To God

be the glory

for the things He hath done.

" In quietness and trust is your strength. "

Isaiah 30:15

DEVELOPMENT OF A BIOMECHANICAL MODEL OF THE INTERFACE BETWEEN THE RESIDUAL LIMB AND PROSTHESIS FOR TRANS-FEMORAL AMPUTEES

By

Lee Vee Sin Peter, BEng.

This thesis is presented for the degree of Doctor of Philosophy at the Bioengineering Unit, University of Strathclyde.

August 1996
Glasgow

ABSTRACT

Prosthetic socket fitting is achieved by the prosthetist applying artisan techniques which are skill dependent and of subjective nature. This study investigates the use of finite element (FE) modelling techniques to predict the biomechanical behaviour at the residual limb / socket interface for the purpose of obtaining a quantitative evaluation of socket fit.

Three dimensional FE models of the residual limb of trans-femoral amputees were generated based on geometrical data obtained using a mechanical digitizer and magnetic resonance (MR) imaging techniques. The inter-segmental loadings at the amputee's hip during standing and walking were applied to the FE models. These were measured with the aid of force platforms and infrared cameras. The material characteristics introduced to the FE models were obtained by testing the residual limb's soft tissue with a computer controlled mechanical indentor. The FE models were validated by comparing predicted and measured pressures at the interface between the residual limb and the socket. The majority of the FE prediction erred within 70% of the measured values.

Detailed internal geometry of two trans-femoral amputees' residual limb in its natural shape and wearing quadrilateral and ischial containment type sockets was studied using MR imaging techniques. At the ischial level, the maximum difference in cross sectional area between the muscles of the sound limb and the residual limb was approximately 62%. The difference in muscles' size can be attributed to muscle atrophy in the residual limb or an increase in the muscle bulk in the sound limb. At similar level, the cross sectional area of the rectus femoris in the residual limb was reduced by as much as 68% from its natural shape when wearing the quadrilateral socket.

Based on the acquired MR images, a two dimensional FE model of a transverse section 30 mm below the ischium was modelled. The model incorporated the interface characteristics between the muscles and intermuscular tissues. The maximum stress was recorded inside the residual limb near muscles / intermuscular tissue interface and at muscles / bone interface.

The FE models generated have shown the potential of predicting stresses and deformation at the residual limb.

ACKNOWLEDGEMENT

I would like to first thank Professor J. P. Paul for giving me the opportunity to carry out the work presented in this thesis, and for his support and advice throughout this study and especially during the writing up of this thesis.

My appreciation is also to Professor J.C. Barbenel the head of the Bioengineering Unit for his continuous encouragement during the period of this study.

My sincere thanks to my supervisor, Mr. S.E. Solomonidis for his invaluable advice, support and criticism in this work. I am also extremely grateful for the encouragement and understanding given to me throughout this project.

My sincere thanks also to the prosthetist, Mr. W.D. Spence for his help, support and advice throughout this work.

I would like to thank Dr. J. Shaw-Dunn, Anatomy Department, University of Glasgow, for his help and advice.

I would like to thank Dr. D Hadley and Dr. B Condon, Southern General Hospital, Institute of Neurological Sciences, for their help and advice, and the use of imaging equipment.

I would like to thank Mr. P. Gross and Mr. S. Griffins for their contribution to the work presented in chapter 10.

I would like to thank all the staff and technicians of the Bioengineering Unit, and in particularly Mr. D Robb, Mr. I. Tullis and Mr. S Murray for their help and advice.

I would like to thank all the subjects who participated in this study.

I would like to acknowledge the financial support from the Overseas Research Student Award and the University of Strathclyde studentship during the period of this study.

I am deeply indebted to my wife Sharon for her understanding, perseverance and encouragement, and also to my son Luke for the joy that keeps me going.

TABLE OF CONTENTS

CHAPTER FIVE : KINETICS AND KINEMATICS

CHAPTER SEVEN : FINITE ELEMENT MODELLING : PART 1

CHAPTER NINE : MRI OF TRANS-FEMORAL RESIDUAL LIMB

CHAPTER ELEVEN : SUMMARY AND FINAL CONCLUSION

CHAPTER ONE
INTRODUCTION

1.1 AIM

1.2 GOOD FIT AND PROSTHETIC SOCKET

1.3 COMPUTER AIDED SOCKET DESIGN AND MANUFACTURE

1.4 FINITE ELEMENT (FE) ANALYSIS

1.5 OBJECTIVES OF THE PRESENT STUDY

1.6 STRUCTURE OF THE PROJECT

1.7 LIMITATIONS

1.8 STRUCTURE OF THE THESIS

1.1 AIM

The project is directed towards the generation of a finite element (FE) model of the trans-femoral amputee's residual limb which is capable of predicting the pressure distribution at the patient / prosthesis interface. The benefit in having this knowledge would be the ability to predict quality of socket fit prior to manufacture. This would allow a reduction of fitting errors and hence improved delivery of service to the physically disabled population.

Currently, prosthetic socket fitting is achieved by the prosthetist applying purely artisan techniques. At the end of his efforts, he confronts the patient with a receptacle into which the amputee must place his residual limb, bear weight and control the prosthesis. If the prosthetist's labours fail disastrously, obvious pain is felt by the patient and the socket is rejected and the process begins again. If these labours are fruitful by being average, above average or magnificent, perhaps the amputee can tell but the prosthetist cannot, neither can he tell in advance. The advantages of producing a truly first class socket are meaningful and worth pursuing.

1.2 GOOD FIT AND PROSTHETIC SOCKET

In the field of lower limb prosthetics the concept of a 'good fit' is always open to much discussion. A good fit is highly dependent on the skill of the prosthetist, his knowledge and experience, he must create a socket that will encourage muscle usage, relieve pressure at pressure intolerant areas, distribute pressure around the residual limb to tolerant areas and maintain suspension of the prosthesis throughout the gait cycle. All of these are achieved through geometrical changes of the socket shape. Many researchers (Appoldt and Bennett 1967, Rae and Cockrell 1971, Pearson et al 1973, Van Pijkeren et al 1980) have related the geometrical modification to interface pressure generated between the residual limb and socket and have developed techniques to measure the pressure. Such advances have opened an avenue of quantitative evaluation of prosthetic socket fit rather than a subjective one.

The socket is of major importance since it forms the interface between man and machine. Currently, there are mainly two types of trans-femoral prosthetic

1.1 AIM

The project is directed towards the generation of a finite element (FE) model of the trans-femoral amputee's residual limb which is capable of predicting the pressure distribution at the patient / prosthesis interface. The benefit in having this knowledge would be the ability to predict quality of socket fit prior to manufacture. This would allow a reduction of fitting errors and hence improved delivery of service to the physically disabled population.

Currently, prosthetic socket fitting is achieved by the prosthetist applying purely artisan techniques. At the end of his efforts, he confronts the patient with a receptacle into which the amputee must place his residual limb, bear weight and control the prosthesis. If the prosthetist's labours fail disastrously, obvious pain is felt by the patient and the socket is rejected and the process begins again. If these labours are fruitful by being average, above average or magnificent, perhaps the amputee can tell but the prosthetist cannot, neither can he tell in advance. The advantages of producing a truly first class socket are meaningful and worth pursuing.

1.2 GOOD FIT AND PROSTHETIC SOCKET

In the field of lower limb prosthetics the concept of a 'good fit' is always open to much discussion. A good fit is highly dependent on the skill of the prosthetist, his knowledge and experience, he must create a socket that will encourage muscle usage, relieve pressure at pressure intolerant areas, distribute pressure around the residual limb to tolerant areas and maintain suspension of the prosthesis throughout the gait cycle. All of these are achieved through geometrical changes of the socket shape. Many researchers (Appoldt and Bennett 1967, Rae and Cockrell 1971, Pearson et al 1973, Van Pijkeren et al 1980) have related the geometrical modification to interface pressure generated between the residual limb and socket and have developed techniques to measure the pressure. Such advances have opened an avenue of quantitative evaluation of prosthetic socket fit rather than a subjective one.

The socket is of major importance since it forms the interface between man and machine. Currently, there are mainly two types of trans-femoral prosthetic sockets in use, the quadrilateral (quad) socket developed in the 1950's (Radcliffe 1955) and the ischial containment socket developed in the 1980's (Long 1985 and Sabolich 1985). Concerning the IC socket Sabolich (1985) stated that : "The old principles of the quadrilateral design simply do not function, since we are dealing with a completely different design in shape, contour, and biomechanical principles." An evaluation of the accuracy of this statement is still high on the agenda of any discussion on trans-femoral socket fittings. In an attempt to clarify the claims made for IC sockets, an international workshop was held in Miami, Florida in 1987, to discuss socket design issues and it was suggested that clinical and biomechanical studies be undertaken (Schuch, 1988).

1.3 COMPUTER AIDED SOCKET DESIGN AND MANUFACTURE

With the recent advent of high speed computers the introduction of high technology software and hardware to lower limb prostheses seems appropriate. Such technology has taken form as computer aided socket design / computer aided manufacturing (CASD/CAM). The CASD/CAM process involves shape acquisition, shape manipulation and physical realisation of the socket design. The initial shape of a residual limb is first recognised through a digitizer. A CASD software package then enables the residual limb shape to be displayed as computer graphics. Manipulating the residual limb shape by decreasing and adding volumes to the original shape, allows a derived shape of the socket to be produced. This procedure is similar to that of a prosthetist taking a wrap cast then modifying the positive mould to a proper socket shape. However using CASD, all these physical work processes are eradicated. It is sometimes necessary for an amputee to require a few fittings before a suitable prosthetic fit is obtained, therefore using CASD modification this could be done more quickly and theoretically more effectively. Manufacturing of the positive mould that defines the socket shape using the CASD system is accomplished through computer codes directed to a numerically controlled milling machine. Manufacturing by these means are termed CAM.

skeletal structures. Currently, the FE method is widely accepted as the method of choice for stress analysis of bone and bone-prosthesis structures, fracture fixation devices and some soft tissue structures. However, the use of finite element method in the area of bulk soft tissues like that in the amputee's residual limb is relatively new.

1.5 OBJECTIVES OF THE PRESENT STUDY

Prior to the creation of an accurate FE model, the mechanical properties of the tissue, geometrical details of the residual limb and the loading and constraints the amputee undergoes during standing and during gait have to be identified. To validate the FE models created, residual limb / socket interface pressures were measured and compared. In addition, the study also attempts to obtain a better understanding of the biomechanical characteristics at the residual limb / socket interface using interface pressure measurement and magnetic resonance imaging techniques. The ongoing controversy regarding the quadrilateral and the ischial containment sockets also provided a suitable case study for the project.

1.6 STRUCTURE OF THE PROJECT

The first part of the study involves the measurement of the residual limb / socket interface pressures. The work involves measurement of three volunteer trans-femoral amputees wearing the quadrilateral and the ischial containment sockets. The measured pressure provided data in the biomechanical analysis of the two types of sockets. The measured pressures were also essential for comparison with predicted pressures by the FE models and hence validation of the models.

To obtain accurate loading conditions for the creation of a finite element model, the magnitude and direction of loading experienced by the amputees were measured using force platforms and infrared cameras tracking the position of the retro-reflective markers placed on anatomical landmarks of the amputee.

The next stage involves characterising the mechanical response of the residual limb soft tissues which is essential to allow any prediction of stresses and deformations on the residual limb imposed by external forces. There are two main skeletal structures. Currently, the FE method is widely accepted as the method of choice for stress analysis of bone and bone-prosthesis structures, fracture fixation devices and some soft tissue structures. However, the use of finite element method in the area of bulk soft tissues like that in the amputee's residual limb is relatively new.

1.5 OBJECTIVES OF THE PRESENT STUDY

Prior to the creation of an accurate FE model, the mechanical properties of the tissue, geometrical details of the residual limb and the loading and constraints the amputee undergoes during standing and during gait have to be identified. To validate the FE models created, residual limb / socket interface pressures were measured and compared. In addition, the study also attempts to obtain a better understanding of the biomechanical characteristics at the residual limb / socket interface using interface pressure measurement and magnetic resonance imaging techniques. The ongoing controversy regarding the quadrilateral and the ischial containment sockets also provided a suitable case study for the project.

1.1.6 STRUCTURE OF THE PROJECT

The first part of the study involves the measurement of the residual limb / socket interface pressures. The work involves measurement of three volunteer trans-femoral amputees wearing the quadrilateral and the ischial containment sockets. The measured pressure provided data in the biomechanical analysis of the two types of sockets. The measured pressures were also essential for comparison with predicted pressures by the FE models and hence validation of the models.

To obtain accurate loading conditions for the creation of a finite element model, the magnitude and direction of loading experienced by the amputees were measured using force platforms and infrared cameras tracking the position of the retro-reflective markers placed on anatomical landmarks of the amputee.

The next stage involves characterising the mechanical response of the residual limb soft tissues which is essential to allow any prediction of stresses and deformations on the residual limb imposed by external forces. There are two main

1.7 LIMITATIONS

Finite element modelling of bulk soft tissue is still in the early stages. In order to create an accurate model of the residual limb, the scope is extremely wide. As outlined earlier, the work involves interface pressure measurement, kinetics and kinematics studies, soft tissue characterisation, geometrical studies including imaging and scaling techniques. Each subject matter is potentially a huge area of study.

The limitations of the study can be briefly discussed according to the input parameters for FE analysis. The geometry of the three dimensional models is limited to uniform structures without differentiation between the different types of soft tissue. This is because with the present state of the art, a model which includes detailed structures of the soft tissues in three dimensions would be impractical with severe numerical problems. This is further supported in the present study with the problems encountered in the 2-D models with detailed musculature.

The loadings applied to the model were based on kinetic and kinematics studies. It becomes clear that this is insufficient to describe the complete state of loading in the residual limb. The lack of geometrical musculature details in the FE model also poses a problem in specifying accurate loading conditions.

The largely unknown material properties of soft tissue presents one of the major problems to the residual limb model. In this study, via mechanical testing and FE analysis of porcine tissues, different material assumptions were studied. The study was able to confirm the accuracy of the different material assumptions applied in the FE method, however, it also highlighted the limited capabilities of the FE method in modelling the complex nature of the soft tissue response to loading.

1.8 STRUCTURE OF THE THESIS

The thesis consists of eleven chapters. Chapter two provides an introductory review on amputation surgery and lower limb prosthetics. Chapter three is a detailed review on the present CASD/CAM technology used in the field of lower limb prosthetics. A review on the use of finite element analysis in the area of biomechanics is also presented in the same chapter. Chapter four discusses residual limb / socket interface pressure measurement. Included in this chapter is a review on interface pressure measurement. This is followed by a description of the techniques used in this study, the results of the amputee subjects measurements and a discussion on the findings. Chapter five describes the kinetics and kinematics studies where the loadings at the anatomical hip joint were determined. The chapter begins with a brief review of the methods of measuring kinetic and kinematics data. This is followed by the experimental and theoretical aspects of the study, and finally a presentation and discussion of the results. Chapter six discusses the mechanical characterisation of biological soft tissue. The chapter begins with a review of soft tissue mechanics. The chapter further describes the *in vitro* studies performed for porcine tissues, which included both experimental and theoretical studies. Subsequently, the chapter details the *in vivo* characterisation of the amputee's residual limb soft tissue.

Chapter seven describes the generation of 3-D FE models of the residual limbs. A comparison between the FE predicted results and the measured interface pressures can be found in this chapter. Chapter eight describes the theoretical and experimental aspects of scaling the human femur. In chapter nine, the procedures and methods of imaging two trans-femoral amputees using magnetic resonance imaging techniques are discussed. The chapter details the observations made based on the morphology and geometry of the internal musculature of the residual limb. Chapter ten describes the creation of a 2-D model of the transverse section of the residual limb with internal musculature detail based on MRI images. The chapter reports the stresses in the residual limb due to the effects of muscle movement and slippage, material non - homogeneity, and loading and boundary conditions. Finally, the conclusion of the study is reported in chapter 11.

CHAPTER TWO
LOWER LIMB PROSTHETICS

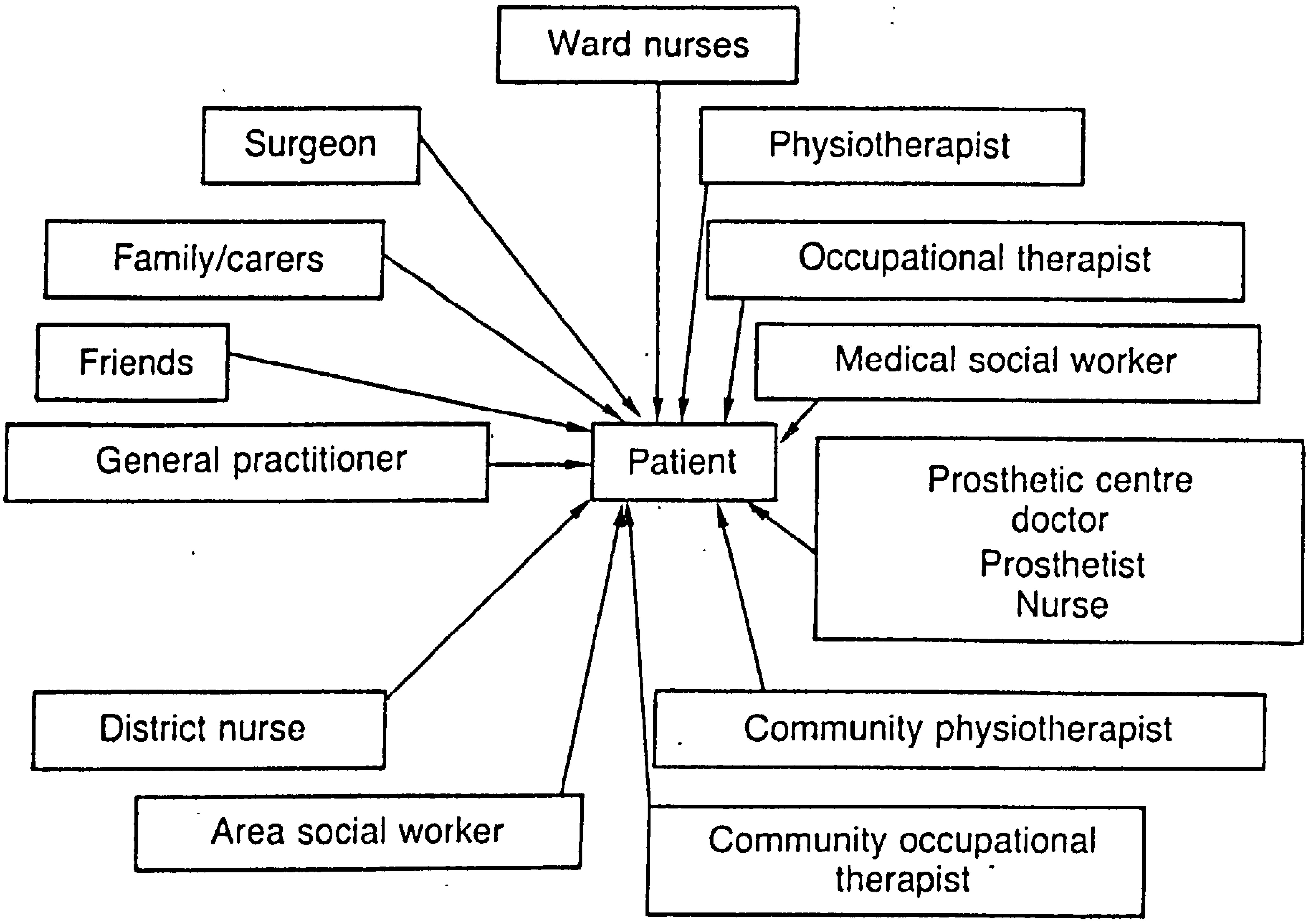

Fig. 2.1.1 The multi - disciplinary team. (Ham and Cotton, 1991)

2.1 INTRODUCTION

The field of lower limb prosthetics practice has in recent years advanced tremendously. New materials, state of the art computer design, manufacturing and control technology have been introduced to artificial limbs. But how much these technologies improve the life of an amputee still depends very much on the patient and the whole rehabilitation process, pre and post operatively. A classic example would be that of a patient prescribed with a first-rate artificial limb who prefers a wheelchair because he/she is simply not educated or convinced of the mobility offered by the limb.

The process for amputee care has always been recognised as a team effort. The amputee team (Fig. 2.1.1) ranges from surgeons to family and assures and enables the patient to return to more or less normal activity with a smooth transition. The multi-disciplinary team approach is widely adopted in the USA. (Burgess and Alexander 1973). In Scotland at Dundee Limb Fitting Centre, the multi-disciplinary team has been functioning since 1965 with good success (Murdoch et al 1988). Ham et al (1987) and Murdoch (1977) have evaluated this team approach and have highlighted many advantages such as an increase in the number of patients prescribed with a prosthesis and rehabilitated, reduced hospital in-patient stay and reduced return for physiotheraphy treatment. It becomes clear that responsibility for the outcome of the patient does not lie with a single professional in the team. Instead each individual responsible should perform to the best of his/her knowledge for optimum results.

It is the aim of this chapter to present a general review of rehabilitation in the field of lower limb prosthetics. Most of the subjects discussed will have their emphasis on the trans-femoral amputee, since the project's primary concern is with this amputee group. The chapter begins with a brief review of the history of amputation, types of lower limb amputation, statistics and techniques of amputation. This will be followed by the introduction of the artificial limb and its biomechanical analysis.

2.2 AMPUTATION

To amputate simply means to cut off. Amputation has been the method

Fig. 2.2.1 Ancient figurine and pottery depicting amputation probably for punitive or ritualistic reasons. (Friedmann, 1972)

adopted for many years now to remove diseased or injured body parts. But the first case of surgical amputation was unlikely to have been a life-saving technique. It was probably ritualistic or punitive. In primitive society, mutilation for ritualistic reasons is common. Friedmann (1972) indicates that ritual amputations were performed to ward off evil spirits and to produce potions and amulets to prevent evil. Parts of the body were burned to ashes and mixed with other substances to make charms or even to be eaten. Evidence of such practices has been found in tribes in Africa, Madagascar, Indonesia, Australia, India and Oceania.

Amputation of the finger or hand was a common method of punishment in primitive cultures and even today. Well (1972) described negative imprints of the hand found in caves in France and Spain showing mutilation by loss of some or all of the fingers. These imprints date as far back as 5000 BC. It was also discovered that most of these imprints show signs of mutilation of the thumb. Mutilation of this sort would render the hand ineffective and thus may have been a punishment for persistent theft. Friedmann (1972) also discussed the strict ancient Peruvian laws 'Do not lie, Do not steal, Do not be lazy.' Discipline had been carried out by amputation of lips and noses, hand and leg for lying, stealing and laziness respectively Fig. 2.2.1. This method of punishment also served as a visual deterrent for would be criminals. In Britain, during the dark ages, offenders were branded on the forehead, amputated of their limbs or tongues to live as examples of punishment for crime. In the Arabic Middle east, Haj (1970) described amputation as a means to exclude individuals from religious society. The community today still practices amputation as a form of punishment. The Times reported a case of five thieves accused of stealing jewellery and electrical goods had their arms amputated at the elbow by the Saudi Arabian authorities in Jeddah (The Times August 6 1994).

2.2.1 Historical development of amputation surgery

Hippocrates (460-380 BC) was cited as the first Greek physician to document the first amputation for vascular gangrene. Celsus (1st century A.D) a translator of Greek medical information recommended that amputation be performed as a

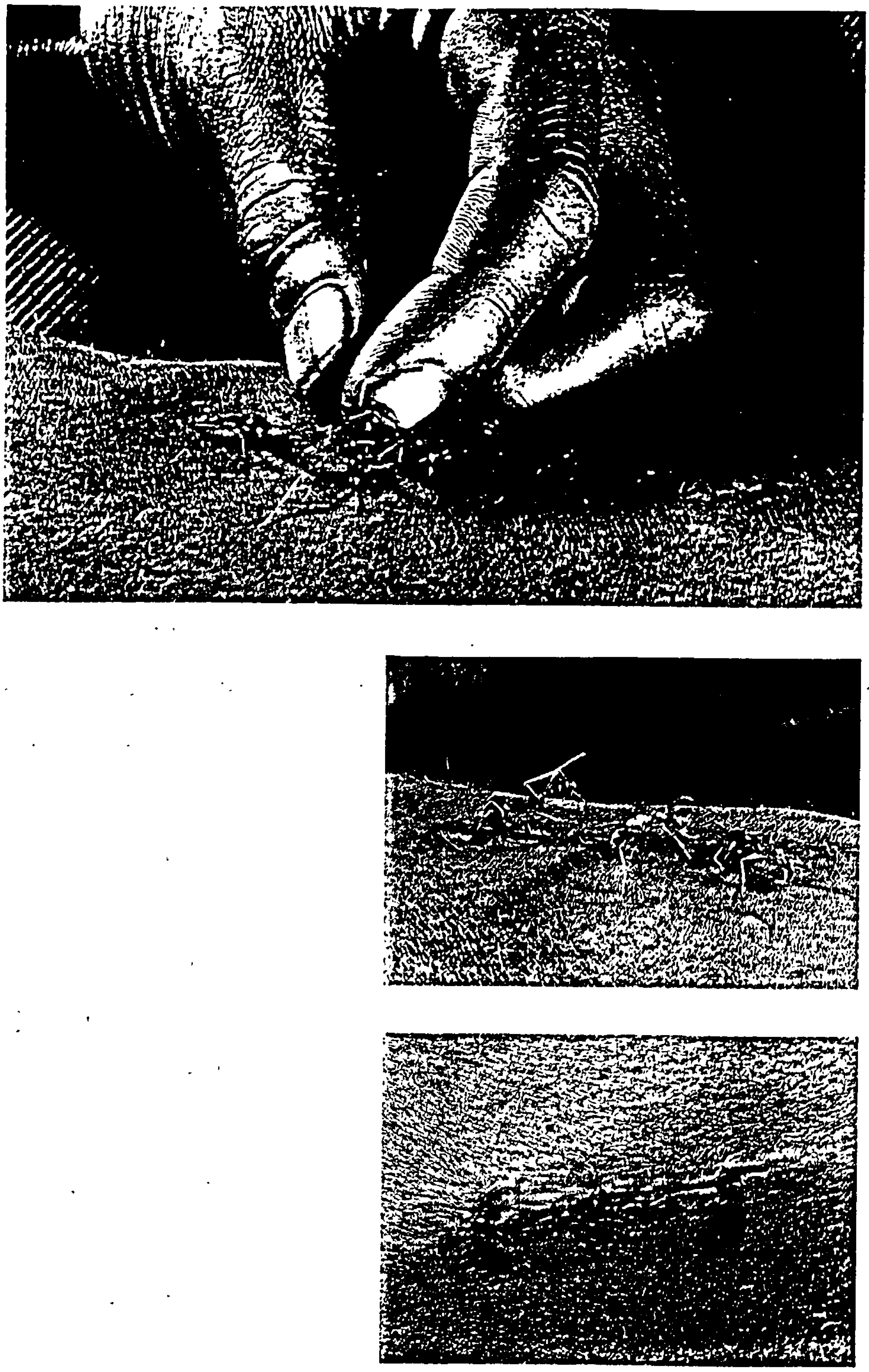

Fig. 2.2.1.1 In Central Africa, soldier ants of the genus *Dorylus*, instinctively bite down and lock their jaws, sealing a wound. The thoraxes and tails of the ants are cut off leaving the jaws in places until the wound heals. (Smolan et al, 1990)

life-saving technique. He mentioned that if medication failed to cure gangrene, amputation becomes a necessity. He also described the use of a flap technique in amputation and ligature to control haemorrhage. During the fifteenth century, amputation became more common due to leprosy and the use of firearms in wars. This increase led to amputation being performed by barbers later differentiated from normal barbers by the name Barber Surgeon (Rang and Thomson 1981). Ambrose Pare (1510-1590) a French Army barber surgeon described many procedures in amputation which still apply in the present day and also emphasized amputation techniques which facilitate prosthetic usage. He reintroduced the use of ligatures for large vessels which was a method which originated from Hippocrates but was gradually lost during the Dark Ages. He was also the first to described the procedure for elbow disarticulation.

The first trans-femoral amputation was reported by William Clowes in 1679. Napoleon's surgeon Dominique Jean Larrey in 1803 described the first knee disarticulation, he was also one of the first to amputate at the hip joint. Jacques Lisfranc of France in 1815 described the disarticulation of the foot at the tarsometatarsal articulation and in 1843, Sir James Syme of Edinburgh reported the Syme amputation at the ankle joint.

In the early amputations, speed was required to reduce complications caused by haemorrhage and pain. It was only after the introduction of the tourniquet by Hans von Gerssdorff of Strassburg in 1517 that surgery could extend for a longer time. Anaesthetics were rarely used in these operations until 1840s when Crawford Williamson Long of Georgia and William Morton, a dentist from Massachusetts discovered the use of ether for surgical anesthesia. In France 1847, Perre Jean Marie Flourens introduced the used of chloroform. Before that alcohol, opium and cocaine were used.

Ligatures, boiling oil and hot iron cautery to prevent haemorrhage were thought to be used by the South American Indians in 1500 B.C and the ancient Peruvians (Friedmann 1972). These methods prevailed during the Dark Ages until the reintroduction of the tourniquet. Early wound closure methods were discovered by

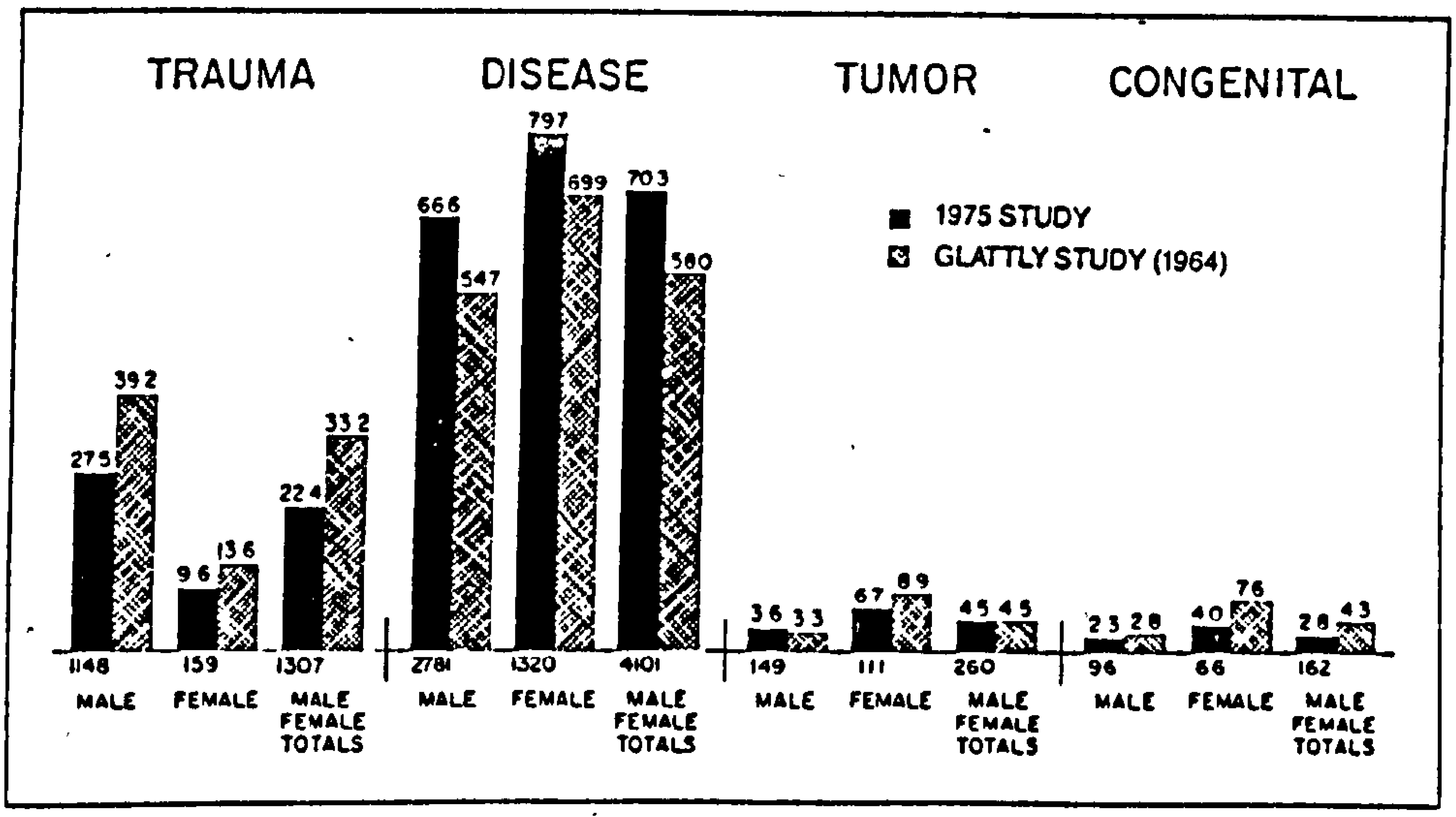

Fig. 2.2.2.1 Distribution of amputees by cause and sex.
(Kay and Newman, 1975)

different civilisations. The Peruvians used cotton for skin suture. Human hairs were used by the South American Indians and in Central Africa, soldier ants that instinctively bite and lock their jaws on the wound, thus sealing the cut had been observed to be useful. Fig. 2.2.1.1

Another remarkable advance in surgery was the introduction of antisepsis by Lord Joseph Lister from Glasgow in 1867. Death caused by infection was reduced to a minimum.

2.2.2 The amputee population

ISPO (1975) reported an estimated of 1000 per million of population lower limb amputees and 200 per million upper limb amputees around the world. The survey was conducted in 33 countries approximating half the world's population.

The number of amputees has increased. Ham et al (1989) reported the number of patients referred to centres for prosthetic prescriptions in the UK in 1961 as 3500. The figure per year had increased to 4559 by 1970 and 5461 by 1985. Dormandy and Thomas (1988) estimated the true amputee population in the UK to be about 8-11000 per year, relying on the assumption that about half of the amputees in the UK are unsuitable for prosthetic limbs, and are statistically not accounted for by the prosthetic services. Presently, there are more than 70000 amputees in England and Wales.

In the United States, the number of new amputees in 1965 was 33000, increasing to 43000 in 1971. The total number of amputees recorded through prosthetic services was 311000 in 1971 and in 1980, had increased to 500000 (Banerjee 1982). A national survey based on household interviews in the 1979 gave a figure of 1849000 non-institutionalised civilians with absence of extremities or parts of extremities, which excludes cases of absence of the tips of fingers and toes (Sanders 1986).

Ebskov (1988) presented a survey of Danish lower extremity amputations from the trans-metatarsal level proximally during the period of 1978-1983 and concluded a significantly increasing trend. In Sweden, the increase in amputation was 17 per 100000 in 1962 to 47 per 100000 population in 1977 (Renstrom 1981) .

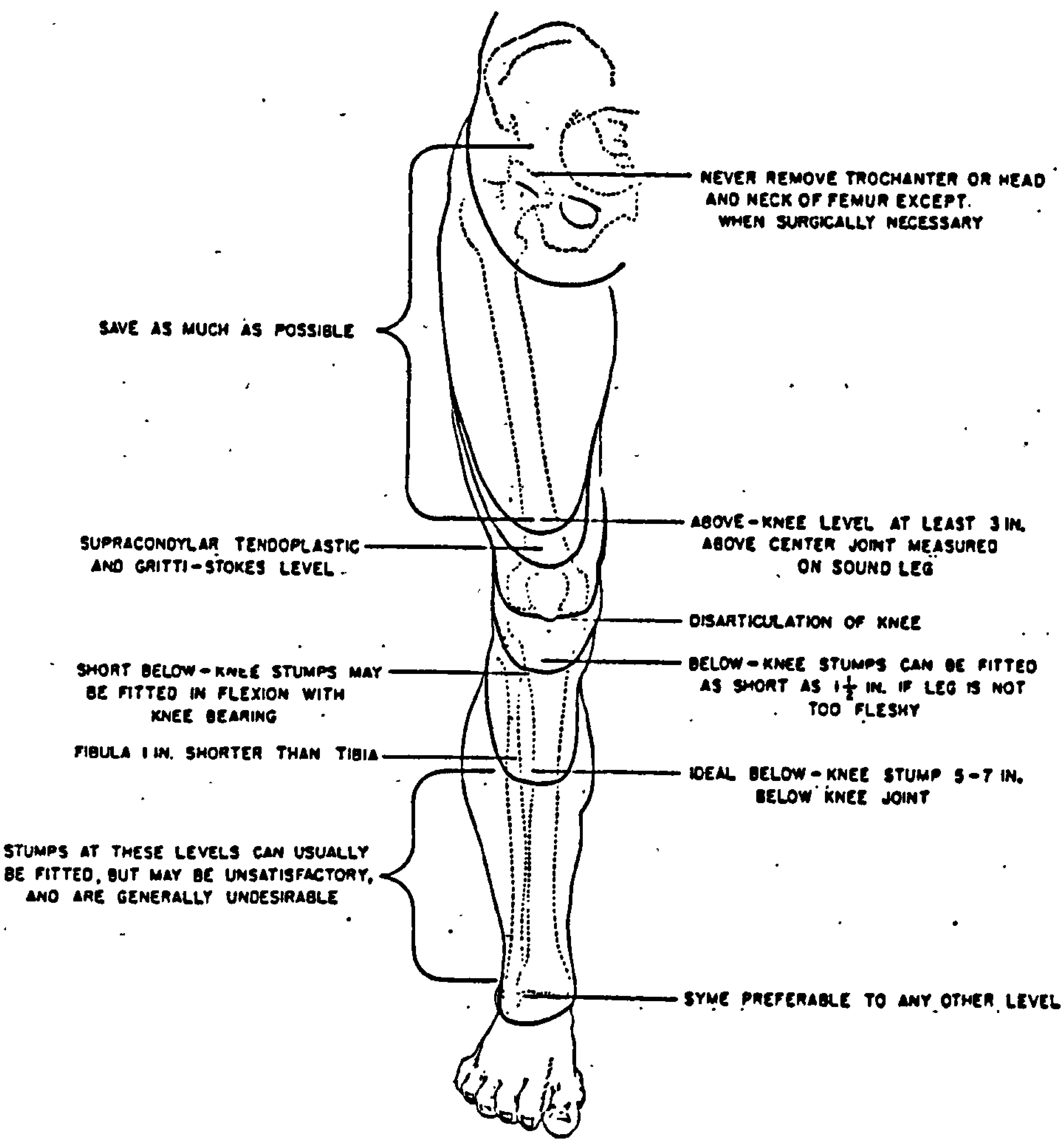

Fig. 2.2.3.1 Level of lower limb amputation.
(Alldredge and Murphy, 1954)

The main causes of amputation are congenital, tumour, trauma and disease. The number of amputations due to each reason varies from place to place. The cause of amputation in developed countries is usually disease. Statistical studies in the United States conducted by Glattly (1963, 1964) in Oct. 1962 to Jan. 1963 with more than 12000 new amputees reported 58% had amputation due to disease. A follow up study by Kay and Newman (1974,1975) in 1973/74 with a further 6000 new amputees showed 70.3% to be of disease origin (Fig. 2.2.2.1). Murdoch (1977) stated 86% of the amputations in Scotland are due to vascular disease and similarly, Furst and Humphrey (1984) reported 85% of the annual 5000 amputations in England and Wales to be of vascular disease origin.

Trauma has been the main reason for amputation in developing and third world countries. Narang and Jape (1982) surveying 14400 cases in India, reported 67% had amputation due to trauma; disease only accounts for 26.3%. Pe (1988) studied the situation in Burma where of 2228 civilian amputees, 55.25% were associated with trauma and 32.45% with disease.

The average age of amputees in developed countries is higher due to the higher occurrence of disease oriented amputation. This age band usually varied between 60 and 70 years. The ratio of male to female amputees is still predominantly higher in trauma related cases but approaches equal incidence in disease related cases.

Detailed statistical studies can be obtained from Glattly (1963,1964), Kay and Newman (1974,1975) and Department of Health and Social Security (DHSS) Amputation Statistics (1971-1989).

2.2.3 Level of amputation

The level of amputation is largely determined by the need to remove dead or diseased tissue. Whatever the level of amputation, it will affect prosthetic fittings, later rehabilitation requirements and certainly the quality of life of the patient. Performing a lower limb amputation involves not just a life-saving operation but also an operation to construct a new organ for locomotion (Vitali et al. 1987). In effect, the end of the stump plays a similar role to the foot of a healthy limb. Common

a) Anterior incision

b) Posterior incision.

Fig. 2.2.3.2 Hindquarter amputation. (Taylor, 1952) surgical practice differentiates the level of lower limb amputation as follows, Fig. 2.2.3.1.

a) Hindquarter and Hip disarticulation

b) Trans-femoral / above-knee

c) Gritti-Stokes level

d) Knee disarticulation / through knee

e) Trans-tibial / below knee

f) Syme

g) Digital and partial foot

Hindquarter amputation demands the removal of the entire lower extremity and the corresponding half of the pelvis (Fig. 2.2.3.2). In hip disarticulation surgery also the entire lower extremity is removed by transection through the hip joint, retaining the ischial tuberosity. These proximal amputations are usually needed in cases of severe malignancy or tumour. Occasionally disarticulation of the hip is called for in failed operations at the trans-femoral level. The techniques of Hindquarter and Hip disarticulation are adequately described in Westbury (1967), Taylor and Rodgers (1953), Boyd (1947), Sugarbaker and Ackerman (1945) and King and Steelquist (1943). Fig. 2.2.3.3 shows a diagram detailing briefly the method of Boyd (1947) for hip disarticulation.

The trans-femoral level is commonly the level preferred by surgeons to ensure primary wound healing. The amputation is above the knee, with an ideal stump length of 25-30 cm from the greater trochanter or approximately two thirds of the length of the intact thigh (Ham and Cotton, 1991).Trans-femoral amputation surgery will be discussed in more detail later in the chapter.

In the Gritti-Stokes amputation, the femur is transected just above the condyles and the patella (Fig. 2.2.3.4). The aim is to provide an end-weight bearing stump. The method is however not recommended as end bearing is difficult to achieve with this operation. Complexity arises in establishing an arthrodesis between the patella and the cut end of the femur. The loss of the femoral epiphysis and the length

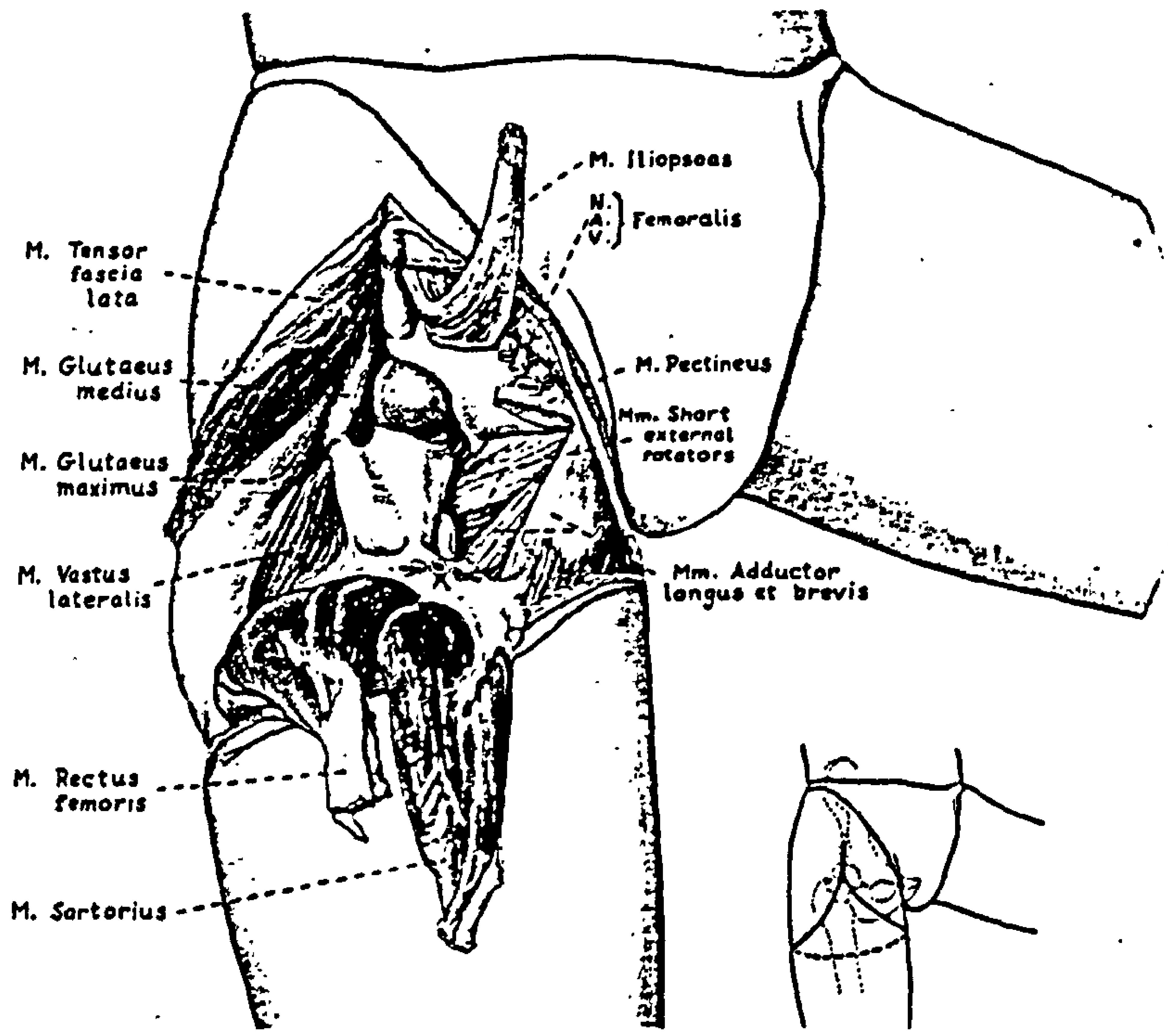

Fig. 2.2.3.3 Boyd method of hip disarticulation. (Boyd, 1947)

of the limb also pose a problem with prosthetic fittings, leaving no space for an artificial knee joint.

The through knee level is much preferred to Gritti-Stokes in achieving end-weight bearing. The operation is relatively bloodless. Burgess's (1977) method of knee disarticulation is briefly described as in Fig. 2.2.3.5. The limb is transected at 15 mm above the condylar ends. The patellar tendon is sewn to the cruciate ligaments and the biceps tendon and medial hamstring are sutured in the intercondylar notch. For surgical closure, the hamstrings are sutured through the femoral notch to the patellar tendon and cruciate ligaments. Major muscle groups in the thigh remain attached and muscle stabilisation is achieved. The operation provides the amputee with a strong residual limb with little muscle atrophy and excellent proprioceptive sensation. Like the Gritti-Stokes amputation, the prosthesis is less cosmetic at the region of the femoral condyles. Removal of the medial, lateral and posterior prominence of the femoral condyle has been suggested to decrease the bulk of the stump providing better fitting of the prosthesis. Development in the polycentric type knee mechanism has also contributed much to the cosmesis and control for this group of amputees.

One of the main aims in trans-tibial amputation is the preservation of the knee joint. The advantages of preservation of the knee joint are highlighted by Castronuova et al (1980). The presence of the knee joint could enable an amputee with average stump length to produce a gait similar to that of a normal subject. A high mobility rate is evident with trans-tibial amputees (Cummings et al 1987). The trans-tibial amputation takes place below the knee approximately 140 mm from the tibial plateau; but more often used as a guide, the lower leg is divided into three equal parts and two thirds removed. A too short or too long stump creates difficulties in fitting prostheses and a knee flexion contracture greater than 15 degrees is unsuitable for a prosthetic device (Ham and Cotton, 1991). The operation techniques are largely divided into two types, amputation for reasons of vascular disease and other reasons like trauma but with normal circulation. The former required the creation of a long posterior and a short anterior flap. This method has been documented as early as 1695 by Pieter

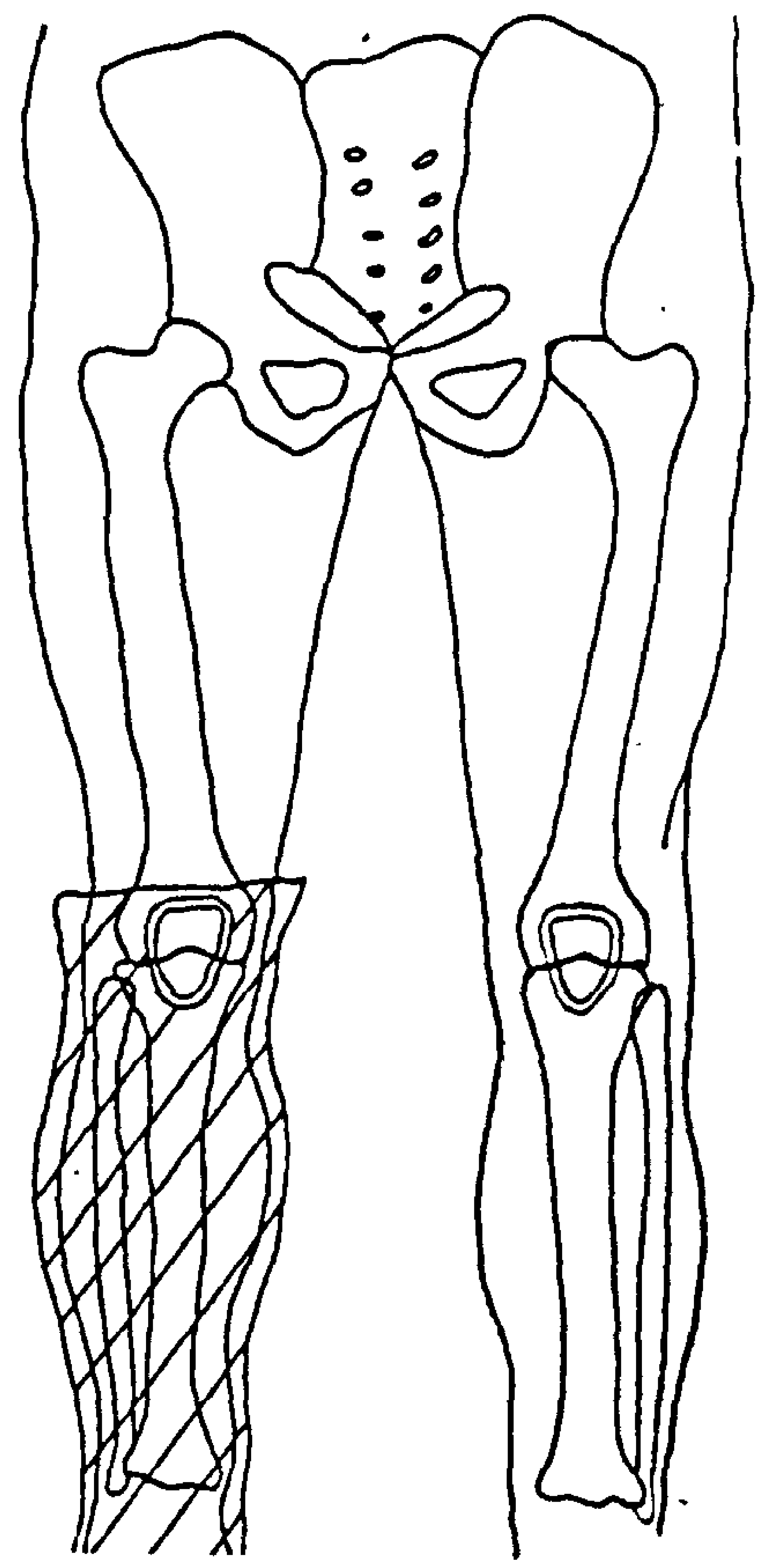

Fig. 2.2.3.4 Level of amputation in Gritti-Stokes amputation.
(Ham and Cotton, 1991)

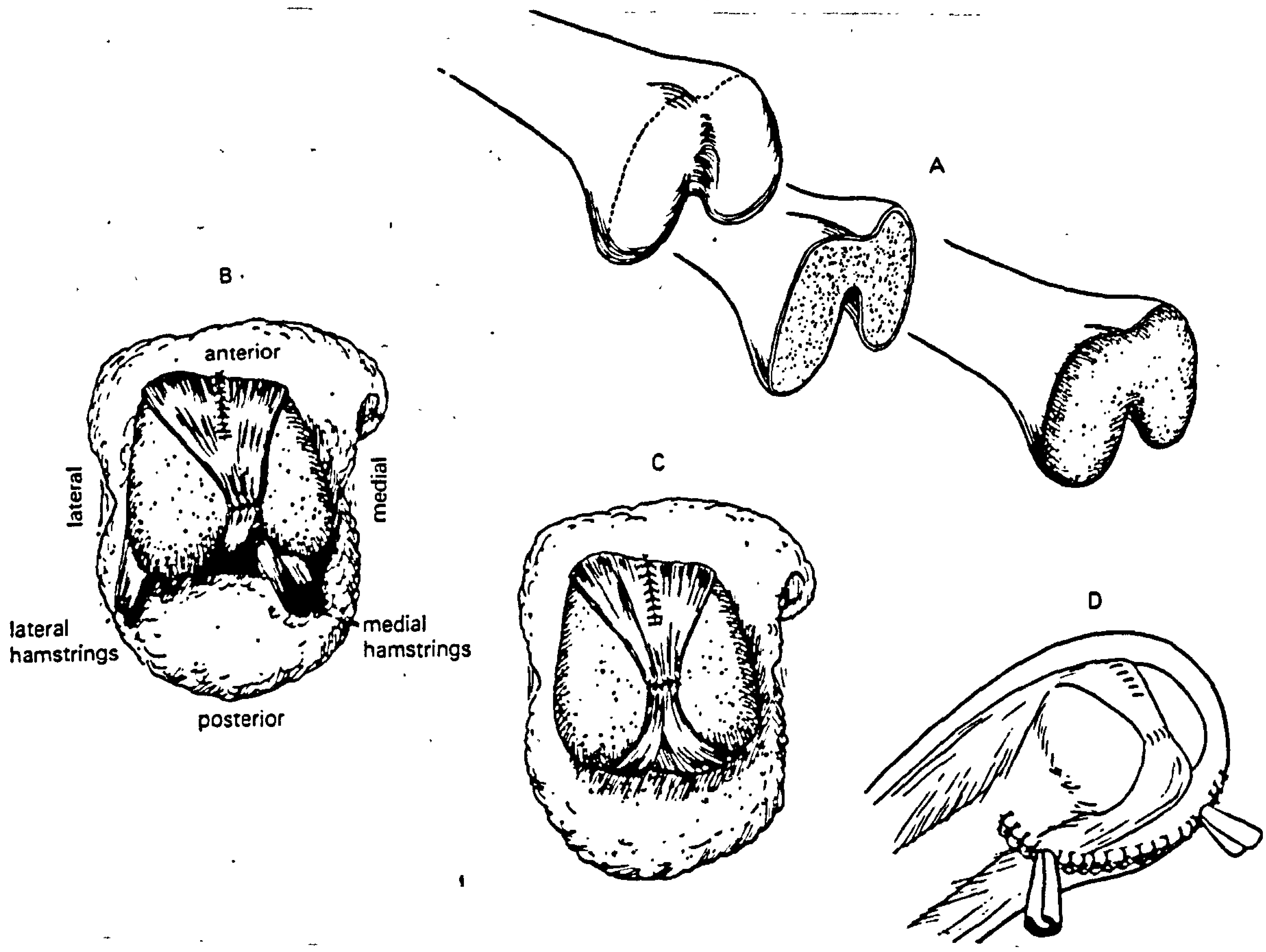

Fig. 2.2.3.5 Burgess method of knee disarticulation. (Burgess, 1977)

Andriaanz Verduyn (Fig. 2.2.3.6), a Dutch surgeon (Gerhardt et al 1982). The method has since been refined and popularised by Burgess (1969) (Fig. 2.2.3.7). The long posterior flap ensures closure without undue tension to the soft tissue. Skin and fascia are highly delicate in a vascular disease case, thus careful handling is needed, maintaining as much blood supply as possible. Amputation for patients with normal unimpaired circulation usually adopts similar surgery but with equal lengths of anterior and posterior flaps. The level of tibial section is usually maintained about an inch lower than the fibular. A long fibula results in excessive pressure from the prosthesis leading to pain. Trans-tibial amputations are well documented by Murdoch (1968), Burgess, Romano and Zettl (1969) and Burgess (1971).

The Syme amputation was named after James Syme of Edinburgh in 1842. The disarticulation is through the ankle joint by an anterior and plantar incision (Fig. 2.2.3.8). The heel flap folds over to the lower end of the tibial for closure. The heel flap, being accustomed to weight bearing, covers the end of the stump. Thus the stump is superior in weight bearing function. Major muscle control of the lower limb is also maintained. Amputation at this level results in a large stump which can lead to difficulties in prosthetic fitting, but more recently cosmetically acceptable Syme prosthesis are available (Sawamura 1988). The Syme amputation is used more often in traumatic cases and on leprosy inflicted patients. Most vascular diseased patients are unsuitable because the diminish blood supply to the distal part of the residual limb would cause difficulties with primary wound healing. There have also been numerous modifications to the amputation method to suit vascular patients, but without much success. An excellent review of the history and technique of Symes amputation is given by Harris (1961).

Digital or partial foot amputations are usually done without any formal flap dissection. Wounds are lightly dressed and left to heal by granulation. The loss of function of the lower limb is minimal. Nowadays prosthetic devices for digital or partial foot with high standards of cosmesis are available (Baumgartner 1988).

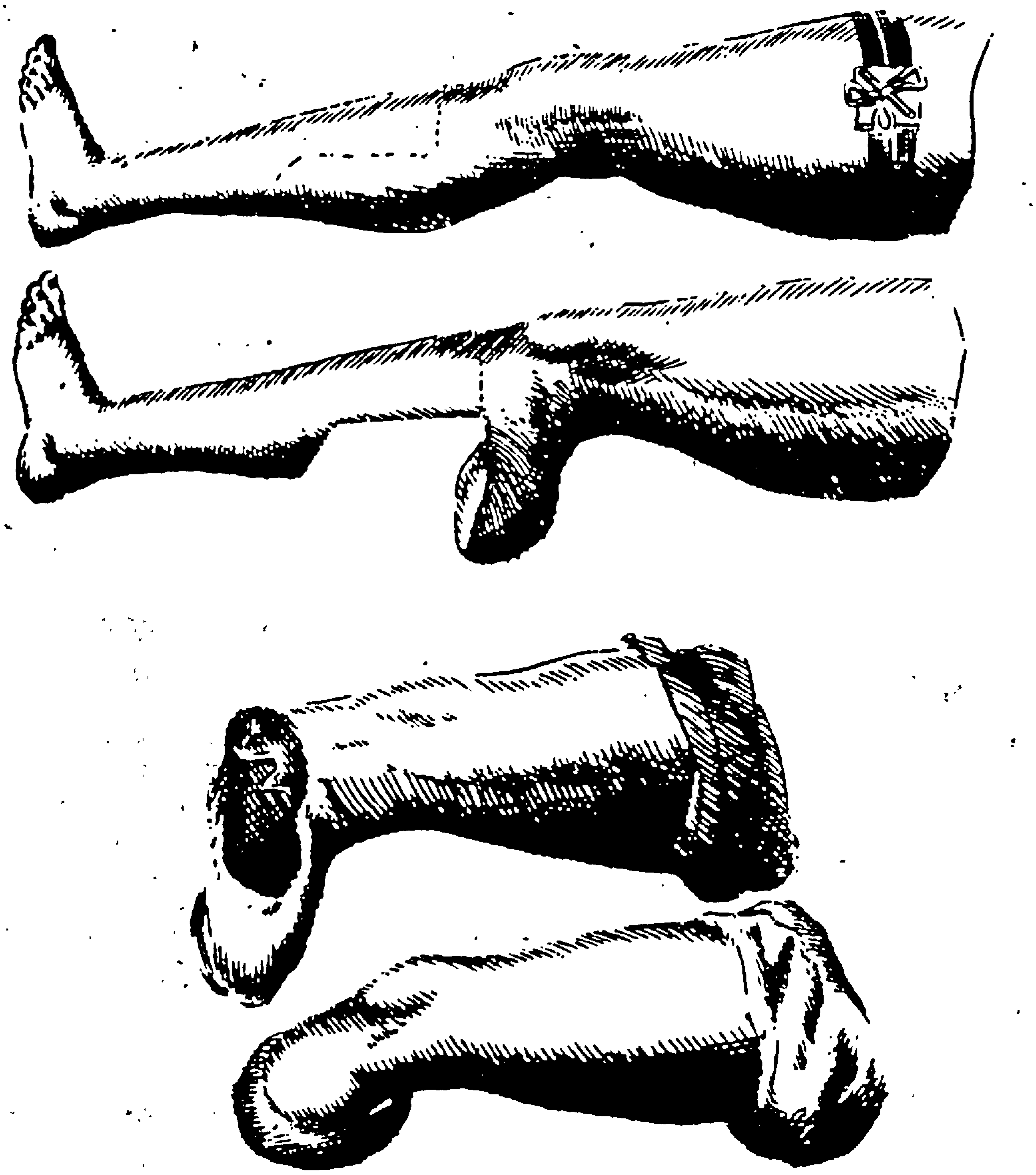

Fig. 2.2.3.6 Trans-tibial amputation using long posterior and short anterior flap method according to Verduyn. (Gerhardt et al, 1982)

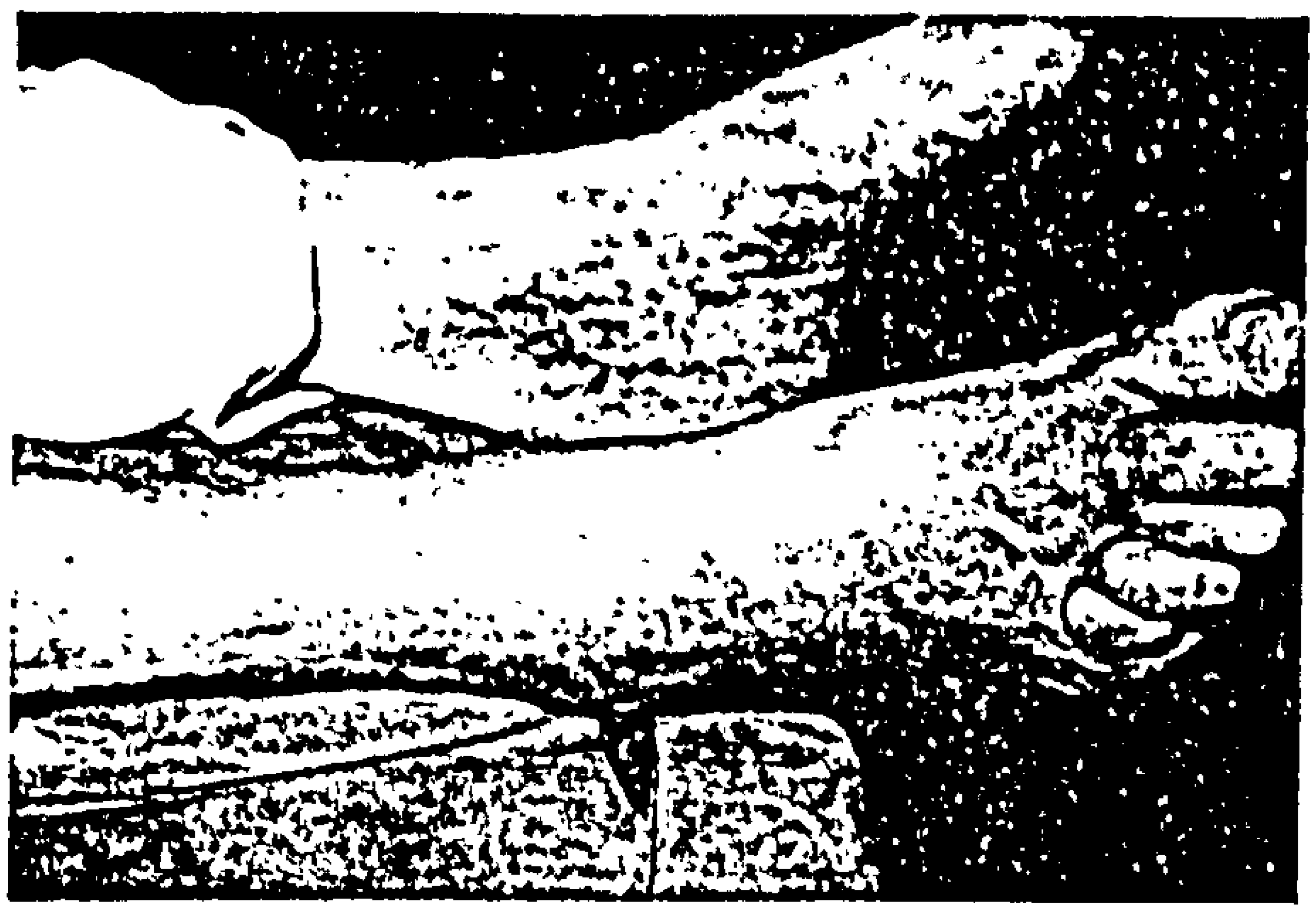

a.) Preoperative condition.

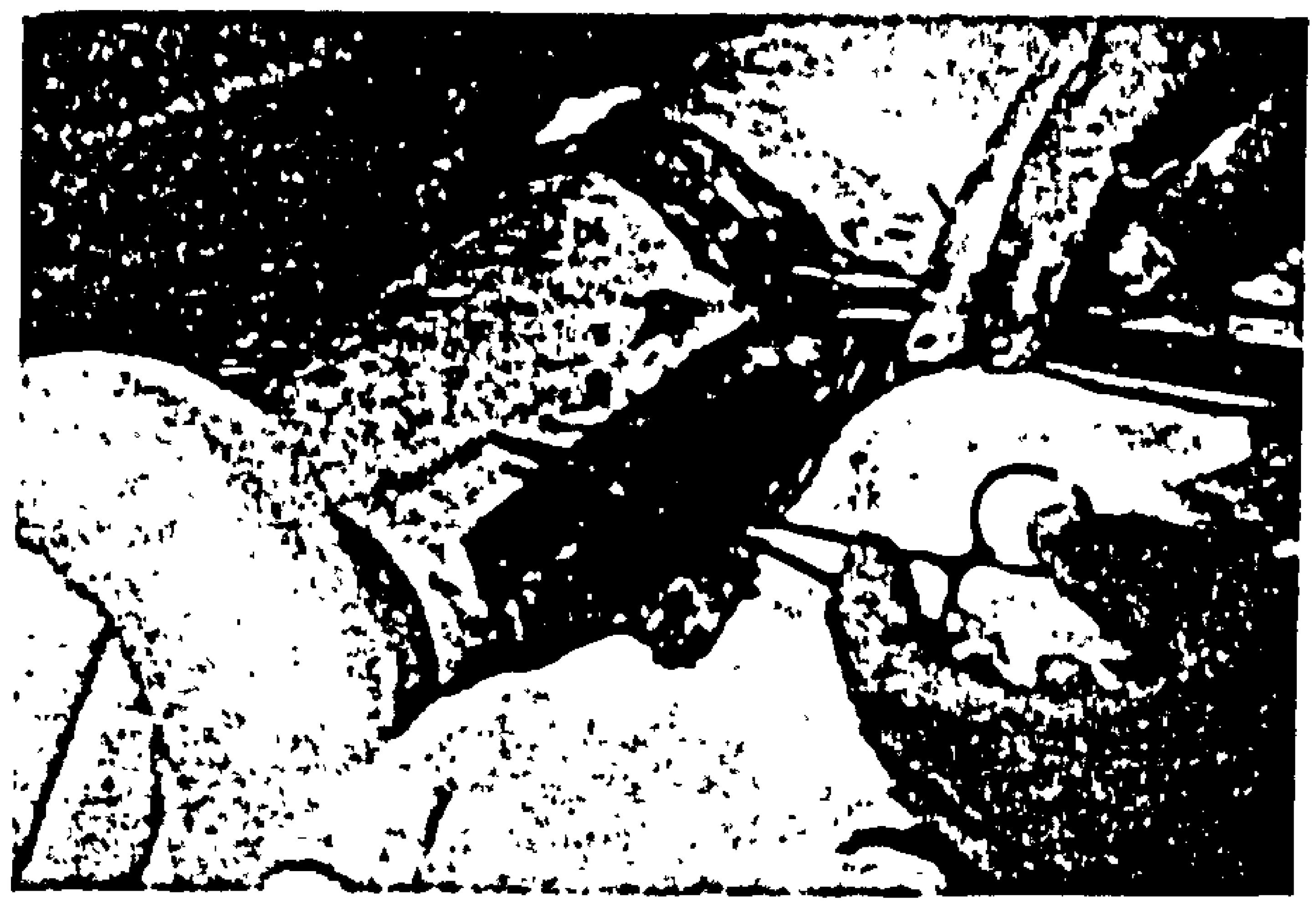

b.) Skin incision with provision for long posterior skin flap.

c.) Tibia and fibula sectioned at level of anterior skin incision.

d.) Tibia carefully rounded.

e.) Muscular flap bevelled.

Fig. 2.2.3.7 Trans-tibial amputation. (Burgess, 1969)

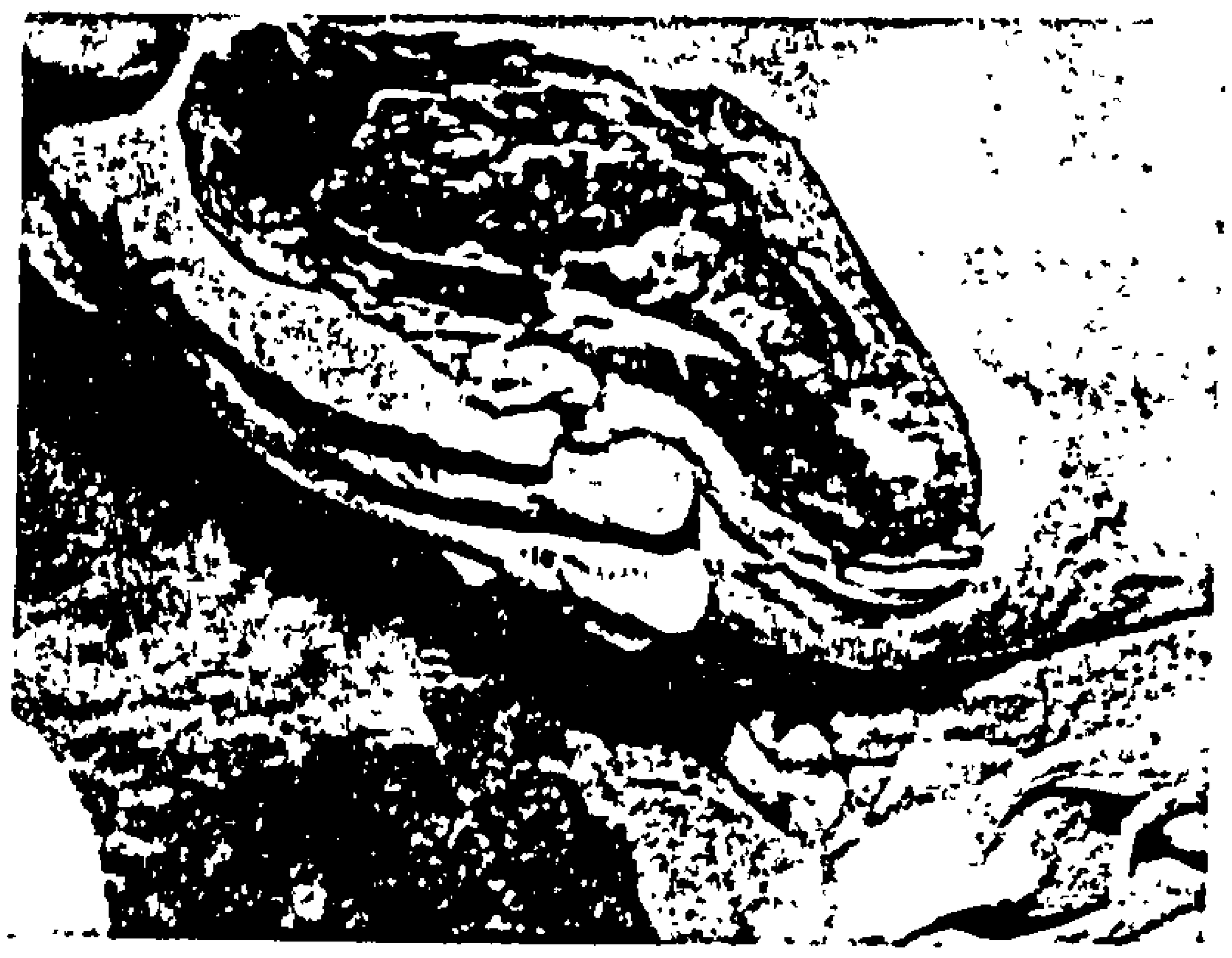

f.) Flap ready to be brought forward.

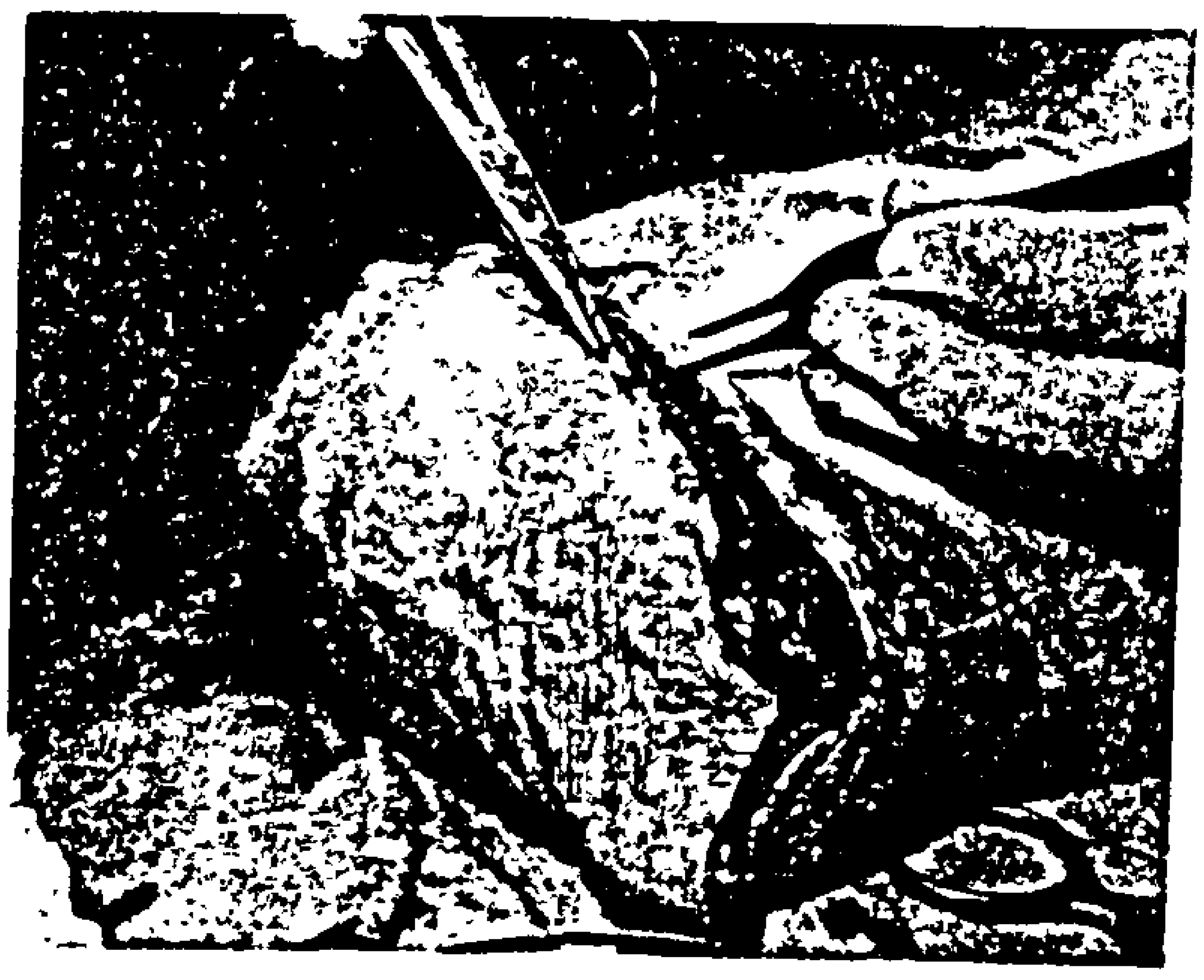

g.) Muscular flap sewn.

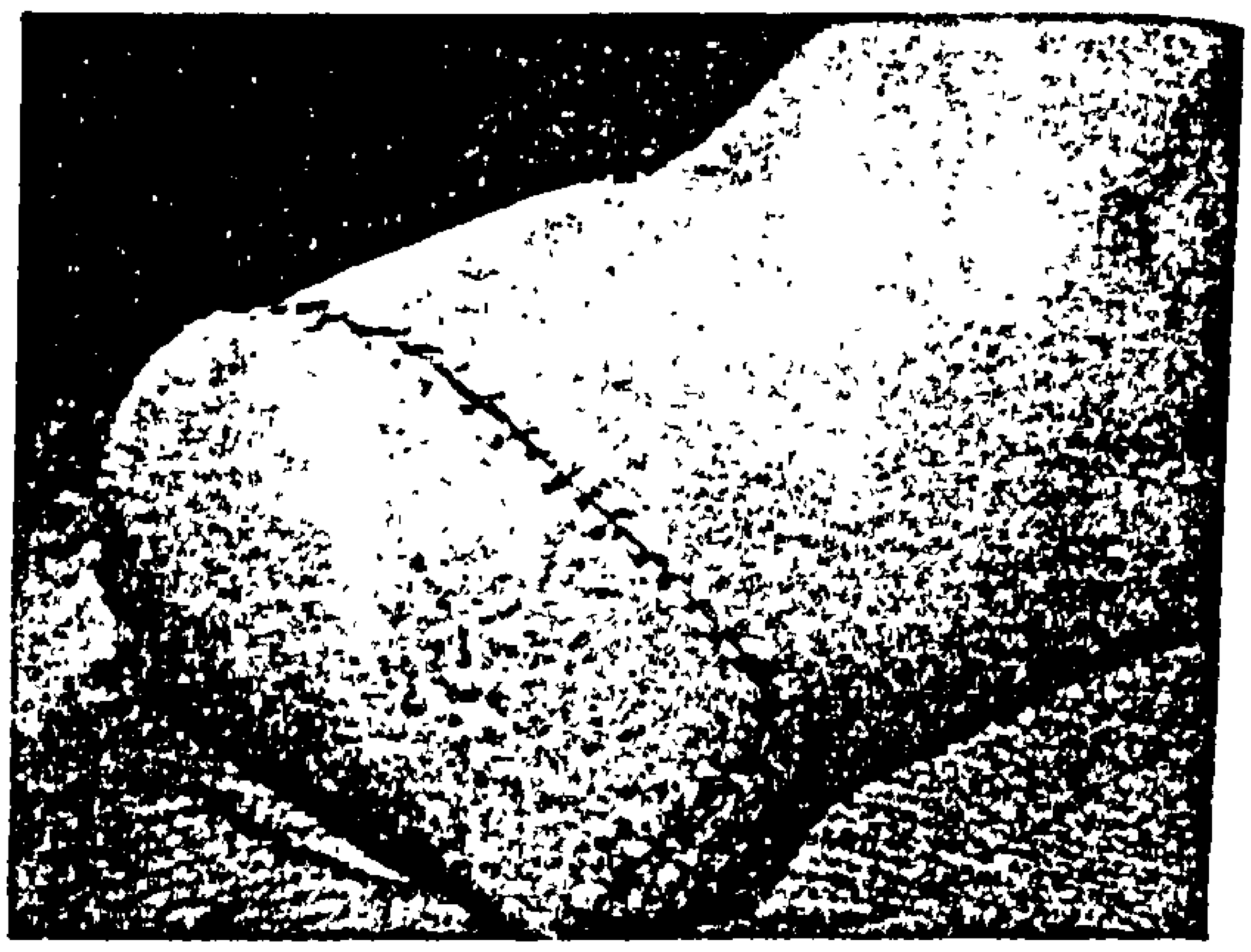

h.) Appearance of residual limb at time of closure.

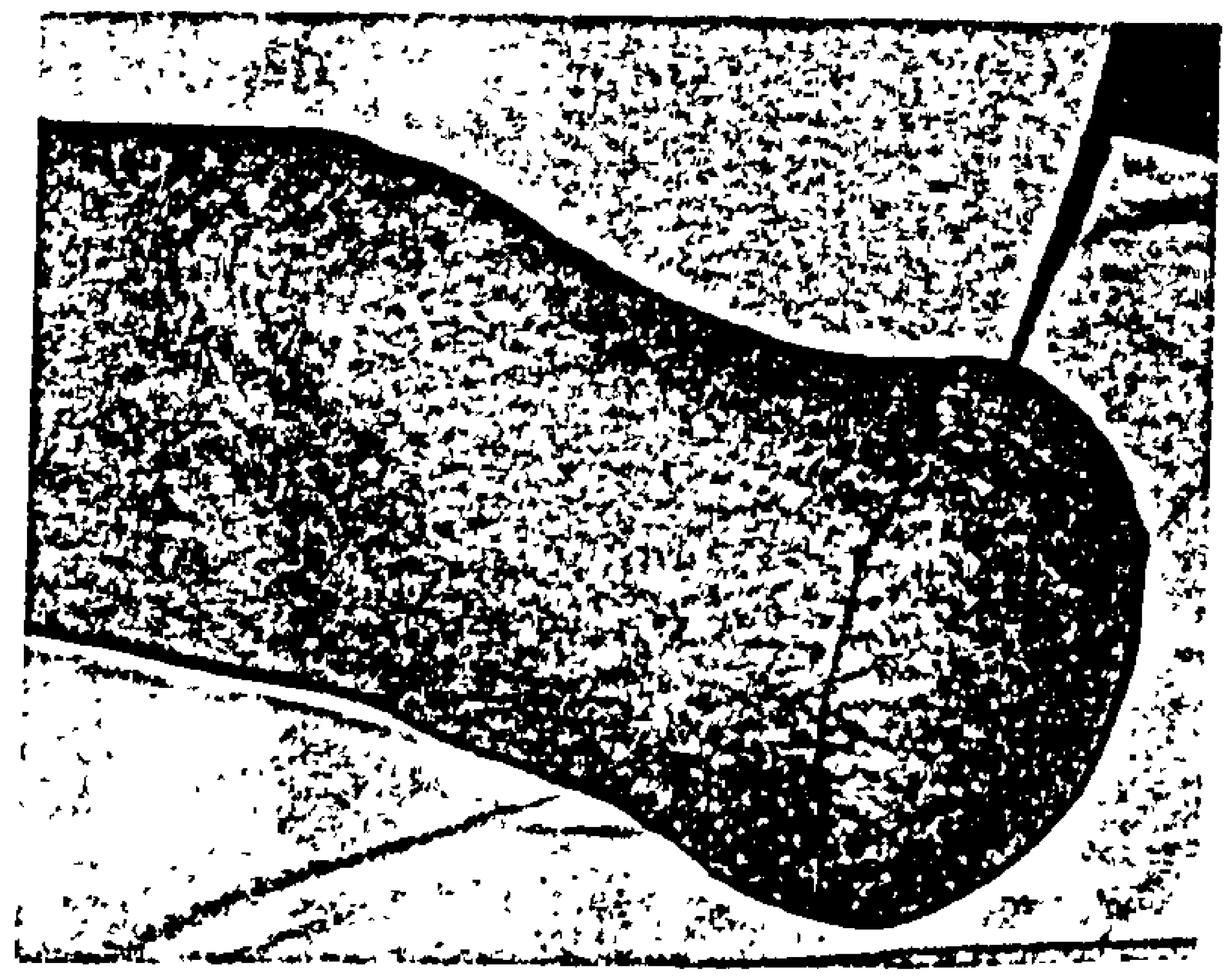

i.) Appearance of residual limb at time of suture removal, 15 days after surgery.

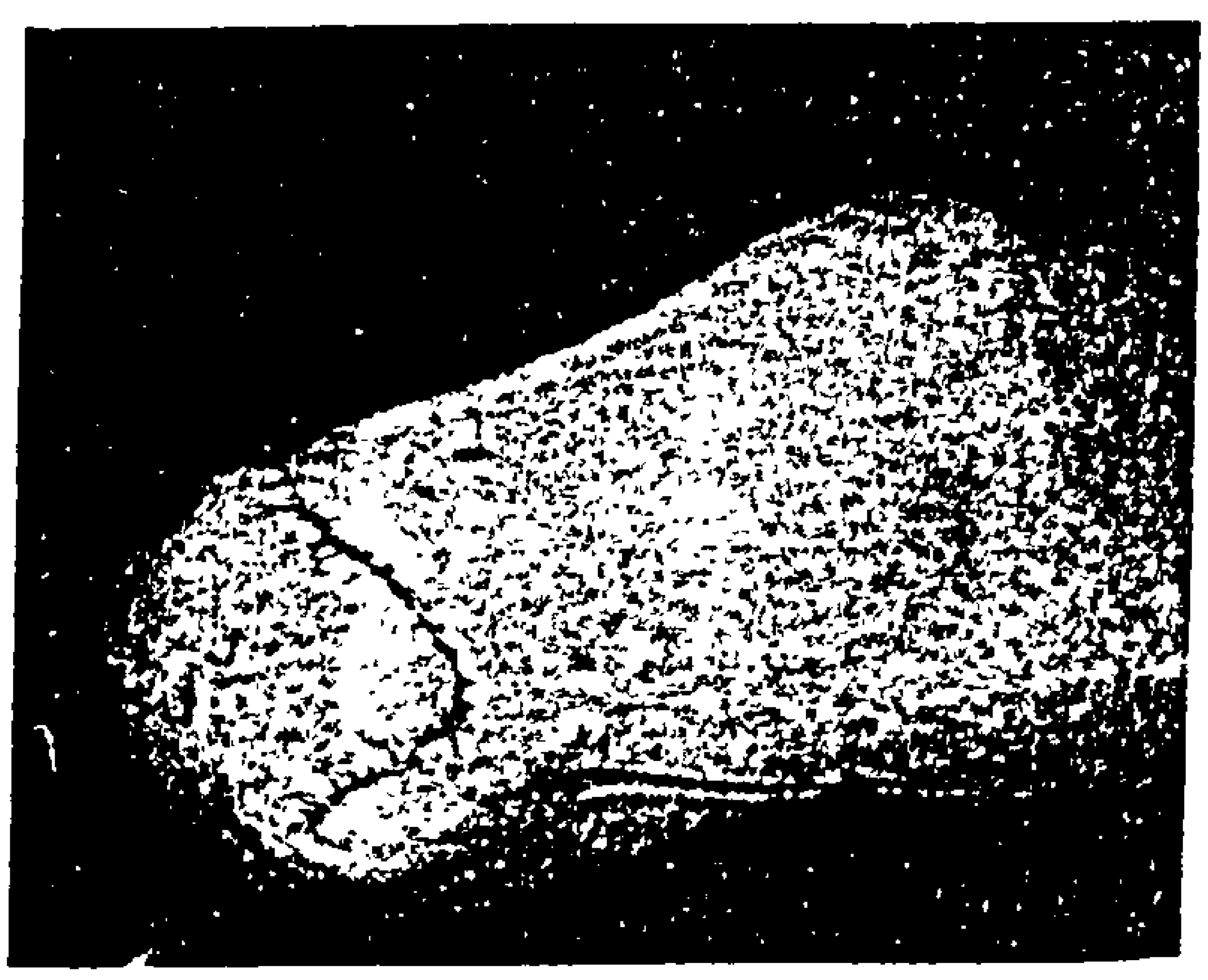

j.) Twenty five postoperative day.

Fig 2.2.3.7 Trans-tibial amputation. (Burgess, 1969)

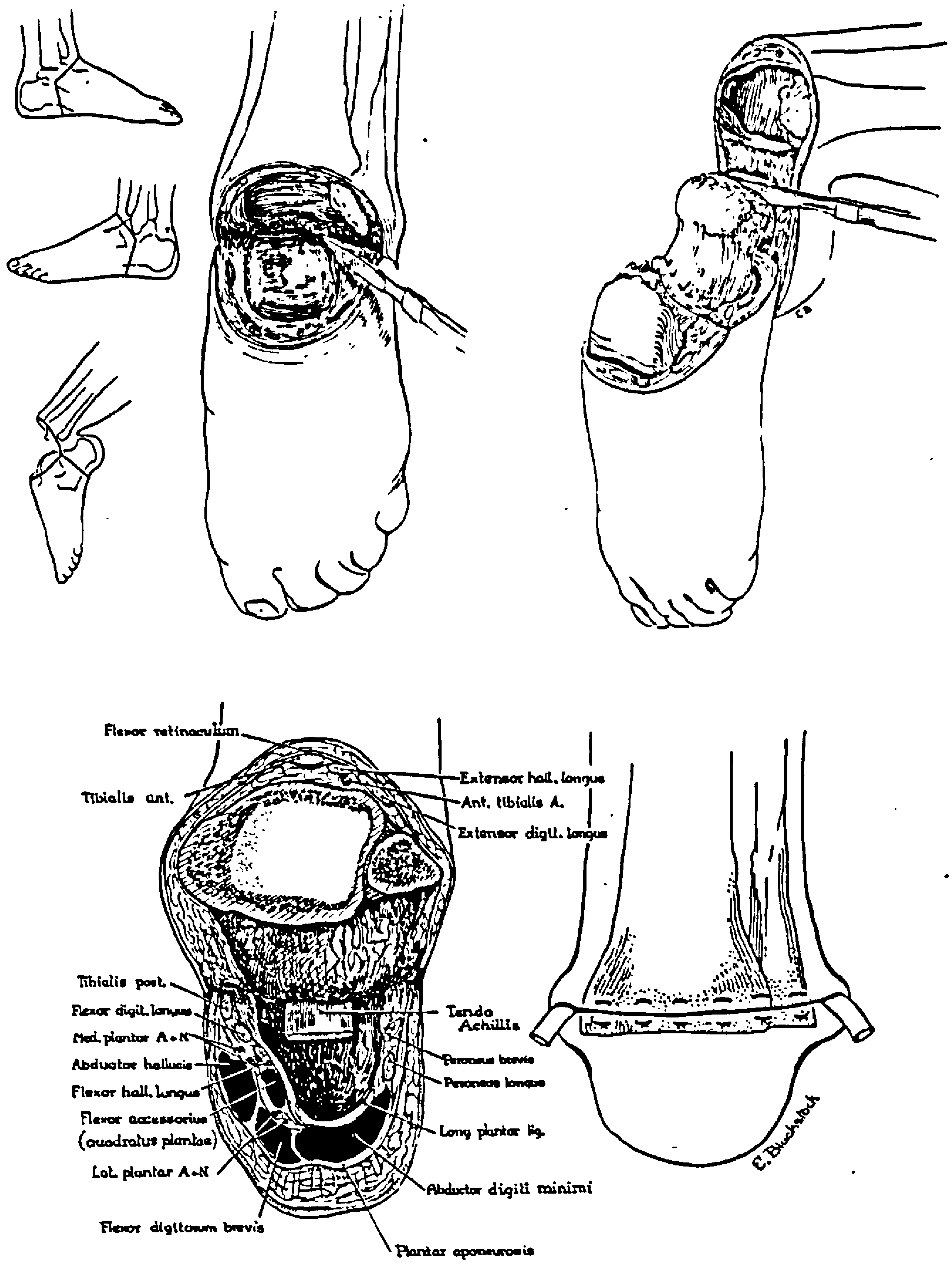

Fig. 2.2.3.8 Symes amputation. (Harris, 1961)

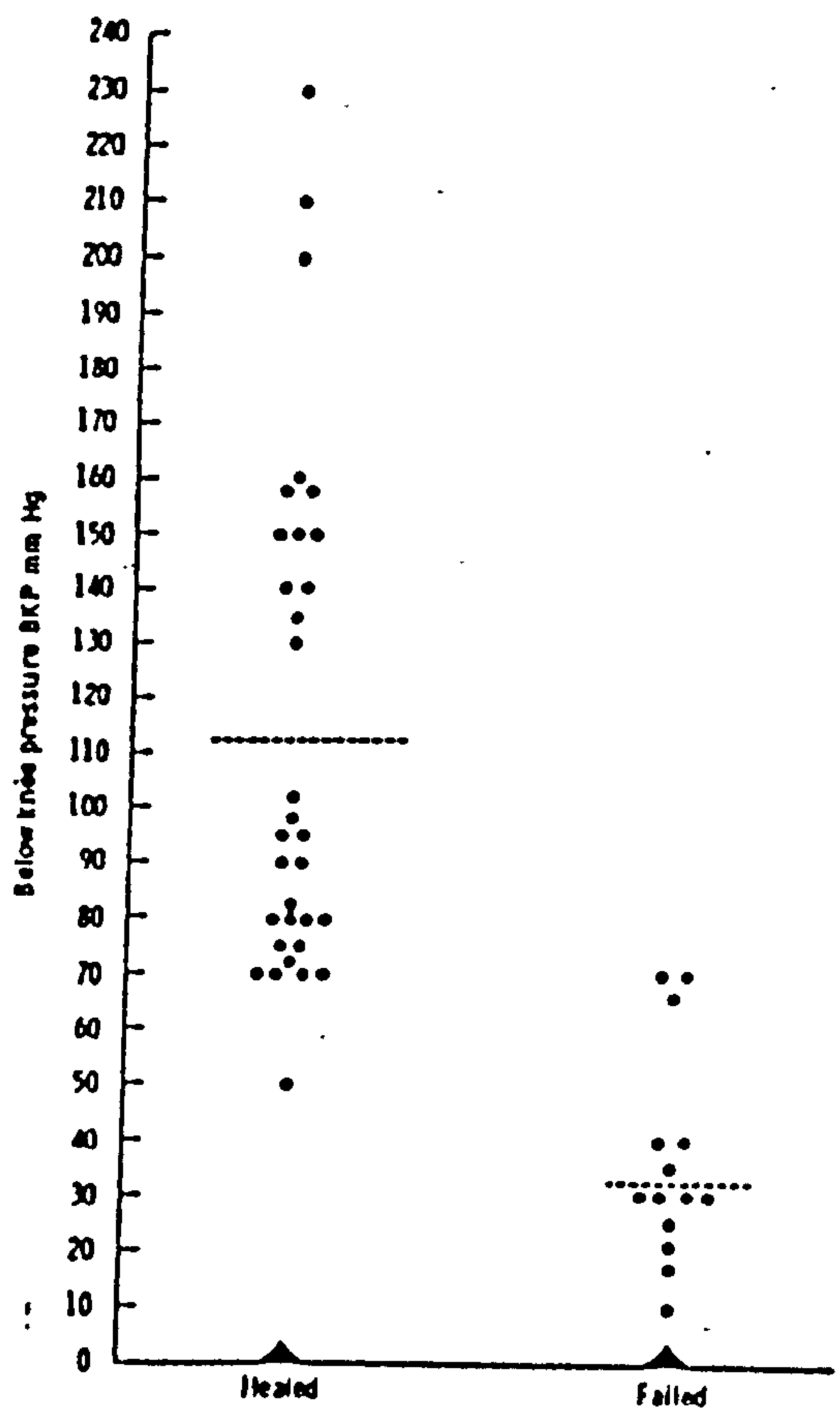

Fig. 2.2.4.1 Using Doppler ultrasound, below knee blood pressure was measured.
31 trans-tibial amputations healed with blood pressure > 70 mm Hg.
1 healed with blood pressure < 70 mm Hg.
14 failed with blood pressure < 70 mm Hg. (Creaney, 1981)

2.2.4 Selection of level of amputation

The level of amputation in traumatic cases is usually obvious, but for vascular reasons, the level is often between that of a trans-fermoral or trans-tibial amputation. This is also because the pattern of ischemia is seldom so favourable to allow partial foot or so severe to require hip disarticulation.

Warren and Record (1983) reported that trans-tibial amputees have a higher percentage (60%) of success with rehabilitation in the use of a prosthesis than trans-femoral amputees (40%). This is largely due to the contribution of the knee joint which is preserved in trans-tibial amputees. To ensure primary wound healing, the surgeon could opt for a trans-femoral amputation. However this measure also sacrifices patients' mobility, cosmetic and rehabilitation outcome due to the loss of the knee joint. Therefore the dilemma is often the case for conserving the knee joint. The tendency nowadays is to recommend trans-tibial amputation where possible. This has led to pre-operative level selection criteria and methods. Besides visual evaluation, many quantifiable level selection techniques have been investigated. Some of the techniques are as follows:

a) Doppler Ultrasound blood pressure measurement (Creaney et al 1981, Pollock and Ernst 1980)

b) Thermography (McCollum et al 1984,1988, Spence et al 1981)

c) Plethysmography (Barnes et al 1976)

d) Skin fluorescence (McFarland and Lawrence 1982)

e) Radioisotope clearance (Malone et al 1981)

Creaney et al (1981) measured the below knee blood pressure, over the posterior tibial or dorsalis pedis artery with a Doppler ultrasonic velocity detector, of 45 vascular disease patients selected for 46 trans-tibial amputations. Out of the 46 amputations, 32 had satisfactory healing of the stump. Fig. 2.2.4.1 shows the correlation between stumps that healed and did not heal with blood pressure. It was concluded that below 70 mmHg only one amputation healed and 14 failed and above this value, there was no failure.

Results of Amputation in 107 Ischemic Limbs

Amputation Level	Amputations Carried Out	No. Achieving Primary Healing	No. Achieving Secondary Healing	No. Requiring Local Wedge Resection	Final No. Achieving Initial Amputation Level	Tp(s)*	No. Requiring Revision to a Higher Level	Tp(f)†
AK	8	7	1	0	8	7	0	0
TK	3	2	0	0	2	1	1	1
BK	69	42	1	6	49	42	20	14
SY	5	1	0	0	1	0	4	4
PF	22	11	1	2	14	5	8	8

* Tp(s): Correct thermographic predictions of successful amputations.
† Tp(f): Correct thermographic predictions of unsuccessful amputations.

Table 2.2.4.1 Level of amputation with successful and unsuccessful prediction using thermography. (Spence et al, 1981)

Analysis of results in AK, TK and BK amputations

Amputation level	*Total*	*Deaths*	*Diabetic*	*1° healing*	*2° healing*	*Revision & type*	*Eventual healing*
Above-knee	28	0	4	24/28 (86%)	3/28 (11%)	1—LWR	28 (100%)
Through-knee	8	0	0	7/8 (88%)	0	1—AK	7 (88%)
Below-knee	150	6	50	103/144 (72%)	3 (2%)	38 9—LWR 4—TK 25—AK	115 (80%)

LWR = Local wedge resection. TK = Through-knee. AK = Above-knee.

Table 2.2.4.2 A 3.2 :1 ratio of trans-tibial amputation to trans-femoral amputation and knee disarticulation was achieved using thermography method for level selection. (McCollum et al 1984)

An extensive study was conducted by McCollum, Spence and Walker in 1981 and 1984 (McCollum et al 1984, Spence et al 1981) with 104 and 186 limb amputations for vascular disease respectively, in an evaluation programme of the use of thermography for preoperative assessment. The initial study involved 104 patients with 107 amputations. The level of amputation was decided by the surgeon on clinical grounds without any thermographic examination results. Thermographic examinations were carried out on all patients, the parameters selected for the interpretation of the thermograms being bilateral temperature asymmetry, analysis of the longitudinal thermal gradient (LTG) and the presence or absence of hypothermia and hyperthermia. Thirty-three of the amputation required revision surgery to a higher level. Table 2.2.4.1 summarises the breakdown of level of amputation, success/failure of the amputation and correct/incorrect thermographic prediction. Thermographic classification of distal amputation was found to be difficult, the predictions were incorrect in 8 out of the 9 cases.

The second study involved amputation of trans-tibial, through-knee and trans-femoral cases. During part of the studies, themographic examination results were used for selecting the levels. The overall investigation resulted in a possibility of maintaining a 3:1 ratio of trans-tibial to trans-femoral with 90% healing (Table 2.2.4.2). McCollum et al (1988) again reported another 100 limb amputations for peripheral vascular disease over a 15-month period. Besides infra red thermography data, measurement of skin blood flow was included to aid in selecting the level of amputation. A 3:1 ratio of trans-tibial to trans-femoral amputation ratio was achieved.

A detailed summary of some of these techniques and their effectiveness is discussed by Murdoch (1975). The implementation of such techniques would mean a reduction in revision surgery, an increase in trans-tibial to trans-femoral amputation ratio, an increase in the use of prostheses by amputees, more successful rehabilitation and a better quality of life for patients.

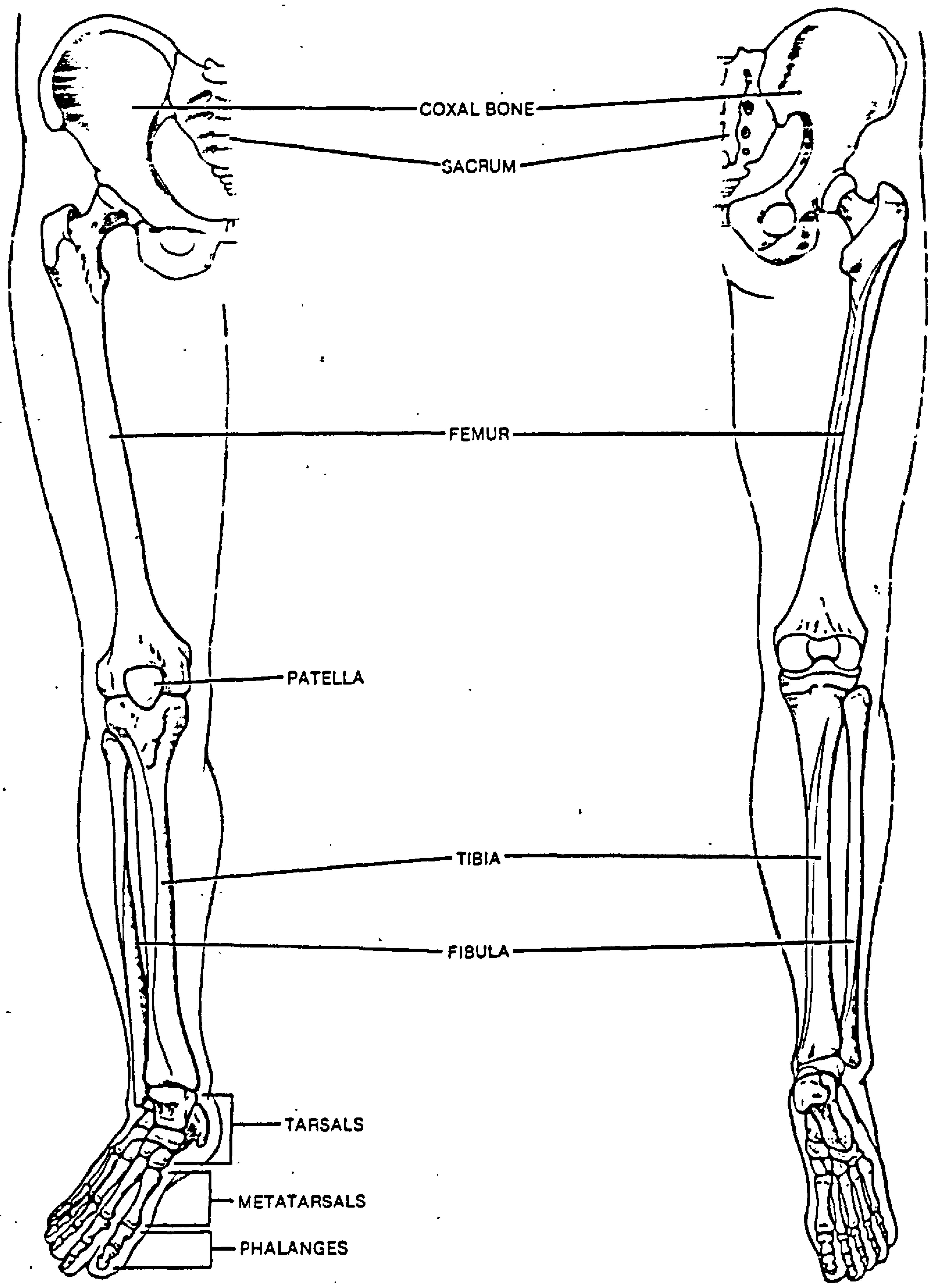

a) Anterior View

b) Posterior View

Fig. 2.3.1.1 Bones of the lower extremities. (Tortora and Anagnostakos, 1990)

2.3 ANATOMY OF THE LOWER LIMB

The general anatomy of the complete limb is discussed, in order to understand the geometry, positions or insertions and functions of both hard and soft tissues. This section also serves as a reference section to the discussion on trans-femoral amputation surgery and the artificial limb.

2.3.1 Bones

The human body consists of a total of 206 bones. In the lower extremities, there are a total of 60 bones (Fig 2.3.1.1) excluding the pelvic girdle. There are two femora, two patellas, fibulas and tibias. The rest of the totals are in the feet (Tarsals 14, metatarsals 10, phalanges 28). These bones will be isolated from the present discussion.

Femur

The femur is the longest and heaviest bone in the body (Fig 2.3.1.2) Proximally, the femoral head articulates with the pelvis at the acetabulum. There are two prominences known as the greater and lesser trochanter at the proximal end that serve as points of attachment for some thigh and buttock muscles. The femoral neck joins the main shaft of the femur at an angle of 125-140^0. Between the trochanters at the anterior surface, a raised trochanteric line marks the distal limits of the articular capsule of the hip joint. The posterior surface of the shaft contains a rough ridge called the linea aspera. Several thigh muscles insert at this ridge. The shafts bow medially bringing the knee joints together, closer to the body's line of gravity. At the distal end of the femur there are two condyles which articulate with the tibia at the knee joint. Posteriorly, the condyles are separated by a deep intercondylar fossa and anteriorly, the two condyles merge producing an articular surface known as the patellar surface where the patella glides. Superior to the condyles are the epi-condyles.

Patella

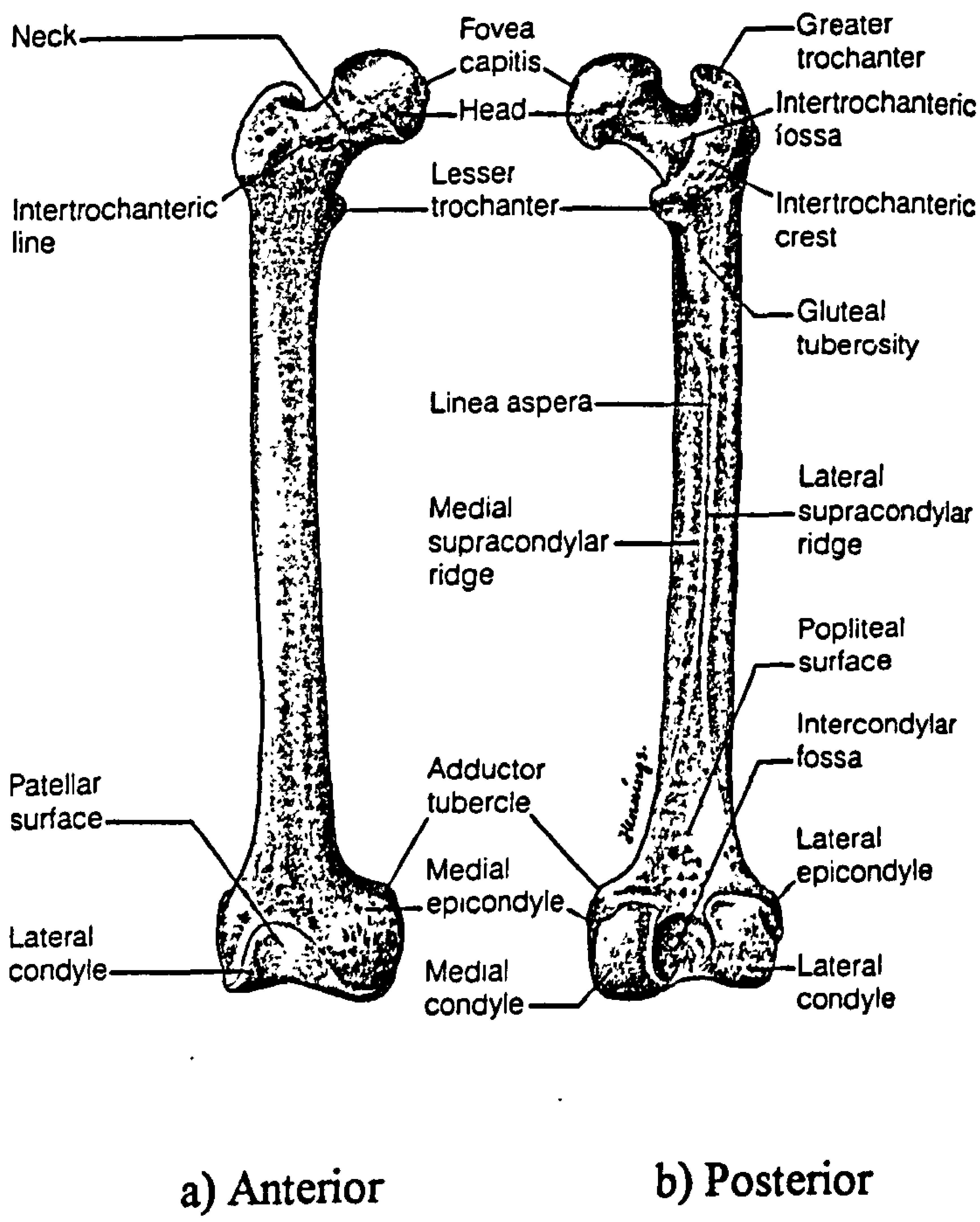

Fig. 2.3.1.2 Femur. (Gaudin and Jones, 1989)

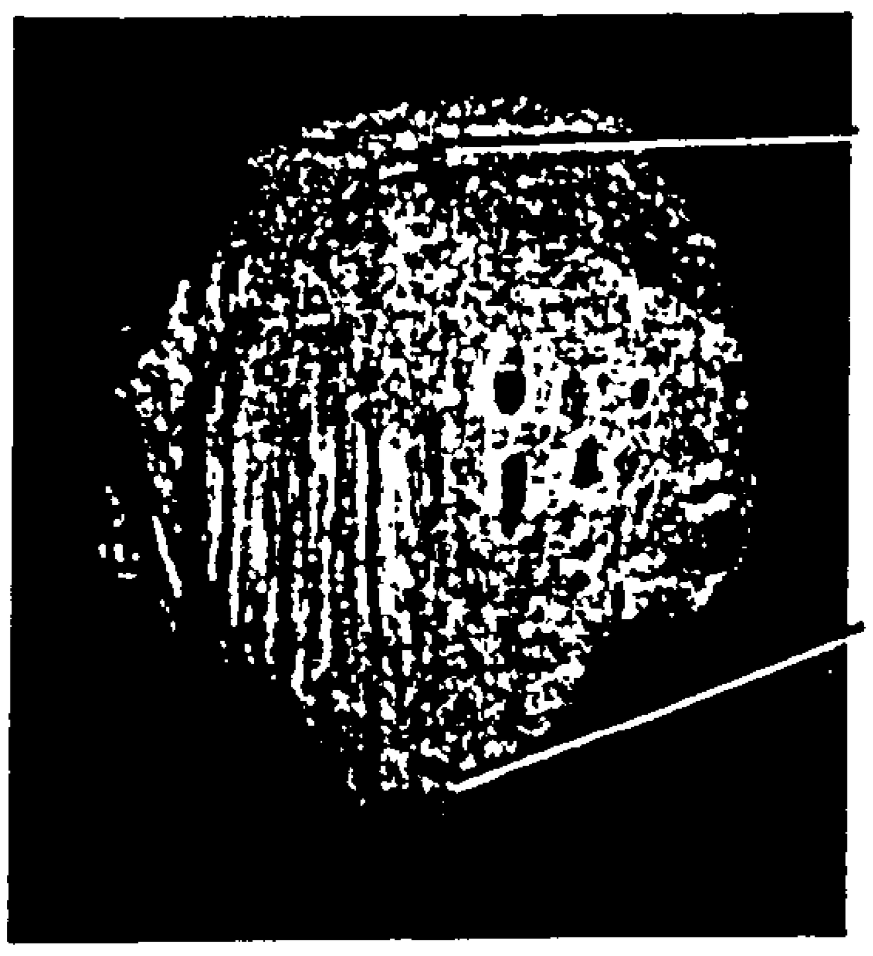

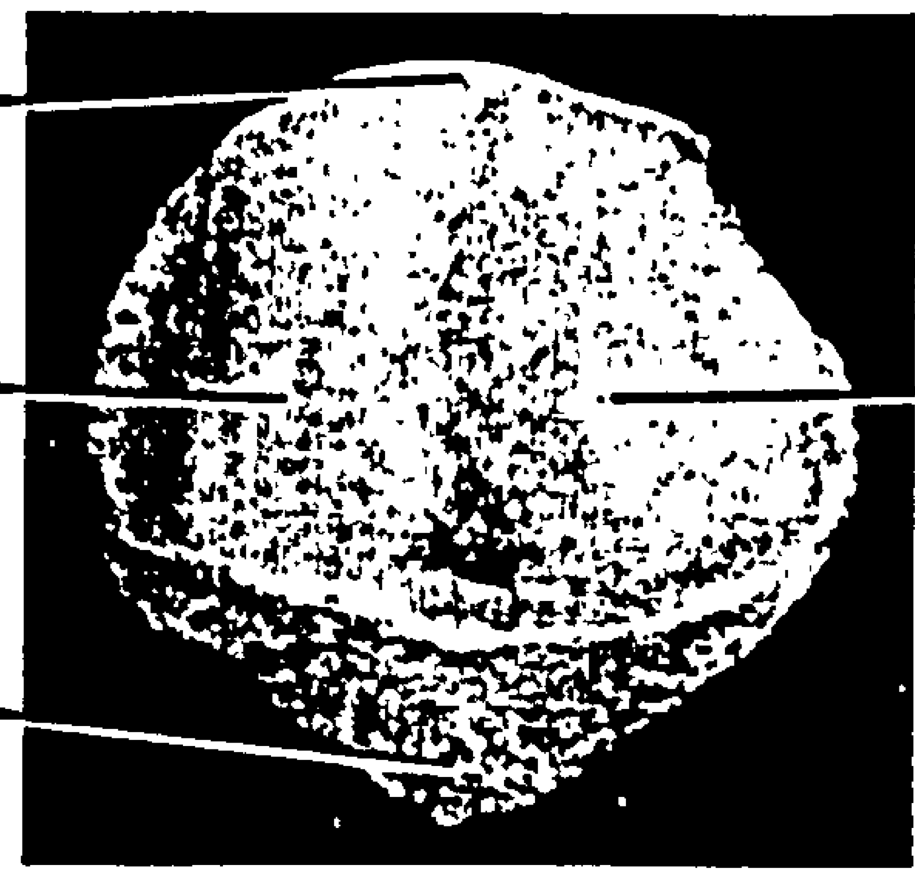

a) Anterior View

b) Posterior View

Fig. 2.3.1.3 Patella. (Tortora and Anagnostakos, 1990)

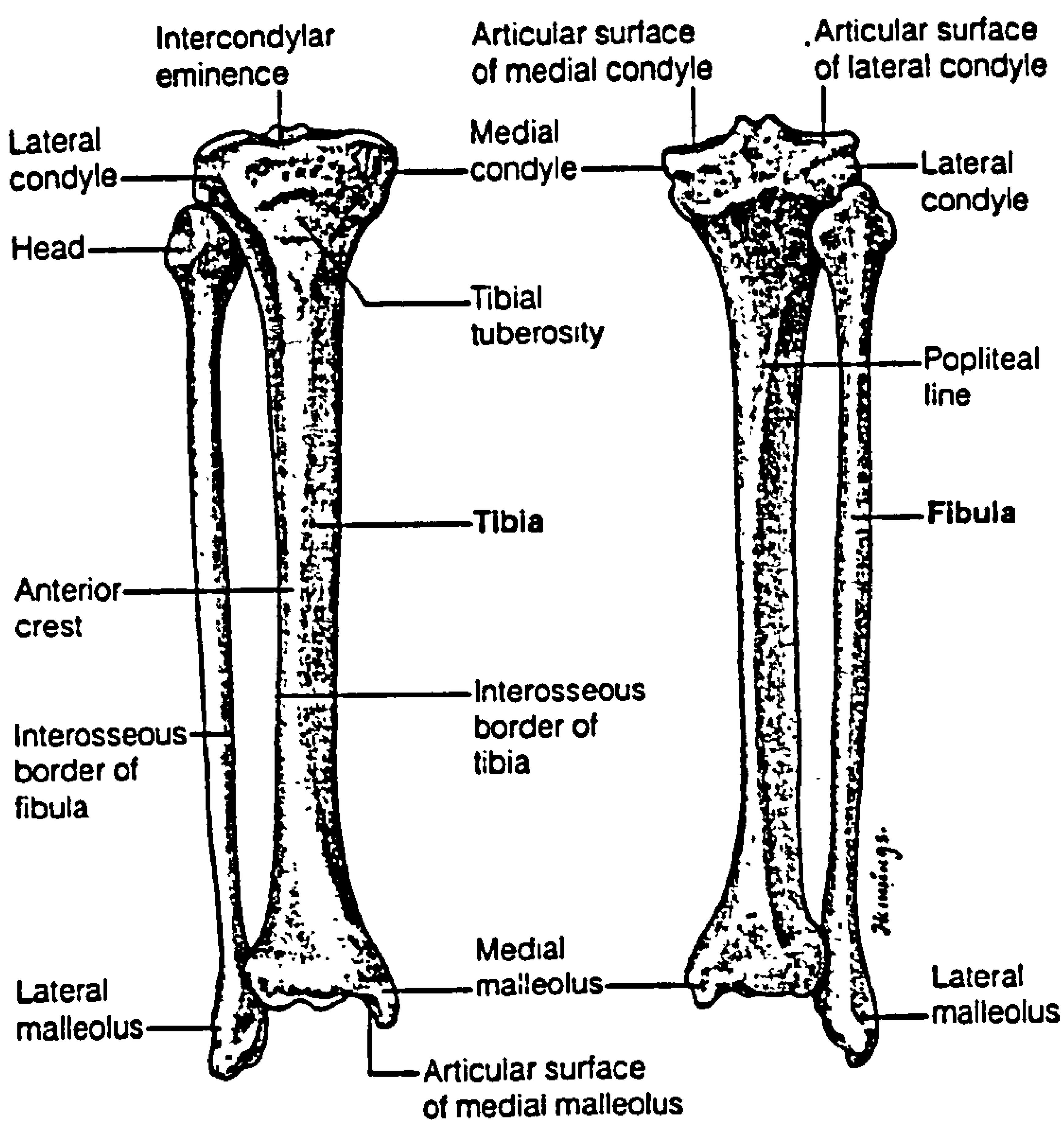

a) Anterior

b) Posterior

Fig. 2.3.1.4 Tibia and fibula. (Gaudin and Jones, 1989)

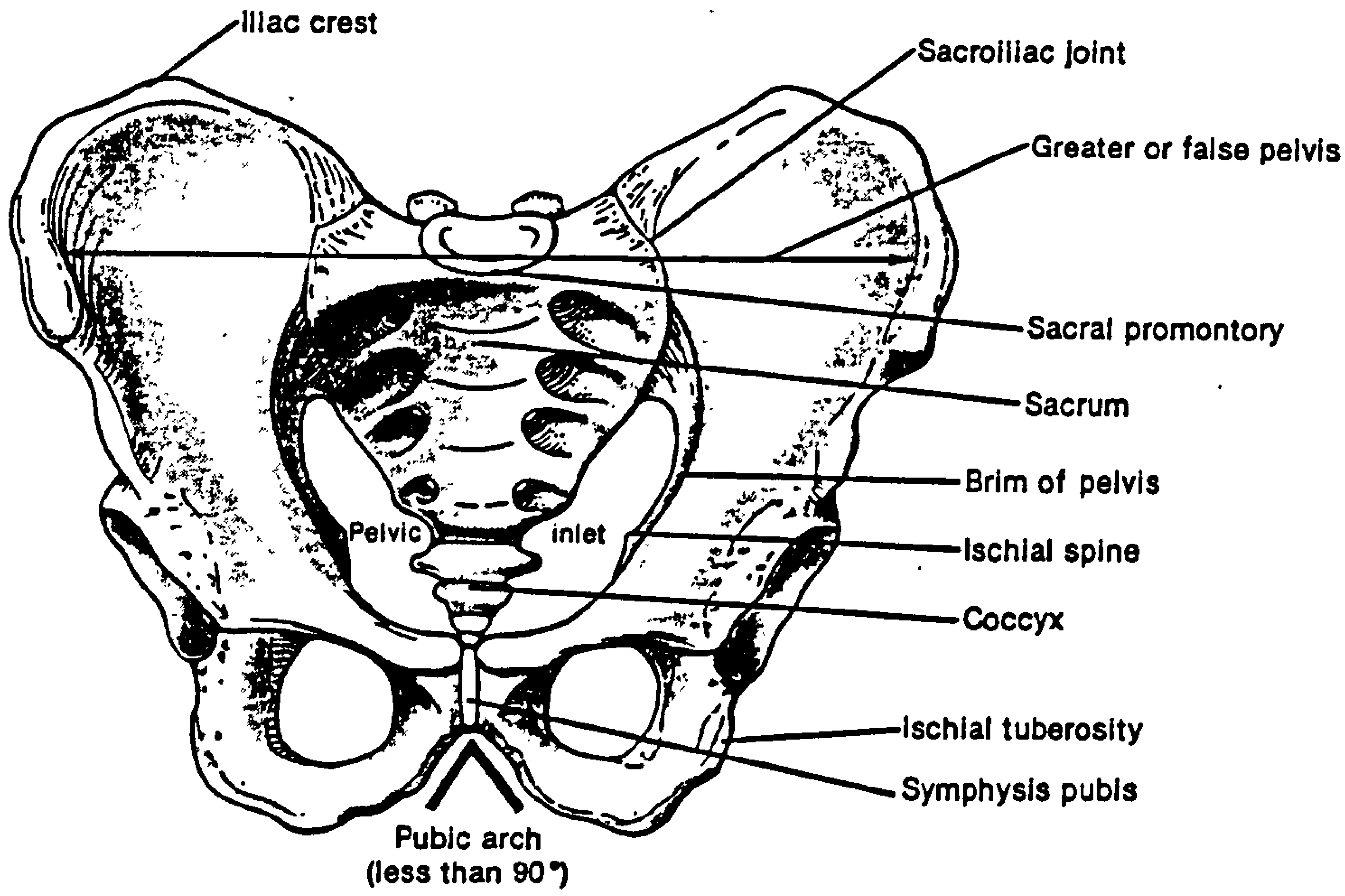

Fig. 2.3.1.5 Pelvic girdle of a male in anterior view.
(Tortora and Anagnostakos, 1990)

The patella (Fig. 2.3.1.3) is a small triangular shaped bone present anteriorly at the knee joint. It is embedded within the quadriceps tendon which converges from the muscles responsible for extending the knee, and provides an anterior bony protection to the knee joint.

Tibia and Fibula

These bones are found in the legs with the tibia being the larger of the two (Fig. 2.3.1.4). The proximal end of the tibia is expanded into a lateral condyle and a medial condyle, articulating with the respective condyles of the femur. The head of the fibula articulates with the inferior surface of the lateral condyle of the tibia. The tibial condyles are separated by a ridge, known as the intercondylar eminence. The tibial tuberosity lies proximally anteriorly and is the point of attachment for the patellar ligament. The fibula lies lateral to and parallel with the tibia. The main purpose of the fibula is not weight bearing since it is completely isolated at the knee joint, but it provides an important surface for muscle attachment.

Pelvic Girdle

Only a brief description of this complicated structure will be attempted. The main parts of the pelvic girdle are the coxae, the sacrum and the coccyx (Fig. 2.3.1.5). The girdle obtains its structural stablility through a series of interconnecting ligaments at its bony prominences, providing a strong and stable support for the lower extremities. Two coxal bones exist in the pelvic girdle and are united anteriorly at the pubis symphysis. The coxal bones consists of three main parts, the ileum, pubis and the ischium. (Fig. 2.3.1.6) The differentiation is obvious in young bones. Eventually the three are fused deeply together into one. The area of fusion is called the acetabulum, where the head of the femur articulates. The larger of the three subdivisions is the ileum. Superiorly the iliac crest of the ileum ends anteriorly at the anterior superior iliac spine (ASIS). The ASIS is often used as an external anatomical landmark for anthropometric measurements and in gait studies. Posteriorly the ilac crest ends in the posterior superior iliac spine. At the gluteal surface of the ileum there

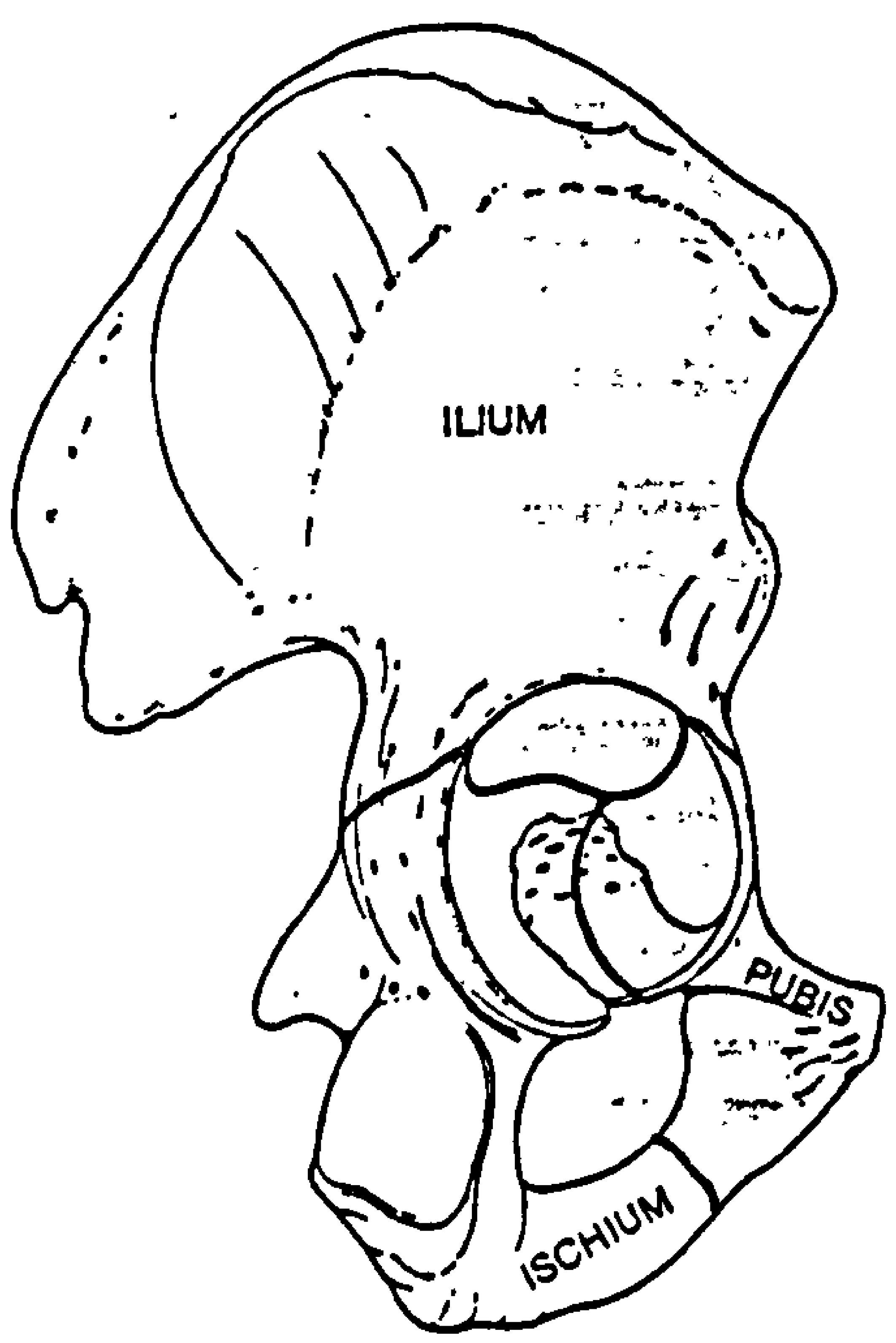

Fig. 2.3.1.6 Coxal. (Tortora and Anagnostakos, 1990)

are three obvious lines known as the posterior, anterior and inferior gluteal line. The lines are sites of attachment of the gluteal muscles. At the ischium, prominent areas are the lesser sciatic notch, ischial tuberosity, ischial spine and the ramus. In the case of trans-femoral amputees, the present prosthetic socket methodolgy places much emphasis on directing a large percentage of prosthetic load to the ischium through the ischial tuberosity. The pubis consists of a superior ramus, an inferior ramus and is where the coxal bones join together.

The sacrum is made up of five sacral vertebrae which are fused together. The sacrum forms a strong structural foundation for the pelvic girdle, positioning posteriorly in the middle of the coxae. The triangular shape of the sacrum forms a base at the superior surface and an apex distally, which is the site of articulation with the coccyx. In the sagittal view, the sacrum is curved, with a convex dorsal surface. Laterally, it has a large articular surface for articulating with the ileum of the coxal bones and posteriorly an area for attachment of ligaments is the sacral tuberosity.

The coccyx continues from the apex of the sacrum and is also triangular in shape. It makes up the last four of the vertebrae bones, known as the coccygeal vertebrae. Fusion of the coccygeal vertebrae takes place between 20-30 years.

2.3.2 Muscles

The muscles in the lower limb can best be described according to their function related to the movement of the thigh and legs. Muscles that move the foot and toes will not be presented here.

The possible actions performed by the muscles are flexion, extension, adduction, abduction, medial rotation, lateral rotation of the thigh and flexion, extension and medial rotation of the leg. A total of 25 muscles are described in Tables 2.3.2.1, 2.3.2.2 and 2.3.2.3 according to the above functions and viewed diagramatically in Fig. 2.3.2.1 to Fig. 2.3.2.2. Most muscles provide two actions especially those of the abductors and lateral rotators of the thighs.

The muscles can also be classified anatomically but often cause confusion due to the area of insertion and origin. But generally the anterior muscle groups are the

Flexion	Extension	Abduction	Adduction	Medial rotation	Lateral rotation
Psoas (1)	Gluteus Maximus (5)	Gluteus Medius (3)	Quadratus Femoris (13)	Gluteus Medius (3)	Psoas (1)
Iliacus (2)	Adductor Magnus (16)	Gluteus Minimus (4)	Adductor Longus (15)	Gluteus Minimus (4)	Iliacus (2)
Tensor Fascia Lata (6)	Semimembranosus (19)	Tensor Fasciae Latae (6)	Adductor Brevis (14)	Tensor Fasciae Latae (6)	Gluteus Maximus (5)
Pectineus (8)	Semitendinosus (20)	Piriformis (7)	Adductor Magnus (16)	Adductor Magnus (16)	Piriformis (7)
Adductor Magnus (16)		Obturator Internus (9)	Pectineus (8)	Adductor Longus (15)	Obturator Internus (9)
		Superior Gemellus (11)		Adductor Brevis (14)	Obturator Externus (10)
		Inferior Gemellus (12)			Superior Gemellus (11)
					Inferior Gemellus (12)
					Quadratus Femoris (13)

Table 2.3.2.1 Muscles providing movement to the thigh in the anatomical position.
(The numbers refer to diagrams of muscles in Fig. 2.3.2.1)

Flexion	Extension	Medial rotation
Biceps Femoris (21)	Rectus Femoris (22)	Sartorius (18)
Semimembranosus (19)	Vastus Intermedius (23)	
Semitendinosus (20)	Vastus Lateralis (25)	
Gracilis (17)	Vastus Medialis (24)	
Sartorius (18)		

Table 2.3.2.2 Muscles providing movement to the leg in the anatomical position.
(The numbers refer to diagrams of muscles in Fig. 2.3.2.1)

Flexion	Adduction	Medial Rotation	Lateral Rotation
Rectus Femoris (22)	Biceps Femoris (21)	Semimembranosus (19)	Sartorius (18)
	Semimembranosus (19)	Semitendinosus (20)	
	Semitendinosus (20)		
	Gracilis (17)		

Table 2.3.2.3 Muscles providing movement to both the leg and the thigh in the anatomical position.
(The numbers refer to diagrams of muscles in Fig. 2.3.2.1)

1. 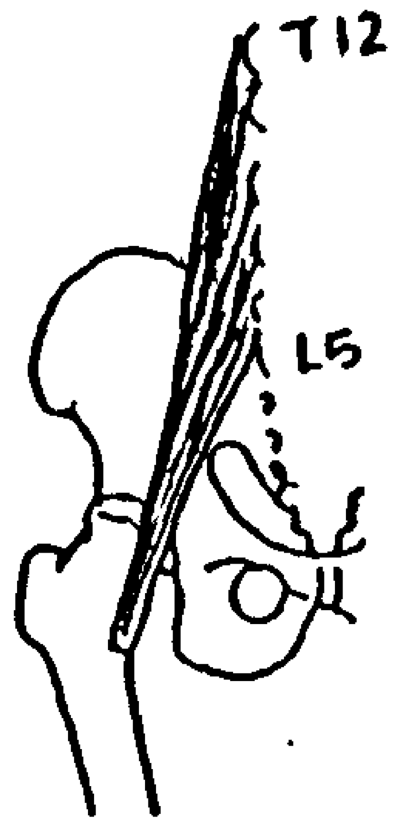 **Psoas** Origin ; Vetebrae T12 to L5. Insertion : Lesser trochanter of femur.	2. 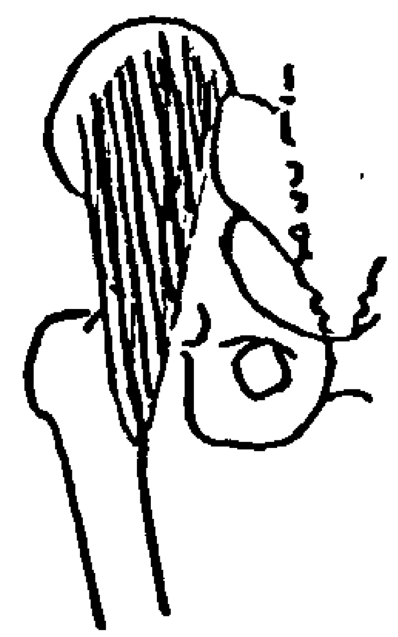 **Iliacus** Origin : Iliac fossa and sacrum. Insertion : Tendon of the psoas.	3.  **Gluteus Medius** Origin : Ilium. Insertion : Greater trochanter of femur.	4. 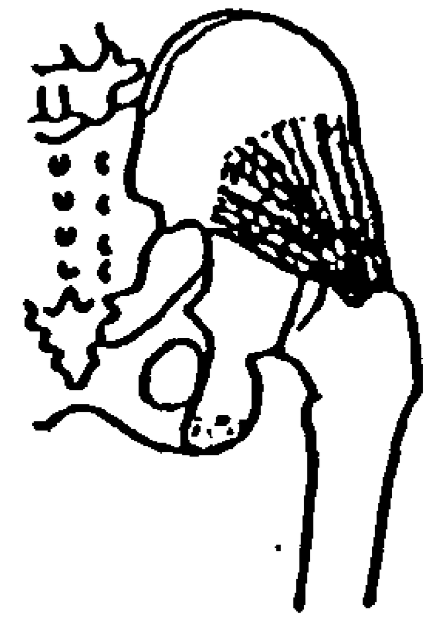 **Gluteus Minimus** Origin ; Ilium. Insertion ; Greater trochanter of femur.
5. 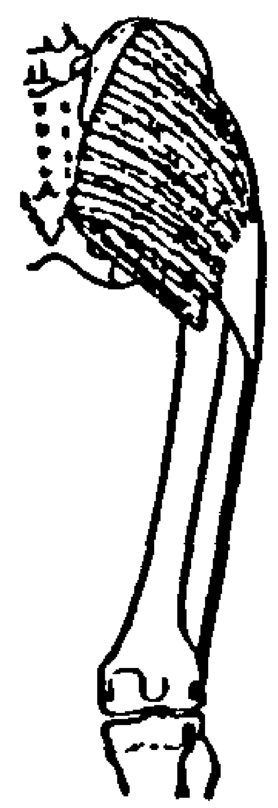 **Gluteus Maximus** Origin : Iliac crest, sacrum, coccyx and sacrotuberous ligament. Insertions ; Gluteal tuberosity of femur and iliotibial tract of fascia lata.	6  **Tensor Faciae Latae** Origin : Iliac crest. Insertion :Iliotibial tract.	7 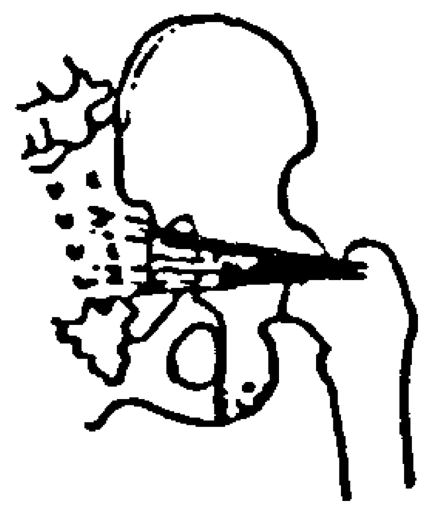 **Piriformis** Origin : Sacrum. Insertion : Greater Trochanter of femur:	8 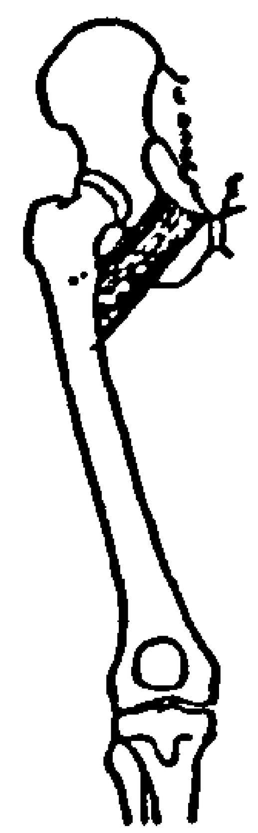 **Pectineus** Origin : Pubis. Insetion ; Pectineal line of femur. (bet[n] lesser tochanter and linea aspera).

Fig. 2.3.2.1 Name and location of muscles in the thigh.

9.. 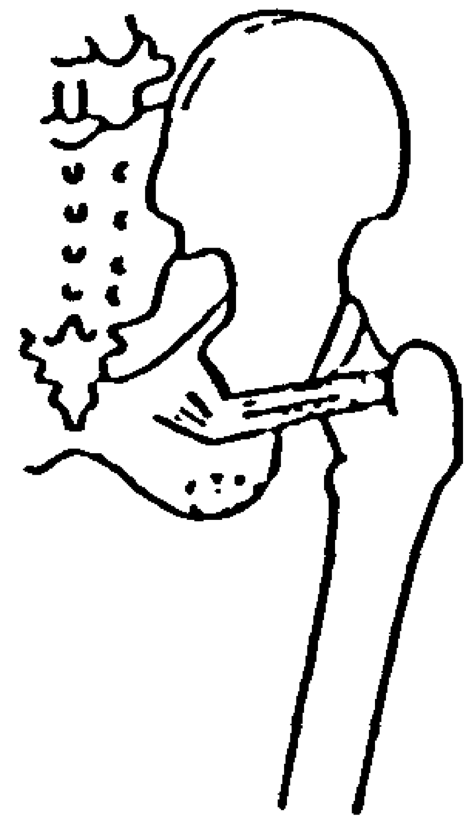 **Internal Obturator** Origin : Obturator membrane (lateral half),pubis and ischium. Insertion : Greater trochnater of femur.	10.. 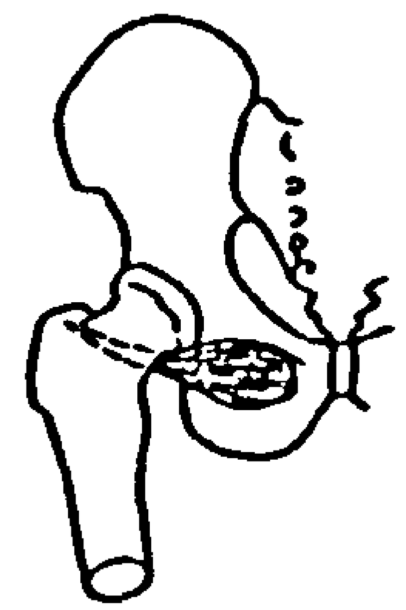 **External Obturator** Origin : Obturator membrane (medial half). Insertion : Trochanteric fossa of femur.	11.. 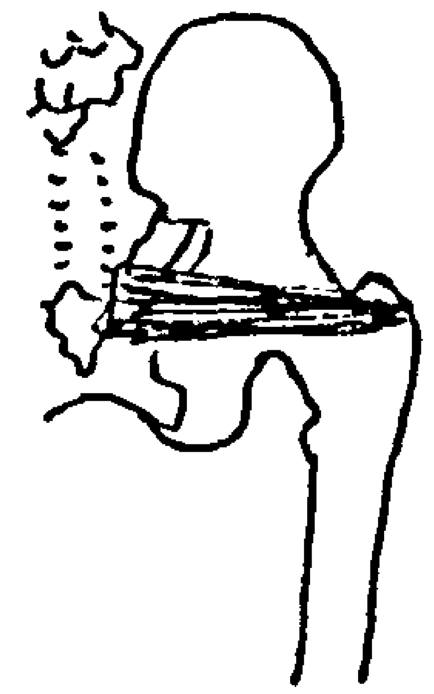 **Superior Gemellus** Origin : Ischial Spine. Insertion : Greater trochanter of femur.	12. 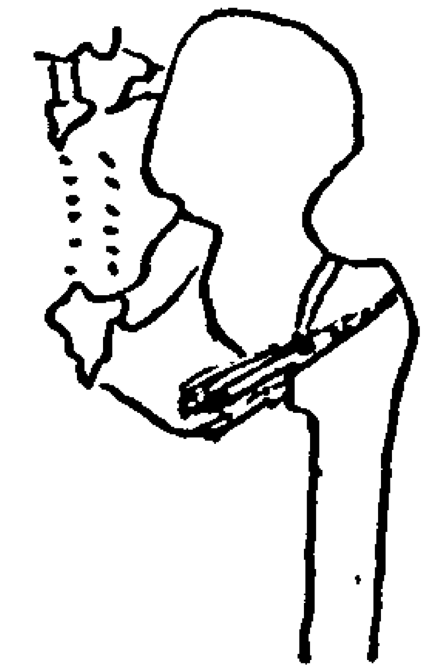 **Inferior Gemellus** Origin : Ischial tuberosity. Insertion : Greater trochanter of femur.
13. 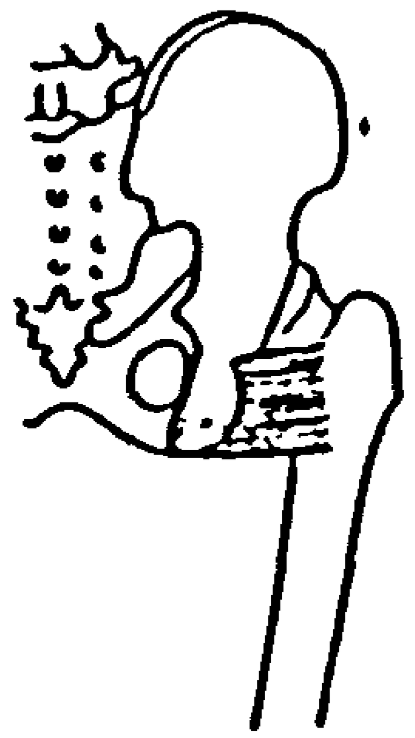 **Quadratus Femoris** Origin : Ischial tuberosity. Insertion : Quadrate tubercle on back of greater trochanter.	14. 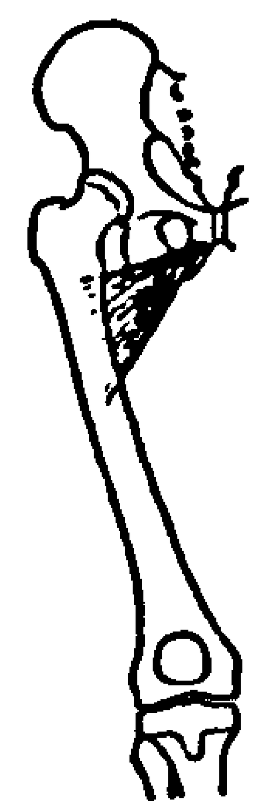 **Adductor Brevis** Origin : Inferior ramus of the pubis. Insertion : Linea aspera of femur.	15.  **Adductor Longus** Origin : Pubic crest and symphysis pubis. Insertion : Linea aspera of femur.	16. 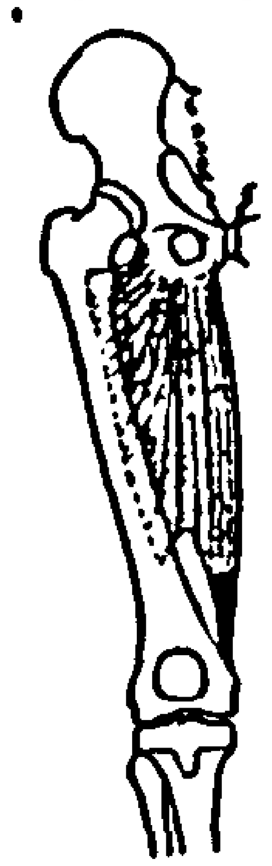 **Adductor Magnus** Origin : Inferior ramus of pubis and ischial tuberosity. Insertion : Along the linea aspera to the adductor tubercle of femur.

Fig. 2.3.2.1 Name and location of muscles in the thigh.

17.  **Gracilis** Origin : Symphysis pubis and pubic arch. Insertion : Medial surfsce of body of tibia.	18. 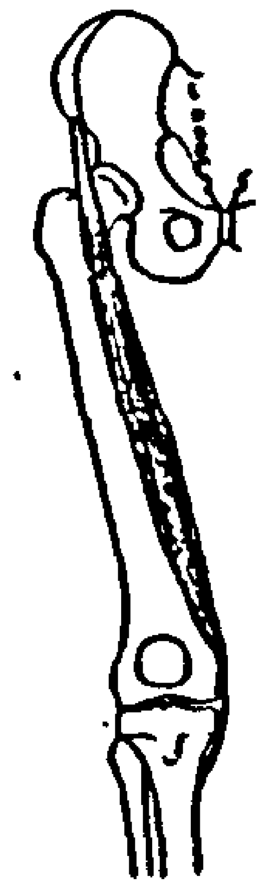 **Satorius** Origin : Anterior superior iliac spine. Insertion : Superior medial surface of tibia.	19. 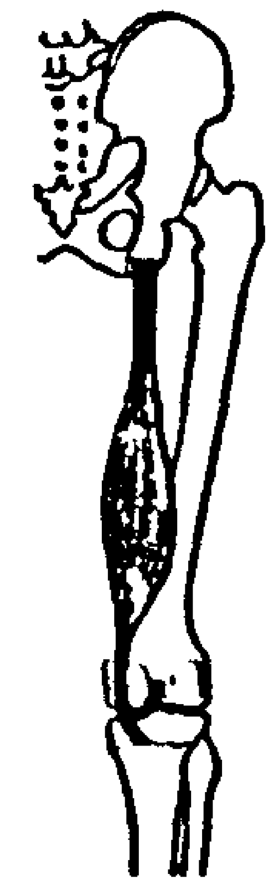 **Semimembranosus** Origin : Ischial tuberosity. Insertion : Medial condyle of tibia.	20. 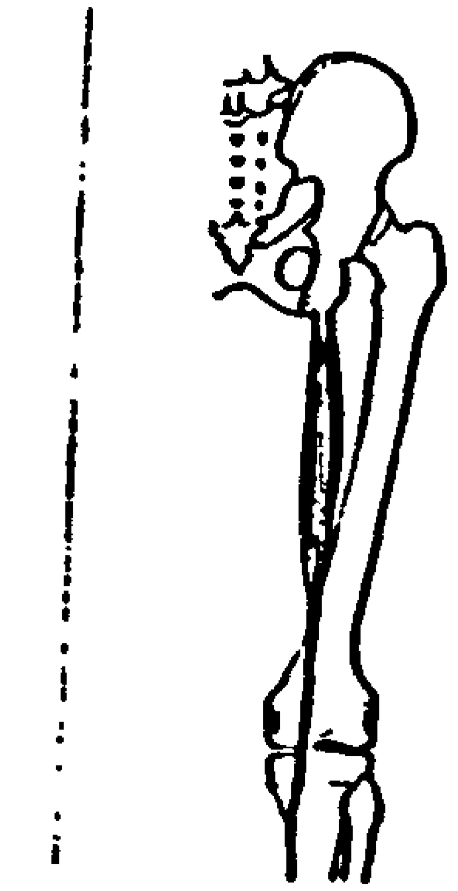 **Semitendinosus** Origin : Ischial tuberosity. Insertion : Proximal medial surface of tibia.
21. 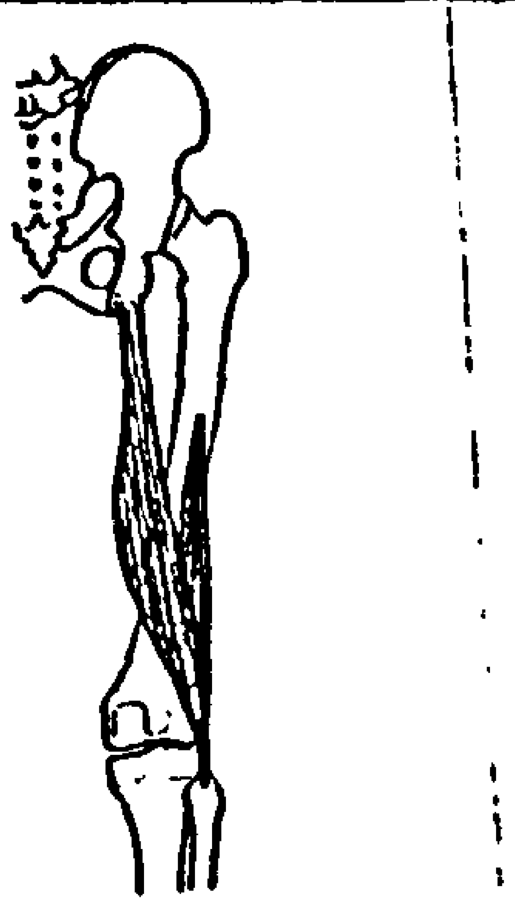 **Biceps Femoris** Origin : Long head, ischial tuberosity. Short head, linea aspera of femur. Insertion : Fibular head and lateral condyle of femur.	22. 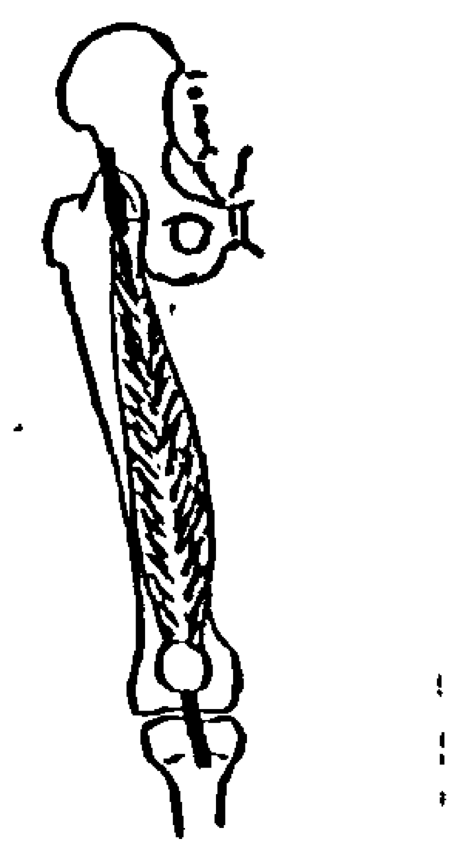 **Rectus Femoris** Origin : Anterior superior iliac spine. Insertion : Upper border of patella.	23. 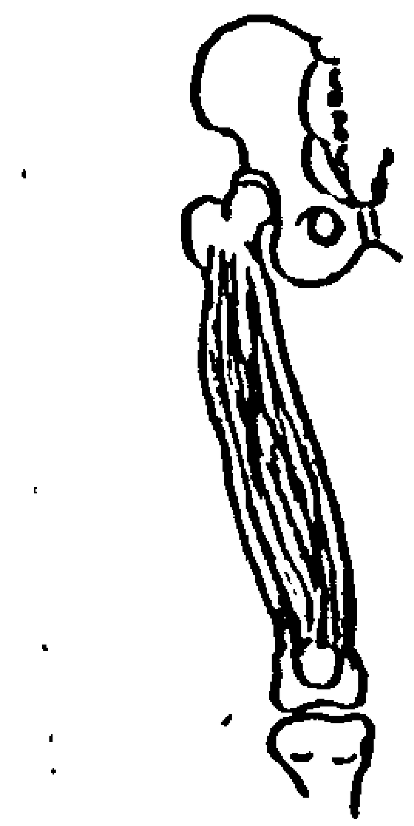 **Vastus Intermedius** Origin : Anterior and lateral surface of femur. Insertion : Upper border of patella.	24. 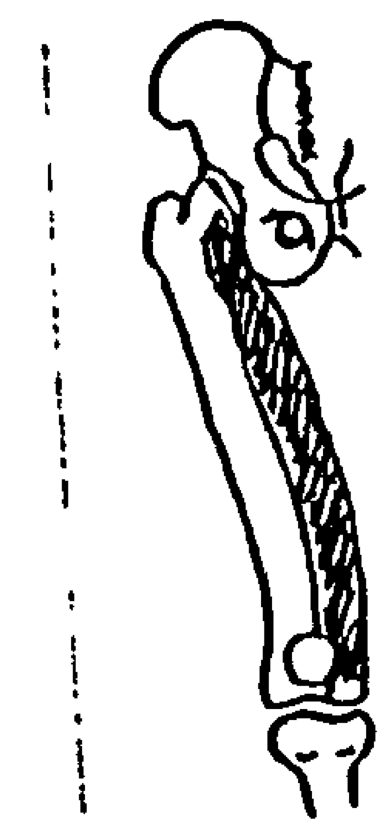 **Vastus Medialis** Origin : Anterior intertrochanteric line, linea aspera and medial epi-condyle of femur. Insertion : Medial border of patella.

Fig. 2.3.2.1 Name and location of muscles in the thigh.

25..

Vastus Lateralis

Origin : Greater trochanter and linea aspera of femur.

Insertion : Upper border of patella.

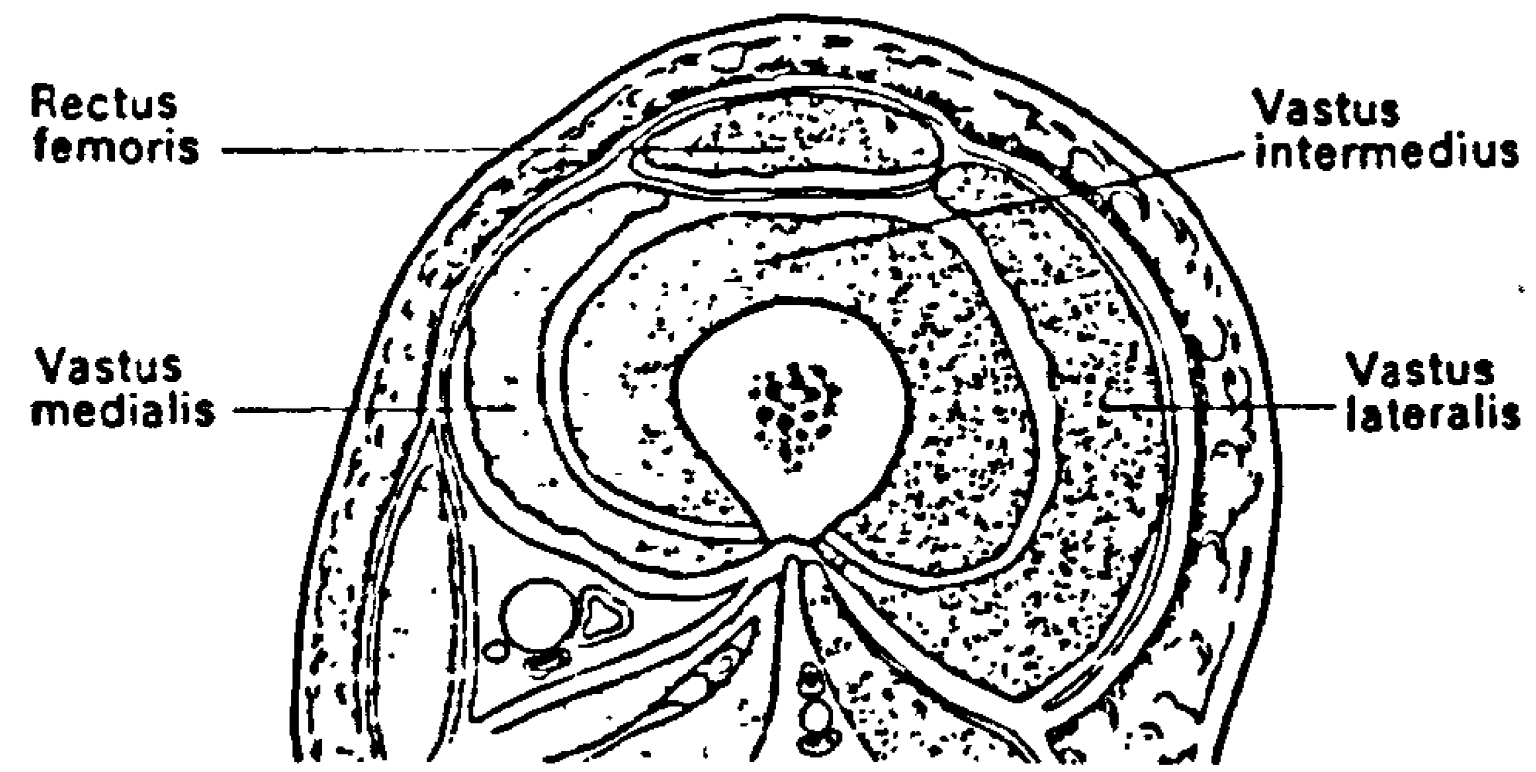

Sectional view of the quadriceps muscles at mid thigh.

Fig. 2.3.2.1 Name and location of muscles in the thigh.

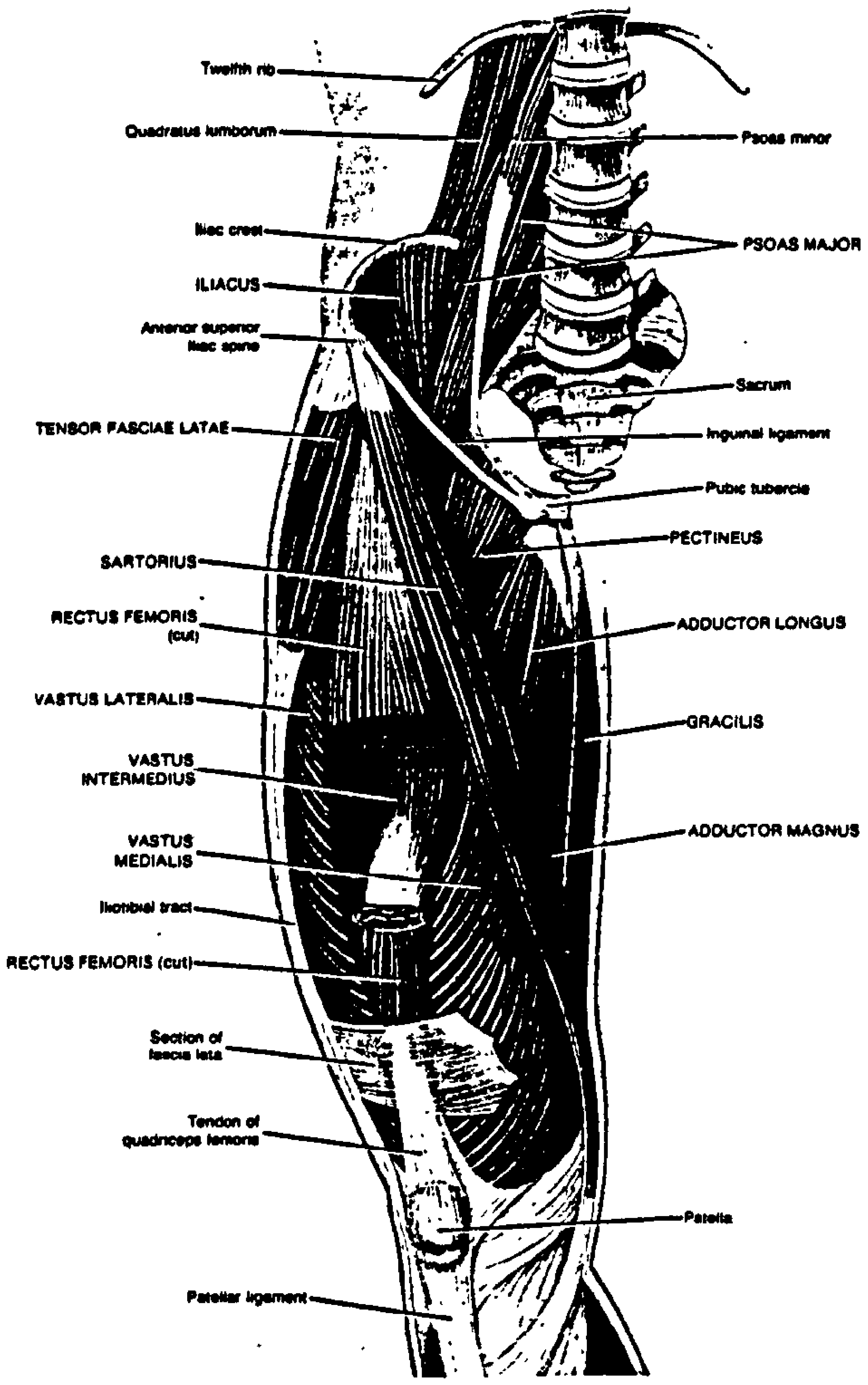

a) Anterior superficial view

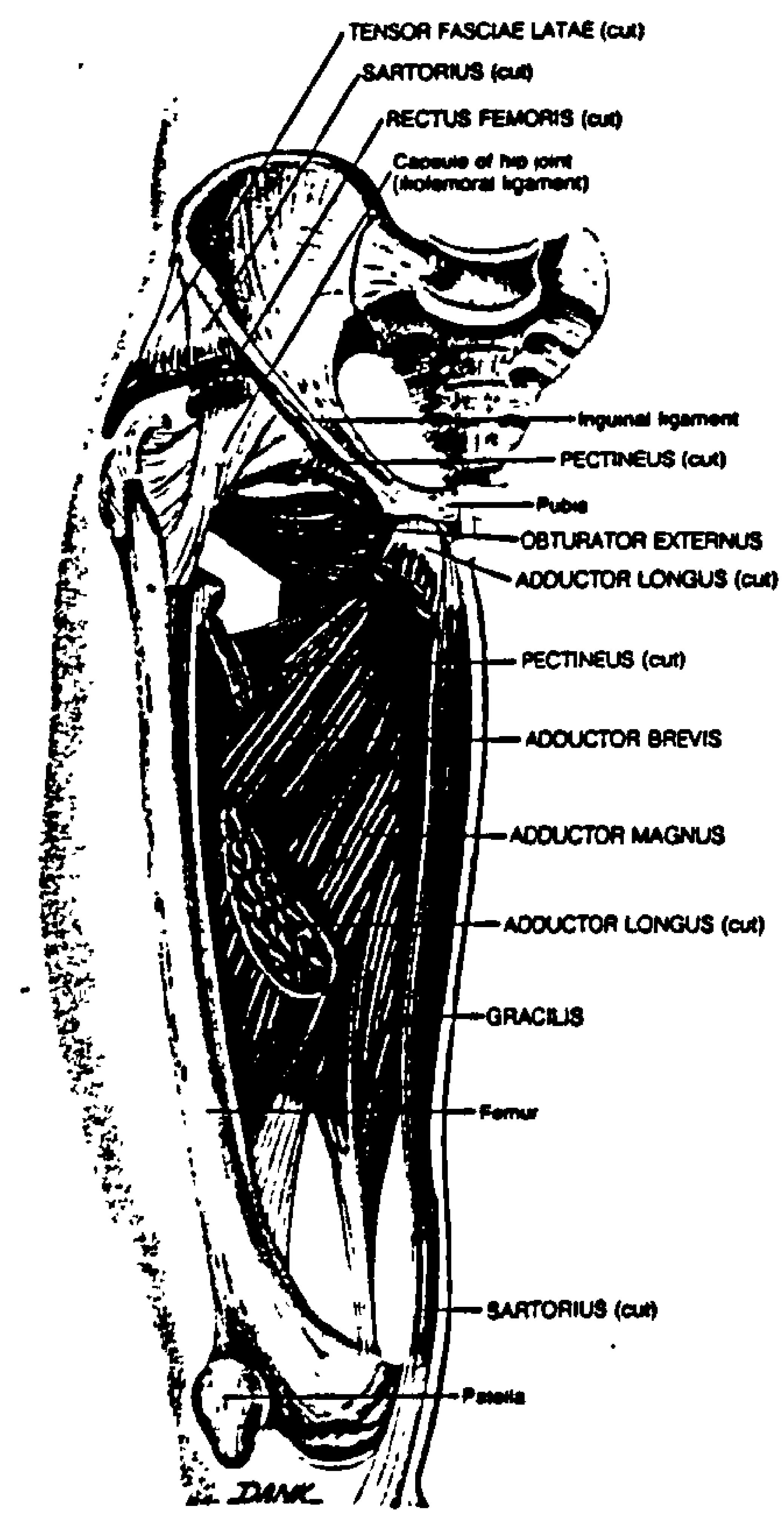

b) Anterior deep view

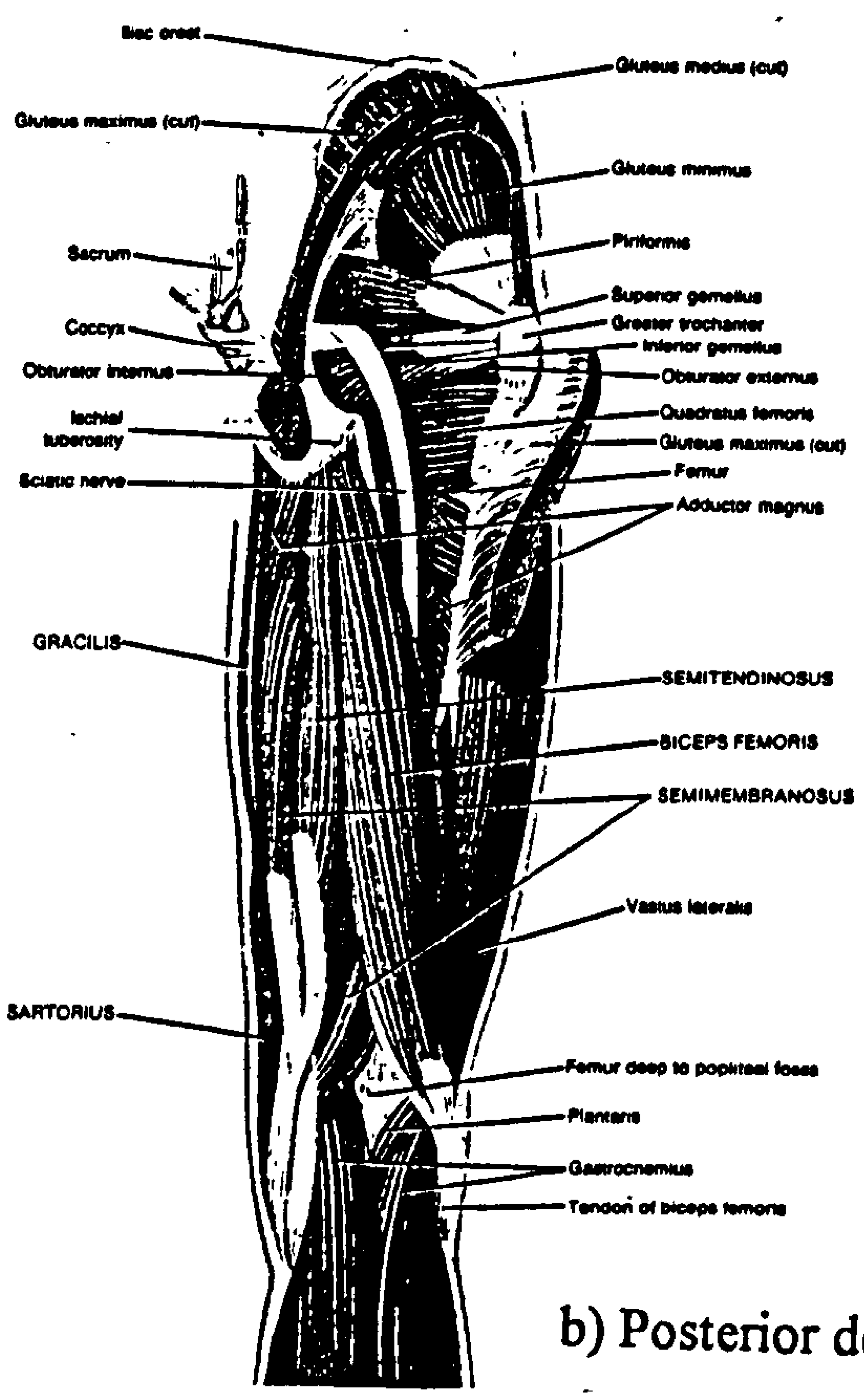

b) Posterior deep view

Fig. 2.3.2.2 Muscles that move the thigh. (Tortora and Anagnostakos, 1990) quadriceps femoris, sartorious iliapsoas muscles and the tensor fascia lata, whose primary actions are flexion, abduction and lateral rotation of the thigh. The medial muscle group consists mainly of the adductors of the thigh, namely the adductor brevis, longus and magnus and the pectineus. The gluteal muscles group viz, the gluteus maximus, medius and minimus are located posteriorly and laterally. These muscles provide abduction to the thigh. The hamstrings are situated inferiorly and posteriorly providing flexion to the legs and extension and adduction of the thigh.

2.4 TRANS-FEMORAL AMPUTATION SURGERY

The following sections describe the various techniques of trans-femoral amputation.

2.4.1 Myoplasty and Myodesis

In the process of amputation, muscles that are divided need to be given a suitable attachment to prevent retraction. Two methods are used, myoplasty and myodesis. In myoplasty, the divided muscles are sutured to opposing muscles and in myodesis, muscles are attached to the bone. Before the introduction of total contact sockets, myoplasty was discouraged so as to reduce the amount of soft tissue at the distal end of the residual limb. This is because in the non-total contact socket, weight bearing is largely proximal to the residual limb creating a situation for distal oedema formation.

Due to amputation at the thigh level, agonist and antagonist muscles are divided unequally. Most of the adductor and hamstrings are severed which can cause an abduction and flexion contracture. In shorter stumps such contracture becomes more pronounced and can cause problems in prosthetic fittings. Suturing antagonist and agonist muscles as in myoplasty, redresses muscle balance and the amount of contracture should be reduced. The procedure also leads to better circulation, decreased phantom pain and better muscle function, discouraging cases of serious muscle atrophy. Myoplasty alone has been known to contribute problems due to the femur of the residual limb migrating in the muscle envelope producing pain and

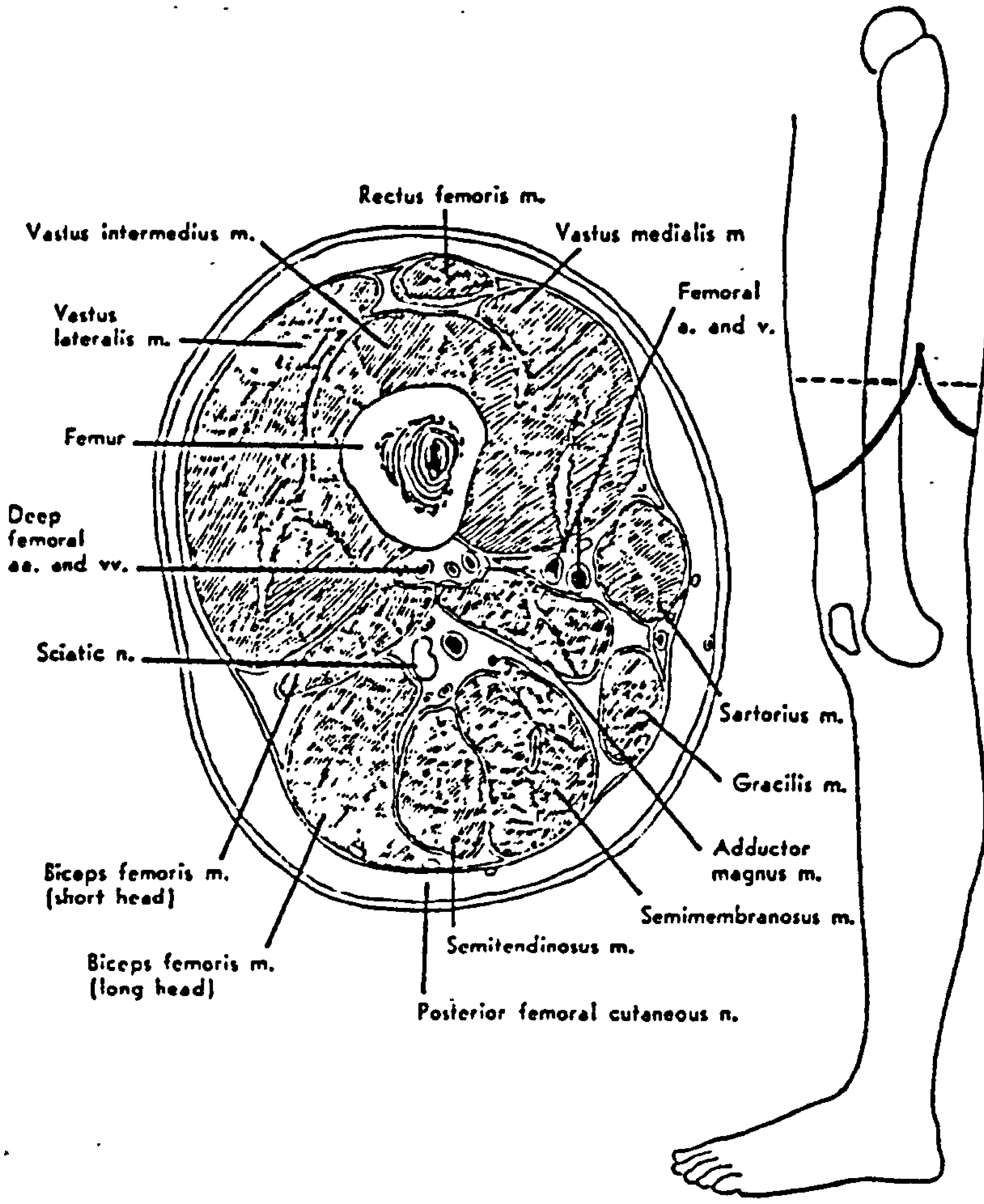

Fig. 2.4.2.1 Incision line and muscles involved in trans-femoral amputation. (Dederich, 1985)

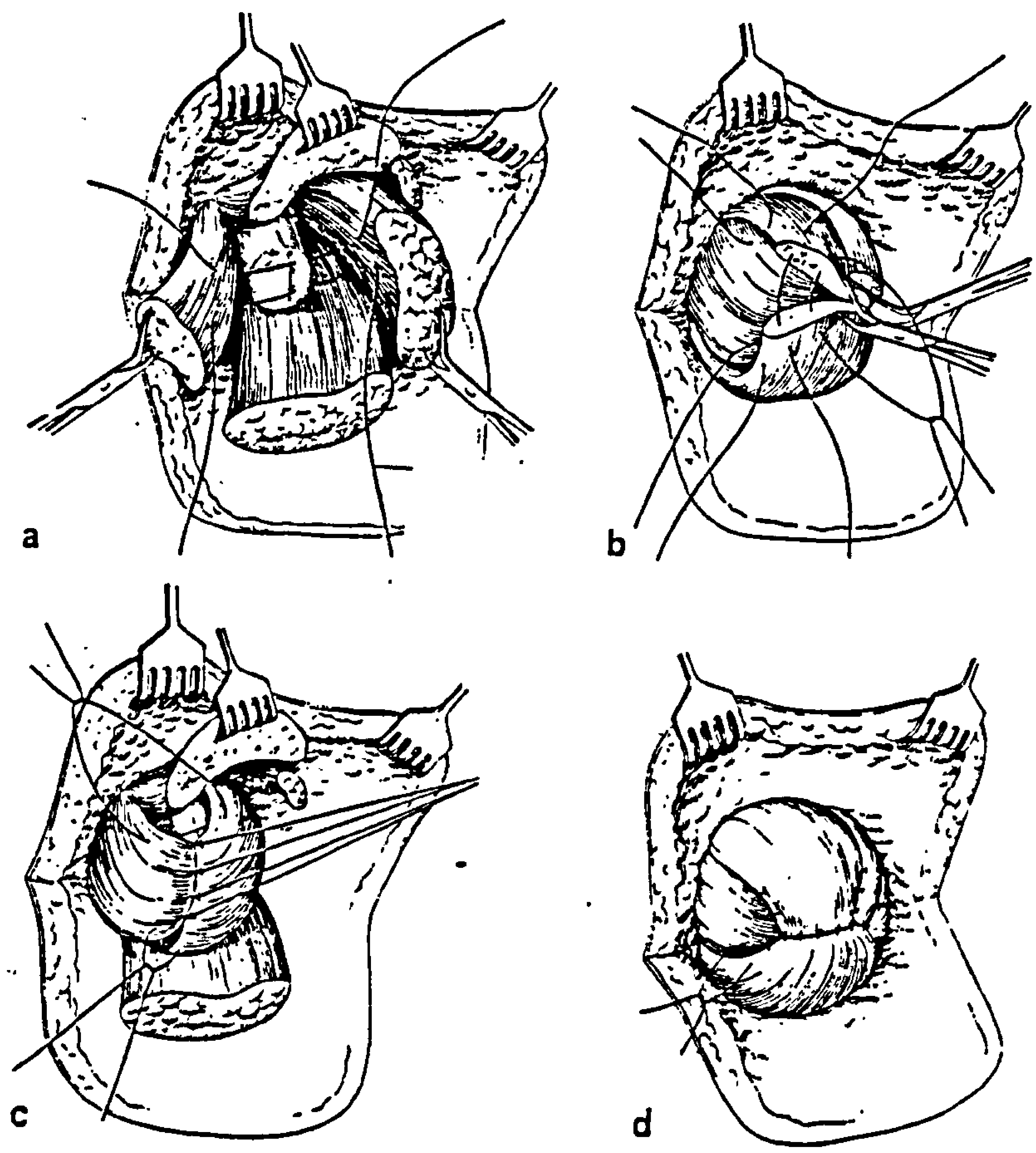

Fig. 2.4.2.2 Trans-femoral amputation according to Dederich. (Dederich, 1985)

compromising prosthetic fittings. Thus myodesis is used to prevent muscles' migration by suturing muscles to the bone before myoplasty commences. This combined method is nowadays widely practised and accepted as the better method.

Myopexy is sometimes carried out in place of myodesis. Muscles are sutured to the periosteum instead of the bone. This is particularly practised in the case of children, preventing any need to drill holes into the bone.

2.4.2 Surgical Techniques

The main difference observed in many transfemoral amputation techniques is in the way in which muscles are attached. Different muscle groups are selected for myoplasty and myodesis. In this section, the methods used by Weiss (1966), Dederich (1963), Murdoch (1968), Burgess (Gerhardt et al 1982) and Gottschalk (1992) are discussed to highlight the variety and procedures in trans-femoral amputation. Once the level of amputation on the thigh is confirmed, commonly the line of incision is marked off to show two flaps (Fig. 2.4.2.1). The anterior flap used to be longer creating a suture line which is posterior, but Neff (1988) recommended in critical cases, wound healing being a priority, the suture line can be directly across the stump. The position of scars is less significant and can be accommodated with modern prosthetic fittings. Tourniquets are seldom used in surgery except in ischaemic disease. Using the marked line as guide, incisions are made through the skin, subcutaneous tissues and deep fascia. Muscles are identified and sectioned to the bone. The muscles of the thigh are divided into four major groups these being the adductors, abductors, extensors and flexors. Femoral vessels and sciatic nerves are ligated and dissected slightly proximally to the bone section. The dissected sciatic nerve is gently separated out of the scar area and covered by deep muscles, reducing the discomfort that can be caused by neuroma formation at the distal scar.

Weiss (1966) introduced myodesis to all the divided muscles. The muscles are sectioned level with the bone section and anchored using suture to drill holes in the femur. Dederich (1985) described myoplasty and myopexy (Fig. 2.4.2.2). The periosteum is sutured over the end of the femoral bone. The adductors and abductors

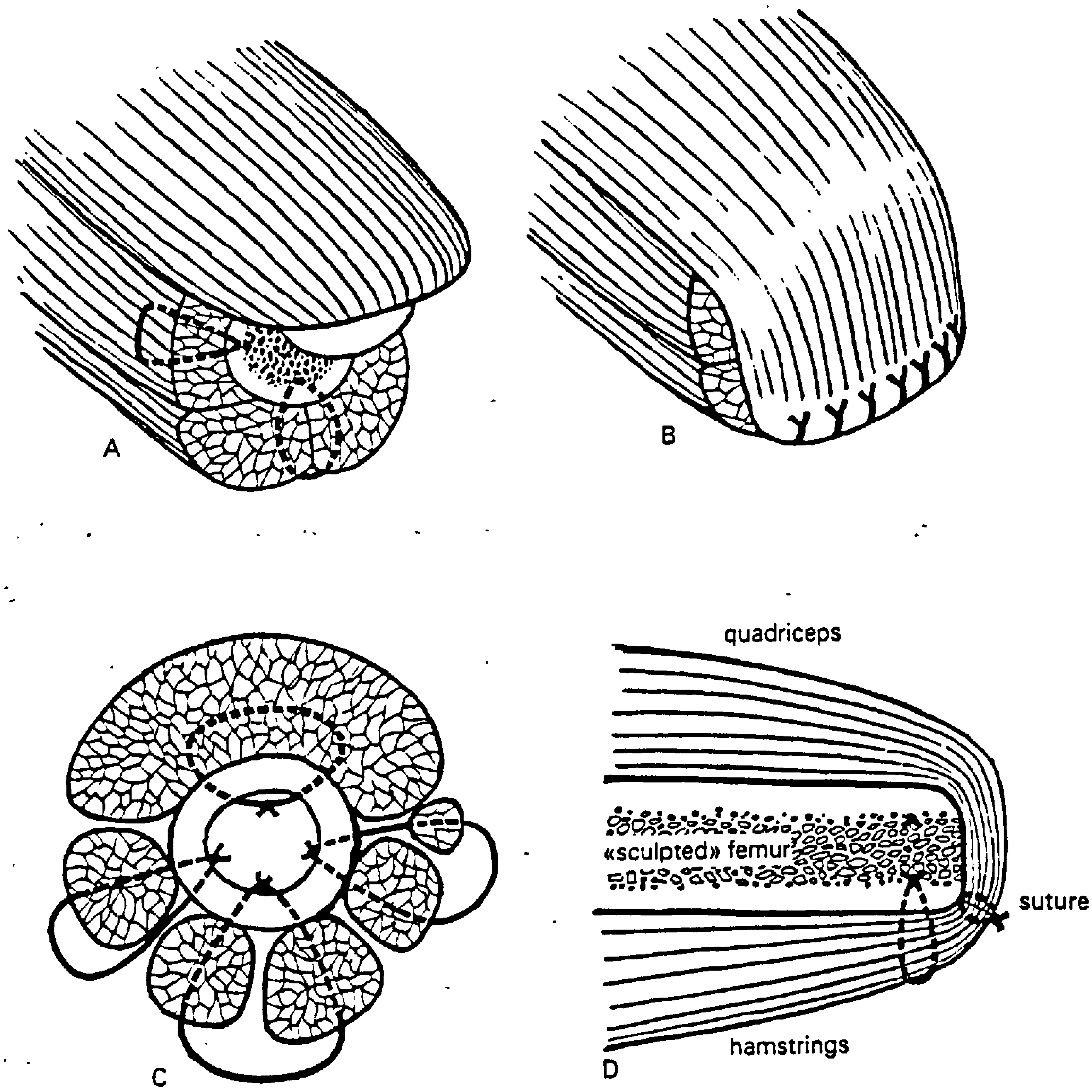

Fig. 2.4.2.3 Murdoch method of trans-femoral amputation.
(Gerhardt et al, 1982)

are then sutured to the periosteum after which they are sutured together over the bony end. The extensor and flexors are sutured together perpendicularly to and over the adductor and the abductor muscles. Murdoch and Burgess' method is basically a combination of the two aforementioned techniques. Murdoch (1968) sectioned all the muscles except the quadriceps to the same level as the sectioned bone (Fig.2.4.2.3). The quadriceps are left long enough to cover the bony end of the femur. Myodesis is performed on all muscles. To complete the surgery, the quadriceps are sutured with the hamstrings covering the end of the femur.

Burgess (Gerhardt et al 1982) similar to Dederich, divided the muscles into four major groups and dissected them longer than the bone section (Fig.2.4.2.4). Holes are drilled at the distal end of the sectioned femur laterally, medially and anteriorly. Myodesis of the quadriceps, adductors and abductors is carried out. The hamstrings are not sutured to the bone but brought over the end of the cut bone to meet with the quadriceps and sutured. The adductors and abductors are then brought crosswise over the sutured hamstrings and quadriceps, and sutured to each other. Sutures are also placed on the overlapped muscle groups..Both Murdoch and Burgess utilise the advantages from myoplasty without any risk of the muscles slipping off the end of the sectioned femur causing pain.

Gottschalk (1992) sutured the adductor magnus tendon to the lateral aspect of the cut end of the femur through drilled holes (Fig. 2.4.2.5). Sutures are also placed anteriorly and posteriorly to prevent the muscle sliding off the bone. The quadriceps are than brought over the adductor magnus and sutured to the posterior aspect of the femur. Finally the hamstrings muscles are sutured to the posterior area of the adductor magnus.

Upon securing the muscles, drain tubes are inserted to lie under the skin flaps. The skin flaps are then sutured together closing the wound with the drain activated to prevent haematoma formation. The wound is dressed with gauze and the stump covered with cotton wool and bandages.

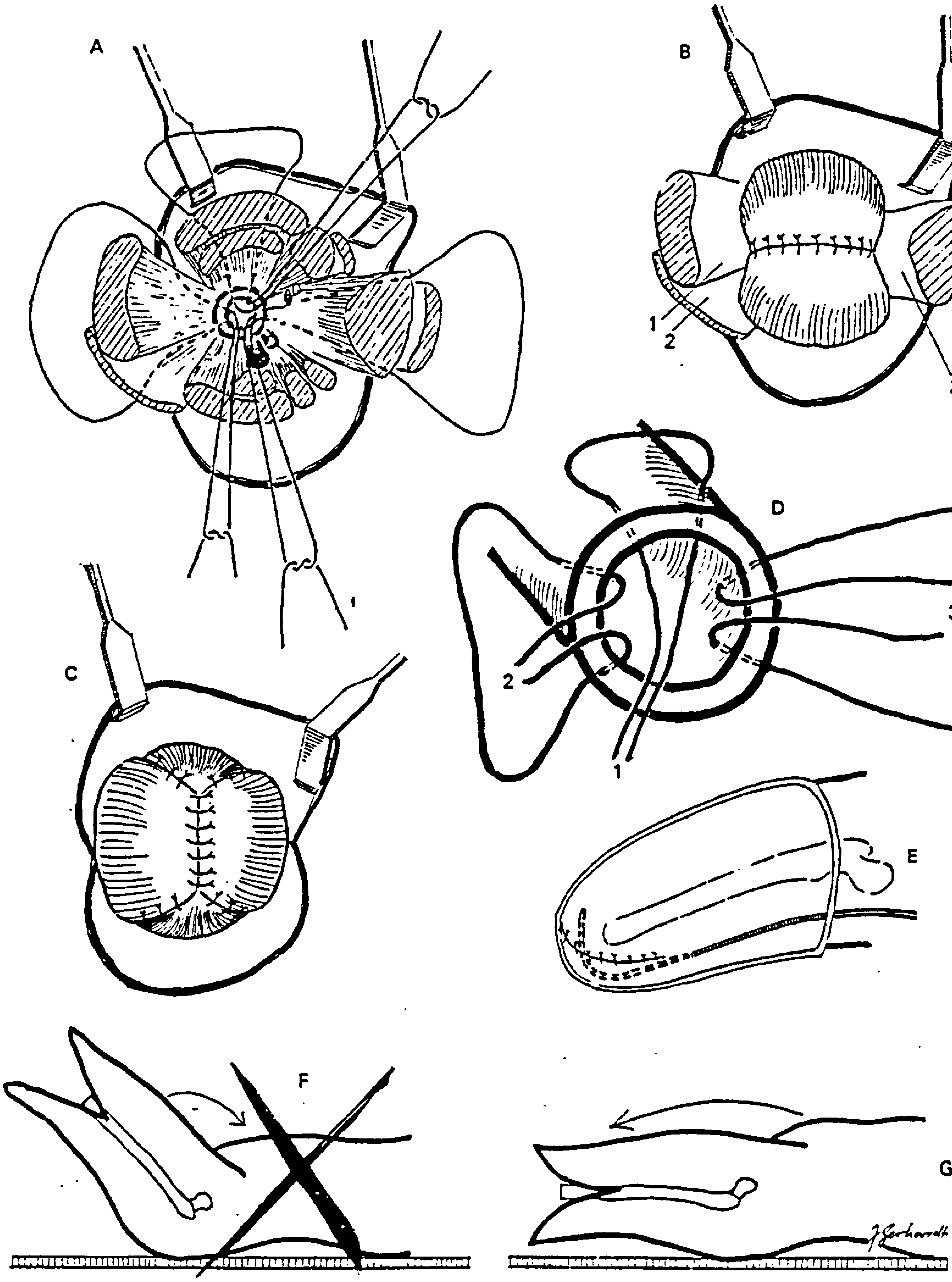

Fig. 2.4.2.4 Burgess method of trans-femoral amputation.
(Gerhardt et al , 1982)

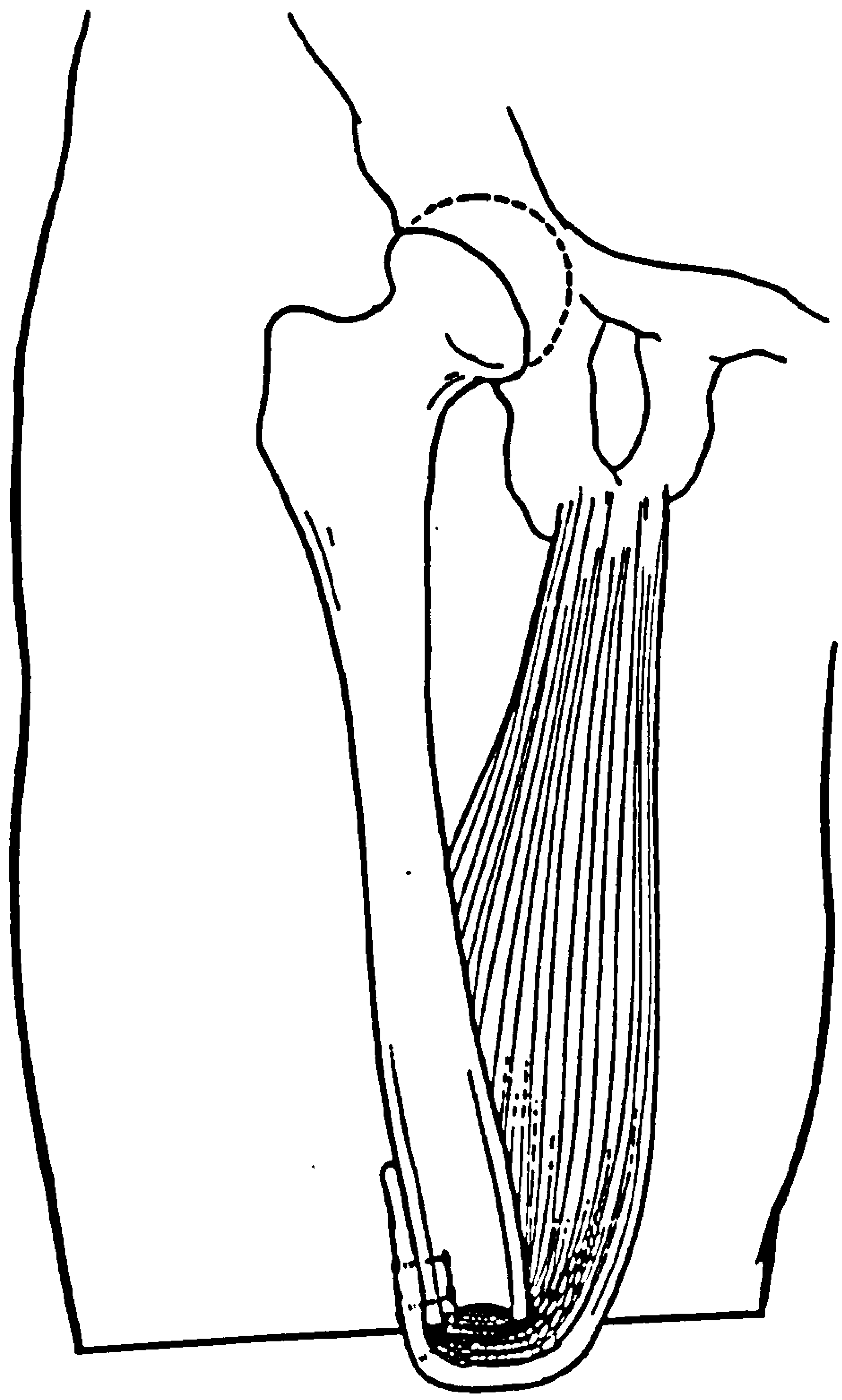

a) Adductor muscles sutured to drill holes of the femur.

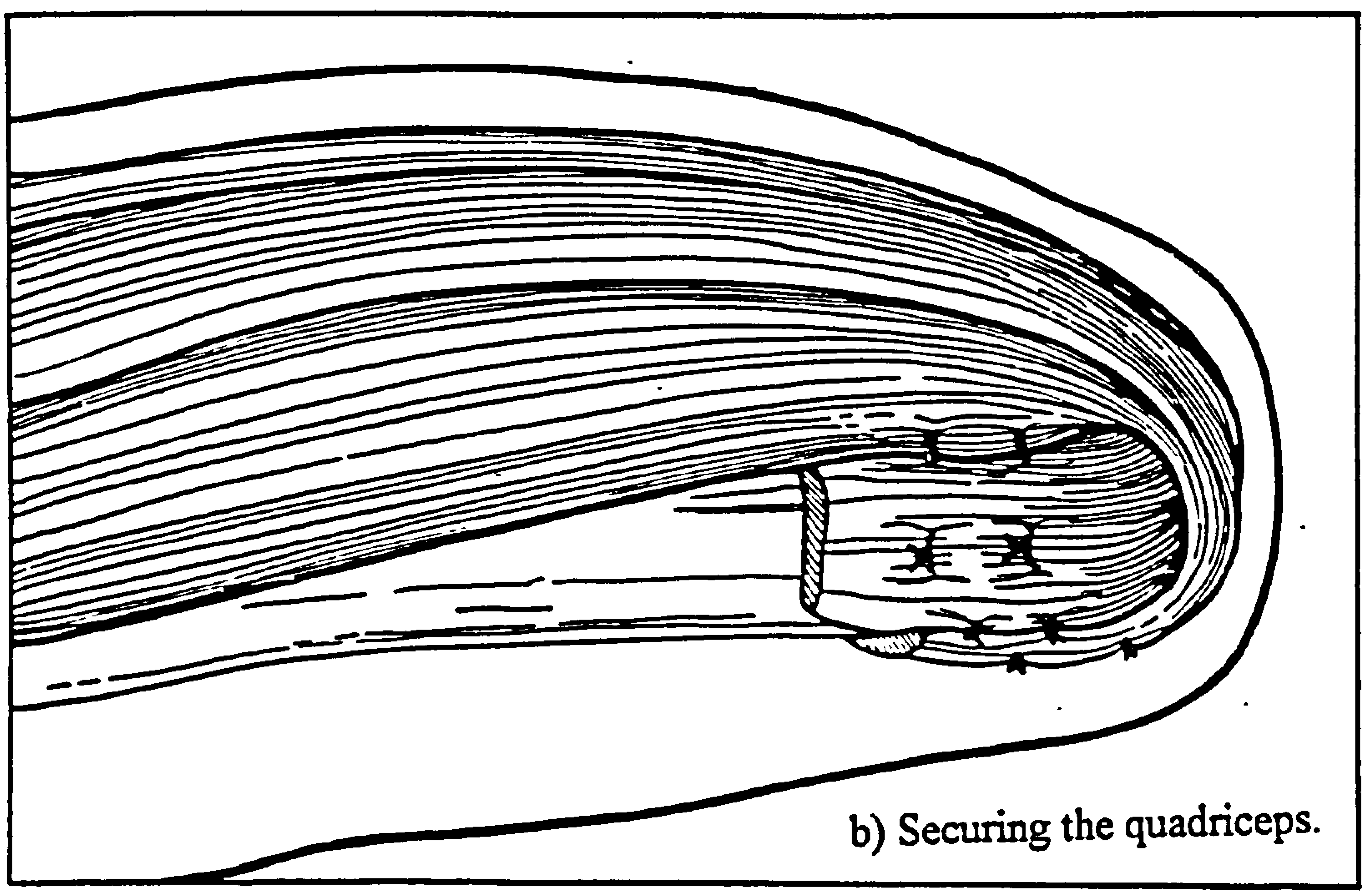

b) Securing the quadriceps.

Fig. 2.4.2.5 Gottschalk method of trans-femoral amputation. (Gottschalk, 1992)

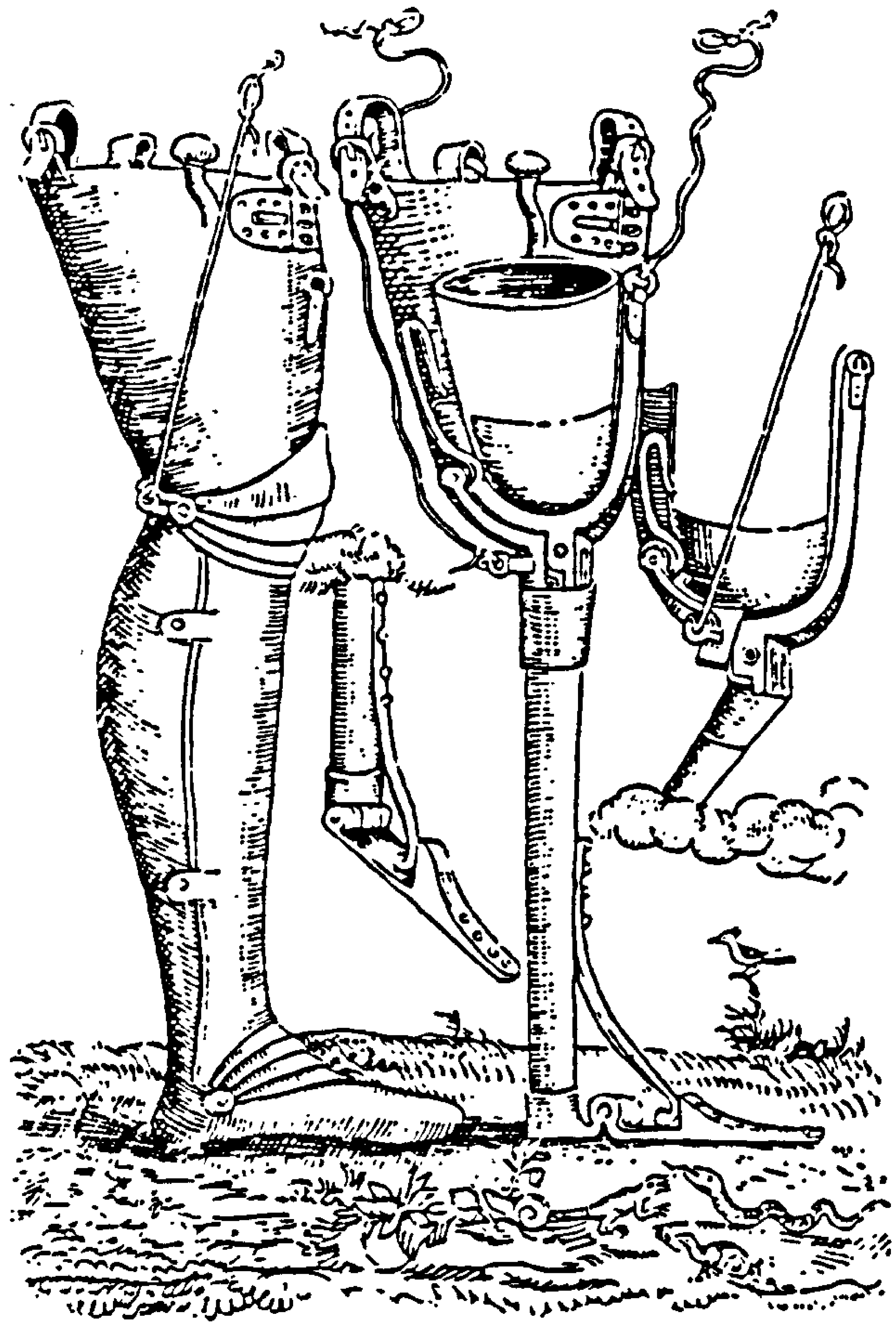

Fig. 2.5.1.1 Ambroise Paré artificial limb. (Wilson, 1970)

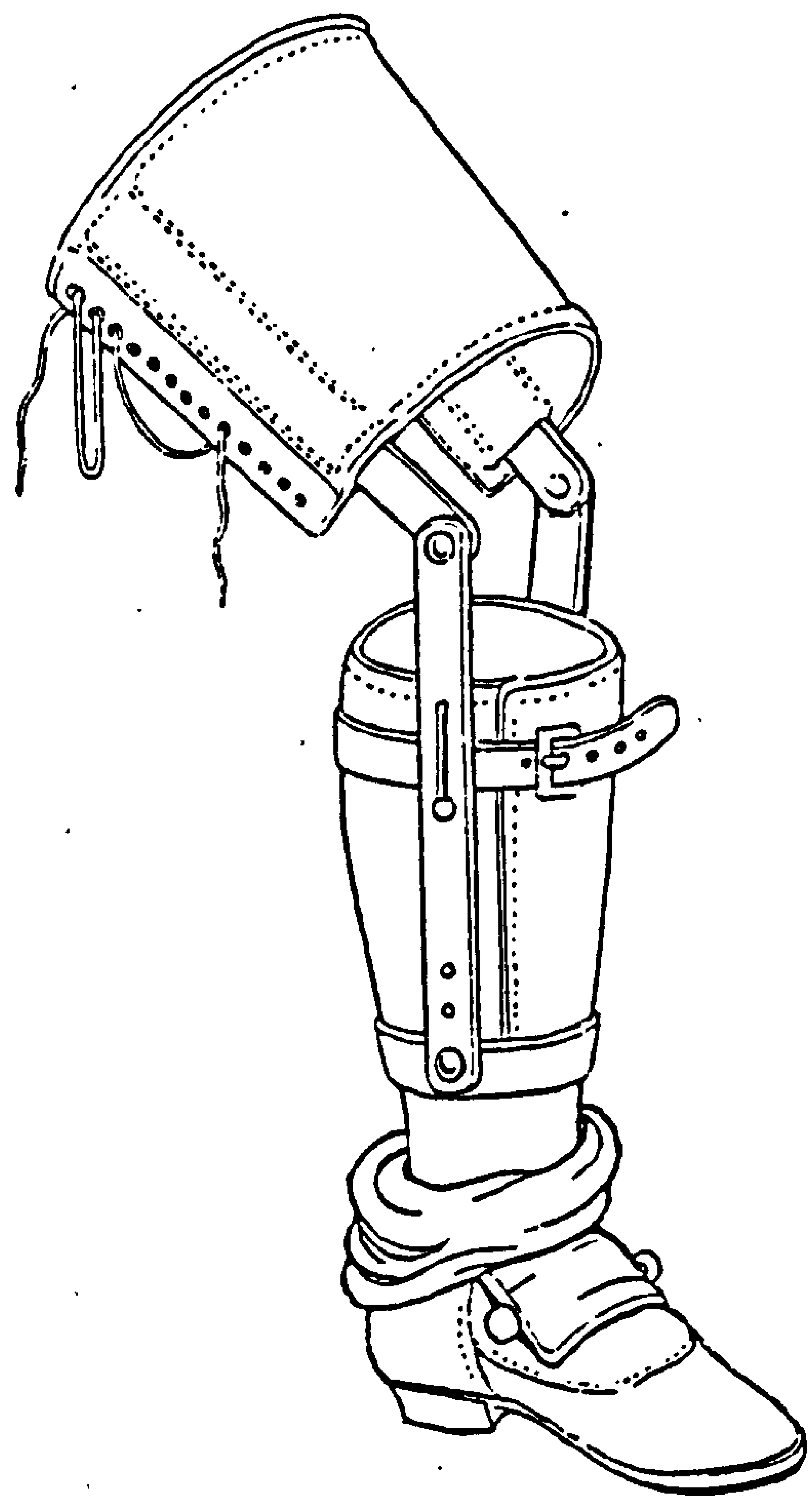

Fig. 2.5.1.2 Verduyn trans-tibial prosthesis. (Sanders, 1986)

2.5 THE ARTIFICIAL LIMB

The components that make up the trans-femoral artificial limb are the socket, knee and the ankle/foot assembly. The use of a suspension system to aid attachment of the artificial limb is no longer prescribed unless a total contact suction socket is found unsuitable for the patient. This section gives a brief review of the history of artificial limbs followed by discussions on sockets, which is the main concern of this project. Readers interested in the knee, ankle/foot assembly can refer to Sanders (1986).

2.5.1 Early history of lower limb prosthetics

An infamous documentation of early prosthesis usage would be that of the case of a Persian soldier Hegosistratus in 484 B.C, who escaped imprisonment by severing his own foot by which he was secured. In replacement, he designed a wooden foot which served its purpose until he was recaptured and executed by the Spartans. Hegosistratus' eagerness to walk normally again prompted him to use a wooden foot. Thus, a prosthesis can be seen as a replacement for appearance and function rather than an addition. Though the original Greek meaning of the word "prosthetic" is "addition".

In the early days, prostheses were fashioned in the likeness of the lost limb. A Roman prosthesis dated as far back as 300 B.C resembled the thigh, knee and calf. Armourers in the 15th century besides manufacturing armour and arms also produced artificial limbs for soldiers who lost their limbs in warfare. These 15th century devices can be functional or just decorative to complete the aesthetic requirement of the suit of armour. For the ordinary peasants, wooden peg legs were widely used to fulfil the functional needs.

In 1529, Ambroise Paré invented the first artificial limb (Fig. 2.5.1.1) for trans-femoral amputees, which employed articulated joints (Wilson 1970). Pieter Adriaanz Verduyn, a Dutch surgeon, in 1696 produced the first artificial limb for transtibial amputees (Fig. 2.5.1.2). The prosthesis bears a similarity to modern prostheses incorporating a leather thigh corset and socket, and hinges that allow articulation at the knee. (Sanders 1986). In 1816, the Marquis of Anglesey made

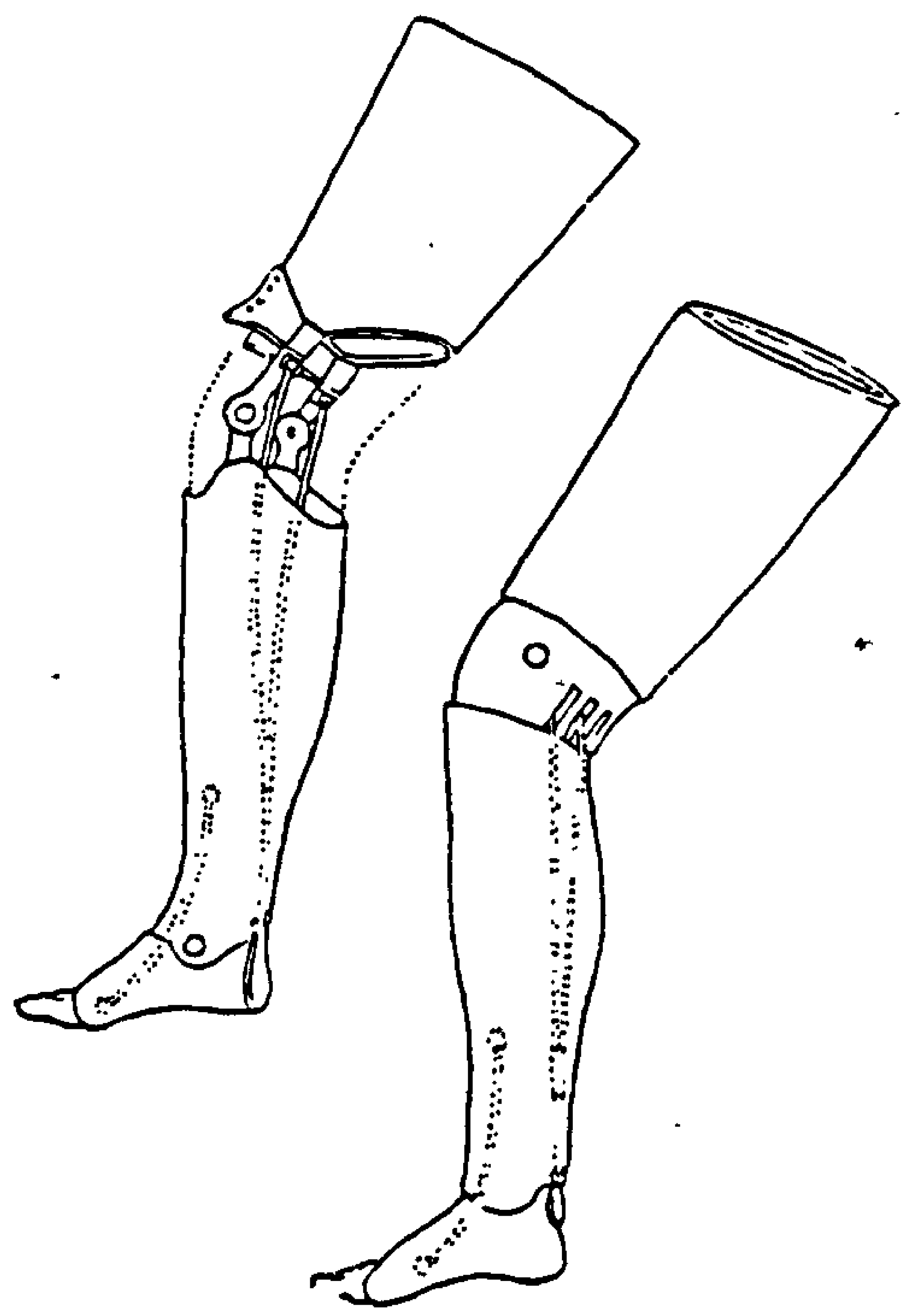

Fig. 2.5.1.3 James Pott's trans-femoral and trans-tibial prostheses.
(Wilson, 1970)

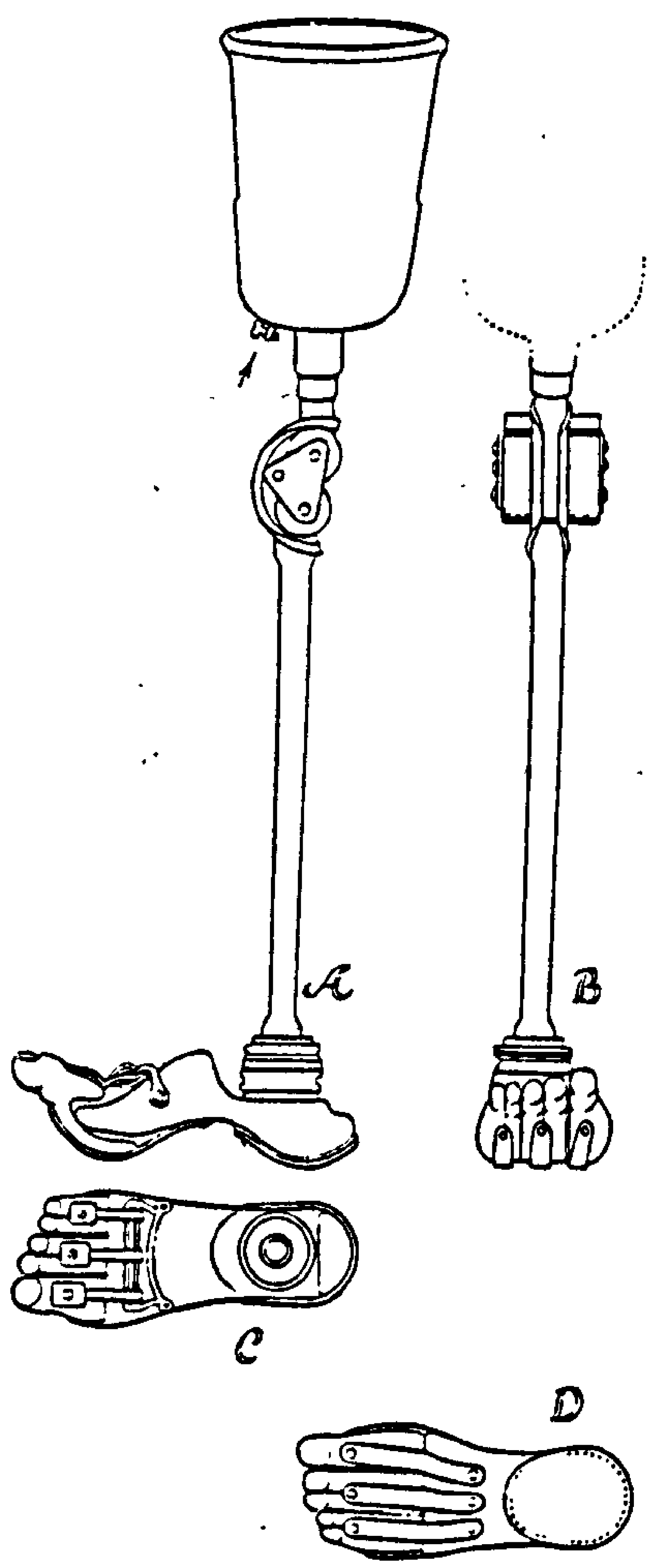

Fig. 2.5.1.4 The Parmelee prosthesis with suction socket.
(Sanders, 1986)

popular the 'Anglesey leg' which was prescribed to him by James Potts of London. These prostheses for both transfemoral and transtibial amputees consist of an articulated foot connected with artificial tendons to the knee (Fig. 2.5.1.3). The Anglesey leg was later introduced to the United States by William Selpho from England. After much modification, it was later known as the American leg. Much of the attention to improving the artificial limb was placed at the articulating joints. Selpho improved the American leg at the ankle using a rubber plate and Benjamin F. Palmer introduced the Palmer leg in 1846, describing movable knee and ankle joints controlled by artificial tendons. In 1859, Amasa A. Marks produced a leg that articulated at the knee, ankle and toes. Dubois D. Parmelee, an American, patented the Parmelee leg which consisted of a multiarticulated foot and a polycentric knee joint in 1863 (Fig. 2.5.1.4). Not much work was done however in improving the socket. In 1831, Jean Gaspard Blaise Goyrand considered designing a socket accommodating the ischial tuberosity for weight bearing purposes. The patented Parmelee leg was the first to introduced the concept of using atmospheric pressure to secure the socket onto the residual limb. The socket at that time was usually shaped to be similar to the residual limb. Its purpose was to contain the residual limb providing functions of the knee, ankle and foot that was lost through amputation. Little consideration was given to the shape of the socket to enhance proprioception, encourage muscle usage and distribute pressure at the residual/limb socket interface, though the success of human and prosthesis interface begins with the shape of the socket. The work in socket design was hampered largely by the only available material and technology available of that time. Unlike the large selection of ferrous and non-ferrous materials suitable for knee and ankle components, the choice of material available for sockets was wood and leather. An example of such a hindrance is the concept of the suction socket by Parmelee which only became a huge success when plastics were introduced to prosthetics.

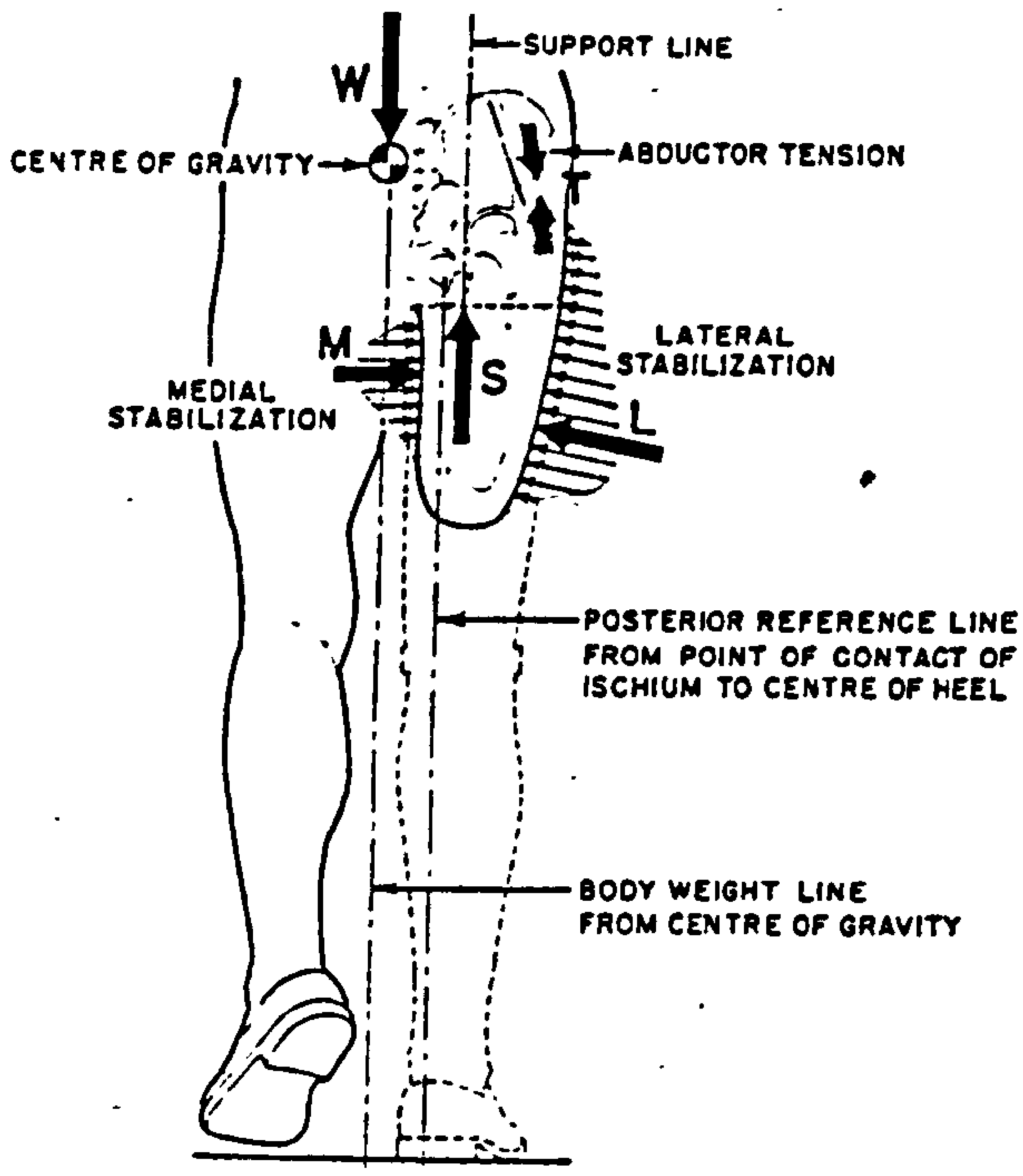

Fig. 2.5.2.1 Medio-lateral stabilisation. (Radcliffe,1977)

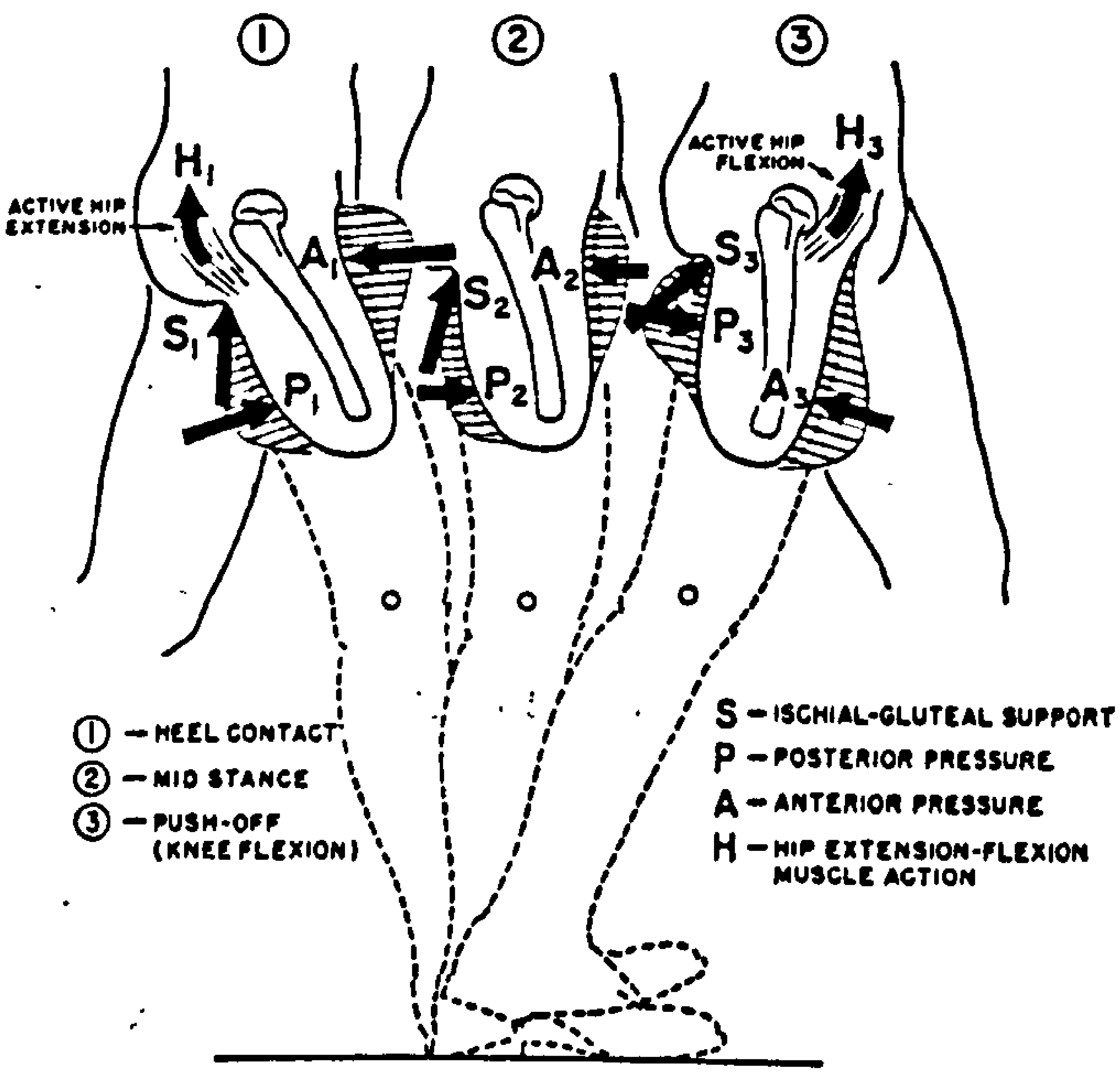

Fig. 2.5.2.2 Anterior-posterior stabilisation. (Radcliffe, 1977)

2.5.2 Biomechanics of the trans-fermoral prosthesis

In a normal subject, the action of walking is accomplished by the action of a series of muscles, stabilising the body. Similarly, the trans-femoral amputee has to achieve body stabilisation with the aid of the artificial limb components and with the existing musculature in the residual limb. Due to the prosthesis being a foreign interface, stabilisation is usually achieved at the expense of cosmetics, gait, comfort and higher physiological energy consumption.

Stability during gait can be viewed in two planes, the medio-lateral (M-L) plane and the anterior-posterior (A-P) plane (Fig 2.5.2.1 and Fig 2.5.2.2). The normal subject in the M-L plane, during walking, exhibits a pelvic tilt towards the unsupported side. To stabilise the pelvis, this tilt is minimised by the hip abductors being active (Fig 2.5.2.3). In the case of the trans-femoral amputee, there exists a support point defined as the centre of action of all vertical supporting forces transmitted through the prosthetic socket. This converts the pelvis into a lever with the support point acting as the fulcrum for two end loads, the body weight and the abductor muscles' tension (Fig 2.5.2.4). In this lever system, the body weight will cause the pelvis to rotate towards the unsupported side. The amputee balances this motion using the abductor musculature. Contraction of the abductor muscles will create a lateral movement of the femur bringing the femur closer to the lateral socket wall. To prevent any large migration of the femur laterally and subsequent pain, the lateral socket wall must provide lateral stabilisation and comfortable pressure distribution. If the lateral socket wall fails in this aspect, the lateral movement of the femur will create localised pressures at the distal end of the residual limb resulting in painful contact. The amputee's reaction to this incommodious situation is to adopt a gait which could relieve the distal pressures by leaning over the prosthesis and walking with a wide base, swaying from side to side. By leaning over the prosthesis, the body weight line which passes through the centre of gravity of the body is brought to coincide with the support point, relieving the work of the abductor musculature thus reducing pressure created at the distal end of the residual limb. Another situation that brings about a similar gait deviation is weak abductor muscles. The weak

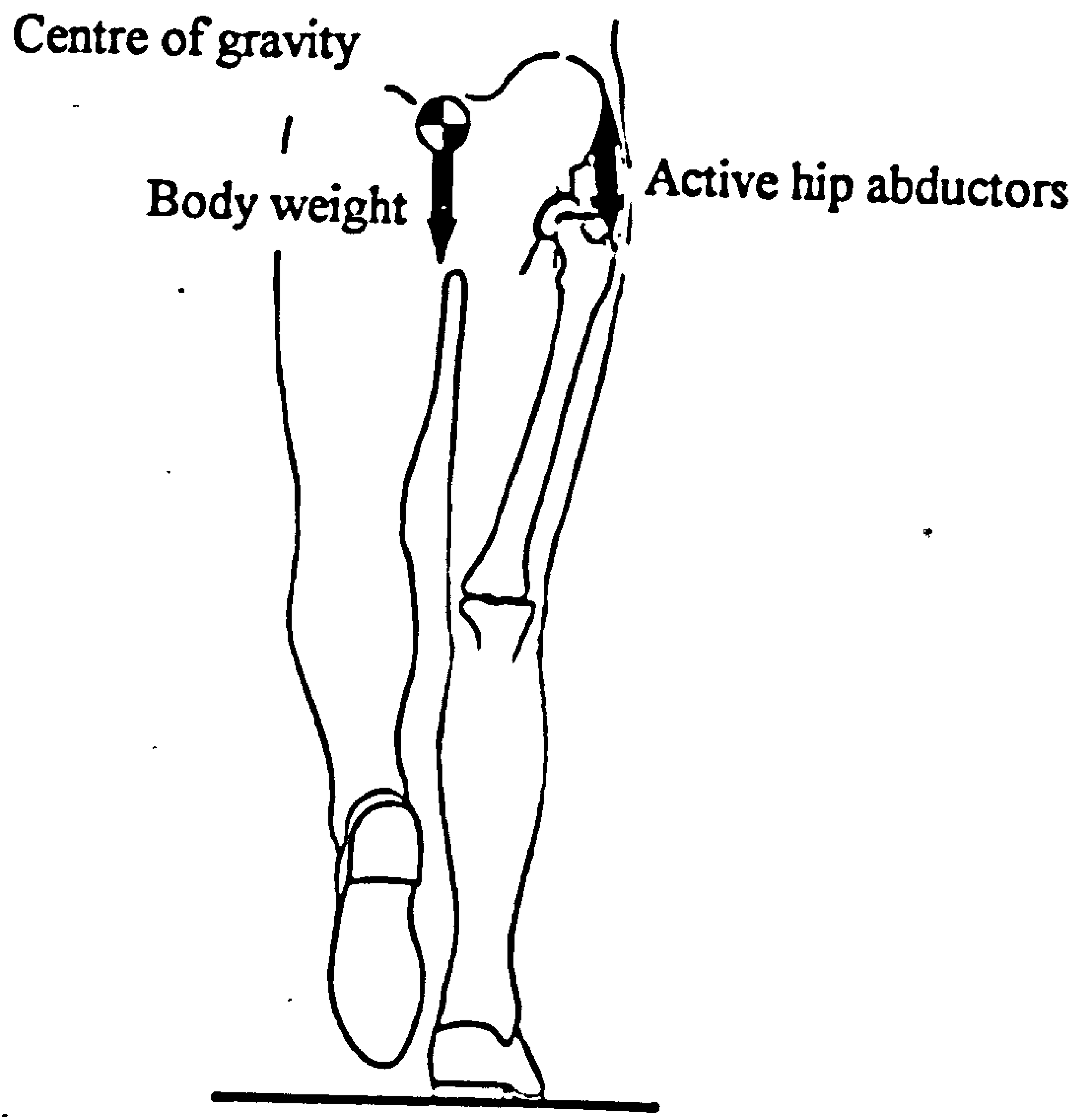

Fig. 2.5.2.3 Pelvis stabilised by active hip abductors.

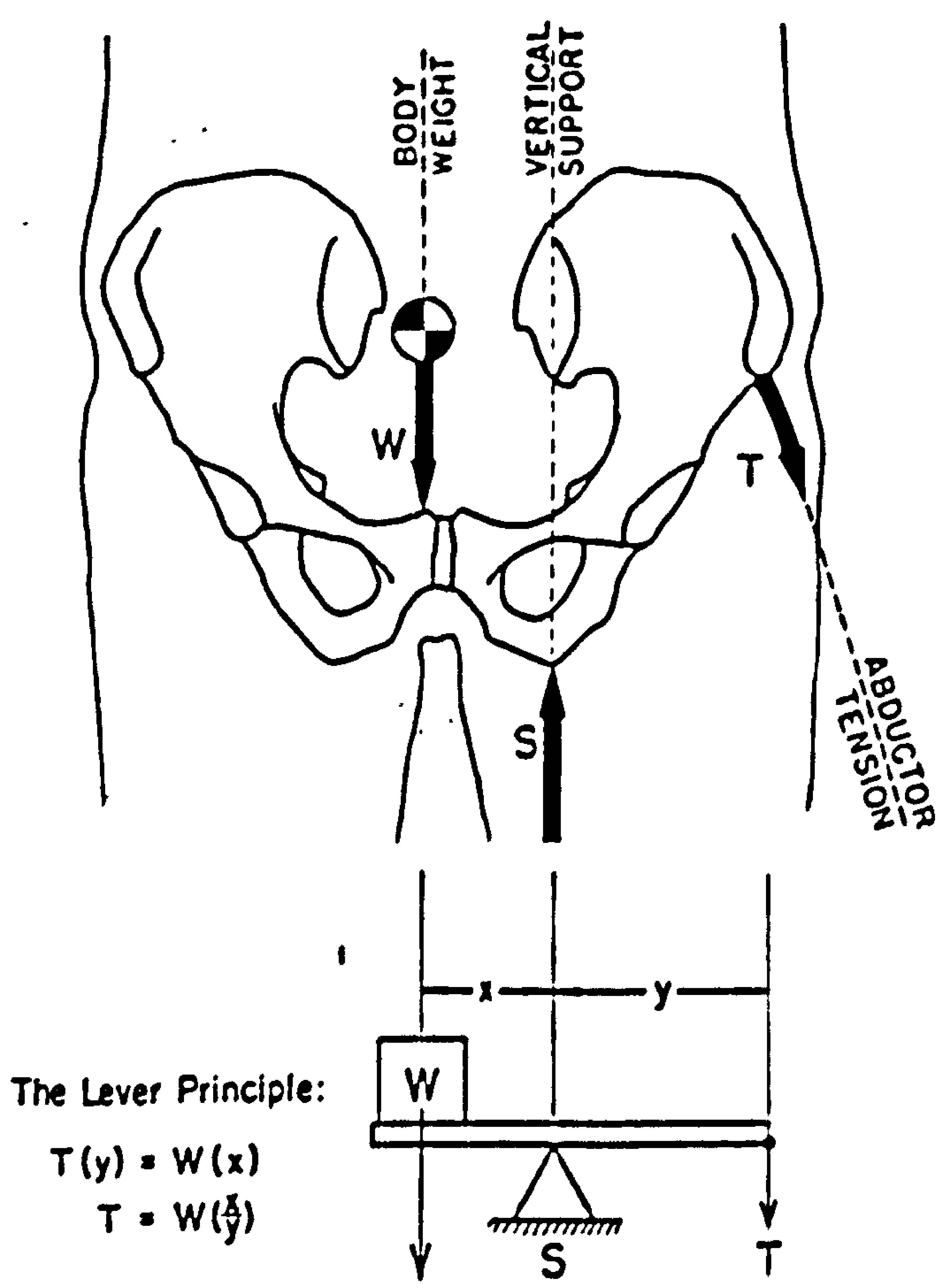

Fig. 2.5.2.4 The pelvic lever system. (Radcliffe, 1955)

musculature cannot prevent the pelvis dipping towards the normal side causing increased pressure at the interface between the residual limb and medial wall of the socket at the crotch area. This pressure is again relieved by leaning over the prosthesis and walking with a wide base gait.

The role of the lateral wall is therefore to provide adequate lateral support with comfortable pressure distribution. The wall keeps the residual limb in adduction, reducing lateral movement of the femur and maintaining the abductor muscles close to their normal rest length in order to work at maximum physiological efficiency. A properly adducted residual limb achieved by the lateral wall of the socket gives rise to only lateral counter-pressure at the medial wall (Fig. 2.5.2.1). Any vertical pressure that can cause discomfort at the crotch area is reduced to a minimum.

The A-P stability may be determined by the position of the knee joint. The knee joint can be locked to provide maximum stability or adjusted to give restricted voluntary knee control. The latter enables the amputee to prevent knee buckling at heel strike but allows controlled movement using hip musculature during the swing phase of gait. Fig 2.5.2.2 shows the A-P residual limb/socket interface pressure pattern during the stance phase of an amputee using a uniaxial knee joint. At heel strike, the muscles' activity is predominantly from the hip extensors, creating counter-pressures at the proximal anterior surface and the distal posterior surface of the residual limb. At mid stance, the abated activity of the hip extensors decreases the pressures experienced at the residual limb/socket interface. The pressure pattern up to this point is still similar since the vertical ground reaction force is in front of the knee joint, ensuring knee stability. It is only at heel off that the ground reaction force appears behind the knee joint, causing the knee to flex. The amputee then begins to initiate the swing phase using the hip flexors. The pressure patterns at the residual limb socket interface change. Anterior pressures are now concentrated distally while posterior pressures are proximal to the residual limb.

Based on the biomechanical principles outlined, the trans-femoral prosthetic socket appears to be more complex than merely a receptacle following the shape of the residual limb. In fact, the final shape of the socket is usually quite different from

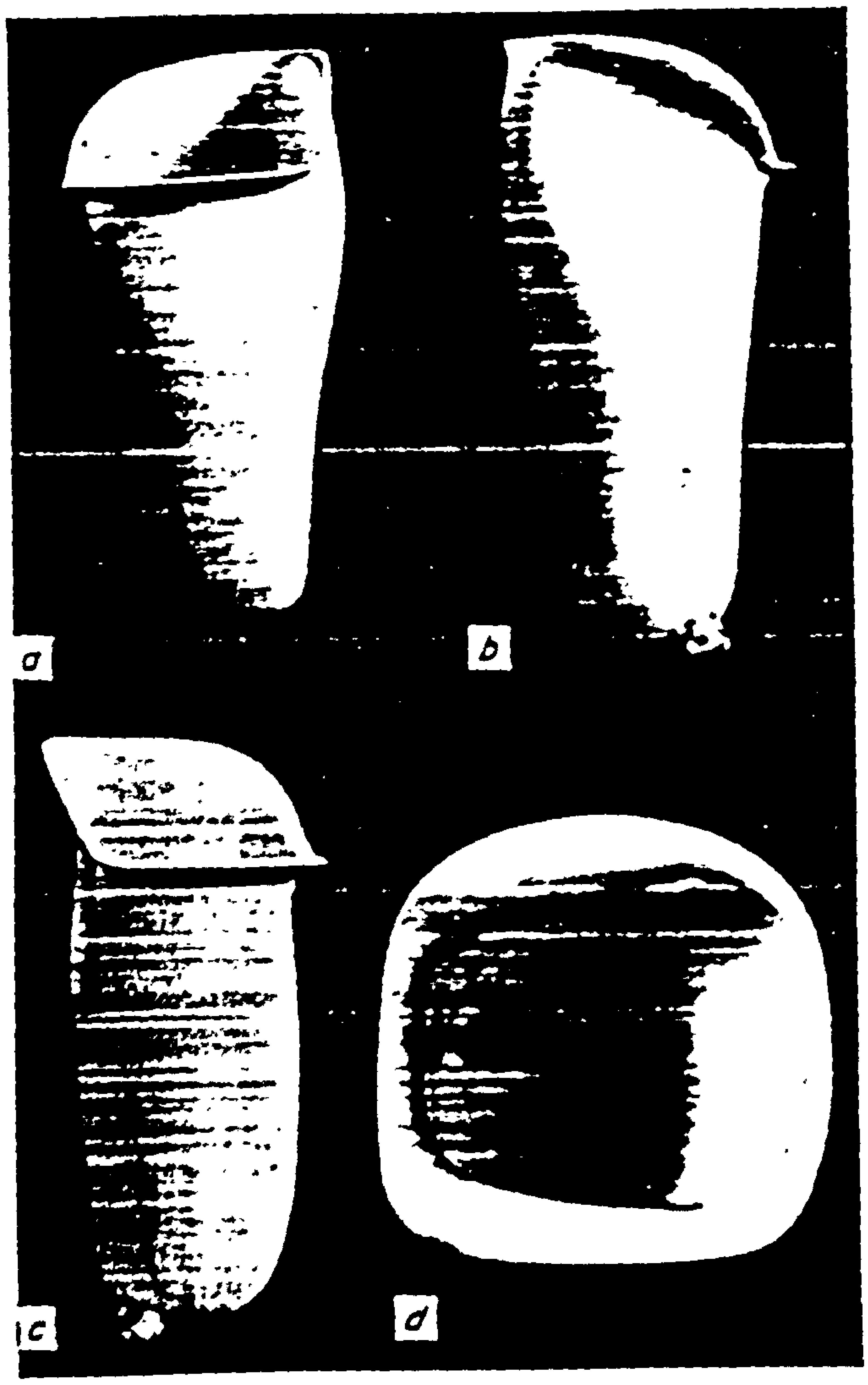

Fig. 2.5.3.1 Quadrilateral socket. (Lyquist, 1970)

the residual limb shape. Consideration must be given to the initial shape of the residual limb, the areas where weight bearing is possible and the pressure distribution expected during standing and gait. Two types of sockets are used in the course of this project, the quadrilateral and the ischial containment socket. The former socket has its origin from Europe and was introduced to the United States by the University of California (Eberhart and Inman 1947). Extensive studies were conducted with this socket shape (Radcliffe 1955) resulting in the socket of choice from 1964 until very recently when the ischial containment sockets emerged in the 1980's .

The author of this thesis at this point would like to draw the attention of the reader to the fact that the biomechanical principles outlined in this section make no reference to the type of socket, though these principles are adopted from Radcliffe (1955, 1977) who is the main developer of the quadrilateral socket. The author views the presented biomechanical principles as principles leading to a good fitting socket regardless of whether they are quadrilateral or other trans-femoral socket types. This view will be expounded later in the following section describing the two types of sockets.

2.5.3 The quadrilateral Socket

The quadrilateral socket takes its name from its appearance when viewed in the transverse plane (Fig 2.5.3.1). There are four distinct walls which make up the quadrilateral shape. At the brim level of the posterior wall, there is a wide seat parallel to the ground known as the ischial seat. A large percentage of weight bearing is directed to the ischial tuberosity resting on the ischial seat. Other sources of vertical support are provided by the gluteal musculature at the posterior wall. A certain amount of vertical support is also possible at the anterior brim of the socket (Radcliffe 1977).

The lateral wall is about 50 mm higher than the ischial seat. Very often the extended wall encloses the greater trochanter, providing M-L stability, especially in shorter residual limbs. Enclosing the greater trochanter also discourages abduction of the residual limb. The lateral wall tapers towards the distal end of the socket

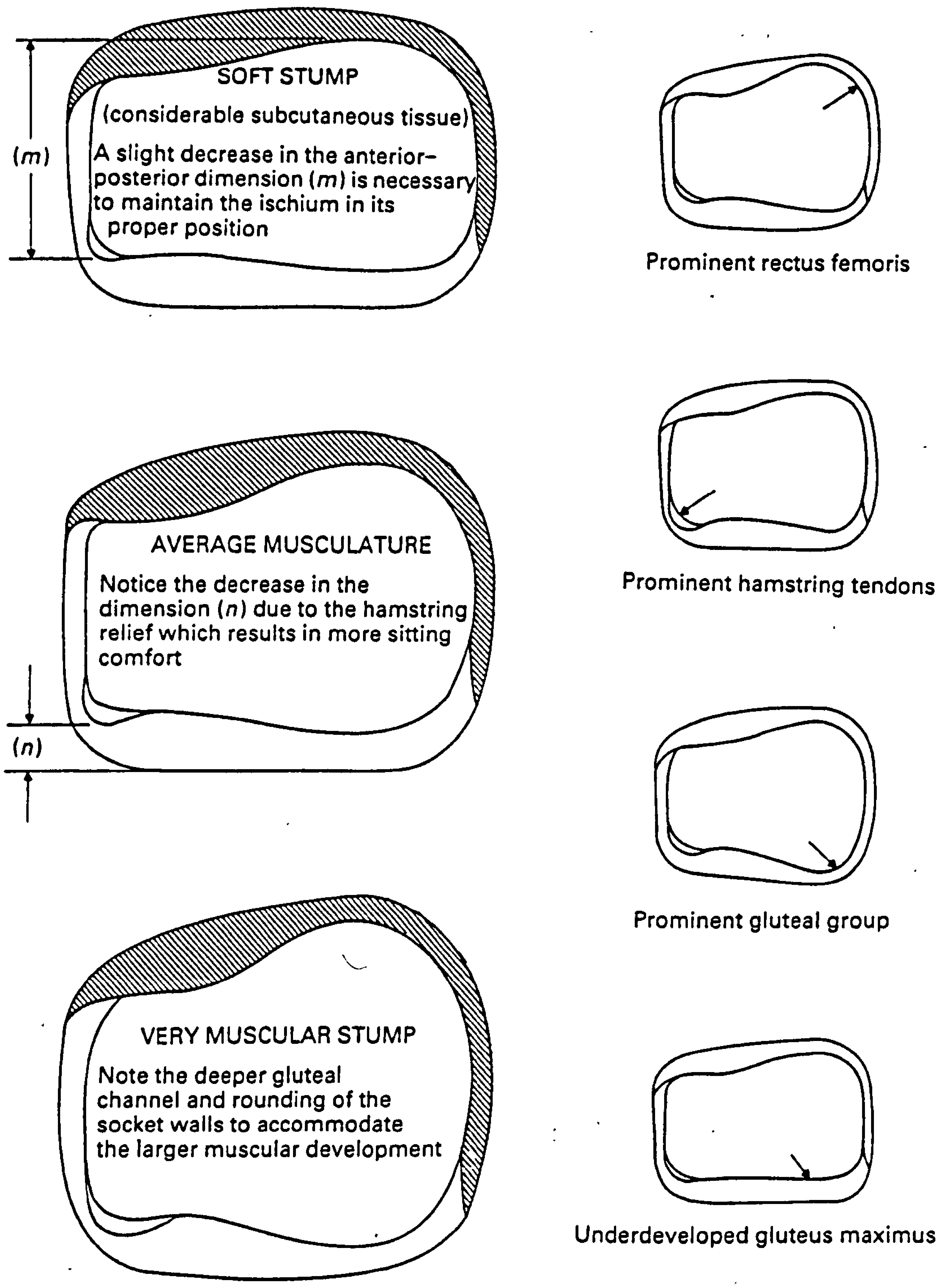

Fig. 2.5.3.2 The quadrilateral socket shape is influence by the muscular development of the residual limb. (Radcliffe, 1955)

providing adduction of the femur to a similar extent to that of the sound femur for unilateral amputees. Firm pressure is exerted along the shaft of the adducted femur by a flattened lateral wall, distributing the lateral pressure over a wider area. The distal end of the lateral wall is contoured to receive the cut end of the femur, and provides a relief to any development of localised pressures.

The height of the medial wall is determined by the crotch line height which usually approximates to the same level as the posterior brim. The A-P dimension at brim level follows the measurement obtained from the adductor longus tendon to the ischial tuberosity. The upper third of the medial wall is flat and perpendicular to the ground. This creates a suitable wall to accommodate pressures that arise during midstance firing of the hip abductors muscles. The flat wall flares outwards towards the perineum forming a comfortable brim proximally at the crotch area.

The vital function of the anterior wall is to maintain the ischium on the ischial seat. The anterior wall is raised by 50-75mm above the ischial seat. The raised section of the anterior wall is flat and protrudes inwards, applying pressure over the area of the Scarpa's triangle and stabilising the position of the ischial tuberosity. Superiorly the anterior brim flares outwards to prevent any pinching of flesh during sitting.

The posterior wall contains the gluteal musculature. Relief of the adductor muscles at the crotch area can be achieved by relieving the gluteus muscles with an enlarged posterior wall. Too tight a fit over the gluteus muscles can cause over crowding of the adductor muscles at the crotch area. At the posterior brim is the ischial seat. The seat should be adequately wide to provide proper positioning of the ischium. It should neither be too wide to cause any discomfort when the amputee sits nor too narrow to cause the ischial tuberosity to slip in or out of the socket.

The overall shape of the quadrilateral socket is highly dependent on the muscular development of the residual limb. Prominent and under developed muscles must be accommodated by a relief or a decrease in dimensions respectively in the socket shape (Fig. 2.5.3.2). Two dimensions are important to the success of the quadrilateral socket. These are the anterior-posterior (A-P) and medio-lateral (M-L) dimensions. The quadrilateral socket is wider at the M-L dimension. The M-L dimension governs the amount of adduction of the femur, when too large, permits the pelvis to drop towards the normal side, increasing the crotch pressure and causing discomfort. A correct A-P dimension ensures the ischial tuberosity location on the ischial seat.

In the past, socket fabrication usually employs a two casts method. The first step involves casting the proximal part of the stump forming the ischial ring. The hardened ring is then removed from the residual limb, reinforced and introduced back in the residual limb forming the ischial seat. The remainder of the residual limb is then wrapped with plaster bandages joining the ischial ring. Presently, the adjustable brim developed by the University of California, Biomechanics Laboratory (Foort 1963) has now largely replaced the need to cast an ischial ring. Fabrication using the adjustable brim will be discussed in chapter 3.

2.5.4 The ischial containment Socket

The potential of an alternative design to the quadrilateral socket began when Long (1975) initiated a study to determine the femoral alignment of transfemoral amputees. Long (1975, 1985) investigated the femoral angle of 100 transfemoral amputees prescribed with the quadrilateral socket and by using X-rays, found 92 to have a difference in angle compared to the sound limb. But the more significant revelation was that 91 of the amputees experienced femoral abduction. Following this finding, new socket designs were attempted which promised to maintain the femur in adduction. The new socket designs bear one similarity in shape which is the enclosure of the ischial tuberosity and ramus in the socket, hence these sockets are generally termed ischial containment sockets or ischial-ramal weight bearing sockets (Schuch 1988). The ischial containment sockets have also come under different names accordingly to their developers. They are ;

a) Normal Shape-Normal Alignment (NSNA) transfemoral prosthesis by Long (1985). The NSNA prosthesis is now adopted and taught by the Prosthetic Education Centre at the Northwestern University in Chicago.

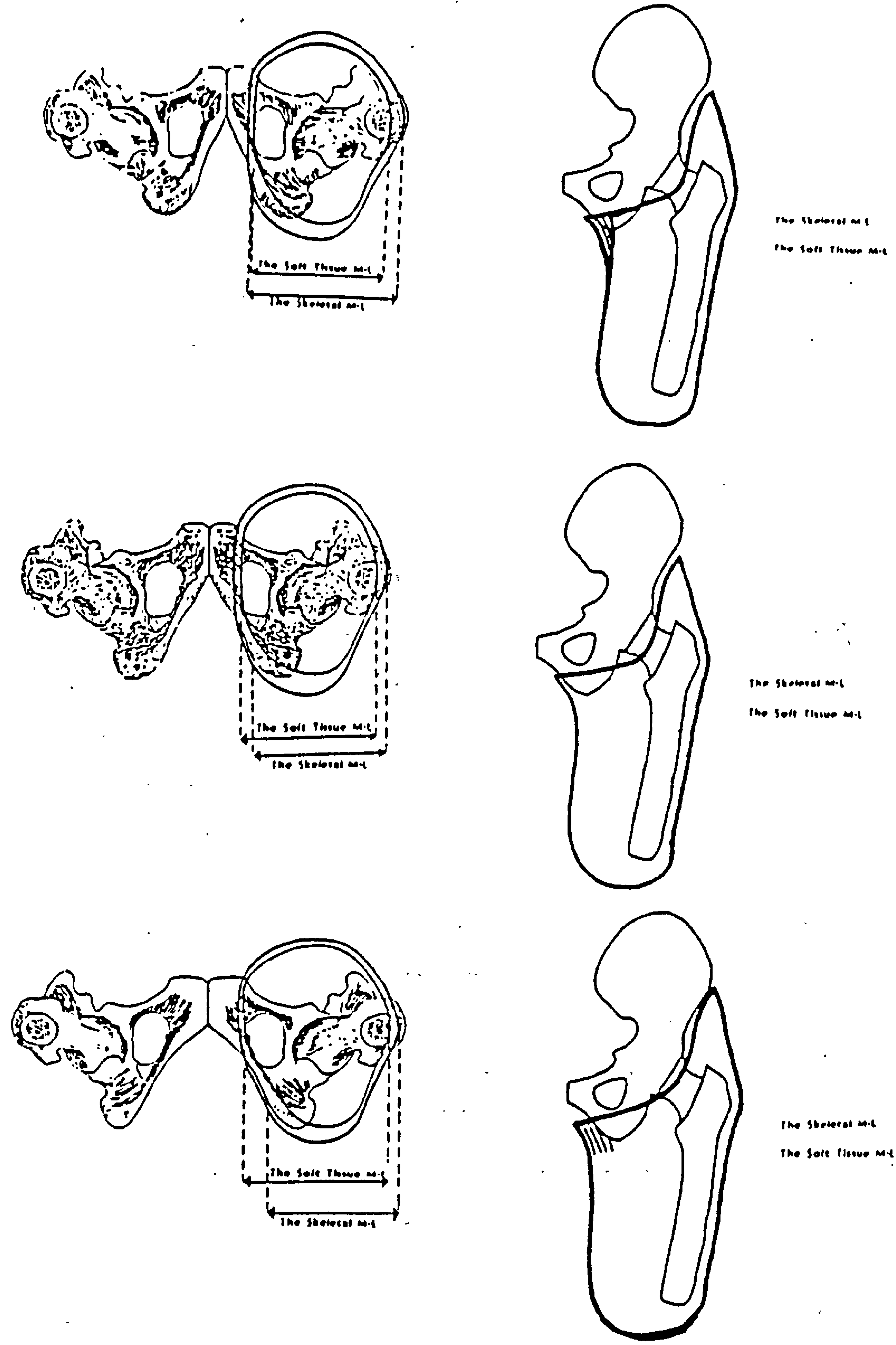

Fig. 2.5.4.1 The variation of the ischial containment socket shape for different pelvic and soft tissue medio-lateral dimensions. (Schuch, 1992)

b) Contoured Adducted Trochanteric-Controlled Alignment Method (CAT-CAM) and Skeletal CAT-CAM (SCAT-CAM) prosthesis by Sabolich (1985).
c) University of California Los Angeles CAT-CAM (UCLA CAT-CAM) prosthesis, which in the beginning resembled the CAT-CAM prosthesis by Sabolich, but through independent research and development has now departed from Sabolich CAT-CAM philosophy.
d) The Shamp brim, for the Narrow ML trans-femoral prosthetic socket. For the Shamp brim type socket, a brim casting system similar to that of the quadrilateral brim casting method is adopted, though the aforementioned ischial containment socket developers have all claimed that hand casting techniques proved to be more successful. (Schuch 1988)

The proximal contours of the ischial containment socket are based on the pelvic skeletal anatomy. Unlike the quadrilateral socket, where muscular variation primarily determines the proximal contours, the medio-posterior brim of the socket slopes proximally to the ischium and captures the ischium and ramus securely (Schuch 1992). Weight bearing is primarily concentrated at this area through the medial aspect of the ischium and the ramus. The amount of ischial ramus containment differs slightly among the types of sockets. The NSNA and the UCLA CAT-CAM sockets provide a limited enclosure, while the CAT-CAM/ SCAT-CAM sockets proceed as far proximally as possible in capturing the ischial ramus. Sabolich (1985) claimed the higher medial brim provides an excellent bony interlock for M-L stability and rotational control. The ischium and ramus are kept in position accurately by two measurements, the skeletal and soft tissue M-L dimensions (Fig. 2.5.4.1). The former is measured from the inferolateral edge of the greater trochanter to the medial aspect of the ischium. Just distal to this measurement is the soft tissue M-L dimension which gives an impression of the overall diameter of the residual limb. Long (1985) reported a tabulated guide to determine the M-L dimension of the socket using the circumference measured just below the ischium (Table 2.5.4.1). These figures were established from about 500 good fitting NSNA sockets averaging eight years old. The

Circumference just below ischium	Goal M-L
9"	−2.5
10"	−2.7
11"	−2.9
12"	−3.1
13"	−3.3
14"	−3.5
15"	−3.7
16"	−3.9
17"	−4.1
18"	−4.3
19"	−4.5
20"	−4.7
21"	−4.9
22"	−5.1
23"	−5.3
24"	−5.5
25"	−5.7

Table 2.5.4.1 Long's table defining M-L dimension of the ischial containment socket. The circumference of the residual limb just below the ischium is measured. Following the table, a circumference of 17" will require a socket M-L dimension of 4.1". (Long, 1985)

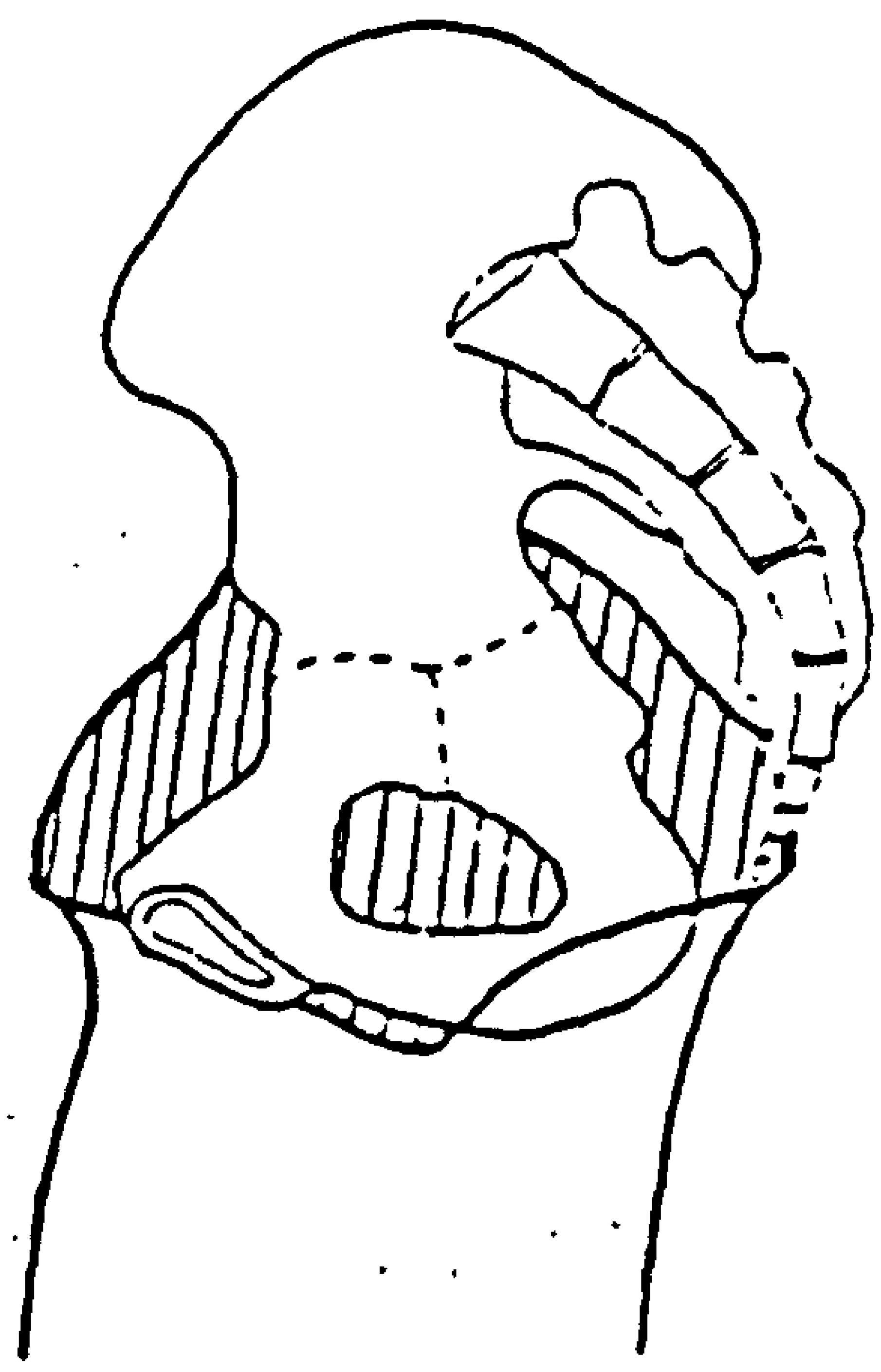

Fig. 2.5.4.2 Medial brim of the ischial containment socket. (Schuch, 1988)

medial brim finally contours distally as it proceeds towards the anterior surface, clearing the pubis ramus and the adductor longus (Fig. 2.5.4.2)

The lateral wall of the ischial containment socket serves two purposes: firstly to keep the ischial ramus in position and secondly to ensure adduction of the femur. The lateral wall rises extensively above the greater trochanter enclosing the bony landmark tightly and maintains the skeletal M-L dimension. Pressure generated at the medial brim is balanced over the greater trochanter enclosure (Fig. 2.5.4.3). Thus a large socket surface area is essential to distribute pressure over the greater trochanter. The lateral wall distal and posterior to the greater trochanter slant aggressively, exerting pressure on the gluteal musculature supplementing weight bearing. The lateral wall is also kept close to the femur throughout the socket length exerting firm lateral pressure to keep the residual limb in adduction.

The posterior brim (Fig. 2.5.4.2) rises above the ischial tuberosity keeping the ischium inside. The brim flares outwards proximally following closely the contours of the soft tissue. The posterior wall encompasses the gluteal musculature which was speculated as a major (about 33%) vertical weight bearing site (Radcliffe 1977).

The anterior brim is just proximal to the inguinal crease. The final height is determined by the brim clearing the superior iliac spine when the patient is sitting.

The emphasis on the ischial containment socket has always been on the M-L stability, hence the M-L dimension. In contrast to the quadrilateral socket, the M-L dimension is less than the A-P dimension.

2.5.5 Comparing quadrilateral and ischial containment sockets

The obvious difference in shape of the ischial containment socket compared with the quadrilateral socket (Fig. 2.5.5.1) presented a case for reviewing the biomechanical requirements of the trans-femoral socket. To quote Sabolich (1985), "The old principles of the quadrilateral design simply do not function, since we are dealing with a completely different design in shape, contour, and biomechanical principles." But how accurate this statement is, is still high on the agenda of any discussions on transfemoral socket fittings. Pritham (1990) investigated such claims

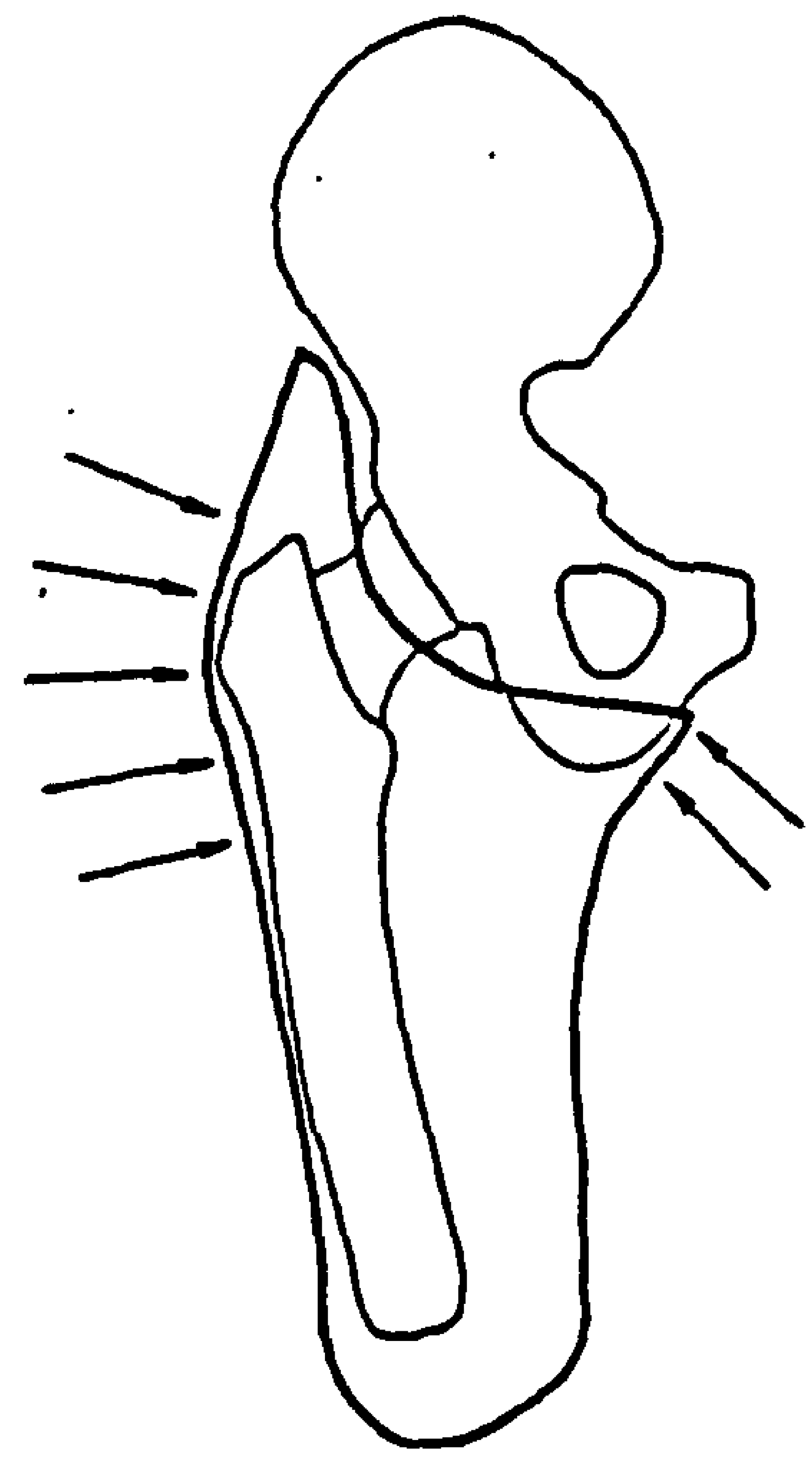

Fig. 2.5.4.3 Counter- pressure developed at the lateral wall over the greater trochanter of the femur. (Pritham, 1990)

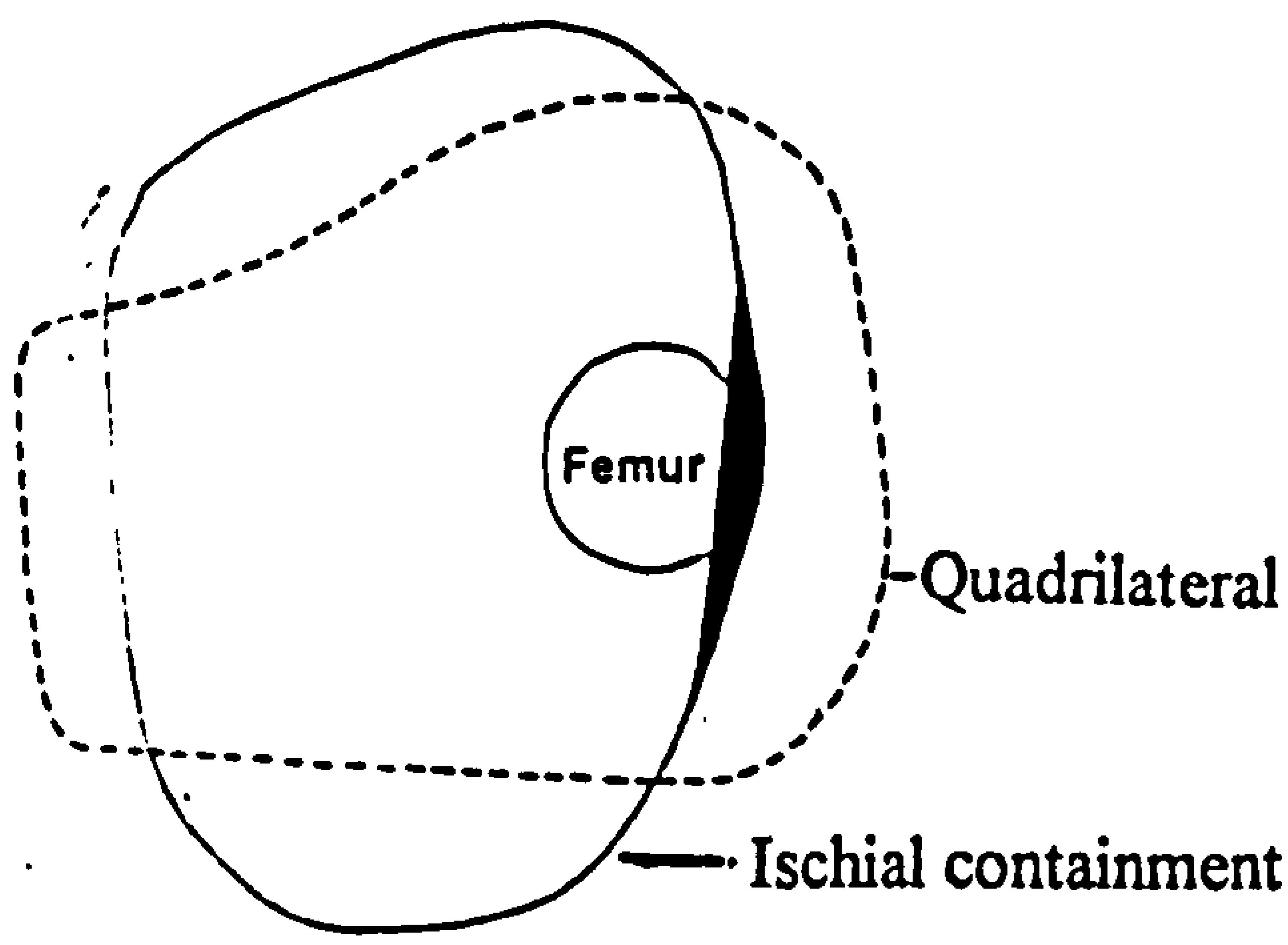

Plan view at brim level of the two type of socket.

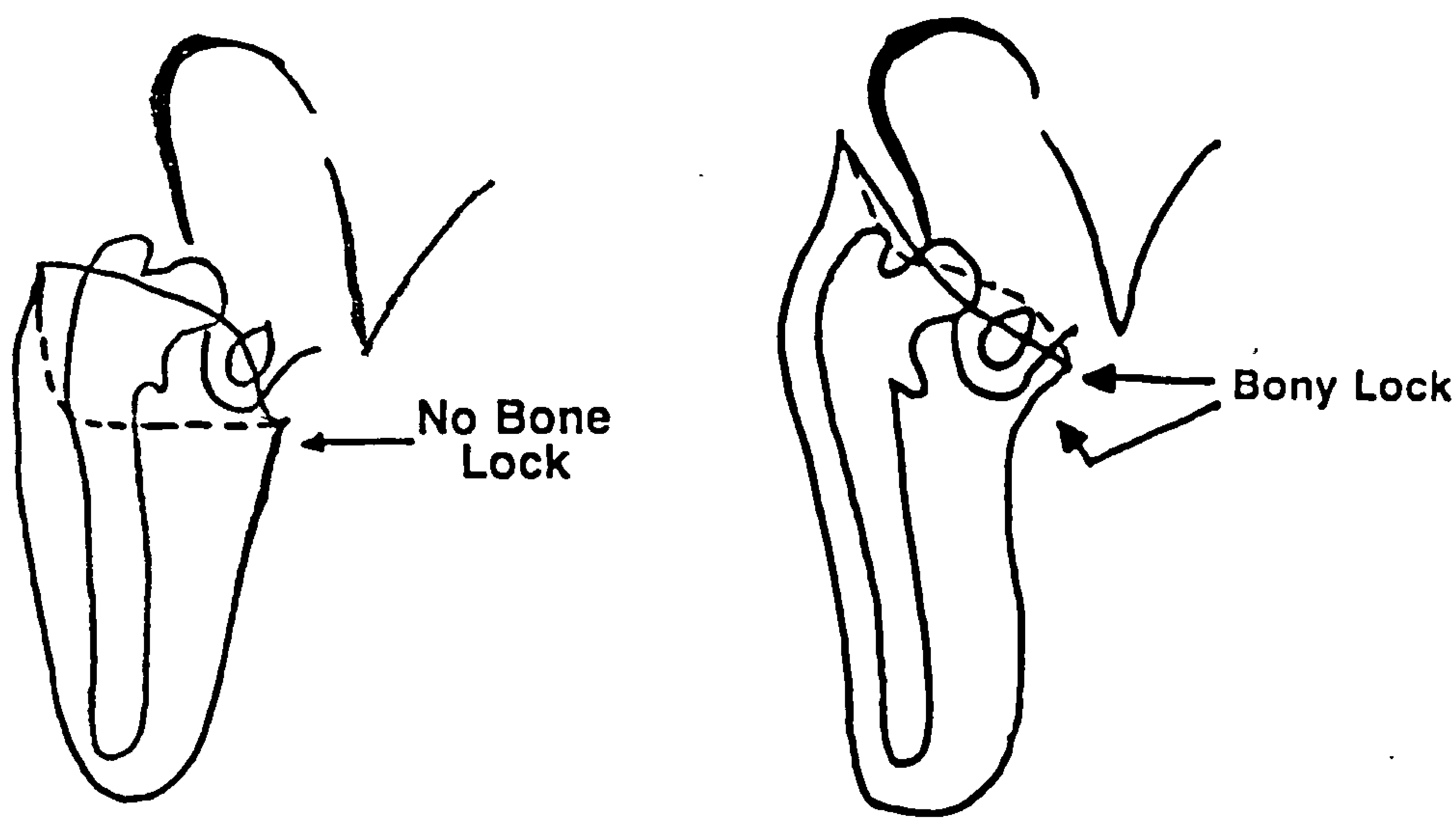

Anterior and posterior view of the two type of socket.

Fig. 2.5.5.1 The difference in shape between ischial containment socket and quadrilateral socket as viewed by Sabolich. (Sabolich, 1985)

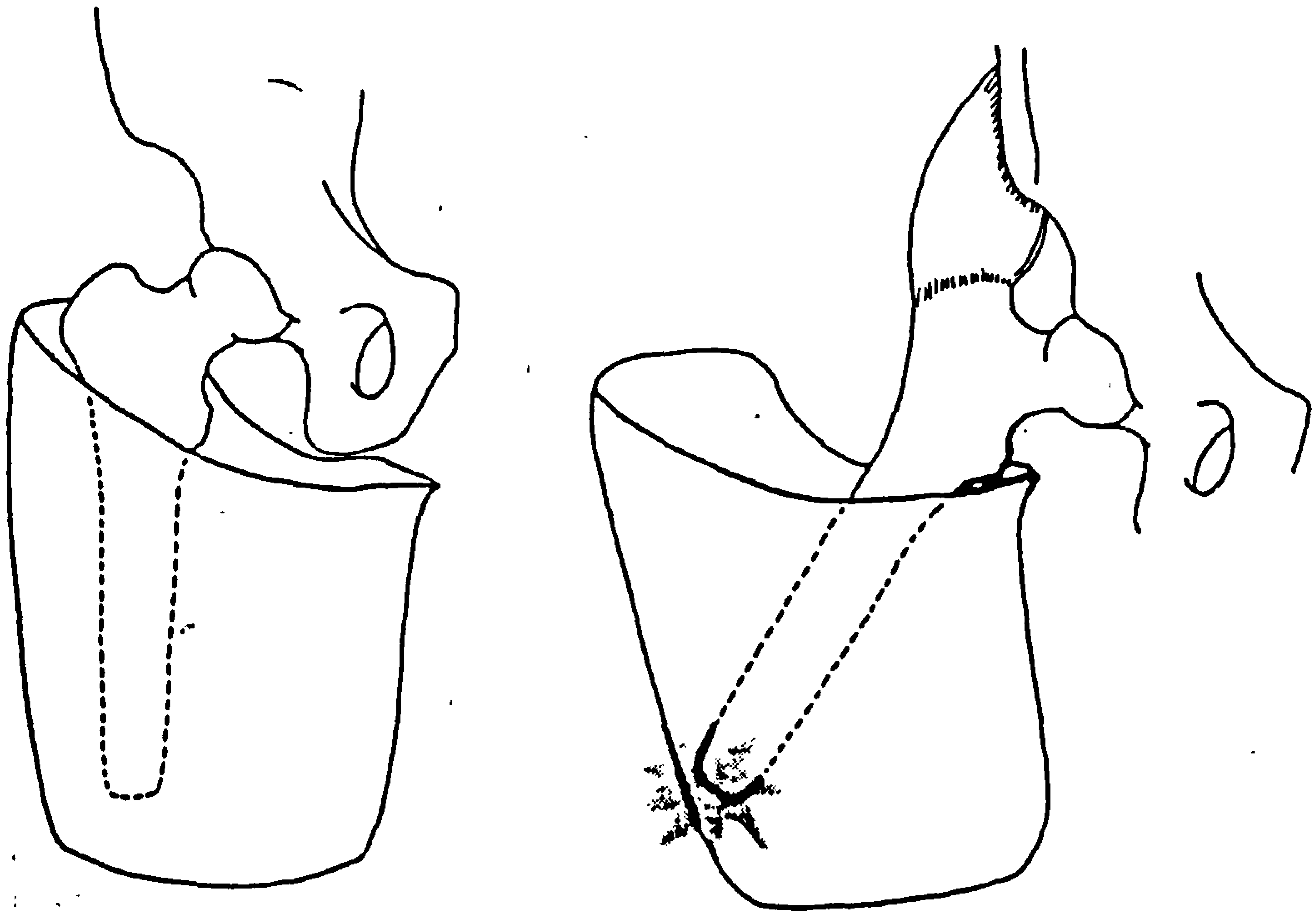

Fig. 2.5.5.2 Active hip abductors forcing femur to abduct in the quadrilateral socket, subsequently producing painful distal end contact. (Flandry et al, 1989)

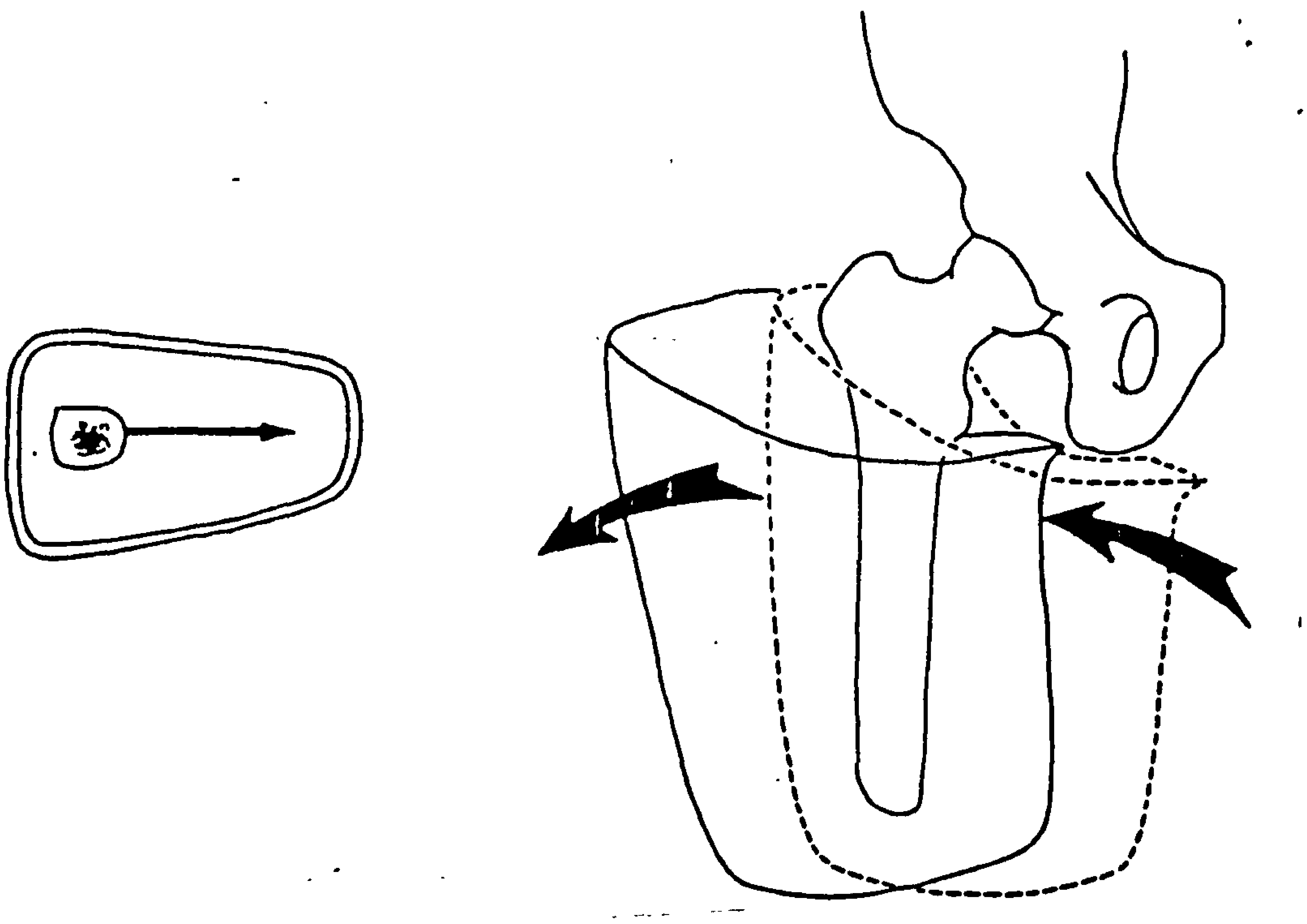

Fig. 2.5.5.3 The absence of a medial bony lock cannot prevent the socket from sliding laterally. (Flandry et al, 1989)

and was convinced that the ischial containment socket does not violate any of the biomechanical principles laid down by Radcliffe (1955). The ISPO workshop in Miami on above knee fittings also clarified a few important points leading to a better understanding of the mechanics of the newer socket (Schuch 1988).

The validity of the quadrilateral socket had been questioned as early as 1969 (Sabolich 1985). But the ischial containment concepts only began to develop after Long (1975) reported abduction of the femur in quadrilateral sockets. Apparently the cause of this abduction was due to two reason. Firstly the M-L dimension is too wide, and secondly the absence of a medial bony lock. In the quadrilateral socket, the ischial tuberosity sits on top of the ischial seat and is free to move. During abductor action, the femur is forced onto the lateral wall of the socket and due to the large M-L dimension, there is enough space between the femur and the lateral wall for femur migration (Fig. 2.5.5.2). Such movement subsequently causes the socket and the ischial seat to slide laterally away from the ischial tuberosity since there is no bony lock to prevent this shift. The lateral movement of the socket creates high shearing forces on the residual limb around the ischial seat and medial brim area of the socket (Fig 2.5.5.3).

The A-P dimension of the quadrilateral socket is kept narrow to ensure the ischial tuberosity on the ischial seat, but this has been a point of criticism by the advocates of the newer socket. The narrow A-P dimension prevented active muscule function from giving good A-P stability. Sabolich (1988) reported that patients changing from the quadrilateral to CAT-CAM socket experienced hypertrophy of the A-P muscles. Therefore the CAT-CAM socket is said to be able to encourage muscles' usage leading to better amputee stability. Suction is also easily maintained in the CAT-CAM suction socket since the muscles are claimed to be kept in more or less the natural shape without undue deformation.

Flandry et al (1989) similarly criticised the quadrilateral socket for its non-anatomical shape. The tight A-P dimension especially distorts the proximal muscles causing discomfort in standing and sitting. Flandry et al also produced CT scans showing in the transverse view, the amount of distortion resulting in the

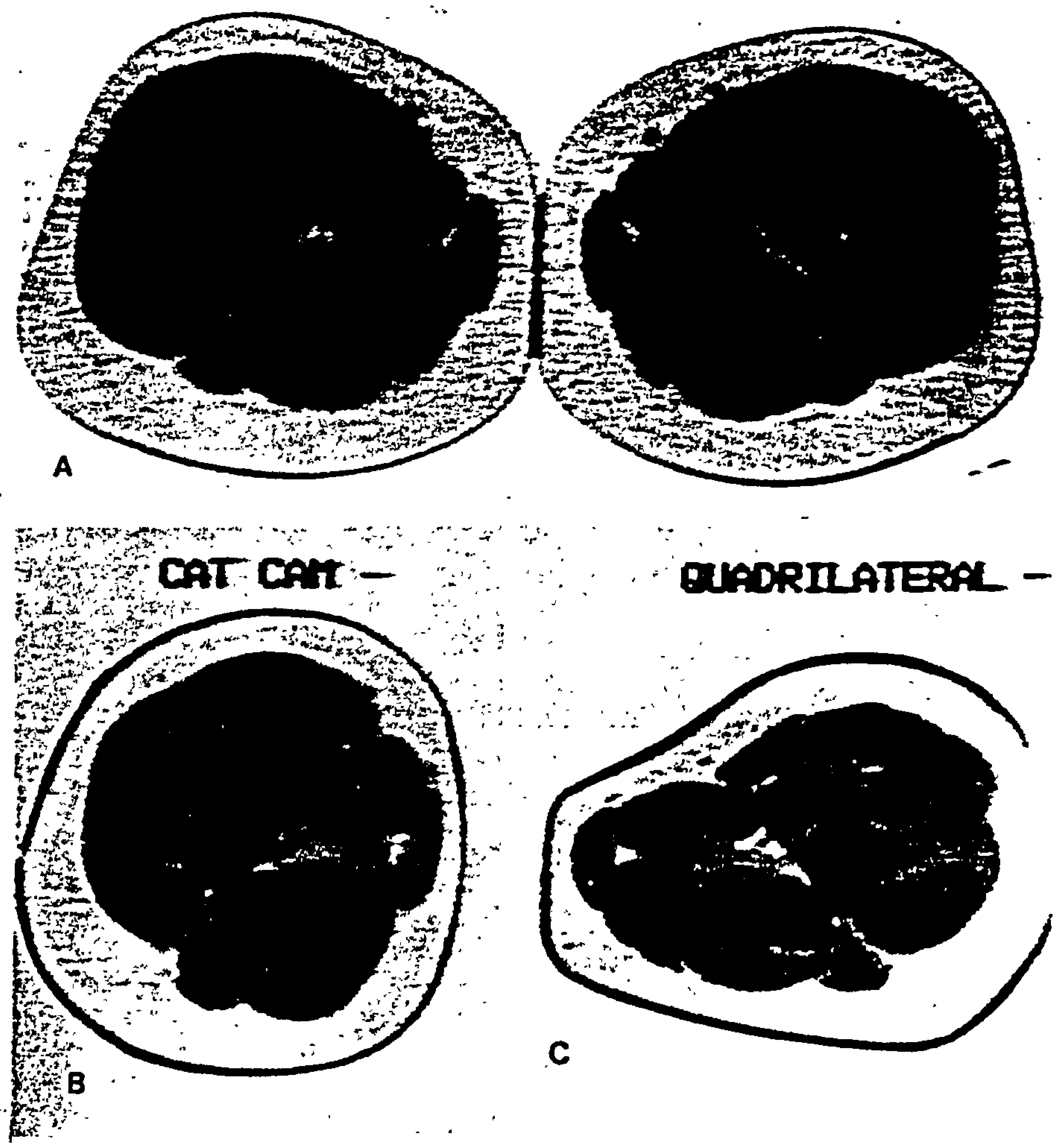

Fig. 2.5.5.4 CT scan showing the transverse view of A) natural limb, B) limb with CAT-CAM shaped sleeve, C) limb with quadrilateral shaped sleeve. High soft tissue distortion was noted with the quadrilateral sleeve. (Flandry et al, 1989)

quadrilateral socket (Fig. 2.5.5.4). The author of this thesis, however, finds that the diagrams highly misrepresent this idea. These geometrical details are produced using socket sleeves fabricated to fit a normal subject, thus cannot represent the amputee population well. The CT scan of the limb with the CAT-CAM socket sleeve has almost identical measurements in the M-L and A-P dimensions, which, of course, contradicts the shorter M-L and longer A-P dimensions philosophy in CAT-CAM socket. Flandry et al results does not agree with that obtained in the present study, where two trans-femoral amputees participated in Magnetic Resonance Imaging (MRI) of the lower limb. Detailed cross sectional images of the entire residual limb without socket, wearing the quadrilateral socket, and wearing the ischial containment socket were captured. From the MRI scans, the geometrical difference between the quadrilateral and the ischial containment socket is distinctive with their opposing A-P and M-L dimensions at the level of the ischial tuberosity. A complete documentation of this study is presented in chapter nine of this thesis.

The concept of ischial weight bearing in the quadrilateral socket was questioned by Lehneis (1985). The author described ischial weight bearing as being not possible throughout the stance phase. The perpendicular distance between the axis of rotation of the hip and the ischial seat changes during the stance phase but the distance from the hip joint to the ischium is constant. The longer perpendicular distance during heel strike causes the ischial tuberosity to leave the ischial seat completely (Fig. 2.5.5.6). This distance decreases towards toe off creating high pressure on the ischial tuberosity (Fig. 2.5.5.7). The ischial tuberosity at this point also acts as a fulcrum, generating rotation of the prosthesis and increasing the gap at the anterior wall. Lenheis suggested a sloped ischial seat on the quadrilateral socket can reduce the effect of the above mentioned problems (Fig. 2.5.5.7). At heel strike a sloped seat prevents any build up of of high pressure at the ischial seat and at toe off the ischium falls inside the socket and pressures are distributed to both the ischium and the gluteus muscles.

The weight bearing area of the ischial containment socket is also indeterminate (Sabolich 1985). Radcliffe (1989) suggested that the ischial tuberosity and the ramus

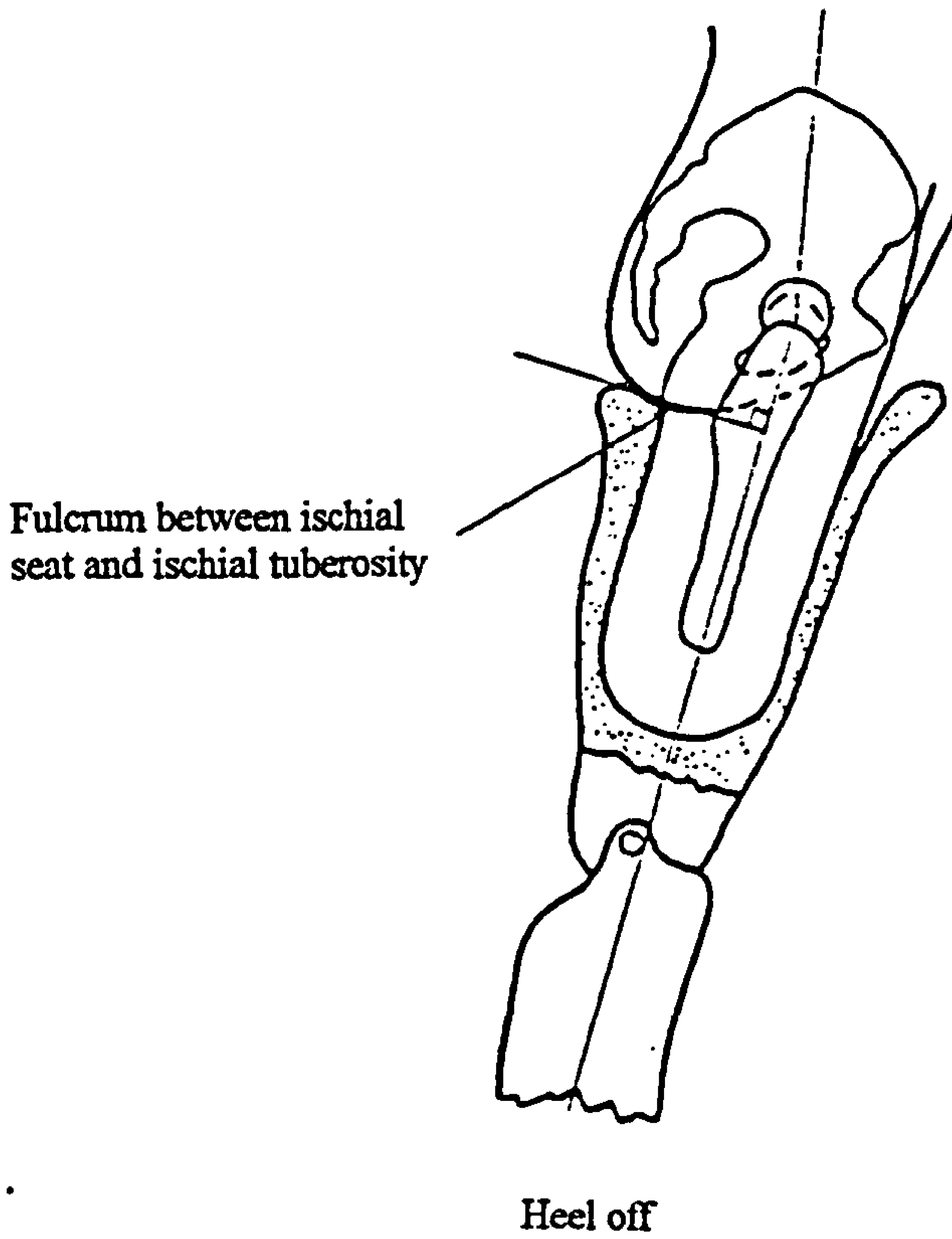

Fig. 2.5.5.5 High pressure at the ischial tuberosity at toe off, with gapping at the proximal anterior wall of the socket. (Lehneis, 1985)

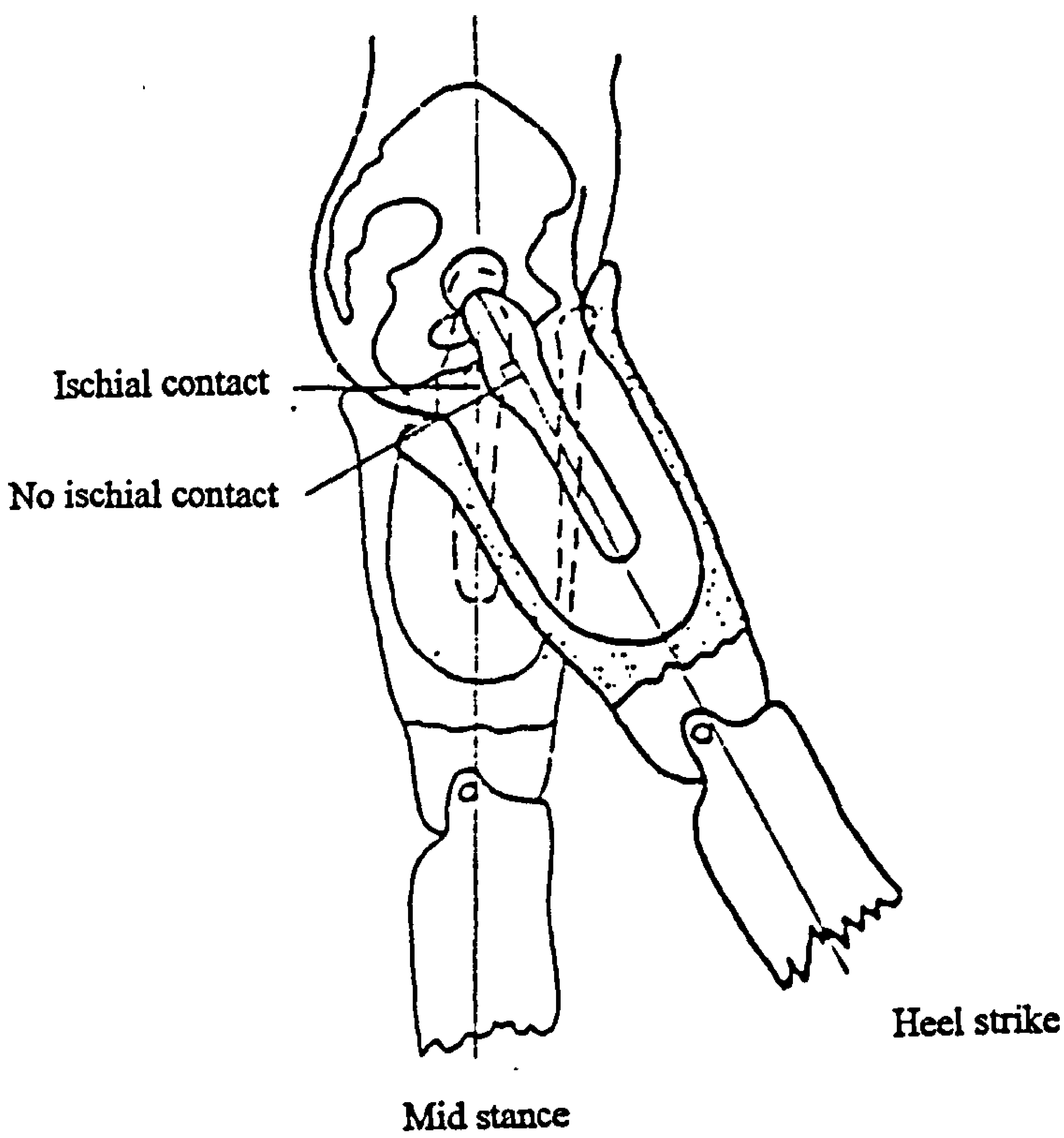

Fig. 2.5.5.6 Ischial leaves the ischial seat at heel strike. (Lehneis, 1985)

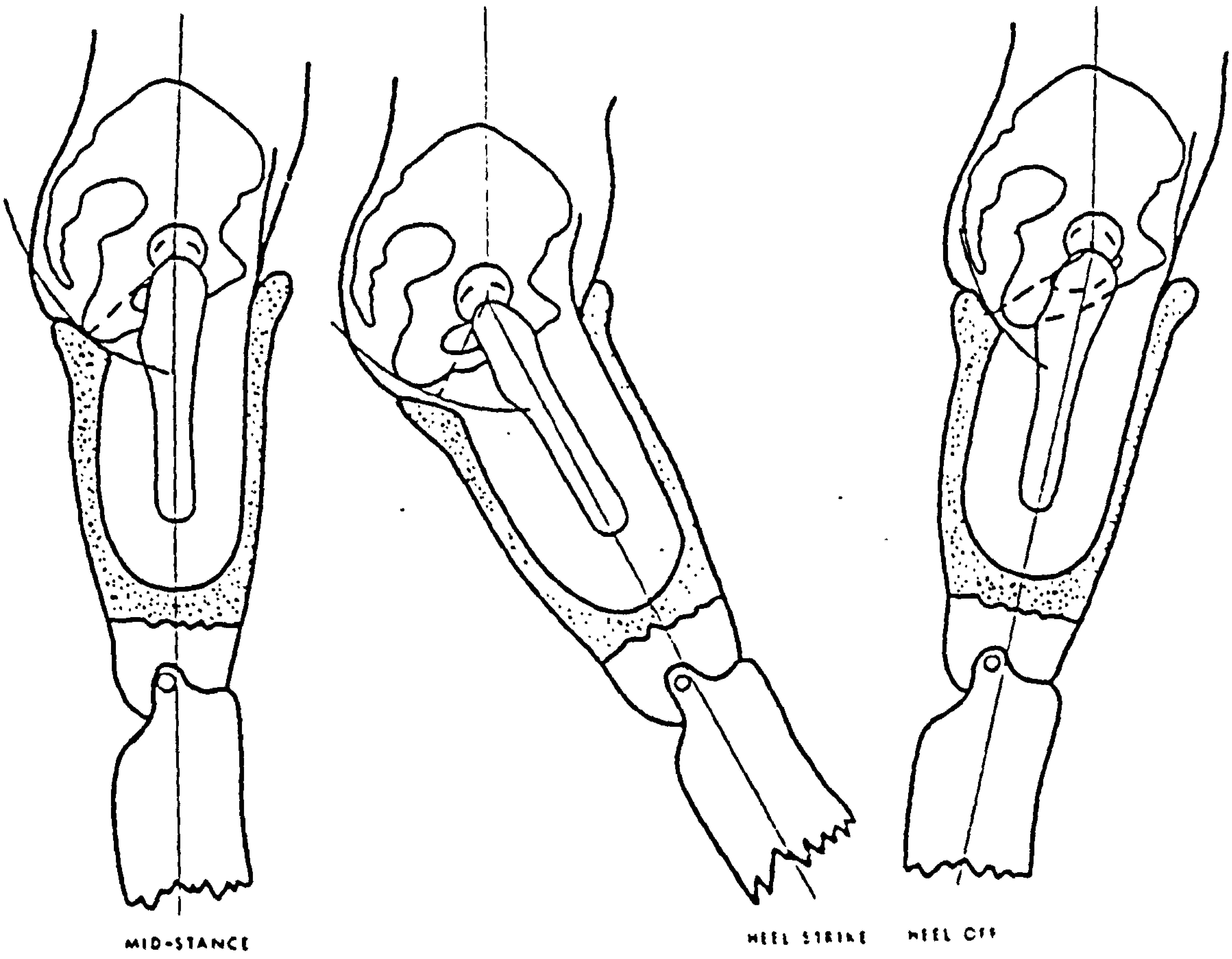

Fig. 2.5.5.7 A slope ischial seat to provide more comfort at the ischial tuberosity. (Lehneis, 1985)

are weight bearing. Sabolich (1985) pointed out the possibility that the femur carried a certain amount of vertical load due to its increased adduction angle. The concept of hydrostatic weight bearing, i.e weight bearing by the soft tissue, developed by Redhead (1979) for the total surface bearing socket, has also been widely accepted as a weight bearing mechanism for the ischial containment socket (Sabolich 1985, Pritham 1990). But the concept of hydrostatic weight bearing raised many questions. Radcliffe (Schuch 1988) claimed that such a system was impossible since the socket and residual limb represent an open system and pressure at the soft tissue will only force the tissue out of the socket. Spence (1994) also mentioned the difficulties in identifying a major load bearing area. With the quadrilateral socket, the amputee is able to locate higher pressure at the ischial seat but for the ischial containment socket, pressures are well distributed and difficulties arise in identifying a major weight bearing area.

Clinical and laboratory evaluations of the ischial containment socket have been carried out by various independent researchers. Flandry et al (1989) converted five transfemoral amputees from quadrilateral to CAT-CAM sockets. Evaluations were conducted depending on subjective acceptance, gait deviation, kinetic measurements, femur adduction and ambulatory demands. Four of the five patients through subjective evaluation considered the CAT-CAM socket to be superior to the quadrilateral socket. The mean stride length improved by 0.23m, mean gait velocity by 4.1 m/min. Femur adduction in the CAT-CAM socket detected using X-rays showed a mean improvement of 6.5° over the quadrilateral socket. The oxygen consumption per metre travelled improved by a mean reduction of 0.078 ml/kg-metre.

A more comprehensive study of energy cost was conducted by Gailey et al (1993). A total of ten unilateral amputee subjects prescribed with the quadrilateral and the CAT-CAM socket participated in the study. Further to the amputees, ten non-amputee subjects were also monitored as the control group. Oxygen consumption (VO_2) and heart rate (HR) were measured at two speeds of ambulation. The subjects were required to walk for eight minutes around a 36 metre, L shaped, industrial carpeted indoor track. The mean results show a clear reduction in the oxygen intake

Means and standard deviations of oxygen uptake and heart rate.

	Slow speed (33.5 m/min)		Fast speed (67 m/min)	
Group	VO_2	HR	VO_2	HR
CAT-CAM	10.37 ± 1.34	101.42 ± 13.27	15.12 ± 1.89	116.42 ± 14.48
QUAD	11.72 ± 2.70	100.82 ± 10.61	18.98 ± 5.52	119.75 ± 16.28
Control	8.48 ± 1.08	83.86 ± 9.22	11.08 ± 1.88	90.04 ± 8.60

Table 2.5.5.1 Oxygen intake by amputees with CAT-CAM and quadrilateral sockets. Table also includes results from non-amputee subjects for controlled comparison. (Gailey et al, 1993)

when amputees use the CAT-CAM socket, about 20% less energy (Table 2.5.5.1). The amputees using the quadrilaterals' socket needed an average of 42% more energy than non-amputees at a 67m/min walking speed, whereas with the CAT-CAM sockets, the average energy required at the same speed was only 27% more.

Visser-Meily et al (1992) converted 13 amputees from quadrilateral to CAT-CAM sockets. A subjective evaluation was conducted through patient interviews after seven months of CAT-CAM socket usage. An improvement in gait and comfort was concluded. There was also an indication that pain at the lower back and groin area were significantly reduced. In other studies involving subjective comparison of the CAT-CAM and quadrilateral socket, the former was also rated the better socket. (Esquenazi et al 1989, Mitchell and Versluis 1990)

The biomechanical principles of the two types of sockets remain the same. M-L and A-P stability is still achieved by pressure and counter pressure developed at the socket walls. The ischial containment socket can be looked upon as an alteration to the quadrilateral socket rather than a completely new idea (Pritham 1990). The objective of ischial containment socket design is to rectify the problems that exist in the quadrilateral socket. However, Radcliffe (Schuch 1988) did not agree that these problems cannot be solved by the quadrilateral socket itself and argued that comparison is often made with bad fitting quadrilateral sockets. The author of this thesis believes that the many trials (presently an average of six) needed to fit an ischial containment socket may be the very reason why the socket produced is a better one. Many quadrilateral sockets are fitted with just one trial. Using the brim method of fitting quadrilateral sockets also contradicts the need for customised fitting. Even though the brim can be adjusted in some aspects, its use introduced a series of limitations which can be vital where the fit of the socket is concerned. It is therefore reckoned that unless a measure of the optimal benefits specified by the advocates of the quadrilateral and ischial containment sockets can be determined, any kind of comparison of the two is inconclusive.

The quadrilateral socket has been in use for more than 30 years now. The current developments of the ischial containment socket highlights the problems that exist with the quadrilateral socket and aimed in solving them. To consider the ischial containment as a new concept unrelated to the quadrilateral socket would be incorrect, since its basis has been in improving the quadrilateral fitted residual limb rather than one which is not fitted with any socket.

CHAPTER THREE

COMPUTER TECHNOLOGY RELATED TO LOWER LIMB PROSTHETIC SOCKET DESIGN AND FABRICATION

3.1 INTRODUCTION

It is no surprise that modern engineering methods applicable to other industries are used in the field of lower limb prosthetic devices and services. However, the implementation of such methods is still a slow process, since the present success of the lower limb prosthetic industry is due mainly to expertise derived from artisan methods. New technology has undoubtedly brought much accomplishment to the lower limb prosthetic industry. How the wooden artificial limb of the 1950's is being transformed to a leg with flexible plastic socket, computer controlled knee, carbon-fibre shank and energy storing foot is certainly commendable. The introduction of new methods is an ongoing process. Some methods have provided significant improvement in fit, comfort and function to the amputee, but the benefits derived from use of other techniques is debatable.

Computer Aided Socket Design and Computer Aided Manufacture (CASD/CAM), and numerical stress analysis using the Finite Element (FE) method, have recently emerged as controversial methods influencing the design and manufacture of prosthetic sockets. The objective of this chapter is to provide a survey of the philosophy and methodology involved in the above mentioned methods. The chapter is divided into four main parts, beginning with a brief description of prosthetic socket design and manufacture using the artisan methods. This section enables the reader to appreciate the type of work involved and also provides a better the understanding of the capabilities and limitations of the newer methods when compared to the artisan method. This will be followed by a discussion on the current CASD/CAM technology and clinical trials. The third main section reviews the use of FE analysis in the field of orthopaedics and lower limb prosthetics. The final sections aim at describing the potential of using FE analysis to enhanced the present CASD/CAM systems.

As many of the present CASD/CAM systems and FE studies focus on the trans-tibial amputee it is necessary in this chapter to consider trans-tibial prostheses and prosthetic methods.

Name ______________________________ Date ____________________

Height ____________ Weight __________ Age ____________ Sex ________

Stump Description: Show the location of stump details

Identify them with the letter code below

AD = Adductor Roll
A = Abrasion
D = Discoloration
E = Edema
S = Scar

LATERAL ANTERIOR POSTERIOR MEDIAL

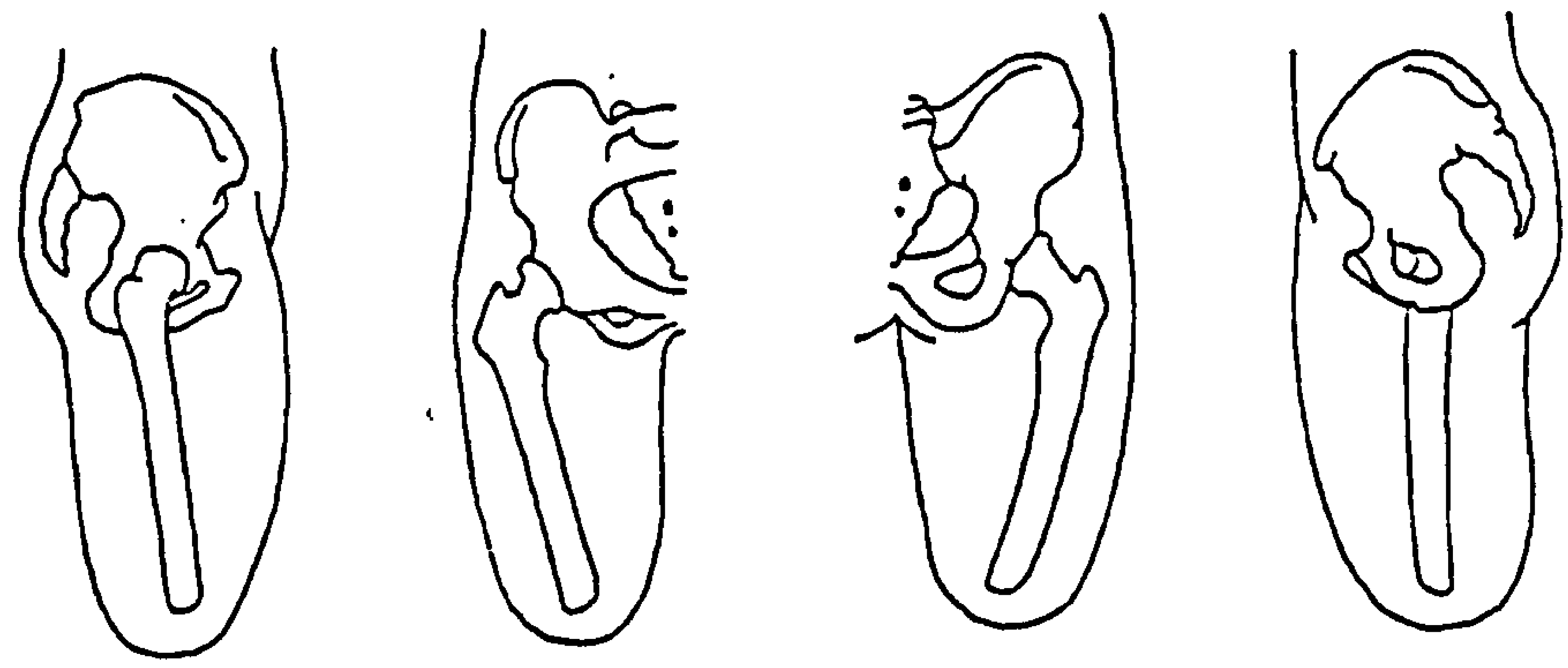

Ischial Area:	Muscle Padding	[ ]	Prominent	[ ]		
	Previous Ischial Bearing:		Yes	[ ]	No	[ ]
Lateral Stump Contour:	Convex	[ ]	Flat	[ ]	Concave	[ ]
Stump Musculature:	Firm	[ ]	Average	[ ]	Soft	[ ]
Flexors -	Strong	[ ]	Weak	[ ]		
Extensors -	Strong	[ ]	Weak	[ ]		
Adductors -	Strong	[ ]	Weak	[ ]		
Abductors -	Strong	[ ]	Weak	[ ]		

Table 3.2.1.1 Trans-femoral amputee's residual limb assessment record. (NCTEPO, 1991)

3.2 PROSTHETIC SOCKET DESIGN AND FABRICATION : THE ARTISAN METHOD

The most important aspect of the artificial limb is the socket, which constitutes the critical interface between the amputee's residual limb and the prosthesis. The design and fitting of the socket is also the most difficult procedure due to the uniqueness of each amputee's residual limb. Every fitting requires much attention from the prosthetist. Although at present, there exists systemisation of the artisan practices to design and fit sockets for different levels of amputation, a successful fitting is still highly dependent on the skill and experience of the prosthetist.

Three main steps, namely, measurement, rectification and fabrication are essential in making a prosthetic socket. The following sections describe briefly these steps with regard to the quadrilateral socket. Manufacture of the ischial containment socket used in the present study follows a similar procedure to that of the quadrilateral socket in its manufacture. However, the measurement and rectification stages are much more complex. The proximal contours of the ischial containment socket are shaped by the prosthetist's hands without the aid of an adjustable brim. Detailed descriptions of the fabrication of the quadrilateral and ischial containment sockets are found in NCTEPO 1991, UCLA 1981 and Hoyt et al 1987.

3.2.1 Residual limb Measurement

A successful socket fitting depends very greatly on careful measurement of the residual limb. Measurements are completed by two procedures, direct measurement using measuring instruments, and shape measurement using a plaster wrap cast.

The residual limb is initially assessed by the prosthetist using a standard form, and a record of muscles' strength, skin condition, bony prominences is made. (Table 3.2.1.1). Any abnormalities like joint contraction, adherent scar, bone spurs and edema are observed and catered for later in socket design.

Direct measurements are recorded with the aid of a prosthetic measurement form (Table 3.2.1.2). The residual limb length is measured from the perineum to its distal end with a perineum gauge (Fig. 3.2.1.1). The femur length is measured

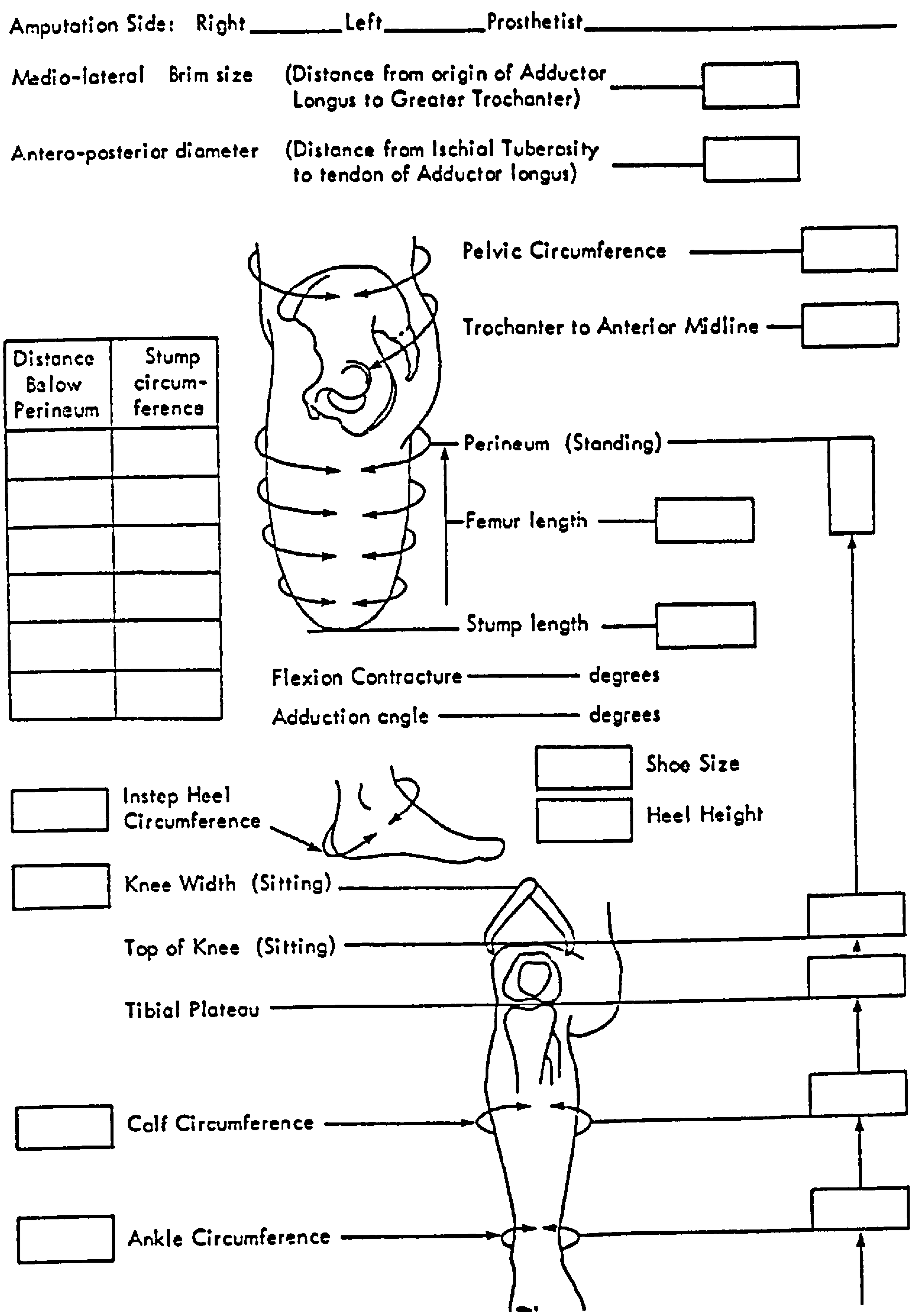

Table 3.2.1.2 Trans-femoral amputee's prosthetic measurements. (NCTEPO, 1991)

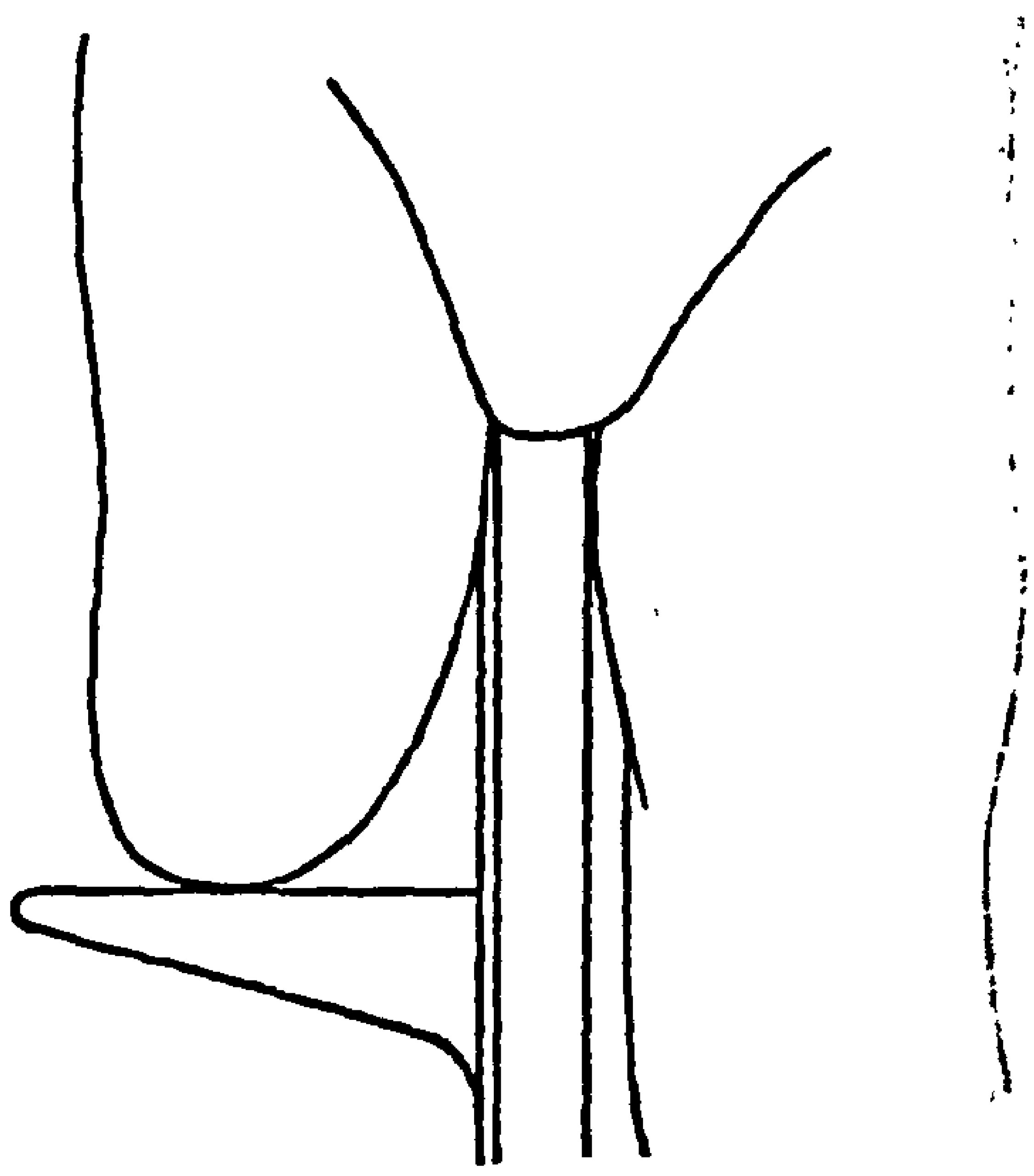

Fig. 3.2.1.1 Residual limb length.
(NCTEPO, 1991)

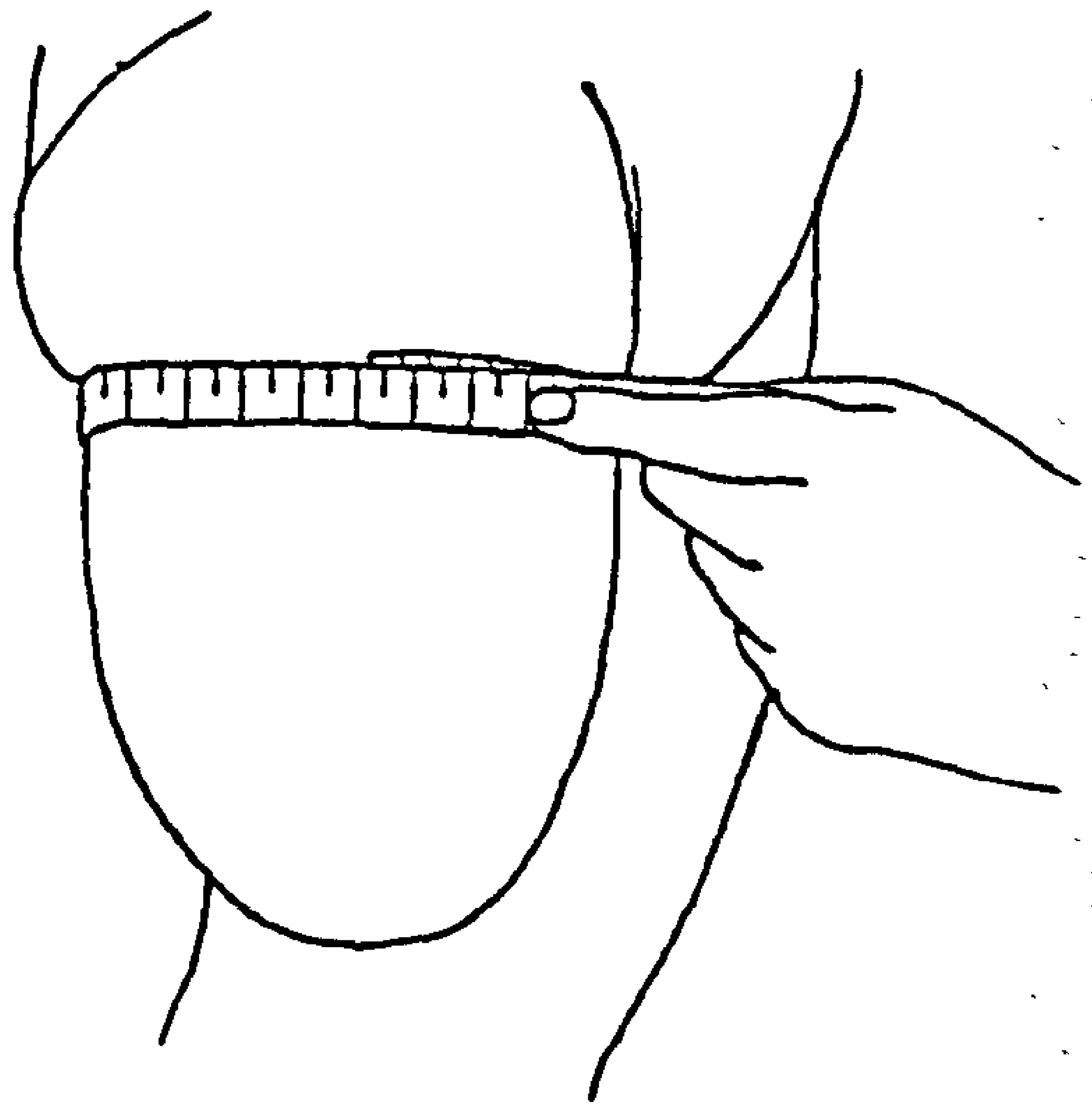

Fig. 3.2.1.2 Circumference of residual limb.
(NCTEPO, 1991)

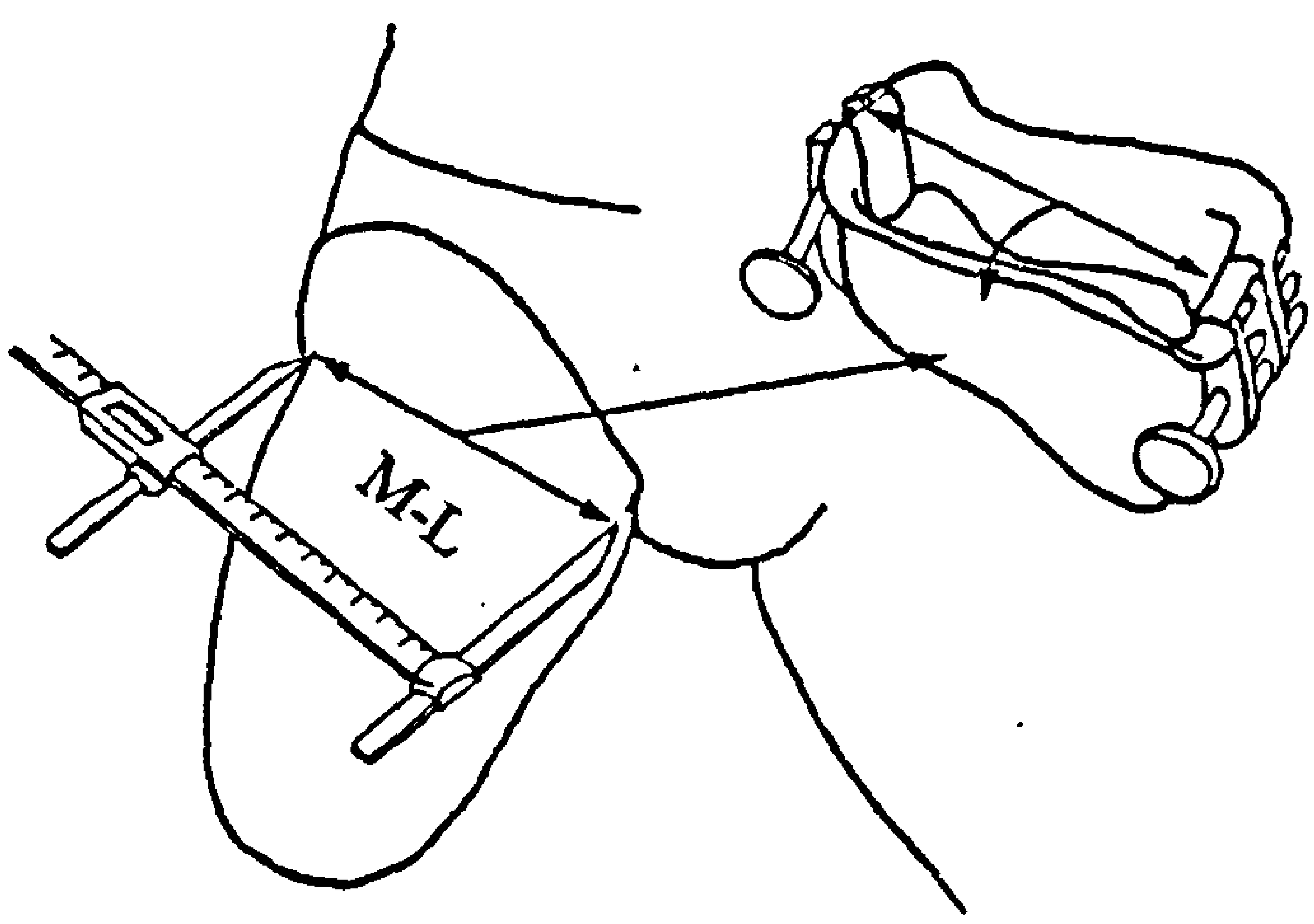

Fig. 3.2.1.4 M-L width of brim.
(NCTEPO, 1991)

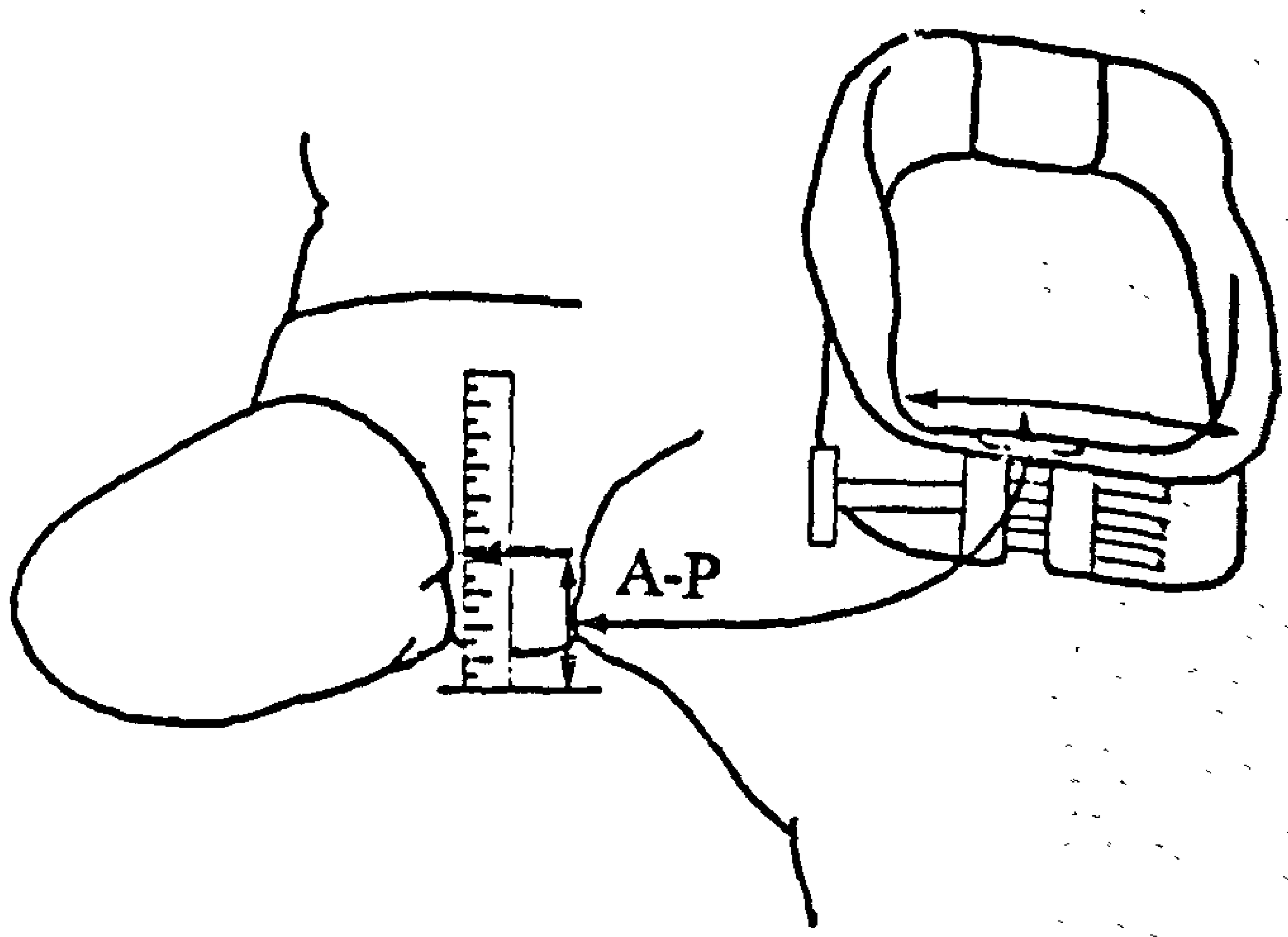

Fig. 3.2.1.3 A-P width of brim.
(Modified from NCTEPO, 1991)

similarly by keeping one of the perineum gauge arms at the perineum while sliding the other moveable arm until it touches the distal end of the femur. The circumference of the residual limb at the perineum is measured using a tape measure, subsequent circumferential measurements are made at 25 mm or 50 mm interval from the perineum to the distal end (Fig. 3.2.1.2).

The quadrilateral socket used in this project was designed using adjustable brim fitting equipment. The brim comes in a series of sizes at 6% increments of the M-L dimension, ranging from 118-200mm. The selection of a suitable brim is based on pelvic measurements. With a caliper, the distance from the greater trochanter to the insertion of the tendon of the adductor longus muscles is measured. The M-L brim size is selected using this measurement (Fig. 3.2.1.3). The A-P width of the brim is adjusted to the vertical distance between the insertion of the adductor longus tendon and the flat surface on which the amputee is sitting i.e. the position of the ischial tuberosity (Fig. 3.2.1.4). The adjusted brim is then fixed onto a stand.

The residual limb is covered with a cast sock suspended from the shoulder and inserted through the brim (Fig. 3.2.1.5). The brim is raised to the correct height and the positions of the adductor longus tendon, greater trochanter and the tuberosity are checked to ensure that the correct brim size was selected (Fig. 3.2.1.6). The brim is adjusted for weight bearing as shown in Fig. 3.2.1.7. The fitting procedures may take considerable time and oedema may develop at the exposed distal part of the residual limb. Thus, before proceeding to the wrap cast, the residual limb should be removed from the brim and elevated in a position to reduce oedema.

The wrap cast is performed with the residual limb in the adjusted brim position, in a weight bearing condition. Two or three rolls of fast setting 100-150 mm width plaster bandages are used. The plaster bandages are wrapped evenly covering the distal section of the brim and all the protruding part of the residual limb (Fig. 3.2.1.8). As the plaster begins to harden, pressure is applied using one hand on the lateral side of the cast to place the femur in the desired position of adduction. Care should be taken not to apply pressure on the cast at the distal end of the femur in order to reduce the possibility of painful contact with the lateral wall of the socket

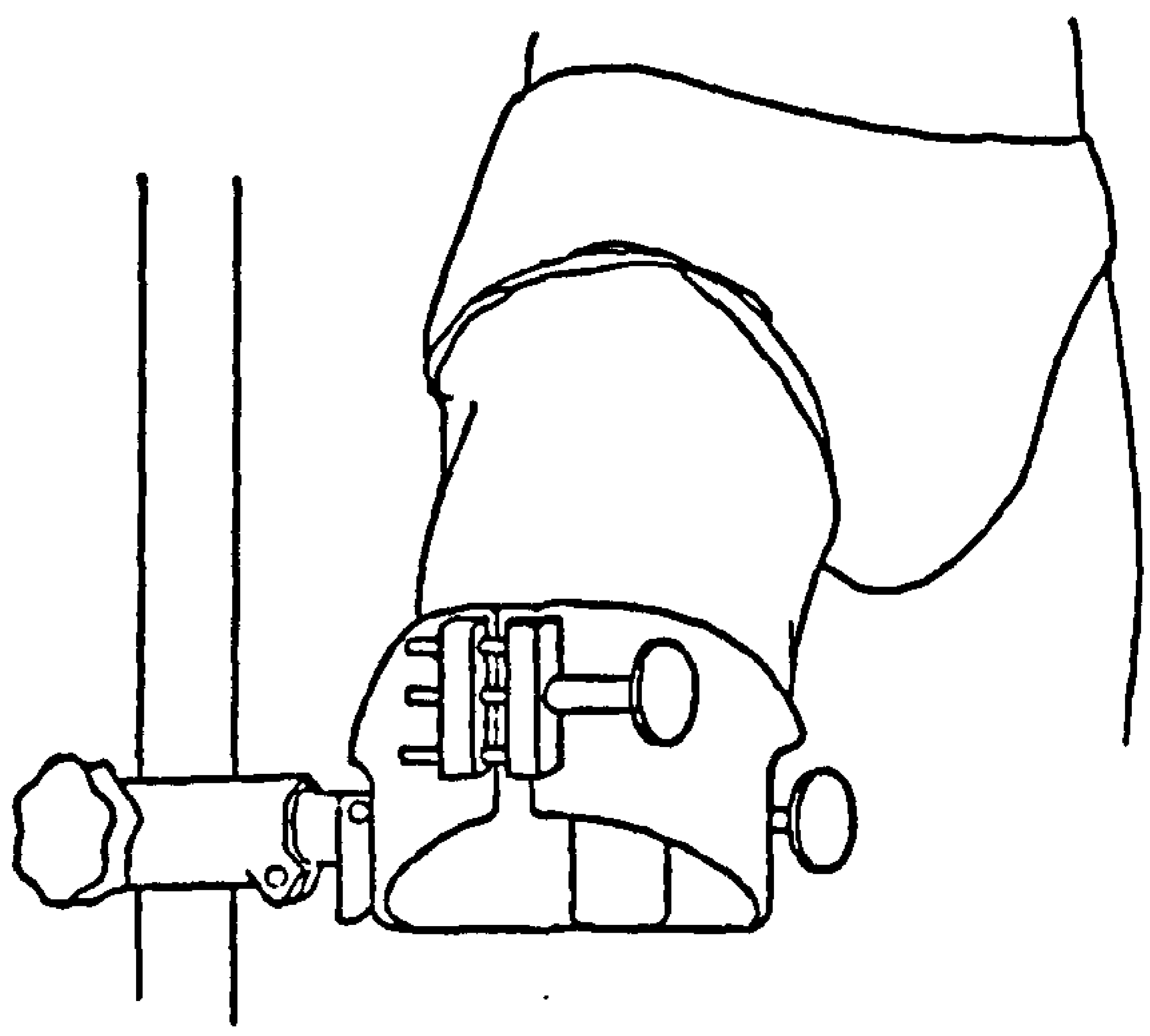

Fig. 3.2.1.5 Brim fitting.
(NCTEPO, 1991)

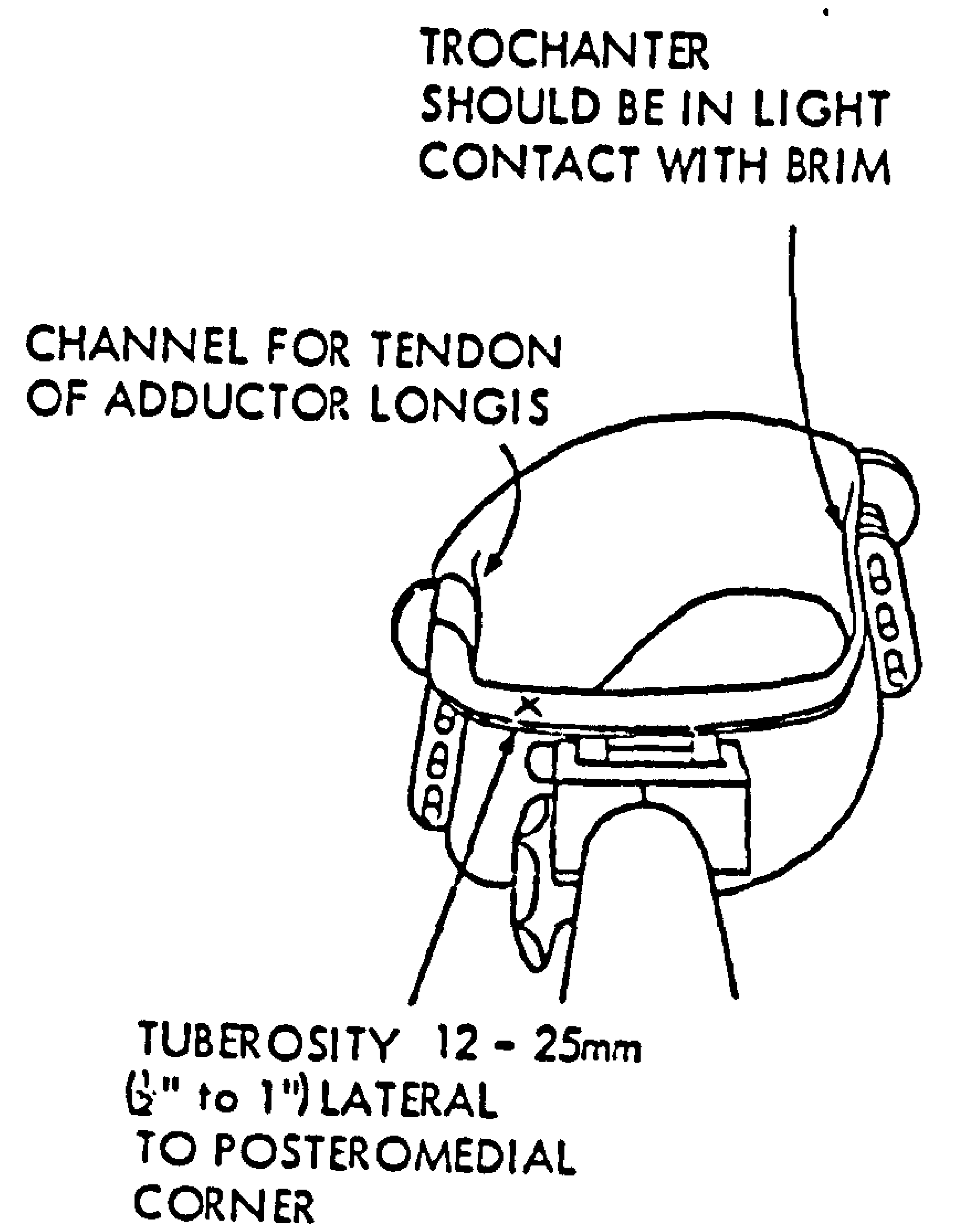

Fig. 3.2.1.6 Anatomical landmarks in relation to the brim.
(NCTEPO, 1991)

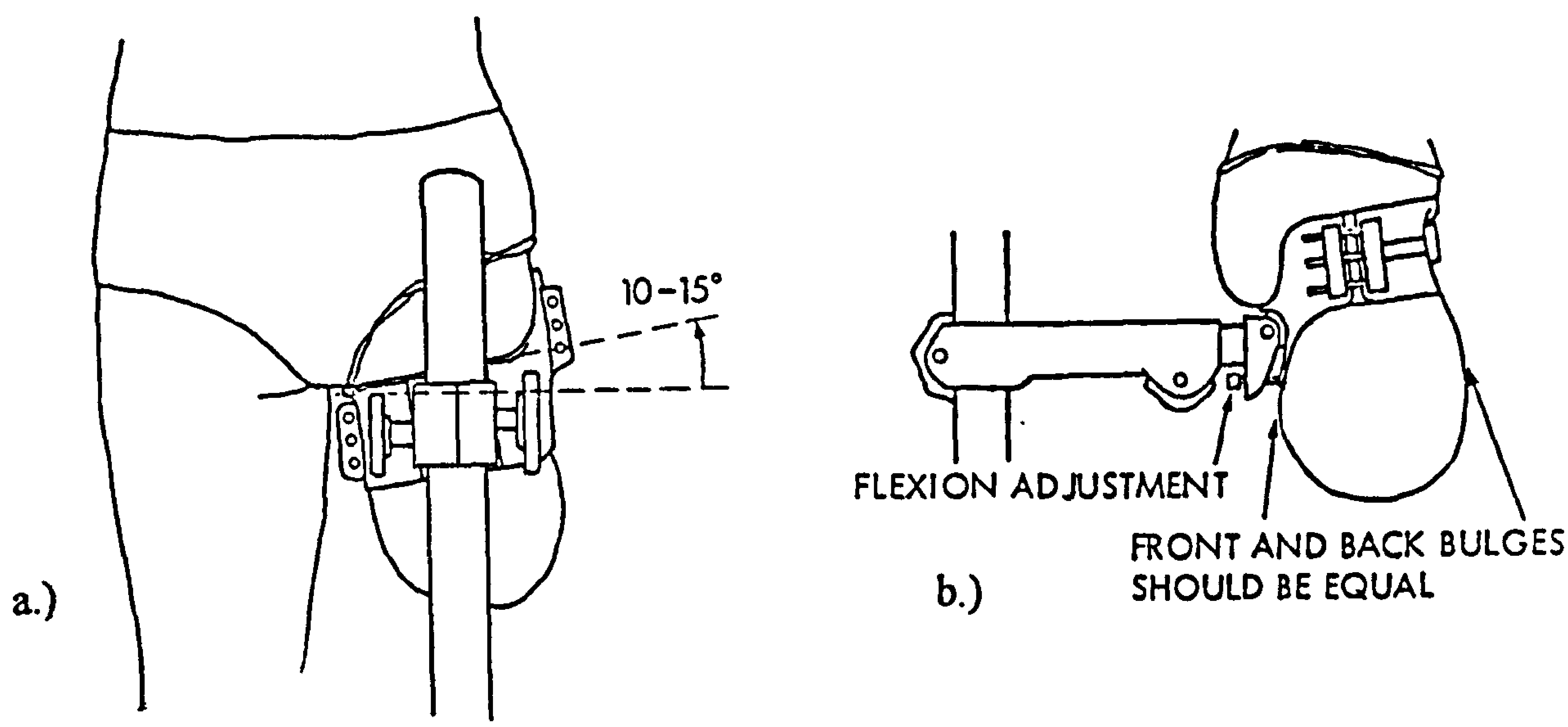

Fig. 3.2.1.7 a.) Residual limb adduction is possible by ensuring that the ischial seat is tilted during weight bearing.
b.) Flexion adjustment enables front and back tissue bulges to be approximately equal. (NCTEPO, 1991)

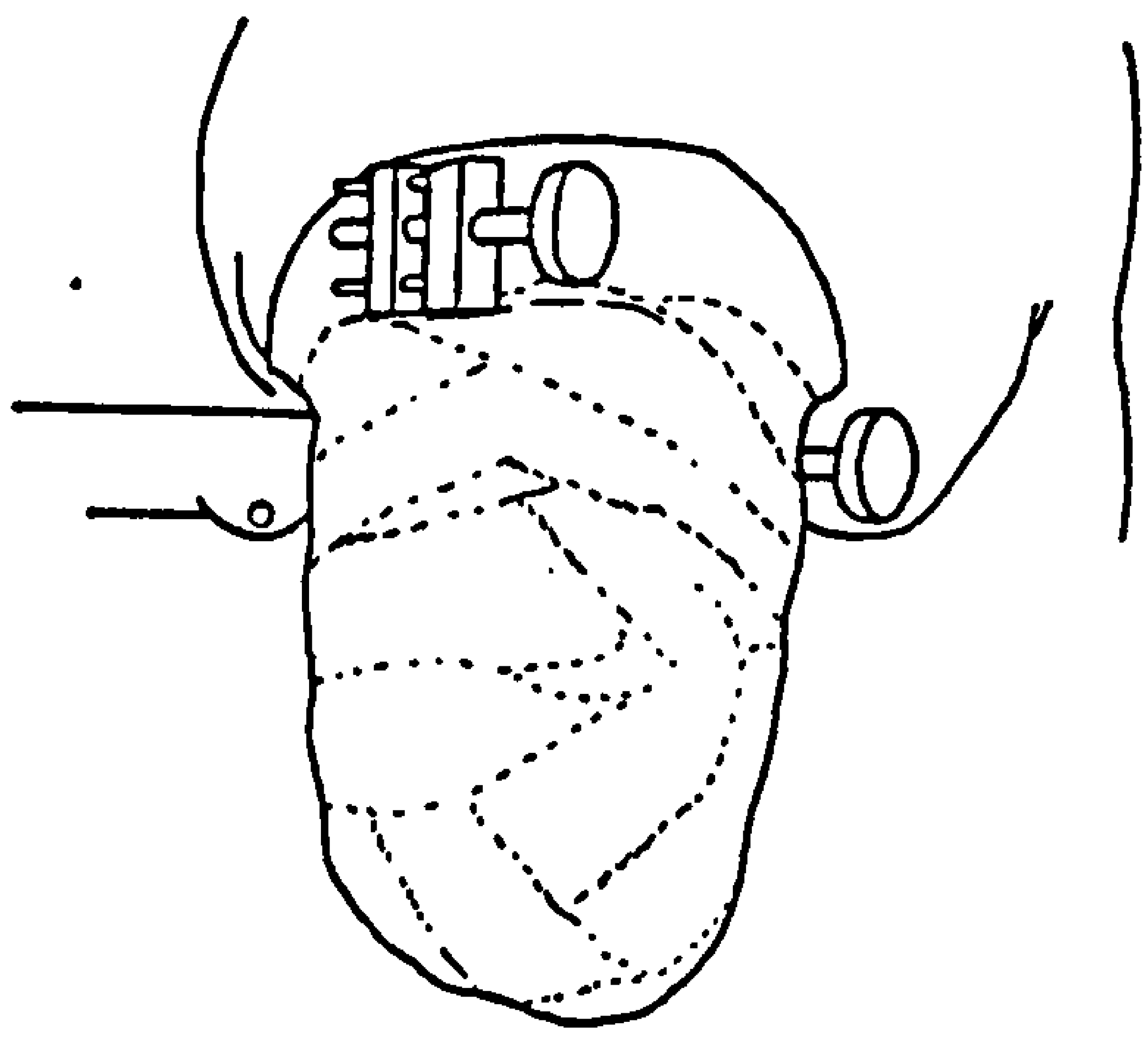

Fig. 3.2.1.8 Completed plaster wrap cast.
(NCTEPO, 1991)

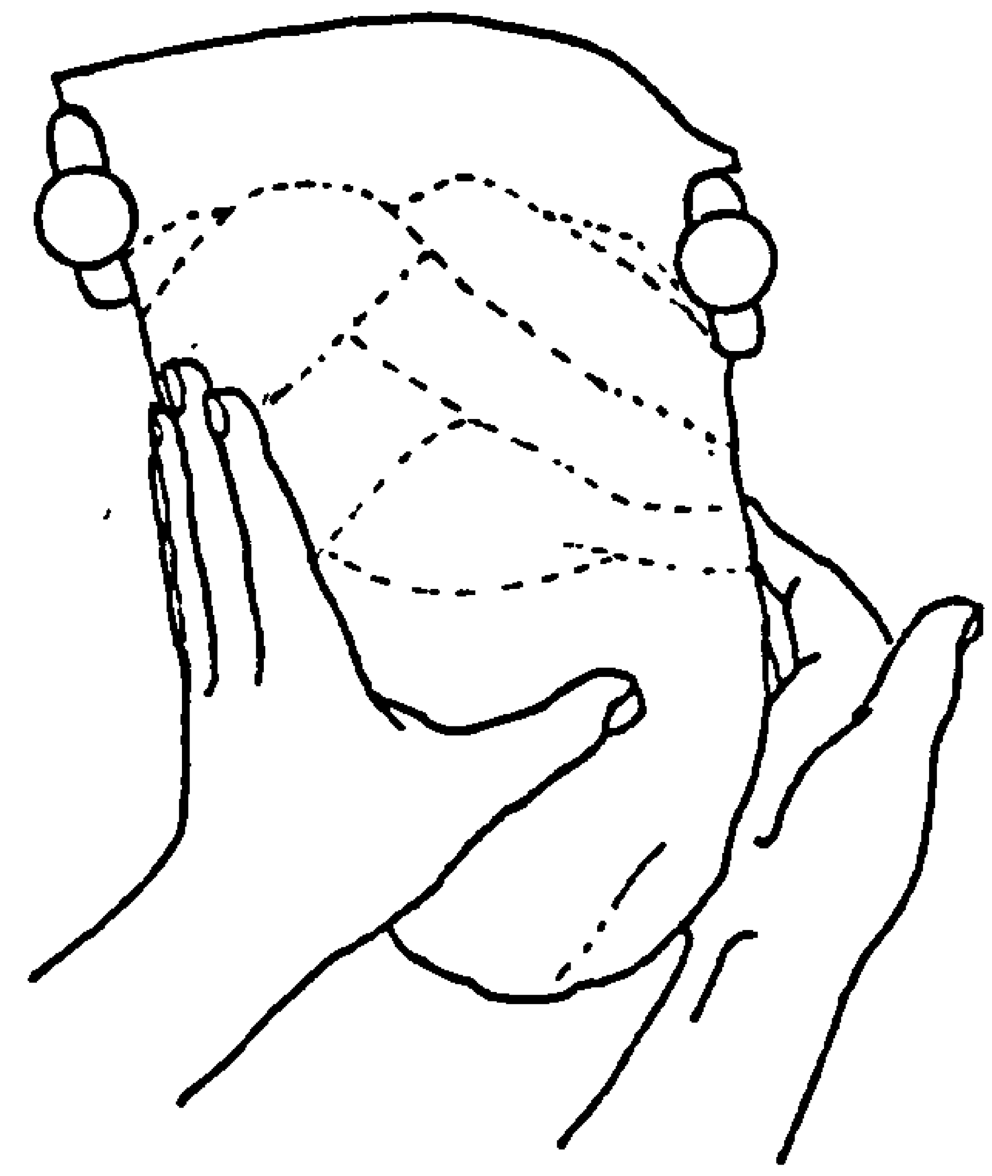

Fig. 3.2.1.9 Controlling limb adduction during cast setting.
(NCTEPO, 1991)

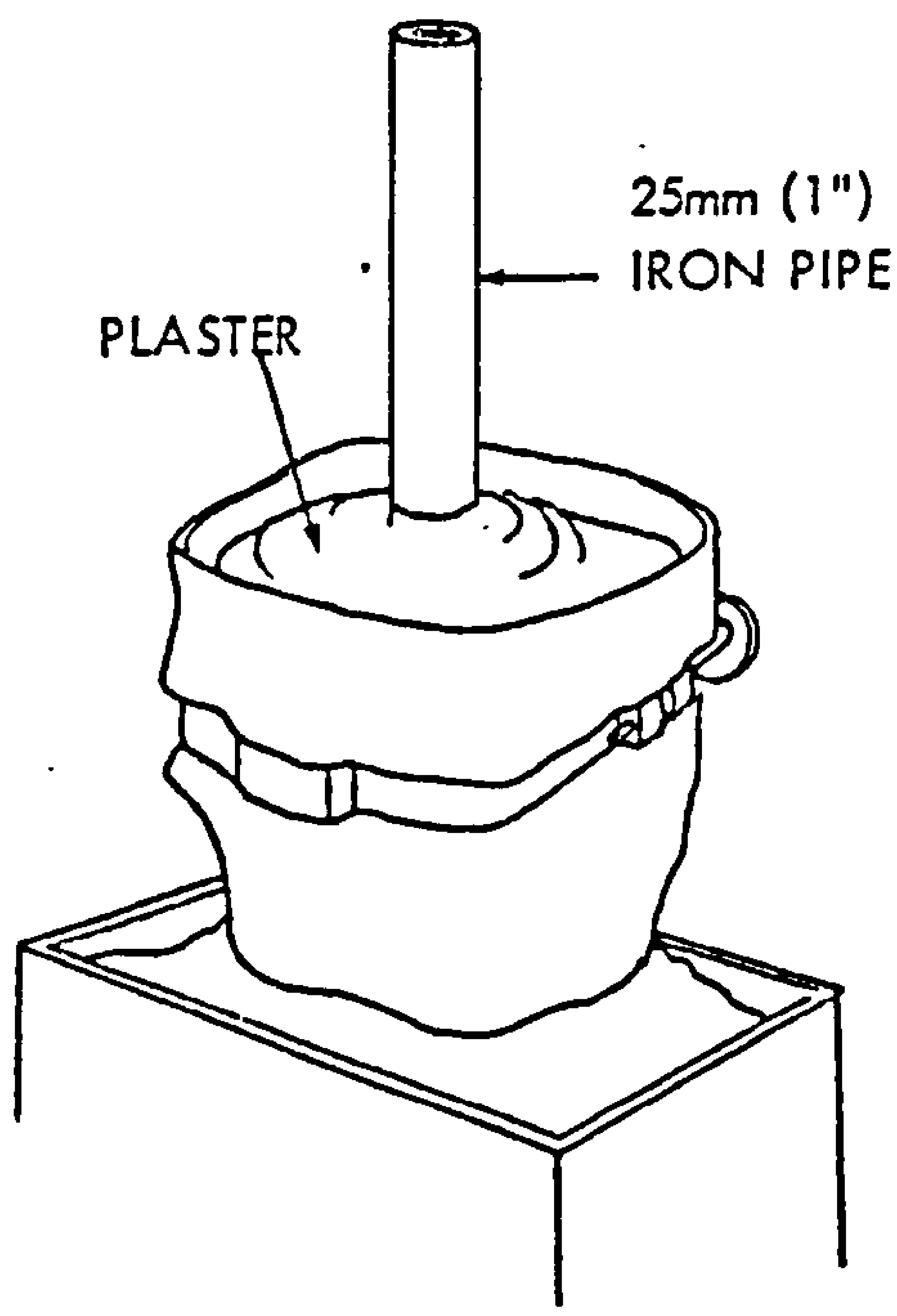

Fig. 3.2.2.1 Positive plaster mould.
(NCTEPO, 1991)

when the femur abducts. The distal end of the wrap cast and the medial side are smoothed to a ensure close fit over the soft tissue with the other hand (Fig. 3.2.1.9). When the cast has set, the brim is detached from its stand, and the wrap cast and the brim are removed from the residual limb together.

3.2.2 Rectification of positive plaster model

A positive plaster model of the residual limb is created by filling the wrap cast and brim assembly with plaster (Fig. 3.2.2.1). Excess plaster at the brim level of the model is shaped and reduced to an appropriate size for the width and flare of the socket brims. Any plaster irregularities on the model surface are smoothed out.

The rectification process begins by taking measurements of the positive model, and comparing them with those previously recorded on the amputee's residual limb. A cast modification and reduction form (Table 3.2.2.1), charts both the measurements of the residual limb and the model. Based on a standard dimensions' reduction table and information which is obtained from past experience, the amount of rectification required is derived, providing the desired dimensions, i.e. the dimensions of the socket. The rectification allows the tissues to be compress in order to form a seal to maintain suction. General areas of the model needing rectification are the overall circumference of the model, the length, A-P dimensions, adduction and flexion angles.

The circumferences of the model are modified at the perineal level and at 50 mm intervals throughout the model length according to Table 3.2.2.1. Initial dimension reduction is carried out by smoothing any irregular areas. Further plaster removal take place at the lateral side of the model or at areas noted as soft in the evaluation Table 3.2.1.1. At the 100 mm level and all other remaining levels from the perinium, the model circumference is reduced evenly throughout by 6 mm. The rectified length usually remains as the model length, unless where the model length exceeds the residual limb by 9 mm, in which case, the rectified length will be 6 mm plus the residual limb length. The A-P goal dimension should register 12 mm less than that measured on the amputee's residual limb. Adduction and flexion angles of the

CAST MODIFICATION AND REDUCTION CHARTS

Patient's Name ______________________________ Date ________________

Prosthetist ______________________________

Amputation type ________________ Tissue consistency ________________

Perineal Level:

Reduce stump measurement by the appropriate value in the table below*

	FIRM	AVERAGE	SOFT
LONG	25mm (1")	31mm (1¼")	37mm (1½")
MEDIUM	25mm (1")	31mm (1¼")	37mm (1½")
SHORT	31mm (1¼")	37mm (1½")	44mm (1¾")

Two inches below perineal level:

Reduce stump measurement 18mm (¾") in all cases *

All other levels:

Reduce cast measurement 6mm (¼") *

* Increase the above reduction values by 6mm (¼") for each 25mm (1") of stump or cast perimeter over 500mm (20")

	MEASUREMENTS		
	1	2	3
	Stump	smoothed but unmodified model	Goal
Perineum			
50mm (2") below Perineum			
100mm (4") below Perineum			
150mm (6") below Perineum			
200mm (8") below Perineum			
250mm (10") below Perineum			
Stump length			
A - P dimension			
Adduction angle			
Flexion angle			

Table 3.2.2.1 Rectification chart.
(NCTEPO, 1991)

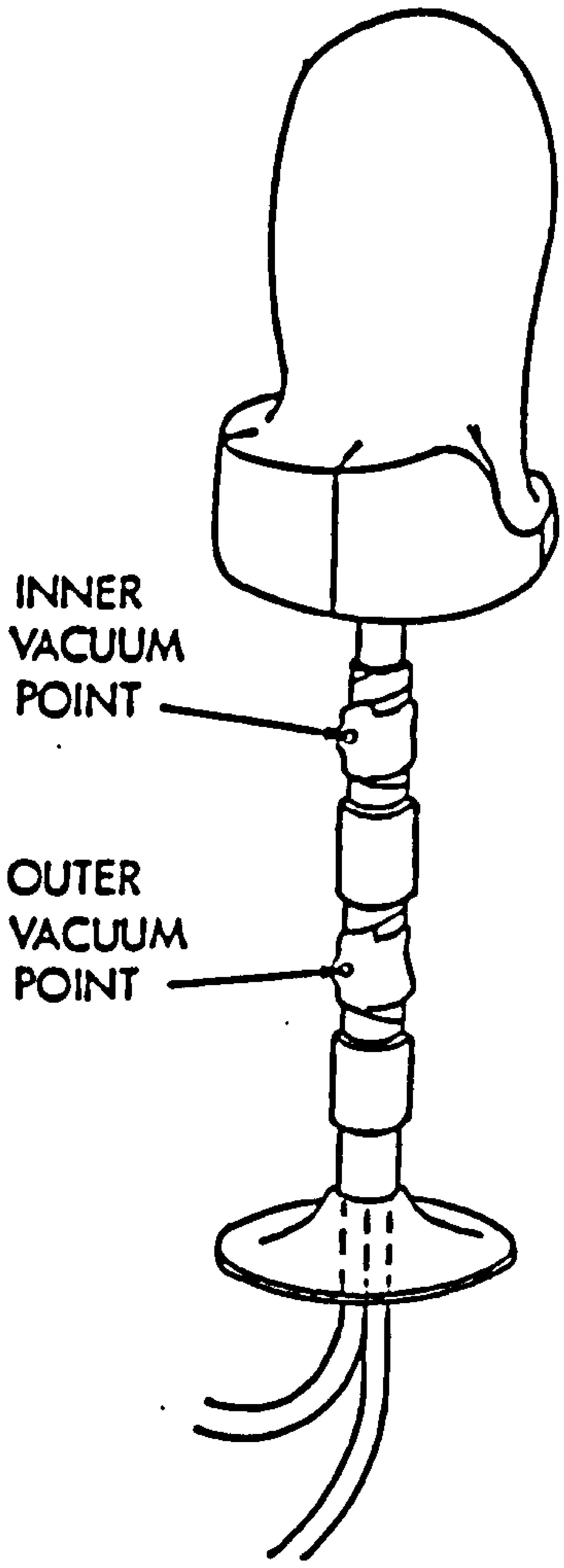

Fig. 3.2.3.1 Two vacuum point mandrel.
(NCTEPO, 1991)

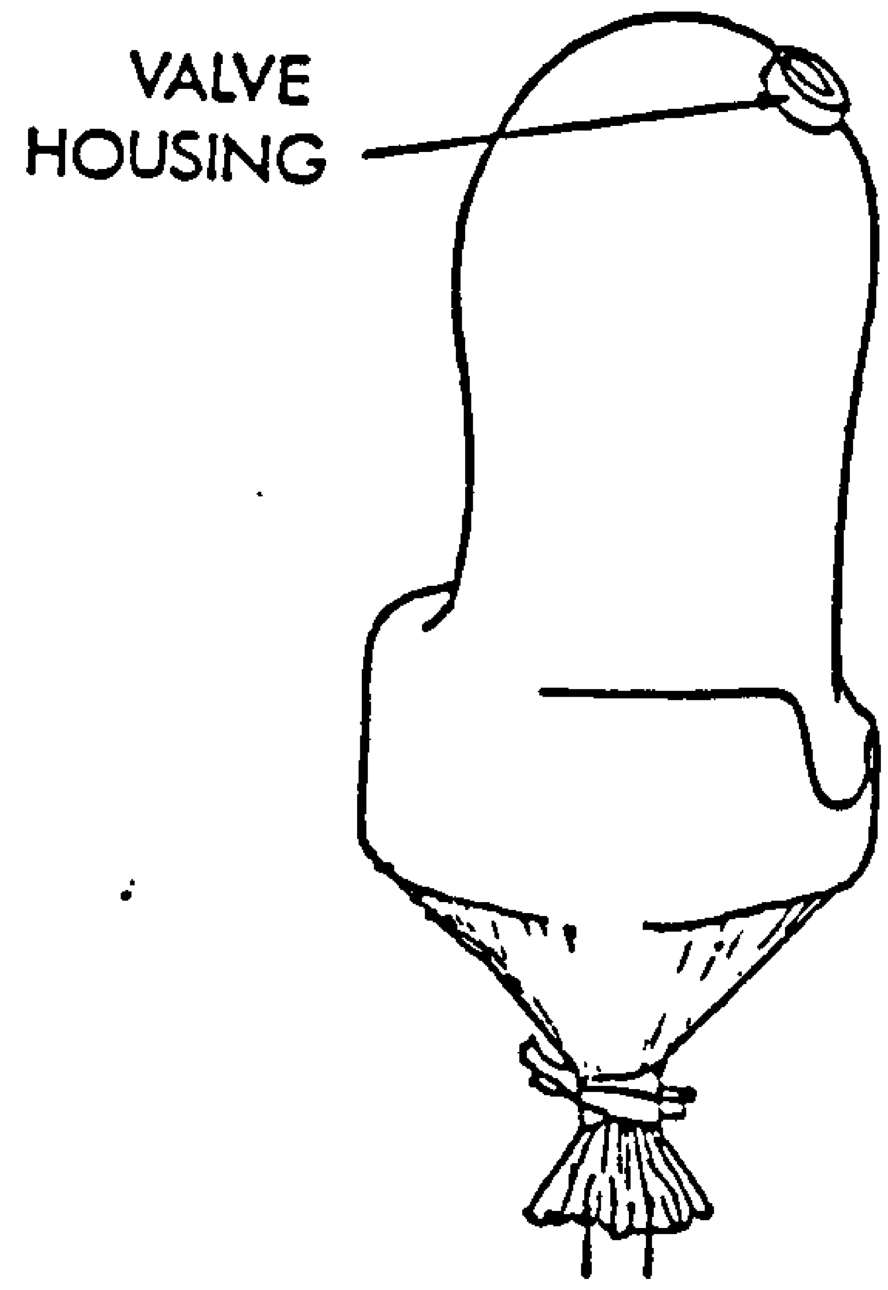

Fig. 3.2.3.2 PVA sheet secured below inner vacuum point.
(NCTEPO, 1991)

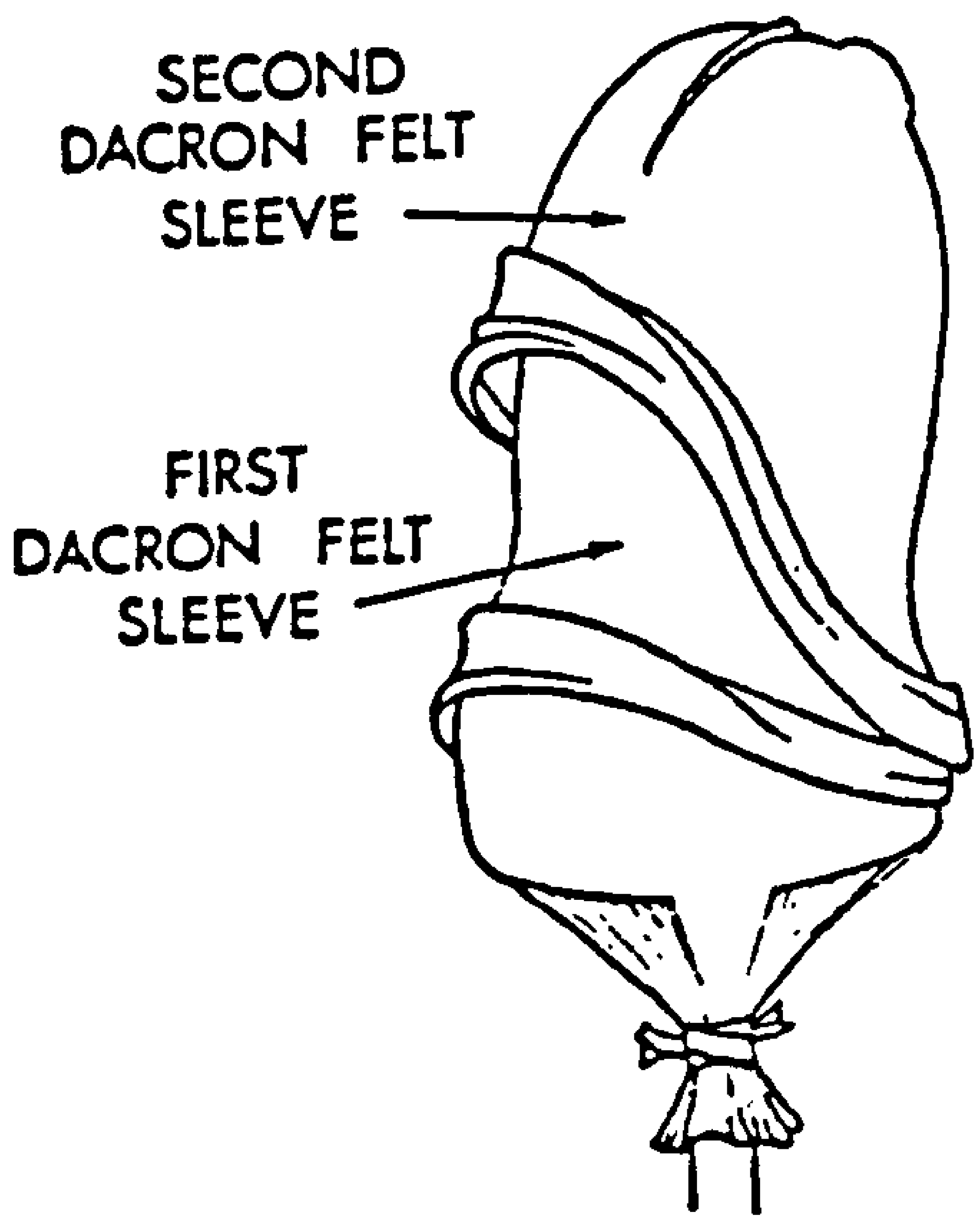

Fig. 3.2.3.3 Dacron felts lay over the PVA sheet.
(Modified from NCTEPO, 1991)

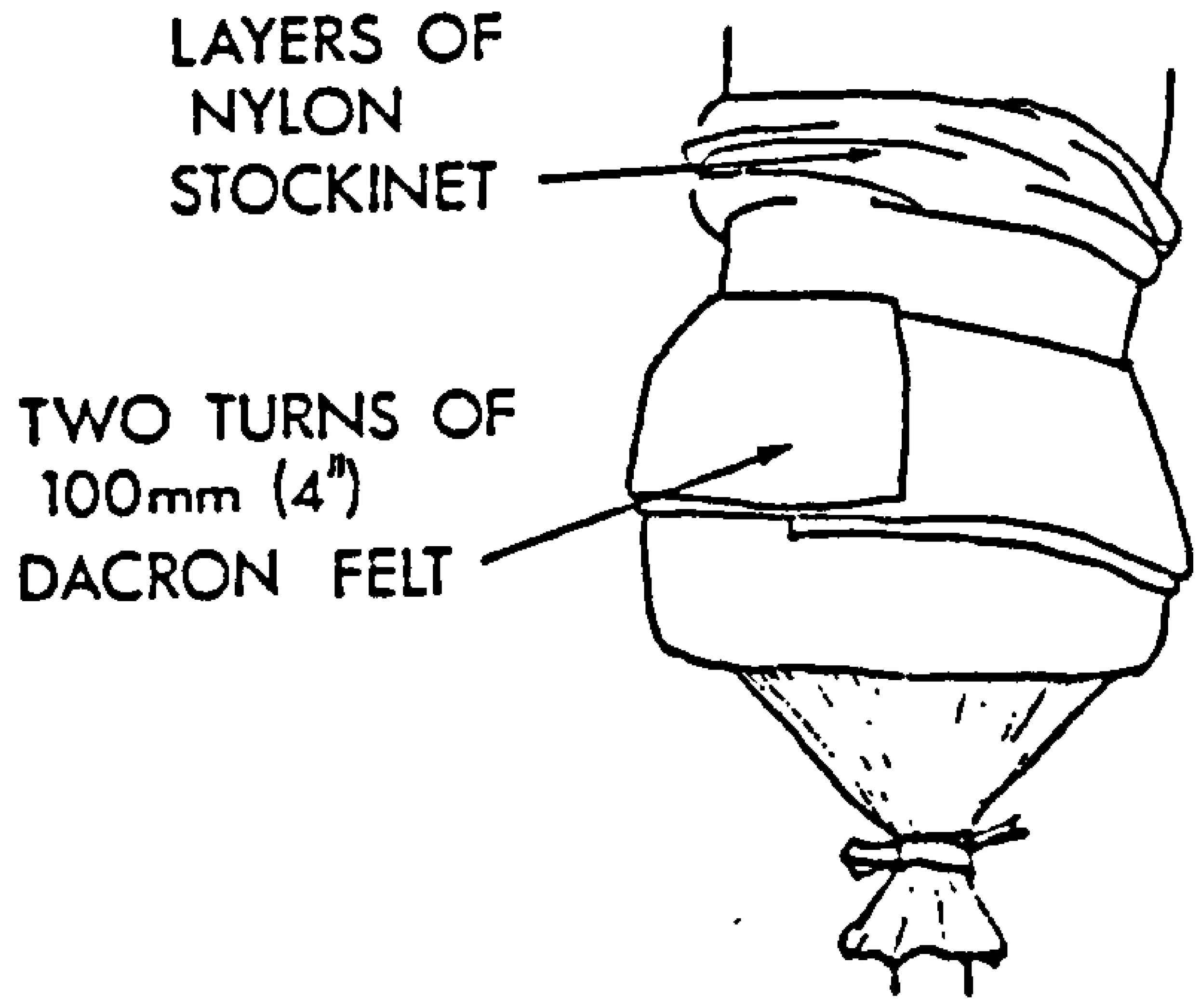

Fig 3.2.3.4 Additional Dacron felt reinforced weight bearing area.
(NCTEPO, 1991)

model are increased or decreased by removing and adding plaster at the gluteal area and the medial brim respectively.

However, the above recommendations are only given as a guide, the prosthetist must consider the unique characteristics of each amputee's residual limb prior to creating a suitable socket. The manufactured socket is an exact negative replica of the rectified model, thus, any major flaw inherent at this stage will lead to an unsuitable socket being manufactured.

3.2.3 Prosthetic socket fabrication

The methods of fabrication depend on the final material selected for the socket. Sockets made of thermoplastics are vacuum formed: heated thermoplastic sheets or pre-formed cones are placed over the positive mould; applying vacuum, the draped material is caused to conform to the mould tightly and left to cure, taking its shape.

Socket lamination is another method commonly applied to the fabrication of the sockets. The socket is made up of a combination of woven materials like Nylon stockinette, Dacron felt and fibreglass cloth, which are held together by polyester in acrylic resin. The process is also vacuum assisted. The positive mould is initially placed on a two vacuum point mandrel (Fig. 3.2.3.1). A moistened poly vinyl alcohol (PVA) sheet then covers the mould surface, which is coated with light oil to prevent wrinkles forming on the PVA sheet. The open end of the PVA sheet is secured tightly by tying it just under the inner vacuum point. A vacuum is applied at this stage to the PVA sheet and maintained throughout the whole process (Fig. 3.2.3.2).

The suction socket valve housing is positioned on the mould surface using plastiscene. Woven materials are then laid over the mould surface and the valve housing, beginning with one sleeve of Dacron felt (Fig. 3.2.3.3). The weightbearing area of the socket is further reinforced by one turn of 100 mm wide Dacron felt (Fig. 3.2.3.4), and the valve housing area is strengthened by three rings of fibreglass cloth. A layer of fibreglass cloth is then placed over the whole surface of the mould, followed by four layers of Nylon stockinette and finally an open ended PVA sleeve.

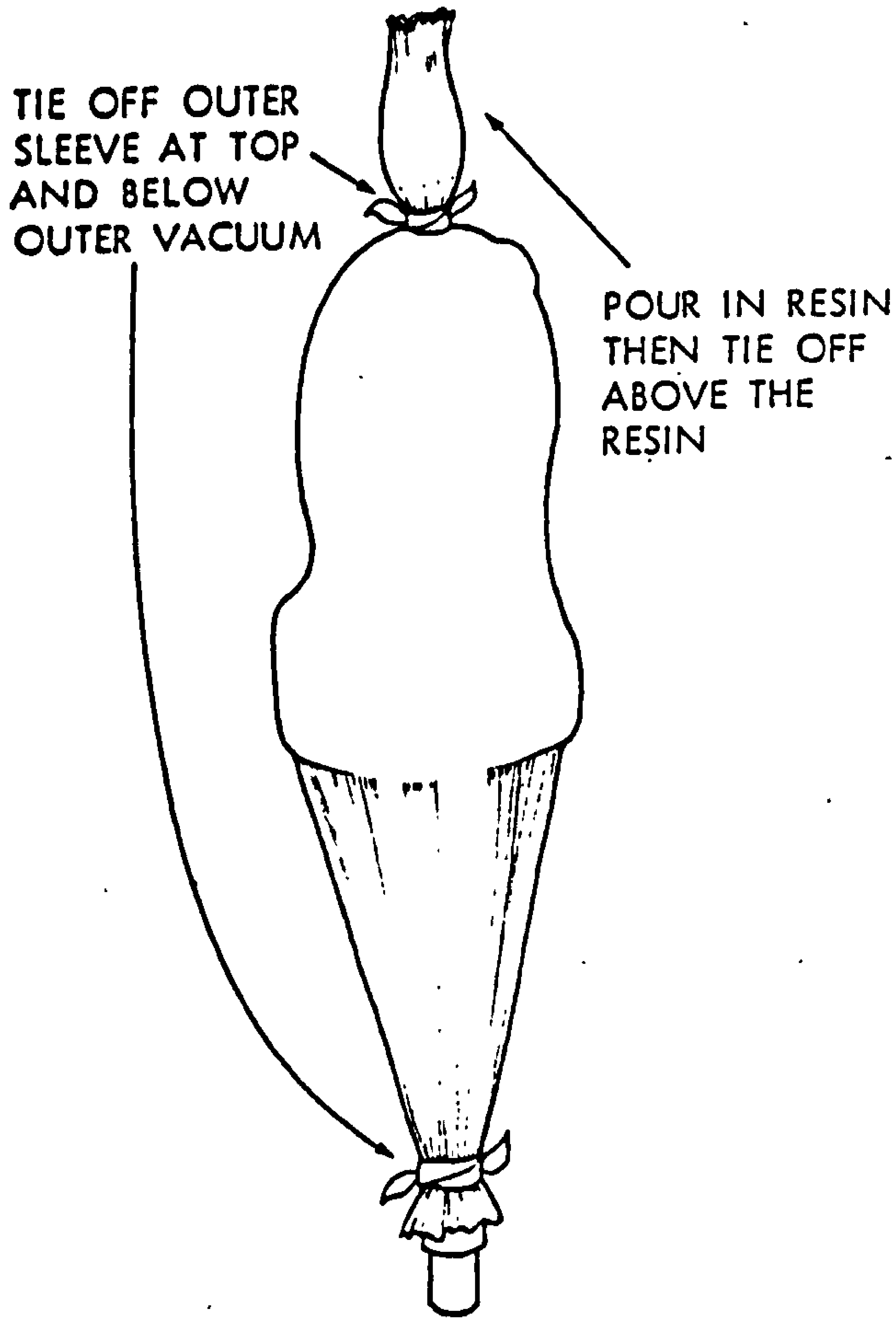

Fig. 3.2.3.6 Tie is released to allow resin to flow into fabrics. (NCTEPO, 1991)

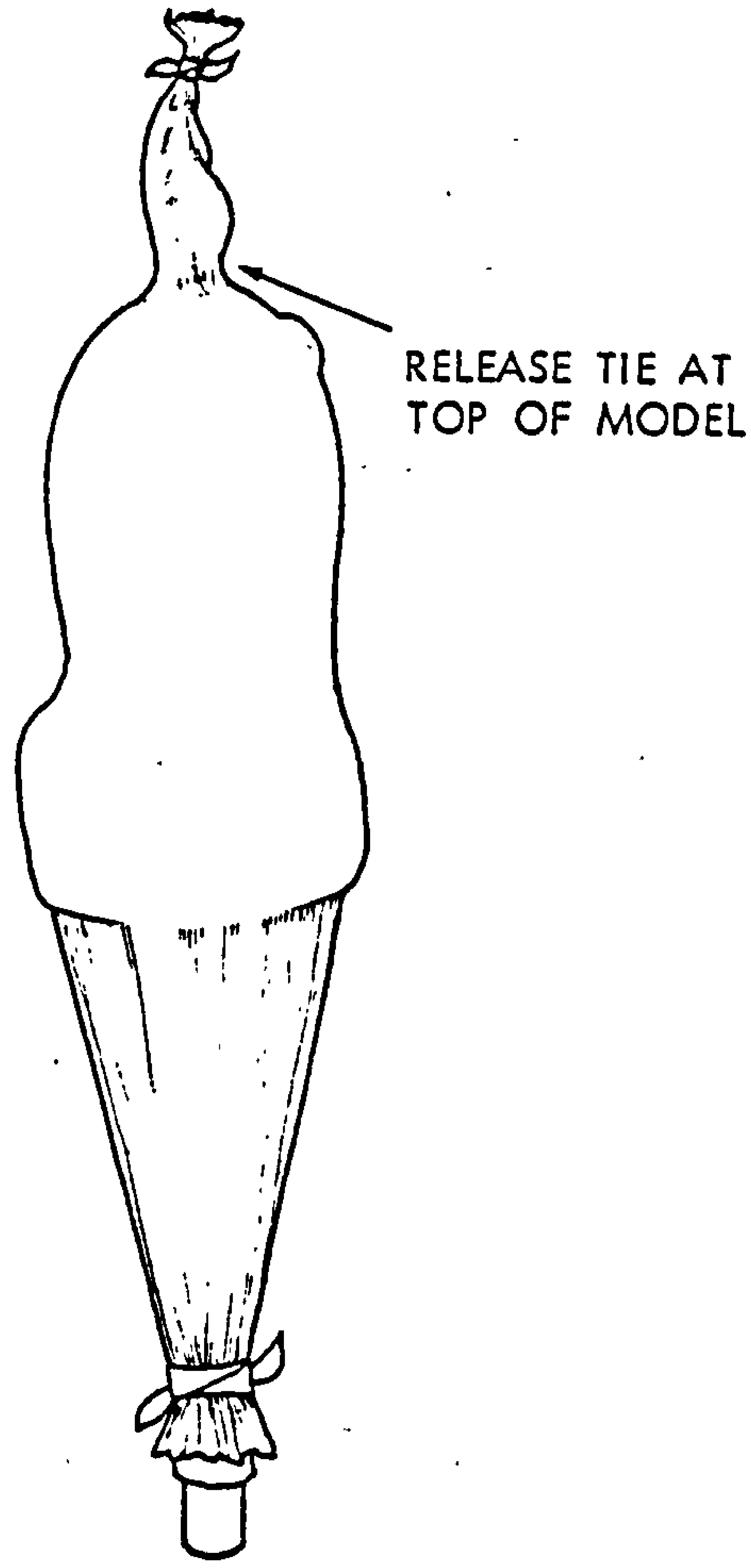

Fig. 3.2.3.5 Second PVA sheet secured below outer vacuum point. (NCTEPO, 1991)

Fig. 3.3.1 Customised hip prosthesis. (Granholm et al, 1987)

The lower end of the PVA sleeve is now secured below the outer vacuum point, while the top end is secured close to the mould, leaving a sufficient extension to contain the resin (Fig. 3.2.3.5). Upon securing the top end, a vacuum is applied and maintained. Resin is poured in at the extension and tied off above the resin. The tie close to the model is released and the resin is left to flow down slowly and into the fabrics (Fig. 3.2.3.6), until they are completely filled and saturated. The resin is left to cure and hardened. The socket is removed by breaking the plaster mould.

3.3 COMPUTER AIDED SOCKET DESIGN AND FABRICATION

Computer aided design and manufacturing, known by the more general acronym, CAD/CAM was introduced to mechanical and manufacturing based industries in the 1960's. The process has since been adopted by a large diversity of other industries. In the field of medicine, dentistry was one of the first to adopt CAD/CAM clinically (Rekow 1992). CAD/CAM has also benefited the orthopaedic field greatly. Granholm et al (1987) and Alexander (1990) described custom made hip prostheses using CAD/CAM. Using computer tomography (CT) scans, 3-D images of hip anatomy and of the femur can be described. Computer software then simulates the surgical procedure where the femoral head and neck are resected exposing the femoral canal for insertion of the prosthetic hip stem. Defining the femoral canal geometry, an optimal fit customised prosthesis can be designed and manufactured (Fig. 3.3.1). Rhodes et al (1987) also discussed the possibility of a main CAD/CAM centre serving numerous local CT scanning clinics providing wide ,fast and low cost services to orthopaedic needs.

CAD/CAM, has also found application in a variety of surgical treatments. Three-dimensional computer graphics and physical model reconstructions of the head (Marsh et al 1985, Klein et al 1992), spine, pelvis and wrist (Totty et al 1984, Vannier et al 1985, Weeks et al 1985) have been produced to assist surgical planning and evaluation.

The idea of using CAD/CAM for external prosthetics of the lower limbs was suggested as early as the 1960's (Foort 1965). Foort presented the idea of modifying a model based on several critical residual limb dimensions to create the complete geometry of the socket, and also discussed the advantages the computer had to offer for the proposed method. Then in 1983, CASD/CAM became a reality. At the 4th ISPO World Congress, delegates witnessed a full working CASD/CAM system designed jointly by the Medical Engineering Resource Unit (MERU) in Vancouver and the University College London Bioengineering Centre (UCL-BC) (Saunders 1983). Ever since, CASD/CAM research has escalated to include work from the United States, Germany, Scotland, Sweden and Japan.

3.3.1 CAD/CAM and its application

It becomes quite uncommon to separate CAD and CAM in modern times, but these techniques have evolved quite separately.

The origin of the acronym CAD was probably coined by Sutherland, at the Massachusetts Institute of Technology during the early 1960's (Hawkes 1992). CAD is a technique in which man and machine are blended into a problem solving team, extracting the best characteristics of each other. Utilising computer technology, it is a design process assisted by sophisticated computer graphics and analytical software. The technique enables the creation, modification, analysis and optimisation of a design.

CAM has its roots in the development of numerically controlled (NC) machining during the 1940's. The increased use of computers in the late 50's led to these NC machines being controlled by the computer, thus giving rise to the terminology CNC, computer numerically controlled. CNC now encompasses many different automatic manufacturing processes like milling, turning, welding, laser cutting. The present use of computers in the manufacturing environment has stretched beyond just controlling NC machines but also embraces inspection and testing. The term CAM thus comes into use as a general heading for all of these disciplines.

CAD/CAM is simply an integration of CAD and CAM techniques into one complete process. This was made possible since both processes are controlled by computer and hence raise no problems with interfacing. This means that whatever

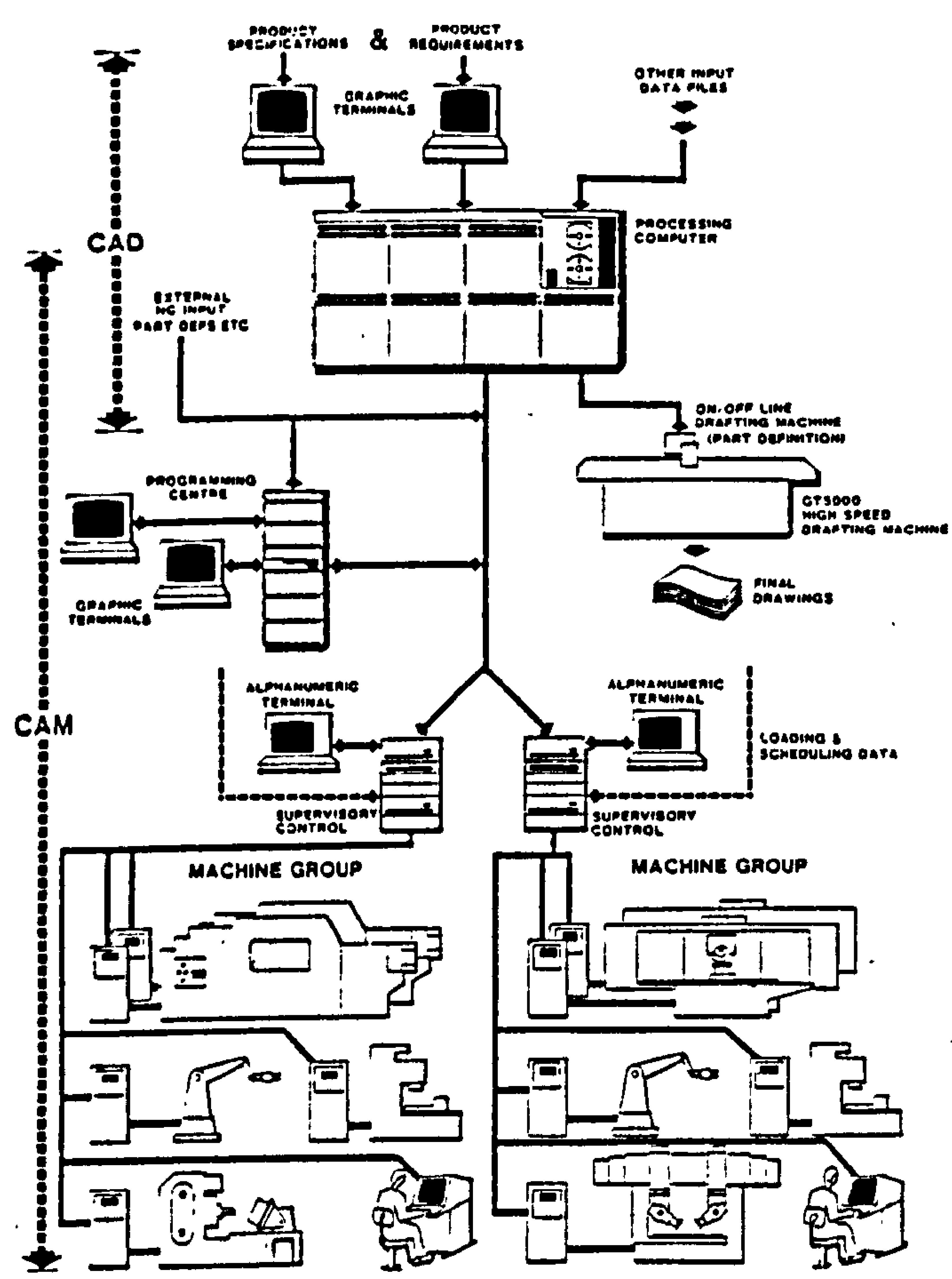

Fig. 3.3.1.1 Computer controlled manufacturing system.
(Hawkes, 1992)

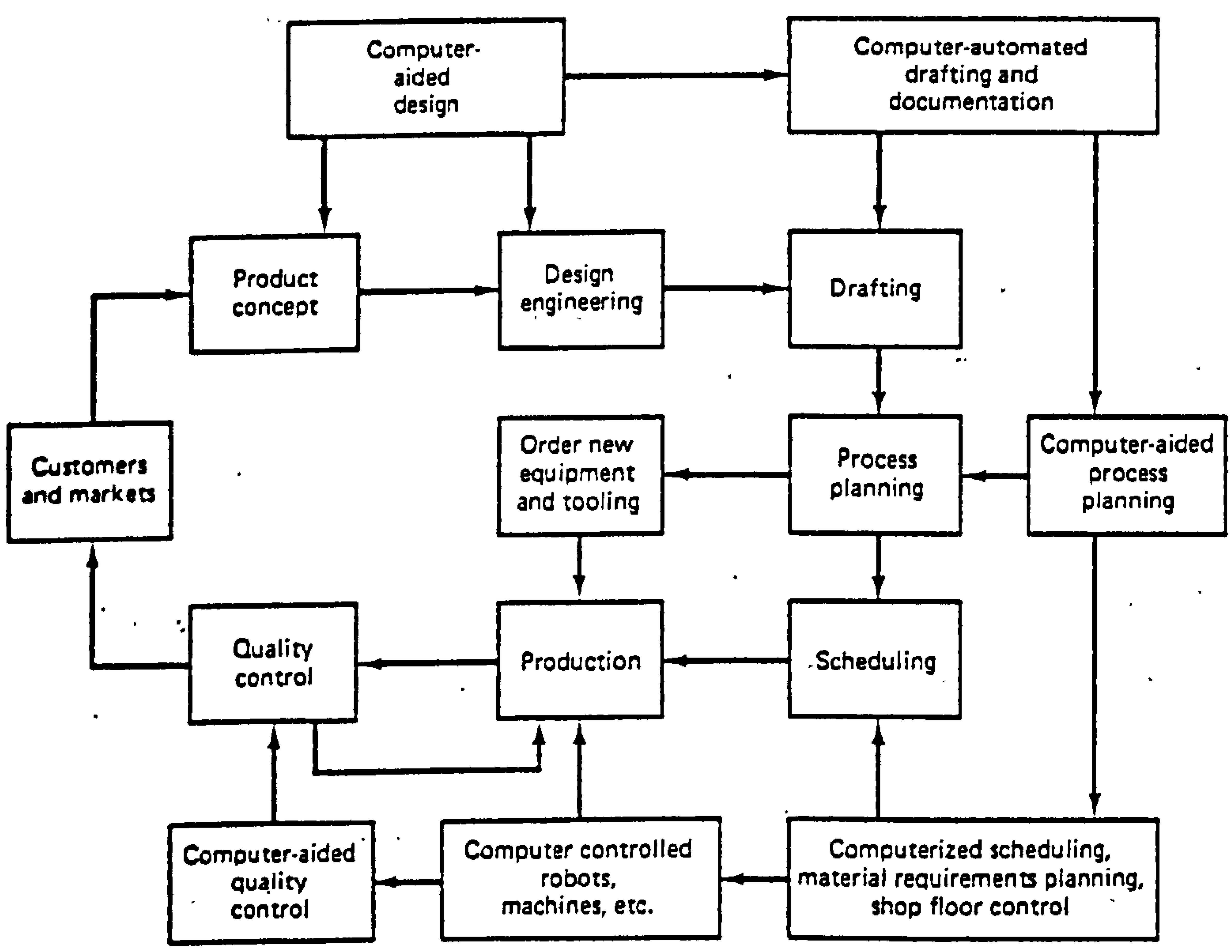

Fig. 3.3.1.2 Implementation of CAD/CAM to the product cycle. (Groover, 1980)

components have been idealised on the computer screen can be communicated in such a way as to produce them physically. Fig. 3.3.1.1 shows a typical computer controlled manufacturing system. After the design cycle is completed, the majority of work contributing to the final product is automatic. Extension of CAD/CAM now includes process planning and management. A complete integrated system will virtually overlay the activities and functions of the conventional product cycle (Fig. 3.3.1.2).

CAD hardware typically includes the computer, graphics' display terminal, keyboard and peripheral equipment like plotters and printers. The software consists of programs to implement computer graphics and application programs to facilitate the engineering functions of the user. Application software includes stress-strain analysis, dynamic response calculation, heat transfer analysis and mass properties' calculation i.e. perimeter, area, moment of inertia and centre of gravity. CAD has provided significant improvements over conventional design methods. Based on mathematical solutions, the user can decide to implement, modify or optimise the design. The computer also provides huge information storage capabilities which do not deteriorate with time, and allow rapid recall of old designs for reference. Information storage also means an increasing database of designer experiences which are accessible by other designers. By integrating CAD and CAM, communication between design and fabrication is enhanced, making no mistake through wrong interpretation of design.

3.3.2 CAD/CAM as in CASD/CAM

The initiation of CAD/CAM in external prosthetics arises from the need to automate procedures, leading to an increase in productivity and quality of products. Most components of the artificial limb are already manufactured under a tight computer controlled automated environment. Therefore introducing the computer to prosthetic socket fabrication should not come as an astonishing revelation, but rather, as described by Foort (1986) like a transition from sail to steam.

The present CASD/CAM system is a much simplified process compared to other manufacturing systems. It is basically made up of a computer controlling a shape acquisition system and a carving machine. The system processes copy the

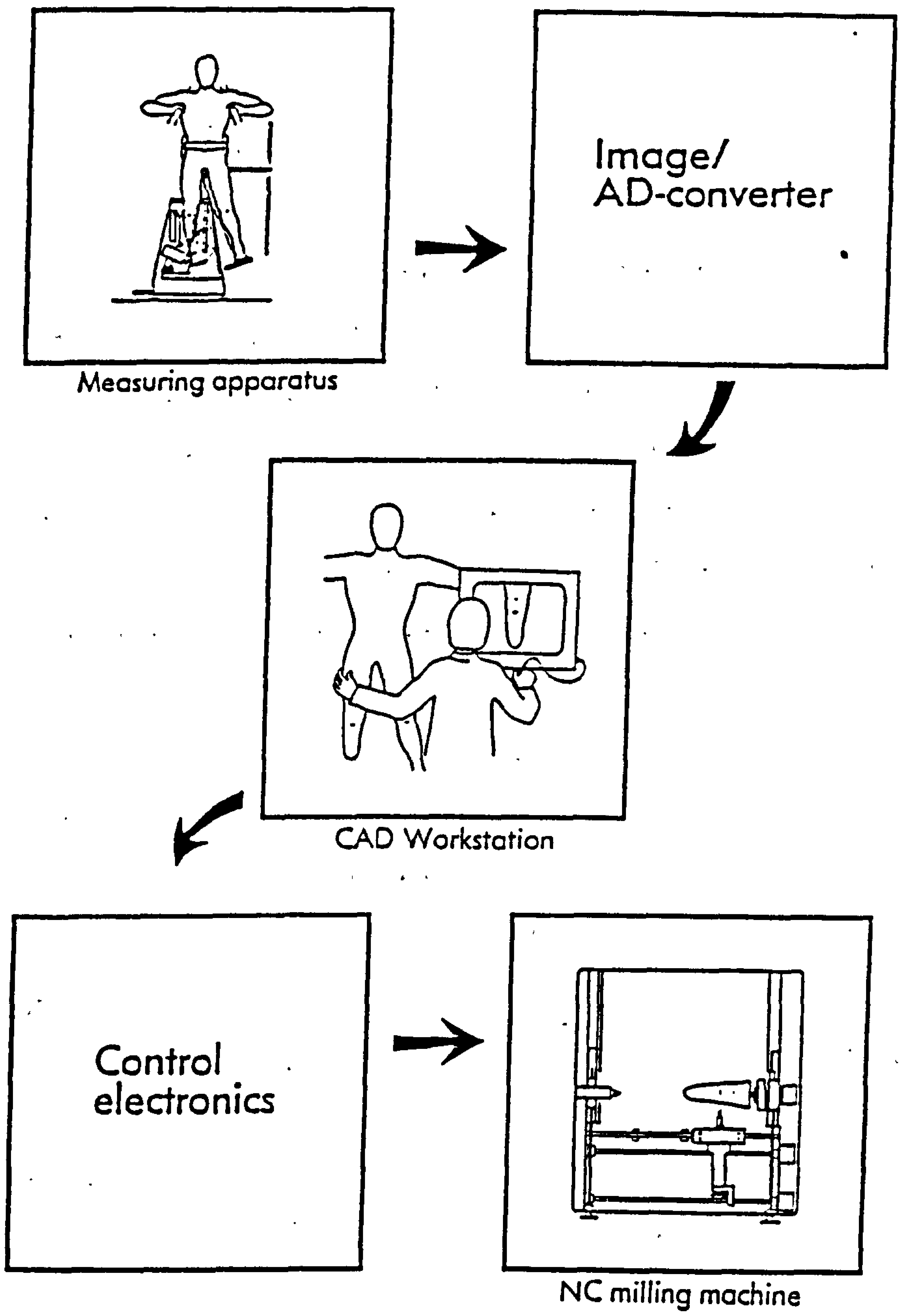

Fig. 3.3.2.1 CASD/CAM process cycle. (Oberg et al, 1987)

artisan techniques' outlined in section 3.2.1 closely. A similar three phase procedure exists consisting of,

a.) measurement of body contours where analogue measurements are converted to digital data recognised by computers,

b.) shape generation and manipulation; a shape rectification process controlled by the user,

c.) and physical realisation of the socket design. (Fig. 3.3.2.1)

The initial shape of the residual limb is first recognised through shape measurement or acquisition techniques. The acquired data are further interpreted by CASD software packages which enable the residual limb shape to be displayed as computer graphics. The rectification phase of the software then allows the acquired shape to be manipulated by decreasing or adding volume to it, moving it to any desired field of view. It is also essential for the software to provide a quantitative feedback of all the dimensional changes in the rectification performed. All these software features contribute to the creation of a desired socket shape represented in computer graphics. Finally, a replica of the final socket shape is manufactured through computer codes directed to a numerically controlled milling machine, which carves on plaster, foam or wax. A socket is then manufactured using the carved model. Alternatively direct fabrication techniques are used, producing sockets without the need of a positive model, but by buliding up layers of material to form the socket (Rogers et al 1992).

Shape measurement and acquisition, CASD software and CAM processes will be discussed in more detail in the following sections.

3.3.3 Shape measurement and acquisition

Shape measurement and acquisition have always been difficult tasks for the prosthetist. The measurement and plaster cast of the amputee's residual limb requires careful attention in order to produce a good fitting socket. CASD/CAM, however seeks to replace this particular stage in the conventional method of socket fabrication with engineering equipment, hoping to give rise to more consistent results.

M.E.R.U. - DEPT. ORTHOPAEDIC SURGERY, UBC
AMPFIT TRANS TIBIAL AMPUTEE MEASUREMENT FORM

Subject Number ______ Date amputated _________ Side _____
This date __________________ Observer ___________________

MEASURE IN INCHES

Residual Limb Measurements in inches, seated and relaxed:
- Minimum Mediolateral Dimension 1" Above Femoral Condyles _____
- (for Condylar Suspension) distance above Tibial Plateau _____
- Mediolateral Dimension .... At Tibial Plateau _____
- Anteroposterior Dimension At Mid Patellar Tendon Level _____

Residual Limb Measurements, NU Suspension Casting System:

• Anteroposterior Dimensions		• Circumferential Dimensions	
At Mid Patellar Tendon	_____	At Mid Patellar Tendon	_____
1" below	_____	1" below	_____
2" below	_____	2" below	_____
3" below	_____	3" below	_____
4" below	_____	4" below	_____
5" below	_____	5" below	_____
6" below	_____	6" below	_____
7" below	_____	7" below	_____
8" below	_____	8" below	_____

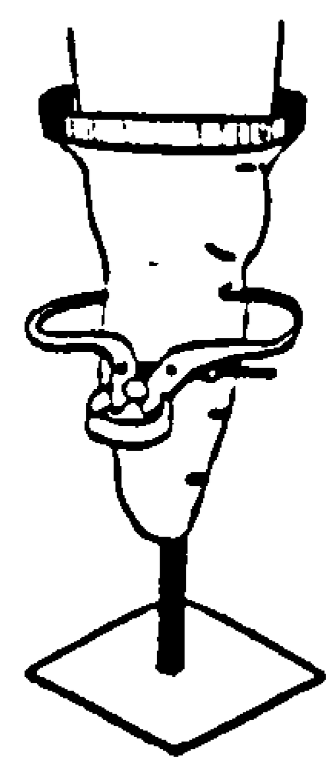

- Length from Tibial Plateau to Tibial Tip .... _____

Sound Limb Standing:
- Mediolateral Dimensions .... Maximum Shank _____
  Minimum Shank _____
- Anteroposterior Dimensions .... Maximum Shank _____
  Minimum Shank _____
- Length from Tibial Plateau to Medial Malleolus .... _____

Residual Limb:
- Tissue Quality: Sparse( ) Soft( ) Heavy( ) Firm( )
- Maturity: Complete( ) Incomplete( )
- Shape: Tapered( ) Cylindrical( ) Bulbous( )

Suspension Plan:
Supracondylar( ) Suprapatellar( ) Cuff( )

Foot Size:
.... _____

Notes: ____

Table 3.3.3.1 Measurement record for MERU trans-tibial CASD/CAM system. (Saunders et al, 1985)

Foort's (1968,1979,1984) investigations found that different transtibial or transfemoral residual limbs are, in fact, sets of geometrically similar shapes. Based on this concept, it was suggested that a suitable socket can be manufactured by modification of a standard socket shape. This idea established the foundation of the MERU CASD/CAM system for transtibial amputees. The system only requires specification of a set of measurements (Table 3.3.3.1) to describe the complete topographical description of a suitable socket (Saunders et al 1985). Using a caliper and a specially designed tool (Fig 3.3.3.1), the A-P, circumferential dimensions and cross-sectional areas are defined 25 mm intervals from the distal end to the mid patellar tendon of the residual limb. A primitive or reference socket which exists in the CASD software is then scaled accordingly to the measurements taken, creating a first customised shape which can be subjected to finer modification. The MERU CASD/CAM system has since continued its development and has become commercialised. Together with Shape Technologies, Inc. the commercial system known as CANFIT transtibial system, holds nine reference sockets instead of one (Saunders et al 1988). The sockets vary in three sizes through small, medium and large. It is further classified into three groups namely, tapered, cylindrical and bulbous according to the amount of distal end tissue. The 3x3 combination thus makes up the nine reference sockets. Upon acquiring the residual limb measurements, the software selects the closest socket size and performs a scaling routine to the correct socket size. Applying similar principles, Torres-Moreno et al (1989, 1992) reported CASD for a trans-femoral amputee using 27 reference socket shapes. The reference shapes of the adjustable brim total contact quadrilateral socket are made up of a 3x3x3 matrix combination of three brim sizes, three different lengths and tissue masses of the residual limb (Fig. 3.3.3.2). Measurements of the residual limb comprise that of the pelvic girdle, femur and the main tissue bulk (Table 3.3.3.2). The measurements are subsequently employed for scaling five separate sections that make up the complete socket (Fig. 3.3.3.3).

Instead of the reference shape concept, a full description of geometry has been popular with other CASD/CAM systems. Dewar (1985) and Houston et al (1992)

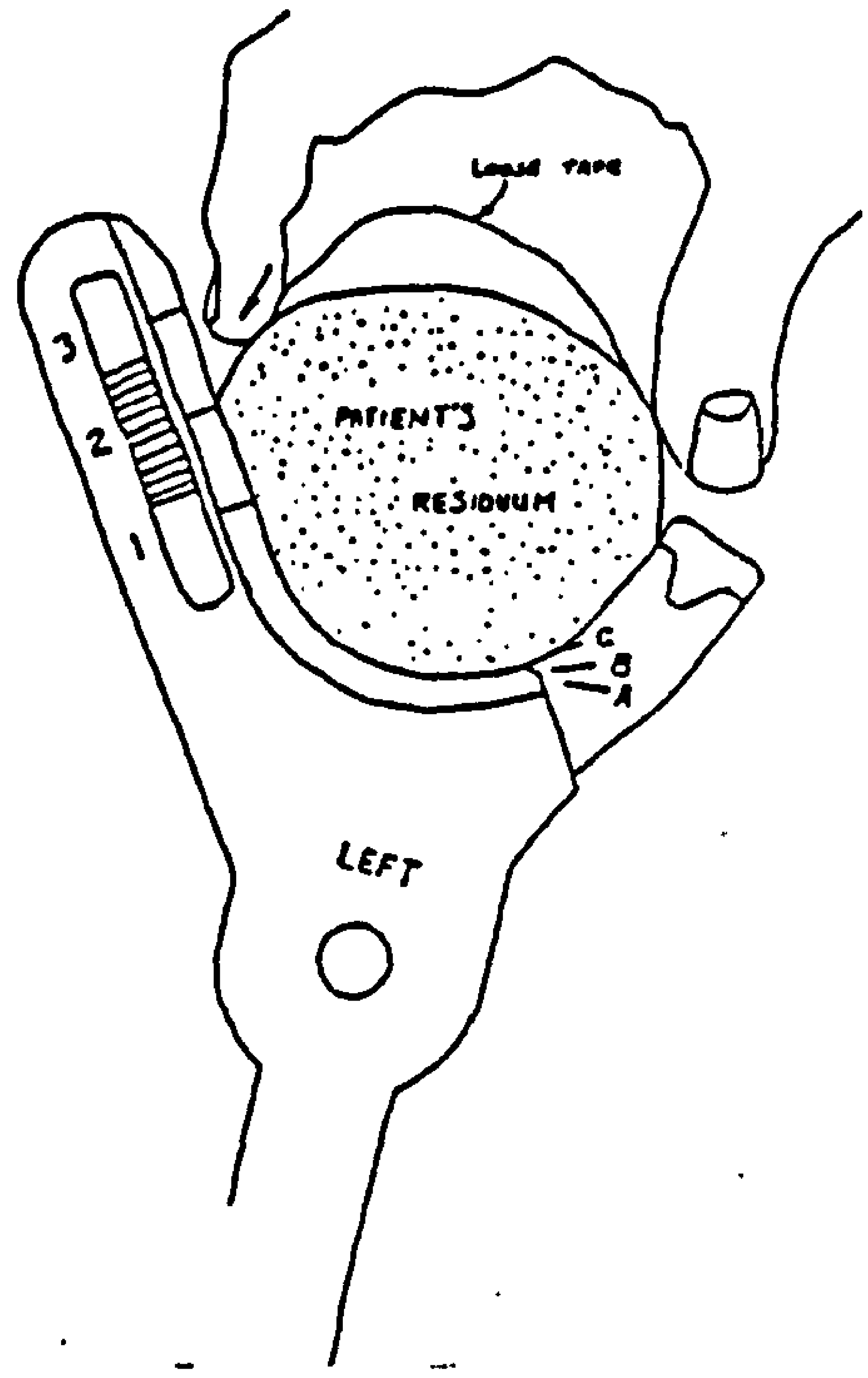

Fig. 3.3.3.1 Cross-sectional area measurement tool for MERU CASD/CAM system. (Saunders et al, 1988)

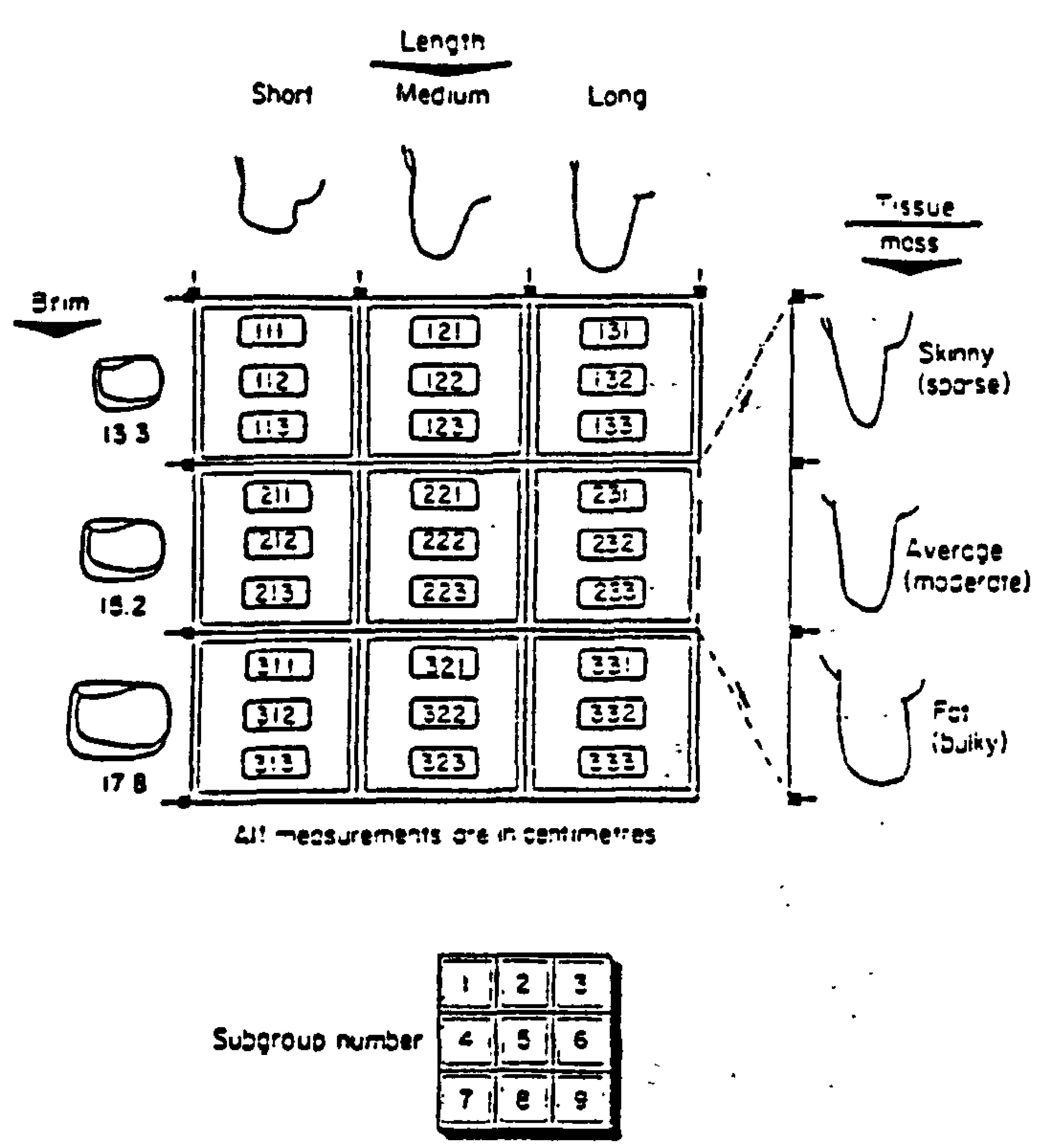

Fig. 3.3.3.2 A combination of reference shapes of the quadrilateral socket. (Torres-Moreno et al, 1989)

Subject information

Year of amputation: May 1978

Cause: train accident

Transfemoral side: right

Stump characteristics: tissue quality soft; maturation complete; shape tapered; distal–lateral bony prominence

Scar across the distal end of the stump, reaching 12.7 cm above on the lateral side, significantly invaginated

Anthropometric measurements

ML, mediolateral dimension: 15.2 cm

AP, anteroposterior dimension: 9.7 cm

SL, stump length: 24.1 cm

PH, pelvic height: 18.7 cm

IFL, intact femur length: 44.5 cm

CIR, perineal circumference: 49.5 cm

CSAR, cross-sectional areas:

Location[a] (cm)	Area (cm^2)
0	195.2
2.5	185.3
5.1	166.3
7.6	152.8
10.2	135.6
12.7	115.5
15.2	93.6
17.8	67.9
20.3	41.6

[a]Location distal from the ischial tuberosity

Table 3.3.3.2 Example measurements record for reference shape based trans-femoral CASD/CAM system. (Torres-Moreno et al, 1989)

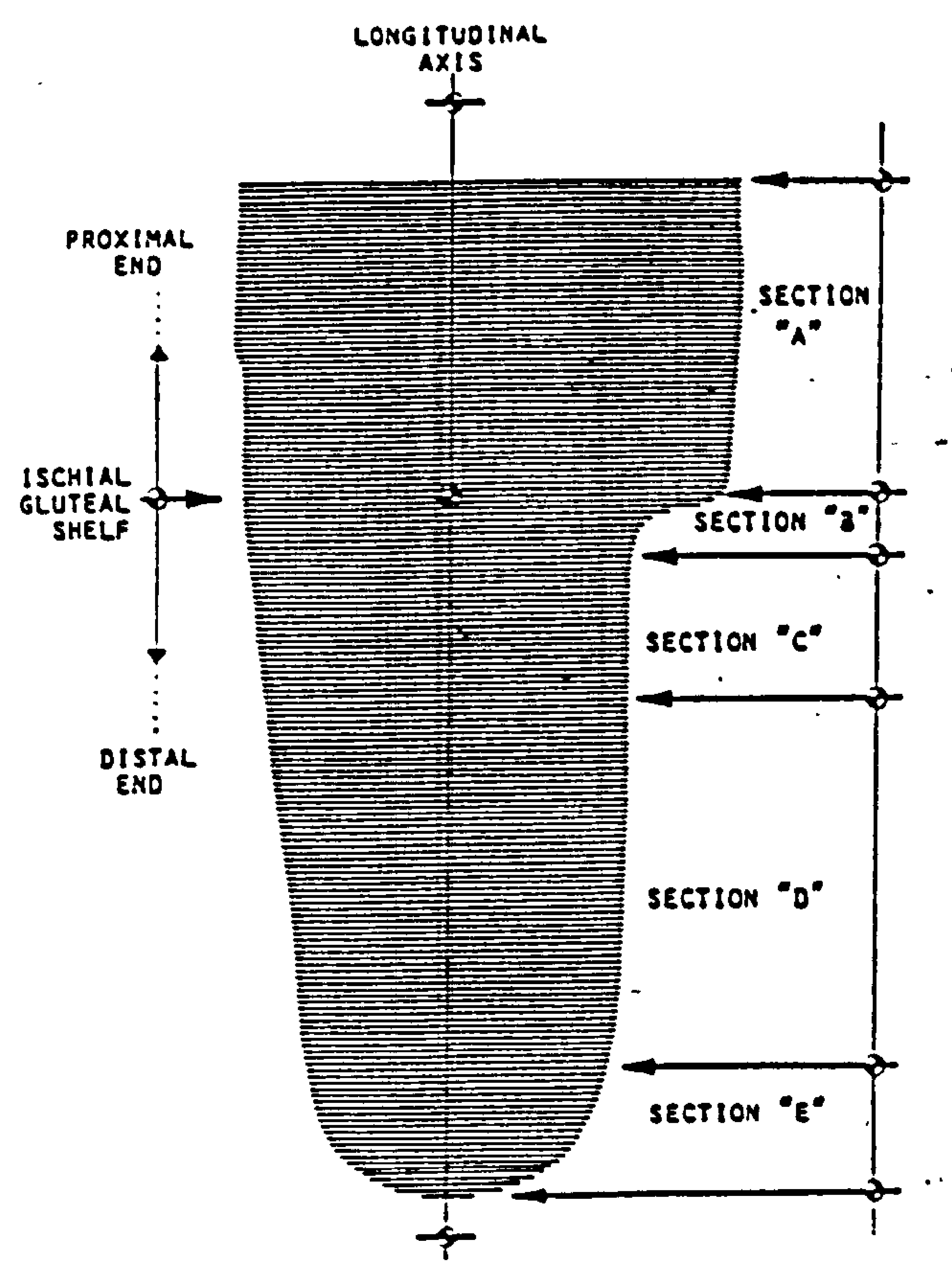

Fig. 3.3.3.3 Quadrilateral socket divided into 5 individual sections for scaling. (Torres-Moreno, 1987)

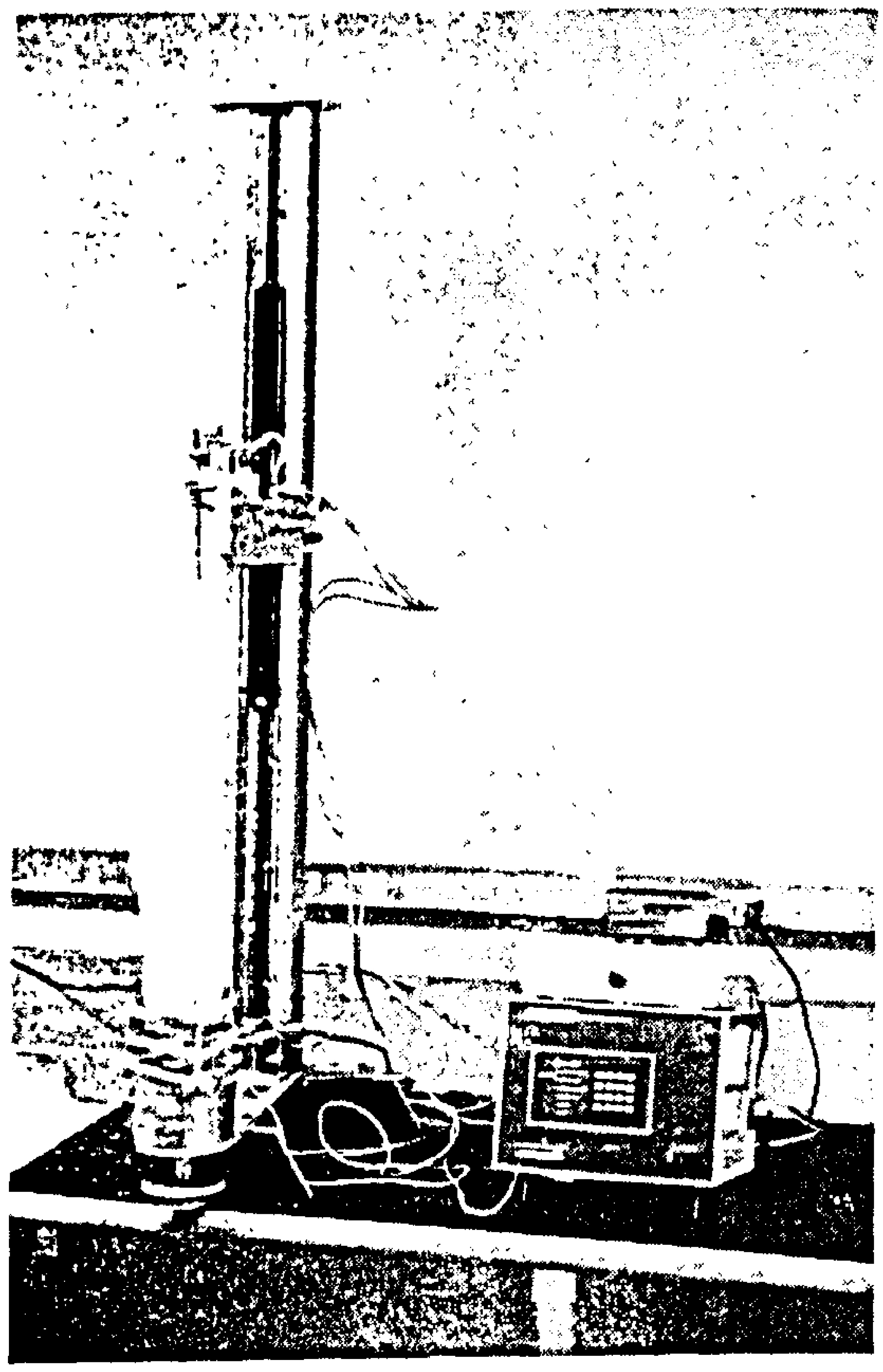

Fig. 3.3.3.4 Mechanical digitiser designed for measuring internal shape of plaster cast. (Houston et al, 1992)

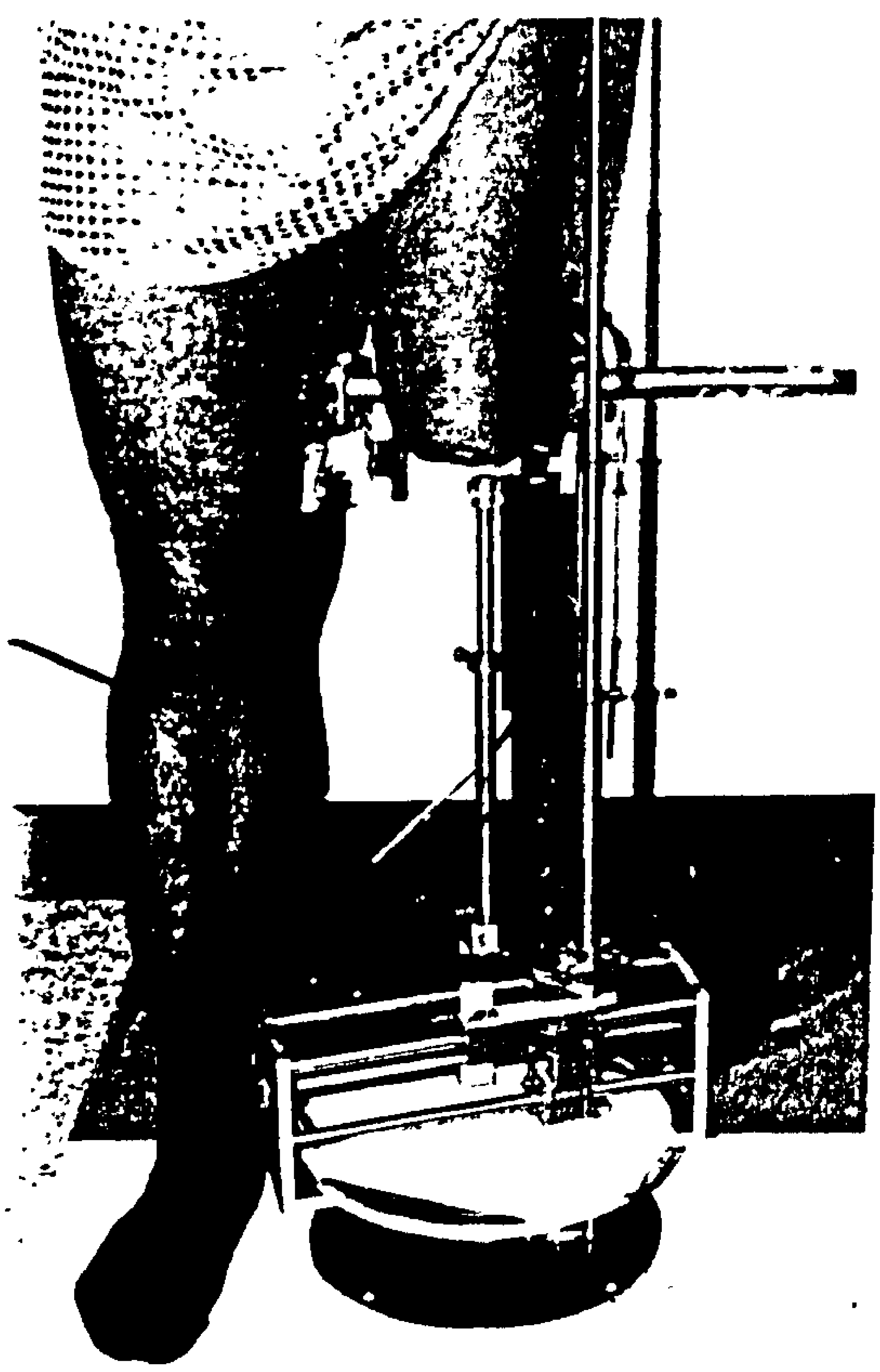

Fig. 3.3.3.5 Mechanical digitiser for trans-femoral amputee's limb. (Krouskop et al, 1988)

gave an account of the UCL CASD/CAM system which makes use of a mechanical digitiser that measures the inside dimension of a plaster wrap cast taken of the residual limb. The cast rotates about its longitudinal axis, while a pivoted arm with a follower attached tracks the inner surface (Fig 3.3.3.4). A potentiometer which outputs analogue signals is placed at the pivoted arm and records the 3-D shape of the cast. For graphical displays, the signals are converted to digital signals presented on a high resolution computer monitor.

Both the MERU and UCL systems have been criticised for the large variability that exists in the measurement results. The use of calipers and tape measures in the MERU systems was found to introduce a great deal of variation between measurements taken by different prosthetists or by the same prosthetist on different occasions (Crawford 1985). The UCL plaster cast wrap is highly subjective and dependent on the skill levels of the prosthetist. The task of producing a plaster wrap cast and subsequently digitising the cast was also deemed time consuming. The move to reduce such variability was to digitise or capture the natural untouched shape of the residual limb. It can be assumed that digitising in this manner subjects the residual limb to minimal deformation and should give rise to more consistent shape definition (Klasson 1985).

The contourgraph, a mechanical system for measuring the trans-femoral residual limb shape, was described by Krouskop et al (1988). A stepper motor drives two opposing sensor heads around the surface of the residual limb, recording circumferential dimensions. Using the two opposing sensors, radial measurements of the residual limb can be described with 180° of sensor travel. The interval of the sensor travel can range from 5-60°. Lengthwise the sensor travel at fixed increments of 5 to 40 mm (Fig. 3.3.3.5). The system is accurate to ± 1 mm and ±2.5 mm at its radial and vertical distance respectively (Krouskop et al 1989). Shape definition for a 330 mm long trans-femoral residual limb can be completed in 6 min with 234 points, though there is no mention of the exact combination of radial and vertical increment. Nevertheless, the author of this thesis would consider the time to be too long for the patient to be comfortable and still.

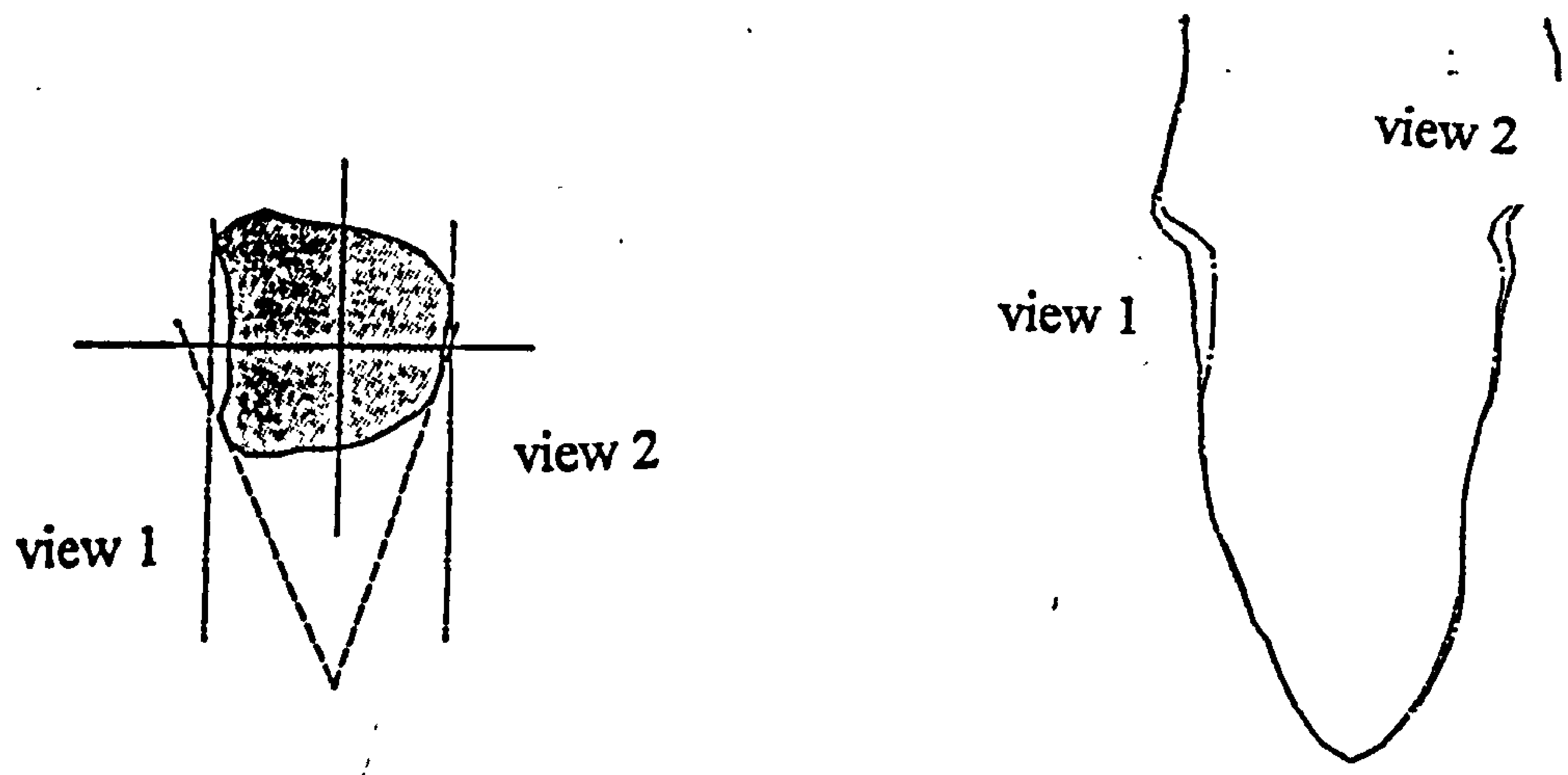

Fig. 3.3.3.6 Silhouette images affected by different distance and position of camera. (Crawford et al, 1985)

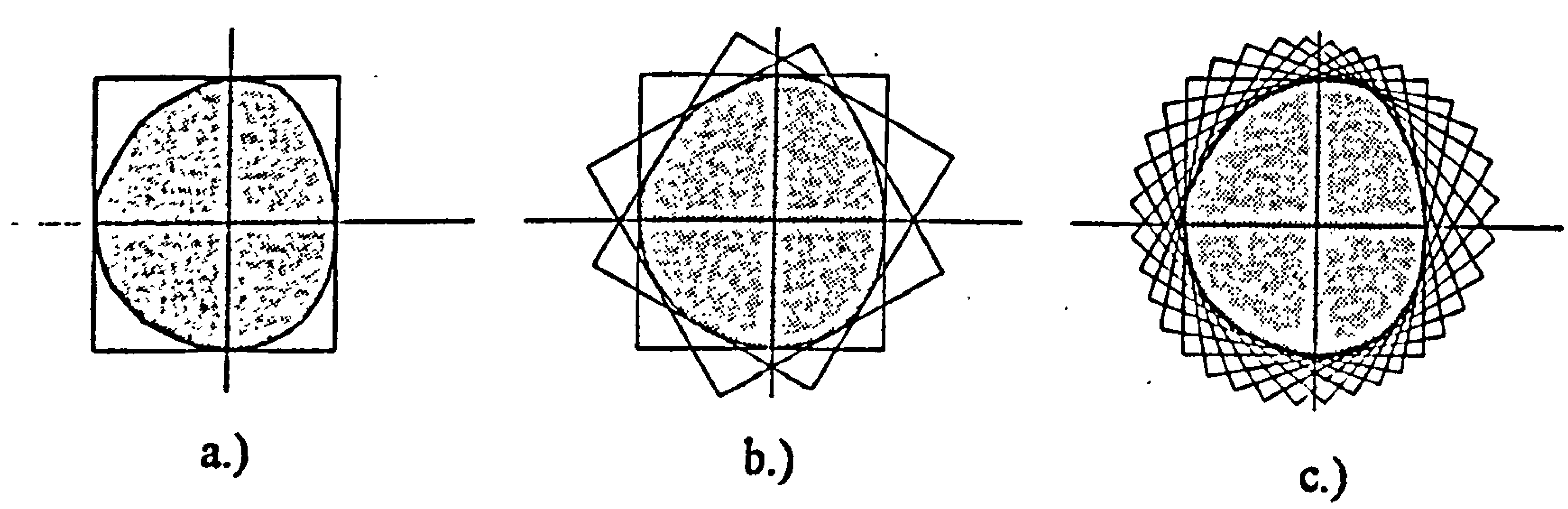

Fig. 3.3.3.7 a.) Two, b.) six and c.) eighteen sets of silhouette data. (Crawford et al, 1985)

Non-contacting optical based shape recognition systems were also introduced to eliminate the non-repeatability associated with caliper measurement and plaster cast. In addition, measurement errors due to mechanical vibration and friction between sensor and residual limb are reduced to a minimum or eliminated. UCL (Crawford et al 1985, Smith et al 1986) explored a method that used silhouette images. By taking photographs of the outline of the residual limb, a 2-D image with respect to the position and distance of the camera can be ascertained (Fig, 3.3.3.6). This image defines the limits within which the shape is contained. Increasing the number of images, it becomes possible to define more accurately the boundaries within which the shape must lie in 3-D (Fig. 3.3.3.7). However, one limititation of this method is that it cannot detect concavities in the horizontal cross-section.

Another form of non-contact measurements adopts the principles and characteristics of laser. Fernie et al (1985) and Oberg et al (1988) have discussed the working principles in much detail. Basically, a laser beam directed through an optical lens is converted to a line of light that projects onto the object to be scanned. The light appears to be following the contour of the object when viewed at a suitable angle. Placing a camera at this particular field of view, the contour line projected onto the object can be captured and represented digitally. By rotating the line of light and simultaneously recording each projected contour, a full 3-D shape of the object can be created. Fernie et al (1985) presented a shape sensing system equipped with 9 cameras positioned at 40° intervals and a light source that is projected onto the diametrically sides of the surface of the scanned residual limb. The rotating arm (Fig. 3.3.3.8) carrying the two lines of light travels 180° for one complete scan. As the line of light rotates, the electric control circuitry selects the appropriately placed cameras for recording. Each camera captures eight sets of data producing a total of 72 sets at 5° intervals around the residual limb.

The commercial CAPOD system from Sweden (Oberg et al 1988) is a similar system but with a single camera and line of light. The camera and light source are both mounted on a rotating table (Fig. 3.3.3.9) and travel 360° around the residual limb. 100 contour images of the residual limb are recorded at 3.6° intervals.

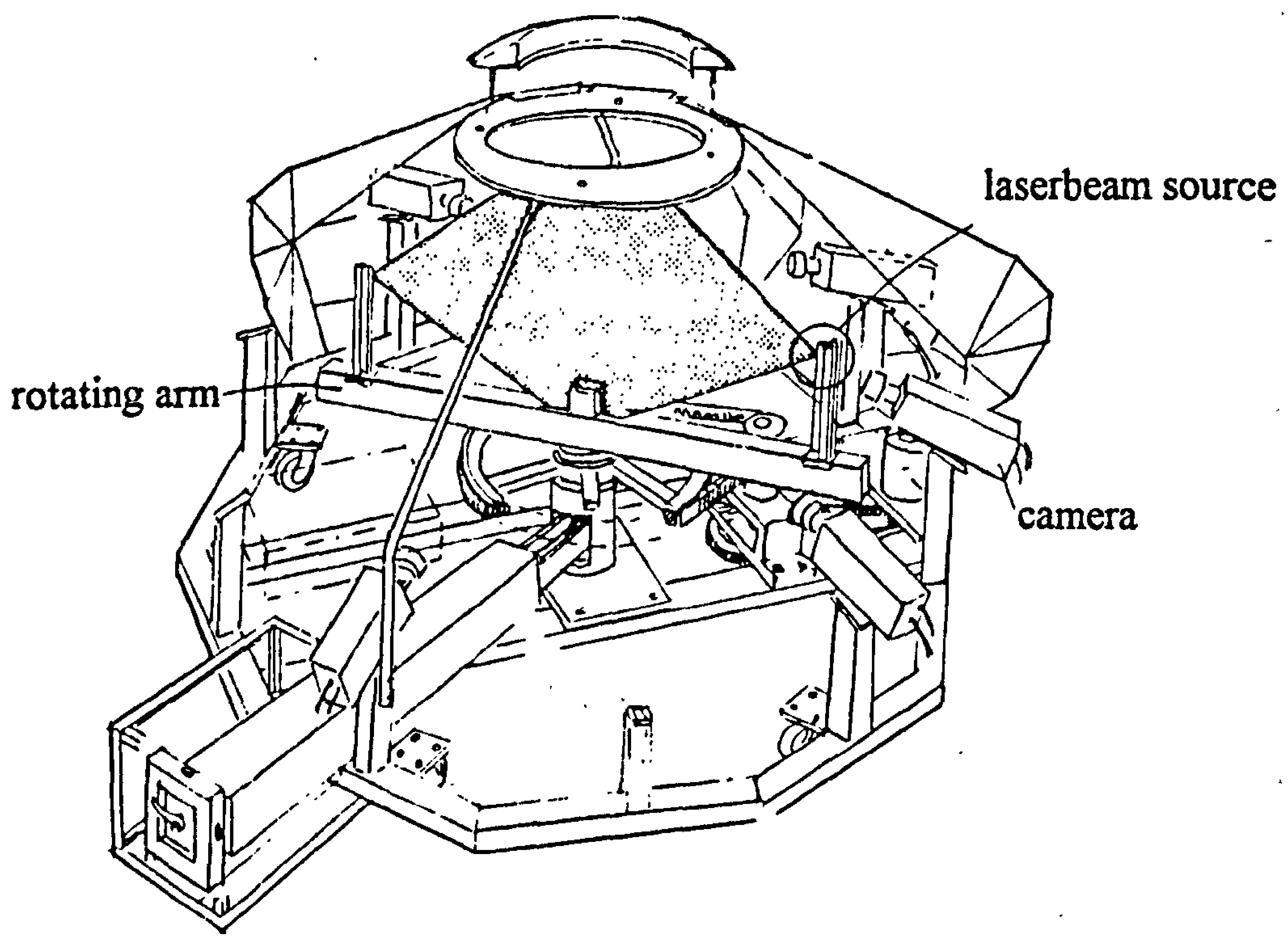

Fig. 3.3.3.8 Residual limb shape sensing based on optical triangulation principle. (Fernie et al, 1985)

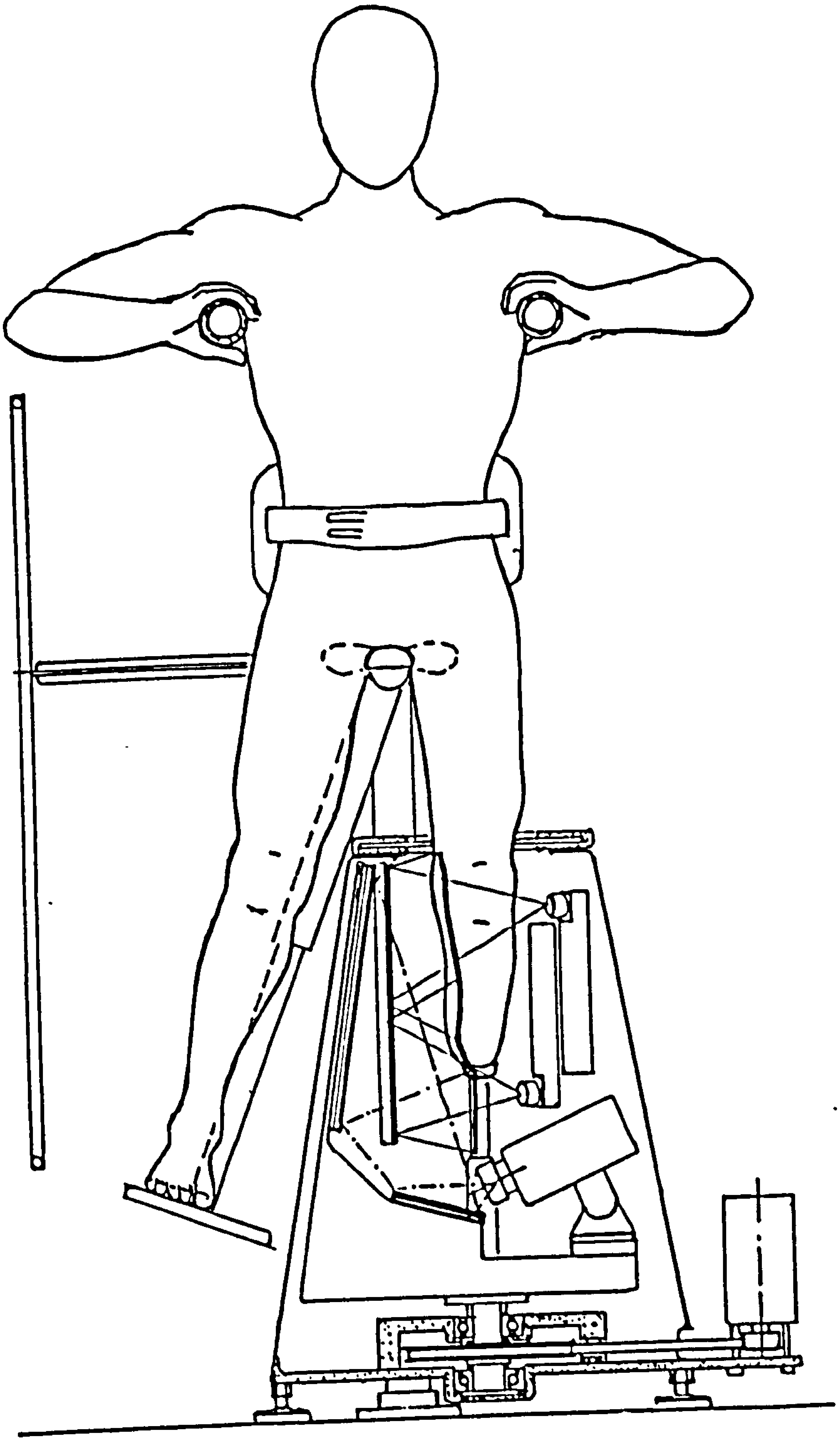

Fig. 3.3.3.9 CAPOD shape sensing system. (Oberg et al, 1988)

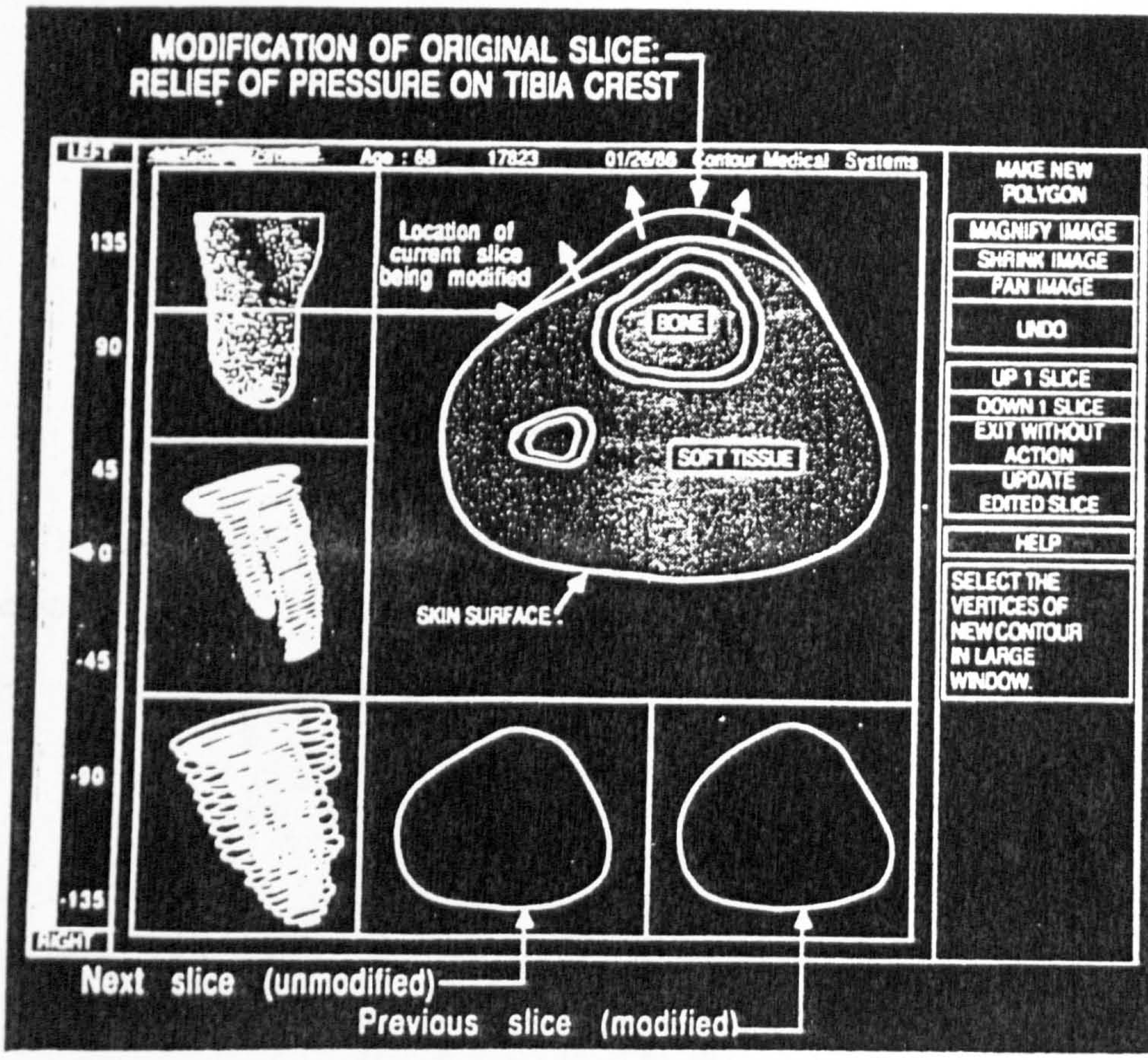

Fig. 3.3.3.10 Shape rectification of CT scans using CEMAX 1000 software. (Faulker and Walsh, 1990)

Cyberware Laboratory Inc. manufacture a laser light shape sensing system that also utilises a single camera and light source. The Cyberware model no. 4012 has been described to be in use in at least two CASD/CAM system (Engsberg et al 1992, Jones et al 1992). Shape sensing using Cyberware can be accomplished under 10 seconds with errors of less that $\pm$1.5 mm.

Researchers at the University of Texas investigated two existing shape acquisition methods, Computer Tomography (CT) scans and ultrasound, with the possibility of describing the internal geometry of the residual limb. CT scans can deliver a collection of accurate 2-D transverse geometry of the residual limb which can be used to build a 3-D model. Faulkner and Walsh (1990) discussed the viability of a CT scan for CASD/CAM purpose. CT scans of a trans-tibial amputee's residual limb were acquired using a GE 9800 scanner. The geometry was formed into a 3-D image by a computer system known as CEMAX 1000, which alternatively also allows modification of the scanned images. Based on biomechanical principles of the transtibial socket, each slice of 2-D image was modified to create a suitable prosthetic socket shape (Fig. 3.3.3.10). The final shape data was transferred to a 3-axis milling machine to fabricate a wax model.

An ultrasonic wave front can detect changes in density through the medium in which it travels. Therefore by placing the residual limb in a tank of water, a wave front directed through the water encounters the tissue producing a return echo that can be detected by a transducer. The return echo provides the basis on which the geometry of the residual limb is defined (Fig. 3.3.3.11). The prototype system produced by Faulkner et al (1988) was configured to measure only the external surface of the residual limb. The complete image can be generated using a commercial CAD program known as the Advance Space Graphics program. The scanning process takes 10 min which was a long time for the patient to keep still. (Fig. 3.3.3.12).

Shape sensing remains the most difficult task in CASD/CAM procedures. (Klasson 1985, Faulkner et al 1988). The methods discussed so far can be generally classed into three basic principles, These are,

a.) residual limb is deformed during measurement,

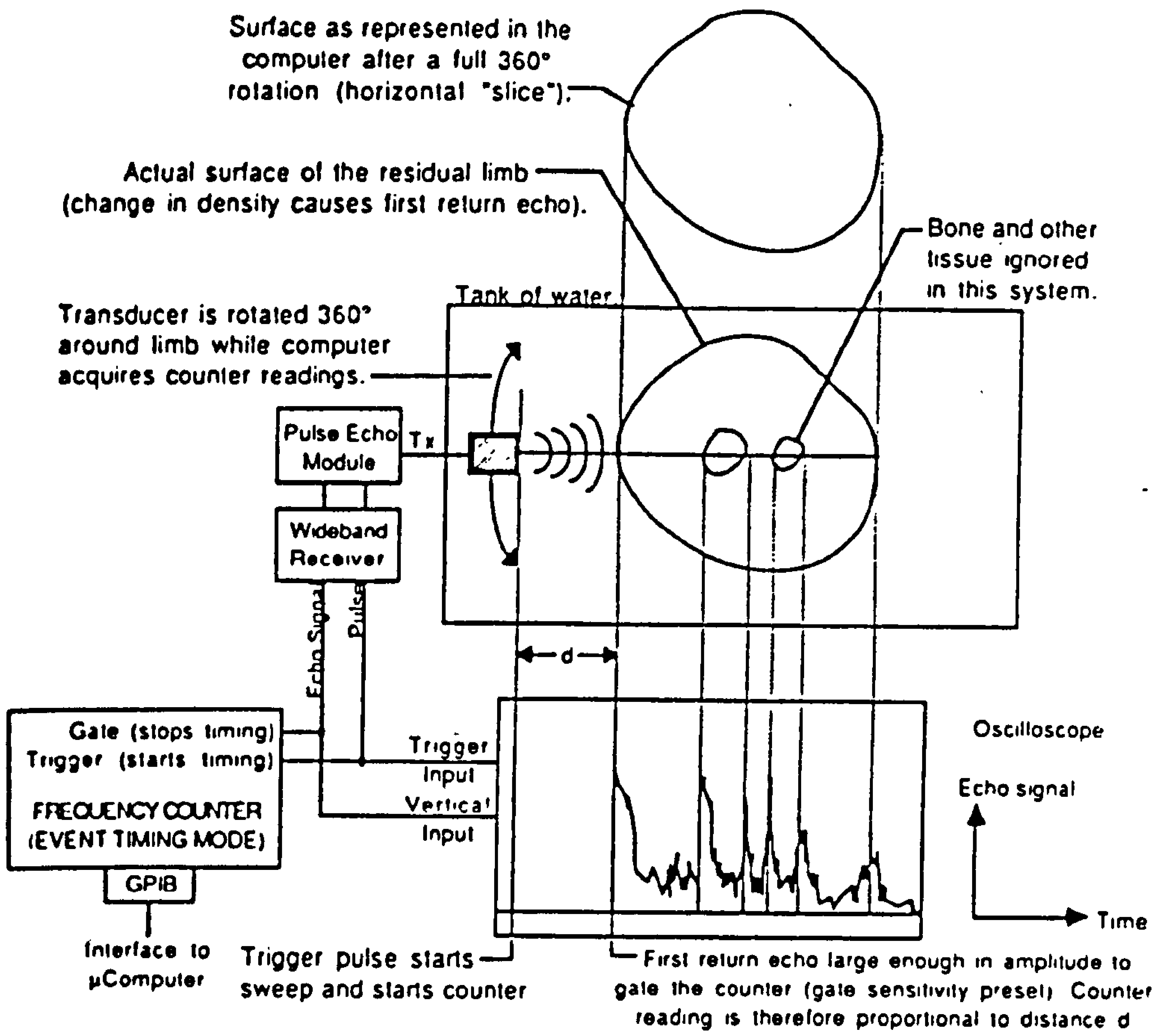

Fig. 3.3.3.11 Ultrasonic shape sensing set up. (Faulkner et al, 1988)

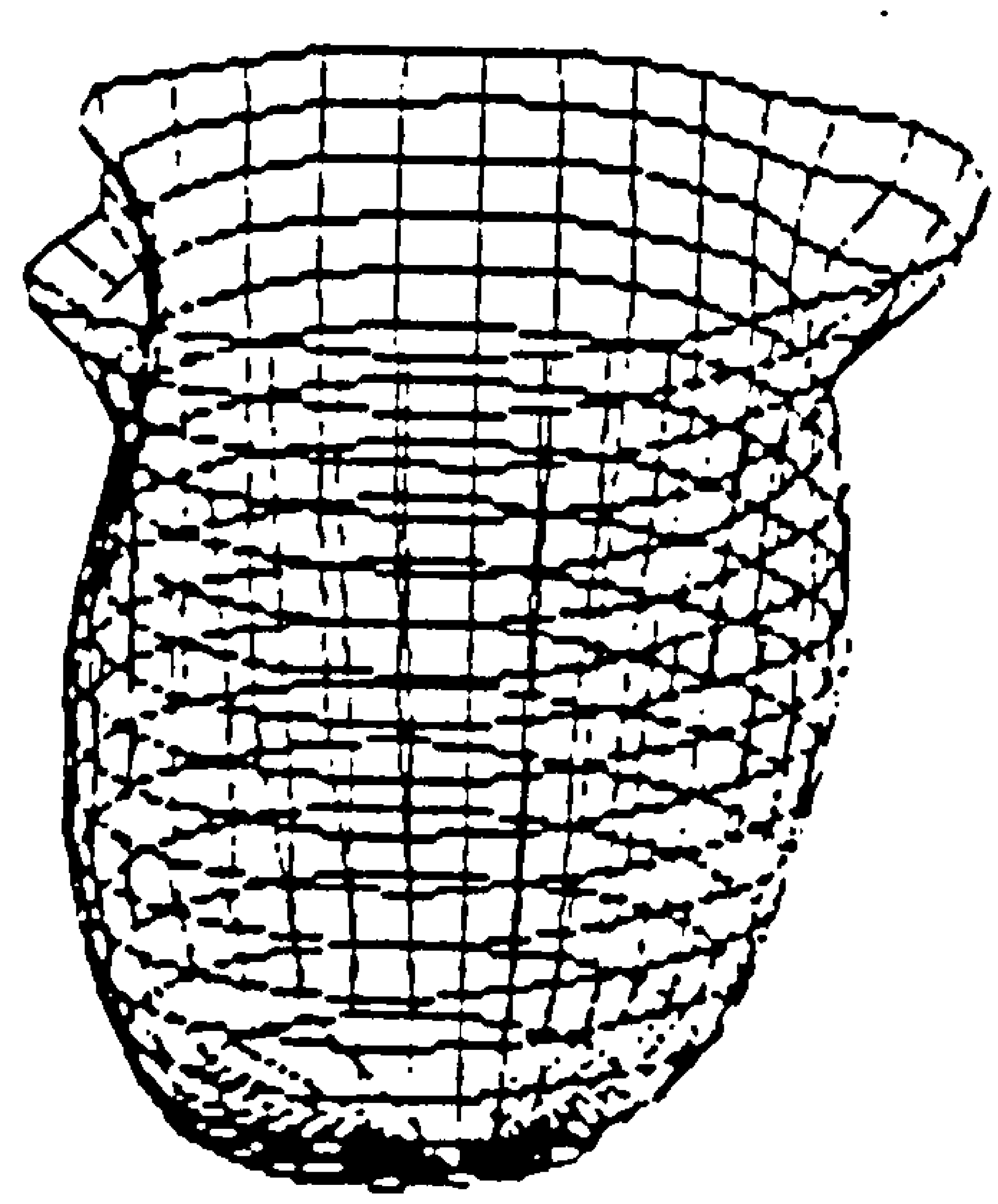

Fig. 3.3.3.12 Residual limb shape defined by ultrasonic shape sensor.
(Faulkner et al, 1988)

b.) residual limb is untouched during measurement and only surface details are captured,

c.) residual limb is untouched during measurement and both surface and internal details are captured.

The tendency nowadays is to proceed with the second option, which explains the popular use of laser light sensing equipment used in many commercial systems. Even CANFIT and the UCL CASD/CAM software have modifications to receive full surface description using this type of scanner. Reasons for adopting the non-contact method are stated as mainly consistency and fast shape definition. Klasson (1985) explains that modification of the shape of the untouched residual limb to a good fitting socket can be mathematically defined, whereas a deformed limb will introduce other variables which may be difficult to quantify. Topper and Fernie (1990) agreed in the evaluation of the CANFIT that a starting shape of the residual limb can be helpful instead of a reference shape, but cautioned against the inadequacies in the non-contact shape sensing system. These systems contradict conventional methods in acquiring shape. In the artisan method, the prosthetist's aim is to shape the plaster cast on the residual limb to be as much as possible similar to the final socket. In the midst of shaping, position of bony location and soft tissue condition are realised. Armed with this information, the areas of relief and weightbearing are catered for in the rectification process. However, information about bone structure and soft tissue properties cannot be found with systems based on the second principle.

Internal geometry and tissue differentiation on the other hand can be determined by non-contact methods like CT scan or ultrasound. However, Faulkner et al (1988) investigation in the use of CT scan only lead to the conclusion that it is too expensive and complicated for CASD/CAM purposes. The use of ultrasound is still much in its infancy and is hampered by long acquisition time.

3.3.4 CASD software

The software's main objective is to permit the CASD system operator to alter the acquired shape of the residual limb in much the same way as a prosthetist would when working with a plaster model. The software also serves as a communication device between the shape acquisition equipment, the operator and socket fabrication equipment. The essential requirements of the CASD software are therefore as follows :

a.) Ability to display graphics in a realistic and informative manner.

b.) The shape editing functions implemented must be familiar to the prosthetist who is use to working with plaster models.

c.) Efficient transfer and handling of data throughout the stages of i) receiving data from shape acquisition device, ii) manipulating shape data to a desired socket shape, iii) conversion and output of data to fabrication devices.

The present CASD software in the commercial market and research groups are mainly unique to the CASD/CAM system to which they belong. The functions are similar but with varying capabilities and methods to display and edit shapes. Some CASD software allows a choice of the type of shape acquisition device i.e. mechanical and optical digitiser, but at the moment there exists no standard software that could incorporate all types of CASD/CAM hardware in the market.

Shapes displayed on computer screens automatically lose their third dimension and physical feel, which is a disadvantage compared to the plaster model. However, computing power nowadays is able to inject a high degree of realism in visualising objects. Jones (1988) described interactive computer graphics and animation which could enable the operator to view objects as though they were held physically, and rotating objects to any angle is achieved by simple mouse or keyboard control. Shaded images also provides a realistic impression of the third dimension. Graphical representation has become an important aspect of CASD/CAM since the prosthetist is customised to performing modifications based on visual information. Most researchers therefore supports the idea of high quality graphics. However CASD, unlike the conventional method of plaster models, has the added advantage of keeping a record of modified and unmodified shapes, the amount of modification performed and the location anywhere in the object in quantitative terms. It is then possible to perform shape modification even with simple 2-D images.

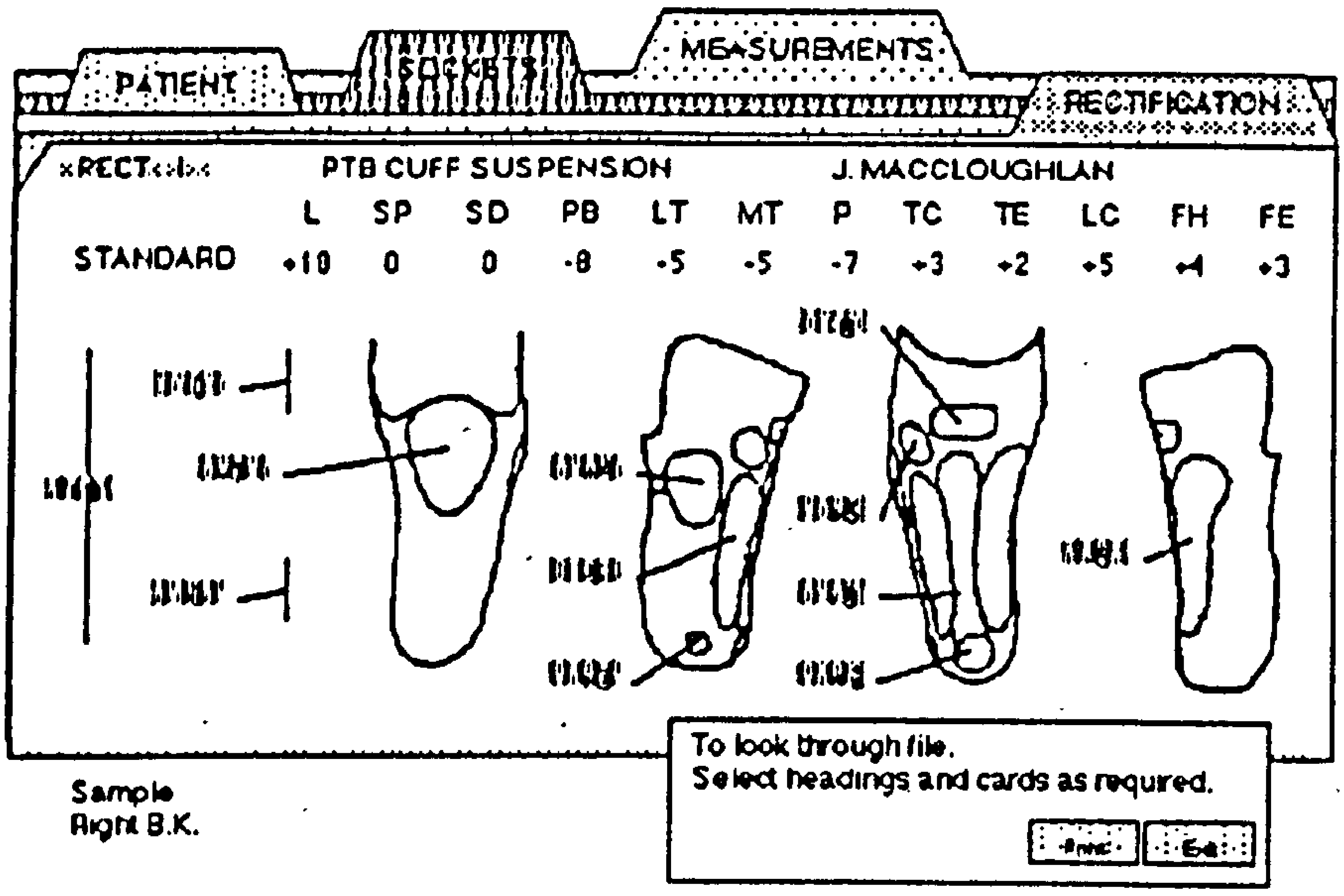

Fig. 3.3.4.1 UCL CASD software display panel. (Dewar et al, 1986)

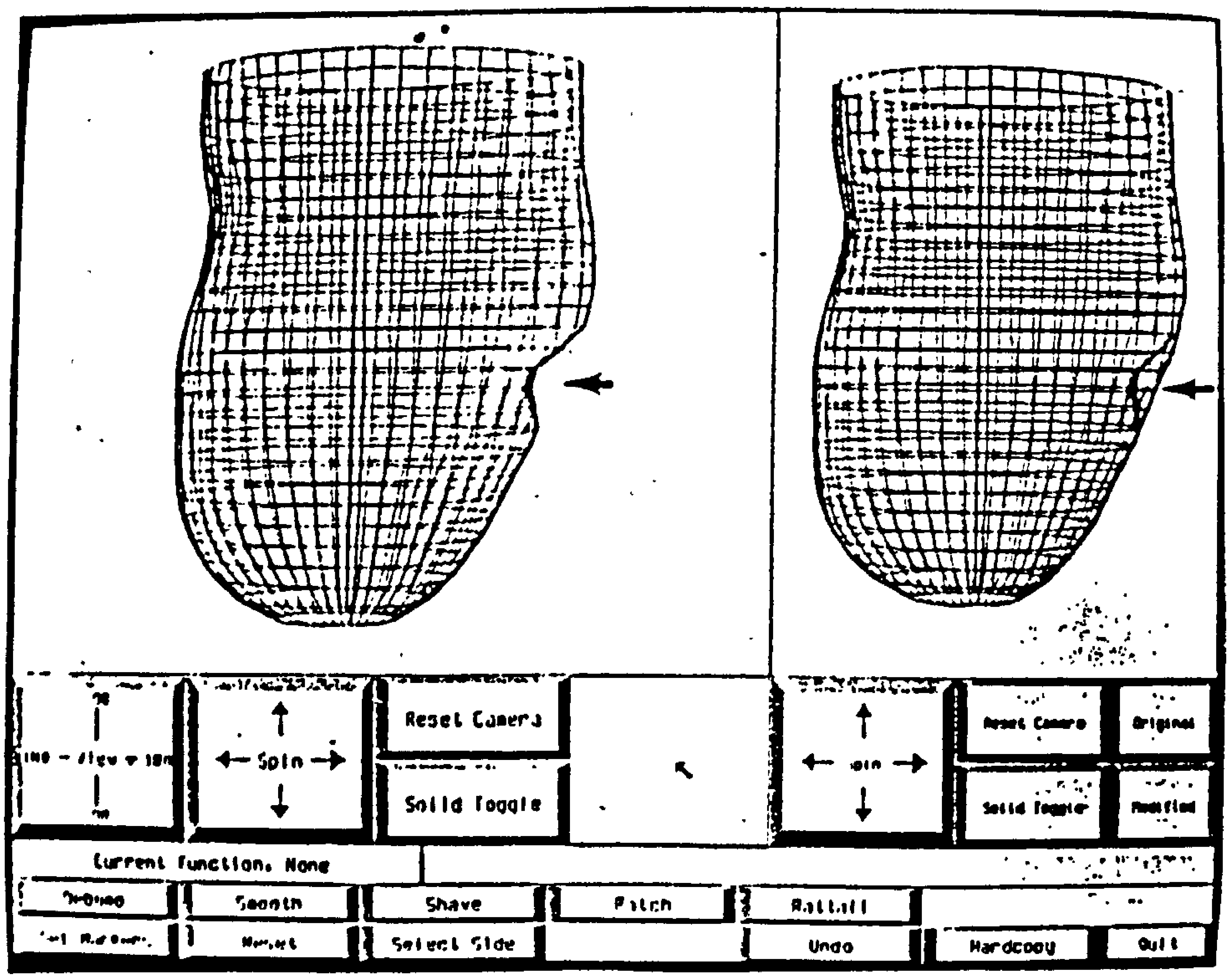

Fig. 3.3.4.2 A two screen display. Modified shape (left) and modified shape superimposed on the original shape (right). (Walsh et al, 1990)

UCL CASD software (Dewar et al 1986, Boone et al 1992) displays 2-D views of a standard stump shape in 4 orthogonal projections with highlights of common rectification areas (Fig. 3.3.4.1). Each rectification area is listed with a default value which can be modified by the operator. Increasing or decreasing the value basically alters the radii at the point that represents the particular area. The final shape can be viewed as a 3-D image before any fabrication processes begins. The concept adopted by MERU (see Section 3.3.3) requires the software to perform an additional scaling procedure on a selected reference socket. After the appropriate image of the socket is obtained, modification is accomplished interactively using a mouse or keyboard controls. Saunders et al (1985) introduced a modification algorithm known as "patching" in the MERU CASD software. The operator can indicate how much relief or compression is required at a specific area at the residual limb by just moving a single point in that area, the software then applies Bi-beta functions to smooth and blend the new point to the surrounding area.

The Rehabilitation Engineering Laboratory (REL), University of Texas presented CASD software (Walsh et al 1990) with powerful graphical capabilities in a user friendly environment developed on a SUN/3160 workstation. Optically scanned images are displayed as 3-D wire-frame or smooth images. A two screen format displays the modified shape and the original shape superimposed by the modified shape (Fig. 3.3.4.2). The software carries a selection of tasks analogous to the conventional methods of plaster modification. The screen displays buttons that represent shape editing functions like "shave", "patch" and "smooth" which allows material to be taken away, added and smoothed similar to the actions of using sandpaper respectively (Fig. 3.3.4.3 and Fig. 3.3.4.4). Areas of modification are first outlined using a mouse and edited by selecting one of the screen displayed buttons. Images can be viewed in different orientations with respect to the position of a fictitious camera controlled by the spin button. The Swedish CAPOD system software (Oberg et al 1988) similarly provides modification to images of the residual limb

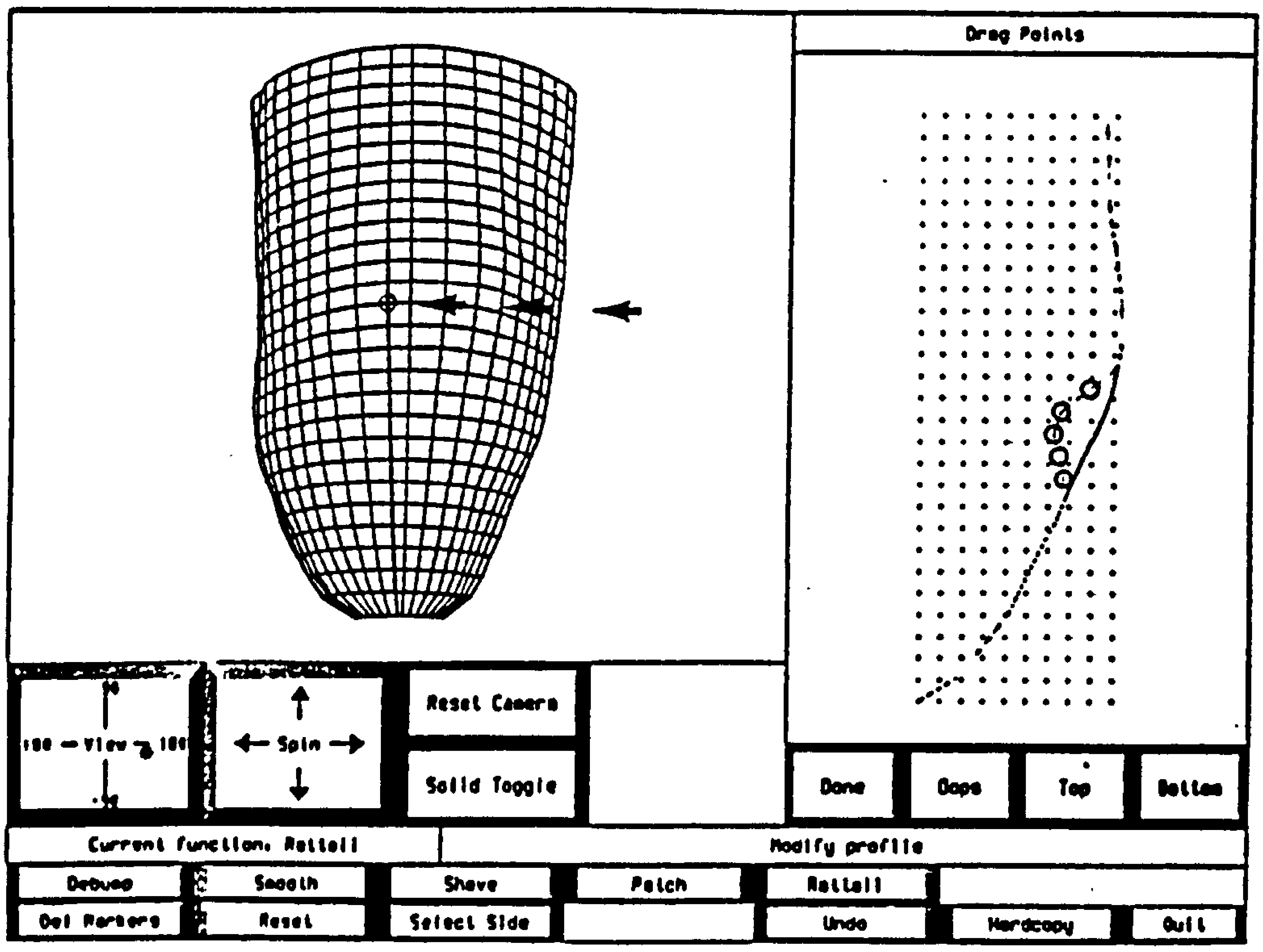

Fig. 3.3.4.3 Modification at the patella tendon bar. (Walsh et al, 1990)

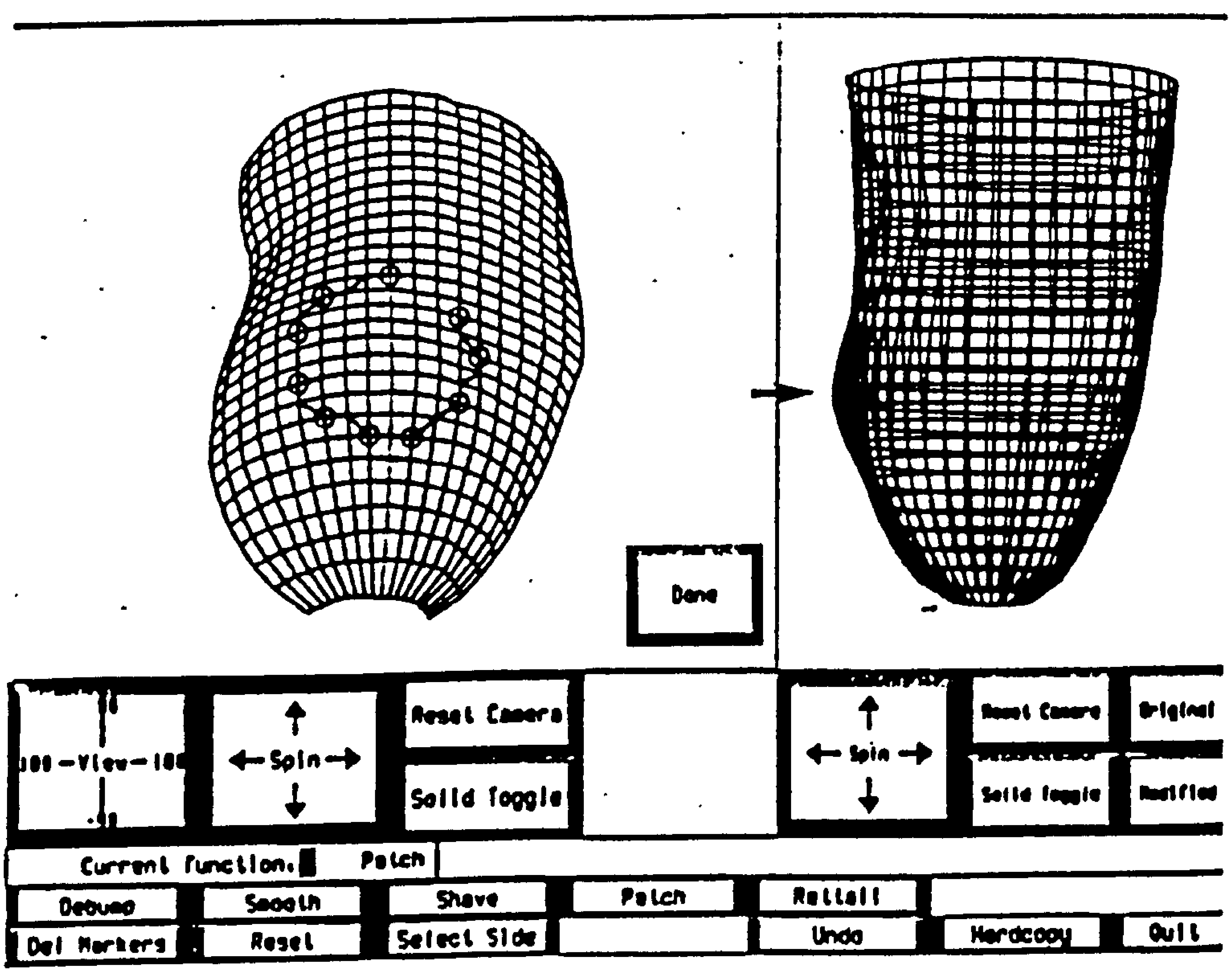

Fig. 3.3.4.4 Modification performed at the fibula head area.
(Walsh et al, 1990)

produced by an optical laser scanner. The shape can be stretched or shrunk at any point along its length. The radius at any cross-section is altered by absolute addition or subtraction, or alternatively by proportional scaling of the length and radius simultaneously. A surface area of the socket can be raised or compressed to form a relief or load bearing area. The modified and unmodified shape can be displayed separately or together for comparison purposes. Diameter and length measurements may be gauged roughly with a ruler displayed on the screen or more accurately using a cursor.

Engsberg et al (1992) explained that most current systems only allow modification to be performed on a 2-D cross-section or profile, though the modified images can be viewed later as 3-D graphics. This may be inadequate and difficult to use in some situations; instead a 3-D wire-frame image was proposed where modification can be performed directly. A standard set of modifications was also developed for the trans-tibial residual limb which when applied, produced the first approximation to the required socket shape. The operator can then further modify the shape to the final socket shape. The Strathclyde CASD software known as MEX (Jones and Mackie 1992), similarly allows modification on a 3-D image. The software utilises a Hewlett Packard 9000/series 400 workstation which provides excellent and fast image generation. Images displayed can be shaded under different simulated light source conditions, wire meshed or a combination of the two. The Berlin CASD/CAM investigators also identify the importance of modification using 3-D surface representation (Boenick and Hasenpusch 1992). The system displays images in either wire-frame or shaded form. Surface geometry can be altered by specifying a point, area or line. The selected entity can then be moved inward or outward, while the contour at the adjacent area affected by such movement can be determined by the operator.

CASD/CAM is still very much at its development stage, therefore software flexibility becomes essential. This allows the user to experiment and produce the optimal benefits achievable. The potential of CASD/CAM has also prompted software developers to cater for other prosthetics and orthotics needs, like that of spinal

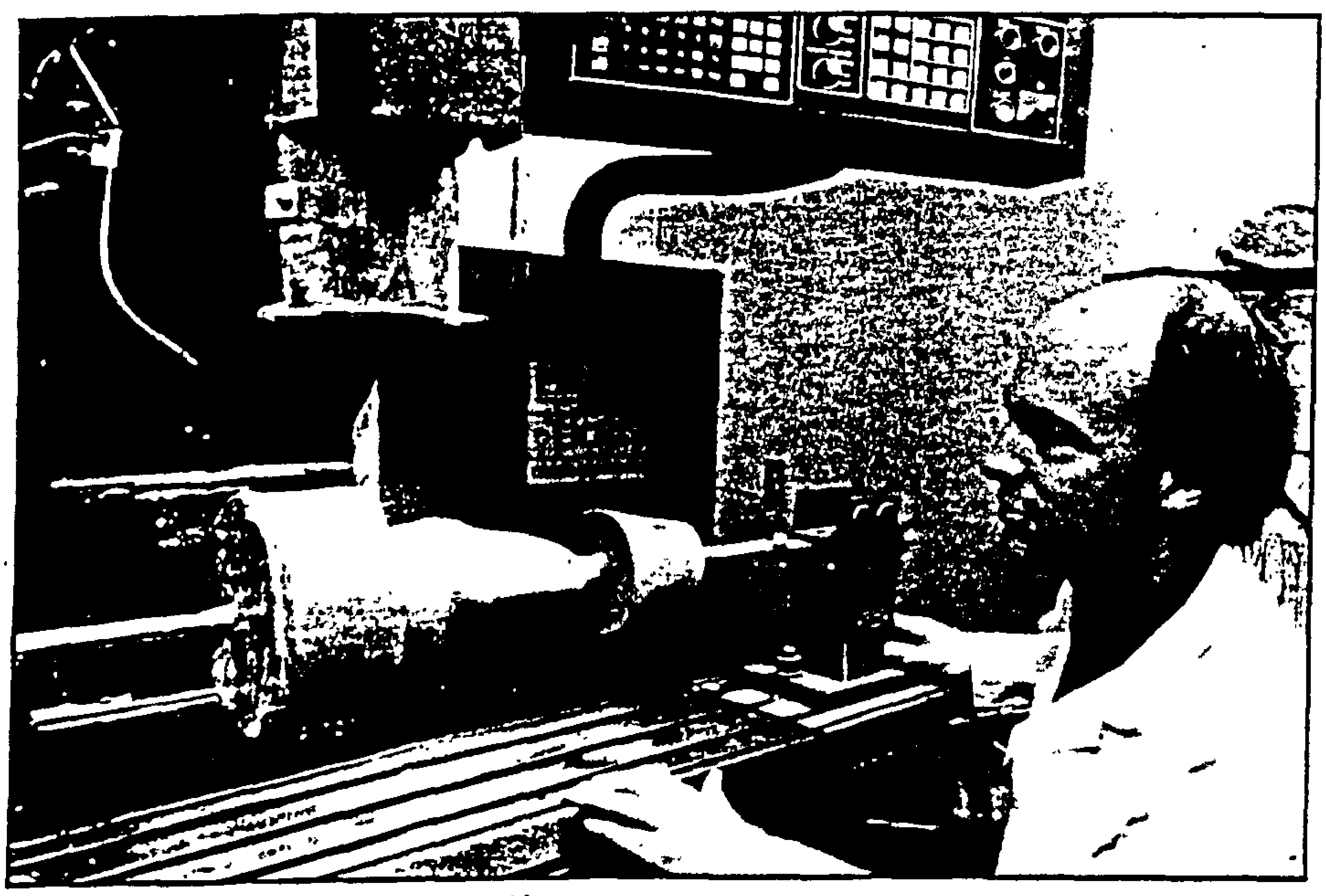

Fig. 3.3.5.1 Commercial milling machine "Excello" used in MERU initial CAM research. (Saunders et al, 1989)

orthotics (Raschke 1992, Scholten and Veldhuizen 1992), prosthetic alignment (Wood et al 1992) and cosmesis (Coombs et al 1985).

3.3.5 CAM of prosthetic socket

The final phase in CASD/CAM involves the manufacture of the computer socket model. Ideally the manufacturing phase should be fully automatic, but present systems still require human intervention. Firstly, numerical data representing the computer socket model is transmitted to a numerically controlled carving machine. The machine carves on plaster, foam, or wax to form a positive replica of the socket. The positive model then acts as a mould to create the socket using conventional methods discussed in section 3.2.3. Effort is currently being made to fabricate socket directly without the need of a positive mould, but such methods are still costly and slow. Direct fabrication methods will be discuss later in this section.

Most carving machines are custom built to suit transtibial, transfemoral prosthetics and also spinal orthotics. Custom built machines are compact, cheaper and lower in machining accuracy compared to standard computer numerical controlled (CNC) milling machines. The manufacture of plaster, foam or wax models for prosthetics and orthotics purposes does not require the high specification available in standard CNC milling machines. However, for research and education purposes, the Strathclyde system (Jones 1988) utilised a 4-axes (x, y, z and rotary) commercial CNC milling machine known as the Deckel 400, Friedrich Deckel AG, Germany. The machine is capable of achieving a least movement of a thousandth of a millimetre. MERU also begun its CAM research using the commercial "Excello" CNC machine (Fig. 3.3.5.1) but collaborated with UCL to create the UCL computer controlled carver. The UCL carver (Lawrence et al 1984, Crawford et al 1985, Crawford and Gellett 1986) is a simplified 3-axes milling machine. Two linear axes determine the tool path while a third axis provides rotation to the workpiece i.e. the plaster block. Minimum linear movement is 0.012 mm and rotation is 3 minutes of an arc. The machine (Fig. 3.3.5.2 and Fig. 3.3.5.3) is housed in a rigid box section frame and its main parts consist of a 3000 rpm cutter motor that slides along two orthogonal slide

Fig. 3.3.5.2 UCL carver 1984 design. (Lawrence et al, 1984)

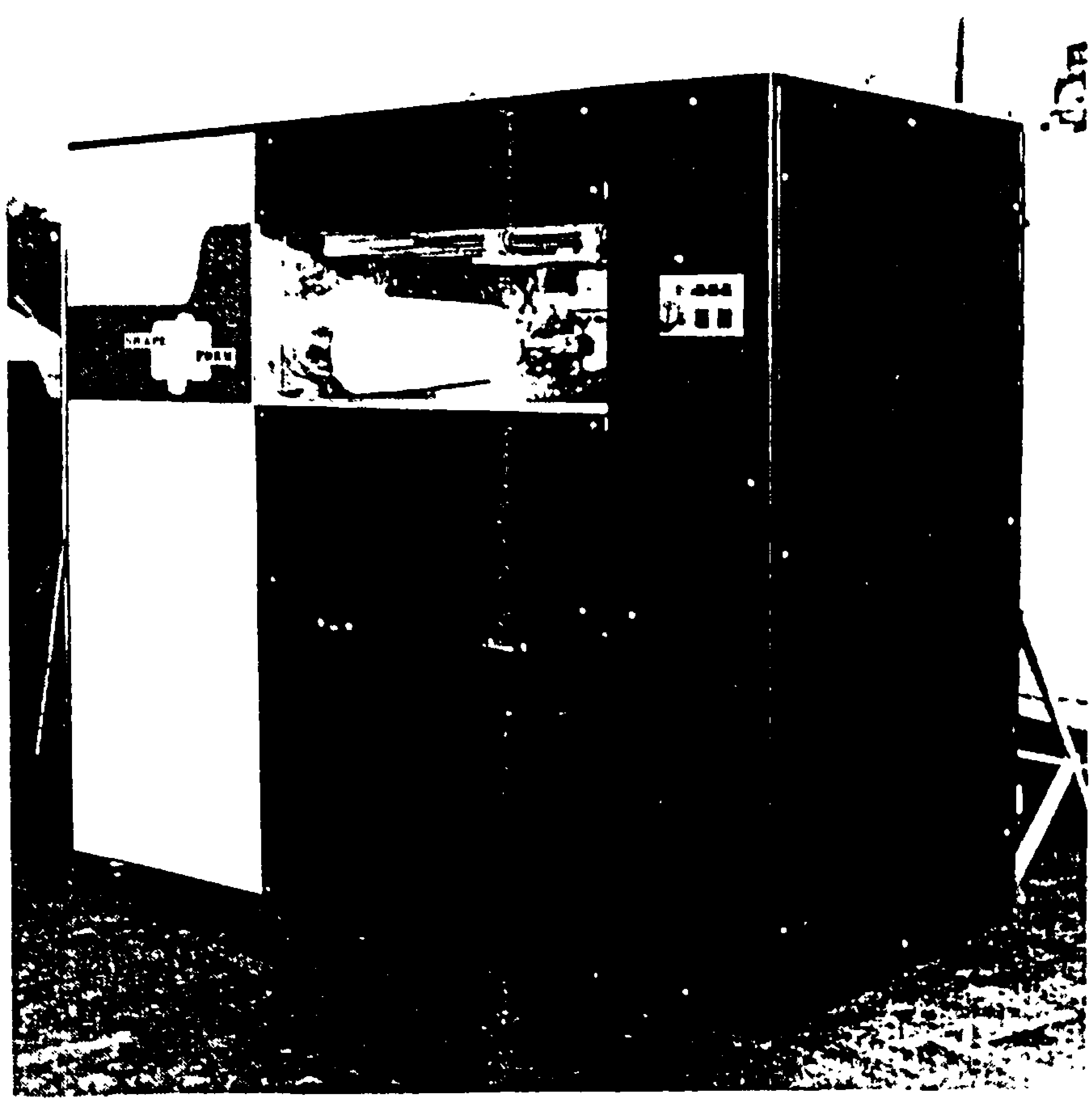

Fig. 3.3.5.3 UCL carver 1986 design. (Crawford and Gellett, 1986)

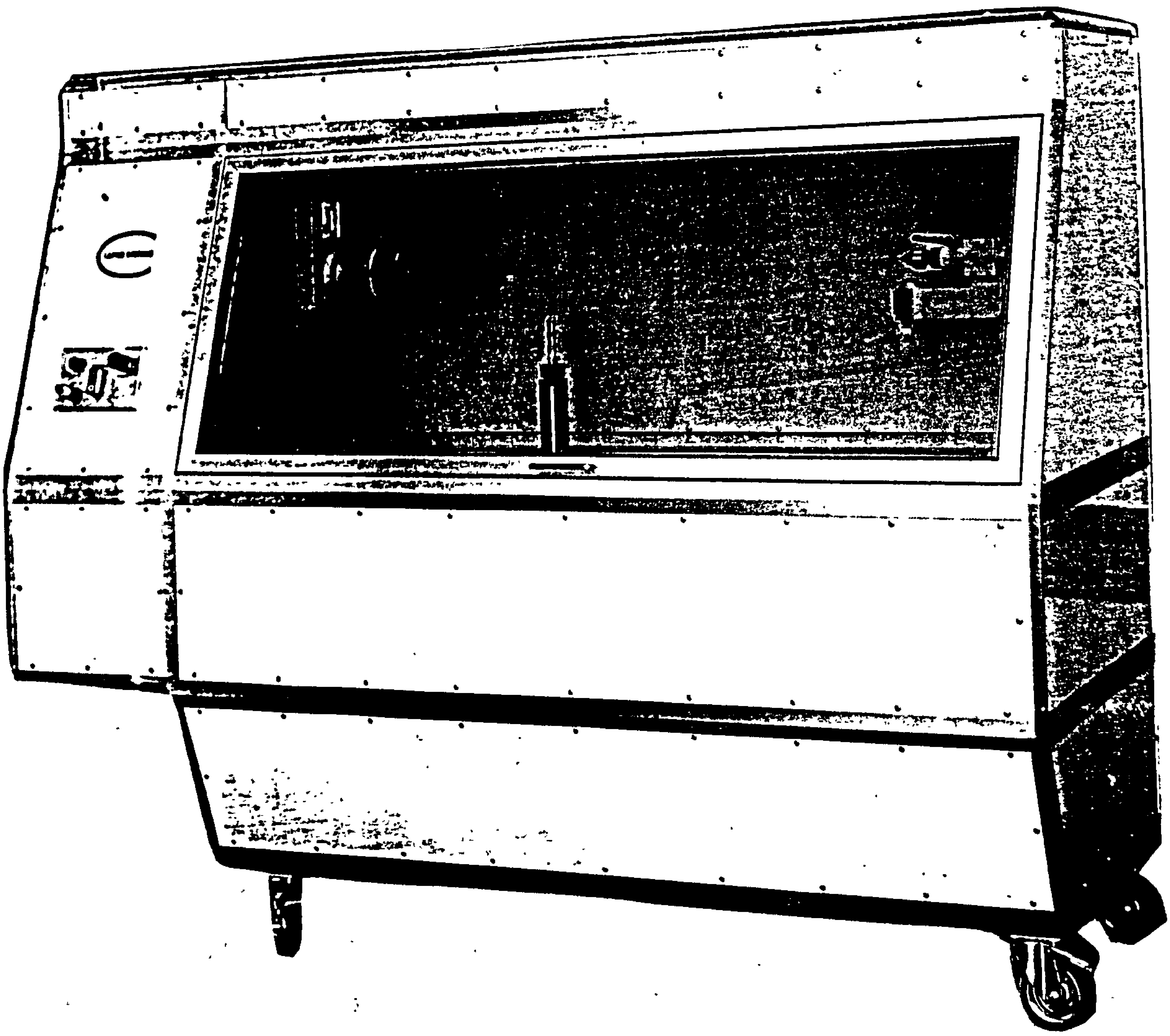

Fig. 3.3.5.4 Three axes CAPOD milling machine. (CAPOD, 1994)

ways controlled by stepper motors. For machining, the plaster block is secured at one end by a tapered mandrel supported on a standard 3-jaw chuck. The UCL carver has an added facility that converts itself to a digitiser enabling the digitization of a plaster cast wrap or positive socket model. For such purposes, a suitable pivot arm similar to the UCL digitiser (see section 3.3.3) is mounted on a carriage adjacent to the cutter motor and a digitising option is selected.

The CAPOD CASD/CAM (Oberg et al 1988) milling machine takes on a much similar construction to that of the UCL system (Fig. 3.3.5.4). Its construction includes three axes, the cutters X and Y axes and a rotating axis imposed onto the workpiece. The motor that drives the cutter remains stationary and power is transmitted to the cutter by gears and bearings. The machine is adequate in size for spinal orthotics and lower limb cosmesis work, and machining time for normal socket positive, as quoted takes less than 10 minutes (CAPOD 1994).

Relatively smooth surface finish of the machined positive mould is nowadays possible with faster and more precise tool control. Lawrence et al (1984) described the effect of surface smoothness with respect to cutters with different endforms (Fig. 3.3.5.5). Selecting a large spherical cutter gives a smoother surface than a small cutter, but there is a tendency that the cutter will remove material from neighbouring points. Correction for possible under-cutting can be provided by using software control (Saunders and Vickers 1983). Smooth surfaces can also be produced by repeated machining using a larger diameter cutter. Other factors affecting the smoothness of the machined mould are the linear and angular pitch between successive tool paths. Wilkinson and Crawford (1986) showed the difference in surface finish obtained with a 18mm diameter hemispherical tip tool, cutting at a pitch of $\frac{1}{4}$, $\frac{1}{8}$ and $\frac{1}{16}$ inch (Fig. 3.3.5.6). In the case of a trans-tibial lined socket, the ripples on the mould will be transferred directly to the soft liner. A study on the effect of ripples created on the Pelite liners from carving at a $\frac{1}{4}$ inch pitch on 28 transtibial amputees showed no disadvantages in terms of comfort. On the contrary, the patients subjectively consider that the rippled liner provides better suspension, reduction in heat build-up and added shock absorption (Wilkinson and Crawford, 1986).

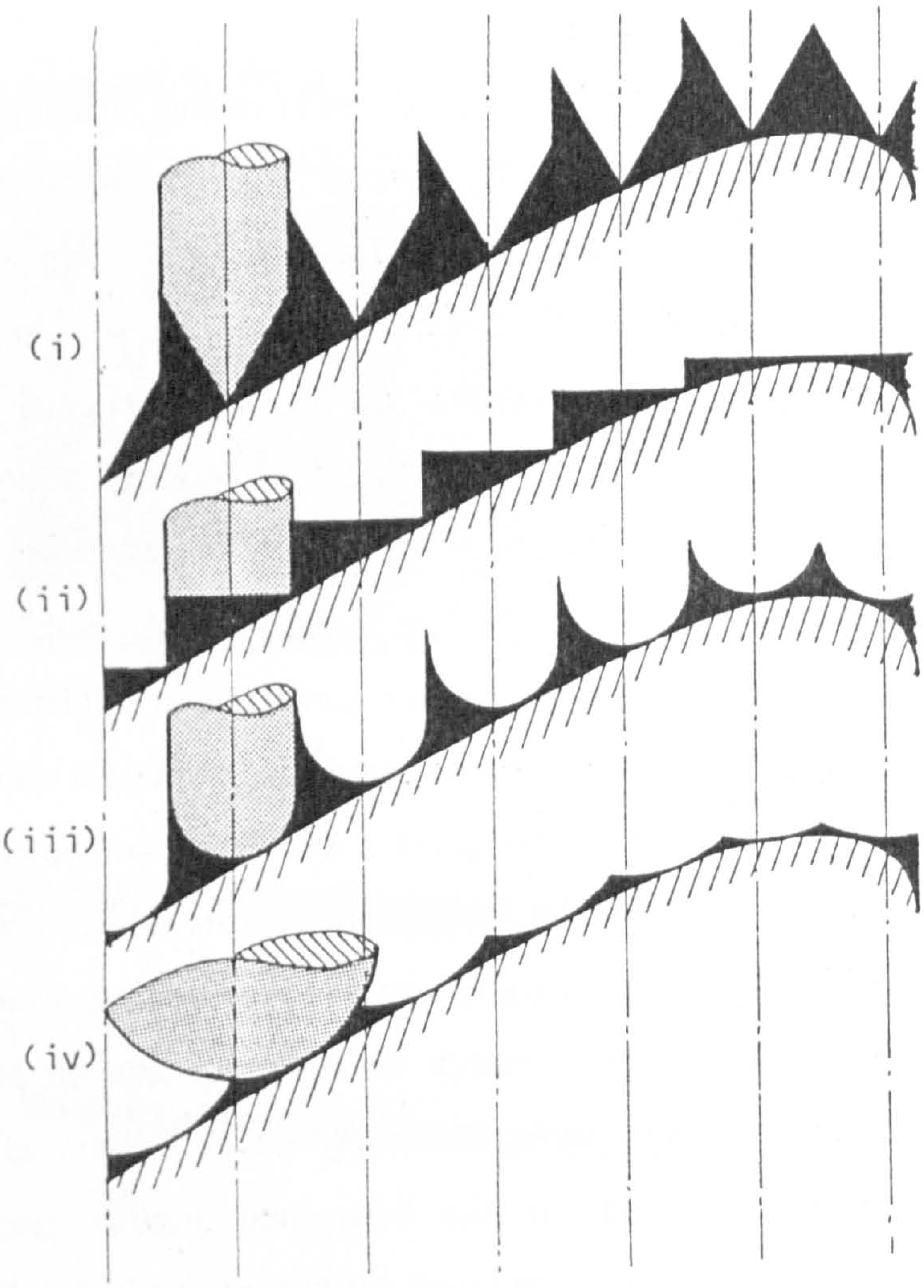

Fig. 3.3.5.5. i.) Conical cutter
ii.) Flat ended cutter
iii.) Small spherical cutter
iv.) Large spherical cutter. (Lawrence et al, 1984)

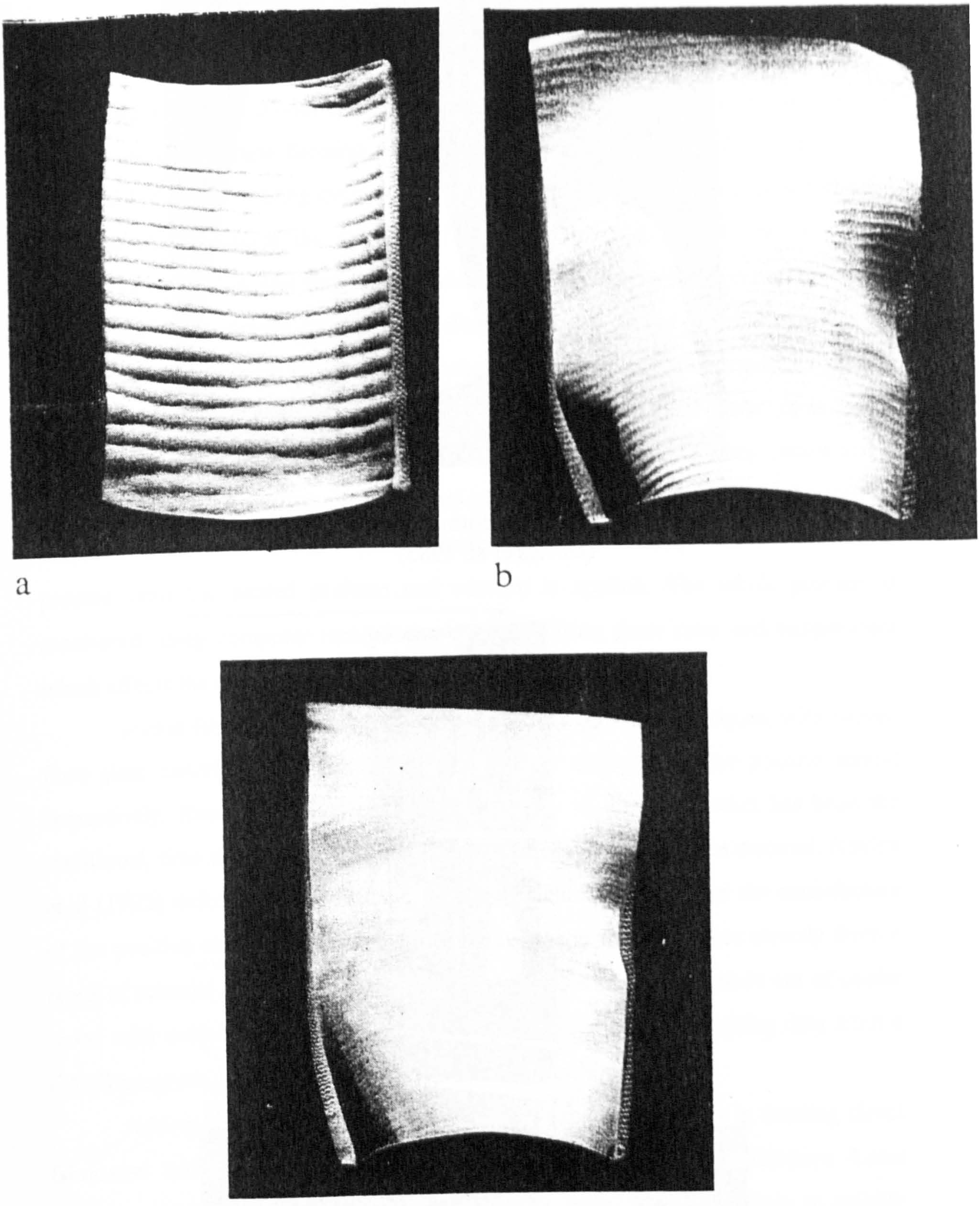

Fig. 3.3.5.6 Socket liner created by plaster model furnished with
a.) 1/4, b.) 1/8 and c.) 1/16 inch carving tool.
(Wilkinson and Crawford, 1986)

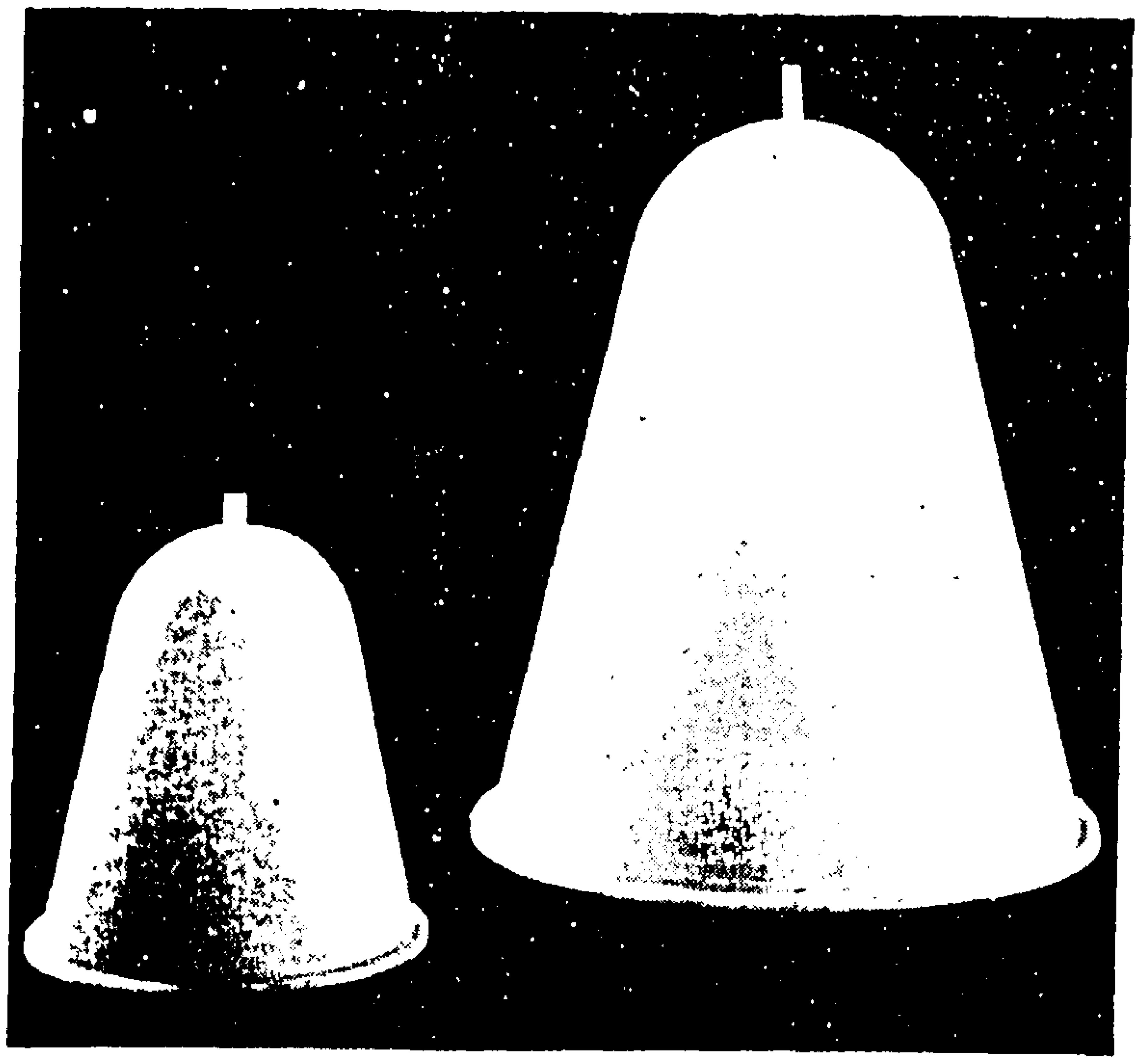

Fig. 3.3.5.7 Plastic preforms for Rapidform machine. (Davies et al, 1985)

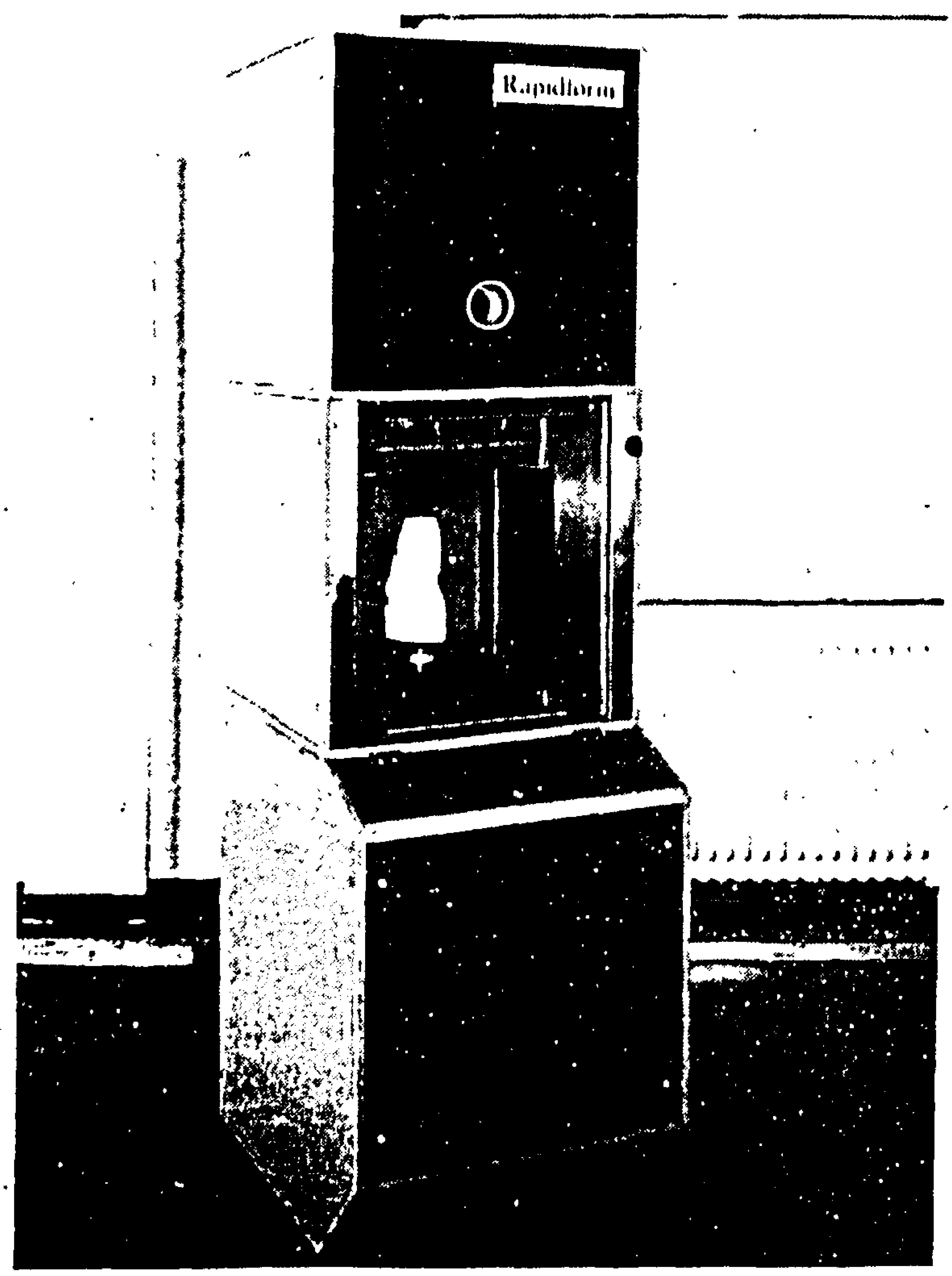

Fig. 3.3.5.8 The Rapidform machine. (Davies et al, 1985)

A worthwhile contribution to the CASD/CAM environment has been the introduction of the Rapidform technique of socket fabrication. The technique initially introduced by UCL (Davies et al 1985) to enhance the production of polypropylene sockets using the drape forming technique, is now widely accepted as part of the CASD/CAM manufacturing cycle. The Rapidform process is divided into two stages. The first stage requires the creation of standard size bell shaped preforms (Fig. 3.3.5.7) for transtibial and transfemoral sockets. The preforms are injection moulded. The second stage drapes the heated preform onto the carved positive mould as a vacuum forming process to create the socket. The second stage is largely automated using the Rapidform machine (Fig. 3.3.5.8). The machine houses three main compartments, an oven at the top, the loading bay for the mould at the centre and a vacuum pump and mechanism for the ram at the bottom. The preform is elevated to the oven and heated to the required temperature, the mould placed on the ram is pressed onto the heated preform and vacuum is applied. The whole process is monitored using computer technology, thus optimising draw ratio and temperature which affects the overall strength of the socket.

Socket fabrication is nowadays dominated by forming techniques, with woven fibre glass material and plastic being laminated or draped onto the positive mould respectively. However, removing materials directly to create a socket has been the traditional, time consuming, way of fabricating sockets with wooden material. Rovick et al (1992) reckon that the advances in CNC machines do not limit the manufacture of the positive mould only, but also the socket shape to be machine directly from a block of material as performed traditionally. A feasible socket was made out of poplar wood with uniform thickness of 7 mm using a CNC machine accepting data from a CASD program, though there was no mention of machining time.

Adding instead of subtracting materials is another possibility in creating direct fabricated sockets. Stereolithography (Rovick et al 1992) and Selective Laser Sintering (SLS) (Rogers et al 1992) involves the use of laser technology to solidify loose materials. Stereolithography utilises lasers to solidify liquid plastic to form the part while SLS applies laser energy to fuse powderised material such as polycarbonate a)

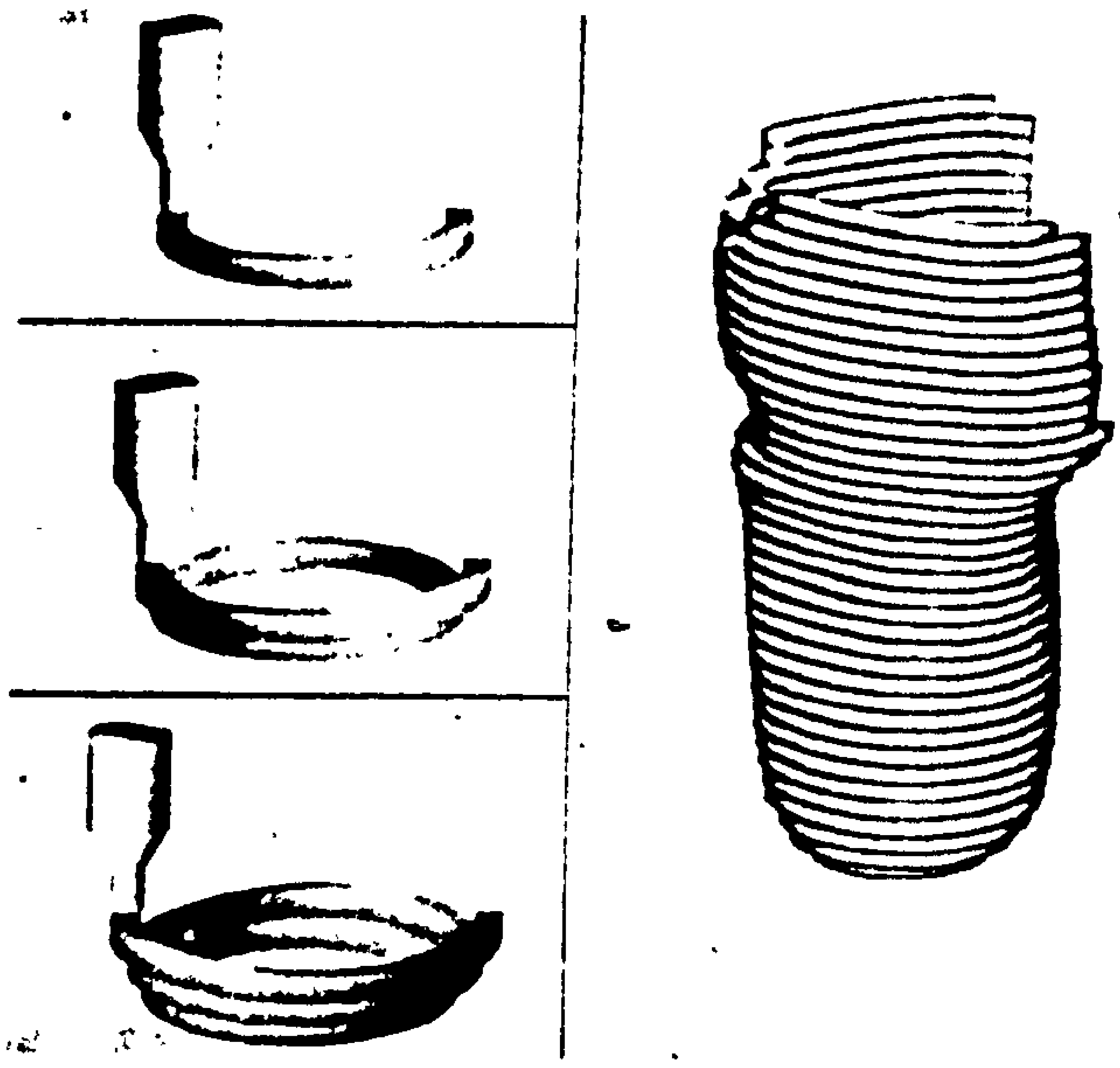

b)

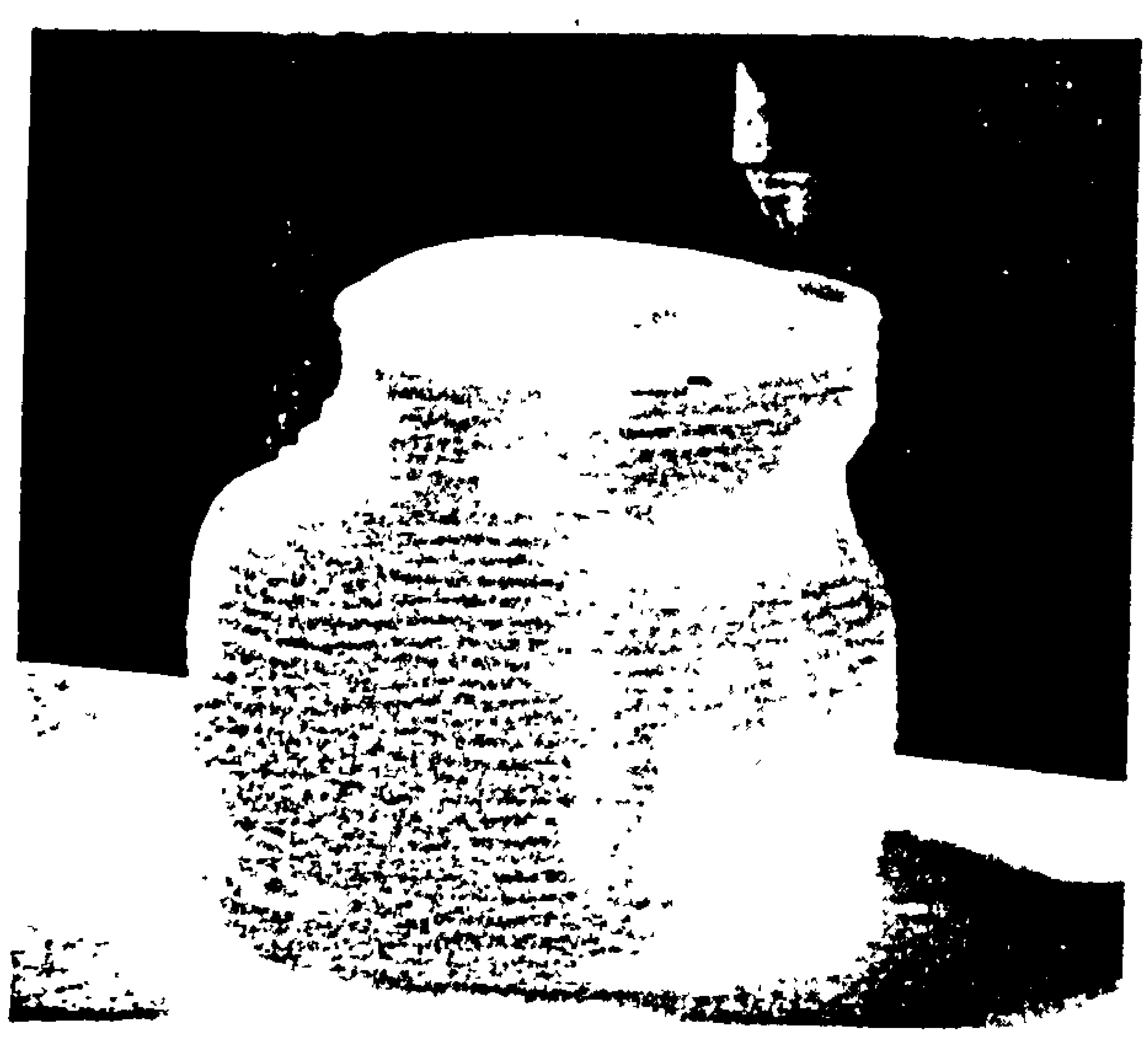

Fig. 3.3.5.9 The additive fabrication technique : Squirt shape system.
a.) Computer simulation of Squirt shape system.
b.) Prototype socket. (Rovick, 1992)

together. Such processes are extremely time consuming. Sterolithography was reported to take as long as 48 hours (Rovick et al 1992). Another faster additive method ($1\frac{1}{2}$ hours for trans-tibial socket) using molten beads of plastic was described by Rovick (1992). Plastic is extruded and deposited layer by layer to form the socket shape (Fig. 3.3.5.9). The system known as Squirt Shape, has a nozzle that squirts molten plastic at a constant pre-set rate, controlled by computer. The nozzle is positioned according to the CASD shape data.

3.3.6 Commercial CASD/CAM systems

The commercial systems have their beginnings in most of the research systems described earlier in this chapter, and therefore have similar methodology as their predecessors. The systems are usually marketed under different names from their predecessors. Collaboration among different groups has also given birth to new systems combining various technologies and due to commercialisation, published literature on the systems is limited, thus tracing the history of the system is usually difficult. Nonetheless, some of the systems available are,

a) CASDaM or System Shape supplied by Applied Biotechnology (ABT) and SHAPE respectively. The systems are similar to that described by literature referred as the UCL CASD/CAM system.

b) CANFIT-PLUS™ (Vorum Research Corporation). CANFIT-PLUS™ now caters for shoe lastfit design, bodyjacket design, trans-tibial and trans-femoral socket design.

c) CAPOD (CAPOD SYSTEMS). The systems remains much the same as reported by Oberg et al (1988), but now includes a torso scanner for spinal orthotics design (Fig. 3.3.6.1).

d) BioSculptor® (Finnieston Group).(Fig. 3.3.6.2)

e) CASDCD-Barlach I/II (ipos® ORTHOPADIE INDUSTRIELL). (Fig. 3.3.6.3)

f) Delta Systems II (CLYNCH Technologies, Inc.).

g) The Seattle CAD/CAM System (M+IND Seattle Medical System Group). (Fig. 3.3.6.4) a)

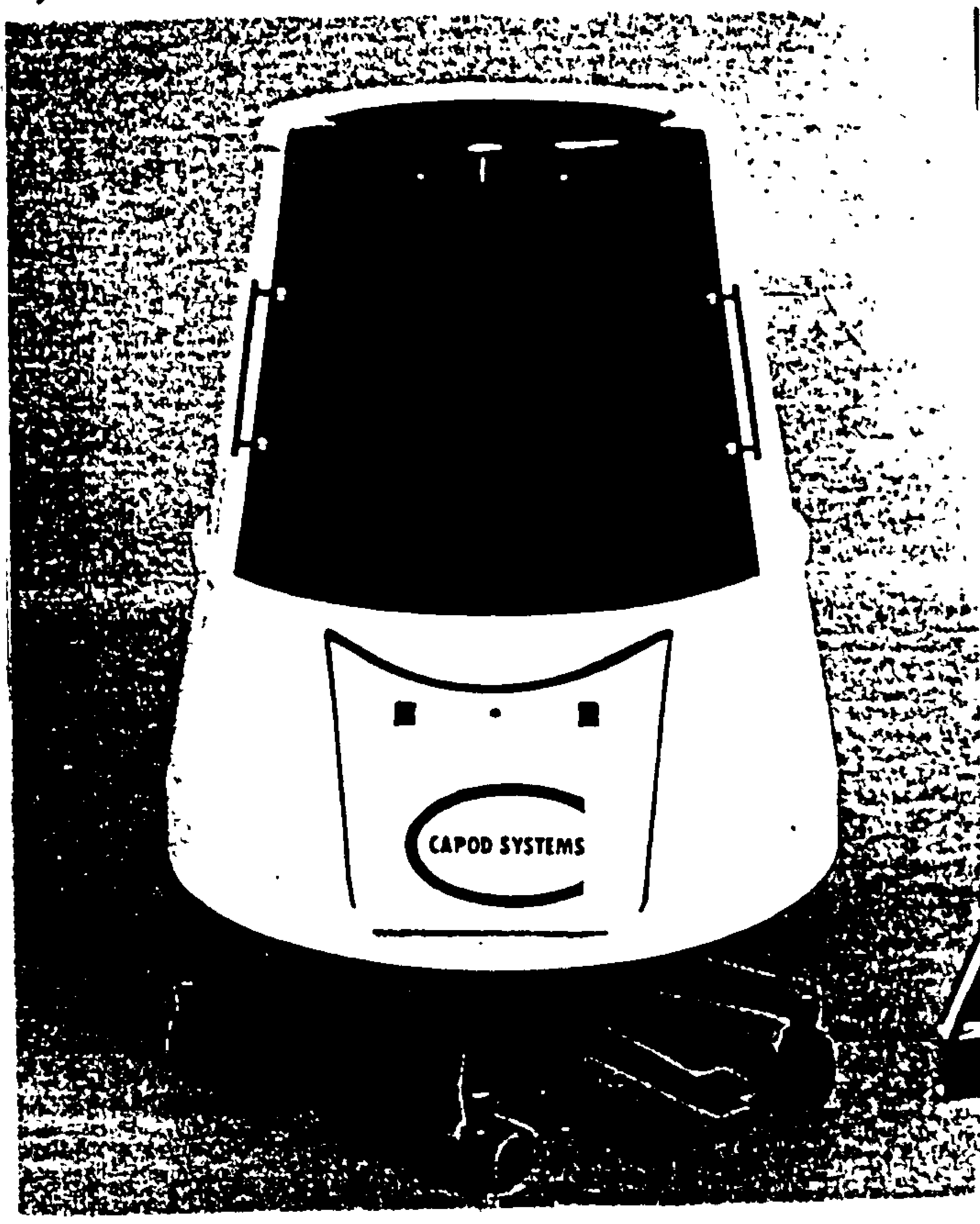

b)

c)

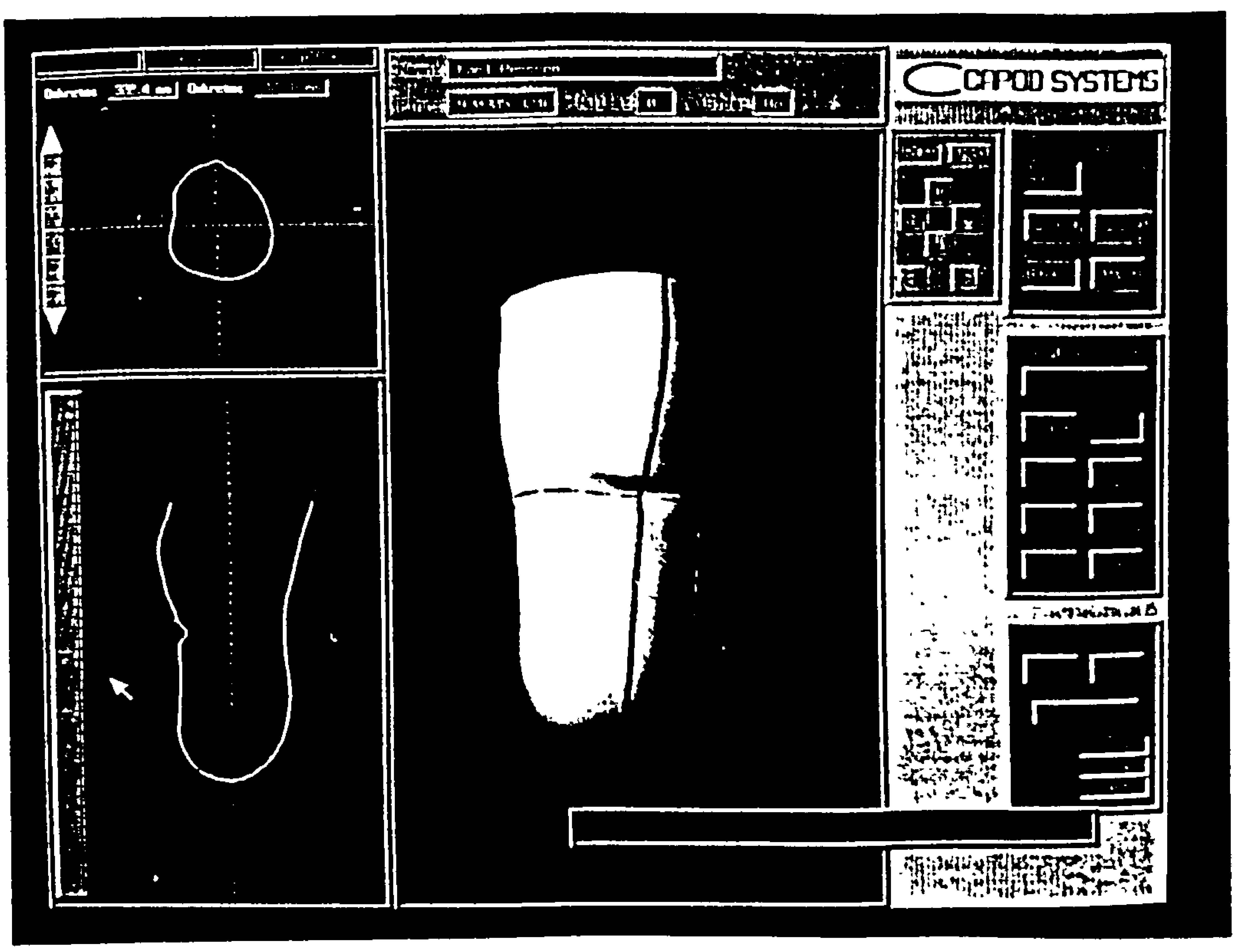

Fig. 3.3.6.1 a.) CAPOD trans-tibial and trans-femoral scanner.
b.) CAPOD torso scanner.
c.) CAPOD software display. (CAPOD, 1994)

a) b)

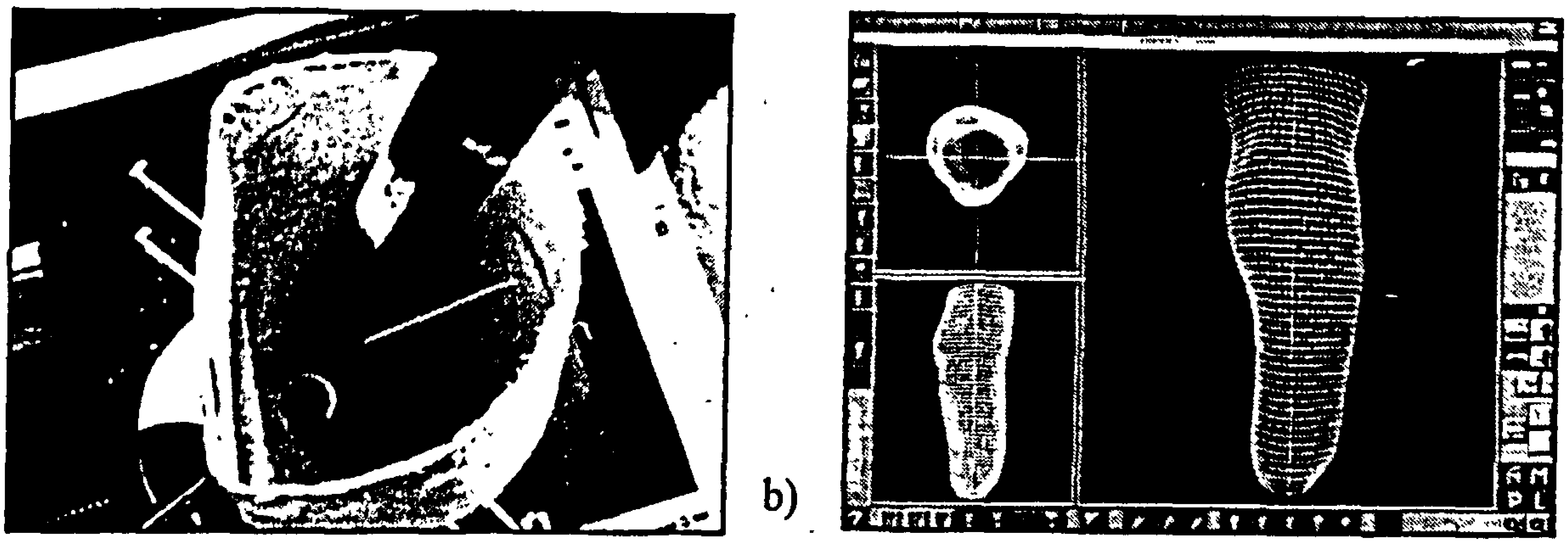

Fig. 3.3.6.2 a.) BioSculptor non-contact laser beam set - up for cast digitisation.
b.) BioSculptor software display panel. (BioSculptor, 1994)

a) b)

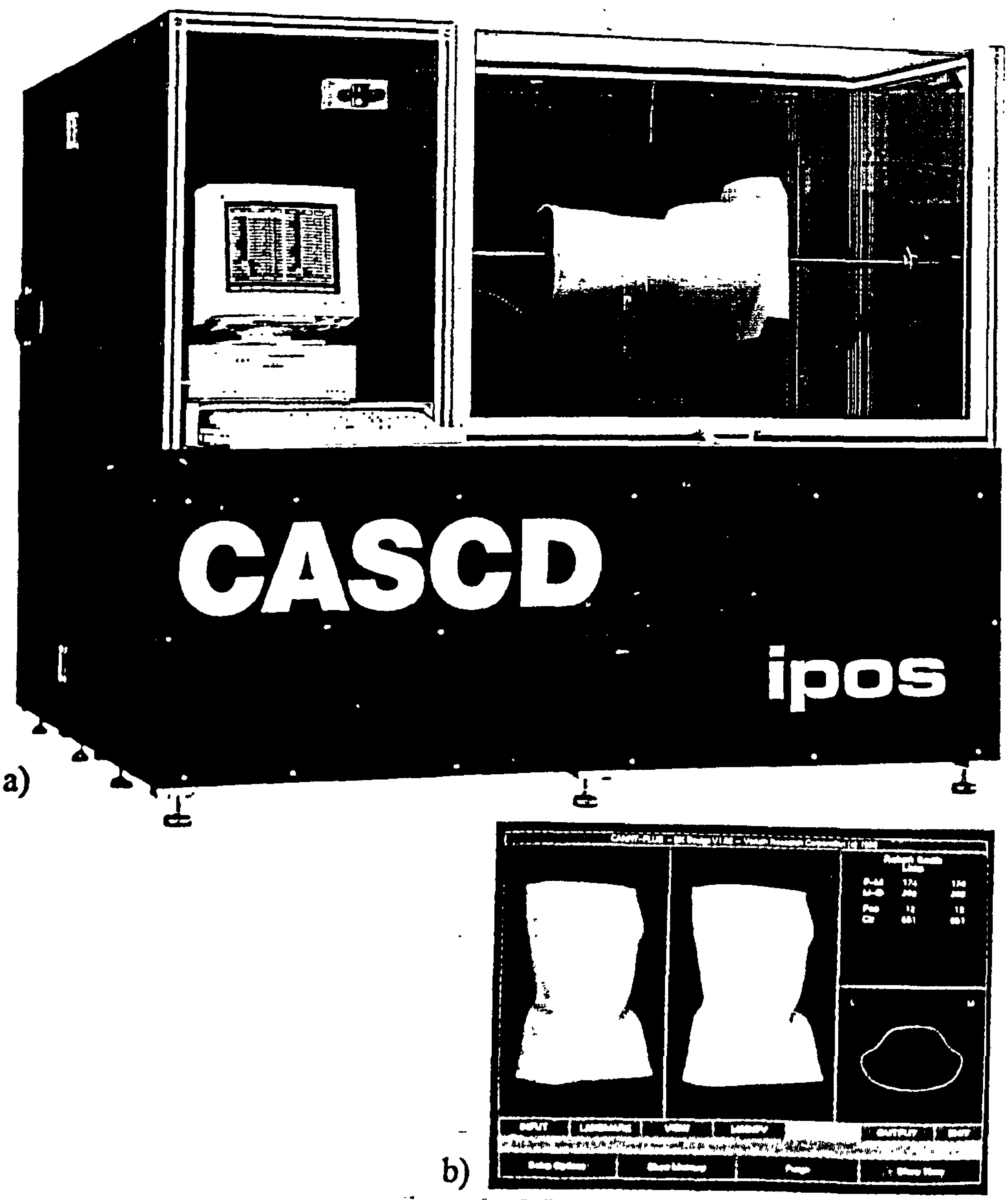

Fig. 3.3.6.3 a.) IPOS carving machine.
b.) IPOS software display panel. (IPOS, 1994)

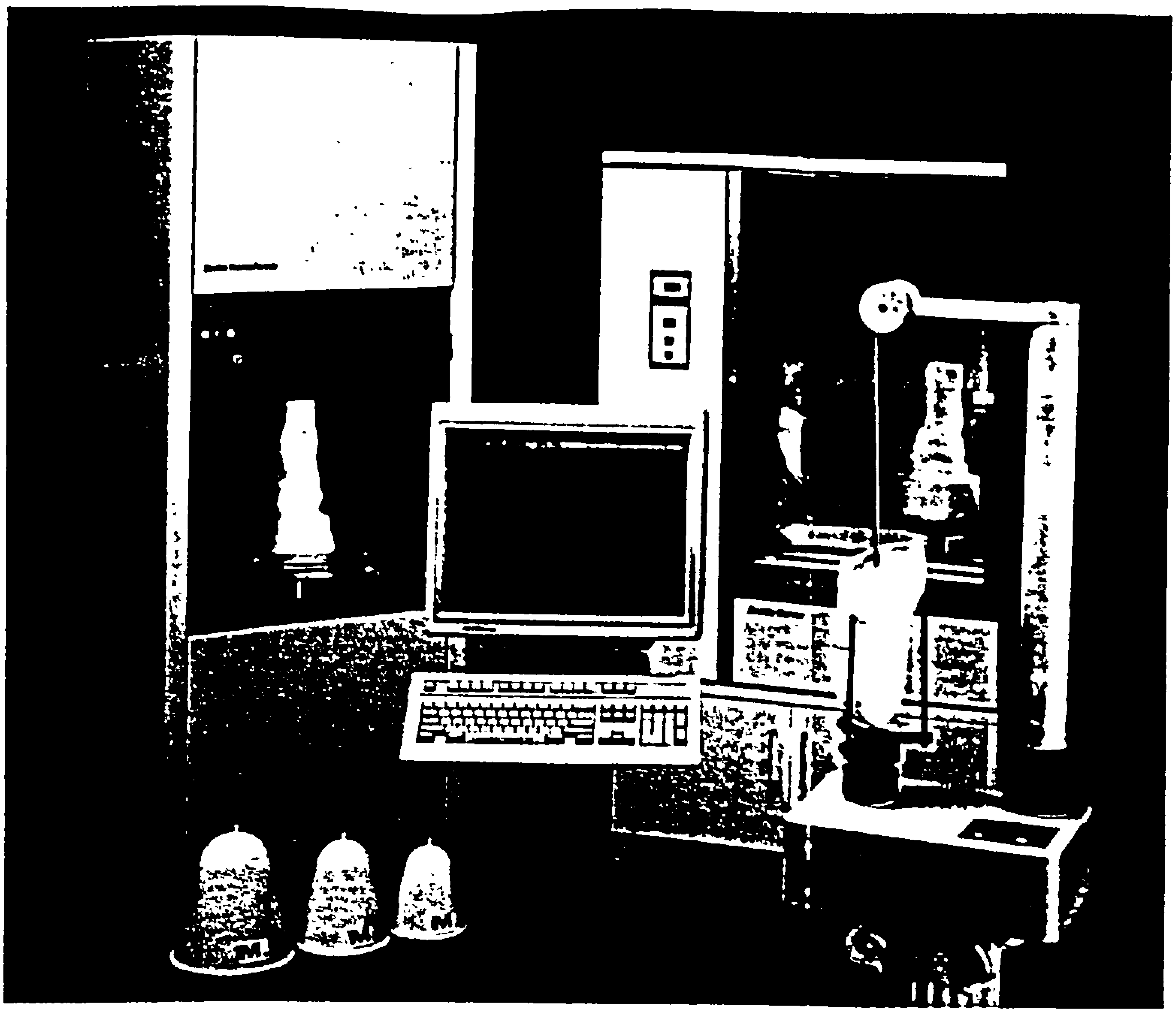

Fig. 3.3.6.4 The Seattle CAD/CAM system.
Clockwise from left, i.) Different size preforms, ii.) The Seattle Rapidform machine iii.) Carving machine, iv.) Digitiser and v.) Personal computer. (MIND, 1994)

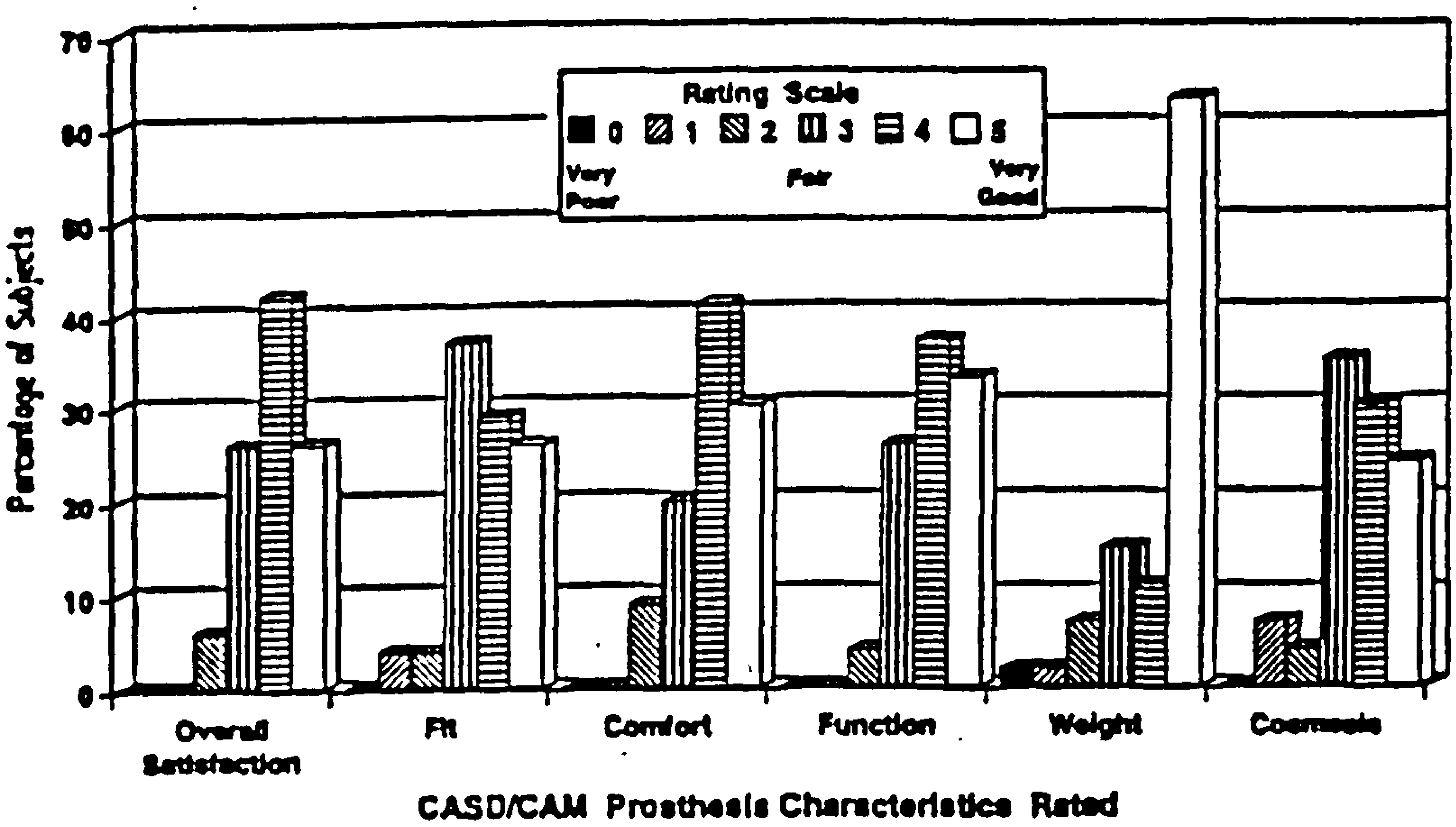

Fig. 3.3.7.1 Test subjects' rating of CASD/CAM sockets and prostheses. (Houston et al, 1992)

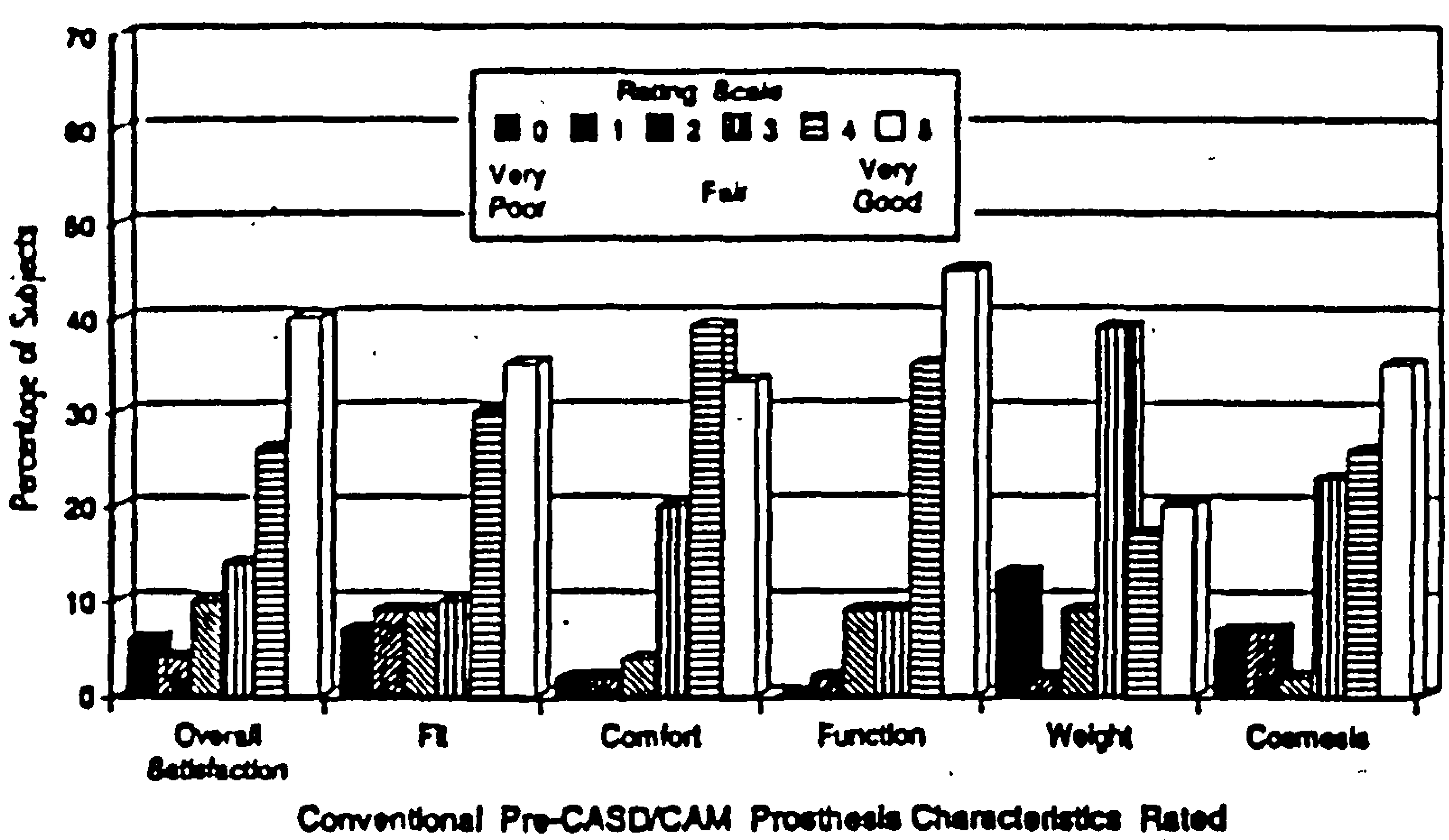

Fig. 3.3.7.2 Test subjects' rating of conventional sockets and prostheses. (Houston et al, 1992)

3.3.7 Clinical trials of CASD/CAM systems

Various clinical trials have been attempted by both developers of the different systems and independent users. The ISPO meeting in Chicago 1992 witnessed a series of results of such clinical evaluation. Dewar and Redhead (1992) assessed the University College London CASD/CAM system and concluded that the implementation for routine prescription of the PTB trans-tibial sockets was a success in terms of fitting with no penalty in terms of time, though no time figures were reported. The assessment involved 147 patients, 70 of them were fitted by the conventional method while the remaining 77 by the CASD/CAM method. The percentages of successful fittings was 95% for both methods. When compared to the patients' previous socket, 89% reported the CASD/CAM sockets are at least as comfortable. In the case of the conventionally fitted patients, 48% reported fits that are better than their previous sockets while only 33% of the CASD/CAM group mentioned similar benefits. Lilja et al (1992) reported 22 trans-tibial amputees fitted using the CAPOD system. No significant difference, except for a reduction in the number of stumps socks, was observed when compared to conventionally fabricated sockets. The National Program for Automated Fabrication of Mobility Aids (AFMA) sponsored by the Veteran Administration Rehabilitation Research and Development Service presented an extensive clinical and developmental evaluation of CASD/CAM sockets and systems for trans-tibial amputees. Published literature related to these studies was reported by Houston et al (1992), Chan et al (1992) and Boone et al (1994). The program which involved three prosthetic research centres in the United States was aimed at introducing CASD/CAM to clinical staff and evaluating it in a clinical setting. The trials are conducted using mainly the UCL CASD/CAM system but also the MERU system. A total of about 90 patients were fitted with CASD/CAM trans-tibial sockets. Six main parameters namely, overall satisfaction, fit, comfort, function, weight and cosmesis were considered for evaluating the sockets. Fig. 3.3.7.1 and Fig. 3.3.7.2 show the percentage of patients rating, in a scale of one to five with respect to the six categories for both CASD/CAM and the pre - CASD/CAM i.e. conventionally designed sockets respectively. Twenty six percent rated the overall satisfaction of their CASD/CAM socket as very good, 68% as good to fair, 6% as poor to fair and none as very poor. Comparing with pre - CASD/CAM sockets, 6% rated them very poor but 40% rated the pre - CASD/CAM socket as very good. In conclusion, it was found that better sockets were achieved in the conventionally designed group, although the worst sockets experienced in the program were in this group also. However, more subjects were satisfied with the CASD/CAM sockets although these sockets did not achieve the highest rating for 5 out of the 6 categories evaluated.

3.3.8 Value of CASD/CAM

The creation of a prosthetic socket has been historically and still, predominantly today, achieved by the prosthetist employing purely artisan techniques. Any attempt to replace these operations using computer technology, will certainly come across much criticism and scepticism. A question that is often asked is, "Can CASD/CAM techniques produce better sockets than those achievable by conventional means ?". Klasson (1985) expressed the opinion that the present CASD/CAM systems do not offer any new principles for optimising socket fit. The author of this thesis shares a similar view. The systems only offer a controlled socket reproduction technique based on conventional tenets. For the system to function efficiently, it is still highly dependent on the prosthetist's skill and experience.

The motivation for the present CASD/CAM system can only be justified in terms of productivity and consistency. Socket manufacturing rate using CASD/CAM can be expected to improve tremendously with high performance computer hardware and software, and the move towards direct socket fabrication. Regardless, one can still remain sceptical since improvements from such technologies will obviously have an impact on conventional socket fabrication techniques, similarly leading to higher productivity. Pritham (1988) suggested the rate of return in a CASD/CAM investment is impracticable given the amount of prosthetic needs handled in the average American facility, and strongly believed that the purchase of a CASD/CAM system cannot pay for itself. Yet there are also economical advantages that could only be realised by CASD/CAM system, such as many low cost shape acquisition systems stationed anywhere around the world constantly sending information to a central CASD/CAM centre where socket can be designed and fabricated.

The author of this thesis reckons that the many arguments for and against the CASD/CAM system arise because a workable system is now possible but not yet optimised. Comparing CASD/CAM with any CAD/CAM techniques in established engineering industries, CASD/CAM lacks the element of analysis and optimisation of a design. The trial and error concept is still dominant as in the conventional process, except that it is now performed faster. A truly computer aided design phase would be one that provides information on whether the design is feasible even before any implementation is undertaken, whereas in the CASD/CAM techniques, a good or bad socket fit is only determined when the socket is donned by the patient.

The author of this thesis firmly believes that the ultimate aim of CASD/CAM should be to equal that being achieved currently in other engineering facilities using CAD/CAM i.e. to produce an excellent and correct socket shape even before any aspect of manufacture is committed. This would lead to a first time fit socket justifying productivity, and more importantly, providing patients every time with the best possible sockets.

Klasson (1988) stated, "a good fit is primarily not defined by a particular shape of socket, but by the accommodation of forces or pressure between the residual limb and the socket, to provide for comfortable and harmless weight bearing, stabilisation and suspension." A good fit is probably attributed to a host of other psychological, physiological and biological issues however, parameters like pressure provide a means to quantify socket design and fit. A few investigations into interface pressure have been attempted. Methods range from the use of transparent check sockets, pressure measurement using mechanical or other types of sensors, and lately, numerical analysis using finite element methods.

The finite element (FE) method enables the prediction of tissue displacement from input forces and pressure and vice-versa. Such a method has great potential in prosthetic socket design and fitting. Being a computational method, its future is

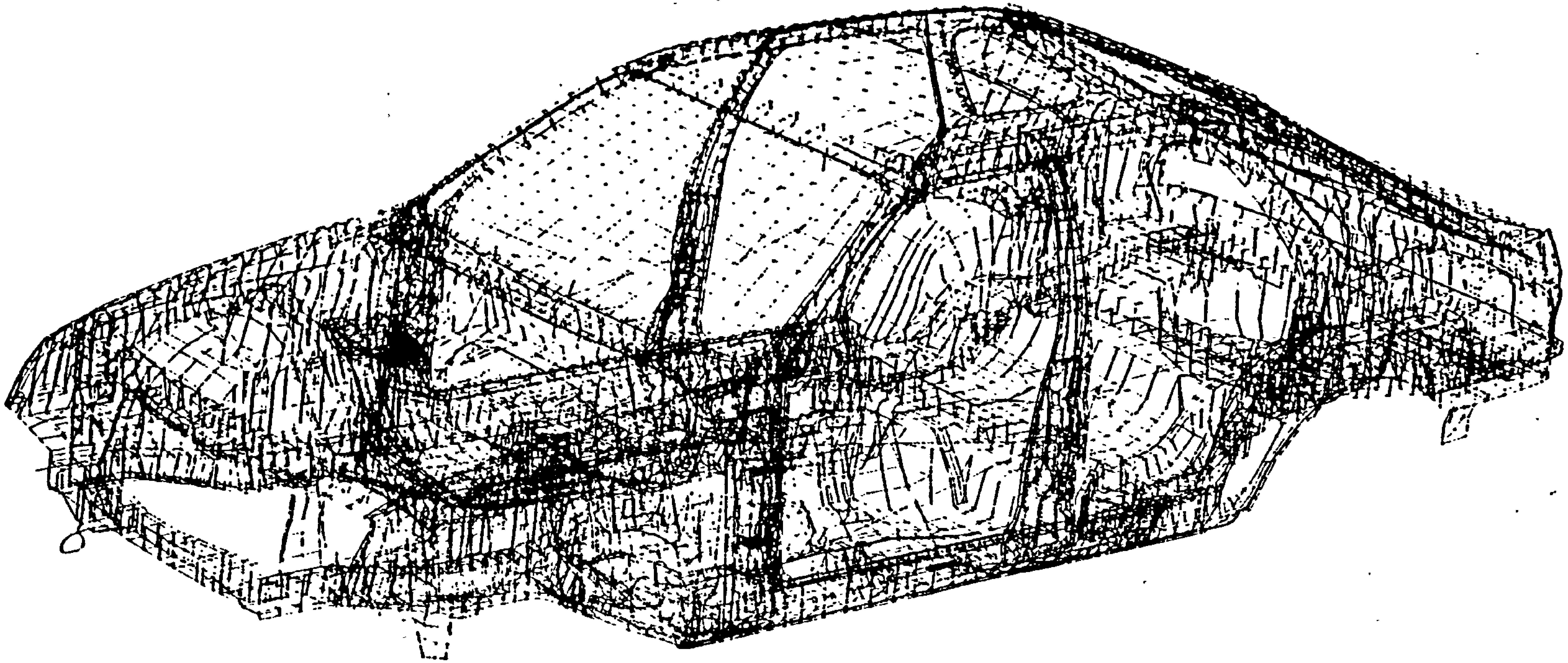

Fig. 3.4.1 Discretization in finite element method enables complicated structures to be analysed. Finite element model of the Ford Sierra. (Hawkes, 1988)

coherent with the implementation of CASD/CAM systems. Far better, its introduction has the potential to enable the CASD/CAM system to become a genuine computer aided design tool.

3.4 THE ROLE OF FINITE ELEMENT MODELLING IN BIOMECHANICS

The FE method was first introduced in the 1950's and originated as a method of stress analysis. Today, the FE method has developed to a highly sophisticated tool and is also used to analyse problems of heat transfer, fluid flow, lubrication, electric and magnetic fields. The FE method is an approximate method of analysis, relying on the concept of discretization. In essence, the FE model is a structure made up of a number of small parts known as elements. Each element is of simple geometry, and pre-defined with a set of material properties and boundary conditions. Therefore, it becomes much simpler to analyse each element than the actual structure itself, Fig. 3.4.1.

The introduction of FE analysis to the area of biomechanics began in 1972 when Brekelmans et al (1972) attempted to analyse the mechanical behaviour of skeletal structures. Currently, the FE method is widely accepted as the method of choice for stress analysis of bone and bone-prosthesis structures, fracture fixation devices and some soft tissue structures. This section of the thesis briefly reviews FE analysis in biomechanics. The first of the three sub-sections concerns orthopaedic biomechanics. A detailed review of this section is not attempted as this would be beyond the scope of this thesis. Interested readers should refer to Huiskes and Chao (1983), Huiskes and Hollister (1993) and Simon et al (1993). Pressure sore studies which involve FE analysis of biological soft tissue will be examined in the next section. This is followed by a review on modelling the amputee's residual limb.

3.4.1 Orthopaedic biomechanics

Interest in the stress analysis of intact bone is evident from early investigation carried out by Meyer (1867), Wolff (1870) and Koch (1971). These studies have provided interesting relationships between stresses and bone architecture. Classical mechanics was the basis for stress analysis in the above mentioned studies and was difficult to apply to a structure of complex shape like bone. The capability of the FE method to tackle complex shape, material and loading behaviour later proved to be extremely advantageous to the study of stresses in bones. The use of FE analysis is further reinforced by the growing interest in artificial joint replacement and new methods of fixation.

Early FE method studies were targeted at demonstrating the viability of the method. Brekelmans et al (1972) and Rybicki et al (1972) demonstrated the possibilities of FE method with 2-D models of the human femur using plane-stress elements. Rybicki's model accounted for non-uniform thickness by varying the Young's modulus of the elements and the results show good agreement between the trabecular structure of the bone and the lines of principal stresses. Several early 3-D FE models of the femur have been achieved, which includes studies by Scholten (1975), Wood (1975), Olofsson (1976), Valliappan et al (1977) Harris et al (1978), Brown and Rohlmann et al (1979). These models showed a more accurate representation of the actual case with out of plane loadings and geometries which cannot be represented with 2-D analysis.

Huiskes and Chao (1983) published a comprehensive survey of finite element studies in orthopaedic biomechanics within a ten year time frame, 1972-1982. The review raised some interesting observations. It was reported that most of the investigations conducted during this time were method oriented rather than problem oriented. Thus, these studies only aim to show the advances in FE methods but generally without producing a solution to real problems. Only a few researchers have attempted to compare theoretical results with experimentation in detail (Valliappan et al 1977, Huiskes et al 1981, Rohlman et al 1982). The review also stated that realistic 3-D geometry had been considered in most cases but, mesh refinement was often poor. Models describing non-linear and anisotropic material properties, and non-linear interface boundary conditions are few, but such models had laid good foundations for more recent studies. Early models are usually restricted by the computer technology and the types of finite elements available and the use of appropriate loading.

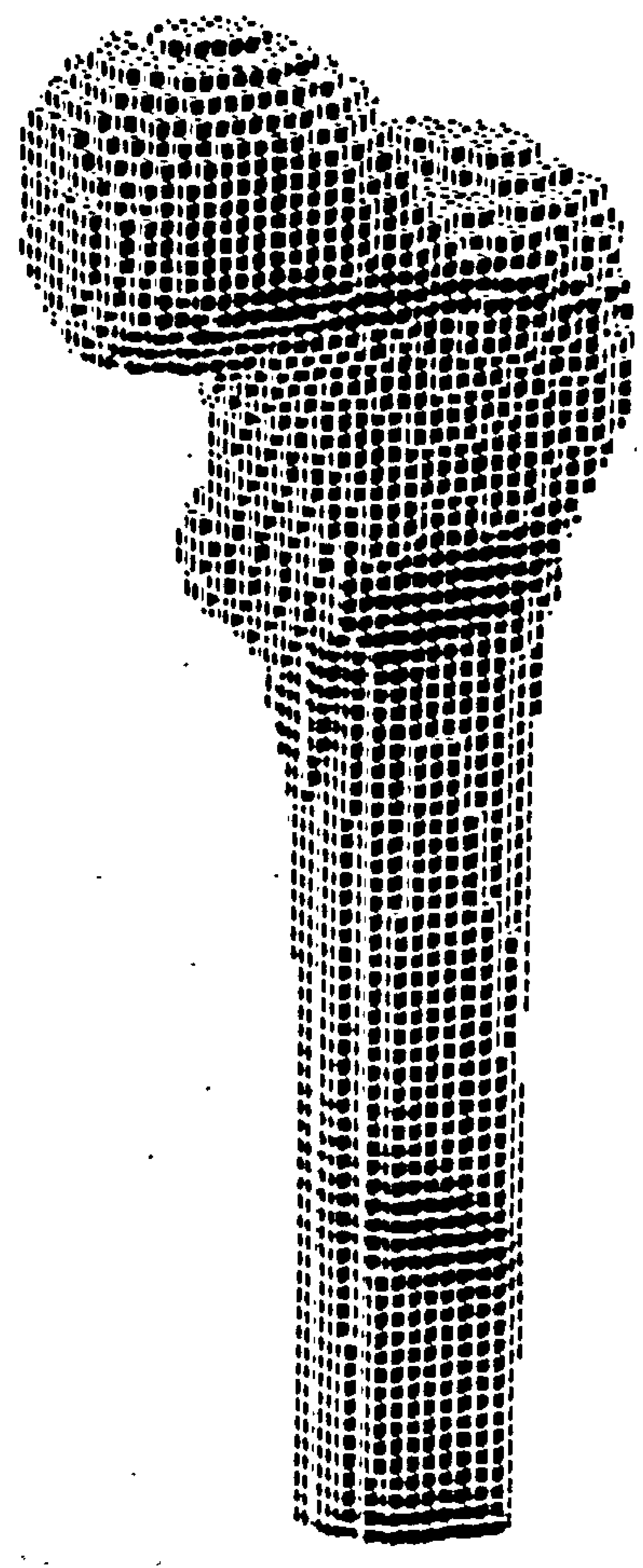

Fig. 3.4.1.1 Finite element model of the proximal femur consisting of 18 691 nodes and 14855 eight noded, linear isoparametric cube elements measuring 3 x 3 x 3 mm. (Keyak et al, 1993)

Computer advancement has influenced efforts in producing more realistic FE models of complicated musculoskeletal structures. Keyak et al (1990,1992,1993) described an automated method of finite element modelling of bone from CT scans. Applying this method, which uses only cube shape hexahedron elements, the proximal femur was modelled with 18691 nodes and 14855 elements (Fig. 3.4.1.1). The model was verified through strain gauge measurement and was found to accurately characterise the strains levels at the diaphysis and neck of the femur when the femoral head is loaded in compression. Geometrically accurate micro-structural modelling of bones (Fig. 3.4.1.2) is now possible with the aid of advanced digital imaging techniques like that of the micro CT scanner described by Feldkamp et al (1989). Van Rietbergen et al (1993) reported a full scale FE model describing the bone elements of a sample of trabecular bone of volume of 5 x 5 x 3.5 mm containing over 296 000 elements. Hollister and Kikuchi (1993) also investigated trabecular bone behaviour using FE methods, modelling both bone and marrow elements of the trabecular bone in a volume of 3 x 3 x 3 mm with 216 000 elements. Such models have provided valuable information to the study of failure mechanism and bone remodelling.

There has been numerous FE analyses attempted on the human spine. Biomechanical models studying spine motion and stability held in position by muscles have been addressed by Detrich et al (1992), Shirazi-Ad (1993) and Goel et al (1993). Stress distribution of the lumbar spine have been reported by Dai et al (1992), Lavaste et al (1992), Swito et al (1992) and Mizrahi et al (1993). Kasra et al (1992) investigated the dynamic characteristic of the lumbar spine. Clinical problems like metatstatic lesions and disc degeneration processes, were discussed by Mzrahi et al (1992) and Natarajan et al (1994) respectively.

Prosthetic devices or implants have received the most attention through FE methods of analysis. Investigations are directed towards extending the functional life of these implants by reducing mechanical failures. The modes of mechanical failure include plastic deformation, fatigue failure, collapse of acrylic cement and loosening at the interface between two different materials. Early 2-D stress analyses on femoral hip prosthetic components have been conducted by McNeice (1974), Andriacchi et al

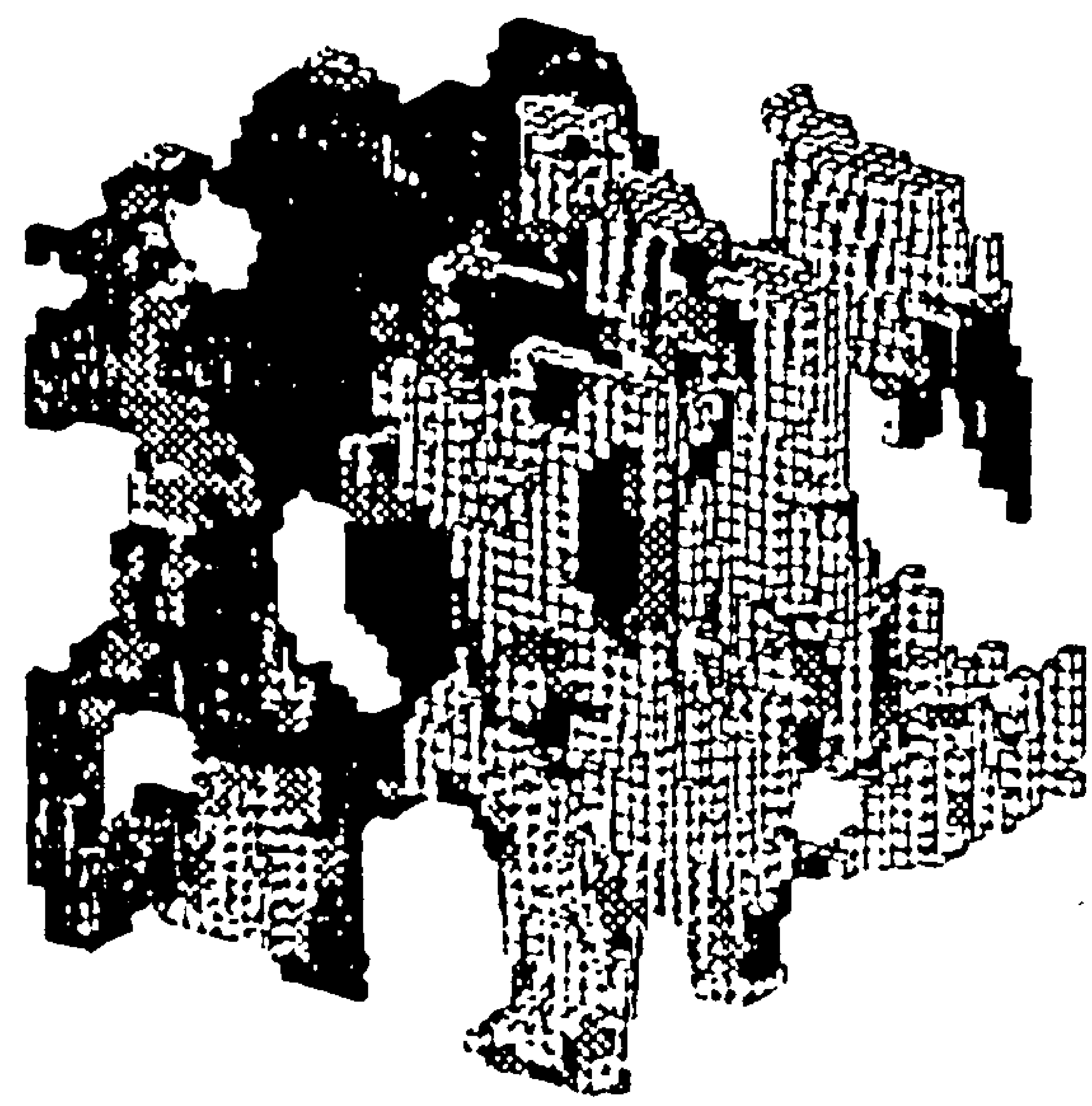

Fig. 3.4.1.2 FE model of a 2 x 2 x 2 mm volume canine trabecular bone.
(Hollister and Goldstein, 1993)

(1976) and Skinner et al (1982). Axisymmetric geometry, considering 3-D elements was attempted by Bartel and Usloy (1975), Bartel (1977) and Huiskes et al (1978). FE models detailing the cross-sectional geometry at the prosthesis cement interfaces have been adopted by Bartel and Desormeaux (1976), McNeice and Amstutz (1976) and Bartel and Samahyek (1976) to examine stresses in the cement.

Some of the latest studies on prosthetic hip implants applying FE methods are outlined as follows :

Adaptive bone remodelling around hip prostheses has been a major problem threatening the long term fixation of uncemented stems. Some believe that this has been caused by stress relief in the bone or stress shielding. Computer simulation models based on adaptive bone-remodelling theory (Cowin and Hegedus 1976), combined with finite element methods have been developed to predict the long term bone resorption phenomenon (Smolinski and Rubash 1992, Weinans et al 1992, Huiskes et al 1992, Levenston et al 1993, Weinans et al 1993a, Huiskes 1993). Applying FE analysis, the mechanism of failure in cemented hip components has been investigated by Harrigan et al (1992) and Jansson et al (1993). Comparative studies of different fixation techniques and different prosthesis materials have been attempted by Mihalko et al (1992) and Cheal et al (1992) respectively. A detailed non-linear FE model constructed using Quantitative Computer Tomography (QCT) scans data to define both geometry and material properties was used to study the effect of porous coating for cementless hip prosthesis (Keavenly and Bartel 1993). Bone reaction to micromotion between bone and implant was discussed by Rubin et al (1993) and Weinans et al (1993b).

The bone-prosthesis interface in total knee replacement was examined by Rakotomanana et al (1992) and Dawson and Bartel (1992). The latter paper gave an account of a linearly elastic, axisymmetrical FE model describing the consequences of an interference fit on porous coated tibial components. Two conditions of long term fixation were considered, the first assuming the bone to have grown into all the porous coating and the second, that the bone had grown only into the single peg of the tibial component (Fig. 3.4.1.3).

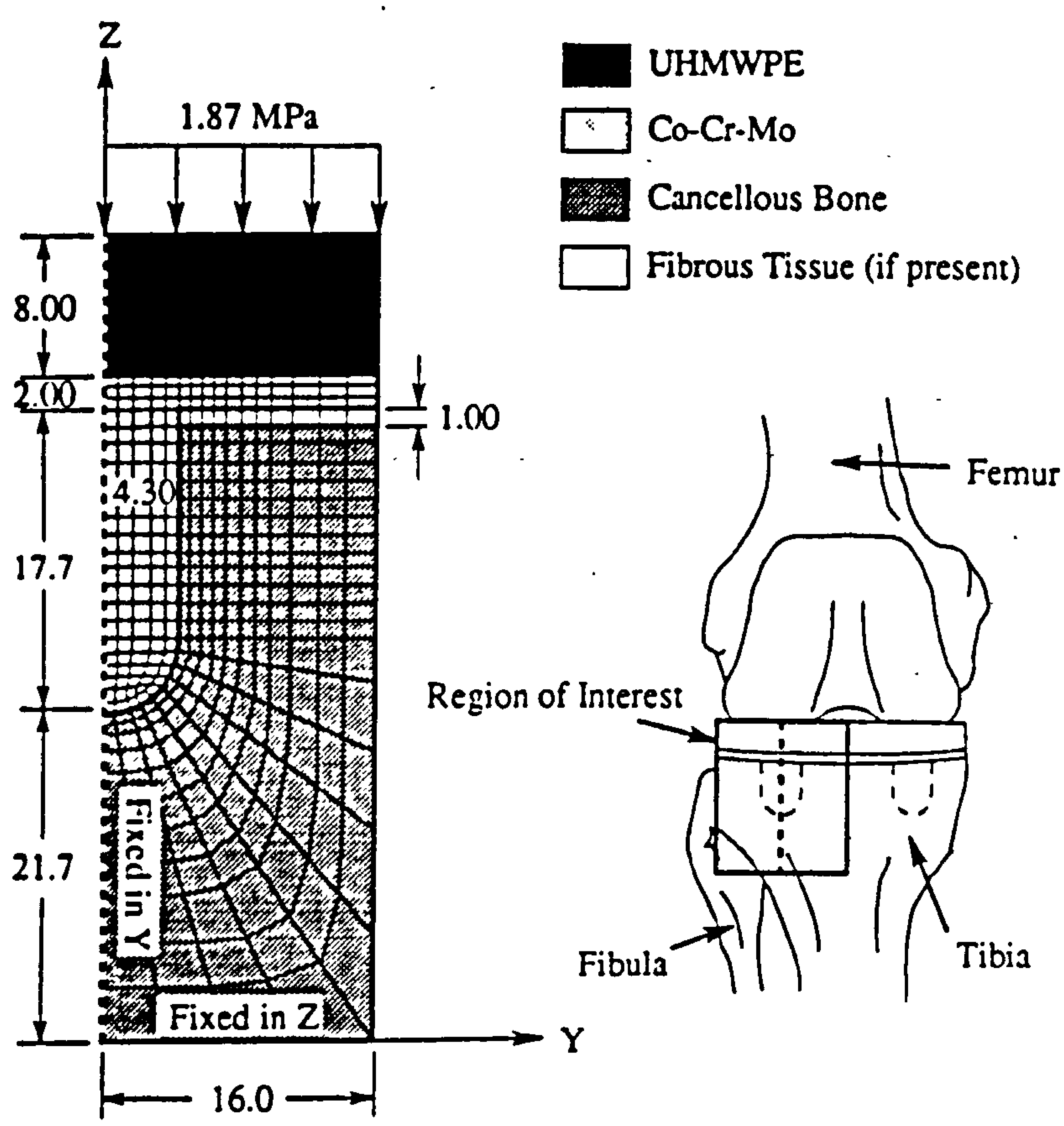

Fig. 3.4.1.3 Axisymmetric model representing the tibia tray, peg and the surrounding cancellous bone. All dimension in mm. (Dawson and Bartel, 1992)

Huiskes's et al review of FE analysis in orthopaedics in 1983 and later in 1993 showed clearly the advancement and the route FE analysis has taken (Huiskes and Chao 1983, Huiskes and Hollister 1993). It was summarised in the later review that FE analysis now fulfils three important roles in orthopaedic research. Firstly, as a method of data evaluation. Experimental data from different time periods can generate FE models that provide an understanding of the investigated biological phenomena. Such models being purely analytical can be more powerful than a statistical model. Secondly, FE analysis can serve as a method of extrapolation. Micro-structural models can extrapolate to a lower level structure, and animal studies can extrapolate to human cases. Thirdly, it has become a method of numerical experimentation. Ideal experimental environment is only possible with a numerical model. Factors affecting the outcome of a numerical experiment can be included or excluded at will, whereas in clinical tests with patients, there are many factors that the researcher has no control over. In addition, the requirement for a numerical experiment is obviously cheaper when compared to most clinical experimental setups.

3.4.2 Pressure sore research

Pressure sores is a major concern for patients who are confined to long periods in a seated or reclining position. Pressure applied to the skin under such conditions is among the many factors contributing to the development of pressure sores (Ryan et al 1989). Most of the FE models discussed in this section concern understanding the mechanical behaviour of soft tissue, and the material behaviour and design of the support mechanism, e.g. wheelchair cushion or matress. The findings' main aim is to prevent the occurence of pressure sores. Numerical modelling of this type is comparable to the modelling of the amputee's residual limb both in methodology and aim. Whilst the aim in the case of an amputee is not as drastic as pressure sore prevention, nonetheless, it is similar when taken into the context of understanding stress distribution in soft tissue for prosthetic socket design. The author of this thesis therefore perceived the benefits of the inclusion of a review of pressure sores studies in this thesis.

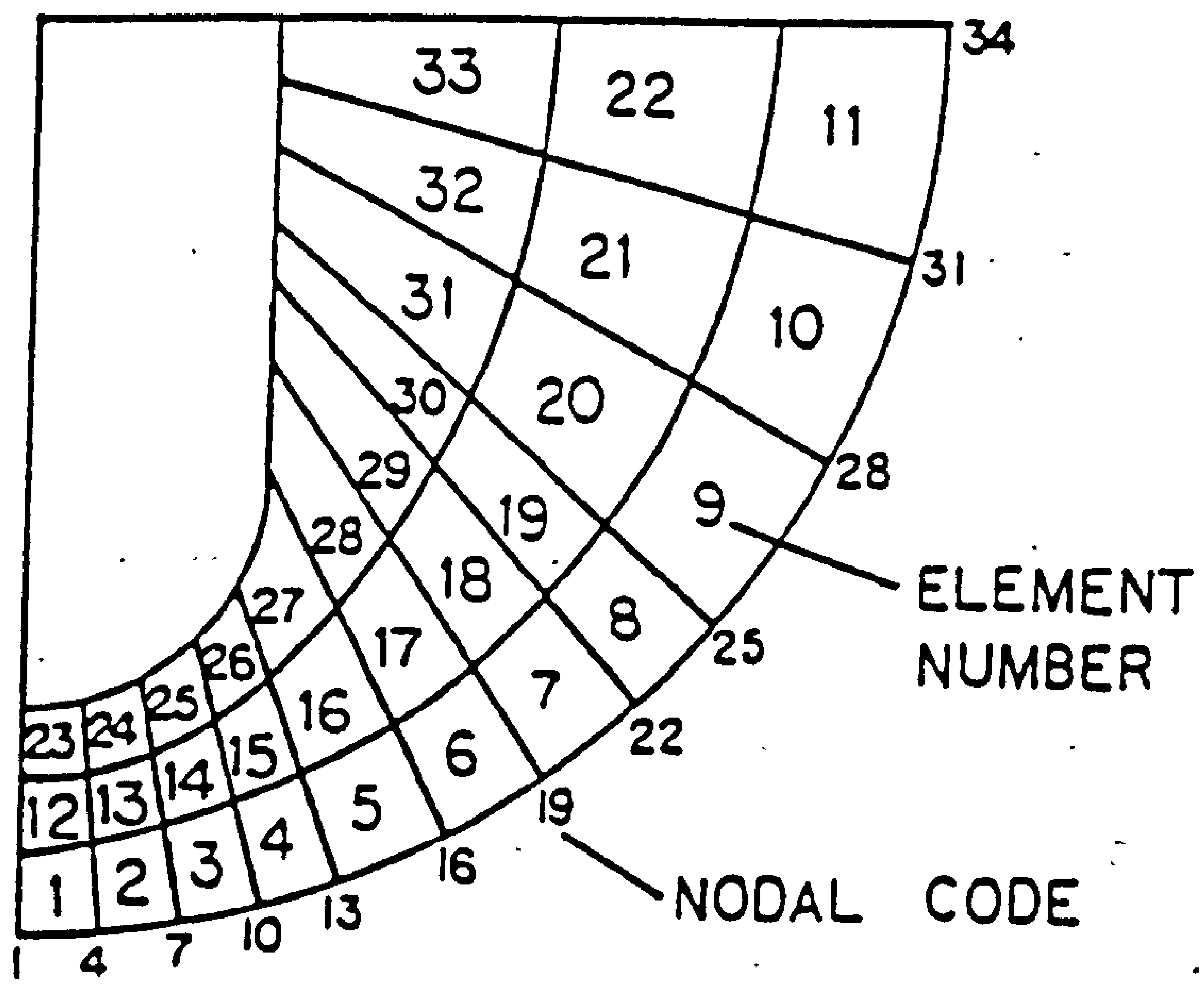

Fig. 3.4.2.1 Axisymmetric FE model of a human buttock.
(Chow and Odell, 1978)

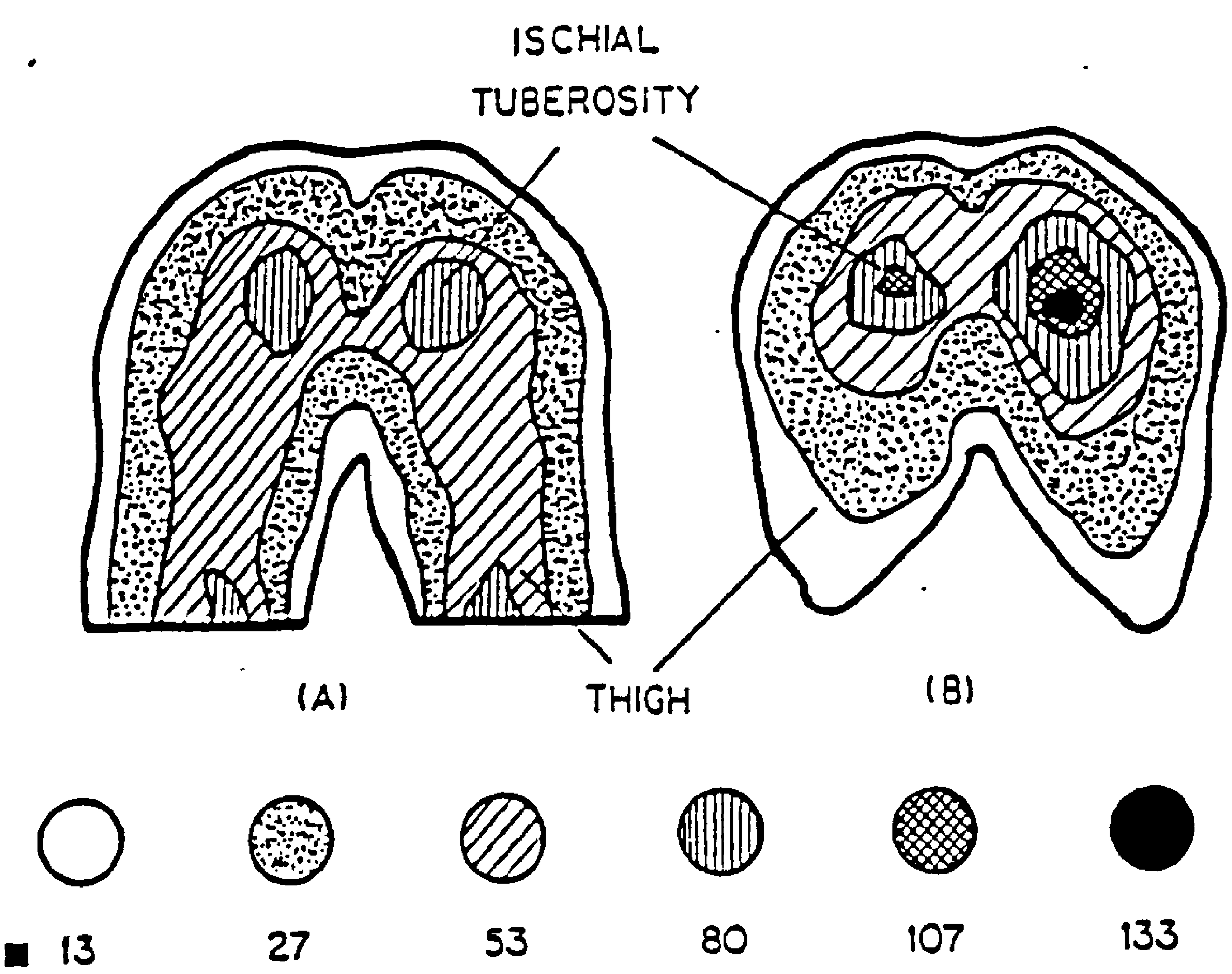

Fig. 3.4.2.2 Pressure distribution at the buttock-cushion interface. All pressures are in x 100 Pa.
a.) Patient's feet hanging free, thigh contact.
b.) Patient's feet supported, minimal thigh contact.
(Chow and Odell, 1978)

Chow and Odell (1978) presented a 3-D axisymmetric FE model of a human buttock. The simplified model described a 100mm radius hemisphere of soft tissue with a rigid core simulating the effect of the ischial tuberosity (Fig. 3.4.2.1). A total of thirty three 12-node isoparametric quadrilateral elements was used. The justification for a axisymmetric model instead of a fully geometrically defined 3-D model was based on the symmetrical stress distribution pattern on the buttock of a seated person. The authors presented soft tissue/cushion interface pressure patterns in two sitting positions (Fig. 3.4.2.2), with and without thigh contact, from Lindan et al (1965) and argue that the position with no thigh contact gives a nearly axisymmetrical pressure distribution. Axisymmetric modelling is further reinforced, since modelling a more critical situation i.e. higher pressure without thigh contact, the supporting medium under evaluation is put under a more severe test. An isotropic material was selected to represent the soft tissue component of the model with a modulus of 15 kPa and Poisson's ratio of 0.49, depicting a nearly incompressible material. A 300 N load was assumed to be transmitted through the buttock-cushion interface in six different ways. These loading conditions are floating on water, floating on mercury, sitting on a flat frictionless rigid surface, pressure applied as a cosine function, foam cushion with friction and foam without friction. Both hydrostatic and von Mises stresses were quoted in the results (Fig. 3.4.2.3). The findings mentioned that uniform presssure and small buttock deformation are possible with flotation support, thus high density fluids may be a promising medium.

Todd and Thacker (1994) produced a 3-D model of the human buttock using MRI techniques to determine the model geometry. Assuming bilateral symmetry, only the tissues around the right ischial tuberosity were included in the model. Two ambulatory subjects, a male and a female, participated in the test. The subjects were placed in supine position and transverse slices of abdominal images were captured at 8mm intervals using an MRI imager (Fig. 3.4.2.4). The images were then digitized slice by slice to form a 3-D model of the buttock. The FE models (Fig. 3.4.2.5) comprises the ischial tuberosity, soft tissue, cushion and an elastic foundation, which were generated using 1008 eight-noded 3-D isoparametric brick elements. Linear

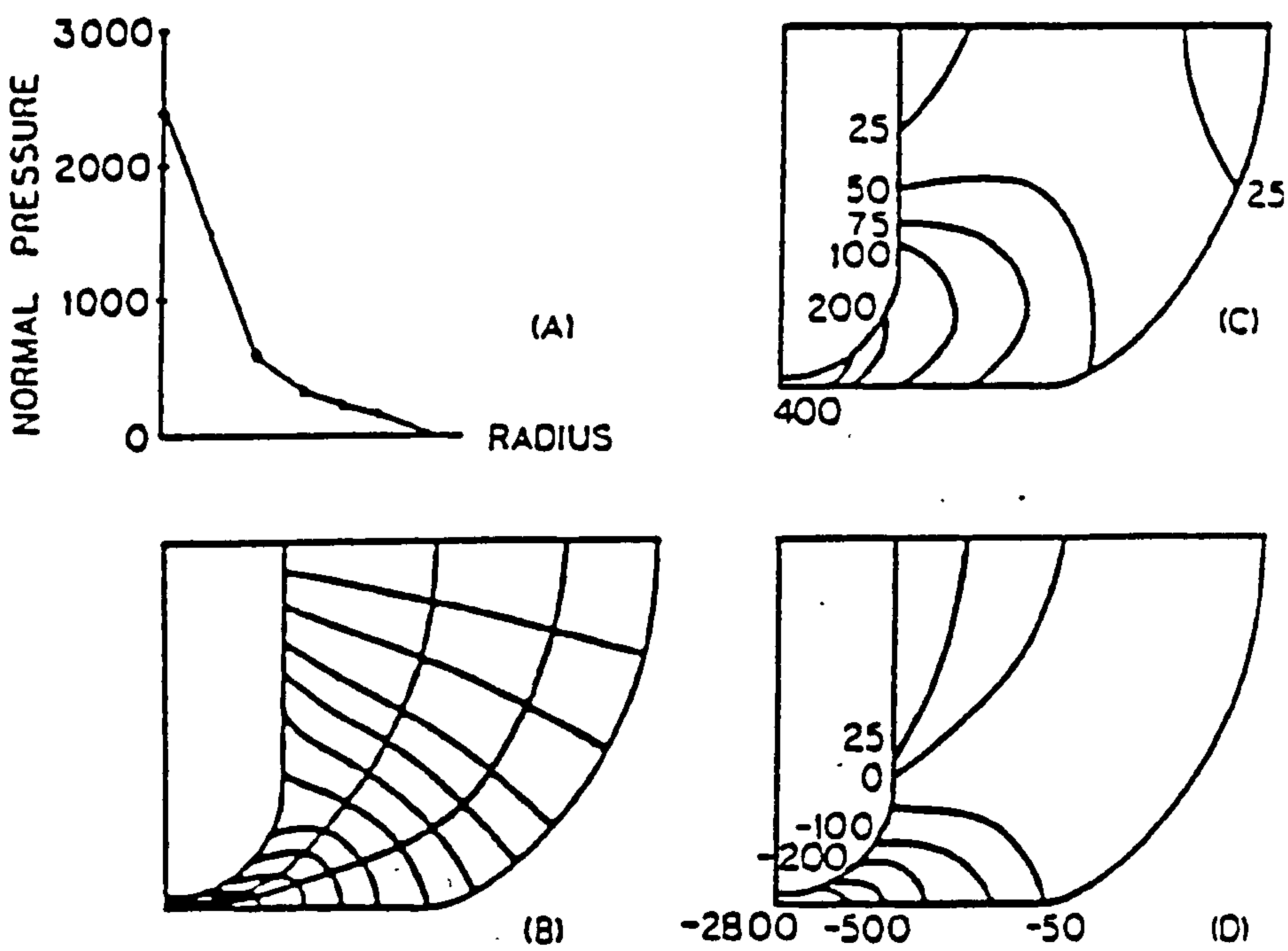

Fig. 3.4.2.3 The model on al flat frictionless rigid surface. All stresses are in x 100 Pa.
A.) Surface pressure distribution, B.) final grid pattern.
C.) von Mises stress contours and D.) hydrostatic stress contours.
(Chow and Odell, 1978)

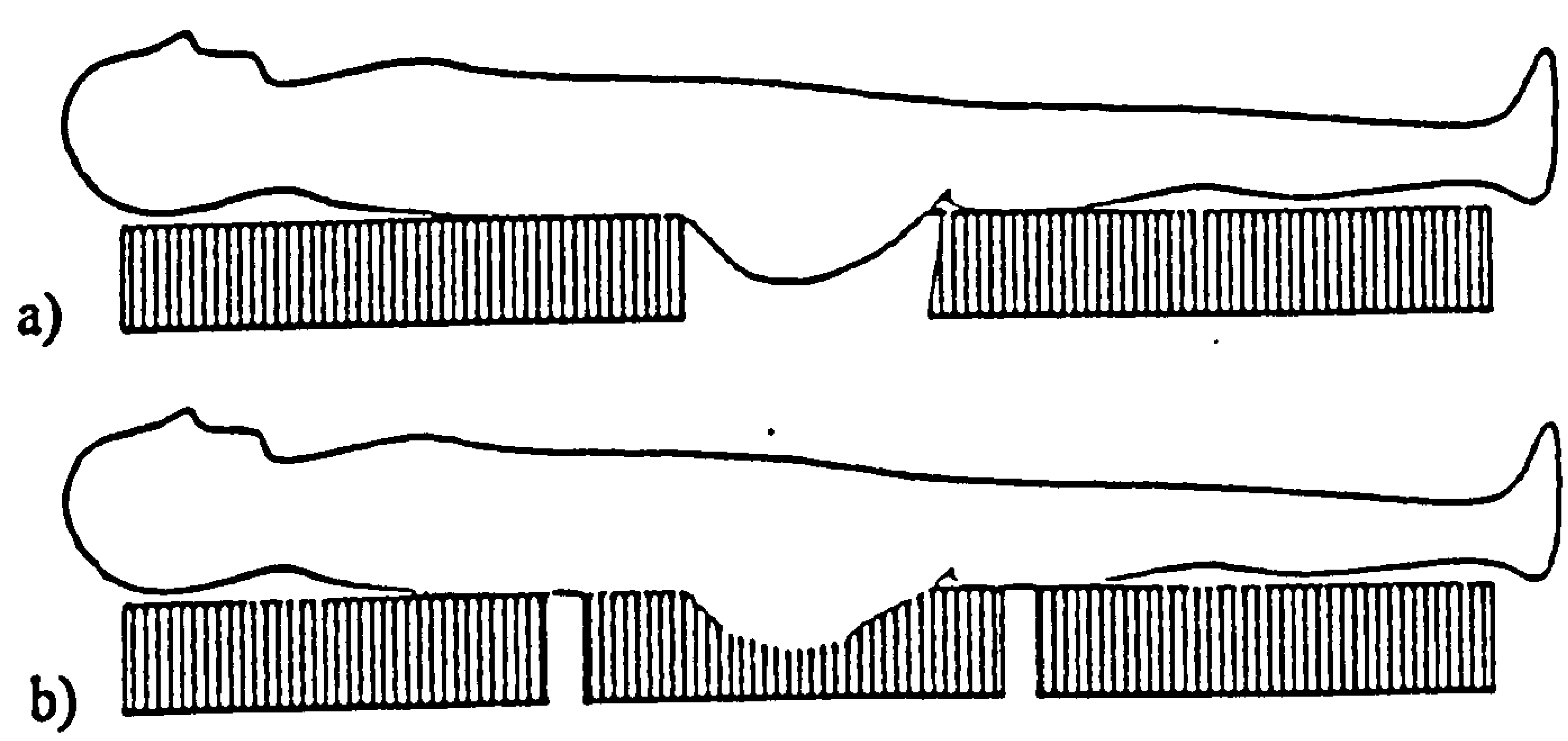

Fig. 3.4.2.4 Subjects' position in the MRI imager. a.) A free hanging buttock geometry is captured for the construction of the FE model.
b.) For model verification subjects were imaged supported on custom - contoured cushions.
(Todd and Thacker, 1994)

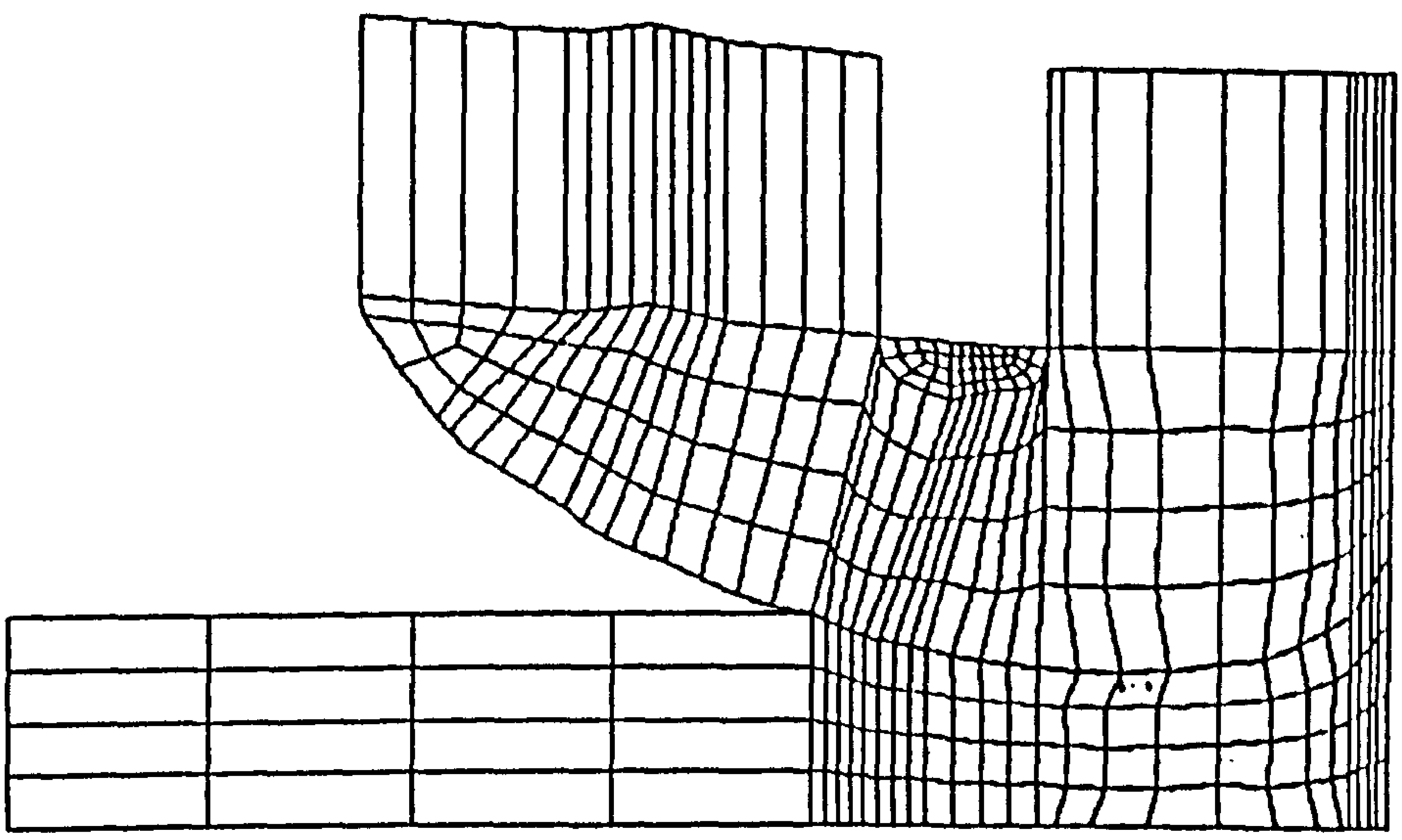

Fig. 3.4.2.5 Cross-section of the 3-D finite element model.
(Todd and Thacker, 1994)

Material	Young's Modulus E (kPa)	Poisson's Ratio ν
Bone	17000	0.31
Cushion	10.2	0.1
Soft Tissue Seated Female	47.5	0.49
Soft Tissue Supine Female	11.9	0.49
Soft Tissue Seated Male	64.8	0.49
Soft Tissue Supine Male	15.2	0.49
Elastic Foundation Supine Female	1.19	0.49
Elastic Foundation Supine Male	25.3	0.49

Table 3.4.2.1 Material properties used in the model.
(Todd and Thacker, 1994)

Position	Computational Displacement (cm)	Experimental Displacement (cm)
Male—supine	1.8	1.7
Male—seated	3.34	Not available
Female—supine	3.81	3.9
Female—seated	3.00	Not available

Table 3.4.2.2 Displacement under the ischial tuberosity.
Experimental displacement obtained from MRI images.
(Todd and Thacker, 1994)

Position	σ_3 (Pa)	°von Mises (Pa)	Oxford Pressure Monitor (Pa)
Male—supine	2,978	2,487	4,100
Male—seated	16,921	16,981	not available
Female—supine	4,667	4,384	2,800
Female—seated	14,955	12,465	not available

Table 3.4.2.3 Predicted hydrostatic and von Mises stresses, and measured buttock - cushion interface normal stresses.
(Todd and Thacker, 1994)

elastic and isotropic material properties were assumed for all elements in the models. Moduli for the soft tissue were obtained by a mechanical indenting device that records force data at 1mm deflection intervals. The moduli of the soft tissue were then estimated by taking the initial portion of the force-deflection curve. Symmetry boundary conditions were specified at the plane of symmetry. Also at the top plane where the model is separated from the rest of the body, an elastic foundation was modelled by a series of semi-infinte elements constrained on the end that is not attached to the soft tissue. However, it was not stated how the modulus for this foundation was arrived at (Table 3.4.2.1). The models were loaded with a concentrated force at the centre of the ischial tuberosity. The magnitude of this force was determined as a percentage of body weight, for male 6.7% and 29.2%, and for female 8.7% and 29.2% for supine and seating positions respectively. Predicted displacement at the ischial tuberosity closely matched the experimental values, which were determined by the MRI images (Table 3.4.2.2). Predicted interface pressures at the buttock/cushion interface were compared with measured pressures obtained using the Oxford pressure monitor. Approximately 50% error was observed (Table 3.4.2.3).

Chow and Odell (1978) and Todd and Thacker (1994) both mentioned improving the FE model to accept non-linear soft tissue properties. Nevertheless, there has been difficulty in finding suitable constitutive relations to represent the highly non-linear behaviour of soft tissue. Many researchers still prefer to model soft tissue non-linear characteristic with a linear approximation. However, Dabnichki et al (1994) suggested the use of Mooney-Rivlin (M-R), hyperelastic material defined in terms of stored energy function (W) to simulate soft tissue behaviour. M-R material is defined as,

$$W=A(I_1-3)+B(I_2-3)$$

or also commonly as,

$$W=C_{10}(I_1-3)+C_{01}(I_2-3)$$

where I_1 and I_2 are functions of principal extension ratios arising as the invariants of the right Cauchy-Green deformation tensor. A, B or C_{10}, C_{01} are constants, which in the case of this investigation are experimentally obtained through material testing. The

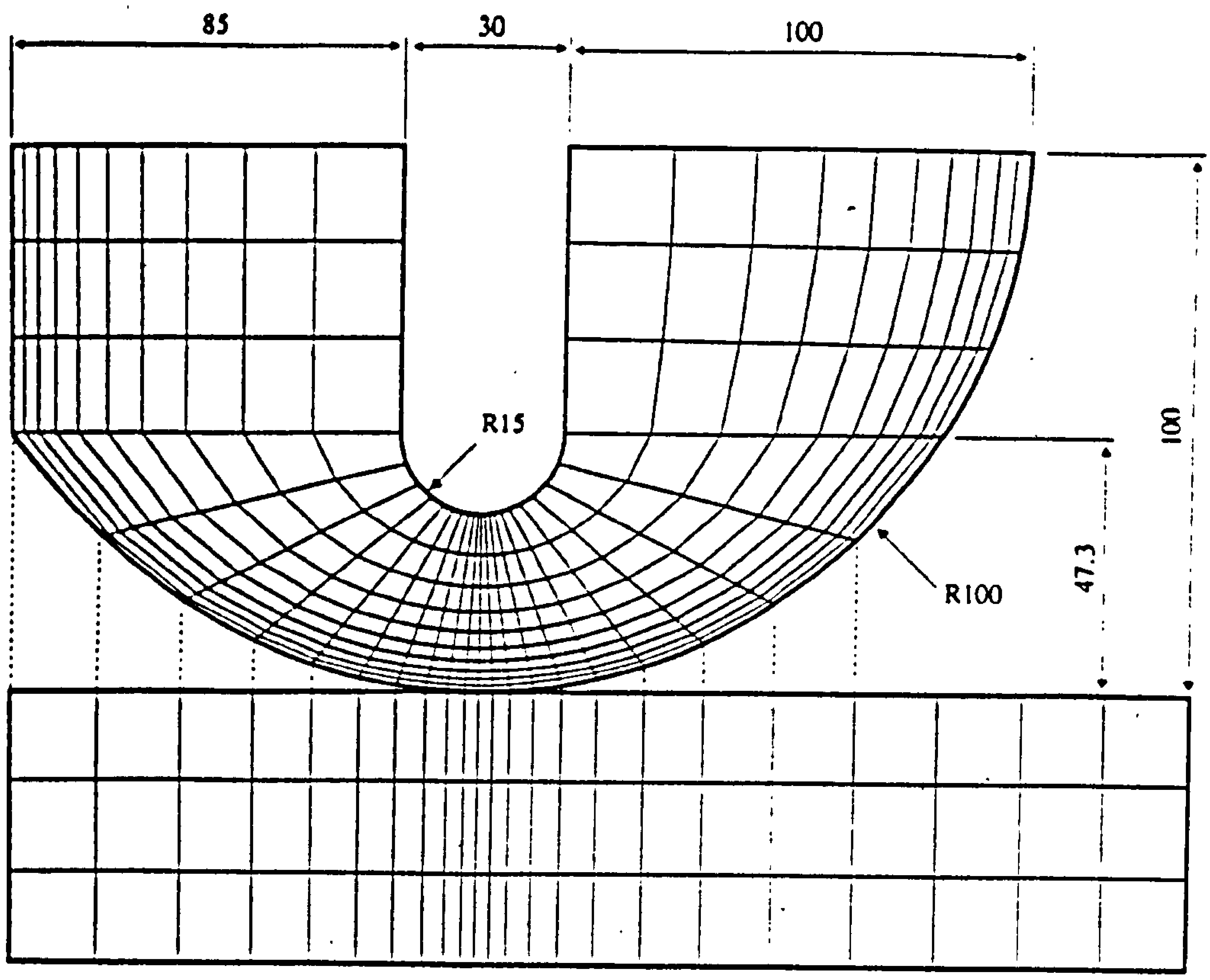

Fig. 3.4.2.6 Idealised FE model of the buttock. All dimension in mm. (Dabnichki et al, 1994)

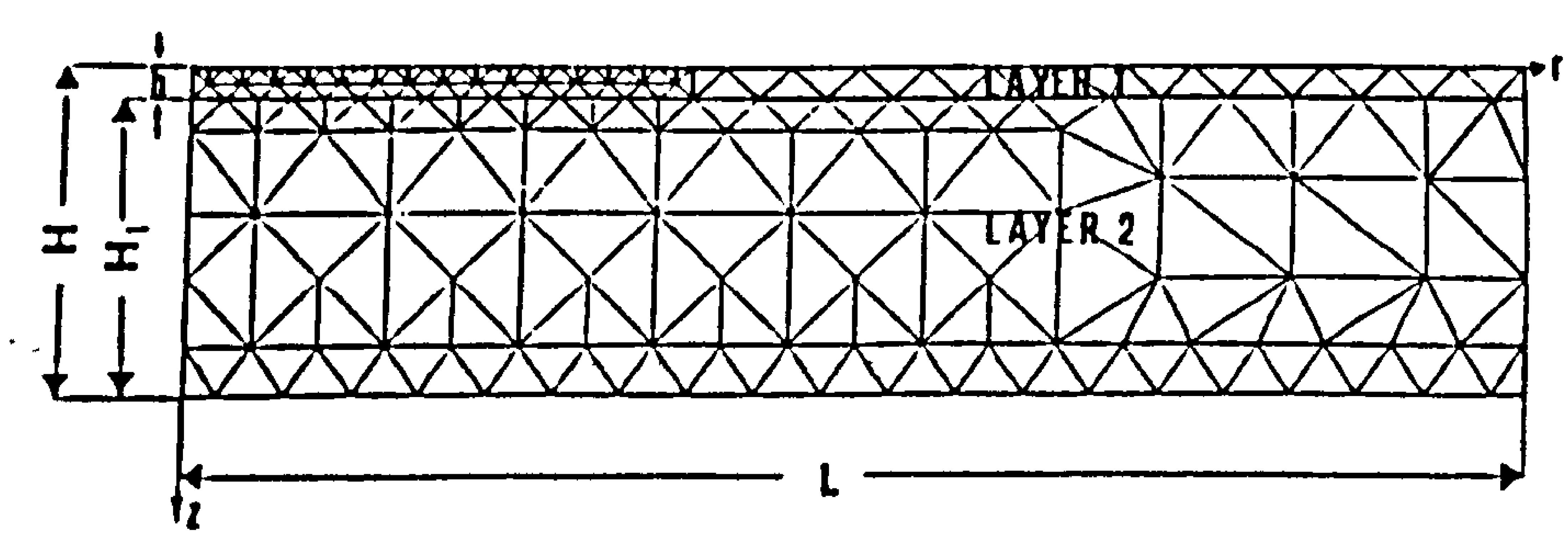

Fig. 3.4.2.7 Axisymmetric FE model for skin (layer 1), and fat together with muscles (layer 2). H = 20 mm, H_1 = 18 mm, h = 2 mm and L = 80 mm. (Brunski et al , 1980)

2-D buttock and cushion model is based on an idealised geometry constructed with 349 elements and 399 nodes (Fig. 3.4.2.6). The authors main emphasis in the studies was the accomplishment of a realistic non-linear FE model using M-R hyperelastic element. Unfortunately the author of this thesis remains sceptical for reasons that the M-R material has been proven in the present study, that it is a worst material choice than a linear elastic material for modelling soft tissues. The experiments and results supporting this statement is presented in detail in chapter six.

Investigation pertaining to the formation of pressure sores in Yorkshire pigs via a constant force indenter were conducted by Brunski et al (1980) and Schock (1981). Brunski simulated the contact problem using a FE method to examine the stresses around the indenter. The general anatomy of the indentation sites was modelled with an axisymmetric FE model of radius 80 mm consisting of 256 six-noded triangular elements (Fig. 3.4.2.7). The model comprises a layer of skin 2 mm thick and another layer of fat together with muscles 18 mm thick.A linear elastic modulus was chosen for both skin and fat plus muscles, respectively, at 2.76 MPa and 162 kPa. Poisson's ratio was 0.49 for both materials. Schock (1981) performed similar numerical experiments but used a finite difference method instead. Both findings show how stresss in indented tissue could be affected by changes in indenter shape, indenter force and tissue mechanical properties.

3.4.3 Amputees' residual limb

A series of projects have been undertaken by the Prosthetic Research Laboratory, Northwestern Univeristy in Chicago to address the possibility of FE analysis in an amputee's residual limb. In the 7th world congress of ISPO, Steege et al (1992) described their goal as to apply desirable surface stress to FE models of residual limbs, use FE analysis to solve for the resultant surface displacements, and output this shape to create a suitable socket. With this aim in mind, research which began in 1986 has since generated interesting results. Steege et al (1987, 1988) gave an account of two phased FE studies of the trans-tibial residual limb. Efforts in both phases concentrated on verifying the FE models with measured pressure at the

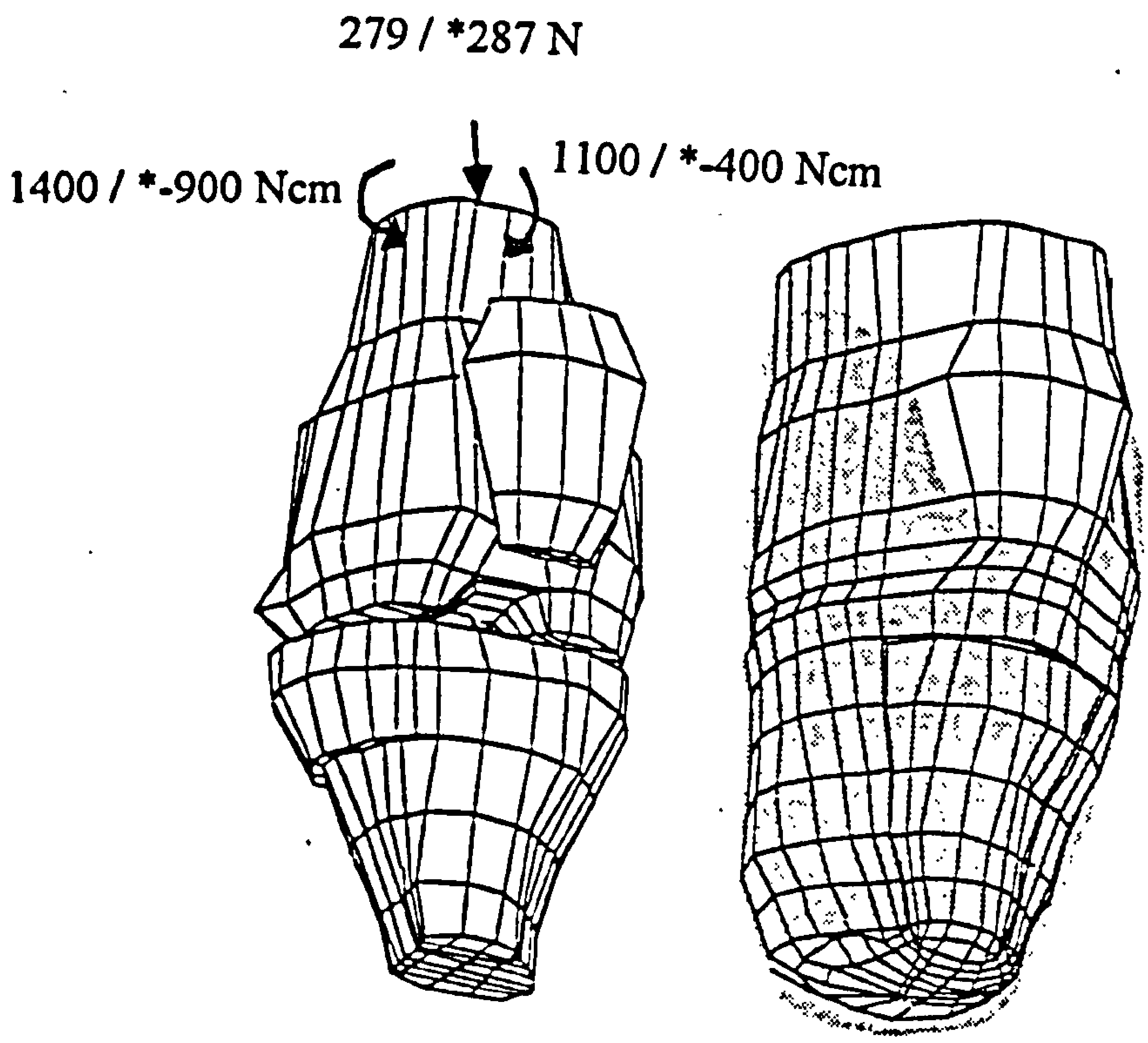

Fig. 3.4.3.1 Three dimensional FE model of the trans-tibial residual limb.
a.) Internal bone elements, b.) Complete model with the conceptual location of the socket liner. Two sets of loading conditions are created. First with the prosthetic foot intact, *second, the prosthetic foot is replaced by a 50 mm diameter ball. Positive forces and moments follow the arrows described in the diagram.
(Steege and Childress, 1988)

residual limb/socket interface. In phase one, two subjects were tested and FE models generated. Commercial FE codes SAPIV and GIFTS were used for model 1 and model 2 respectively (Fig. 3.4.3.1). Mesh for model 1 consisted of 1017 linear 8-noded isoparametric brick elements representing the soft tissue, bones and cartilage, while another 340 linear spring elements represented the socket liner, giving rise to a total of 1282 nodes. Model 2 consisted of 1578 similar 8-noded isoparametric brick elements and 1976 nodes, which represents all the elements of the model including the socket liner.

Geomertical details of the models were acquired by manual digitization of multiple transverse CT scans at 10 mm intervals. 13 and 14 transverse images were deemed sufficient for the creation of model 1 and 2 respectively. Material properties assigned to the models are as tabulated in Table 3.4.3.1. Bone and cartilage properties were obtained from literature. The modulus of the socket liner (Pelite) was established through standard material testing. Soft tissue load-deflection behaviour was ascertained through an *in vivo* mechanical indentation test. Loadings for the models were directed at the femur i.e. the proximal end of the models. The magnitudes and directions of the load actions were obtained with the aid of a CODA-3 motion analysis system and two AMTI force platforms. The subjects were positioned such that their body weight was distributed equally over the force platforms. Several retroreflective markers recognised by the CODA-3 system were placed on the prostheses and subjects. Markers' position, ground reaction forces and also residual limb/socket interface pressures were acquired simultaneously. Knowing the exact co-ordinates of the strategic markers enabled the GRF to be transformed to actual forces and moments experienced at the proximal femur, which are then employed in the FE models. Two different loading conditions were created by replacing the prosthetic foot with a 50mm diameter ball, with the intention of reducing moments on the limb. The direction and magnitude of load actions at the femur are as shown in Fig. 3.4.3.1.

Interface pressures at seven locations around the PTB socket were measured and compared to the FE analysis prediction. Results are as tabulated in Table 3.4.3.2.

TABLE I : Material Property Information

Material	Bone	Tissue	Cartilage	Pelite™
Young's modulus E (N/cm²)	1.55 x 10^6	6.00	79.00	38.00
Poisson's ratio υ	0.28	0.49	0.49	0.49

Table 3.4.3.1 Material properties assigned to the model.
(Steege and Childress, 1988)

Measurement Location	Subject A w/foot Exp.	Subject A w/foot FEA	Subject A w/ball Exp.	Subject A w/ball FEA	Subject B w/ball Exp.	Subject B w/ball FEA	Isherwood †	Pearson •
Distal End	10.7	5.4	0.0	5.1	0.0	0-2	0.8	-
Popliteal Area	0.0	0.7	4.0	0.8	8.1	4-6	4.3	-
Medial Tibial Condyle	4.7	0	8.6	0	0.0	0-2	-	1.0
Patellar Tendon Bar	4.8	10.5	12.5	9.4	8.0	2-12	6.4	3.4
Medial Flare Proximal Tibia	-	3.0	-	1.7	5.9	0-2	3.4	-
Distal Lateral Contact Area	7.7	2.2	12.8	1.6	6.5	0-2	-	-
Fibular Shaft	4.8	0.9	7.2	0.3	3.1	0-2	4.7	-

Table 3.4.3.2 Experimental and predicted interface pressure values (N/cm²).
(Steege and Childress, 1988)

The overall range in the measured (0-12.8 N/cm^2) and predicted (0-10.5 N/cm^2) pressures matches well, but a direct one to one correlation was not possible. Distal end pressures highlighted such a case, since pressure predicted for the foot and ball trial for subject A was both 5 N/cm^2 while the measured pressure was 10.7 and 0 N/cm^2 respectively. The insensitivity to changes in loading condition in the models neccessitated a further 2nd phase study.

Phase two analysis converted the original two models to MARC FE code which was claimed by the authors to provide better capabilities for non-linear soft tissue modelling. Alterations were also made to the socket liner now modelled only as a linear elastic foundation. Elastic foundations were also placed at the proximal end of the model to simulate the effects of the rest of the unmodelled thigh. Treated as a small strain problem, the MARC FE code predicted almost identical pressure contours to the phase one analysis, except with lower magnitude. Under the two different loading conditions, the foot and ball analysis, pressure patterns remain similar. The inability of the model to differentiate pressures between the two conditions was further investigated with non-linear modelling. The non-linear analysis was based only on the top third of a generic residual limb modelled with one hundred and twenty 9-noded isoparametric brick elements (Fig. 3.4.3.2). Large deflection theory was adopted requiring the analysis to take place iteratively. Elastic foundations were placed at both the proximal and distal end of the model to represent the unmodelled limb (E=6 N/cm^2), and at the sides of the model representing the socket liner (E=38 N/cm^2). Soft tissue material was represented by M-R material as was done by Dabnichki et al (1994). However, the values of C_{01} and C_{10} were not obtained experimentally but assumed to satisfy the following conditions :

$$C_{01} = 0.25\, C_{10} \text{ and } E = 6\,(C_{01} + C_{10}).$$

The results of the preliminary analysis predicted stress patterns which are generally similar to the phase one study, but also with some area of obvious difference. The authors suggested that these differences were encouraging enough to pursue such non-linear modelling. Later investigations were reported in the 7th world congress of ISPO (Steege et al 1992), but there was no mention if the soft tissue was modelled as

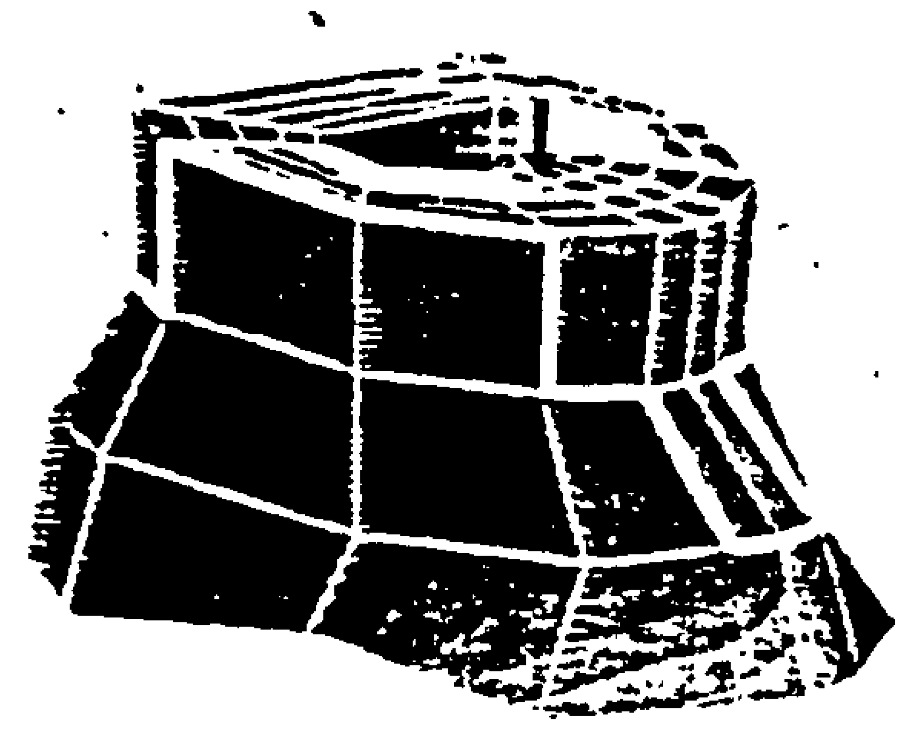

Fig. 3.4.3.2 Non-linear FE model simulating only the top third of the residual limb. (Steege and Childress, 1988)

MODEL CASE	E_{skin} (kPa)	G_{skin} (kPa)	E_{muscle} (kPa)	G_{muscle} (kPa)
1	5.2	1.7	131	44.0
2	6.9	2.3	131	44.0
3	3.5	1.2	131	44.0

Table 3.4.3.3 Soft tissue material properties combination. (Sanders and Daly, 1993)

M-R hyperelastic materials. However, the generation of the FE model was greatly improved through the use of EXTRACT, a program that handles CT scans data and provides edge detection facilities, thus there is no need for manual image digitisation. A model of the trans-tibial limb was created using 85 levels of CT data and current work is being carried out to manufacture a socket with equal pressure around the limb in a non-weight bearing state. Although the benefit of a socket with equally distributed pressure is still questionable.

From the same research group, Silver-Thorn and Childress (1992) presented a generic geometric FE model of the trans-tibial residual limb in order to do away with costly imaging procedures. An existing FE model was scaled appropriately to the amputee's residual limb prior to the numerical analysis. Results obtained show predicted pressures were of the same order of magnitude when compared to the measured pressures at the residual limb/socket interface, but significant errors are seen in the way these predicted pressures are distributed.

Finite element modelling of the trans-tibial residual limb was also attempted by Sanders and Daly (1993). MRI techniques were adopted to determine the residual limb geometry. A total of 19 transverse scans were acquired for 3-D model generation. The model comprises of Pelite, skin, muscles, bone, prosthetic shank and socket. Eight-noded isoparametric brick elements were used for skin, fat, muscles and Pelite while bone was modelled as a rigid surface. The socket was modelled with quadrilateral shell elements and the prosthetic shank with beam elements. The complete mesh consisted of 840 elements with 795 nodes. Three sets of material properties sourced from the literature were assigned to skin and muscles (Table. 3.4.3.3). Pelite was subjected to a uniaxial compression test and a suitable modulus of 1.8 MPa was selected. The Poisson's ratio of for Pelite was 0.39. Input load actions were specified at the distal end of the model which were measured using a 20 strain gauge mounted pylon transducer situated at the prosthesis' shank. Shank forces and moments were collected for 8 s with the subject walking on a 18m x 1.2m pathway. These data were collected concurrently with residual limb/socket interface pressure measurements attempted at five measurement sites around the socket. Predicted and

NORMAL STRESS

alignment	site: postero-proximal	antero-medial proximal	antero-lateral proximal	antero-lateral distal	postero-distal
plantarflexion	under 90%	over 49%	over 95%	over 550%	under 16%
zero	under 89%	under 29%	over 63%	over 221%	under 25%
dorsiflexion	under 86%	under 83%	over 52%	over 197%	under 19%

RESULTANT SHEAR STRESS

alignment	site: postero-proximal	antero-medial proximal	antero-lateral proximal	antero-lateral distal	postero-distal
plantarflexion	under 82%	under 19%	under 49%	under 51%	under 44%
zero	under 87%	under 11%	under 53%	under 74%	under 51%
dorsiflexion	under 88%	under 1%	under 57%	under 75%	under 54%

Table 3.4.3.4 Comparison of predicted and experimental normal and resultant shear stresses. Under and over implies, FE results underestimated and over estimated respectively. (Sanders and Daly, 1993)

experimental peak interface pressures during the stance phase of the gait cycle were compared at three different alignment positions of the prosthesis. The angular settings of the socket relative to the shank in the sagittal plane were zero, 12° plantarflexion and 4° dorsiflexion. The results are shown in Table. 3.4.3.4. Very large errors were observed at the anterior - lateral distal sites (197% - 550%) of the trans-tibial limb. Majority of the sites recorded percentage errors ranging from 40% to 90%. The model's sensitivity to changes in skin modulus affected stress prediction. An increase in skin modulus from 3.5 to 6.9 kPa recorded a decrease in the peak stance phase interface pressure of less than 30%.

In order to understand the effects of friction and interface pressures, Reynolds (1988) constructed an axisymmetric model of the trans-tibial limb. The geometry was derived from X-ray views and basically idealised. The model's soft tissue utilised linear elastic, isotropic material properties of E=170 kPa and v=0.45. The model demonstrated the contribution of shear forces in vertical weight bearing through varying friction at the socket/residual limb interface. Further 3-D modelling was attempted which included details of soft tissue, bones and socket. The effects of rectified and unrectified sockets in terms of interface pressures were also compared. Generally the model predicted higher pressures than most published experimental measurements. The work of Reynolds was further expanded by Zhang and Roberts (1993). The model created (Fig. 3.4.3.3) accepts large displacement analysis and the use of interface elements. Soft tissue and socket liner were meshed with 972 and 486 3-D 8-noded isoparametric brick elements respectively, and between the two, 486 interface elements were specified. Commercial FE codes installed in a Convex C3840 Supercomputer were utilised. ABAQUS FE codes served as the numerical solver and FEMVIEW as the pre-processor. The interface elements provided the added capabilities of the model to study micromotion slips, but the authors were unable to verify the predicted slip due to obvious difficulties in conducting experimental measurements. Pressures predicted were lower than reported measurements (see section 4.2.2, a review of trans-tibial pressure measurements in chapter 4), but this was largely attributed to the hypothetical loading described for the model.

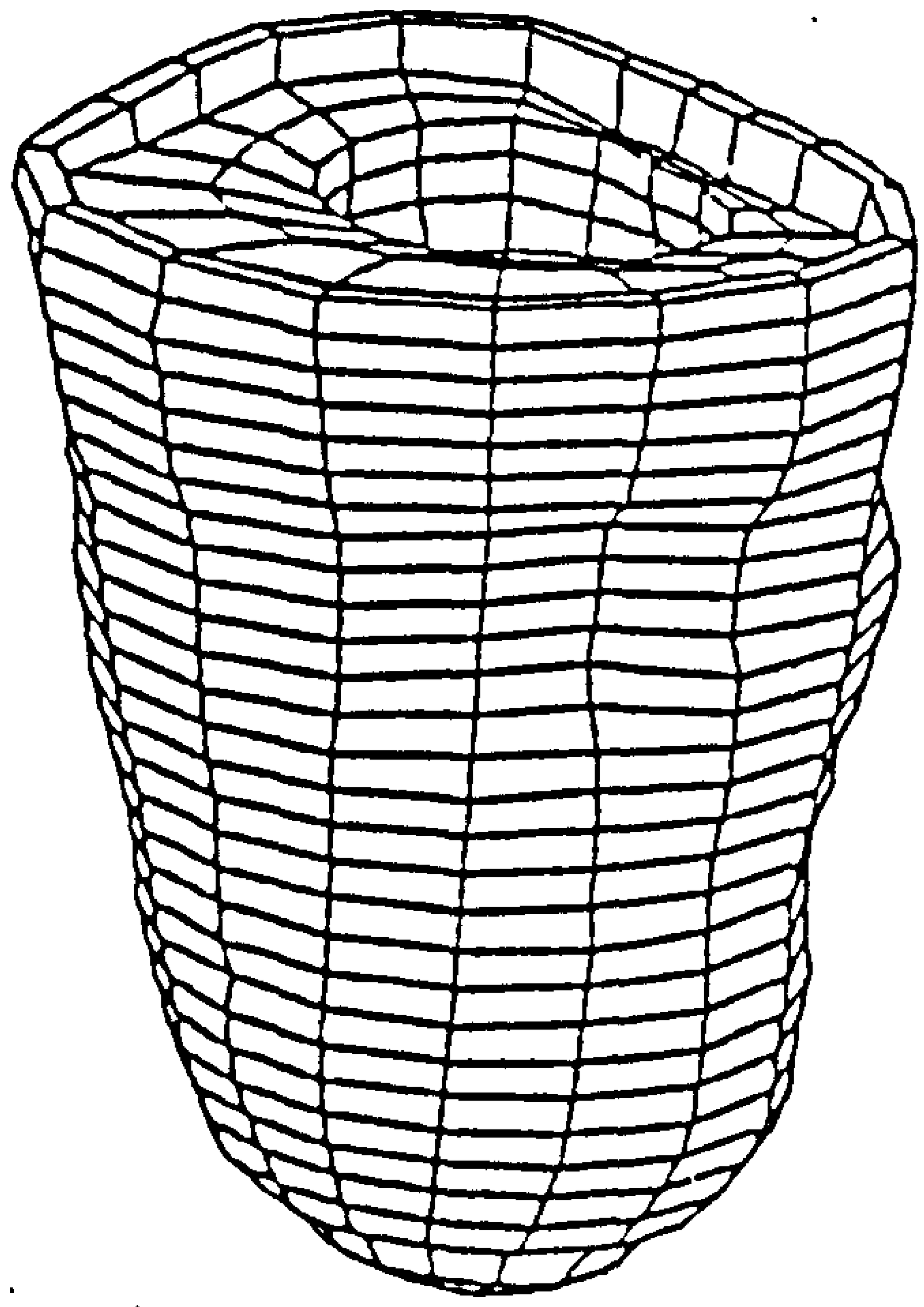

Fig. 3.4.3.3 FE model of the trans-tibial limb incorporating interface elements between the soft tissue and socket liner. (Zhang and Roberts, 1993)

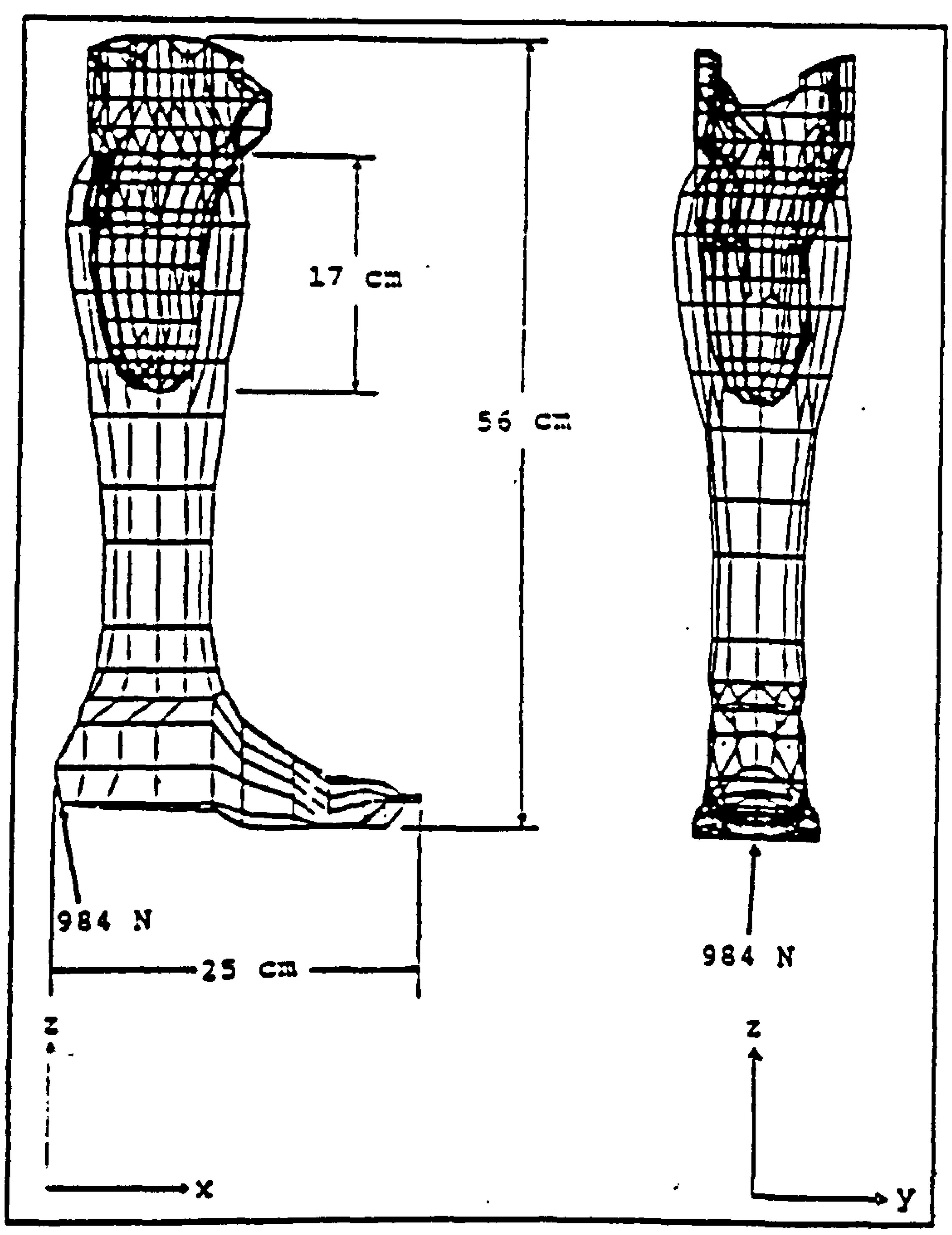

Fig. 3.4.3.4 FE model of trans-tibial PTB prosthesis and residual limb. (Quesada and Skinner, 1991)

Instead of modelling only the residual limb, Quesada and Skinner (1991) attempted modelling the complete trans-tibial PTB prosthesis (Fig. 3.4.3.4). The model with 636 nodes and 655 elements contained quadrilateral and triangular shell elements. The soft tissue components were modelled as a spring, with a linear spring constant at each node of the residual limb/socket interface. Applying a numerical optimisation routine, suitable spring constants were assigned . The geometrical detail of the socket was determined by digitising transverse slices of the socket mould, while the rest of the prosthesis geometry was directly measured. A load of 1.5 times the body weight was applied at the heel of the model to simulate heel strike. Various material properties and geometrical alterations were introduced to the model in order to investigate their effects on interface pressures. These changes included increasing the elastic modulus of the socket by 10 times, lengthening and shortening the residual limb/socket by 20 mm. The authors maintained that the results are specific to the FE model created, nonetheless, predicted interface pressures managed to fall within the range of most measurements in published literature. Several general observations were made pertaining to these alterations to the model. Interface pressures can be significantly reduced by a) decreasing the socket elastic modulus, b) using a suction socket and c) increasing residual limb/socket length.

FE modelling of the trans-femoral limb has been attempted by Krouskop et al (1987, 1989), Brennan and Childress (1991) and Torres-Moreno (1991). Krouskop et al (1987, 1989) described a CASD/CAM procedure that implements FE analysis to predict socket shape. Geometry of the residual limb was captured using a mechanical probe digitizer, whereas soft tissue material properties were ascertained by an ultrasonic Doppler system specially designed to allow *in vivo* measurements. The soft tissue properties were idealised as linear elastic, isotropic and homogeneous in the model. The bone (femur) was assumed to be rigid and its position determined through the use of an ultrasonic probe. However, the exact geometry of the bone was not included and simply assumed as cylindrical (Fig. 3.4.3.5). Residual limb/socket interface pressures of 12 subjects with well fitted quadrilateral sockets were recorded. Based on these measured pressures, a generalised pressure profile was defined. This

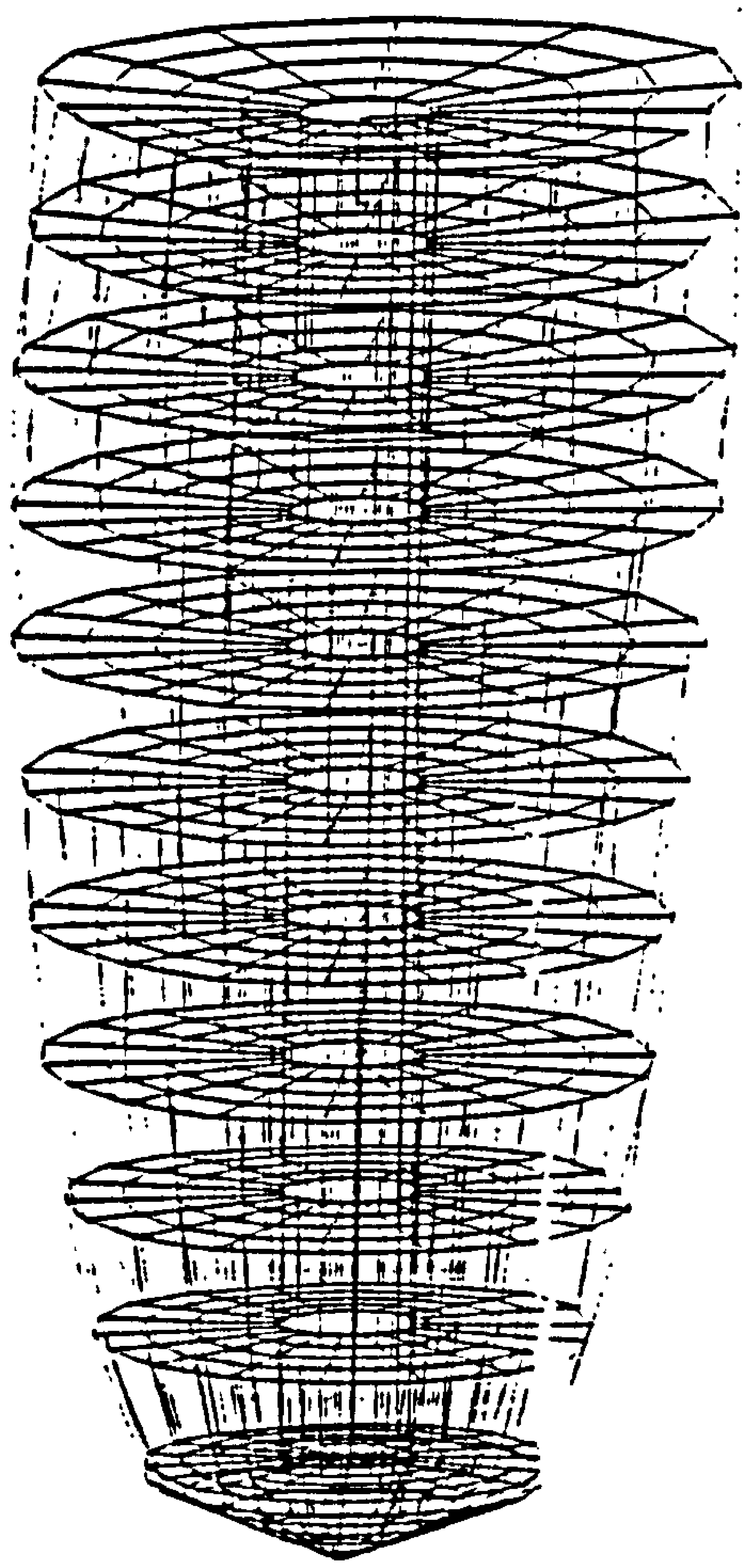

Fig. 3.4.3.5 FE model of the trans-femoral residual limb.
(Krouskop et al, 1987)

pressure profile served as the loading condition to the FE model created. Using ANSYS FE code, the FE model generated computes a suitable socket shape which was then manufactured with the aid of an NC carving machine. The authors claimed the process was successful with the two amputees tested. The sockets prescribed required no further modification after the CASD/CAM procedures and were described to be as good as the subjects' previous prostheses. The author of this thesis thought that in the study, the authors did not realise the advantage of numerical analysis, and instead opted for a subjective rather than quantitative evaluation of the sockets produced. The loading implemented in the model was based on a generalised interface pressure profile at the residual limb / socket. Applying pressure, the model will be expected to deform, predicting a socket shape. The shape of the predicted socket is difficult to verify experimentally, as in the case of Krouskop's et al investigations, the sockets could only be evaluated subjectively. Due to the uncertain behaviour of any initial FE model, the author of this thesis feels that the fitting of the two amputees were premature, since no model verification was attempted through experiment.

A comparative study involving the quad and two types of IC sockets, namely the partial and total ischial ramal containment sockets were discussed by Brennan and Childress using FE analysis. A FE model of an unloaded trans-femoral residual limb, i.e. without socket, was first created, which was deformed according to the different types of sockets evaluated by displacing the model's nodal positions. The model was first constructed by digitizing a plaster wrap cast of the undeformed limb. The positions of the femur and the pelvis were scaled linearly from existing CT scans to fit bony prominences marked on the wrap cast. The FE mesh consisted of 3845 nodes and 2672 eight-noded hexahedral solid elements. The loading conditions were approximated by half the subjects body weight, applied vertically over the proximal hip. Nodal displacements were then imposed on the model according to the type of socket. The nodal displacements were determined by first digitizing the socket and then taking the difference between the digitised data of the socket and the plaster wrap cast. The material properties of the model were assumed to be linear elastic,

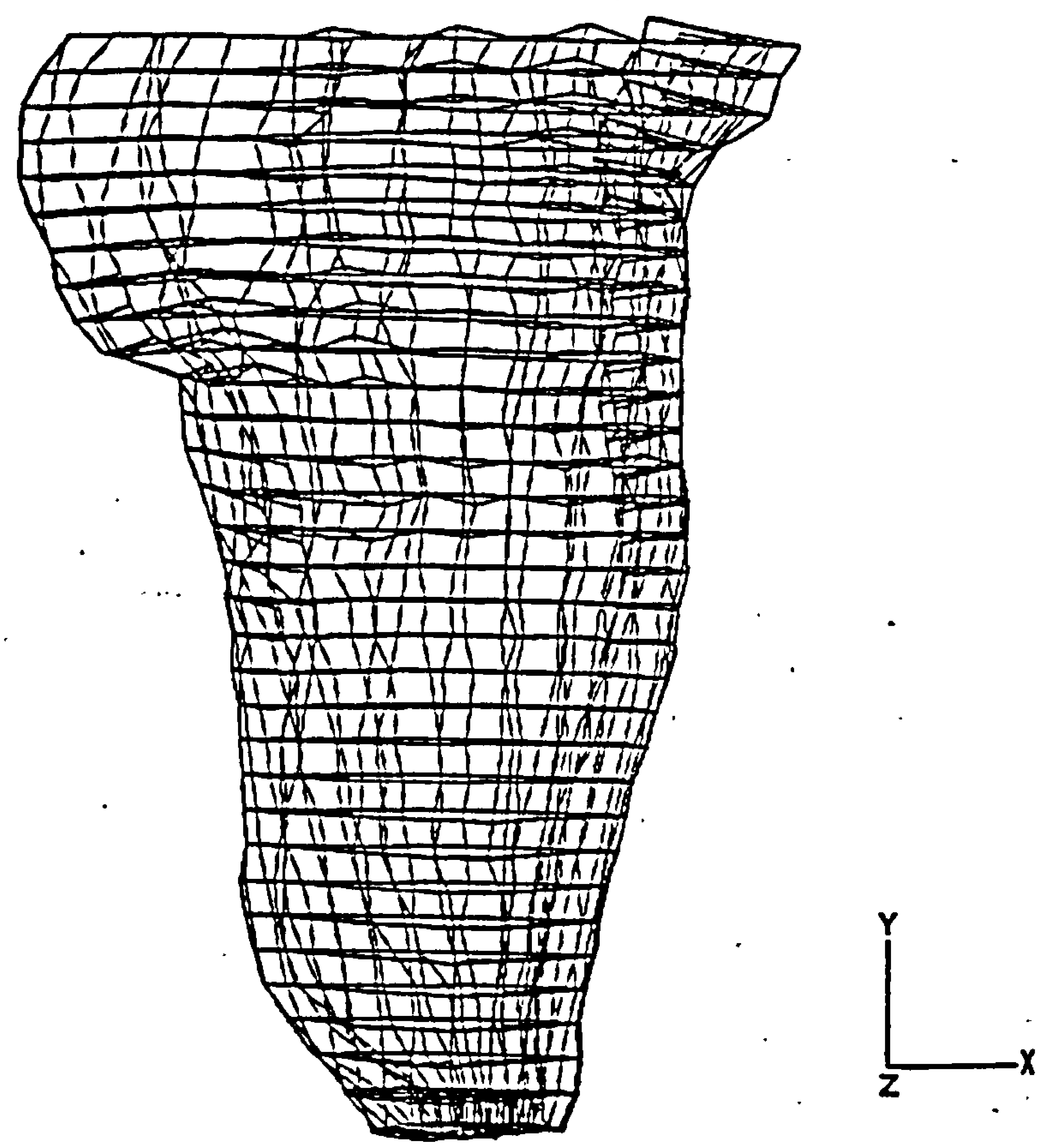

Fig. 3.4.3.6 Displacement results of a FE model of trans-femoral residual limb with the quad socket. (Torres-Moreno, 1991.)

homogeneous and isotropic (Bone : E=15.5 MPa, ν=0.28. Soft tissue : E=60 kPa, ν=0.49). The model was validated by interface pressure measurement at 7 sites around the residual limb using diaphragm type transducers, similar to those described by Steege et al (1988). The FE model predicted pressures at the Scarpa's triangle area and under the ischial tuberosity of the quad socket to be about 65 kPa and 130 kPa respectively. However, at the mid area of the quad socket, almost zero pressure was predicted. The partial and total IC socket predicted pressures at the mid area ranging from 40-120 kPa. The high pressures were predicted around the ischium with values ranging from 90-150 kPa. Experimentally measured pressures were much lower, with pressures around the ischium ranging from 25-40 kPa and pressures around the mid limb sites at about 20 kPa for all three types of socket. Nevertheless, the authors maintained that an agreeable trend exists when FE and experimental pressure profiles were compared, thus fulfilling the main aim of the study which was comparison of the different types of sockets quantitatively using FE analysis.

Torres-Moreno (1991) described the construction of a FE model (Fig. 3.4.3.6) of a trans-femoral amputee's residual limb with a quad socket. The geometry for the model was based on an undeformed limb, with details of both femur and the surrounding soft tissues captured by a whole body MRI imager. The FE model was then subjected to nodal displacements at the proximal end. These nodal displacements were according to the size and shape of the adjustable brim used to make the quad socket. Loadings were assigned to the model as normal pressures distributed over the entire surface of the residual limb, which were initially measured at 12 sites around the residual limb with a quad socket using resistance strain gauge type pressure transducers. A further vertical load was directed at the proximal end of the femur which approximates to half body weight. Twelve elastic moduli derived from mechanical indentation tests were chosen to describe the soft tissue properties of the residual limb at different locations (E=27 to 146 kPa and ν=0.49), while the femur was assigned a modulus of 17.6 MPa and Poisson ratio of 0.3. The model comprised 1962 nodes and 2628 3-D isoparametric solid elements consisting of both hexahedral and tetrahedral shaped elements. The model was validated by comparing predicted

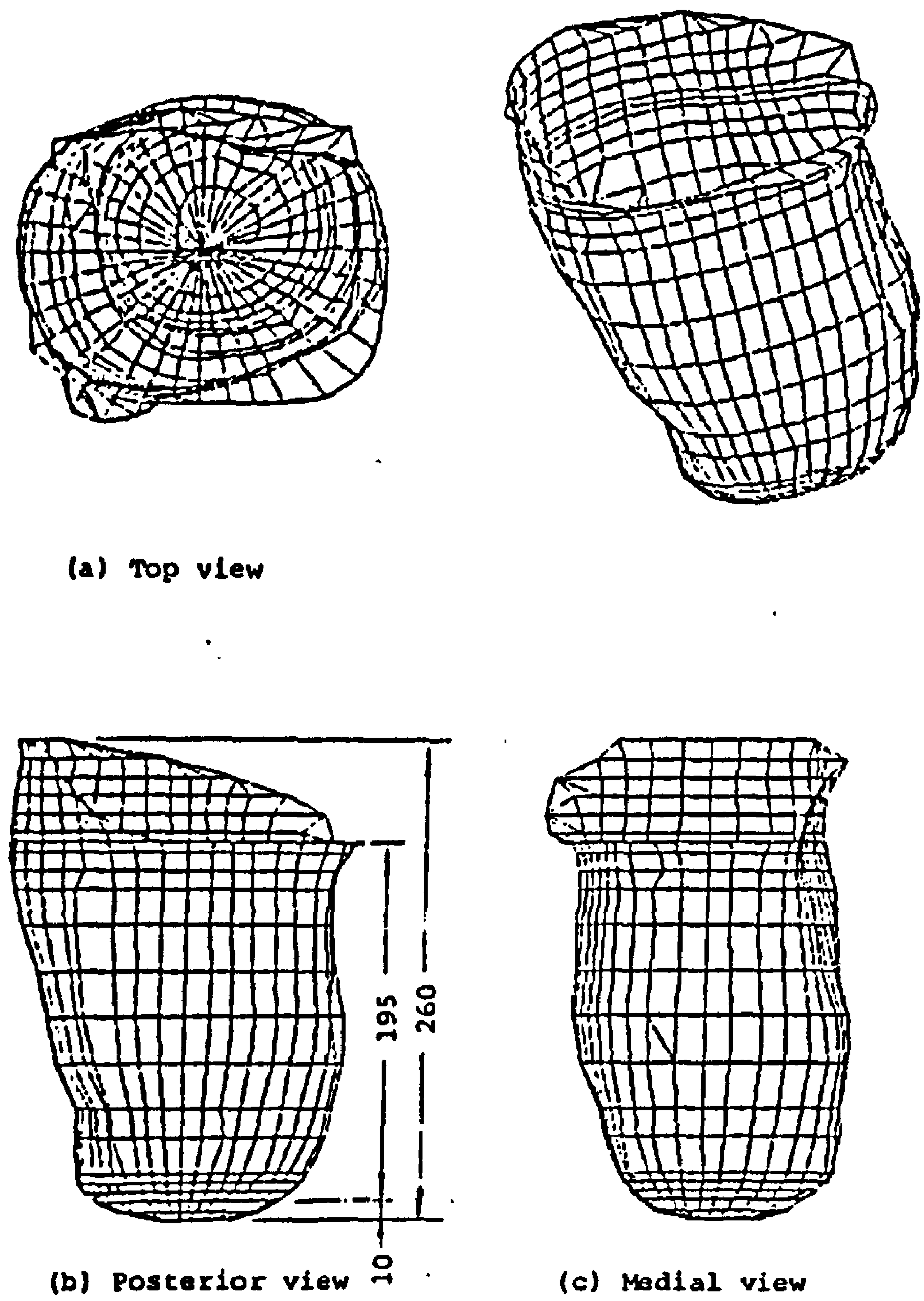

Fig. 3.4.3.7 FE model of the quad socket. (Seguchi et al, 1988)

and measured pressures. The results were reported to be encouraging with values closely matched. The shape of the final residual limb also follows that of the quadrilateral socket closely, though this was not validated through measurement procedures. However, the author was not prepared to comment on a 'one to one' correlation of the predicted and measured pressure, since the measured pressure was performed on a different subject to that which the model was based on. The subject who participated in the MRI scans on which the model was based on, did not continue for the rest of the investigation. The author of this thesis reckons that Torres-Moreno's model, like to that of Krouskop et al's (1988), should be validated by comparing the model's final shape with that of the physical socket. Interface pressures were input as part of the model's loading conditions, and to compare the same input pressure profiles with the output results of the FE model seems questionable. Whereas pressures measured at the residual limb/socket interface were input as loading conditions to the FE model, ideally the model should predict the shape of the socket where pressure measurements were initially made, thus model validation should be based on socket shape rather than interface pressures.

A different approach was proposed by Seguchi et al (1988) to predict residual limb/socket interface pressure. Instead of modelling the residual limb, a FE model of the prosthetic socket was created (Fig. 3.4.3.7). The quad socket geometry was first defined with an industrial CT scanner. Applying the ANSYS FE code, a model was generated with 683 nodes and 694 quadrilateral thin shell elements. The model was first validated by comparing calculated strain levels with strains recorded from 24 strain gauges instrumented on a quad socket. The walls of the socket was loaded with the aid of a mechanical spring actuator in the anterior posterior plane. The model was then treated as an optimisation problem in which a minimum energy is attained to produce an observed deformation. The interface pressure was therefore estimated by the load required to produce a known displacement in the model. The loading conditions applied were largely hypothetical, with case one having uniform contacting pressure on the inner surface of the entire socket and case two, weight was fully concentrated at the ischial seat.

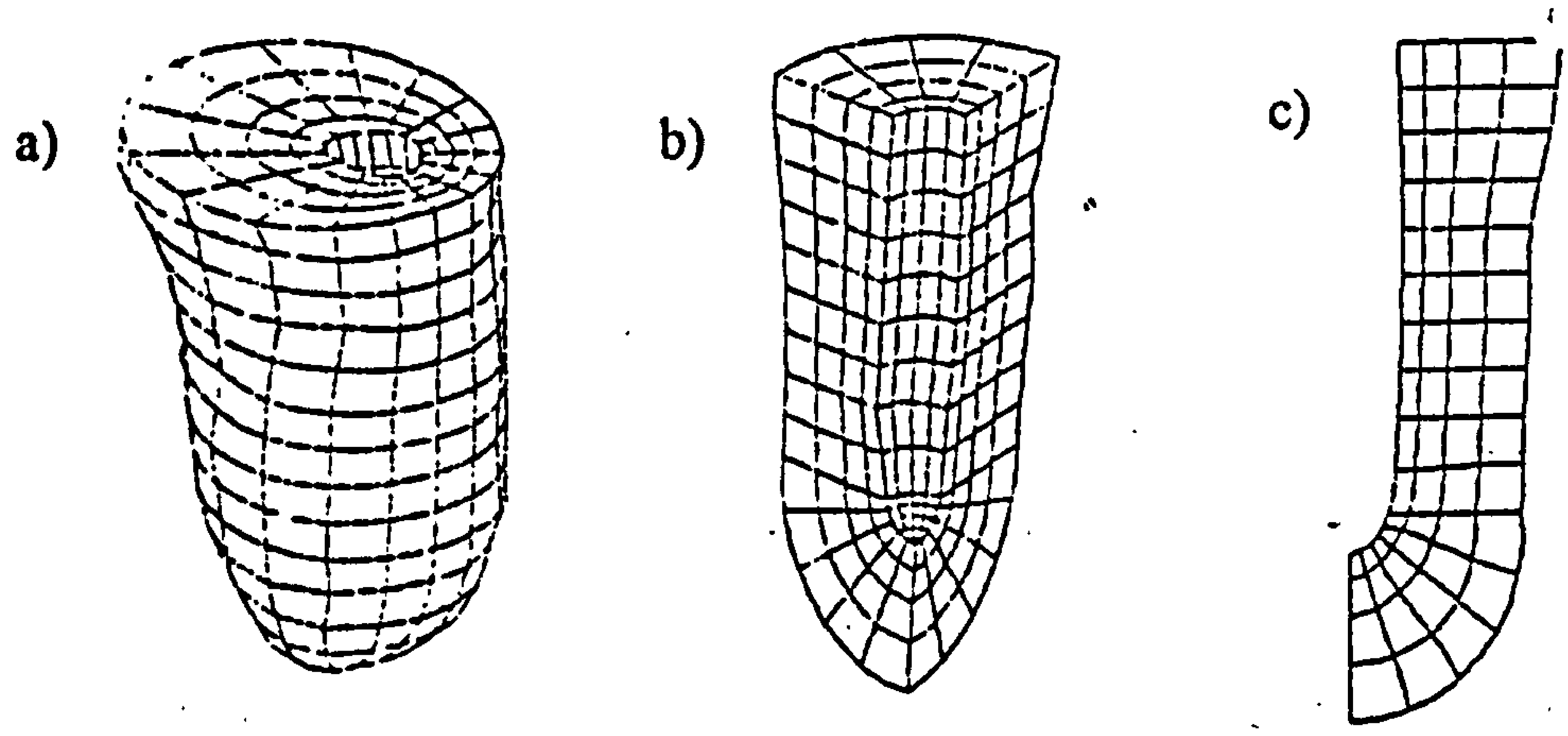

Fig. 3.4.3.8 Geometrical simplification in the FE model of a trans-femoral residual limb. a.) 3-D model, b.) elliptical model and c.) axisymmetric model. (Mak et al, 1992)

Mak et al (1992) investigated the possibility of simplifying the geometrical specification in an FE model of the residual limb. An initial 3-D model was created which was later simplified to an elliptical model and subsequently an axisymmetrical model (Fig. 3.4.3.8). Stresses calculated with the simplified models compare well with those of the 3-D model.

In summary, FE modelling techniques of the residual limb vary mainly in loading and boundary conditions. Geometrical details are still usually obtained through CT or MRI scans and the use of a digitizer, though methods of anthropometric scaling are evolving (Silver-Thorn and Childress 1992, Lee et al 1994). Material properties adopted are most likely linear elastic, isotropic and homogeneous for both soft tissue and bone. Some researchers recommended the use of hyperelastic material for soft tissue, but as discussed earlier, this material definition for such a purpose is highly questionable. Socket material has been modelled as a non-linear and anisotropic material by Soh et al (1990), but the 2-D model presented was highly simplified in terms of geometry which made it difficult to evaluate the need for material non-linear modelling. Socket liner material (Pelite) in trans-tibial sockets has been modelled using linear elastic or hyperelastic materials, or simply as an elastic foundation (Steege et al 1987). The types of finite element selected to represent the residual limb are usually 3-D isoparametric solid hexahedron elements, and quadrilateral shell elements are commonly used to describe the socket.

The main ongoing efforts in the above mentioned investigations are centred on validating FE models with experimental methods. Validation procedures usually takes the form of comparing predicted and measured pressure. It requires careful selection of a set of loading and boundary conditions to apply to the model, so that meaningful predictions can be correlated with experimentally measured values. The investigation of Steege et al (1988) and Sanders and Daly (1993) are the only two studies that include realistic load actions at the anatomical joints, with the former utilising a motion analysis system and the latter a pylon transducer for such data. Other investigators commonly assumed a vertical force equivalent to half body weight (to simulate standing) or full body weight (to simulate mid stance) at the proximal end of the femur. In addition to the loadings applied, boundary conditions had been prescribed in several fashions by different researchers. Steege et al (1990) and Sanders and Daly (1993) created the FE model of the residual limb in the deformed state i.e. with the prosthetic socket on. The FE analysis therefore begins at a zero stress level with the model already in the deformed state, which means the soft tissues were not considered to be in a pre-stressed situation, leading to under estimation. The tissues pre-stressed state has been addressed by Brennan and Childress (1991) and Zhang and Roberts (1993) by introducing nodal displacements on an undeformed model of the residual limb, so that the model finally takes on the shape of the socket. Soft tissue pre-stress values in the trans-femoral amputees have been measured by Redhead (1979) to be about 2.34 kPa. However, studying the results presented by Steege et al and Sanders and Daly, it was possible for the FE model to predict interface pressures with percentage errors of over estimation of 550%. Therefore, the author of this thesis believes that though the inclusion of soft tissue pre-stress may be important in this type of modelling, it certainly cannot be the vital assumption that affects the large percentage error that still exists in these type of studies.

Finite element modelling of the amputee's residual limb is still largely limited by the amount of available information required for the creation of the model. On the other hand, the studies presented in this chapter clearly show the possibility and the potential of such techniques. In addition, FE methods and computer technology are expected to advance rapidly thus the future FE model of the residual limb can only be expected to be more accurate.

CHAPTER FOUR
RESIDUAL LIMB / SOCKET INTERFACE PRESSURE MEASUREMENT

4.1 INTRODUCTION

The primary aim of this part of the study is to implement an experimental procedure that allows quantitative assessment of the biomechanical behaviour at the residual limb/socket interface. Pressures at the interface are measured for both the quad and the IC socket. This should lead to a better understanding of the way interface pressures are distributed with respect to the biomechanics of the two types of socket design. In addition, the measured pressures were essentially used to validate the FE models' results presented in the later part of the thesis.

Chapter 4 begins with a review of the past and current work in pressure measurement at the body/external support interface. This is followed by a complete documentation of the experimental procedures which includes patient selection, preparation of test equipment, measurement procedures and results.

4.2 LITERATURE REVIEW

Excessive pressure or pressure applied over a long period on superficial tissue can cause damage in the form of skin ulcers (pressure sores). The relationship between tolerable pressure and time of pressure application has been studied by Husain (1953), Kosiak (1961) and Dinsdale (1973), who had managed to induce skin ulceration to animals via an indentation system. Though pressures at the surface are often discussed as the main cause of pressure sores, studies (Daniel et al 1985, Nola and Vistnes 1980) also indicate that deeper tissue, like muscles is likely to undergo necrosis in less severe conditions than the superficial tissues. Tissues nearer to bony prominences are also likely to experience higher pressures than the superficial tissue when subjected to external forces, thus the mechanics of pressure sore formation has been believed to arise from the internal tissue to the external superficial tissues (Crenshaw and Vistnes 1989). However, despite the high pressure usually experienced in the trans-tibial or even the trans-femoral amputees at the residual limb/socket interface, the occurrence of pressure sores is rare. This may be attributed to the fact that skin and tissue can tolerate much higher cyclic pressure than constant pressures (Kosiak 1961). As in the case of an amputee, socket interface pressure can be intermittently relieved during the swing phase of the prosthetic limb. Also, an amputee is usually conscious of any severe discomfort on the residual limb caused by the prosthesis, thus possesses the ability to reject the prosthesis before there is any chance of a pressure sore developing. Pressure measurement in prosthetic sockets is therefore aimed at understanding socket design and the physiology of the residual limb (Appoldt and Bennett 1967) rather than preventing pressure sore occurrence.

4.2.1 Pressure transducers

Suitable transducers are limited due to the nature in which interface pressures are acquired in prosthetics. Ideally, the transducer must disturb the so called true interface pressure as little as possible. In establishing a perfect transducer, it should possess the following characteristics :

a) minimal size and low in weight

b) ability to measure pressure applied at a point

c) does not distort pressure distribution

d) flexible, with the ability to measure pressure in regions of small radius of curvature

e) capable of measuring both normal and shear stresses

f) maintain stability with changes in temperature and humidity

g) safe in contact with human skin and

h) low in cost.

In addition, most conventional pressure transducers base their principles on the deformation of a material to generate a pressure related change, therefore the characteristics of the deformable material i.e. linearity, hysteresis, creep and yield also influence the overall operating characteristic of the transducer.

Numerous types of commercial pressure transducers have been adopted or modified by researchers in the area of body/support interface pressure measurement, and the most common type are electrical transducers, whose measuring properties are based on changes in electrical resistance. Such transducers in their simplest forms appear as wire or foil strain gauges. However, silicon technology has provided the means to produce semiconductor strain gauges which are highly stable. They adopt a

a.)

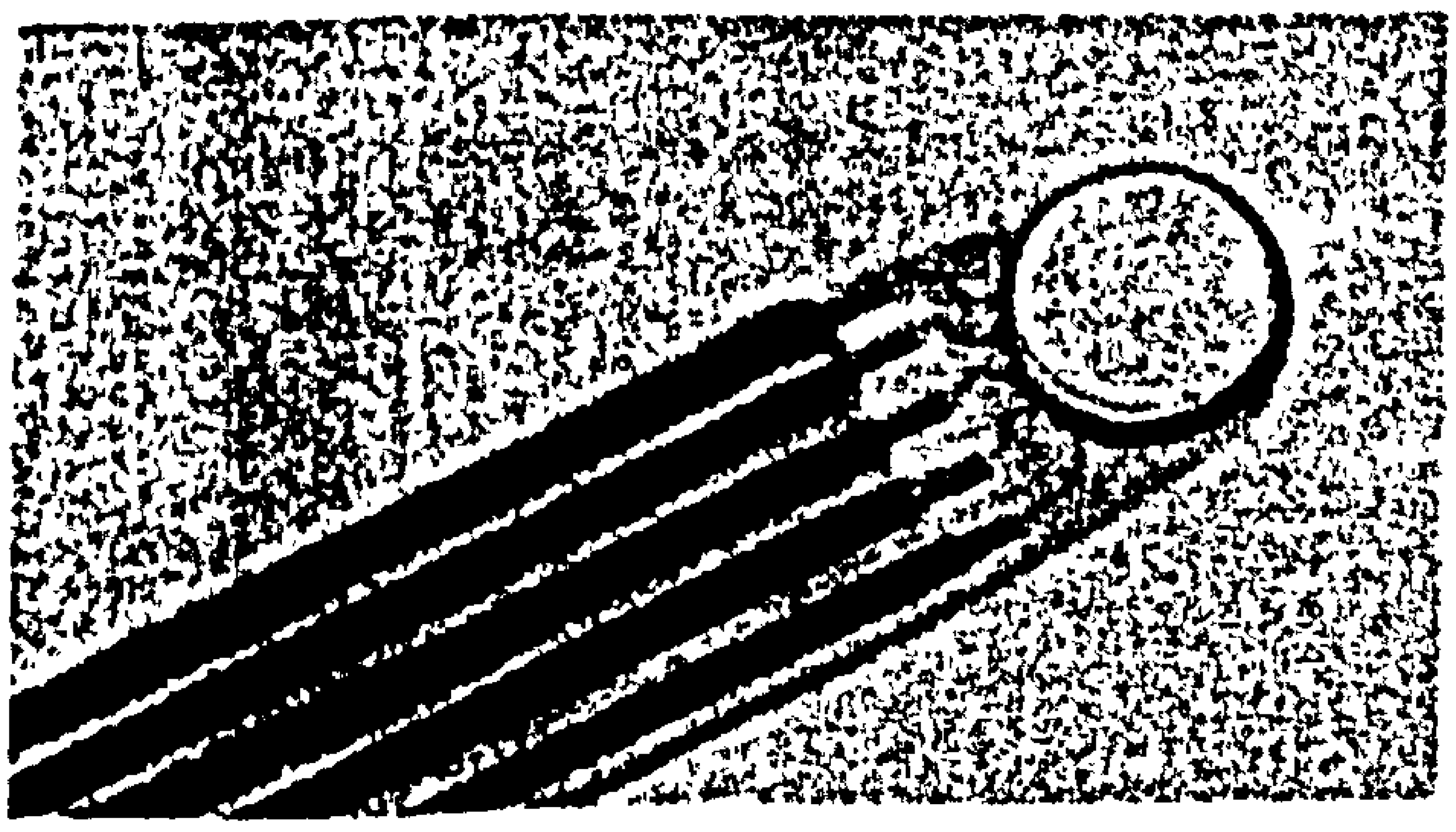

b.)

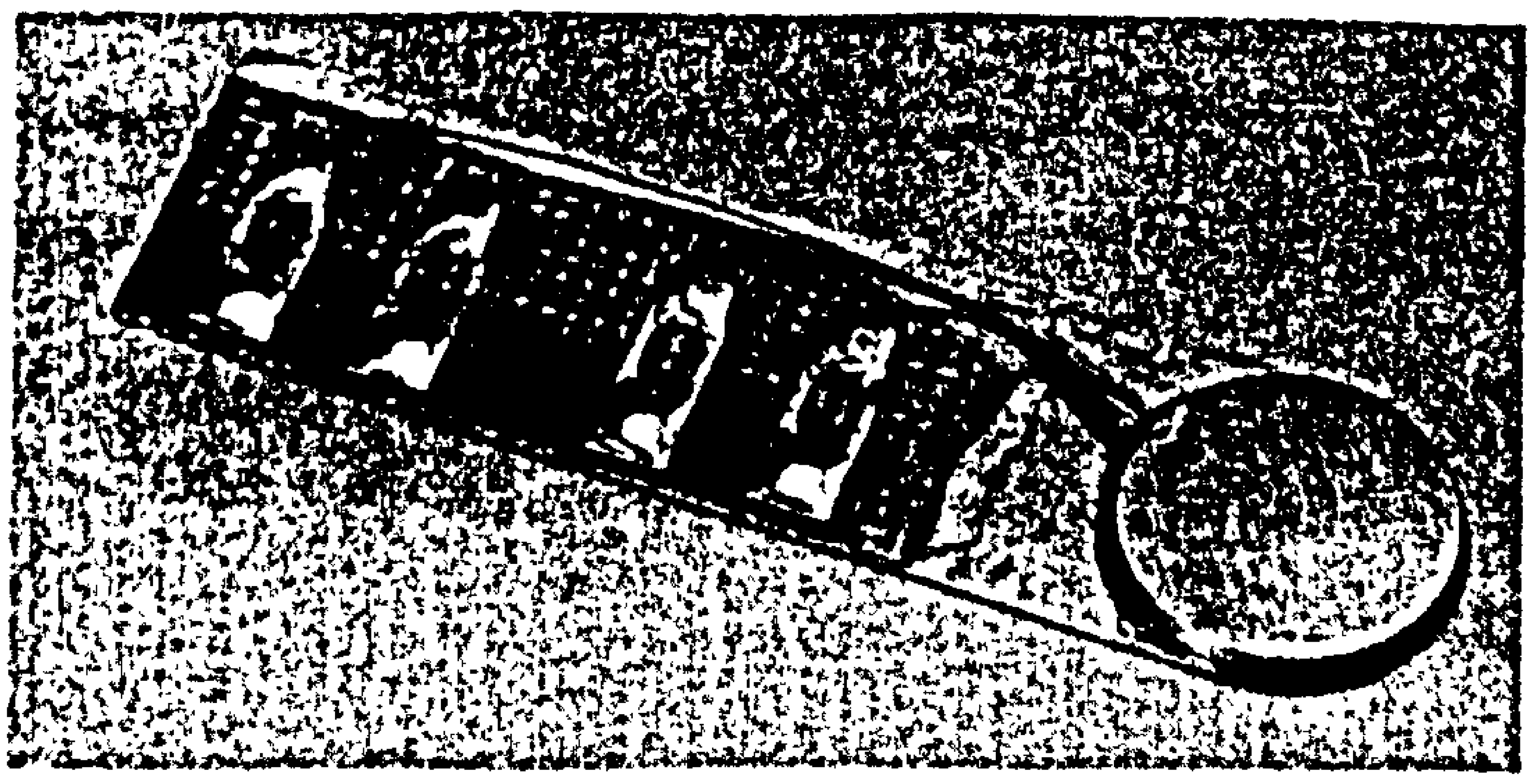

Specification	Kulite LPS-125-500	Scientific advances M-7F-100
Diameter	0.125 in.	0.250 in.
Thickness	0.030 in. max.	0.027 in. max.
Internal pressure	—(sealed)	—(sealed)
Pressure range	0–500 p.s.i.a.	0–100 p.s.i.a.
Natural frequency	350 KHz	—
Overpressure	100% F.S.	25% F.S.
Excitation	5 VDC or ACRMS	3 VDC or ACRMS
Impedance (nom.)	350 ohms	120 ohms
Zero balance	±3% F.S. max.	—
Sensitivity (nom.)	0.05 mv./v./p.s.i.	0.01 mv./v./p.s.i.
Temperature effect on zero	±0.02% F.S./°F.	±0.2% F.S./°F.
Temperature effect on sensitivity	±0.03% F.S./°F.	±0.08% F.S./°F.
Nonlinearity and hysteresis	±1.0% F.S.	±0.5% F.S.
Repeatability	±0.2% F.S.	±0.25% F.S.

Fig. 4.2.1.1 Miniature semiconductor gauges
a.) Kulite (LPS-125-500)
b.) Scientific Advances (M-7F-100)
(Rae and Cockrell, 1971)

silicon diaphragm which has elastic limit greater than steel and can be stressed repeatedly while retaining accuracy. These gauges are usually arranged in a Wheatstone Bridge configuration with four active arms for maximum sensitivity. The application of external load produces a bending stress on the diaphragm producing a piezoresistive effect, i.e. the variation of resistance with strain in strips of silicon. Hysteresis and creep are negligible in these types of transducers and non-linearity is significantly small. However, they are temperature dependent, hence compensation techniques like the four-arm Wheatstone Bridge are usually employed.

Appoldt and Bennett (1967) investigated two types of resistive gauges for trans-femoral residual limb/socket interface pressure measurement, the Micro-Systems (semiconductor gauge) and the NYU pressure transducer (foil gauge), both comprising four active strain gauges arranged as a Wheatstone Bridge. The transducers were flush mounted by drilling holes onto the socket. Results obtained with both type of gauges appear similar. Rae and Cockrell (1971) introduced miniature semiconductor gauges manufactured by Scientific Advances (M-7F-100) and Kulite (LPS-125-500) mounted between the socket inner wall and the trans-tibial residual limb (Fig.4.2.1.1). These transducers were reported as responding "reasonably well to the environment and that sizing was approximately correct", assuming that the authors meant negligible disturbances were introduced to the interface pressure distribution. The authors, however, raised questions about the applicability of the transducers to function in areas of extreme curvature, the condylar flare, medial and lateral plateaux of the tibia in the trans-tibial socket.

The effect of placing miniature transducers (Kulite LQ-125) as surface mounted (protrude) and flush mounted through a countersunk transducer seat was studied by Davis (1986). The transducers' responses were tested by applying known static load through foam/rubber mediums under the two different mounting conditions. Fig. 4.2.1.2 shows that the transducers' responses in both mounting conditions give similar loading profiles to the known load, except that a constant offset was evident in the case of the surface mounted. The author discusses that this offset exists as a protrusion pressure artifact and if carefully taken into account,

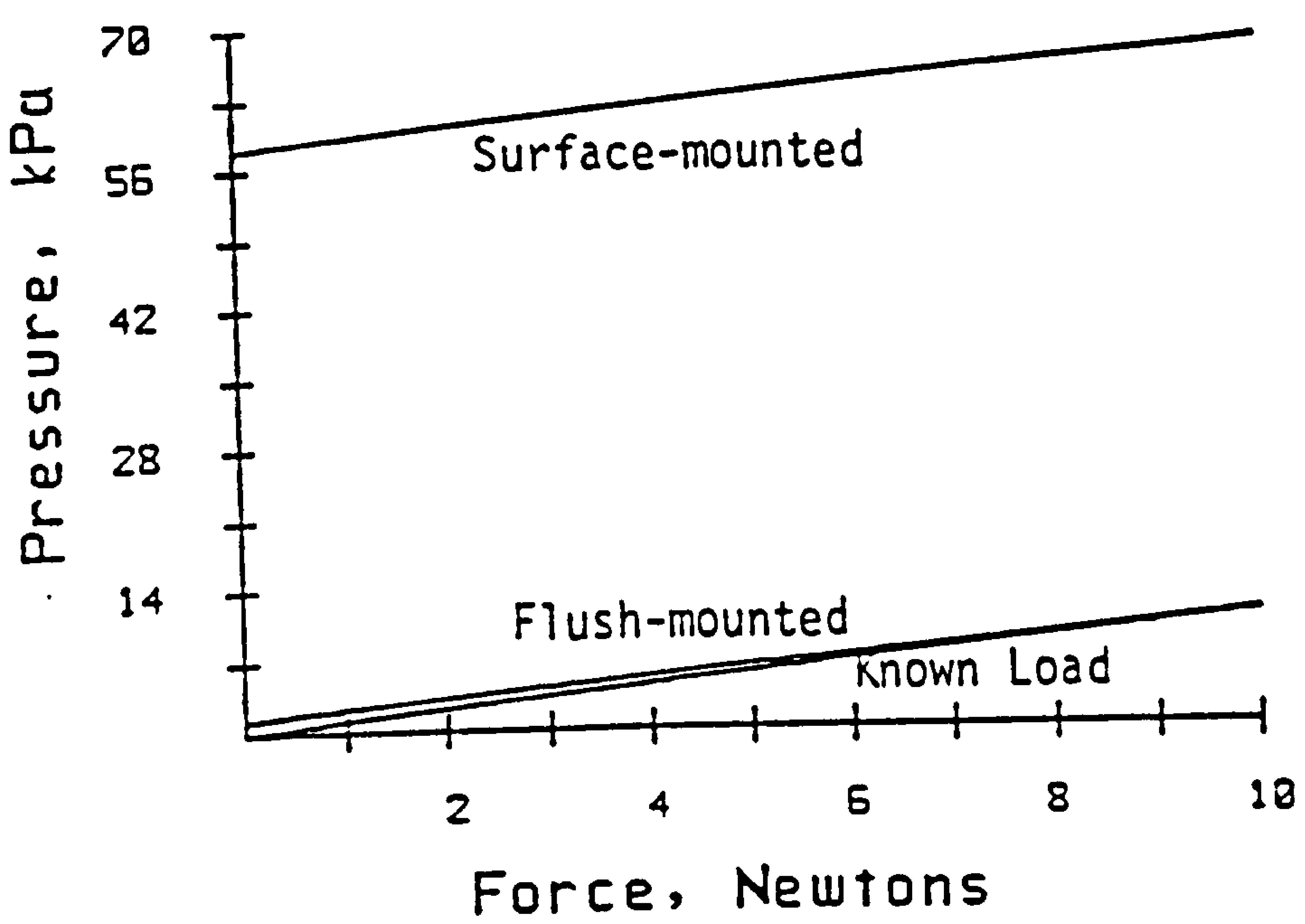

Fig. 4.2.1.2 A plot of static load evaluation of pressure monitoring capability of the transducer, one mounted so that sensing surface is flush with the surface and one mounted on the contact surface such that sensing surface protrudes into the interface space. Soft tissue model is a low density, flexible foam (2 mm thick) encased in a elastomer (2 mm thick). (Davies, 1986)

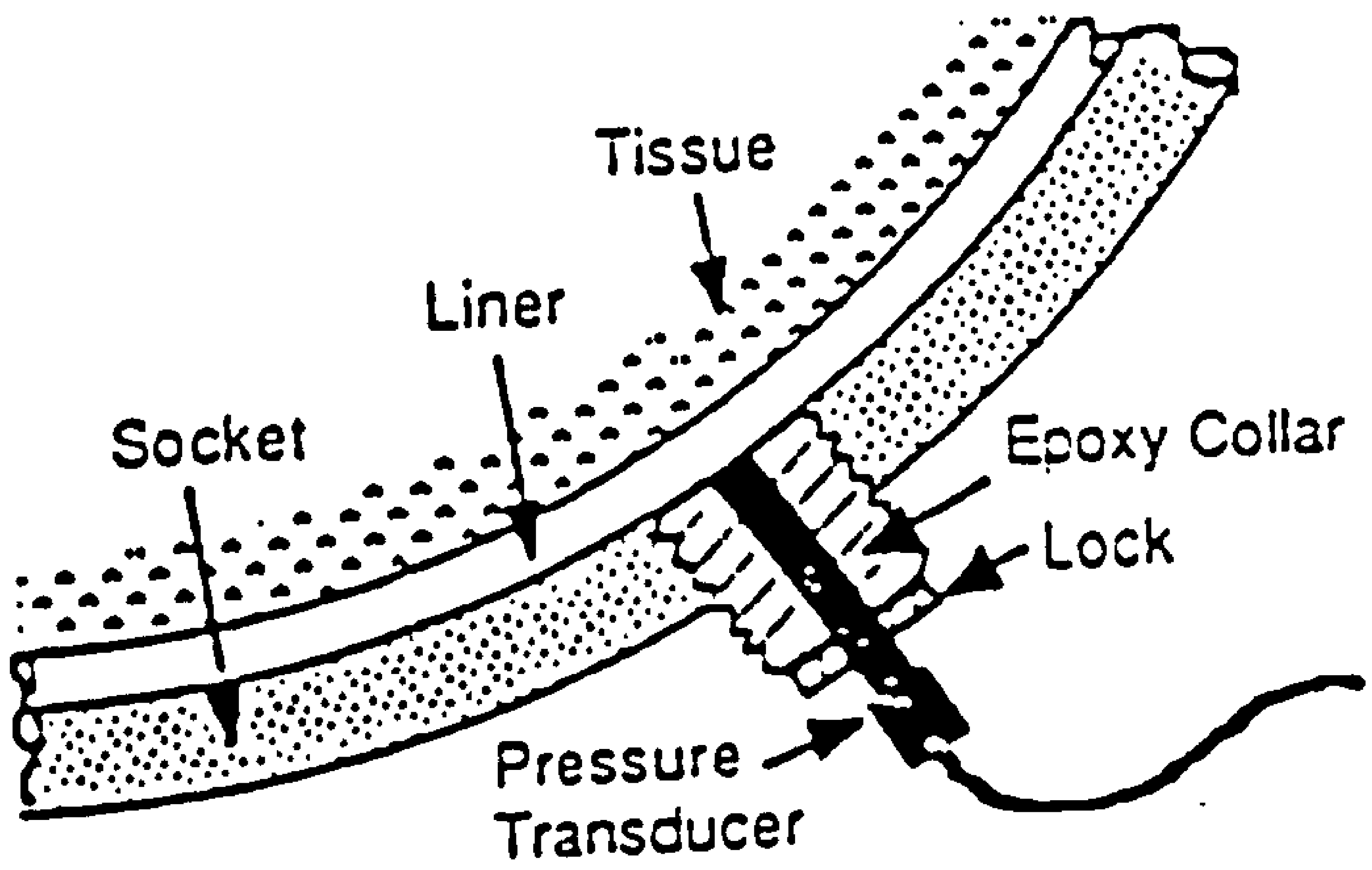

Fig. 4.2.1.3 Miniature transducers (Kulite XTM-190) in epoxy collar surface mounted in socket. (Steege et al, 1987)

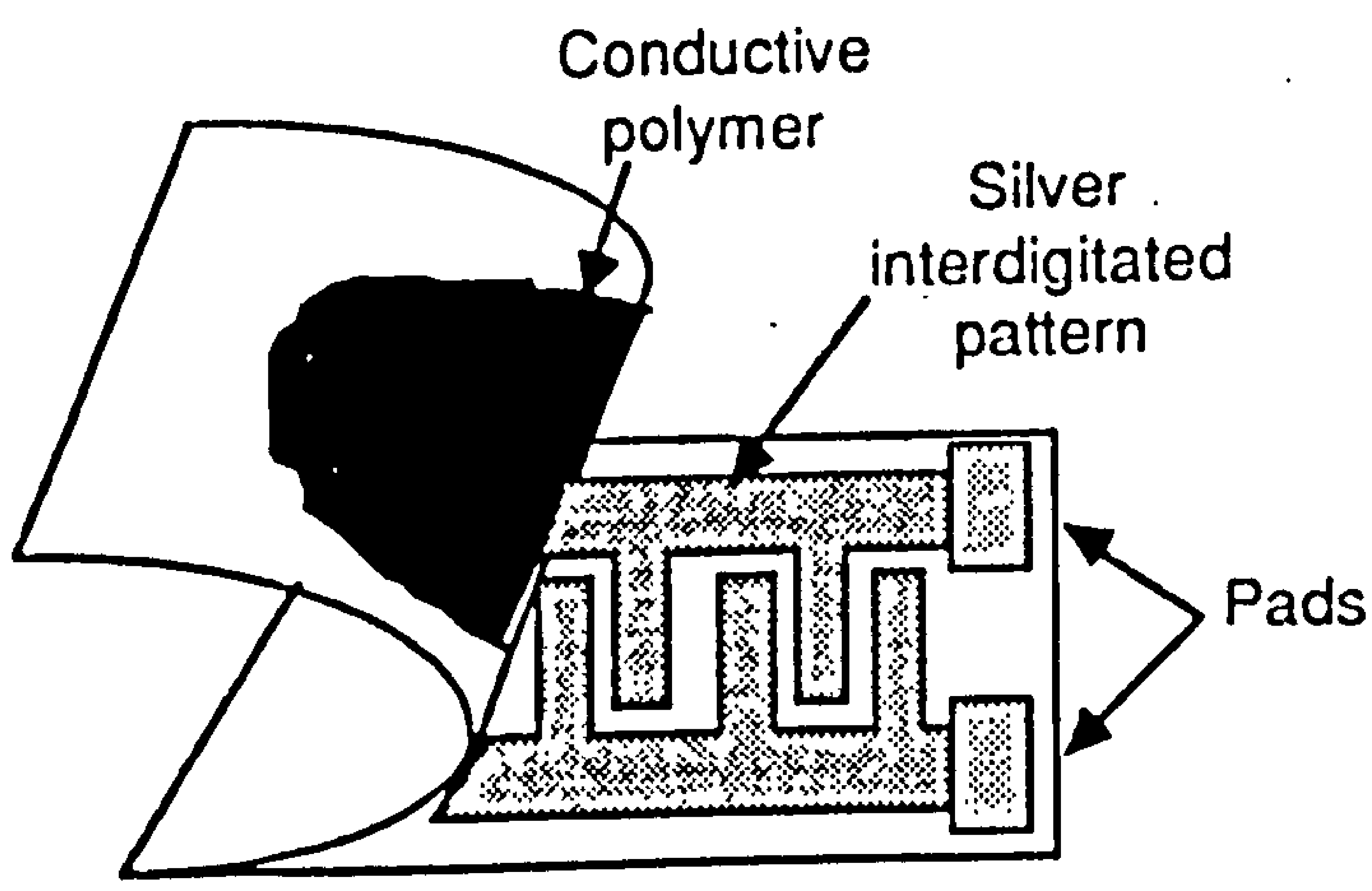

Fig. 4.2.1.4 Force sensing resistor (FSR) construction. (Olson, 1991)

provides similar accuracy to a flush mounted transducer. Further studies were then performed using surface mounted transducers for trans-femoral prosthetic limb measurement during stance. However, the author of this thesis reckons that it is difficult to determine the offset protrusion pressure accurately during gait. Unlike that of a membrane filled with gas, the residual limb is nonhomogeneous in nature, protrusion pressure will not remain constant with time. In addition, the amount of muscular contraction and internal bone movement in the residual limb differ during stance and during gait, which made determination of the protrusion pressure during gait almost impossible. Appoldt et al (1969) similarly studied the effect of a protruding transducer (1.6 mm protrusion) and concluded that overestimation of pressure frequently exceeded 1.5 times, and at areas near bony prominences, i.e. high tissue stiffness, about 4 times. Steege et al (1987) initially employed miniature transducers (Kulite XTM-190) surface mounted on trans-tibial prosthesis, but was unable to obtain consistent results. An epoxy mounting (Fig. 4.2.1.3) was further introduced to ensure that the transducer's face was flushed with the inner socket wall to ensure proper use of the gauge. However, Burgess and Moore (1977) discussed the possibility of surface mounting Kulite LQ-125 transducer in the evaluation of swing phase interface pressure on trans-tibial prostheses. The authors predicted that the low pressure experienced during swing phase, hence negligible protrusion pressure, justified the use of surface mounted transducer.

Conductive polymer pressure transducers, commonly known as force sensing resistor (FSR) also rely on electrical resistance to indicate pressure. FSR is basically an assembly of two sheets of polymer, usually with the top sheet coated with an elastomer containing carbon or metal powder while the lower sheet has a silk screened pattern of interdigitated silver conductors (Fig. 4.2.1.4). The application of force on the FSR causes an increase in contact area resulting in a decrease in electrical resistance. The attractiveness of these types of transducers are their extreme thinness (250-400 μm) and flexibility. Nevertheless, some researchers who have evaluated such transducers found them unsuitable for accurate determination of interface pressure (Steege et al 1987). The repeatability of the transducer is highly dependent upon the geometry of the transducer when a load is applied. The transducer's

Fig. 4.2.1.5 Rincoe socket fitting system. (DAW Industries textbook)

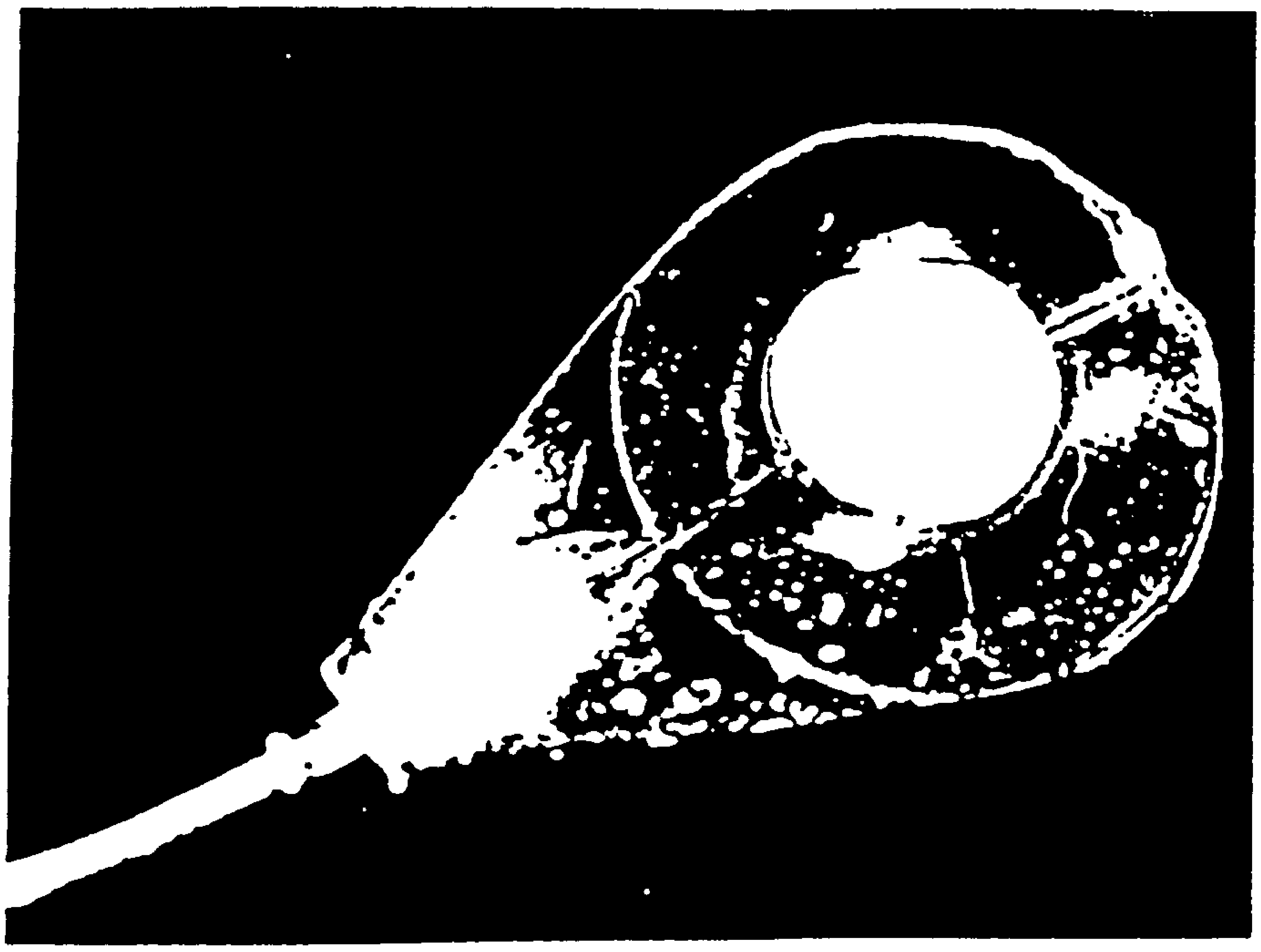

Fig. 4.2.1.6 PVC transducer bag. (Van Pijkeren et al, 1980)

response curve becomes unpredictable if it is allowed to flex during measurement. These transducers also exhibit non-linearity, hysteresis and creep, thus requiring tedious calibration procedures. Due to creep, long term pressure measurement becomes unreliable. Upon static load, the resistance of the transducer could decrease with time. These transducers have been popular in the measurement of pressure under the foot (Maalej et al 1987, Zhu et al 1990), since minimal modification is required to shoes and insoles. Similarly, one such system known as Rincoe Socket Fitting System (formerly DAW CPA) (Fig. 4.2.1.5) which utilises six long polymer strips containing 10 Interlink FSR is available commercially to obtain interface pressures for both trans-tibial and trans-femoral prostheses. The present system only captures interface pressure during standing and at heel strike, mid-stance and toe off with the aid of foot switches. The Strathclyde Bioengineering Unit has acquired one such system, and preliminary trials show the need to overcome non-linearity, hysteresis and creep before accurate interface pressure could be determined. However, the system has proved to be a valuable and simple indicative tool.

Pressure transducers which require a fluid medium have been used for measuring pressure at body/support interfaces. The fluids commonly chosen are oil based liquids (hydraulic) and air (pneumatic). The transducer construction takes the form of a bag (PVC, urethane film) filled with fluid. The bag is then connected to an external pressure transducer through a fluid filled tube. The application of force on the bag will cause an increase in fluid pressure which will be sensed by the external transducer. Van Pijkeren et al (1980) described the use and manufacture of a hydraulic pressure transducer. The transducer bag is made by heat sealing two disks of PVC, 0.25mm thick and 30 mm in diameter, which is further filled with silicone oil (Fig. 4.2.1.6) . An oil filled tube then connects the bag to a National Semiconductor pressure transducer LX 1600. No mention was made of the exact type of this external transducer. The total thickness of the fluid filled bag is approximately 0.6mm. The flexibility of the bag was reported as sufficient to meet both flat and convex or concave surfaces in prosthetic sockets (Fig. 4.2.1.7).

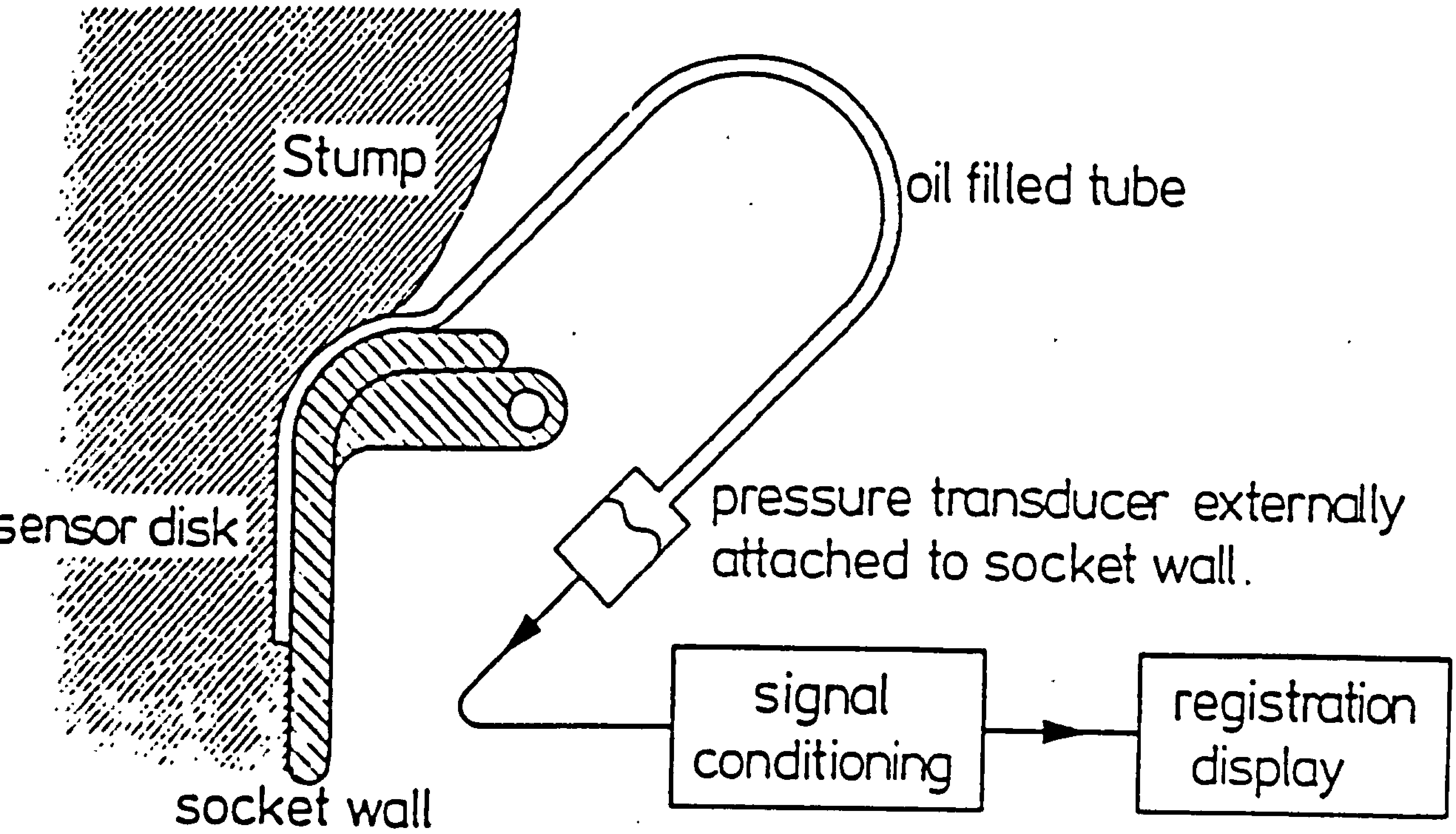

Fig. 4.2.1.7 Pressure measurement set-up utilising oil filled PVC transducer bag, which was suitable for both concave and convex surfaces. (Van Pijkeren et al, 1980)

The flexibility provided by this type of transducer also made it possible to measure pressure beneath bandages. Barbenel and Sockalingham (1990) reported such usage with transducer bags filled with oil connected to an electro-hydraulic piezoresistive pressure transducer. One of the main difficulties experienced with oil filled bag transducers is that extreme care is required to fill the bags with oil so as to exclude any air enclosure (Van Pijkeren et al 1980). The common material used for the manufacture of the transducer bag, urethane, also has the tendency to harden after prolonged contact with oil, thus producing inaccuracy if interpretation is based on initial transducer calibration.

The use of air instead of oil is less harmful to the bag transducer. However, it will introduce a response delay to the overall system due to air being compressible. One such system regularly used in measurement of seating pressure is the Oxford Pressure Monitor (Talley Medical Equipment, UK). It is made up of an array of 12 pneumatic cells 20mm in diameter covering an area of 9000 mm^2. Another form of air cell incorporates electrical contacts on the inside surface of the air bag. As air is released from the bag, electrical contact is established indicating that the pressure applied on the bag is similar to that on the inside. Both pneumatic and hydraulic transducers exhibit low frequency responses which make them suitable only for quasi-static loading conditions. Its sensitivity to load as compared with other types of transducers is lower due to the larger area involved in the fluid filled bags.

4.2.2 Pressure measurement at the trans-tibial residual limb / socket interface

An investigation on the interface pressure between the trans-tibial residual limb and the patellar-tendon-bearing prosthesis was presented by Pearson et al (1973). Measurement of interface pressure at critical areas (patellar tendon, distal anterior tibial, lateral tibial condyle and medial tibial condyle) of the unilateral amputee's residual limb was attempted under different standing conditions and altered prosthetic alignment. A total of ten amputee subjects participated in the studies. Kulite semiconductor pressure transducers measuring 3.18 mm in diameter and 0.76 mm in thickness were used. These transducers were inserted between the prosthetic socket

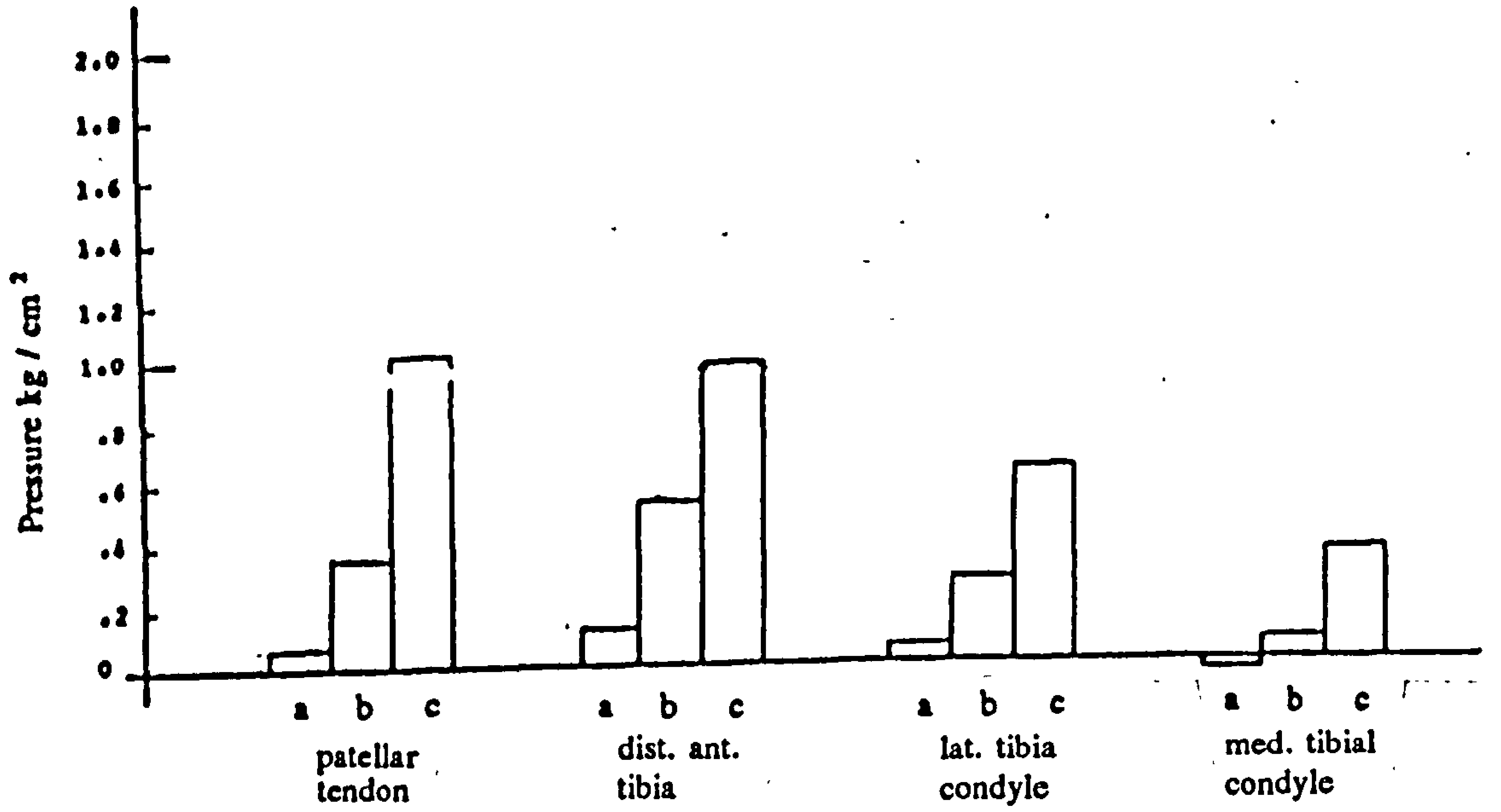

Fig. 4.2.2.1 Average values of the pressures in the critical regions for three modes of support in postural stance, i.e. a.) prosthesis suspended, b.) double support with weight on both feet c.) and prosthesis support only. Residual limb muscles are relaxed. (Pearson et al, 1973)
Note : 0.1 kg / cm² = 9.81 kPa.

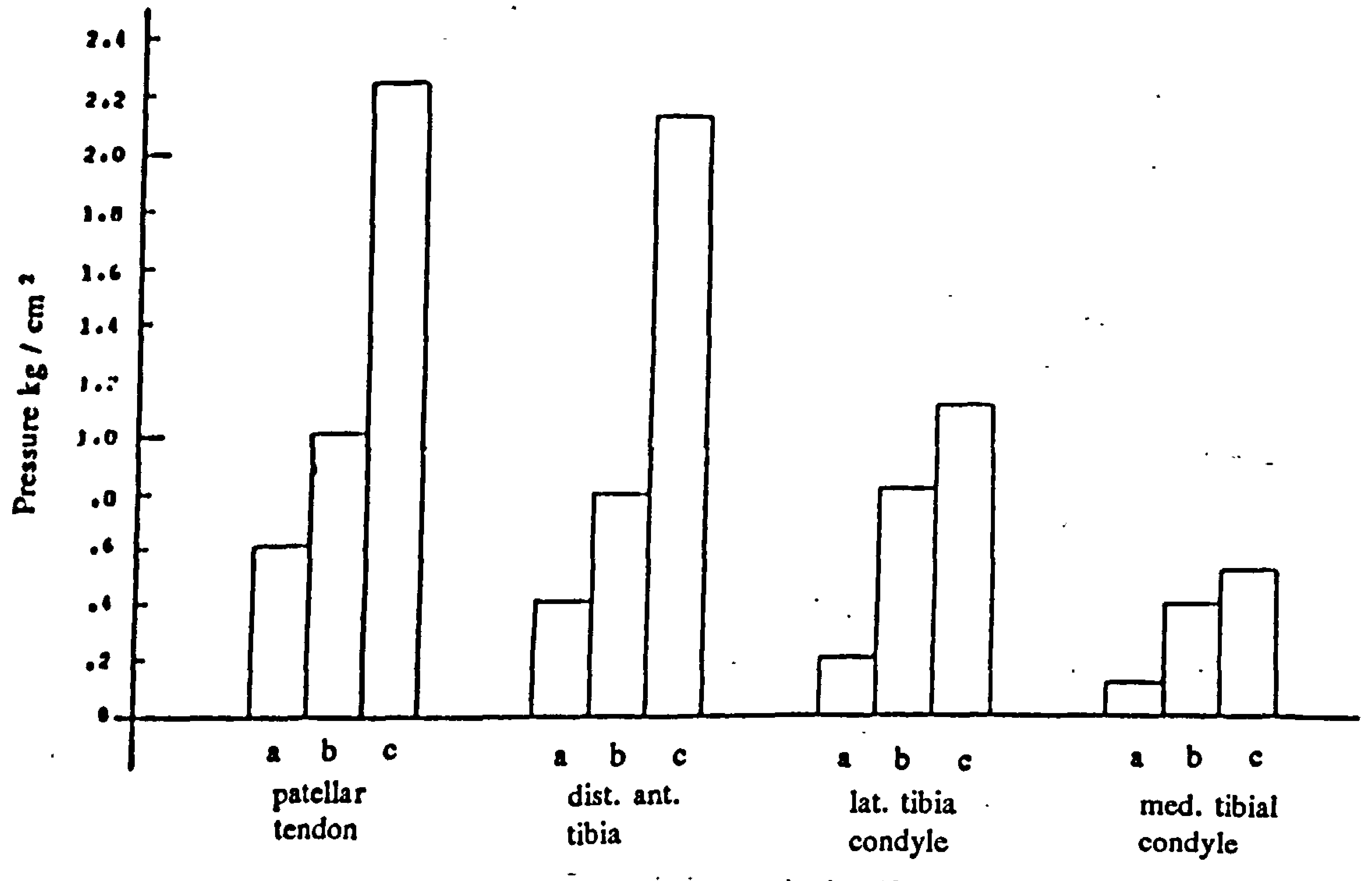

Fig. 4.2.2.2 Average values of the pressures in the critical regions for three modes of support in postural stance, i.e. a.) prosthesis suspended, b.) double support with weight on both feet c.) and prosthesis support only. Residual limb muscles are tensed. (Pearson et al, 1973)
Note : 0.1 kg / cm² = 9.81 kPa.

and the residual limb. Foot switches were also placed at the prosthetic feet, and goniometers were specially fabricated for the prosthetic limb at the hip and the knee.

Interesting results were presented by Pearson's team. Fig. 4.2.2.1 and Fig. 4.2.2.2 display the interface pressures at the critical areas of the residual limb examined for three modes of static support. These were prosthesis suspended, double support and prosthesis support only, under the conditions of relaxed and tensed residual limb musculature. Peak pressure was recorded at the patellar tendon area. However, pressure at the distal anterior tibial region was notably high, since the amount of soft tissues tends to be less. In the process of tensing the residual limb muscles (Fig. 4.2.2.2), a significant increase in pressure, as much as a 100% was seen for all three static conditions. Comparisons were also made between the maximum dynamic pressure occurring during heel strike with two previously mentioned static conditions, namely double support and prosthetic support only with tensed musculature (Fig. 4.2.2.3). The authors concluded from the comparison that the recorded dynamic pressure includes muscle contraction effects plus inertia and leverage effects due to the prosthetic limb configuration. Extreme changes in prosthetic alignment were also implemented to show the effect on the phasing or time relationship of the interface pressures. Peak pressure in such cases remained aprroximately similar in magnitude but occurred later and earlier for maximum altered posterior and anterior alignment respectively (Fig. 4.2.2.4 and Fig 4.2.2.5).

Pearson et al suggested from the study that the pressure measured for prosthesis support only with tensed residual limb muscle could be effectively used as an indication of the maximum dynamic pressure expected during normal gait. The authors further concluded that interface pressures when used as a criterion of judgment of the quality of fit and alignment depends upon a definition of tolerance level. However, pressure experienced by amputees is unlikely to cause pain immediately, thus suggesting that tolerance levels will eventually be defined in terms of the cumulative effect upon a localized region.

The use of a Kulite semiconductor pressure transducer similar to Pearson et al (1973) has been attempted before by Rae and Cockrell (1971). Instead of using a

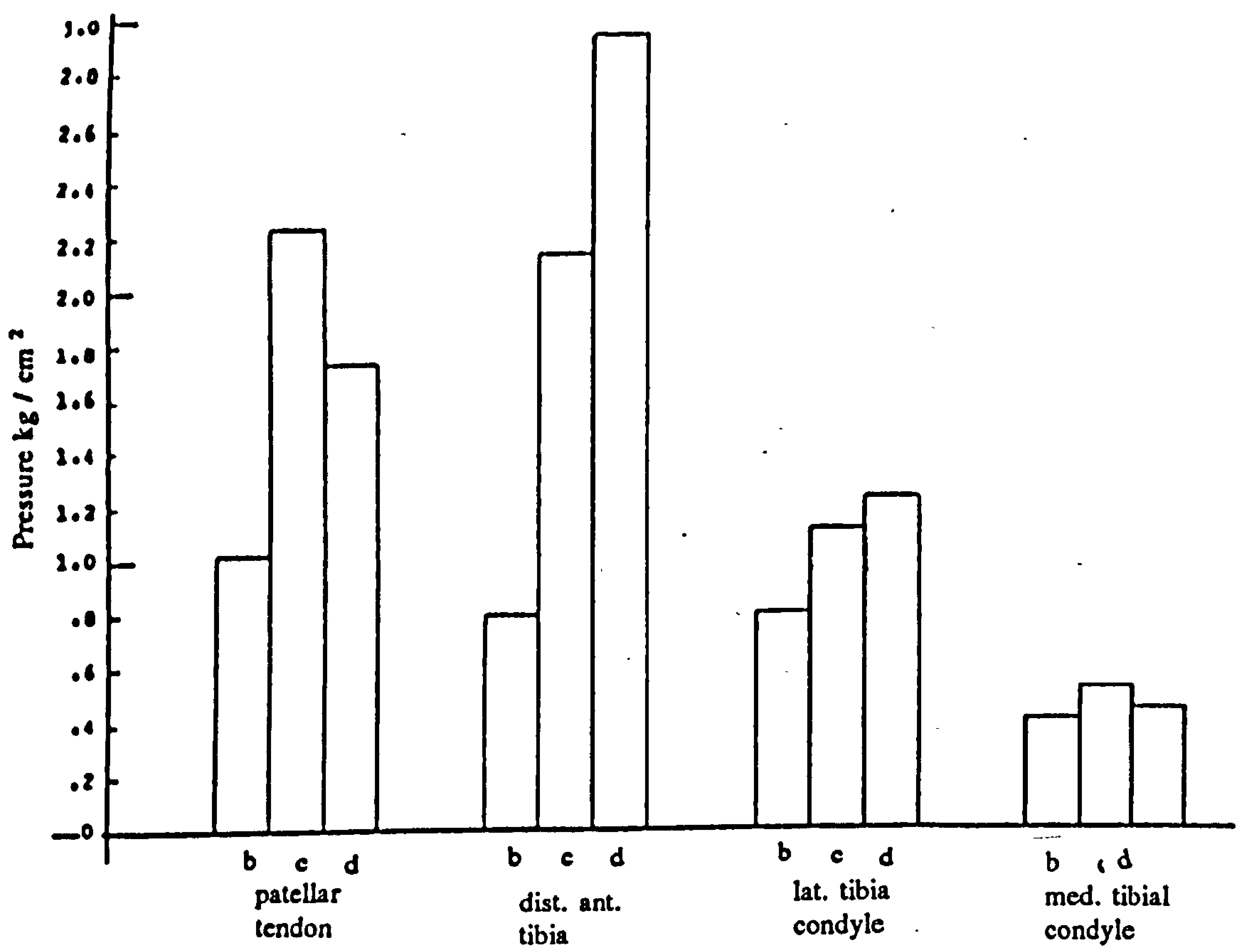

Fig. 4.2.2.3 Average values of pressures with tensed residual limb muscles in postural stance. b.) Double support, c.) prosthesis support only and d.) maximum dynamic pressure occurring at heel contact. (Pearson et al, 1973)
Note : 0.1 kg / cm^2 = 9.81 kPa.

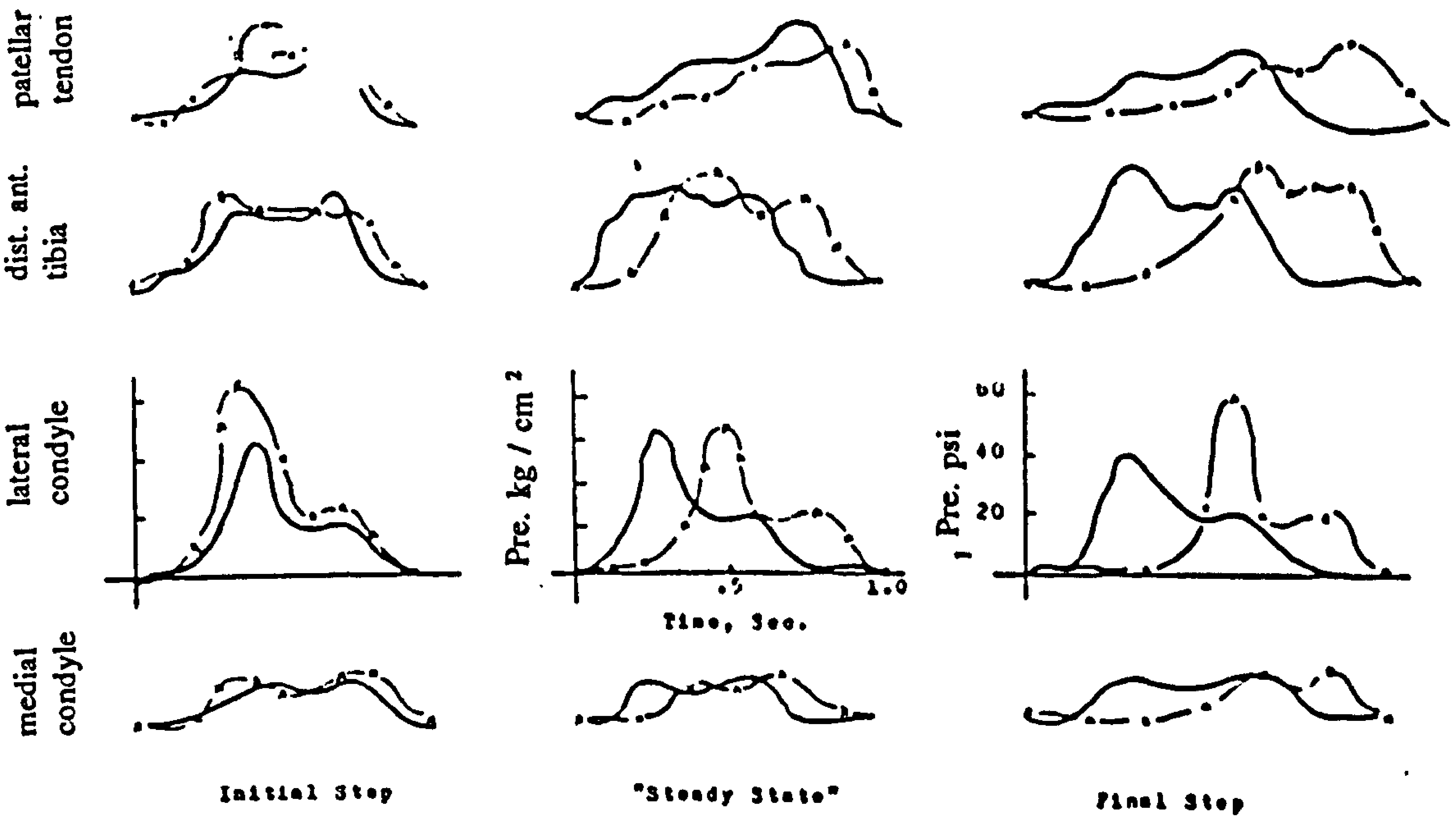

Fig. 4.2.2.4 Comparison of interface pressure at the critical regions for neutral (---) and maximum posterior (--x--x--) alignment offset.
(Pearson et al, 1973)
Note : 0.1 kg / cm^2 = 9.81 kPa and 1 psi - 6.895 kpa.

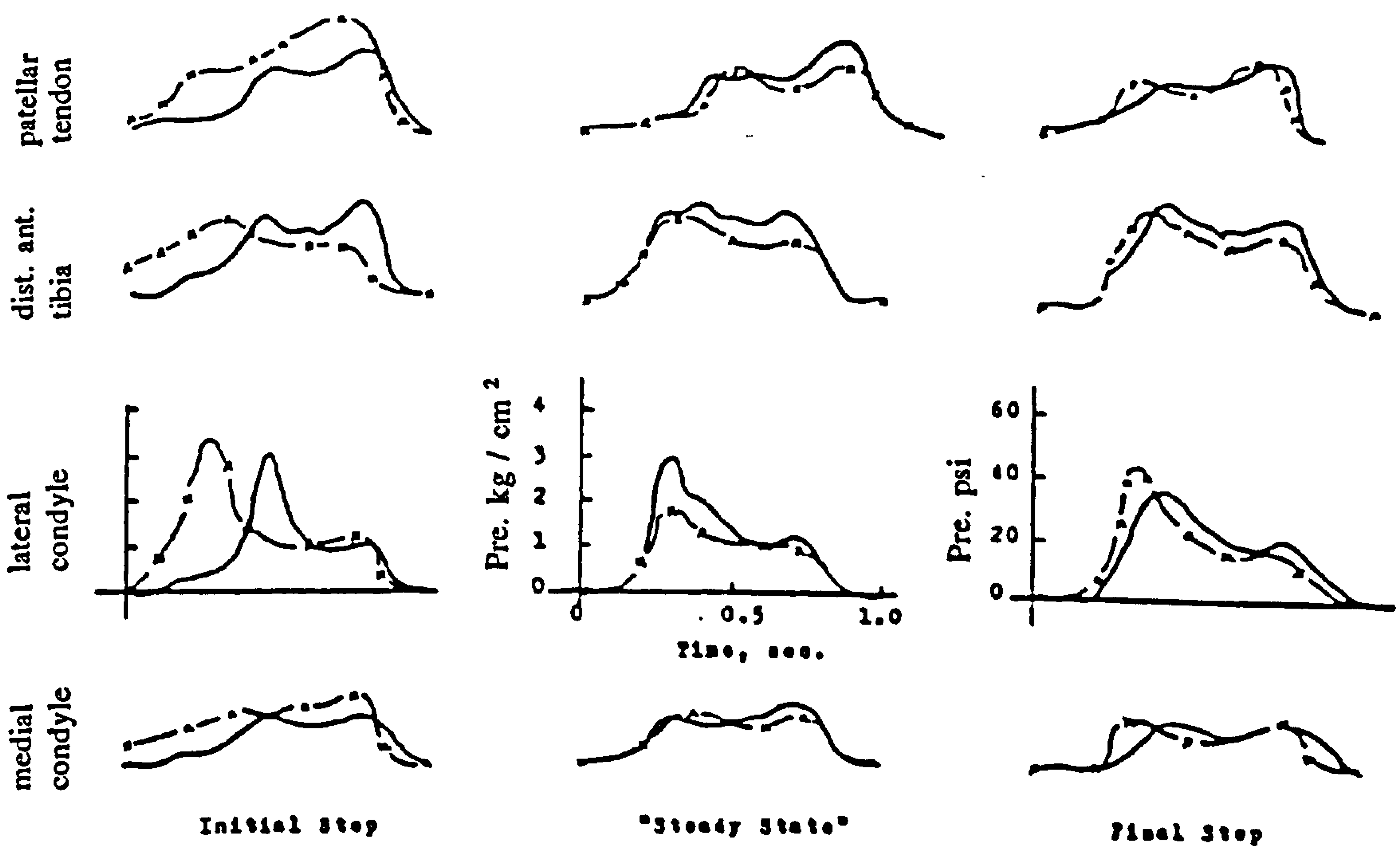

Fig. 4.2.2.5 Comparison of interface pressure at the critical regions for neutral (---) and maximum anterior (--x--x--) alignment offset.
(Pearson et al, 1973)
Note : 0.1 kg / cm^2 = 9.81 kPa and 1 psi - 6.895 kpa.

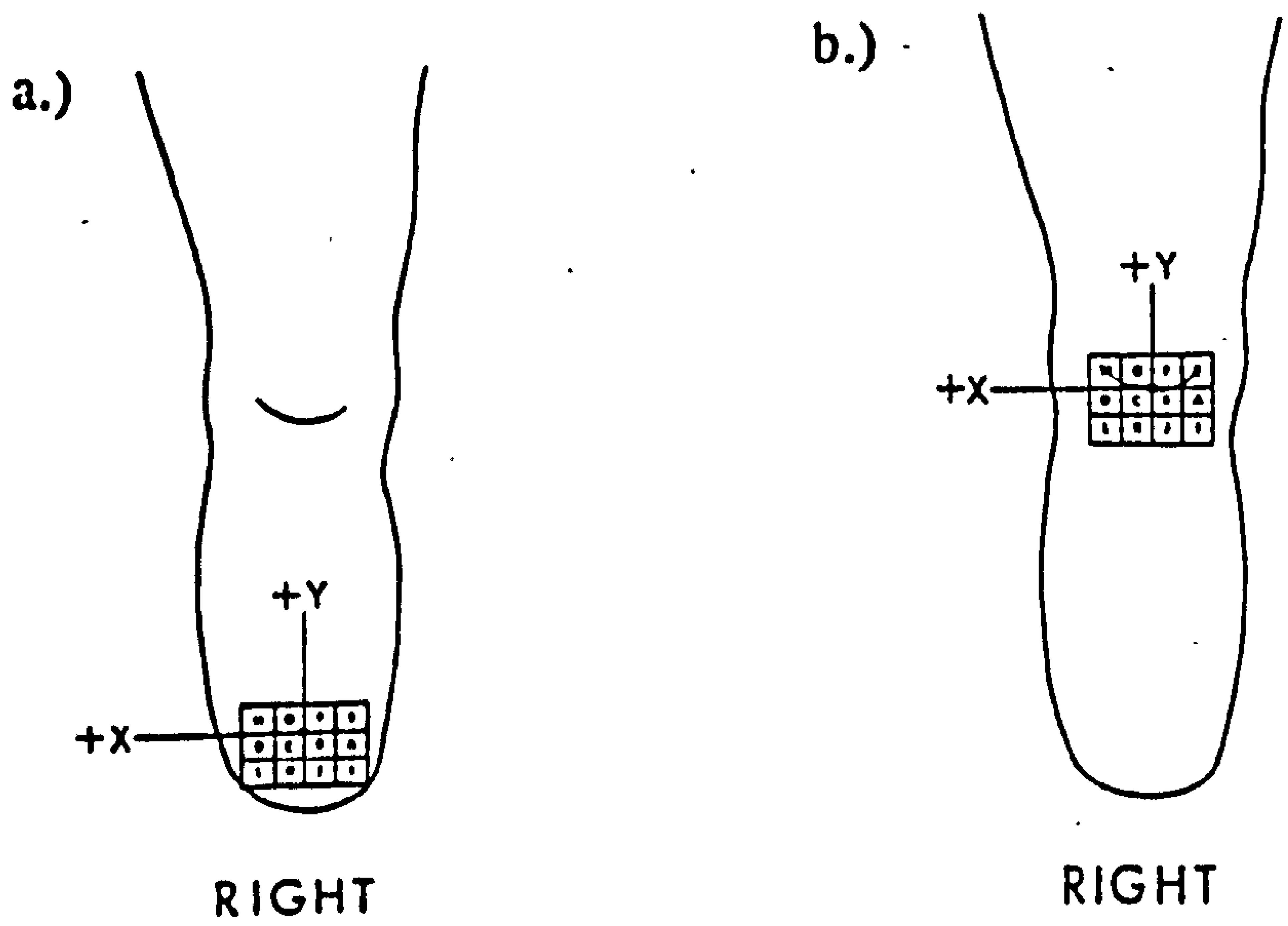

Fig. 4.2.2.6 a.) Kick point and
b.) Patellar point for right amputee (anterior view)
(Rae and Cockrell, 1971)

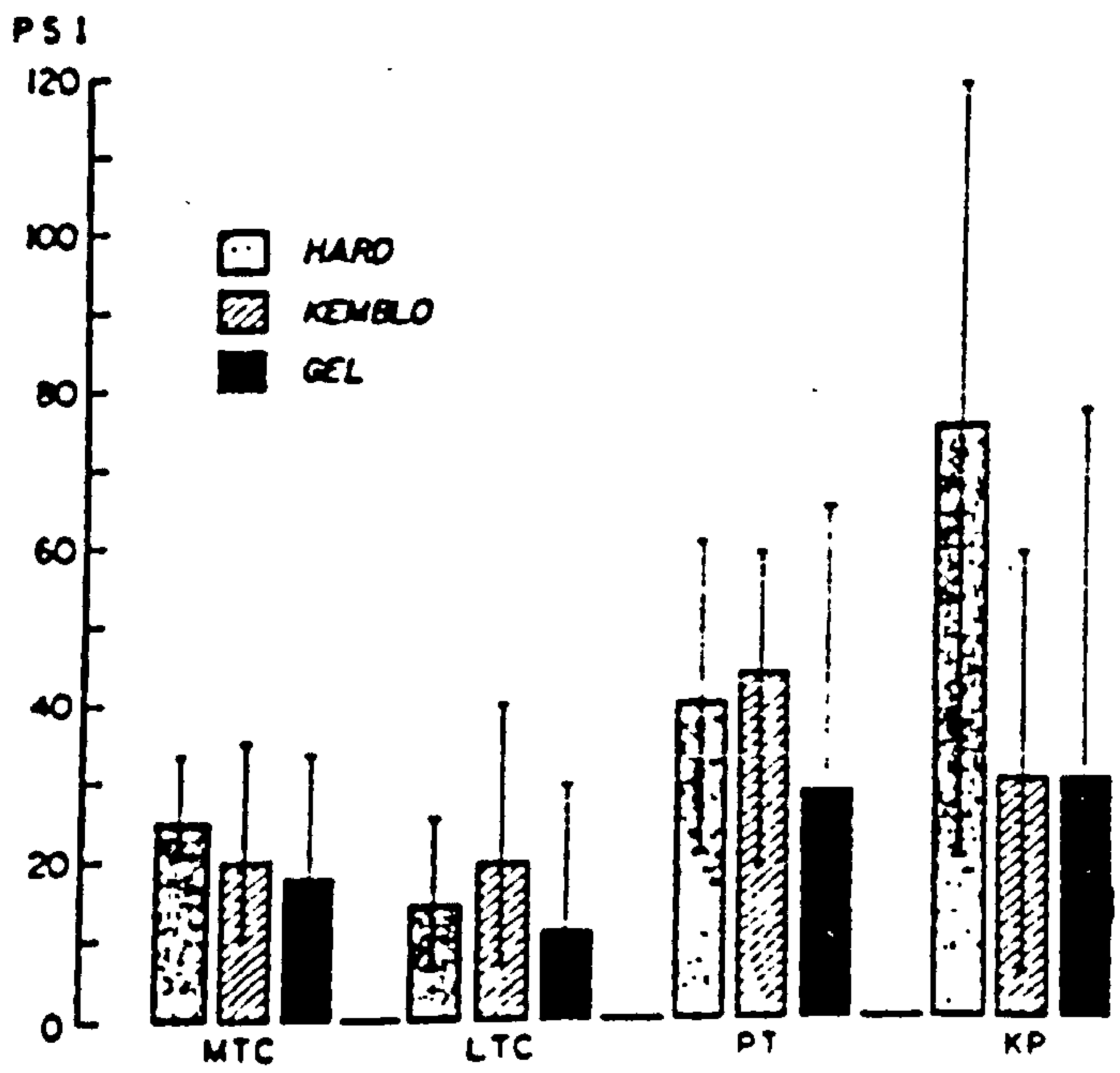

Fig. 4.2.2.7 Interface pressure at MTC (medial tibial condyle), LTC (lateral tibial condyle), PT (patellar tendon), KP (kick point) with Hard (no liner), Kemblo and Gel liner. (Sonck et al, 1990)
Note : 1psi = 6.895 kPa.

single transducer describing the pressure at a localised area of the trans-tibial residual limb, Rae and Cockrell adopted a matrix configuration requiring five transducers arranged within a 12.7mm square, four forming a square with the fifth in the centre. Alternatively the transducers were also placed in a straight line 12.7mm apart. Both of these configurations allow pressure distribution on a surface to be reproduced by curve fitting the data. Two areas, namely the kick point i.e. anterior distal end and the patellar tendon area were of interest to the authors (Fig. 4.2.2.6). PTB sockets were used in the study, and the maximum peak pressures recorded for the two areas repectively were 104 kPa and 276 kPa.

An attempt was also made to record peak pressure experienced during normal walking with different types of liner and no liner (Sonck et al 1970). Similar transducers placement to that of Rae and Cockrell (1971) was adopted. A peak pressure of 500 kPa ecountered at the kick point decreases to about 215 kPa when liner material was introduced (Fig. 4.2.2.7).

Engsberg et al (1992) introduced a system known as Tekscan for prosthetic limb interface pressure measurement. The transducers were based on FSR technology and appear in the form of a thin pressure mat of size 300 by 80 mm wide and 1mm thick. The pressure mat was secured on the residual limb by tape and a PTB socket was then fitted onto the limb with the pressure mat conforming to the final limb shape. As discussed earlier in section 4.2.1, the measurement yield by FSR is highly dependent on the final geometry of the transducer. The authors shared similar views, reporting that sensing capabilities of the pressure mat were lost due to wrinkle forming in high curvature areas. However, the system allows an interpolation routine with adjacent data in order to fill in the missing data. Interface pressures were measured for two subjects (male, 10 years and 30 years old) during standing and during gait, results are presented in Fig. 4.2.2.8. One of the main achievements stated by the authors in this study was the introduction of a simple clinical system for pressure measurement. Nevertheless, the author of this thesis felt that the system is still premature for clinical implementation. The inherent properties of FSRs leading to inaccuracy in pressure measurement need to be further investigated for such purposes.

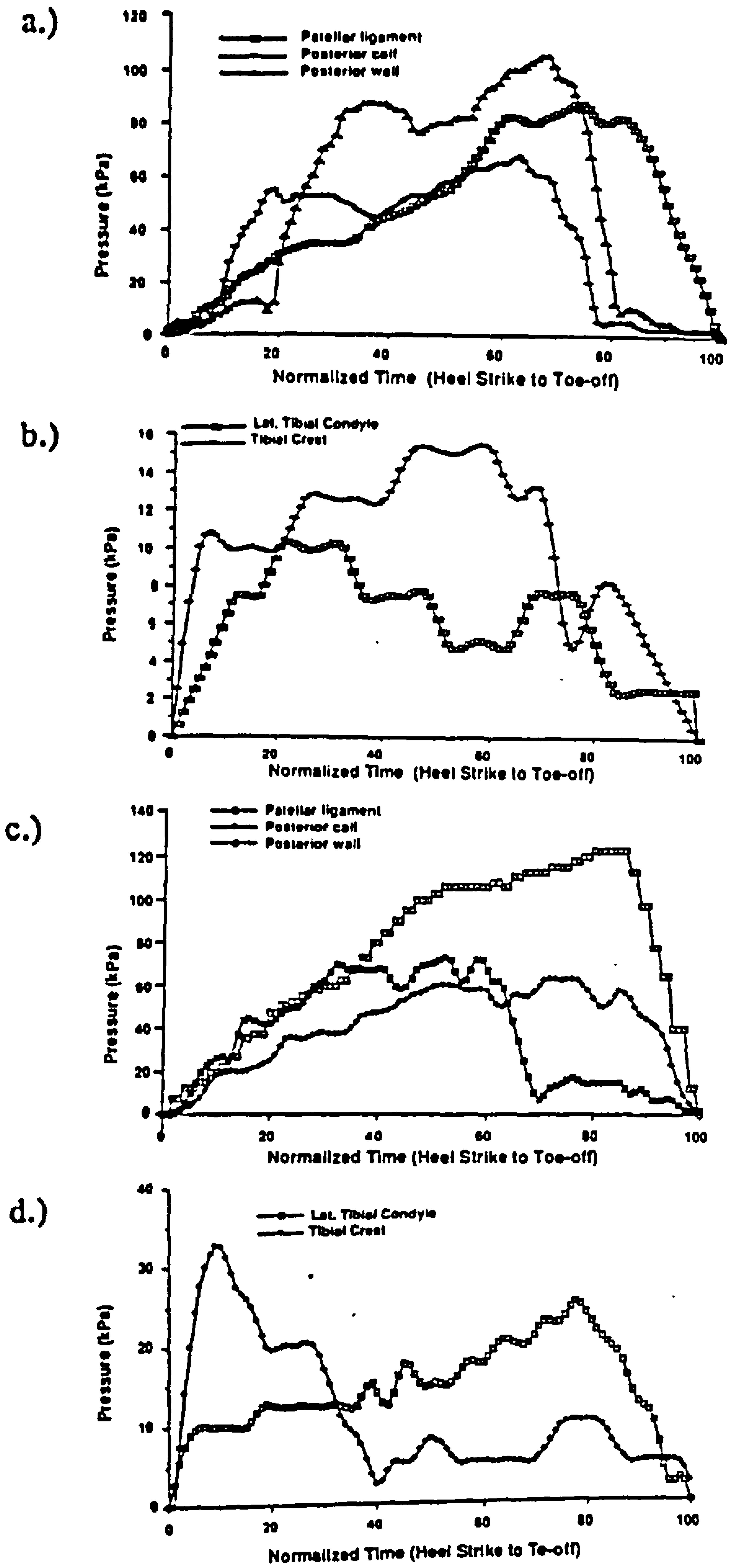

Fig. 4.2.2.8 a.) Selected high pressure sites for Adult during walking.
b.) Selected low pressure sites for Adult during walking.
c.) Selected high pressure sites for Child during walking.
d.) Selected low pressure sites for Child during walking.
(From Engsberg et al 1992)

A satistfactory calibration procedure for the transducers has to be achieved, catering for geometrical changes. Secondly, the introduction of a 1mm thin pressure mat may initially seem unimportant, however, considering the area of the mat (300 by 80 mm), a significant volume of 24000 mm^3 was added. A discussion with an experience prosthetist working with CASD/CAM system, indicated that the resultant volume being removed and built-up from the original plaster model could be less than 24000 mm^3 for a typical adult trans-tibial residual limb (Hulshof 1995). An additional volume of 24000 mm^3 would therefore have a considerable effect on prosthetic fittings.

The need for experimental validation of the finite element model of the residual limb required Steege et al (1987) to perform interface pressure measurement. The transducers were Kulite model XTM-190. These were mounted flush with the inside surface of the socket instead of being sandwiched between the residual limb and the prosthesis. Standing pressures were monitor at seven locations and magnitudes ranged from 0 to 128 kPa.

Interface pressures that were discussed in the above mentioned studies can only be identified as normal pressure or normal stress, which acts perpendicularly to the interface. However, shear stresses which act in the plane of the interface exist along with normal stresses. Shear stresses have been directly related to tissue distortion which is common at the prosthesis brim (Bader and Hawken 1986), and have been known to cause blisters and abrasion within the epidermis and skin respectively (Kenedi et al 1965). Sanders et al (1992, 1993) attempted to measure interface shear stresses during walking in trans-tibial amputees. A custom made transducer was used (Fig. 4.2.2.9). Shear measurements was made possible by mounting two metal-foil strain gauges on an aluminium beam of 1.52 mm square cross - section. The gauges were configured in two four - arm Wheatstone bridges. The differences in bending moment between the gauges is thus measured which is proportional to shear force applied to the end of the transducer in a plane perpendicular to the strain gauge surfaces. The transducer construction also includes a full bridge diaphragm strain gauge which detects normal stress. The transducers were calibrated to a full scale output (FSO) of 75 kPa and 175 kPa for the shear and

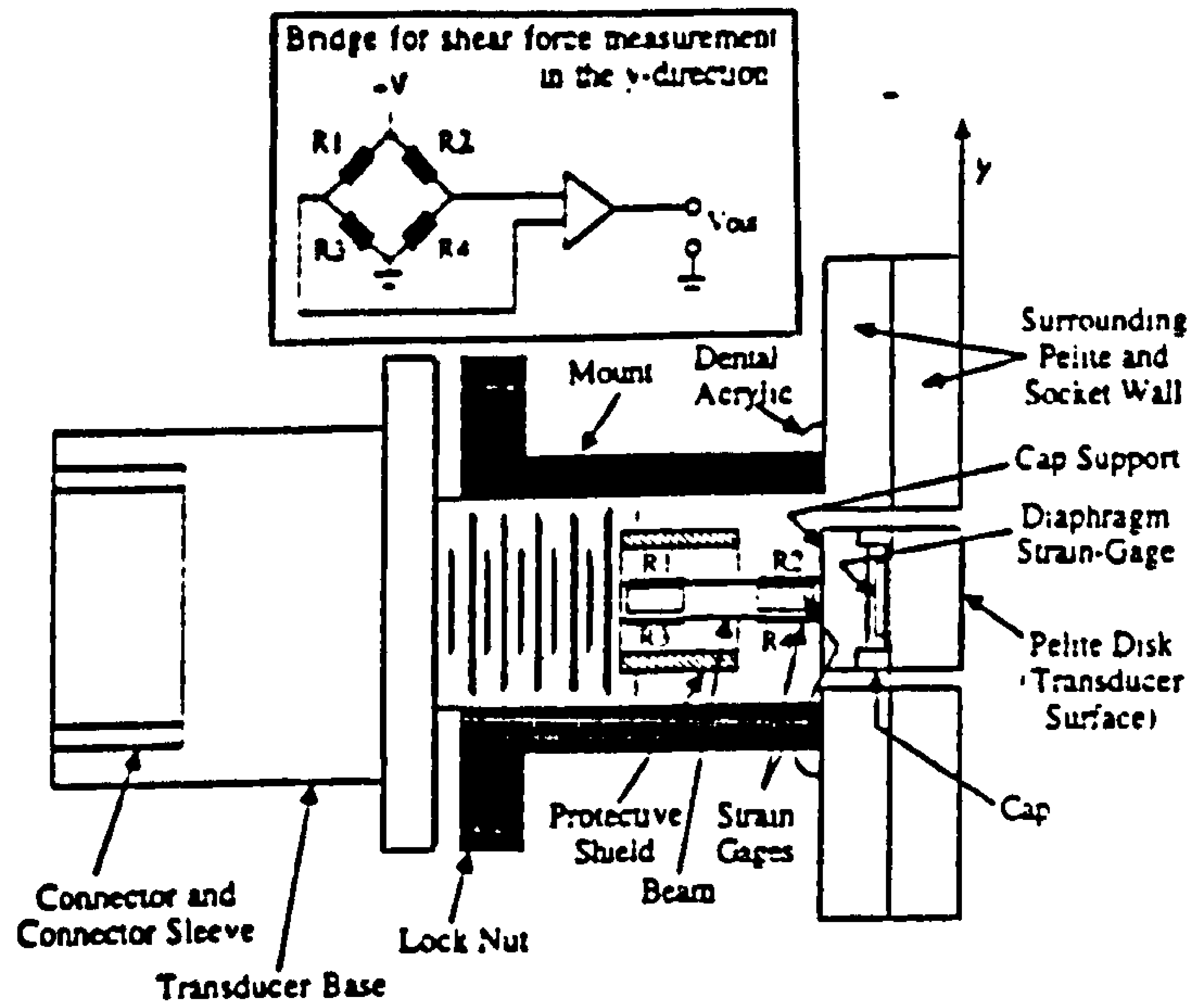

Fig. 4.2.2.9 Transducer construction. (Sanders et al, 1993)

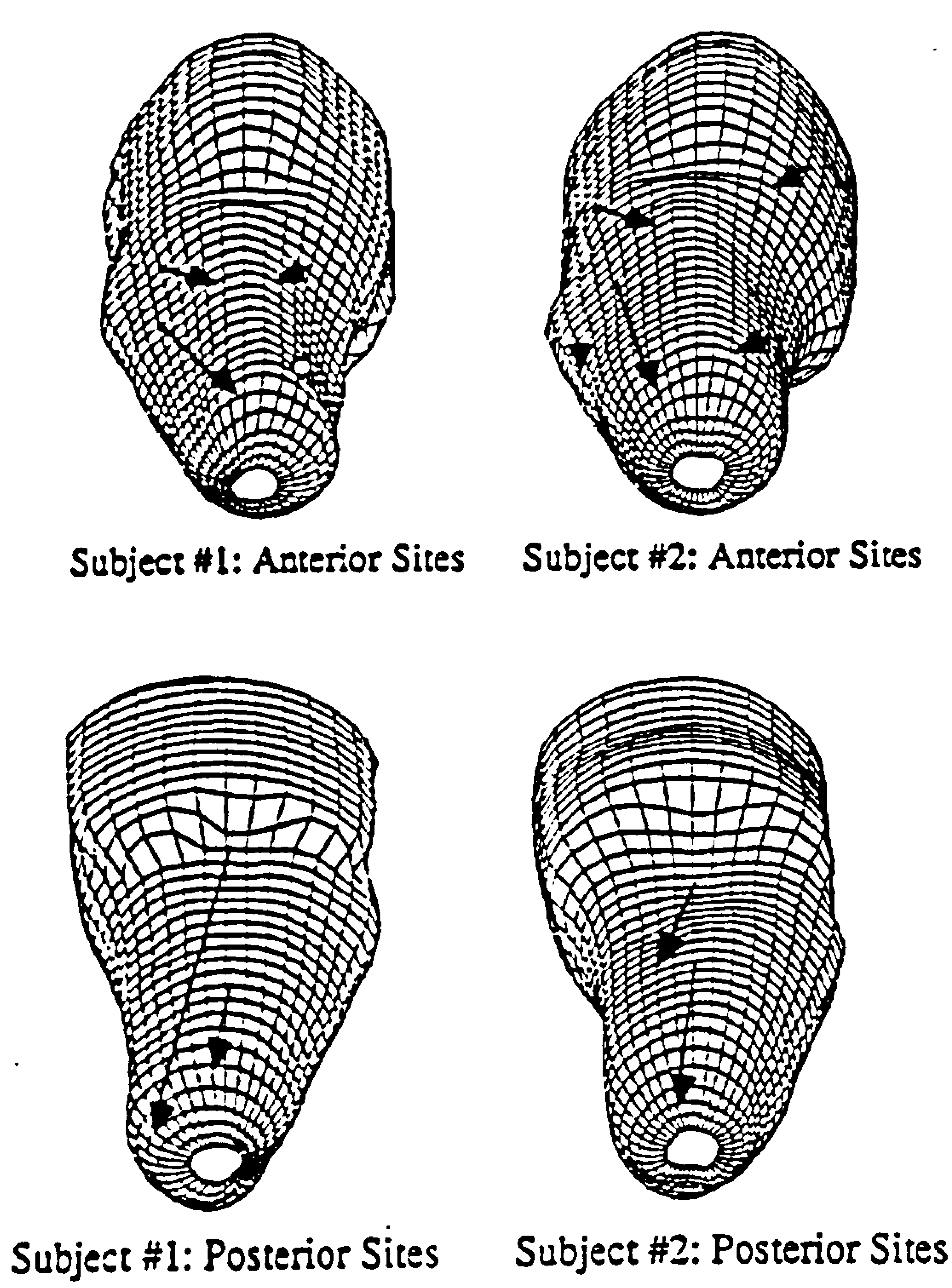

Fig. 4.2.2.10 Resultant shear stresses from a time 50% into stance phase for 2 subjects (right amputees). Arrows length are proportional to magnitude. (Sanders et al, 1992)

normal stresses respectively. The crosstalk between normal and shear directions was less than 1% FSO. Error due to hysteresis was 0.31% FSO and 3.01% FSO, and nonlinearity was 2.11% FSO and 0.31% FSO for shear and normal respectively. Peak magnitudes for normal stress and resultant shear stress were 205 kPa and 54 kPa respectively. The directions in which the resultant shear stresses act at a time of 50% into the stance phase are shown in Fig. 4.2.2.10. At the anterior surface, resultant shear stresses were directed toward the apex of the socket, which was likely to cause stretching of the skin at the crest of the tibia. Posteriorly, they were directed downward almost perpendicular to the ground. Willaims et al (1992) also presented a transducer that enabled shear and normal force measurement in prosthetic sockets (Fig. 4.2.2.11). Preliminary measurements were made with one trans-tibial amputee, recording peak normal force of approximately 35N and a longitudinal shear force of 6N. Circumferential shear force was almost zero in magnitude. The ratio of normal to shear magnitudes was 5.8 compared to Sanders et al (1992) which was only 3.8.

This section outlined briefly the methodology and results achieved in some studies. Upon comparing the results of these investigations, a significantly wide range of pressures could be noticed at similar sites of measurement. This is inevitable since each prosthetic socket has been customized for an individual patient, and furthermore, created by different prosthetists. It clearly illustrates the difficulties involved in producing consistent sockets even with well established and standardised methods of manufacturing. Nevertheless, pressure measurement has been advocated to be one of the best possible ways of quantifying prosthetic fit. Individual aspects of the socket could be investigated. Katz et al's (1979) study showed that the PTB socket could be improved by transferring more load to the distal end of the residual limb. The experiments were conducted by measuring end bearing pressure on a specially designed PTB socket. Hulshof (1995) with the aid of CASD/CAM produced several sockets where the volume was controlled by altering the amount of rectification over the PTB area. Interface pressure recorded for both static and dynamic conditions presented a strong argument against the effectiveness of PTB sockets. Mizrahi et al (1986) altered the patellar tendon insertion in the socket and measured the dynamic

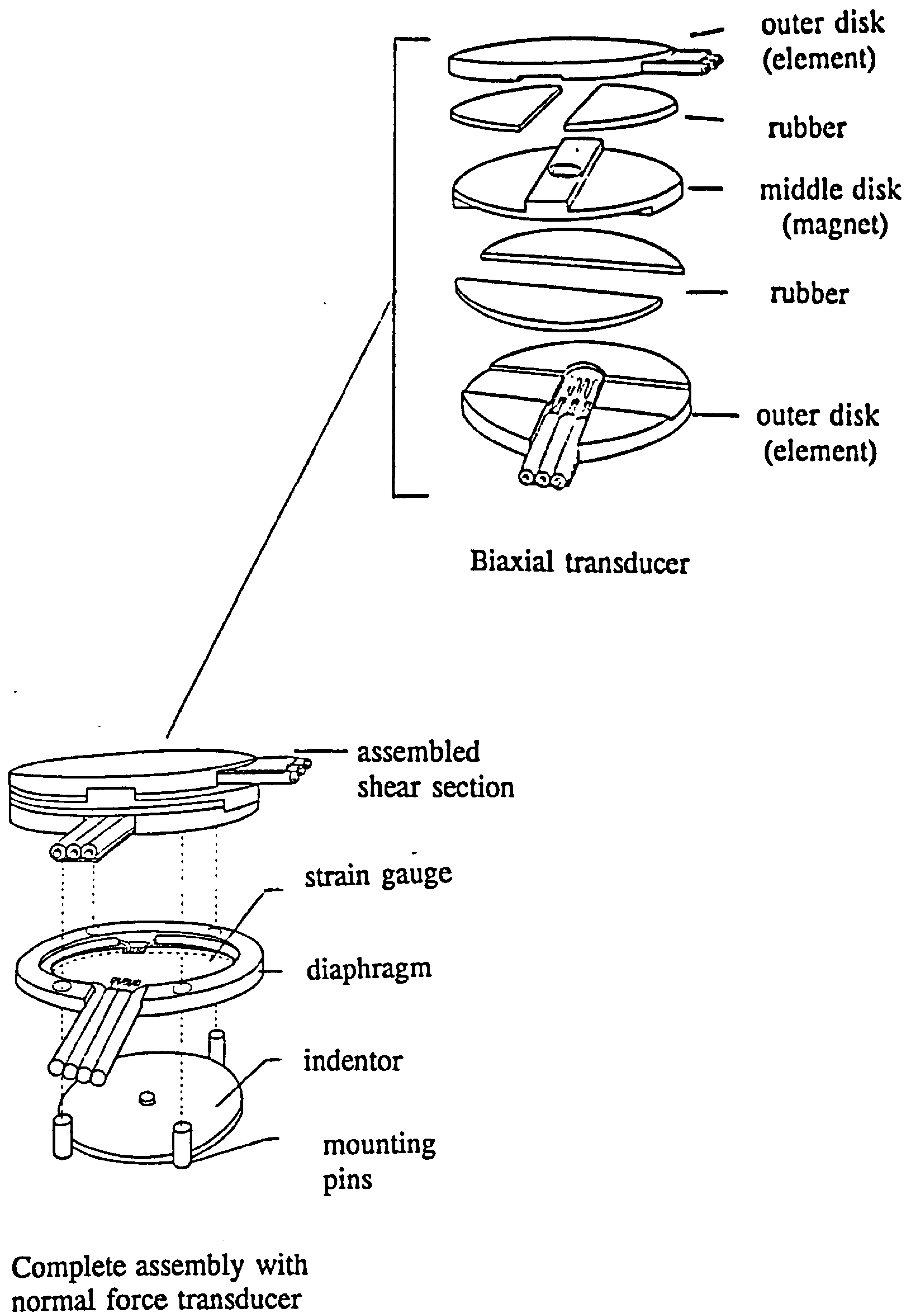

Fig. 4.2.2.11 The transducer's construction is based on the principle of transduction, which depends on the resistance of a semiconductor resistor varying with the strength of an applied magnetic field. (Williams et al, 1992)

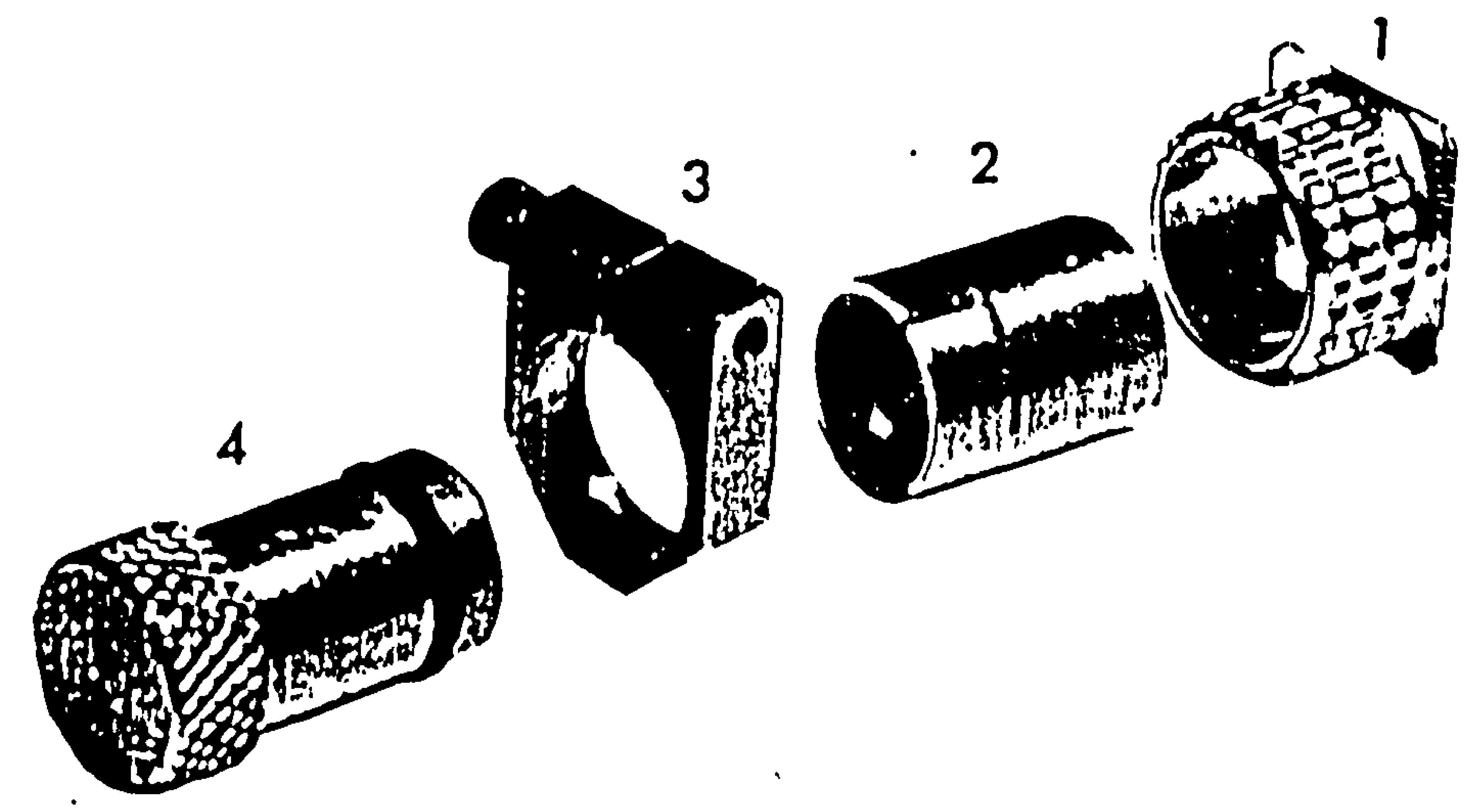

Fig. 4.2.3.1 Transducer mount. (Appoldt and Bennett, 1967)

1. Insert, flanged tube with knurled outer face.
2. Mounting tube, slit for one quarter of its length.
3. Split clam ring.
4. Metal plug for sealing the mount.

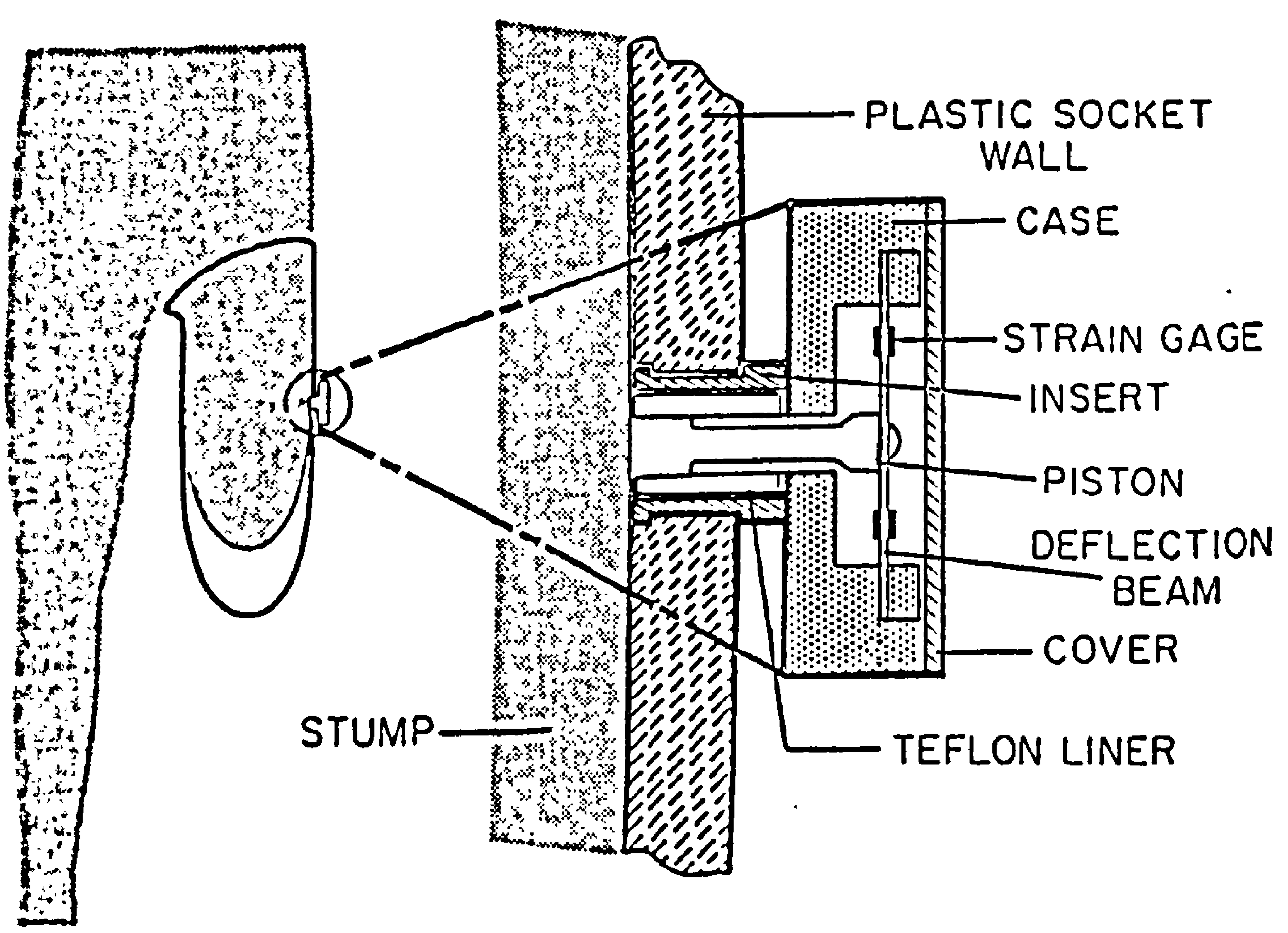

Fig. 4.2.3.2 NYU transducer assembly. (Appoldt and Bennett, 1967)

load through the patellar tendon. Results obtained were used to discuss adaptation and compensentory mechanisms developed by the patients over changes in prosthesis component variations.

4.2.3 Pressure measurement at the trans-femoral residual limb / socket interface

One of the earlier trans-femoral pressure measurements was attempted by Appoldt and Bennett (1967) from New York University (NYU). In this preliminary trial, pressures at 25 sites on a quadrilateral socket were measured. The sites were arranged in four columns, evenly distributed accordingly to the anterior (6 sites), medial (4 sites), posterior (4 sites) and lateral (6 sites) areas of the socket. In addition, five sites were located at the medial and posterior (ischial seat) brims. At each of these sites, a transducer mount was fixed to the socket wall, which enabled the sensing head of the transducer to be flush with the inner surface of the socket. The transducer mount was made up of four pieces (Fig. 4.2.3.1) with a metal plug to seal the site where measurement was not attempted. A series of different types of pressure transducer was investigated. Nevertheless, only the Micro-System and the NYU pressure transducers, both strain gauge type transducer were selected (Fig. 4.2.3.2). The former was calibrated using gas in a small chamber while the latter either by direct application of weight or gas pressure. The pressure measurement test was conducted in two different prosthetic alignment, normal and 2^0 abducted shanks. The results presented showed peak pressures that occurred at 100, 300, 470 and 540 ms after heel-contact (Fig. 4.3.2.3 and 4.3.2.4 and 4.3.2.5). Generally, pressure ranged from 0-56 kPa at the walls while highest pressure of 166 kPa was observed at the lateral-posterior ischial seat. Anterior-posterior wall pressures were highest at 100 ms after heel contact, peaking at the proximal posterior site and gradually reducing towards the distal end of the residual limb. Towards the end of the gait cycle, pressure distribution behaved conversely peaking instead at the anterior distal end (see Fig. 4.3.2.3). The wall pressures were not affected considerably both in magnitude and distribution by the 2^0 abducted shank, however brim pressure at posterior lateral site reduced from 166 kPa to only 97 kPa.

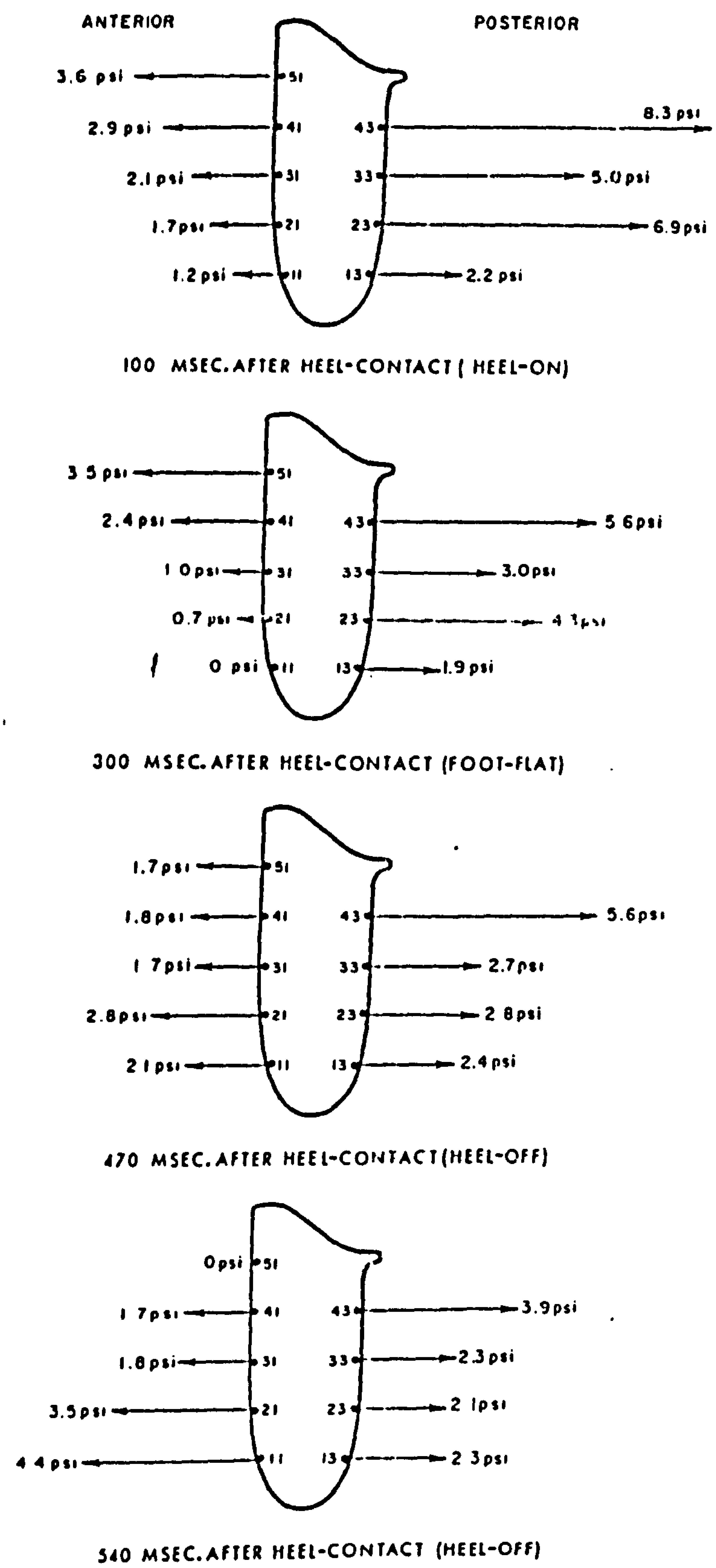

Fig. 4.3.2.3 Anterior and posterior wall pressure at 100, 300, 470 and 540 ms after heel contact. (Appoldt and Bennett, 1967)

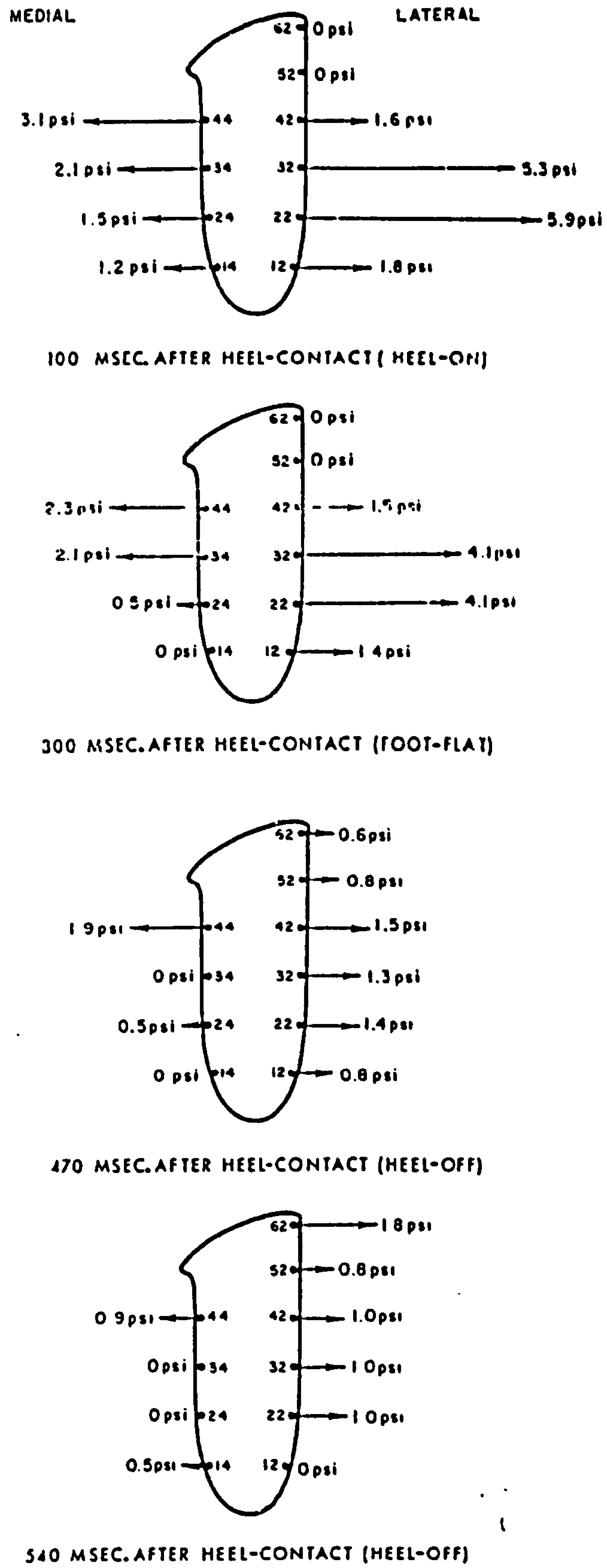

Fig. 4.3.2.4 Medial and lateral wall pressure at 100, 300, 470 and 540 ms after heel contact. (Appoldt and Bennett, 1967)

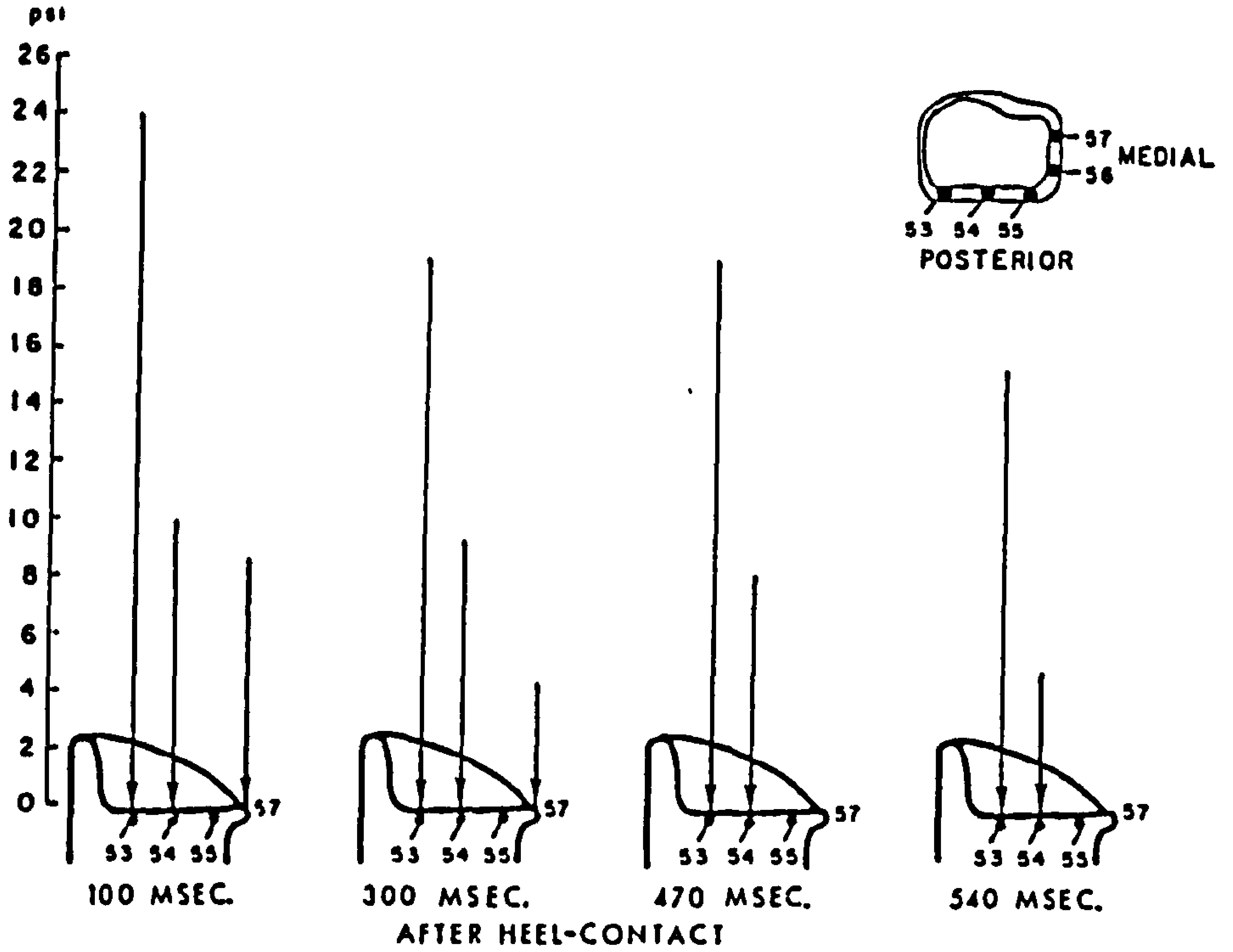

Fig. 4.3.2.5 Posterior and medial brim pressure at 100, 300, 470 and 540 ms after heel contact. (Appoldt and Bennett, 1967)

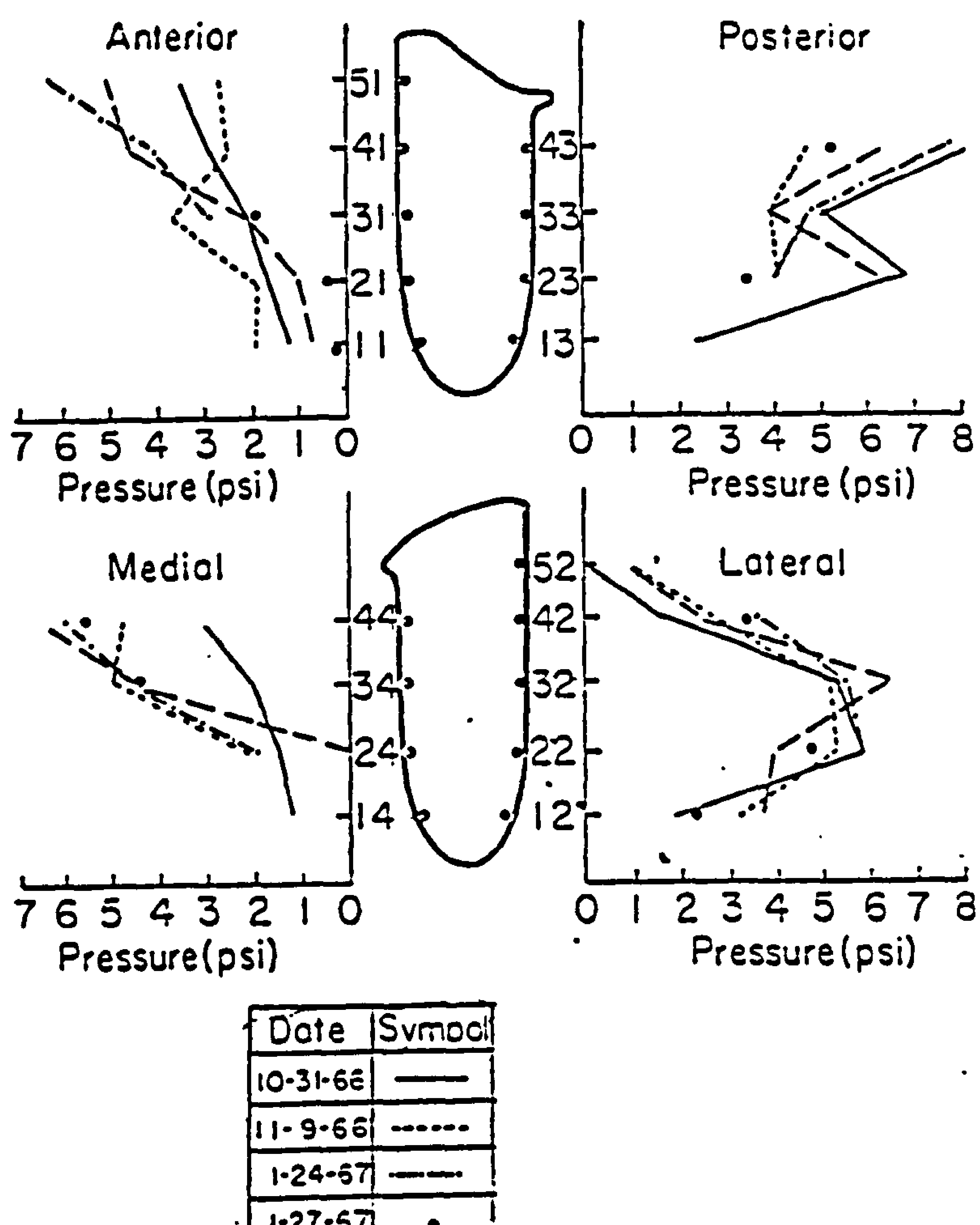

Fig. 4.3.2.6 Socket pressure as a function of time. (Appoldt et al, 1968)

In another study by the NYU group (Appoldt et al 1968), two subjects were tested for day to day and week to week interface pressure variations. The findings showed these variations were indeed significant (Fig. 4.3.2.6). The authors discussed that the potential sources for such differences included instrumentation errors, subjects gait variation, donning of prosthesis, fatigue and changes in residual limb sizes.

Leavitt et al (1970) described a system to quantify prosthetic gait and socket/ residual limb interface pressure (Fig. 4.3.2.7). Knee angle was captured on the anatomical leg with the aid of a goniometer attached on a knee cage type brace, placed approximately on the mechanical axis of the knee, while another goniometer was placed directly on the prosthetic leg at the knee bolt. Temporal-distal measurement were obtained by the use of three foot switches each foot and interface pressure measured at the contact area of the ischial tuberosity and the socket. The exact location of the ischial tuberosity measurement site was determined using x-ray. The pressure transducer used was stated as sensitive and temperature compensated, however, the make and type was not described. The report did not highlight any result since it was only a preliminary description of the method of measurement, but a further study by the same group (Leavitt et al 1972) on 35 male trans-femoral amputees yielded useful information. Out of the 35 amputees, 20 has been subjectively rated as amputees with good gait while the other 15 with bad gait. A total of three pressure transducers were located at the ischial seat, medial and lateral mid third of the socket walls respectively. Several cases of subjects with abnormal gait patterns were highlighted with respect to interface pressure. A subject with prolonged heel time on the prosthetic limb recorded 290 kPa at the ischial seat. Another subject with increased double stance time in order to reduce pain at the groin area recorded pressure of only 34 kPa on the ischial seat, but about 152 kPa on the lateral mid-third wall. The study also evaluated a series of modular prosthetic components. The effect of combining different prosthetic components on interface pressure was highlighted in one particular case, where upon replacing a conventional foot with the SACH foot, the ischial seat pressure increased from 76 kPa to 130 kPa. However the authors did

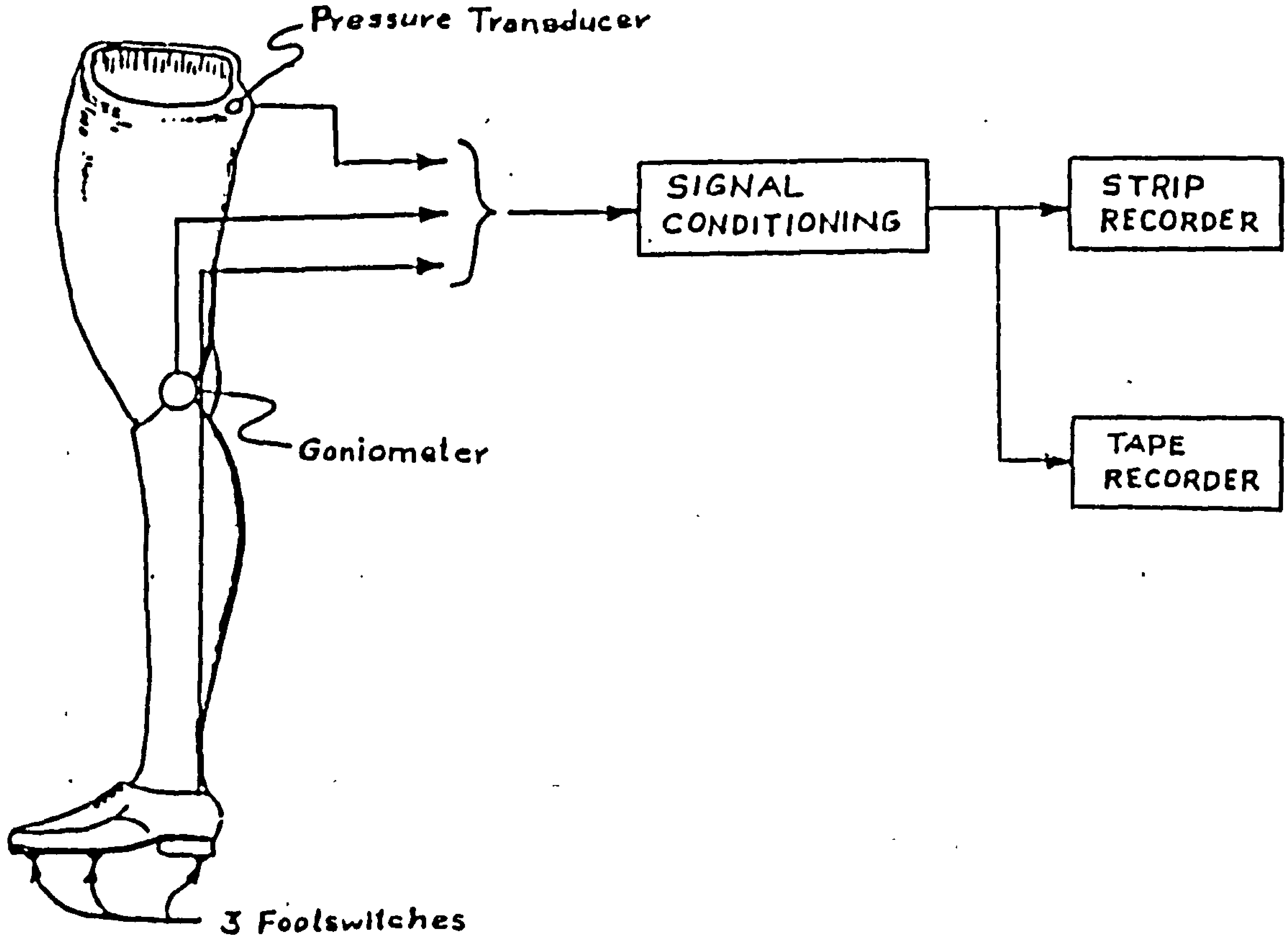

Fig. 4.3.2.7 Pressure measurement set-up. (Leavitt et al, 1970)

not attempt to explain the effects of the different prosthetic feet. It concluded that gait pattern and residual limb / socket pressures reflected the change and additional subjects need to be studied before valid conclusions can be drawn.

Van Pijkeren et al (1980) introduced a fluid filled bag (hydraulic) transducer as reviewed in section 4.2.1. for interface pressure measurement. Naeff and Van Pijkeren (1980) used the transducer to study the relationship between interface pressure and the curvature at the ischial brim of the quadrilateral socket. The brim medio-posterior section (Fig. 4.3.2.8) was divided into 44 points where interface pressures were measured. In addition, six different curvatures at the brim were used, 7.5 mm (sharp corner), 15 mm, 22.5 mm, 30 mm, 45 mm and 200 mm (almost vertical wall). Fig. 4.3.2.9 plots the pressures measured at the brim for curvatures 7.5 mm, 15 mm and 200 mm during the stance phase. It was observed that pressure at the ischial tuberosity peaks at approximately 200 kPa and was unaffected by the variation in radius of curvature. However, a greater radius of curvature reduces the pressure on the gluteus muscles significantly. The authors continued to relate comfort to radius of curvature. The test subjects reported that 30 mm and 45 mm were more comfortable than the 7.5 mm curvature which caused an abrasion to the skin. Also, the 200 mm was considered comfortable by the subjects, nevertheless, the authors concluded the large curvature actually gave rise to a plug fit socket with no gluteal-ischial seating, which will be totally different from the quadrilateral socket.

Pneumatic transducers based on similar principles to the hydraulic transducer, were applied by Krouskop et al (1987) to measure interface pressures of 18 trans-femoral amputees. Nine of them were fitted with the quad sockets, while five were fitted with the NSNA sockets. These sockets were considered comfortable, while another four subjects had sockets which caused discomfort, three being NSNA and one quad. In the NSNA sockets, tissue loading was concentrated around the proximal third of the socket and around the distal femur. Some areas around the distal end of the femur with the quad sockets were also reported as highly loaded. The distribution of pressure between the two sockets were noted to vary significantly, but with pressure values of about the same magnitude. Most of the tissues were subjected

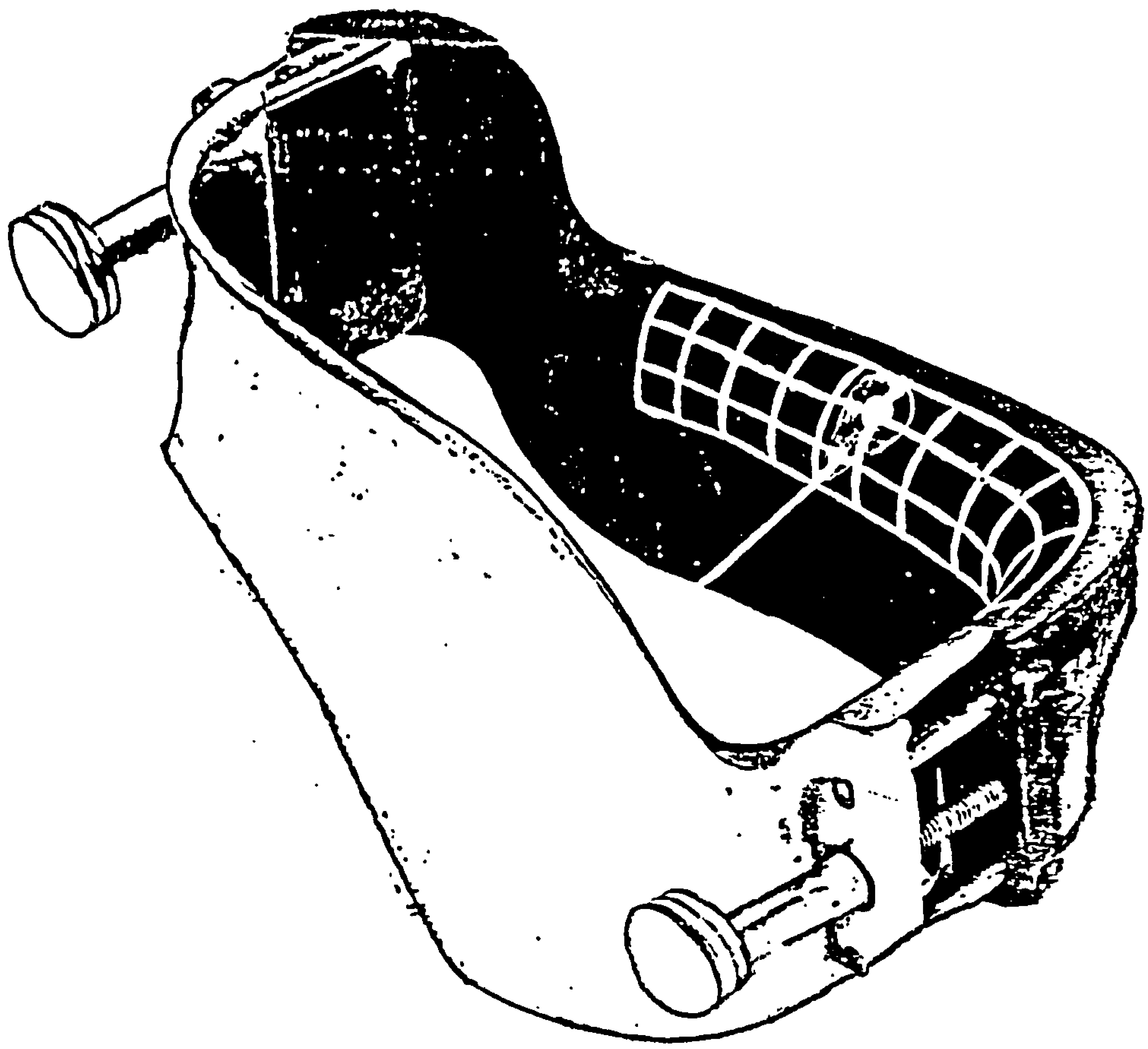

Fig. 4.3.2.8 Hosmer casting brim with network of lines for transducer placement.
(Naeff and Van Pijkeren, 1980)

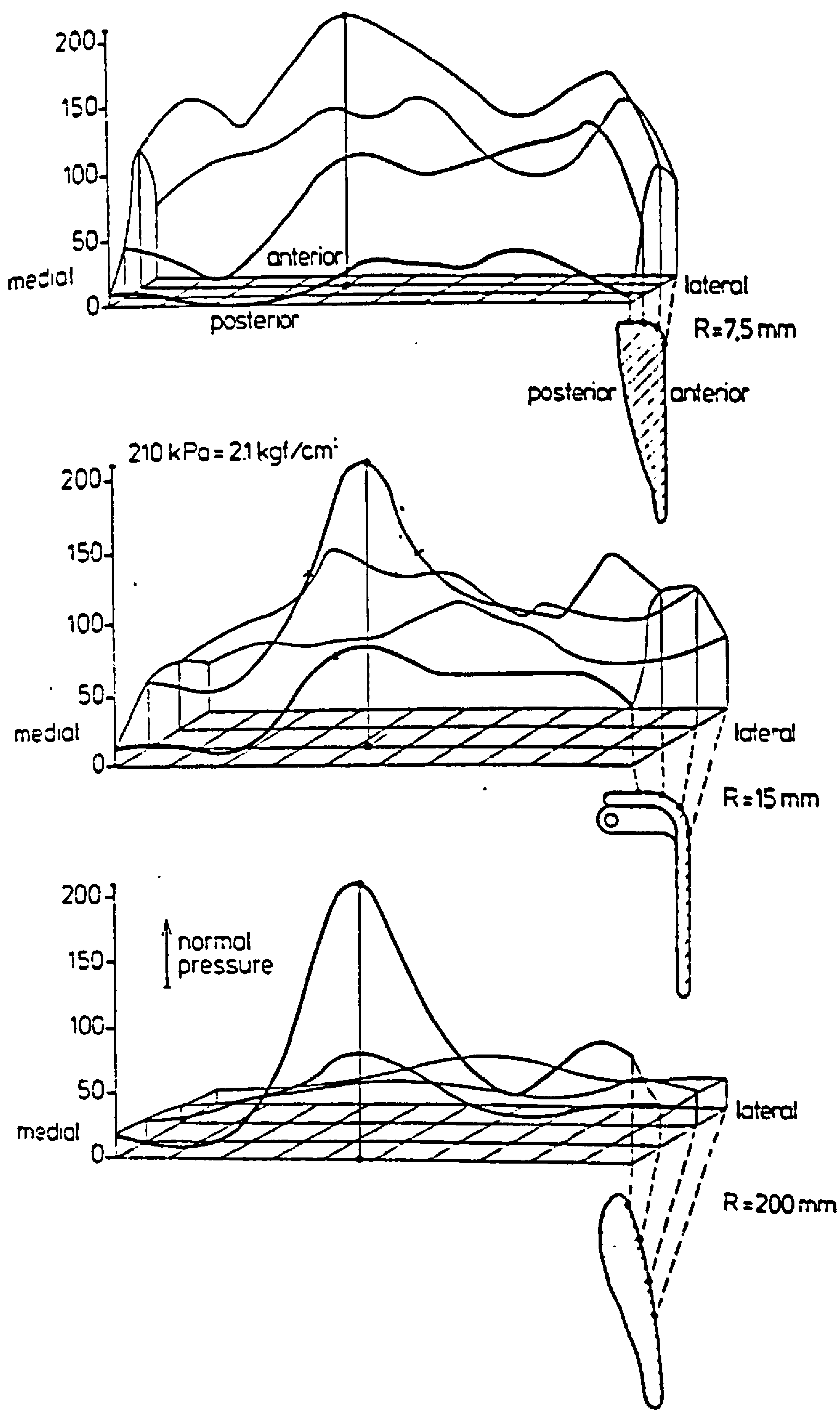

Fig. 4.3.2.9 Interface pressure located at the brim according to the network of lines in Fig. 4.3.2.8 for three radius of curvature.
(Naeff and Van Pijkeren, 1980)

to a pressure of about 7 kPa and peak pressure of one subject with bad gait reached 12.6 kPa. The author of this thesis considers that the study lacks consistency in evaluating socket types, since the two types of sockets were not prescribed for the same subject. The loading and load distribution on each subject's residual limb was expected to vary due to the unique shape and comfort requirements of the individual. Thus, comparison made with different subjects on different sockets could be highly inconclusive.

4.3 PRESSURE MEASUREMENT TEST

The amputee has to achieve body stabilisation with the aid of the artificial limb and with existing musculature in the residual limb. Due to the prosthesis being a foreign interface, stabilisation is usually achieved at the expense of good gait, comfort and higher physiological energy consumption. The socket has been a major aspect of prosthetics research, since it represent the initial interface between human and machine. The complex behaviour at the interface can be appreciated through quantifiable measurement like that of pressure. Interface pressure measurement indicates the mechanism of load transfer between the residual limb and socket which is the primary aim in prosthetic socket design.

4.3.1 Brief description of the test

The primary aim of the test was to provide a means to validate the finite element models of the residual limb. Nevertheless, in line with the general aim of the study, the test also allows socket designs to be investigated. Thus, the test encompass a study into the design of the quadrilateral (quad) and the ischial containment (IC) socket.

A two part study was adopted. Interface pressures were initially measured on three subjects prescribed with IC sockets. Only two of the three subjects proceed to part two of the study where measurements were performed on both quad and IC sockets that were prescribed by another prosthetist. The second part of the study aimed to eliminate some of the inconsistencies by using one prosthetist to fit both types of sockets to the same patient. In summary, the study hoped to achieve the following ;

a.) Validation of FE models of the residual limb,

b.) Quantify the pressure variation in IC sockets designed by different prosthetists,

c.) Study the biomechanics of the quad and the IC socket prescribed for the same subject by the same prosthetist.

Pressure was only measured at predetermined discrete points over the whole surface of the socket for subjects during standing and during normal walking. The test sockets were therefore modified to incorporate pressure measurement sites, ranging from 16-20 depending on the type and size of the socket prescribed for the individual subjects. These sites were basically holes made in the socket for the pressure transducers to make contact with the residual limb. Strain gauge load transducers were used. These were housed in nylon adapters which allowed connection to the socket. More details of the socket and pressure transducer will be discuss.

4.3.2 Subjects

Three volunteer trans-femoral amputees participated in the test. The subjects (H, U and M) are currently active wearers of the IC type socket, but in the past have been on the quad socket. The selected amputees represented the general population of the amputees in Scotland reasonably well, and are active users of their prostheses. Prior to the test, an assessment of the amputees' residual limb condition was carried out by an experienced prosthetist. The assessment was performed under the guidance of a standard document described by Wall (1987). Information regarding skin, state of tissue, circulation, pain, amputation, joint function and muscle strength were recorded. The level of activity of the subjects was also indicated using Day's (1981) activity level assessment. The assessment provides the subject with questions regarding daily activities and multiple choice answers leading to positive or negative scores. The overall scores rate the amputees' activity level in five categories, very high, high, average, restricted and inactive. All three subjects are reasonably active and found to be highly dependent on their artificial limb in their daily activities.

Subjects	Year of amputation	Age (yrs)	Mass (kg)	Day's Activity Level	General state of residual limb
H	1985	66	67	+ 8	Shape conical, skin normal with no sores, circulation normal, no obvious pain.
U	1957	58	80	+ 4	Shape conical, skin slight redness, evidence of old distal odema, phamtom pain - dull ache.
M	1967	47	77	+ 23	Shape cylindrical, tissue flabby, skin normal, circulation normal, pain at hip joint.

Left/Right indicates side of amputation.
Day's activity score full range between -70 and +50.
More than +30 = Very High, +10 to +29 = High, -9 to +9 = Average, -40 to -10 = Restricted, Less than -40 = Inactive.

Table 4.3.2.1 Subjects' descriptions.

The assessments according to the above mentioned documents are listed in Appendix A, while Table 4.3.2.1 provides a brief summary.

4.4 PRESSURE TRANSDUCER

Fig. 4.4.1 shows a photograph of the transducer and Fig. 4.4.2 shows the schematic cross-sectional view of the transducer mount assembly. The transducer (A) selected is commercially available and is manufactured by Entran International (model ELM 601-2). Its construction consists of a stainless steel casing housing a sensitive diaphragm bonded with miniature strain gauges in full Wheatstone Bridge configuration. Load is transferred to the diaphragm through a miniature piston. The transducer measures 15 mm in diameter and 6 mm in thickness. However, in order to secure it flush with the inner surface of the socket, the transducer was housed in a nylon mount (B), increasing the overall dimension to 35 mm diameter and 17 mm thick. The mount provides a recess to fit the transducer, while a cylindrical piston (C) in contact with the Entran miniature piston serves to transfer normal loading from the tissue to the transducer. For easy coupling, a locking ring (D) provides a threaded lock to the adapter (E) that is embedded in the socket. The locking ring can rotate independently around the transducer mount, thus preventing the whole assembly from rotating which could cause problems with the transducer wires. Only four transducers were available for the test, therefore the assembly was designed to ensure secure placement and easy transfers between measurement sites. Sites which were not measured were secured with air tight nylon plugs (Fig. 4.4.3), thus maintaining the vacuum essential for suspension of the artificial limb.

4.4.1 Selection of transducer

An important criterion of the pressure sensor was the ability to provide accurate representation of pressure at the residual limb, which allows validation of the FE models created. Thin sensors like that of the FSR were considered, however, their ability to give accurate readings has been doubted. A strain gauge transducer possessing high sensitivity, low hysteresis, high frequency response and linearity in its

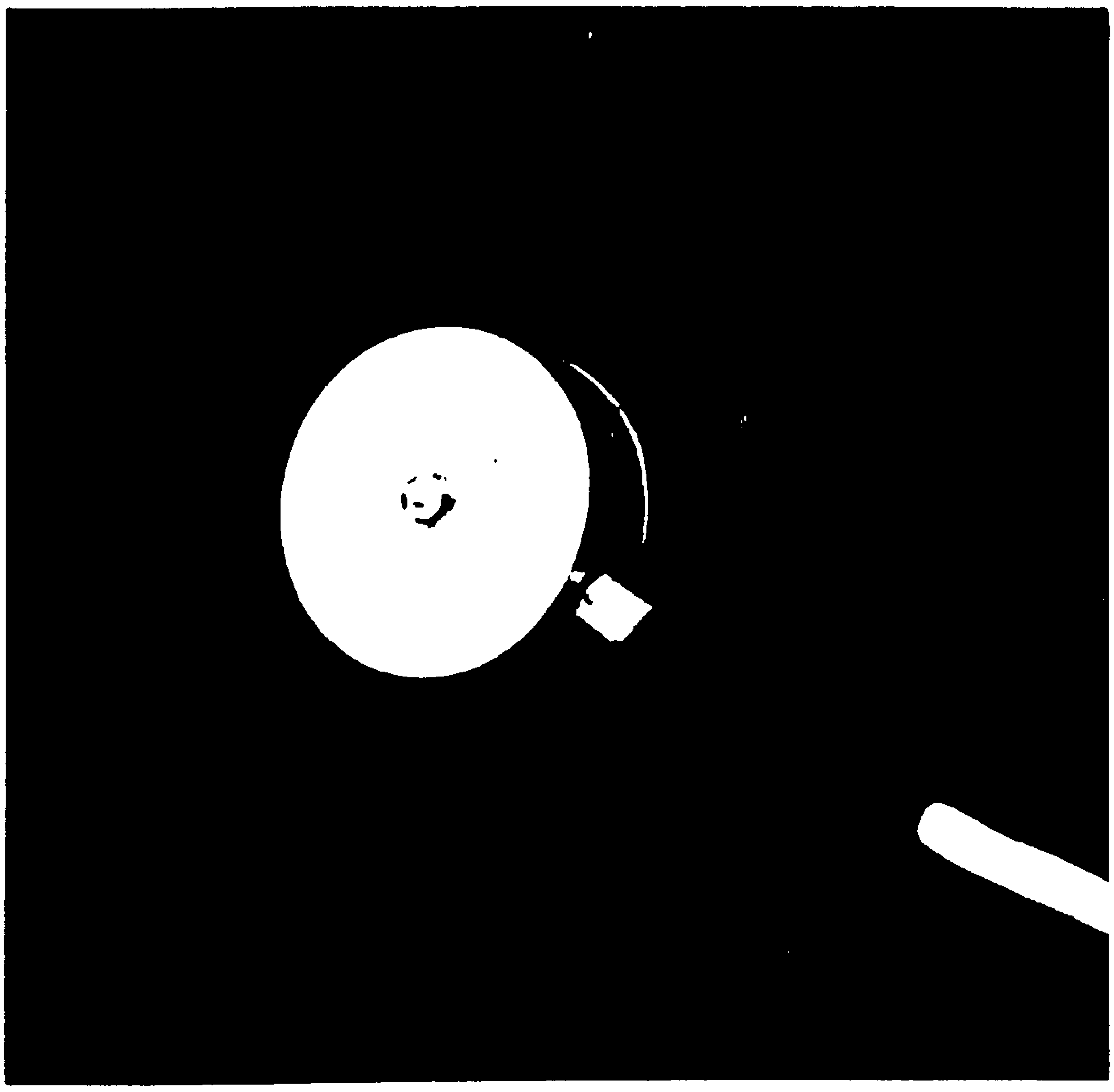

Fig. 4.4.1 Entran transducer (Model ELM-601-2)

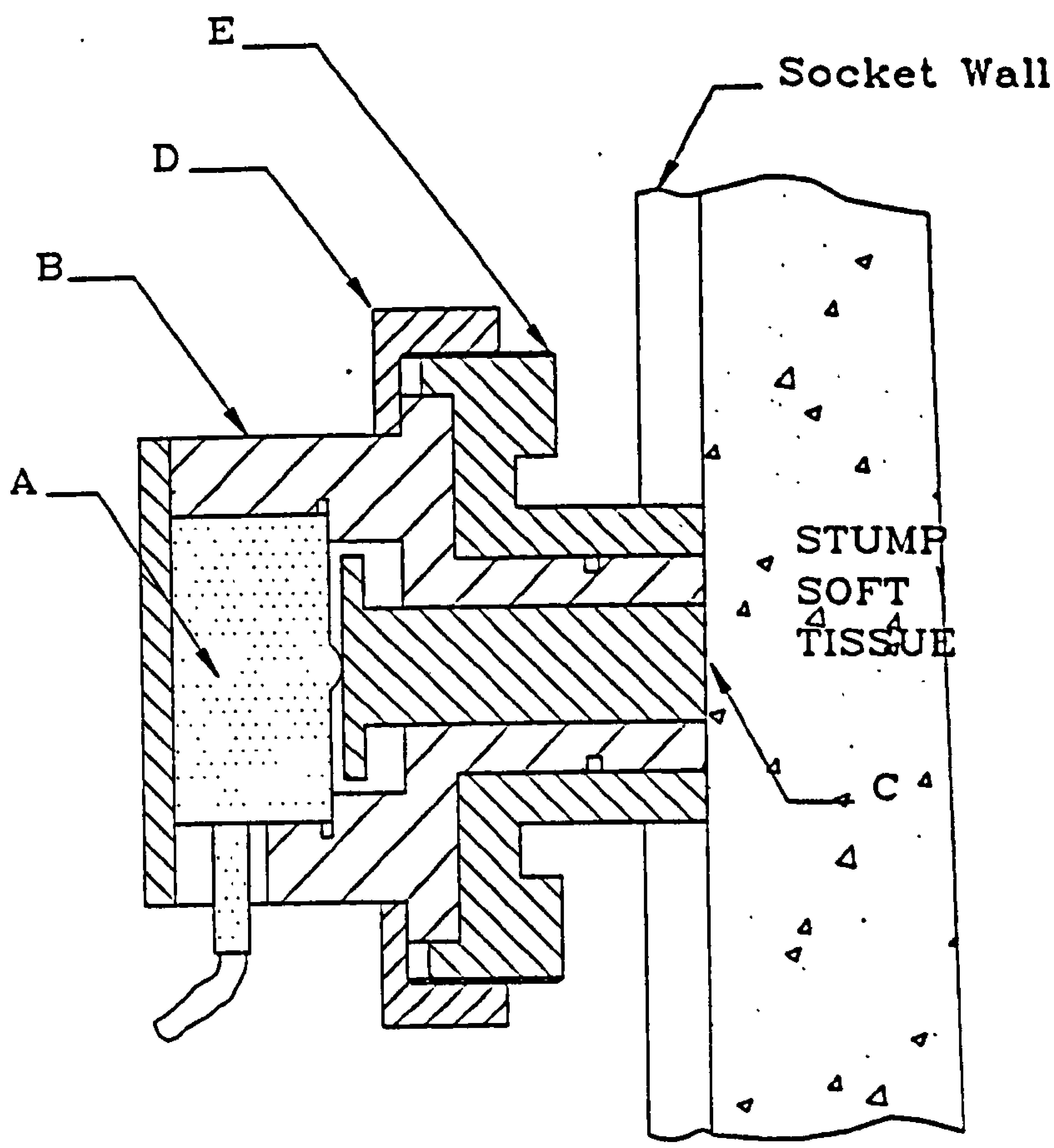

A.) Entran transducer
B.) Mount
C.) Piston
D.) Locking ring
E.) Adapter

Fig. 4.4.2 Transducer assembly

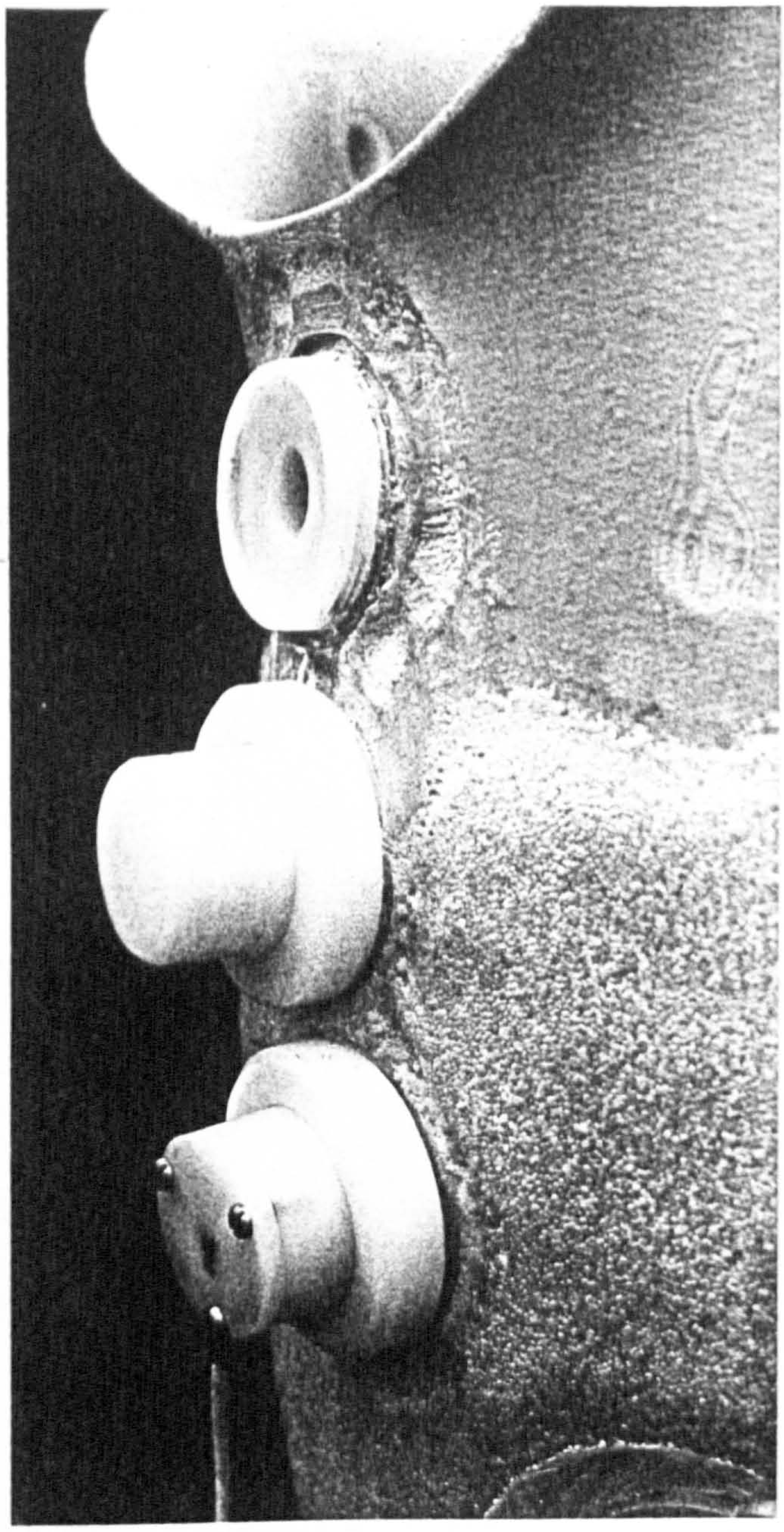

Fig. 4.4.3 Prosthetic socket with adapter, air tight plug and transducer.

measurements was chosen. Other factors considered are cost, size and load range. Unlike thin miniature transducers, the Entran ELM-601-2, was too thick to allow placement between the socket and the residual limb. However, as previously discussed in section 4.2.1, the protrusion pressure caused by such placement could result in significant errors during measurement. Thus, in this study there was no intention to adopt such placement, instead the socket was modified to allow the transducer sensitive area to be mounted flush with the inside surface of the socket.

The load range of the transducer was selected corresponding to the size of the sensor area, which is discussed in the next section.

4.4.2 Selection of transducer's pressure sensitive area

One of the main concerns was selecting a suitable sensitive area for the pressure transducer i.e. the nylon cylindrical piston. The load applied to the transducer is not uniform. Pressure gradients and shear stresses therefore exist at this area giving rise to the difference between mean and peak pressures experienced on the sensor surface. Ideally, the sensitive area has to be as small as possible, however, this is often constrained by practical problems. The estimates of the size of the sensitive area was based on a theoretical analysis performed by Ferguson-Pell (1980). It assumes a transducer with uniform sensitivity and an output per unit area which is directly proportional to the mean pressure acting across its area. However, this is not achievable in many types of transducer especially that of the diaphragm strain gauge type transducer. Nevertheless, the analysis provides an understanding to the parameters involved when selecting a sensitive area.

Fig. 4.4.2.1 represents pressure contours encountered by the sensor, where the shaded area represents the sensing area determined by radius r'. The pressure across the region R is a function of r and θ in the cylindrical co-ordinates where,

$$0 \leq r \leq r' \text{ and } 0 \leq \theta \leq 2\pi$$

therefore

$$P_m = \frac{\iint_R P(r,\theta)\, r\mathrm{d}\theta\, \mathrm{d}r}{\iint_R r\mathrm{d}\theta\, \mathrm{d}r} \qquad (4.4.2a)$$

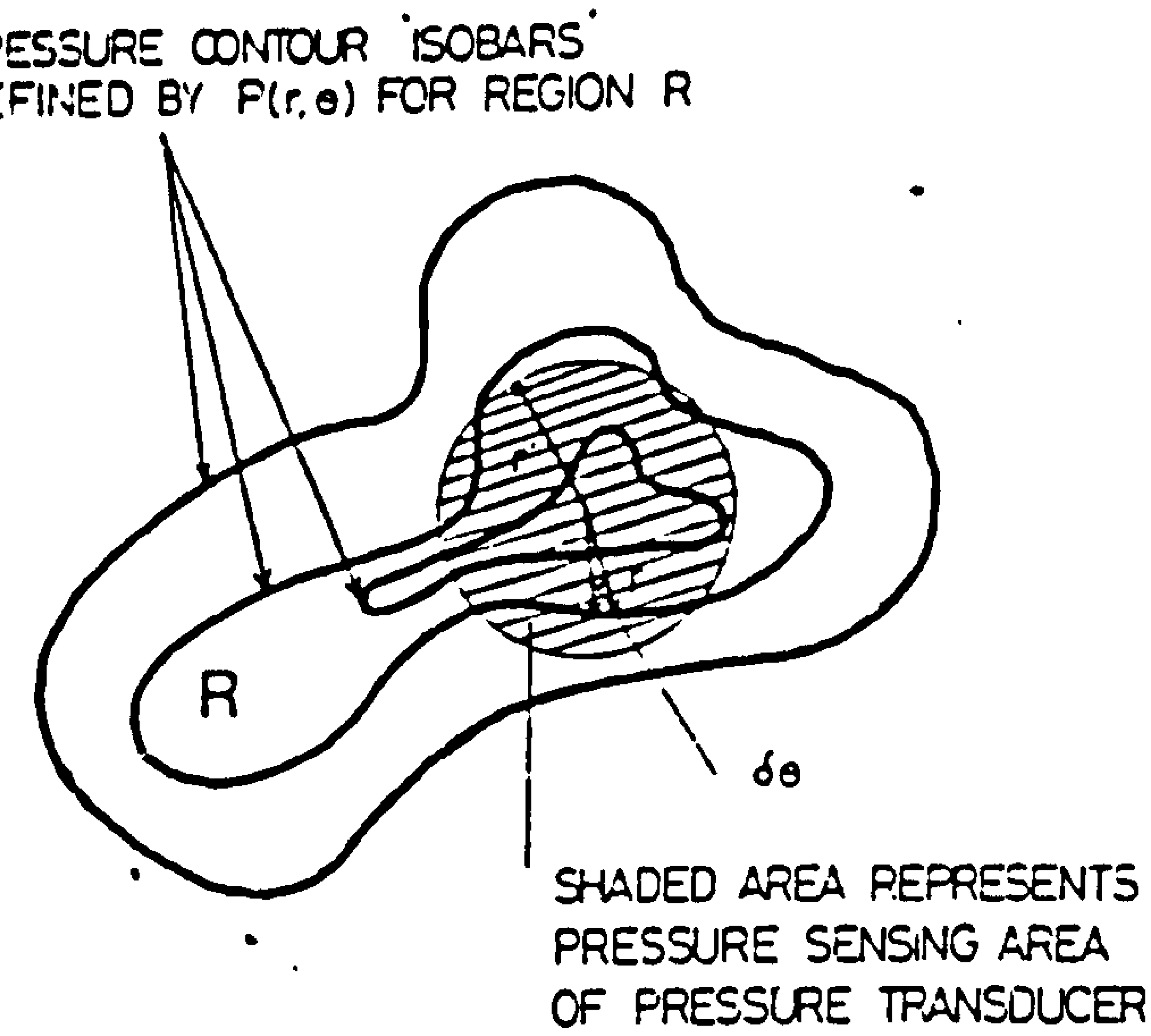

Fig. 4.4.2.1 Relationship between transducer diameter and pressure gradient.
(Ferguson-Pell, 1980)

Source of results	Transducer used, size and separation	Support material	Support position	P_m, kPa	K, kPa mm	Radius of device to measure pressure peak pressure to 5% accuracy, mm
Kosiak *et al* (1958)	Butterfly valves 20 mm × 10 mm 40 mm apart	25 mm foam	Sitting	34.6	0.49	5.2
		50 mm foam	Sitting	18.7	0.16	8.7
Lindan (1961)	Bed of spring-loaded nails Spring constant 8.2 kPa mm 14 mm apart	Bed of nails	Supine	8.0	0.07	8.6
			Sitting, legs supported	13.3	0.13	7.7
Reswick *et al* (1964)	Electro-pneumatic switches 10 mm × 10 mm 10 mm apart	25 mm foam	Sitting	27.9	0.37	5.6
Houle (1969)	Butterfly valves 20 mm × 10 mm 40 mm apart	Contoured foam 76 mm thick	Sitting	16.0	0.20	6.0

Table 4.4.2.1 Recommended sensor size for sitting position.
(Ferguson-Pell, 1980)

where P_m is the mean pressure and $P(r,\theta)$ is a function denoting the distribution of pressure measured. Assuming the pressure to be isotropically distributed and proportional to its distance from the centre of the distribution,

$$P(r,\theta) = P_p - kr \qquad (4.4.2b)$$

where k is a constant pressure gradient and P_p is the peak pressure at the centre of the distribution. Therefore substituting (b) into (a),

$$P_m = P_p - \frac{2kr}{3} \qquad (4.4.2c)$$

P_p and P_m can be expressed as percentage error E by,

$$E = \frac{P_p - P_m}{P_p} \times 100\% \qquad (4.4.2d)$$

and substituting (c) into (d) and replacing r by r',

$$E = \frac{200kr'}{3P_p}\% \qquad (4.4.2e)$$

and assuming a 5% error, the sensor radius can be expressed as,

$$r' = \frac{3P_p}{40k} \qquad (4.4.2f)$$

Ferguson - Pell has included in the study the recommended sensor size based on the data provided by Kosiak et al (1958), Lindan (1961), Reswick et al (1964) and Houle (1969) for subjects in a sitting position (Table 4.4.2.1). The sensors' radius ranged from 5.3 to 8.7 mm. However, the peak pressure measured and pressure gradient expected at the socket / residual limb interface would be greater. Therefore a smaller sensor would be required for accurate measurement. Assuming a peak pressure (P_p) of 30 kPa and a pressure gradient (k) of 0.8 kPa/mm, at 5% error, the estimated

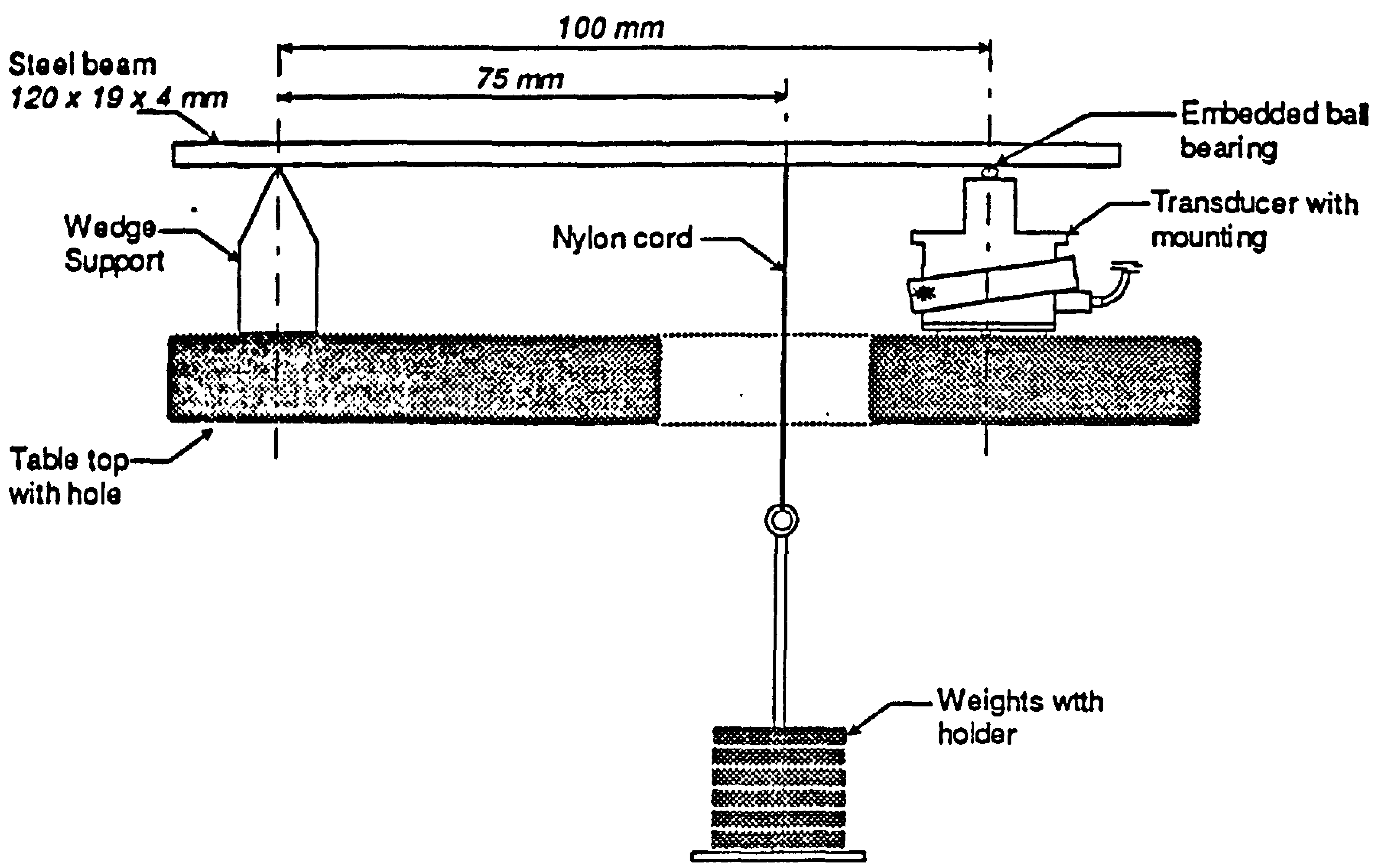

Fig. 4.4.3.1 Transducer calibration setup

radius is 2.81mm. Considering that the 30 kPa peak is on the low side, increasing the peak pressure to 100kPa with the estimated sensor radius of 2.81mm, a 5% error could still be maintained when the pressure gradient increases to 2.67 kPa/mm. The majority of the interface pressures measured in previous studies for trans-femoral amputees fall within the 0-100 kPa range, except at bony areas of the residual limb where localised pressure of above 200 kPa has been reported. In order to cater for such loading, the transducer chosen has a load range of 0 - 9 N, which gives a maximum pressure of 362 kPa based on the selected circular radius of 2.81 mm.

4.4.3 Calibration of the pressure transducers

The pressure transducer was calibrated using dead weights in its complete assembly. Each of the four transducers was individually calibrated since it was stated by the manufacturer that they posses different sensitivities (2.835, 3.088, 2.860 and 2.295 mV/lb). The transducer housing was taken apart, cleaned thoroughly and reassembled before calibration began. Calibration was performed again if the transducer had been left unused for a period of more than one month, nevertheless the transducer has shown to be extremely stable when previous calibration values were compared.

The complete pressure measurement system (described in more detail in section 4.4.4), was set-up prior to the procedures of calibration. A simple system was used to transfer loading to the sensitive area of the transducer. A steel beam supported at one end by a knife edge and the other by the transducer sensitive face, enabled weights to be hung (Fig. 4.4.3.1). The contact point on the transducer face was reduced to a point load by a ball bearing embedded in the beam. Weights were hung at 75 mm and 25 mm away from the knife edge and the transducer respectively. Thus, the total load acting on the transducer sensitive face was 75% of the hung weights. The transducer output signals were recorded on-line using a personal computer with the aid of the Acquire software or the Kistler Bioware software in either computer units or voltages respectively. The transducer was loaded and unloaded three times by sequentially placing or taking weights on or off the beam. A

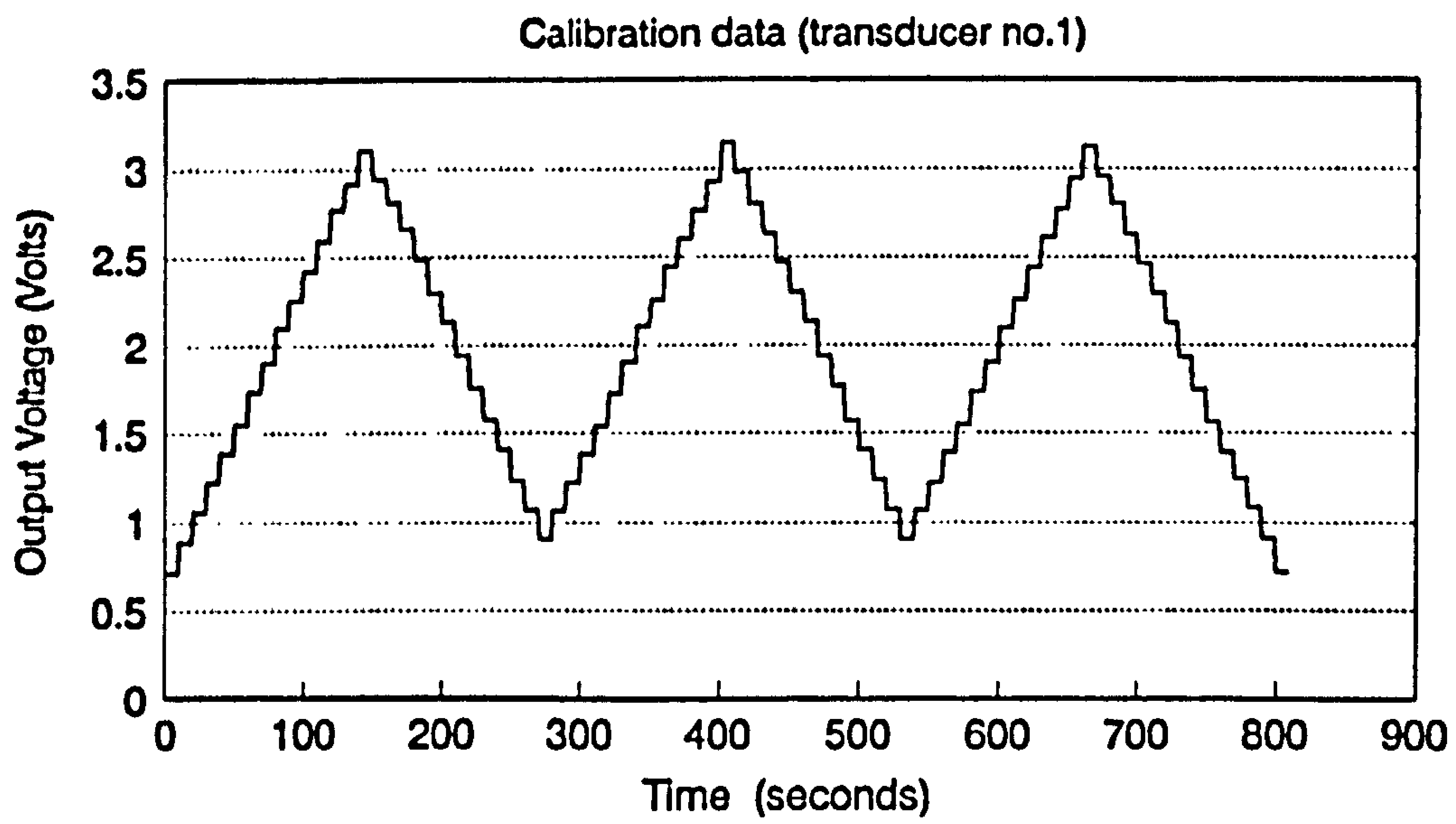

Fig. 4.4.3.2 Output signal during the process of calibration.

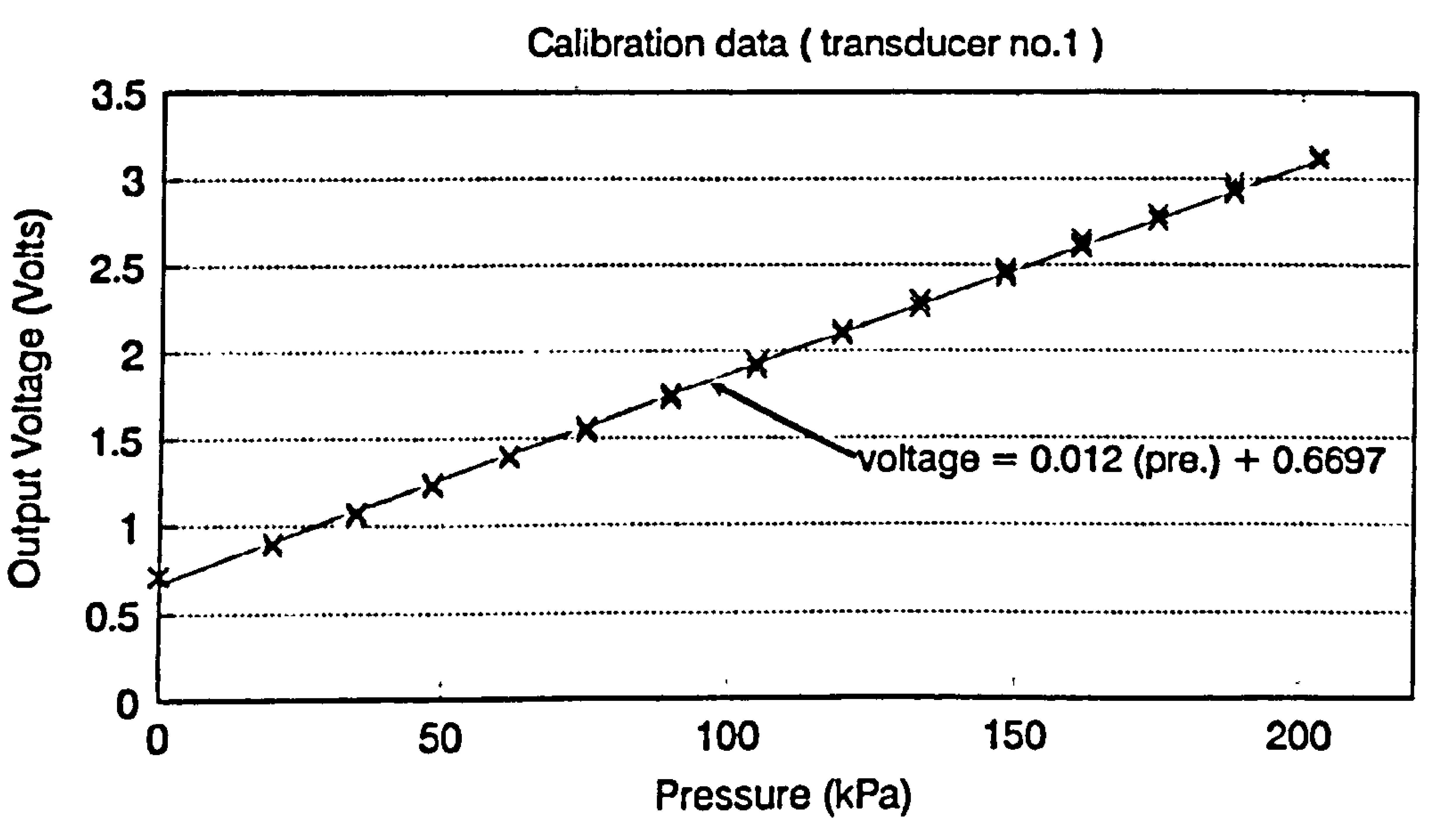

Fig. 4.4.3.3 Least square method was used to determine transducer's calibration equation.

total of 13 weights ranging from 45 to 51 grams were used. Upon placement or removal of each weight, a wait time of 10 seconds was allowed for the transducer output to be stabilised. Fig. 4.4.3.2 shows the output signals of transducer no.1 obtained over three loading and unloading cycles, recording a total of 80 points. The relationship between the output signals and the weights (expressed in pressure based on the sensitive area of the transducer) described the calibration values of transducer no. 1. Fig. 4.4.3.3 shows the plot of the transducer output voltage against pressure. A high degree of linearity could be observed. The transducer could therefore be calibrated by a simple equation of the form $y = mx + c$, where y and x are variables which in this case describes output voltage and pressure respectively, m represents the slope of the line and c the y-intercept. A least squares linear regression was used to determine this equation. The 80 points produced during the calibration process for transducer no.1 was therefore 'fitted' by a straight line $y = 0.012\,x + 0.6697$.

4.4.4 Equipment set-up

Fig. 4.4.4.1 describes the set-up for pressure measurement. The main components were the pressure transducers, the power supplies, amplifiers, control box, force platform, an axial load transducer and data acquisition system.

The transducers were connected to individual power supplies with built in amplifiers recommended by the manufacturer, model Entran PS30A-2. The power supplies were powered by the mains at 240V AC, 100mA, 50 Hz while the sensor excitation was ± 1 to ± 7.5 VDC adjustable, with a maximum current of 100 mA. The amplifiers have adjustable gain to translate the output of the transducers into output of 0 to ± 10 V with gains up to 100 times.

The full description in the circuitry of the control box is documented by Torres-Moreno (1991). The box provided signal conditioning to the inputs from the Entran transducers. However, the signals were found to be highly stable and low in noise even without the control box, thus its use became optional. Nevertheless, the control box provided an emergency stop switch which was essential for the tissue indenting device described in Chapter 6.

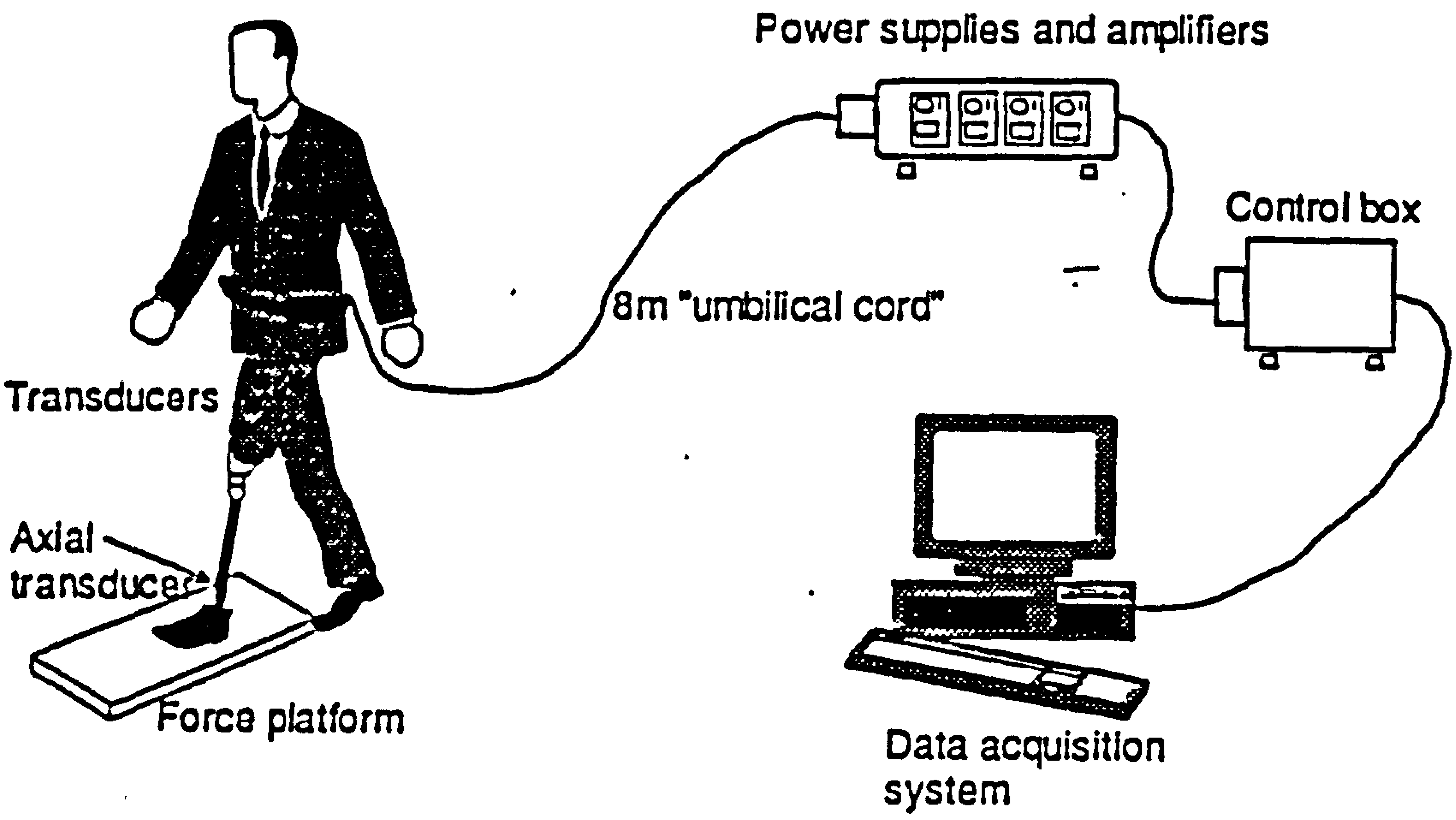

Fig. 4.4.4.1 Pressure measurement set-up

The data acquisition system consisted of a PC 286, Amplicon PC26 A/D converter card and the Acquire software. The system was later upgraded to a PC 486 using the Bioware software. The Acquire software is a general purpose acquisition software developed in the Bioengineering Unit. It allows sampling at up to 16 channels at 200 Hz. The Bioware software is available commercially from Kistler and designed for use with Kistler force platforms and transducers. The software is highly versatile in handling and processing raw data. Using this software, simultaneous data capture was possible for four pressure transducers, one Kistler force platform and also a Kistler axial load transducer (Load washer model 9031A). A total of 11 channels were used, four for pressure measurement, six for ground reaction forces and moments from the force platform and one for the axial transducer.

The commercially available axial transducer was constructed as a ring of external and internal diameter of 28.5 mm and 13 mm respectively with a thickness of 11 mm. It was fitted between the foot and shank of the prosthetic limb using the foot bolt (Fig. 4.4.4.2). Initially it was obtained to measure axial loading on the artificial limb, however, the device was able to detect moments which affected the axial load recorded significantly. In this study, only temporal information was extracted from the axial transducer, which served only as a switch to indicate heel strike and toe off.

4.5 PROSTHETIC SOCKET

As mentioned earlier in section 4.3.1, the pressure measurement test consisted of two parts. In the first part, subject H, M and U were prescribed with IC sockets by prosthetist A. In the second part, subjects M and U continued with a further test and had IC and quad sockets manufactured by prosthetist B. During the whole period of the pressure measurement test, all donning of the sockets and alignment checks were supervised and handled by the prosthetist involved.

The test sockets were modified to incorporate pressure measurement sites. These sites were basically holes made in the socket for the pressure transducers to make contact with the residual limb. Fourteen sites were allocated for the IC sockets in part one of the study. However, in part two of the study, the sockets were

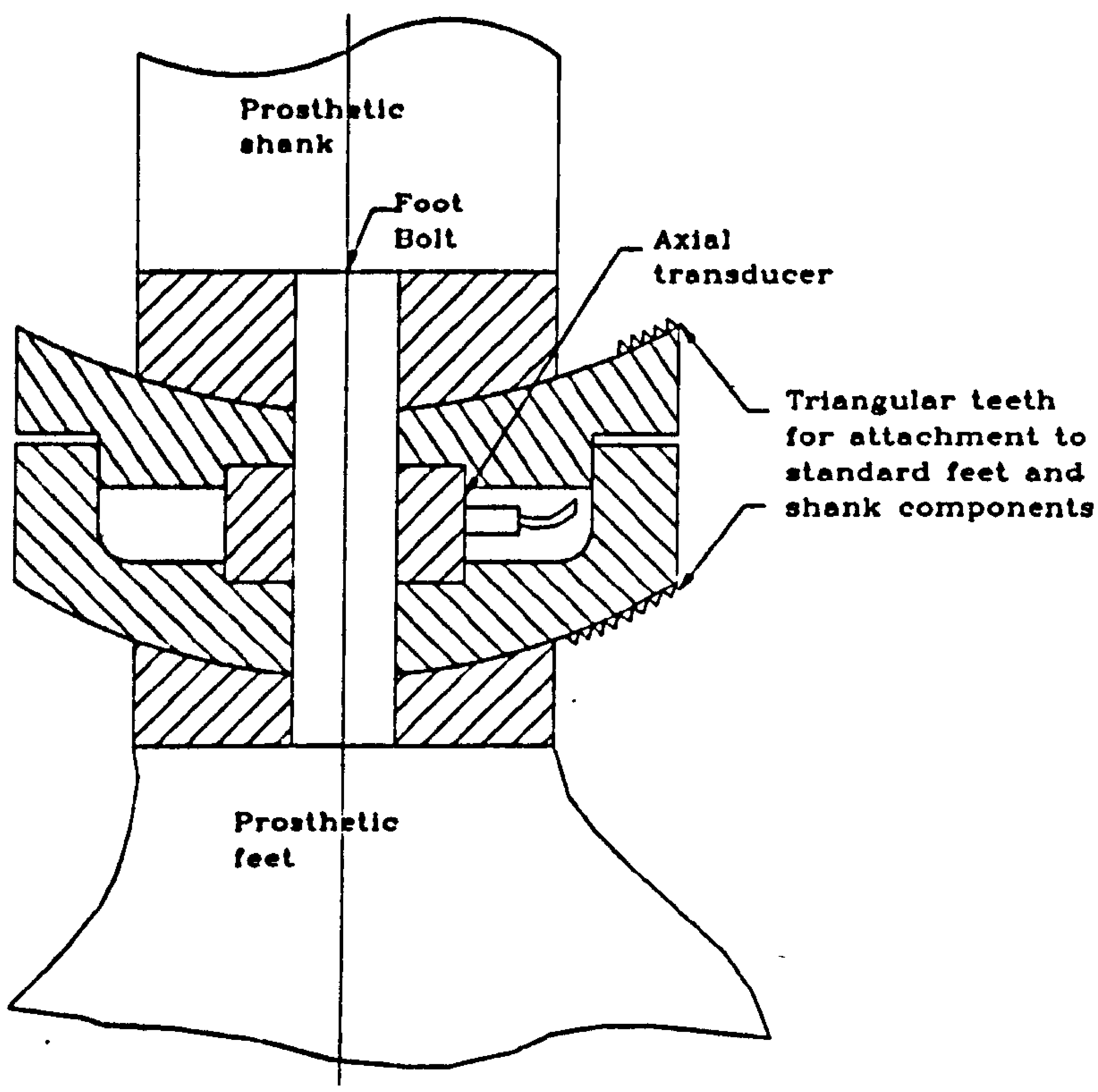

Fig. 4.4.4.2 Axial transducer assembly

laminated instead of draped, thus providing structural strength for a total of 17 sites for the IC and 15 sites for the quad socket

4.5.1 Measurement sites

The location of the measurement sites were based on a process of sub dividing the subjects' socket according to its long axis. The long axis could be defined using the procedures established at the Bioengineering Unit, with the aid of a Socket Axis Locator (SAL) (Fig. 4.5.1.1) The use of the SAL is described in detail by Szulc (1983). Briefly, the SAL was placed inside the socket and positioned with all the pointers, which were held by springs, in contact with the socket (Fig. 4.5.1.2a). The long axis of the SAL in this position was also the long axis of the socket. Such a method was used because a common axis for all the test sockets was impossible due to the unique shape of each socket. This method has been thoroughly tested and shows good repeatability. Upon defining the long axis, measurement sites could be determined. The SAL was replaced by a steel pipe while maintaining the long axis with the aid of an adjustable support. (Fig. 4.5.1.2b). The steel pipe was then permanently fixed in position by filling the socket with plaster of paris, creating a positive mould of the socket (Fig. 4.5.1.2c). With the socket removed, the positive mould was held in its long axis by clamping the steel pipe in the three-jaw chuck of a lathe (Fig. 4.5.1.2d). By rotating the plaster mould, location of measurement sites could be marked with respect to the long axis.

Two transverse planes were initially defined, 50 mm proximal to the distal end, and 25 mm distal to the medial brim of the positive mould i.e. the amputee's perineum area. Between the two transverse planes, three measuring sites were allocated at the anterior, posterior, medial and lateral sections of the socket. Another two sites ,anatomically determined, were the ischial tuberosity and the greater trochanter. The total of 14 sites applies to the IC sockets for part one of the study (Fig. 4.5.1.3a). The later IC sockets have three additional sites which were located above the proximal sites at the anterior, posterior and lateral sections, thus making a total of 17 sites (Fig. 4.5.1.3b). The quads, however, could not contain an additional

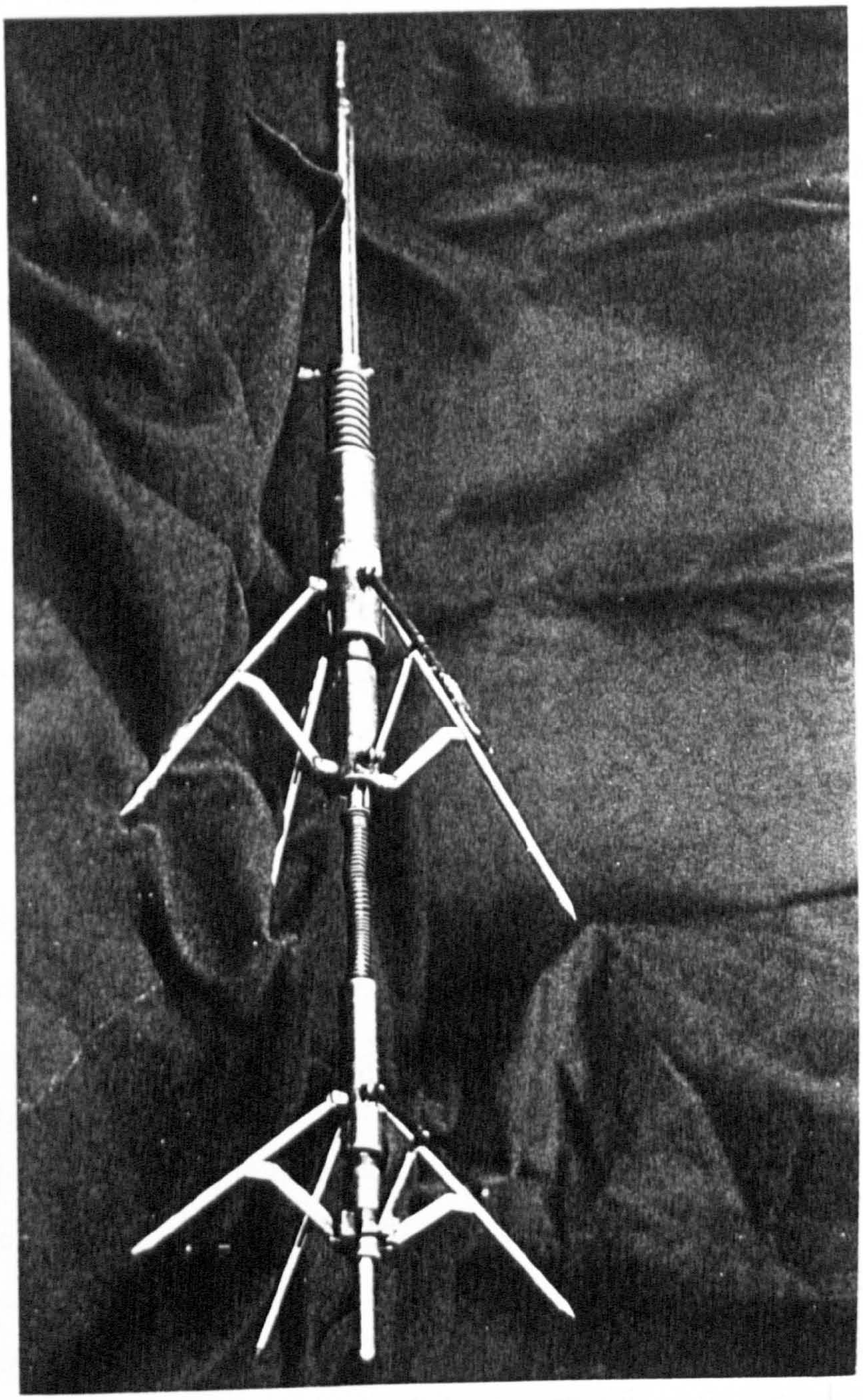

Fig. 4.5.1.1 Socket axis locator (SAL)

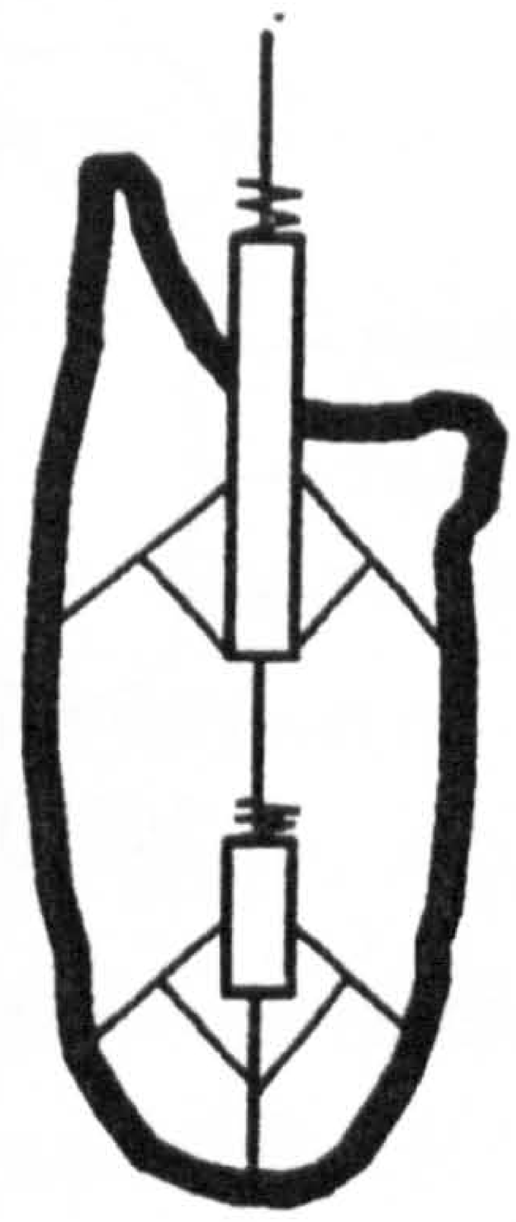

a.) Socket axis determined by SAL centre shaft.

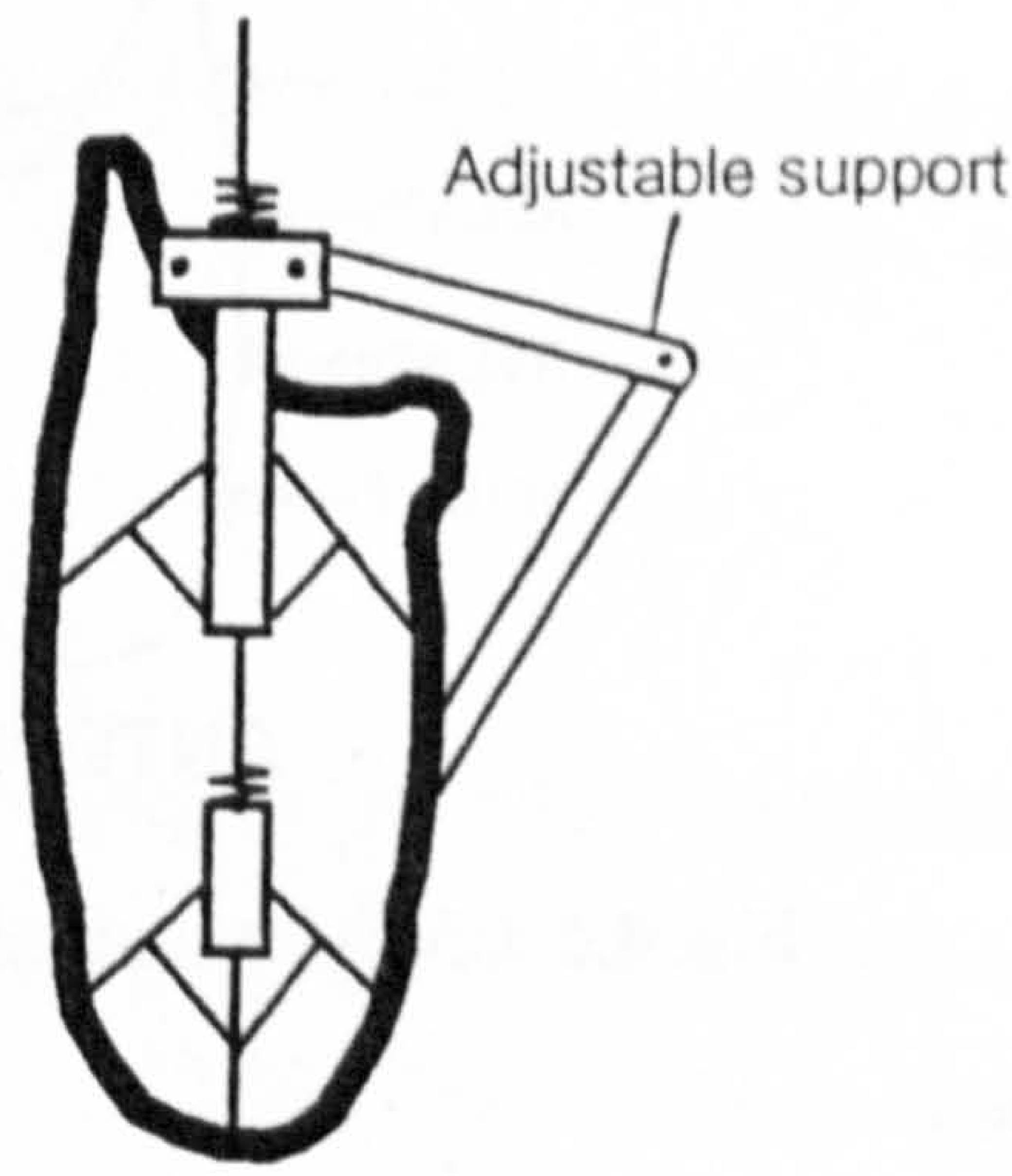

b.) An adjustable support fixed to the external socket wall kept the axis location after the SAL was removed.

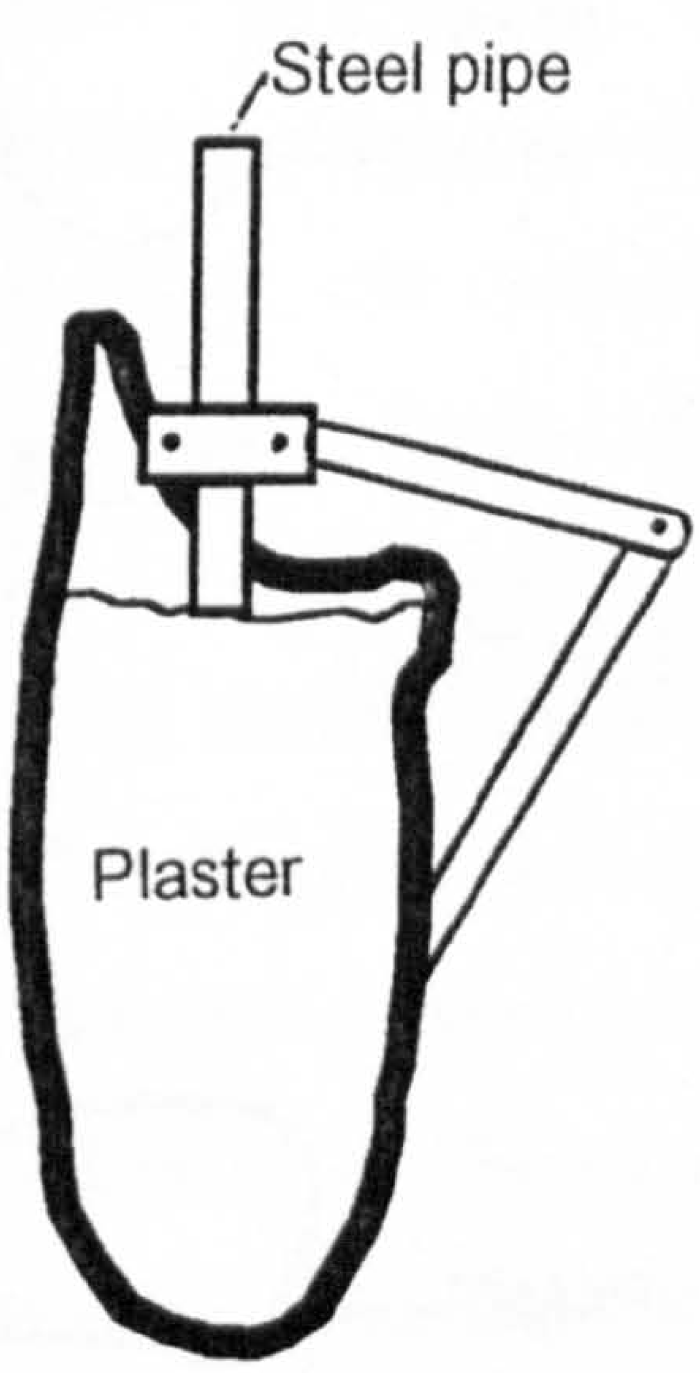

c.) The SAL was replaced by a steel pipe and plaster was poured into the socket creating a positive mould.

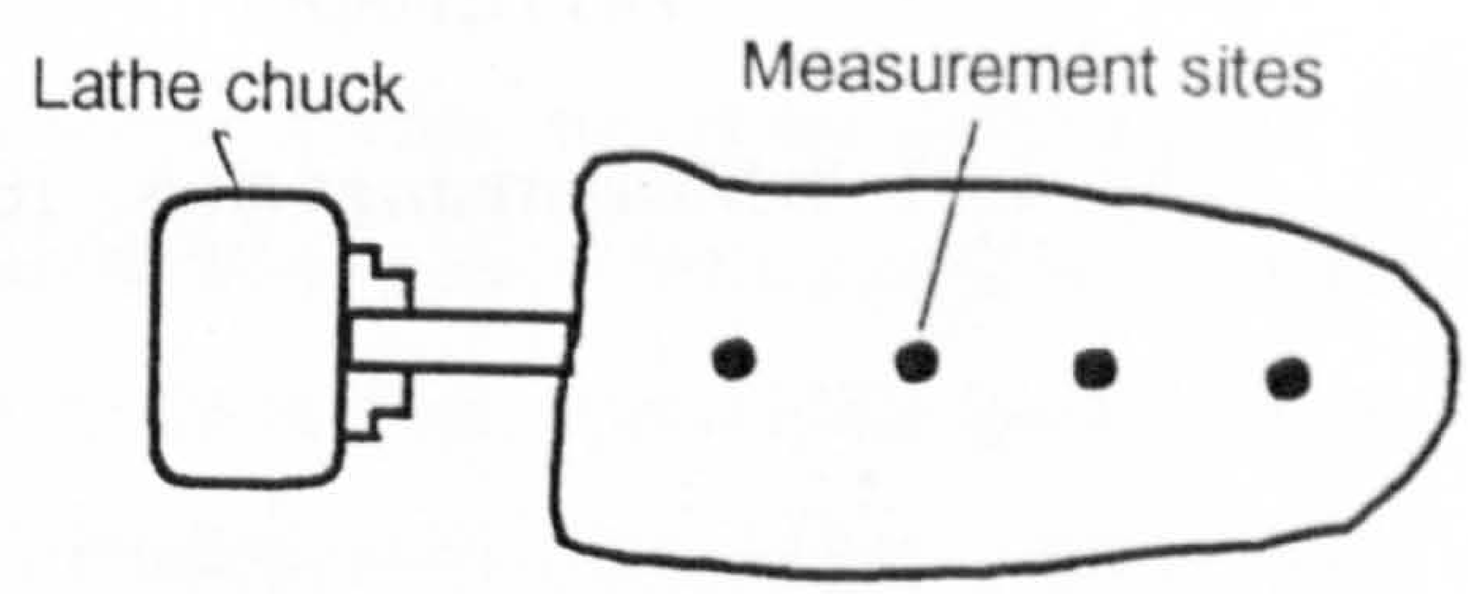

d.) The plaster mould was held in the lathe to determine the measurement sites.

Fig. 4.5.1.2 Procedures in locating measurement sites

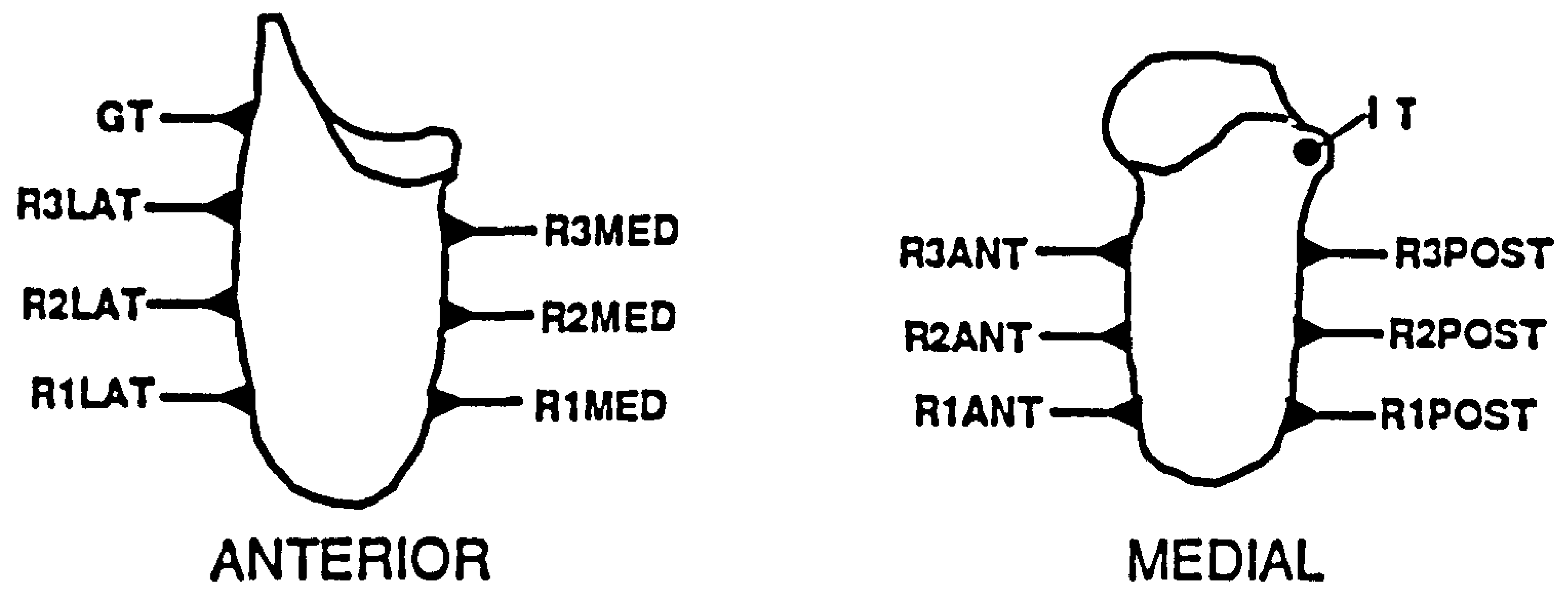

Fig. 4.5 1.3a Measurement site - IC Socket (Part One)

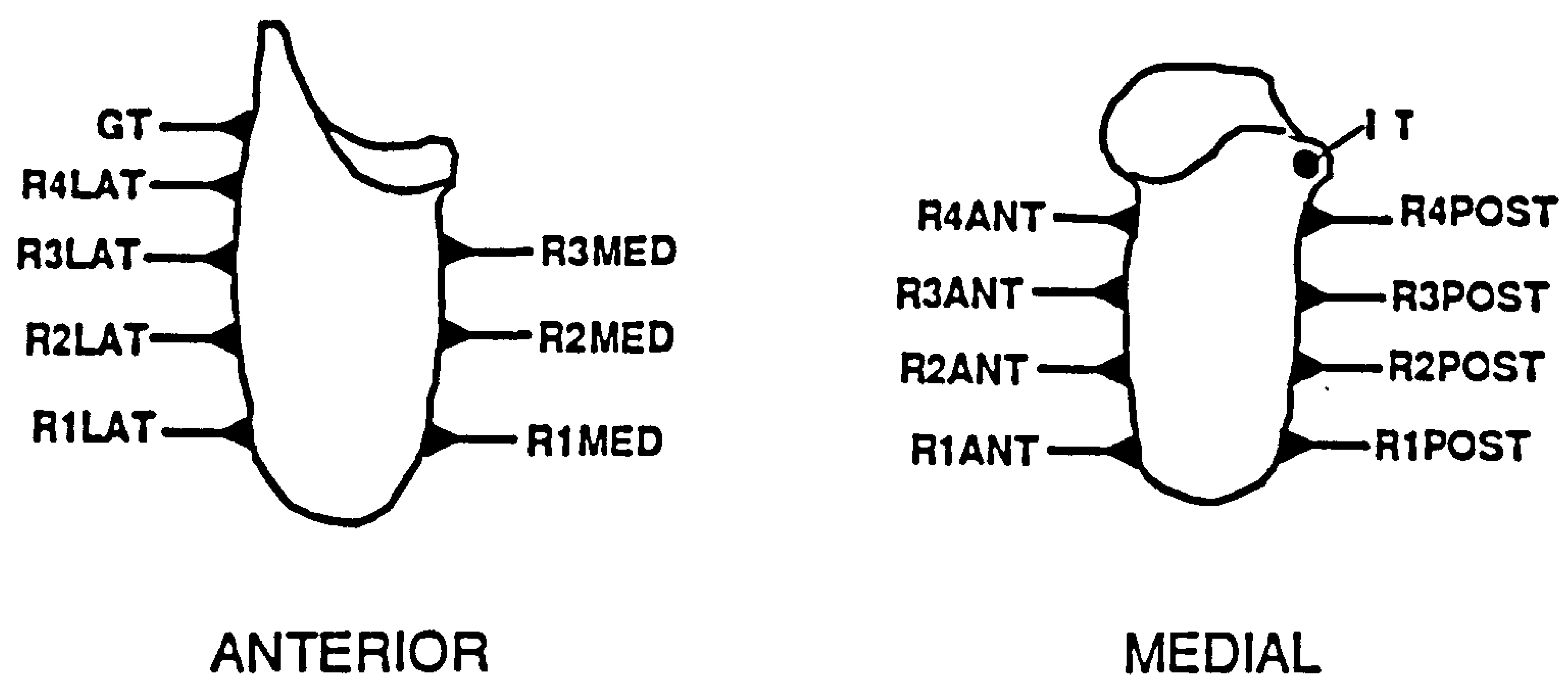

Fig. 4.5.1.3b Measurement sites - IC Socket (Part Two)

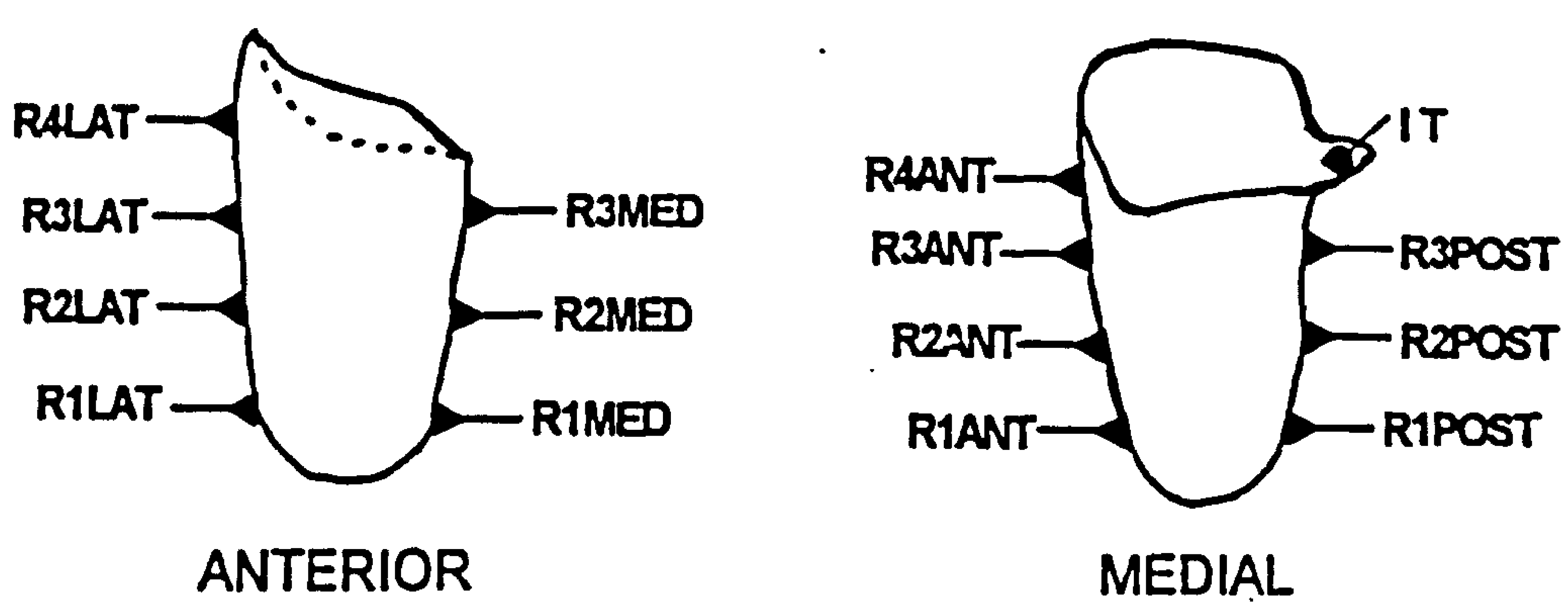

Fig. 4.5.1.3c Measurement sites - Quad Socket (Part Two)

site in the short anterior wall and did not have lateral walls that stretch over the greater trochanter, therefore they could only contain 15 sites (Fig. 4.5.1.3c). The sites were named accordingly to the anterior (ANT), posterior (POST), medial (MED) and lateral (LAT) sections corresponding to the row R1, R2, R3, R4 distally to proximally.

4.5.2 Manufacture process

The test sockets were manufactured by two traditional methods, draping for sockets in part one and lamination for sockets produced for part two. In the former case, the positive mould with measurement site markings was draped with polypropylene forming the socket. Prior to the socket removal from the mould, all site markings were transferred onto its surface. Pilot holes were drilled at the site markings which were later reamed to the correct size to fit the transducer adapters. The adapters were glued onto the socket using a two part adhesive, Loctite Prism 406 and 757 specially formulated for polypropylene and other plastics. Though the adhesive performed relatively well, due to the need for the transducer to be placed in a site several times, the adapters came loose occasionally. This led to a revised method of manufacture for the later sockets.

Standard procedures of lamination were adopted except for the inclusion of the adapters. The marked plaster mould was initially covered with a polyvinyl alcohol (PVA) bag. The adapters were positioned at the marked sites on the surface of the mould using pins and plasticine, with their threaded sections protected by PTFE tape. Dacron and fibre glass fabrics were then wrapped around the mould leaving the adapter's area clear. A further PVA bag sandwiched the entire mould and acrylic resin was then introduced between the PVA bags under a vacuum environment. The Dacron and fibre glass fabrics and the adapters were therefore embedded together by the resin forming the test socket.

4.6 STAGES OF PRESSURE MEASUREMENT TEST

Pressure, ground reaction forces and temporal parameters were collected simultaneously. Prior to any measurement, the subjects were given at least 15 min walking with the prosthesis to get used to the test socket. Once a comfortable fit was established, all data collection was performed on the same day without the subjects doffing the socket at any interval during the test. Due to subject fatigue, the test was limited to only one socket per test day.

The tests for each subject were divided into static, dynamic and unloaded stages.

4.6.1 Static test (normal standing interface pressure)

In the static test, the subject was positioned close to the force platform. Force platform data and interface pressure acquisition began about 2-4 seconds prior to the subject stepping onto the force platform, with feet an equal distance apart as in a normal standing position. Recording was continued for a further 6-8 seconds, enabling a collection of stable static measurements of pressure and ground reaction forces. The data were acquired at a frequency of 50 Hz. The axial transducer was disabled during the test.

4.6.2 Dynamic test (normal walking interface pressure)

The dynamic test required the subject to walk a distance of approximately 8 metres at normal walking speed, stepping onto the force platform at approximately midway through the walk. Data capture lasted for 10 seconds at 200 Hz and began only after one complete step of the artificial limb. Data collected included ground reaction forces, interface pressures and axial transducer signals indicating heel strike and toe off.

4.6.3 Socket suspension interface pressure measurement

In the final test sequence, an attempt was made to record the interface pressure caused purely by the socket fitting. The prosthetic limb was fully dismantled

Transducer placement set number.	MEDIAL			LATERAL				POSTERIOR				ANTERIOR					
	R1	R2	R3	R1	R2	R3	R4	R1	R2	R3	R4	R1	R2	R3	R4	IT	GT
1	PT1 PT1*			PT2 PT2*				PT3 PT3*				PT4 PT4*					
2		PT1 PT1*			PT2 PT2*				PT3 PT3*				PT4 PT4*				
3			PT1 PT1*			PT2 PT2*				PT3 PT3*				PT4 PT4*			
4			PT1*				PT2				PT3				PT4 PT4*	PT3*	PT1 PT2*
5	PT2 PT2*	PT3 PT3*	PT4 PT4*													PT1	PT1*
6	PT2*		PT2	PT1 PT1*	PT3 PT3*	PT4 PT4*											PT1*
7								PT1 PT1*	PT2 PT2*	PT4 PT4*					PT3 PT3*		
8											PT4	PT1 PT1*	PT2 PT2*	PT3 PT3*		PT4*	
9							FT1		PT2							PT3	PT4

Table 4.6.4.1 Order of transducer placement.
PT (1,2,3,4) indicate transducers' number, IC socket.
PT (1,2,3,4)* indicate transducers' number, quad socket.

after the dynamic test, leaving the socket on the residual limb. The subjects were then requested to rest the residual limb on a stool adjusted to a suitable height that enabled normal standing posture to be adopted. Data capture at 50 Hz began and after 2 seconds, the subject was cautioned to stand on the good limb while the stool was removed. After another 8 seconds, the stool was placed back in position. This test was only performed for subjects U and M in part two of the study.

4.6.4 Transducer placement and number of test

A total of eight and nine sets of transducer placements respectively for the quad and the IC socket (four transducer at a time) were required to complete the pressure measurements in each test routine. The sequence of transducer placement adopted is explained in Table 4.6.4.1. The placements enabled each measurement site to be visited by at least 2 different transducers, thus maintaining a check for faults and consistency in the equipment. For each transducer placement, three recordings were made. Therefore a total of six sets of data were collected for each site. This meant that the subject with the quad socket was required to stand 24 times each in the static and the unloaded test and walk 24 times in the dynamic test, while in the case of the IC socket 27 times. Due to fatigue, the patient was requested to rest 5 min at every phase of transducers repositioning.

4.7 INTRODUCTION TO RESULTS

The results will be presented in two main parts as described earlier in section 4.3.1. i.e. part one are pressures measured on three subjects prescribed with IC sockets and part two, pressures on two of the three subjects that participated in the further test fitted with both quad and new IC sockets. In each of the two parts, results will be separated into static, dynamic and unloaded. All pressure values will be indicated in kPa. Ground reaction forces and temporal-distance measurement will not be discussed in detailed in this chapter. These will be reserved for in chapter five, where the gait of the subjects will be analysed.

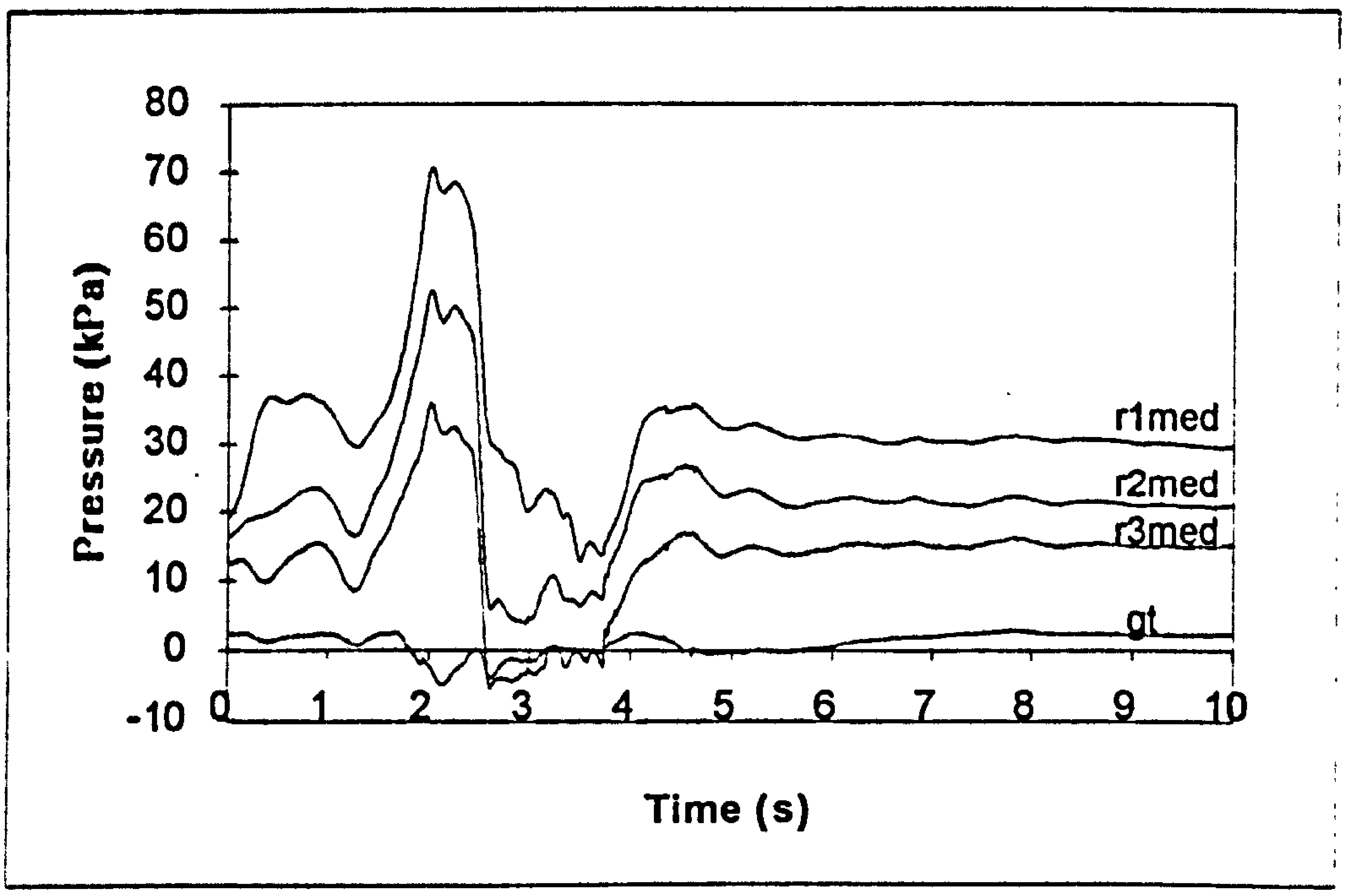

Fig. 4.7.1.1 Stable interface pressure obtained after approximately 6s during standing test. (Subject H)

4.7.1 Analysis of results

Basically, the pressures at individual measurement sites were averaged to produce a mean interface pressure. In the static and socket suspension test, the sampled pressures were averaged during the period of data capture and then further grouped accordingly to the measurement sites and averaged for different trials. At the initial phase of data capture, the data collected were considered unstable, since this involved the amputee stepping onto the force platforms or resting on the stool in the static and socket suspension test respectively. Thus the data that were analysed began only when the transducer output remained stable. The stable signal could be identified clearly when the output signal was plotted against time (Fig. 4.7.1.1).

In the dynamic test situation, only pressures at the particular step where the prosthesis contacted the force platform were considered. At the start and end of gait, the dynamic pressure profile differed significantly from pressures recorded at the middle of the walkway i.e. near the force platform, largely due to the effects of acceleration and deceleration during gait. Nevertheless, steps which were near the force platform produced pressure profiles that were repetitive. However, there was no attempt to average these pressures for individual steps within one trial because force platform data were only available for one step. In the construction of the FE model, loading calculated from the force platform was introduced as loading condition. In order to be consistent in the verification procedure, pressure values that were used to verify the model must also correspond to the force platform reading. Therefore the pressures and force platform data were only averaged between trials but not between the steps in a single trial. The data collected at different trials were subjected to variability in terms of number of points collected, since the subject speed was expected to change from step to step. Simply averaging the data between trials would produced distorted pressures profile. Thus, prior to the process of averaging, the data had to be normalised to 100% of the gait cycle.

4.7.2 Normalising dynamic interface pressures

Normalisation was performed using Fourier analysis. The dynamic pressure profiles could be represented in the form of sine and cosine terms with Fourier coefficients. The acquired data q_i (i = 1, 2, 3.....N), where N is the number of actual points collected between heel strikes were normalised to 100 points (M), indicating 100% of the gait cycle.

Andrews (1982) discussed the need to firstly detrend the data to avoid introducing bias in the reconstructed patterns. This was performed using the equation,

$$\hat{q}_i = q_i - q_1 - \tfrac{q_N - q_1}{N-1}(i-1) \qquad (4.7.2a)$$

where i = 1,2,3 ..... N and $\hat{q}_i$ are the detrended data and q_i is the point under consideration.

The Fourier coefficients were obtained using the following relations :

$$A_o = \tfrac{2}{N-1}\sum_{i=1}^{i=N}\hat{q}_i \qquad \text{and}$$

$$A_j = \tfrac{2}{N-1}\sum_{i=1}^{i=N}\hat{q}_i.\cos\frac{2\pi j(i-1)}{(N-1)} \qquad \text{and}$$

$$B_j = \tfrac{2}{N-1}\sum_{i=1}^{i=N}\hat{q}_i.\sin\frac{2\pi j(i-1)}{(N-1)} \qquad (4.7.2b)$$

where j = (1,2,3 .... N) and N = 10.

The final normalised data were reconstructed as ,

$$q_k = q_1 + \tfrac{q_N - q_1}{M-1}(k-1) + \tfrac{A_o}{2} + \sum_{j=1}^{j=n} A_j.\cos\frac{2\pi j(k-1)}{M-1} + \sum_{j=1}^{j=n} B_j.\sin\frac{2\pi j(k-1)}{M-1} \qquad (4.7.2c)$$

where k = 1,2,3 ...... N and M =100.

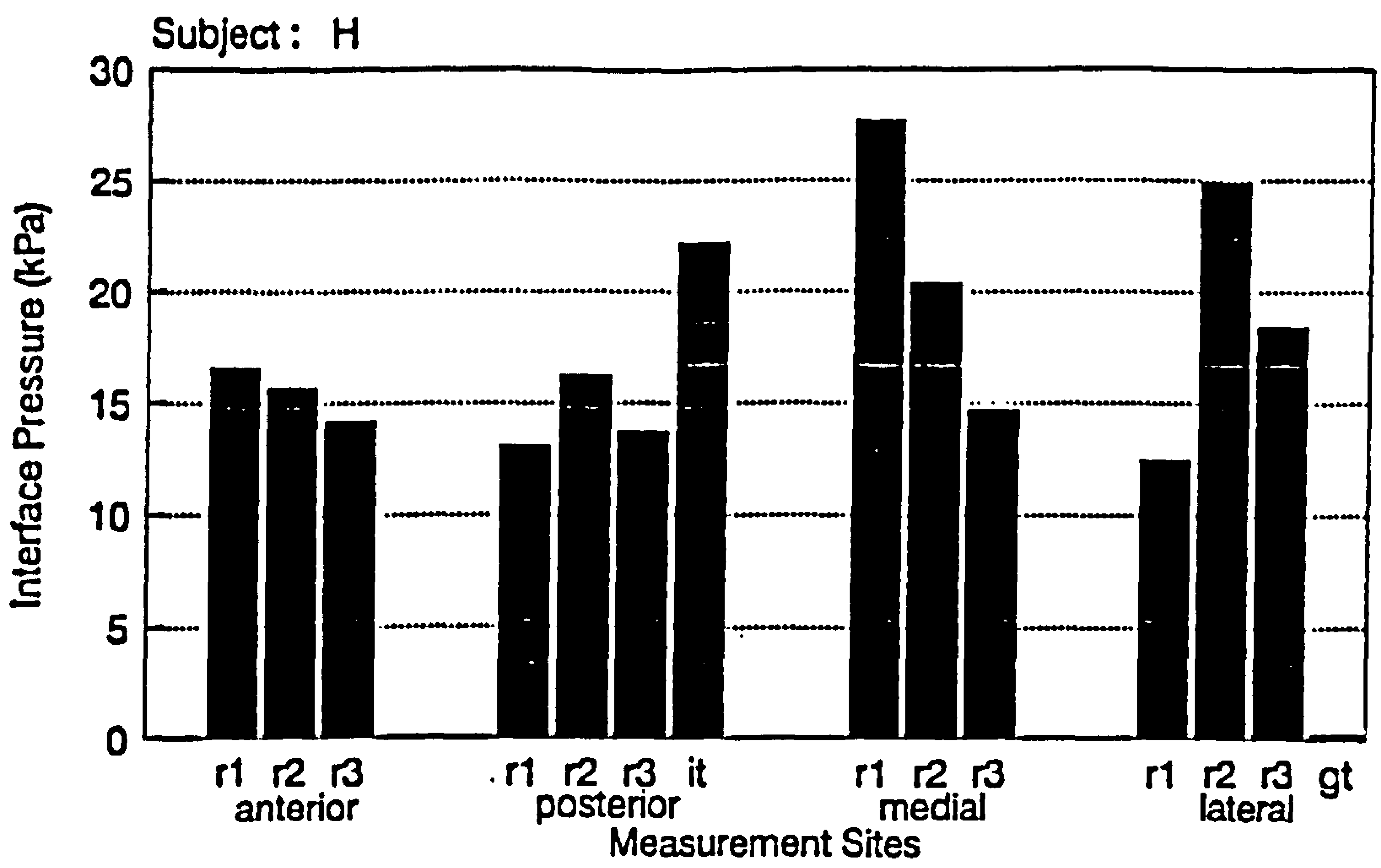

Fig. 4.8.1.1 Subject H standing pressures

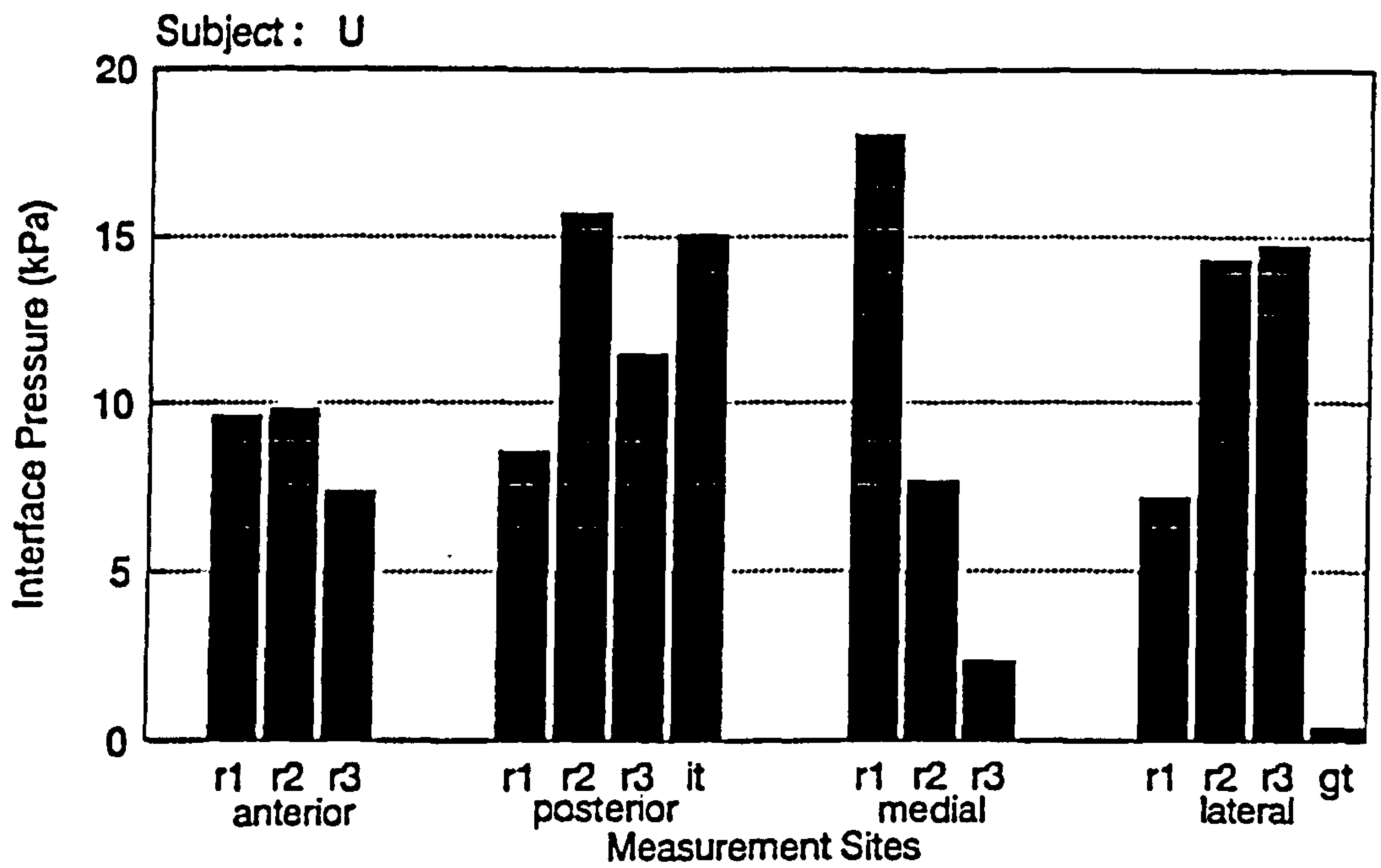

Fig. 4.8.1.2 Subject U standing pressures

The procedure thus enable the measured pressures to be express as 100% of the gait cycle.

4.8 RESULTS : PART ONE

This section consist of pressures measured using the IC sockets described as part one of the study with subjects H, U and M.

4.8.1 Normal standing pressure

Fig. 4.8.1.1, 4.8.1.2 and 4.8.1.3 illustrate the standing pressures experienced by the three subjects. The pressures measured in subject H ranged from 12 -28 kPa with the exception of site GT where almost zero pressure was recorded. Other than site GT, the pressures were distributed relatively evenly throughout the residual limb. Pressures at the medial side increased towards the distal end peaking at 28 kPa. A detectable trend could be seen in the pressure profiles at the lateral side which were opposite to that of the medial side, decreasing towards the distal end. Anterior and posterior walls pressures were very consistent and around 15 kPa. Pressure at the ischial tuberosity (IT) was the third highest and measured at 23 kPa.

The pressure profiles in subject U were very similar to subject H but of lower magnitude. Measured pressures ranged from 2-17 kPa, again with the exception that site GT, near zero pressure was recorded. The medial wall pressures increased towards the distal end while lateral wall pressures increased towards the proximal end of the residual limb. Maximum pressure was recorded at site R1MED, similar to subject H. Anterior and posterior walls pressures were distributed evenly at approximately 10 kPa except at site R2POST (16 kPa).

Subject M's standing pressures were significantly different from the other two subjects. Pressures measured at two particular sites, R2ANT (33 kPa) and IT (30 kPa) were about 60% higher than the rest of the other sites, where pressures recorded were within a small range of 9-14 kPa. Also by contrast to the subjects H and U, site GT pressure was noticeable and of the same order of magnitude as the majority of the other sites.

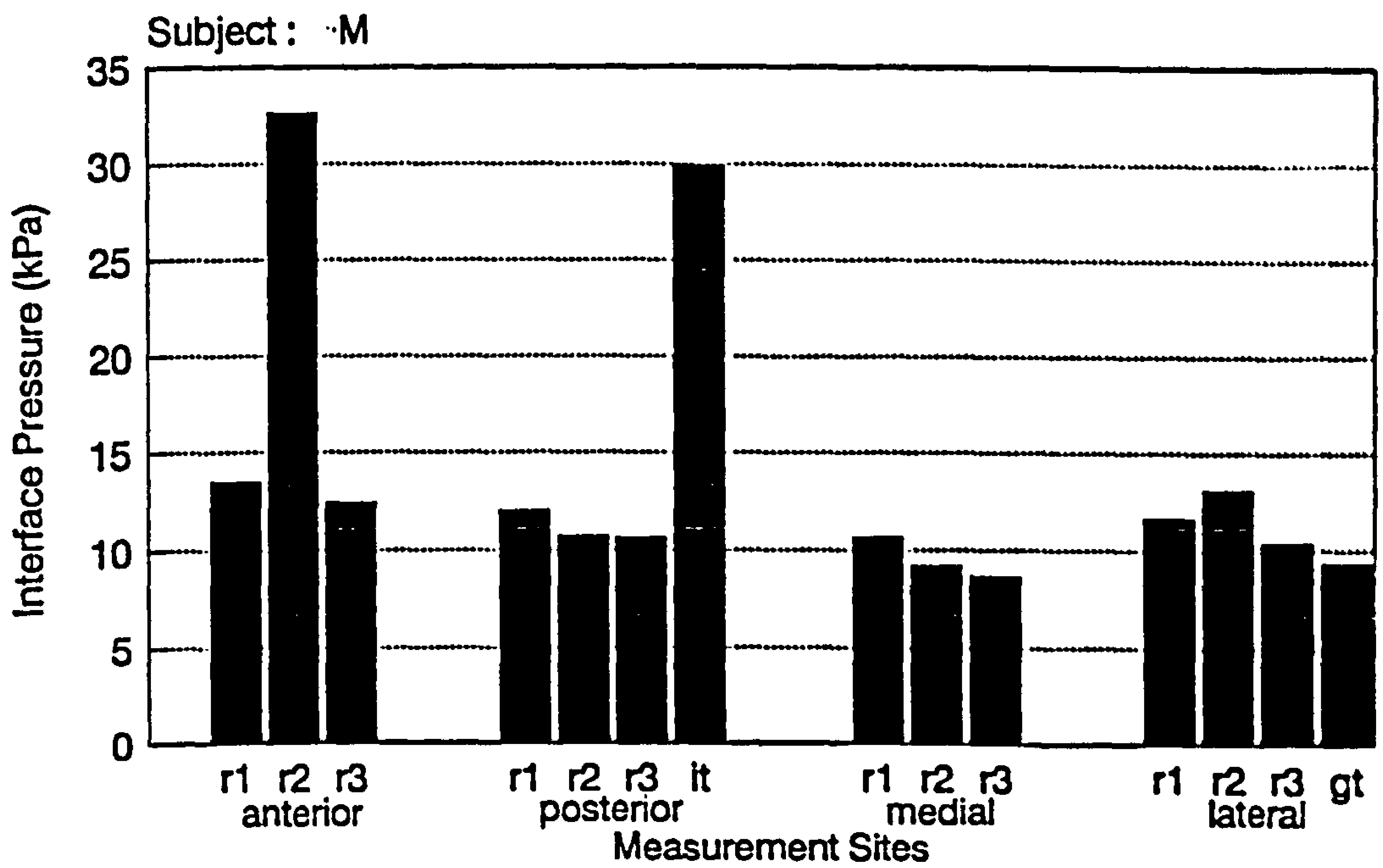

Fig. 4.8.1.3 Subject M standing pressures

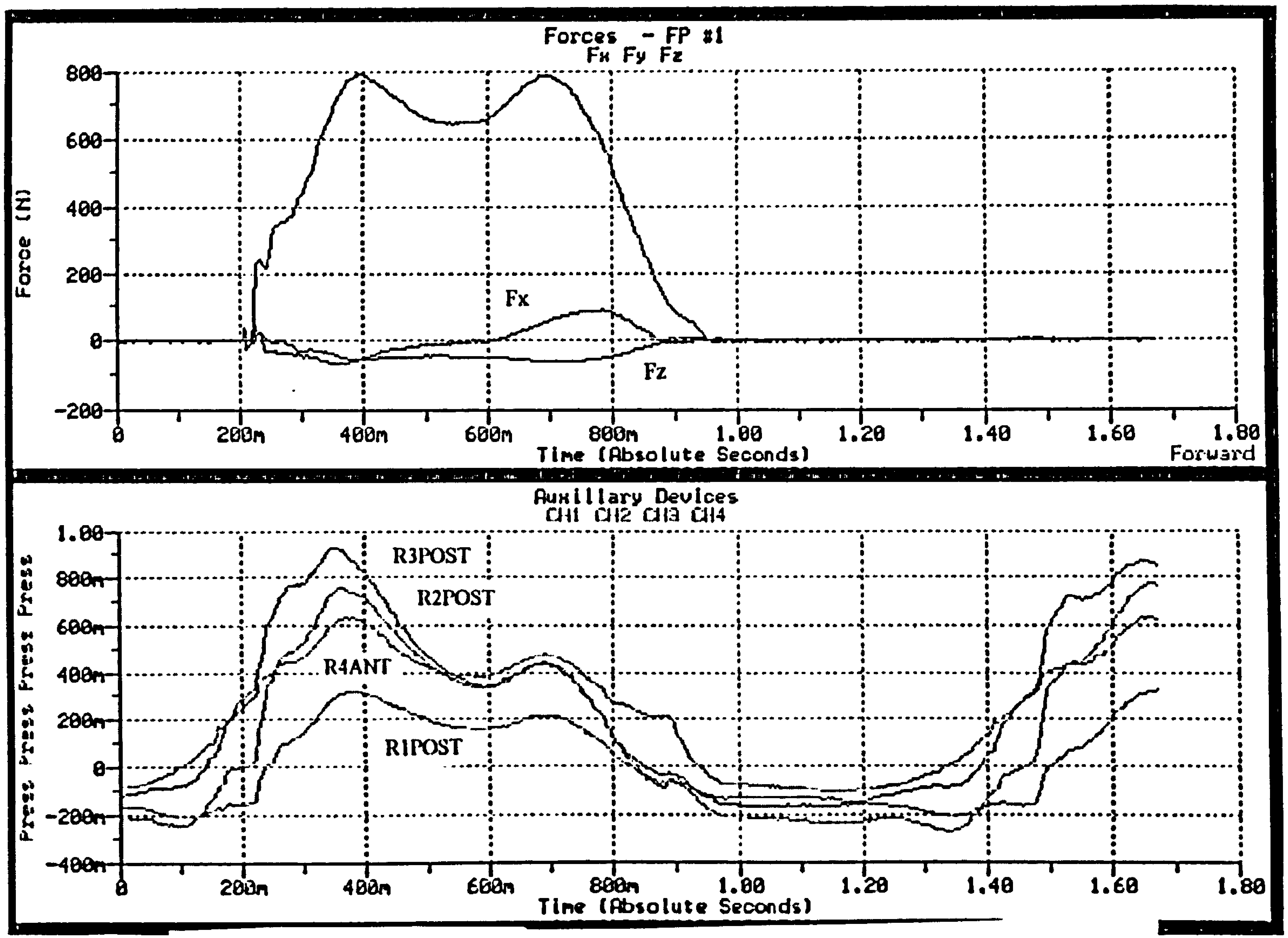

Fig. 4.8.2.1 Raw data showing ground reaction forces (GRF) and measured pressures.
Note : Y- axis scale for GRF in Newtons.
Y- axis scale for pressures in Volts.

4.8.2 Normal walking interface pressure

The interface pressures during the stance phase of walking at most sites showed a two peak and a trough pattern. This pattern followed closely to the vertical component (Fy) of the ground reaction force (GRF). Fig. 4.8.2.1 plots the raw data of both interface pressures and ground reaction forces recorded simultaneously. The plot is fairly representative of the interface pressures measured during walking in this study, thus will be generalised as a typical dynamic pressure profile.

Prior to heel strike ($\approx$100 ms), the pressures began to increase gradually. This was due to musculature contraction in preparation for heel strike. In a previous study by Pearson et al (1974), muscular contraction in the trans-tibial residual limb has been shown to produce pressures twice those that occur when the muscles were relaxed. The rate of increase in pressures in this short time frame before heel contact was dependent on the residual limb pre-stress (suspension) pressures and the location of the sites. Higher rates of increase were seen at the proximal sites which had higher pre-stress pressures.

At heel strike, the pressures increased almost instantaneously which was followed by a steep climb to the first peak. The pressure profiles at early stance consisted of high frequency components which could be due to the deformation of the prosthetic foot or musculature activity. Comparing the measured pressures with the Fy component of the GRF, the first peak in the pressure profiles occurred about 50 ms before Fy reached a peak value. After the first peak, pressures began to decline forming the trough portion of the two peaks' profile. The lowest point in the trough did not occur at the same time as that in Fy, but was delayed by about 100 ms. It was not clear why the first peak and the lowest point of the trough did not match that of Fy. The time difference may be due to slippage between the residual limb and the socket during gait, and the mechanical response of the soft tissues.

During push off, pressures increased to form a second peak which was lower in magnitude than the first, yet Fy displayed similar magnitude in both first and second peak. A probable explanation may be found in the viscoelastic behaviour of the soft tissue in the residual limb when subjected to loading. At heel strike, the residual limb soft tissue was subjected to load which could cause a migration of fluids changing its overall mechanical properties. When subjected to further loading, the soft tissue response would therefore be different from the first applied load. There was little chance for the residual limb to return to the physical state prior to heel contact since it was constantly under load during stance. The second peak in the measured pressure was in phase with the second peak in Fy. Pressures decreased gradually towards the end of stance and high frequency components which again may be due to slippage at the interface or muscles' activities could be seen at this stage.

Fig. 4.8.2.2 to 4.8.2.7 plot the interface pressure over 100% of the gait cycle for subjects H, U and M.

Subject H

The pressures measured in Subject H fall between -10 kPa and 78 kPa. The negative pressures indicated that suction occurred at the residual limb / socket interface. Although the transducers have been calibrated in depth for positive pressures only, preliminary calibration test using a manometer set up indicated that the transducers were able to detect negative pressures. However, it must be cautioned that the accuracy of the negative pressures was questionable, since the transducers were originally designed by the manufacturer for positive load only. As seen later in the results, the negative pressures usually occurred during the swing phase in very short period. In this study, positive pressures are investigated in more detail.

Maximum pressure was recorded at site R2LAT at 10% of the gait cycle. The pressure profile observed in most sites differs from the typical two peak profile. An initial rise in pressure just after heel strike was followed by a more or less constant pressure profile throughout stance with undulating peaks. Pressures at the medial, posterior and anterior walls were evenly spread. Lateral wall pressures recorded high values at the mid section. Almost zero pressure was recorded at site GT. The GT site was considered as a pressure intolerant site due to the bony prominence of the greater trochanter, thus the prosthetist aimed to create a relief at this area in the socket while

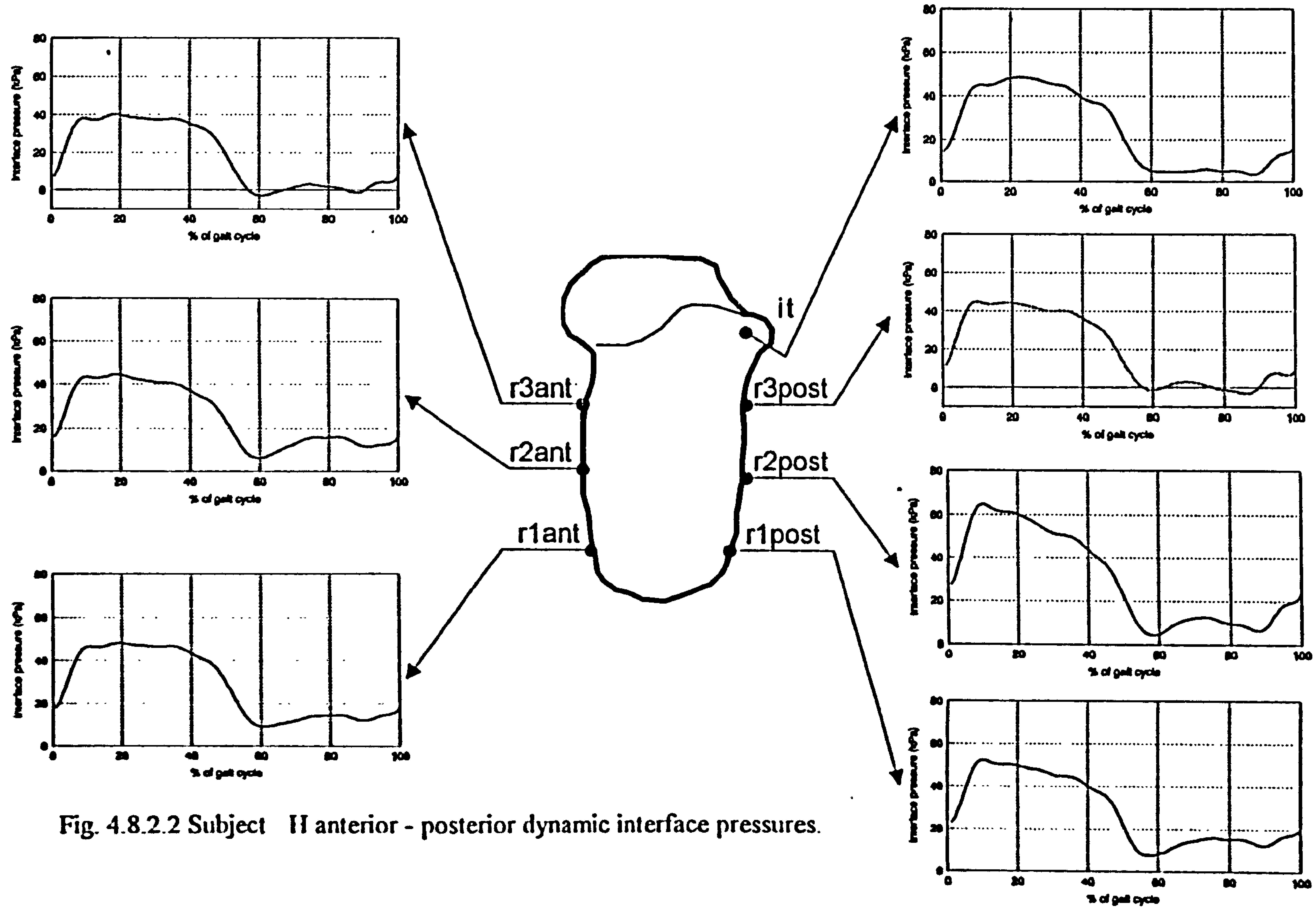

Fig. 4.8.2.2 Subject II anterior - posterior dynamic interface pressures.

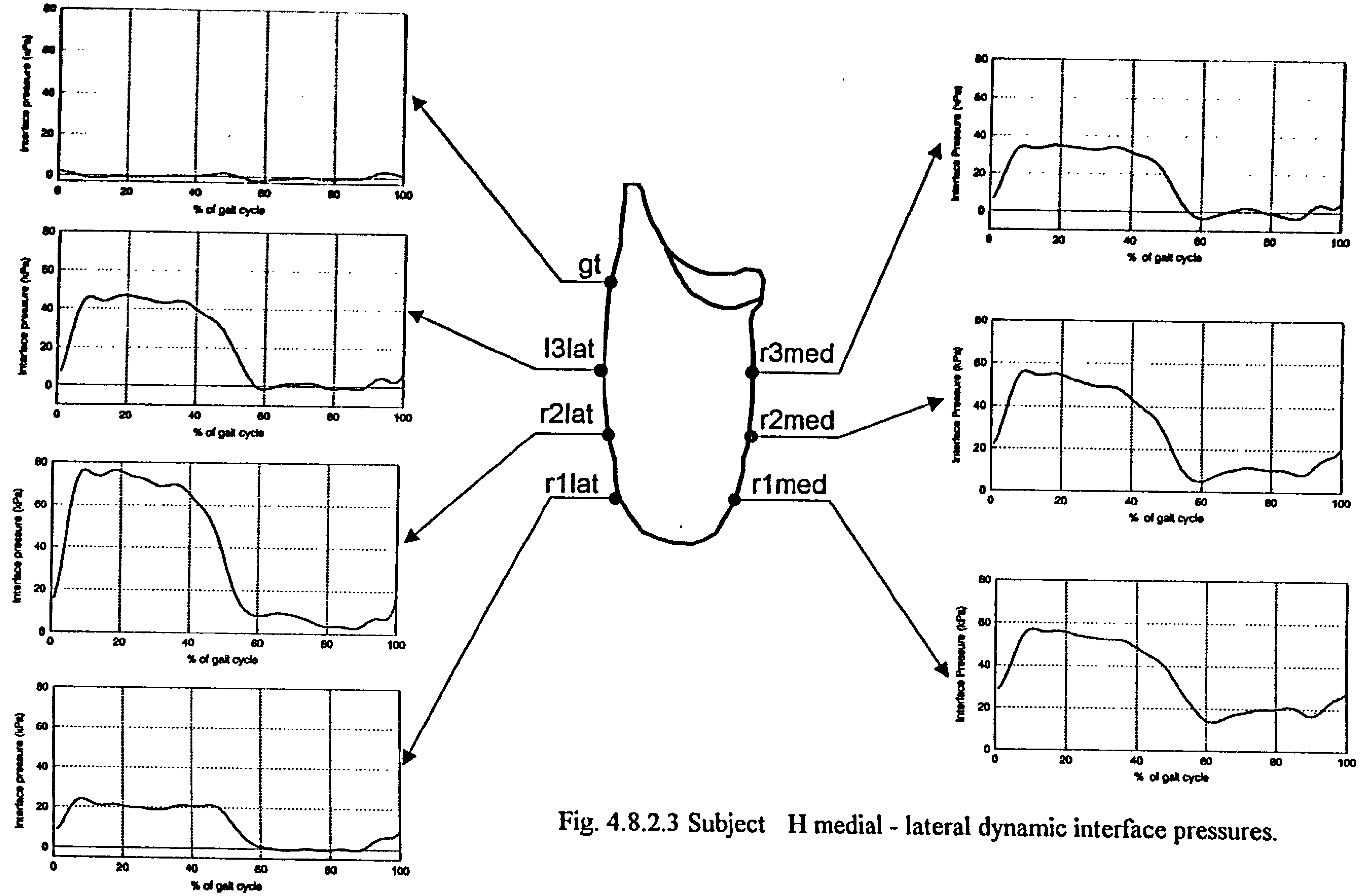

Fig. 4.8.2.3 Subject H medial - lateral dynamic interface pressures.

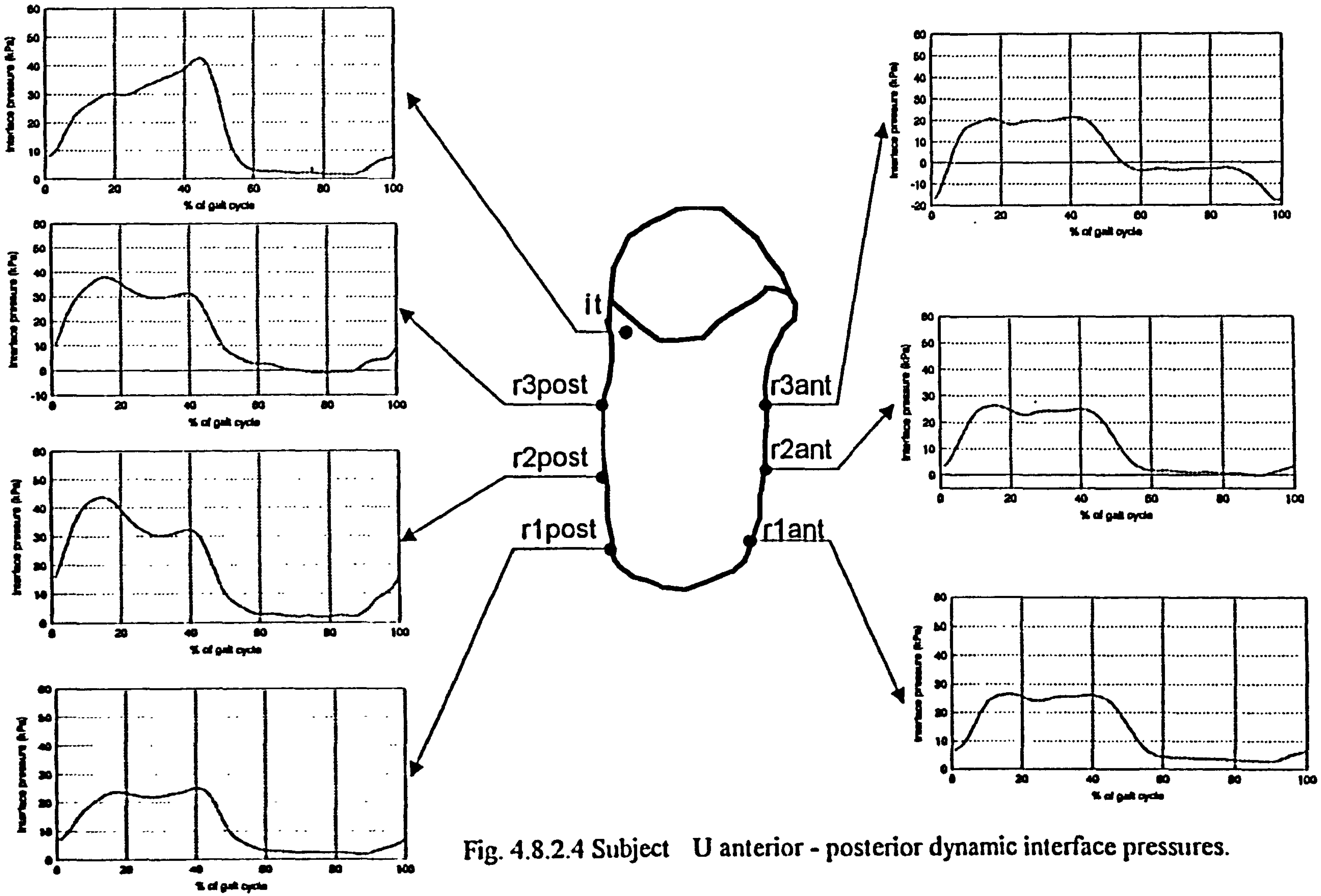

Fig. 4.8.2.4 Subject U anterior - posterior dynamic interface pressures.

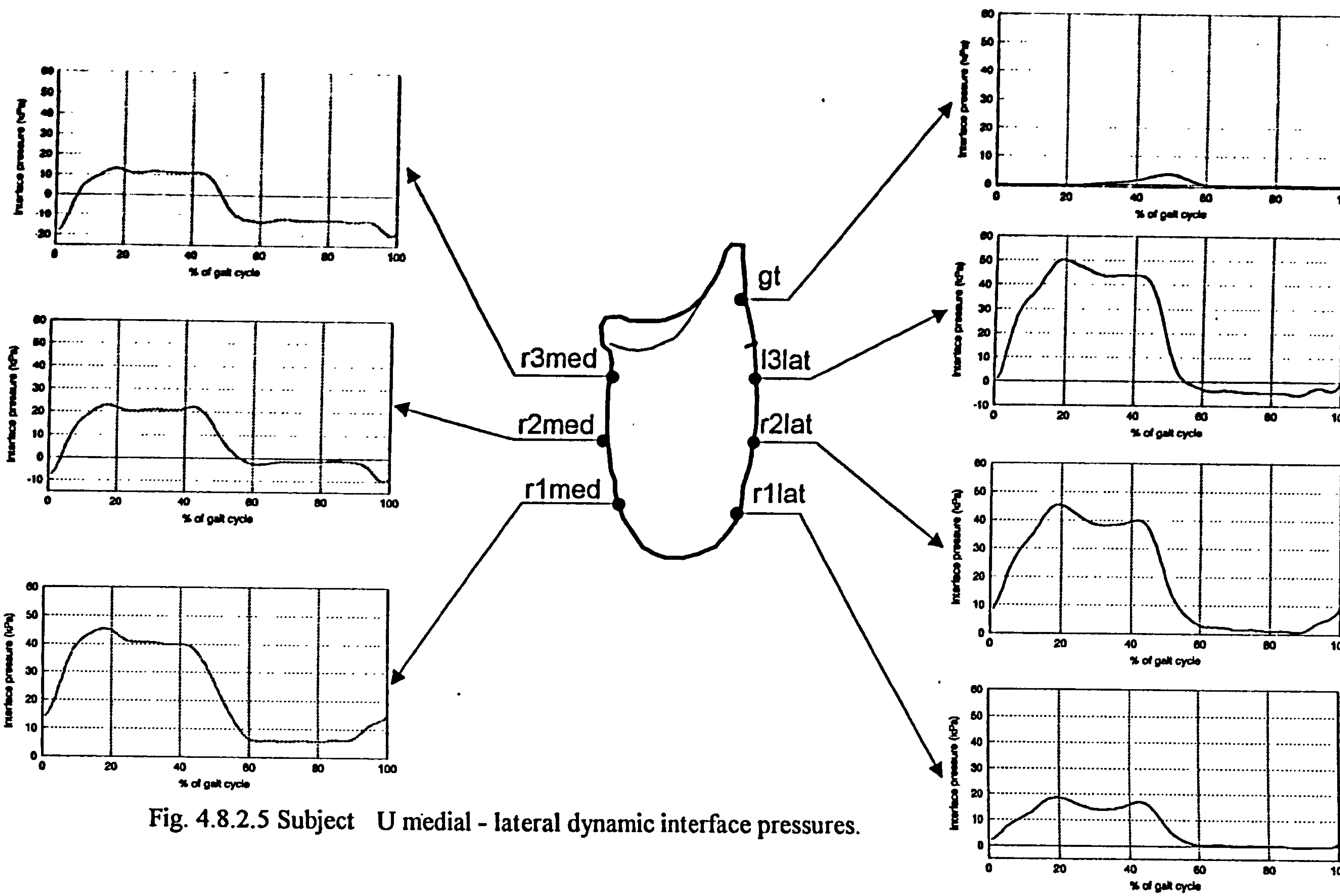

Fig. 4.8.2.5 Subject U medial - lateral dynamic interface pressures.

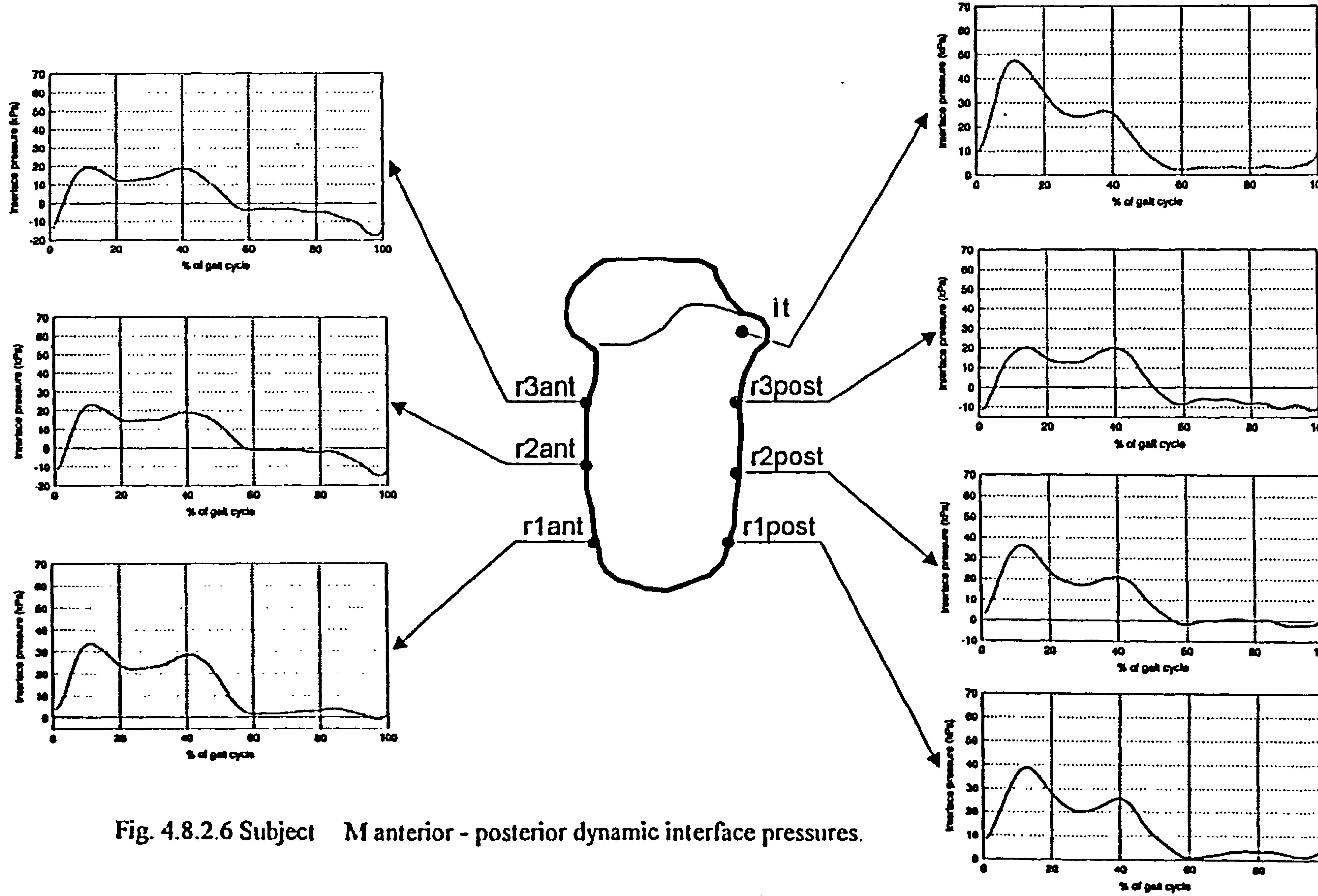

Fig. 4.8.2.6 Subject M anterior - posterior dynamic interface pressures.

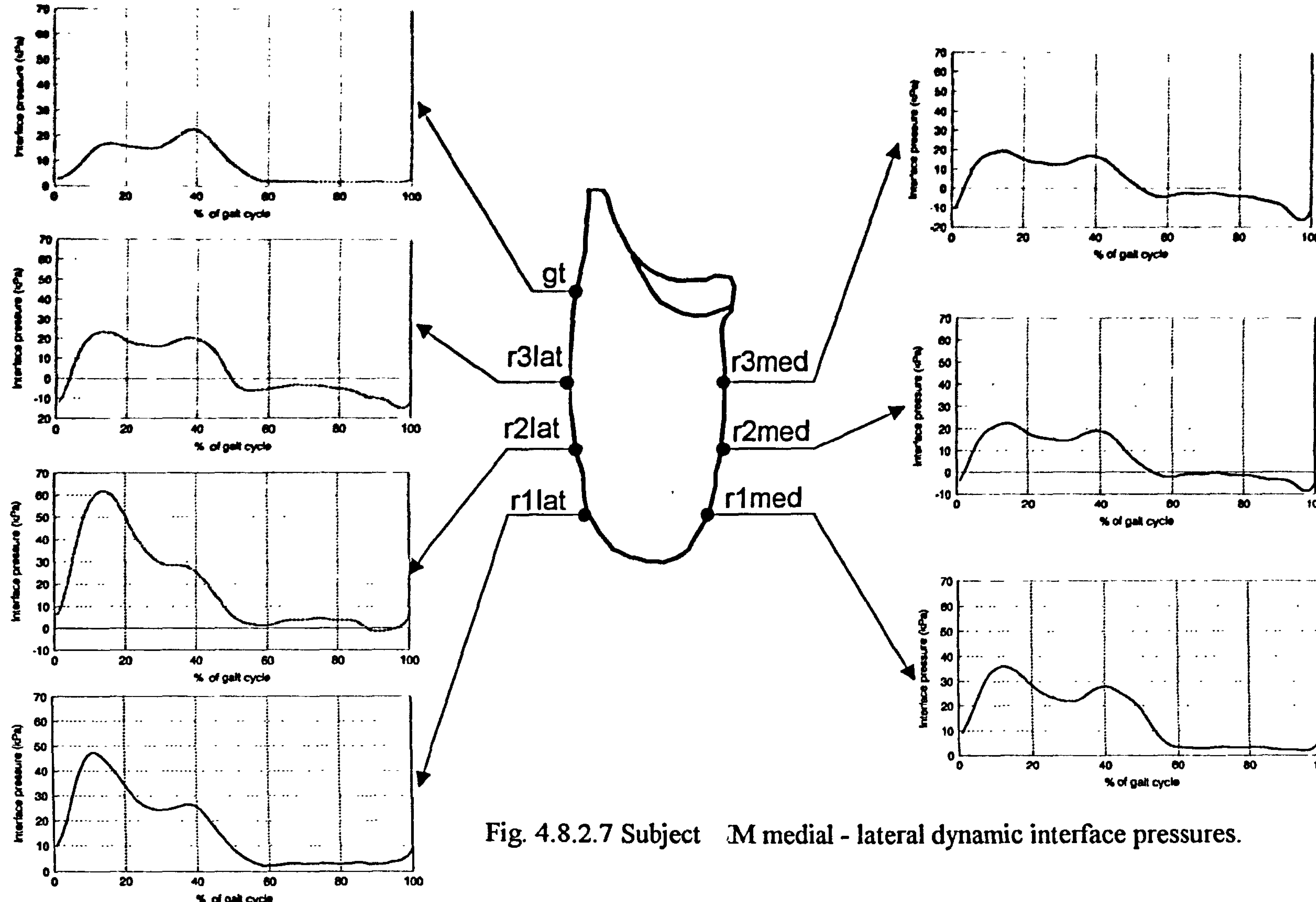

Fig. 4.8.2.7 Subject M medial - lateral dynamic interface pressures.

still maintaining total contact. In this case, the relief might have been too severe since from the pressure measurement, it was obvious that no contact was maintained throughout the gait cycle.

Subject U

The double peak pressure profile was recorded at all sites except site GT. The stance phase lasted approximately 55% of the gait cycle. Pressures ranged from -20 kPa to 50 kPa with the maximum at site R3LAT at 18% of the gait cycle. Site GT recorded the lowest pressure during stance at 5 kPa at 55% of the gait cycle. Generally, pressures at the anterior, posterior and lateral walls decreased towards the distal end while pressures at the medial wall decreased towards the proximal end of the residual limb. Higher pressures were recorded at the lateral and posterior walls than the medial and anterior walls. Pressure at the IT site (43 kPa) peaks towards the end of stance at about 50% of the gait cycle.

Subject M

Subject M's pressures ranged from -18 kPa to 62 kPa. A typical double peak profile occured at all the sites. It was observed that in the proximal sites, the profile were almost symmetrical, i.e. the two peaks in the profile were approximately of the same magnitude and equally spaced during the period of stance, while profile at the distal sites displayed a higher first peak. As discussed earlier, the unsymmetrical profile may be caused by fluid migration in soft tissue. It can be assumed that there was a high tendency at the distal sites for the soft tissue fluid to be forced into a unidirectional flow proximally, thus a low chance for the distal tissue to recover its original physical state before push off. Maximum pressure was recorded at R2LAT at 13% of the gait cycle. Peak IT loading of 48 kPa occured at early stance. Pressures at the socket walls were evenly distributed peaking between 20 kPa to 30 kPa, except at distal lateral sites where higher pressures (60 kPa) were recorded. Unlike the previous two subjects, pressure at the GT sites registered a magnitude of the same order as the other lateral wall sites.

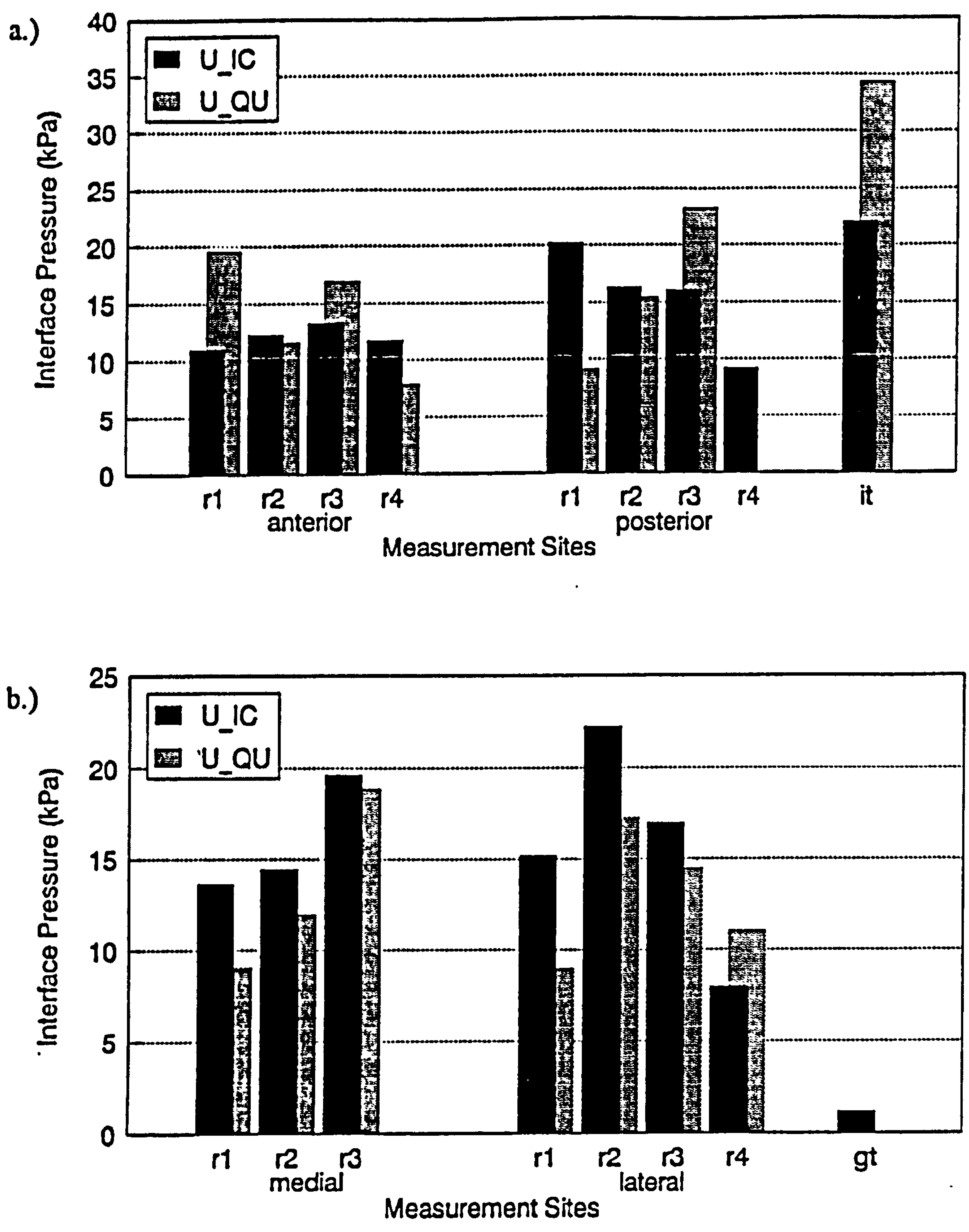

Fig. 4.9.1.1 Normal standing interface pressure in subject. U. a) Anterior-posterior sites, b) Medial-lateral sites. QU - Quadrilateral socket, IC - Ischial containement socket.

4.9 RESULTS : PART TWO

Interface pressures of subjects U and M with both the IC and the quad sockets described as part two of the study will be presented. The results of the two different types of sockets for each subject will be introduced together for the purpose of comparison.

4.9.1 Normal standing interface pressure

Fig. 4.9.1.1 and Fig. 4.9.1.2 show the pressures generated at the interface while standing for subject U and M respectively. The pressure ranged from 1-34 kPa and 7-19 kPa for subjects U and M respectively. The highest pressure (34 kPa) was recorded on subject U using the quad socket at site IT and the highest pressure on subject M was 19 kPa at site R3POST of the quad socket. Comparing the two types of sockets, in the case of subject U, the quad indicated the existence of a decreasing pressure pattern from the anterior distal end to the proximal brim. However, the IC exhibited more evenly distributed pressure at similar sites. At the quad's posterior sites, higher pressure existed at the proximal brim and decreased towards the distal end. On the contrary, the IC reveals decreasing pressure towards the posterior proximal brim. At the medial and lateral sites, pressures on all sites except R4LAT for the IC were higher than those of the quad and the difference was more pronounced at the distal sites.

The standing pressures measured in subject M showed greater variations in both magnitude and distribution when compared to those of subject U. As already discussed, inter subject comparison of this nature is highly dependent on the subjects' unique shape, biomechanical properties and physiology of the stump. However, comparing subject's M quad and IC sockets, it was noted that the pressure at all sites in the quad except at IT, was higher than those measured in the IC. In addition, the pressure gradient seen in the IC was similar to that of subject U's IC socket, whereas in the quad, pressures were largely evenly distributed and of about the same magnitude. Pressure at site IT was surprisingly lower in the quad than that in the IC. The author reckoned that this could be due to the difficulty in locating the exact

a.)

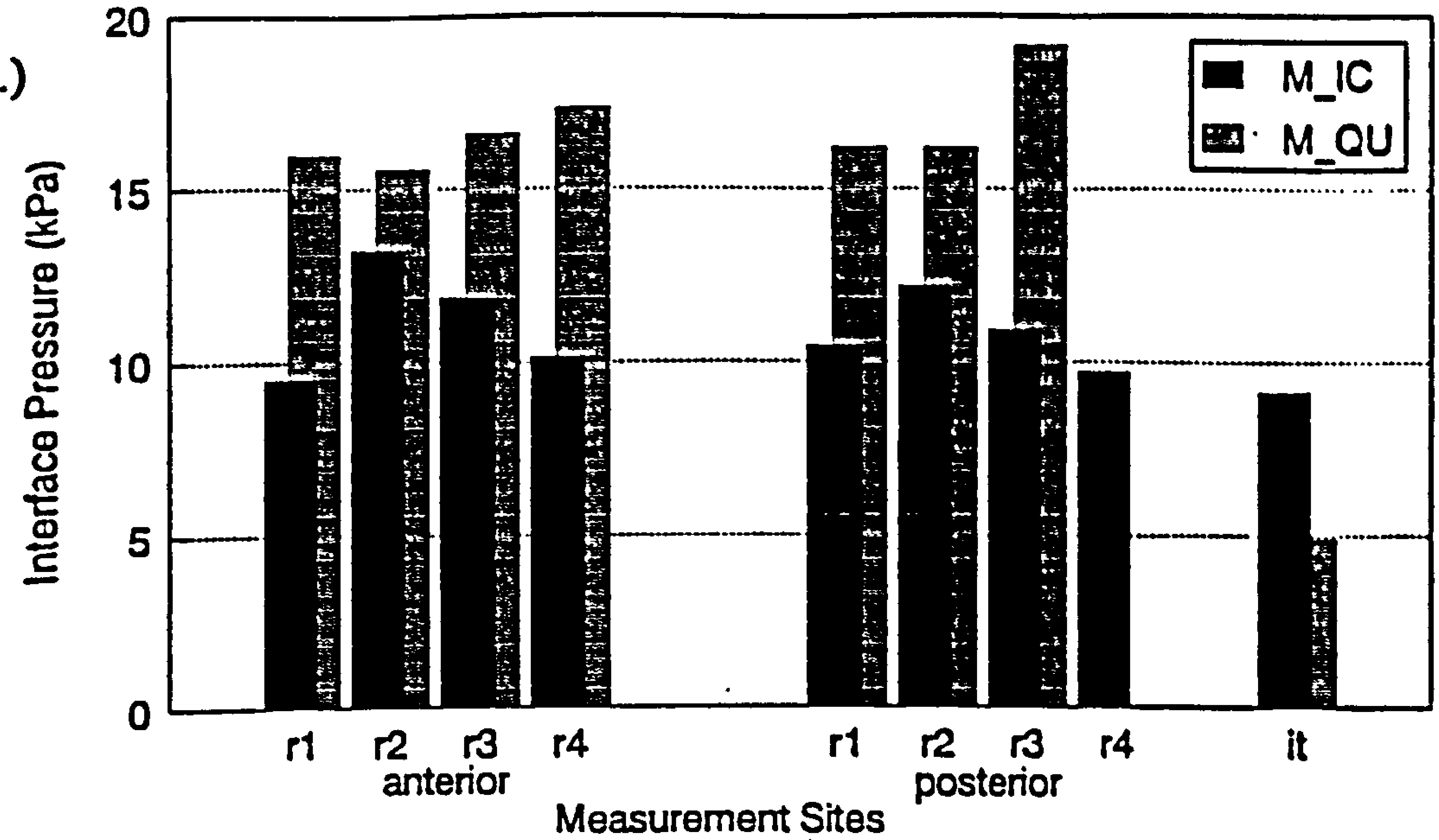

b.)

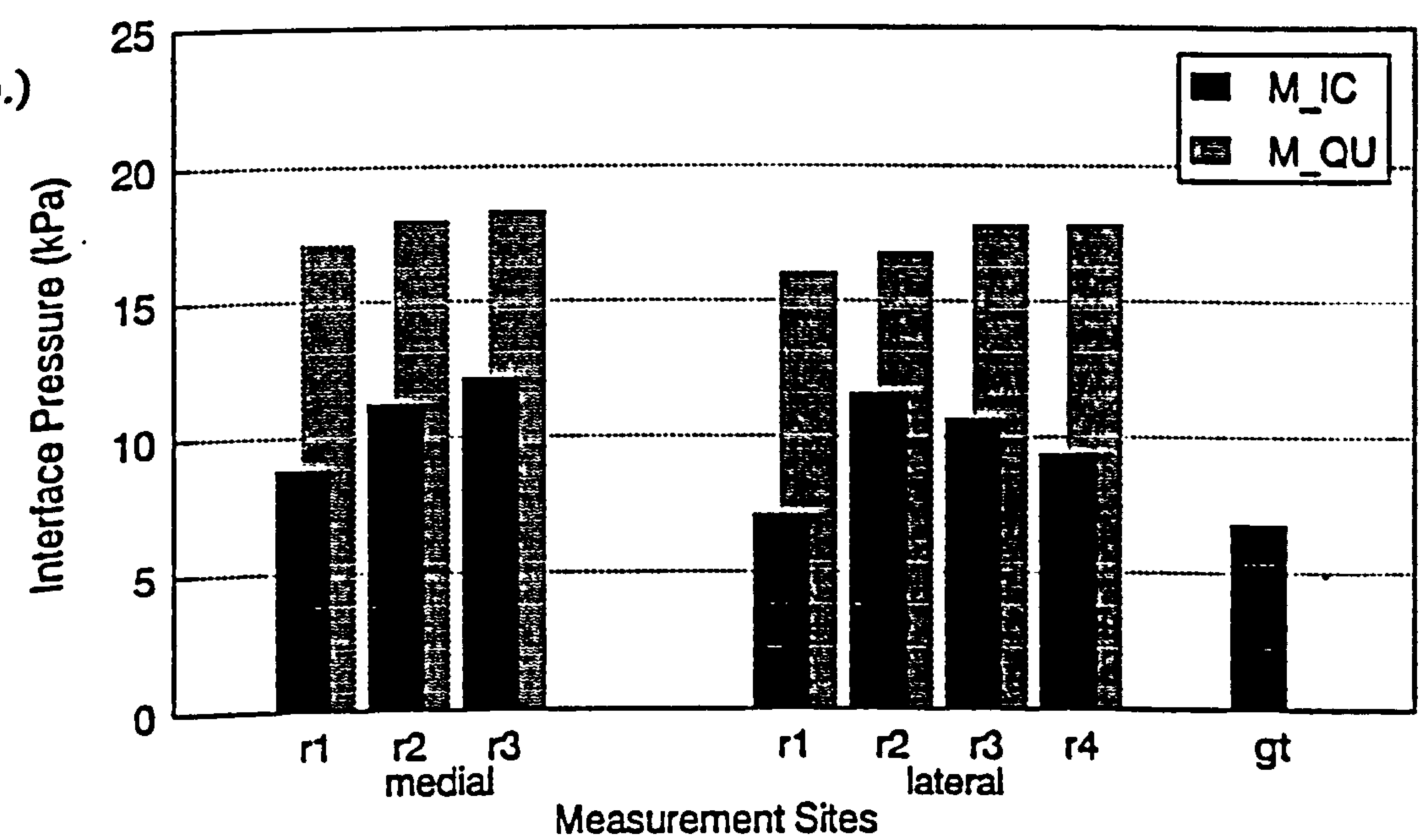

Fig. 4.9.1.2 Normal standing interface pressure in subject M. a) Anterior-posterior sites, b) Medial-lateral sites. QU - Quadrilateral socket, IC - Ischial containement socket.

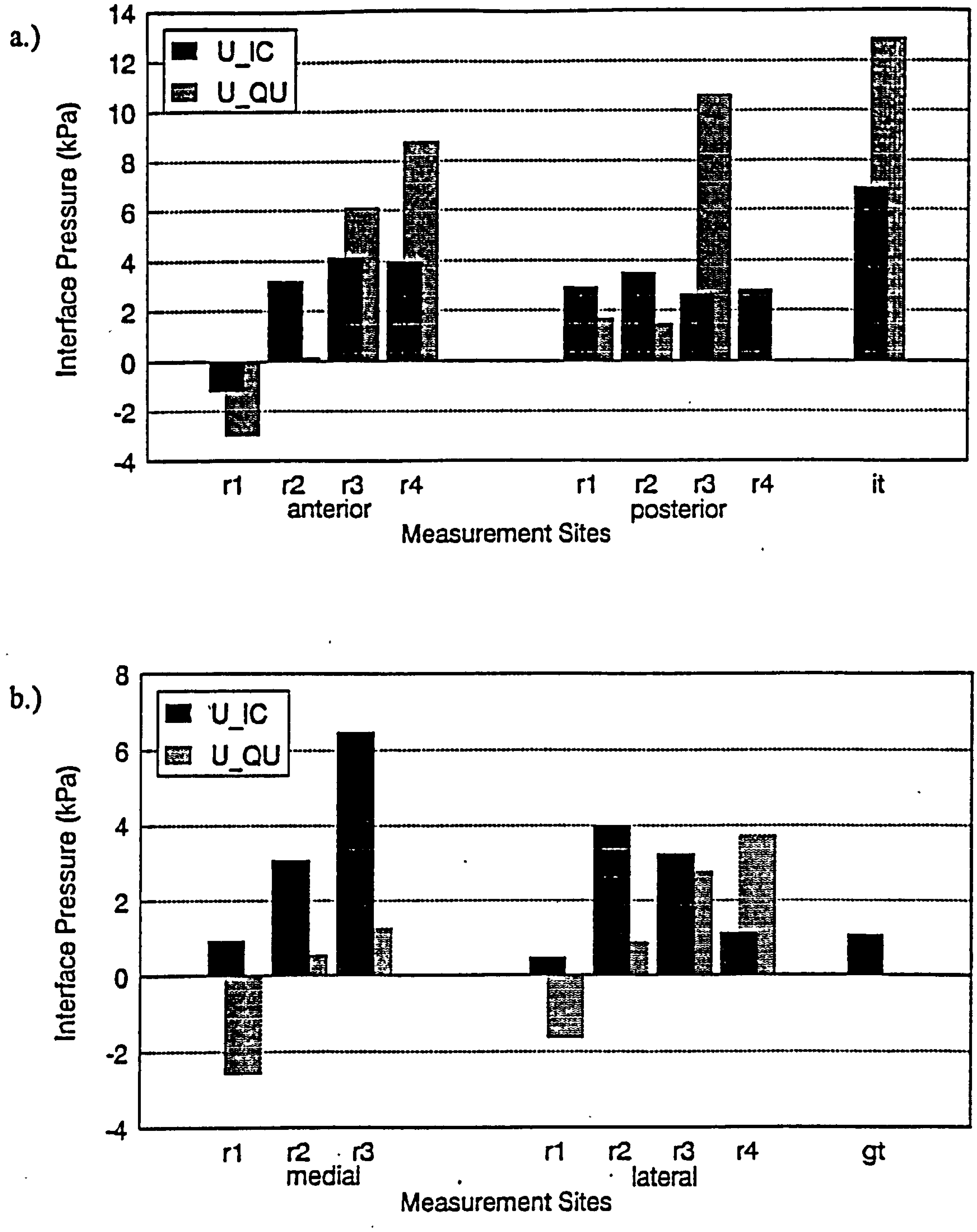

Fig. 4.9.2.1 Socket suspension interface pressure in subject U. a) Anterior-posterior sites, b) Medial-lateral sites. QU - Quadrilateral socket, IC - Ischial containement socket.

position of the ischial tuberosity inside the socket. However, it was also perceived that the lack of weight bearing at the IT in this particular quad socket could indicate the increase in pressure that was recorded at all the other sites, especially at R3POST where the gluteal muscles could be acting as the main weight bearers.

4.9.2 Socket suspension interface pressure

Fig. 4.9.2.1 & 4.9.2.2 shows pressures measured during the unloaded test procedures. Generally, pressures increased toward the proximal sites, with the majority of distal end pressures indicating negative magnitudes. Pressures ranged from -3 to 13 kPa and -3 to 5 kPa for subjects U and M respectively. Peak pressure (13 kPa) was recorded in U quad socket site IT. The geometrical difference of the two types of socket brim could be seen in the way pressures were distributed. U quad pressures were higher at the anterior and posterior sites and lower at the medial and lateral sites when compared to pressures in the IC socket, reflecting the narrow AP and wider ML dimension of the quad socket. However, this was not clear in the case of subject M's quad, since equivalent pressures were recorded in both the AP and ML sites.

4.9.3 Normal walking interface pressure

The dynamic test results were normalised to 100% of the gait cycle based on the exact time of heel strike and toe off detected by the axial transducer. In both subjects, the pressure variations throughout stance in majority of the measurement sites showed the typical two peak curve, with the first peak being at approximately 12-16% and the second at about 37-44% of the gait cycle. The measured pressures for both subjects in the quad and IC sockets ranged from -20 kPa to 92 kPa. In this section, the results for each subject with the respective sockets (IC and quad) will be displayed in a set of three figures, the first and second being plots of the anterior and posterior, medial and lateral walls pressures over 100% of the gait cycle repectively. The third figure illustrates the peak pressures corresponding to the percentage of the gait cycle.

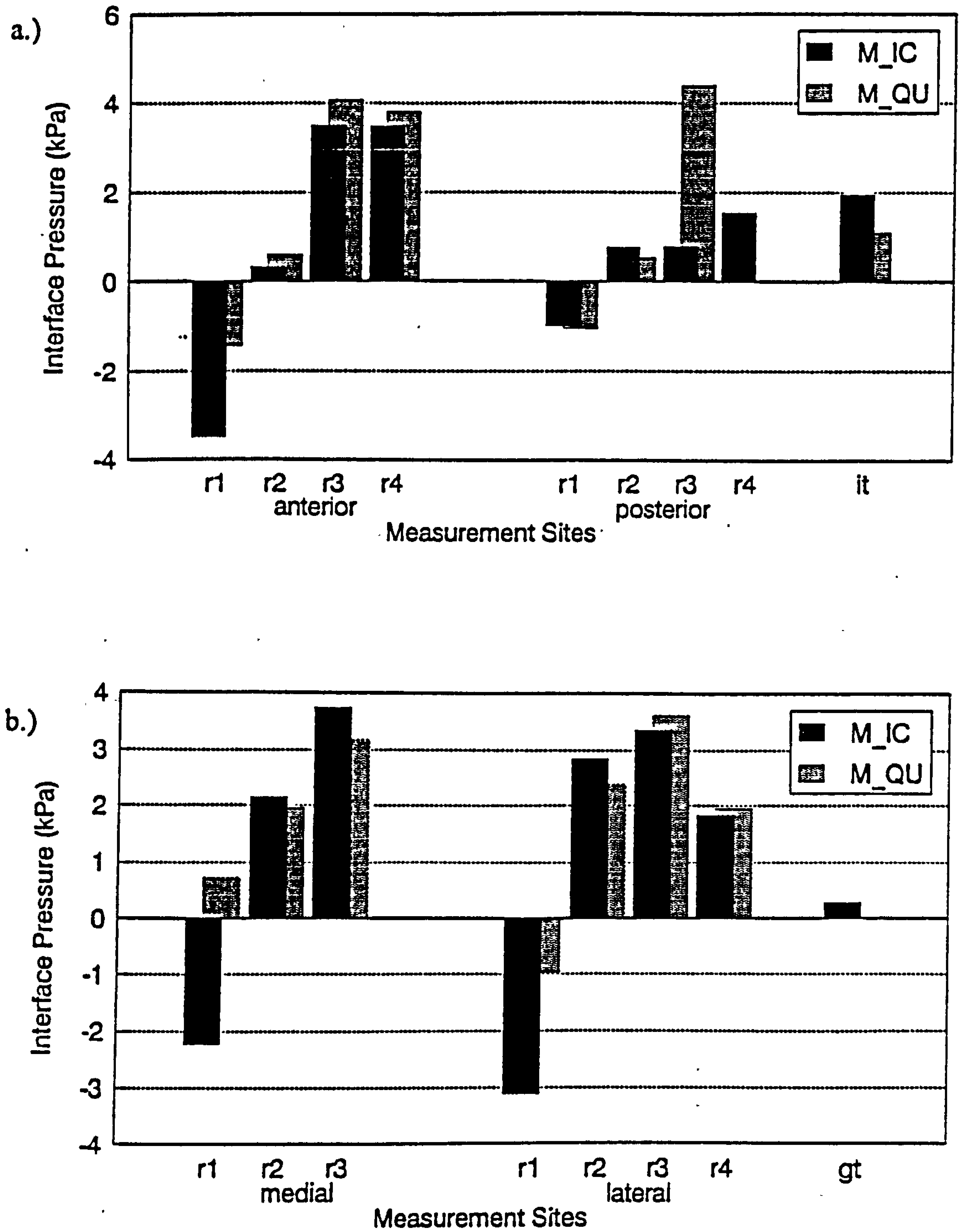

Fig. 4.9.2.2 Socket suspension interface pressure in subject M. a) Anterior-posterior sites, b) Medial-lateral sites. QU - Quadrilateral socket, IC - Ischial containement socket.

Subject U

Subject U's interface pressures with the quadrilateral socket is described in Fig. 4.9.3.1 and Fig. 4.9.3.2 and Fig. 4.9.3.3. Generally, the pressures at the proximal brim level were higher than the distal end. The measured pressures ranged from -20 kPa to 92 kPa. In most sites during the beginning of stance, the measured pressures increased up to a maximum at 12% of the gait cycle. Upon reaching this maximum value, the pressures decreased slightly leaving a peak profile. The pressure profile then continued in a fairly consistent manner until late stance where a second peak could be observed at about 43% of gait. Most measured sites possessed the two peak pressure profile except at sites IT, R1LAT and R4LAT where a single peak profile was exhibited. A maximum pressure of 92 kPa was located at site IT at 33% of the gait cycle.

In the IC socket, Subject U's interface pressures ranged from -8 to 72 kPa (Fig. 4.9.3.4, Fig. 4.9.3.5 and Fig. 4.9.3.6). All sites except site GT displayed a two peak pressure profile with the first peak occurring at approximately 10% to 14%, and the second peak at about 31% to 44% of the gait cycle. Proximal pressures during stance were higher than distal end pressures at the medial wall of the socket, while pressures at the lateral wall recorded low proximal and high distal end pressures. Maximum pressure was measured at R2LAT at 37% of the gait cycle, and peak pressure at site IT occurred at 12% of the gait cycle with a magnitude of 56 kPa.

Subject M

Subject M quadrilateral socket interface pressures are displayed in Fig. 4.9.3.7, Fig. 4.9.3.8 and Fig. 4.9.3.9. Pressures ranged from -12 to 63 kPa. Maximum pressure occurred at 12% of the gait cycle at site R3POST. Pressure at site IT reached a maximum of 41 kPa at 44% of the gait cycle. All measured sites produced a two peak pressure profile, though at site IT, the two peaks were only separated by 9% of the gait cycle and occurred during late stance. Pressures at the anterior, posterior and lateral walls during stance recorded high pressures proximally which

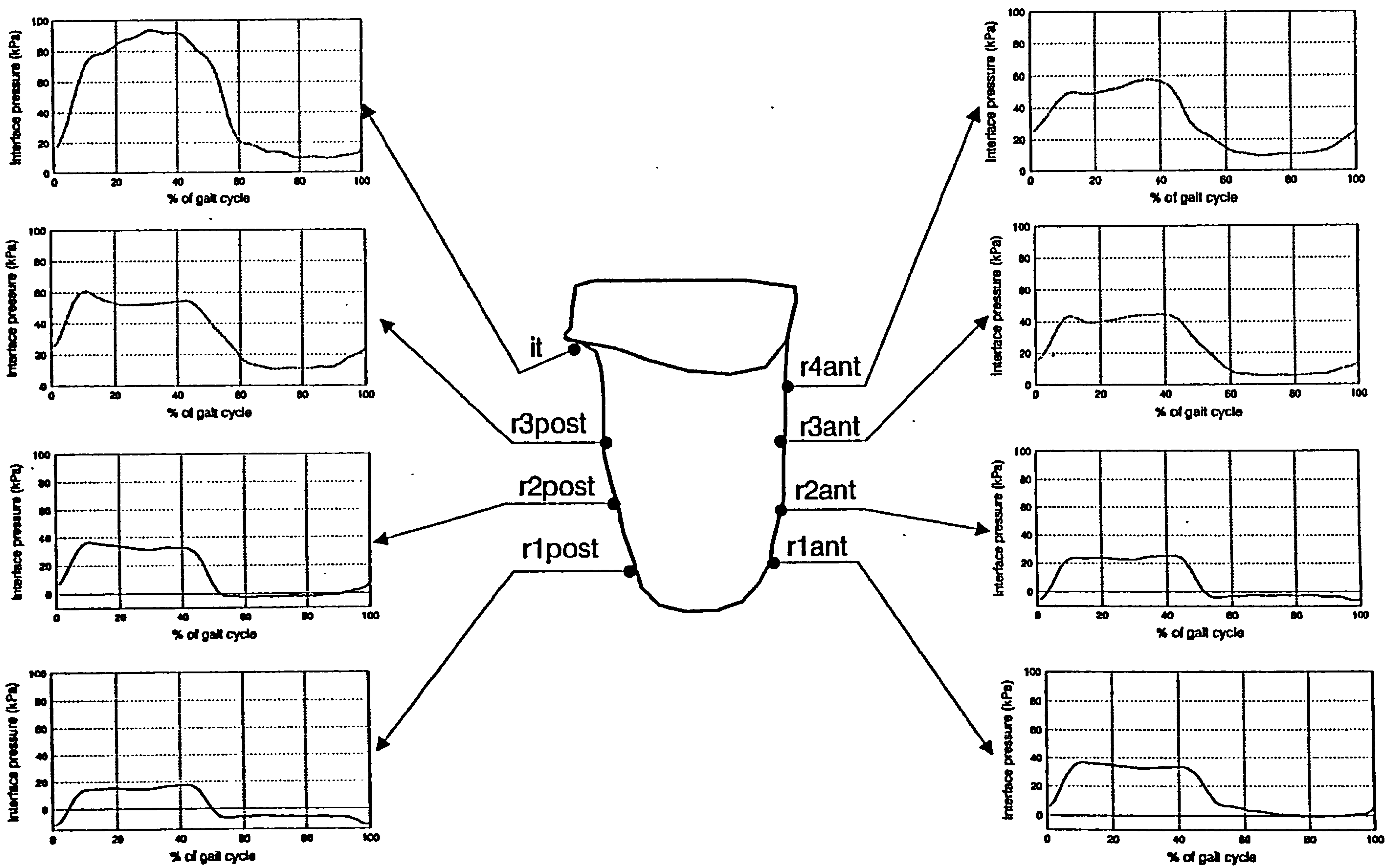

Fig. 4.9.3.1 Subject U quad socket anterior - posterior dynamic interface pressures

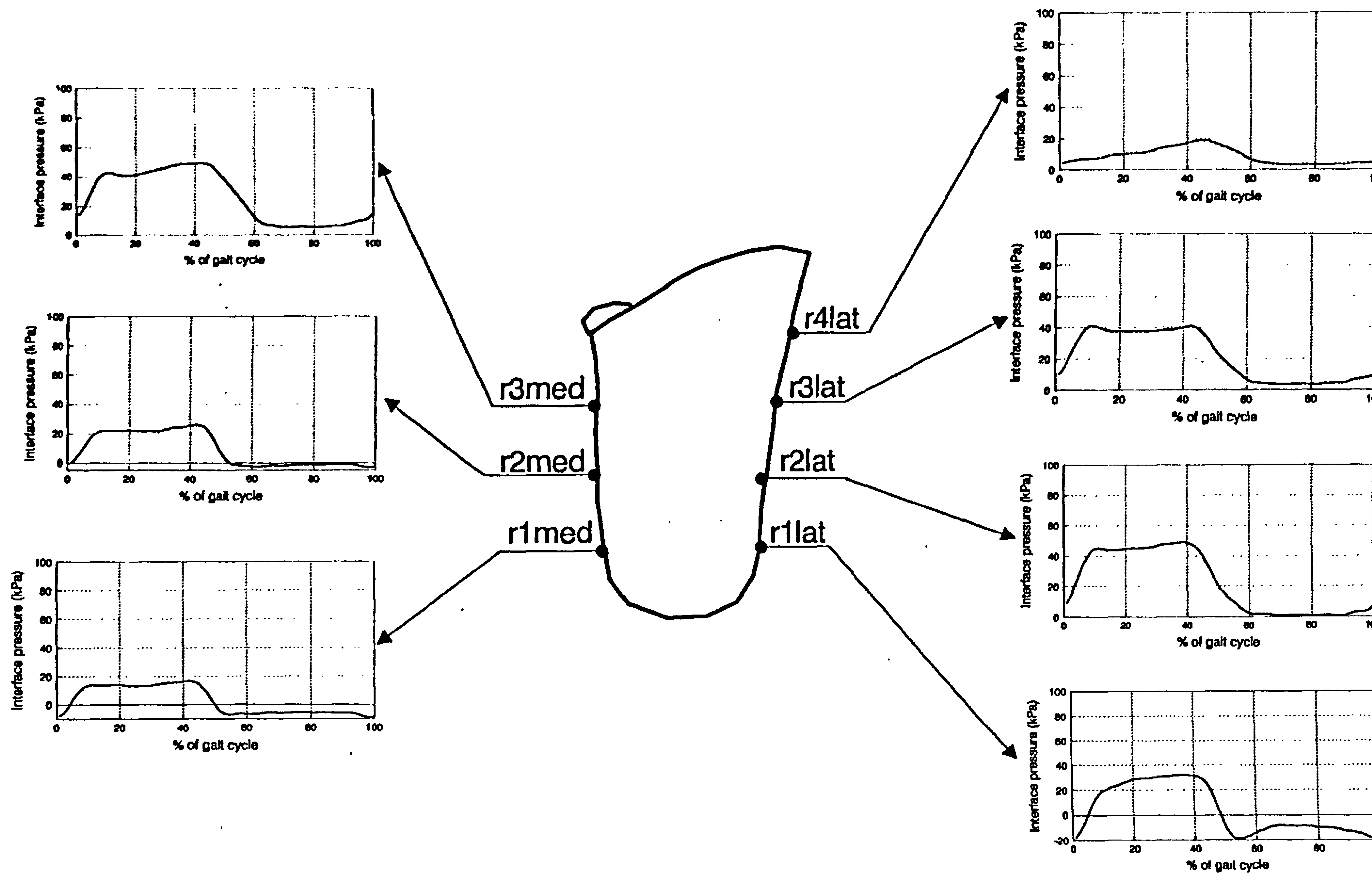

Fig. 4.9.3.2 Subject U quad socket medial - lateral dynamic interface pressures

a.)

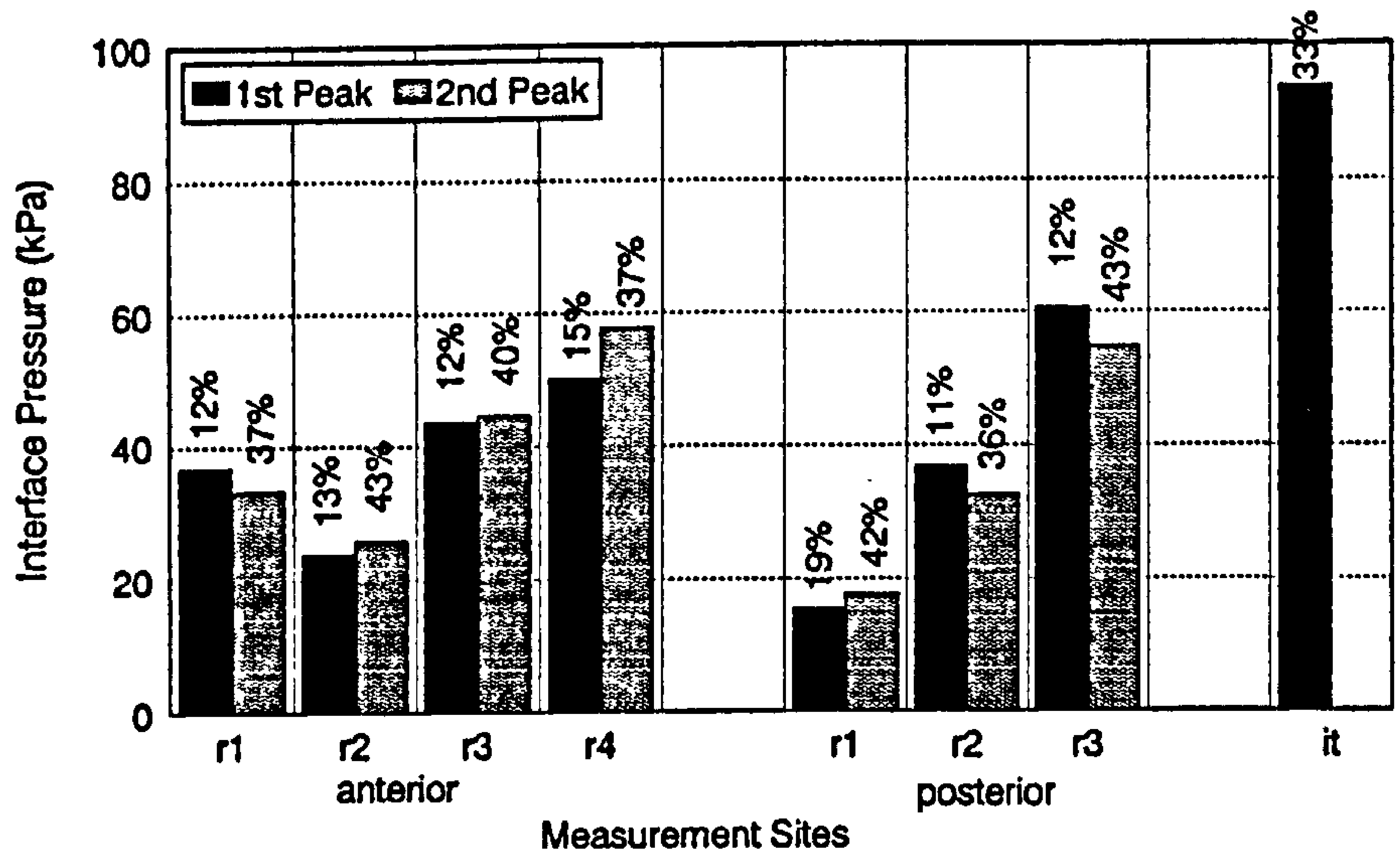

b.)

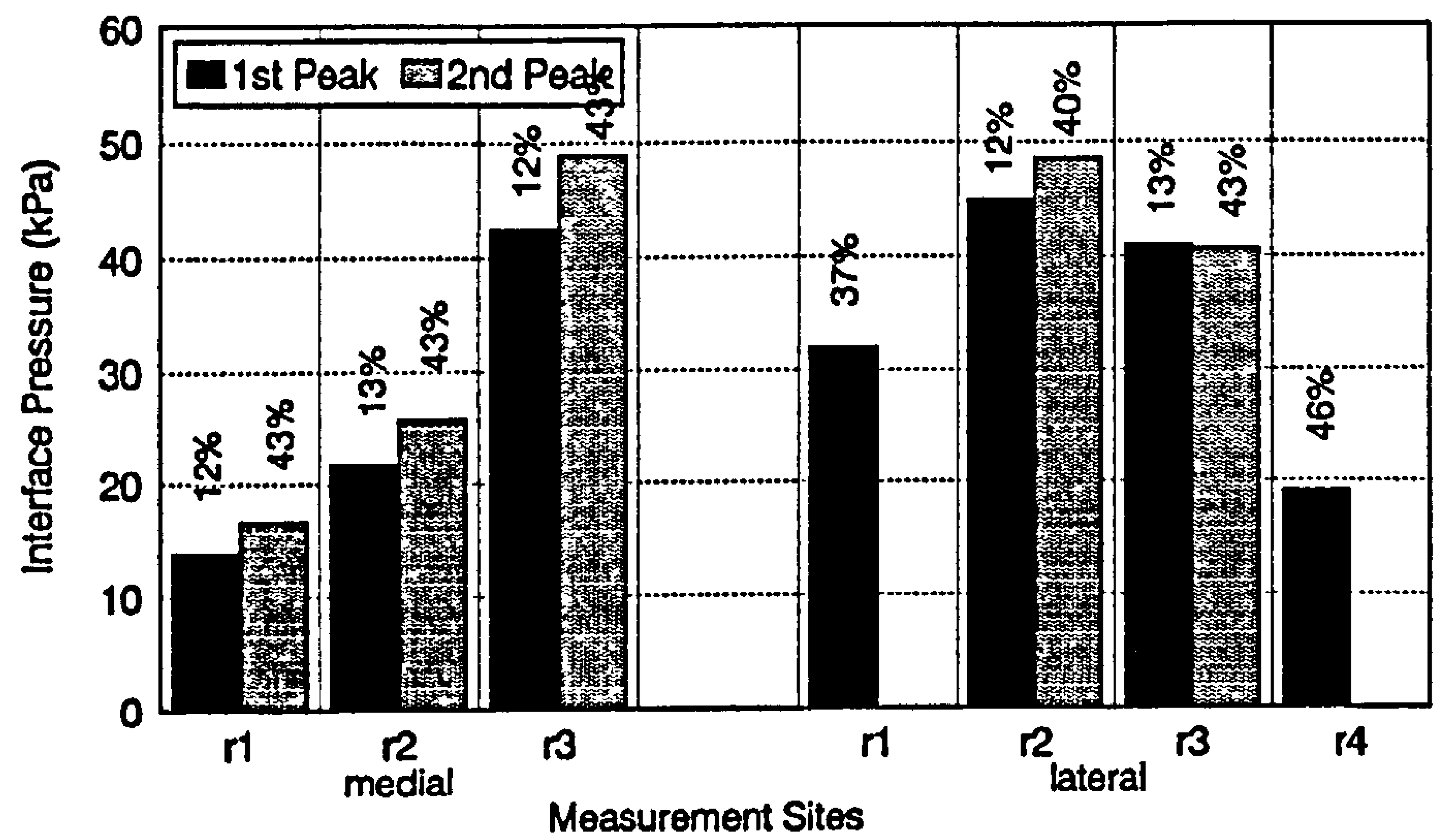

Fig. 4.9.3.3 Peak pressures corresponding to % of gait cycle
in subject U quad socket.
a.) Anterior posterior sites
b.) Medial lateral sites

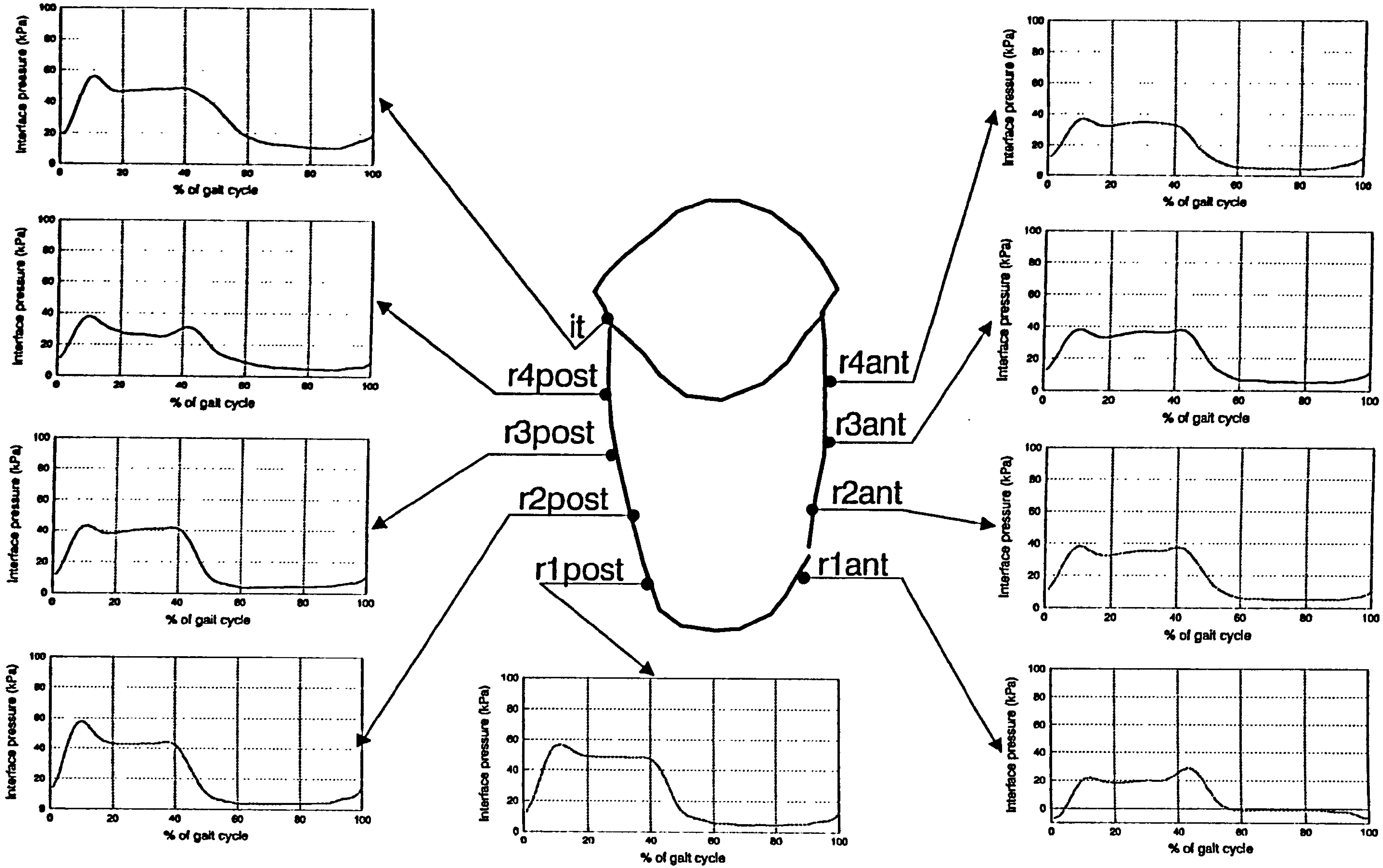

Fig. 4.9.3.4 Subject U 1C socket anterior - posterior dynamic interface pressures.

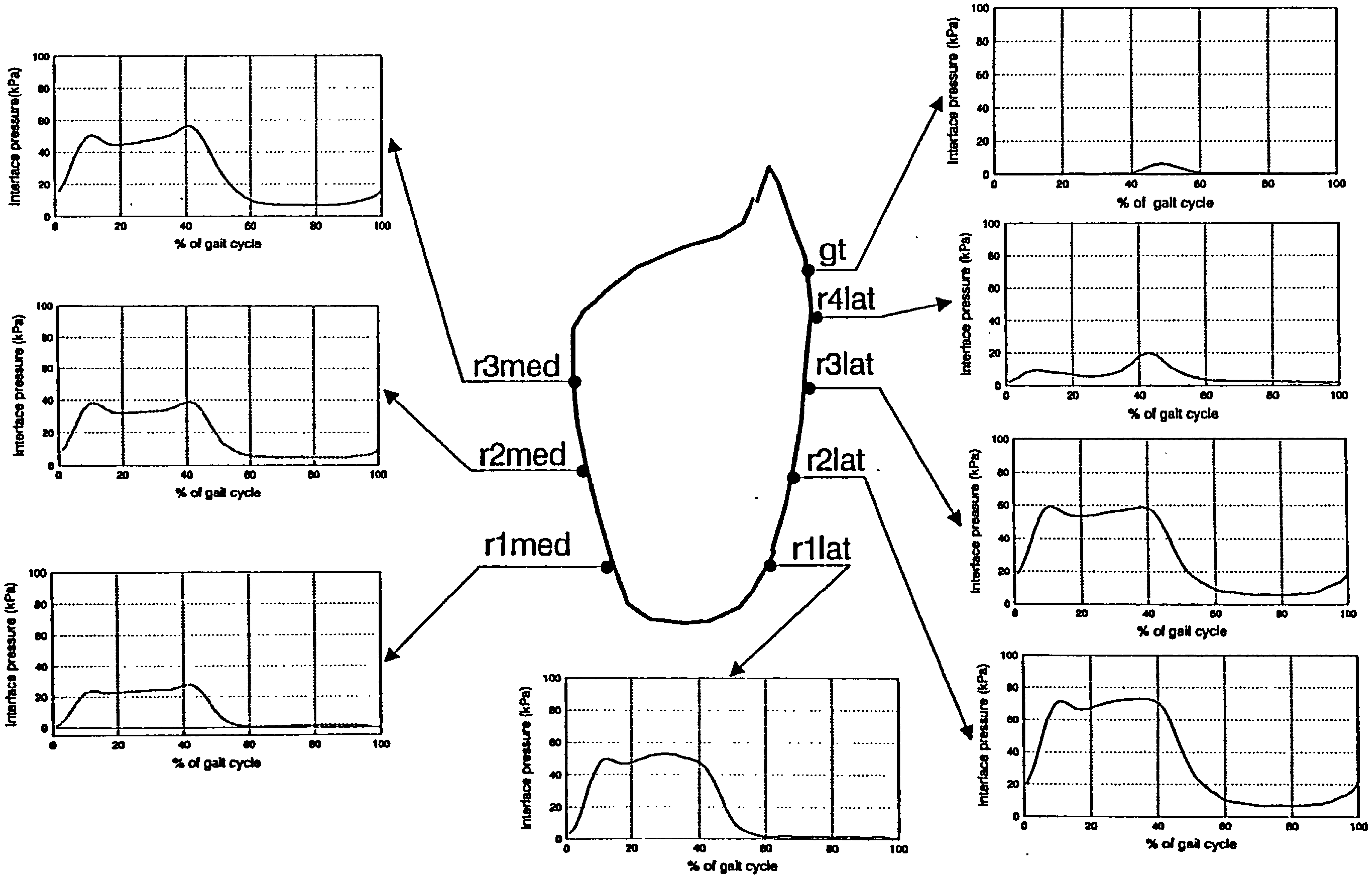

Fig. 4.9.3.5 Subject U IC socket medial - lateral dynamic interface pressures.

a.)

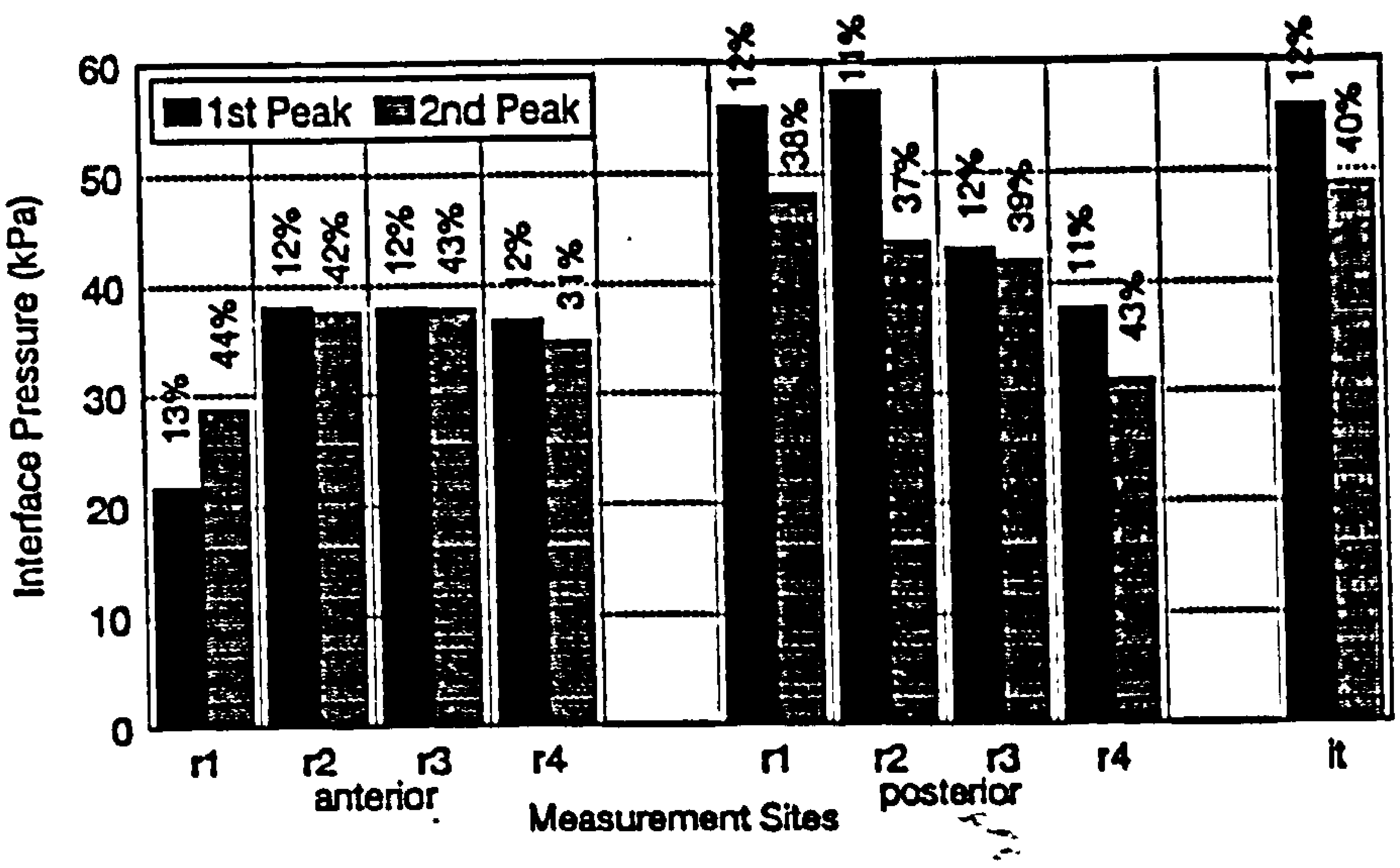

b.)

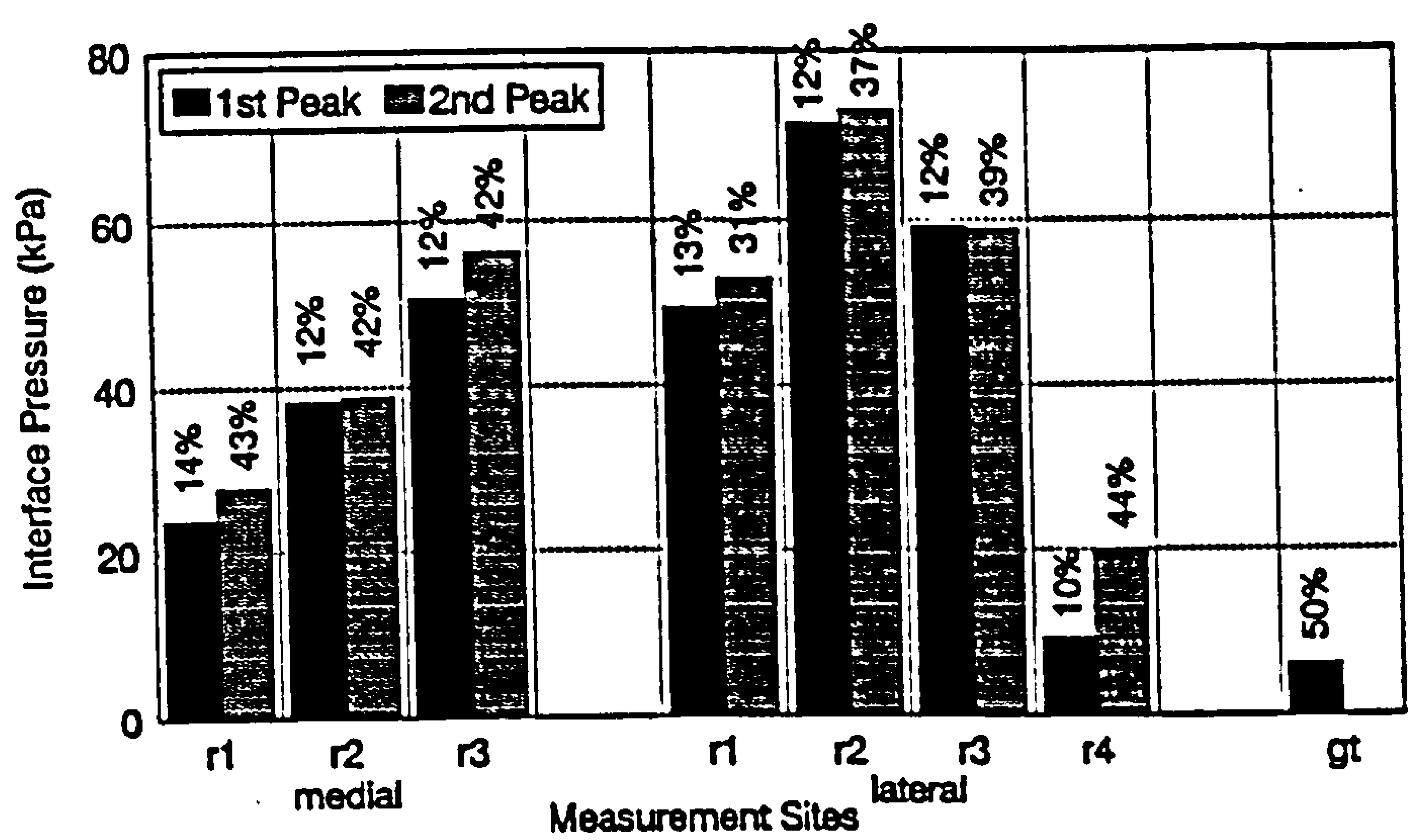

Fig. 4.9.3.6 Peak pressures corresponding to % of gait cycle
in subject U IC socket.
a.) Anterior posterior sites
b.) Medial lateral sites

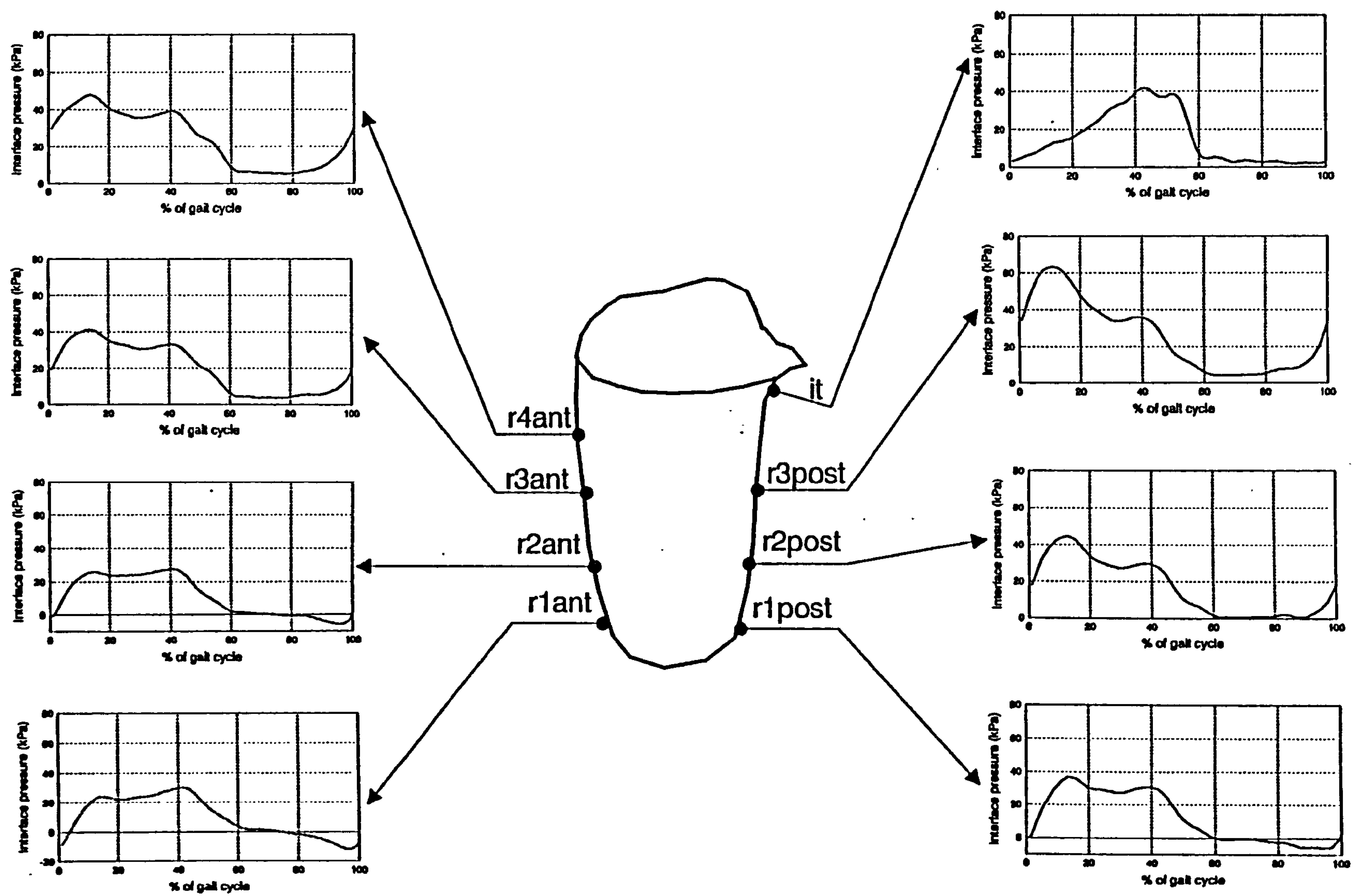

Fig. 4.9.3.7 Subject M quad socket anterior - posterior dynamic interface pressures.

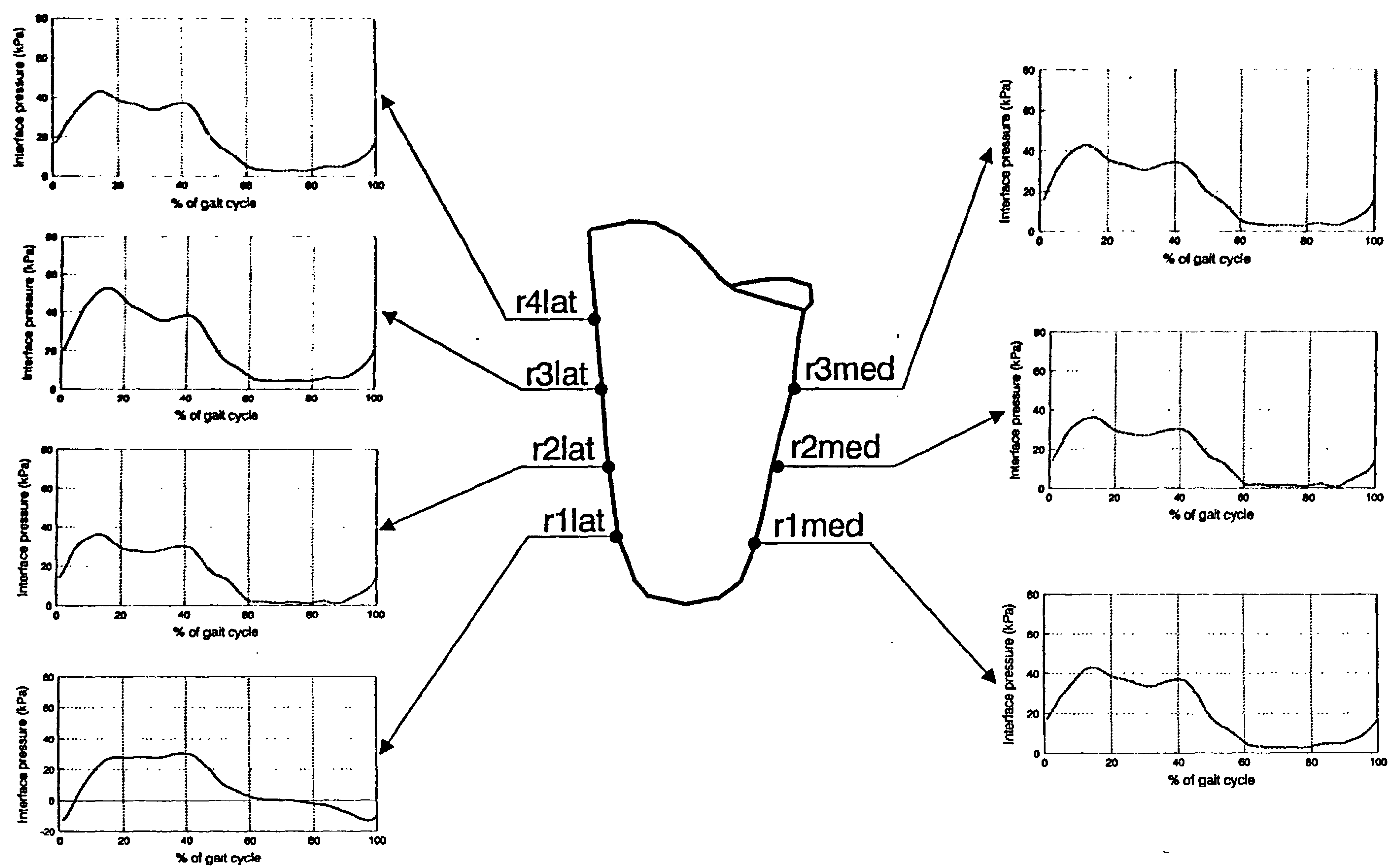

Fig. 4.9.3.8 Subject M quad socket medial - lateral dynamic interface pressures.

a.)

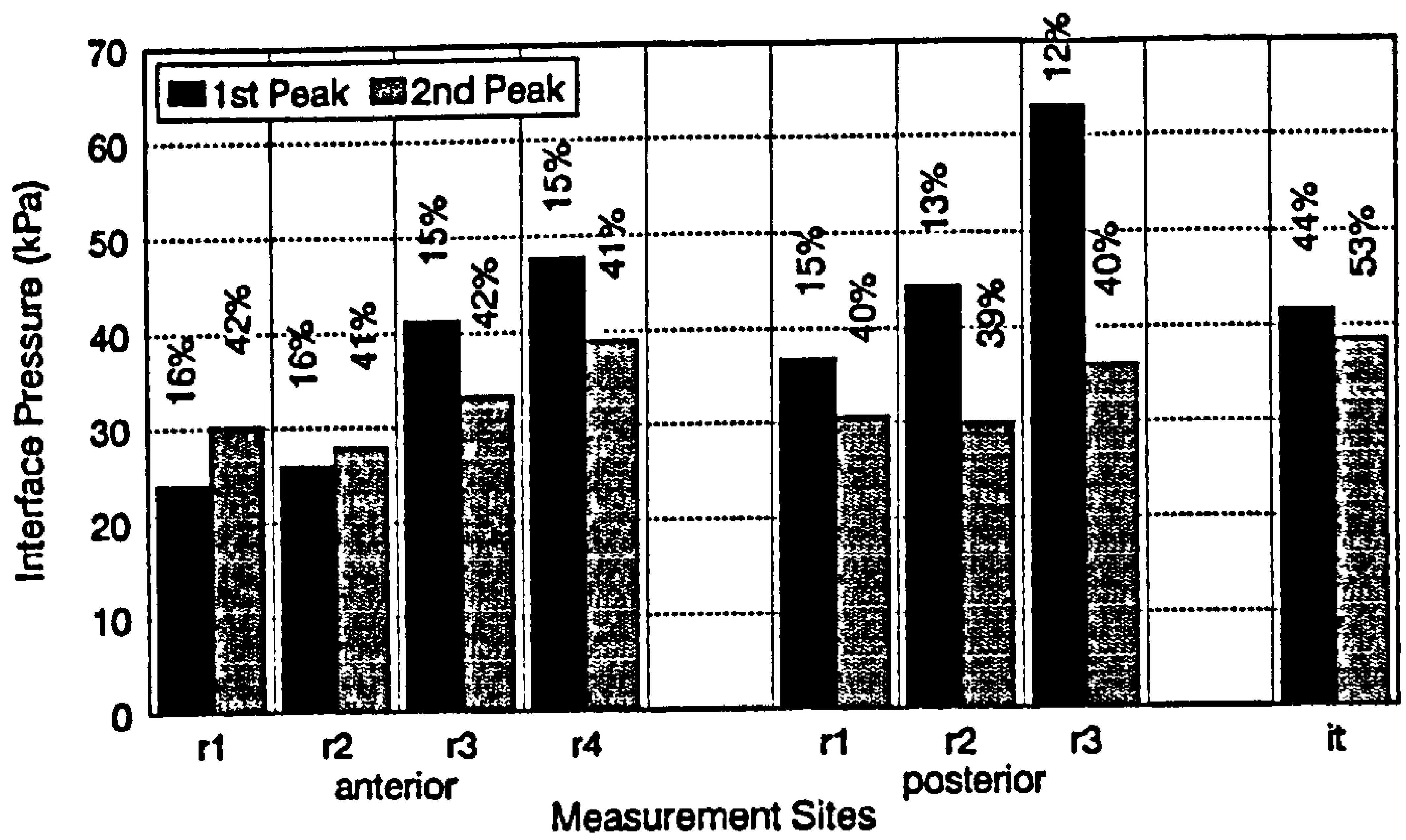

b.)

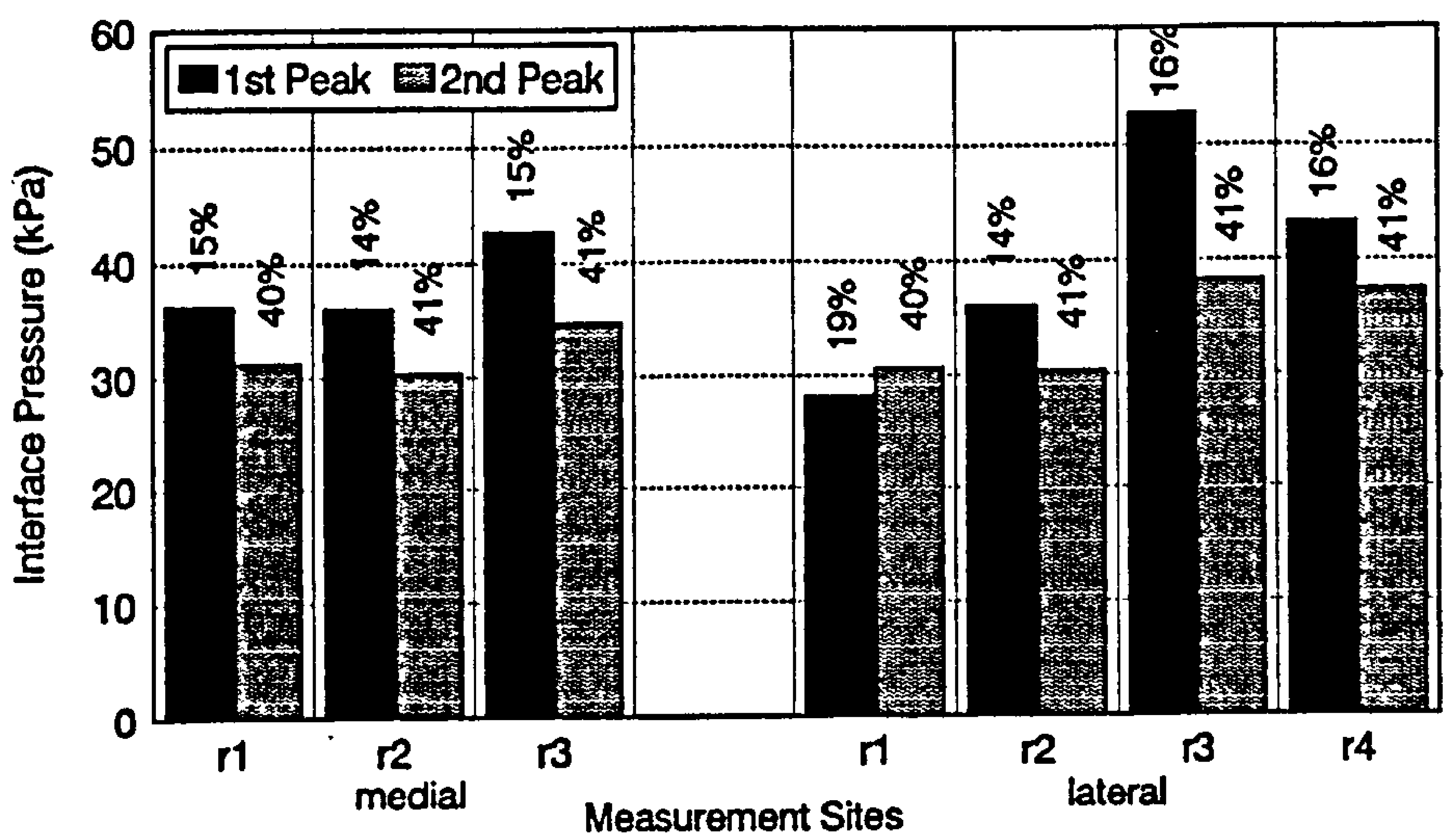

Fig. 4.9.3.9 Peak pressures corresponding to % of gait cycle
in subject M quad socket.
a.) Anterior posterior sites
b.) Medial lateral sites

decreased toward the distal end, whereas the medial wall pressures remained fairly even throughout stance.

Fig. 4.9.3.10, Fig. 4.9.3.11 and Fig. 4.9.3.12 show the interface pressures measured in subject M with the IC socket. The pressures ranged from -20 kPa to 69 kPa. Maximum pressure occurred at site R2LAT at 19% of the gait cycle, which was the only single peak pressure profile. All other sites possessed a two peak profile with the first peak occurring at about 13% to 18% and the second about 34% to 47% of the gait cycle. The pressures during mid stance in most of the sites were about the same, just below 20 kPa. However in site R2LAT, both pressure profile and magnitude varied significantly from the other measurement sites. The pressure at this site rose quickly to a peak of 69 kPa after heel contact which was about 40% higher than most first peaks recorded in other sites.

In summary, the highest pressure was found at the IT site of subject U quad socket, while subject M highest pressure was located at R2LAT site of the IC socket. Both were single peak pressure profiles. Subject M IT site in the quad socket did not register the highest pressure but instead at site R3POST. Several distal sites in both subjects recorded negative swing phase pressures.

4.10 COMPARISON OF RESULTS WITH THOSE OF APPOLDT AND BENNETT'S (1967) INVESTIGATION

A comparison is made with results presented by Appoldt and Bennett (1967) since this is one of the most detailed investigations. The reader is advised that the comparison should be viewed in a qualitative basis, since an exact match of the measurement sites was not possible and these measurements were performed for different subjects. Appoldt and Bennett measured dynamic pressures at 100 and 470 ms after heel strike. In the comparison, these timings were assumed to approximate 10% and 40% of the gait cycle respectively. Comparisons were made only with U and M quads, since the quad socket was used by Appodlt and Bennett. The results are graphically depicted in Fig. 4.10.1 and Fig. 4.10.2. The pressure distributions were quite similar during 10% of gait cycle for all socket walls. However, the low

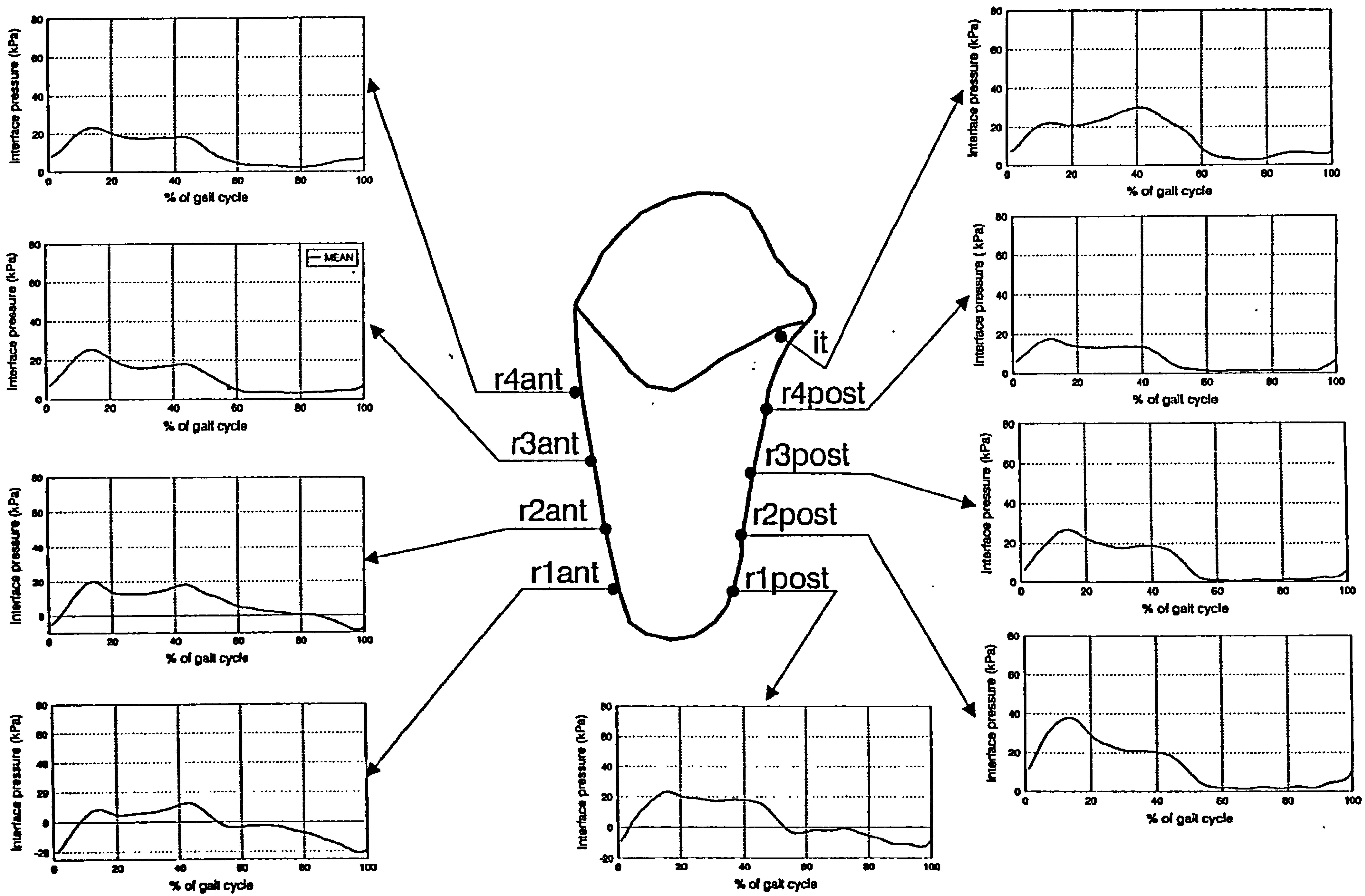

Fig. 4.9.3.10 Subject M IC socket anterior - posterior dynamic interface pressures.

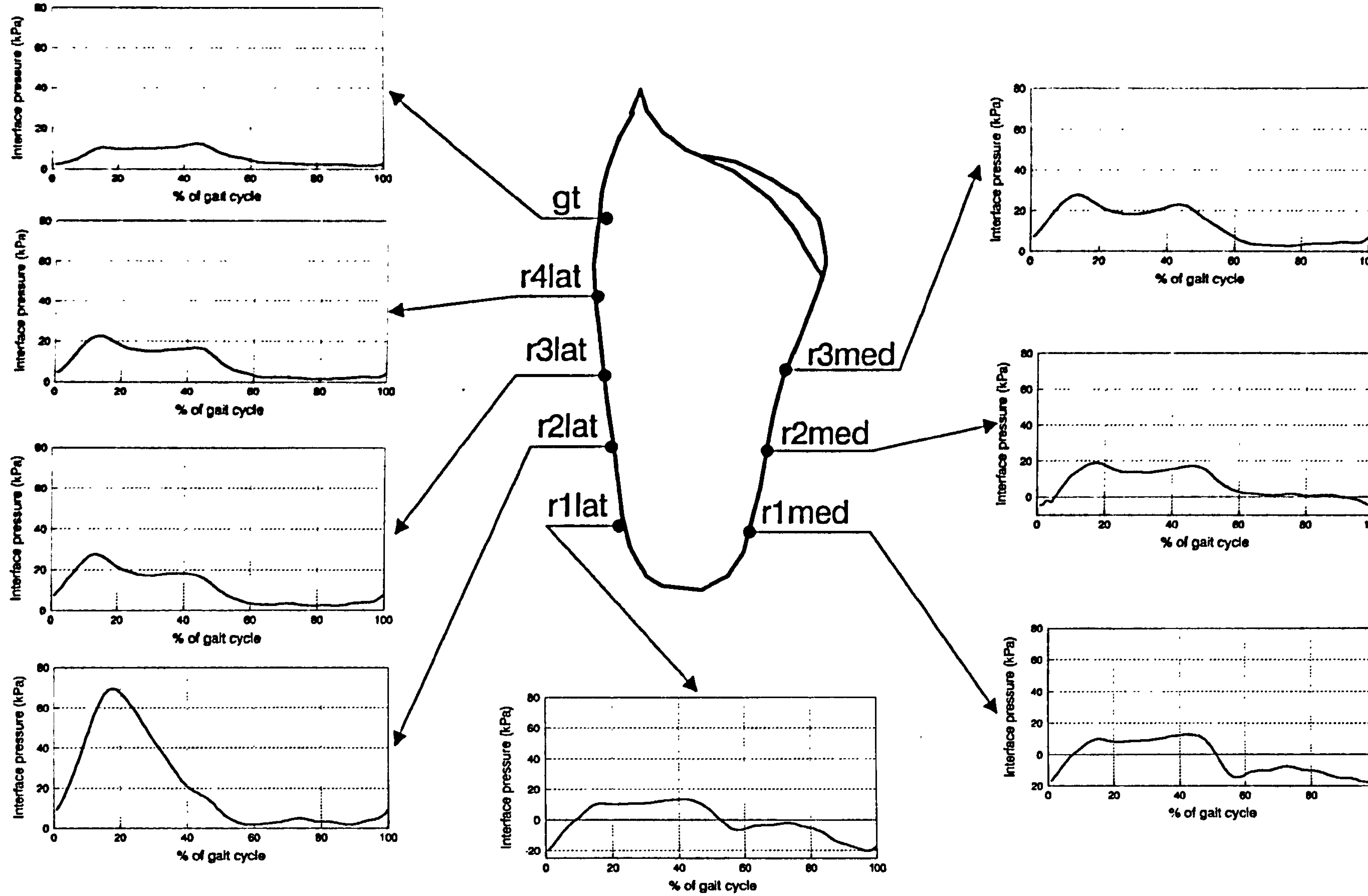

Fig. 4.9.311 Subject M IC socket medial - lateral dynamic interface pressures.

a.)

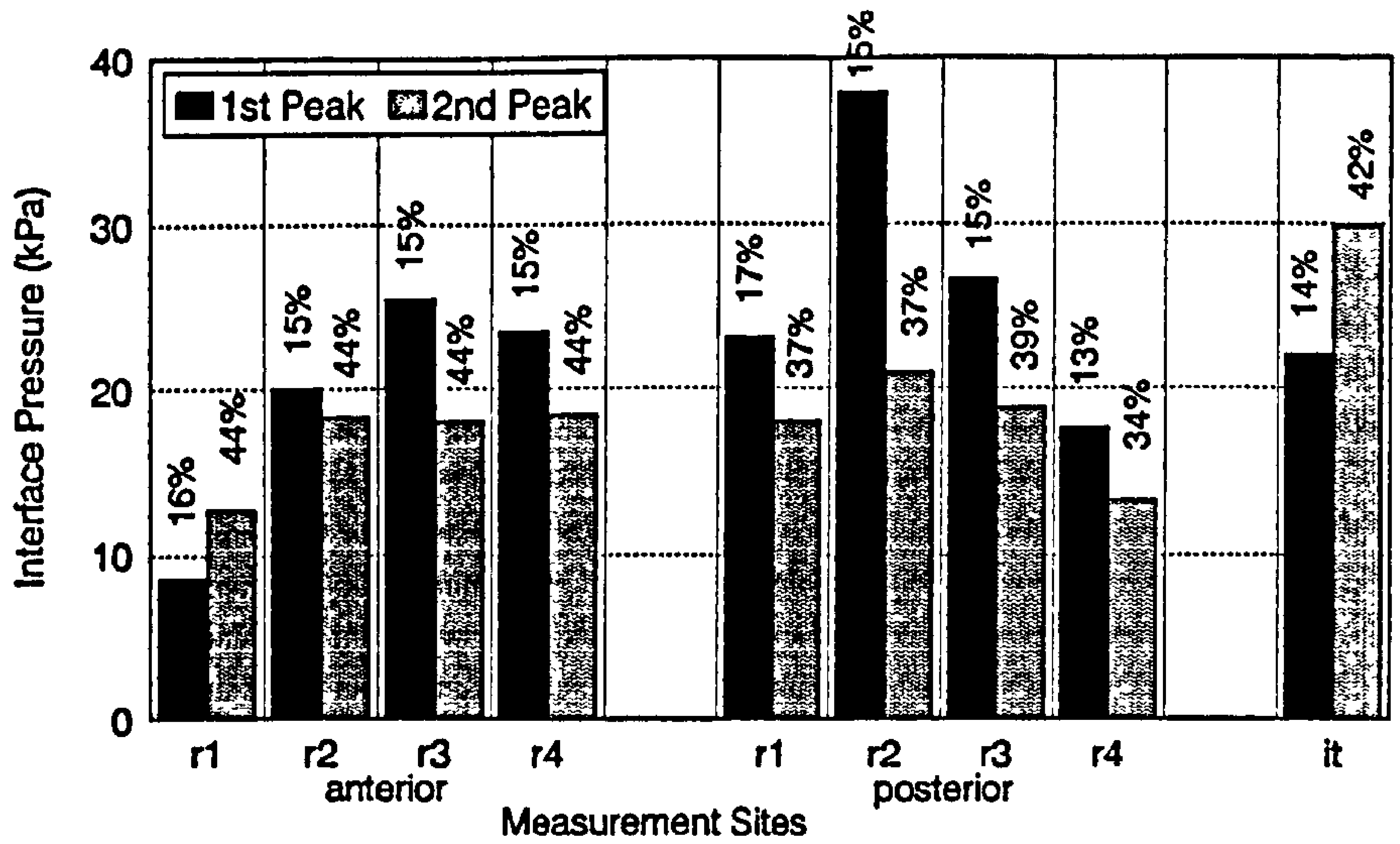

b.)

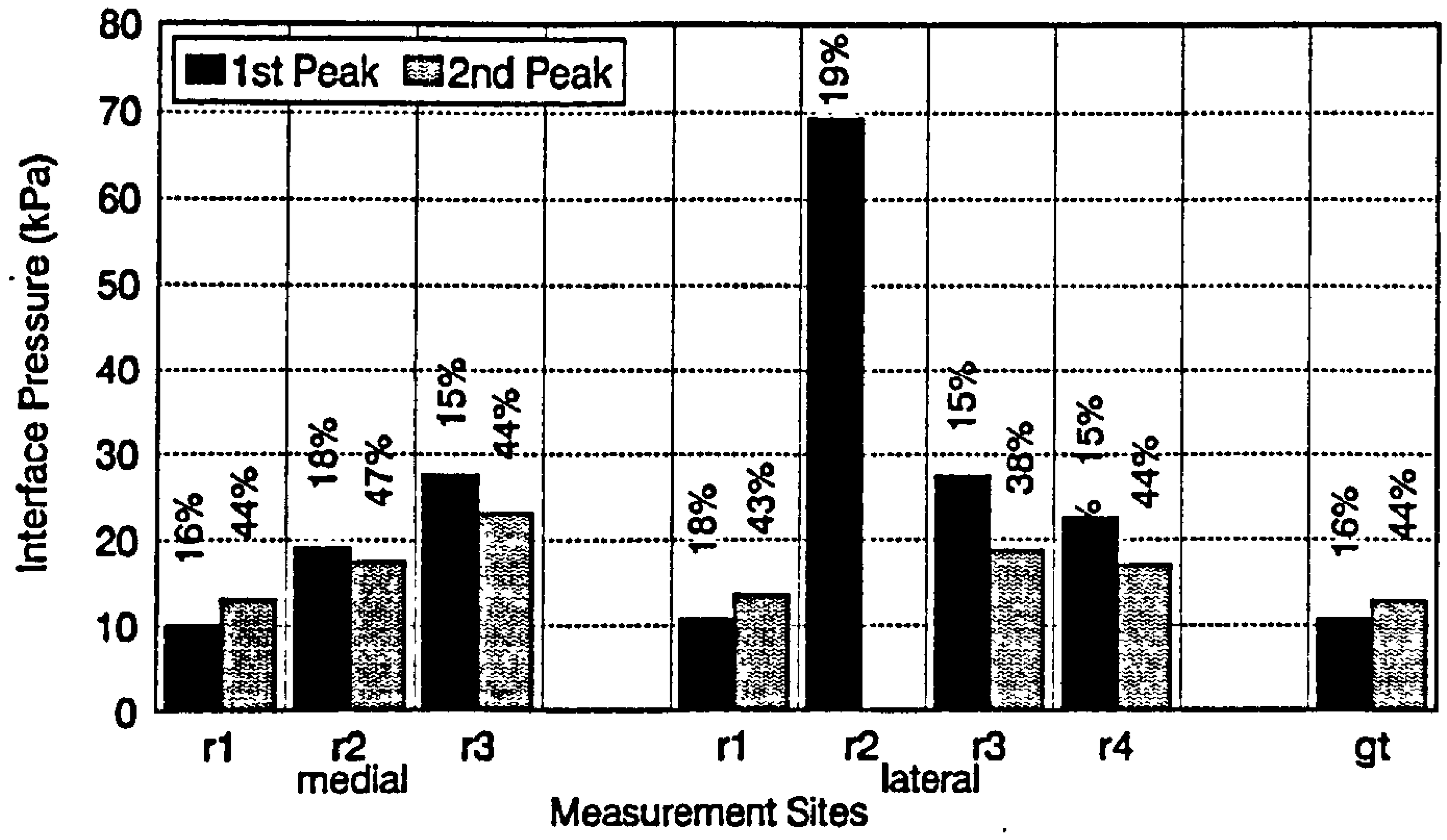

Fig. 4.9.3.12 Peak pressures corresponding to % of gait cycle in subject M IC socket.
a.) Anterior posterior sites
b.) Medial lateral sites

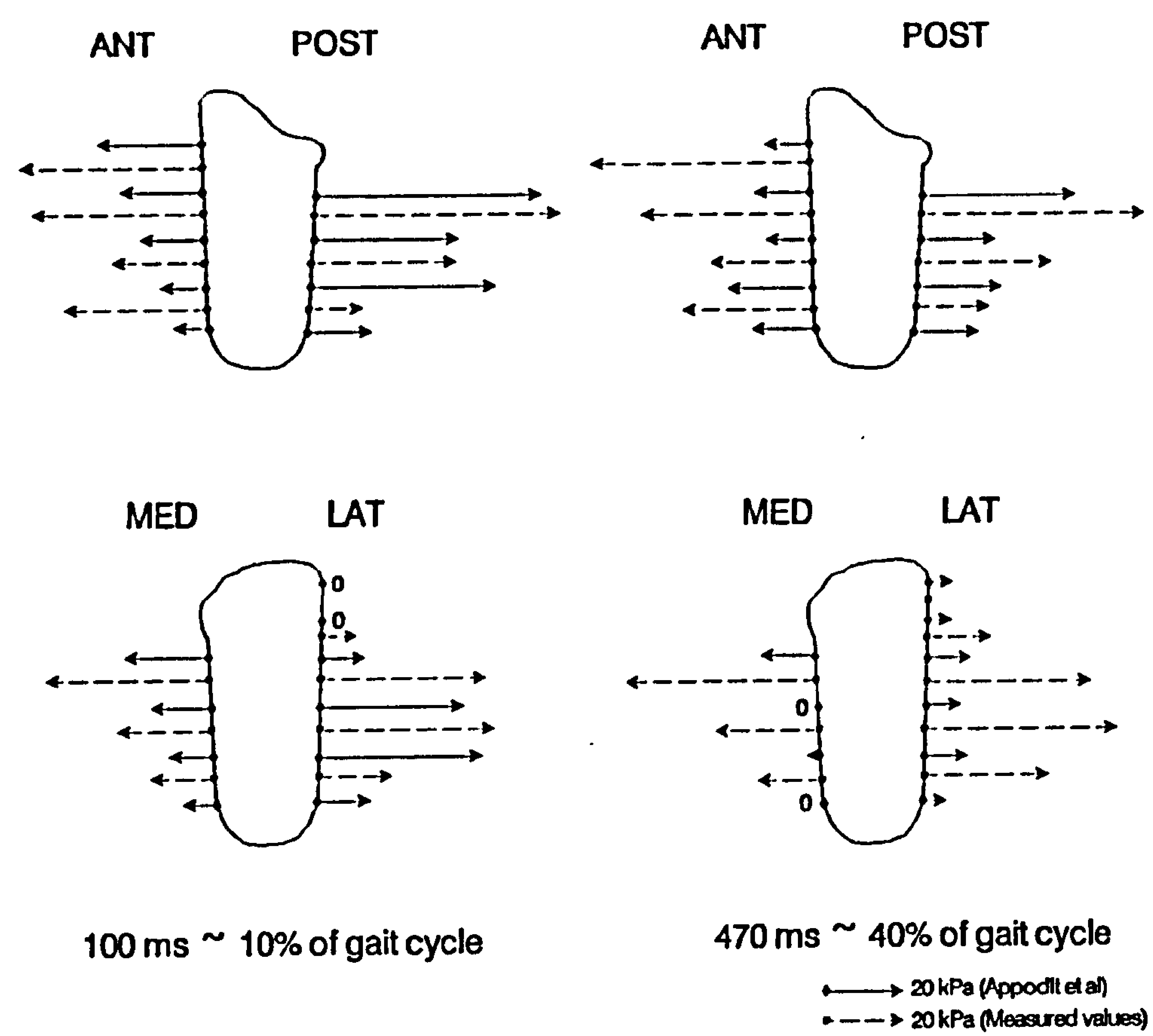

Fig. 4.10.1 Comparison of subject U's quad pressures with Appoldt and Bennett's study.

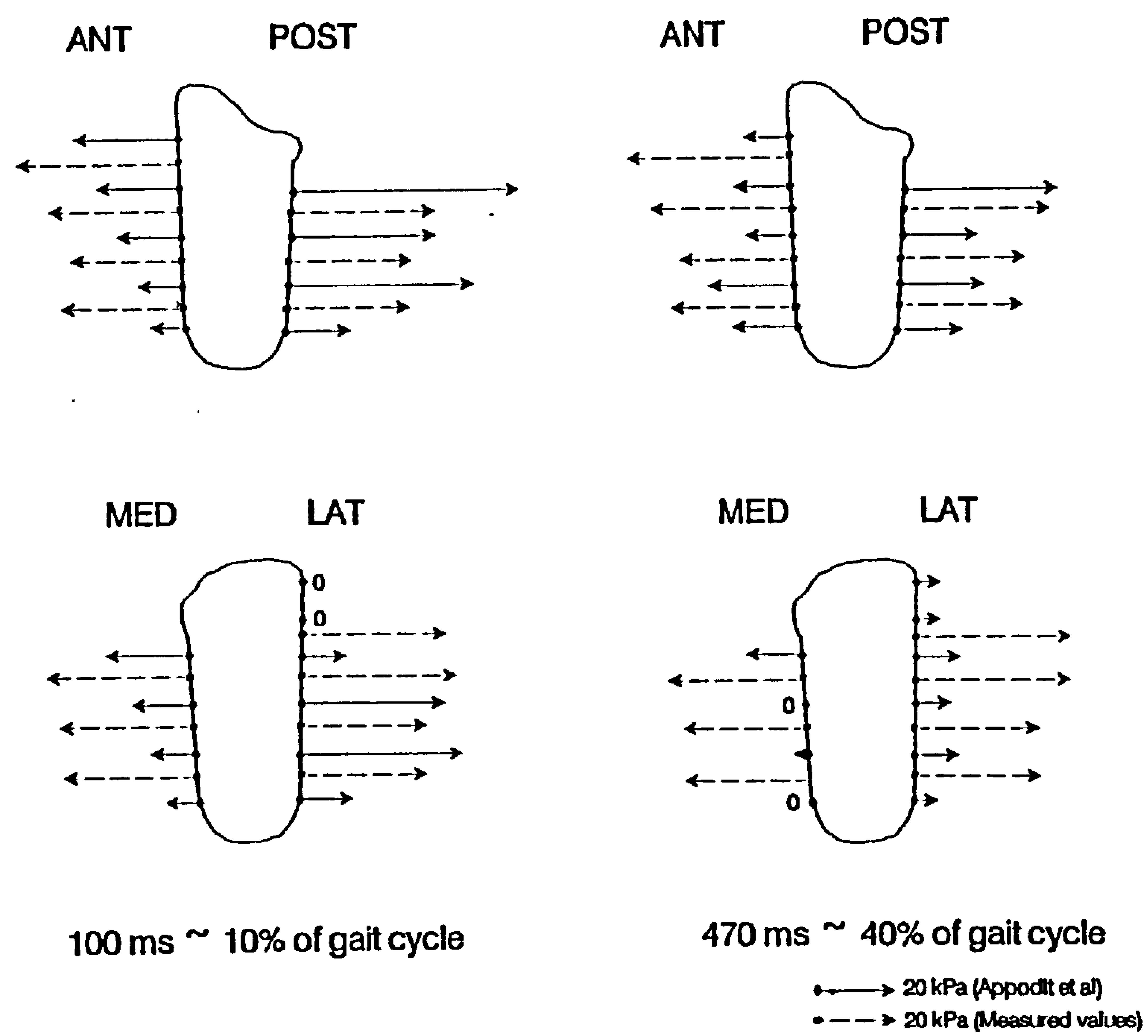

Fug. 4.10.2 Comparison of subject M's quad pressures with Appoldt and Bennett's study

pressures reported by Appoldt and Bennett at the ML wall at 40% of gait were not seen in the present study.

4.11 DISCUSSION

The discussion is separated into two main parts. The first looks at the pressure measurement system and procedures. The second discusses the pressures measured in part two of the study where the biomechanical differences between the quad and the IC are evaluated.

4.11.1 Pressure measurement system and procedures

The transducers adopted were found suitable in providing quantitative measurement of socket / residual limb pressure. It was obviously desirable to incorporate a large number of measurement sites in order to obtain a detailed pressure distribution. However, there is a physical limitation to the number of measurement sites that can be included. Improvement in this area is probably best investigated through selecting other types of transducers rather than improving the present Entran transducer attachment. The increasing use of conductive polymer pressure transducers, commonly known as force sensing resistors (FSR), in body/support measurement has spurred the development of commercial systems like the DVA-TEKSCAN (Houston et al, 1994) for socket pressure measurement. The main advantage of such a system is the thickness of the transducer (0.11mm) which allows the transducer to be sandwiched between the residual limb and socket without any modification to socket construction. Numerous pressure transducers can be incorporated without difficulty thus providing a more representative pressure map of the residual limb. However, as previously mentioned in the review section of this thesis, the FSR output is non-linear, and hysteresis and creep are present. Nevertheless, this type of transducer should not be overlooked as it is the most promising one available in terms of the advantages mentioned above.

Only static calibration was attempted with the Entran transducer used in this study, though dynamic interface pressure had been acquired. Difficulties were encountered in calibrating the transducer dynamically due to its delicate construction. The transducer is sensitive only to loading directed to the piston which in turn activates the encased strain gauge diaphragm. The option of subjecting the transducer to a pressurised chamber would be inappropriate since loading would not be isolated only to the transducer's piston. Subjecting the piston to a load displacement test using equipment like the INSTRON also proved to be difficult since the maximum displacement the transducer piston allows is only 0.012 mm.

The sockets used in the experimental procedures were different in several aspects to normally prescribed sockets. Due to the need to attach transducer adapters, the socket manufactured by the laminating procedure using resin was most successful, with no loose adapters and air leakage. Modern sockets are usually manufactured by draping flexible polyethylene and strengthened by a skeletal frame, which is significantly lighter in weight compared to these test sockets. This in turn will affect amputee gait to a certain extent, though it is not clear how interface pressure would be affected by the lighter weight and more flexible sockets.

The ambulatory demand on the subjects in the pressure measurement test was considerable since only four transducers were available for each data acquisition. Subjects' performances were expected to decrease due to fatigue though appropriate measures were taken to ensure sufficient rest in between test trials. Furthermore, the pressure variability due to time could affect results obtained for comparison between the quad and the IC sockets. In a study by Appodlt and Bennett (1968), it was shown that interface pressure in trans-femoral amputees vary significantly from day to day and week to week. It was not possible in this study to test the two types of sockets within the same day due to subject fatigue. Therefore the time interval between testing the first and the second socket for the same subject was about two weeks.

4.11.2 Comparing Quad and IC sockets

The comparison will be discussed under three subheadings relating to the amputee's stabilisation in the medio - lateral and anterio - posterior planes and the loading at the ischial tuberosity.

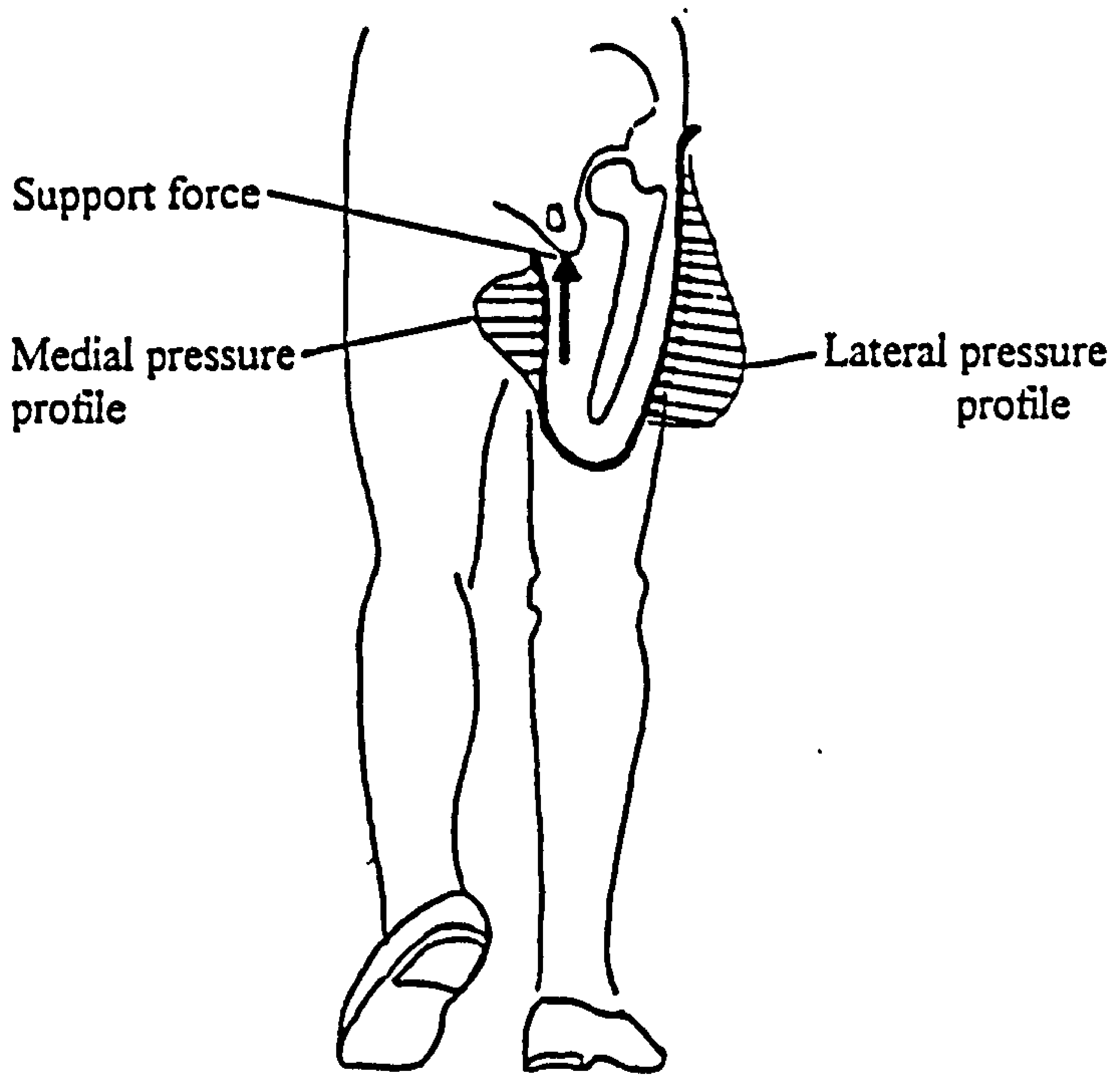

a.) Predicted interface pressure pattern and support force during stance in the medio lateral plane

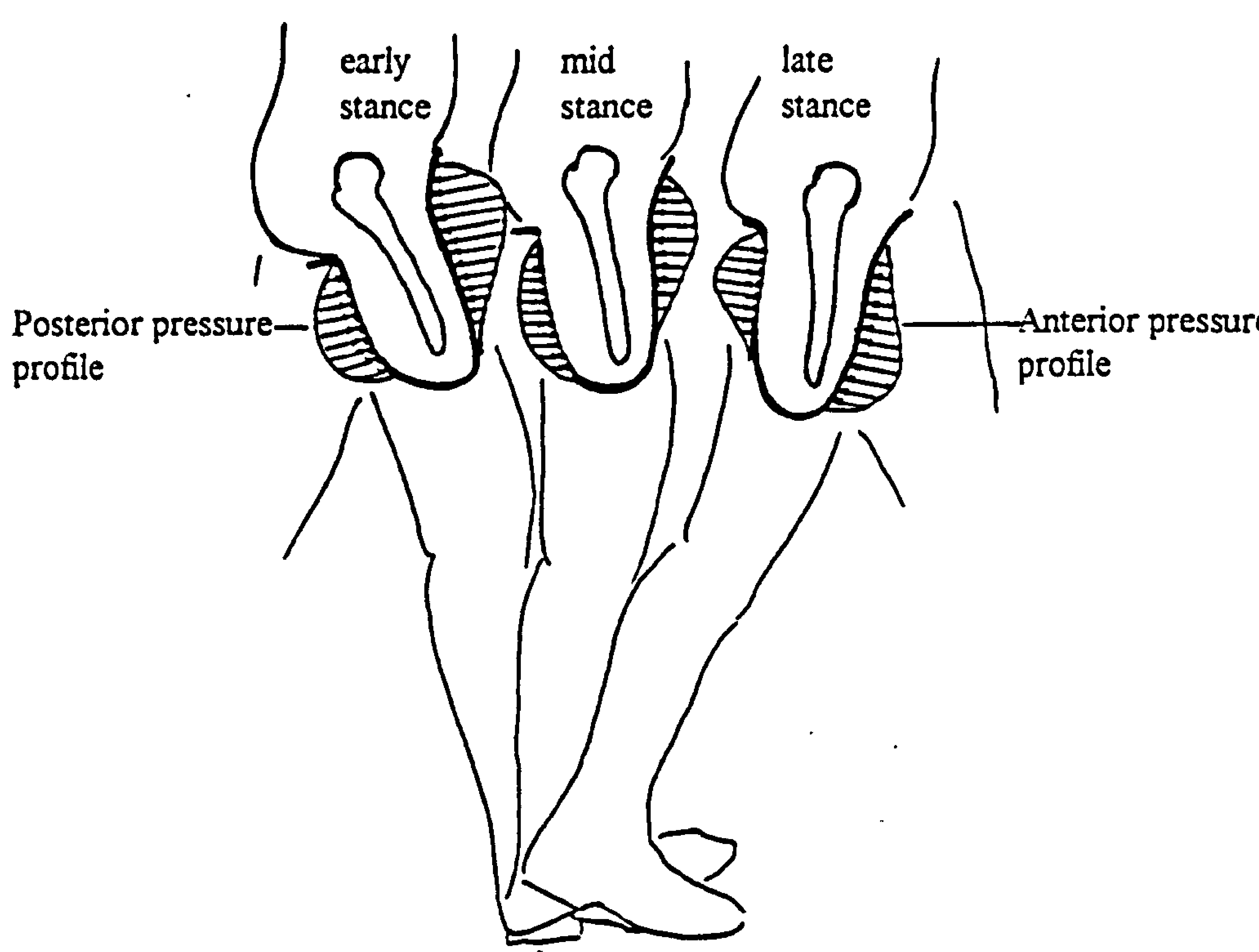

b.) Predicted interface pressure pattern due to the action of the hip musculature only, (supporting force not shown) in the anterior - posterior plane.

Fig. 4.11.2.1 predicted pressure distribution pattern in the quad socket.

Medio - lateral stabilisation

An indication of the direction and the anticipated distribution of forces acting on the residual limb of the trans-femoral amputee during gait are given by Radcliffe (1977) as shown in Fig. 4.11.2.1. According to Radcliffe the resultant of the vertical forces acting between the stump and the socket passes through a point, the support point. This support point acts as a fulcrum with the pelvis as a lever subjected to two end loads, the body weight and abductor muscles tension. During prosthetic leg stance phase, body weight will cause the pelvis to rotate towards the unsupported side, restriction of this motion, and thus maintenance of an approximately level pelvis, occurs by contraction of the abductor muscles of the supporting leg. Abductor contraction creates a lateral movement of the femur bringing the femoral remnant, especially the cut distal end, closer to the lateral wall of the socket. The abduction movement of the femur and stump against the socket ML walls generates a moment which leads to an increase in the distal lateral and proximal medial pressures. Without accommodation the localised pressure at the distal lateral aspect can lead to severe discomfort and hence to gait deviations. The prosthetist, therefore, aims to reduce this distal tip pressure by creating a small relief in the lateral wall whilst maintaining an intimate contact with the remainder of the lateral aspect of the stump.

The pressures observed at 10% and 50% of the gait cycle from the medial and lateral socket walls follow the expected pressure distribution, as described above, for both subjects on both sockets. Fig. 4.11.2.2 illustrates the pressure distribution for one subject (U) in the ML plane for both IC and quad sockets. The lateral pressures increase towards the distal end reaching a maximum at the second last site, then reducing at the most distal site showing that the desired relief was achieved. Medially, the proximal site shows that high pressure exists and this pressure is reduced by more than 50% towards the distal end.

Anterio - posterior stabilisation

Prosthetic knee stability can be achieved by a variety of methods, e.g. locked knee, weight activated locks and voluntary control by the amputee. The theory

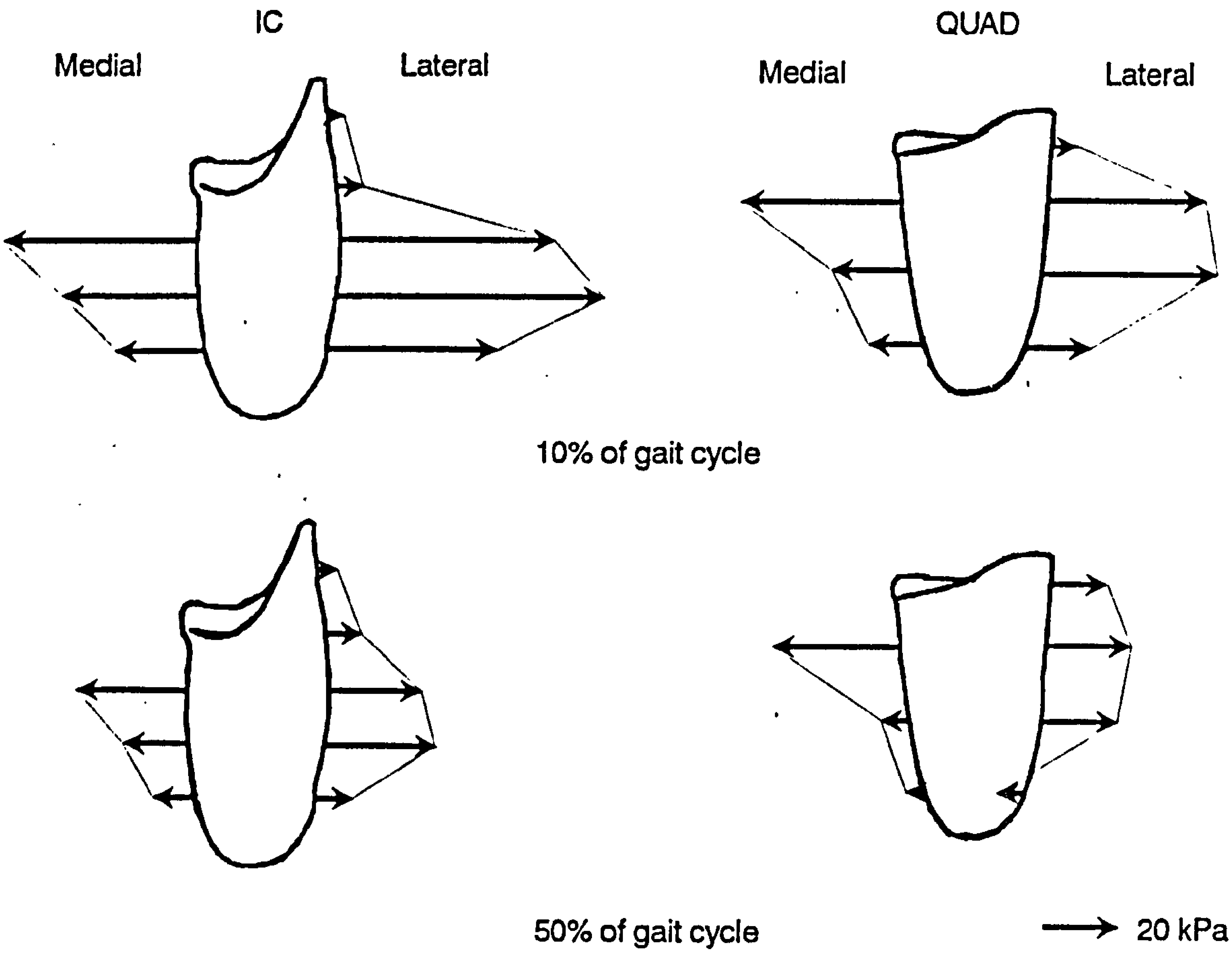

Fig. 4.11.2.2 Interface pressure in Subject U at 10% and 50% of the gait cycle in the ML plane.

relating to the last method suggests that at heel strike the hip extensors create counter pressure at the proximal anterior and distal posterior socket walls. This pattern maintains up to the point of heel off when the ground reaction force vector passes behind the knee joint. In late stance anterior socket pressure is concentrated distally while posterior pressure can be found proximally as the hip flexes to propel the prosthesis into swing phase (Fig. 4.11.2.1).

The AP pressure distribution for subject U wearing the IC socket at 10% of the gait cycle is shown in Fig. 4.11.2.3. The diagram follows the expected pressure distribution pattern shown in Fig. 4.11.2.1 at early stance but the difference between the pressure pattern on the anterior and posterior walls of the socket is less pronounced. At the 50% point the pattern remains the same but with the pressures decreased. This is not in agreement to the pattern predicted in Fig. 4.11.2.1 which shows a reversal of the load actions from hip extensors being active to the hip flexors. The pressure distribution throughout stance on subject M with the IC socket displays similar characteristics.

In the quad socket during early stance, the pressures are concentrated at the proximal part of the socket with much reduced pressures at the distal part of the socket. As with the IC socket, no reversal of the pressure distribution at late stance takes place, the pattern remaining the same as in early stance but with reduced values. Exactly why the measured pressure pattern in the anterio - posterior plane differs from that predicted in Fig. 4.11.2.1 at this stage of the investigation is not clear. A reason for the difference could be due to the fact that Fig. 4.11.2.1 assumes a free knee under voluntary control whereas, the prosthesis used in this study was fitted with a stabilised prosthetic knee. Furthermore, the recorded pressures comprise the combination of pressures caused by weight transmission and by the propulsion forces. Before comparisons can be made these two effects must be separated. However, it is considered that additional measuring sites are necessary before such in depth analysis of the data can be undertaken.

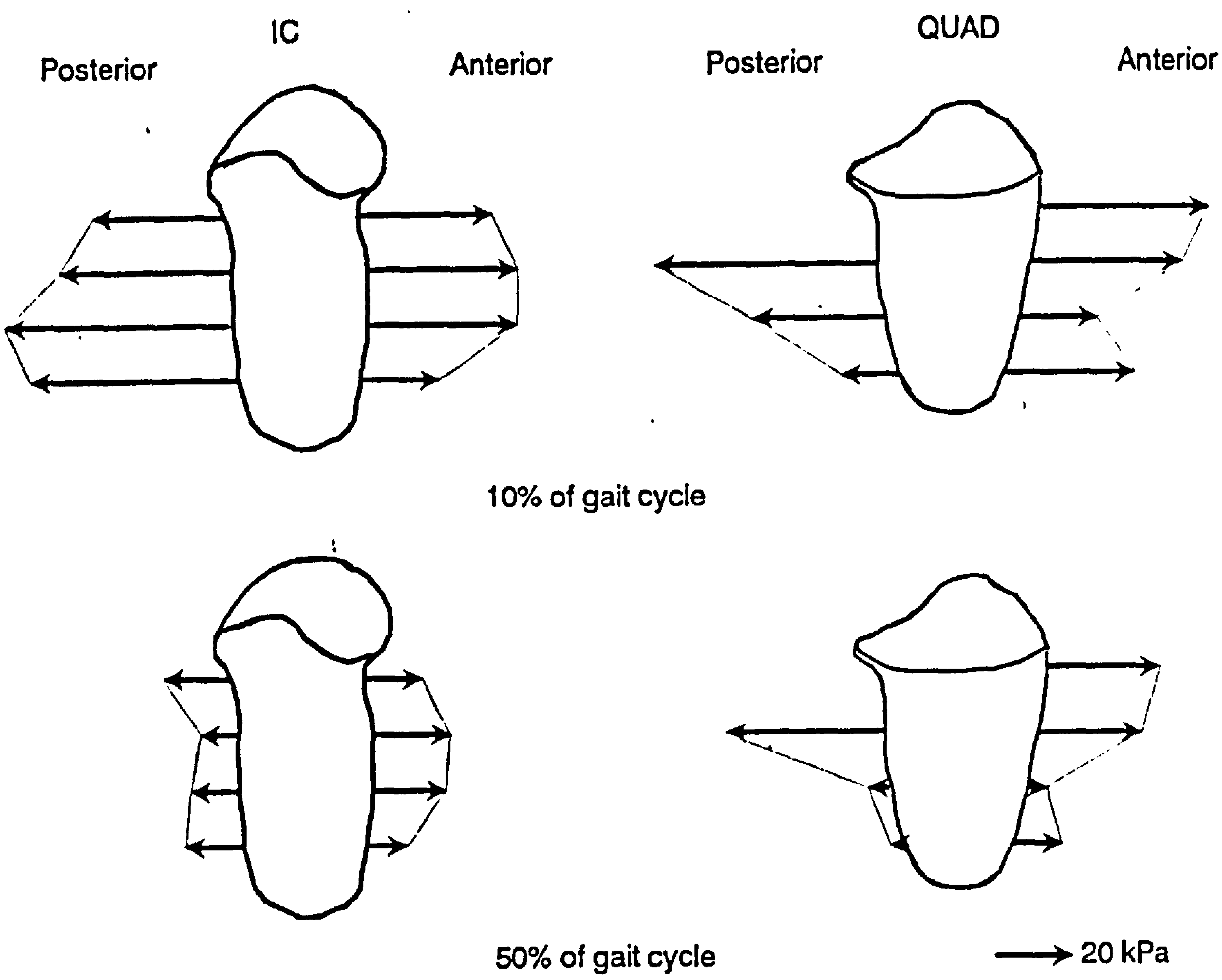

Fig. 4.11.2.3 Interface pressure in Subject U at 10% and 50% of the gait cycle in the AP plane.

Ischial tuberosity loading

Subject U displays high ischial loading during gait in both IC and quad sockets, with the latter approximately 35% higher. However, in the case of subject M, ischial loading at 10% of cycle is 20 kPa and 9 kPa in the IC and quad respectively. At 50% of the cycle, these pressures increase to 29 and 39 kPa respectively. In comparison, subject U's ischial loading (up to 92 kPa) which is much higher than subject M's suggested several ideas. The author reckons that this could simply be due to the difficulties in ensuring that the transducer site corresponded with subject M's ischial tuberosity since visual verification is impossible and tactile inspection is extremely difficult when the socket is in situ. However, subject M lower pressure at 10% of gait which subsequently increases at 50% of gait could also mean that the ischial tuberosity was not fully loaded at the early phase of stance. Such a theory has been put forward by Lehneis (1985) . The distance between the axis of rotation of the hip and the ischial seat on the socket changes during the stance phase but the distance from the hip joint to the ischial tuberosity is constant. Therefore the ischial tuberosity is expected to separate from the ischial seat at early stance (Fig. 4.11.2.4). Nevertheless, if this is true, it applied only to subject M, since subject U shows a consistent ischial loading throughout the stance phase. Comparing the IC and the quad, it could be noted that the magnitude of pressure at the ischium of the IC is not much higher than the proximal walls. The slope and raised ischial brim of the IC tend to serve two purposes, distribute pressure and maintain consistent loading throughout gait.

4.12 CONCLUSION

The results presented in this study helped in discussing several concepts of prosthetic socket fitting. However, the author felt that it is too early to arrive at a definite conclusion regarding which is the better between the IC and the quad, since while pressure measurement allows quantitative information to be collected with regard to the external features of the stump, it provides little concerning the geometry and tissue properties of the residual limb. Nevertheless, the results have contributed to

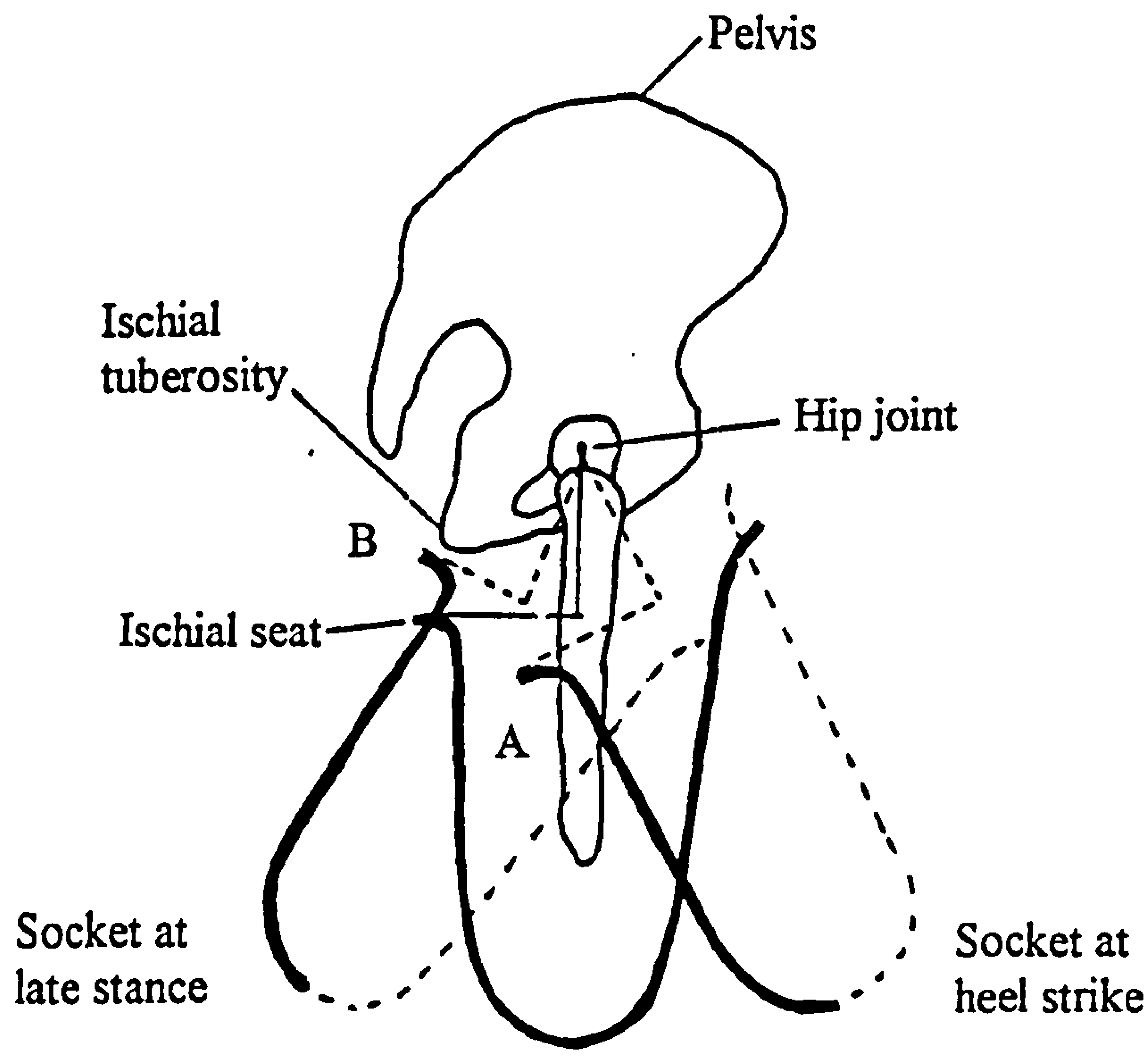

(A) At heel strike seat leaves ischial tuberosity
(B) At late stance seat presses hard against ischial tuberosity

Fig. 4.11.2.4 Ischial tuberosity position with respect to the quad socket during gait.

expanding a database concerning the comparison of the two types of sockets. This study also forms part of an investigation to build accurate finite element models of the stump, where the interface pressures measured were used to validate the models.

The transducers adopted were found suitable in providing quantitative measurement of socket / residual limb pressure. It is obviously desirable to incorporate a large number of measurement sites in order to obtain a detailed pressure distribution. However, there is a physical limitation to the number of measurement sites that can be included.

The pressures recorded for the two types of sockets indicated that there is a significant difference in the way pressures are distributed. The quad socket provides good proximal support, increasing pressure at the brim while reducing distal end pressure. The IC relaxes loading at the brim, allows transfer of load to the distal end and thus produces a more evenly distributed pressure profile throughout the socket. In general, the ML dynamic pressure distribution was similar for both the IC and the quad socket, which approaches that predicted in Fig. 4.11.2.1. However, pressures at the AP plane is somewhat unclear, which require further work.

CHAPTER FIVE
KINETICS AND KINEMATICS

5.1 INTRODUCTION

It must be highlighted at the beginning of this chapter that the kinematics and kinetics studies performed on the amputee subjects were not used to investigate factors that influence gait, i.e. types of prosthesis components, alignment of prosthesis or socket fit. The main aim was to established the actual loading conditions experienced at the anatomical joints. These loadings served only as realistic inputs to the FE models of the residual limb. The effort and cost required in performing these studies were indeed massive, thus one could argue the justification for such a purpose. Nevertheless, the need to provide accurate input to FE model could not be more important. It becomes unacceptable when the validating pressures were carefully recorded while the inputs to the model were just guesswork.

The chapter begins with a brief review in the studies of human locomotion. Methods of kinetics and kinematics measurements are discussed with reference to the different types of equipment used. This is followed by a short review on normal and lower limb amputee gait analysis, in order to define most of the gait analysis terminology used in this study.

5.2 LITERATURE REVIEW

Walking is itself a complex action. A control system is required to govern the changing forces and motions of walking, where anatomy, physiology and mechanics have to be considered altogether. Borelli (1680) was the first to perform force analysis in the study of locomotion, though the studies were largely considered static. Dynamic studies began in the late 1800's through techniques of photography. Marey (1882) and Muybridge (1887) used photographic plate to record sequence of human locomotion acts. The results were relatively good for qualitative observation of movements. With the work of Braune and Fischer (1895) the fundamentals in biomechanics were established. Human body segments were represented as rigid bodies and 3-D trajectories of moving points fixed on the body segments could be identified. The development of an instrument to measure forces between the foot and the ground by Amar (1916) also advanced the research in locomotion. This

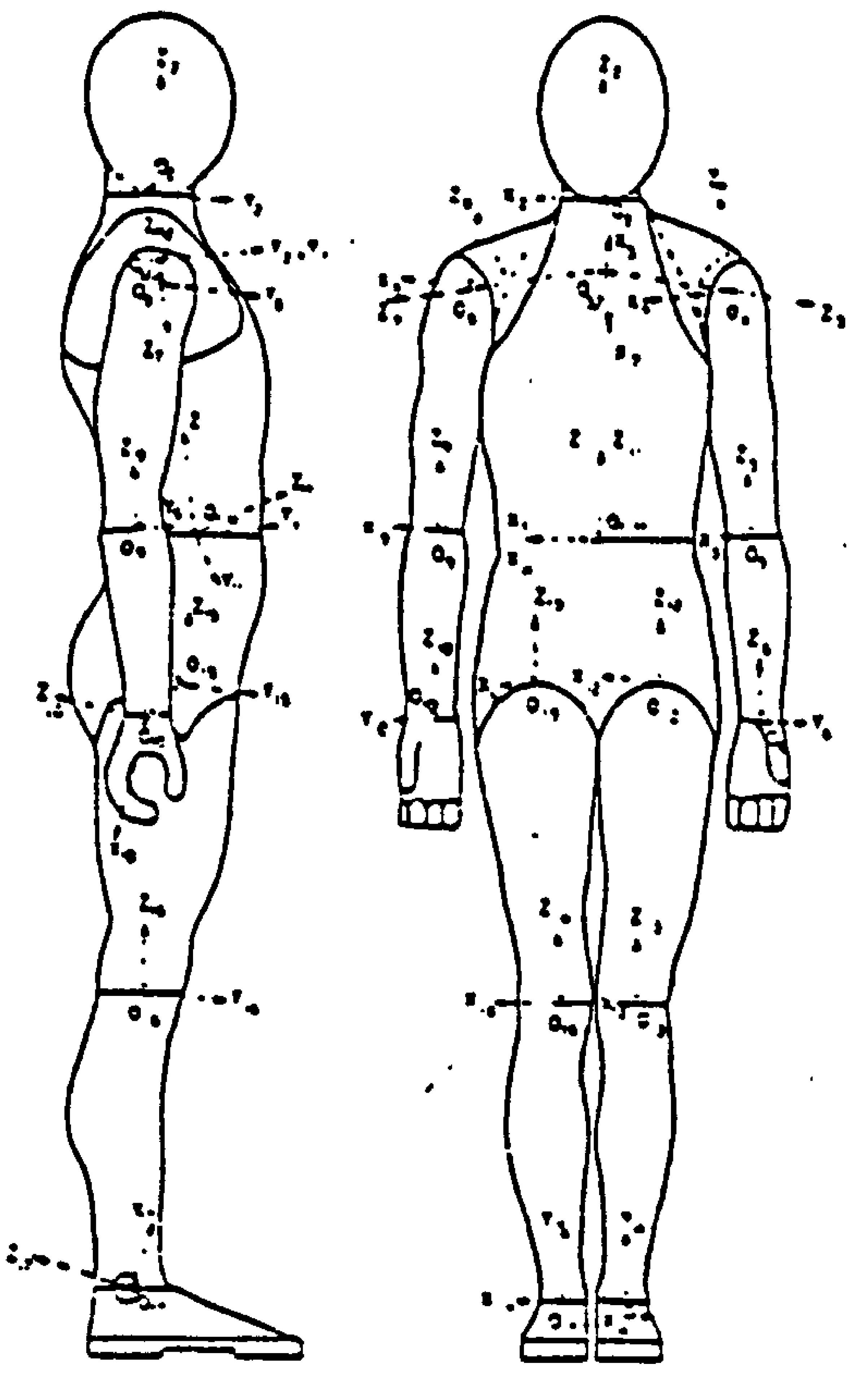

Fig. 5.2.1.1 Human model consisting of 17 segments.
(Hatze, 1980)

mechanical instrument records the deflection of springs supporting a platform upon loading.

In 1947, an extensive programme to study human locomotion was formed in the University of California. The group has been responsible for what is now known as the modern force platform, providing knowledge of the ground reaction forces (GRF) generated at the foot (Eberhart et al 1947, Cunningham and Brown 1952). In the programme, information regarding movements, velocities, accelerations, forces, moments and muscles' activities in limb segments were obtained for normal and amputee subjects.

5.2.1 Human Body segments

The human body presents itself as a complicated structure for biomechanical analysis and therefore has to be simplified. Simplification takes the form of breaking down the body into segments. A segment is thus defined by two ends possessing synovial joints, i.e. where two or more bones articulate.

Aleshinsky and Zatsiorsky (1978) described a 15 segments model which was used to determine moments at major joints. Hatze (1980) reported a human body made up of 17 segments (Fig. 5.2.1.1) and Goh (1982), Lang (1988) and Marmar (1993) used an eight segment model to study trans-femoral gait. The eight segment model has been tested by Lang (1988) and gave comparable results to previous investigators. The same eight segment model will be used in this study.

5.2.2 Kinetics measurement

Two forms of kinetic measurements relating to human gait are the measurement of foot to ground reaction forces and pressure distribution under the foot. The device that is used in the former measurement is commonly known as the force platform and the latter is with a custom built pressure sensitive shoe insole or a pedobarograph. Another device used to obtain force measurements in amputee subject is the strain gauged pylon transducer (Berme et al 1975). The device is usually connected between the prosthetic foot and shank and thus has the advantage of acquiring data for every single step, unlike the force platform.

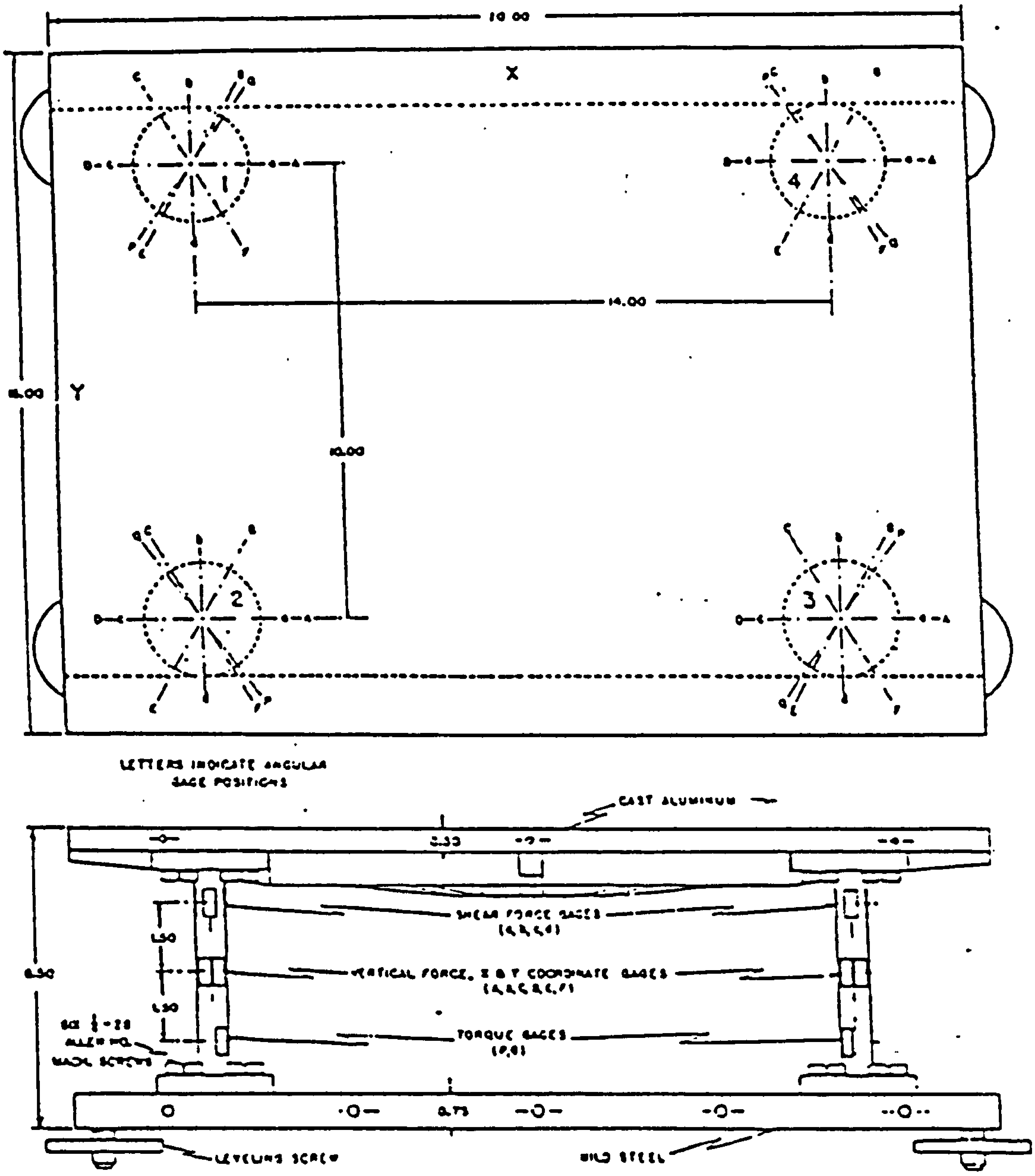

Fig. 5.2.2.1 Force platform designed by Cunningham and Brown, 1952.

The force platform designed by Cunningham and Brown (1952) Fig. 5.2.2.1, was made up of two aluminium plates separated by four columns. The columns were mounted with electrical resistance strain gauges to record the resultant forces and moments. Based on the same principles, Kistler Instruments (1975) has a commercial system utilising pizeoelectric transducers. A cast aluminium plate or glass plate is supported on another lower plate by four multicomponent piezoelectric transducers at the corners. Signals corresponding to three orthogonal forces and three orthogonal moments could be produced by electrically summing and coupling the appropriate components of the transducers. The natural frequency of the system is between 125 Hz and 800 Hz, which is higher than most of the applied frequency involved in the measurement of floor reaction forces (Crowninshield and Brand 1978).

5.2.3 Kinematics measurement

Kinematic studies are generally conducted using imaging methods in the form of photography or optoelectronics. Photography techniques are now largely replaced by newer developments in optoelectronics. There are several types of optoelectronics systems which are highlighted below.

Television/video computer systems are based on the principle of digitally sampling and registering images of the markers that are attached on the subject by a video camera and analysis circuits. The markers positions could then be defined in the x and y co-ordinates. One of the first descriptions of such a system by Furnee (1967) was applied in the study of arm movements. The updated system is now marketed under the name PRIMAS (Furnee 1988). Jarrett (1976) developed a system (Strathclyde system) that identified markers that were brighter than the background recording them as x and y co-ordinates at a resolution of 0.1% and 0.3% respectively (Fig. 5.2.3.1). The markers were retro reflective and illuminated by tungsten halogen light sources positioned close to the cameras. The system utilised a PDP12 mini computer managing two cameras, nevertheless, the system was capable of accommodating up to six cameras. Andrews (1981) continued the development improving the accuracy and ease of operation of the system. The improved camera operated with infrared light, thus there was no need for the distracting tungsten

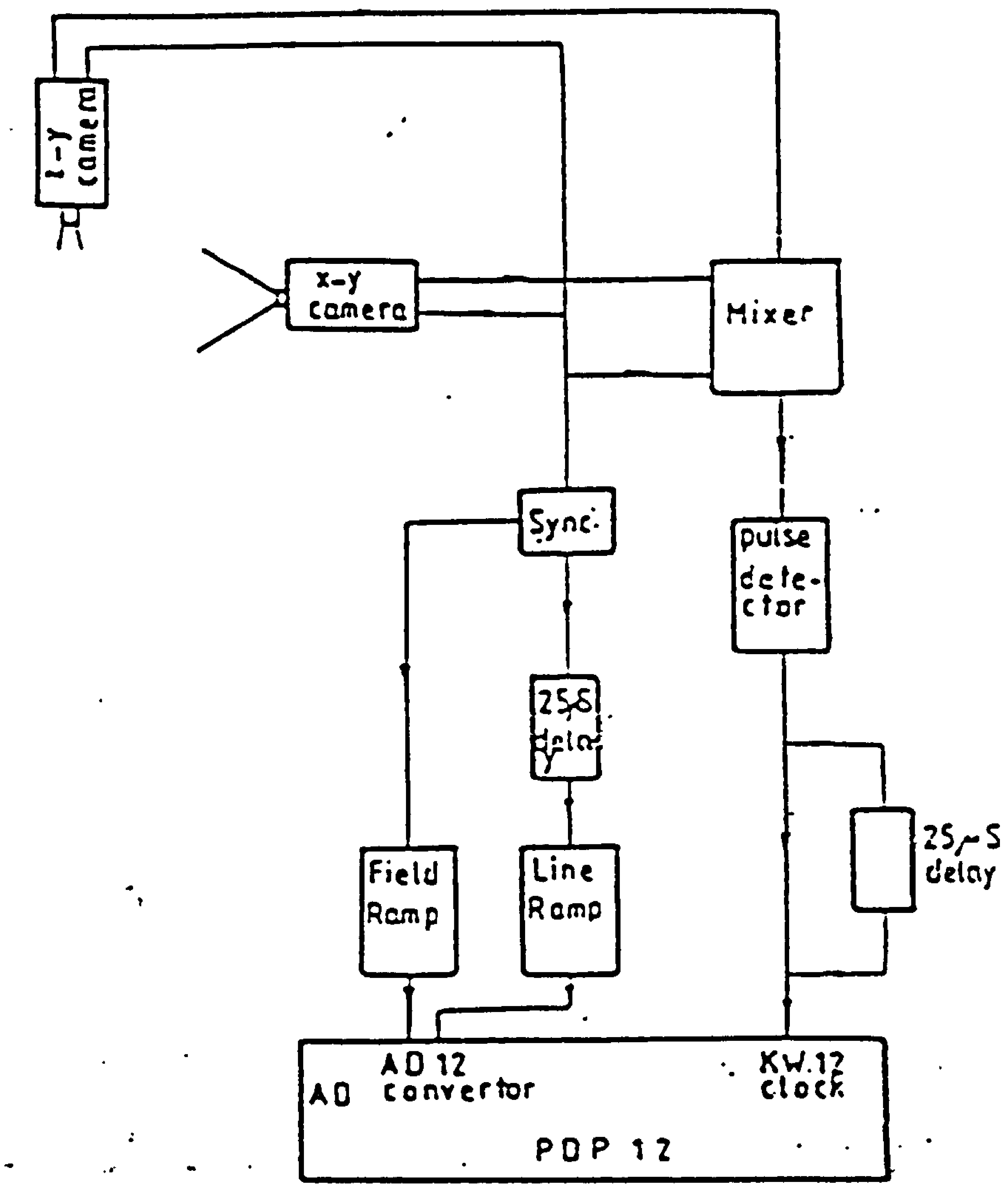

Fig. 5.2.3.1 Schematic layout of Strathclyde system.
(Jarrett, 1976)

halogen light source as used in the previous system. A third camera was also added enabling 3-D analysis of the whole body.

The Strathclyde system is now available commercialy under the name VICON from Oxford Metrics Ltd. The system has an accuracy of 0.1% of the field of view and capability of accommodating seven cameras. The Vicon has been widely used and evaluated. Whittle (1982) looked at the frame to frame variation of the system by capturing a stationary marker for 20 frames and found it to be 2 mm or less. Li (1993) did a similar test but with 20 markers recorded for 20 frames, the mean variation for x, y and z axes was 2.493 mm (Table. 5.2.3.1). Morris (1991) proposed a test protocol for evaluating the Vicon system. The dynamic test was performed by tracking the motion of three pendulums. A standard deviation of 0.579 mm, 0.496 mm and 0.543 mm was found. A further dynamic test was carried out using a rod of 978 mm length with two end markers, and moving it in four directions. The mean and standard deviations of the recorded length are 979.38 ± 0.56, 978 ± 0.65, 979.07 ± 0.74, 978.79 ± 0.57 mm. The reliability of measuring joint kinematics using the Vicon was evaluated by Rao et al (1992). Ten healthy male subjects participated in the test where kinematics of free and fast walking were obtained. Statistical analysis was performed upon which the authors concluded, " the inherent static system measurement error was low, and the measured gait kinematics were highly reliable ".

The Vicon has attracted a wide and diverse group of users. The study of normal gait was attempted by Bastian et al (1991), correlating lumbar lateral flexion with pelvic rotation. Novick (1990) reported a study examining 20 subjects to determine the effect of foot orthoses during walking. Postema et al (1994) compared an energy storing foot and a conventional foot in 10 trans-tibial amputees and concluded that there was a small difference in the acceleration during walking. The application of Vicon or other motion analysis systems has been growing in the treatment of children with cerebral palsy. A preliminary study was reported by Thomas et al (1992) where the gait of 200 children with cerebral palsy were clinically evaluated using Vicon. These cases were seen for reasons of pre-orthopaedic surgery, pre-rhizotomy assessment, post surgical assessment, clinical correlation and orthotic assessment. Preoperative gait analysis was performed by Lee at al (1992) on 23

Marker No.	Measured marker position (Mean)			Real marker position		
	X	Y	Z	X	Y	Z
1	-1552.32	1341.93	437.10	-1552.0	1341.5	437.0
2	-1552.79	941.84	436.61	-1552.0	941.5	437.0
3	-1549.88	541.46	436.04	-1552.0	541.5	437.0
4	-1549.86	201.15	436.15	-1552.0	201.5	437.0
5	-1550.69	141.10	436.96	-1552.0	141.5	437.0
6	-733.87	1340.41	-602.21	-733.5	1340.3	-601.0
7	-733.05	938.77	-600.74	-733.5	940.3	-601.0
8	-732.19	538.32	-600.71	-733.5	540.3	-601.0
9	-732.35	200.02	-600.46	-733.5	200.3	-601.0
10	-732.47	139.46	-600.17	-733.5	140.3	-601.0
11	1156.42	1337.22	-712.65	1156.0	1336.5	-712.0
12	1155.46	936.40	-711.81	1156.0	936.5	-712.0
13	1154.95	536.72	-711.45	1156.0	536.5	-712.0
14	1153.23	196.83	-711.72	1156.0	196.5	-712.0
15	1152.84	136.70	-711.85	1156.0	136.5	-712.0
16	1151.84	1343.15	1024.60	1151.0	1342.1	1023.0
17	1151.67	1001.46	1022.43	1151.0	1002.1	1023.0
18	1151.40	940.82	1022.47	1151.0	942.1	1023.0
19	1148.77	540.17	1021.82	1151.0	542.1	1023.0
20	1149.23	141.38	1022.00	1151.0	142.1	1023.0

(Mean residual 2.493mm)

Table 5.2.3.1 Frame to frame variability of 20 static markers.
(Li, 1993)

children with cerebral palsy using Vicon. Surgery was then conducted based on gait assessments and other clinical evaluations. The authors concluded that gait assessment contributed significantly to the process of treatment.

A light recognition system, originally designed by Lindholm (1974), is now marketed under the name of SELSPOT by Selcom, Sweden. Similar to the above mentioned systems, markers have to be placed at anatomical joints. Instead of passive markers, these markers are active infrared LEDs flashing sequentially. The flash is picked up by a camera focusing the light on a built in silicon photo-diode which produces an electrical signal corresponding to the x and y co-ordinates. Paul and Nicol (1981) evaluated the system for biomechanical purposes. It was found that the reflected stray light could distort the acquired data. It was also difficult to fix the LEDs to some anatomical sites. SELSPOT has also been widely used in the study of human motion. Goel et al (1987) measured the movements of spine using SELSPOT. The accuracy of the system for a 0.2m x 0.25m x 0.2m measuring field was reported to be less than 0. 5 mm in translation. Stokes et al (1989) studied pelvis and thorax movements during locomotion. Areblad et al (1990) used SELSPOT to investigate the kinematics of running.

Other than the two commercial systems mentioned, there are the CODA-3, developed in Loughborough University marketed by Movement Techniques Limited; the WATSMART system, Northern Digital Incorporated; and a video based system known as ExpertVision by Motion Analysis Corporation. Literature regarding these systems could be found in Mitchelson (1988), Northern Digital Inc. (1983) and Motion Analysis System (1990) respectively.

5.2.4 Gait analysis

Gait analysis is the study of human walking. A complete gait analysis includes the study of temporal-distance measurements, kinematics and kinetics analysis, energy factors and muscular activities. In this study, only the first three analyses were attempted which was sufficient to fulfil the aim of this work.

Several reviews of lower limb amputees gait analysis have been published over the years. Porter and Roberts (1989a and 1989b) reviewed the topic in two parts,

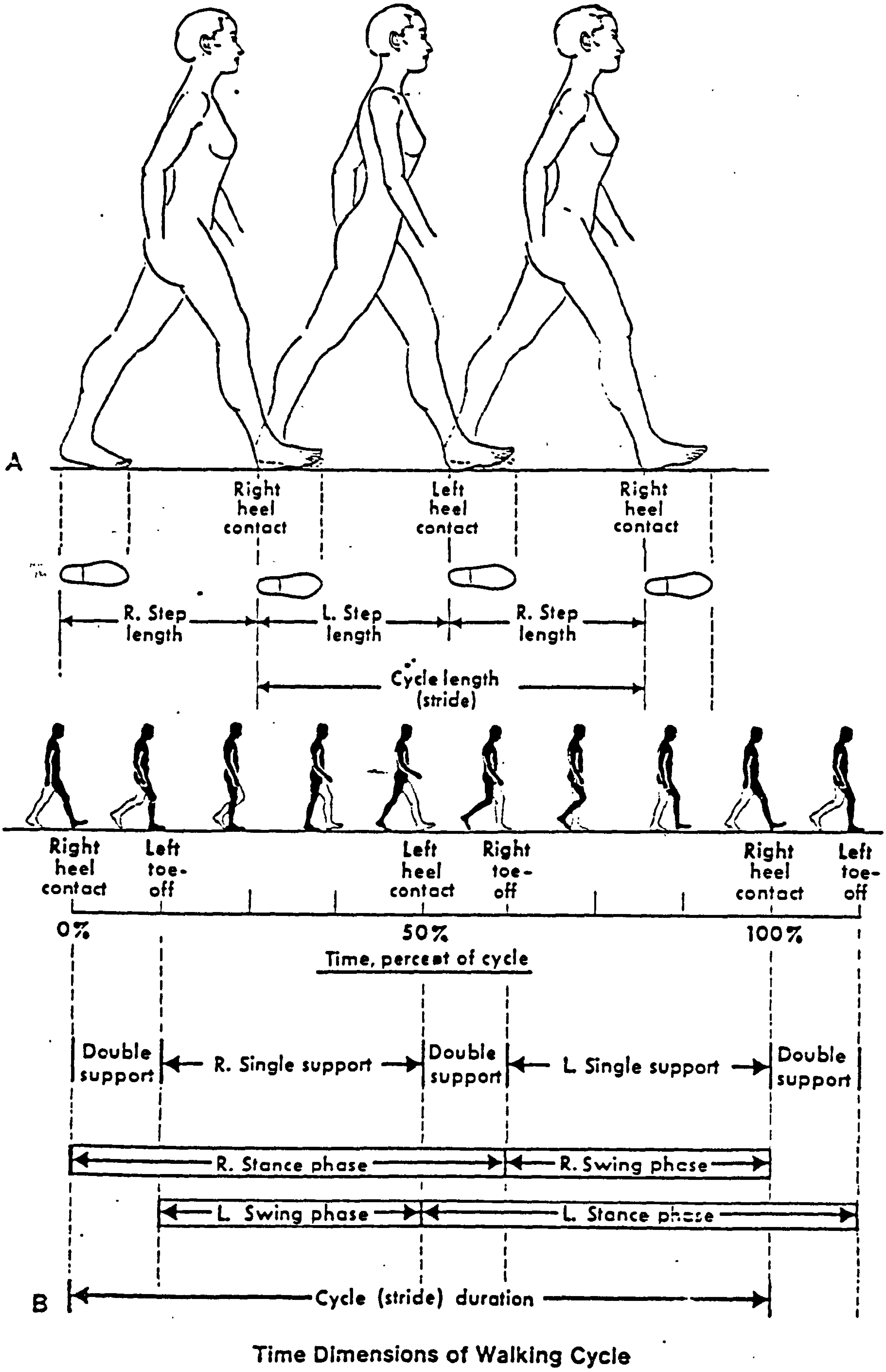

Fig. 5.2.5.1 Temporal-distance parameters. (Inman et al, 1981)

temporal / kinematics and kinetics / metabolic analysis. Skinner and Effeney (1985) and Gage and Hicks (1985) provided a brief and concise summary of gait analysis in amputees.

5.2.5 Gait Analysis :- temporal - distance measurements

The position of the leg for a normal human walking can be broken down into repetitive cycles consisting of a swing and stance phase. At swing phase the foot moves through the air and during stance or support phase, the foot is in contact with the ground. The latter phase is also called the support phase. Inman et al (1981) presented a graphical illustration of temporal-distance parameters (Fig. 5.2.5.1). Human gait could be described in the following measurements ;

a.) Velocity is the distance covered by the whole body in a given time in the forward direction, expressed in metre /second or metre / minute.

b.) Stride length (expressed in metre) is the distance between two successive placements of the same foot, example heel contact to heel contact.

c.) Step length (expressed in metre) is the distance between heel contacts made by different feet. A stride length is made up of two step length, a left and a right.

d.) Cadence (expressed in steps / minute) is the number of steps accomplished in a given time.

d.) Gait cycle (expressed in seconds) is the time interval between two successive occurrence during walking. It is common to use the heel strike of one foot. For example, the time between the right heel contact to the next right heel contact forms the gait cycle. The stance phase and swing phase for normal free walking is about 60% and 40% of the gait cycle respectively.

e.) Double support time (expressed in seconds) is the period when heel contact of one foot occurs while the other foot is still on the ground, i.e. right heel contact to left toe off or vice -versa.

e.) Single limb support time (expressed in seconds) is the period when one foot leaves the ground while the other foot in still in contact. Thus, at the beginning of swing phase of the left side (left toe off), right single support begins and the period stops when the left heel comes back into contact with the ground.

Level	Velocity (m/min)	Cadence (steps/min)	Stride Length (m)	Gait cycle (sec)	Single limb prosthetic	support normal	Reference
AK	60	87	1.36	1.38	0.43	0.58	Murray et al 1981
AK	*	*	*	1.43	0.48	0.6	Zuniga et al 1972
AK	52	84	1.21	1.44	*	*	Godfrey et al 1975
AK (Dysvacular)	36	72	1	*	*	*	Waters et al 1976
AK (Traumatic)	52	87	1.2	*	*	*	Waters et al 1976
AK	56.4	85	1.29	1.41	0.49	0.61	James et al 1973
BK (Dysvascular)	45	87	1.02	*	*	*	Waters et al 1976
BK	71	99	1.44	*	*	*	Waters et al 1976
BK	64.2	96	1.32	*	*	*	Robinson et al 1977
Normal (Free Walking)	90.6	113	1.56	1.06	*	0.41	Murray et al 1966

Table. 5.2.5.1 Summary of temporal-distance investigations. (Skinner and Effeney, 1985)

There have been several reports on amputees, both trans-femoral and trans-tibial temporal-distance measurements. Skinner and Effeney (1985) provided a summary from these investigations as seen in Table. 5.2.5.1. The traumatic trans-femoral amputees walk about 40% slower than normals, increasing the duration of the gait cycle by an average of 0.36 second and reducing the stride length by about 20%. In general, the trans-tibial amputees walk faster than the trans-femoral amputees. Comparing dysvascular with traumatic amputees, the former walk slower with a smaller stride length. The comparison in temporal-distance measurements between amputees, and amputees with normal subjects provided an understanding of abnormal gait. Zuniga et al (1972) gave a good example of abnormal gait investigation using temporal-distance parameters, leading to suitable prosthetic prescriptions. The effectiveness of six different types of knee joint has also been investigated through similar measurements (Godfrey et al 1975). However, though simple to acquire temporal-distance parameters are affected by many factors, for example age and built (Murray et al 1964), thus limiting their usefulness when used alone.

5.2.6 Gait analysis :- Kinetics and kinematics measurement

Calculation of inter-segmental forces and moments require both kinetics and kinematics data to be present. One of the most extensive studies in amputees gait would be that performed by the University of California, Berkeley (Eberhart 1947, Eberhart et al 1954). The work has set the background in amputee gait studies for the present which are usually involved with the evaluation of prosthetic equipment. Murray et al (1980) study the kinematics of the sound and prosthetic limbs of ten trans-femoral amputees. Fig. 5.2.6.1 illustrated the knee angle against percentage of gait, which clearly showed continued knee extension of the prosthetic limb in the early stance phase when the sound limb registered flexion. Krebs and Tashman (1985) evaluated the conventional socket made of rigid themosetting resins and the ISNY flexible socket by studying the gait of one trans-femoral amputee. The kinematics are displayed in Fig. 5.2.6.2, which showed little difference between the two types of sockets.

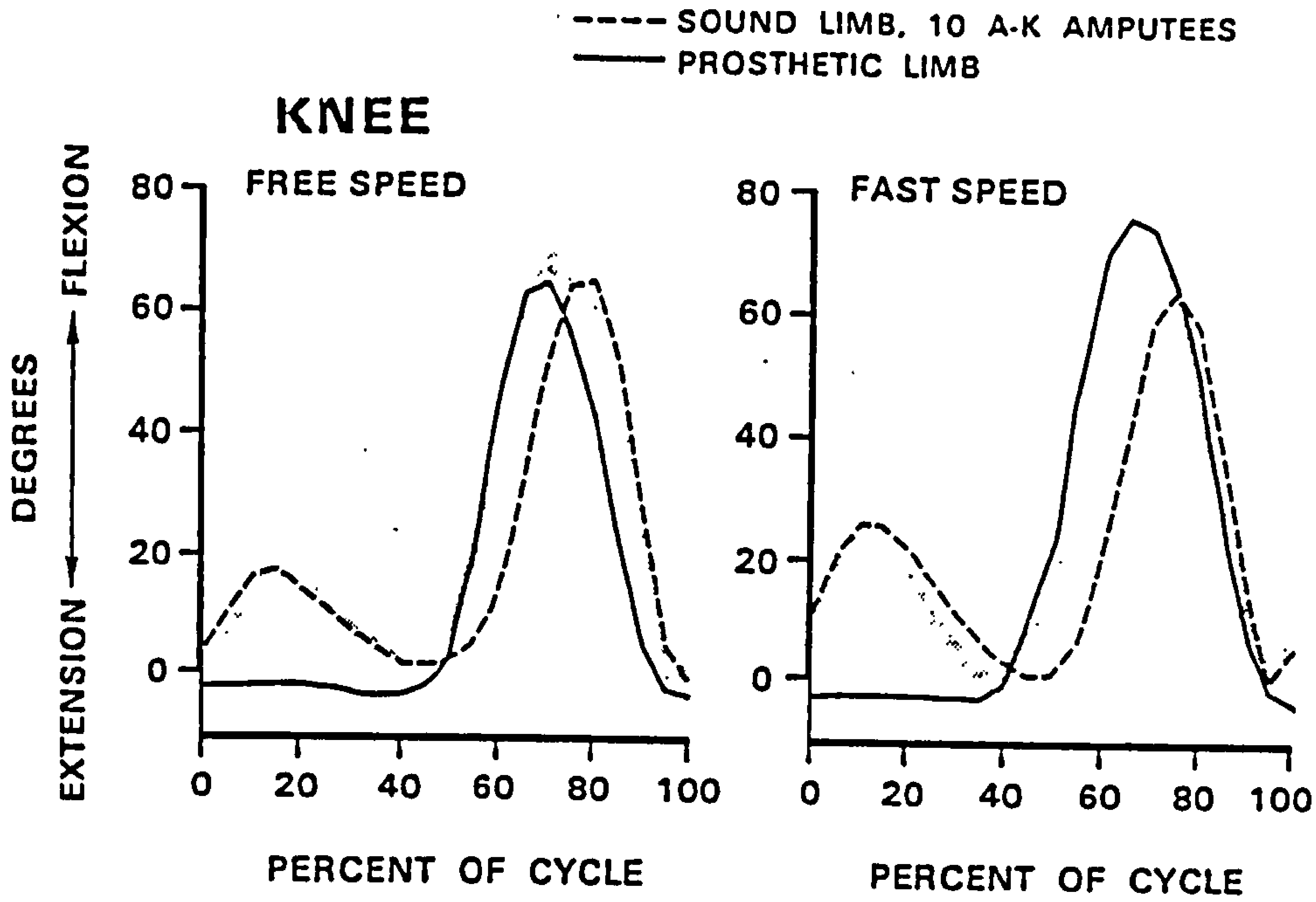

Fig. 5.2.6.1 Knee flexion and extension angles of sound and prosthetic limbs of trans-femoral amputee subjects. (Murray et al, 1980)

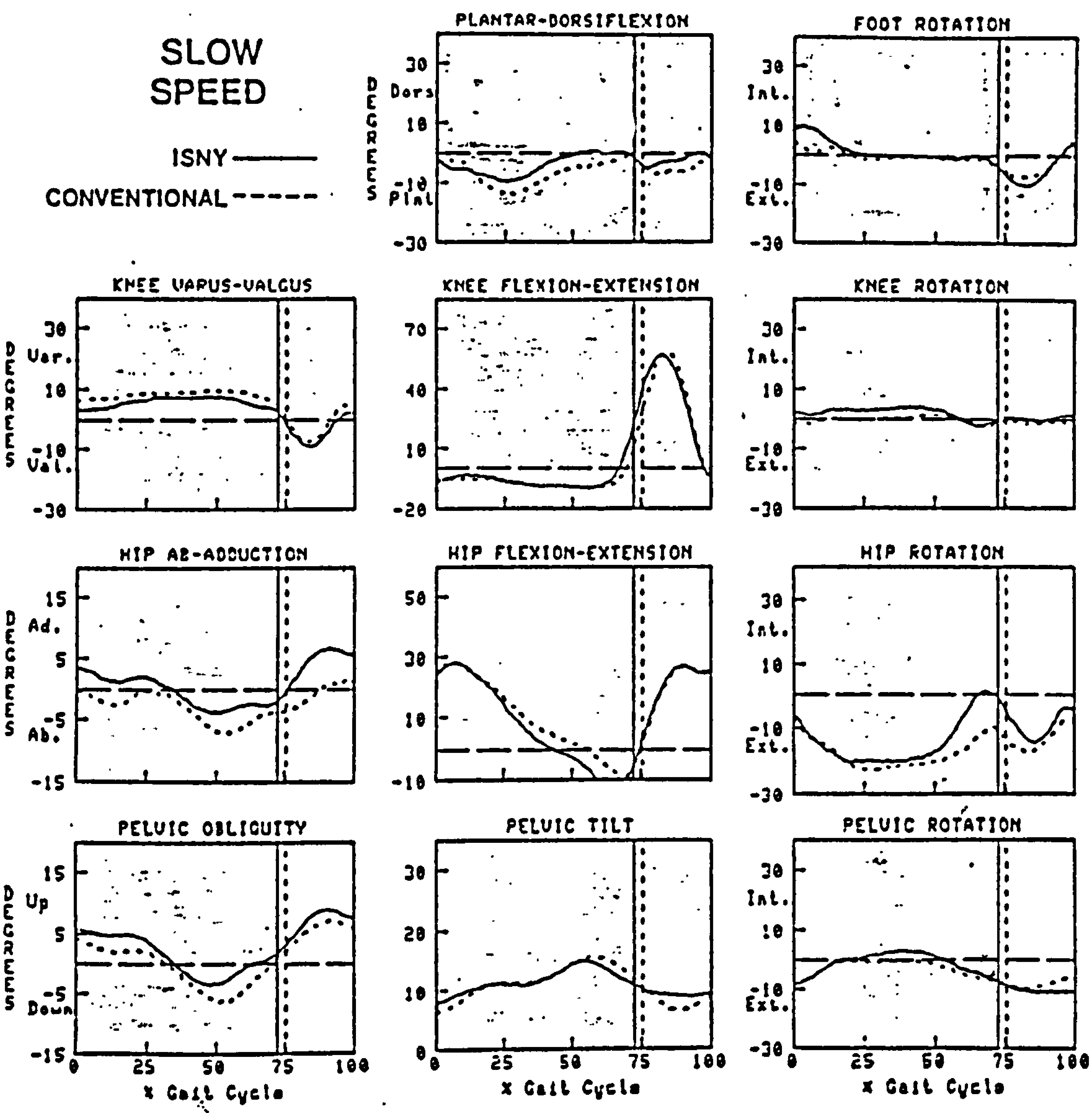

Fig. 5.2.6.2 Kinematics of trans-femoral amputees with conventional and ISNY sockets. (Krebs and Tashman, 1985)

The University of Strathclyde has always been at the forefront in amputee gait analysis. The work has a wide scope ranging from the design of pylon transducers (Berme et al 1975), evaluation of prosthetic components (Goh 1982) to prosthetic alignment studies (Zahedi et al 1988, Lang 1988, Marmar 1993). Several investigations from this group will be used to illustrate typical gait parameters observed in amputees.

Most of the above mentioned gait studies performed a comparison between amputees and normal subjects. The ground reaction forces of five normal subjects are seen compared with five amputee subjects with the quad sockets in Fig. 5.2.6.3. The axes system is similar to that adopted in the present study displayed in Fig. 5.3.1.1 in the experimental methods section (section 5.3) of the thesis. No significant difference were noticed between the right and left foot for normal subjects, but this was not the case for the unilateral amputees tested. Normal subjects force pattern in the x-direction (FPX) identified a braking force in the beginning of stance, and changing its direction at the end of stance to indicate a push off force. Force in the vertical direction (FPY) displayed a two peak and a trough pattern. The peaks were the results of the inertia force acting on the body mass in a direction opossite to its upward acceleration. The trough part was generated when the centre of gravity of the body is at the highest position. The downward acceleration of the body at this point is at its maximum value. The inertia force acting on the body is therefore directed upwards reducing the total force acting on the ground. FPZ was the medio-lateral force which acts in the opposite direction for the left and right foot. FPZ indicated a force tending to cause the foot to move outwards at the beginning of stance (about 0-11%), and the force changes direction (opposite to that in the beginning of stance) for the remainder of the gait cycle. The differences in the ground reaction force (GRF) between normal and amputee subjects is explained in Table 5.2.6.1. In general, larger magnitude of forces could be observed in normal subjects, and in the case of the amputees, larger forces were seen on the sound side.

Angular displacement at the saggital plane has been reported by Lang (1988) and Marmar (1993). Fig. 5.2.6.4 shows the angular displacement against the gait cycle. The foot usually goes into plantar flexion following heel strike, then dorsi flexes

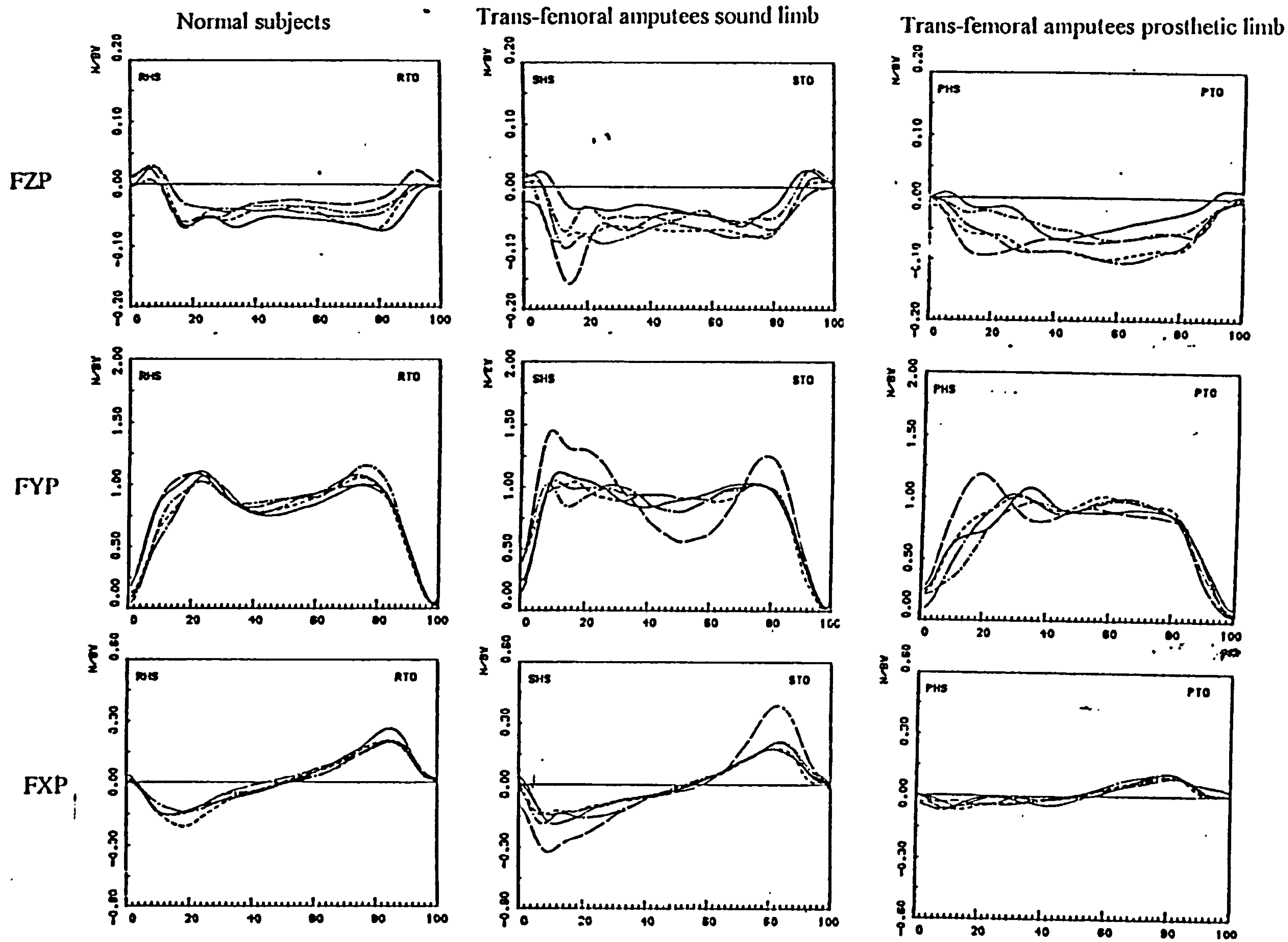

Fig. 5.2.6.3 Ground reaction forces (Newton/Body Weight) expressed in percentage of stance phase. (Marmar, 1993)

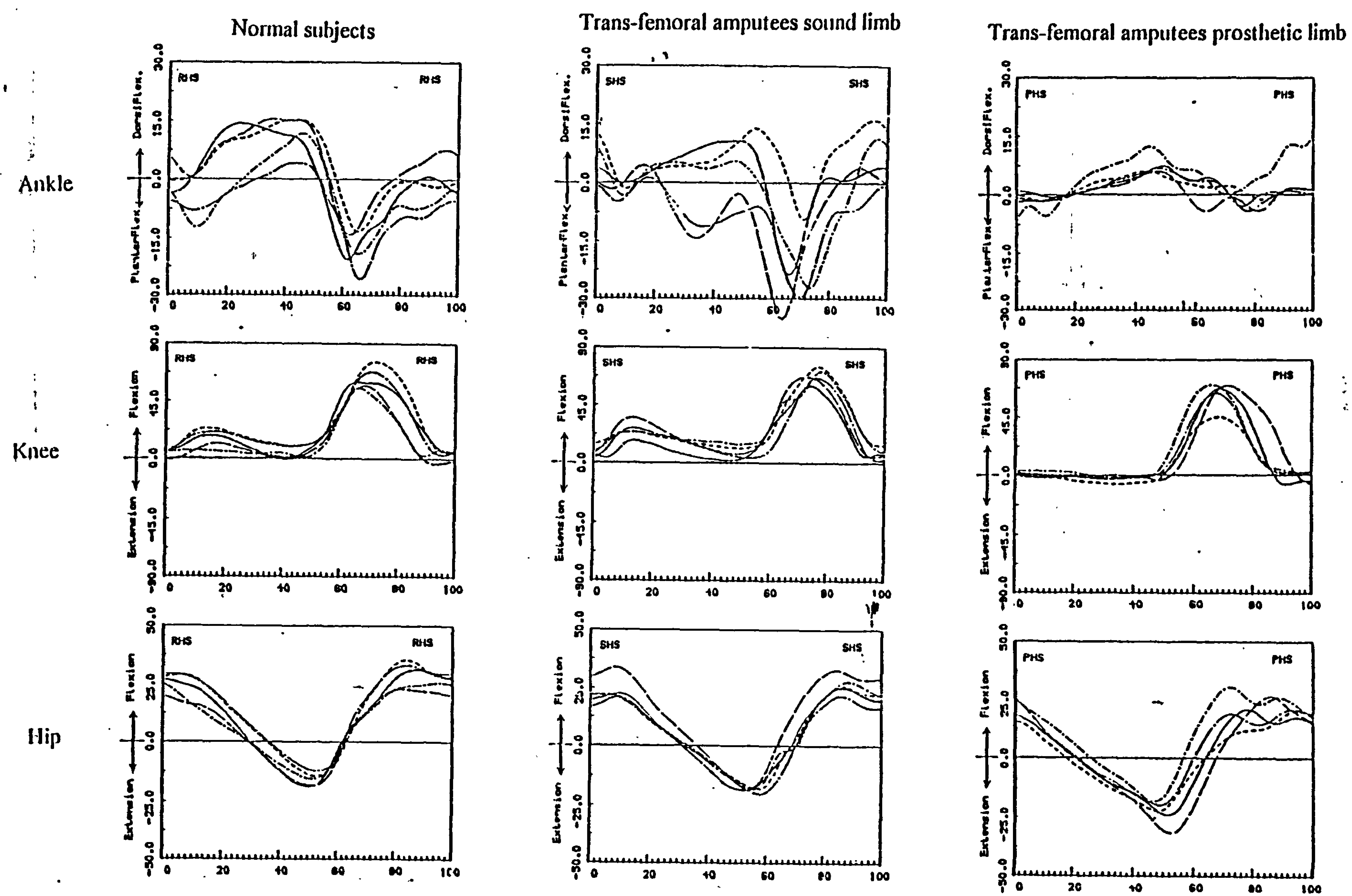

Fig. 5.2.6.4 Anterior - posterior plane angular displacement (Degrees) of lower joints expressed in % of gait cycle. (Marmar, 1993)

GRF	Difference between normal and amputee's sound leg	Differences between normal and prosthetic leg
FX	Small variation	Very low force was experienced in the prosthetic leg. The braking force is usually reduced by the amputee on purpose so as prevent the knee mechanism from flexing providing added stability.
FY	A third peak appearing at mid stance can sometime be seen in the sound leg, due to a "vaulting" action adopted by the amputee to provide clearance for swinging the prosthetic leg. The first peak in the sound leg occurs at about 10% of stance earlier than the normal.	Prosthetic leg first peak occurs at about 33% of stance. The magnitude of the two peaks also reduces significantly.
FZ	Sound leg indicates a shorter period of force causing the foot to move outwards at the beginning of stance phase.	The force causing the prosthetic foot to move outwards is not seen throughout stance due to poor medio-lateral stability.

Table 5.2.6.1 Differences in the GRF between normal and amputee subjects.
(Refer to Fig. 5.3.1.1 for axis system.)

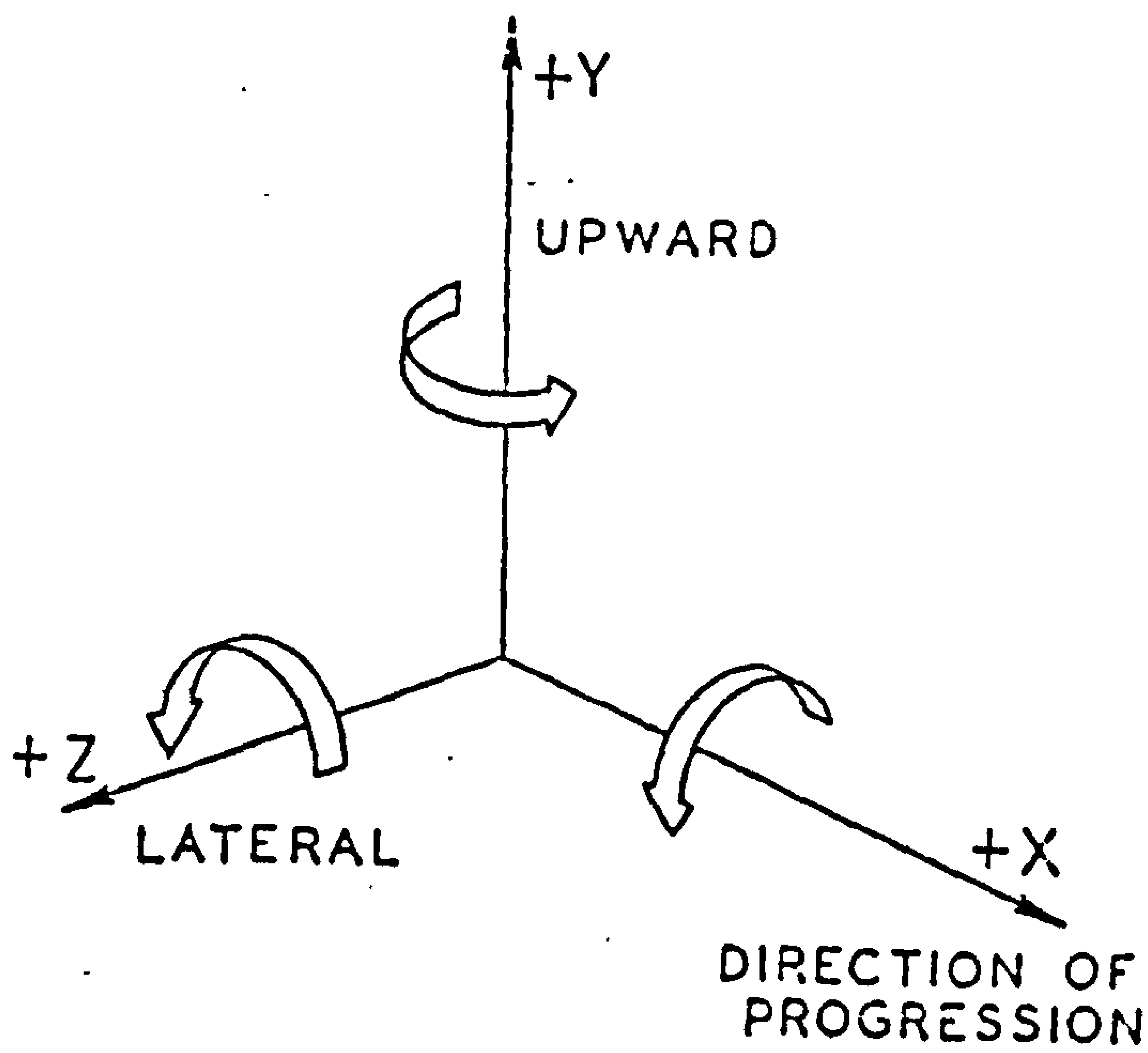

Fig. 5.3.1.1 Cartesian coordinate system used in gait laboratory for this project.

during mid stance and plantar flexes again at push off. Knee flexion begins immediately after heel contact, and at the beginning of swing phase flexion angle increased up to 60°. Hip flexion (about 20°) existed at the beginning of heel contact. The hip was then extended by approximately the same amount towards late stance and returned back to flexion during the swing phase. The angular differences between the normal and amputee's sound limb was minimal, except for the consistent ankle dorsi flexion through the gait cycle for several subject. At the prosthetic side, the stiff prosthetic foot causes low ankle plantar and dorsi flexion. The prosthetic knee showed practically no flexion during stance. This is typical in most amputee's gait because when the knee is purposely placed in full extension, it is prevented from buckling thus providing added stability during stance.

The body inter-segmental moments and forces are also particularly useful parameters in gait analysis, these will be discussed in more detail later in the chapter.

5.3 EXPERIMENTAL METHODS

This section describes equipment set-up, calibration and accuracy. It further highlights the biomechanical test procedures and data processing.

5.3.1 Coordinate system

The selected coordinate system for gait analysis is that recommended by the Committee on Prosthetic Research and Development (CRPD, 1975). The Cartesian system shown in Fig. 5.3.1.1 described x as the forward direction of progression, y upward and z to the right. Direction of positive moments is clockwise when view along the corresponding axis in the positive direction.

5.3.2 Biomechanics laboratory

Fig. 5.3.2.1 shows a plan view (not to scale) of the biomechanics laboratory in the Bioengineering Unit. The equipment consist of the Vicon motion analysis system (Oxford Metrics Ltd. UK) and three force platforms (Kistler Instrument AG, Switzerland). The former is made up of six infrared cameras, calibration poles used only during calibration of the system and the Etherbox which houses the control

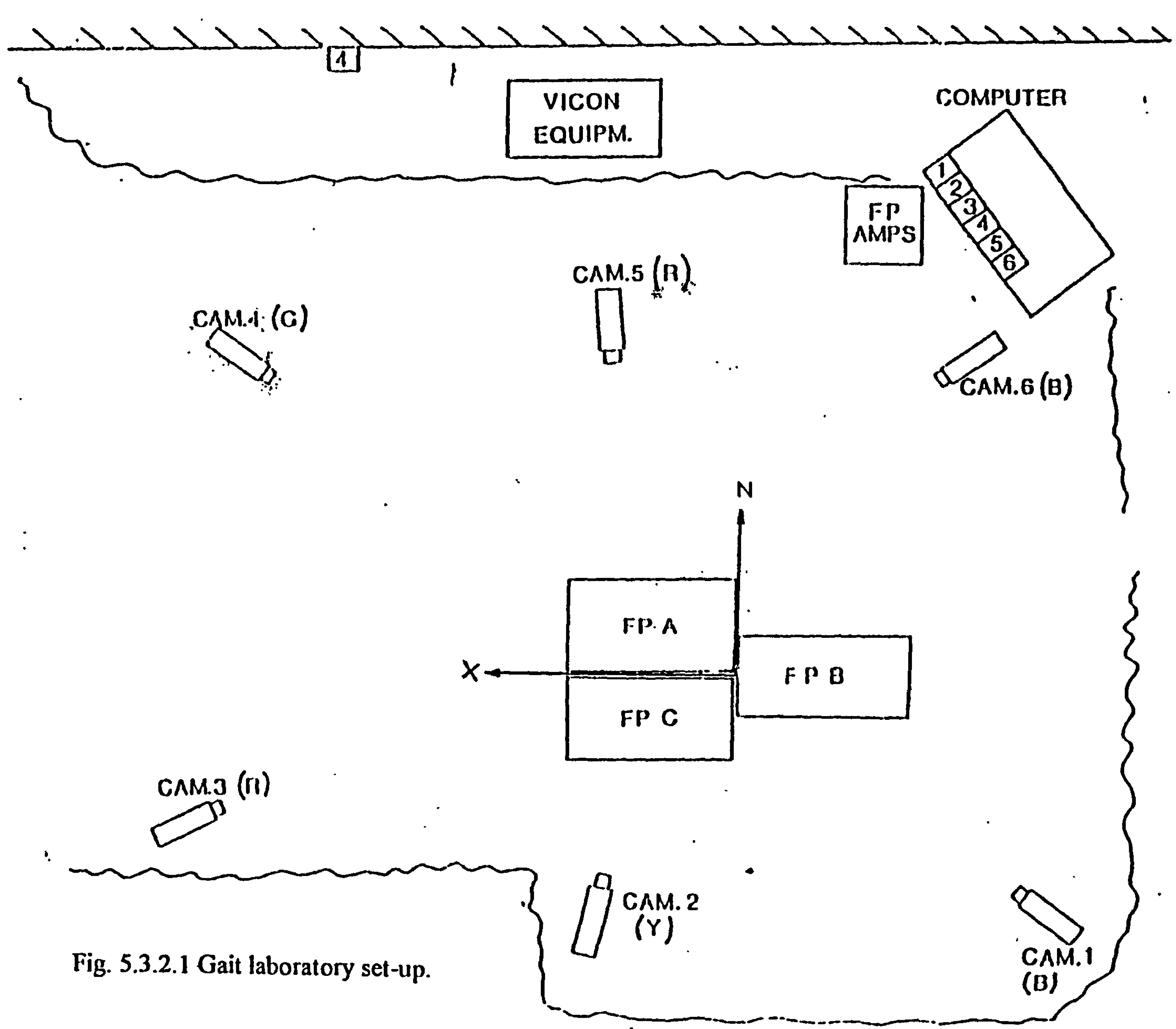

Fig. 5.3.2.1 Gait laboratory set-up.

electronics. The force platforms with charge amplifiers are linked to the Vicon through the Etherbox. The one system is operated under the control of the MicroVax 3100 computer. The MicroVax is networked to the computer centre main Vax, thus providing a host of support software. The position of the cameras are not fixed, but generally the described positions in Fig. 5.3.2.1 are adopted. The floor space is sufficient to provide a walkway of 20 metres length with the force plate positioned midway. The laboratory is situated on the ground floor, well suited for mounting force platforms and easy access for the disabled. Dark coloured curtains (black and dark blue) could be drawn to isolate the measurement area to improve the Vicon capability.

5.3.3 Vicon calibration

A procedure known as linearisation was performed with the six cameras imaging an array of points in order to reduce lens distortions and imperfections. However, this procedure is not commonly repeated unless the system is under suspicion of acquiring incorrect results. Another calibration procedure which must be executed prior to any data acquisition uses four standard poles with 20 markers attached. The four poles were hung absolutely stationary from the ceiling, forming the four columns of a box which determined the cameras' field of view. This volumetric space of about 5.4 m^3 was situated over the force platforms midway along the walkpath .With the position of the cameras established, the Vicon software was set-up in the calibration mode and data was captured for 1 s. The exact positions of the markers had been previously entered into the Vicon software. Based on these values, the software reports the success and or failure of the calibration process and tabulates the mean residual (see section 5.4.3) for each camera. A residual of 4.5 mm and below is normally accepted. The calibrated cameras must be left untouched in their positions during the whole period of the test, if moved a re calibration would be necessary.

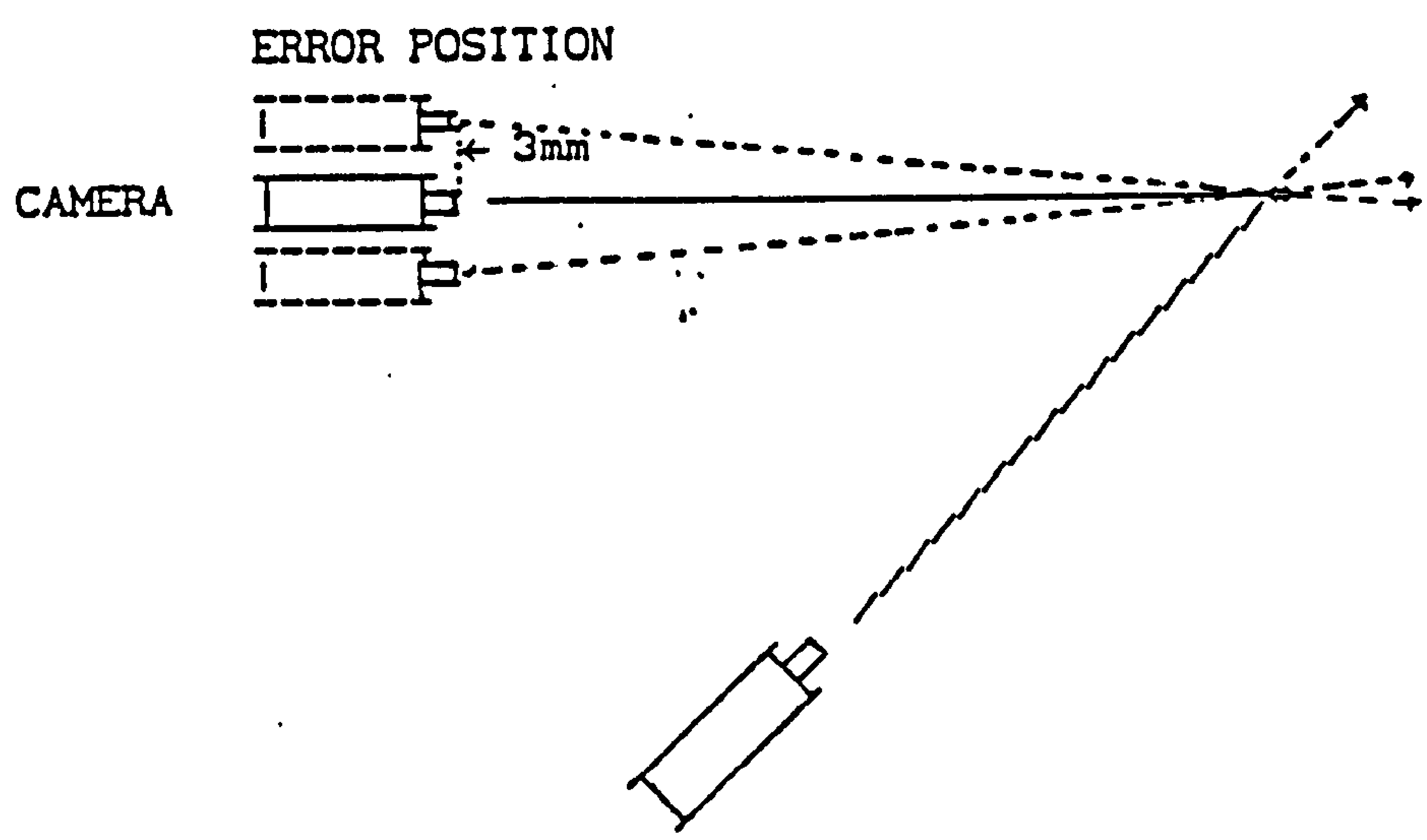

Fig. 5.3.4.1 Errors in the Vicon system. (Li, 1993)

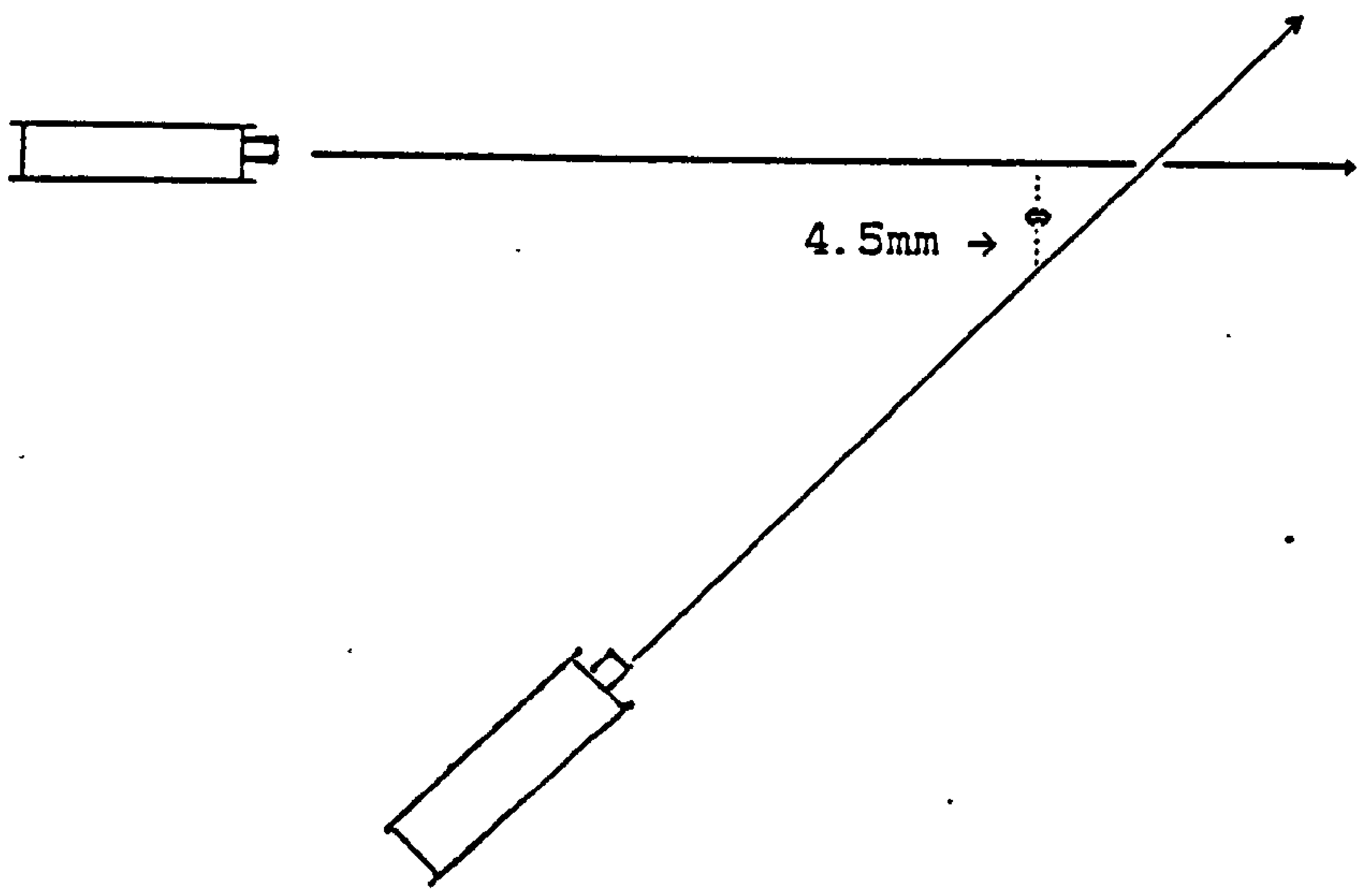

Fig. 5.3.4.2 Residuals in the Vicon system. (Li, 1993)

5.3.4 Accuracy of the Vicon

Two forms of errors exist in the Vicon system which can be alleviated by the procedures of cameras linearisation and calibration. The former error was limited to a maximum of 3 mm and the latter 4.5 mm. The error in linearisation meant that the ideal position of the camera could be out by ±3 mm (Fig. 5.3.4.1), while the reported residual during calibration (4.5 mm) represented the shortest perpendicular distance from the seen marker to the camera's infrared ray (Fig. 5.3.4.2).

5.3.5 Marker system

The marker system was designed to distinguish the different segments of the body. The segments were two foot, shank and thigh segments, one pelvic and upper torso segment. The upper torso segment included the head and the upper limb.

The marker was made up of a polystyrene ball of 25 mm diameter. It was made sensitive to the infrared cameras by covering it completely with small strips of retro-reflective paper. The polystyrene ball was held using a pin as shown in Fig. 5.3.5.1, which gave the marker a base for attachment to the subject's skin surface using double sided adhesive tape.

The markers were placed according to the subjects' anatomical landmarks located through palpation. An exception was made for markers placed onto the prosthetic socket. At the prosthetic socket, the markers' locations were approximated according to the part of the socket that defined the anticipated anatomical landmark. The markers were schematically presented in Fig. 5.3.5.2 and described in detailed in Table 5.3.5.1. A total of 22 markers were used. The marker system was separated into static and dynamic. The static and dynamic markers were required during the static test, where data was captured with the subject in a normal standing position. This was achieved in order to obtain anatomical joint centres and data to relate different frames of reference which will be discussed later in the thesis. During the dynamic or free walking test, the static markers could be taken out for better comfort leaving the rest of the dynamic markers behind.

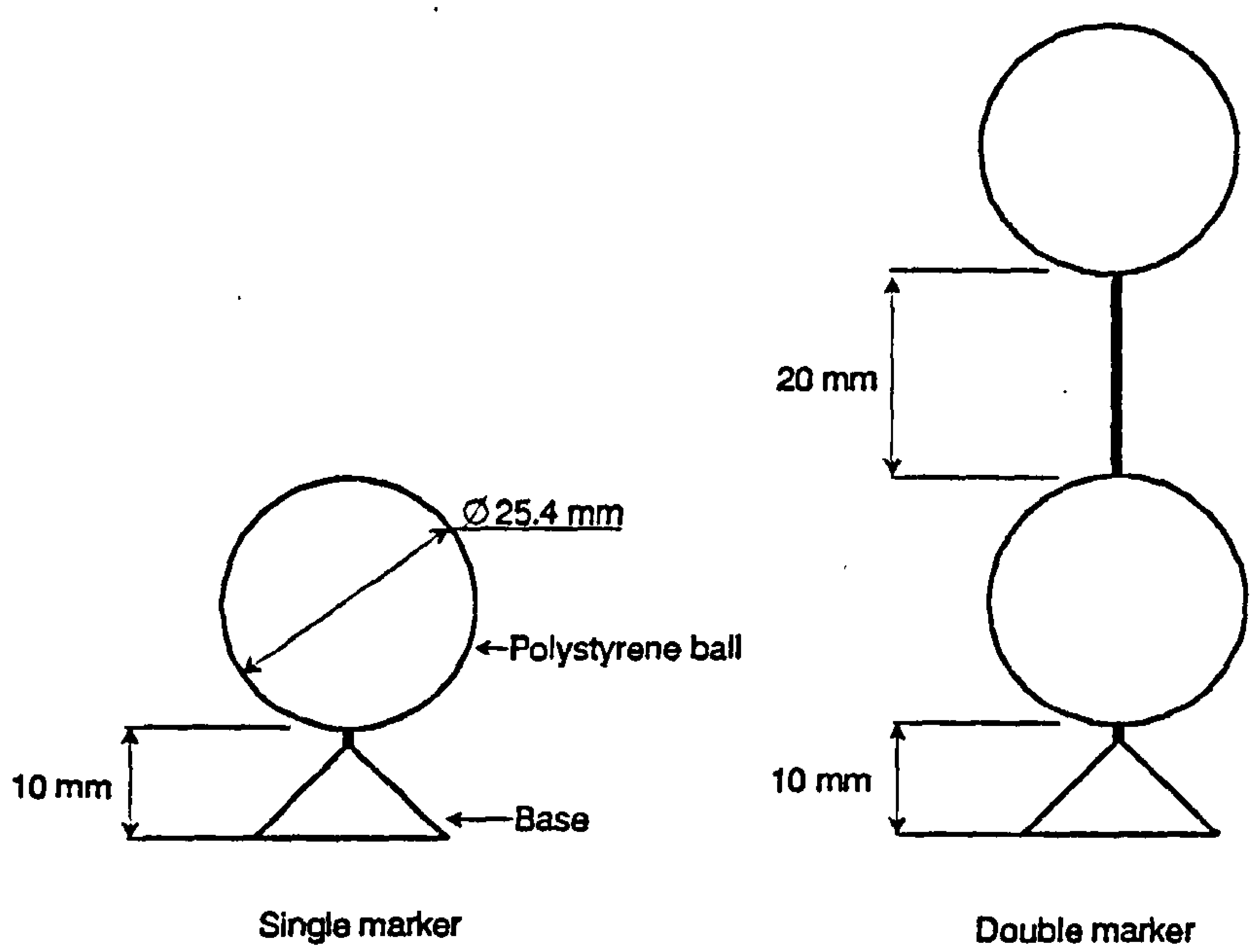

Fig. 5.3.5.1 Markers

No.	Name	Marker position
1	RAJL	Right ankle joint lateral malleolus
2	RAJM	Right ankle joint medial malleolus
3	RTMF	Right tibia middle front
4	RKJL	Right epicondyle of femur
5	RKJM	Right medial condyle of femur
6	RASIS	Right anterior superior iliac spine
7	LASIS	Left anterior superior iliac spine
8	BWCL	L4 spine lower marker
9	BWCH	L4 spine higher marker
10	LAJL	Left ankle joint lateral malleolus
11	LAJM	Left ankle joint medial malleolus
12	LTMF	Left tibia middle front
13	LKJL	Left epicondyle of femur
14	LKJM	Left medial condyle of femur
15	RGT	Right greater trochanter
16	LGT	Left greater trochanter
17	RFMF	Right femur middle front
18	LFMF	Left femur middle front
19	RFF	Right foot front
20	RFB	Right foot back
21	LFF	Left foot front
22	LFB	Left foot back

Table 5.3.5.1 Markers name and location

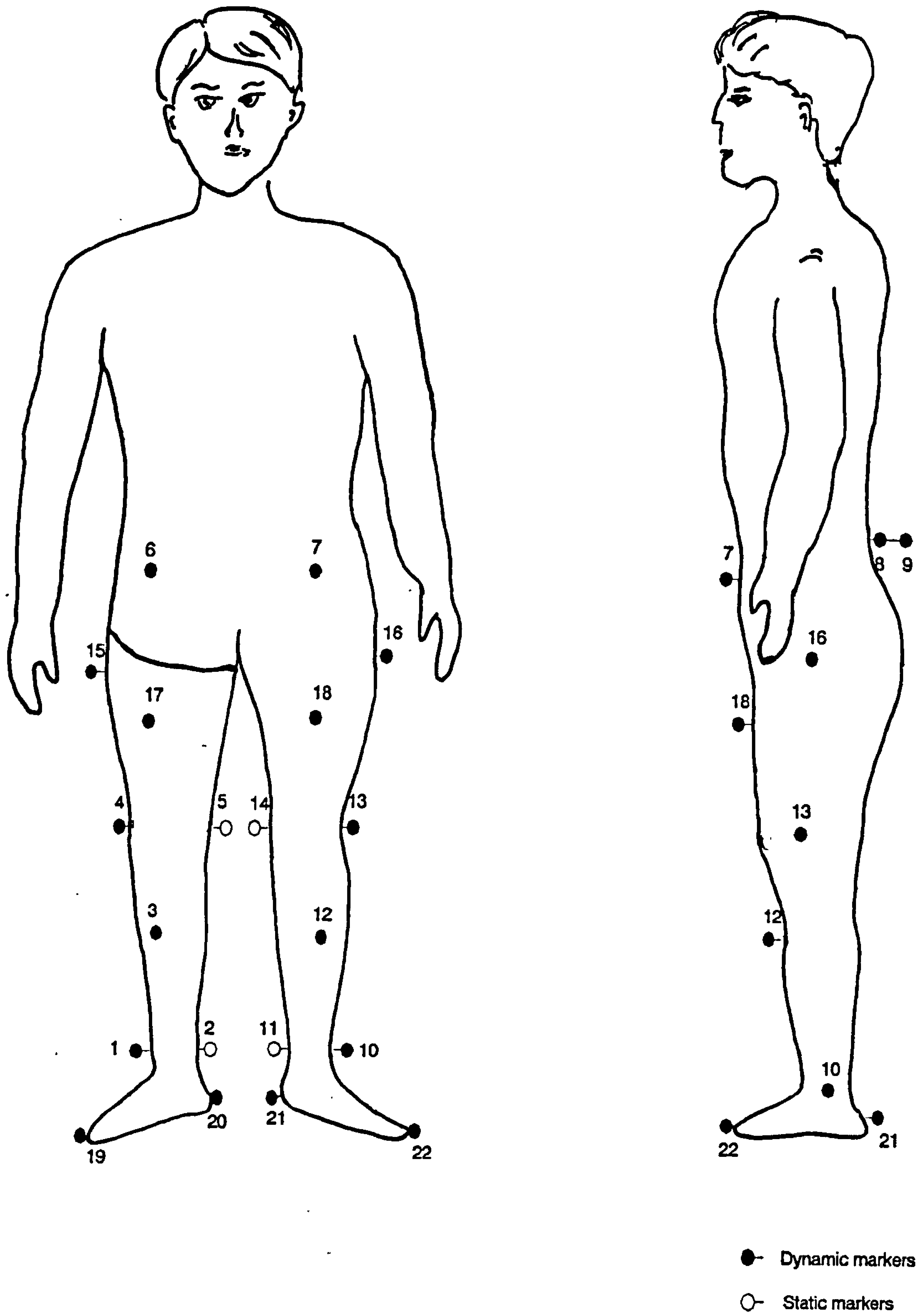

Fig. 5.3.5.2 The marker positions in a right amputee.

5.3.6 Static and dynamic test procedures

The reader is reminded that the pressure measurement test described in chapter 4 was executed simultaneously with gait measurements. The pressure measurement system however, was not linked to the Etherbox but rather a standalone system. During data acquisition, different operators were responsible for the two systems. There was no requirement for the two operators to activate data capture at exactly the same time.

The test was divided into two stages, static and dynamic. The additional stage in the pressure measurement test where the unloaded residual limb pressures were measured (section 4.6.3) did not involve the Vicon nor the force platforms. Upon attaching the static markers onto the assigned landmarks, the subject was asked initially to stand near the force platforms but not on it for the static test. Data acquisition began, after 2-4 seconds the subject was requested to step onto the force platforms A and C, maintaining a normal standing posture, facing the x-direction of the chosen co-ordinate system stated in section 5.3.1. Data acquisition continued for another 6-8 seconds.

The static markers were removed for the dynamic test. The subject was given time to get used to walking in the artificial leg with all the dynamic markers and pressure transducers attached. Several walking trials were then necessary to ensure that the subjects' feet landed on force platforms B and C or B and A, placed midway between the walk path. The subjects were requested to maintain a normal walking style without paying any attention to the force platforms, while the investigators kept track of the subjects' starting point relative to the feet positions on the force platforms. A starting point was then ascertained and marked on the floor where the subjects would be requested to start at the following test trials. The dynamic test began with the subject walking freely, stepping over the platforms midway through the walk. The pressure measurement system was activated first, capturing interface pressure at the beginning. As the subject approached the force platform, the Vicon and force platforms were activated. The Vicon and force platforms were activated later because any data collected outside the Vicon calibration frame could not be used. Thus, prior to the subject entering the calibrated volume, approximately 2-3 steps before hitting the platforms, a 5 s long data capture was activated. The acquisition frequency was 50 Hz for the Vicon and 200 Hz for the force platforms. The number of trials were dependent on the pressure measurement test, 24 and 27 walk for the quad and the IC sockets respectively. Due to the limited number of pressure transducers (four transducers), in order to complete the pressure measurement test, a large number of trials is required (see section 4.6.4). However, this was considered to be in excessive for gait analysis, thus only five good trials were obtained for the analysis.

Temporal-distance information were also collected during the dynamic test. The position of the markers at the foot allowed temporal-distance parameters to be calculated using the Vicon, though limited to a distance of about 2.3 m in the walking direction due to the calibrated volume. Nevertheless, the Kistler axial transducer in the pressure measurement system also provided additional data for this purpose. The full distance of the walkway was marked at the beginning and the end by infrared light switches. The switches activate a digital timer which records the time between the beginning and the end of the walkway. This enables the mean velocity of the amputee to be tracked during the test, keeping the walking speed consistent for the different trials.

5.3.7 Data processing

The Vicon and force platform data were collected and stored in a microVax 3100 computer. Data handling could also be managed using the computer centre mainframe Vax computers where full compatibility was maintained. After data capture using the Vicon software, the data were reconstructed generating .SEG files. The Vicon software using this file type could then display the markers seen by the cameras graphically, enabling the markers to be identified according to the specified marker set discussed in table 5.3.5.1. Upon identifying the markers, a .C3D file was generated. The .C3D file is a file consisting of binary data which is used by the Vicon software to produce graphical plots, example stick and butterfly diagrams. Included in the .C3D file are also the force platform data. The .C3D file was further transformed into a

.A3D file consisting of ASCII text. Finally, a program written in Fortran read the .A3D file and output segmental forces and moments.

5.4 THEORETICAL ANALYSIS

This section outlined the theoretical aspects of the kinematics and kinetics analysis carried out in this study.

5.4.1 Symbols and Notations

Various symbols and notations are used to describe frames of reference, joint centres etc. The following are used consistently in this thesis ;

a.) In order to distinguish data measured or derived between static and dynamic test, the former is represented by upper case letters and the latter by lower case letters.

b.) The position vector of any point in space is written as follows ;

$$\text{Static : } \vec{R}^{\Phi}_{\alpha\beta} = \left[X^{\Phi}_{\alpha\beta}, Y^{\Phi}_{\alpha\beta}, Z^{\Phi}_{\alpha\beta}\right]$$

$$\text{Dynamic : } \vec{r}^{\Phi}_{\alpha\beta} = \left[x^{\Phi}_{\alpha\beta}, y^{\Phi}_{\alpha\beta}, z^{\Phi}_{\alpha\beta}\right]$$

where ,

Φ	=	g	ground frame of reference
		m	marker frame of reference
		p	principal segment frame of reference
		f	force plate frame of reference
α	=	r	right limb
		l	left limb
β	=	a	for ankle joint centre
		k	for knee joint centre
		h	for hip joint centre
		s	centre of gravity of the shank
		t	centre of gravity of the thigh

As an example, the static position vector of the right ankle joint with reference to the ground frame of reference can be written as $\vec{R}^{g}_{ra}$.

c.) The vector of an axis of a co-ordinate system of reference is written as follows;

$$\vec{D}_i^{\alpha\Delta} = [D_{i1}, D_{i2}, D_{i3}]$$

$$\vec{d}_i^{\alpha\Delta} = [d_{i1}, d_{i2}, d_{i3}]$$

where i = x, y, or z and

$\Delta =$	s	for the shank
	t	for the thigh
	g	for ground

d.) The notation for forces and moments is as follows ,

$$\vec{F}_{\alpha\beta}^{\Phi} = \left[FX_{\alpha\beta}^{\Phi}, FY_{\alpha\beta}^{\Phi}, FZ_{\alpha\beta}^{\Phi}\right]$$

$$\vec{M}_{\alpha\beta}^{\Phi} = \left[MX_{\alpha\beta}^{\Phi}, MY_{\alpha\beta}^{\Phi}, MZ_{\alpha\beta}^{\Phi}\right]$$

respectively. Thus, $\vec{F}_{lh}^{p}$ will describe the force at the left hip joint centre in the principal segment frame of reference.

e.) The directional cosines for the three different frames of reference are as follows;

$$[\vec{D}C_{\delta}^{\alpha\Delta}]_{\Phi\leftarrow\Phi} = \begin{bmatrix} d_{11} & d_{21} & d_{31} \\ d_{12} & d_{22} & d_{32} \\ d_{13} & d_{23} & d_{33} \end{bmatrix}$$

where,

$\delta =$	s	for static
	d	for dynamic

As an example, the directional cosine of the principal axes of the left shank related to the ground frame of reference is $\left[\vec{D}C_{s}^{ls}\right]_{p\leftarrow g}$.

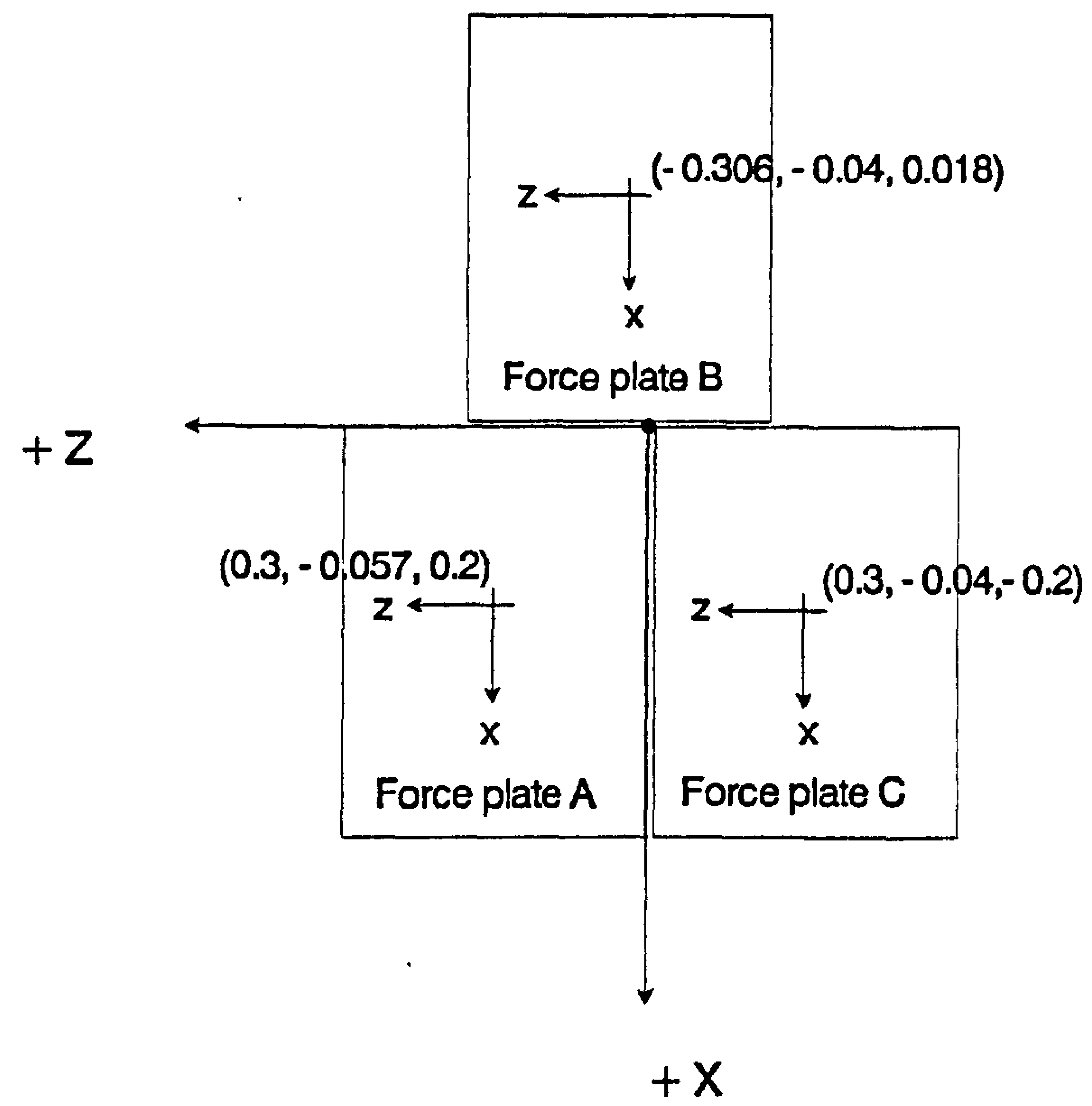

Fig. 5.4.4.1 Co-ordinates of the centre of the force platforms relative to the Vicon origin in the ground frame of reference. The y axes of the Vicon system and the force platforms point vertically upwards. (All values are stated in m)

5.4.2 Data Filtering

The inherent electronic noise in the measured signal was initially subjected to a digital filter written in Fortran 77 programming language. Several studies have previously attempted to design a suitable filter specially for signals acquired during gait analysis (Miller and Nelson 1973, Winter 1974, Pezzack et al 1977, Andrews 1988). The filter selected for this project is a fourth-order Butterworth low pass digital filter developed by Andrews (1982). Its form is as follows ;

$$\begin{aligned} Y_k = \frac{1}{C_6}[C_1(x_k + 4x_{k-1} + 6x_{k-2} + 4x_{k-3} + x_{k-4}) \\ -(C_2 y_{k-1} + C_3 y_{k-2} + C_3 y_{k-2} + C_4 y_{k-2} + C_5 yk - 4)] \end{aligned}$$

where,

x_k is the co-ordinate of the point to be filtered

y_k is the co-ordinate of the filtered point

C_1, C_2, C_3, C_4, C_5, C_6 are constants expressed as functions of cut off frequency f_{cut} (Hz) and the sampling interval T (s). In this work, f_{cut}= 5 Hz and T = 0.02 s.

5.4.3 Normalization gait analysis data

The acquired signals need to be normalized into a common time base, in this case in percentage of the gait cycle. This procedure further allows the signals to be averaged and standard deviations defined. The normalization process is exactly the same as that described in section 4.7.2, where dynamic interface pressures were normalised to 100% of gait cycle using a Fourier analysis technique.

5.4.4 Frame of reference

In the theoretical analysis, three frames of reference will be commonly referred to. All three are described in the Cartesian co-ordinate system outlined in section 5.3.1, the first being the ground frame of reference. The origin of this reference is positioned approximately at the centre of the three force platforms. Its exact location relative to the force platforms is shown in Fig. 5.4.4.1. The second frame of reference is referred to as the principal axes of segments. It is also commonly named according

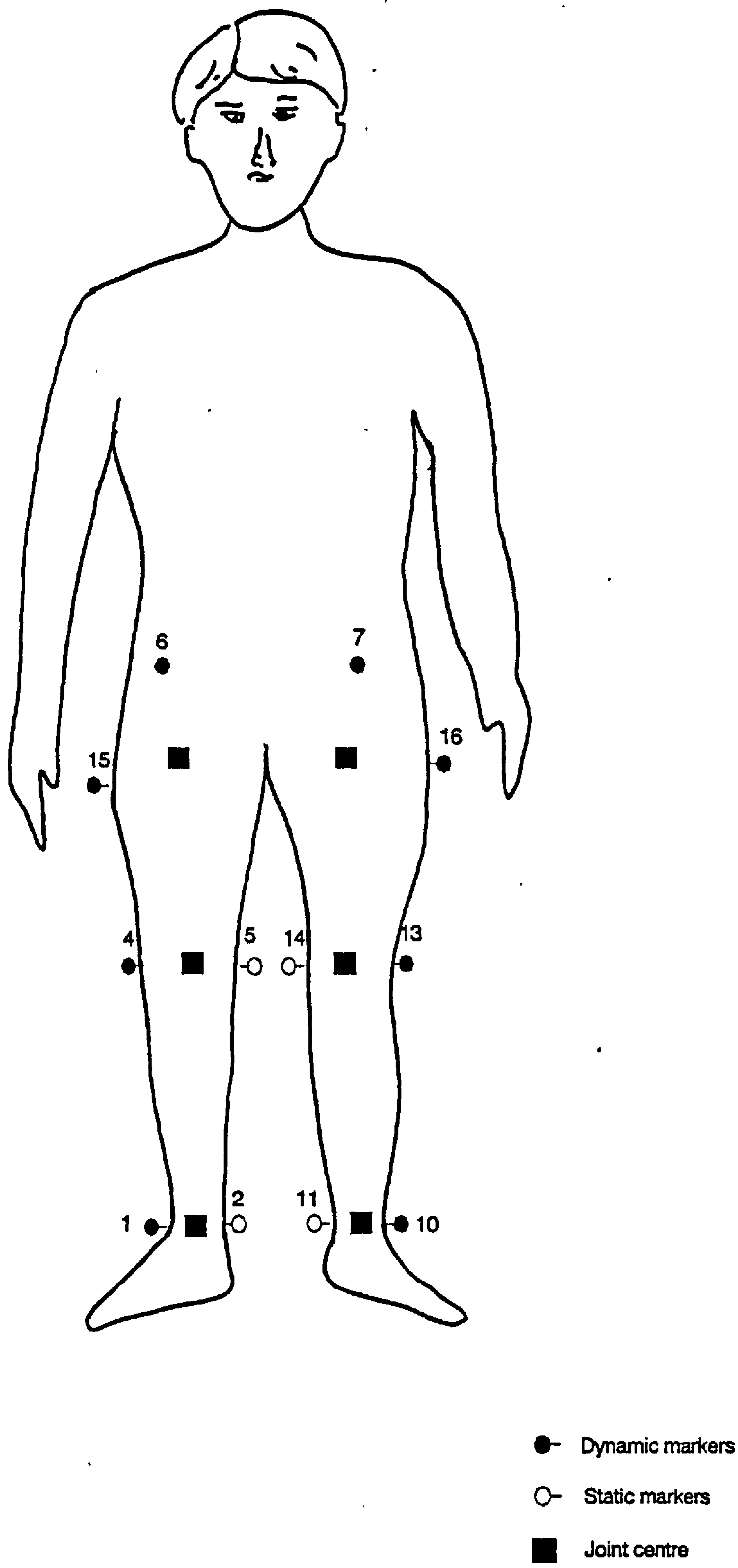

Fig. 5.4.5.1 Positions of joint centres relative to the markers.

to the segments, example thigh frame of reference. The third frame of reference system is the marker frame of reference. The principal axes of segments and the marker frame of reference will be described under their own headings in the later part of this chapter.

5.4.5 Determination of joint centres in the static condition

The joint centres were identified through markers used during the static test. Fig. 5.4.5.1 shows the positions of the joint centres together with the markers. The two markers placed on the lateral and medial sides of the ankle and knee joints defined a line through the joint centres. Assuming the joints rotate along this line in the saggital plane, the joint centres could be defined as the midpoint of their respective two markers. In the ground frame of reference, the left ankle joint centre is therefore ;

$$\vec{R}^g_{la} = \begin{bmatrix} X^g_{la} \\ Y^g_{la} \\ Z^g_{la} \end{bmatrix} = \begin{bmatrix} (X_{10} + X_{11})/2 \\ (Y_{10} + Y_{11})/2 \\ (Z_{10} + Z_{11})/2 \end{bmatrix}$$

and the left knee joint as ;

$$\vec{R}^g_{lk} = \begin{bmatrix} X_{lk} \\ Y_{lk} \\ Z_{lk} \end{bmatrix} = \begin{bmatrix} (X_{13} + X_{14})/2 \\ (Y_{13} + Y_{14})/2 \\ (Z_{13} + Z_{14})/2 \end{bmatrix}$$

Similar procedures were adopted for the remaining right ankle and knee joints. There was no distinction in the way the calculations were done regarding anatomical or prosthetic ankle and knee centres. However, the placement of the markers on the latter depends on the mechanical axis of the prosthetic ankle and knee joints.

The anatomical hip joint centres were calculated based on the study performed and proposed by Bell et al (1989, 1990). Bell et al investigated 31 subjects, 15 males and 16 females and concluded that a fairly accurate prediction of the hip centre could be obtained using the distance between the right and left anterior superior iliac spine

(ASIS). The 3-D location of the hip joint centre was defined as a percentage of the inter-ASIS distance, 30% distal, 14% medial and 22% posterior to the ASIS. Therefore using the above mentioned proposal, the left hip joint centre is given by,

$$\vec{R}^g_{lh} = \begin{bmatrix} X^g_{lh} \\ Y^g_{lh} \\ Z^g_{lh} \end{bmatrix} = \begin{bmatrix} X_7 - (AX \times 0.22) \\ Y_7 - (AX \times 0.30) \\ Z_7 + (AX \times 0.14) \end{bmatrix}$$

where AX is the distance between the right and left ASIS. In the right side, marker number 6 is used instead and calculated as follows ;

$$\vec{R}^g_{rh} = \begin{bmatrix} X^g_{rh} \\ Y^g_{rh} \\ Z^g_{rh} \end{bmatrix} = \begin{bmatrix} X_6 - (AX \times 0.22) \\ Y_6 - (AX \times 0.30) \\ Z_6 - (AX \times 0.14) \end{bmatrix}$$

There was no difference in the way the hip joint centre was obtained for both the residual and the good limb. In the residual limb, the presence of the socket did not interfere with the placement of the ASIS marker.

5.4.6 Principal axes of segments

The principal axes of segments were related to the ground frame of reference by directional cosine matrices. Thus in each segment i.e. shank, thigh and pelvis, a principal axis was defined.

The principal axes of the shank are ;

Ys = from the ankle joint centre to the knee joint centre and

Xs = at right angle to Ys and pointing forward and

Zs = at right angles to Ys and pointing in the same direction as Zt of the thigh segment.

The shank directional cosine of Ys can therefore be derived as;

$$\vec{D}^{as}_y = \frac{\vec{R}^g_{ak} - \vec{R}^g_{aa}}{\left|\vec{R}^g_{ak} - \vec{R}^g_{aa}\right|}$$

and directional cosine of Zs is calculated as the cross product of the ground x-axis with Ys of the shank;

$$\vec{D}_z^{\alpha s} = \vec{D}_x^{\alpha g} \times \vec{D}_y^{\alpha s}$$

and $\vec{D}_x^{\alpha g} = [1 \ 0 \ 0]$ representing the x-axis on the ground. The directional cosine of Xs of the shank is than calculated as the cross product of Ys and Zs ;

$$\vec{D}_x^{\alpha s} = \vec{D}_y^{\alpha s} \times \vec{D}_z^{\alpha s}$$

The directional cosine of the principal axes of the shank in the static condition is therefore ;

$$[\vec{D}C_s^{\alpha s}]_{p \leftarrow g} = \begin{bmatrix} \vec{D}_x^{\alpha s} \\ \vec{D}_y^{\alpha s} \\ \vec{D}_z^{\alpha s} \end{bmatrix}$$

A similar procedure was adopted for the thigh principal axes in deriving the directional cosine matrix. The thigh principal axes are defined as follows ;

Yt = from the knee joint centre to the hip joint centre and

Xt = from the knee joint centre at right angle to Yt and Zt and

Zt = from the knee joint centre to the right, at right angles to Yt and parallel to a line joining the condyles of the femur.

The directional cosine of Yt is therefore,

$$\vec{D}_y^{\alpha t} = \frac{\vec{R}_{\alpha h}^g - \vec{R}_{\alpha k}^g}{\left|\vec{R}_{\alpha h}^g - \vec{R}_{\alpha k}^g\right|}$$

The directional cosine of Zt can be obtained by cross product as;

$$\vec{D}_z^{\alpha t} = \vec{D}_x^{\alpha s} \times \vec{D}_y^{\alpha t}$$

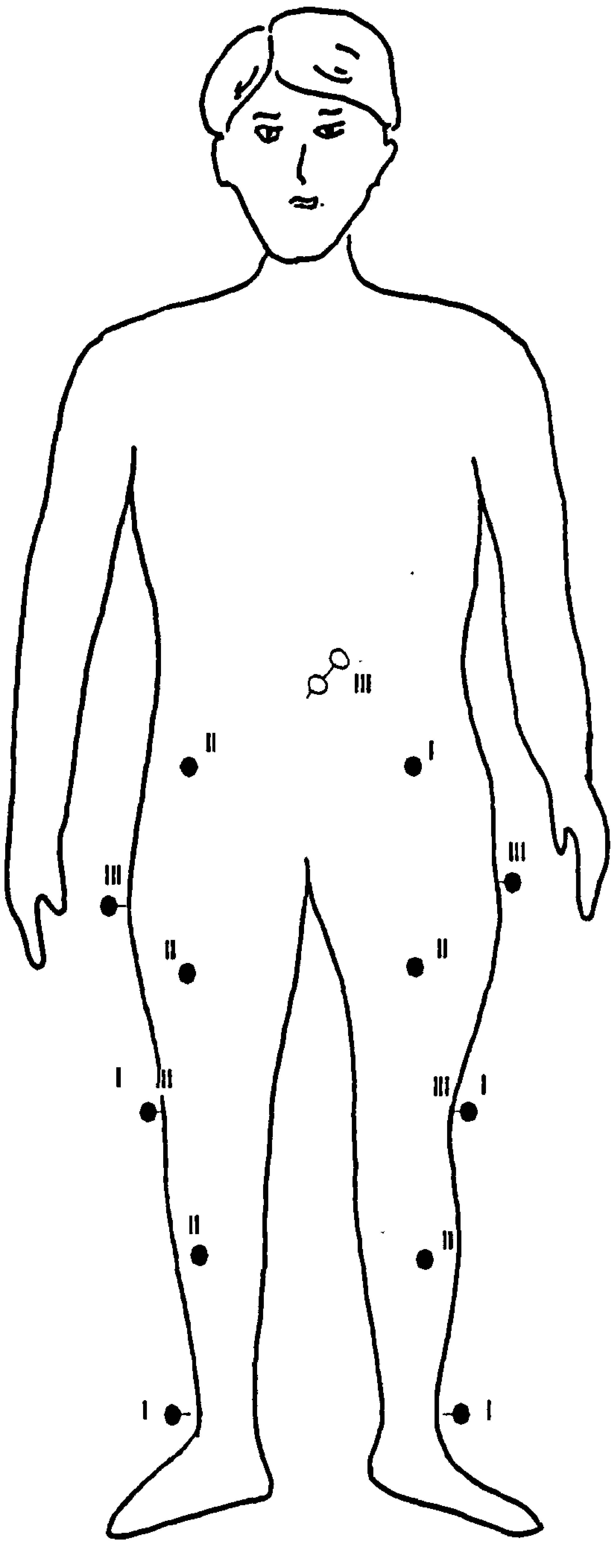

Fig. 5.4.7.1 Numbering system for marker frame of reference

and finally the direction cosine of Xt is ;

$$\vec{D}_x^{\alpha t} = \vec{D}_y^{\alpha t} \times \vec{D}_z^{\alpha t}$$

Rewriting, the directional cosine matrix of the principal axes of the thigh is ;

$$[\vec{D}C_s^{\alpha t}]_{p \leftarrow g} = \begin{bmatrix} \vec{D}_x^{\alpha t} \\ \vec{D}_y^{\alpha t} \\ \vec{D}_z^{\alpha t} \end{bmatrix}$$

5.4.7 Marker frame of reference

The marker frame of reference for different segments of the body was determined by the position of the markers affixed on the subject's body. Its purpose was to provide a relationship between the ground and principal segment frame of reference. In order to calculate the segment's marker frame of reference, the position vectors of three markers attached to the particular segment were required. These markers were numbered I, II and III for each segment with the origin of the marker frame of reference assigned to marker I (Fig. 5.4.7.1). The general formulations shown below are for working out the directional cosine of the marker frame axes for all segments in relation to the ground frame of reference for both static and dynamic conditions. Naming axes of the marker frame as Ym, Xm and Zm, where Ym is directed from marker I to marker III and its directional cosine can be given by (Note : the general formulation will disregard the left and right limb, and also the static and dynamic notations) ;

$$\vec{D}_y^{\Delta} = \frac{\vec{R}_{III}^g - \vec{R}_I^g}{\left|\vec{R}_{III}^g - \vec{R}_I^g\right|}$$

Thus the directional cosine of Xm is therefore ;

$$\vec{D}_x^{\Delta} = \frac{\vec{R}_{II}^{g} - \vec{R}_{I}^{g}}{\left|\vec{R}_{II}^{g} - \vec{R}_{I}^{g}\right|}$$

and $\vec{D}_z^{\Delta}$ is obtained from cross product as follows;

$$\vec{D}_z^{\Delta} = \vec{D}_x^{\Delta} \times \vec{D}_y^{\Delta}$$

Therefore the directional cosine defining the marker frame of reference in relation to the ground frame of reference for static and dynamic conditions is ;

$$[\vec{D}C^{\Delta}]_{m\leftarrow g} = \begin{bmatrix} \vec{D}_x^{\Delta} \\ \vec{D}_y^{\Delta} \\ \vec{D}_z^{\Delta} \end{bmatrix}$$

5.4.8 Segment orientations

Up to this point, the following directional cosine matrices have been discussed ;

- $[\vec{D}C_s]_{p\leftarrow g}$, relating the segments principal axes of inertia to the ground frame of reference for static condition. (section 5.4.6)

-$[\vec{D}C_s]_{m\leftarrow g}$ and $[\vec{D}C_d]_{m\leftarrow g}$, relating markers axes to the ground frame of reference for static and dynamic conditions respectively. (section 5.4.7)

In order to study the dynamic situation i.e. walking, the dynamic orientation of the segments need to be defined. Similar to $[\vec{D}C_s]_{p\leftarrow g}$ for static condition, $[\vec{D}C_d]_{p\leftarrow g}$ will relate the segment axes of inertia to the ground frame of reference during walking. This is obtained by firstly using the transpose of $[\vec{D}C_s]_{m\leftarrow g}$ to get the relationship between the principal axes of inertia and the marker frame of reference in the static condition as follows;

$$[\vec{D}C_s]_{p\leftarrow m} = [\vec{D}C_s]_{p\leftarrow g}[\vec{D}C_s]_{m\leftarrow g}^{T}$$

It can be seen that $[\vec{D}C_s]_{p\leftarrow m}$ remained the same during static and dynamic conditions, which allowed the dynamic relationship between the principal axes and the ground frame of reference to be determined by the following formulation ;

$$[\vec{D}C_d]_{p\leftarrow g} = [\vec{D}C_s]_{p\leftarrow m}[\vec{D}C_d]_{m\leftarrow g}$$

5.4.9 Dynamic position of joint centres

Regardless of static or dynamic conditions, the joint centres have fixed positions in relation to the marker frames of reference. Therefore in order to achieve the dynamic position of joint centres in relation to the ground frame of reference, the joint centres acquired in the static test are firstly related to the marker frame of reference corresponding to the different segments. In this study, the ankle and knee joint centres were related to the shank's marker frame of reference while the hip joint centres to the pelvis's marker frame of reference. The formulation is described below taking the knee joint centre as an example.

The static left knee joint centre with respect to the marker frame of reference is ;

$$\begin{bmatrix} X_{lk}^{m} \\ Y_{lk}^{m} \\ Z_{lk}^{m} \end{bmatrix} = [DC_s^{ls}]_{m\leftarrow g} \begin{bmatrix} X_{lk}^{g} - X_{lll}^{g} \\ Y_{lk}^{g} - Y_{lll}^{g} \\ Z_{lk}^{g} - Z_{lll}^{g} \end{bmatrix}$$

X_{lk}^{m}, Y_{lk}^{m} and Z_{lk}^{m} do not change during walking, thus the dynamic knee joint centre with respect to the ground is obtained by ;

$$\vec{r}_{lk}^{\,g} = \begin{bmatrix} x_{lk}^{g} \\ y_{lk}^{g} \\ z_{lk}^{g} \end{bmatrix} = \begin{bmatrix} x_{lll}^{g} \\ y_{lll}^{g} \\ z_{lll}^{g} \end{bmatrix} + \left[DC_d^{ls}\right]_{m\leftarrow g}^{T} \begin{bmatrix} X_{lk}^{m} \\ Y_{lk}^{m} \\ Z_{lk}^{m} \end{bmatrix}$$

Channel	Force and moment	Factor
Force plate A		
1	FZ	0.31252
2	FZ	0.31252
3	FX	-0.31381
4	FX	-0.31381
5	FY	0.63356
6	FY	0.63356
7	FY	0.63356
8	FY	0.63356
Force plate B		
9	FX	0.26749
10	FY	0.96922
11	FZ	-0.24822
12	MX	0.26001
13	MY	0.06563
14	MZ	-0.25452
Force plate C		
15	FX	-0.24930
16	FY	1.01344
17	FZ	0.25248
18	MX	-0.27450
19	MY	0.06549
20	MZ	0.26159

Table 5.4.10.1 Force plates calibration factors

$$\vec{r}^{\,g}_{lk} = \begin{bmatrix} x^g_{lk} \\ y^g_{lk} \\ z^g_{lk} \end{bmatrix} = \begin{bmatrix} x^g_{III} \\ y^g_{III} \\ z^g_{III} \end{bmatrix} + \left[DC^{ls}_{d}\right]_{g\leftarrow m} \begin{bmatrix} X^m_{lk} \\ Y^m_{lk} \\ Z^m_{lk} \end{bmatrix}$$

5.4.10 Ground reaction forces and moments acting at the centre of the force plate

The ground reaction forces (Fx, Fy and Fz) as a result of the subject standing or walking were recorded with the aid of force platforms as previously discussed. Simultaneously, the moments acting at the centre of each force plate (Mx, My and Mz) were also recorded. The force platforms data were represented in computer units (1-4096), and related to the individual force plate frame of reference. The force plate frame of reference was located at the centre of the force plate parallel to the ground frame of reference of the Vicon motion analysis system. In order to represent forces and moments in SI units, the computer units recorded by the force platforms have to be converted by a set of calibration factors. The computer units were firstly subtracted by 2048, the mid point of a 12 bit ADC, and multiplied by the calibration factors shown in table. 5.4.10.1. In the case of force plate A, further calculations were performed to obtain the forces and moments,

$F_x = F_{x1+4} + F_{x2+3}$

$F_y = F_{y1} + F_{y2} + F_{y3} + F_{y4}$

$F_z = F_{z1+2} + F_{z3+4}$

$M_x = a\,(-F_{y1} + F_{y2} + F_{y3} - F_{y4}) / 0.975$ 5.4.10a

$M_y = b\,(-F_{z1+2} + F_{z3+4}) + a\,(F_{x1+4} - F_{x2+3}) / 0.955$ 5.4.10b

$M_z = b\,(F_{y1} + F_{y2} - F_{y3} - F_{y4}) / 1.031$ 5.4.10c

where a = 0.12 m and b = 0.2 m.

The sensitivities of the force plates have been checked in detailed by Fleming et al (1992). Table 5.4.10.2 and 5.4.10.3 shows the sensitivity and crosstalk represented in mean absolute values in percentage for force plate A and B respectively. The main effects for the three force components were negligible (99.608 % to 100.29%), while the main effects in the three components of moments are

University of Strathclyde Force Platform A			
Parameter	Mean Absolute Value	Standard Deviation	N
Fx %TFx	99.884	0.487	30
Fy %TFx	0.9119	0.2312	30
Fz %TFx	1.027	0.785	30
Fx %TFy	0.1201	0.0779	12
Fy %TFy	99.608	0.486	12
Fz %TFy	0.3264	0.0907	12
Fx %TFz	0.4258	0.2573	29
Fy %TFz	0.6227	0.3183	29
Fz %TFz	99.938	0.456	29
Mx %TMx	97.545	1.832	29
My %TMy	95.595	0.771	39
Mz %TMz	103.07	1.60	29
Mx Nm/kNTFx	0.8622	0.4568	30
My Nm/kNTFy	1.120	0.2196	12
Mz Nm/kNTFz	0.877	0.742	29

Table 5.4.10.2 Sensitivity and crosstalk on force plate A. (Fleming et al, 1992)

University of Strathclyde Force Platform B			
Parameter	Mean Absolute Value	Standard Deviation	N
Fx %TFx	99.975	0.281	19
Fy %TFx	1.611	0.506	19
Fz %TFx	0.3846	0.1440	19
Fx %TFy	0.3913	0.3721	17
Fy %TFy	99.364	0.428	17
Fz %TFy	0.2978	0.0637	17
Fx %TFz	1.0023	0.4713	36
Fy %TFz	1.337	0.831	36
Fz %TFz	99.466	0.732	36
Mx %TMx	100.22	1.89	30
My %TMy	101.09	0.92	38
Mz %TMz	100.29	1.29	30
Mx Nm/kNTFx	1.775	0.998	19
My Nm/kNTFy	0.4932	0.2728	17
Mz Nm/kNTFz	1.755	1.166	36

Table 5.4.10.3 Sensitivity and crosstalk on force plate B. (Fleming et al, 1992)

slightly larger varying from 95.595 % to 103.07 %, requiring correction factors as reflected in equations 5.4.10a, 5.4.10b and 5.4.10c. The cumulative error due to cross effect at maximum loading experienced during normal walking, are estimated to be about 0.6%, 0.3% and 5% for Fx, Fy and Fz respectively. Similarly, based on the maximum moment experienced during walking, extreme cross effect error estimated on Mx from Fx, on My from Fy and Mz from Fz were 0.3%, 10% and 0.4%. The cross-effect error was considerably larger on My from Fy due to the lower magnitude of My recorded during walking.

Forces and moments calculated above are related to the individual force plate frame of reference. These have to be transferred to the ground frame of reference of the Vicon motion analysis system for later use in calculating the inter segmental joint loads. Since the force plate and ground frame of reference are parallel to each other differing only in position of their origins, the transfer does not affect the components of the ground reaction forces, thus ;

$$FX^g = FX^f\,;\ FY^g = FY^f\,;\ FZ^g = FZ^f$$

However, transferring the moments to the ground frame of reference require the following computation ;

$$\vec{M}^g = \vec{M}^f + \vec{R} \times \vec{F}^f$$

where $\vec{R}$ is the position vector of the centre of the force plate related to the ground frame of reference which was obtained through measurement and ;

$\vec{R} = [-0.303\ -0.057\ 0.2]$ for force plate A

$\vec{R} = [0.303\ -0.04\ -0.2]$ for force plate B

$\vec{R} = [-0.306\ -0.04\ 0.018]$ for force plate C

5.4.11 Position of centre of gravity and segment mass

The mass of the good leg was calculated using the method reported by Clauser et al (1969). Several information were required to calculate the mass of shank and foot, and thigh. These were shank circumference at the calf (C_S), tibia height (H_T), ankle circumference (C_A), body weight (BM) in kg, foot length (L_F), upper thigh circumference (C_{TH}) and p the thickness of the folded iliac fat. All dimensions were measured in cm except for p which was in mm. The mass of shank and foot is therefore,

$$m_s(kg) = 0.111C_S + 0.047H_T + 0.122C_A + 0.003BM + 0.027L_F$$

and the mass of thigh,

$$m_t\,(kg) = 0.074BM + 0.123\,C_{TH} + 0.027\,(\,0.78p - 0.27\,)$$

The position of the centre of gravity (CG) was calculated using coefficients presented by Goh (1982). The distance from the knee joint centre to the CG of the shank and foot is,

$$L_{ms}\,(m) = 0.4673L_{sh}$$

and the distance from the hip joint centre to the CG of the thigh is given by,

$$L_{mt}\,(m) = 0.4169L_{th}$$

where L_{sh} is the ankle height plus the shank length and L_{th} is length of the thigh.

The mass of the prosthetic shank and foot was measured using a spring balance and the CG of the shank and foot assembly was obtained by balancing the assembly on a sharp edge. The mass of the thigh on the prosthetic side included the mass of the socket (m_{so}) and the residual limb (m_{rl}). The mass of the socket was again

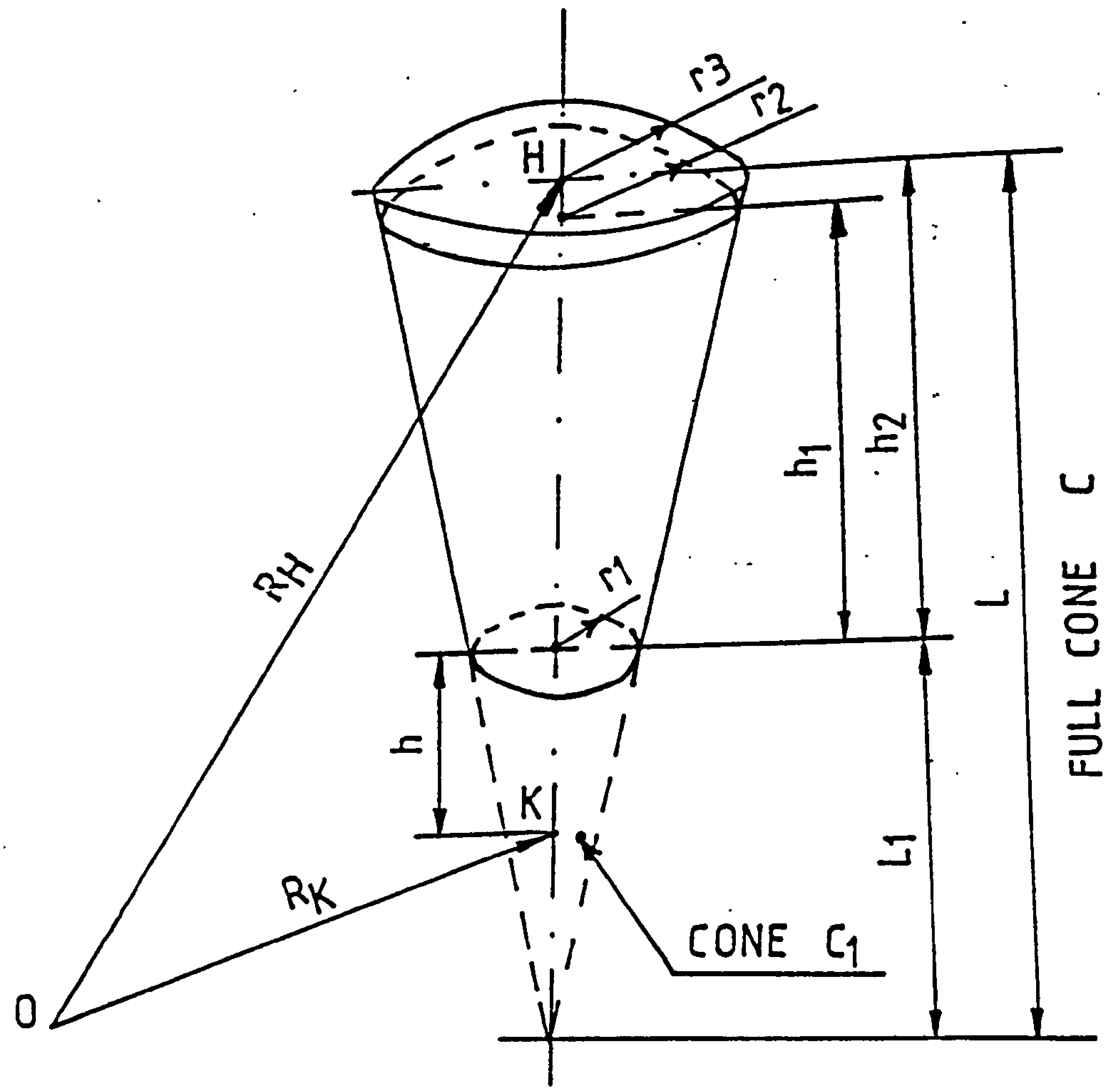

Fig. 5.4.11.1 Residual limb model for calculation of mass and position of centre of gravity. (Marmar, 1993)
K - Knee joint centre.
H - Hip joint centre.

obtained using a spring balance, while the mass of the residual limb was approximated using the following calculations ;

$$m_{rl} = \rho v_{rl}$$

where v_{rl} is the volume of the residual limb in m^3 and ρ is the body density by Contini (1972) which is equal to 1065.2 kg/m^3.

The volume of the residual limb was computed by assuming it to be a truncated cone. Referring to Fig. 5.4.11.1,

$$v_{rl}\ (m^3) = \tfrac{\pi}{3} h_2 (r_3^2 + r_3 r_1 + r_1^2)$$

Therefore ,

$$m_{rl}\ (kg) = \tfrac{\pi}{3} \rho h_2 (r_3^2 + r_3 r_1 + r_1^2)$$

and r_3 which could not be measured was calculated using,

$$\frac{h_2}{r_3 - r_1} = \frac{h_1}{r_2 - r_1}$$

The distance from the hip joint centre to the CG of the residual limb was acquired using the fomulation given by Shames (1980),

$$L_{mrl}\ (m) = \frac{h_2 (r_3^2 + 2 r_3 r_1 + 3 r_1^2)}{4 (r_3^2 + r_3 r_1 + r_1^2)}$$

Similar to that of the shank and foot segments, the distance of the hip joint centre to the CG of the socket (L_{mso}) was based on balancing the socket on a sharp edge. Finally, the distance of the hip joint centre to the CG of the thigh at the prosthetic side was given by combining the residual limb and the socket. Thus,

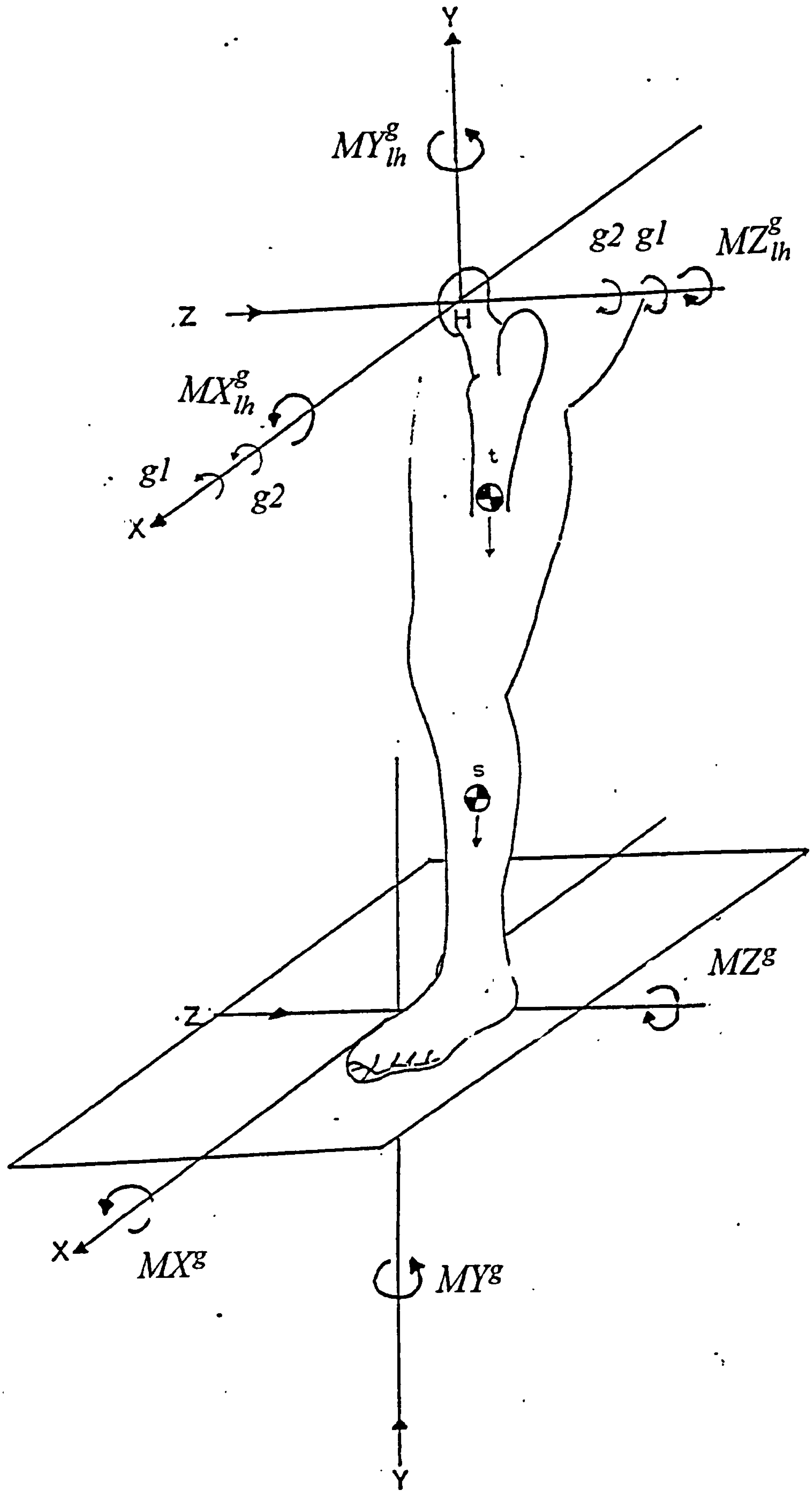

Fig. 5.4.12.1 Free body diagram of left lower limb.
(Modified from Li, 1993)

$$L_{mpt}\,(m) = \frac{m_{rl}L_{mrl} + m_{so}L_{mso}}{m_{rl} + m_{so}}$$

5.4.12 Inter segmental loads

The inter segmental loads were calculated firstly in the ground frame of reference using the kinematics information of the model segments and the ground reaction forces recorded with the force plates. The calculated values were then transformed accordingly to the principal frame of reference as discussed previously in section 5.4.7. The example below showed the calculations for the moments and forces at the hip for the left good limb. Referring to Fig. 5.4.12.1,

$$MX^{g}_{lh} = (FZ^{g} \times y^{g}_{lh}) - (FY^{g} \times z^{g}_{lh}) + MX^{g} + g1 + g2$$

where g1 and g2 are the moments due to the weight of the shank and foot, and thigh respectively, these are calculated as follows ;

$$g1 = (\vec{r}^{\,g}_{ls} - \vec{r}^{\,g}_{lh}) \times m_{sh} \times 9.81$$

$$g2 = (\vec{r}^{\,g}_{lt} - \vec{r}^{\,g}_{lh}) \times m_{th} \times 9.81$$

where $\vec{r}^{\,g}_{ls}, \vec{r}^{\,g}_{lt}, \vec{r}^{\,g}_{h}$ are the position vectors for the shank and foot mass centre, thigh mass centre and the hip joint centre for the left limb respectively. And,

$$MY^{g}_{lh} = (FZ^{g} \times x^{g}_{lh}) - (FX^{g} \times z^{g}_{lh}) + MY^{g}$$

$$MZ^{g}_{lh} = (FX^{g} \times y^{g}_{lh}) - (FY^{g} \times x^{g}_{lh}) + MZ^{g} - g1 - g2$$

Therefore the inter segmental moments at the hip in the principal frame of reference are ;

$$\begin{bmatrix} MX_{lh}^{p} \\ MY_{lh}^{p} \\ MZ_{lh}^{p} \end{bmatrix} = \begin{bmatrix} \vec{D}C_{\delta}^{lh} \end{bmatrix}_{p \leftarrow g} \begin{bmatrix} MX_{lh}^{g} \\ MY_{lh}^{g} \\ MZ_{lh}^{g} \end{bmatrix}$$

and the inter segmental forces at the hip in the principal frame of reference are ;

$$\begin{bmatrix} FX_{lh}^{p} \\ FY_{lh}^{p} \\ FZ_{lh}^{p} \end{bmatrix} = \begin{bmatrix} \vec{D}C_{\delta}^{lh} \end{bmatrix}_{p \leftarrow g} \begin{bmatrix} FX^{g} \\ FY^{g} \\ FZ^{g} \end{bmatrix}$$

5.5 RESULTS AND DISCUSSIONS

The results discuss in this section comprise of the temporal - distance parameters, the ground reaction forces and the inter segmental moments at the hip. The forces and moments were obtained for the three amputee subjects during walking and during standing.

5.5.1 Temporal - distance parameters

The temporal - distance parameters for the three trans-femoral amputee subjects are listed in table. 5.5.1.1. The mean values listed were the average of five walking trials conducted within the same day. The walking speed was the preferred normal walking speed of the amputee subjects. Among the three subjects, subject M walking speed was the faster (1.319 m/s) possessing the largest stride length (1.462 m). Nevertheless, the average velocity of the three amputees in this study (1.152 m/s) was in agreement with previous study attempted on trans-femoral amputees (Marmar 1993 and Murray et al 1983 obtained average velocity of 1.022 m/s and 1.07 m/s respectively). The average stride length was 1.33 m, which was comparable to those reported by Marmar (1983) measuring 11 trans-femoral amputees obtaining an average value of 1.36 m. It was observed that the step length at the prosthetic side was longer than the sound side, however, in subject M the difference was minimal (2 mm). The average step length for the three subjects in the prosthetic and sound side

	Subject U	Subject M	Subject H
Parameters	Mean (± Std. Dev)	Mean (± Std. Dev)	Mean (± Std. Dev)
Velocity (m/s)	1.015 (0.013)	1.319 (0.018)	1.124 (0.017)
Stride length (m)	1.278 (0.128)	1.462 (0.018)	1.251 (0.026)
Left step length (m)	0.611 (0.069)	0.726 (0.03)	0.566 (0.023)
Right step length (m)	0.589 (0.051)	0.728 (0.022)	0.658 (0.031)
Stride period (s)	1.211 (0.11)	1.114 (0.036)	1.327 (0.036)
Left stance period (s)	0.716 (0.031)	0.743 (0.013)	0.931 (0.019)
Left swing period (s)	0.52 (0.028)	0.378 (0.027)	0.403 (0.019)
Right stance period (s)	0.854 (0.051)	0.651 (0.025)	0.77 (0.027)
Right swing period (s)	0.367 (0.046)	0.45 (0.017)	0.567 (0.082)
Cadence (step/min)	95.32	108.32	101.61

Table 5.5.1.1 Temporal-distance measurement for subject U (left amputee), subject M and H (right amputee).

were 0.665 m and 0.627 m respectively. The difference between the two step lengths were slightly lesser than some of the previous studies. The prosthetic and sound side step lengths obtained by Marmar (1993) were 0.7 m and 0.61 m and Murray et al (1983) were 0.76 m and 0.67 m respectively.

The average stance period on the prosthetic and the sound side for the three subjects was 0.71 s and 0.84 s respectively. The respective average swing periods were 0.51 s and 0.38 s.

5.5.2 Ground reaction forces during walking

The ground reaction forces of the subjects' (H, U and M) sound limb are plotted in Fig. 5.5.2.1, 5.5.2.2 and 5.5.2.3 respectively. The subsequent ground reaction forces of the subjects' prosthetic limb are plotted in Fig. 5.5.2.4, 5.5.2.5 and 5.5.2.6 respectively. The plots showed the mean values and the mean values plus and minus the standard deviation based on five walking trials. The forces FX, FY and FZ are according to the Cartesian co-ordinate system shown in Fig. 5.3.1.1. Similar force profiles were observed when comparing with previous studies discussed earlier in sectioned 5.2.6. Majority of the forces recorded higher values at the sound side than at the prosthetic side for all three subjects. However, in subjects M and H, the peak force in FZ at the prosthetic side was approximately 10 N more than the sound side.

FX indicates the braking and push off force during the stance phase. The absolute peak force recorded ranged between 80 N to 250 N for the three subjects. In the sound limb, the braking force lasted approximately up to 40 % of the gait cycle. This was followed by the push off force which was opposite in direction to that of the braking force which lasted from 40% to 60% of the gait cycle. The FX profile in the prosthetic limb was generally similar to the sound limb. However, the magnitude of force was lower and the profile also showed a shorter braking force stage, up to 20% of the gait cycle instead of 40% in the sound limb. Also unlike the sound limb, the transition to push off force did occur at the end of the braking force stage. Instead, as seen in subject H and M, the force profile flatten out and remained close to 0 N from 20% to 30% of the gait cycle. In subject U, a third peak of low force magnitude was observed between 20% and 30% of the gait cycle prior to the beginning of the push

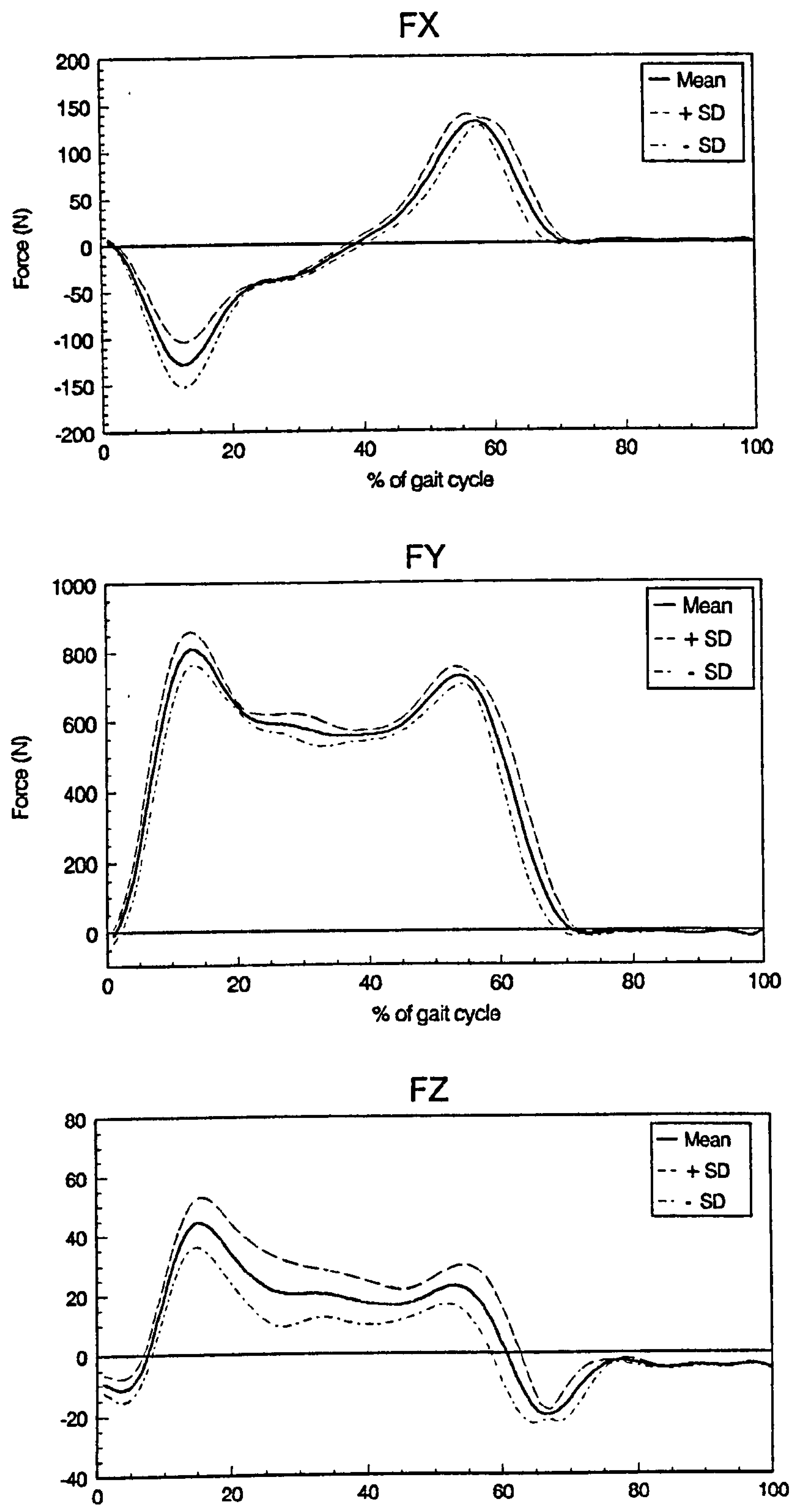

Fig. 5.5.2.1 Ground reaction forces at the sound side of subject H

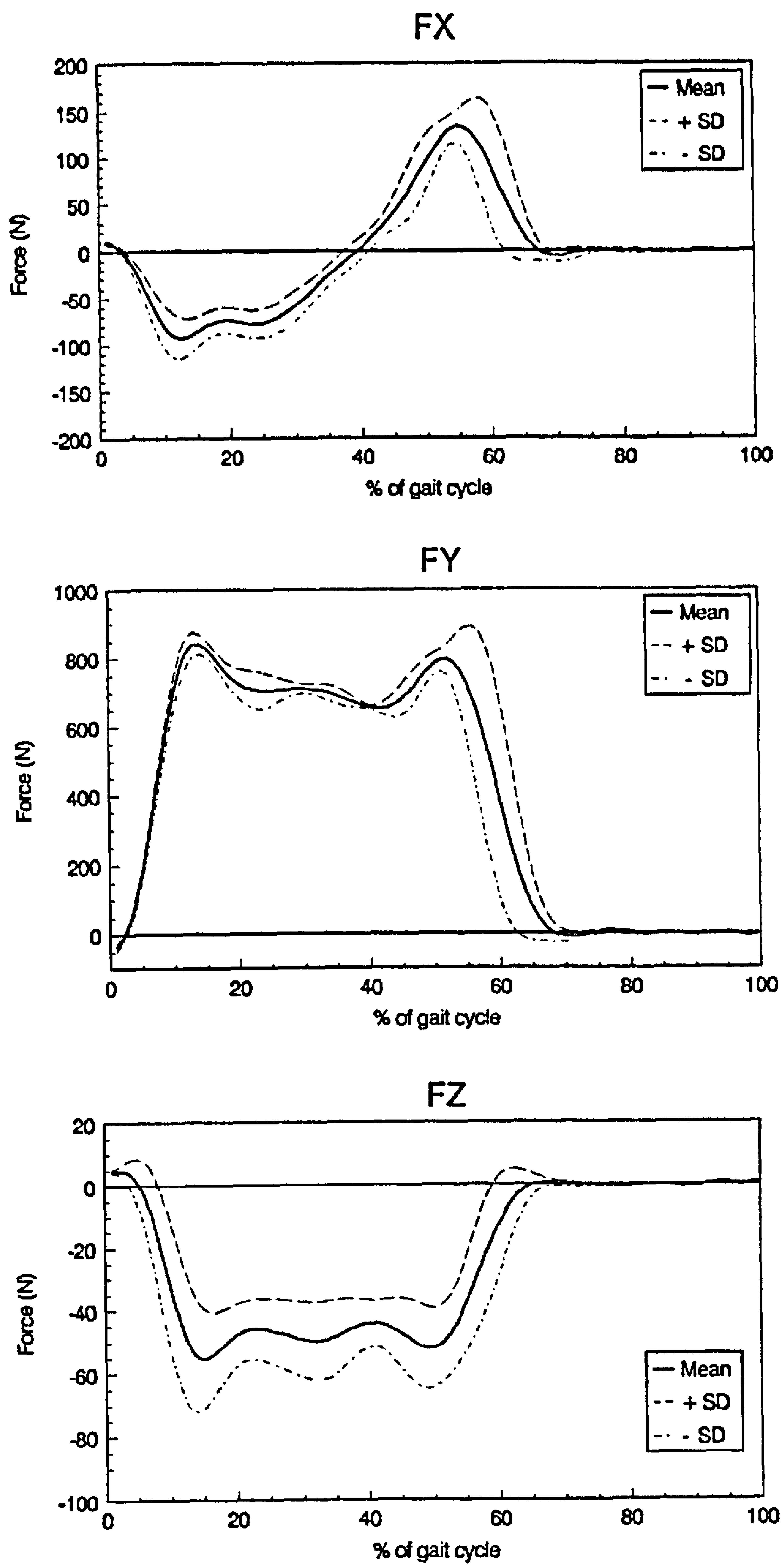

Fig. 5.5.2.2 Ground reaction forces at the sound side of subject U

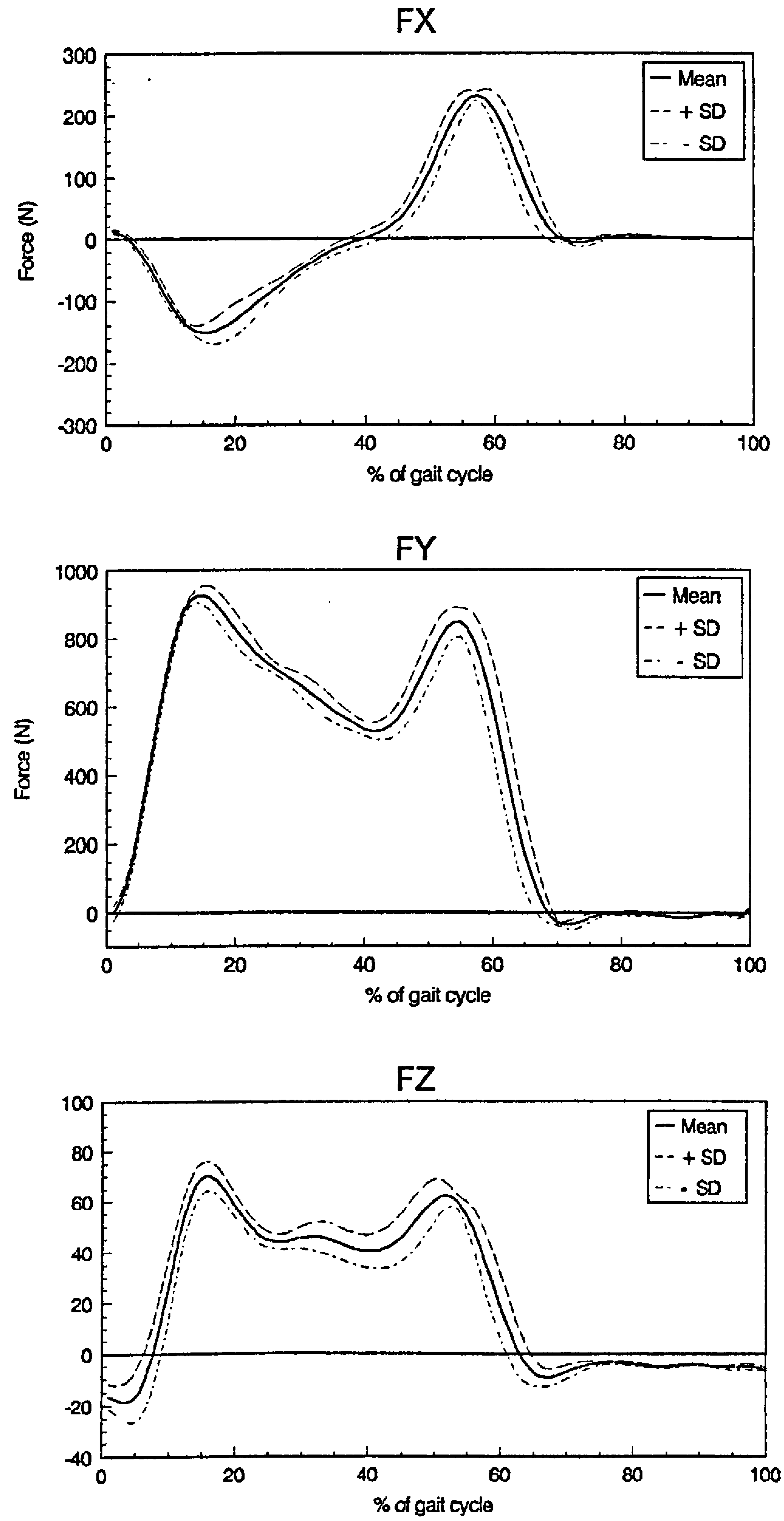

Fig. 5.5.2.3 Ground reaction forces at the sound side of subject M

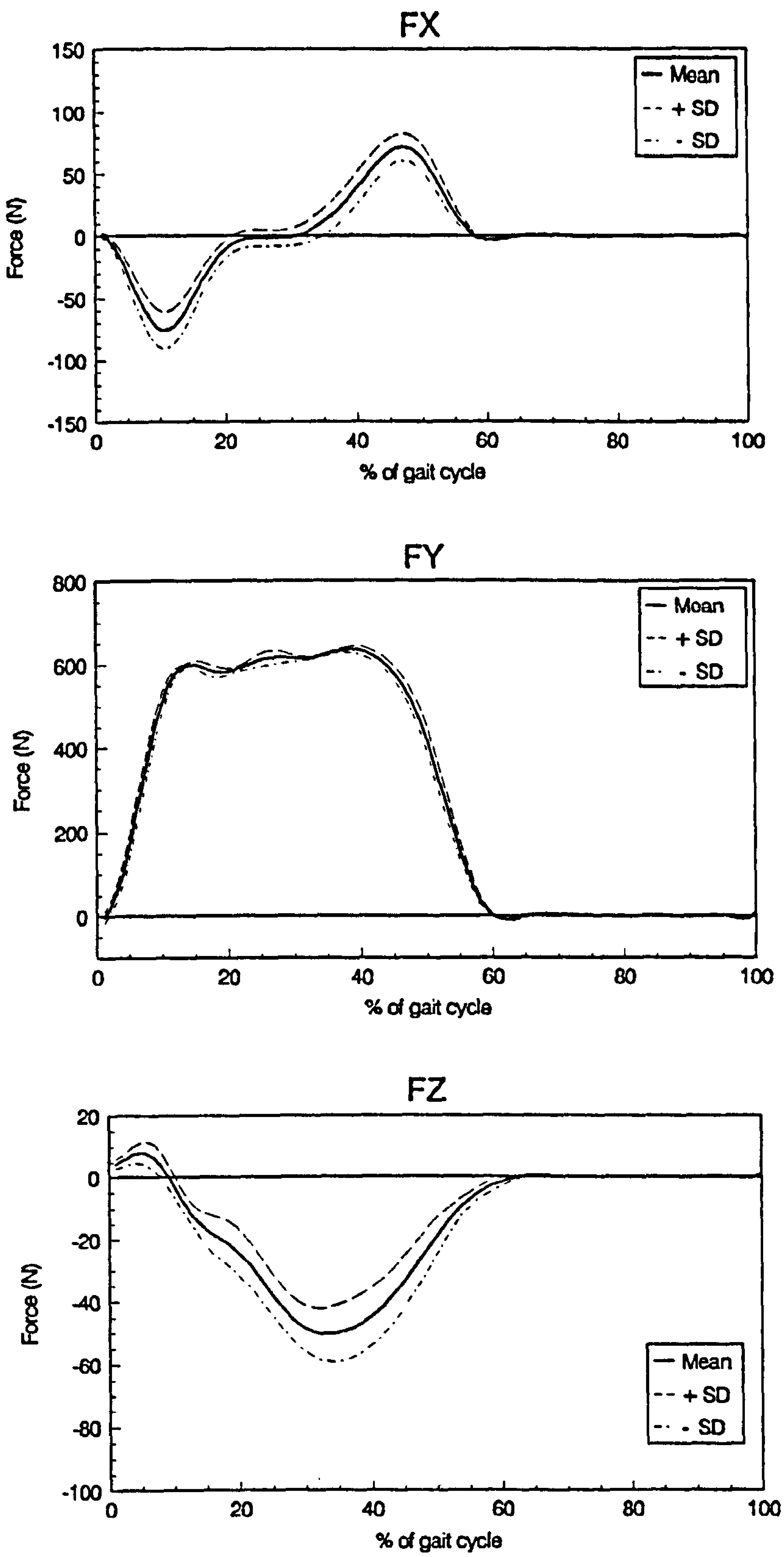

Fig. 5.5.2.4 Ground reaction forces at the prosthetic side of subject H

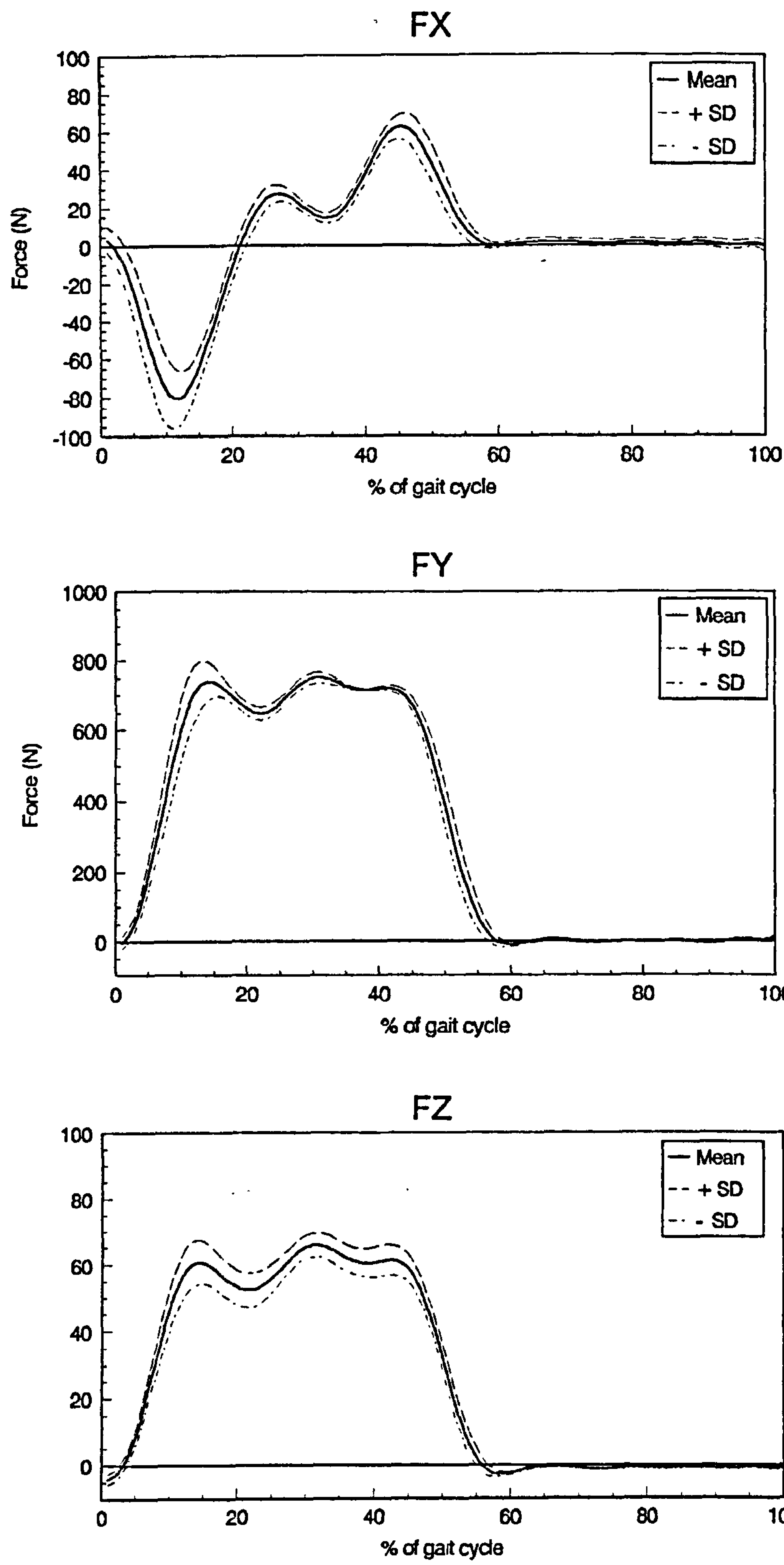

Fig. 5.5.2.5 Ground reaction forces at the prosthetic side of subject U

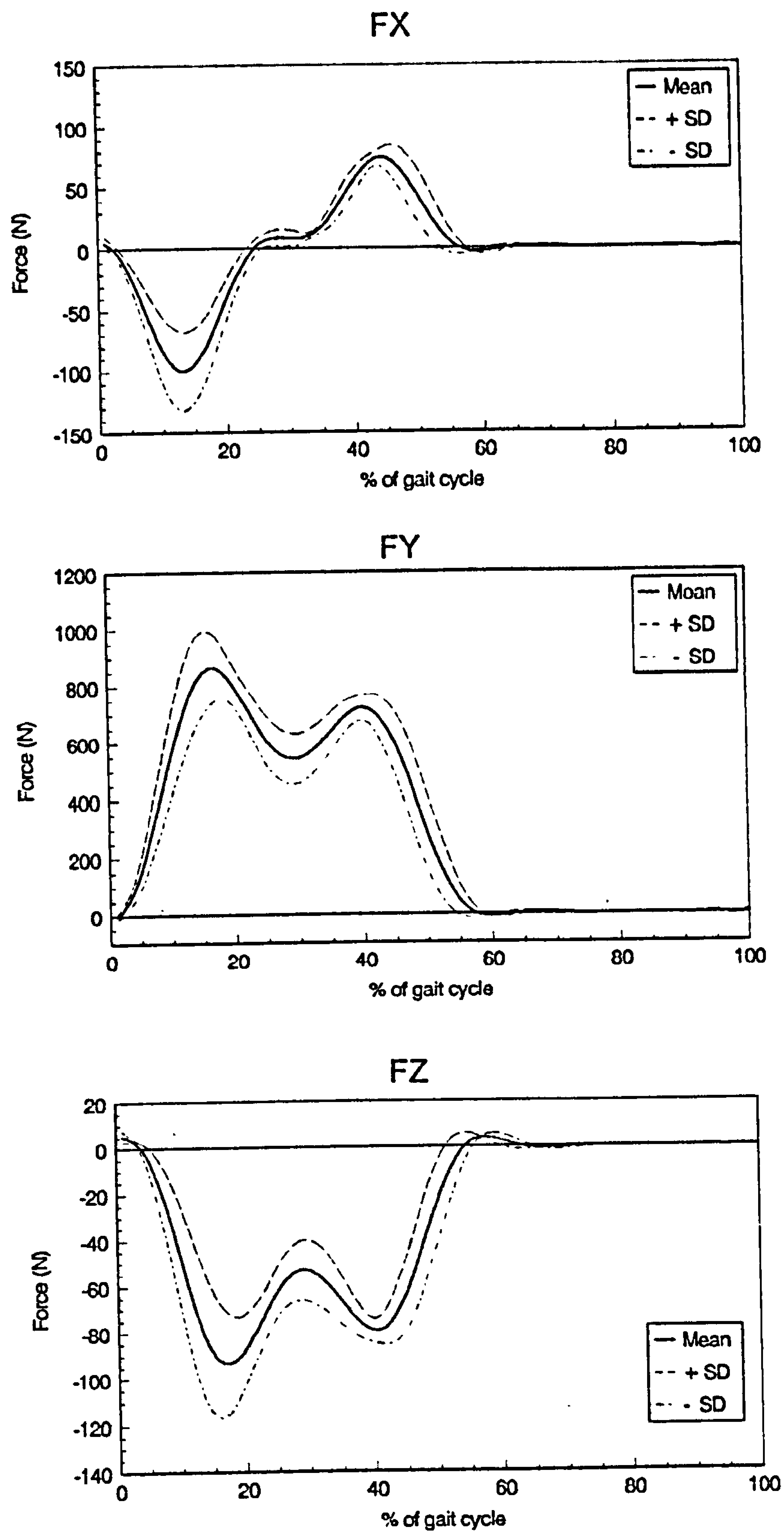

Fig. 5.5.2.6 Ground reaction forces at the prosthetic side of subject M

off force. The push off force at the prosthetic side for the three subjects lasted from 30% to 55% of the gait cycle.

The FX force profile at the prosthetic side could be explained by considering the stability at the prosthetic knee. A large braking force would cause the prosthetic knee to flex. However in the amputee subjects tested, the braking force was deliberately reduced and shorten during gait in order to provide the assurance of stability with the prosthetic knee.

The peak vertical force FY for the three subjects ranged from 750 N to 950 N. The force profile on the sound limb exhibited the typical two peak and a trough pattern. The two peaks occurred at approximately 12% and 40% of the gait cycle. On close observation, a third peak could also be seen at approximately 30% of the gait cycle. This peak was due to the common action known as vaulting, where the subject rose the sound foot to provide clearance for swinging the prosthetic feet. Vaulting could be caused by the prosthetic leg being too long, misalignment and socket loosening due to lost of suction. At the prosthetic side, the two peaks and a trough pattern was not clear. Especially in subject H, the force profile increased to the first peak at 14% of the gait cycle and remained almost flat throughout the stance phase. For the three subjects tested, it was also observed that the first peak in the sound limb (12% of the gait cycle) occurred earlier than that of the prosthetic limb (14% of the gait cycle). This could be due to the lack of confidence with the prosthetic limb or uncomfortable socket, which caused the subject to load the sound limb faster leading to a more secure and comfortable situation.

The peak absolute force recorded in the FZ direction ranged from 50 N to 95 N for the three subjects. The force profile recorded in the sound limb were very similar to that of FY, also possessing the two peaks and a trough pattern. There was minimal difference in the force profile between the sound and the prosthetic side. Except for subject H, the FZ on the prosthetic side was a single peak profile.

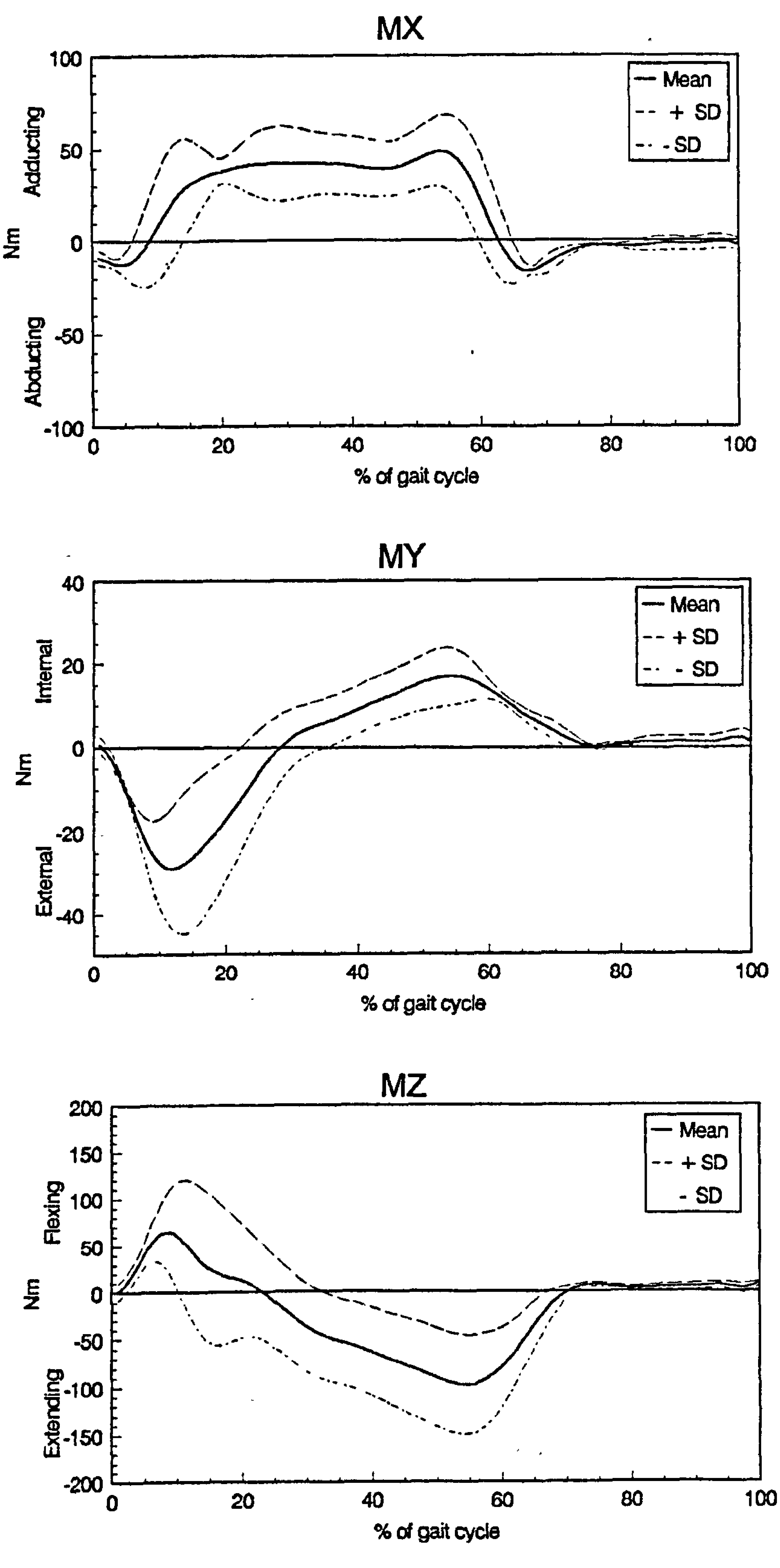

Fig. 5.5.3.1 Inter segmental hip moments at the sound side of Subject H.

5.5.3 Inter segmental hip moment during gait

The inter segmental hip moments at the sound side for subject H, U and M are presented in Fig. 5.5.3.1, 5.5.3.2, 5.5.3.3 respectively. The respective plots for the prosthetic side are presented in Fig. 5.5.3.4, 5.5.3.5 and 5.5.3.6.

The moment MX generated at the medio-lateral plane were mainly causing the thigh to adduct. The adducting moment was larger in the sound side than in the prosthetic side. Peak moments recorded for the three subjects at the sound side ranged from 50 Nm to 145 Nm, and at the prosthetic side the peak moments ranged from 45 Nm to 80 Nm. The values presented in this study compared well with previous study by Marmar (1998) which recorded moments ranging between 15.5 and 93 Nm. It was also observed that an abducting moment was generated just after heel strike to approximately 10% of the gait cycle in the sound limb of subject U and M. However, in all three subjects measured, no abducting moment was indicated in the prosthetic side. It was reckoned that the weak adductors at the residual limb cannot compensate for an abduction moment.

The moment about the y - direction denotes the moment tending to rotate the thigh. In the sound limb of subject H and U, an external rotation moment was generated from early stance to mid stance. From mid stance to the end of stance, the moment changed direction causing the thigh to be internally rotated. However at the sound side of subject M, the external rotation moment lasted from heel strike to about 18% of the gait cycle instead of mid stance. Thereafter, an internal rotation moment was maintained until the end of stance. At the prosthetic side, the external moment generated in subject U during early stance was very low. Similar to the sound side, the moment changed direction at mid stance and the internal rotation moment was about the same magnitude as that of the sound side. However at the prosthetic side of subject H and M, the moment generated were mostly causing the thigh to rotate internally througout stance. The maximum magnitude of the internal rotation moment recorded for the three subjects ranged from 7 Nm to 25 Nm, and the external rotation moment ranged from 3 to 35 Nm.

The moment about the z - direction showed a flexing moment at the hip at early stance when the ground reaction force vector passed ahead of the hip joint

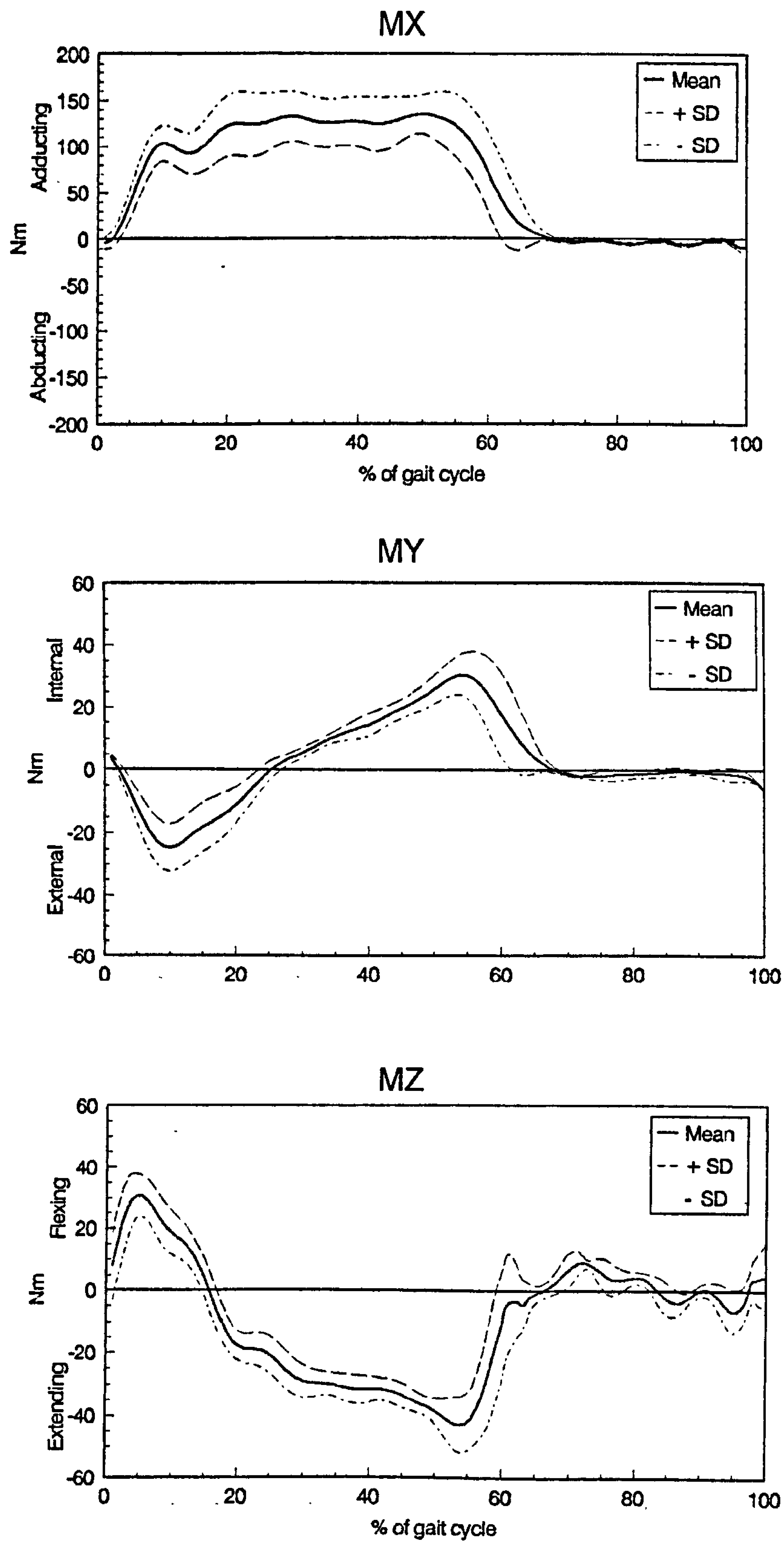

Fig. 5.5.3.2 Inter segmental hip moments at the sound side of subject U

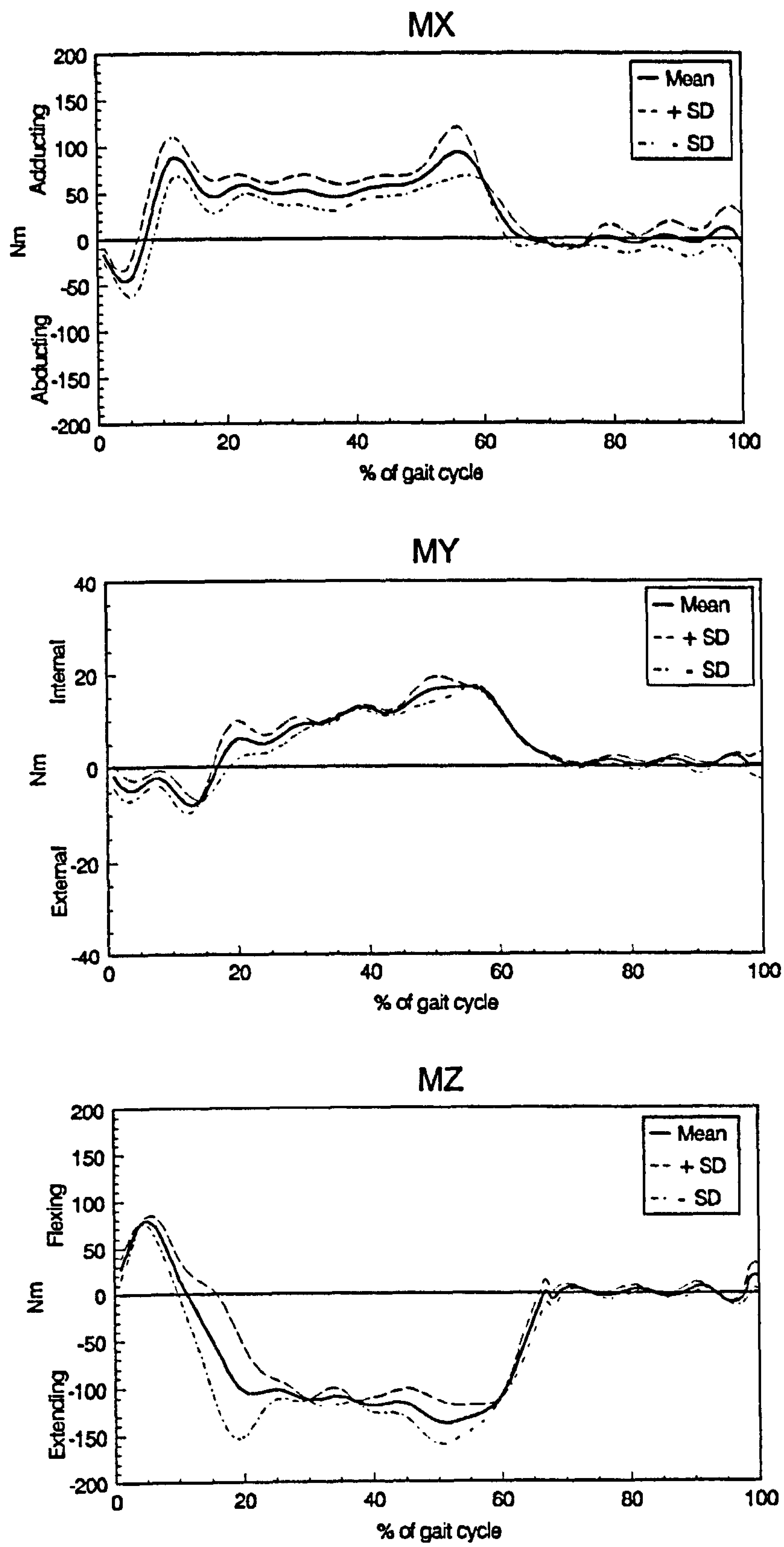

Fig. 5.5.3.3 Inter segmental hip moments at the sound side of Subject M

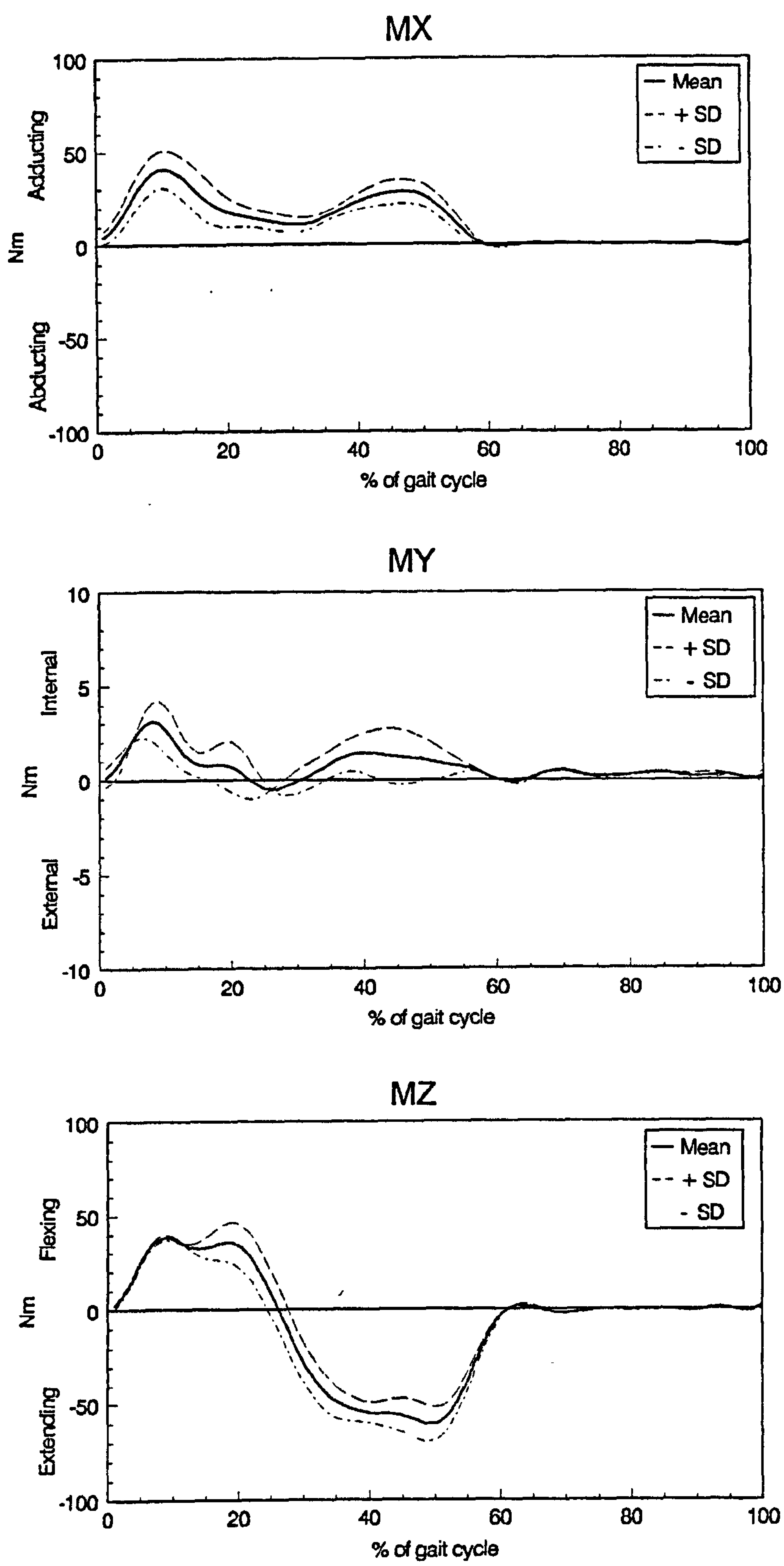

Fig. 5.5.3.4 Inter segmental hip moments at the prosthetic side of subject H

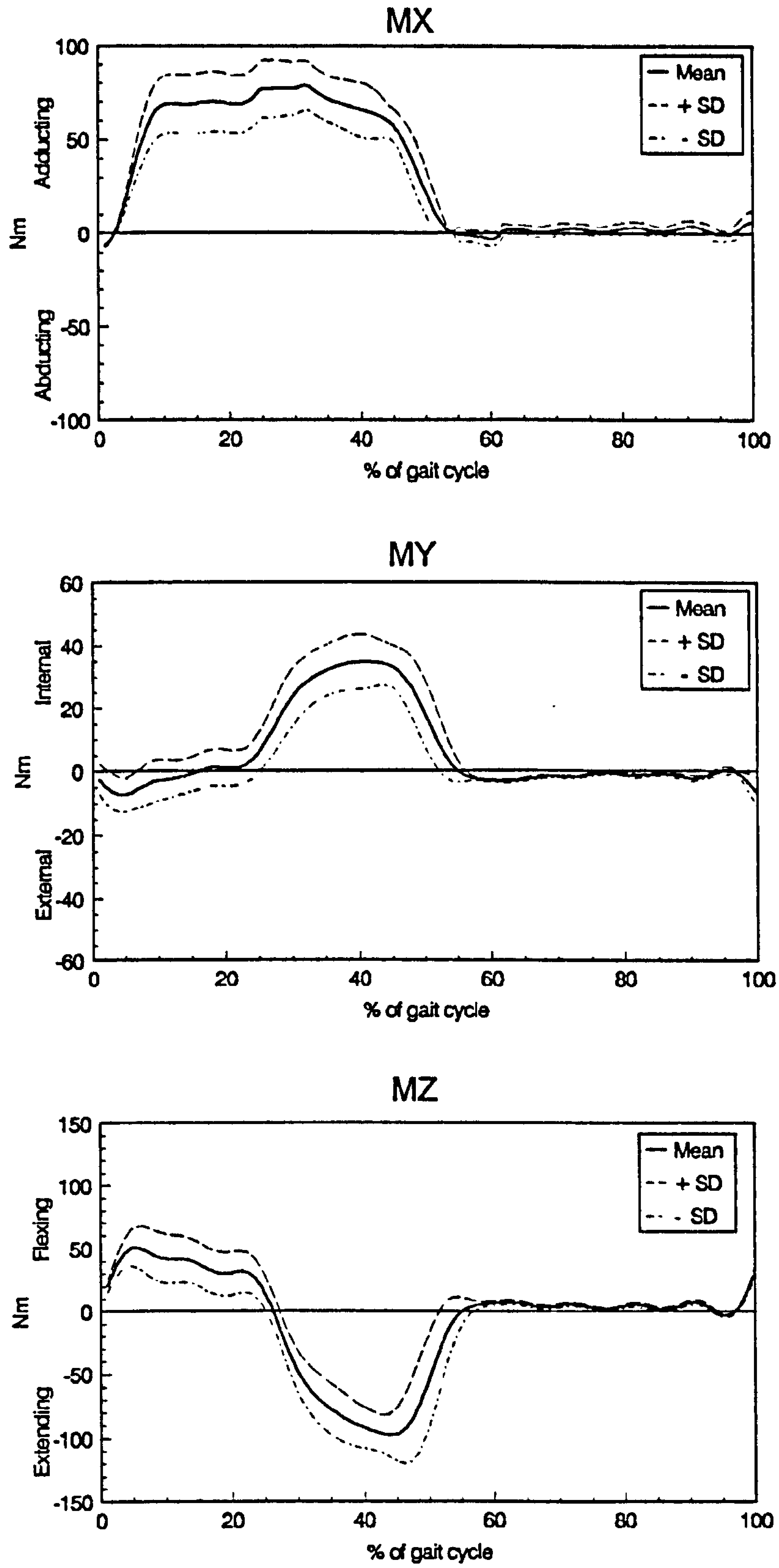

Fig. 5.5.3.5 Inter segmental hip moments at the prosthetic side of Subject U

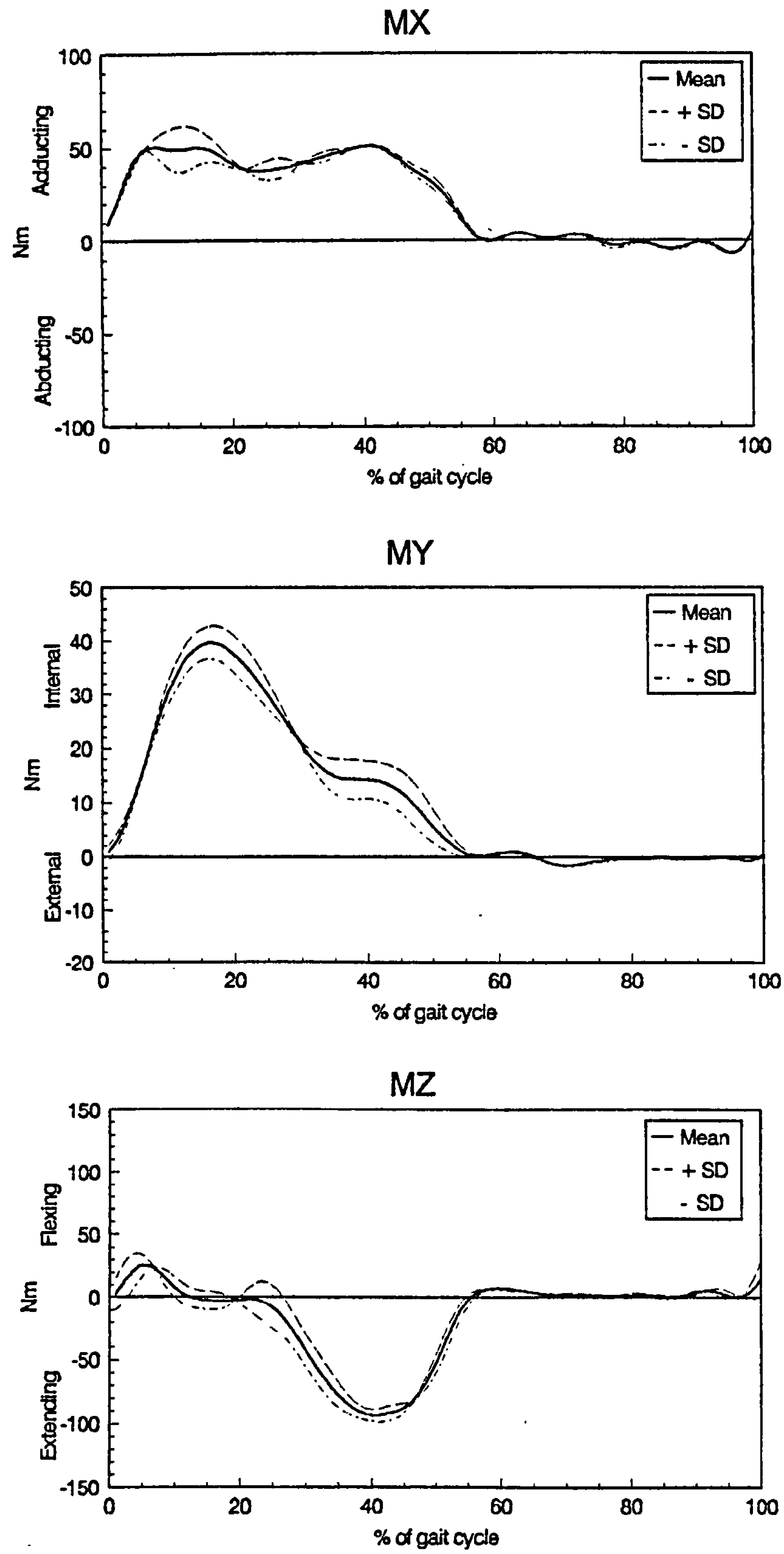

Fig. 5.5.3.6 Inter segmental hip moments at the prosthetic side of Subject M

centre. Towards late stance as the force vector passed behind the hip joint centre, an extending moment began to built up. The maximum flexion and extension moment corresponded approximately to the two peaks of the vertical ground reaction force (FY) in early and late stance i.e. 12% and 50% of the gait cycle. The maximum flexion moment for the three subjects ranged from 30 Nm to 90 Nm while maximum extension moment ranged from 40 Nm to 130 Nm. These values were comparable to previous values obtained with amputee subjects. Marmar (1993) obtained flexion moment ranging from 38 Nm to 107 Nm and extension moment ranging from 0 to 83 Nm. Goh (1982) produced average flexion moment of 100 Nm and extension moment of 50 Nm. The flexion and extension moments recorded in subject H and M sound side were larger than that of the prosthetic side. This was mainly due to the higher vertical ground reaction force recorded in the sound limb than in the prosthetic limb for the two subjects. However, in subject U the flexion and extension moments in the prosthetic limb were actually slightly larger than that of the sound limb. This could be due to the minimal difference in FY between the sound and prosthetic limb, and also the high braking and push off force (FX) recorded in the prosthetic limb with this subject. In the three subjects tested, the transition from flexion to extension occurred earlier in the sound side (approximately 15% of the gait cycle) than in the prosthetic side (approximately 25% of the gait cycle).

5.5.4 Ground reaction forces and inter segmental moments at the hip during standing

Table 5.5.4.1 presents the ground reaction forces which were recorded with the subjects in a standing position. The forces tabulated are the mean of five standing trials and are according to the co-ordinate system shown in Fig. 5.3.1.1. It was noticed for the three subjects the vertical force (FY) acting on the sound limb was larger than the prosthetic limb. In subject H and M, approximately 52% of the vertical load was acting on the sound limb. In the case of subject U, the percentage of load acting on the sound limb was much larger at 64%.

The inter segmental moments recorded during standing were much lower than the peak moments obtained during walking. This was due to the lower vertical force

	FX (N)		FY (N)		FZ (N)	
Subjects	Sound	Prosthetic	Sound	Prosthetic	Sound	Prosthetic
H	-16.9	22.6	352.1	298.2	-13.5	1.8
U	-0.8	5.2	489.2	274.9	-12.8	6.3
M	13.5	1.8	384.4	354.4	-12.1	6.7

Table 5.5.4.1 Ground reaction forces during standing

	MX (Nm)		MY (Nm)		MZ (Nm)	
Subjects	Sound	Prosthetic	Sound	Prosthetic	Sound	Prosthetic
H	8.4 (Add)	21.6 (Add)	2.1 (Er)	8.8 (Ir)	1.1 (Ext)	6.2 (Ext)
U	25.6 (Add)	19.4 (Add)	4.2 (Er)	1.3 (Ir)	15.6 (Ext)	18.1 (Ext)
M	29.9 (Add)	36.5 (Add)	2.6 (Er)	6.9 (Ir)	3.2 (Flex)	2.1 (Ext)

Add - Adduction ; Flex - Flexion ; Ext - Extension ; Er - External rotation ;
Ir - Internal rotation

Table 5.5.4.2 Inter segmental hip moments during standing component and the position of the lower limbs i.e. short moment arm. Table 5.5.4.2 show the mean inter segmental moments at the hip for five standing trials. An adducting moment (MX) was seen in both the sound and the prosthetic limbs for the three subjects. The flexion or extension moments (MZ) recorded at the hip were relatively small since the ground reaction force vector passed near the hip joint. External and internal rotation (MY) moments were also relatively small compared to the adducting moment. Nevertheless, it was observed that an external rotation moment was present at the sound side and an internal rotation moment at the prosthetic side.

5.5.5 Input forces and moments for the finite element (FE) model of the residual limb

The forces and moments measured for standing and walking were used as loading conditions in the corresponding FE models of the residual limb generated for the three subjects. The details of the FE models are presented in chapter seven. The forces and moments were introduced to the femoral bone component of the FE model, reproducing the actual loading conditions experienced by the amputee subject during standing and during gait. However, due to the laborious mathematical procedure in the FE method, modelling was only performed for standing and for walking conditions at 10%, 25% and 40% of the gait cycle only.

The loading implemented in the FE models were that of the prosthetic side only. Prior to adopting the ground reaction forces in the FE models, the forces need to be transformed to the thigh principal frame of reference as discussed earlier in section 5.4.12. However, the inter segmental moments applied in the FE models would be similar to that discussed in the results sections as these were already in the thigh principal frame of reference. Table 5.5.5.1 shows the magnitude and direction of loading used in the FE models.

5.6 CONCLUSION

The ground reaction forces, inter segmental forces and moments at the hip were obtained for three trans-femoral amputees during standing and during walking.

Standing	Subject U	Subject H	Subject M
FX (N)	-63.5	-26.8	-66.4
FY (N)	264.1	295.1	353.2
FZ (N)	49.2	-74.4	-18.2
MX (Nm)	-19.4	21.6	36.5
MY (Nm)	-1.3	8.8	6.9
MZ (Nm)	-18.1	-6.2	-2.1
10 % of gait cycle			
FX (N)	-96.9	72.6	-150.3
FY (N)	819.2	494.9	521.7
FZ (N)	-18.4	27.2	205.1
MX (Nm)	-68.4	40.7	49.6
MY (Nm)	2.73	2.69	30.2
MZ (Nm)	41.8	37.4	8.1
25 % of gait cycle			
FX (N)	-163.9	33.1	-206.5
FY (N)	641.1	598.5	545.2
FZ (N)	-5.1	15.4	189.4
MX (Nm)	-76.7	13.9	37.9
MY (Nm)	-6.1	-0.43	29.9
MZ (Nm)	13.8	8.6	-8.1
40 % of gait cycle			
FX (N)	-330.1	67.7	-317.5
FY (N)	640.9	619.1	585.1
FZ (N)	3.1	58.1	264.9
MX (Nm)	-65.7	23.2	50.9
MY (Nm)	-34.8	1.43	14.32
MZ (Nm)	-91.9	-54.3	-93.1

Fig. 5.5.5.1 Inter segmental forces and moments at the hip applied to the FE models of the residual limb. The forces and moments are according to the Cartesian co-ordinates system shown in Fig. 5.3.1.1. Note : Subject U is a left amputee, thus according to the co-ordinates system negative MX is an adducting moment and negative MY denotes an internal rotation.

The information were obtained for the purpose of applying realistic loading conditions in the three dimensional FE models of the residual limb.

The ground reaction forces and the inter segmental moments at the hip presented in this study were found to be comparable with previous studies attempted on evaluating trans-femoral amputee gait (Marmar, 1993 and Goh, 1983).

CHAPTER SIX
MECHANICAL PROPERTIES OF SOFT TISSUE

6.1 INTRODUCTION

Characterising the mechanical properties of soft tissues is essential to allow any prediction of stresses and deformations on the body imposed by external forces, as in the case of an amputee experiencing pressure at the residual limb / socket interface. To model such a problem proved to be a difficult task, predominantly due to the complex mechanical behaviour of the soft tissues inside the residual limb. Even though using different hypotheses, many workers have proposed mathematically the mechanical behaviour of different types of soft tissue like skin, vessels and muscles, but these proposal have been obtained under specific experimental procedures and often impossible to incorporate to a composite structure like that of the residual limb. Furthermore, it has been reckoned that regarding the stress - strain behaviour of soft tissue, no general mathematical descriptions have yet been developed successfully (Barbenel et al 1978).

There are two main parts in this chapter, consisting of *in vitro* and *in vivo* studies of soft tissue. The first investigation leads to the use of finite element analysis to predict soft tissue behaviour under compression. A series of compression tests performed on the Instron machine with PVC gel and porcine tissue were carried out to validate finite element predictions. The second part investigates the use of an *in vivo* mechanical indentation device on the amputee's residual limb to characterise its mechanical properties.

A review of related works in soft tissue mechanics will also be presented in this chapter.

6.2 STRUCTURE AND COMPOSITION OF SOFT TISSUES

In the residual limb, the soft tissue components can be generally grouped into three main types, skin, fascia and skeletal muscles. The structures and compositions of these tissues have been extensively studied and established, providing much information to their mechanical properties. Before an attempt to review their mechanical properties, their structures and compositions are discussed briefly.

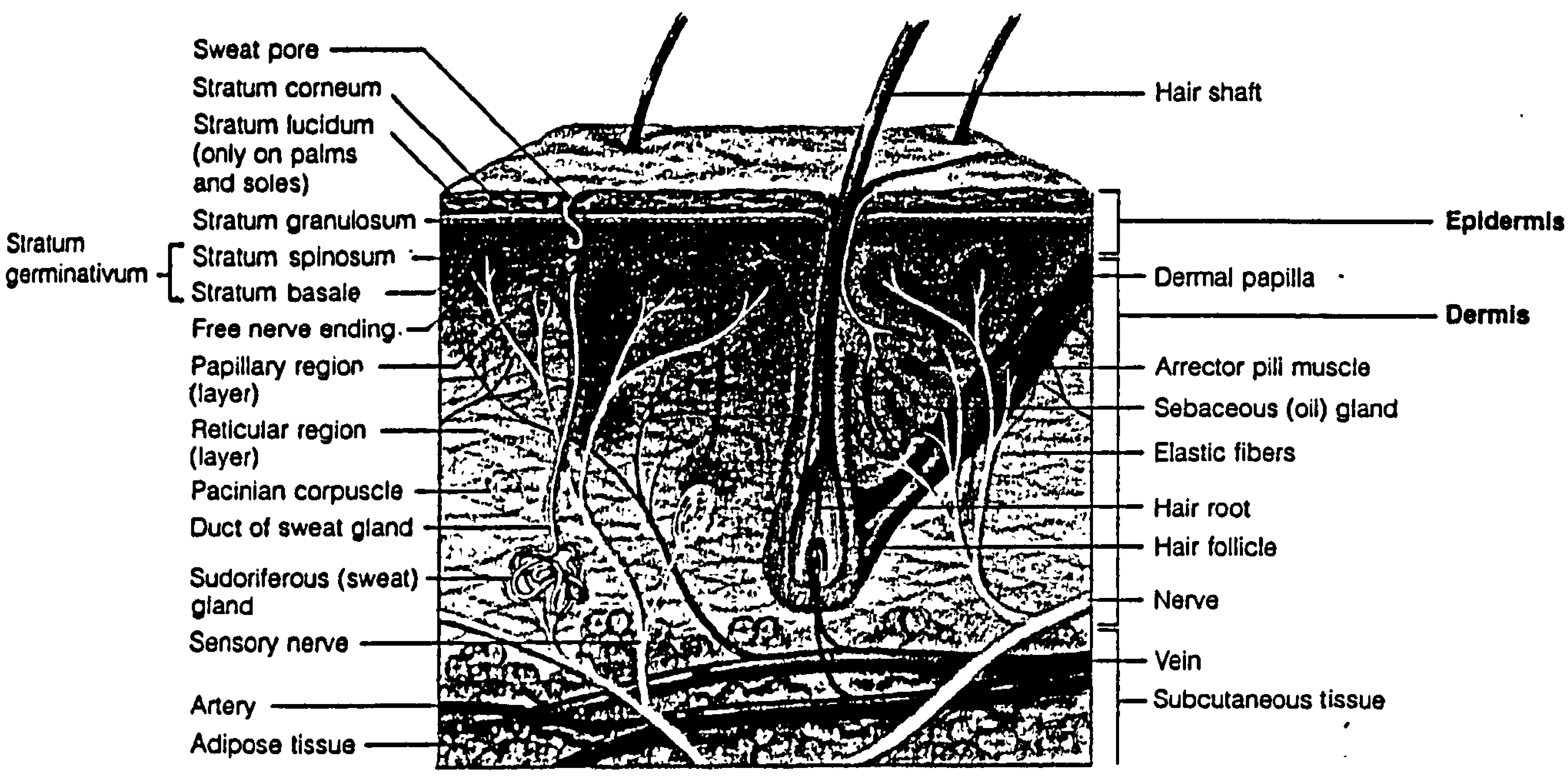

Fig. 6.2.1.1 Epidermal layers of skin. (Gaudin and Jones, 1989)

6.2.1 Skin

Skin forms the outermost covering of the body and contributes to a variety of functions leading to homeostasis of the body, which includes protection against mechanical damage, production of vitamin D and immunity. Skin is divided into two major layers (Fig. 6.2.1.1), the epidermis and the deeper dermis. The epidermis is made up of stratified squamous epithelium consisting of several layers of cells, with the outermost layer called the stratum corneum and the innermost layer stratum basale. New cells are formed through cell divisions at the basal layer and these cells progressively moved outwards to the stratum corneum by even newer cells. The dermis is mainly connective tissue containing collagenous and elastic fibres. Collagenous fibres usually exist in bundles with their unique minute fibres running parallel to each other forming a wavy band. Elastin or elastic fibres come in branching mesh and are smaller than collagenous fibres. Two layers can be distinguished in the dermis, the papillary (upper) region, consists mainly of fine elastin and the reticular region, where a dense network of collagen and coarse elastin exists.

6.2.2 Fascia

Between skin and muscles or skin and bones, lies the region called the hypodermis (subcutaneous tissues or superficial fascia). Hypodermis consists of loose connective tissue of collagen and elastin fibres, and adipose tissues which is a another form of loose connective tissue where fats cells are a majority. This region functions as insulation and shock absorber for the body and also provides a pathway for nerves and vessels. Deep fascia which is a denser connective tissue extends to the skeletal muscles' area, holding muscles together, surrounding and separating them into different muscle groups. This allows free movement between muscle groups and also serves to provide a passageway for nerves and blood vessels.

6.2.3 Skeletal muscles

Skeletal muscles are voluntary muscles and are responsible for movement of bones. Movements of bones are produced by muscles contracting, thus exerting

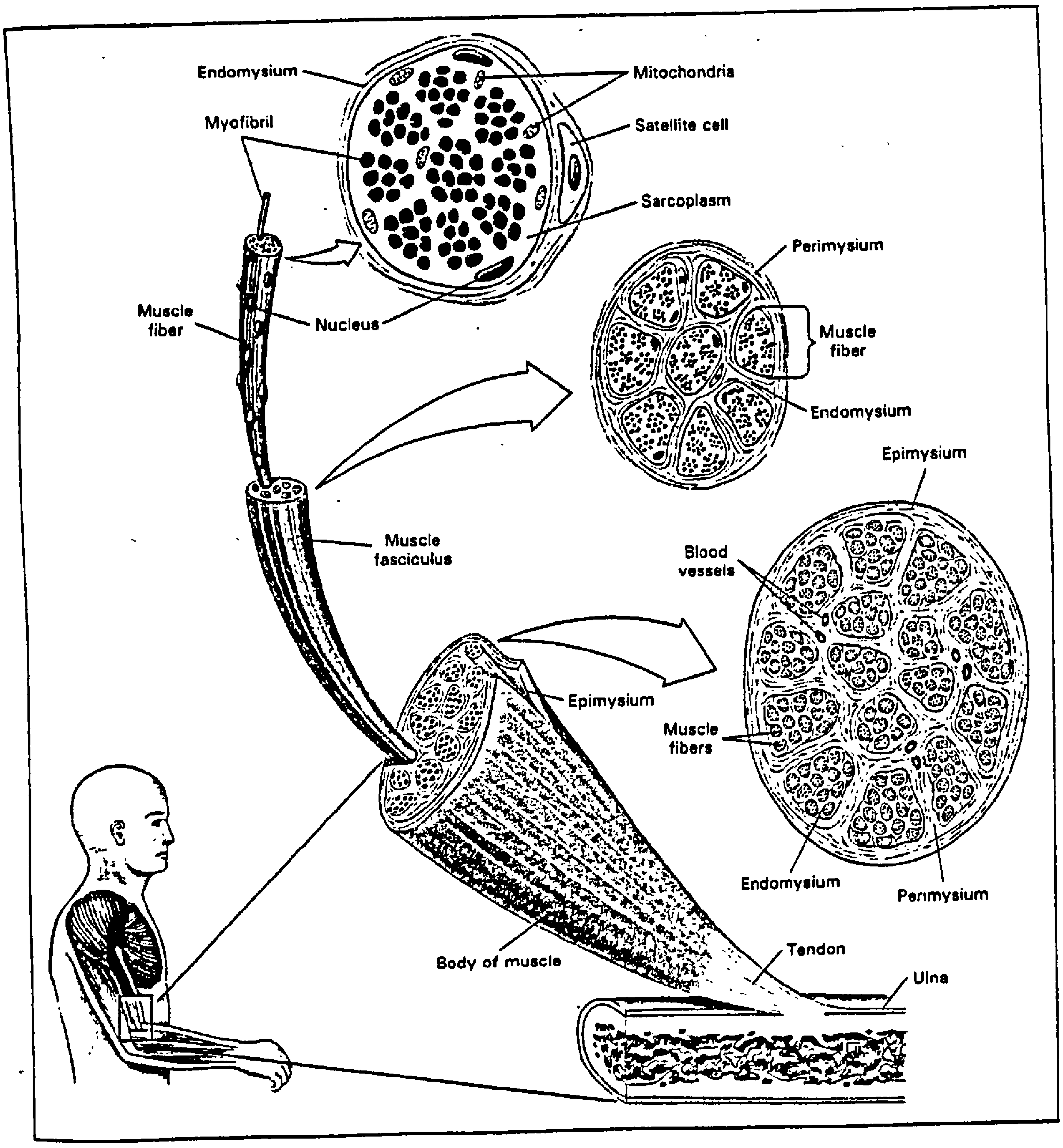

Fig. 6.2.3.1 Structures of muscles. (Martini, 1992)

forces on the tendons, which connect muscles to bone. Skeletal muscles are striated muscles. When viewed along the long axes of the fibres, alternating light and dark bands run perpendicularly. A single muscle fibre ranges from 1-40mm in length and from 10-100 μm in diameter. Therefore in most long muscles, fibres are arranged from end to end.

The structure of muscles is described in Fig. 6.2.3.1. Separating the muscles' fibres are the endomysium, a fibrous connective tissue with numerous reticular fibres. Perimysium, a denser connective tissue groups muscle fibres into fasciculus. And the entire muscle is wraped in deep fascia and epimysium, a collagenous connective tissue. Each muscle fibre is surrounded by sarcolemma, the muscle's fibre cell membrane (Fig. 6.2.3.2). And within each muscle fibre, there are myofibrils, a threadlike structure measuring about 1-3 μm in diameter. Under the electron microscope, the myofibrils can be distinguished into lines and bands, where muscles' contraction can be explained (Fig. 6.2.3.3).

6.3 LITERATURE REVIEW

There are many published works on soft tissue mechanics and soft tissue responses to mechanical stresses. In this review, only selected key articles will be discussed.

6.3.1 Mechanical properties of biological tissues

Skin mechanical properties have been investigated by numerous authors, and these form the basis for most soft tissue work. The mechanical strength of skin is mainly due to the dermis, where connective tissue consisting of collagenous and elastin fibres is present. Collagens are tougher then elastins and are responsible in resisting forces. Nevertheless, elastin also provides strength and is able to stretch to strains of about 50% (Daly 1969). The load - deformation plot of skin in uniaxial tension shows large deformation produced by small loads in the initial phase. Upon continuing loading, the stiffness of the skin increases abruptly. This gave rise to a non-linear stress-strain behaviour (Fig. 6.3.1.1) thus deviating from Hooke's law. This law applies to many engineering materials and is expressed as $\sigma = Ee$, where σ is

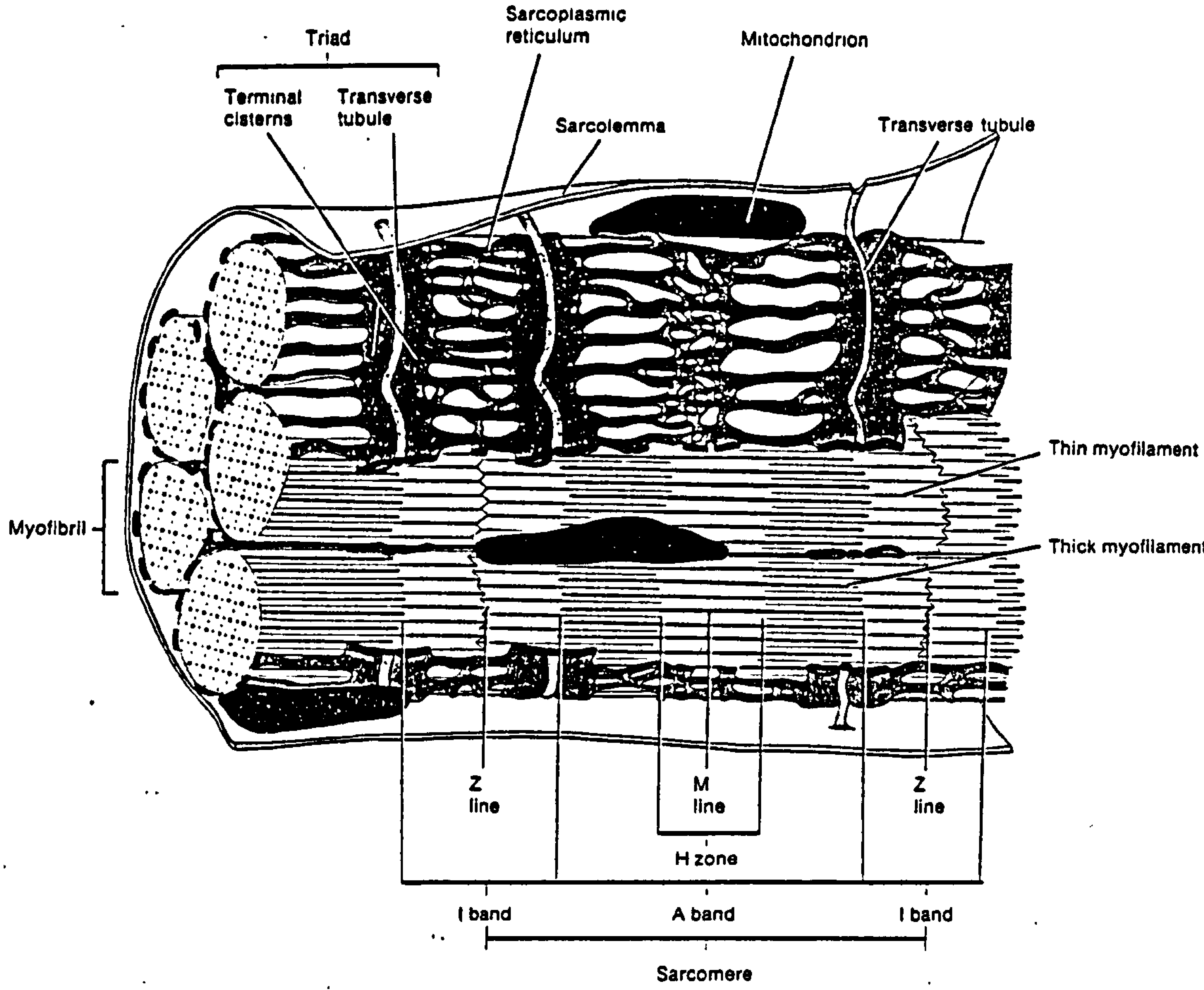

Fig. 6.2.3.2 Muscle's fibre cell membrane. (Tortora and Anagnostakos, 1989)

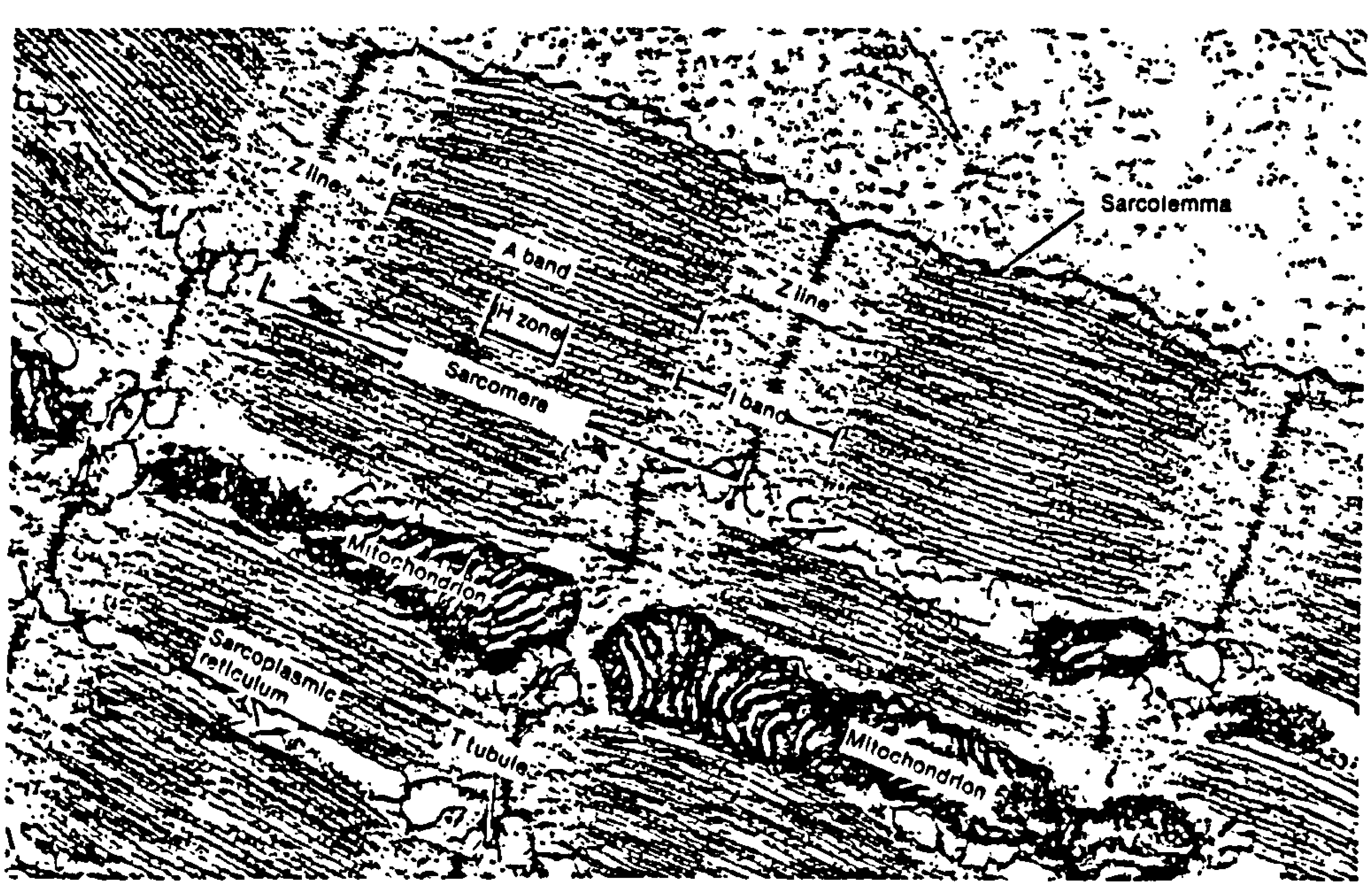

Fig. 6.2.3.3 Arrangement of filaments in a myofibril.
(Tortora and Anagnostakos, 1989)

stress, E is a constant often referred as Young's modulus and e is strain. Hooke's law is only applicable for material with a linear stress-strain relationship and for small strains. In the case of soft tissue, the stress at a given point at any instant of time depends not only on the strain at that time but also on the strain history (Fung 1993). Soft tissue possesses the characteristics of elastic solids and viscous liquids, giving rise to a viscoelastic material which exhibits time dependence with stress relaxation, creep and hysteresis.

Soft tissue is a complex structure consisting of cells, blood vessels, lymphatics and nerves. However, its mechanical properties are mainly contributed by the extracellular fibrous materials, i.e. collagen and elastin fibres (Fig. 6.3.1.2). The load - deformation behaviour of soft tissues is dependent on three factors relating to the mechanical properties, proportion and mesh arrangement of the collagen and elastin fibres. Different types of soft tissues have different proportion and mesh arrangement of collagen and elastin fibres. In tendon and skin, there is a high proportion of collagen fibres, 75% and 60% of dry weight respectively. However, tendon and skin behave differently mechanically because the collagens are oriented differently. In tendon, the collagens are oriented in alignment with the tensile stresses that the tendon undergoes physiologically, whereas skin in a relaxed state has fibres that are not in any order. This explain the difference between tendon and skin in their stress - strain curve especially at the initial lax phase, which is characterised by the wavy collagen straightening to the direction of pull. Any further deformation to the collagen fibres at their maximum unstretched length will then contribute to an increase in material stiffness, which happens earlier with tendon than skin due to the arrangement of the collagen fibres. Figure 6.3.1.3 shows the stress - strain relationship for different types of soft tissue.

6.3.2 Constitutive equations proposed for biological soft tissues

Prior to any theoretical approach to the problem of residual limb / socket interface, a mathematical description of the stress - strain history of soft tissue is required. However, as discussed earlier, the constitutive equations for biological tissues are not completely known. Practical difficulties like handling delicate

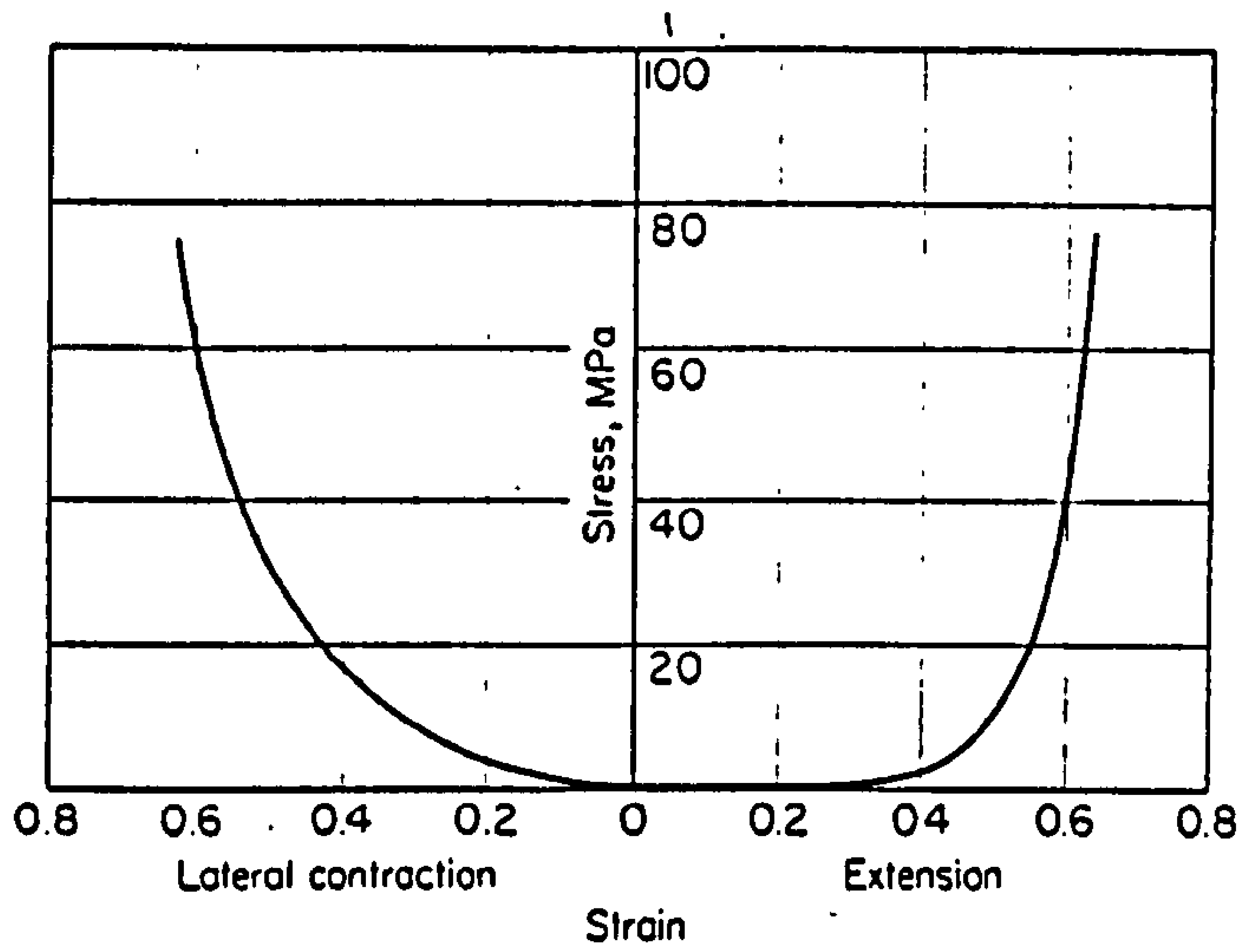

Fig. 6.3.1.1 Non-linear stress - strain behaviour of skin. (Barbenel et al, 1978)

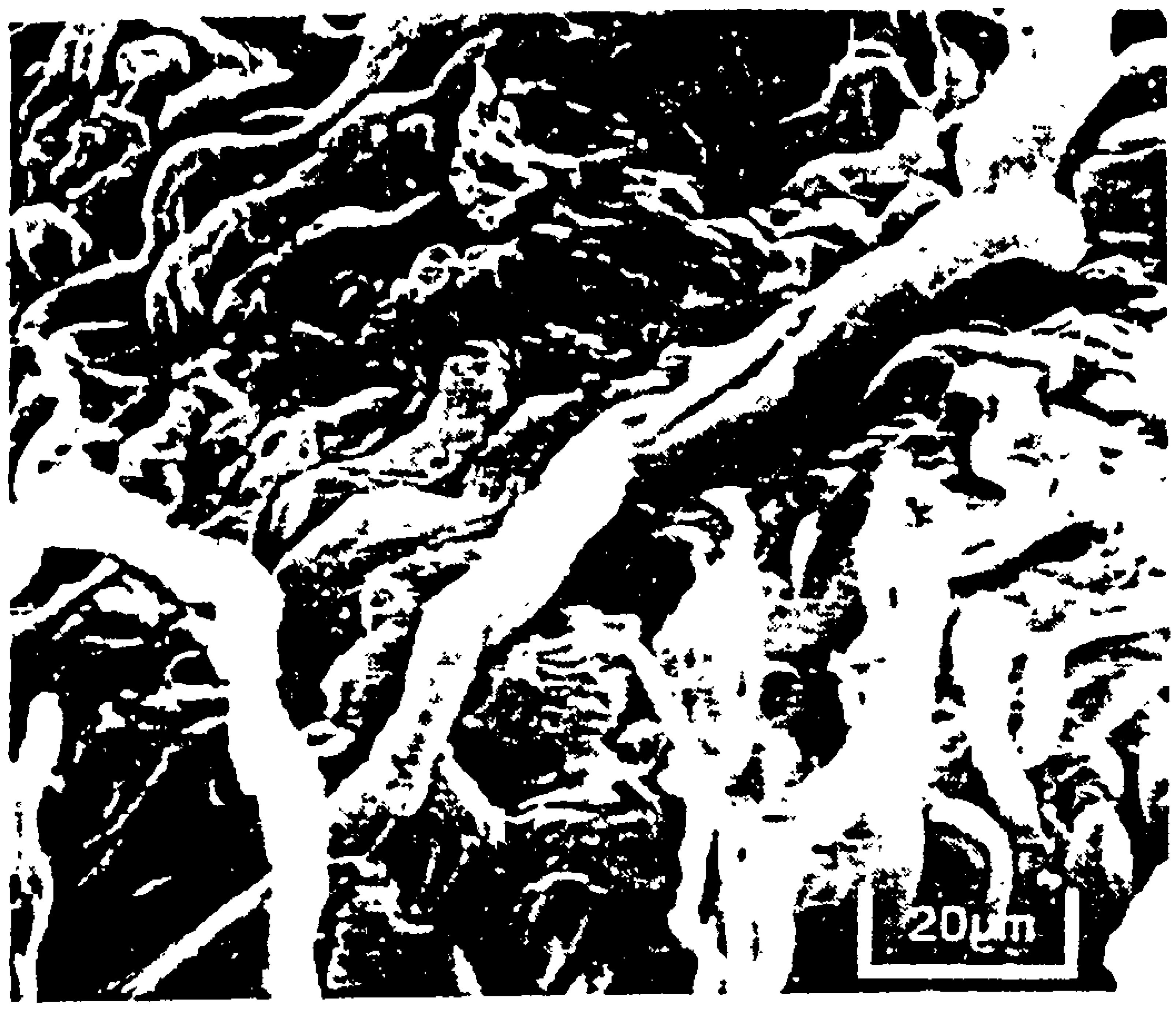

Fig. 6.3.1.2 Collagen in skin. (Barbenel et al, 1978)

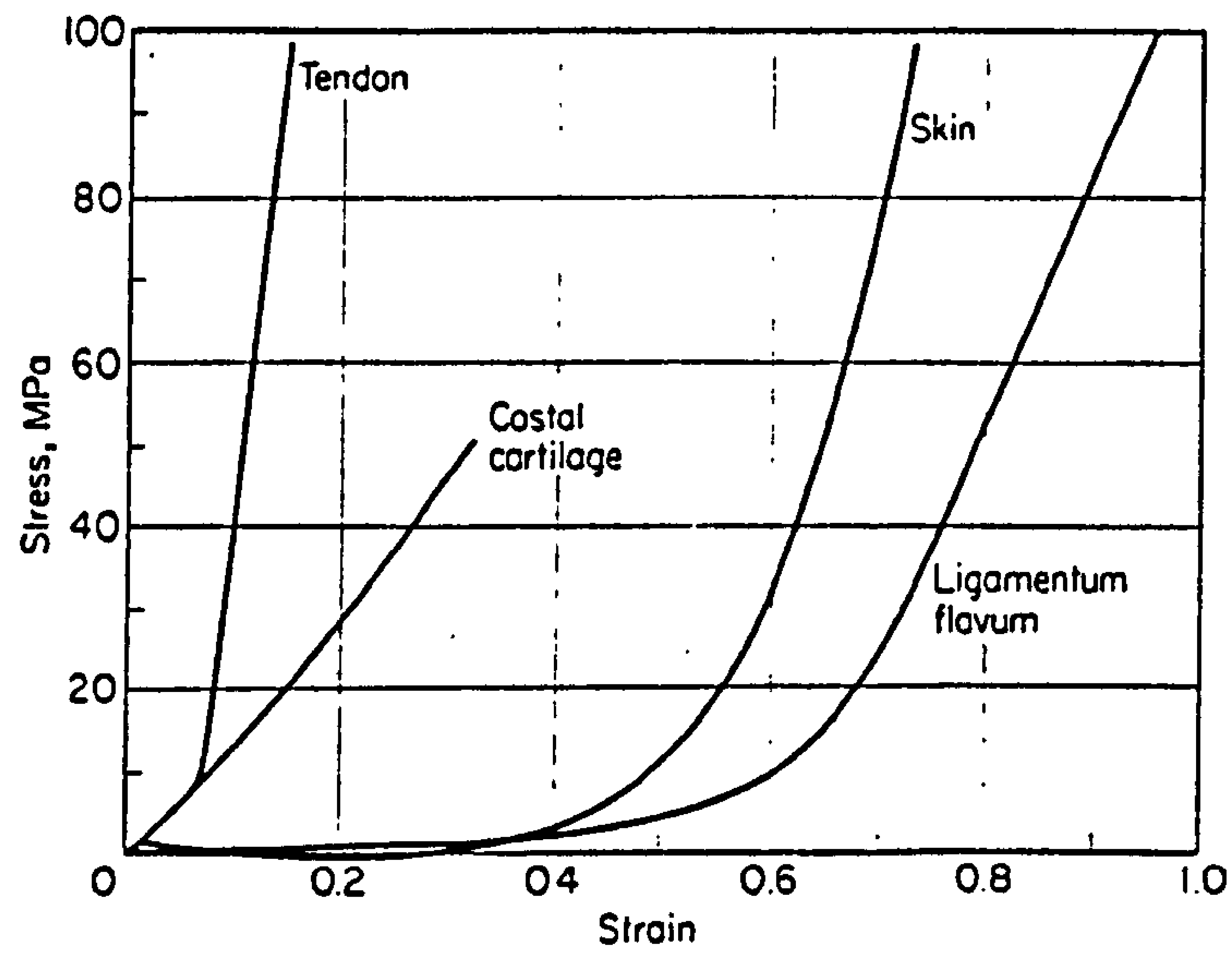

Fig. 6.3.1.3 Stress - strain relationship of different types of tissue.
(Barbenel et al, 1978)

specimens that must be maintianed at a level close to that in the living condition hampered 2 or 3-dimensional test (Fung 1993). Nevertheless, the non-linear stress - strain response of soft tissues has been investigated in great detail. This section will discuss some of these investigations.

The different types of constitutive equations proposed for soft tissue stress - strain response fall mainly into two categories, exponential and power laws in stress or strain, and strain energy functions. Ridge and Wright (1966) divided the force extension curve of human skin into three phases, the first phase corresponded to the straightening out of the collagen fibres which is followed by the increased in the stiffness of the fibres, and lastly a yielding phase where the fibres break. Based on the experimental data, phase one and phase two were found to follow logarithmic and power law relationships respectively.

Fung (1967) described the elastic stress for rabbit mesentery as essentially an exponential function of the extension ratio. The relationship was derived from a simple tension test on a relaxed specimen assuming isotropy and incompressibility. Therefore,

$$\lambda_2 = \lambda_3 \qquad (6.3.2a)$$

and

$$\lambda_1 \lambda_2 \lambda_3 = 1 \qquad (6.3.2b)$$

where $\lambda_1, \lambda_2, \lambda_3$ are the three principal extension ratios i.e. $\lambda_1 = 1 + e_1$ in simple tension. The only non zero stress in simple tension test is σ_1, which is equal to the force (F_1) divided by the current cross sectional area. σ_1 is also commonly called the true stress, and in Fung's paper, described as the Eulerian stress. If the original dimensions of the specimen are l_1, l_2, l_3, the strained dimensions are therefore $l_1\lambda_1, l_2\lambda_2, l_3\lambda_3$ respectively. Therefore,

$$\sigma_1 = \frac{F_1}{l_2\lambda_2 l_3\lambda_3} = \frac{F_1}{l_2 l_3}\left(\frac{1}{\lambda_2\lambda_3}\right) \qquad (6.3.2c)$$

and the engineering stress or Lagrangian stress (i.e. force divided by the original cross sectional area) is given by,

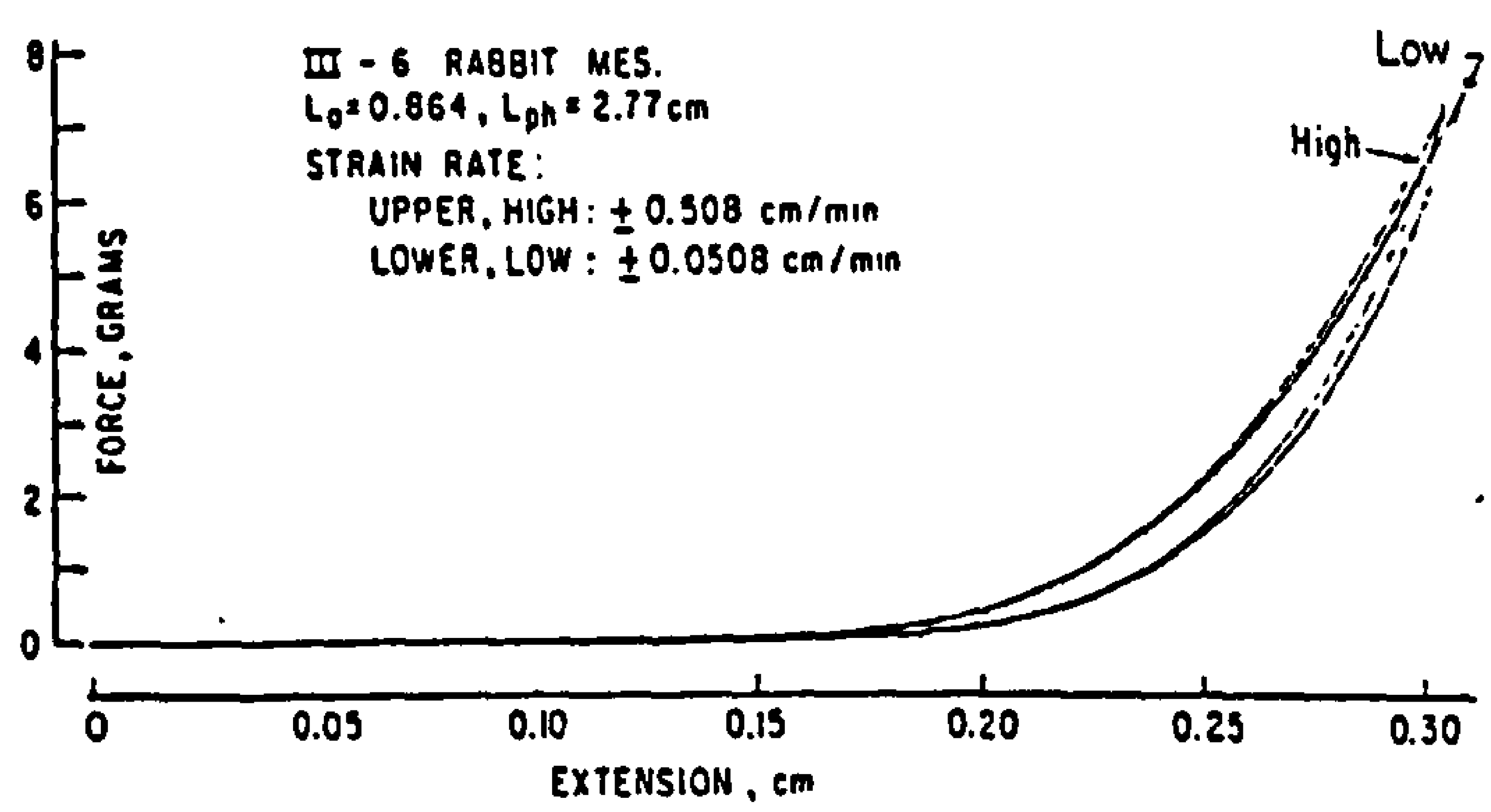

Fig. 6.3.2.1 Hysteresis curve of rabbit mesentery. (Fung, 1967)

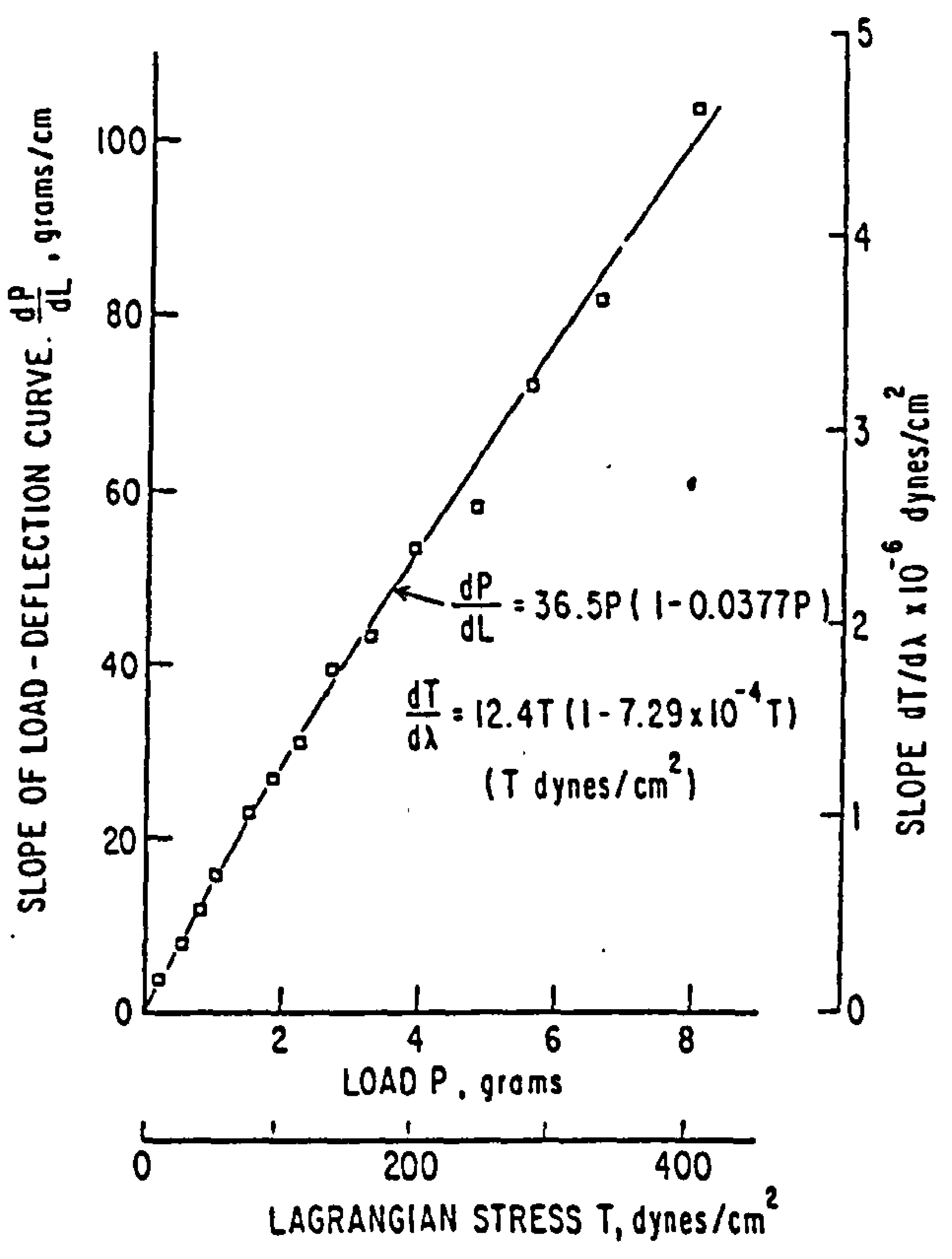

Fig. 6.3.2.2 Slope of load - deflection versus load, and $\frac{dT}{d\lambda}$ versus T where T is engineering stress and λ is the extension ratio. (Fung, 1967)

$$s_1 = \frac{F_1}{l_2 l_3} \qquad (6.3.2d)$$

Therefore substituting 6.3.2d into 6.3.2c,

$$\sigma_1 = \frac{s_1}{\lambda_2 \lambda_3} \qquad (6.3.2e)$$

And from 6.3.2a and 6.3.2b, equation 6.3.2e can be expressed as,

$$\sigma_1 = \lambda_1 s_1 \qquad (6.3.2f)$$

which shows that simple tension can be described by a single component of stress and a single extension ratio. In Fung's paper (1967), T was used to denote the engineering stress or the Lagrangian stress giving the general form of equation 6.3.2f as,

$$\sigma = T\lambda \qquad (6.3.2g)$$

Fung continued to show that for mesentery, T and λ are related by,

$$\frac{dT}{d\lambda} = aT \qquad (6.3.2h)$$

Using the loading phase of the load - deflection hysteresis curve obtained from rabbit mesentery as shown in Fig. 6.3.2.1, Fung plotted the slope of the load - deflection curve versus load, and $\frac{dT}{d\lambda}$ versus T as shown in Fig. 6.3.2.2. It can be seen that the slope of the load - deflection curve is not constant when compared to that of a Hookean material, in which $\frac{dT}{d\lambda} = const.$ As a first approximation, the straight line in Fig. 6.3.2.2 can be represented by equation 6.3.2h thus integrating gives,

$$T = \frac{1}{c} e^{a\lambda} \qquad (6.3.2j)$$

where a and c are constants. However, Fung also realised that T becomes zero when $\lambda \rightarrow \infty$ in equation 6.3.2j, where by definition T should be zero when λ equals one. Equation 6.3.2h was then modified by adding a small constant β giving,

$$\frac{dT}{d\lambda} = a(T+\beta) \qquad (6.3.2k)$$

and integrating gives,

$$T+\beta = \frac{1}{c}e^{a\lambda} \qquad (6.3.2m)$$

and if $T = T^*$ when $\lambda = \lambda^*$, then

$$c = \frac{e^{a\lambda^*}}{T^*+\beta} \qquad (6.3.2n)$$

Therefore substituting 6.3.2n into 6.3.2m,

$$T = (T^* + \beta)e^{a(\lambda-\lambda^*)} - \beta$$

Thus when $T = 0, \lambda = 1$,

$$\beta = \frac{T^* e^{-a(\lambda^*-1)}}{1-e^{-a(\lambda^*-1)}} \qquad (6.3.2p)$$

As an alternative to adding the constant β as described above, Fung (1967) derived an equation based on theory of elasticity and strain energy function, which introduced a polynomial factor that vanishes at $\lambda = 1$. The use of strain energy is a common approach to modelling bodies which undergo finite deformation. In order to deform an elastic body from its unstressed state, it is necessary to do a certain amount of work, which is stored in the body as strain energy (W), and is a function of the deformation gradients. Therefore,

$$W = W(I_1, I_2, I_3)$$

where the strain invariants I_1, I_2 and I_3 are given by Green and Akins (1960) as,

$$I_1 = \lambda_1^2 + \lambda_2^2 + \lambda_3^2 \qquad (6.3.2q)$$

$$I_2 = \lambda_1^2\lambda_2^2 + \lambda_2^2\lambda_3^2 + \lambda_3^2\lambda_1^2 \qquad (6.3.2r)$$

$$I_3 = \lambda_1^2\lambda_2^2\lambda_3^2 \qquad (6.3.2s)$$

and assuming isotropy and incompressibility as in equations 6.3.2a and 6.3.2b respectively, the Eulerian stress for simple tension via strain energy function is given by,

$$\sigma = 2(\lambda_1^2 - \tfrac{1}{\lambda_1})(\tfrac{\partial W}{\partial I_1} + \tfrac{1}{\lambda_1}\tfrac{\partial W}{\partial I_2}) \qquad (6.3.2t)$$

and the Lagrangian stress is,

$$T = 2(\lambda_1 - \tfrac{1}{\lambda_1^2})(\tfrac{\partial W}{\partial I_1} + \tfrac{1}{\lambda_1}\tfrac{\partial W}{\partial I_2}) \qquad (6.3.2u)$$

If $\frac{\partial W}{\partial I_1}$ and $\frac{\partial W}{\partial I_2}$ are finite and continuous at $\lambda = 1$, equation 6.3.1j can be expressed in the form,

$$T = const(\lambda - \tfrac{1}{\lambda^2})e^{\tilde{a}\lambda} \qquad (6.3.2v)$$

Evaluating the constant and differentiation of the above gives,

$$\frac{dT}{d\lambda} = T\left[\tilde{a} + \frac{3\lambda^2}{\lambda^3 - 1} - \frac{2}{\lambda}\right] \qquad (6.3.2w)$$

Fung goes on to say that the exponential factor in equation 6.3.2v is so powerful that as far as mesentery is concerned the plots produced by equation 6.3.2k and equation 6.3.2w are almost the same with slight difference between a and $\tilde{a}$.

In a paper by Hildebrandt et al (1969) titled 'completing the length tension curve of tissue', Hildebrandt et al showed that Fung's proposed function as described by equation 6.3.2v could only fit extension data, but performed badly when $\lambda < 1$ i.e. compression. Experiments were initially carried out on a narrow strip of condom rubber which was shown to follow equation 6.3.2t, which could also be written in the form below,

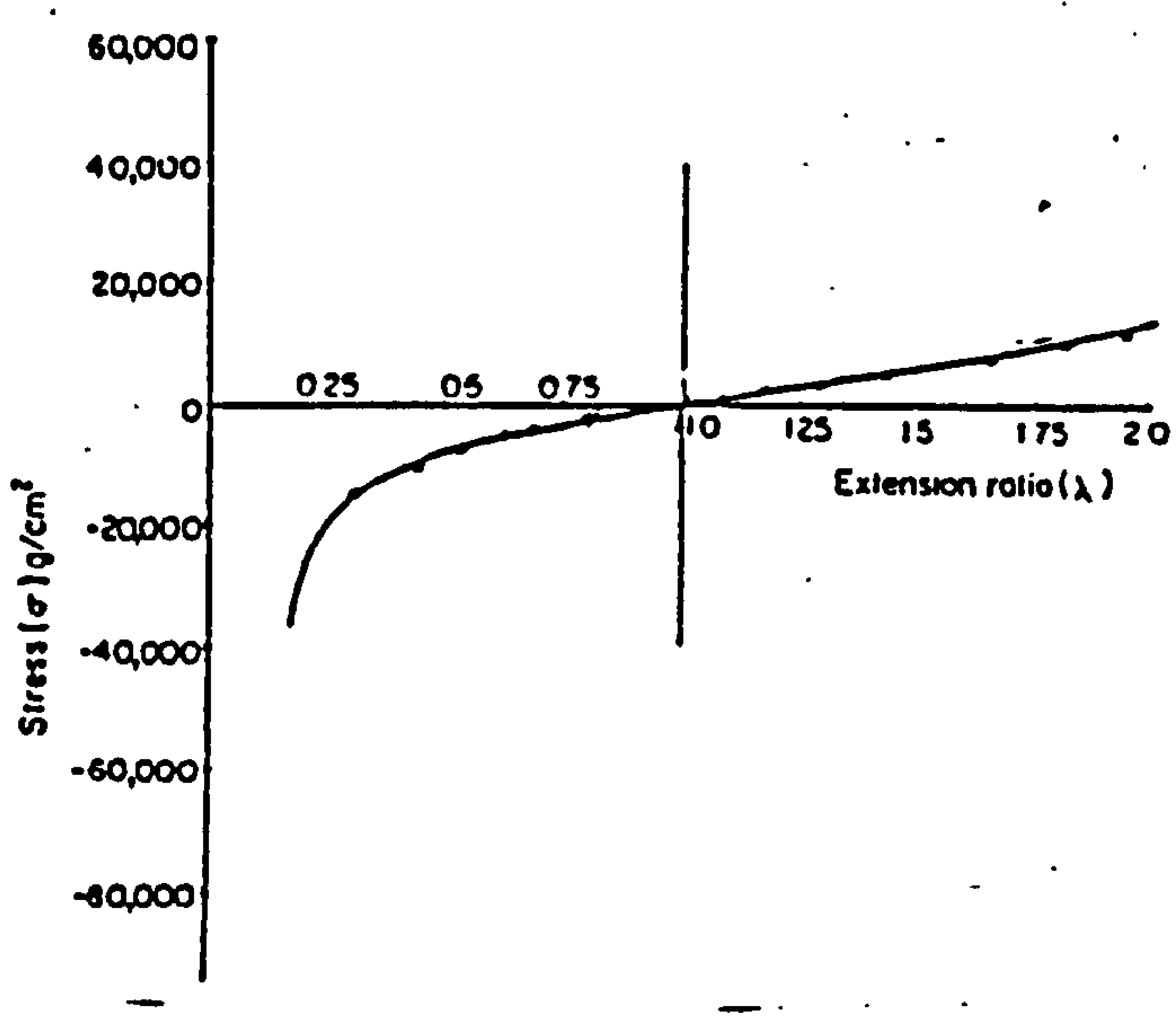

Fig. 6.3.2.3 Stress versus extension ratio for condom rubber from simple extension and equi-biaxial extension test. (Hildebrandt et al, 1969)

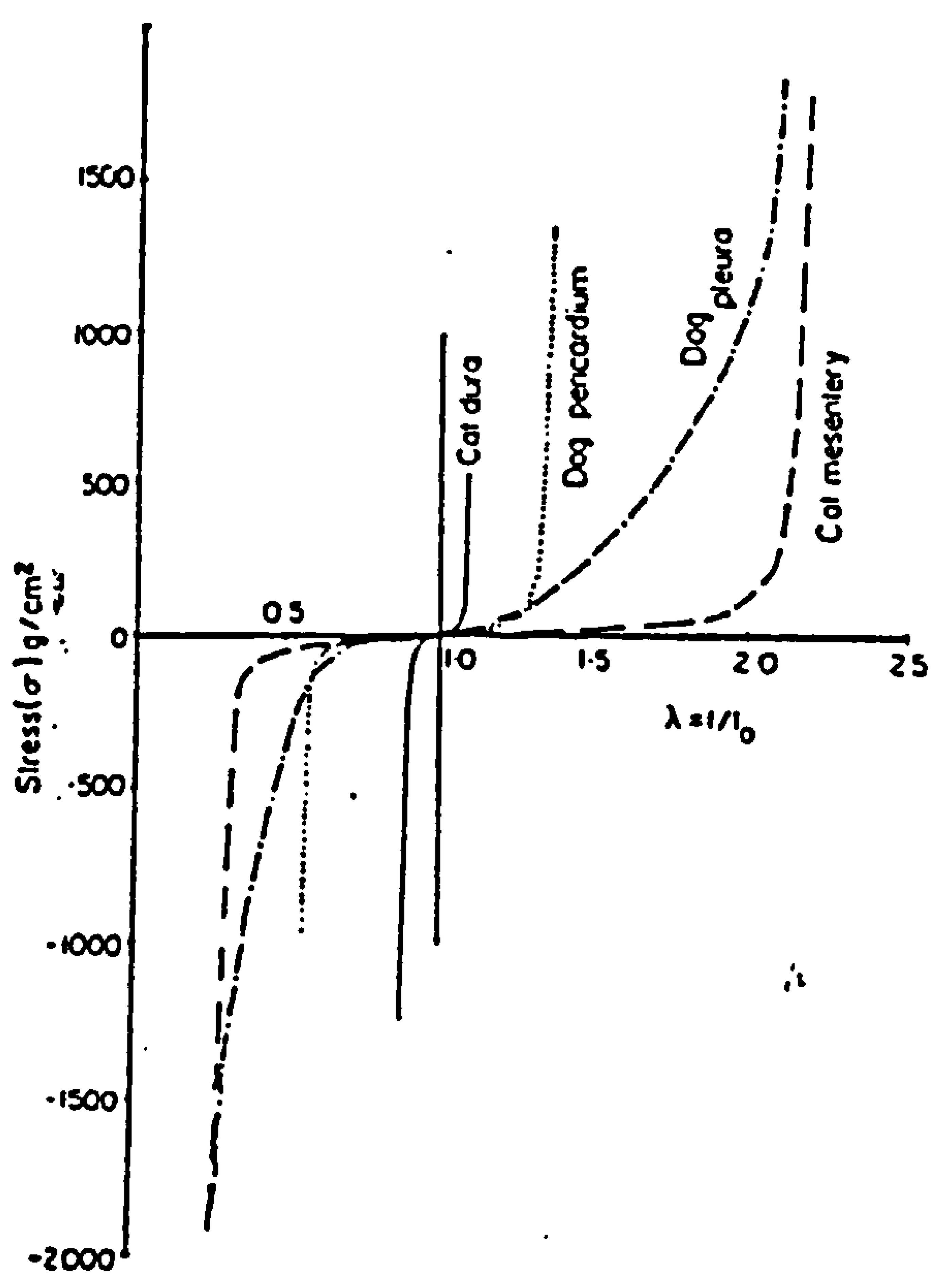

Fig. 6.3.2.4 Stress versus extension ratio for four biological tissue. (Hildebrandt et al, 1969)

$$\sigma = 2(\lambda^2 - \tfrac{1}{\lambda})(c_1 + \tfrac{1}{\lambda}c_2) \qquad (6.3.2x)$$

where c_1 is in the order of 2000g/cm^2 for rubber and $c_2 = 0.1c_1$. The experiments also showed that compression of the rubber could be achieved by equi-biaxial extension test, whereby conditions for $\lambda < 1$ could be obtained (Fig. 6.3.2.3). The paper further presented four different tissue types (cat dura, dog pericardium, dog pleura and cat mesentery) subjected to similar extension and equi-biaxial extension experiments as the condom rubber. Fig. 6.3.2.4 plots their stress versus extension ratio curve. Returning to Hildebrandt et al's disagreement with Fung, they produced a curve (Fig. 6.3.2.5) which showed that an exponential function would fail when $\lambda < 1$. Instead a hyperbolic function replacing Fung's exponential function in equation 6.3.2v was proposed which was applicable for the complete range of λ (note : equation 6.3.2v is written in Lagrangian stress whereas in Fig. 6.3.2.5 Eulerian stress are plotted). Expressing equation 6.3.2x as,

$$\sigma = (\lambda^2 - \tfrac{1}{\lambda})f(\lambda) \qquad (6.3.2y)$$

The hyperbolic form which Hidebrandt et al proposed was ;

$$f(\lambda) = \frac{k_1}{(\lambda_{max}-\lambda)^p} + \frac{k_2}{(\lambda-\lambda_{min})^q}$$

where λ_{max} and λ_{min} are the upper and lower strain asymptotes, and k_1, k_2, p and q are constants determined from curve fitting equation 6.3.2y.

The use of strain energy functions was further expanded by Veronda and Westmann (1970). The protocol for their investigations was similar to those mentioned above, whereby simple extension tests was performed on cat skin from which a suitable mathematical function was derived. Fig. 6.3.2.6 shows the non-linear stress - strain behaviour of soft tissue under simple extension test obtained from 9 samples of cat skin. By plotting the lateral extension ratios, λ_2 and λ_3 against λ_1, the authors maintained that the samples were anisotropic and compressible respectively (Fig. 6.3.2.7 and Fig. 6.3.2.8). Two mathematical models were derived, the first based on the tissue being isotropic and compressible and the second, isotropic

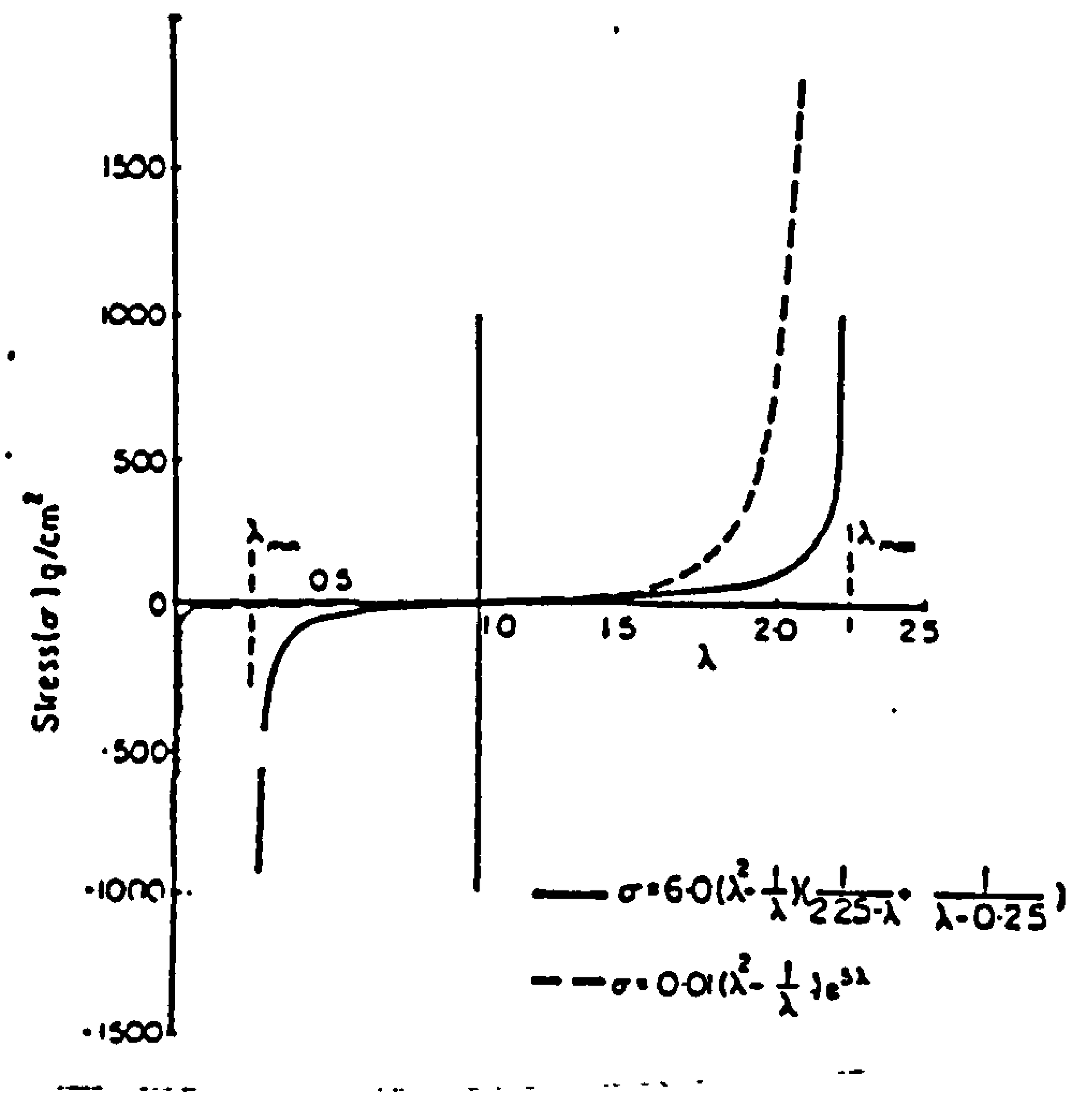

Fig. 6.3.2.5 Dotted line - Fung's exponential function which failed at $\lambda < 1$.
Solid line - Hildebrandt et al's hyperbolic function.
(Hildebrandt et al, 1969)

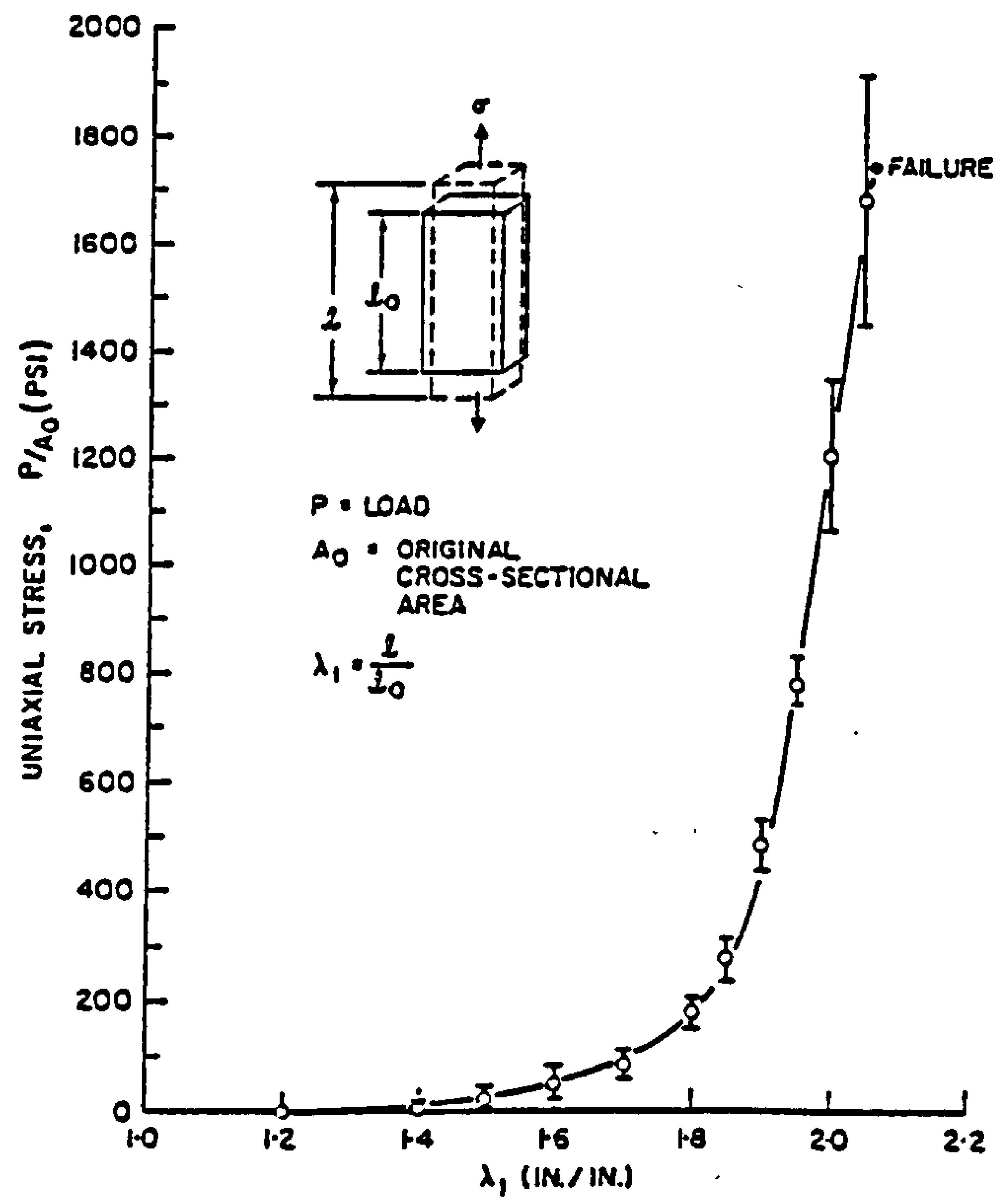

Fig. 6.3.2.6 Stress versus extension ratio of nine samples of cat's skin.
Note : 1 psi = 6.895 kPa.
(Veronda and Westmann, 1970)

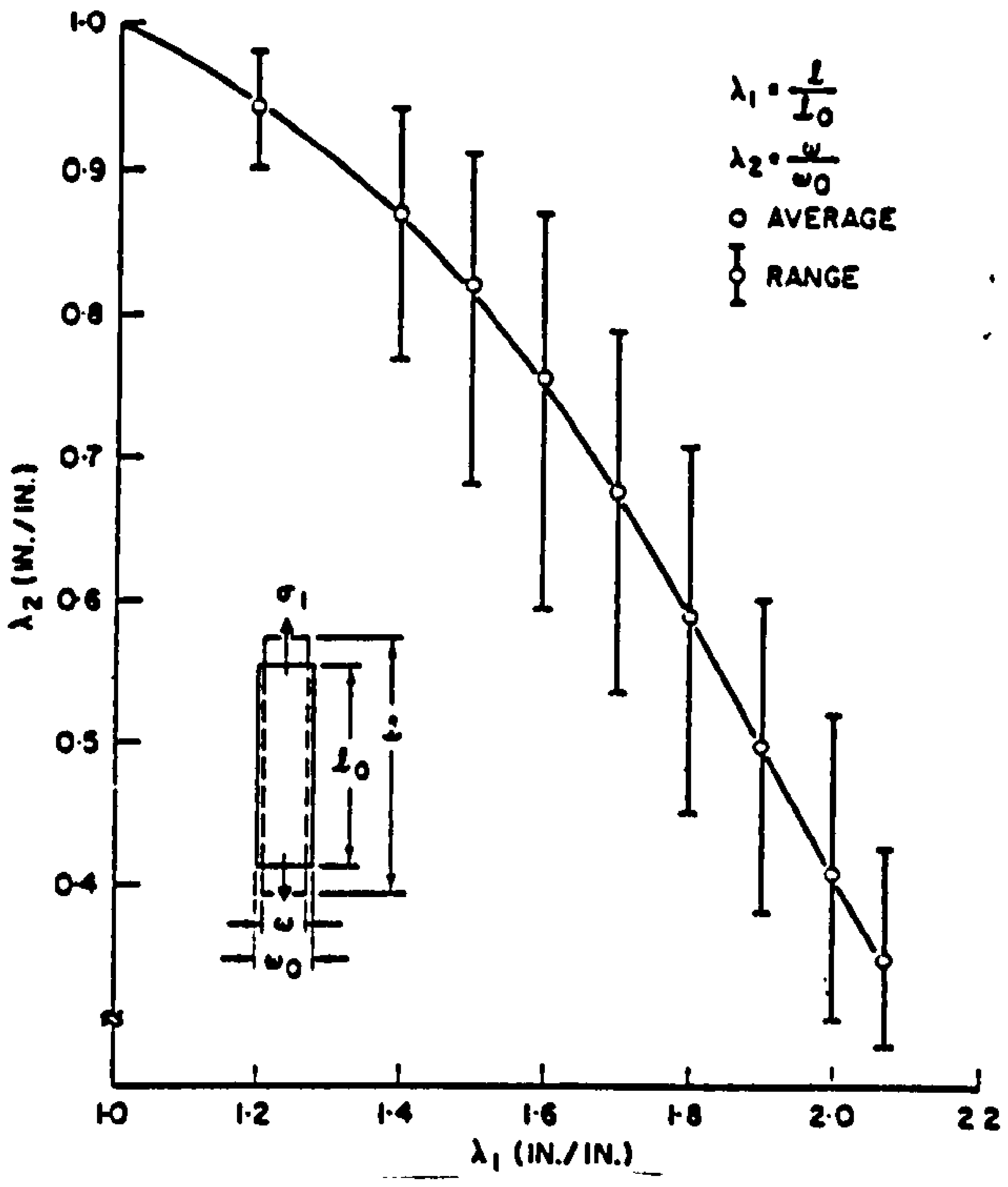

Fig. 6.3.2.7 Lateral extension ratio λ_2 versus longitudinal extension ratio λ_1.
Note : 1 in = 0.0254 m. (Veronda and Westmann, 1970)

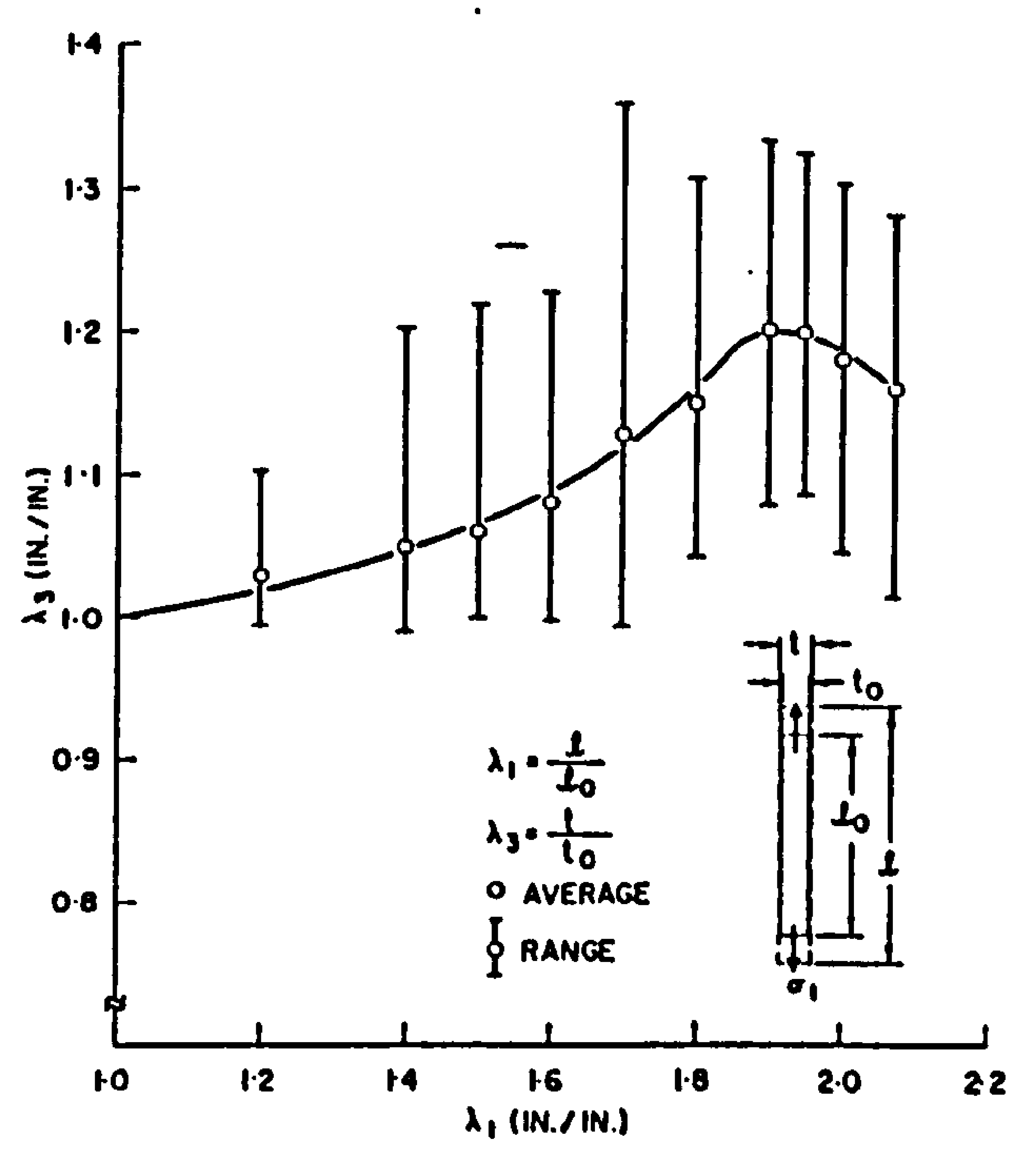

Fig. 6.3.2.8 Lateral extension ratio λ_3 versus longitudinal extension ratio λ_1.
Note : 1 in = 0.0254 m. (Veronda and Westmann, 1970)

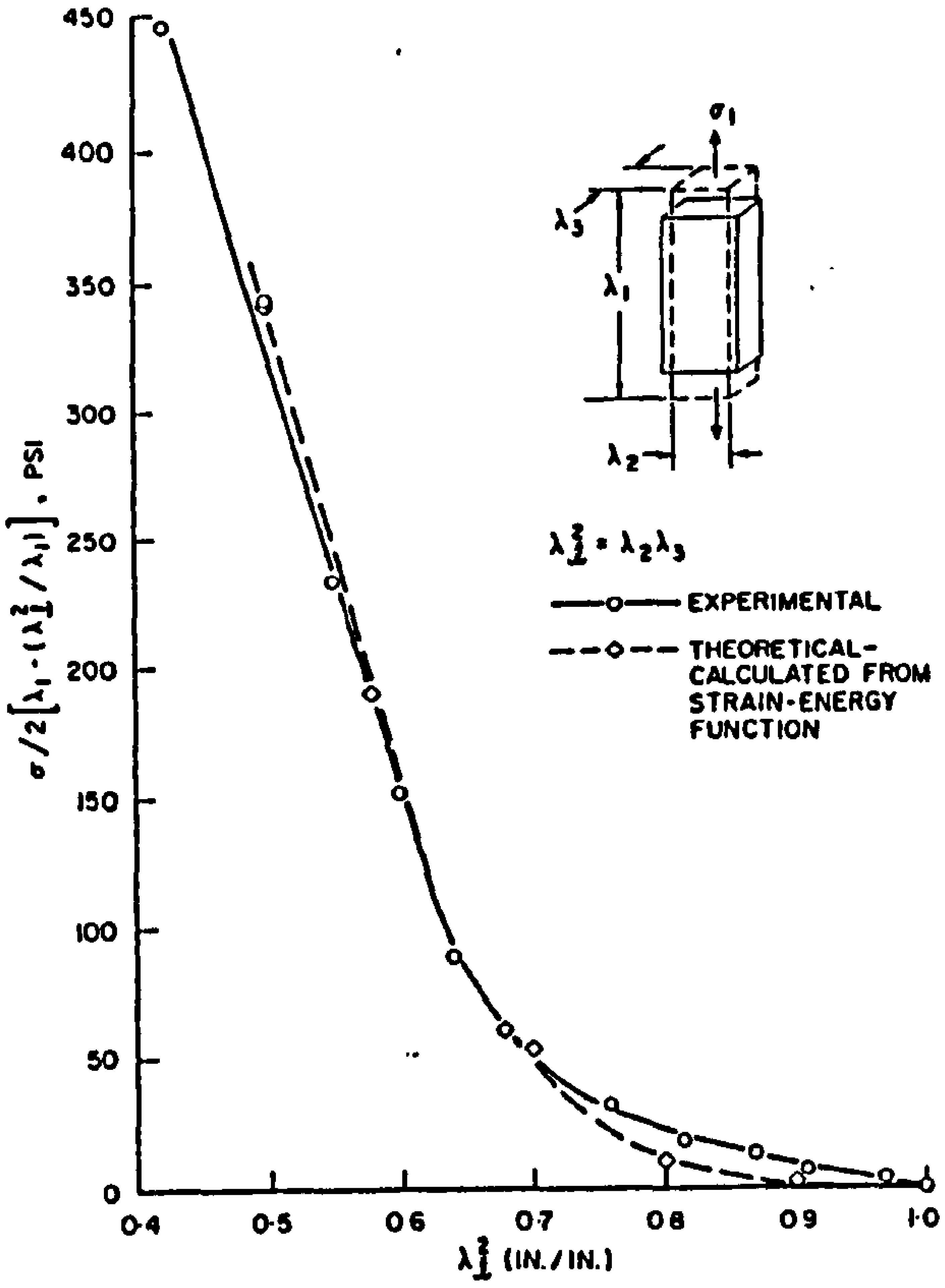

Fig. 6.3.2.9 Plot of $\dfrac{\sigma}{2(\lambda_l - \frac{\lambda_l^2}{\lambda_1})}$ versus λ_l^2 did not produced a straight line, hence it is not of the Mooney - Rivilin character. The theoretical strain - energy proposal is based on the compressible approach.

Note : 1 psi = 6.895 kPa. (Veronda and Westmann, 1970)

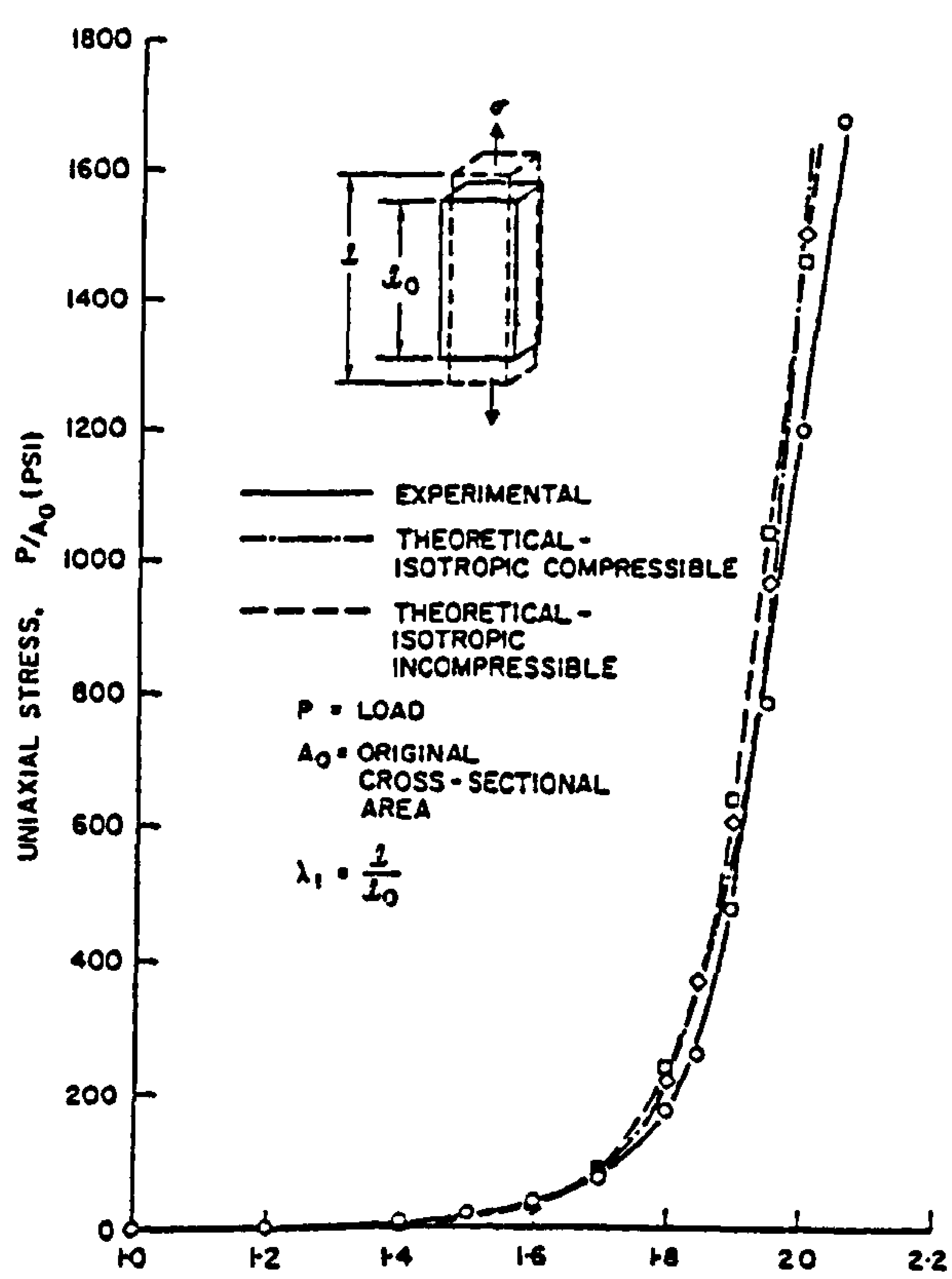

Fig. 6.3.2.10 Uniaxial stress versus longitudinal extension ratio λ_1. The two theoretical proposals were plotted against experimental values.

Note : 1 psi = 6.895 kPa. (Veronda and Westmann, 1970) and incompressible. Therefore in both cases anisotropy was not considered, instead it was assumed that $\lambda_2^2 = \lambda_3^2 = \lambda_2\lambda_3$, so that the material was isotropic. By introducing a mean extension ratio known as $\lambda_l = \sqrt{\lambda_2\lambda_3}$, the first of the two models (isotropic and compressible) was given by modifying equation 6.3.2t,

$$\frac{\sigma}{2\left(\lambda_l - \frac{\lambda_l^2}{\lambda_1}\right)} = \frac{\partial W}{\partial I_1} + \lambda_l^2 \frac{\partial W}{\partial I_2} \qquad (6.3.2z)$$

The authors also further showed that the Mooney-Rivilin function for rubber,

$$W = C_1(I_1 - 3) + C_2(I_2 - 3) \qquad (6.3.2aa)$$

where $C_1 = \frac{\partial W}{\partial I_1}$and $C_2 = \frac{\partial W}{\partial I_2}$ are constants suitable for rubber material, cannot be applied to soft tissue since a plot of $\frac{\sigma}{2\left(\lambda_l - \frac{\lambda_l^2}{\lambda_1}\right)}$ versus λ_l^2 should produce a straight line where $\frac{\partial W}{\partial I_1}$ would be the y-intercept and $\frac{\partial W}{\partial I_2}$ the gradient. However, the plot in Fig. 6.3.2.9 did not show a straight line but a non-linear curve. The authors proposed an exponential function of $\frac{\partial W}{\partial I_1}$ instead, where the strain energy functions appeared in the form,

$$W = C_1[e^{\beta(I_1-3)} - 1] + C_2(I_2 - 3) + g(I_3) \qquad (6.3.2bb)$$

where C_1, C_2 and β are constants and $g(1)=0$. The constants were obtained from fitting the experimental curve as previously shown in Fig. 6.3.2.9. However, equation 6.3.2bb predicted the existence of non-zero lateral stress in simple tension. To rectify this, the authors produced an alternative function based on an incompressible material where the last term of equation 6.3.2bb was removed. Similarly the constants C_1, C_2 and βwere obtained from the experimental data. The following two functions i.e. compressible and incompressible, based on cat skin in simple tension were therefore plotted on Fig. 6.3.2.10. and written as follows;

$$W = 0.00394[e^{5.03(I_1-3)} - 1] - 0.01985(I_2 - 3) + g(I_3)$$

and

$$W = 0.0134[e^{4.4(I_1-3)} - 1] - 0.0295(I_2 - 3)$$

The authors reckoned that the compressible model fitted the data better. They also suggested that a simple tension test alone cannot characterise the material completely. Further multiaxial testing should be performed to verify the strain energy function proposed.

In summary, characterising the stress - strain relationship in soft tissue often involves complex curve fitting procedures. However, it can be realised that the proposed mathematical functions are based on the modification of Hooke's Law i.e. elastic theory or the well known Mooney-Rivilin (M-R) strain energy function for rubber. The limitation of Hooke's law is clear, since in soft tissue specifying a single Young's modulus is meaningless unless a strain level is stated (Fung, 1967). Alternatively, the use of the M-R function (equation 6.3.2x) in a plot of $\frac{S}{2(\lambda_1-\frac{1}{\lambda_1^2})}$ versus $\frac{1}{\lambda_1}$ cannot produce a straight line for soft tissue, thus the two constants needed to define the material cannot be obtained. These issues will be further expanded in a later part of the thesis where experiments and theoretical analyses are performed for rubber and porcine tissues.

6.3.3 Characterisation of residual limb soft tissue

There have been several *in vivo* attempts to study the mechanical properties of the soft tissues in the residual limb *in vivo*. The aim was mainly related to understanding the load transfer mechanism involved at the residual limb / socket interface. The objectives could range from obtaining a quantitative measure for healthy tissues in the residual limb (Mak et al, 1994) to that of creating a finite element model of the residual limb (Steege et al, 1987). However, as seen later in all of these studies, the viscoelastic behaviour of soft tissue was ignored. Furthermore, the different curve fitting procedures described in section 6.3.2 were not applied. This was largely due to the lack of information in an *in vivo* examination of this type. Unlike an *in vitro* study, constitutive equations can be derived under strict loading conditions with known dimensions of excised specimen. Another difficulty encountered in an *in vivo* examination of the residual limb is that bulk soft tissues (skin, fascia, muscles) are involved. Application of constitutive equations derived from a single type of soft tissue, for example skin, becomes inaccurate. With these difficulties, investigators usually assume soft tissue properties of the residual limb to be an elastic material obeying Hooke's Law, where a modulus of elasticity (Young's Modulus) can be defined.

Presently, there are two known methods of characterising the mechanical properties of residual limb tissue. The first is a mechanical compression test, where an indentor is introduced to deform the soft tissues. The load acting on the indentor and the amount of deformation can be recorded to give a load - deformation curve. The second method used pulsed Doppler ultrasound techniques to detect tissue motion under a known mechanical perturbation. This will be discuss later in more detail.

Steege et al (1987, 1988) discussed the use of a manually controlled plunger device consisting of a miniature load cell and a linear variable differential transformer to obtain load displacement data on the soft tissue of trans-tibial residual limb. This device was used in conjunction with a preliminary finite element model of the residual limb to obtain a suitable value of Young's modulus (E) of the soft tissue. The device was fitted to an adapter embedded on the socket and indentation of the residual limb was performed by 'injecting' the plunger. Load - displacement curves were output on an x - y recorder where an initial E value was derived. In the preliminary FE model of the residual limb, the indentation procedure was modelled using fixed nodal displacement and with the initial measured E value. The FE model output reaction forces which was compared to the load experienced in the plunger device. The process produced an average E value of 60 kPa.

A similar procedure was attempted by Reynolds (1988) where mechanical indentation together with finite element modelling were used to obtain suitable values of E for a trans-tibial residual limb. The indentor had a hemispherical tip and diameter

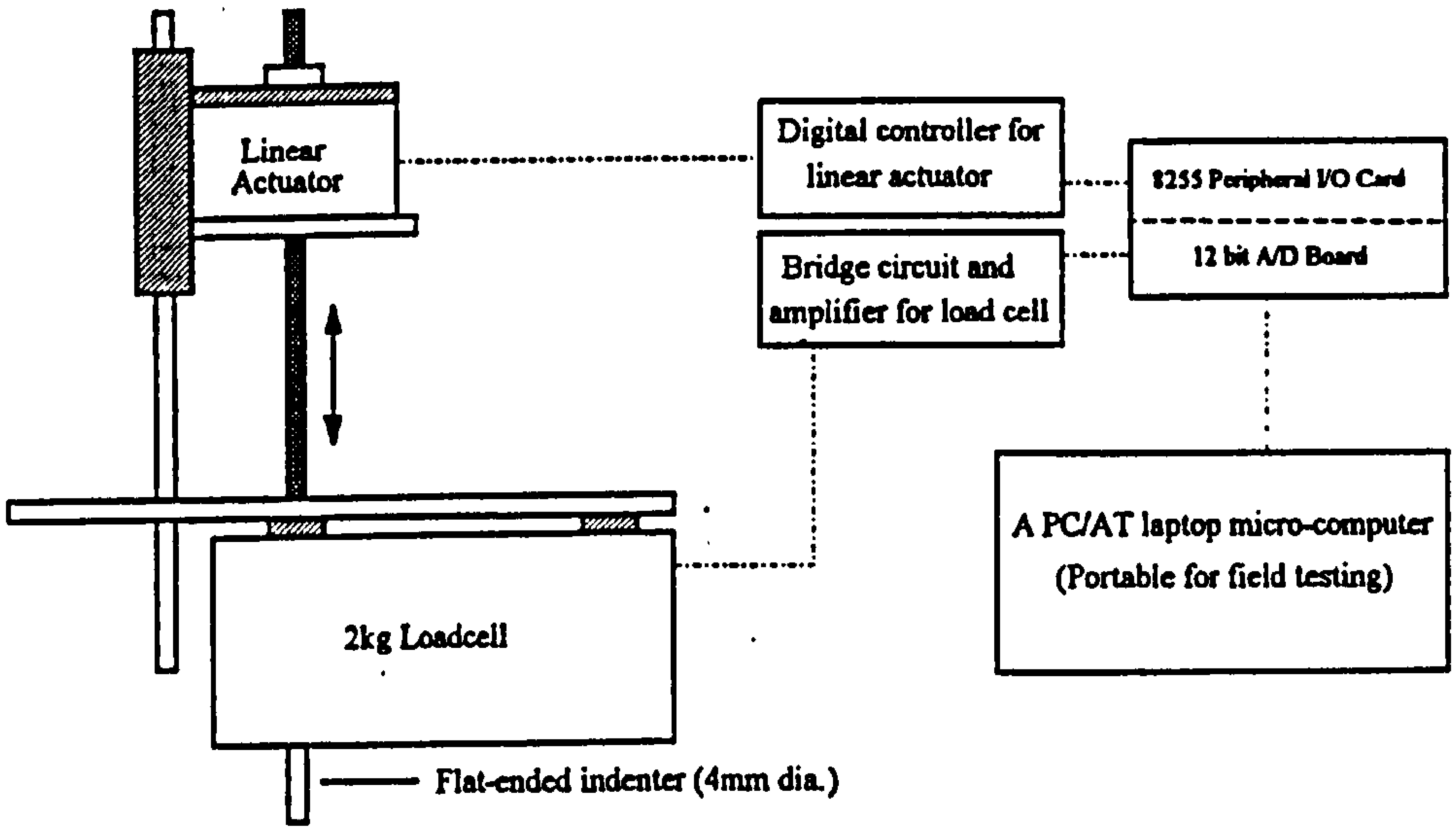

Fig. 6.3.3.1 Schematic diagram of indentation device.
(Mak et al, 1994)

of 20 mm. Indentation was performed manually at an approximate strain rate of 0.05 s^{-1} at four sites over the residual limb. The sites were the patellar tendon, popliteal region and the anterior aspects of the medial and lateral regions of the tibia. The E values at these respective sites were 145, 50, 50 and 120 kPa.

An improved system where the indentation process was computer controlled was designed by Torres-Moreno (1991) in the Strathclyde Bioengineering Unit. The principle behind the system was similar to the fore mentioned investigations. However, the system allowed the exact rate of loading to be specified and controlled. This system was used in the present study and will be discussed in the later part of the thesis.

Mak et al (1994) also designed a computer controlled indentation device to assess the soft tissue properties for both normal subjects (6 male) and subjects with trans-tibial amputation (2 male and 6 female). The schematic diagram in Fig. 6.3.3.1 shows the system's main components. A linear actuator controls the depth of indentation and a 20 N load cell records the load experienced on the flat ended indentor of 4 mm diameter. The entire system operation was monitored and data recorded with the aid of a laptop microcomputer. A total of three indentation sites was selected, the patellar tendon area, the lateral side of the lower leg between the fibula and the tibia, and a site directly opposite to the lateral site on the medial side. Indentation was conducted at a rate of approximately 4 mm/s up to a depth of 5 mm for medial and lateral sites and 3 mm at the patellar tendon site. At maximum displacement, the indentor was held for 2-3 seconds where stress relaxation was observed. The modulus of elasticity was derived based on a formula suggested by Hayes et al (1972) for modelling intact articular cartilage and subchondral bone as below;

$$E = \frac{P(1-\upsilon^2)}{2awk(a/h,\upsilon)} \qquad (6.3.3a)$$

where E is the modulus of elasticity, w is the depth of indentation, P *is* the force applied to the indentor at w indentation, υ is the Poisson's ratio, h is the thickness of

Location	Time after Amputation	Soft Tissues at Relaxed state 3 weeks* Mean (SD) kPa	Soft Tissues at Relaxed state 6 months** Mean (SD) kPa	Soft Tissues at Contracted state 3 weeks* Mean (SD) kPa	Soft Tissues at Contracted state 6 months** Mean (SD) kPa
Medial Side	E_{eq}	55.9 (8.6%)	61.5 (7.7%)	69.4 (7.9%)	74.9 (7.7%)
	E_{in}	64.4 (9.9%)	68.1 (10.0%)	80.8 (9.1%)	83.9 (9.5%)
Lateral Side	E_{eq}	77.9 (12.8%)	81.6 (13.1%)	87.6 (18.5%)	92.0 (18.7%)
Between Tibia/Fibula	E_{in}	90.4 (12.4%)	93.5 (12.4%)	101.1 (18.1%)	107.5 (19.9%)
Patella Tendon Areas	E_{eq}	29.1 (17.0%)	29.8 (16.7%)		
	E_{in}	30.6 (14.3%)	31.7 (13.7%)		

SD = standard deviation
kPa = 1000 N/m²

*Measured before prosthetic fitting (~3 weeks postamputation)
**Measured at first follow-up (~6 months postamputation)

Table 6.3.3.1 Elastic moduli at three locations around the trans-tibial residual limb. (Mak et al, 1994)

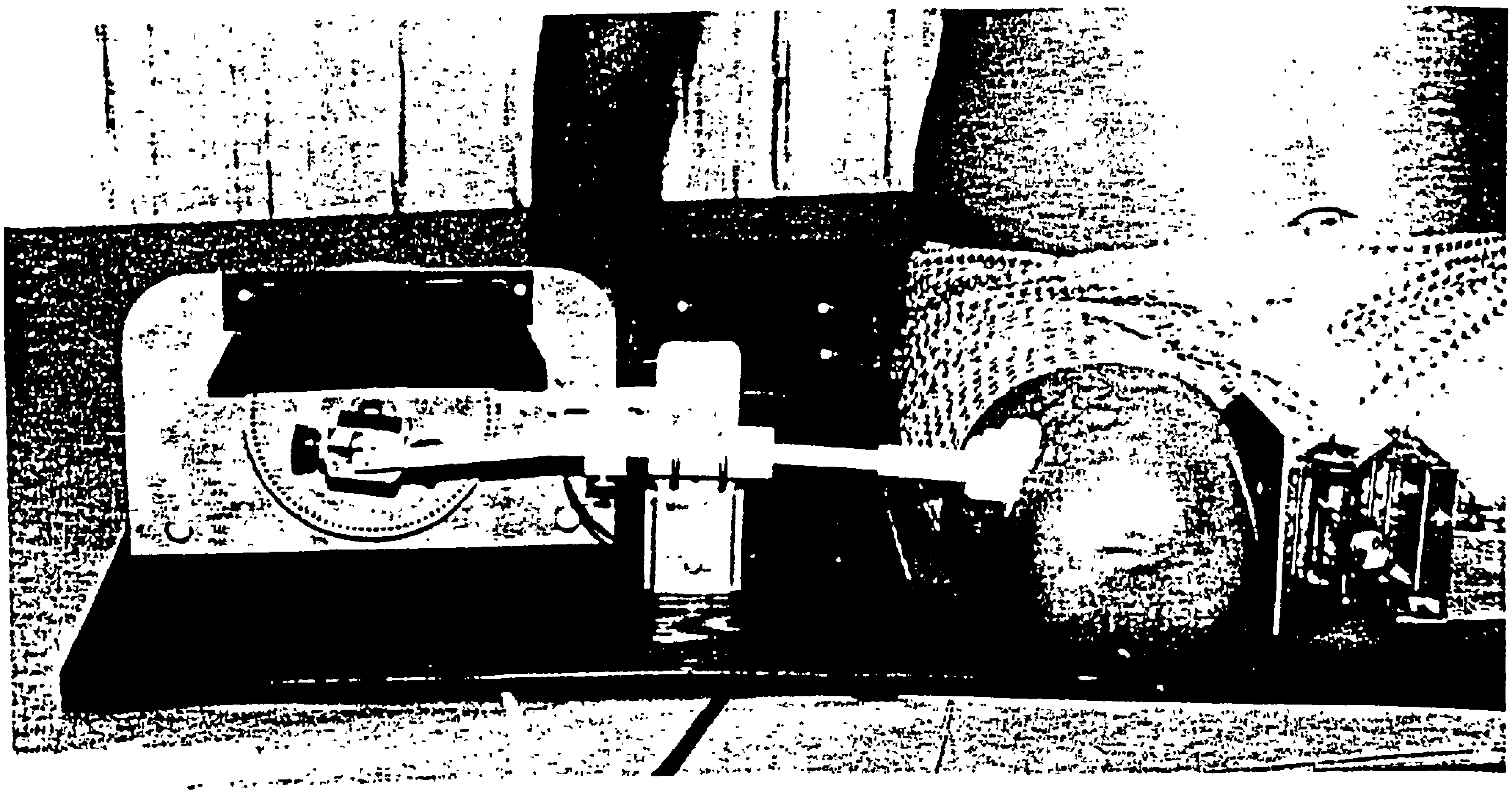

Fig. 6.3.3.2 Set-up for *in vivo* residual limb measurement using ultrasound techniques. (Krouskop et al, 1987)

of 20 mm. Indentation was performed manually at an approximate strain rate of 0.05 s^{-1} at four sites over the residual limb. The sites were the patellar tendon, popliteal region and the anterior aspects of the medial and lateral regions of the tibia. The E values at these respective sites were 145, 50, 50 and 120 kPa.

An improved system where the indentation process was computer controlled was designed by Torres-Moreno (1991) in the Strathclyde Bioengineering Unit. The principle behind the system was similar to the fore mentioned investigations. However, the system allowed the exact rate of loading to be specified and controlled. This system was used in the present study and will be discussed in the later part of the thesis.

Mak et al (1994) also designed a computer controlled indentation device to assess the soft tissue properties for both normal subjects (6 male) and subjects with trans-tibial amputation (2 male and 6 female). The schematic diagram in Fig. 6.3.3.1 shows the system's main components. A linear actuator controls the depth of indentation and a 20 N load cell records the load experienced on the flat ended indentor of 4 mm diameter. The entire system operation was monitored and data recorded with the aid of a laptop microcomputer. A total of three indentation sites was selected, the patellar tendon area, the lateral side of the lower leg between the fibula and the tibia, and a site directly opposite to the lateral site on the medial side. Indentation was conducted at a rate of approximately 4 mm/s up to a depth of 5 mm for medial and lateral sites and 3 mm at the patellar tendon site. At maximum displacement, the indentor was held for 2-3 seconds where stress relaxation was observed. The modulus of elasticity was derived based on a formula suggested by Hayes et al (1972) for modelling intact articular cartilage and subchondral bone as below;

$$E = \frac{P(1-\upsilon^2)}{2awk(a/h,\upsilon)} \qquad (6.3.3a)$$

where E is the modulus of elasticity, w is the depth of indentation, P *is* the force applied to the indentor at w indentation, υ is the Poisson's ratio, h is the thickness of

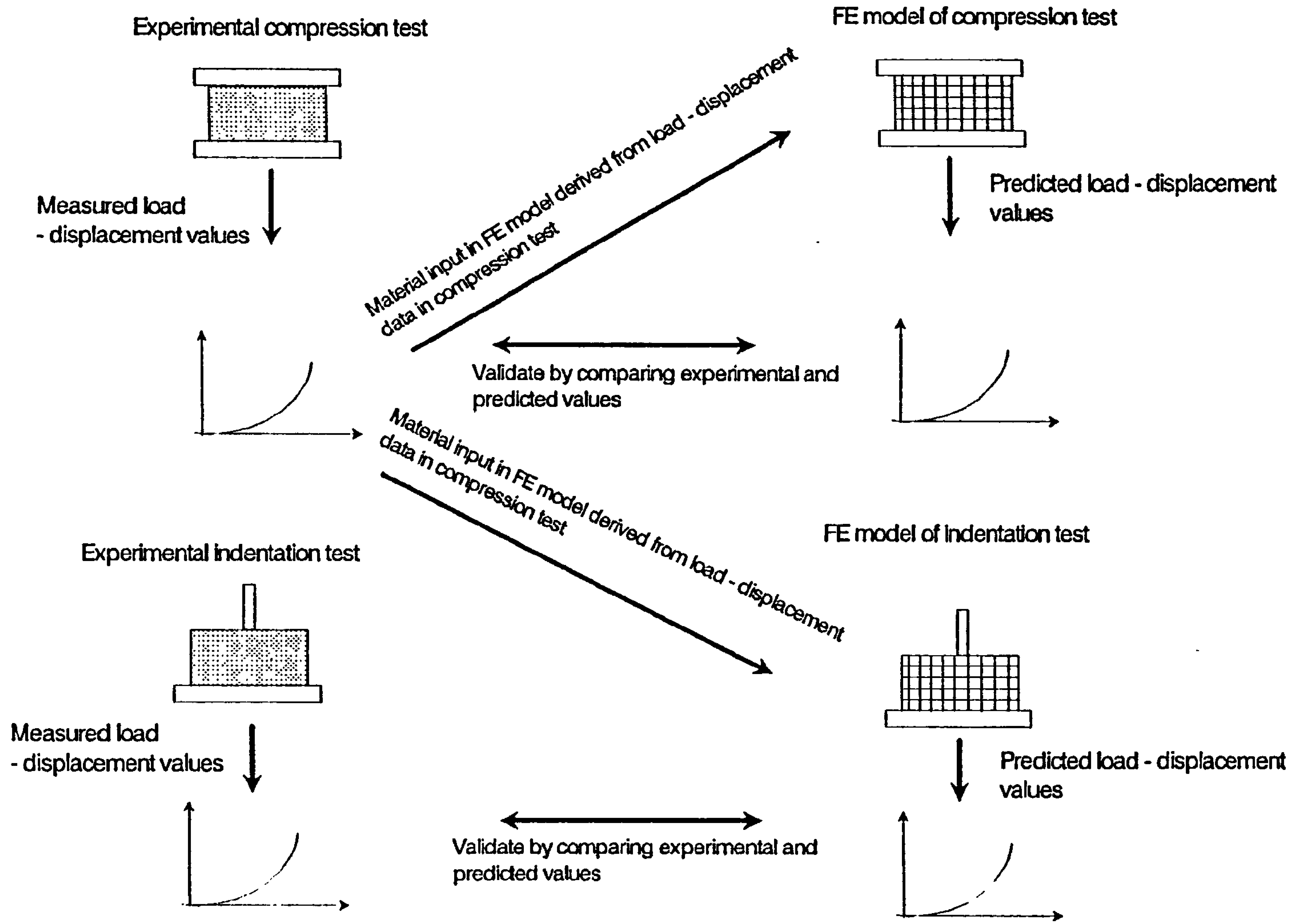

Fig. 6.4.1 Stages of compression and indentation studies on rubber and porcine tissue

where ρ is the density of the soft tissue and ω is the frequency of the cyclic displacement. Using this method, Krouskop's et al reported the average modulus of the relaxed thigh was 6.2 kPa, on mild contraction 40 kPa and on maximum contraction to be 109 kPa. Malinauskas et al (1989) reported the measurement of nine trans-femoral amputees using the same procedure at the anterior, lateral, posterior and medial aspects of the residual limb. The moduli were 141.4 kPa ± 79.1, 57.9 kPa ± 31.1, 53.2 kPa ± 30.5 and 72.3 kPa ± 45.5 respectively. It was also discovered that the modulus of the superficial tissue (average modulus of 117.6 kPa ± 63.0) was significantly (t- tests set at 0.01) stiffer than the underlying tissues (average modulus of 59.1 kPa ±74.0).

6.4 *IN VITRO* COMPRESSION AND INDENTATION TEST

Compression tests were performed in order to characterise the mechanical properties of non-linear material (rubber and porcine tissue). Upon determining the properties, FE models can be created and validated. The test procedures are outlined in Fig. 6.4.1. The specimen was initially subjected to a mechanical compression test where suitable material properties were derived from the load - deflection curve. Subsequently, a FE model was constructed based on the specimen's geometry, loading and boundary conditions as in the experiment. The FE predicted displacement was then compared with the specimen's displacement recorded during the compression test. Indentation tests on the specimen were also performed to evaluate FE modelling techniques.

The aim of the exercise was to determine the limitation in FE modelling of a non-linear material. The author of this thesis considered it improper to model the residual limb without firstly understanding the capability of the FE method on non-linear biological material. Most researchers in the past have proposed FE models of the residual limb (Steege et al 1988, Sanders et al 1993, Zhang et al 1995) and buttocks (Dabnichki et al 1994) without firstly testing the material properties assigned to their model. Attempting a FE model of the residual limb involves complex geometry and loading conditions, which make it difficult to assess the effects of material properties introduced. The experiments and modelling techniques in this study were designed with simple geometrical and loading constraints in order to address issues that concern material properties. A better understanding of how biological structures behave under compression should be accomplished. In the next section, material testing will be discussed.

6.4.1 Specimen material selection and preparation

Two types of materials were selected, PVC rubber and porcine tissue. Rubber's behaviour under compression has been well documented. Its properties can be considered homogeneous and isotropic and non linear in its stress - strain relationship. The rubber used in the experiment was obtained in liquid form and moulded to a rectangular block. The rubber block was manufactured by pouring it into an aluminium mould of 100 x 50 x 50 mm internal dimensions and leaving it in the oven at 150 °C for 15 minutes. Shrinking was evident and the final dimensions of the PVC rubber were 95.50 x 48.96 x 49.50 mm in length, width and height respectively.

The porcine tissue was specially ordered from a butcher with the following specifications. The tissue was fresh (i.e. straight from the abattoir) and a portion from the hind thigh of the pig consisting skin, fat and muscles was cut out. The tissue was further dissected into smaller samples of rectangular shape suitable for the compression and indentation test. Initially, the specimens prepared included skin, fat and muscle tissues. However, difficulties arise in several areas. It was difficult to prepare a sample with stable dimensions due to the soft fat between the skin and muscles. Furthermore, the soft fat acts as a layer of low friction between the skin and the muscles allowing sliding to occur when compressive load is applied to the specimen. Finally, the amount of fluid loss from the fat after compression was considerable, thus upsetting the specimen dimensions. Taking all these into consideration, it was decided only to test the muscle tissue. Satisfactory dimensions could be achieved by cutting the muscle tissue with a very sharp razor blade. The specimens were prepared with the following dimensions, approximately 66 x 37 x 36

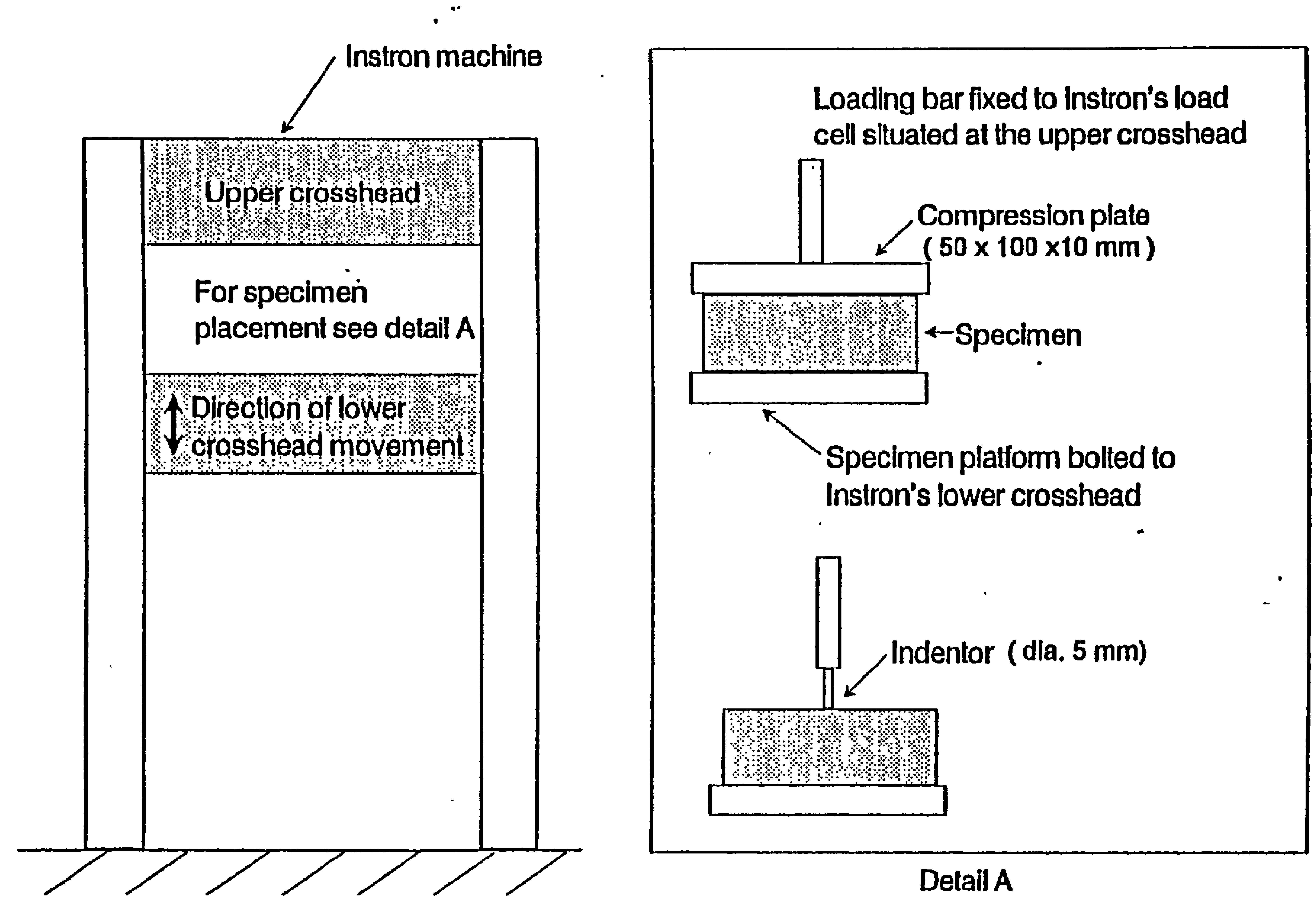

Fig. 6.4.2.1 Schematic diagram of compression and indentation test set up

mm. Unlike rubber, the fragility of the porcine tissues would mean a new specimen for each test. Thus prior to each test, the exact dimensions of the porcine tissues were recorded.

6.4.2 Experimental set-up

Fig. 6.4.2.1 shows a schematic diagram of the test set-up. The mechanical testing machine used was an Instron model 4505. Detail drawings of the fixtures used with the Instron in the experimental set-up is shown in Appendix B. Both the rubber and porcine specimens were placed freely onto the specimen platform. The specimen platform movement towards or away from the compression plate or indentor was achieved by moving the Instron lower crosshead, which was controlled by a personal computer or the Instron control panel. The rate of movement and location of the lower crosshead could be pre-set, controlled and program on the personal computer.

The loads experienced with testing rubber were much higher (about 25 times) than porcine tissue, thus the Instron had to be set up for two different sensitivities. This was achieved by changing the load cell mounted at the upper cross head, using a 10 kN cell for rubber and a 1 kN cell for porcine tissue. Upon mounting the appropriate load cell, the load cell had to be zeroed to accommodate the weight of the compression plate or indentor. After this, the specimen was placed onto the specimen platform and brought to just about touching the compression plate or indentor. A fine adjustment control on the Instron control panel was than used to bring the specimen into contact with the compression plate or indentor. Contact was indicated by a digital meter on the control which shows the load acting on the load cell to be just slightly above zero.

In the compression test, it was hoped to achieve only normal forces acting on the specimen. Precautions were taken to ensure that the specimen was centrally located and flat on the compression plates. However, a totally flat surfaces was not possible especially with the porcine tissue. Furthermore, due to friction, shear stresses were present between the specimen and the compression plates. In the case of PVC rubber, lubricant was applied to the interface between the rubber and the compression

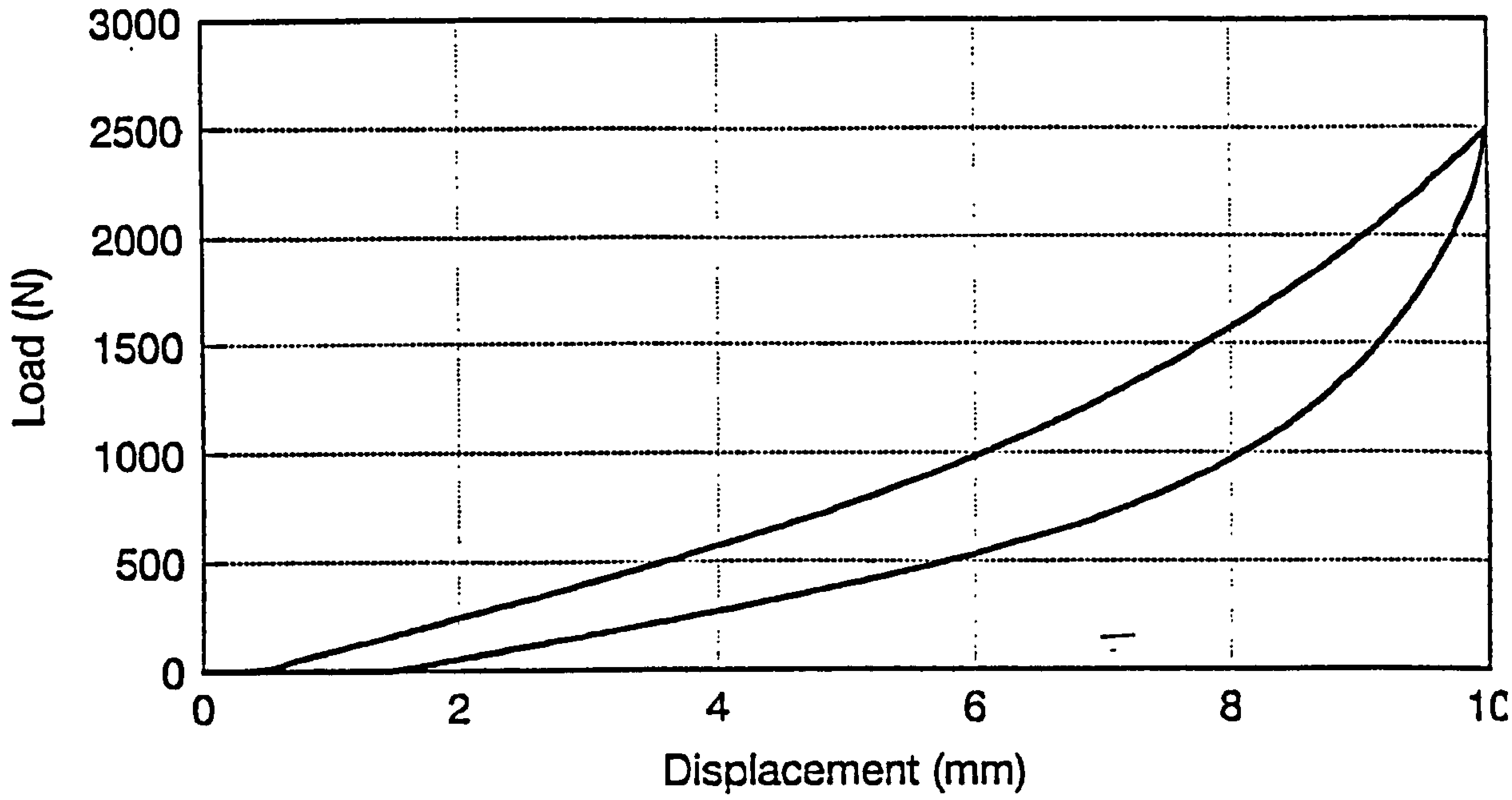

Fig. 6.4.5.1 Loading and unloading of rubber at rate of 10 mm/min in compression test

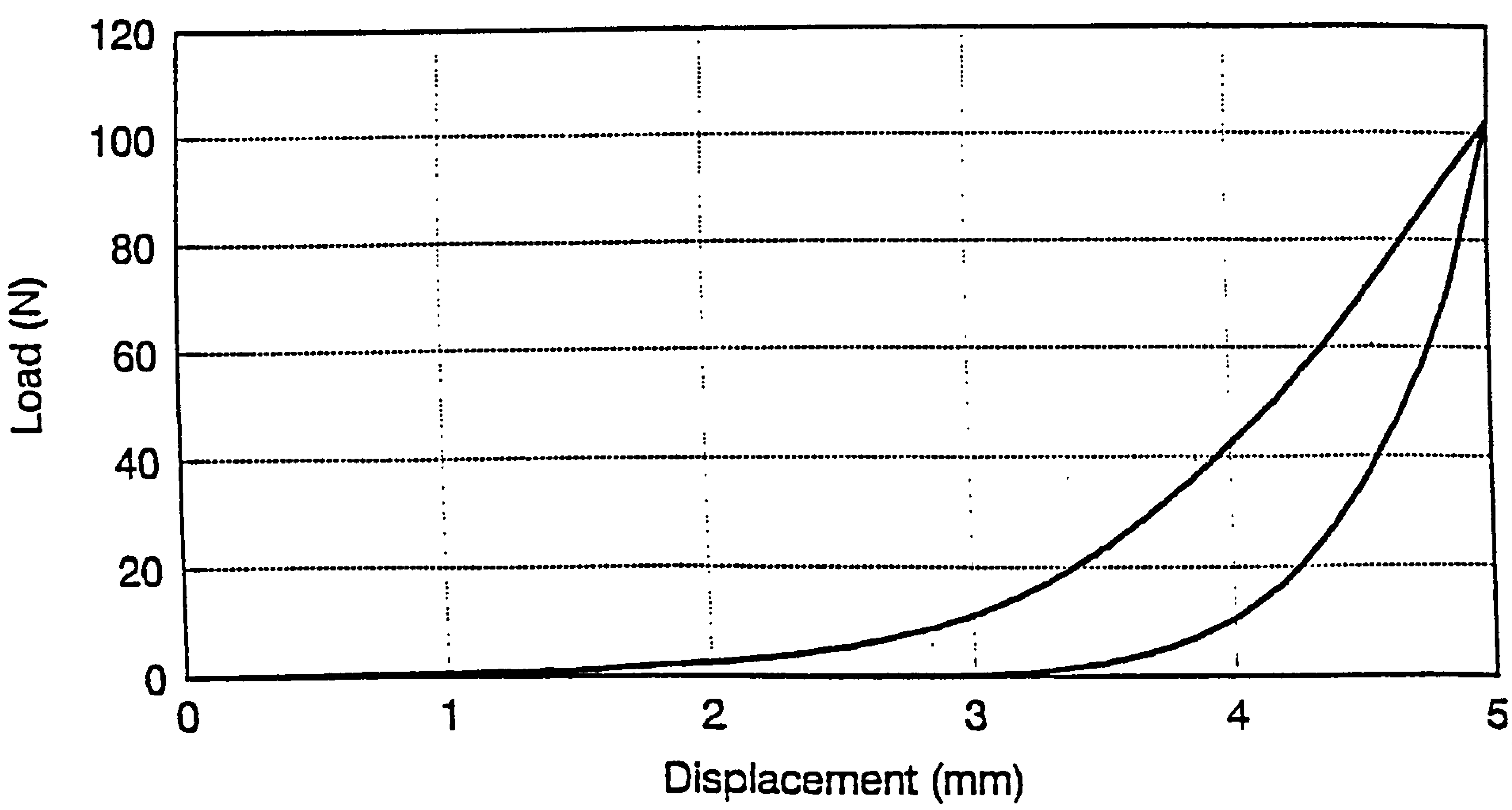

Fig. 6.4.5.2 Loading and unloading of porcine tissue at rate of 10 mm/min in compression test

plates to reduce the effect of shear. It was observed that during compression, the rubber specimen performed well by not sticking onto the compression plates retaining most of its rectangular shape. In the porcine test, no lubricant was applied. It was considered that the lubricant would not be effective in this case and might alter the properties of the tissue in some way.

6.4.3 Methodology : Compression test

Prior to the actual test, the specimens were preconditioned by a series of loading and unloading cycle. The rubber specimen was compressed to a maximum depth of 10 mm, approximately 0.2 strain. Five different rate of loading and unloading were applied, these were 5, 10, 50, 100 and 200 mm/min. For each rate of loading and unloading, load - deformation data were recorded. In the porcine tissue, the five different rate of loading and unloading were kept similar, however the amount of displacement was reduced to 5 mm. The tissue specimen was thinner, thus the compression strain was still maintained at approximately 0.2. ?

6.4.4 Methodology : Indentation test

A 5 mm diameter flat indentor was used. Indentation was performed up to a depth of 10 mm for rubber and 5 mm for porcine tissue. The rate of of loading and unloading was 5 mm/min.

6.4.5 Results : Compression test

Load - deflection curve

Fig. 6.4.5.1 and Fig. 6.4.5.2 show the typical loading and unloading curves from rubber and porcine tissue. Hysteresis was present for both materials and in porcine tissue more pronounced. The area bounded by the loading and unloading curves indicates the energy lost. In rubber, this energy dissipates as heat but in the case of porcine tissue, besides heat loss there was also a loss of cellular fluids leading to permanent deformation. However, in the case of rubber, unloading the specimen did not return the specimen to its original dimensions immediately, but this effect was

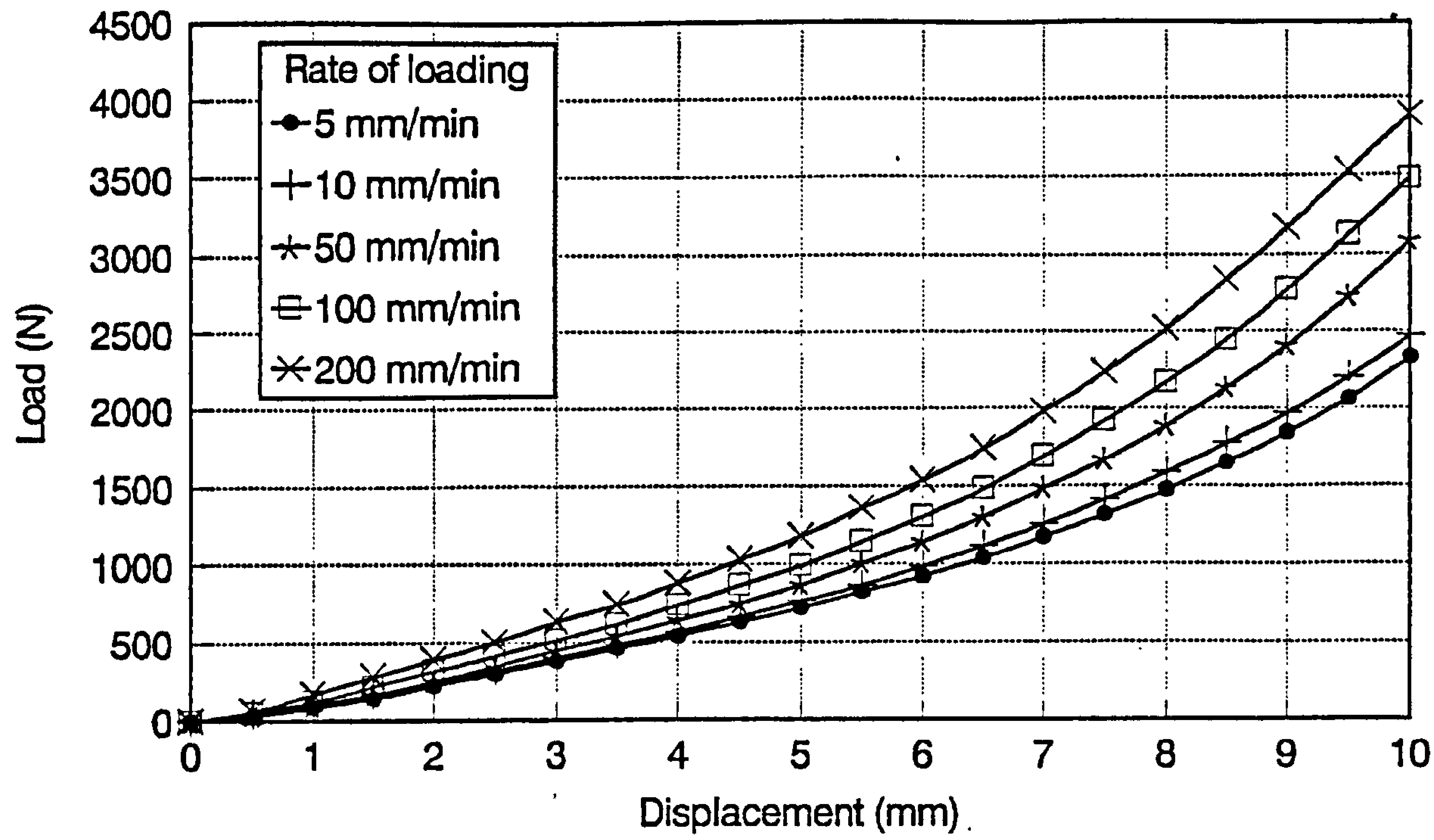

Fig. 6.4.5.3 Rubber compression test

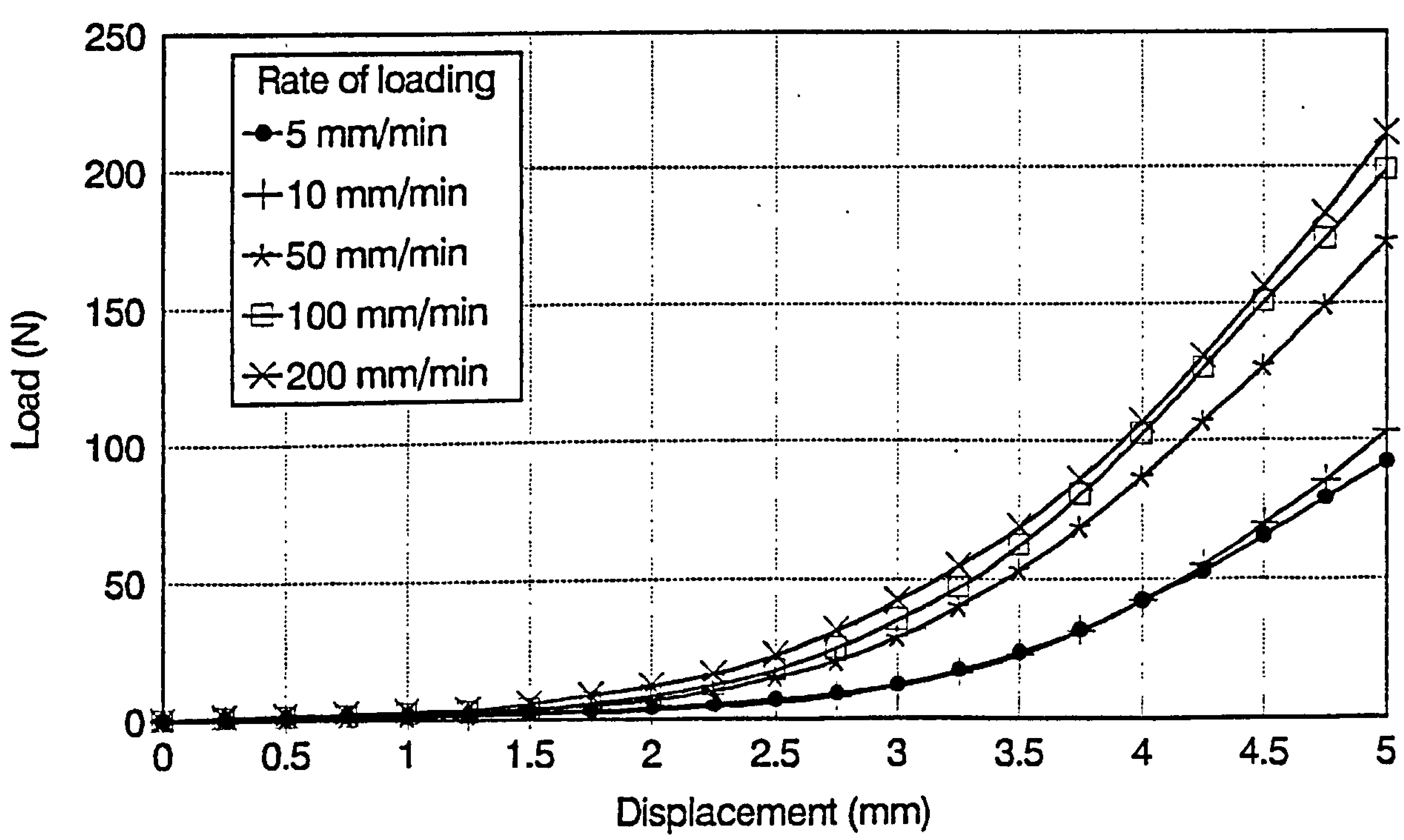

Fig. 6.4.5.4 Porcine tissue compression test

not permanent and the specimen usually recovered its original dimensions quickly prior to the next compression test. The state of unloading in the porcine tissue was therefore dependent on factors which are uncertain. It was therefore considered that only the loading phase of the compression test should be analysed and modelled for both rubber and porcine tissue.

Fig. 6.4.5.3 and Fig. 6.4.5.4 show the load - displacement curves for rubber and porcine tissue at different rates of loading. It must be pointed out that unlike the tests for rubber where only one specimen was used throughout the different rates of loading, a new specimen was used in each rate of loading in the test for porcine tissue. The load deflection curve was therefore dependent on the specimen size. Nevertheless, variability between the porcine tissue specimen sizes have been kept to within a close tolerance. But in any case, the stress - strain plots described later take the individual specimen size into consideration. The load - displacement plots indicated clearly that the maximum load corresponding to the maximum displacement increases with the rate of loading. The maximum force encountered at 200 mm/min in rubber was 3890 N while in porcine tissue it was 212 N. Both rubber and porcine tissue produced non-linear curves with the latter showing higher non linearity. The porcine tissue required a very low load to bring it to a displacement of 1.5 mm. Within this range of displacement, the effect due to different rates of loading was minimal.

<u>Stress - strain curve</u>

In evaluating the stress - strain relationships of the compression test, both engineering and true stress - strain relationship have been considered. Engineering stress was obtained by force divided by the original cross sectional area while true stress was computed by having the applied force divided by the current cross sectional area. Therefore engineering stress, which is based on the unloaded cross-sectional area would be higher than true stress for compressive loading. Engineering strain was computed by the displacement divided by the initial thickness of the specimen. The

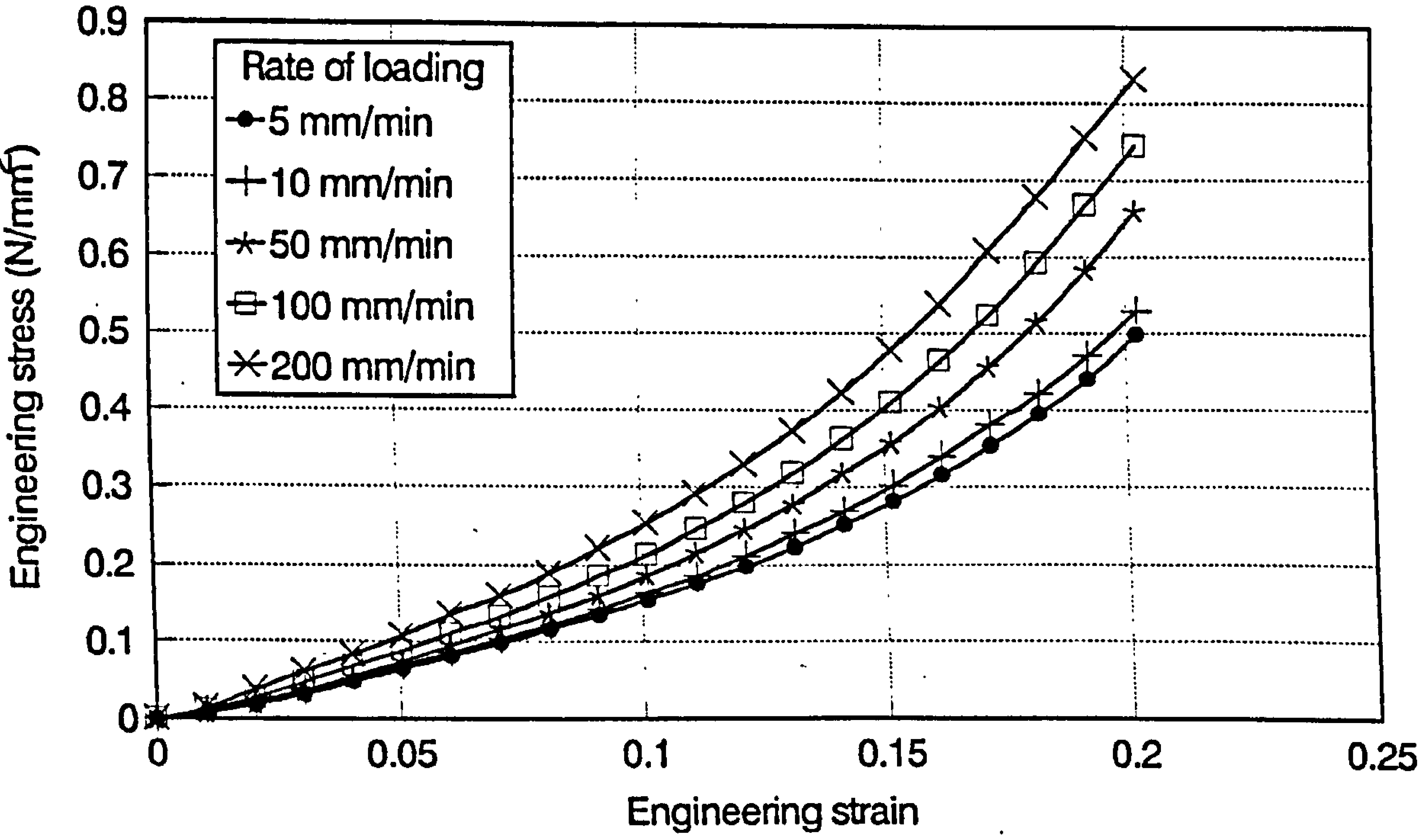

Fig. 6.4.5.5 Engineering stress - strain plot in rubber compression test

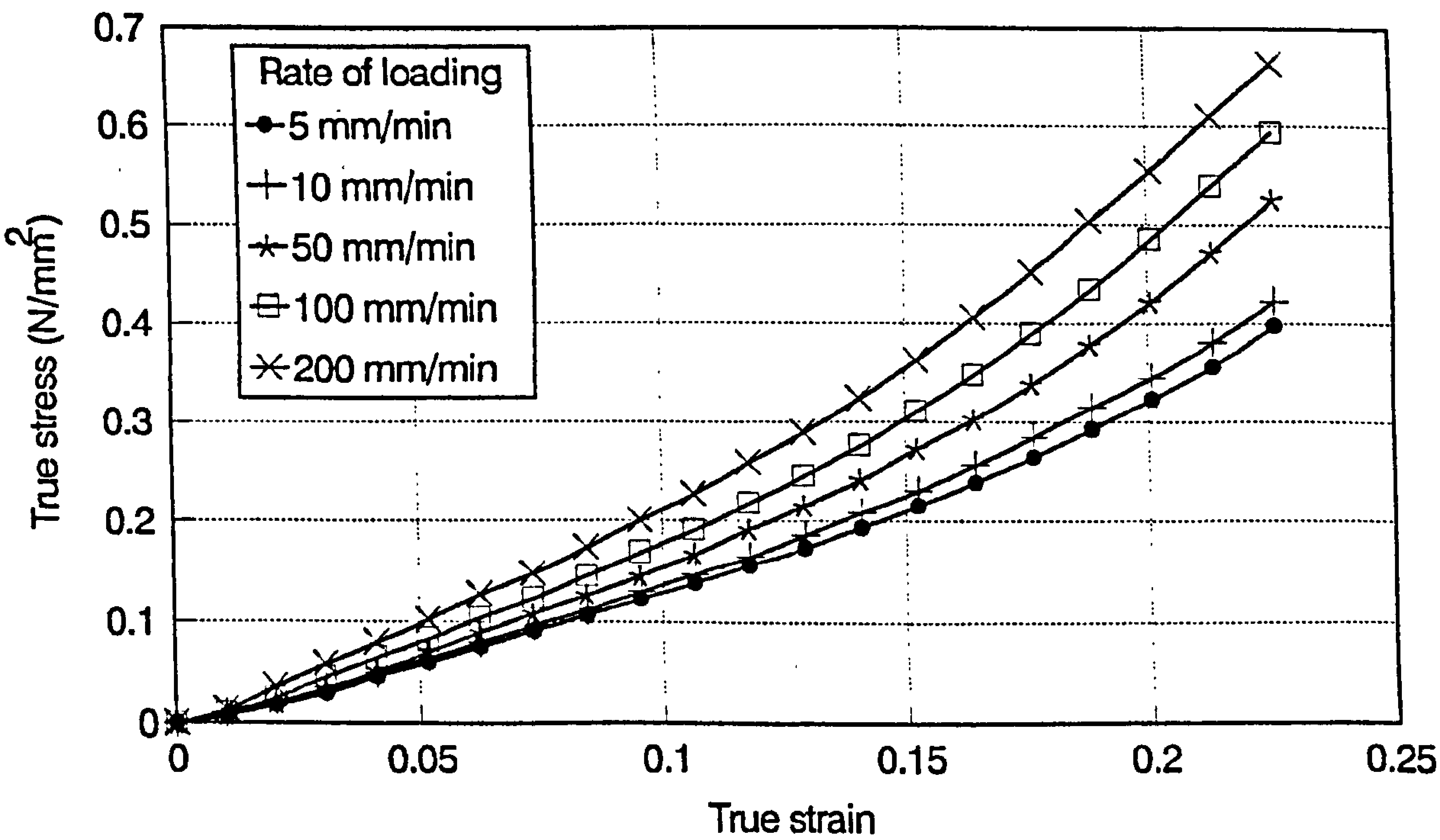

Fig. 6.4.5.6 True stress - strain plot in rubber compression test

true strain, however, is the sum of each incremental change in the thickness ΔL divided by the instantaneous thickness L. Therefore ,

$$\varepsilon = \Sigma\left(\frac{\Delta L}{L}\right) = \ln\left(\frac{L_i}{L_f}\right) \qquad (6.4.5a)$$

where L_i is the initial thickness and L_f is the final thickness. The concept of engineering stress would be inappropriate for materials that undergoes large displacement where true stress and strain are more suitable. Nevertheless, both engineering and true stress - strain will be investigated in this study.

Fig. 6.4.5.5 and Fig. 6.4.5.6 show the stress - strain plots for rubber. The curves at different rates of loading bear similarity with those of load - deflection curves in Fig. 6.4.5.3. Increasing the loading rate gradually increases the gradient of the curves. In the true stress - strain plots, the curves approached a more linear characteristic especially at lower rates of loading. In porcine tissue, as shown in Fig. 6.4.5.7 and 6.4.5.8, the stress - strain plots were highly non linear. There was little difference between the curves obtained at 5 and 10 mm/min rate of loading. A much steeper gradient was seen with strain greater than 0.1 at 50 mm/min rate of loading than at 5 and 10 mm/min. However, increasing the rate of loading from 50 mm/min up to 200 mm/min, the increase in gradient of the curve was not considerable.

Poisson's ratio

Poisson's ratio is usually derived traditionally from engineering strains where,

$$\upsilon = \frac{e_t}{e_a}$$

where e_t and e_a are engineering strains in the transverse and axial directions. It can be shown that due to incompressibility, Poisson's ratio is a function of strain alone. From a cube of 1 x 1 x 1 unit, it can be shown that ;

d = axial elongation

e = axial engineering strain which is also equal to d, since $\frac{d}{1} = e$

incompressibility gives,

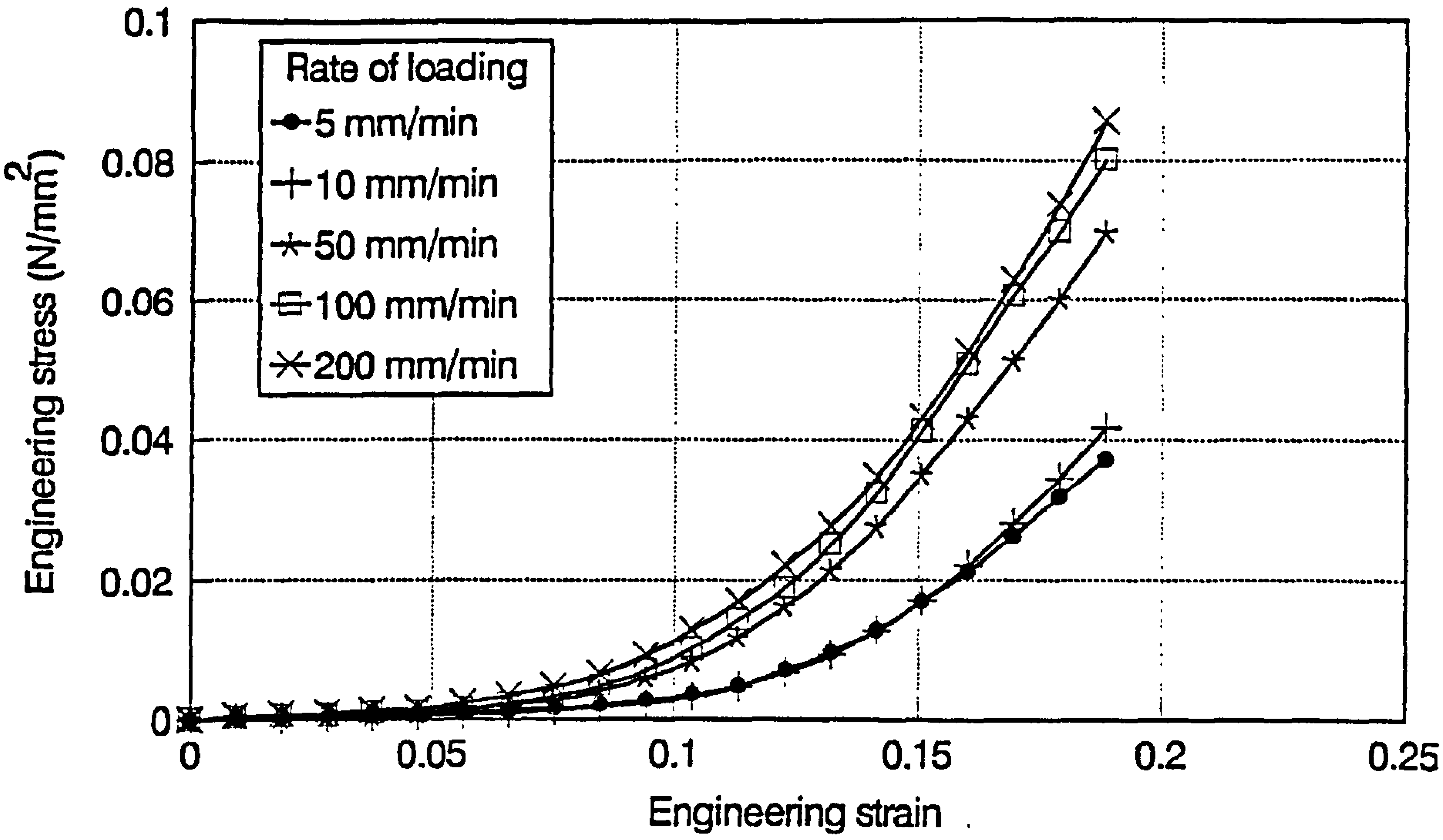

Fig. 6.4.5.7 Engineering stress - strain plot in porcine tissue compression test

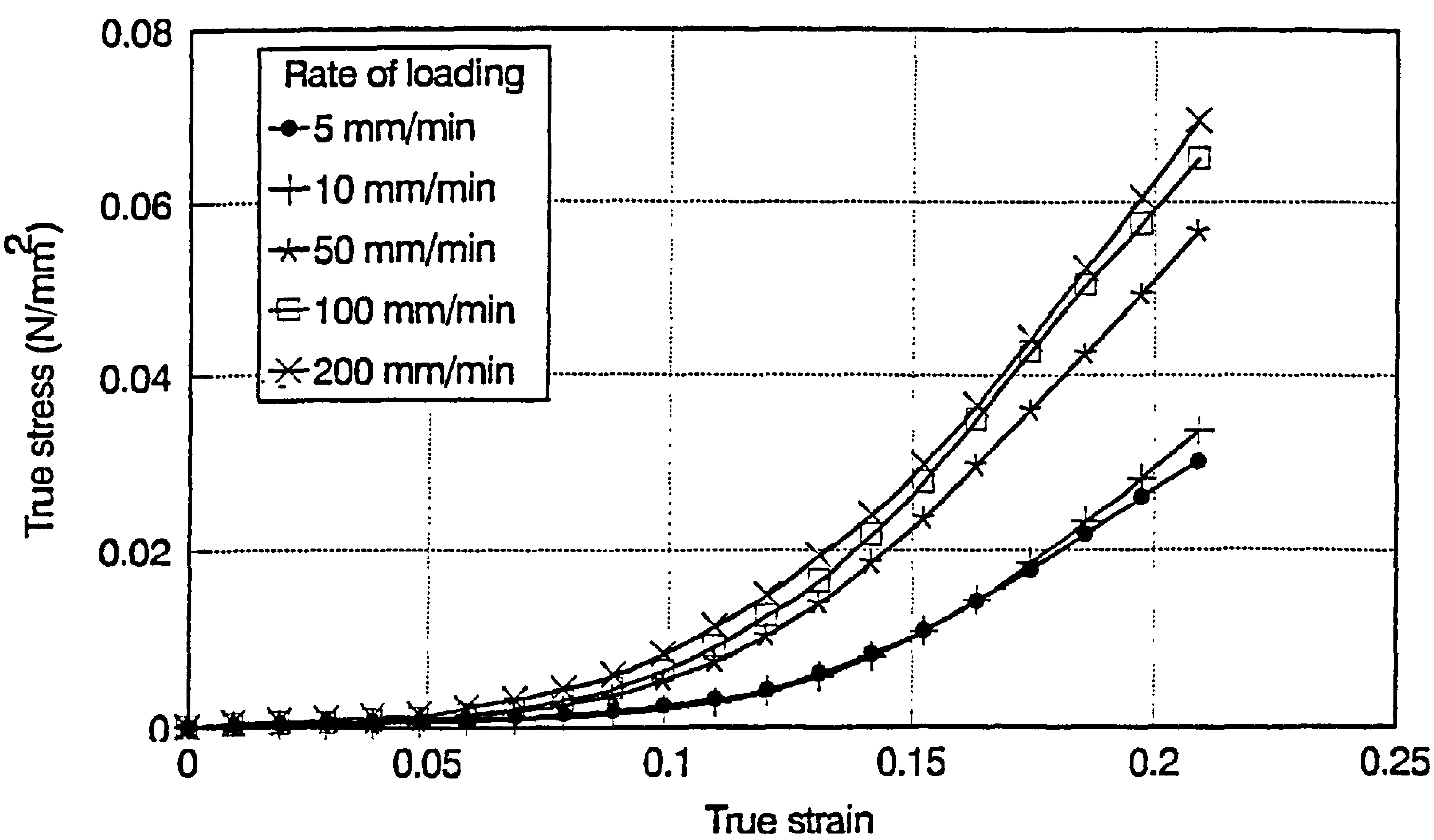

Fig. 6.4.5.8 True stress - strain plot in porcine tissue compression test

initial volume = final volume

1 = (final length) x (final width)^2

$$1 = (1+e)(1-\upsilon e)^2$$

$$1 = (1+e)(1-2\upsilon e+\upsilon^2 e^2)$$

$$\upsilon^2(e+e^2)+\upsilon(-2-2e)+1=0$$

$$\upsilon = \frac{(2+2e)\pm\sqrt{(4+8e+4e^2)-4(e+e^2)}}{2(e+e^2)}$$

$$\upsilon = \frac{1+e\pm\sqrt{1+e}}{e+e^2} \qquad (6.4.5b)$$

For a range of strains, Poisson's ratio is greater than 0.5 for large compressive strains and less than 0.5 for large tensile strains and 0.5 for small strains as shown in the plot of equation (6.4.5b) in Fig. 6.4.5.9. In the rubber and porcine compression test the range of strain and Poisson ratio is as indicated in the same figure. However, again for an incompressible material, it can be shown that based on true strains that Poisson's ratio is 0.5 for any strains. In such a case, incompressibility gave rise to the following;

$$\frac{L_{1f}L_{2f}L_{3f}}{L_{1i}L_{2i}L_{3i}} = 1$$

where L_{1f}, L_{2f}, and L_{3f} are the final length, width and thickness and L_{1i}, L_{2i}, and L_{3i} are the initial length, width and thickness. Therefore the above can be expanded as,

$$\ln\left(\frac{L_{1f}}{L_{1i}}\right)+\ln\left(\frac{L_{2f}}{L_{2i}}\right)+\ln\left(\frac{L_{3f}}{L_{3i}}\right)=0$$

and from equation 6.4.5a, the above can be written as,

$$\varepsilon_1+\varepsilon_2+\varepsilon_3=0$$

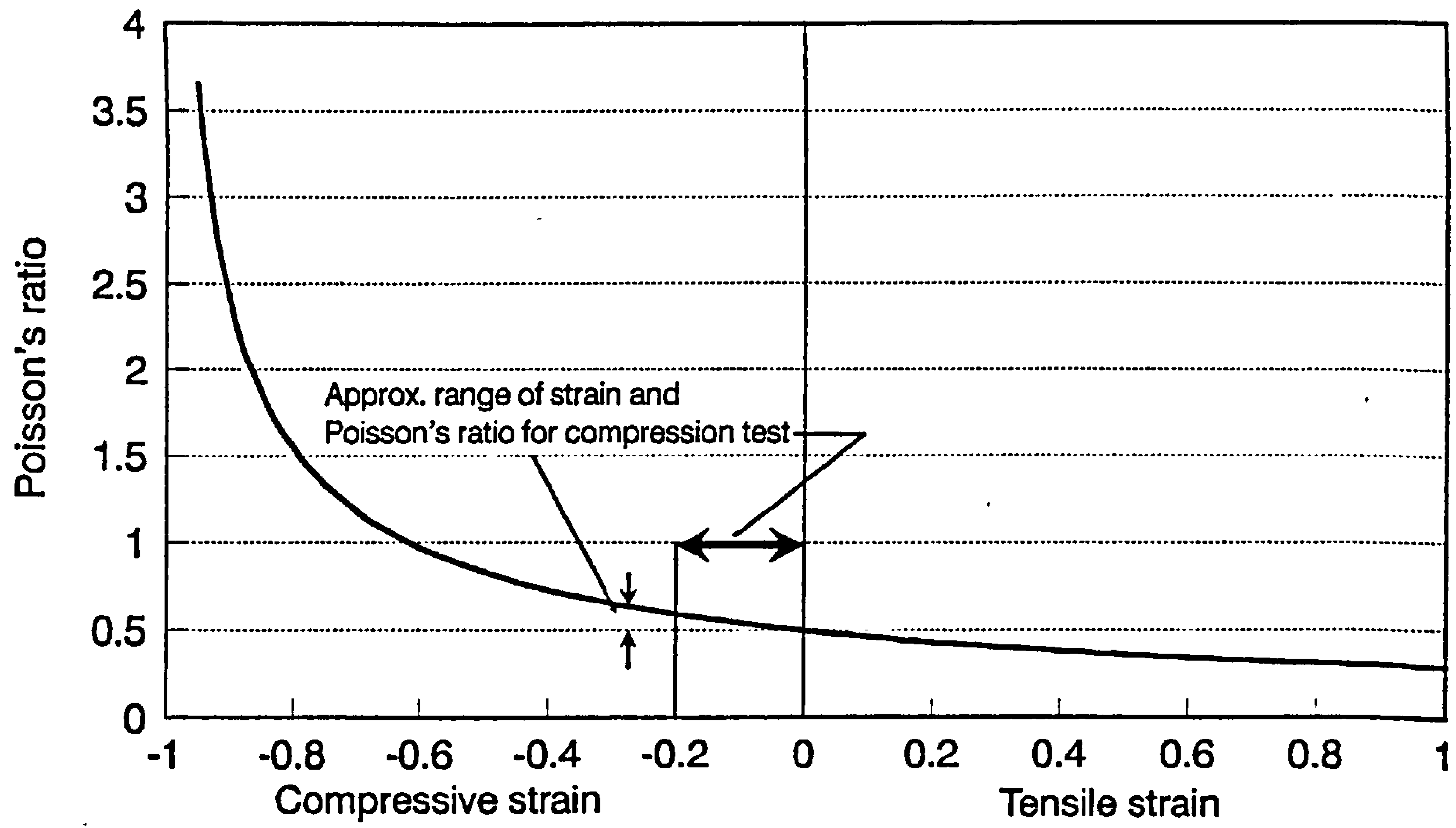

Fig. 6.4.5.9 Plot of $\upsilon = \frac{1+e-\sqrt{1+e}}{e+e^2}$, where υ is the Poisson's ratio and e is the tensile or compressive strain.

and due to uniaxial loading in an isotropic material,

$$\varepsilon_2 = \varepsilon_3$$

$$\varepsilon_1 = -2\varepsilon_2$$

and $$\upsilon = \frac{\varepsilon_1}{\varepsilon_2} = -0.5$$

Modulus of elasticity

The next section looks at the secant modulus of elasticity based on the engineering and true stress - strain plots. The engineering and true modulus are described respectively as follows ;

$$E_{eng} = \frac{S}{e}$$

and

$$E_{true} = \frac{\sigma}{\varepsilon}$$

Fig. 6.4.5.10 to Fig. 6.4.5.13 shows the plot of engineering and true modulus versus strain for both rubber and porcine tissue respectively. For a linear material, the plots should indicate a straight horizontal line. In the case of rubber, the modulus increases with increasing strain. As shown in Fig. 6.4.5.10 and Fig. 6.4.5.11, the initial phase of the curve between 0 - 0.05 strain shows a steep gradient. This was follow by a region showing gradual increase in the modulus. The modulus calculated from engineering stress and strain was considerably larger than that obtained from true stress and strain. The former recorded a maximum modulus value of 4.12 N/mm^2 and the latter 2.94 N/mm^2 at a rate of loading of 200 mm/min. The moduli were also very much dependent on the rate of loading. It was observed that compressing the specimen at a low rate produced low moduli that varied less with strain (i.e. approaching that of a linear material) than at a higher rate.

Fig. 6.4.5.12 and Fig. 6.4.5.13 show plots of modulus versus strain for porcine tissue. Unlike rubber, the initial phase of the curve within the range of 0 - 0.1 strain

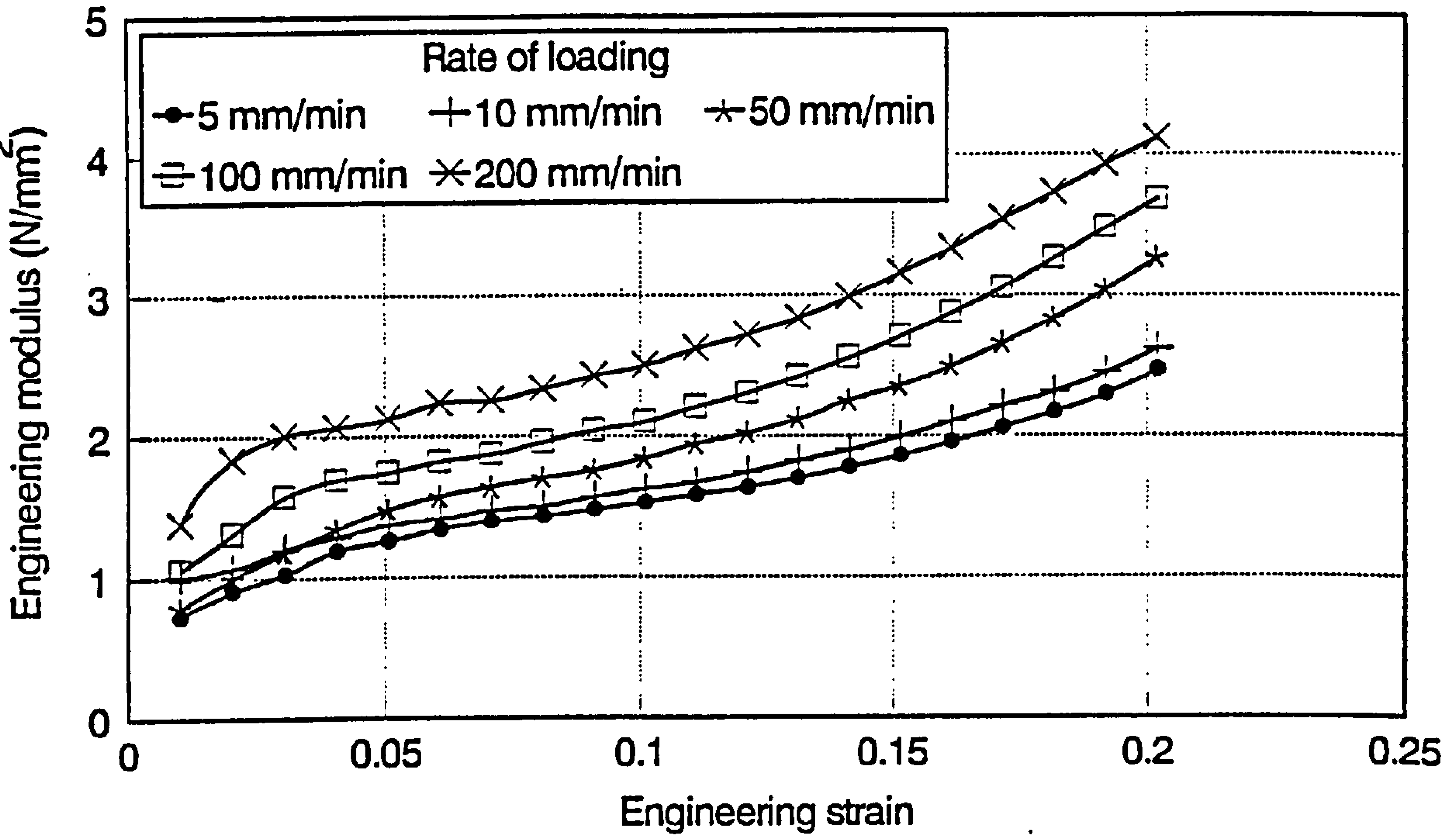

Fig. 6.4.5.10 Engineering modulus versus engineering strain for rubber

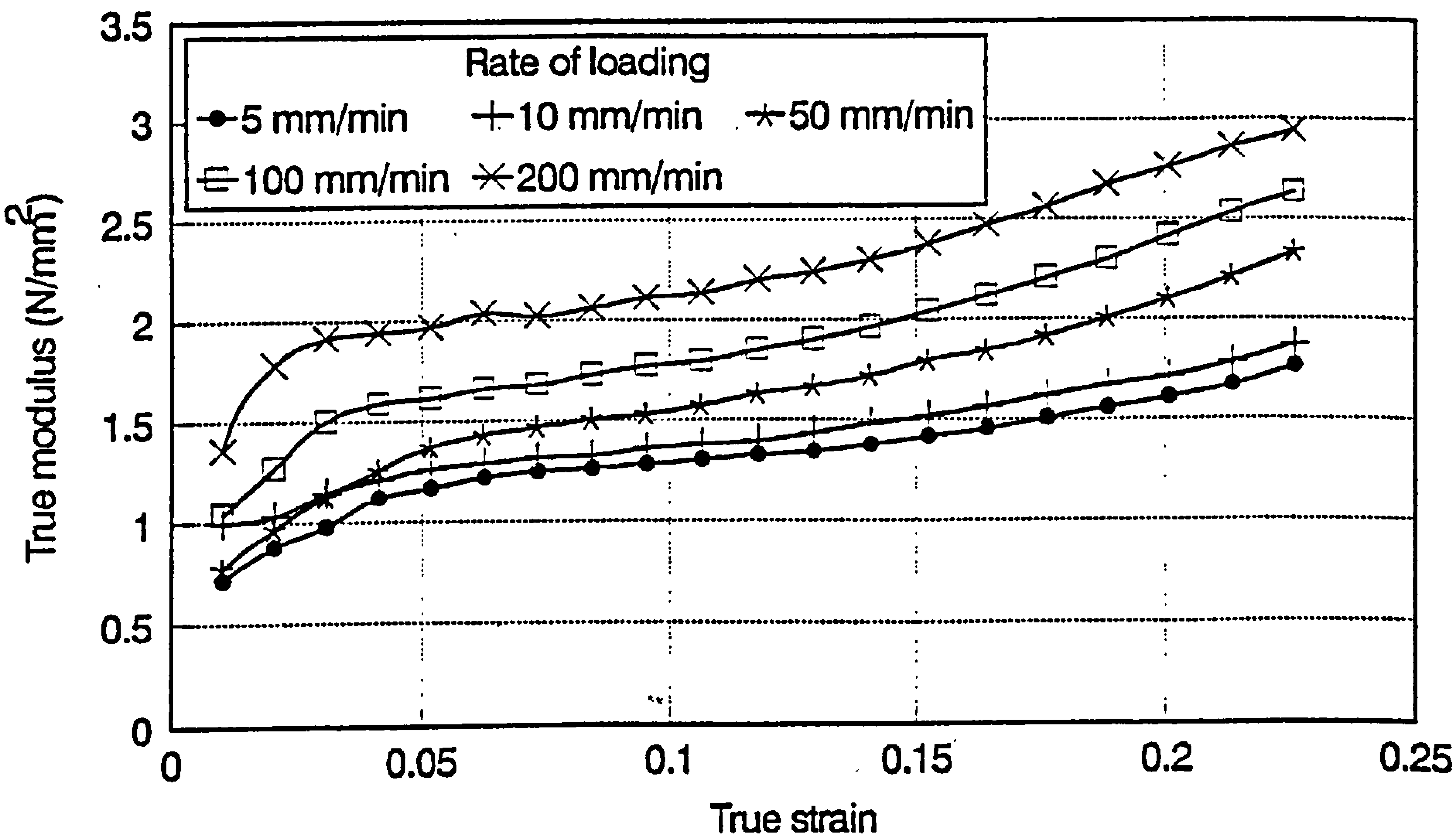

Fig. 6.4.5.11 True modulus versus true strain for rubber

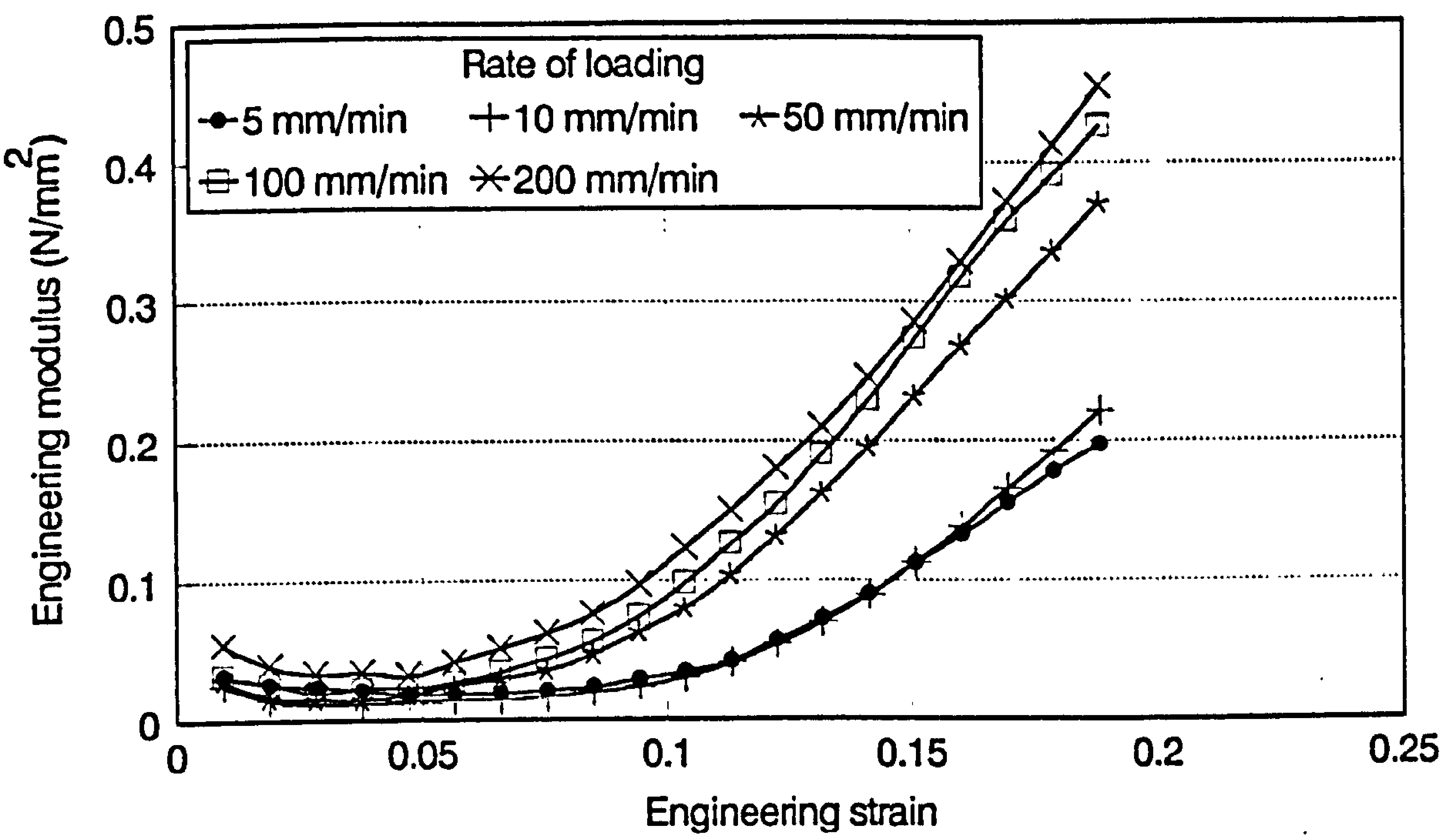

Fig.. 6.4.5.12 Engineering modulus versus engineering strain in porcine tissue

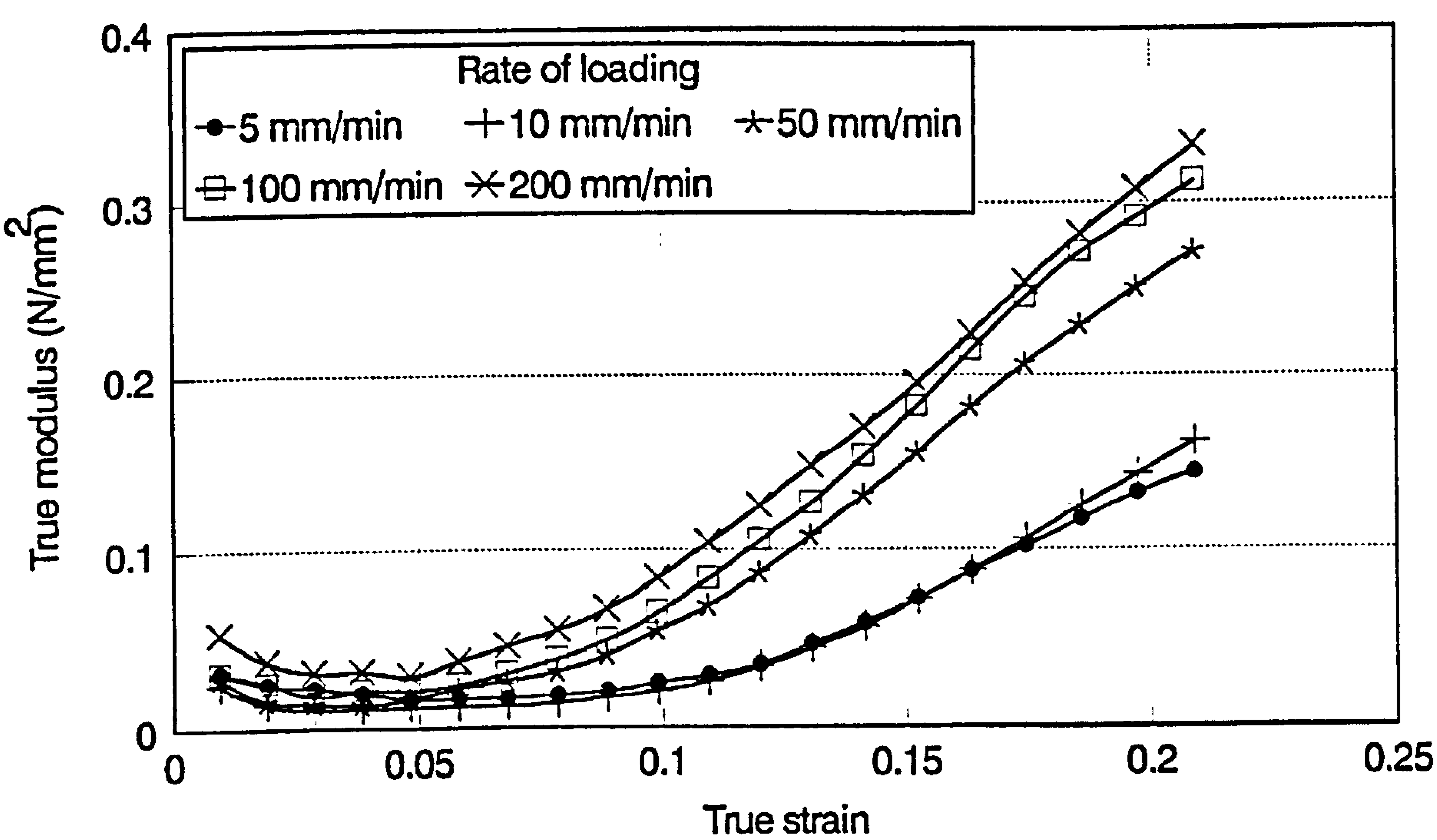

Fig.. 6.4.5.13 True modulus versus true strain in porcine tissue

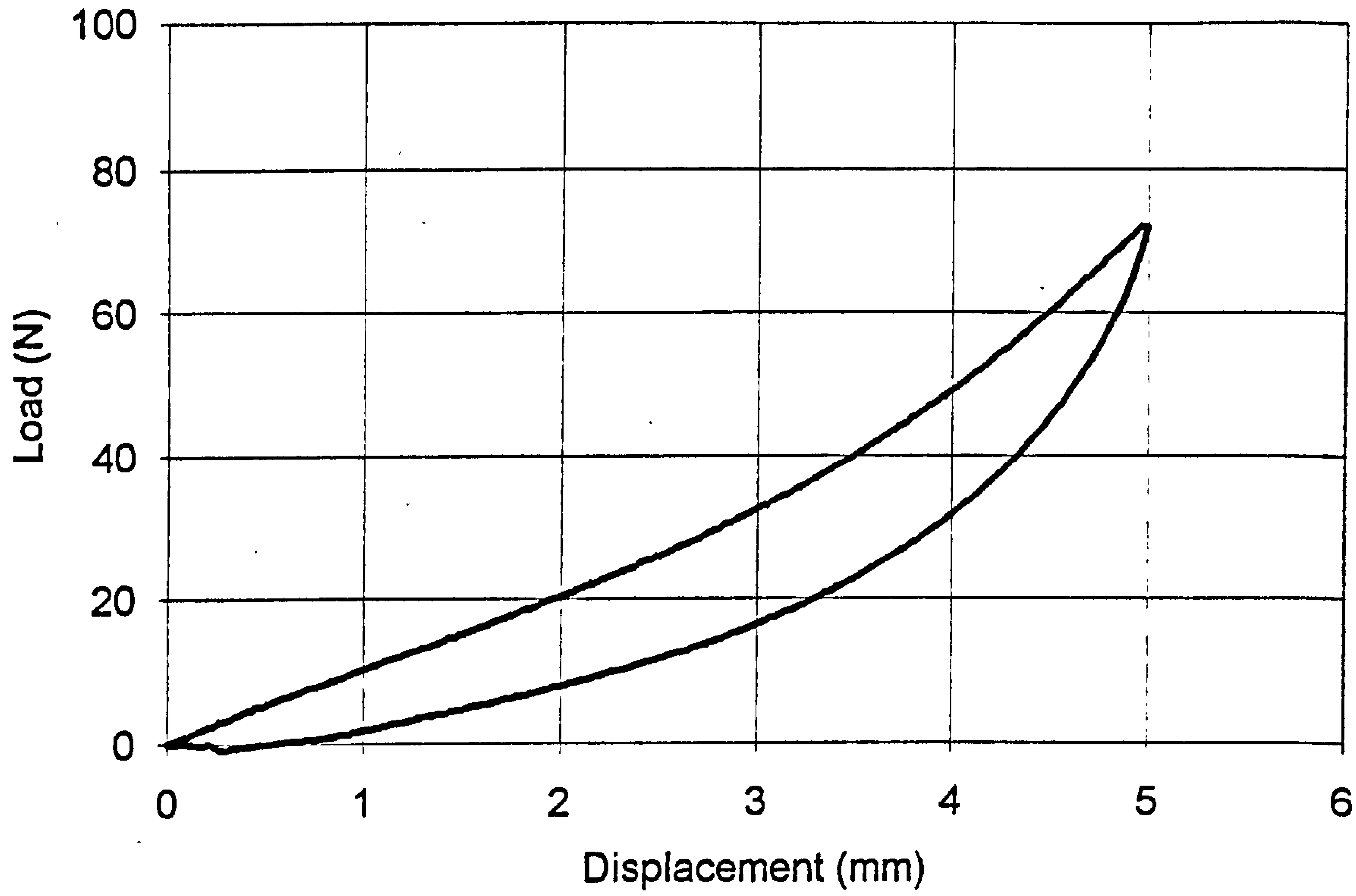

Fig. 6.4.6.1 Load - deflection plot of rubber indentation.
Rate of loading 5mm/min, indentor diameter 5mm.

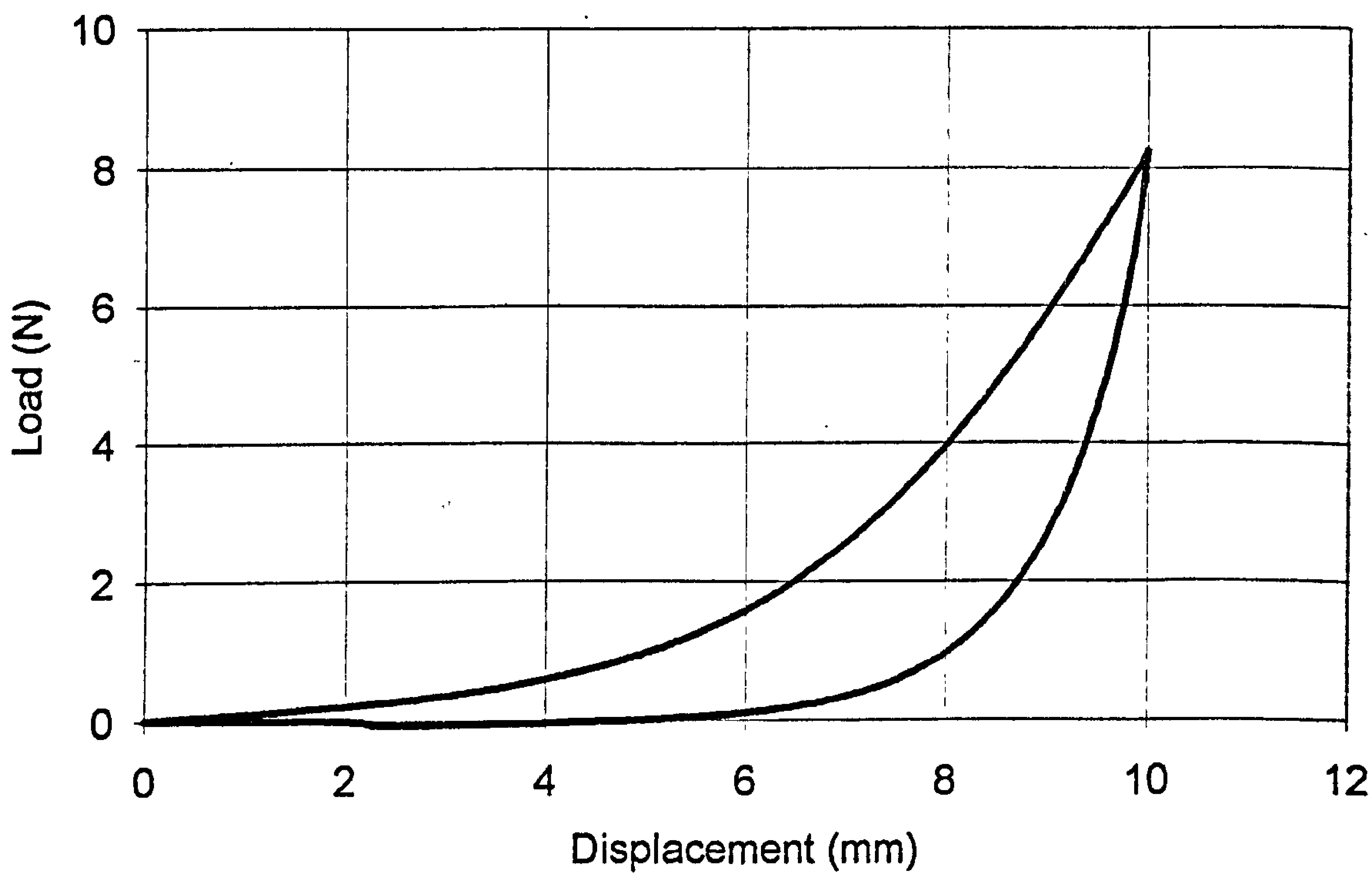

Fig. 6.4.6.2 Load - deflection plot of porcine indentation.
Rate of loading 5mm/min, indentor diameter 5mm.

shows little change in the gradient. After 0.1 strain, the moduli increases quickly producing a steep slope. Similar to rubber, the moduli were affected by the rate of loading, and a low rate of loading produce a lesser change in modulus with strain. The figures also shows that at 5 and 10 mm/min between 0 - 0.1 strain, the specimen behaves like a linear material with constant moduli. This was the region in the stress - strain curve where a low load produces large deflection in the specimen.

It was clear from these figures that it is insufficient to specify a single modulus for both rubber and porcine tissue without relating it to strain.

6.4.6 Results : Indentation test

The indentation tests were performed further to evaluate the FE models created under different material properties specifications. The results of the indentation test will be compared to a 3-D FE model of the indentation test, by matching the experimental and predicted load - deflection curve. In this section, the load - deflection data from the indentation tests are presented.

Fig. 6.4.6.1 and Fig. 6.4.6.2 show the load - deflection curves for rubber and porcine tissue when subjected to an indentor of 5 mm at a rate of loading of 5 mm/min. The maximum loads observed for rubber and porcine tissue were 71.82 N and 8.24 N. Both curves were non-linear, with porcine tissue showing a higher state of non linearity as expected. However, due to the low load experienced in the indentation test of the porcine tissue, the non-linear curve obtained differs from that commonly seen in tissue compression or tension. The three phases in the curve (i.e. the small slope due to large deformation produced by small load, the transition phase and the steep slope due to increase tissue stiffness) were not as clear as in the compression test.

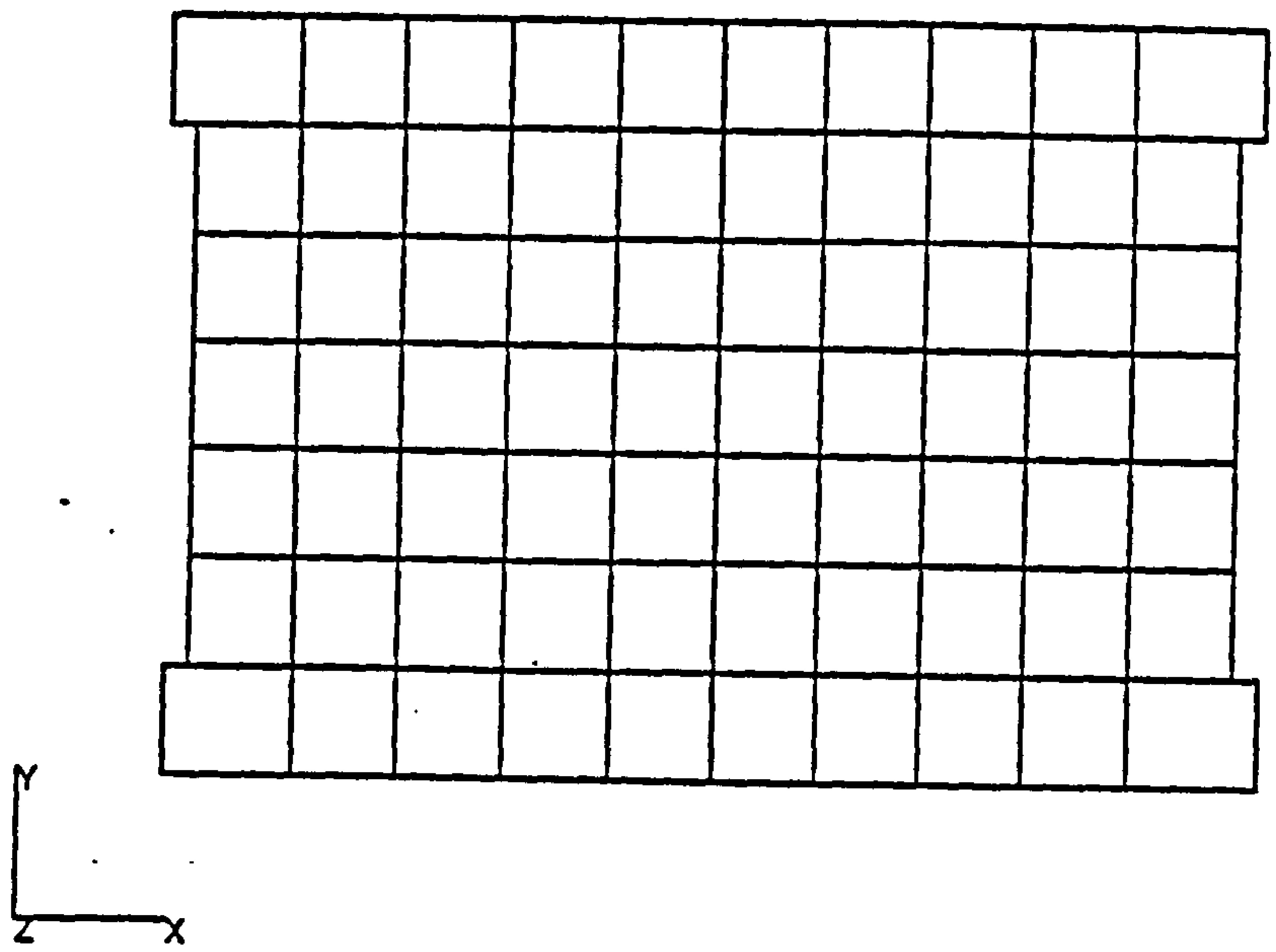

Fig. 6.5.1.1 Two dimensional FE model of rubber compression test.

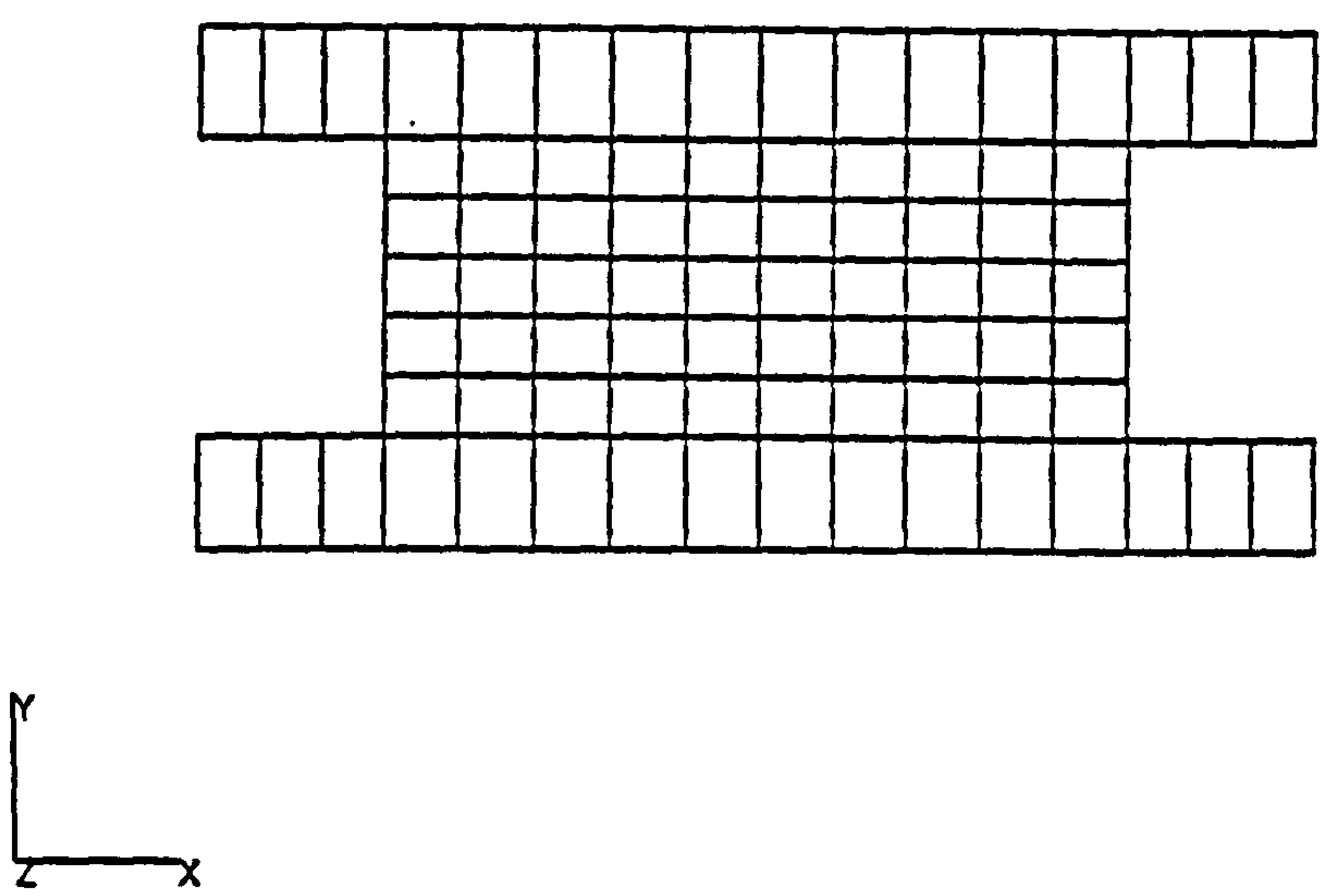

Fig. 6.5.1.2 Two dimensional FE model of porcine compression test.

6.5 FINITE ELEMENT MODELLING OF COMPRESSION AND INDENTATION TEST

Finite element models were created for rubber and porcine tissue under compression and indentation. The experiments described in section 6.4 were modelled with three types of material specifications, linear elastic, non-linear elastic and hyperelastic. Both engineering and true stress - strain conditions were considered for the three fore mentioned material specifications. The models were verified based on displacement data from the Instron test.

FE modelling was performed using commercial FE packages installed on SUN SPARC or Silicon Graphics Indigo II workstations. The FE packages were PATRAN version 2-5 (PDA Engineering, USA) and ABAQUS version 5.0 (Hibbitt, Karlsson and Sorensen, Inc. USA), where the former was used as a pre and post processor and the latter a solver.

6.5.1 FE model of the compression test

The FE model of the compression test was two dimensional, assuming plane stress conditions where the thickness of the material was considered. The FE models for rubber and porcine tissue are as shown in Fig. 6.5.1.1 and Fig. 6.5.1.2. Two types of finite elements were used in the models. The compression plates and specimen were meshed with two dimensional 4 noded quad elements (ABAQUS CPS4) Fig. 6.5.1.3. A total of 70 and 82 quad elements consisting 121 and 134 nodes were used for the rubber and porcine tissue models respectively. At the surface where the compression plates contact the specimen, a second type of element known as interface elements (ABAQUS INTER2) were sited Fig. 6.5.1.4. These elements are 2 dimensional and a total of 10 at each contact surfaces were assigned for both rubber and porcine tissue models. The interface elements allowed the specimen to slide freely at its contact surfaces at a direction tangential to the applied force. The amount of motion, hence shear stresses at the contact surfaces is dependent on the coefficient of friction (μ) specified at the contact surfaces. For both rubber and porcine tissue, μ was assumed as zero. This was a realistic value for the rubber compression test, since lubricant was applied in the experiments. In porcine tissue, μ was likely to range from

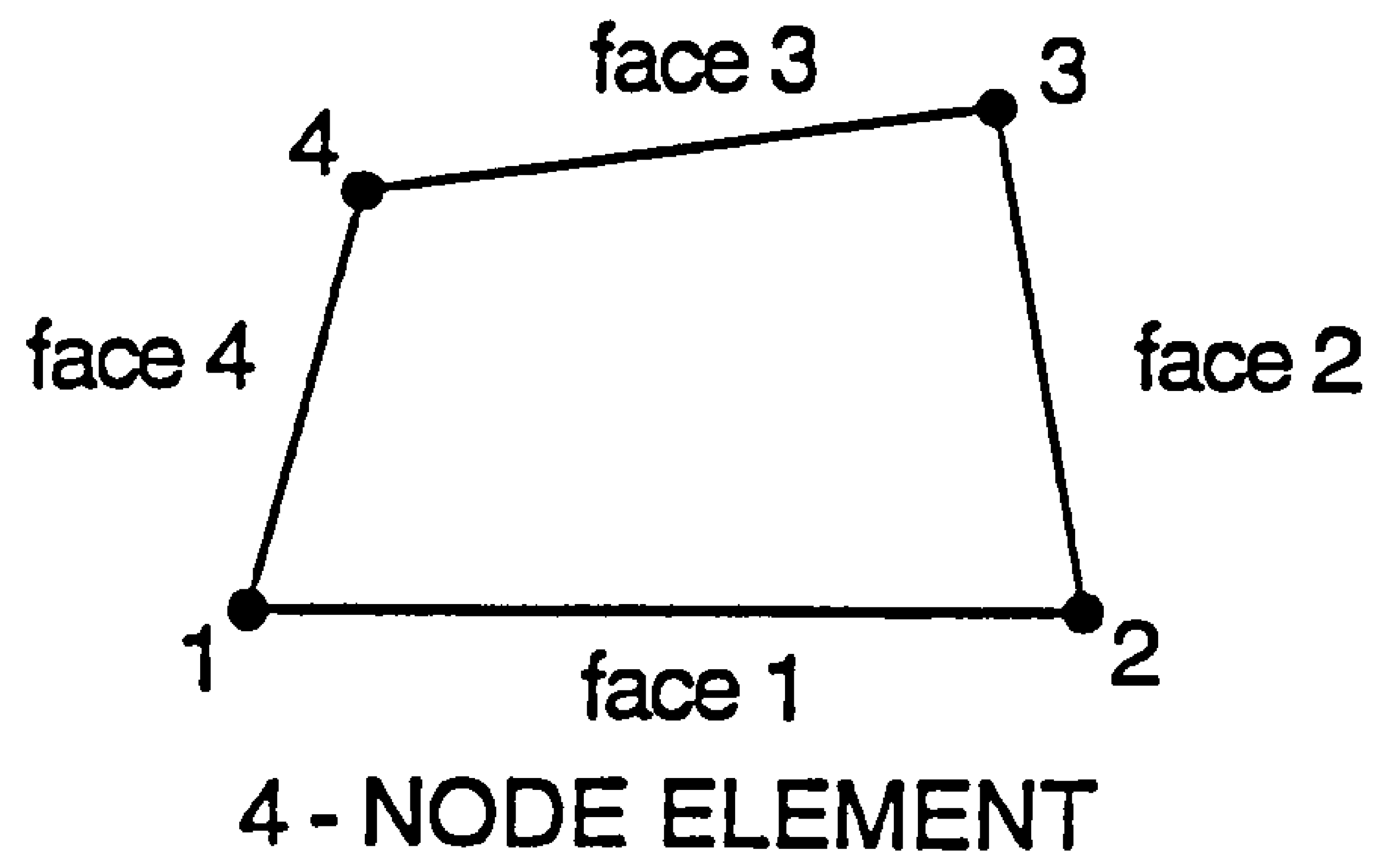

Fig. 6.5.1.3 Two dimensional 4 noded quad element (ABAQUS CPS4).

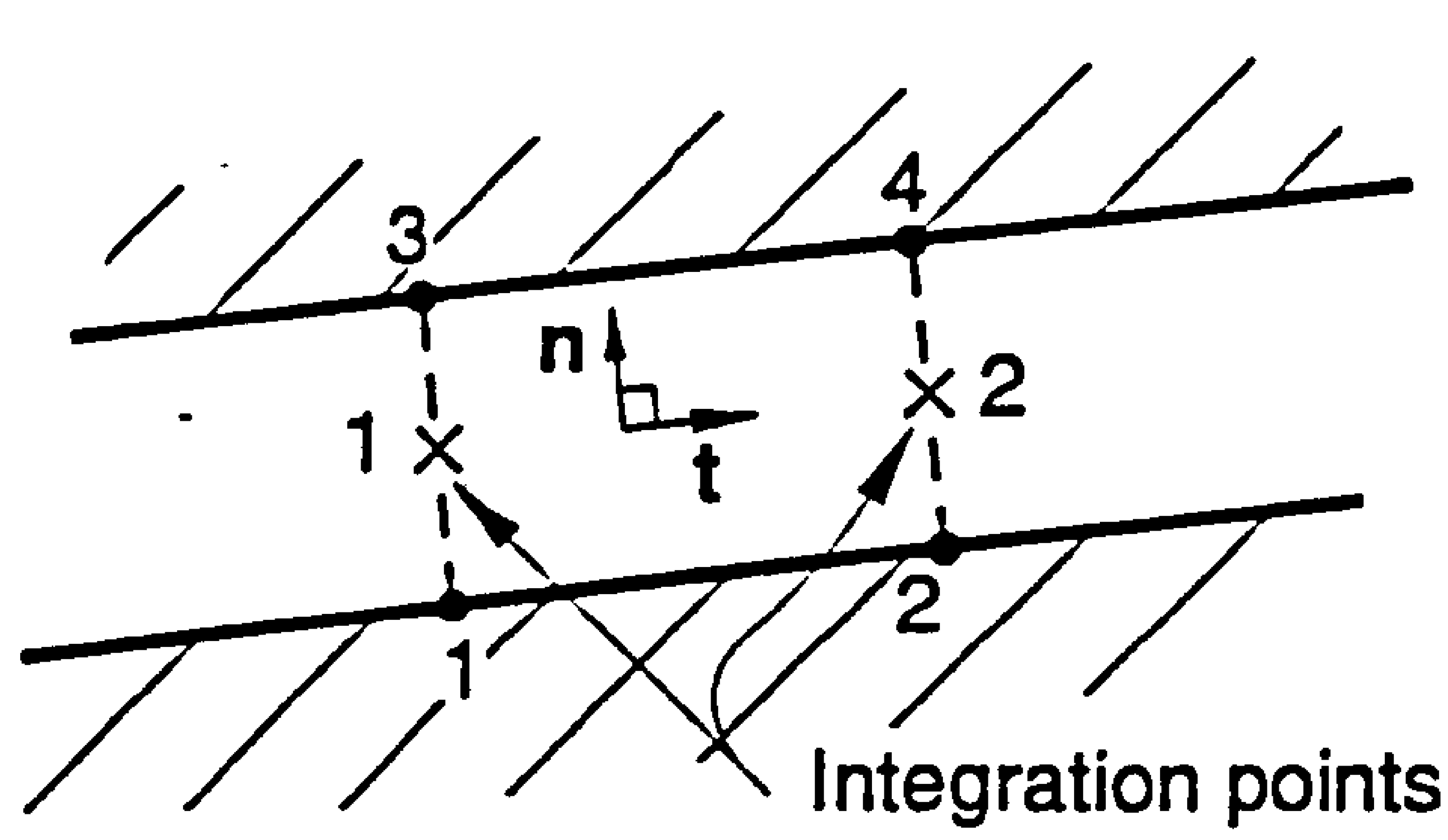

Fig. 6.5.1.4 Interface element (ABAQUS INTER2) use with 4 noded quad element.

0 to 0.2. However, zero was chosen to prevent numerical convergence problems, especially in cases when the models were assigned with non-linear material properties.

The boundary and loading conditions allocated to the models were as follows ; the bottom compression plate was fixed in the x and y direction and distributed forces were applied over the entire surface of the top compression plate. A central node of the specimen had to be fixed in the x direction. This was necessary to prevent the specimen from "falling out" of the compression plates or moving away from its central position with respect to the compression plates, causing numerical convergence problems.

Upon specifying the geometry, boundary and loading conditions, the subsequent inputs to the model were the magnitude of loading and the material properties. Both loading and material properties were derived from the specimen load - deflection curve from the experimental compression test. The material properties inputs were differentiated to give three types of FE analysis, linear elastic, non - linear elastic and hyperelastic as described in the following sections.

6.5.2 Linear elastic and non - linear elastic compression model

Table 6.5.2.1 and table 6.5.2.2 show the different linear elastic models attempted corresponding to the different parameters for rubber and porcine tissue specimens. Take for example model rub1 to model rub5. The force introduced to these FE models corresponded to the maximum load (2332.35 N) experienced in the experimental compression test of 10 mm displacement at a rate of loading of 5 mm/min. The elastic modulus (E_{1eng}) used in the FE analysis of rub1 was based on the experimental engineering stress - strain values as plotted in Fig. 6.4.5.10 and corresponded to the engineering strain of 0.0101 at a loading rate of 5 mm/min. Model rub2 elastic modulus (E_{2eng}) was also based on engineering stress - strain except it corresponded to the maximum engineering strain of 0.2020. Model rub3 elastic modulus (E_{1true}) was based on the true stress - strain values as previously plotted in Fig. 6.4.5.11 at a true strain of 0.0102, while model rub4 E_{2true} also based on the true stress - strain values was obtained at a maximum true strain value of 0.2258.

Model nos.	Rate of loading (mm/min)	Applied force (N)	Material properties (N/mm²)
rub1	5	2332.35	E_{1eng} = 0.729
rub2	5	2332.35	E_{2eng} = 2.469
rub3	5	2332.35	E_{1true} = 0.718
rub4	5	2332.35	E_{2true} = 1.763
rub5	5	2332.35	E*= 1.350
rub6	10	2474.55	E_{1eng} = 1.014
rub7	10	2474.55	E_{2eng} = 2.619
rub8	10	2474.55	E_{1true} = 0.998
rub9	10	2474.55	E_{2true} = 1.871
rub10	10	2474.55	E*= 1.430
rub11	50	3085.95	E_{1eng} = 0.790
rub12	50	3085.95	E_{2eng} = 3.267
rub13	50	3085.95	E_{1true} = 0.778
rub14	50	3085.95	E_{2true} = 2.333
rub15	50	3085.95	E*= 1.780
rub16	100	3480.37	E_{1eng} = 1.058
rub17	100	3480.37	E_{2eng} = 3.684
rub18	100	3480.37	E_{1true} = 1.042
rub19	100	3480.37	E_{2true} = 2.632
rub20	100	3480.37	E*= 2.012
rub21	200	3890.13	E_{1eng} = 1.376
rub22	200	3890.13	E_{2eng} = 4.118
rub23	200	3890.13	E_{1true} = 1.355
rub24	200	3890.13	E_{2true} = 2.941
rub25	200	3890.13	E*= 2.235

Table. 6.5.2.1 The finite element models attempted for rubber based on engineering and true modulus obtained from the experimental compression test. E* denotes the modulus which enables the FE analysis to predict the exact final displacement achieved in the compression experiment, i.e. 10 mm. This value is obtained by trial and error in the FE analysis.

Model nos.	Rate of loading (mm/min)	Applied force (N)	Material properties (N/mm^2)
po1	5	92.10	E_{1eng} = 0.0321
po2	5	92.10	E_{2eng} = 0.197
po3	5	92.10	E_{1true} = 0.0316
po4	5	92.10	E_{2true} = 0.144
po5	5	92.10	E* = 0.109
po6	10	103.22	E_{1eng} = 0.0251
po7	10	103.22	E_{2eng} = 0.221
po8	10	103.22	E_{1true} = 0.0248
po9	10	103.22	E_{2true} = 0.162
po10	10	103.22	E* = 0.119
po11	50	173.37	E_{1eng} = 0.0295
po12	50	173.37	E_{2eng} = 0.371
po13	50	173.37	E_{1true} = 0.0291
po14	50	173.37	E_{2true} = 0.272
po15	50	173.37	E* = 0.202
po16	100	199.02	E_{1eng} = 0.0321
po17	100	199.02	E_{2eng} = 0.426
po18	100	199.02	E_{1true} = 0.0317
po19	100	199.02	E_{2true} = 0.312
po20	100	199.02	E* = 0.234
po21	200	212.49	E_{1eng} = 0.0545
po22	200	212.49	E_{2eng} = 0.454
po23	200	212.49	E_{1true} = 0.0545
po24	200	212.49	E_{2true} = 0.333
po25	200	212.49	E* = 0.248

Table. 6.5.2.2 The finite element models attempted for porcine tissue based on engineering and true modulus obtained from the experimental compression test. E* denotes the modulus which enables the FE analysis to predict the exact final displacement achieved in the compression experiment, i.e. 5 mm. This value is obtained by trial and error in the FE analysis.

Model nos.	Rate of loading (mm/min)	Applied force (N)	Material properties
nrub1	5	2332.35	Eng. stress - strain values
nrub2	5	2332.35	True stress - strain values
nrub3	10	2474.55	Eng. stress - strain values
nrub4	10	2474.55	True stress - strain values
nrub5	50	3085.95	Eng. stress - strain values
nrub6	50	3085.95	True stress - strain values
nrub7	100	3480.37	Eng. stress - strain values
nrub8	100	3480.37	True stress - strain values
nrub9	200	3890.37	Eng. stress - strain values
nrub10	200	3890.37	True stress - strain values

Table 6.5.2.3 Finite element models attempted for rubber with non-linear elastic material properties.

Model nos.	Rate of loading (mm/min)	Applied force (N)	Material properties
npo1	5	92.10	Eng. stress - strain values
npo2	5	92.10	True stress - strain values
npo3	10	103.22	Eng. stress - strain values
npo4	10	103.22	True stress - strain values
npo5	50	173.37	Eng. stress - strain values
npo6	50	173.37	True stress - strain values
npo7	100	199.02	Eng. stress - strain values
npo8	100	199.02	True stress - strain values
npo9	200	212.49	Eng. stress - strain values
npo10	200	212.49	True stress - strain values

Table 6.5.2.4 Finite element models attempted for porcine tissue with non-linear elastic properties.

Finally, rub5 elastic modulus (E*) was selected through a process of trial and error so that when it was introduced to the model, it would predict an exact final displacement of 10 mm as in the experimental compression test for rubber.

The Poisson's ratio used in the analysis was 0.4999 approaching that of an incompressible material. The material was also assumed to be isotropic. The analysis was performed under incremental loading (load steps at 10% of maximum load), which accounts for the large displacement effect seen in the rubber and porcine tissue during compression.

In the non-linear elastic model, the material properties for rubber and porcine tissue were defined by the complete stress - strain curve obtained in the compression test. In other words, the analyses take into consideration a set of Young's moduli which vary with strain. An incremental analysis with load steps at 5% of maximum load was applied. The specimens were again assumed to be isotropic and nearly incompressible (Poisson's ratio of 0.4999).

Referring to section 6.4.5, the experimental engineering and true stress - strain values for the five loading rates (5, 10, 50, 100 and 200 mm/min) were input as material properties in ABAQUS. These values are already plotted in section 6.4.5 as Fig. 6.4.5.5 to Fig. 6.4.5.8. Loading and boundary conditions were kept similar as in the elastic model discussed above. Therefore the non-linear material models for rubber and porcine tissue are as tabulated in table 6.5.2.3 and table 6.5.2.4.

6.5.3 Hyperelastic compression model

Hyperelastic or the Mooney- Rivlin (M-R) material was the third material property considered. As discussed earlier in section 6.3.2, the strain energy function is given by,

$$W = C_{10}(I_1 - 3) + C_{01}(I_2 - 3) \qquad (6.5.3a)$$

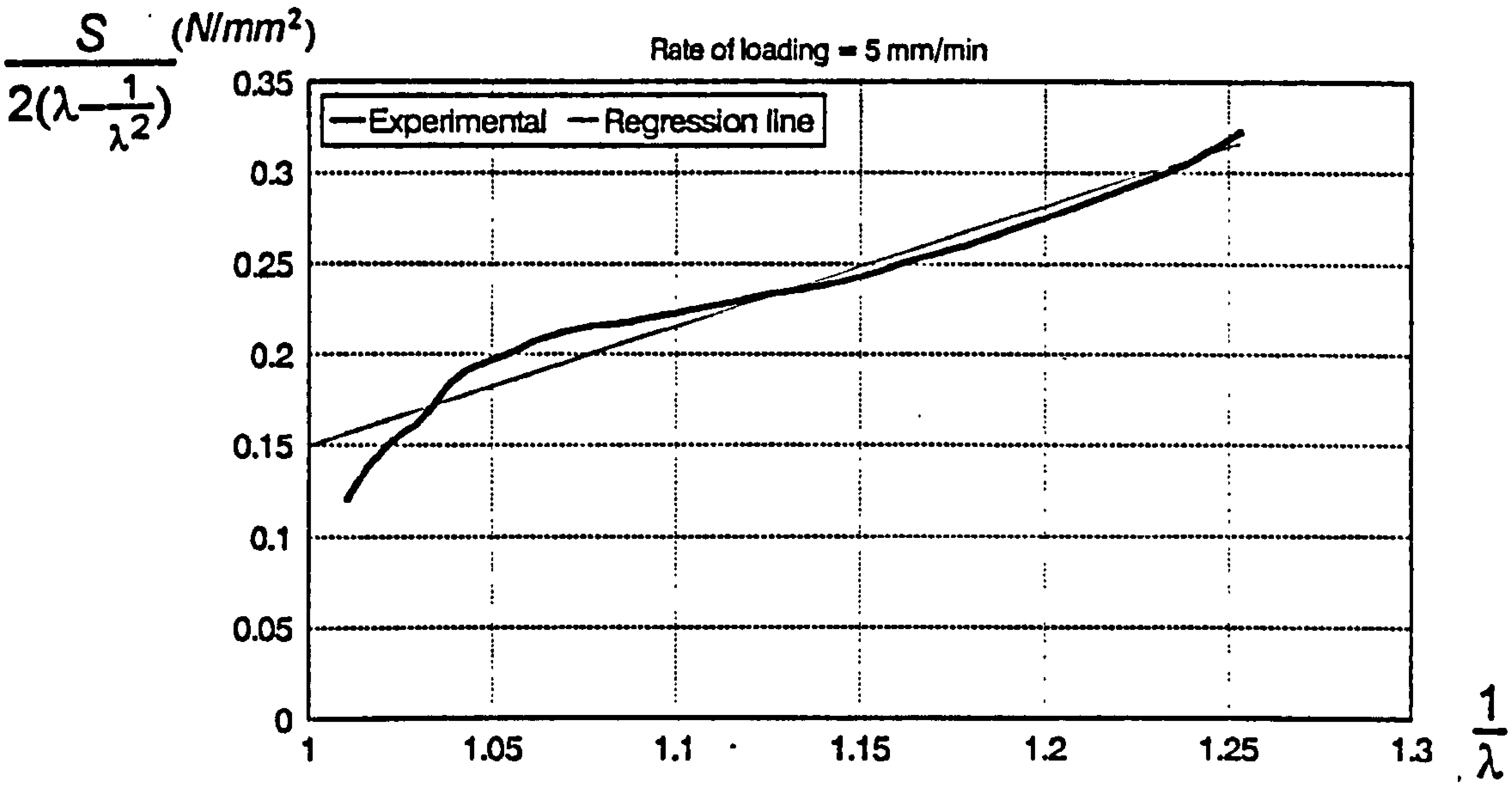

Fig. 6.5.3.1 Plot of $\frac{S}{2(\lambda-\frac{1}{\lambda^2})}$ versus $\frac{1}{\lambda}$. Mooney - Riv.lin constants C_{10}= -0.5097 N/mm^2 and C_{01}=0.6592 N/mm^{2}for rubber loaded at 5 mm/min.

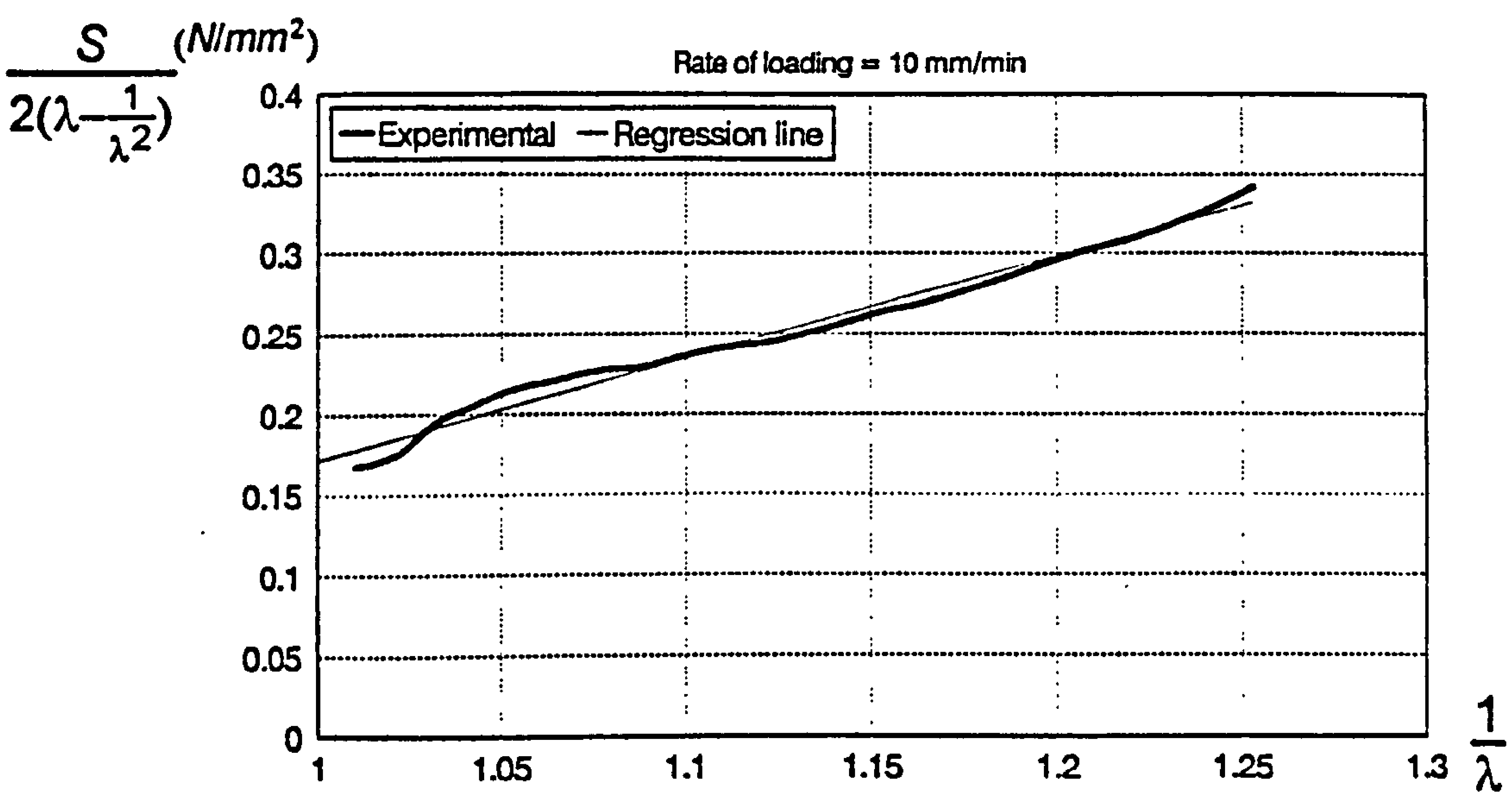

Fig. 6.5.3.2 Plot of $\frac{S}{2(\lambda-\frac{1}{\lambda^2})}$ versus $\frac{1}{\lambda}$. Mooney - Riv.lin constants C_{10}= -0.4649 N/mm^2 and C_{01}=0.6362 N/mm^2 for rubber loaded at 10 mm/min.

where $C_{10} = \frac{dW}{dI_1}$ and $C_{01} = \frac{dW}{dI_2}$ are constants. I_1 and I_2 are the principal extension ratio as previously defined in equation 6.3.2q and 6.3.2r respectively. Assuming isotropy and incompressibility, for cases of simple tension or compression, the following equation can be derived,

$$\frac{S}{2(\lambda - \frac{1}{\lambda^2})} = C_{10} + \frac{1}{\lambda} C_{01} \qquad (6.5.3b)$$

where S is the engineering stress and λ the extension ratio. Also discussed in section 6.3.2, any material obeying the M-R expression should produce a straight line when $\frac{S}{2(\lambda - \frac{1}{\lambda^2})}$ is plotted against $\frac{1}{\lambda}$, yielding C_{10} as the y-intercept and C_{01} as the gradient. In the compression FE model, ABAQUS requires C_{10} and C_{01} as inputs to define a M-R material. The two constants were therefore obtained by plotting the experimental compression test in the form of equation 6.5.3b for rubber and porcine tissue for the different rate of loadings.

Fig. 6.5.3.1 to Fig. 6.5.3.5 show the plots of $\frac{S}{2(\lambda - \frac{1}{\lambda^2})}$ versus $\frac{1}{\lambda}$ for rubber loaded at 5, 10, 50, 100 and 200 mm/min respectively. The plots produced a straight line with slight deviation observed between $\frac{1}{\lambda}$=1 to 1.1. This deviation increases as the rate of loading increases. In order to obtain the constants, the least squares method, which chooses a straight line that gives the smallest deviation from the experimental values was used. From this straight line C_{10} and C_{01} were calculated. Table 6.5.3.1 tabulates the five FE models performed for rubber with their respective loadings and M-R constants.

A similar plot of $\frac{S}{2(\lambda - \frac{1}{\lambda^2})}$ versus $\frac{1}{\lambda}$ was performed for the compression test on porcine tissue loaded at 5 mm/min as shown in Fig. 6.5.3.6. The plot produced a non-linear curve with decreasing gradient between $\frac{1}{\lambda}$=1 to 1.1, and an increasing gradient between $\frac{1}{\lambda}$= 1.1 to 1.25. The non-linear curve clearly showed that M-R function could not be applied to porcine tissue. As discussed previously in section 6.3.2, the study by Veronda and Westmann (1970) had already shown that the M-R

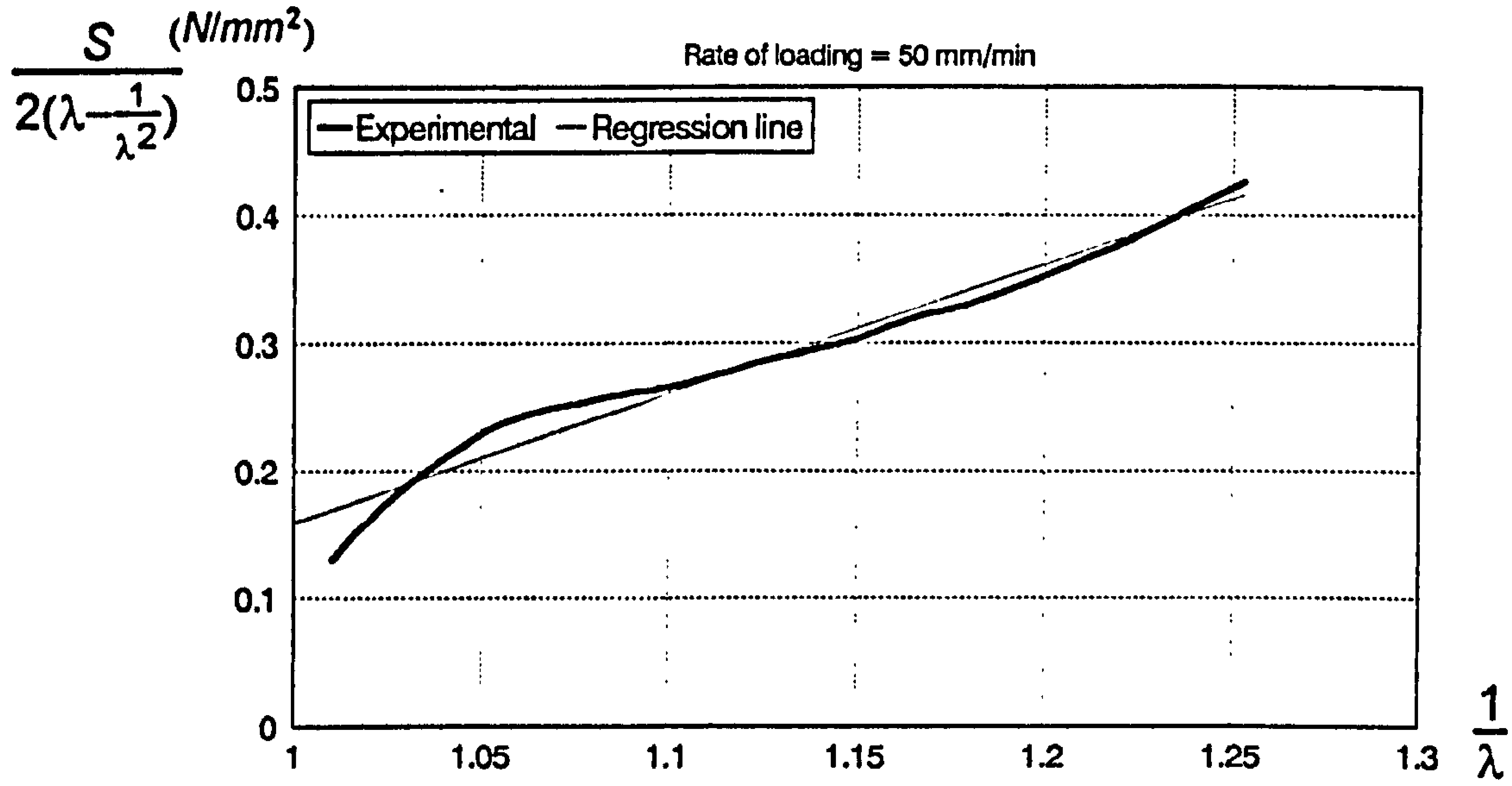

Fig. 6.5.3.3 Plot of $\frac{S}{2(\lambda-\frac{1}{\lambda^2})}$ versus $\frac{1}{\lambda}$. Mooney - Rivlin constants C_{10}= -0.8575 N/mm^2 and C_{01}=1.0166 N/mm^2 for rubber loaded at 50 mm/min.

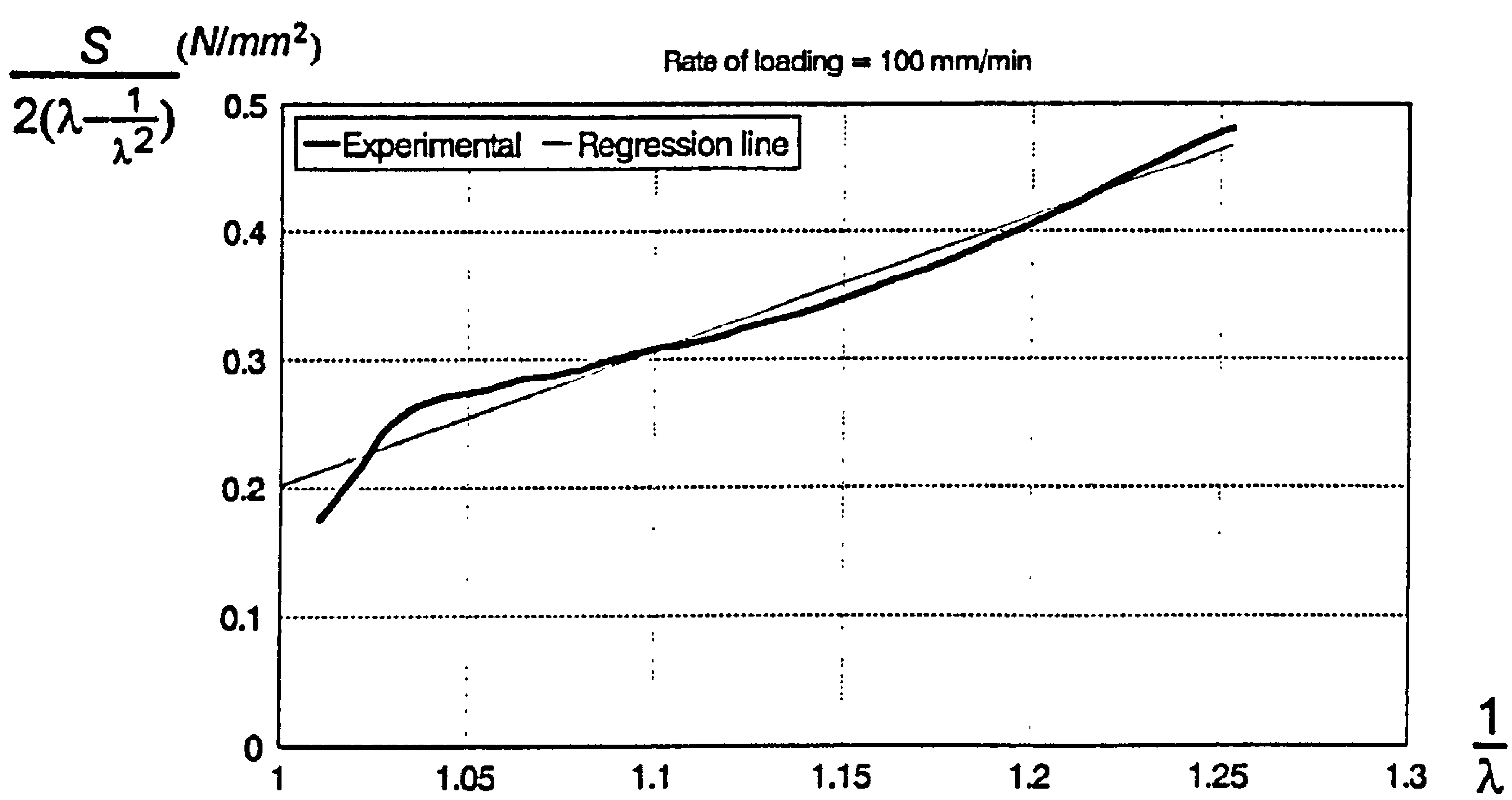

Fig. 6.5.3.4 Plot of $\frac{S}{2(\lambda-\frac{1}{\lambda^2})}$ versus $\frac{1}{\lambda}$. Mooney - Rivlin constants C_{10}= -0.8465 N/mm^2 and C_{01}=1.0487 N/mm^2 for rubber loaded at 100 mm/min.

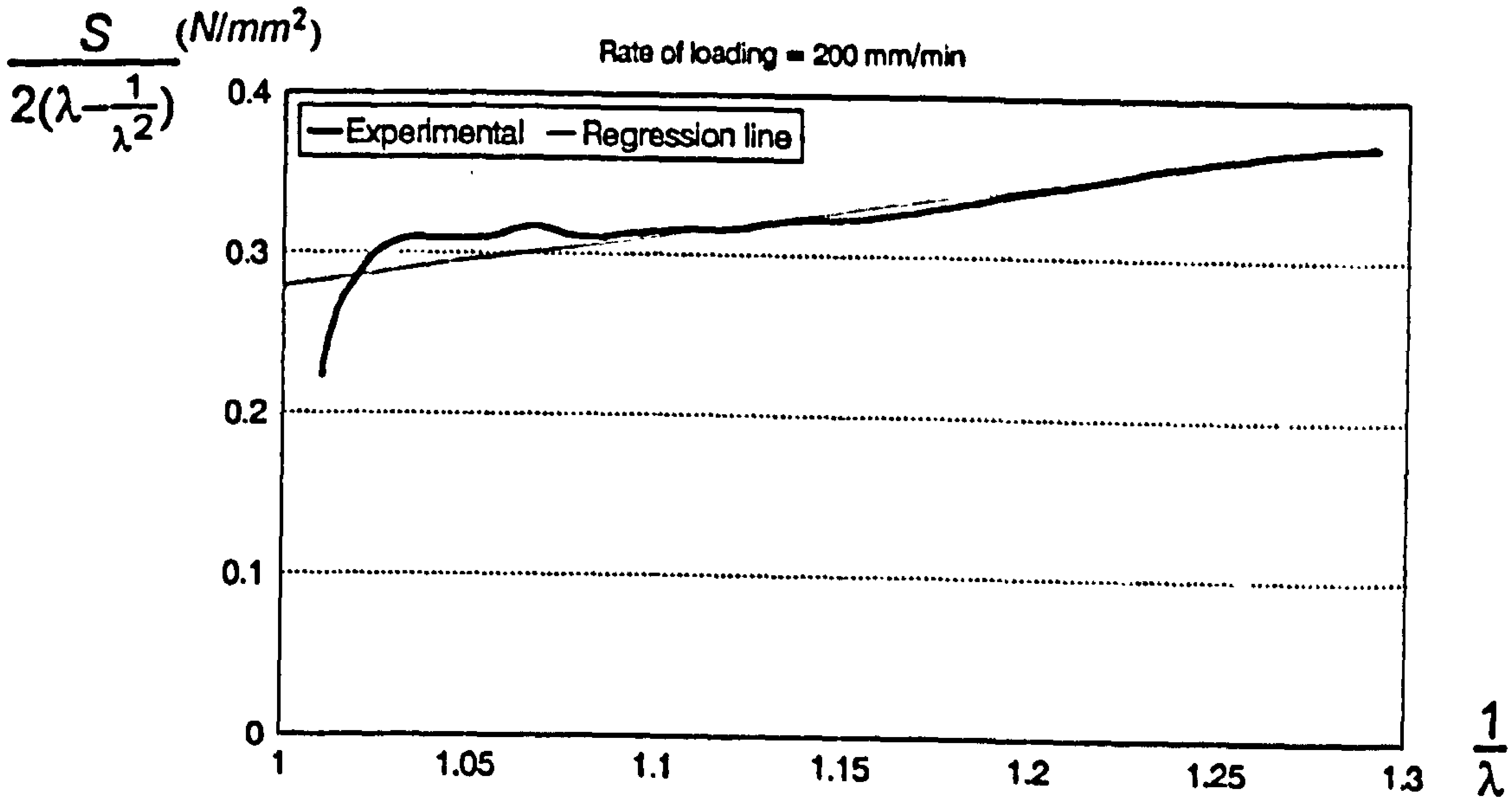

Fig. 6.5.3.5 Plot of $\frac{S}{2(\lambda-\frac{1}{\lambda^2})}$ versus $\frac{1}{\lambda}$. Mooney - Rivlin constants C_{10}= -0.0430 N/mm^2 and C_{01}=0.3229 N/mm^2 for rubber loaded at 200 mm/min.

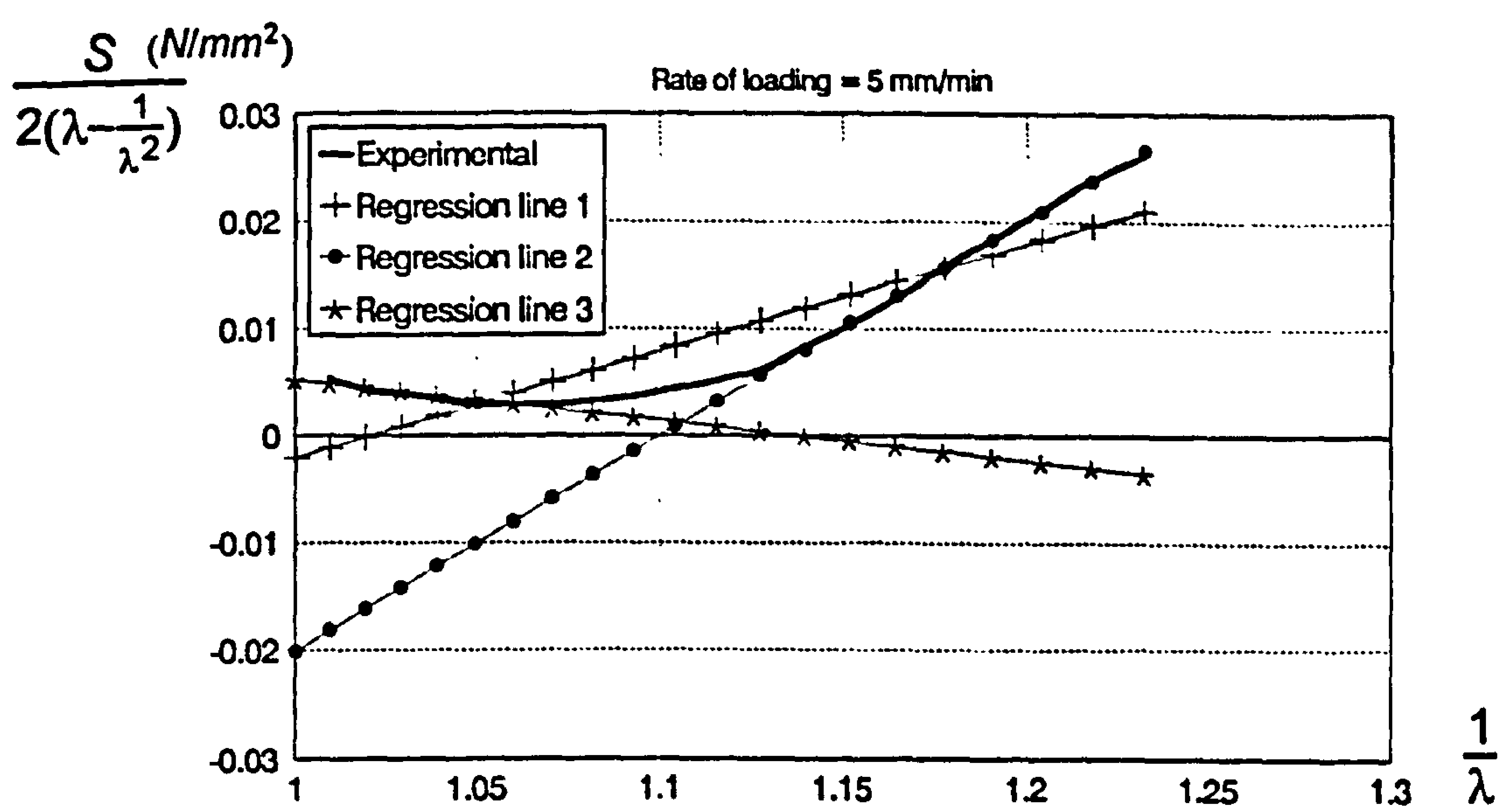

Fig. 6.5.3.6 Plot of $\frac{S}{2(\lambda-\frac{1}{\lambda^2})}$ versus $\frac{1}{\lambda}$ for porcine tissue loaded at 5 mm/min.

-Regression line 1 based on data ranging from $\frac{1}{\lambda}$ = 1 to 1.24 where Mooney - Rivlin constants are C_{10}= -0.1018 N/mm^2 and C_{01}=0.0997 N/mm^2.

-Regression line 2 based on data ranging from $\frac{1}{\lambda}$ = 1.12 to 1.24 where Mooney - Rivlin constants are C_{10}= -0.2212 N/mm^2 and C_{01}=0.2011 N/mm^2.

-Regression line 3 based on data ranging from $\frac{1}{\lambda}$ = 1 to 1.08 where Mooney - Rivlin constants are C_{10}= 0.0424 N/mm^2 and C_{01}= -0.0373 N/mm^2.

Model nos.	Rate of loading (mm/min)	Applied force (N)	C_{10}	C_{01}
hrub1	5	2332.35	-0.8575	1.0166
hrub2	10	2474.55	-0.8465	1.0487
hrub3	50	3085.95	-0.5097	0.6592
hrub4	100	3480.37	-0.4649	0.6362
hrub5	200	3890.13	-0.0430	0.3229

Table 6.5.3.1 Finite element models attempted for rubber based on hyperelastic materials.

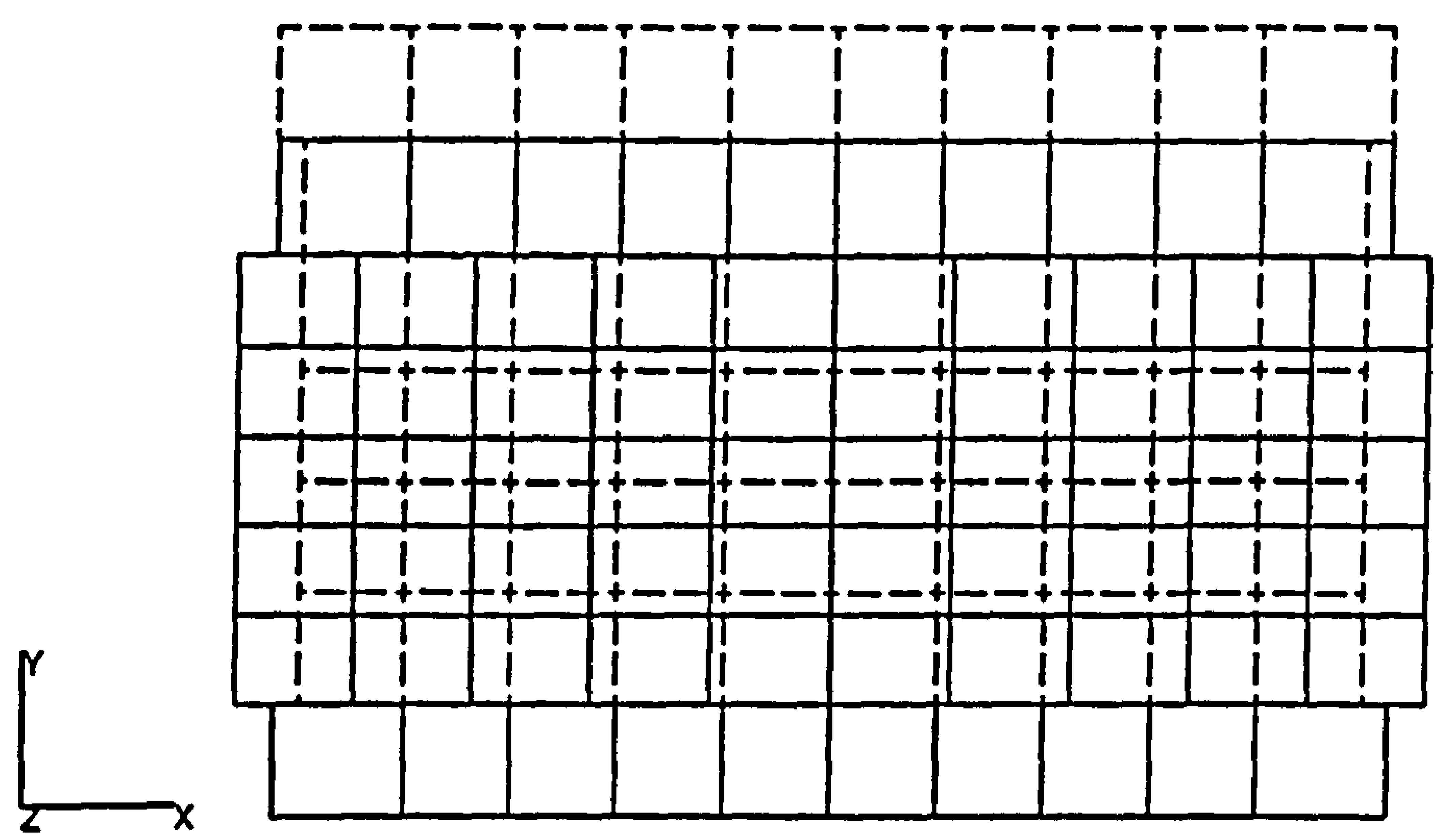

Fig. 6.5.4.1 Rubber compression model displacement plot.
(dashed line - original model, continous line - deformed model)

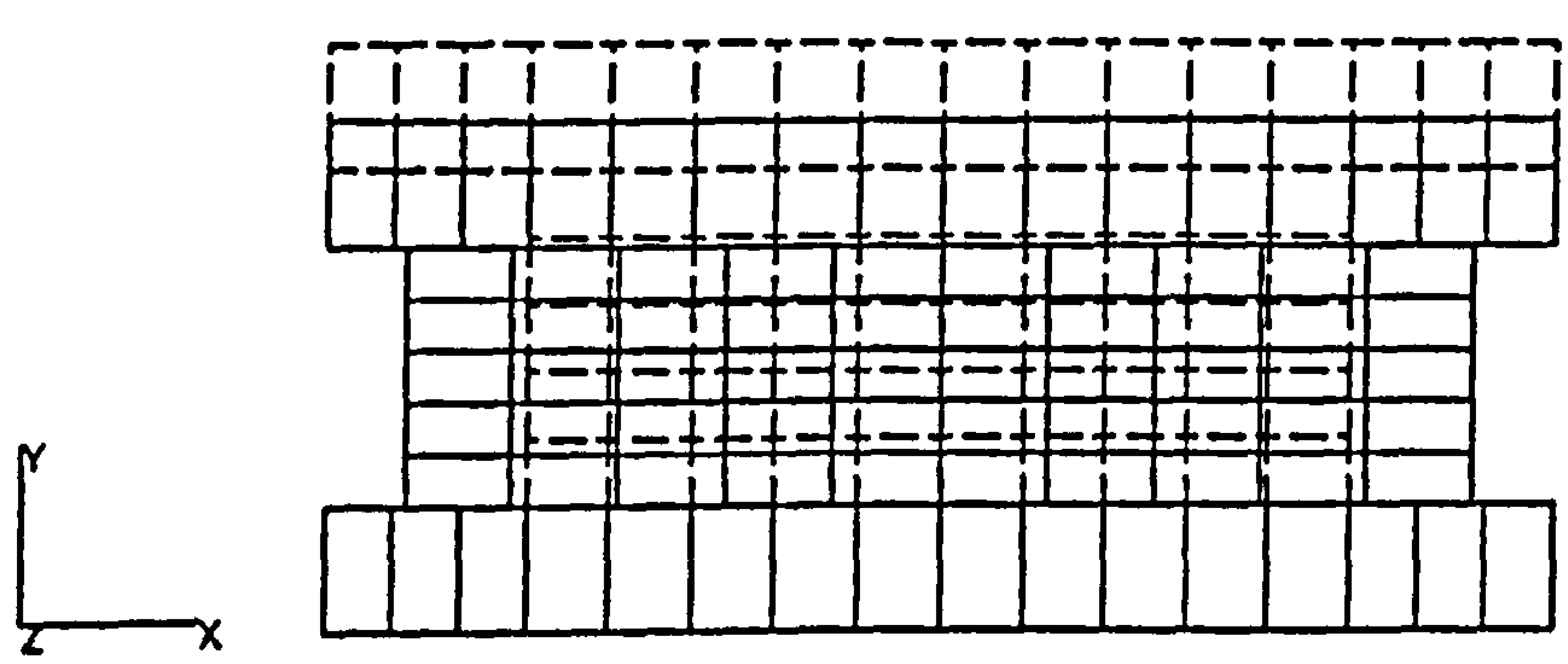

Fig. 6.5.4.2 Porcine tissue compression model displacement plot.
(dashed line - original model, continous line - deformed model)

function was insufficient to model cat skin. Nevertheless, in this study, using the least square method, three regression lines were derived to give three sets of M-R constants. Regression line 1 was based on the complete curve, while regression line 2 and 3 were based on the curve ranging from $\frac{1}{\lambda}$=1.12 to 1.24 and $\frac{1}{\lambda}$=1 to 1.08 respectively. The three sets of material constants were than implemented in FE model of the porcine tissue compression test at a loading rate of 5 mm/min. Unlike rubber, further FE modelling for the other rate of loading was not performed. This was because the FE analysis for the present model (5 mm/min) had failed to converge. More details will be discussed in the result.

Both the rubber and porcine FE models were performed under incremental loadings. In rubber, increments was set to 5% of the maximum load whilst in the porcine tissue model, automatic step loading was performed. Automatic step loading requires the first load step to be specified and in the porcine tissue model, this was set to 0.1% of the maximum load. ABAQUS performed the first load step using this increment, and if convergence occurred the increment was automatically increased. The procedure repeated until the maximum load had been reached. Automatic step loading was chosen for the porcine tissue model because of the convergence problems encountered.

6.5.4 Results of compression model : linear elastic analysis

Fig. 6.5.4.1 and Fig. 6.5.4.2 show the FE model displacement plots for rubber and porcine tissue. The use of interface elements allowed the specimens to slide along the compression plates, modelling effects due to compression loads only. To assess the validity of the models using linear elastic material properties, the predicted displacements were plotted against the experimental load - displacement data. The results were presented in the following manner ;

For each rate of loading two graphs were drawn, one for the analysis which based its material properties on the engineering elastic modulus, and the other on the true elastic modulus. Each graph contained four plots of displacement versus load data. These were obtained from,

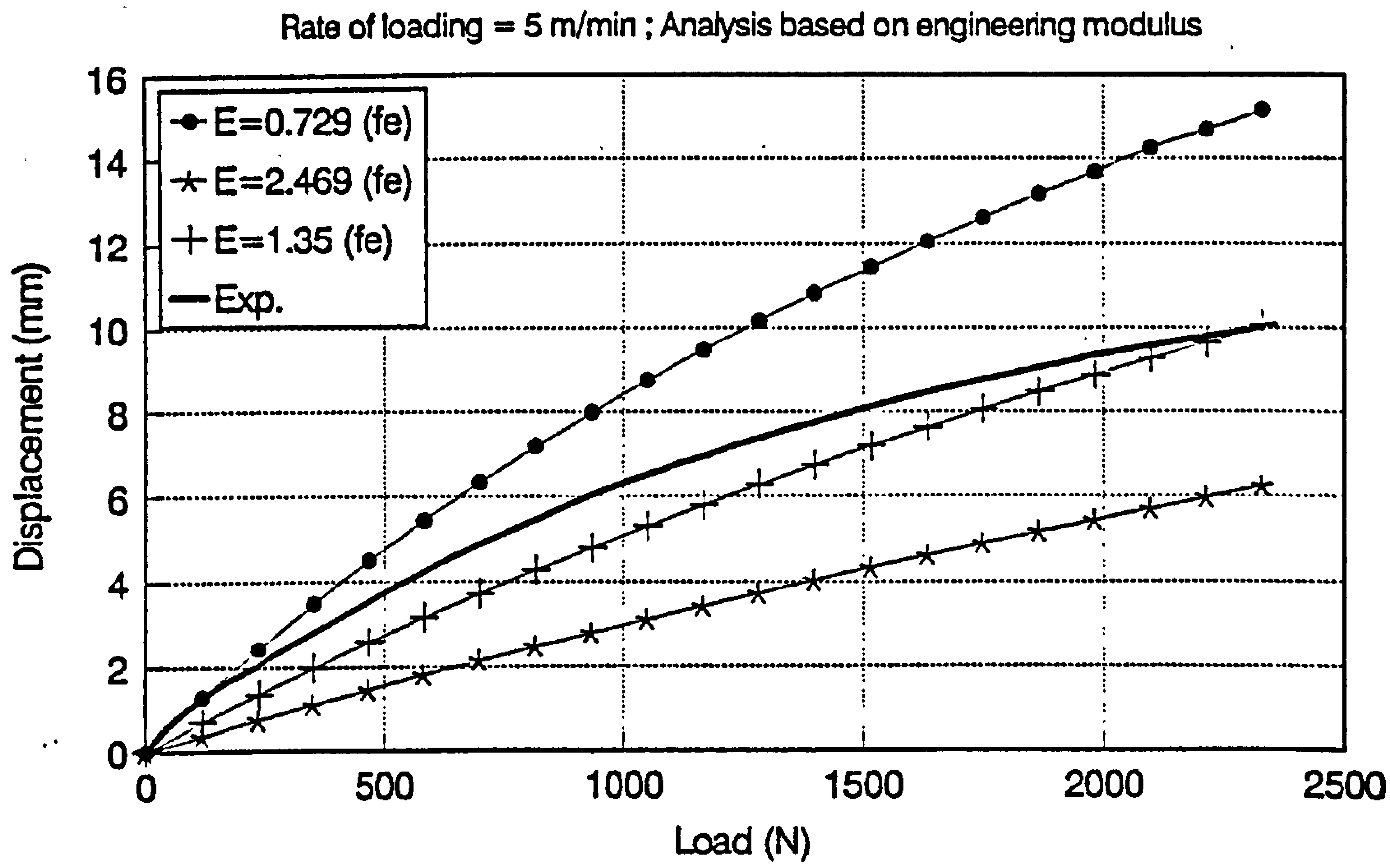

Fig. 6.5.4.3 Comparison between FE and experimental results.
(Rate of loading 5 mm/min ; FE model rub1, 2, and 5)

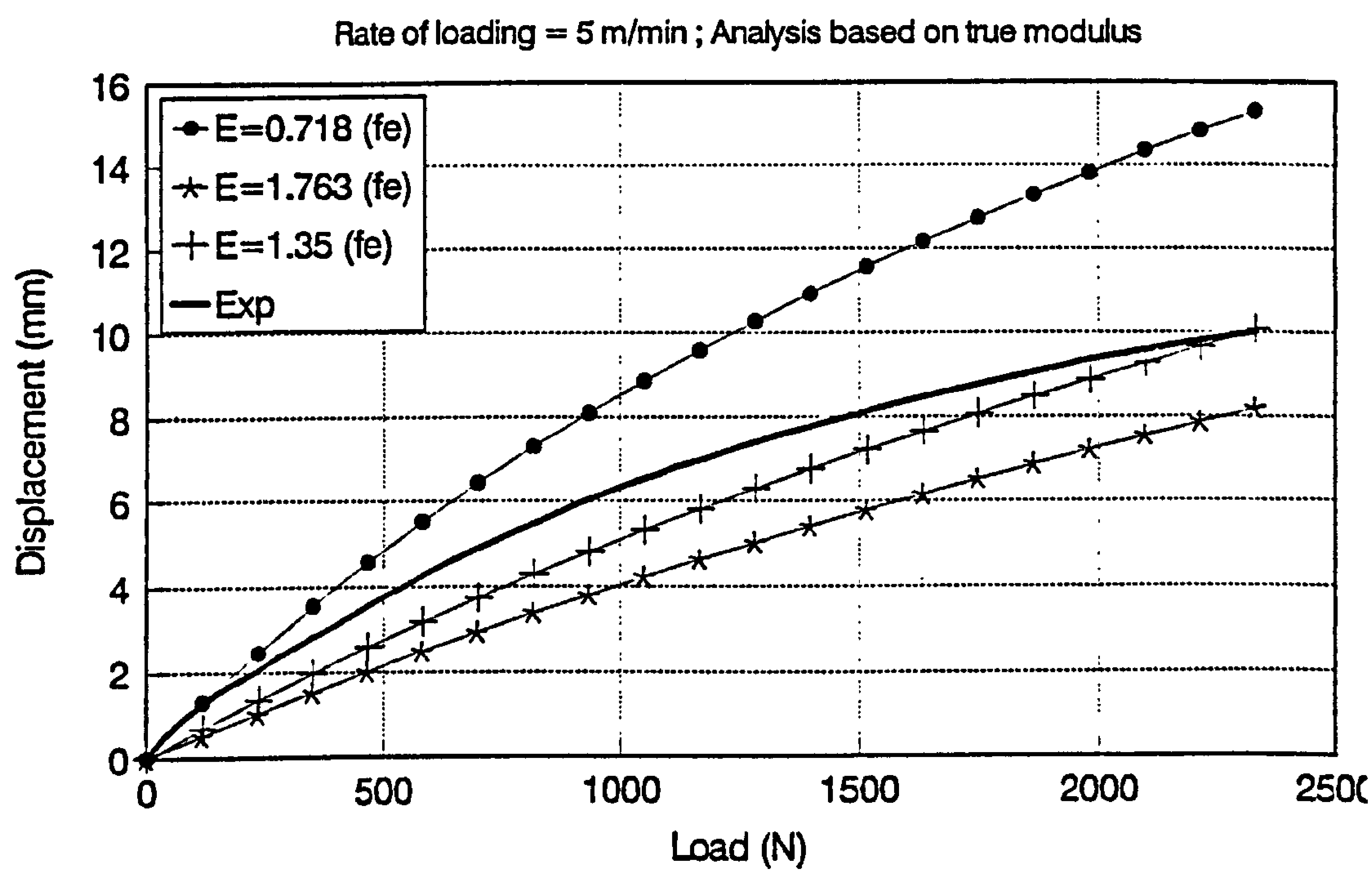

Fig. 6.5.4.4 Comparison between FE and experimental results.
(Rate of loading 5 mm/min ; FE model rub3, 4, and 5)

a) FE model assigned with elastic modulus corresponding to small strains,

b.) FE model assigned with elastic modulus corresponding to maximum strains,

c.) FE model assigned with elastic modulus that gave an exact final displacement similar to that obtained during experimental compression test and

d.) the experimental compression test.

Fig. 6.5.4.3 to Fig. 6.5.4.12 plot the results for rubber and Fig. 6.5.4.13 to Fig. 6.5.4.22 plot the results for porcine tissue.

From these plots, the following general observations can be made ;

- The FE analyses predicted displacements showed a larger deviation from the experimental values when engineering modulus was used instead of true modulus.

- The predicted displacements based on both engineering and true modulus failed to follow the experimental curve closely. The predicted curves using a modulus at small strains were only slightly non - linear, while a modulus based on maximum strains produced a straight line.

- The exact final displacement can be predicted if a suitable modulus (E*) was selected. E* was within the range of moduli that were calculated based on small (E_{1eng} and E_{1true}) and maximum strain (E_{2eng} and E_{2true}) for different rate of loadings. It was also observed that the mean percentage difference achieved by $\frac{E_{2true} - E^*}{E_{2true}}$ or $\frac{E_{2eng} - E^*}{E_{2eng}}$ for all five different rate of loadings were 23.65 ± 0.22 % and 45.46 ± 0.15 % for rubber and 25.42 ± 0.83 % and 45.36 ± 0.55 % for porcine tissue respectively. The percentage difference varied little regardless of strain rate as seen by the minimal standard deviation. The small standard deviation also suggested the possibility that E* can be approximated by,

$$E^* = 0.45\, E \qquad (6.5.4a)$$

where E is the engineering elastic modulus at maximum strain condition. This therefore provides a guideline in choosing a suitable modulus for modelling a non-linear material using linear elastic material properties in the finite element method.

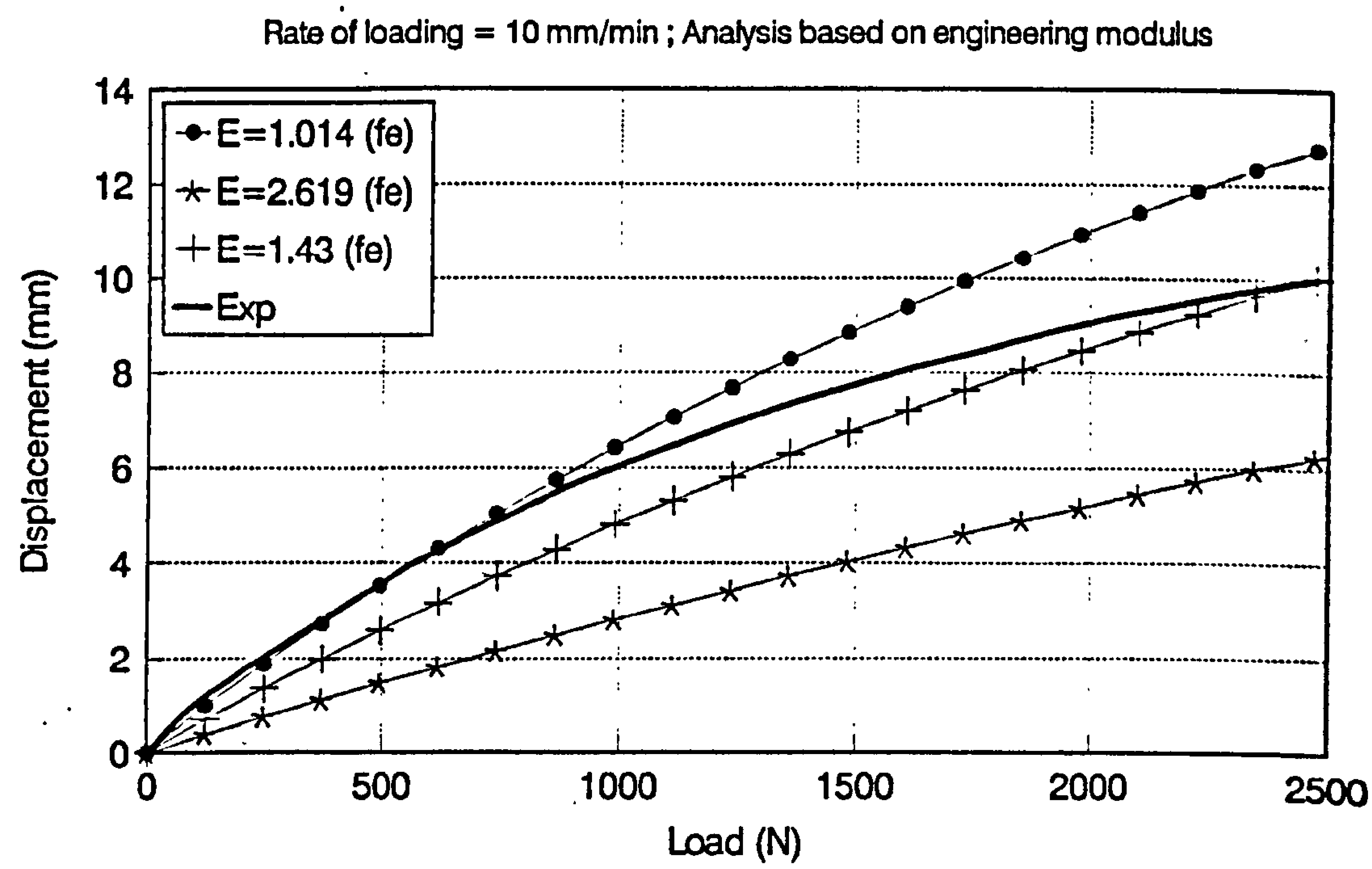

Fig. 6.5.4.5 Comparison between FE and experimental results.
(Rate of loading 10 mm/min ; FE model rub6, 7, and 10)

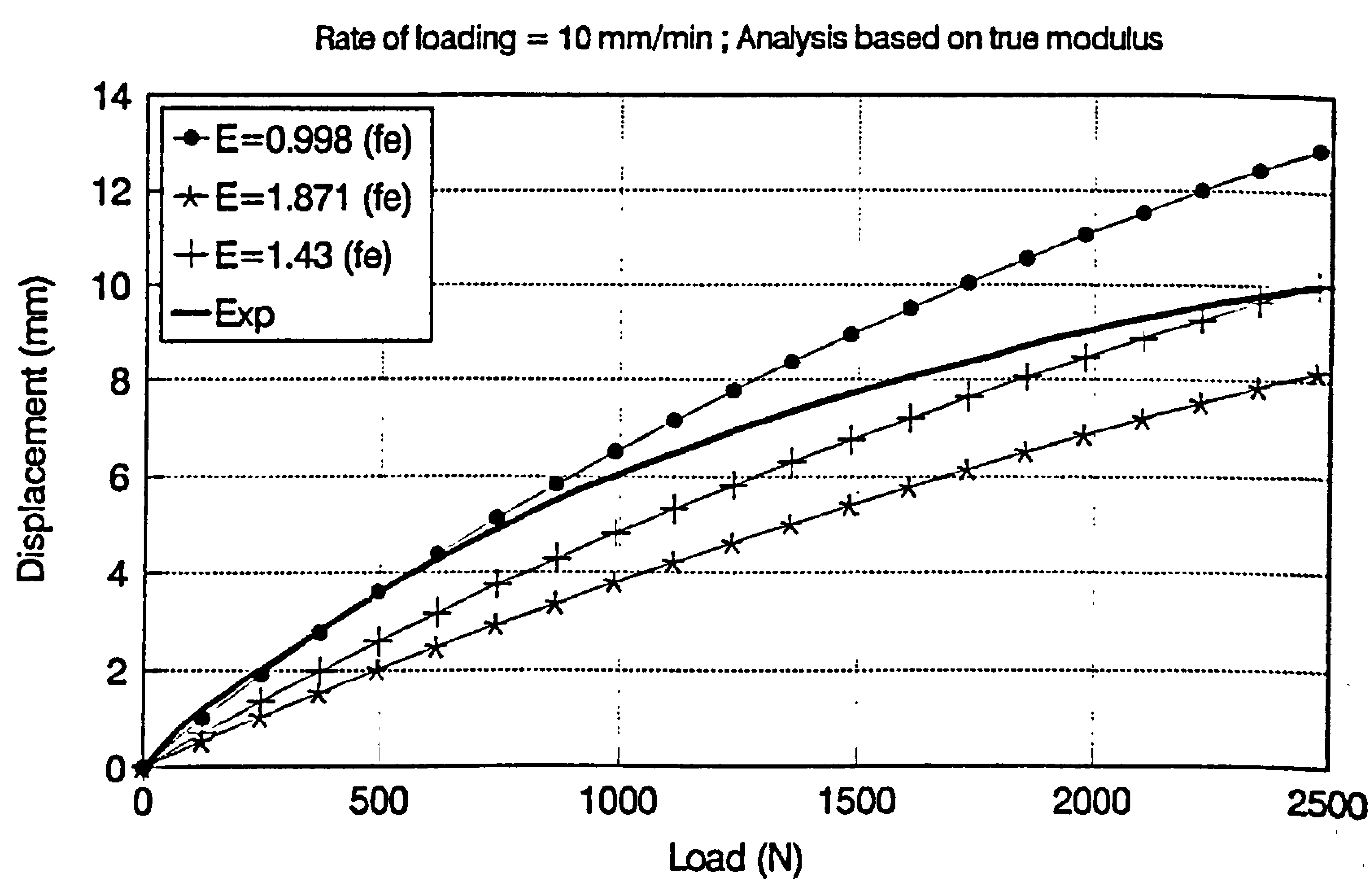

Fig. 6.5.4.6 Comparison between FE and experimental results.
(Rate of loading 10 mm/min ; FE model rub8, 9, and 10)

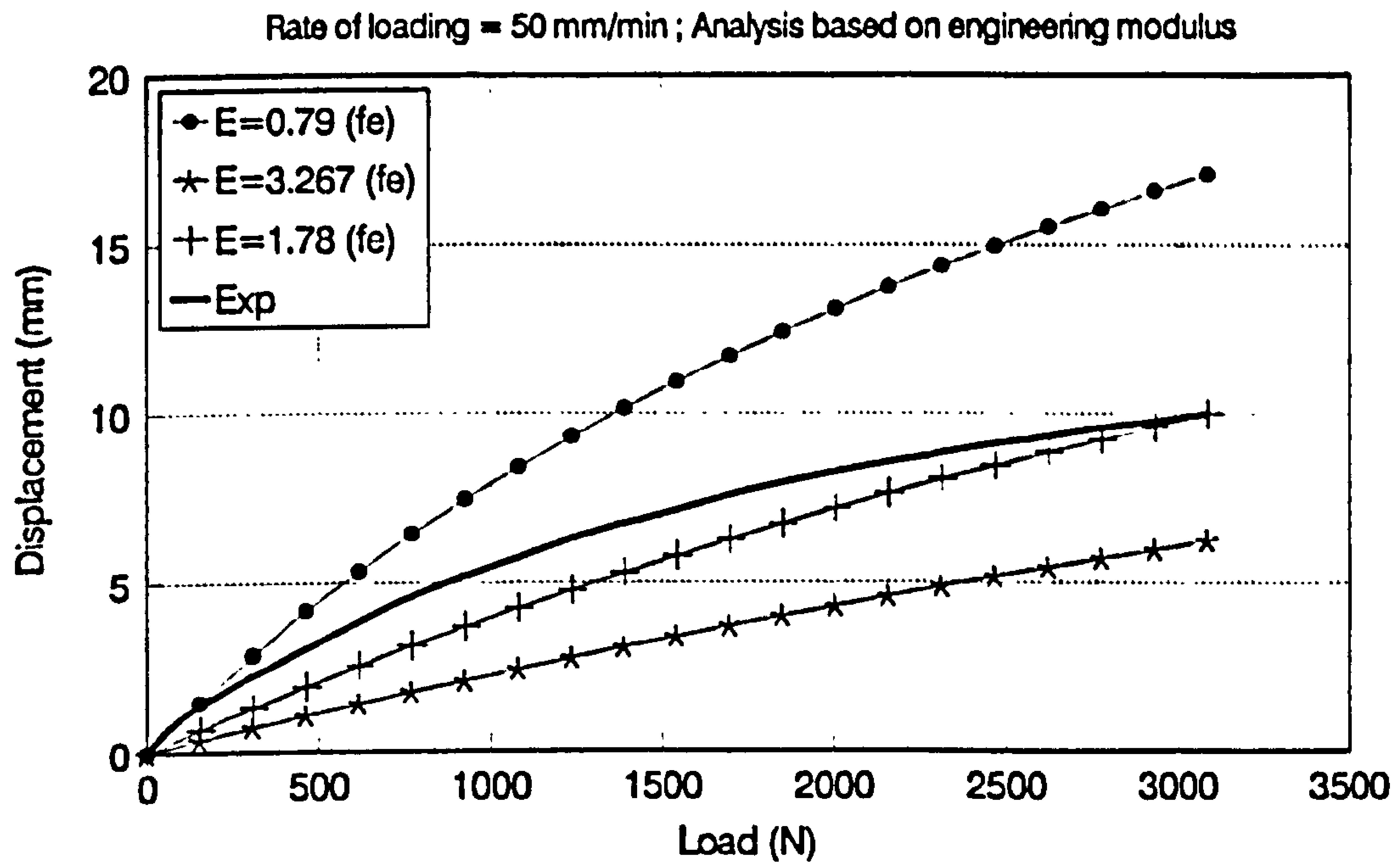

Fig. 6.5.4.7 Comparison between FE and experimental results.
(Rate of loading 50 mm/min ; FE model rub11, 12, and 15)

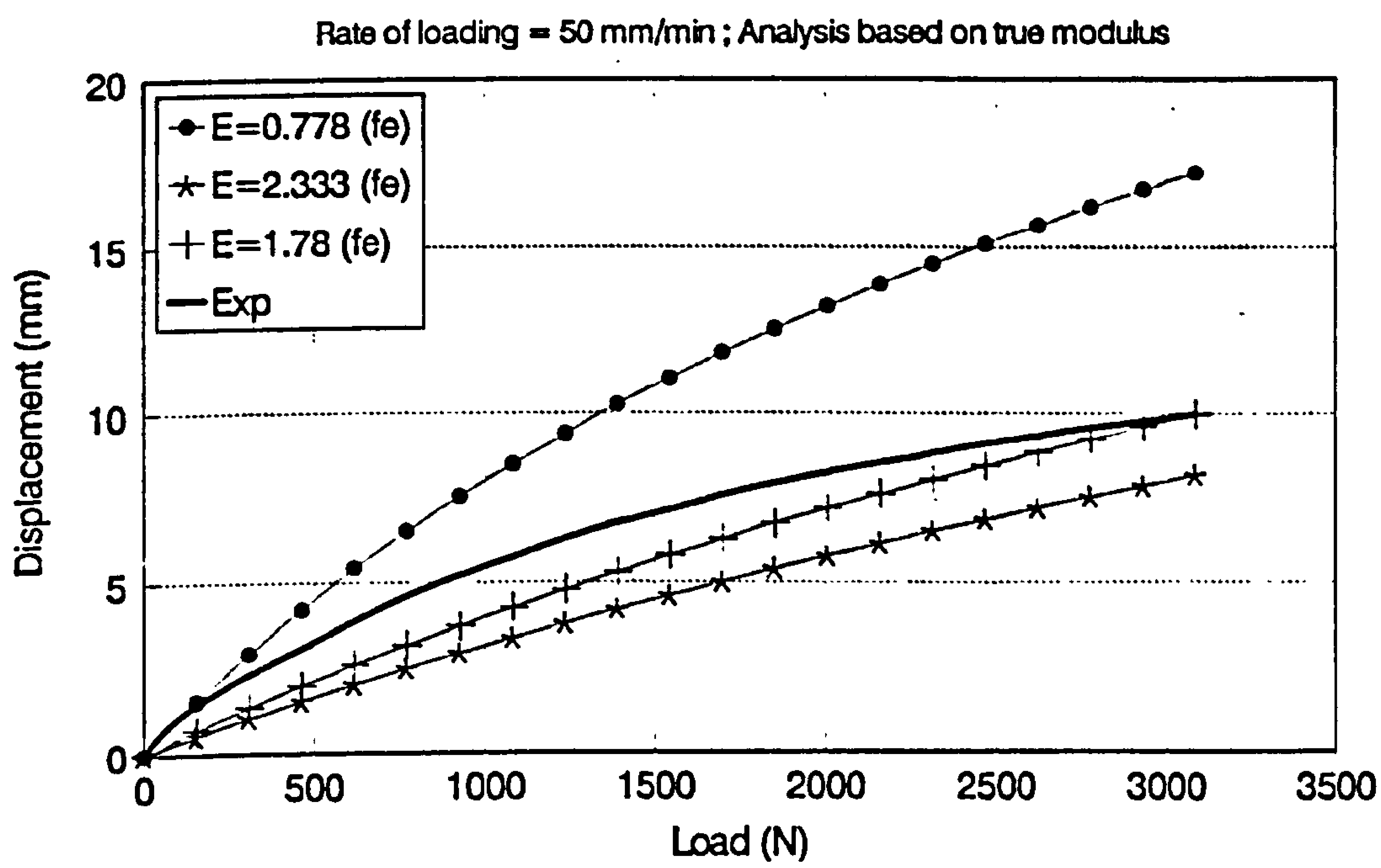

Fig. 6.5.4.8 Comparison between FE and experimental results.
(Rate of loading 50 mm/min ; FE model rub13, 14, and 15)

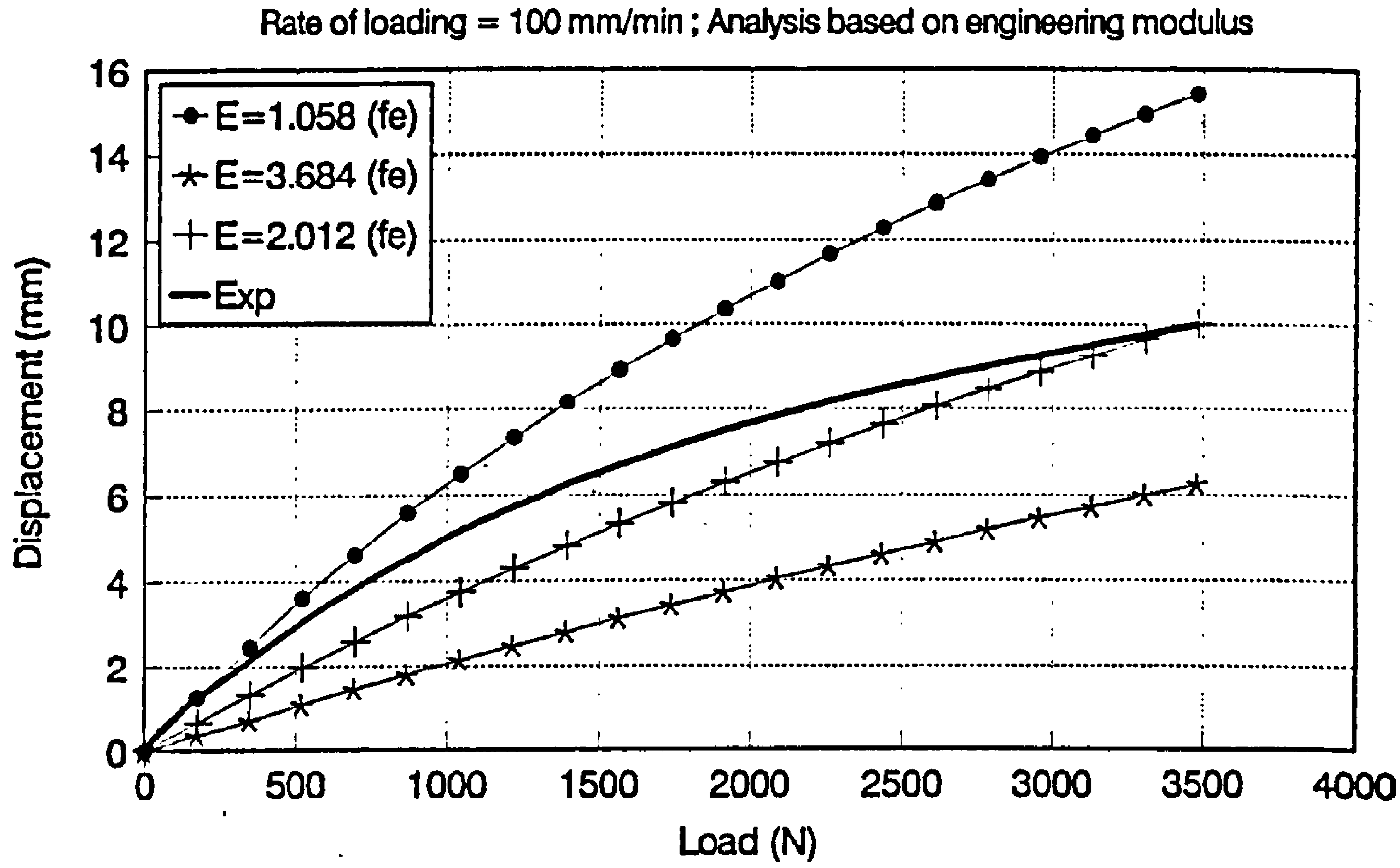

Fig. 6.5.4.9 Comparison between FE and experimental results.
(Rate of loading 100 mm/min ; FE model rub16, 17, and 20)

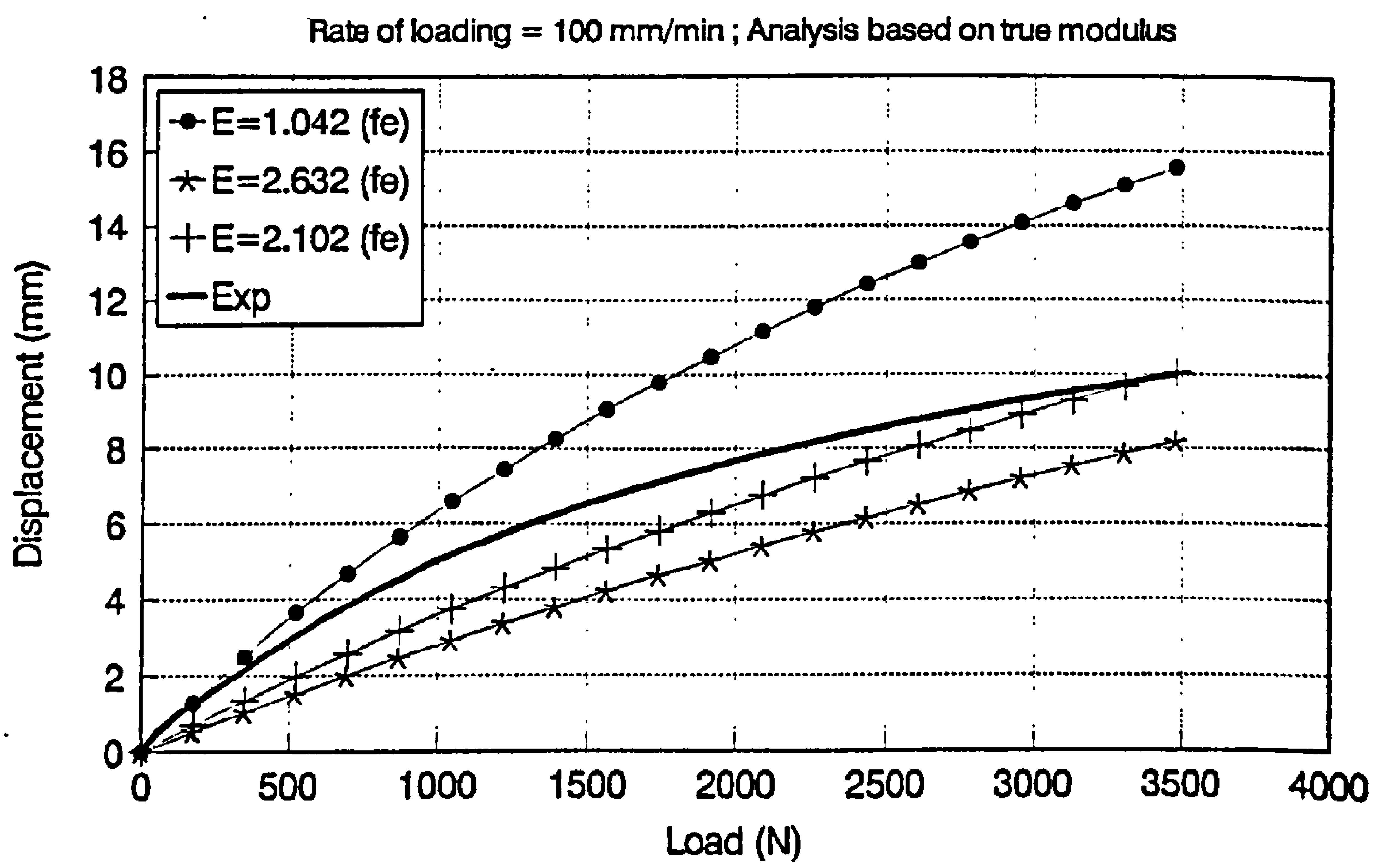

Fig. 6.5.4.10 Comparison between FE and experimental results.
(Rate of loading 100 mm/min ; FE model rub18, 19, and 20)

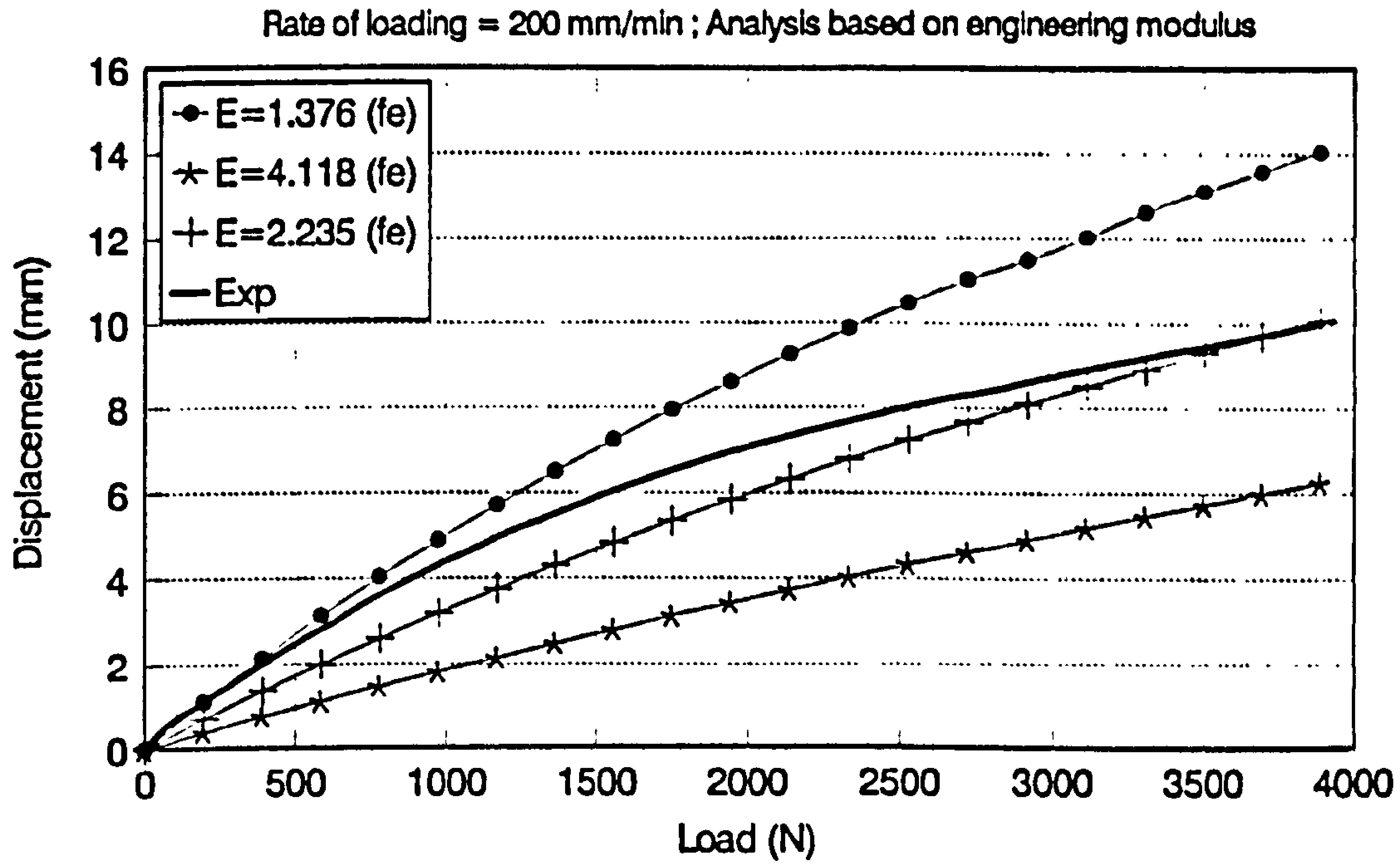

Fig. 6.5.4.11 Comparison between FE and experimental results.
(Rate of loading 200 mm/min ; FE model rub21, 22, and 25)

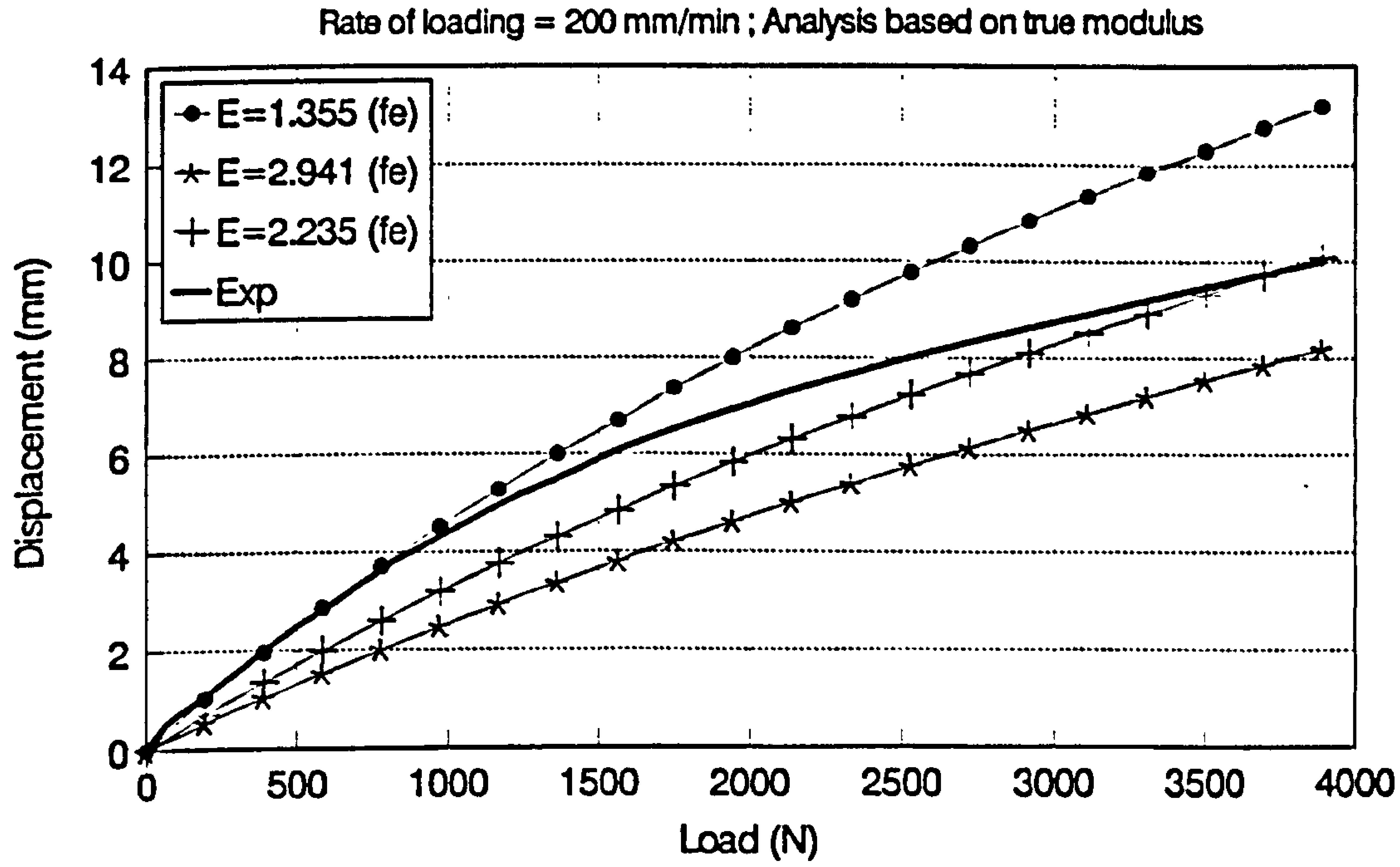

Fig. 6.5.4.12 Comparison between FE and experimental results.
(Rate of loading 200 mm/min ; FE model rub23, 24, and 25)

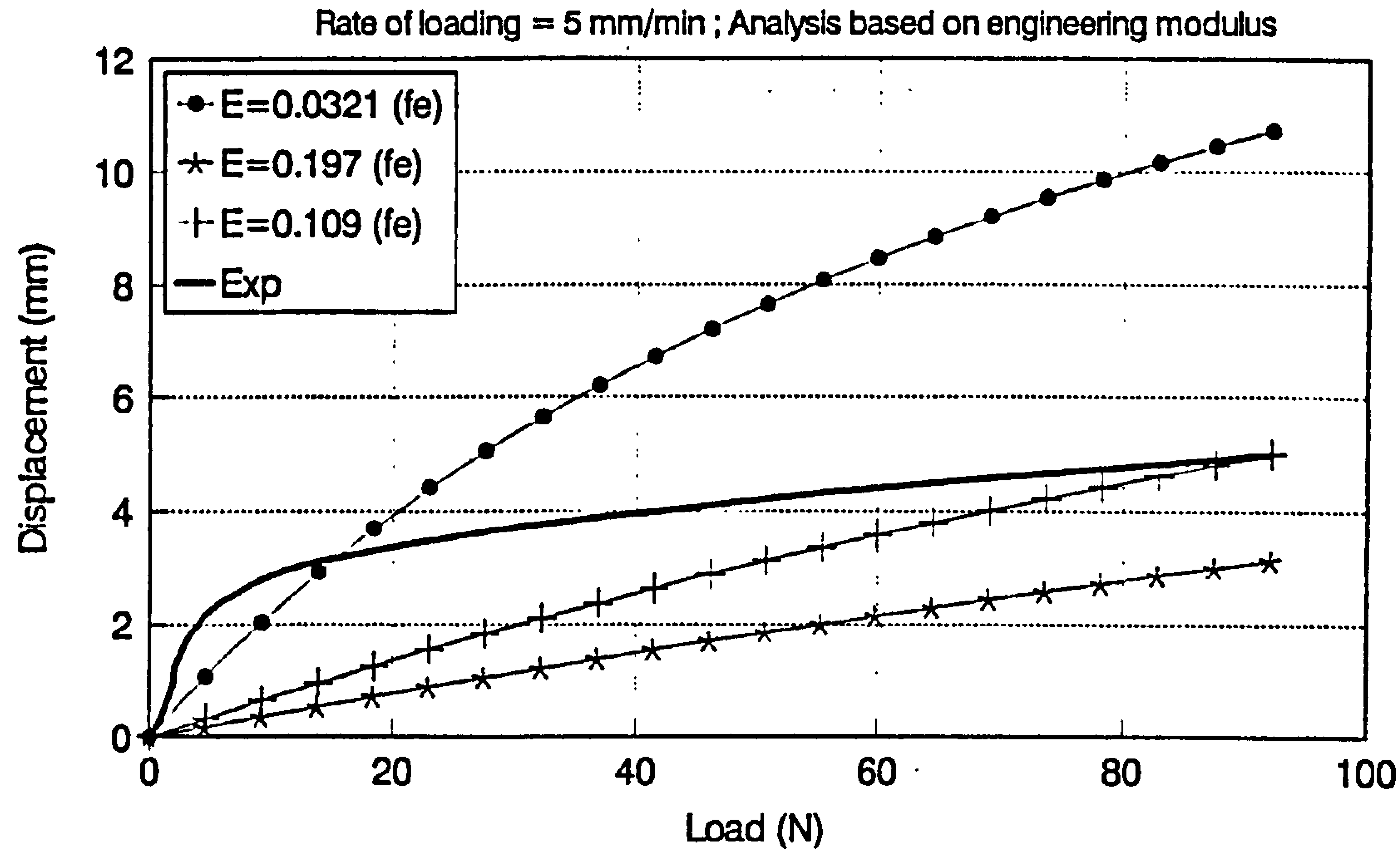

Fig. 6.5.4.13 Comparison between FE and experimental results.
(Rate of loading 5 mm/min ; FE model po1, 2, and 5)

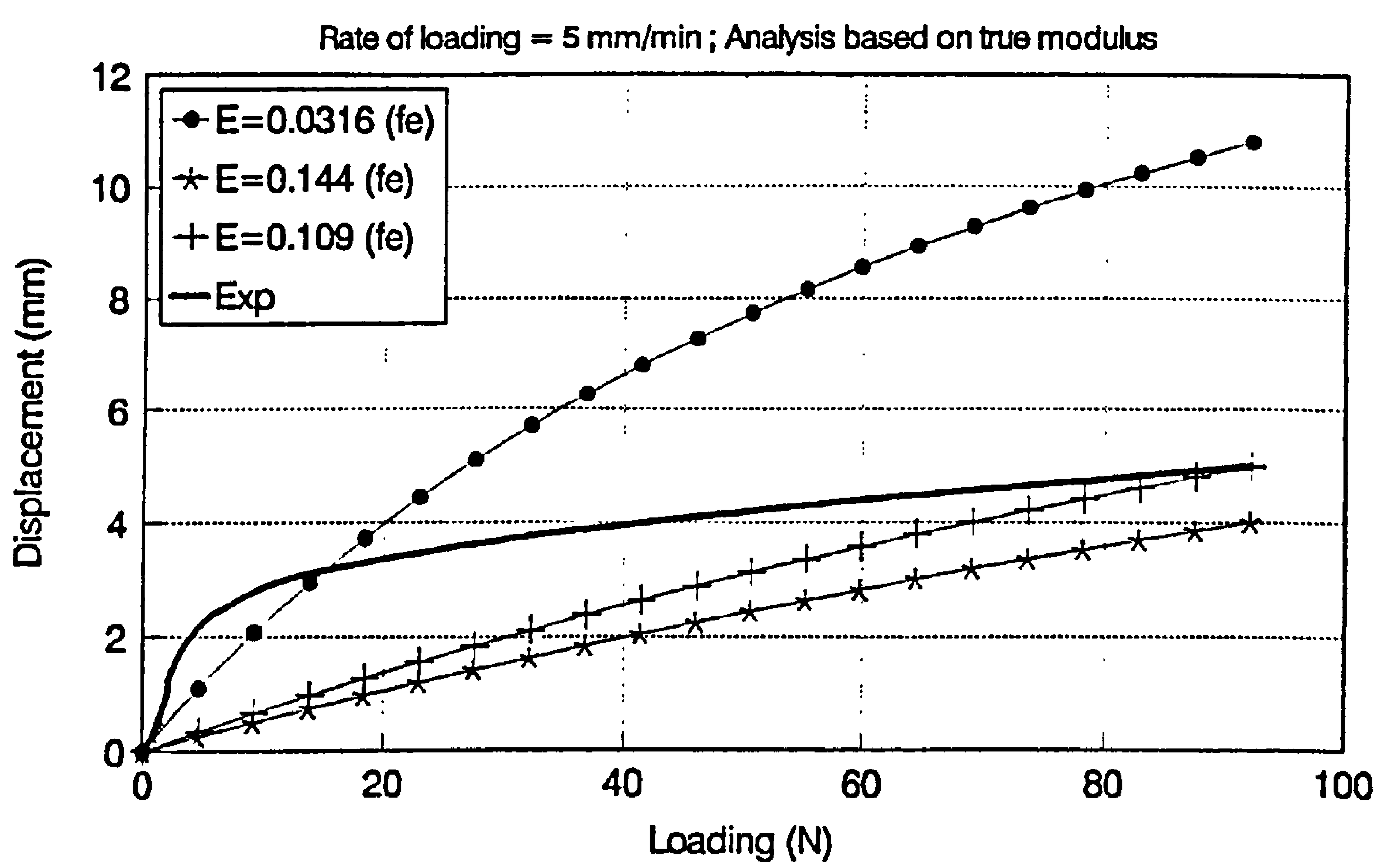

Fig. 6.5.4.14 Comparison between FE and experimental results.
(Rate of loading 5 mm/min ; FE model po3, 4, and 5)

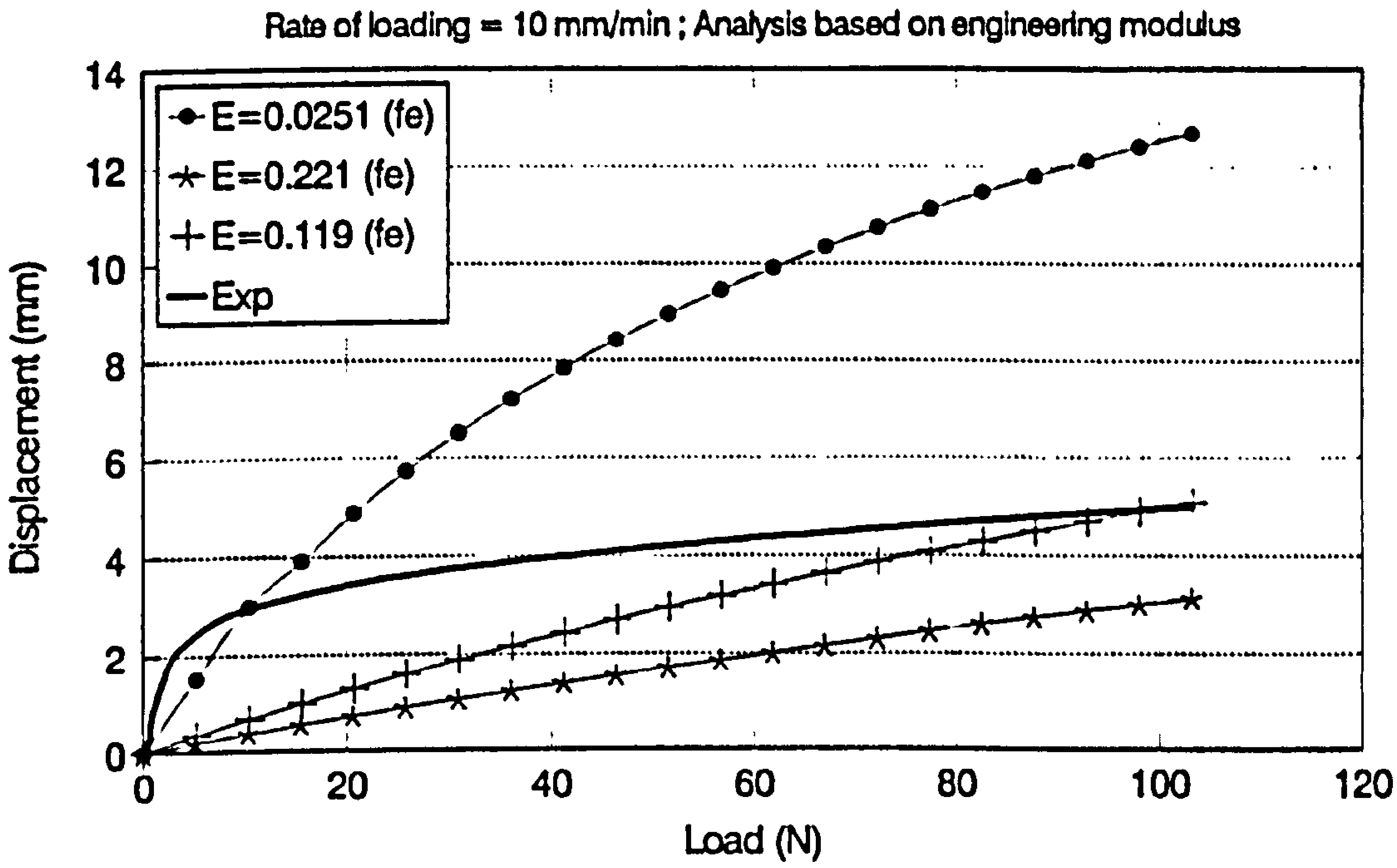

Fig. 6.5.4.15 Comparison between FE and experimental results.
(Rate of loading 10 mm/min ; FE model po6, 7, and 10)

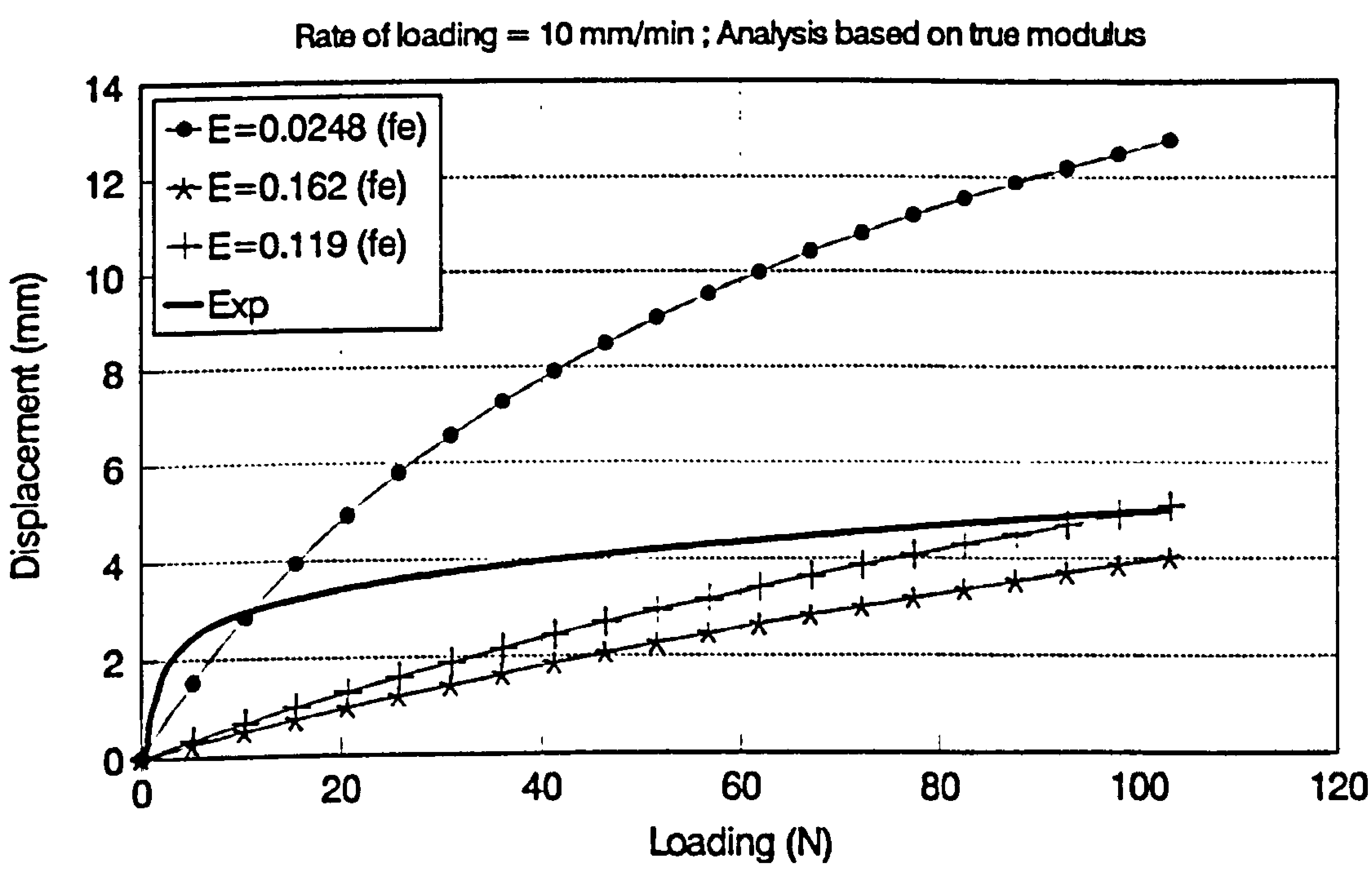

Fig. 6.5.4.16 Comparison between FE and experimental results.
(Rate of loading 10 mm/min ; FE model po8, 9, and 10)

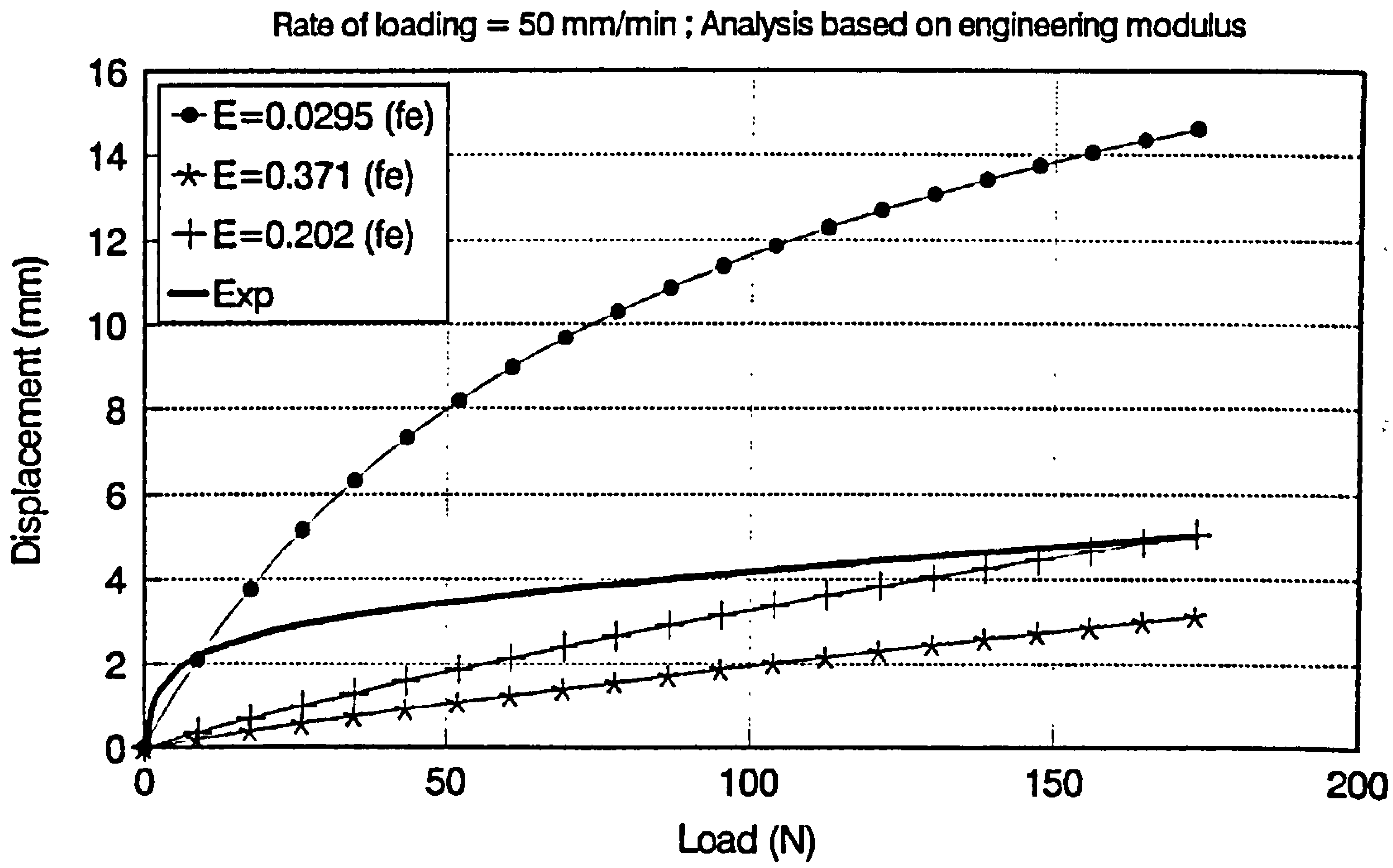

Fig. 6.5.4.17 Comparison between FE and experimental results.
(Rate of loading 50 mm/min ; FE model po11, 12, and 15)

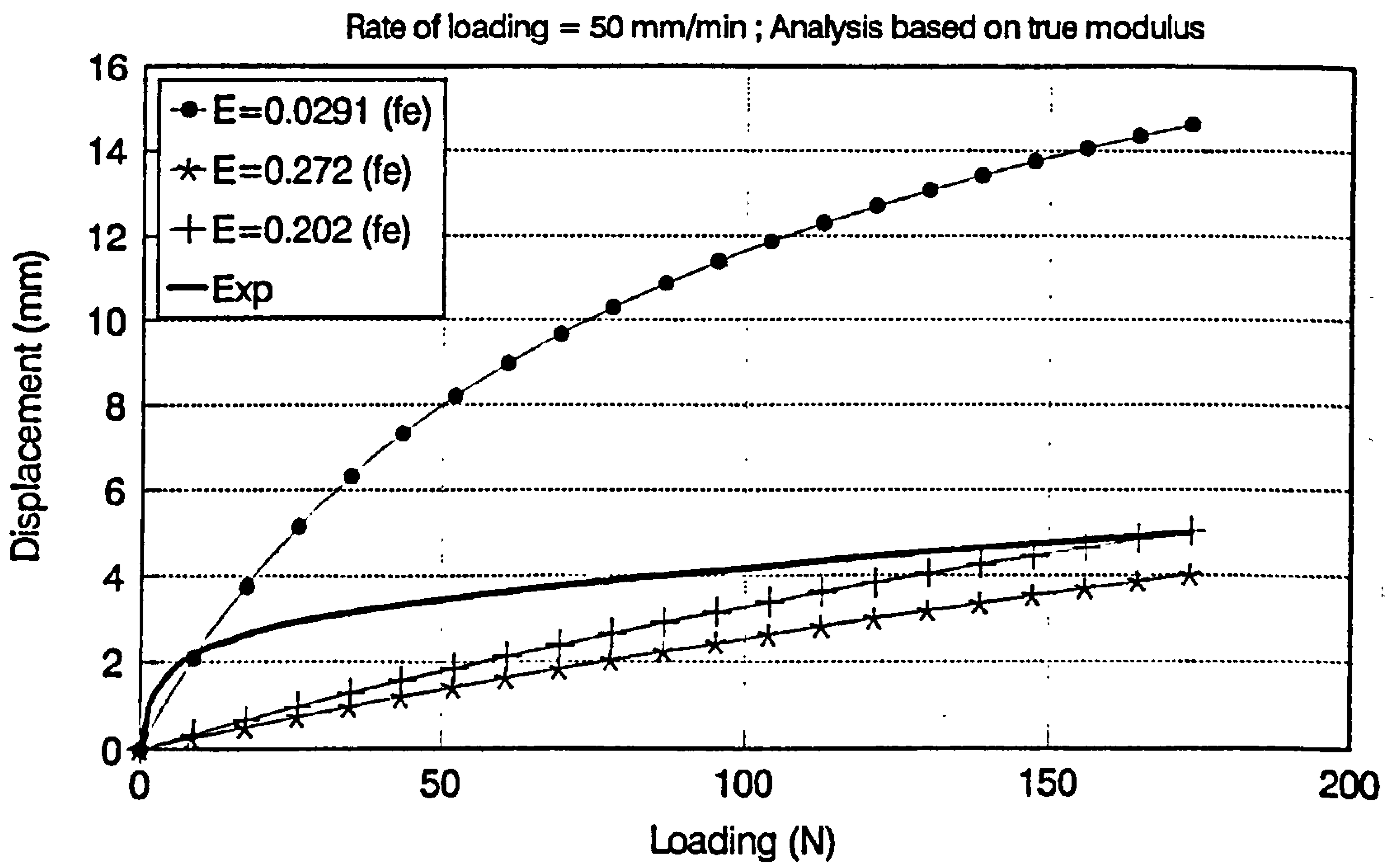

Fig. 6.5.4.18 Comparison between FE and experimental results.
(Rate of loading 50 mm/min ; FE model po13, 14, and 15)

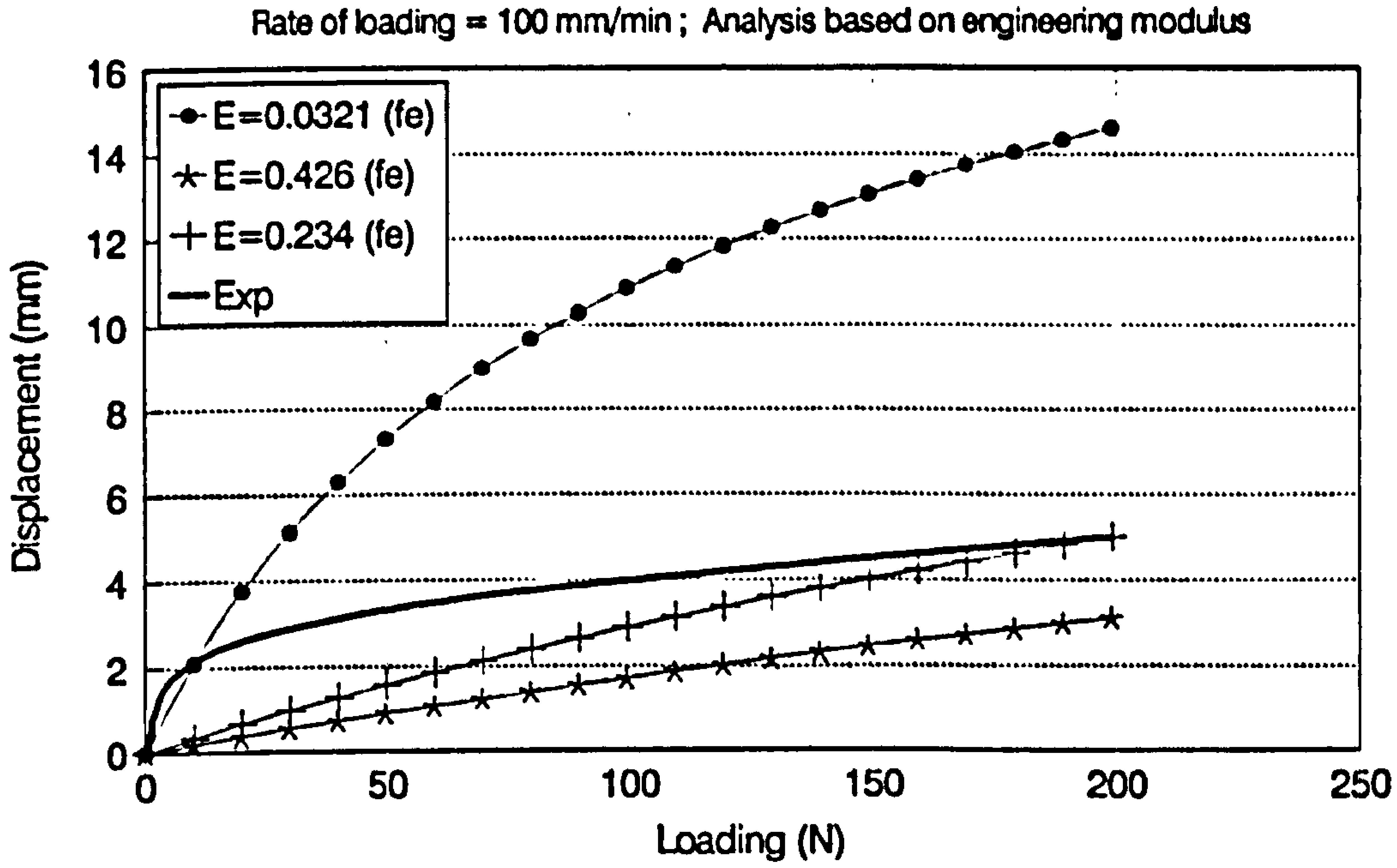

Fig. 6.5.4.19 Comparison between FE and experimental results.
(Rate of loading 100 mm/min ; FE model po16, 17, and 20)

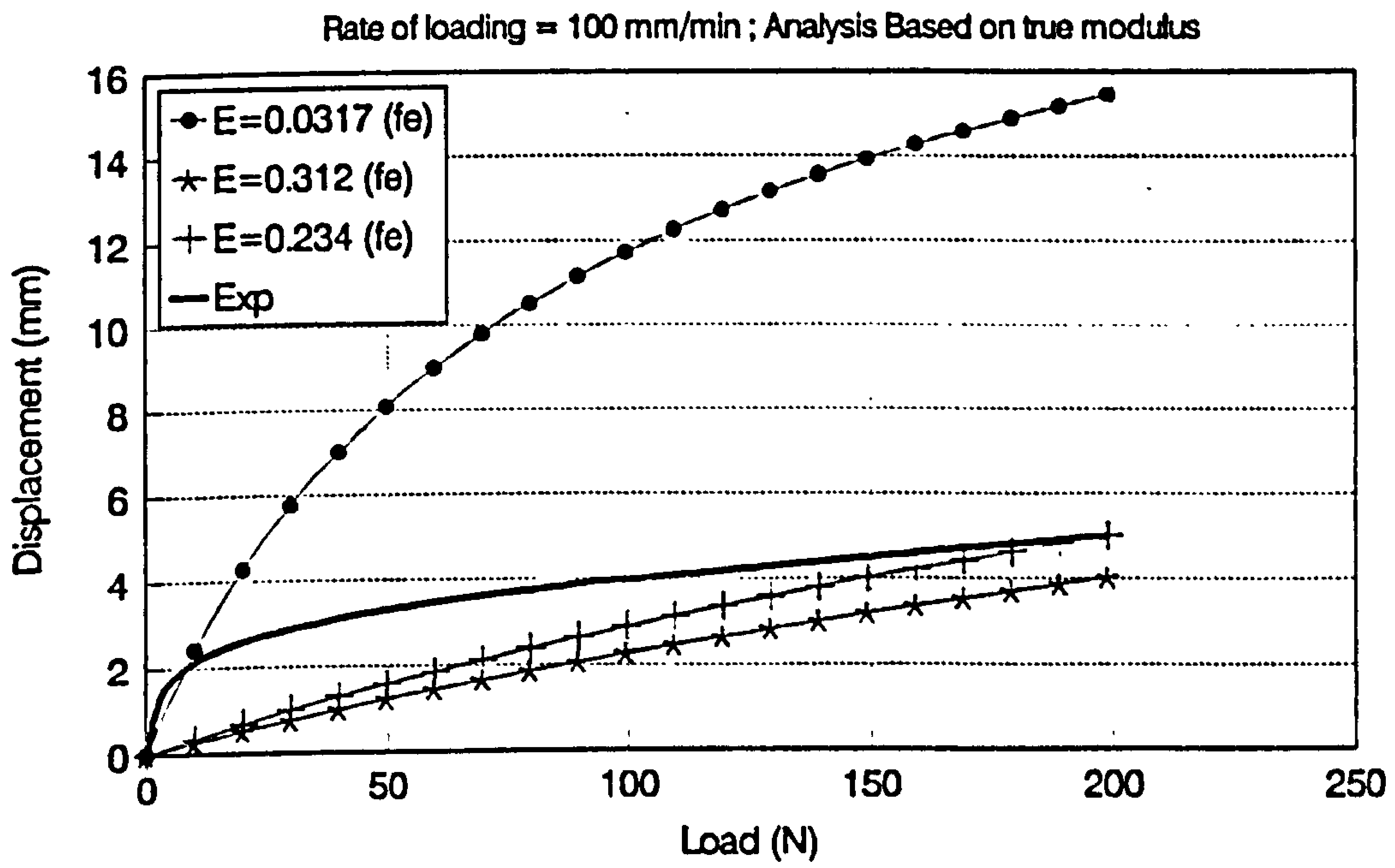

Fig. 6.5.4.20 Comparison between FE and experimental results.
(Rate of loading 100 mm/min ; FE model po18, 19, and 20)

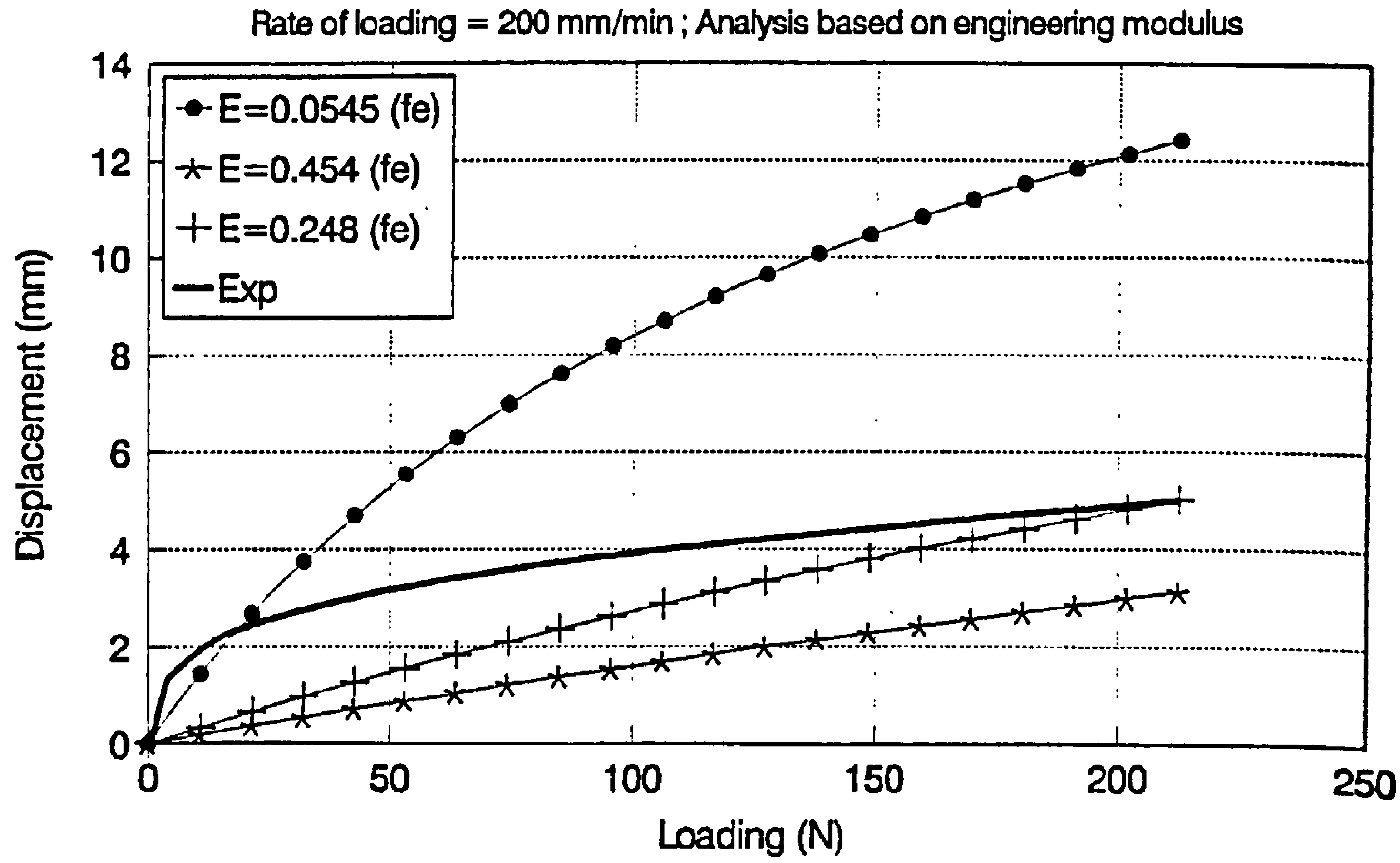

Fig. 6.5.4.21 Comparison between FE and experimental results.
(Rate of loading 200 mm/min ; FE model po21, 22, and 25)

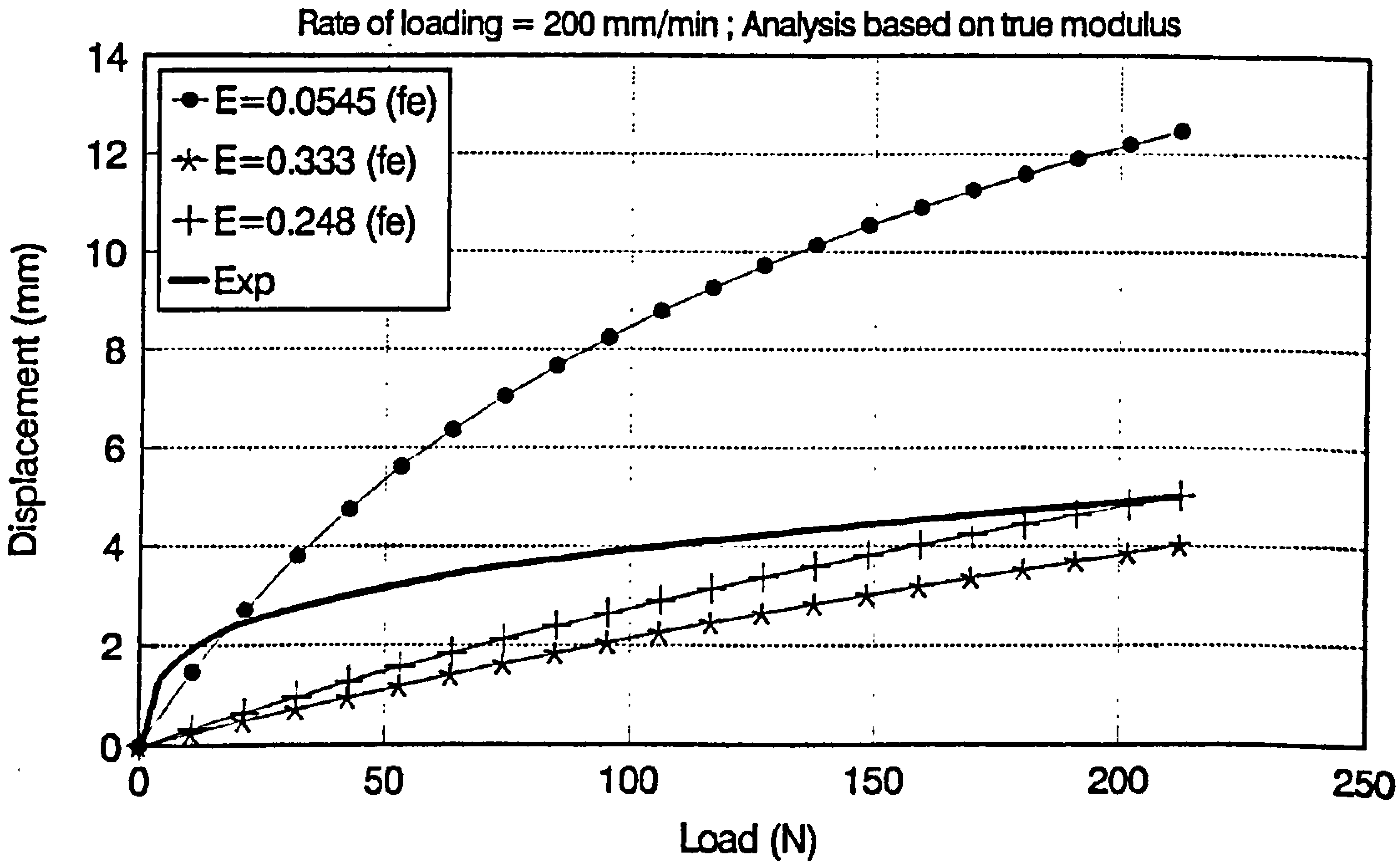

Fig. 6.5.4.22 Comparison between FE and experimental results.
(Rate of loading 200 mm/min ; FE model po23, 24, and 25)

The displacement - load curve predicted by using E^* gave the closest possible match to the experimental curve in the linear elastic analysis. Regardless, the predicted curve using E^* still approaches that of a straight line. Thus, at the section where the experimental curve's curvature is at its maximum, maximum error will be encountered in the FE prediction.

6.5.5 Results of compression model : non - linear elastic analysis

The predicted results of the non - linear elastic analysis are presented in graphical plots of displacement versus load. Similarly, the FE predictions are compared to the experimental values. For each rate of loading, three curves were drawn, these are ;

a.) FE predictions using values obtained from engineering stress - strain,

b.) FE predictions using values obtained from true stress - strain and

c.) the experimental data.

Fig. 6.5.5.1 to Fig. 6.5.5.5 show the results for the rubber model and Fig. 6.5.5.6 to Fig. 6.5.5.10 for the porcine tissue model. On the whole, a close match was obtained when FE predicted curves were compared to the experimental curves. A closer match was obtained when using true stress - strain values in the rubber model, however this was not the case with the porcine model where engineering stress - strain inputs give better predictions.

In the rubber model, the maximum error encountered with the FE predictions occurred at approximately 0.12 strain when true stress - strain values were used in the model, however, maximum error occurred at maximum strain when engineering stress - strain values were used. With the porcine model, using values obtained from engineering or true stress - strain, maximum predicted errors occurred at maximum strain. The porcine model was able to predict the initial non-linear part of the load - displacement curve (approximately 0.06 strain) closely, above this strain level, the predicted values were larger but follow the experimental curvature closely.

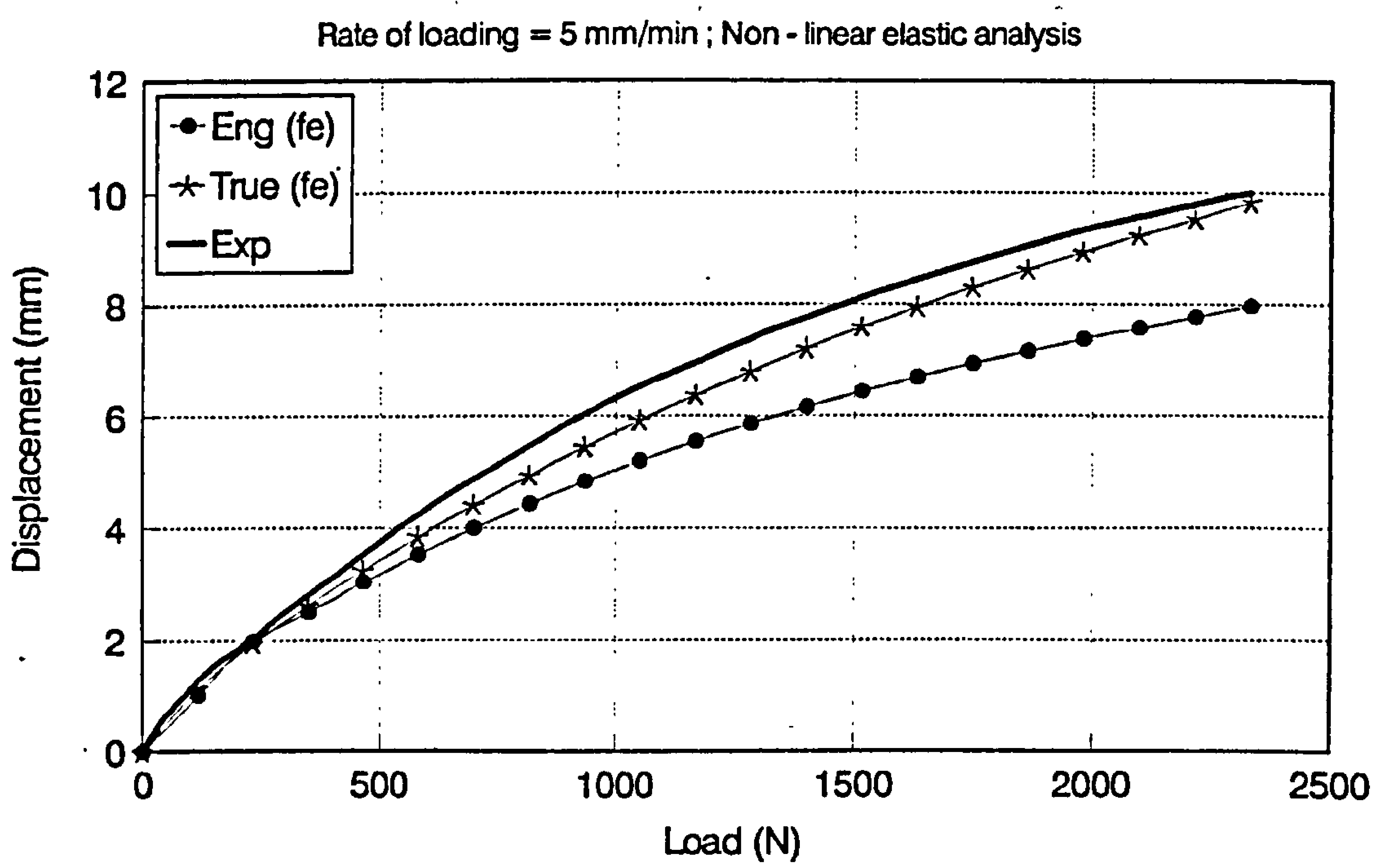

Fig. 6.5.5.1 Comparison between FE and experimental results.
(Rate of loading 5 mm/min ; FE model nrub1 and 2)

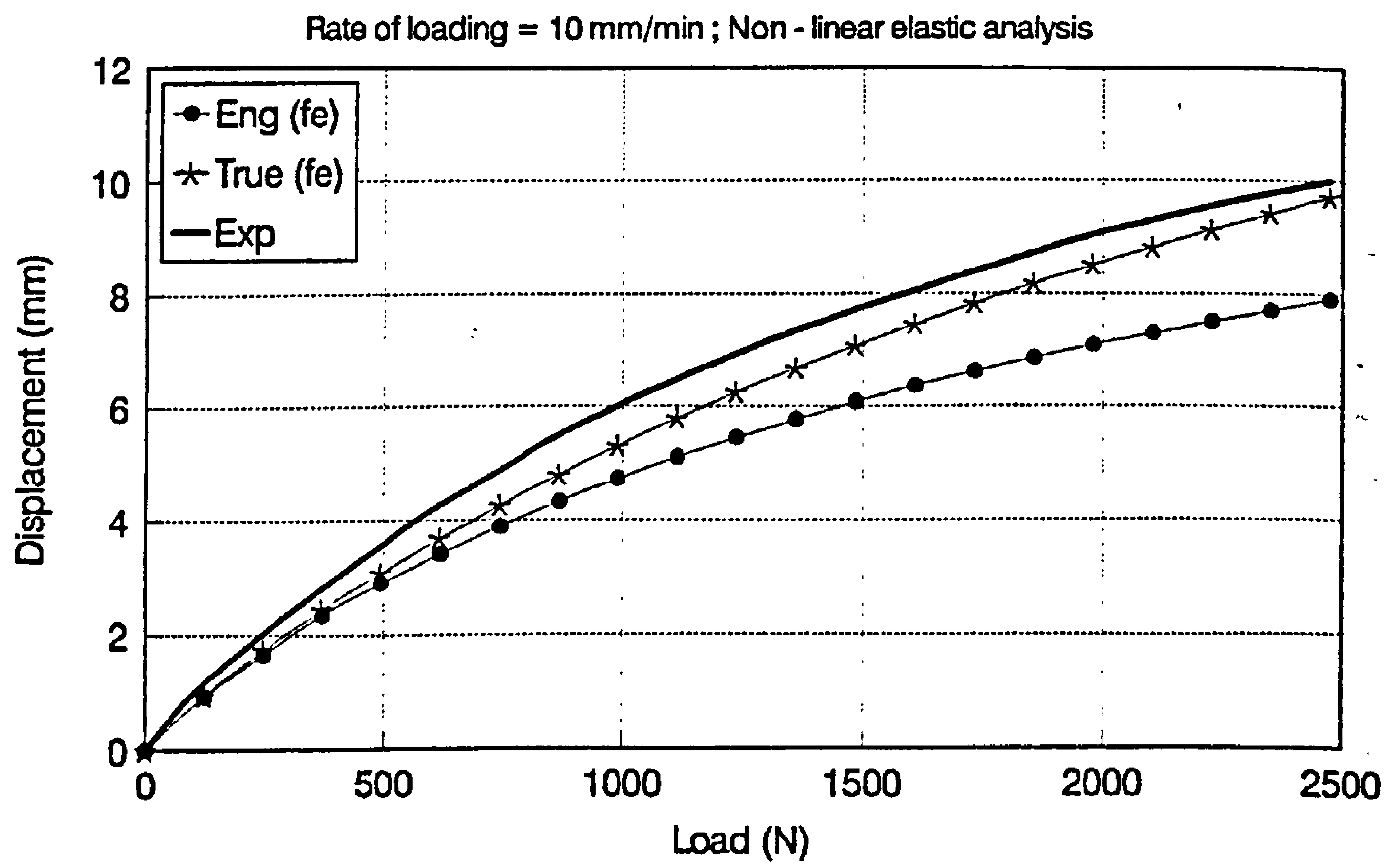

Fig. 6.5.5.2 Comparison between FE and experimental results.
(Rate of loading 5 mm/min ; FE model nrub3 and 4)

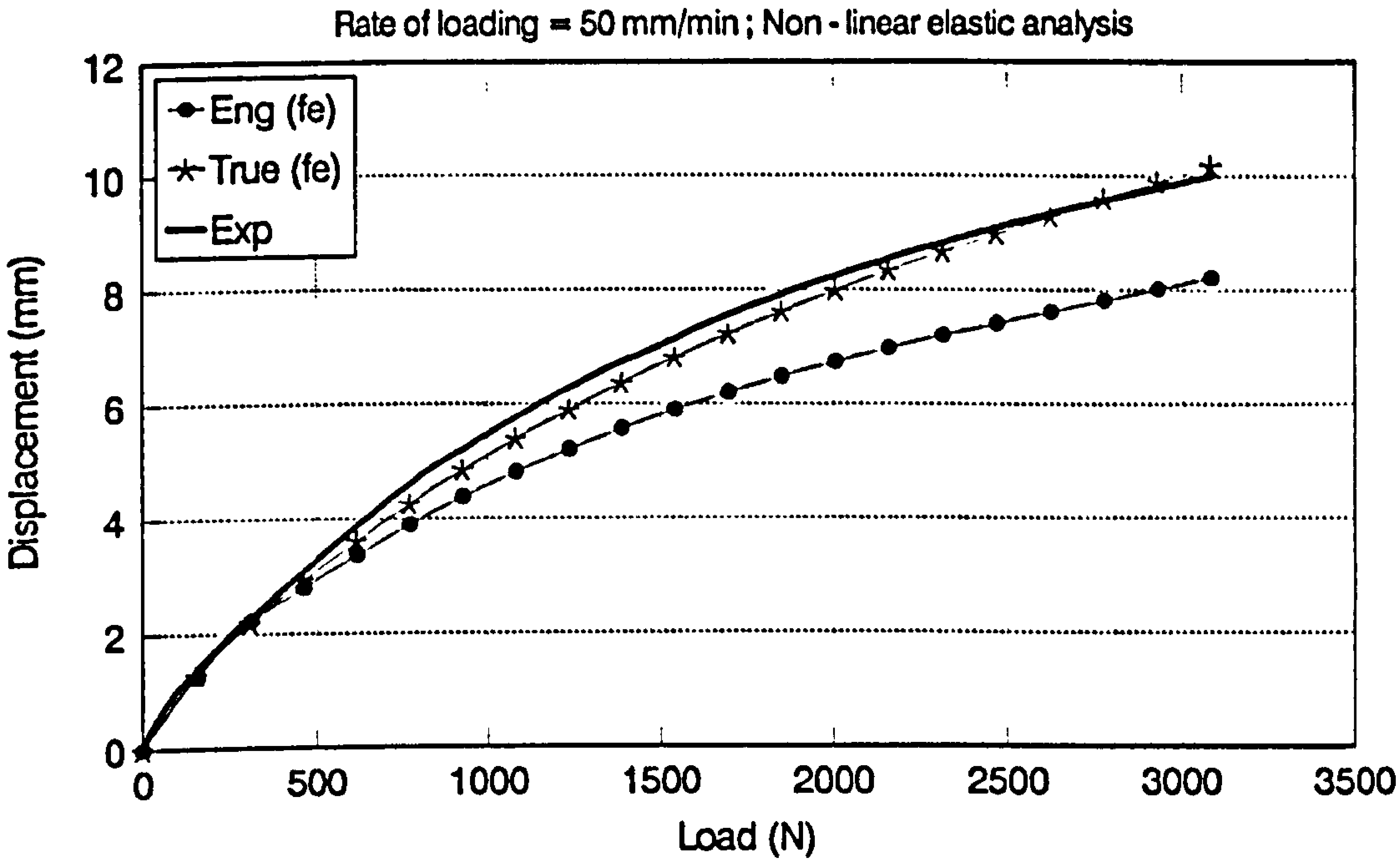

Fig. 6.5.5.3 Comparison between FE and experimental results.
(Rate of loading 5 mm/min ; FE model nrub5 and 6)

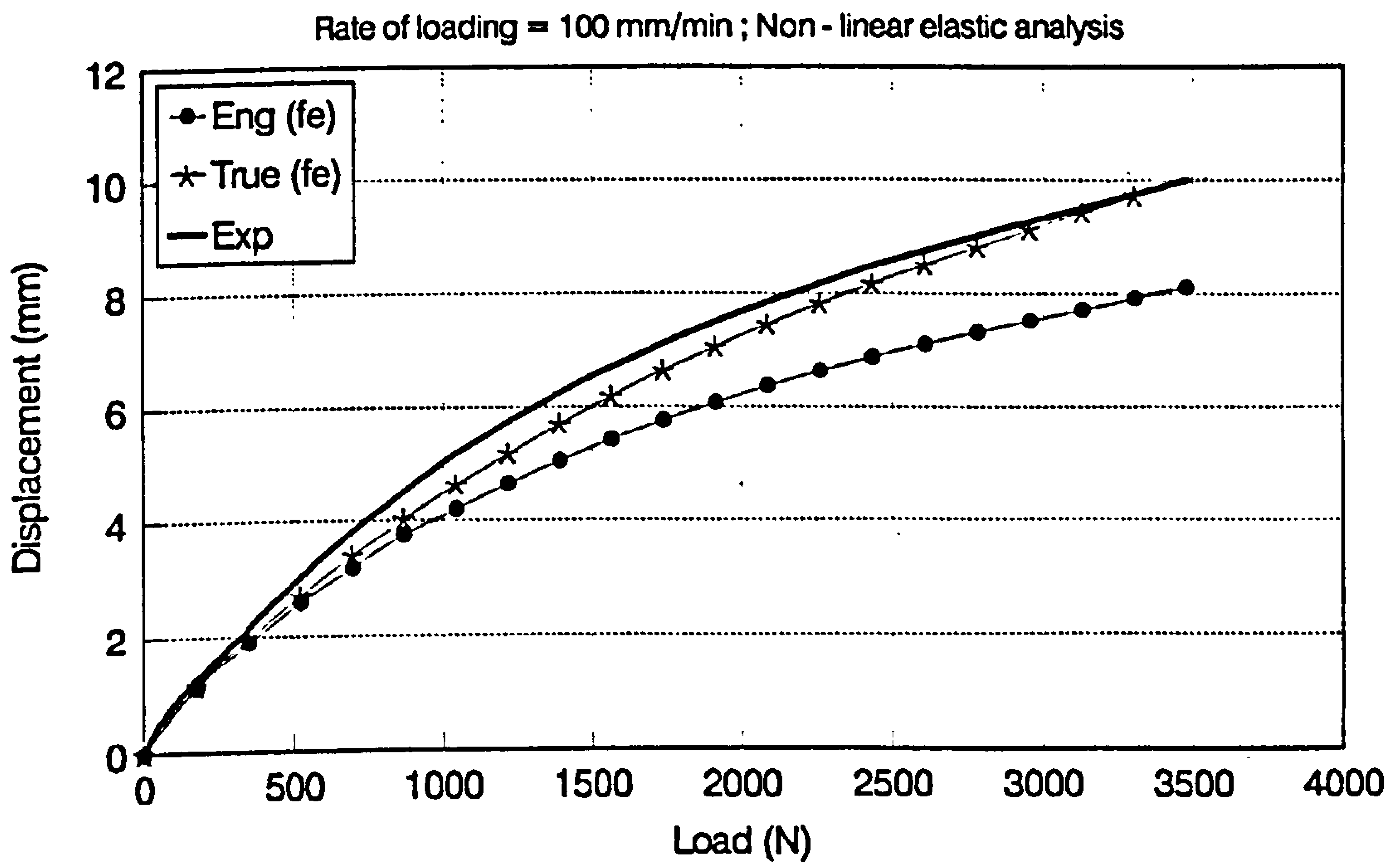

Fig. 6.5.5.4 Comparison between FE and experimental results.
(Rate of loading 5 mm/min ; FE model nrub7 and 8)

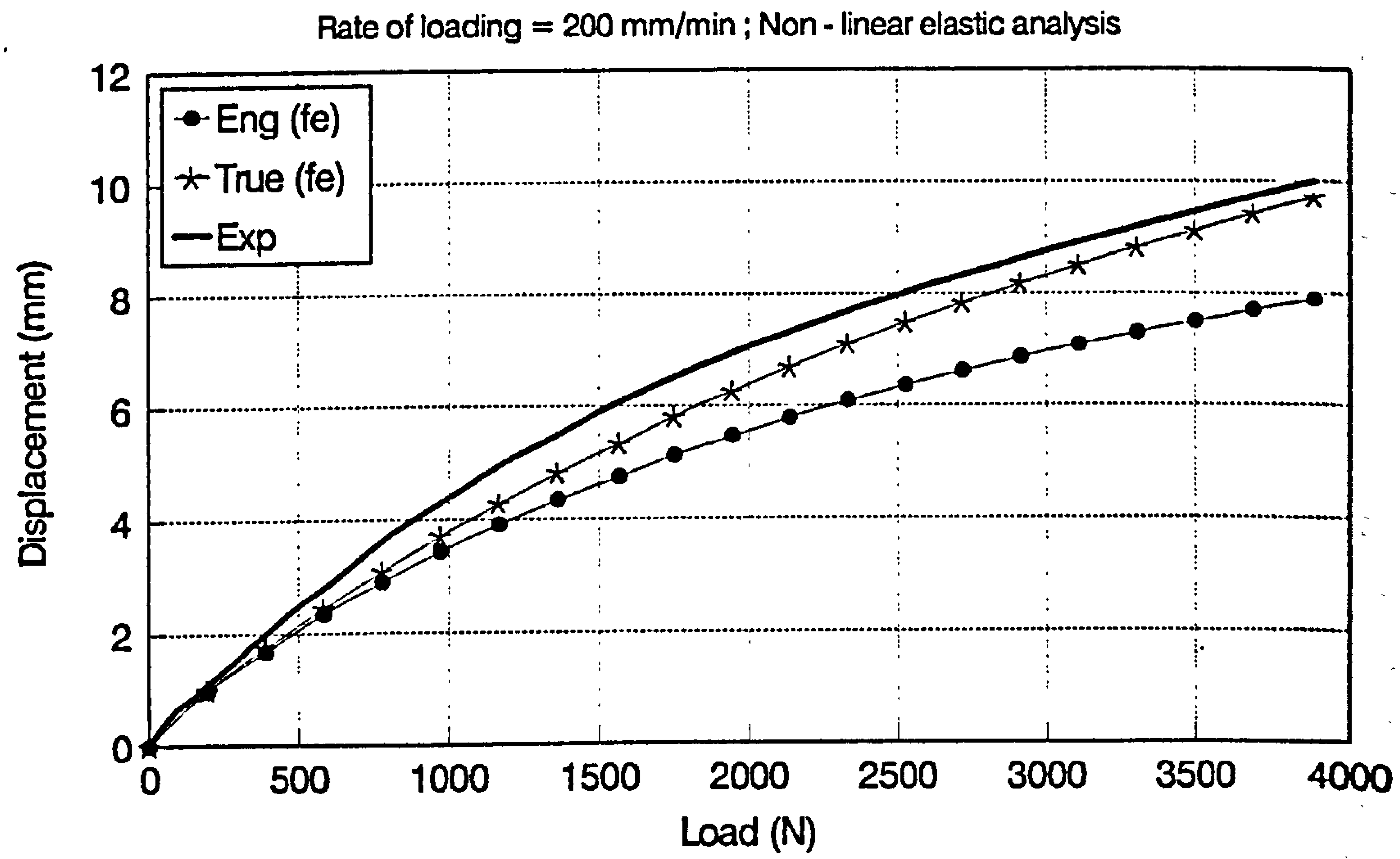

Fig. 6.5.5.5 Comparison between FE and experimental results.
(Rate of loading 5 mm/min ; FE model nrub9 and 10)

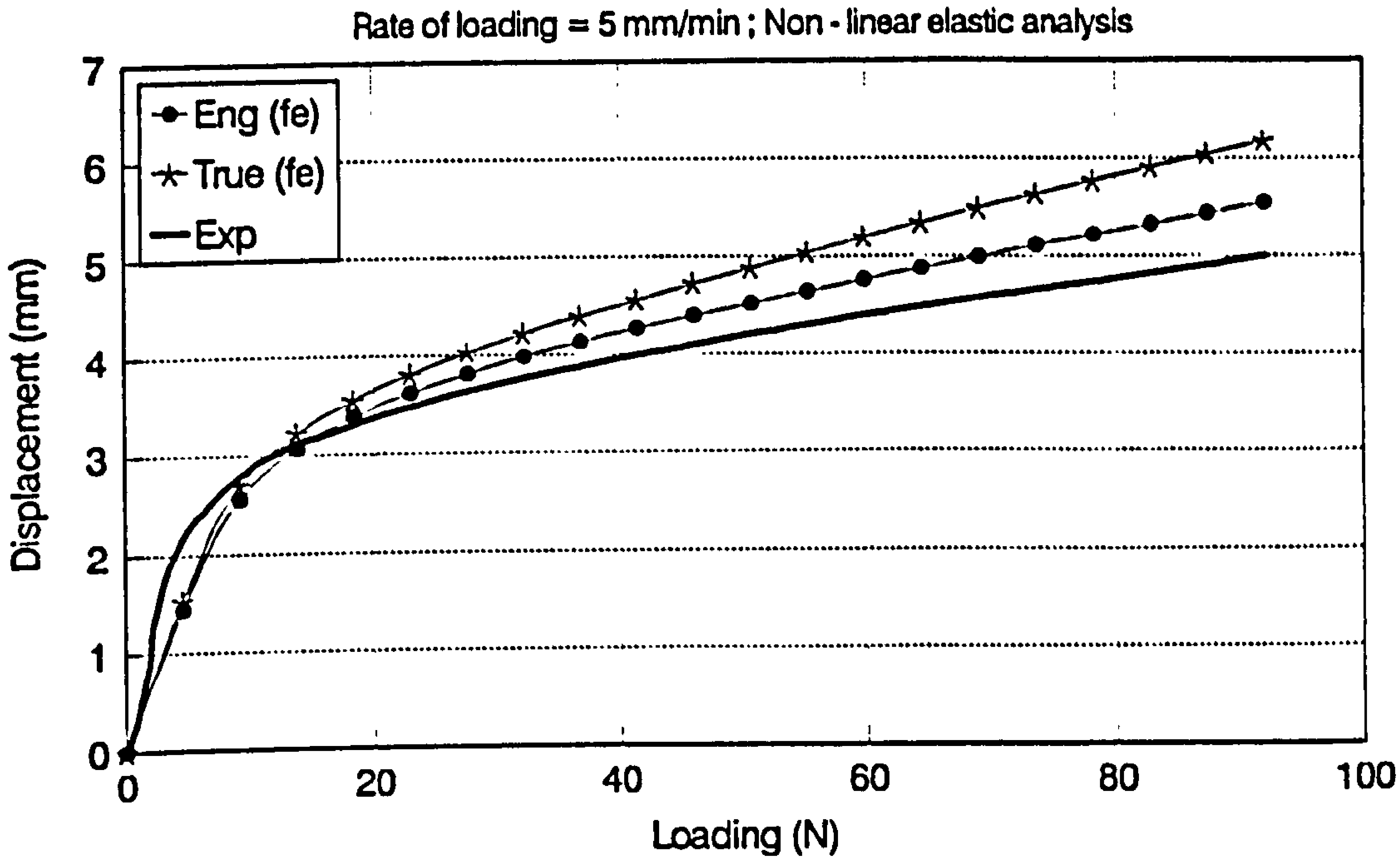

Fig. 6.5.5.6 Comparison between FE and experimental results.
(Rate of loading 5 mm/min ; FE model npo1 and 2)

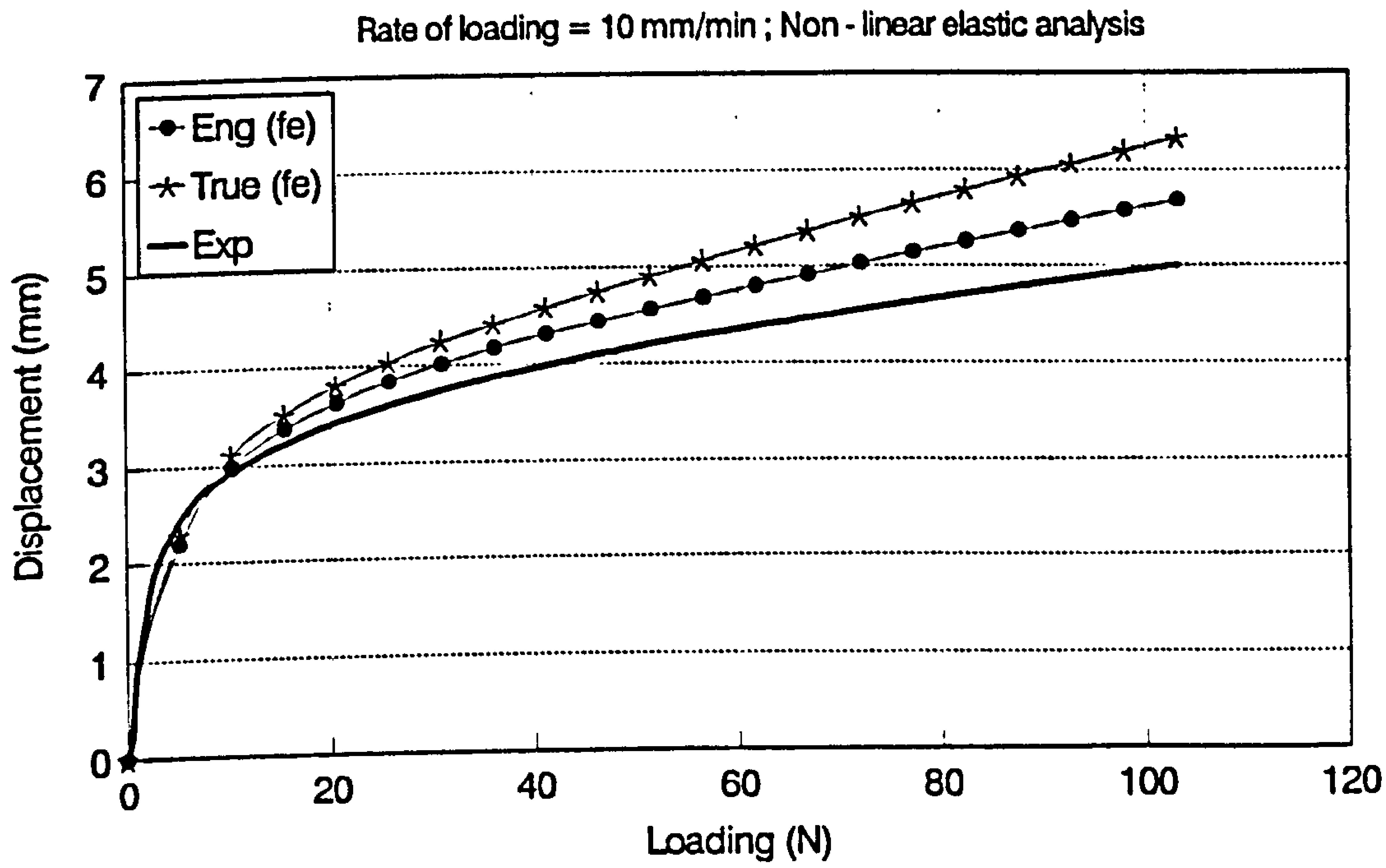

Fig. 6.5.5.7 Comparison between FE and experimental results.
(Rate of loading 10 mm/min ; FE model npo3 and 4)

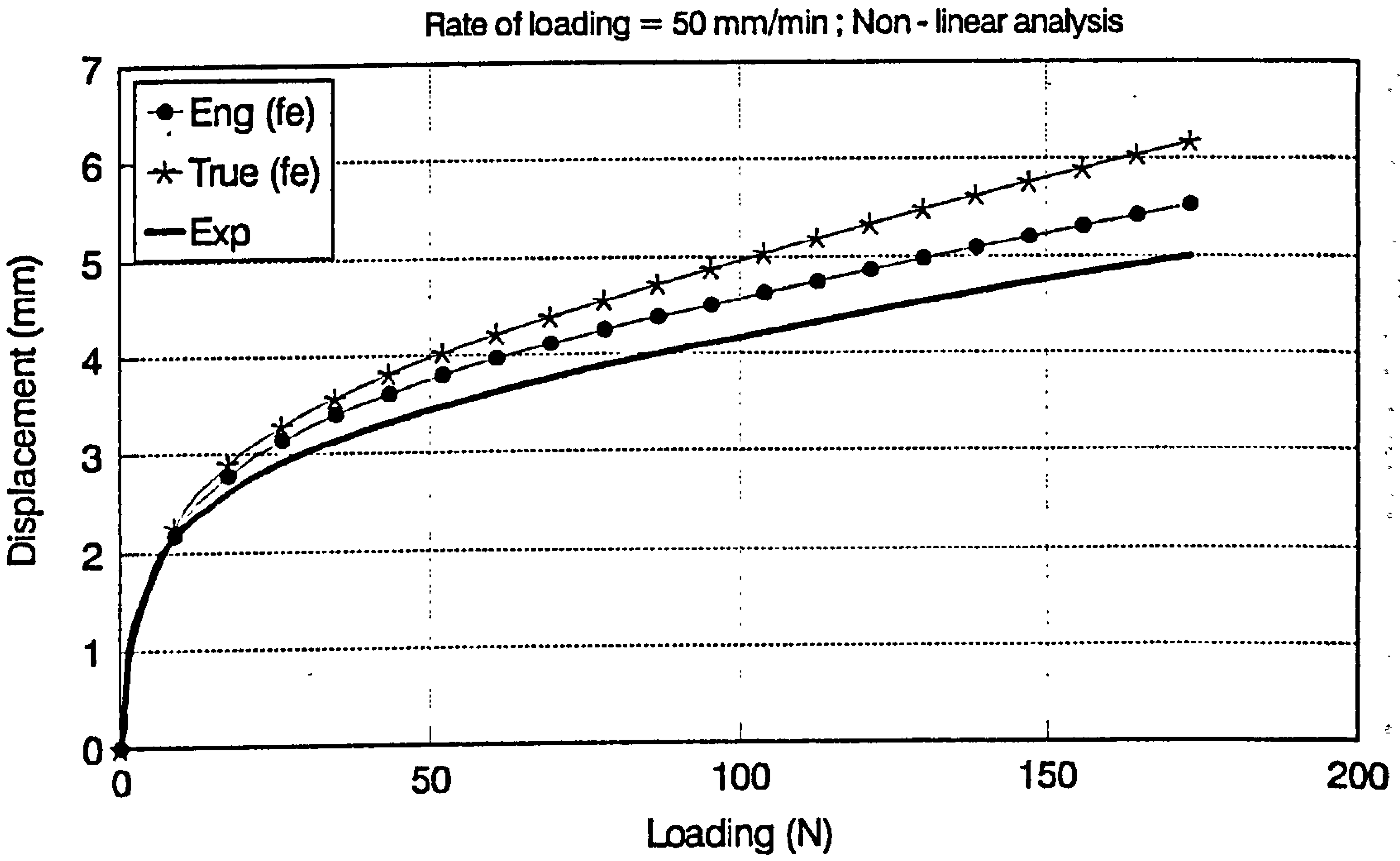

Fig. 6.5.5.8 Comparison between FE and experimental results.
(Rate of loading 50 mm/min ; FE model npo5 and 6)

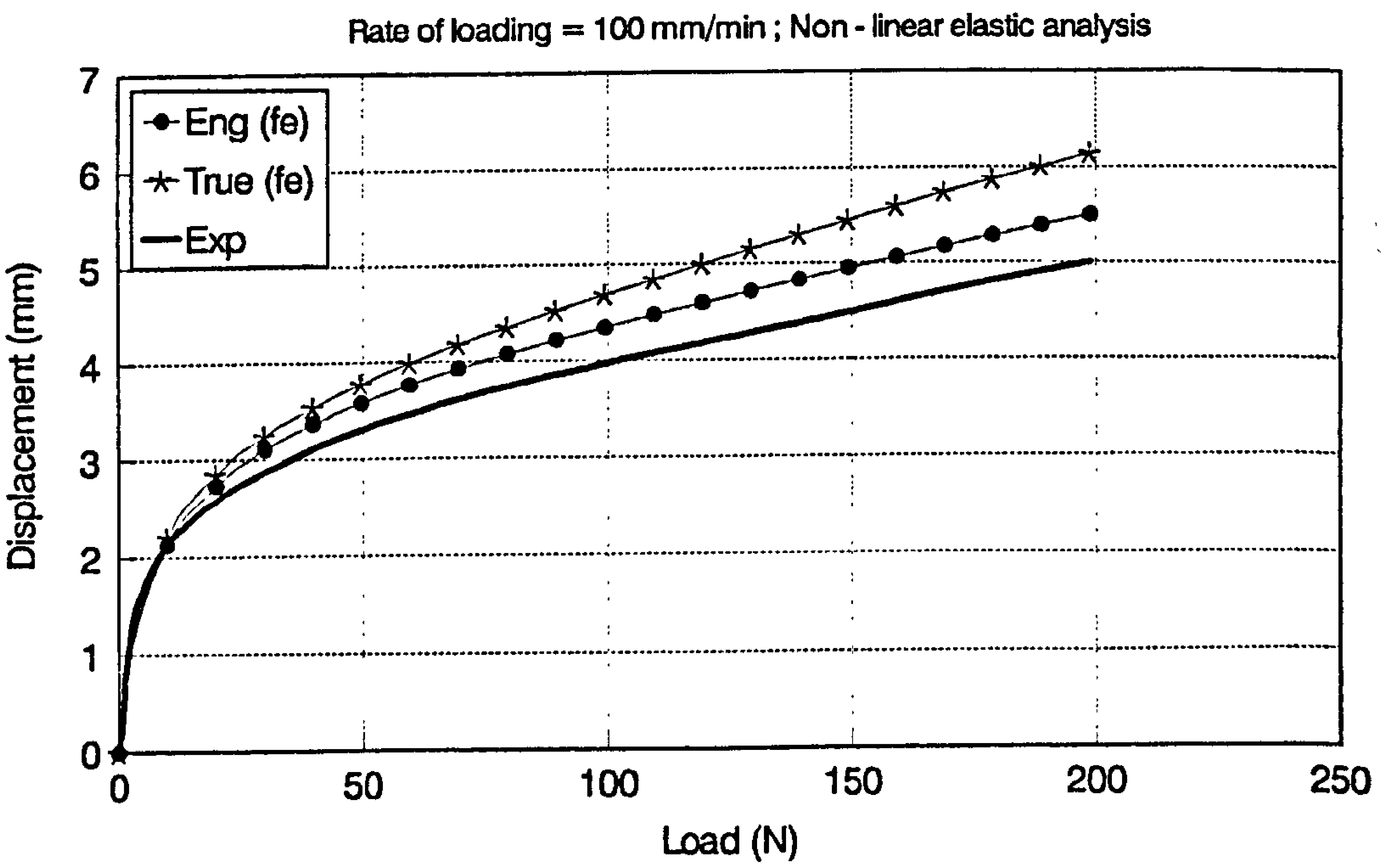

Fig. 6.5.5.9 Comparison between FE and experimental results.
(Rate of loading 100 mm/min ; FE model npo7 and 8)

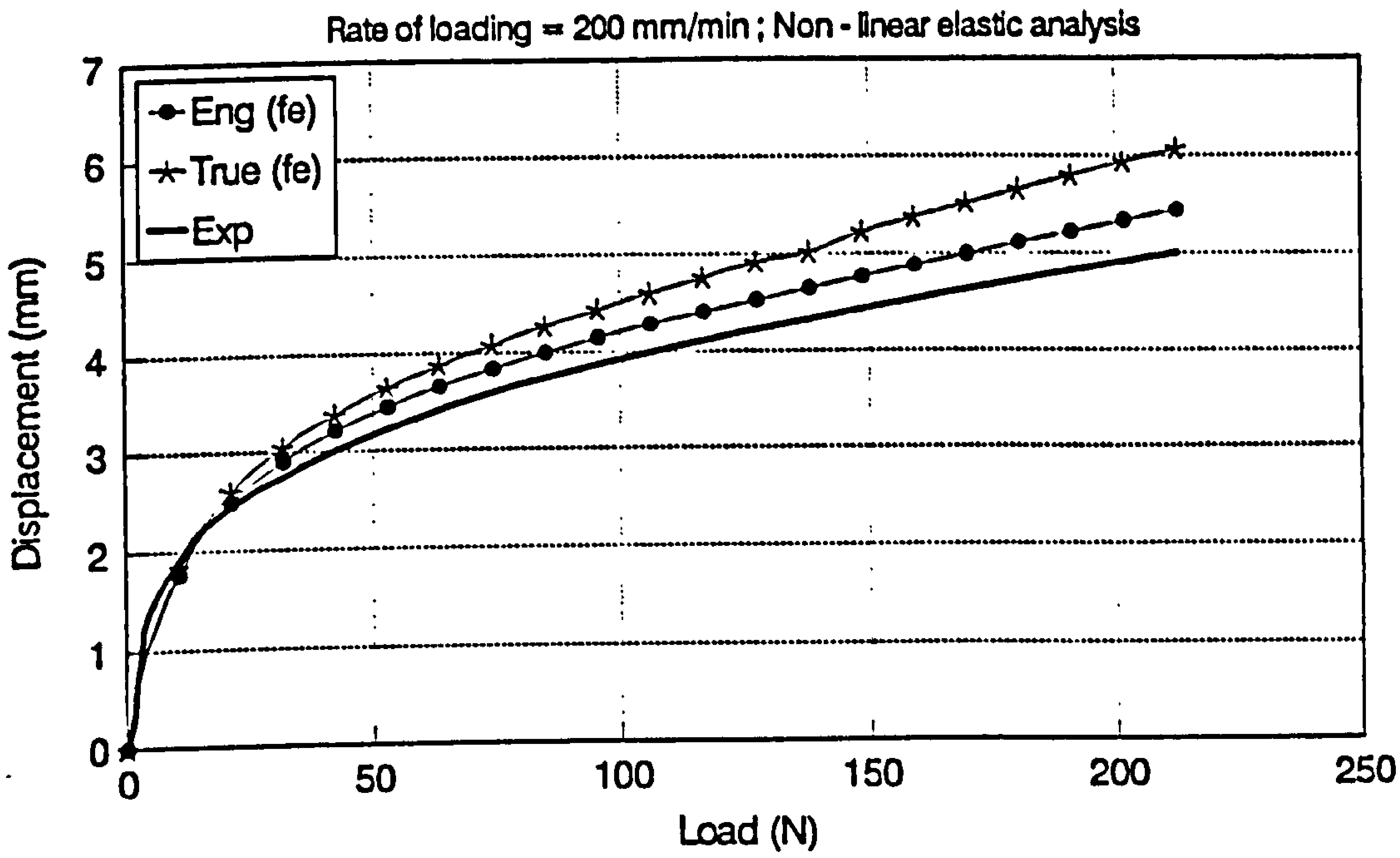

Fig. 6.5.5.10 Comparison between FE and experimental results.
(Rate of loading 200 mm/min ; FE model npo9 and 10)

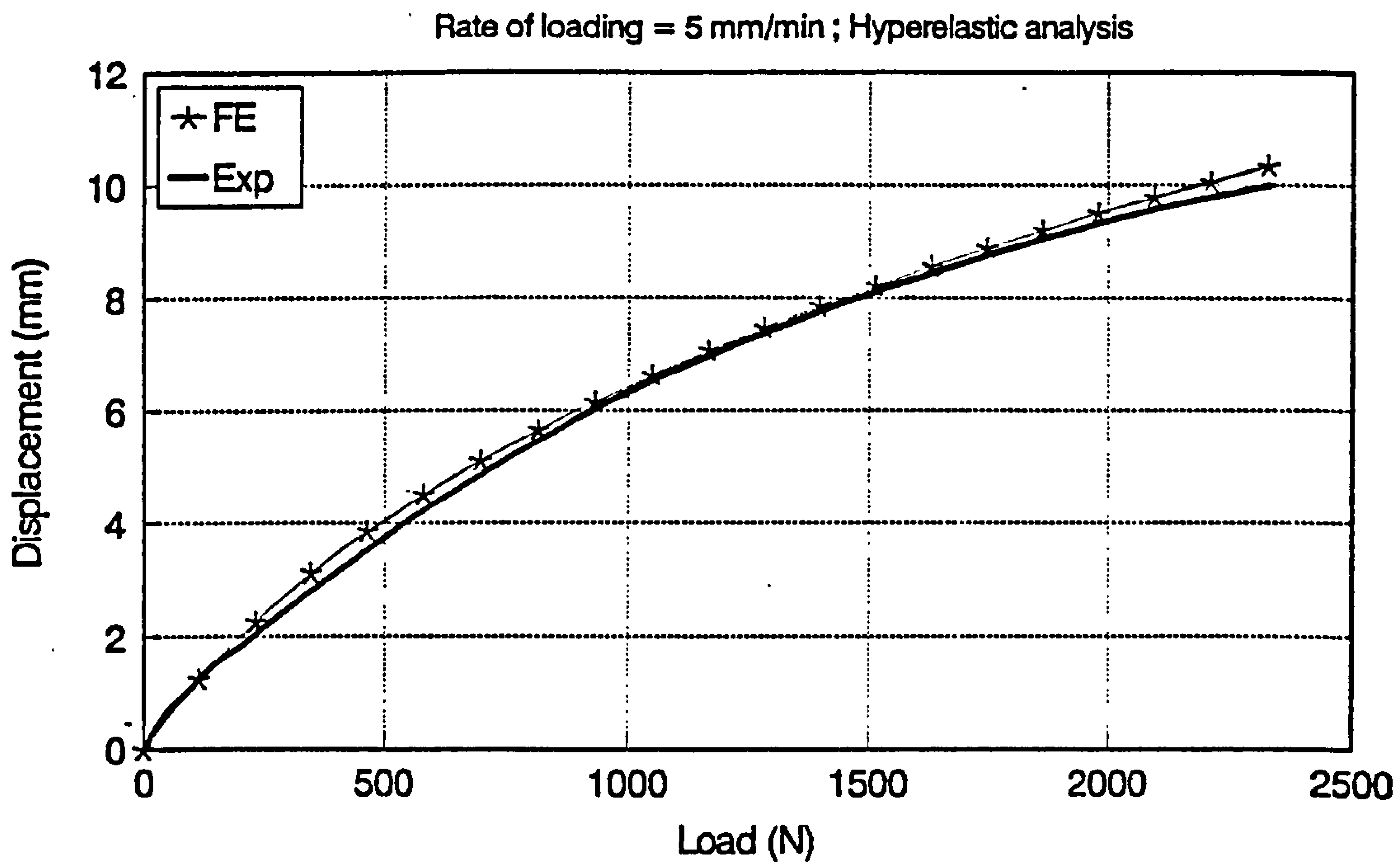

Fig. 6.5.6.1 Comparison between FE and experimental results.
(Rate of loading 5 mm/min ; FE model hrub1)

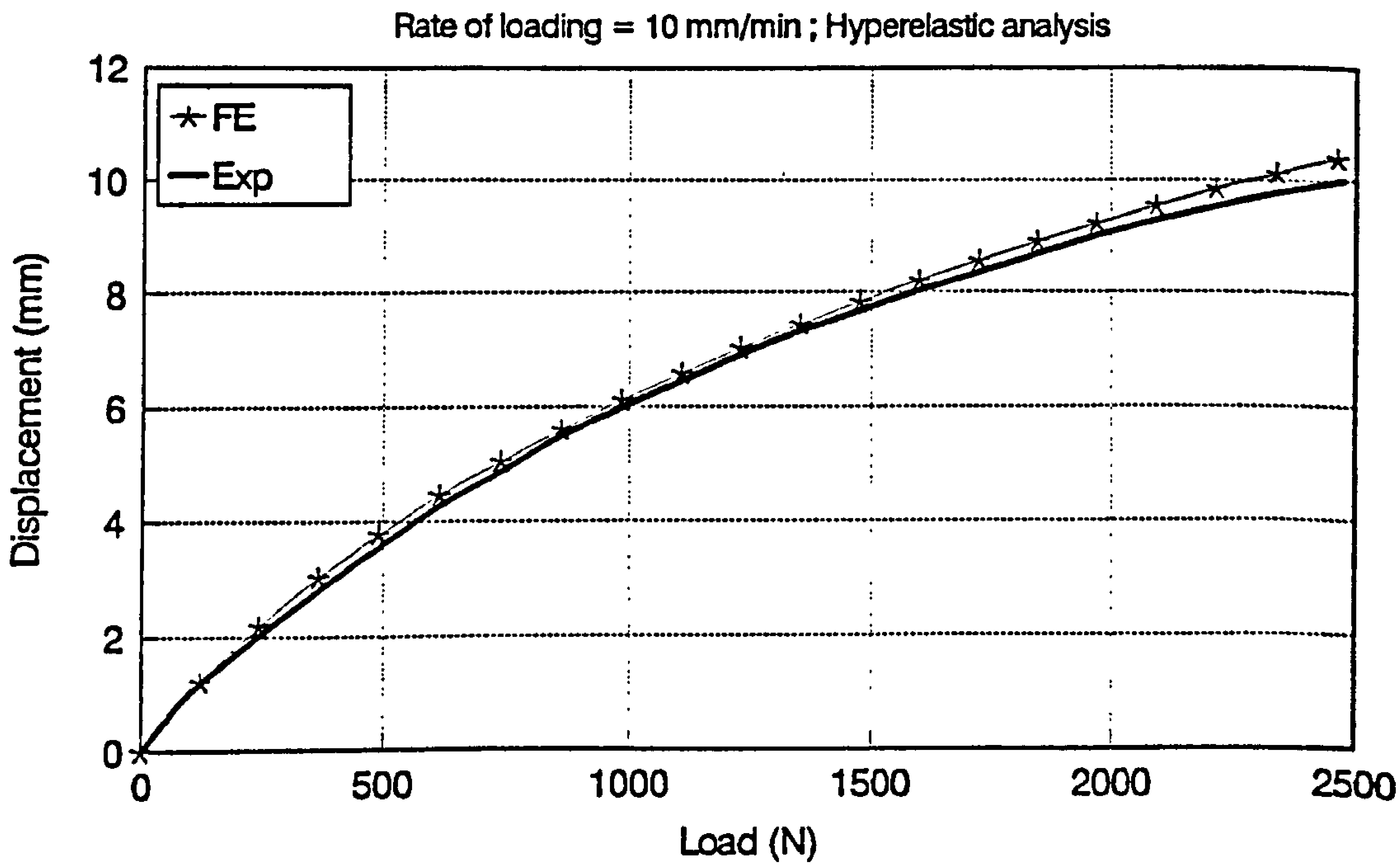

Fig. 6.5.6.2 Comparison between FE and experimental results.
(Rate of loading 10 mm/min ; FE model hrub2)

6.5.6 Results of compression model : hyperelastic analysis

The results of the hyperelastic analysis for rubber are presented in Fig. 6.5.6.1 to Fig. 6.5.6.5. The plots show the predicted and the experimental displacement - load curves. Among the three types of analysis for the rubber model, the use of hyperelastic material properties yield the most accurate FE predictions. The predicted curves match extremely well at all level of strain measurements. This may well be expected since the hyperelastic material is known to represent elastomers. However, in the porcine model, the use of hyperelastic material proves to be inaccurate. Firstly, as discussed in section 6.5.3, instead of one set of hyperelastic constants, three sets had to be defined in order to characterise the load - deflection curve of the porcine tissue. Secondly, upon feeding these constants into the porcine tissue model, a solution cannot be obtained due to numerical problems encountered.

6.5.7 FE model of the indentation test

Two models were constructed to model the rubber and porcine tissue indentation tests. The models were constructed in 3-D so that the geometry and the position of the indentor with respect to the specimen could be defined accurately. Fig. 6.5.7.1 and Fig. 6.5.7.2 display the FE models. The dimensions of the specimen were as mentioned in section 6.4.1 (rubber 95.5 x 48.96 x 49.5 mm ; porcine 66 x 37 x 36 mm). The indentor used was 5 mm in diameter. Both models were meshed with 3-D hexahedron elements (ABAQUS C3D8) Fig. 6.5.7.3. The number of elements used in both models were similar. The indentor was meshed with 144 elements containing 236 nodes, while the specimen was meshed with 1920 elements containing 2409 nodes. Loadings were assigned to the top surface of the indentor as distributed loads. The base of the specimen was fixed in the x, y and z directions while the indentor was fixed in the x and z directions. The assigned boundary conditions assumed there was no movement at the specimen base and the indentor was only allowed to travel perpendicularly to the specimen.

The steel indentor was given a material property of E=200 000 N/mm^2 and a Poisson's ratio of 0.3. Similar to the compression models, different types of analyses

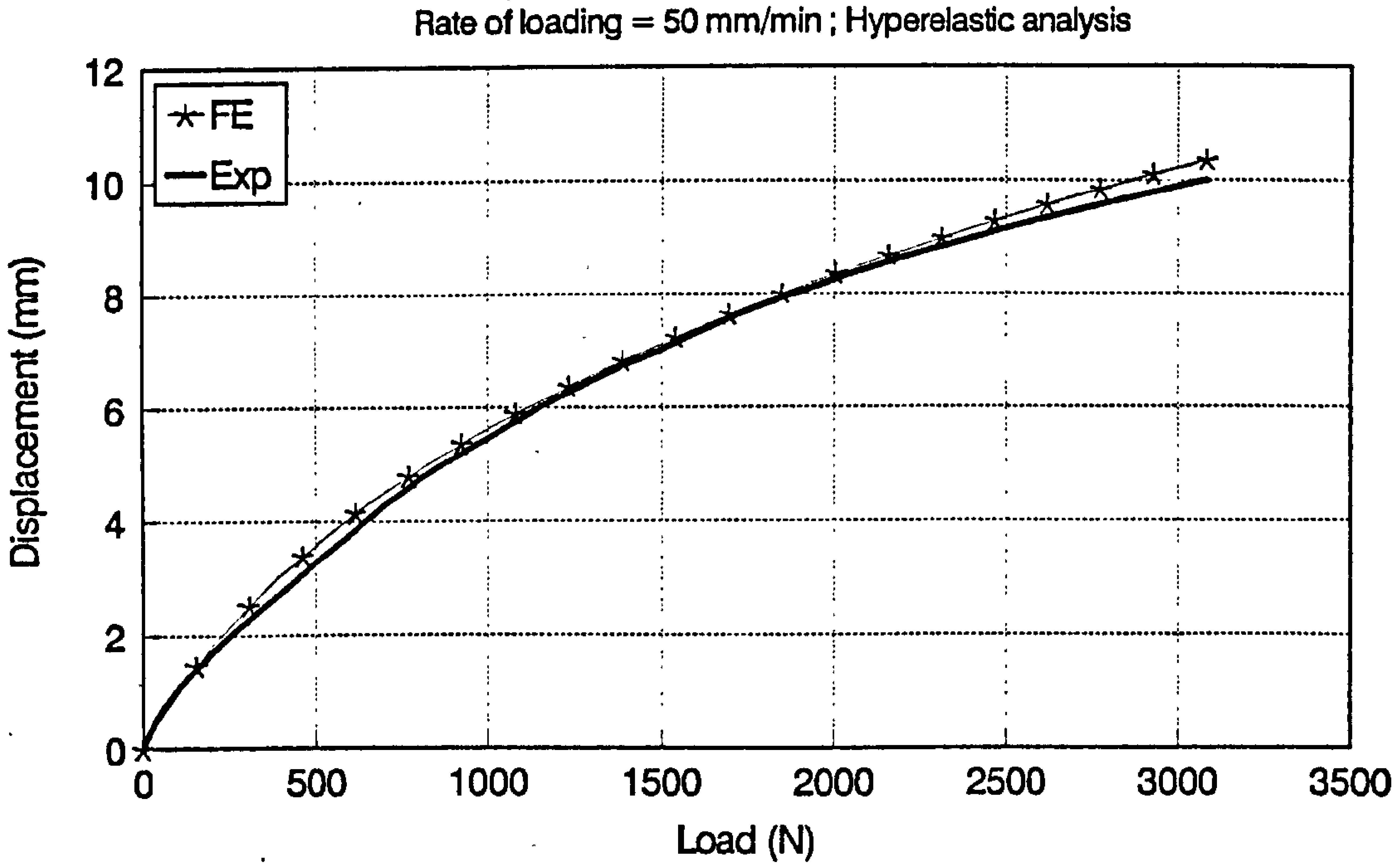

Fig. 6.5.6.3 Comparison between FE and experimental results.
(Rate of loading 50 mm/min ; FE model hrub3)

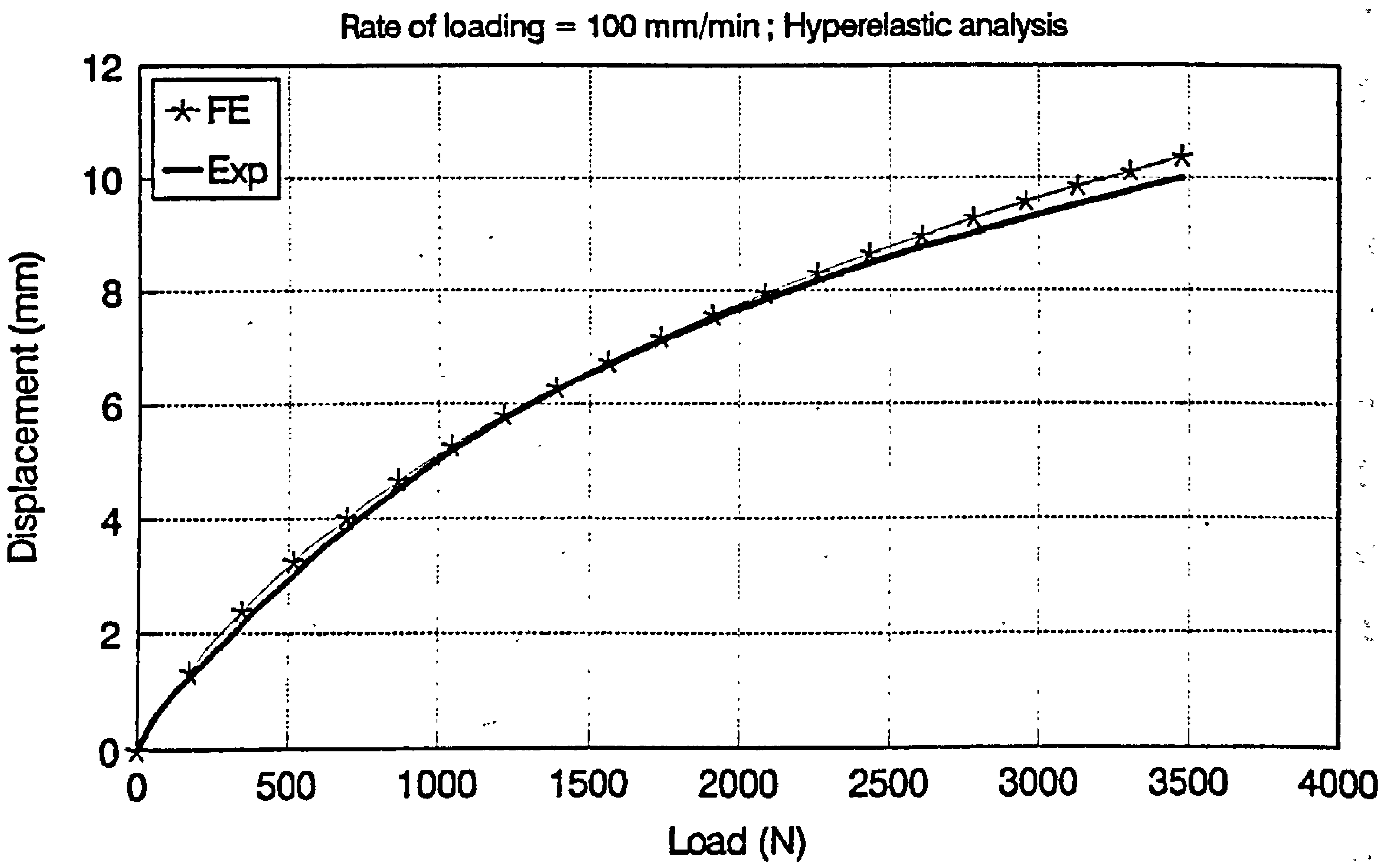

Fig. 6.5.6.4 Comparison between FE and experimental results.
(Rate of loading 100 mm/min ; FE model hrub4)

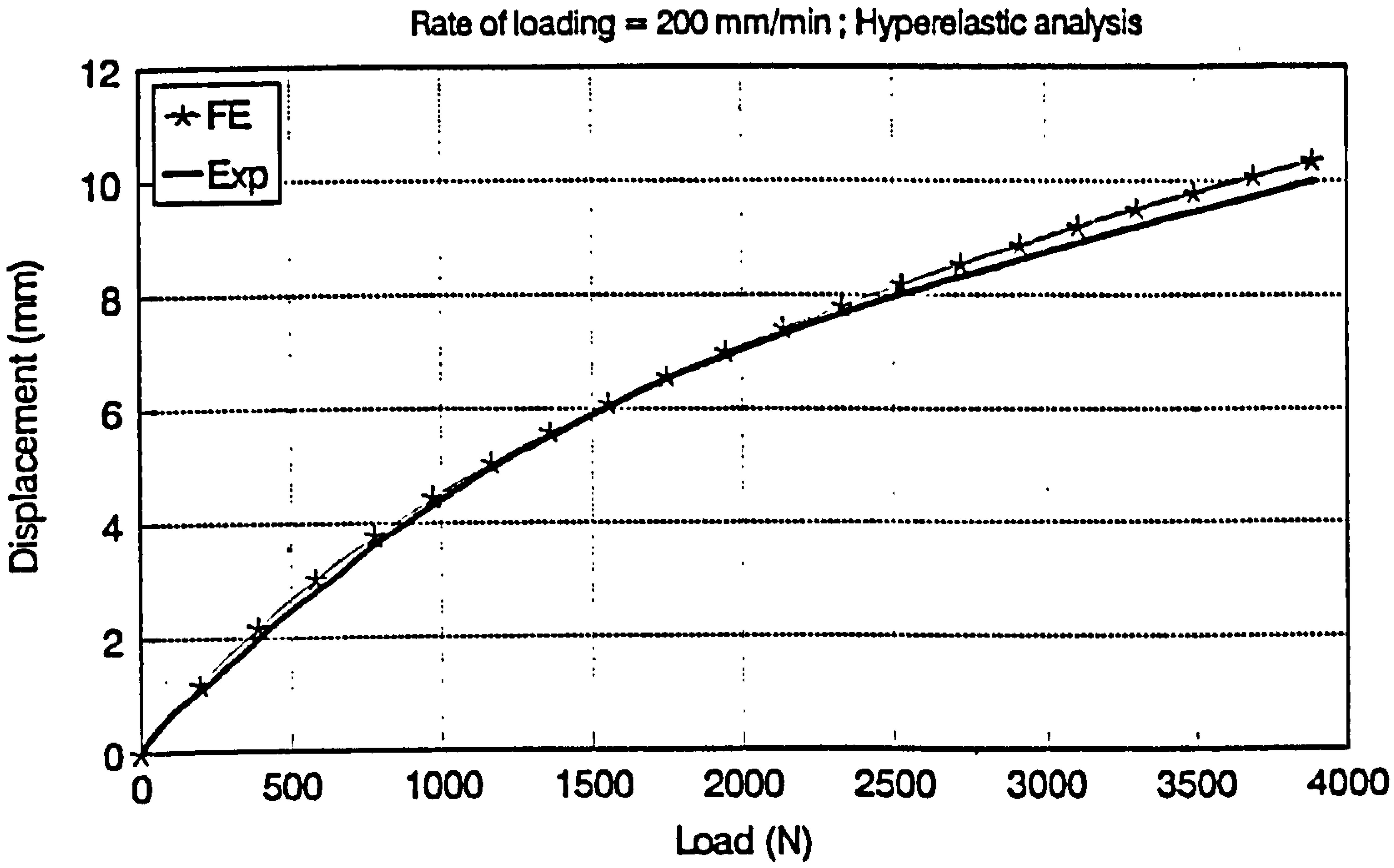

Fig. 6.5.6.5 Comparison between FE and experimental results.
(Rate of loading 200 mm/min ; FE model hrub5)

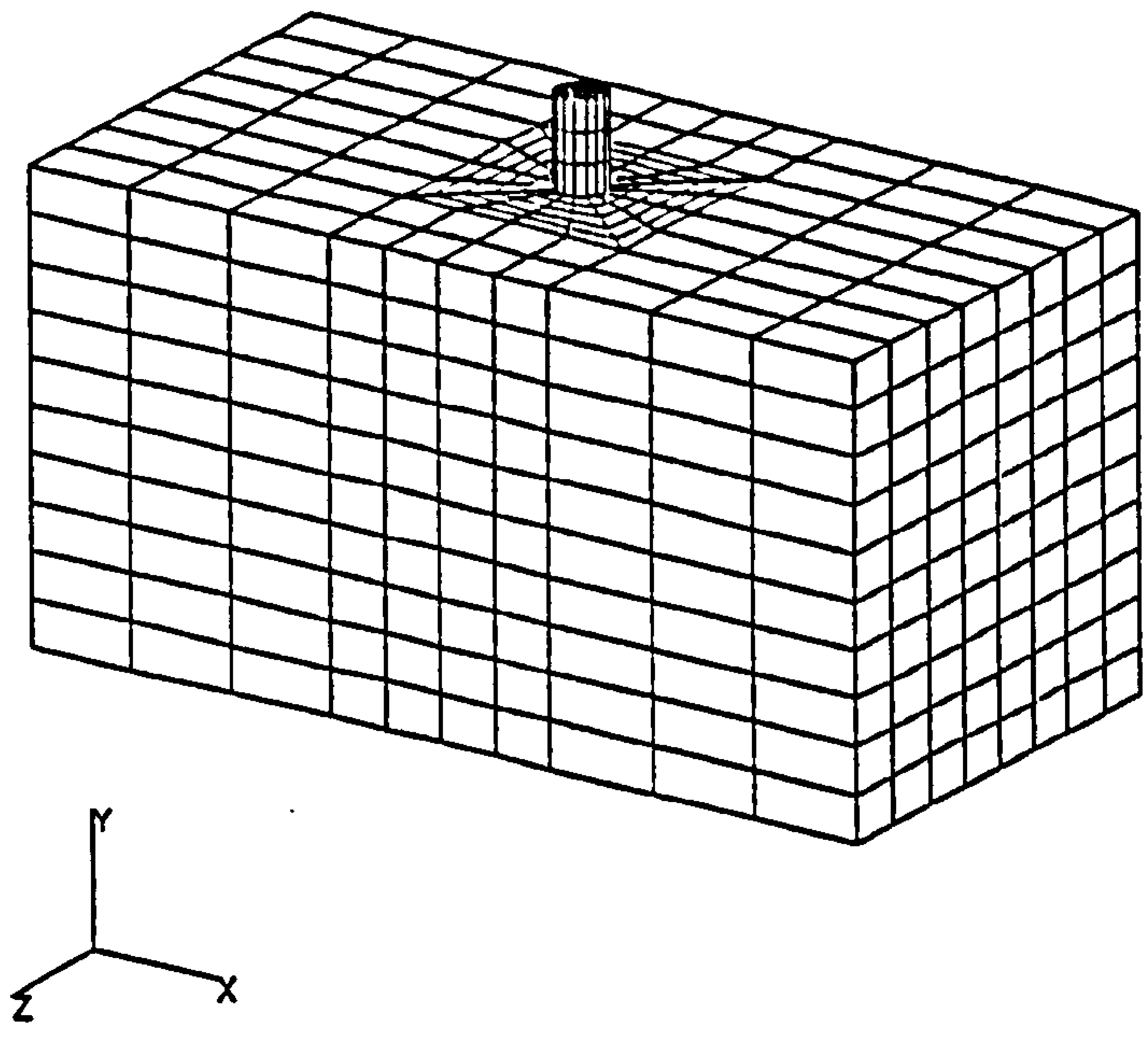

Fig. 6.5.7.1 FE model of rubber indentation test.

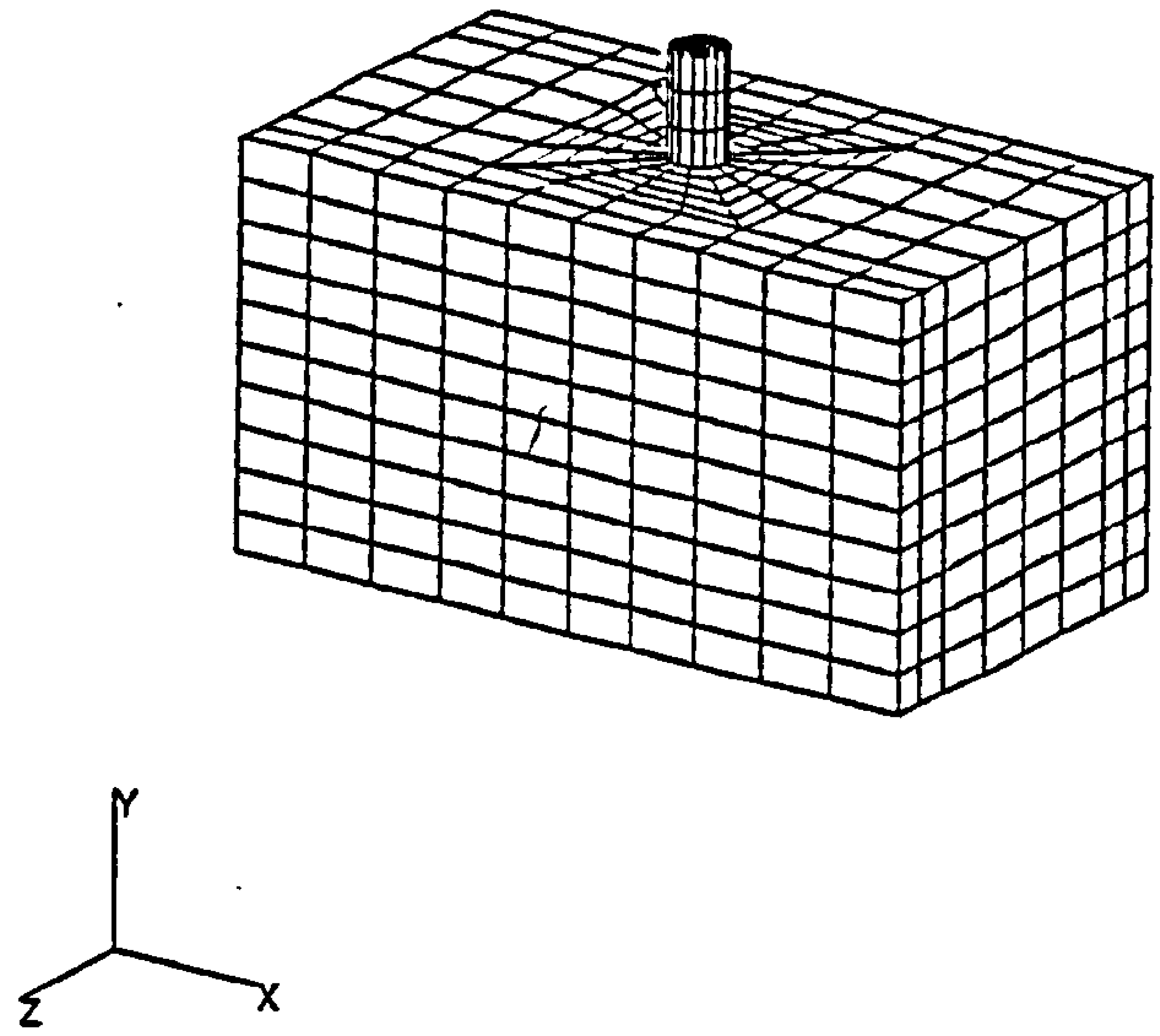

Fig. 6.5.7.2 FE model of porcine indentation test.

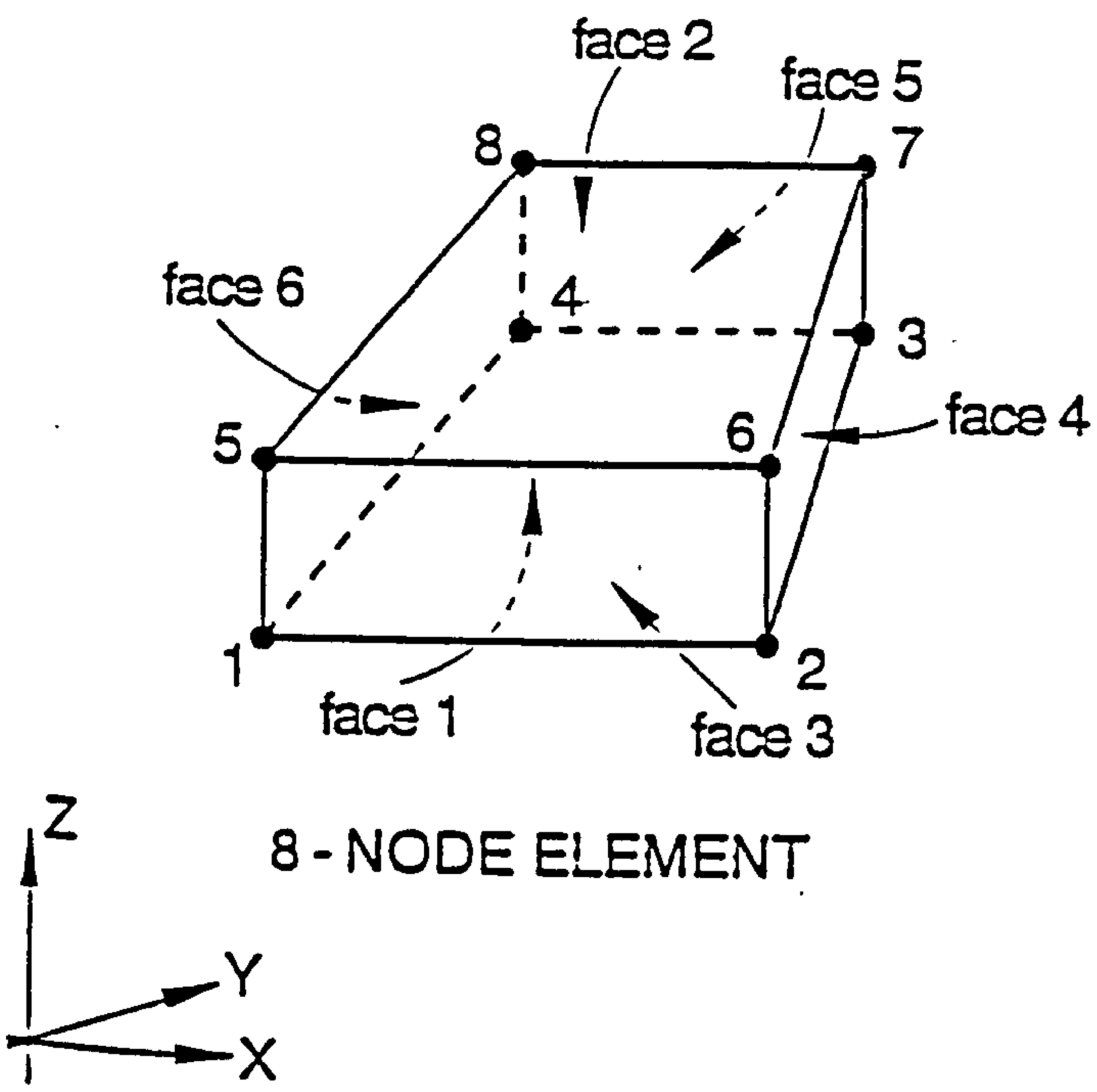

Fig. 6.5.7.3 Three dimensional hexahedron element (ABAQUS C3D8).

based on different material properties were conducted. However, unlike that of the compression test, the number of studies was reduced to only two types of material properties, linear and non-linear elastic. Hyperelastic analysis was not considered as it has been shown in section 6.5.6 to be unsuitable for porcine tissue. All the indentation analyses were attempted for a loading rate of 5 mm/min only.

In summary, the material inputs for the linear and non-linear indentation models are tabulated in table 6.5.7.1. All modelling was performed under large displacement analysis assuming geometrical non - linearity.

6.5.8 Results of indentation model : linear elastic analysis

Fig. 6.5.8.1 and 6.5.8.2 show the deformation plots of the rubber and porcine tissue indentation models. In rubber, the FE model predicted maximum indentation of 6.8 mm against that of 5 mm which was experimentally recorded (Fig. 6.5.8.3). The numerical solution converges after 17 incremental loadings and 40 iterations in total. The predicted values match the initial part of the experimental displacement - load curve very well up to approximately 4 mm indentation depth. After this point, predicted values were larger than the measured values and continued to increase with load producing more or less a straight line.

The predicted results from the porcine indentation test is as shown in Fig. 6.5.8.4. It can be seen that the numerical solution failed to converge at loads above 83.6 % of the maximum applied load of 8.24 N. The maximum displacement predicted at this load (6.8 N) was 7.732 mm compared to the experimental value of 10 mm at maximum load. The numerical solution diverges after 53 incremental loadings and 210 iterations. The failure for the solution to converge at 100% of the applied load was mainly due to highly deformed elements in the model at high loads. The applied load which should subject the model to predict a 10 mm indentation depth was high enough to cause some elements to have the effect of being turned inside out causing numerical problems. Furthermore, numerical divergence could also be caused by the large difference in the modulus of elasticity between the indentor and porcine tissue. Nevertheless, fitting a best straight line (linear regression) to the FE a.) Rubber model

Model	Rate of loading (mm/min)	Applied force (N)	Material properties
rub_ind_elas	5	71.82	$E^*=1.35\ N/mm^2$
rub_ind_non_e	5	71.82	Eng. stress - strain values
rub_ind_non_t	5	71.82	True stress - strain values

b.) Porcine tissue model

Model	Rate of loading (mm/min)	Applied force (N)	Material properties
po_ind_elas	5	8.24	$E^*=0.109\ N/mm^2$
po_ind_non_e	5	8.24	Eng. stress - strain values
po_ind_non_t	5	8.24	True stress - strain values

Table 6.5.7.1
Linear and non-linear elastic indentation models for a.) rubber and b.) porcine tissue. The material properties are defined from the experimental compression test. E* was used previously to predict the exact final experimental displacement in the compression FE model. The same E* was used for the linear elastic indentation model. For the non-linear elastic model, the material properties were defined by the engineering and true stress-strain curve from the experimental compression test.

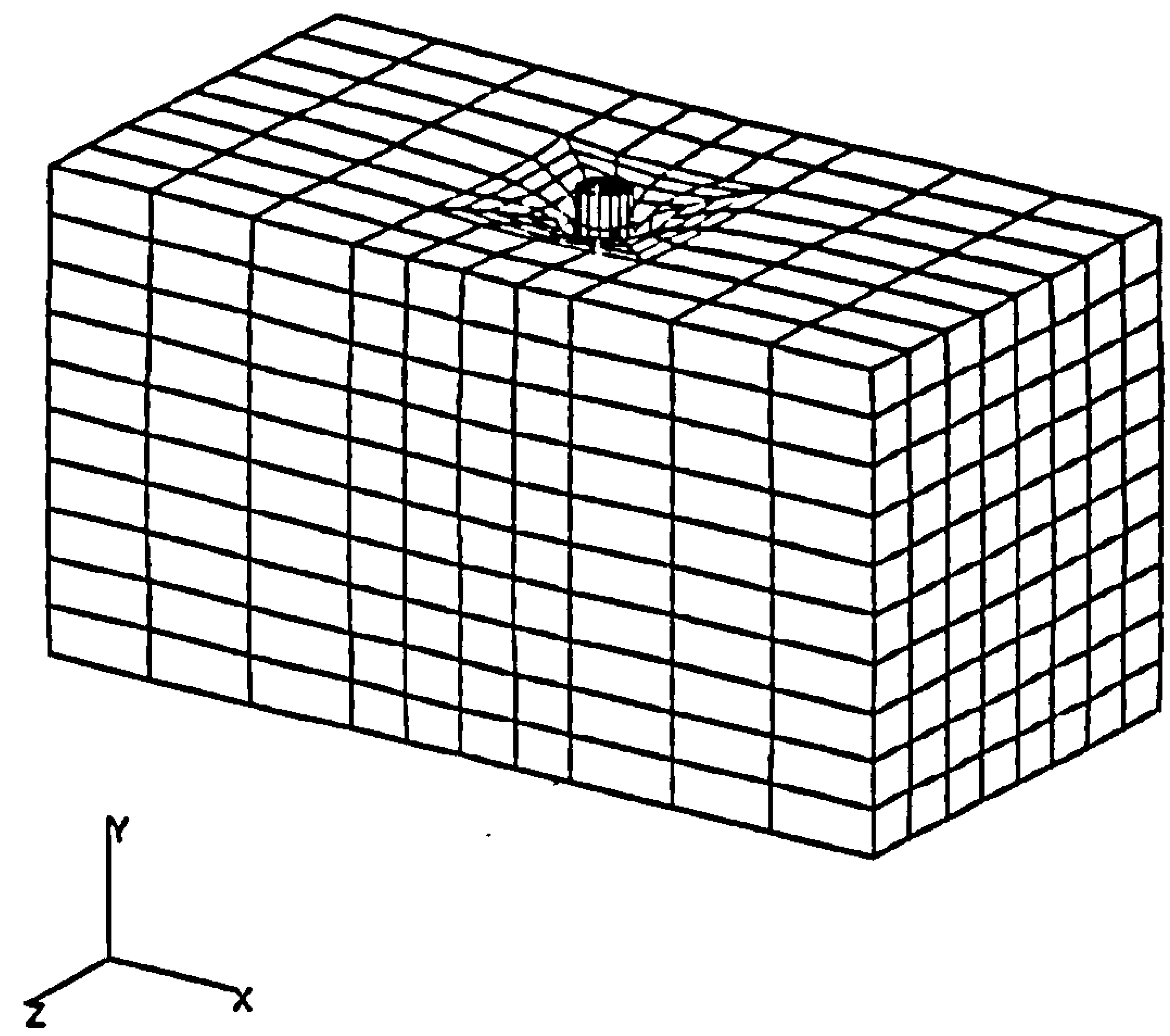

Fig. 6.5.8.1 Plot of deformation of rubber indentation model.

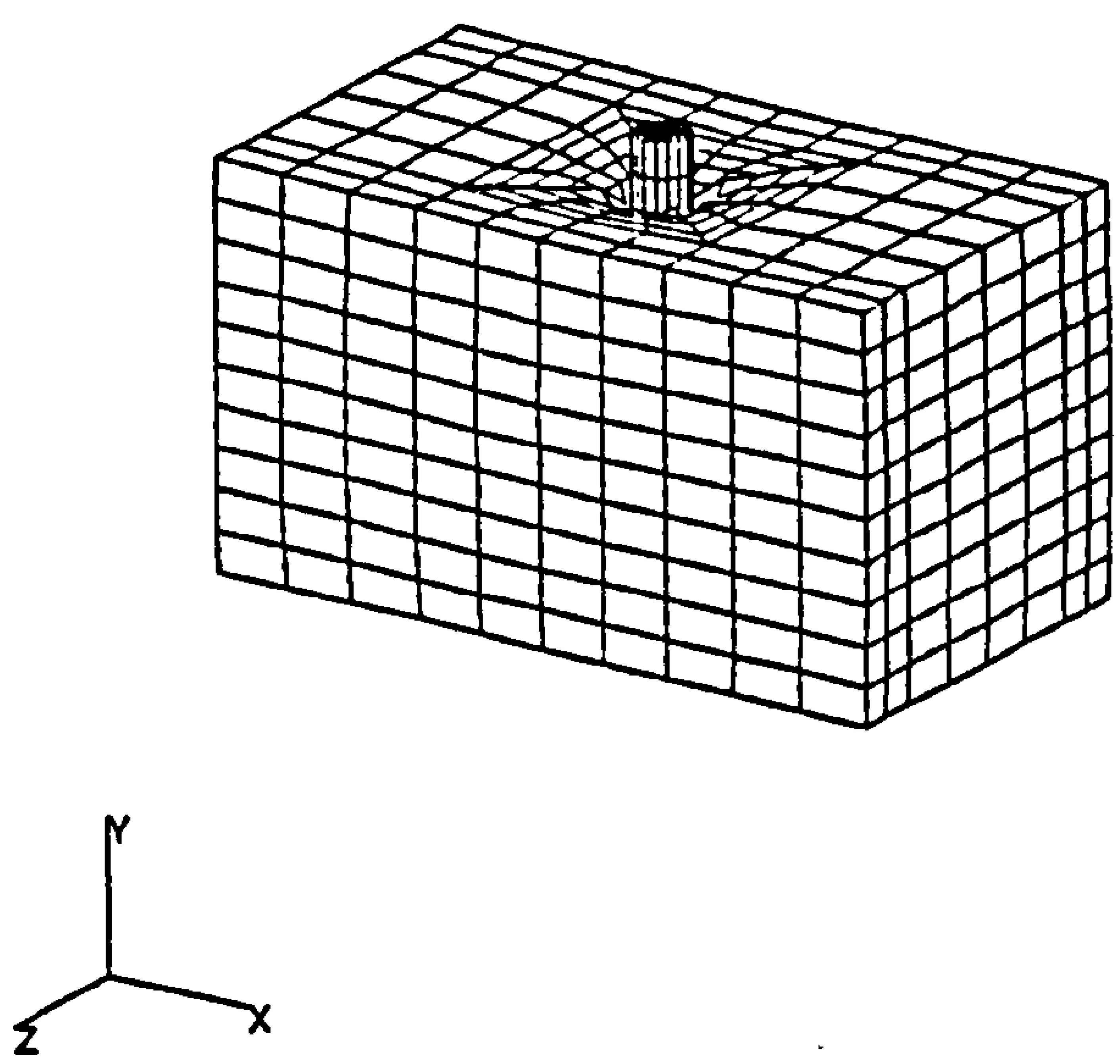

Fig. 6.5.8.2 Plot of deformation of porcine indentation model.

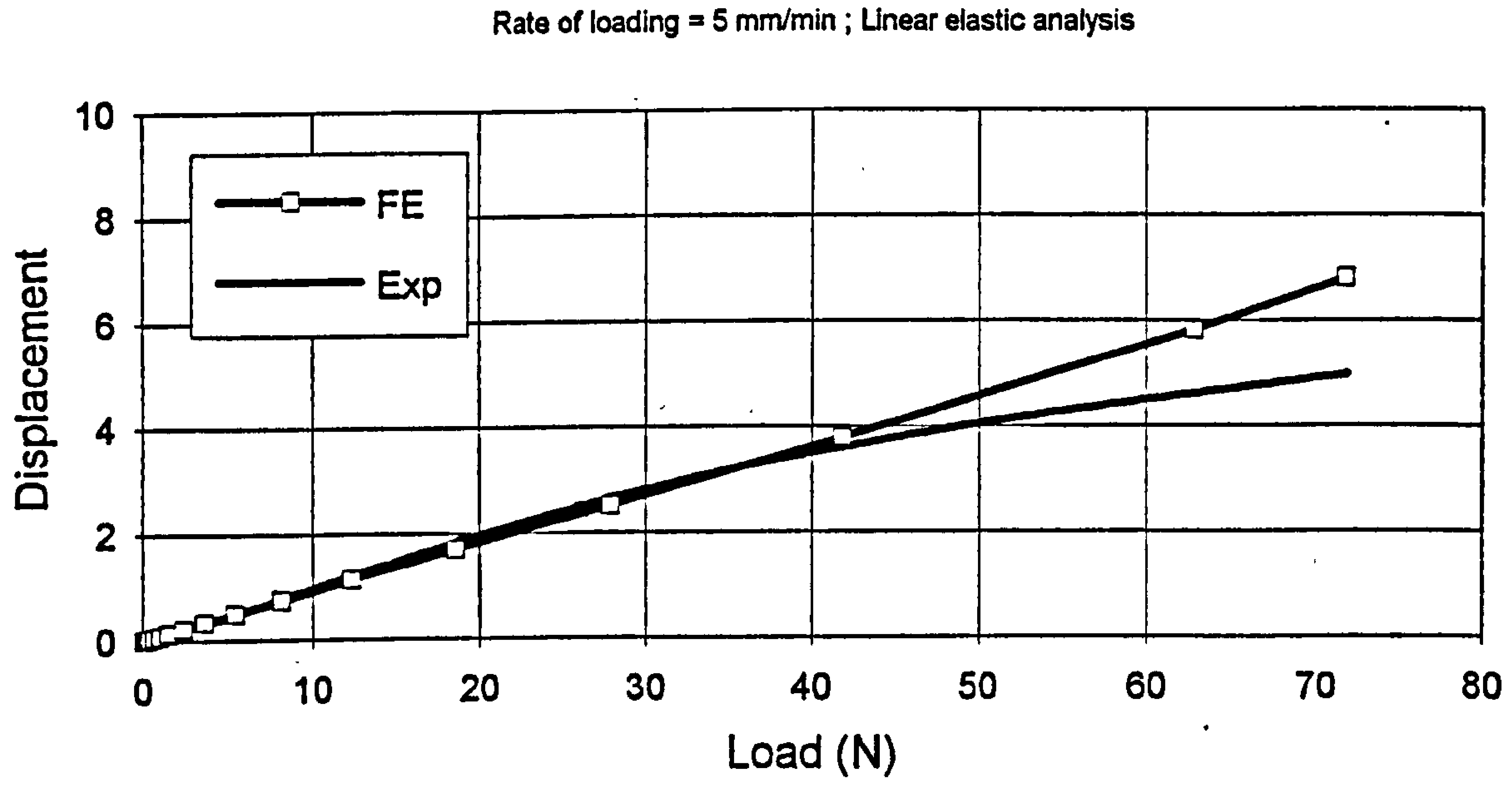

Fig. 6.5.8.3 Comparison between FE and experimental results.
(Rate of loading 5 mm/min ; FE model rub_ind_elas)

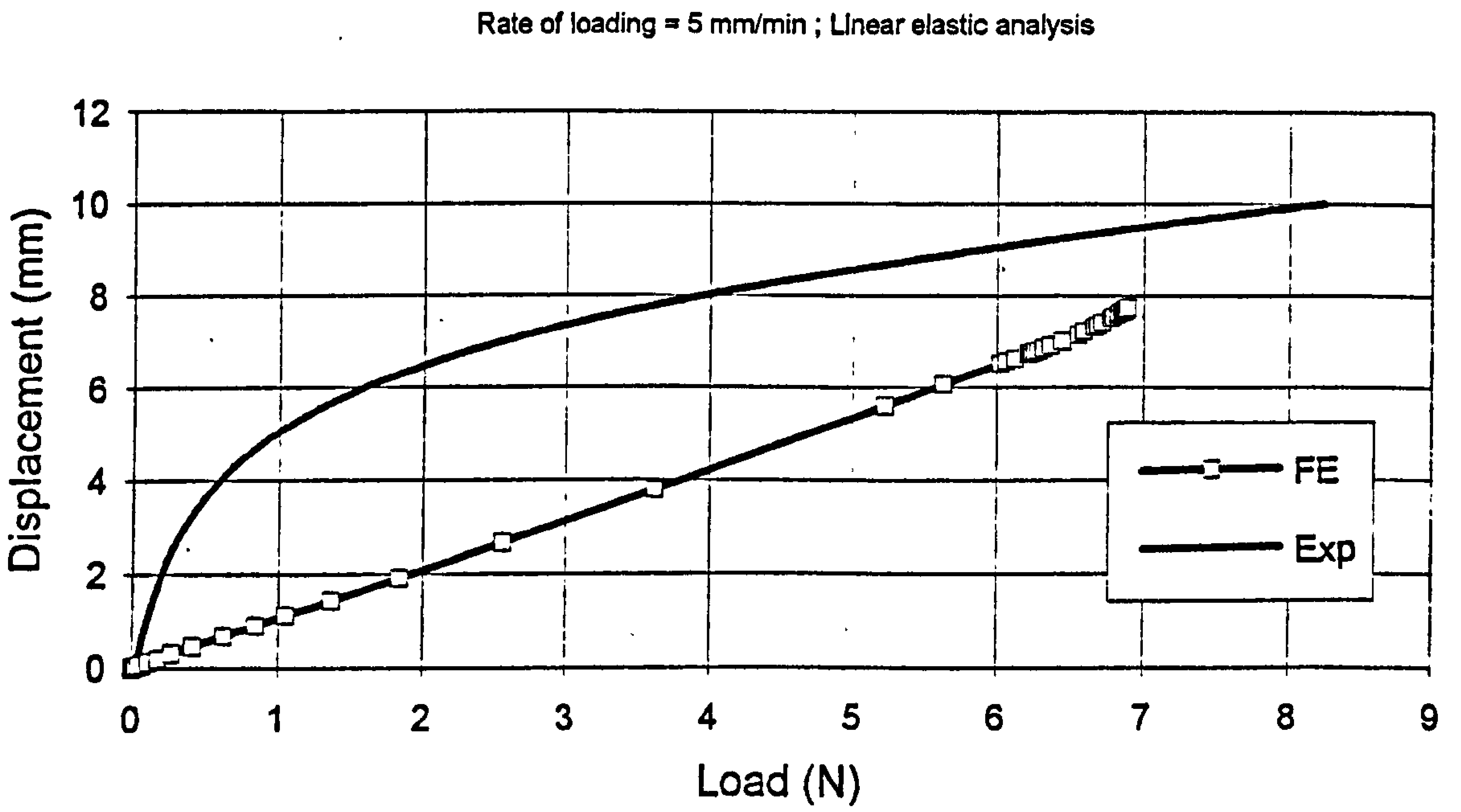

Fig. 6.5.8.4 Comparison between FE and experimental results.
(Rate of loading 5 mm/min ; FE model po_ind_elas)

predicted curve and extrapolating the displacement to 100% of the applied load, produced a displacement of 9.05 mm which was close to experimental value of 10 mm. Though the extrapolated final displacement may be within an acceptable range, the predicted curve however approaches that of a straight line and was not able to replicate the experimental curve.

6.5.9 Results of indentation model : non-linear elastic model

Both the non-linear elastic models for rubber and porcine tissue predicted realistic results. Also in both models, applying the engineering stress - strain values to describe the material properties gave a better prediction than using the true stress - strain values. In the rubber model (Fig. 6.5.9.1), the predicted curve based on engineering stress - strain matches the experimental curve very well up to 4.3 mm indentation depth, after which the predicted values increased beyond the experimental values giving a maximum predicted depth of 5.45 mm. The predicted displacement using true stress - strain values were consistently higher than the experimental values, where maximum predicted indentation was 6.39 mm.

In the porcine model, the predicted curves were not able to follow the experimental curve closely (Fig. 6.5.9.2), especially at the initial part of the curve when a low indentation load produced a large displacement. Using the engineering stress-strain values as material input to the model, lower displacement values were predicted throughout the incremental loads applied. However, the final predicted displacement was 9.88 mm, close to the experimental indentation depth of 10 mm. Whereas using the true stress - strain values, the predicted displacement were also lower than the experimental values up to a load of about 5N at 9 mm indentation depth. At higher incremental loadings, the predicted displacements exceeded the experimental values producing a final displacement of 11.61 mm.

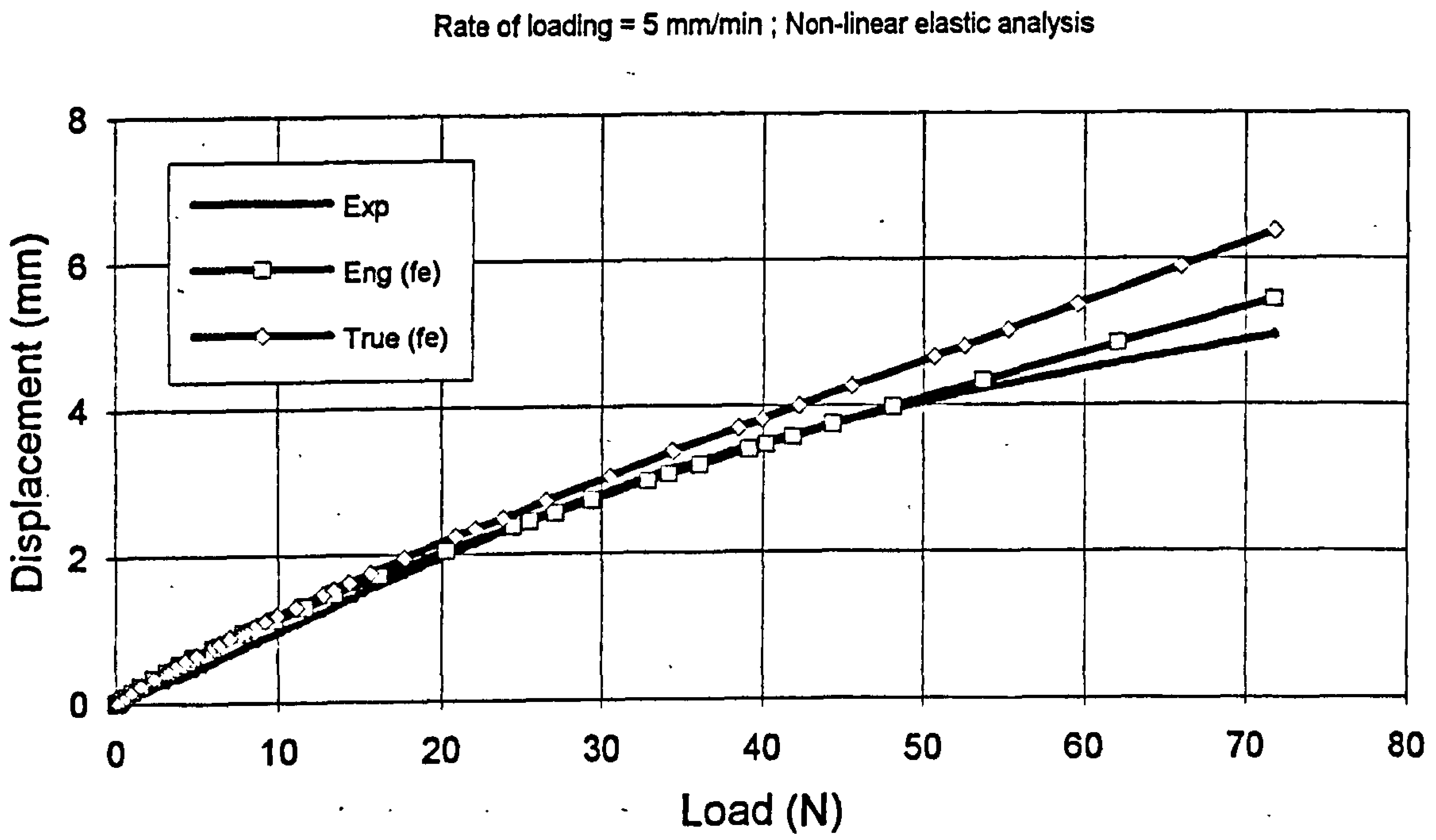

Fig. 6.5.9.1 Comparison between FE and experimental results.
(Rate of loading 5 mm/min ; FE model
rub_ind_non_e and rub_ind_non_t)

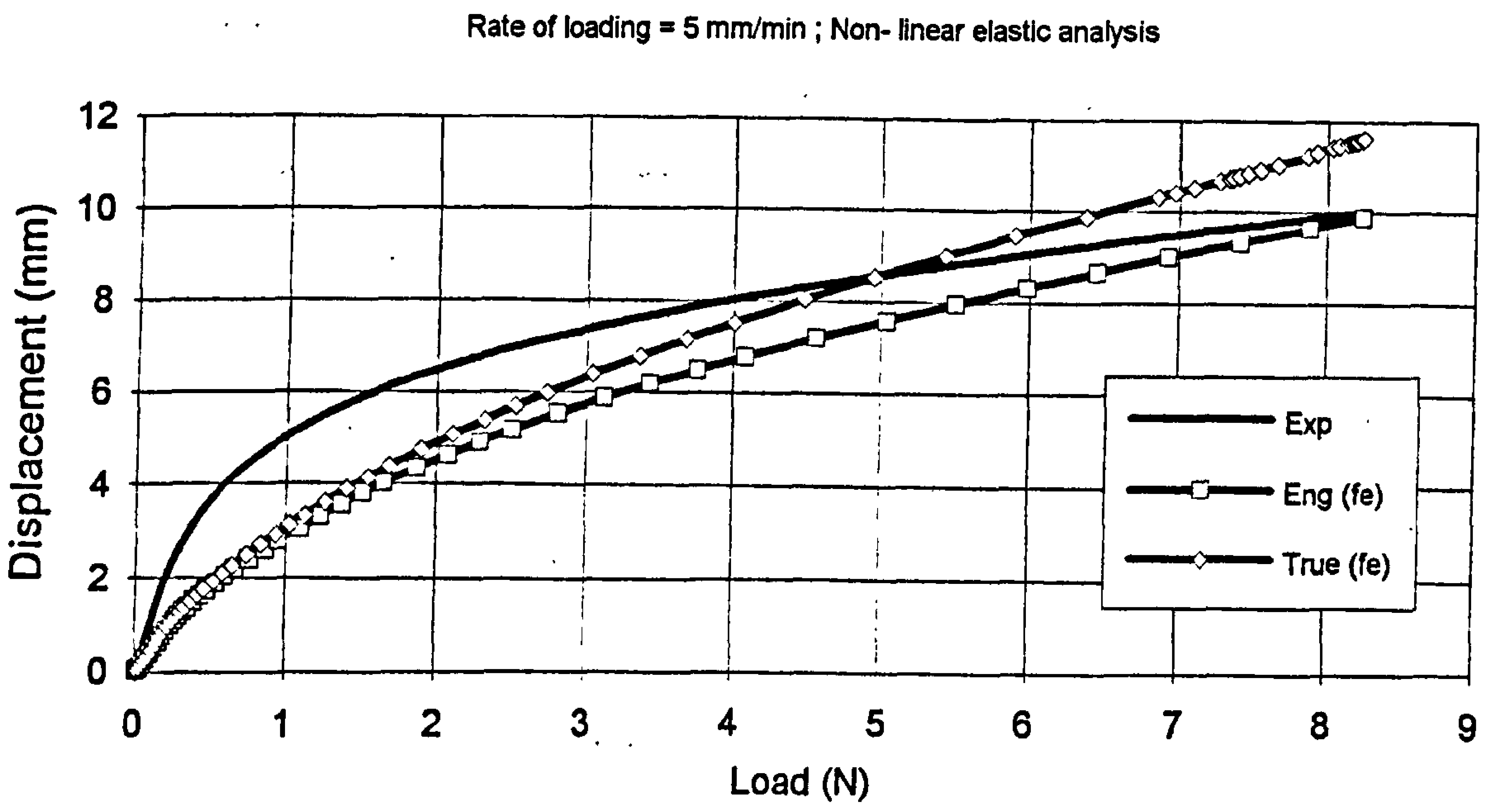

Fig. 6.5.9.2 Comparison between FE and experimental results.
(Rate of loading 5 mm/min ; FE model
po_ind_non_e and po_ind_non_t)

6.6 DISCUSSION : *IN VITRO* STUDY

This section will discuss the implication which arises from the *in vitro* study.

A number of investigations using FE method to model soft tissue behaviour in the areas of prosthetic sockets (Steeges et al 1987, Sanders et al 1993) and seating (Todd and Thacker 1994, Dabnichki et al 1994) have used material properties assumptions with little or no documentation. In the present study of two non - linear materials, rubber and porcine tissue, the author of this thesis has provided a concise picture of what is involved in modelling soft issue mechanical behaviour using FE method. The present study dealt with the selection of suitable material properties for FE analysis, indicating clearly the errors involved by comparing with experimental data.

Prior to the experimental and theoretical part of the study, a review of past literature has shown the limitation in producing a suitable constitutive equation that could represent soft tissue mechanical behaviour. With this in mind, this study was carried out assuming soft tissue to be nearly incompressible, isotropic and exhibiting no viscoelastic behaviour. Soft tissue has been considered to be virtually incompressible because of the high ratio of bulk modulus to shear modulus, which is very much the same as rubber where the bulk modulus is about 10000 times greater than the shear modulus. However, incompressibility poses problems since the stress - strain relationship for an incompressible material is indeterminate. In this study, to overcome this indeterminacy, the Poisson's ratio selected for the elastic and non-linear elastic analysis was 0.4999 i.e. nearly incompressible. Vannah and Childress (1993) reported FE modelling of narrowly contained soft tissue in which predicted results were highly sensitive to the selection of Poisson's ratio around the 0.5 limit. Using the MARC finite element code, with specially formulated elements, the authors produced an idealised axisymmetric model of the trans-femoral residual limb and subjected it to a selection of Poisson's ratios ranging from 0.45 to 0.5. Assuming linear elastic material properties (E=0.0207 MPa) under small displacement analysis, the idealised femur was displaced 5 mm vertically (Fig. 6.6.1). The FE predictions are tabulated in table 6.6.1. The results showed that assuming a Poisson's ratio of 0.499 to 0.5, there

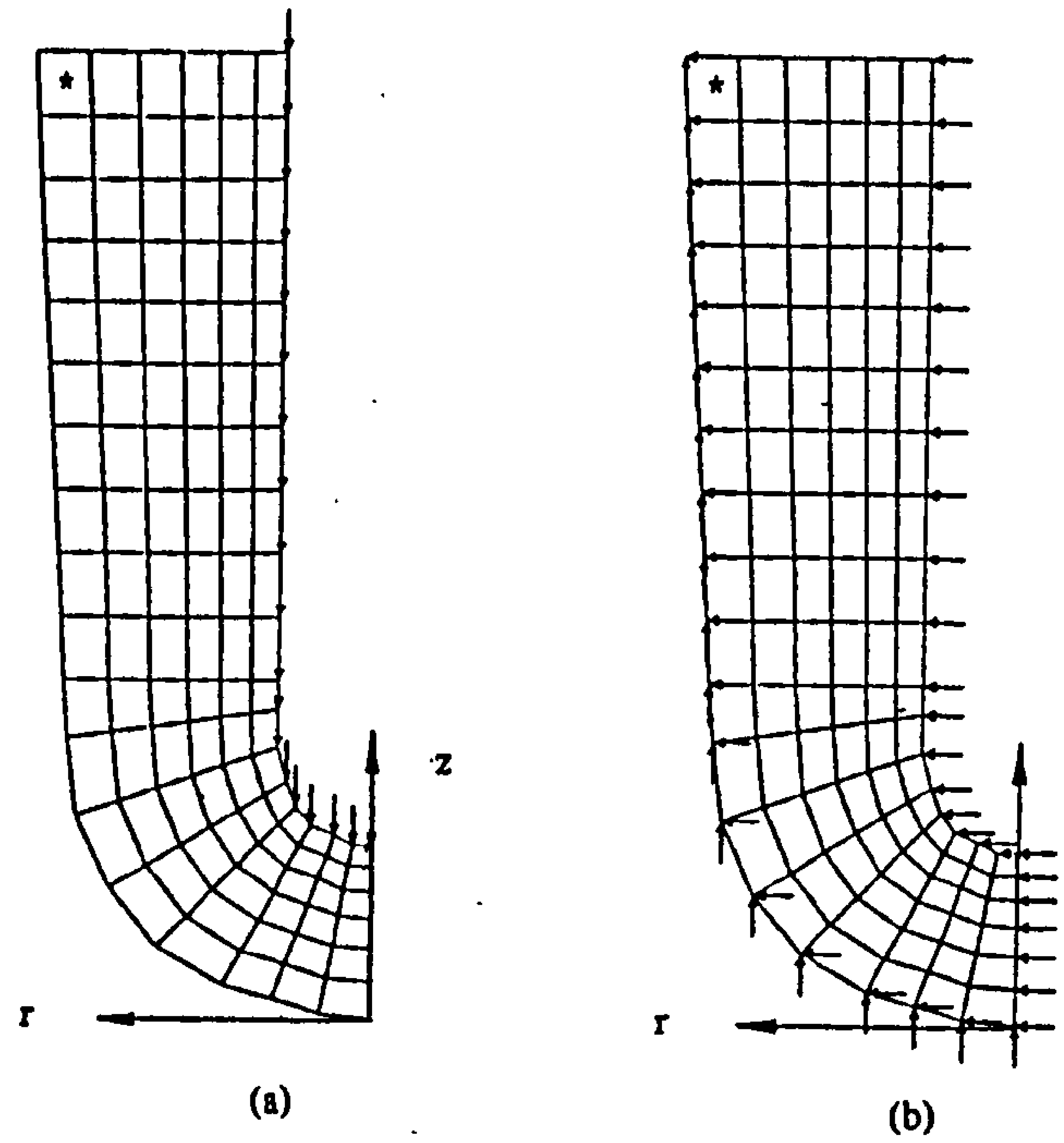

Fig. 6.6.1 Idealised axisymmetric FE model of the trans-femoral residual limb.
a.) Displays the vertical nodal displacements and
b.) Displays the nodal boundary conditions.
(Vannah and Childress 1993)

(displacement = 5.0 mm).

Poisson's Ratio	Reaction Force (N)	von Mises Stress (MPa)
0.4500	44.7	0.12
0.4900	64.5	0.15
0.4990	91.4	0.66
0.4999	91.4	0.66
0.5000	91.4	0.66

Table 6.6.1 Effects of Poisson's ratio on element ' * ' as shown in Fig. 6.6.1.
(Vannah and Childress 1993)

was no change in the FE predictions. Therefore in the present study, the use of 0.4999 for the Poisson's ratio was a reasonable figure describing the incompressibility of the rubber and the porcine tissue studied.

Assuming the model to be isotropic, elastic and exhibiting no viscoelastic behaviour i.e. no hysteresis, no stress relaxation and no creep, actually reduced the problem to one of non-linearity only. This was considered the best way to tackle the problem of selecting a suitable material property for use in the FE modelling. If one was to consider anisotropy in a three dimensional Hookean solid, multiple elastic constants are required. The compression test set-up used in this study was not sufficient to obtain these multiple elastic constants. However for an isotropic material, the problem is greatly simplified, having only one elastic constant and Poisson's ratio, which was within the reach of the compression test performed. The assumption of isotropy and incompressibility made it possible to define the properties of a three dimensional solid using two dimensional experimental data.

The viscoelastic behaviour of biological soft tissue has been modelled previously by several researchers. These models were based on the combination effect of a linear spring (elastic modulus) and dashpot (viscosity), also commonly known as the Maxwell and Voigt models (Jamison et al 1968 and Barbenel 1979). To include viscoelasticity in the present study was considered premature. To the knowledge of the author of this thesis, there has been no previously published information on the accuracy of a biological soft tissue FE model using the different elastic material properties (i.e. linear elastic, non-linear elastic and hyperelastic) as attempted here. However, it is highly recommended that viscoelasticity be considered in future studies.

The present study was aimed at evaluating the different material characteristics in order to model biological soft tissue. Three types of material properties have been investigated, these were linear elastic, non-linear elastic and hyperelastic. Linear elastic analysis assumes that the material tested obeys Hooke's law. In the non-linear elastic analysis, the material assumes an elastic behaviour but the stiffness varies with strain. Finally, hyperelastic material is based on the M-R functions for rubber like

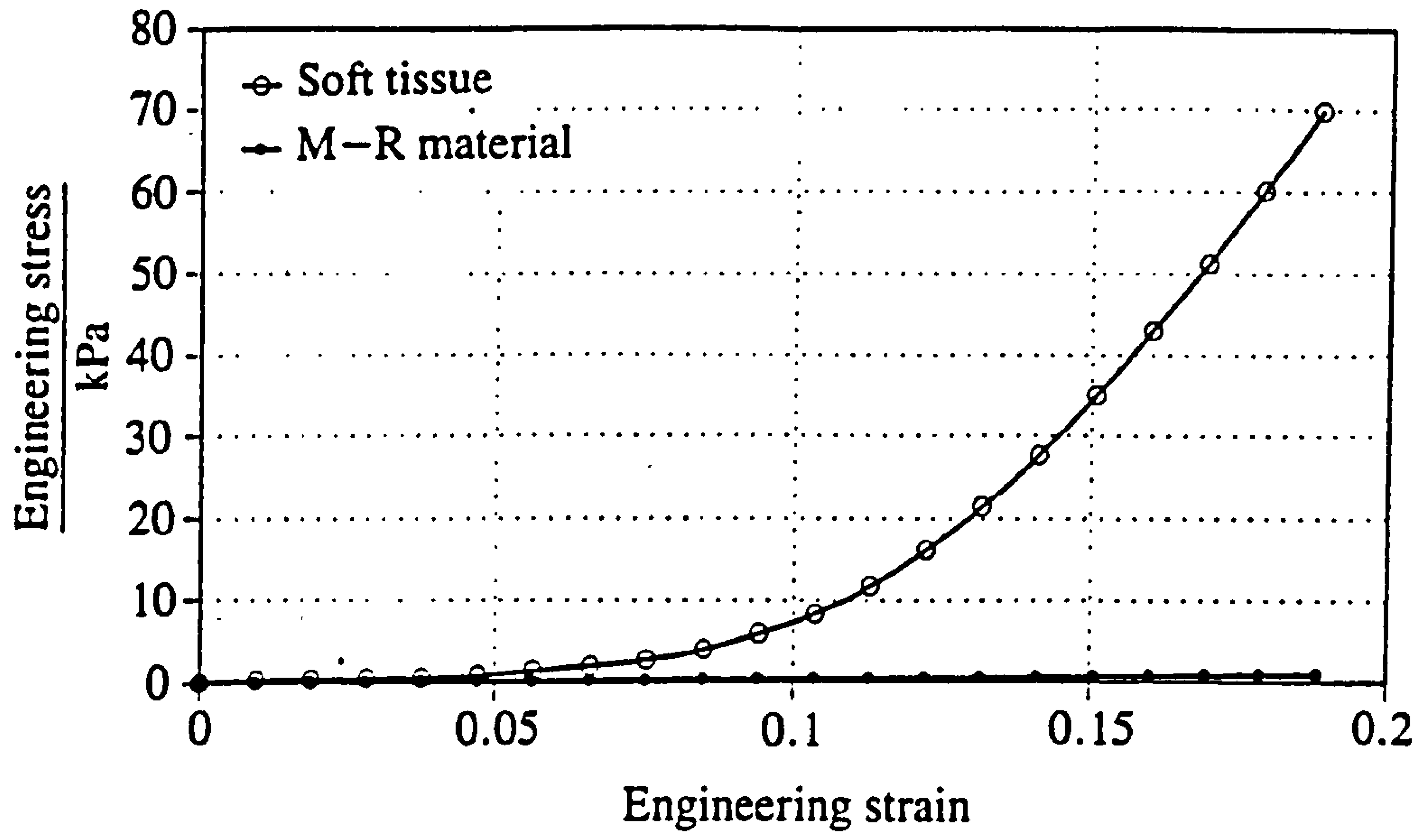

Fig. 6.6.2 A typical porcine soft tissue response to compression compared with the M-R material with parameters suggested by Dabnichki et al (1994).

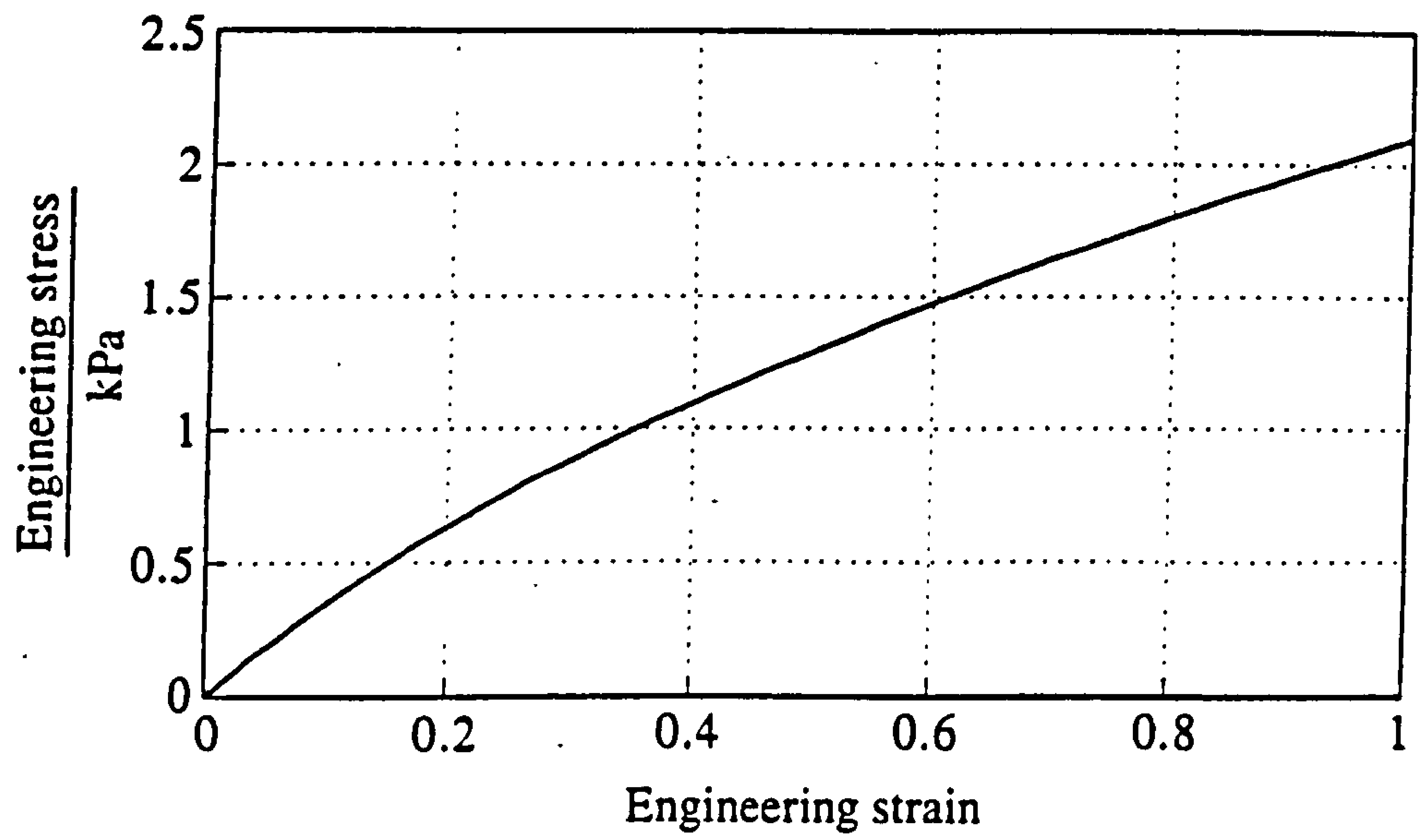

Fig. 6.6.3 Response of M-R material to simple tension using parameters suggested by Dabnichki et al 1994.

material derived from strain energy. The results had clearly shown that for biological tissue, non-linear material properties with non-linear geometry, i.e. large displacement analysis where the geometry is updated incrementally, provided the closest match to the experimental values for both the compression and indentation models. In the elastic model, the predicted curve approached a straight line. Though the linear analysis included the non - linear geometrical properties of the model, it was insufficient to accommodate the high degree of non - linearity experienced by the porcine tissue.

The use of Mooney-Rivlin (M-R) material has been cited as a possible choice of material by several authors in modelling bulk soft tissue (Dabnichki et al 1994 and Steege et al 1987). However, as shown in this study the M-R material has failed to model soft tissue. A discussion was generated between Dabnichki et al (1994) and Barbenel and Lee (1994) regarding the use of M-R material and several points from the discussion will be highlighted here. The M-R function is non-linear, isotropic and elastic. Thus, the best that the M-R function could achieve was to model the non-linearity experienced upon loading soft tissue, which was similar to the other two previous analyses (elastic and non-linear elastic). In order to use the M-R function, a minimum of two constants have to be defined. However, it has been shown clearly in section 6.5.3, that unlike rubber, two M-R constants were insufficient to define the complete loading curve of porcine tissue under compression. In fact the stress-strain relationship predicted using the M-R function as expressed in equation 6.5.3b of section 6.5.3 was only mildly non-linear, which was suited to the mild non-linearity experienced in compressing rubber. However, when applied to soft tissue, the M-R material cannot model the marked increased in stiffness displayed by the porcine tissue (Fig. 6.6.2). It was only at a much higher strain that the mild non-linearity in M-R material began to surface. And even this mild non-linearity was only shown at unphysiologically large compressive strain.

Finally, in a model of the residual limb or buttock, both compressive and tensile stress states exist. However, in simple tension, equation 6.5.3b shows that the M-R material displays a monotonically decreasing gradient with increasing strain (Fig.

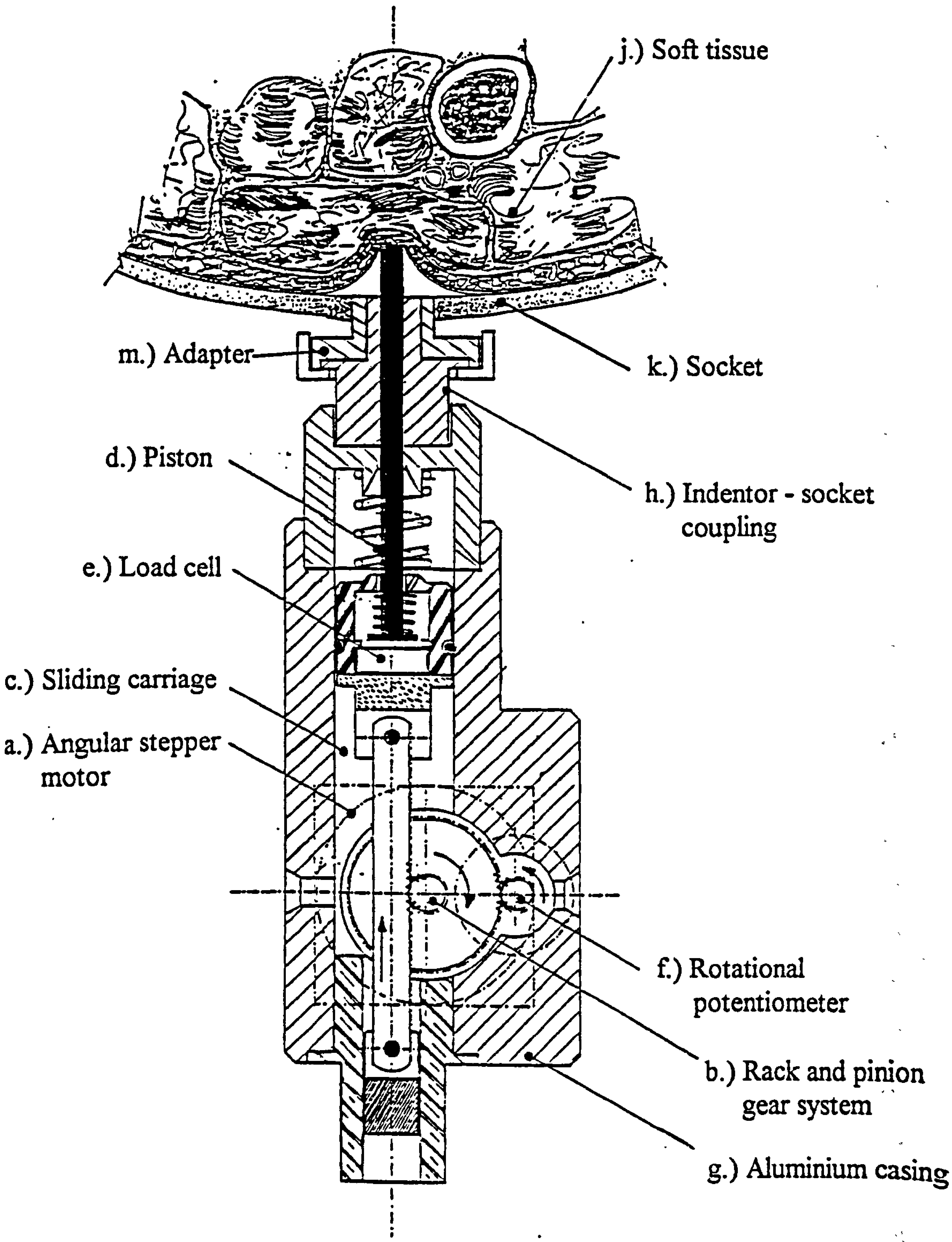

Fig. 6.7.1.1 Mechanical Indentor (Modified from Torres-Moreno, 1991)

6.6.3). This behaviour is exactly the opposite of that of the behaviour shown by tissue in simple tension, clearly indicating the M-R material does not model the mechanical behaviour of soft tissue in simple tension.

This study has shown the effect of considering the three commonly used material assumptions in modelling bulk soft tissue. The investigation indicated that the use of non-linear elastic material properties gave the best correlation between FE prediction and experimental results in FE modelling of porcine tissue. Linear elastic behaviour was able to provide a reasonable FE prediction when the elastic modulus describing the material was carefully selected. Its selection was dependent on the maximum stress or strain experienced by the material. Lastly, the use of hyperelastic material in the modelling of porcine tissue was not successful and the FE models experienced numerical convergence difficulties.

6.7 *IN VIVO* INDENTATION TEST

This section of the thesis discusses the use of a mechanical indentation device to characterise the mechanical properties of the amputee's residual limb. The device used in this study was designed by Torres - Moreno (1991) in the University of Strathclyde Bioengineering Unit. Only minor changes have been introduced to the indentor in order to facilitate easy coupling during indentation while the rest of the device's construction has been kept similar to that proposed by Torres-Moreno. The full details of the indentor construction and calibration can be found in the report by Torres-Moreno (1991).

6.7.1 Mechanical indentor

The indentor is as shown in Fig. 6.7.1.1. Its main parts are ;

a.) an angular stepper motor (Model RS 332-082, RS Components Ltd. UK),

b.) rack and pinion gear system,

c.) a sliding carriage system which also includes the housing for the load cell and the load sensitive indentor piston,

d.) circular solid indentor piston with a sensitive area of 23.16 mm^2 (5.43 mm in diameter),
e.) load cell (Model 601-2, Entran International, France) similar in type used in the pressure measurement system described in chapter 4 of this thesis,
f.) rotational potentiometer (Model RS 173-388, RS Components Ltd. UK),
g.) aluminium casing,
h.) indentor - socket coupling.

The device is driven by the stepper motor which is controlled using a personal computer. The stepper motor rotation is converted to a linear displacement through the rack and pinion system. Referring to Fig. 6.7.1.1, the linear displacement therefore pushes the piston out of the indentor - socket coupling indenting the soft tissue (j) contained within the socket (k). The adapter (m) which is fixed securely to the socket is exactly the same as that used in the pressure measurement system described in chapter 4. The indentor is held onto the adapter on the socket using the indentor - socket coupling. The coupling allowed the indentor to be fixed to the socket without the need of rotating the indentor, thus easing moving the indentor from site to site. The coupling and adapter combination also provided a means for locating the piston to sit flush with the inside wall of the socket prior to indentation.

6.7.2 Subjects and prosthetic socket

The subjects tested have been similar throughout this study and have been described in chapter 4 section 4.3.2 of this thesis. The subjects are coded H, U and M. Each of the three subjects has been prescribed and fitted with an IC socket, which was modified to contain 14 pressure measurement sites. The indentation test was performed on the same pressure measurement sites. The location of the 14 sites has been described in section 4.5.1 in figure 4.5.1.3a. Indentation was performed for each site except the proximal medial site (R3MED) where there was a space constraint in fitting the indentor.

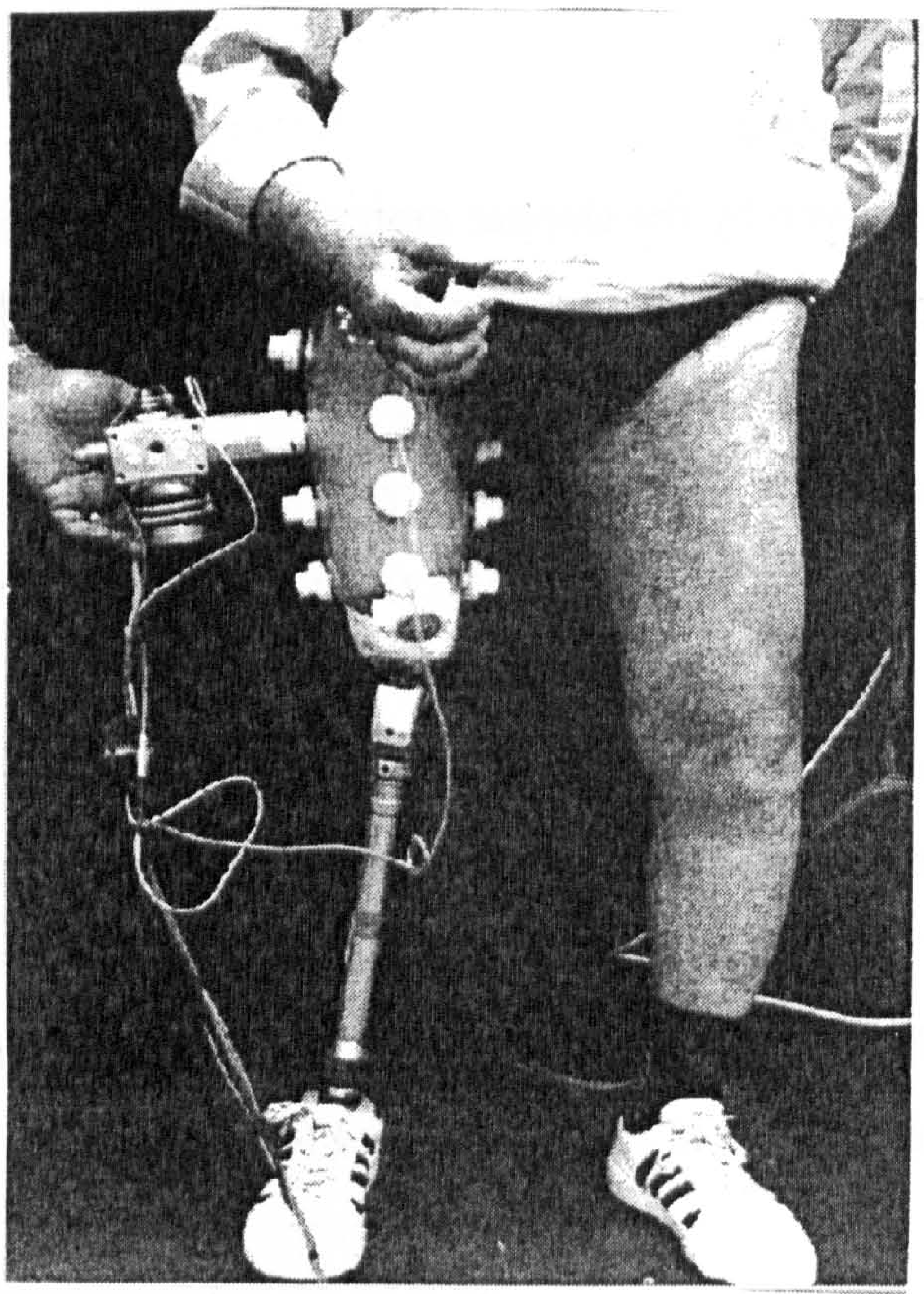

Fig. 6.7.3.1 Indentation test carried out with the subject in a standing position.

6.7.3 Indentation protocol

The indentor was fixed onto each of the 13 sites one at a time. Six consecutive indentation cycles were performed on each site, where each cycle consisted of a loading and unloading phase. The first three cycles were termed the preconditioning cycles where data would not be recorded. Only the following three cycles' load - displacement data would be recorded for further analysis.

Indentation was performed with the subject in a standing position with approximately equal weight on both feet (Fig. 6.7.3.1). The complete indentation routine was performed with the subject in the same standing position. However, due to the discomfort of standing for long periods, rest periods were given at the subject's request. Thus, in order to ensure the subject return to approximately the same position, the positions of the subject's feet were marked on the floor.

6.7.4 Maximum depth and load of indentation

Torres - Moreno (1991) reported that the maximum radial differences obtained at the ischial- gluteal and inguinal flare regions in the quad socket ranged from 23 to 26 mm. Based on this amount of tissue displacement, the maximum depth of indentation was limited to 20 mm. However, the pressure created by the small area of the indenting piston would be considerable higher than that caused by the socket wall. To prevent any risk of puncturing the soft tissue, an additional parameter limits the compressive load acting on the piston to 6.4 N, giving a pressure of 275 kPa. Therefore, which ever parameter is reached first, i.e. 20 mm depth or 6.4 N load, the indentor piston would retract.

The actual indentation depth achievable by the device was 19.78 mm instead of 20 mm. This was due to the mechanical limitation imposed by the stepper motor and the rack and pinion system.

6.7.5 Rate of loading

The rate of indentor loading was decided based on the duration of the gait cycle. As a first approximation, the soft tissue contained in the socket would be subjected to load for the duration of the gait cycle. From past literature (Yang, 1988), the average duration of the gait cycle in normal walking for a trans-femoral amputee averaged 1.38 s. The rate of loading was then calculated based on the time of 1.38 s to complete a 19.78 mm indentation. The indentation frequency of 0.72 Hz (1/1.38s) gave a loading rate of 854.5 mm/min for 19.78 mm indentor piston travel (19.78 x 60 x 0.72).

6.7.6 Safety aspects

The device was subjected to an assessment from the Safety Committee at the Bioengineering Unit. No indentation was performed on sites where scar tissue was present. In addition to the limited indentation load and depth, the risk of the indentor cutting into the soft tissue was reduced by having the indentor's piston chamfered at its edge. The indentation routine was carried out automatically under computer control. However, an emergency control switch would be held by the subject during the indentation routine. The switch enable him to disrupt the indentation routine at any time, setting the indentor piston to its original retracted position. If all of the preventive features fail, the maximum indentation depth would be 26 mm.

6.7.7 Derivation of a pseudo Young's Modulus

The *in vitro* study performed with porcine tissue and the problems discussed in section 6.3.3 regarding *in vivo* mechanical characterisation of soft tissue necessitate the present study to apply linear elastic theory.

Considering the small radius of the indentor piston relative to the thickness of the residual limb, the pressure distribution under the indentor's piston can be assumed the same as for a flat rigid cylindrical die resting on a semi-infinite homogeneous isotropic elastic continuum, as theoretically defined by Timoshenko and Goodier (1970) to be ;

$$q = \frac{P}{2\pi a\sqrt{a^2-r^2}} \qquad 6.7.7a$$

where q is the pressure intensity, P is the load acting on the die, a is the radius of the die and r is the distance from the centre of the die. The pressure directly under the die is at its minimum i.e. when $r = 0$, and reaches infinity when r approaches a. Following equation 6.7.6a, Timoshenko and Goodier (1970) provided a solution to determine the displacement of the die for any given load acting on a material as,

$$d = \frac{P(1-\nu^2)}{2aE} \qquad (6.7.7b)$$

where d is the displacement of the die, P is the load acting on the material and ν the Poisson's ratio of the material and E is the Young's modulus of the material. Rearranging equation 6.7.6b, the Young's modulus of the material can be obtained by

;

$$E = \frac{P(1-\nu^2)}{2da} \qquad (6.7.7c)$$

Further consideration that soft tissue is incompressible $\nu = 0.5$, equation 6.7.6c can be simplified to,

$$E = \frac{3P}{8da} \qquad (6.7.7d)$$

Therefore with the radius of the indentor piston kept constant, E is a function of applied indentation load and the resulting deformation occurring in the soft tissue. Equation 6.7.6d can be further simplified by applying an indentor piston of radius 2.715 mm used in the present study, giving

$$E = \frac{0.138P}{d} \qquad (6.7.7e)$$

where E is in N/mm^2, P is in N and d is in mm.

6.7.8 Results of indentation test

The results of the indentation test are presented as load - displacement curves as shown in Fig. 6.7.8.1. The first three indentation cycles applied to the residual limb for the purpose of preconditioning the soft tissue are not plotted, only the following 4th, 5th and 6th indentation cycles are displayed in the graph. The loading and unloading cycles were fairly repeatable indicating that the preconditioning was sufficient. The plot possesses the typical characteristic of soft tissue response to mechanical loading. The pseudo Young's modulus was derived using the loading phase of the cycle only by applying equation 6.7.7e. The moduli calculated would vary with load and displacement due to the non-linear load - displacement characteristic. In the present study, only three moduli were selected based on the following conditions,

a.) at maximum indentor load,

b.) at 4 mm indentation depth and

c.) at 1N indentor load.

The three moduli are known as E_{max}, E_{disp} and E_{one} respectively in this thesis. Thus, for each indentation test, the final E_{max}, E_{disp} and E_{one} could be obtained by averaging the 4th, 5th and 6th cycle as shown in the table in Fig. 6.7.8.1.

The load - displacement data obtained from the indentation test were non-linear and exhibited large hysteresis. Similar characteristics could be observed when comparing the indentor test (*in vivo*) with that of the *in vitro* porcine indentation in section 6.4.6 Fig. 6.4.6.2. Both curves were non-linear and exhibited hysteresis. However, the amount of non-linearity was less in the *in vivo* indentor test. This was likely due to the stiffer soft tissue in the residual limb caused by the enclosed prosthetic socket compared to the more compliant excised porcine tissue. The low load limitation (6.4 N) in the mechanical indentor also reduced the amount of non - linearity produced in the load - displacement curve.

A monotonically increasing gradient with increasing strain was not always the case with the indentor test load - displacement results. At several sites approximately between 0 to 1 mm displacement, the load - displacement data displayed a

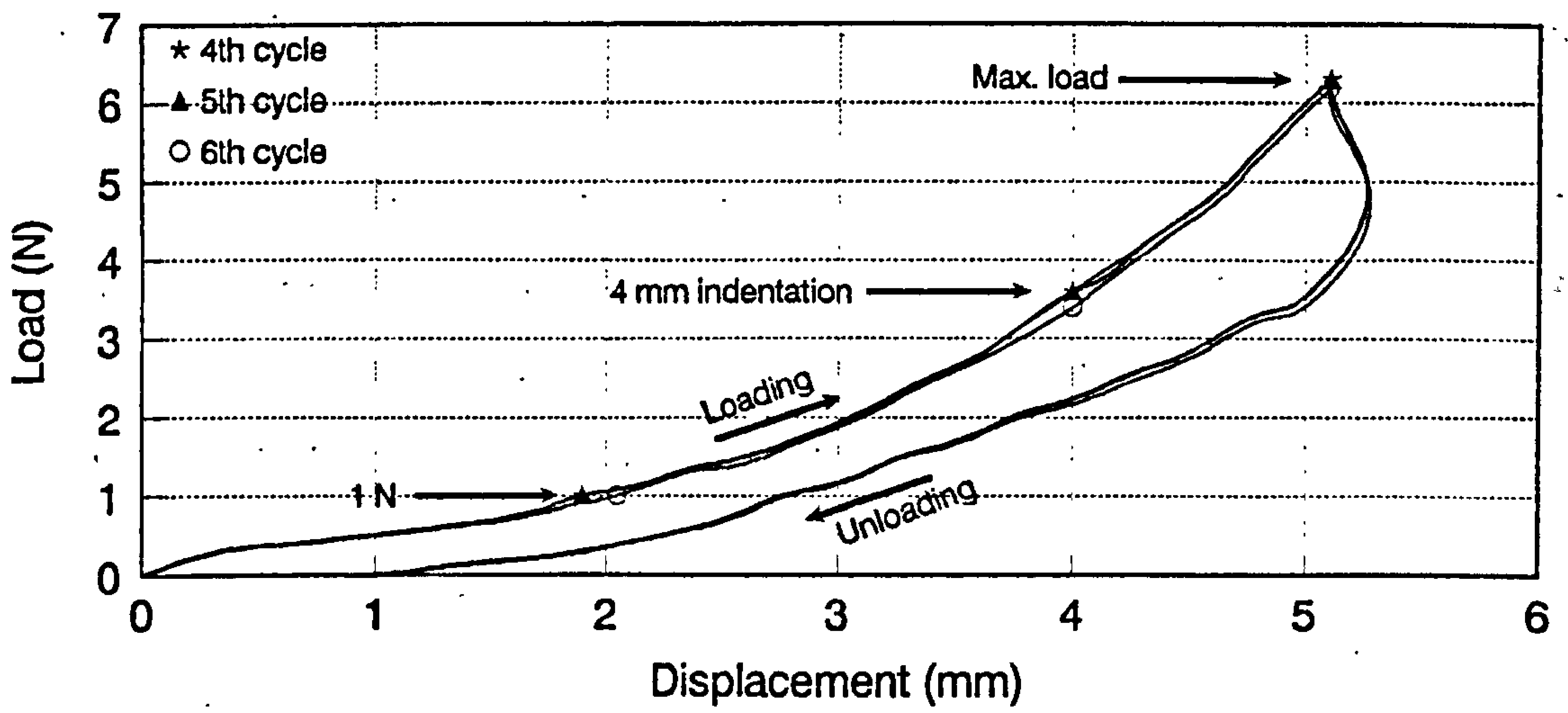

Young's modulus	4th cycle	5th cycle	6th cycle	Average
E_{max} (kPa)	170.2	170.01	166.93	169.05
E_{disp} (kPa)	124.20	124.20	117.31	121.90
E_{one} (kPa)	72.63	72.63	67.31	70.85

Fig. 6.7.8.1 Subject M site R3POST load - displacement curve. E_{max}, E_{disp} and E_{one} obtained at maximum indentor load, 4mm indentation and 1N indentor load respectively

monotonically decreasing gradient with increasing strain as shown in Fig. 6.7.8.2. Under such circumstances, the moduli calculated at a lower load - displacement value could be higher than that obtained at a higher load -displacement value. For example, in Fig. 6.7.8.2, the moduli calculated at 0.5 N gave 169 kPa which was higher than 75 kPa calculated at 1 N. The author of this thesis reckons that this effect was due to experimental difficulties in making sure that the indentor was absolutely flush with the inner wall of the socket. In the case where the indentor was displaced slightly away from the socket wall, a small pocket would be formed at the indentation site. The amputee applying weight on the socket would displace the soft tissue into the small pocket prior to the indentation test. The soft tissue contained in the small pocket was therefore much stiffer, causing the initial increase in gradient in the indentor load displacement curve.

Fig. 6.7.8.3 shows the average pseudo Young's moduli derived from the load - displacement curves for all the sites measured in subject U. The highest E_{max} (176 kPa) was recorded at site R2MED and the lowest E_{max} (101 kPa) was located at site R1 POST. Generally, high moduli were recorded at the anterior proximal tissues of the residual limb. Fig. 6.7.8.4 shows the load displacement curves for site R3ANT in subject U and tabulates the moduli calculated at the 4th, 5th and 6th cycle. At the distal region, the residual limb was stiffer at the lateral side. Fig. 6.7.8.5 shows the load - displacement curve at site R1LAT. At the medial side, the mid region showed an increased in modulus. Distally from the mid region, the moduli dropped about 20%. Fig. 6.7.8.6 plots the load displacement data at site R2MED. Posteriorly, the stiffness of the residual limb soft tissue varied mildly, increasing at site IT (E_{max}=168.35 kPa) located near the ischial tuberosity. Fig. 6.7.8.7 shows the load - displacement data at site R2POST.

Fig. 6.7.8.8 shows the average pseudo Young's moduli for subject M. The maximum modulus of 165.28 kPa was located at the distal posterior site while the minimum E_{max} of 110.35 kPa was measured at site R2MED. The lateral tissues were stiffer than those in the medial side, however, these were not as stiff as those in the

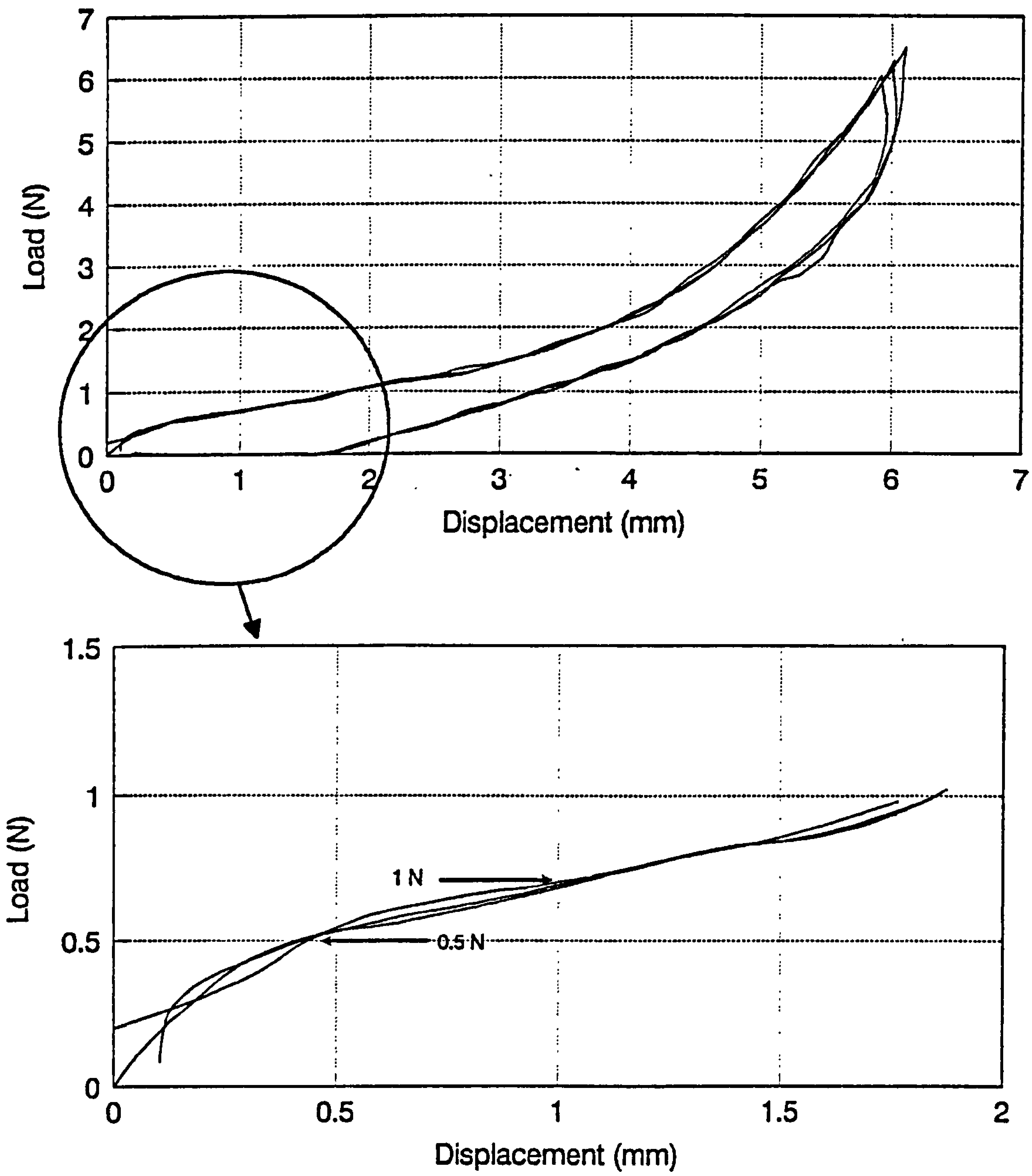

Young's modulus	4th cycle	5th cycle	6th cycle	Average
E at 0.5 N (kPa)	173.41	149.02	169.47	163.96
E at 1 N (kPa)	74.51	76.84	75.24	75.53

Fig. 6.7.8.2 Load displacement data at site R3ANT in subject H.
Between 0 to 1 mm displacement, the load - displacement data display a monotonically decreasing gradient with increasing strain.

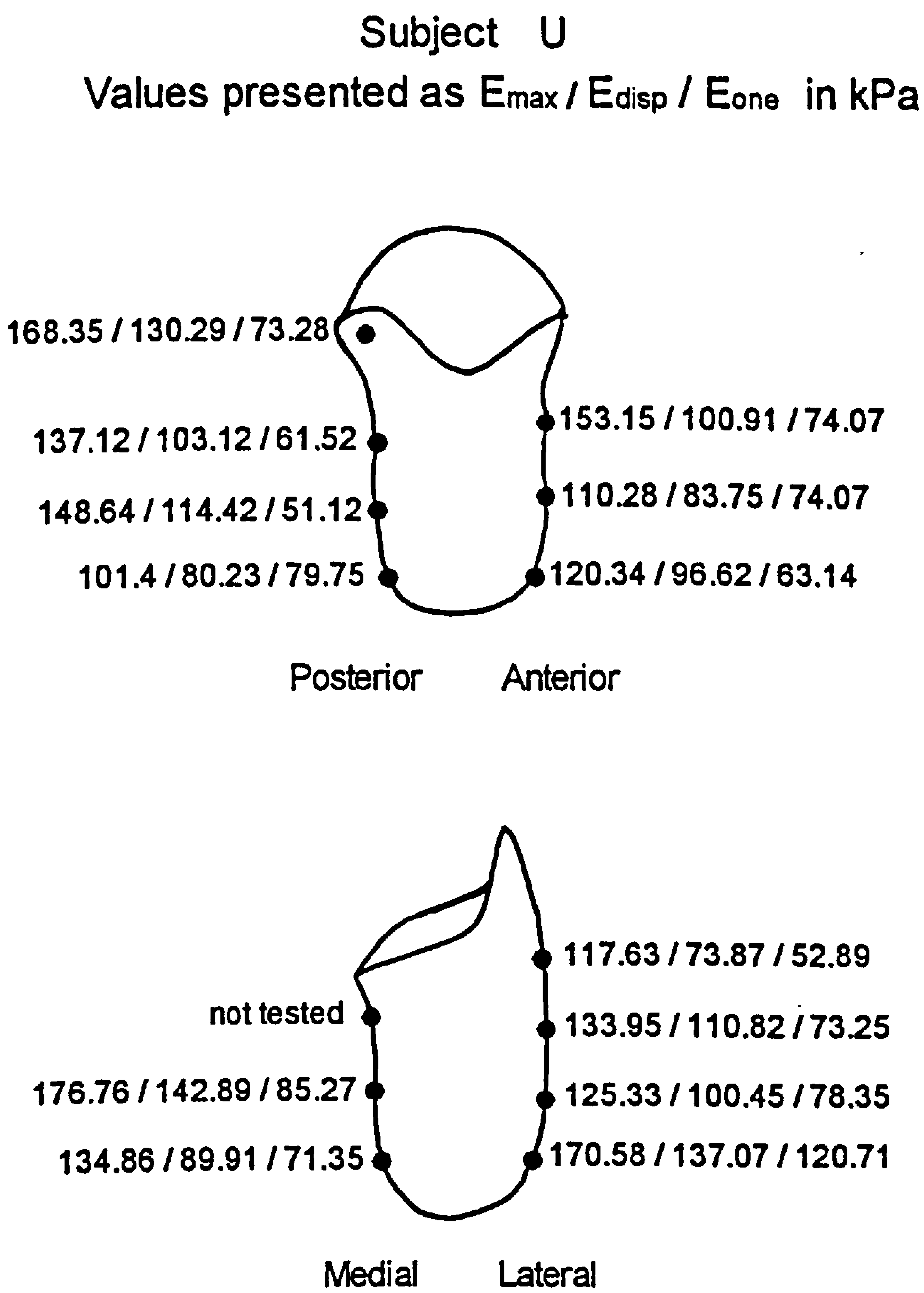

Fig. 6.7.8.3 Moduli measured in subject U.

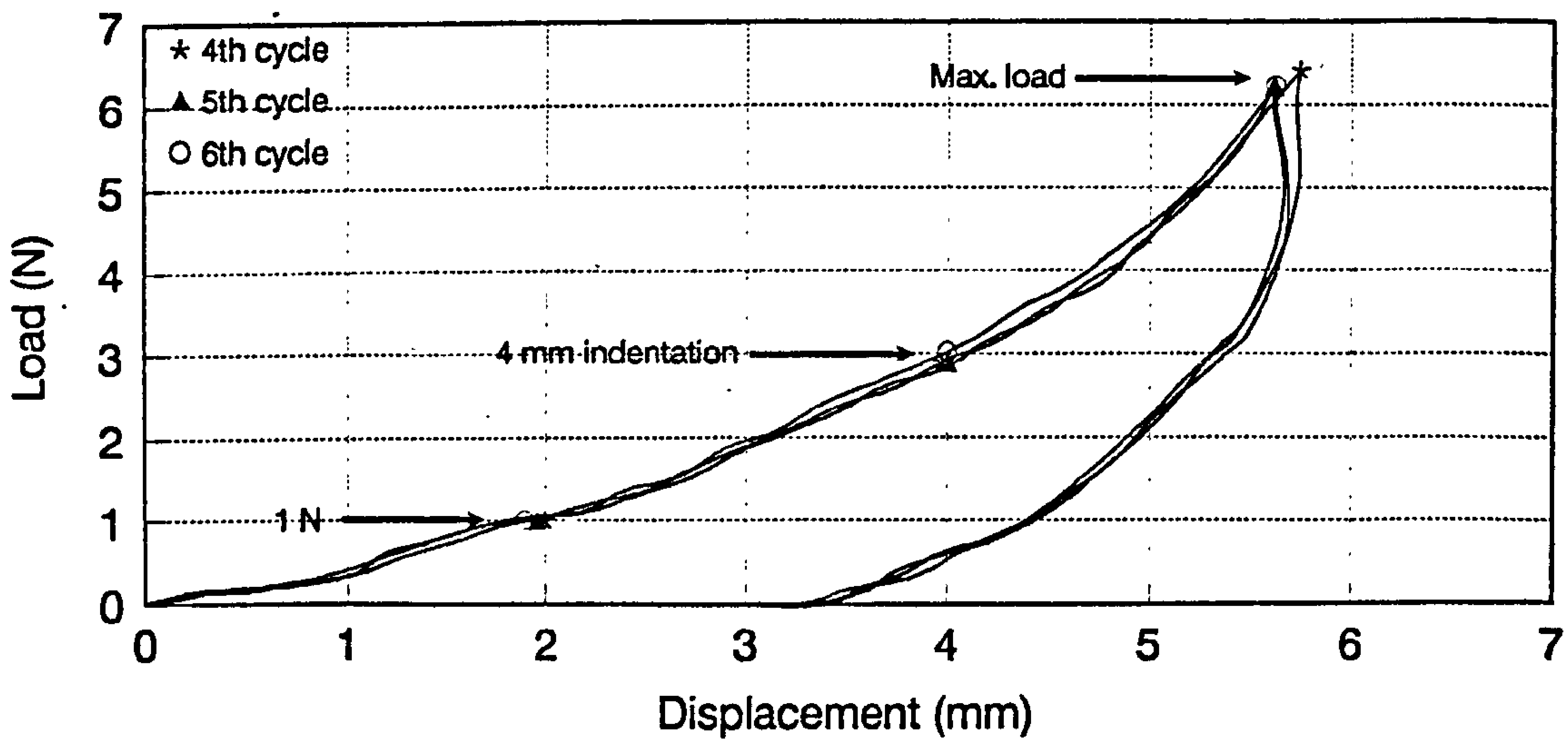

Young's modulus	4th cycle	5th cycle	6th cycle	Average
E_{max} (kPa)	154.15	152.73	152.56	153.15
E_{disp} (kPa)	100.76	97.79	104.19	100.91
E_{one} (kPa)	72.27	73.78	76.18	74.07

Fig. 6.7.8.4 Subject U site R3ANT load - displacement curve. E_{max}, E_{disp} and E_{one} obtained at maximum indentor load, 4mm indentation and 1N indentor load respectively.

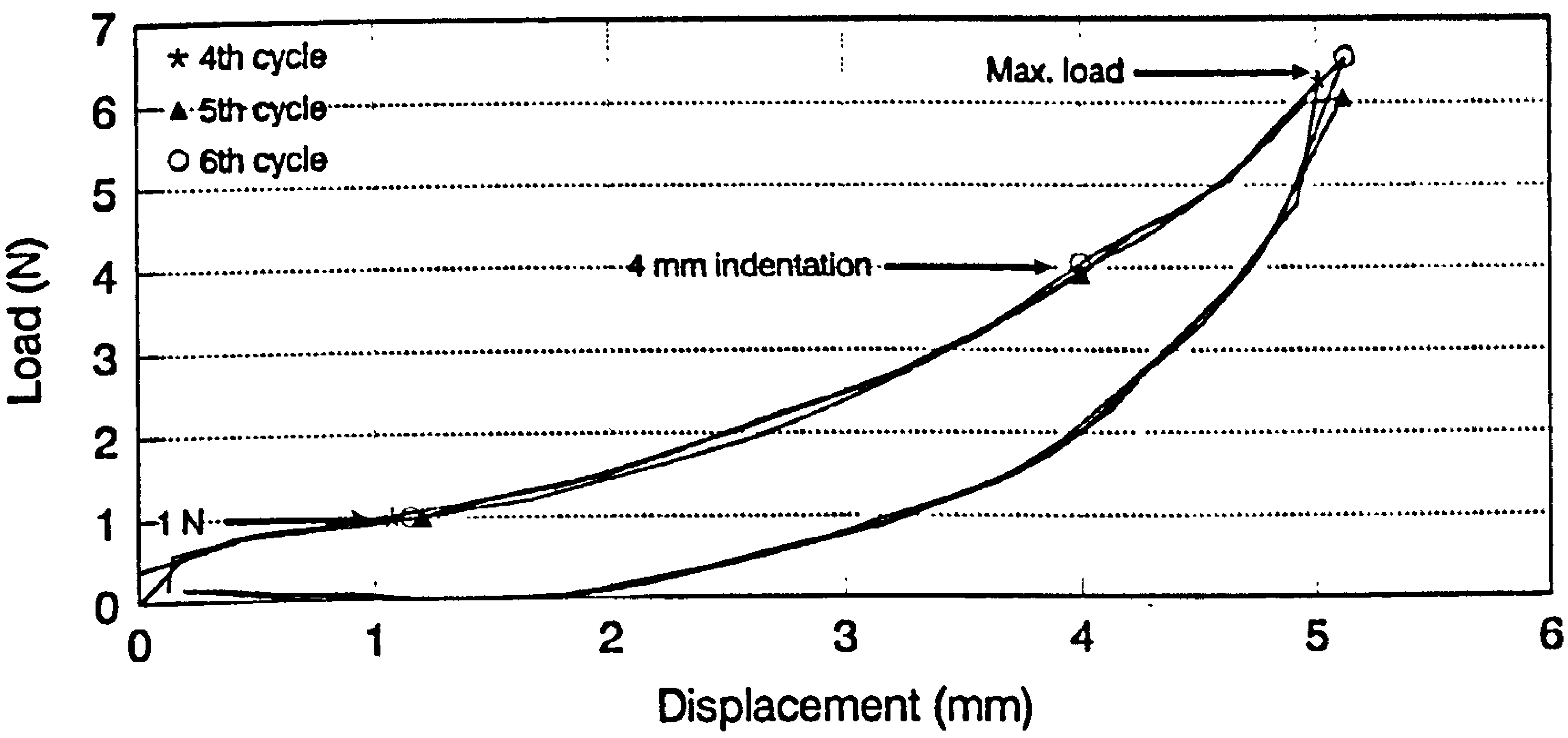

Young's modulus	4th cycle	5th cycle	6th cycle	Average
E_{max} (kPa)	172.29	163.42	176.04	170.58
E_{disp} (kPa)	136.27	135.24	139.72	137.07
E_{one} (kPa)	128.97	115.01	118.15	120.71

Fig. 6.7.8.5 Subject U site R1LAT load - displacement curve. E_{max} , E_{disp} and E_{one} obtained at maximum indentor load, 4mm indentation and 1N indentor load respectively

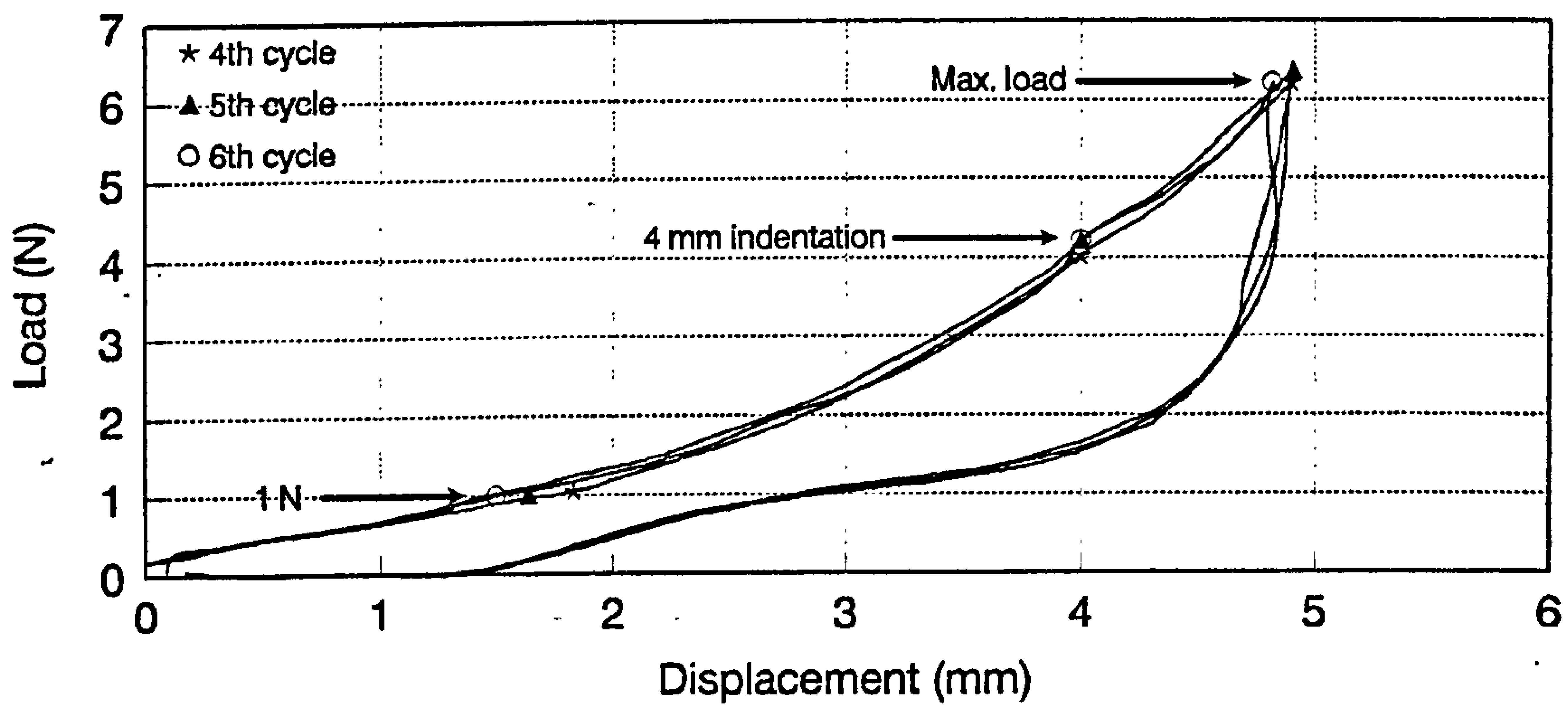

Young's modulus	4th cycle	5th cycle	6th cycle	Average
E_{max} (kPa)	174.55	178.37	177.37	176.76
E_{disp} (kPa)	138.87	144.91	144.90	142.89
E_{one} (kPa)	79.10	84.62	92.11	85.27

Fig. 6.7.8.6 Subject PU site R2MED load - displacement curve. E_{max} , E_{disp} and E_{one} obtained at maximum indentor load, 4mm indentation and 1N indentor load respectively

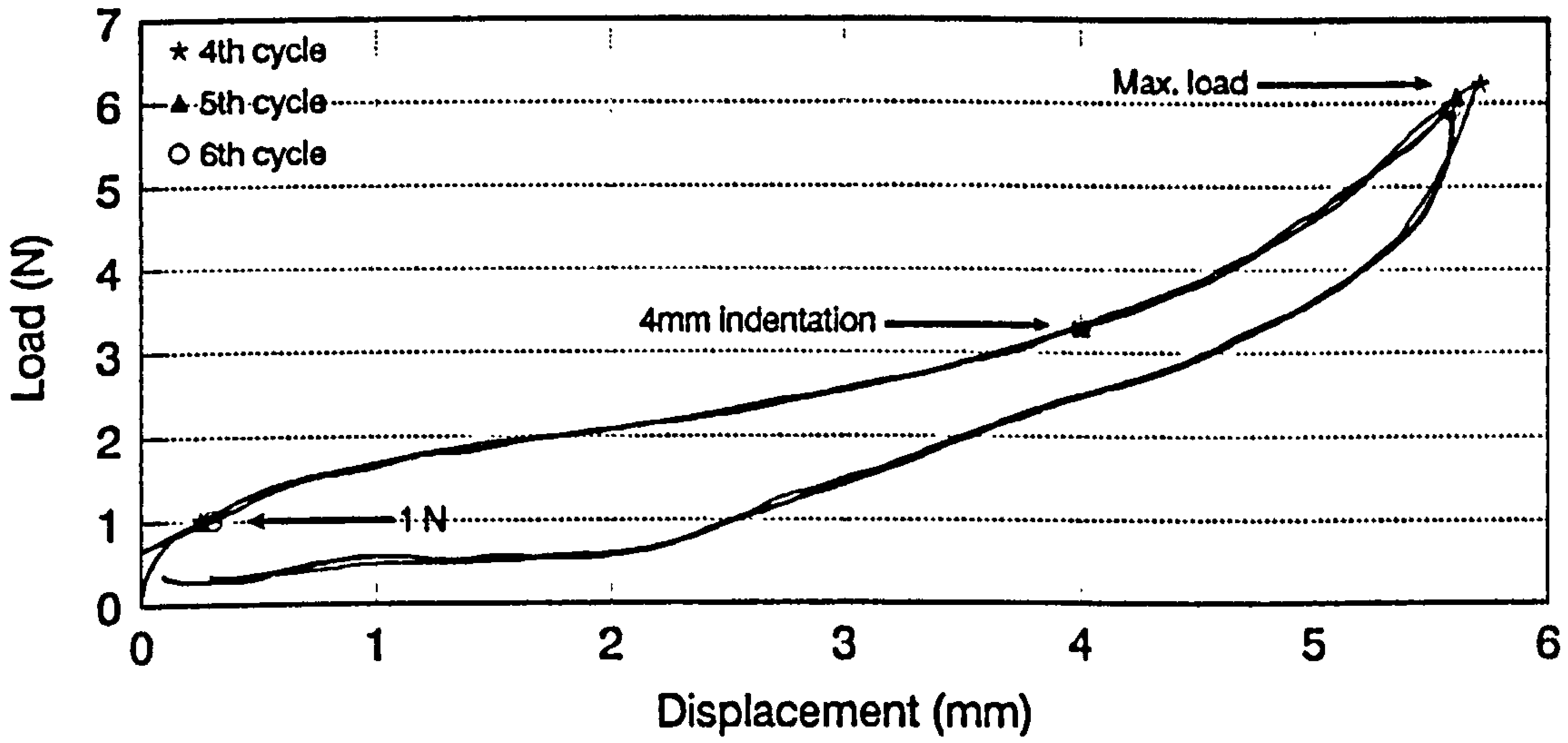

Young's modulus	4th cycle	5th cycle	6th cycle	Average
E_{max} (kPa)	150.49	149.46	145.97	148.64
E_{disp} (kPa)	115.57	113.85	113.85	114.42
E_{one} (kPa)	51.95	55.2	46.21	51.12

Fig. 6.7.8.7 Subject U site R2POST load - displacement curve. E_{max} , E_{disp} and E_{one} obtained at maximum indentor load, 4mm indentation and 1N indentor load respectively

Subject M

Values presented as E_{max} / E_{disp} / E_{one} in kPa

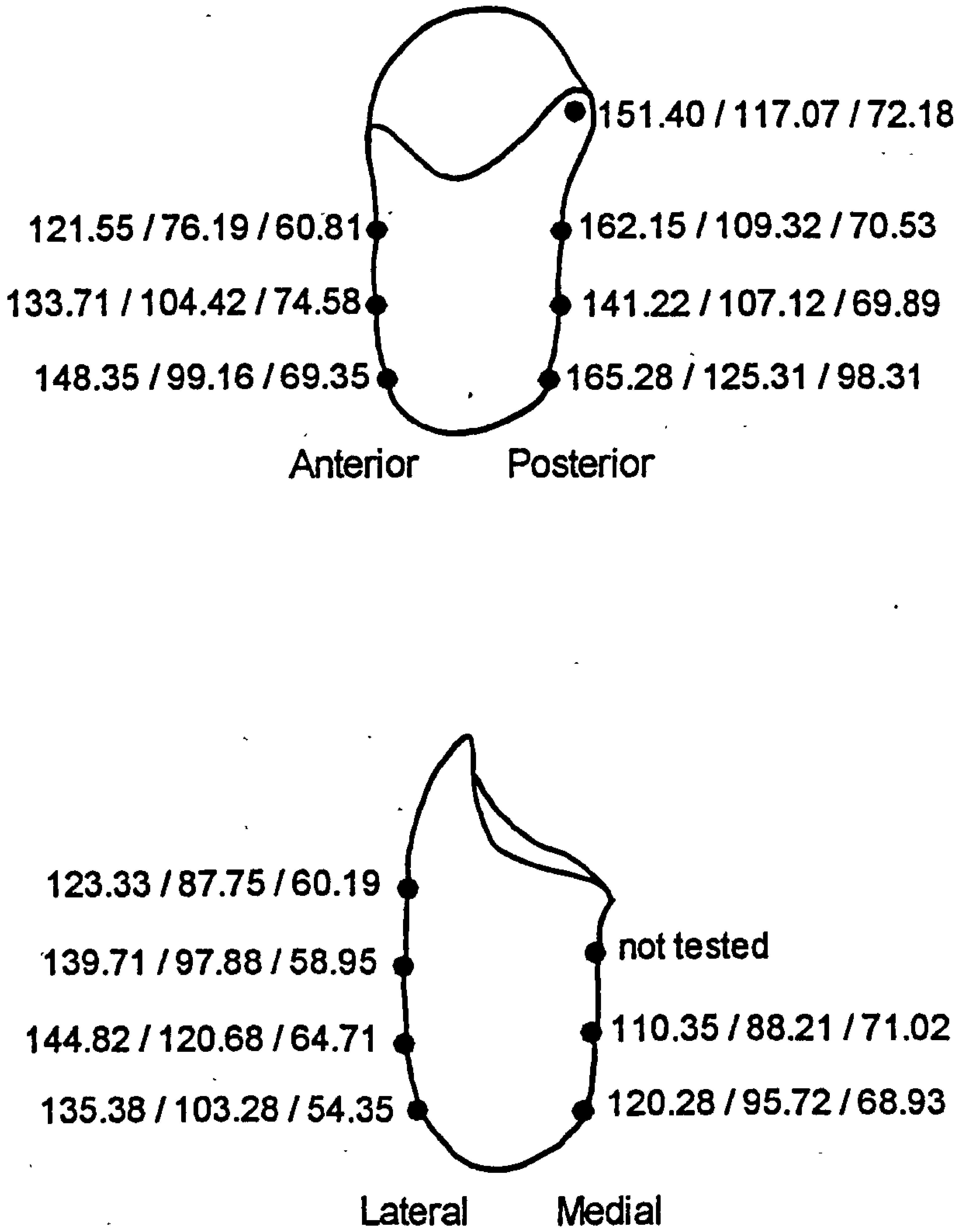

Fig. 6.7.8.8 Moduli measured in subject M.

posterior region. Unlike subject U, stiff proximal anterior tissues were not seen in subject M, instead the distal anterior tissues were slightly stiffer.

The average pseudo Young's moduli for the different sites in subject H are displayed in Fig. 6.7.8.9. The maximum and minimum E_{max} were 169.88 kPa and 125.21 kPa and site R3POST and R1LAT respectively. The stiffness at the proximal posterior region is about 10% higher than most of the other sites measured. At the anterior side, the stiffness at the mid region was about 15% higher than the distal and proximal regions. In the medial and lateral regions of the residual limb, the moduli did not vary considerably and the E_{max} for all the sites at the two regions averaged at about 136 kPa. Overall, the anterior and posterior regions of the residual limb recorded higher moduli than the medial and lateral regions.

6.7.9 Elastic modulus selected for FE modelling

The modulus used in the FE models presented in chapter 7 of this thesis was based on an indentation depth of 4 mm (E_{disp}). As discussed earlier, the maximum load allowable during indentation of the residual limb tissue was 6.4 N (275 kPa) which resulted in maximum indentation depths ranging between 5 to 7 mm for the three subjects tested. A 4 mm indentation depth was arbitrarily chosen as a suitable representation to derive the modulus for FE modelling. At lower indentation depth, the modulus derived could be unstable due to experimental errors as discussed previously in Fig. 6.7.8.2. It should be highlighted that there was an amount of uncertainty that E_{disp} selected at 4 mm indentation was the most appropriate choice. It was considered that the indentation test was performed with the residual limb in a loaded state i.e. with the amputee in a standing position. Therefore the amount of deformation that could occur when the residual limb was already in the loaded state should be considerably less than when the residual limb is in a relaxed state. The E_{disp} calculated not only described the soft tissue's behaviour but also reflected the boundary conditions. Therefore the 4 mm deformation selected is probably a reasonable value based on the possible amount of deformation occurring from the residual limb in a loaded state and the limited depth of indentation with the mechanical

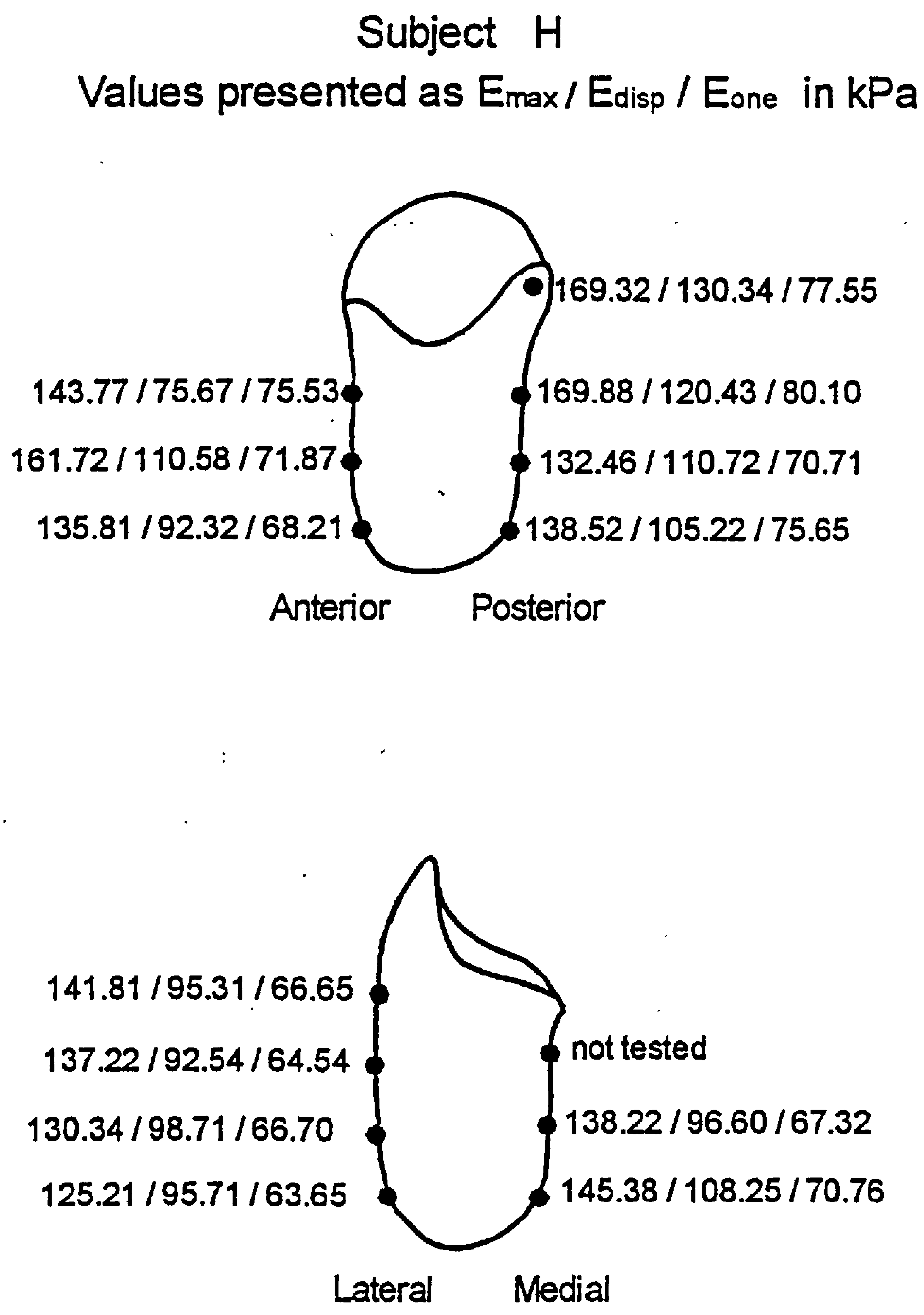

Fig. 6.7.8.9 Moduli measured in subject H.

indentor. The selected E_{disp} ranged from 73.87 kPa to 137.07 kPa and is about 30% lower than E_{max} and 20% higher than E_{one} in most cases. The E_{disp} selected in this study compares well to previous FE studies of residual limb or buttocks where E was chosen based either on literature or experiment. Steege et al (1987) applied a value of 60 kPa to all soft tissue components in the FE model of the trans-tibial residual limb. Similarly, the muscles in the trans-tibial residual limb have been modelled by Sanders and Daly (1993) using an E value of 131 kPa, Reynolds (1988) and Zhang and Roberts (1993) using an E value of 170 kPa. In models of buttocks, Todd and Thacker (1994) applied an E value ranging between 11.9 to 64.8 kPa to the soft tissue components.

To apply the E_{disp} to the FE models of the residual limb for subjects U, M and H, the models were firstly divided into equal sections corresponding to the indentation sites. In the transverse view, four sections were defined and in the long axis, three sections were defined (Fig. 6.7.9.1). At the proximal medial side where indentation was not performed, the E_{disp} of site R2MED was used instead. At the proximal lateral region, an average E_{disp} based on site GT and R3LAT was used. The E_{disp} of site IT was not used in the FE models since the ischial tuberosity was not included in the models described later in chapter 7.

6.8 DISCUSSION : IN VIVO INDENTATION TEST

There are several factors that can affect the pseudo Young's modulus obtained in the indentation of residual limb tissue. The modulus is dependent on the general health of the residual limb, its muscular activity during indentation and the different indentation sites. These factors are therefore subject and time dependent. Two other experimentally dependent factors affecting the modulus are the rate and depth of indentation. Due to the viscoelastic behaviour of soft tissue, different load - displacement curves could be obtained by introducing different rates of indentation. The non-linear load-displacement characteristic of soft tissue would also mean that one modulus is insufficient to described the complete material. Instead, to describe the

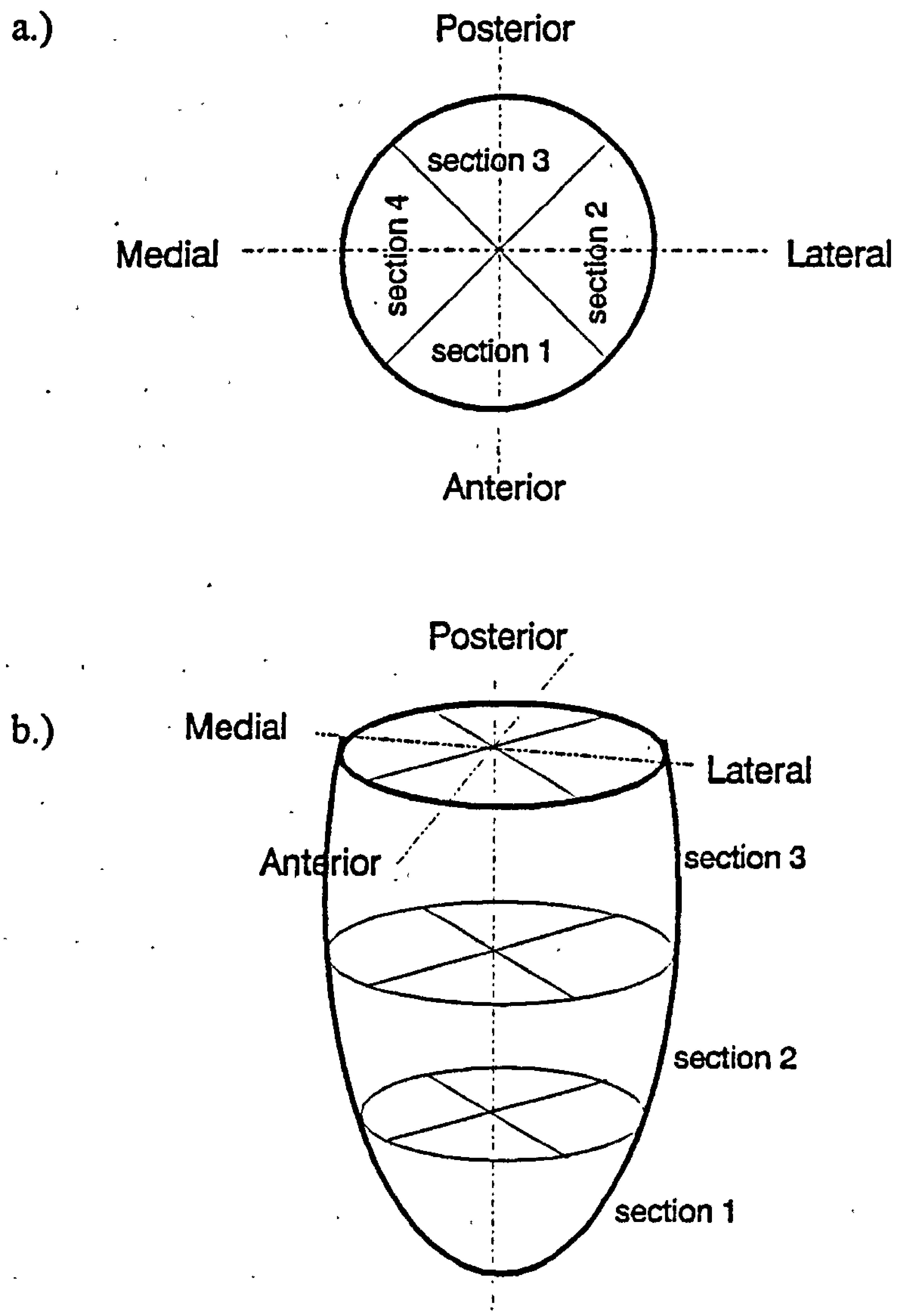

Fig. 6.7.9.1 The FE model of the residual limb is divided into 12 sections. The material properties defined for the particular section is therefore the E_{disp} measured at the corresponding indentation site.
a.) transverse view.
b.) 3-D view.

material fully a series of moduli is required since the load at any instant of time is dependent on the displacement.

The results of other studies reviewed previously in section 6.6.3 could be compared to the present study. However, the comparison should be viewed conservatively as the moduli obtained are highly subject and experiment dependent as mentioned above. Mak et al (1994) performed indentation on both normal and trans-tibial amputees. The rate of indentation was 4 mm/s and two depths of indentation of 5 mm and 3 mm were performed. The moduli derived ranged from 56 kPa to 141 kPa for both normal and amputee subjects. Upon muscles' contraction, the moduli increased about 40% (143 kPa to 194 kPa) in normal and approximately 20% (69 kPa to 101 kPa) in the amputee subjects. In the present study, the moduli obtained ranged from 73.87 kPa to 137.07 kPa. The present indentation test was conducted with the subject in a comfortable standing position at a loading rate of 854.5 mm/min (14.2 mm/s) and an indentation depth of 4 mm. The muscles in the residual limb that were likely under contraction would be the hip extensors and the abductors muscles. In all three subjects tested, the moduli at the posterior sides of the residual limb were generally higher (E_{disp} = 64 kPa to 130 kPa) and in subject M, the moduli on the lateral side were also high (E_{disp}= 88 kPa to 103 kPa). The state of muscles' contraction in Mak's studies was obtained by requesting the subjects to performed voluntary contraction in a sitting position. The lower limb muscles undergoing voluntary contraction would probably be significantly stiffer than that required for balancing the body in a normal standing position, which might explain the lower values obtained in the present study.

Using pulsed Doppler ultrasound techniques, Malinauskas et al (1989) measured nine trans-femoral amputees and reported the average moduli in the posterior, anterior, lateral and medial region to be 141 kPa, 58 kPa, 53 kPa and 72 kPa respectively. The values were obtained with the subject in a sitting position. The authors discussed that the posterior muscles were in general, the stiffest and suggested that this stiffness may be an acquired condition or that the posterior muscles were normally stiffer. Both the studies of Mak et al and Malinauskas et al were attempted without any constraints of a prosthetic socket on the residual limb. The author of this thesis is unsure if the effect of prosthetic socket is large on the measured moduli, nevertheless, the aim in this study was to obtain the moduli for the purpose of modelling the interface conditions between the residual limb and the socket. Thus the former condition without any restraints on the residual limb was not attempted. Torres - Moreno (1991) measured the tissue stiffness of three trans-femoral amputee using a method similar to that presented in the present study. The moduli were derived based on 1 N indentation load. Indentation was performed with the amputee wearing a prosthetic socket with the residual limb in a relaxed state, which was achieved by requesting the subject to adopt a supine position. The moduli obtained ranged from 36 to 146 kPa. In the present study, based on a indentor load of 1N, the moduli measured ranged from 51 to 111 kPa.

The state of soft tissue in the residual limb changes continuously during gait due to active musculature. As shown by Mak et al (1994), the stiffness in the residual limb tissues could increased by 20% in the contracted state. Thus, in order to model the residual limb during gait, the dynamic material properties should really be considered. However, the present method of indentation is only possible with the amputee in a static position. The author of this thesis believes that a possible way to track the muscles activity and their relationship to tissues mechanical properties would be to attempt the indentation test with the assistance of electromyography. The procedure would be to firstly identify the different muscles' EMG signals during gait which could be normalised to the maximum voluntary contraction. Subsequently, the indentation test could be performed in the static situation requesting the patient to voluntary contracting the muscles to a similar state to that achieved during gait through the assistance of feedback EMG signals.

The estimation of a suitable elastic modulus using the indentation test results is dependent on the assumed value of Poisson's ratio. The Poisson's ratio in the present study was assumed as 0.5, identifying the soft tissue as incompressible. Referring to equation 6.7.7c, assuming a Poisson's ratio of 0.4 would reduce the estimated modulus by 11%. The validity of soft tissue being incompressible has been discussed previously in section 6.3.2. Mak et al (1994) also viewed the assumption of a constant Poisson's ratio for various sites and different muscular activity to be a rather bold one. Nevertheless, it highlights the problem of obtaining a modulus based on theory of elasticity.

The modulus obtained in the present study is site dependent and relates to that of the bulk soft tissue in the residual limb. The study further assumes that the modulus achieved also represents the underlying tissue. This again, is a bold assumption, since the soft tissue in the residual limb are non homogeneous, consisting of different structures of skin, fascia, muscles and vessels. Malinauskas et al (1989) applying ultrasound have detected that underlying tissues can be up to 50% less stiff than surface tissue. The muscles in the residual limb are also compartmentalised and surrounded by low friction connective tissues known as the intermuscular septum. The intermuscular septua allows muscles to slide relative to each other. Introducing a mechanical indenting force can therefore displace the position of the muscle instead of measuring its material properties. Though, it can be assumed that the tendency of this happening may be unlikely if the muscles are in the contracted state.

6.9 CONCLUSION

The *in vitro* porcine tissue studies had shown the limitations involved in modelling biological tissue's mechanical response using the finite element method. Three material assumptions were studied in detailed. These were elastic, non-linear elastic and hyperelastic. The investigation clearly indicated the use of non-linear elastic properties gave the closest correlation between FE and experimental results.

In vivo indentation tests conducted on the residual limbs of three trans-femoral amputees, donning prosthetic sockets and adopting a standing position, indicated that the posterior tissues were slightly stiffer than the lateral, medial and anterior tissues. The pseudo elastic moduli obtained at 4 mm indentation depth and a rate of loading of 14.2 mm/s ranged from 74 to 137 kPa. These values were subsequently implemented in the FE models of the residual limbs reported later in chapter 7 of this thesis.

CHAPTER SEVEN
FINITE ELEMENT MODELLING : PART 1

7.1 INTRODUCTION

Finite element modelling part one, describes three FE models of the residual limb of subjects U, M and H. These models were based on the amputees' wearing the IC socket from part one of the interface pressure measurement test (refer to section. 4.3). Unlike the previous chapters, a literature review will not be given here since this was already dealt with in chapter three. An overview of the FE method will not be included in this chapter. A good introduction to finite element analysis can be found in Fagan, 1992. The chapter will therefore begin directly with the steps involved in creating the FE models of the residual limb. Results that were already presented in chapter 4, 5 and 6 will be constantly referred to in this chapter for two main purposes, to determine the inputs to the models and validating the FE models' results.

7.2 THE FINITE ELEMENT MODEL

The creation of a FE model of the residual limb required the following parameters ;

a.) Geometrical detail of the limb,

b.) Load actions at the anatomical joints (Loading conditions),

c.) boundary conditions defined by the prosthetic socket and

d.) material properties of the local tissues.

7.2.1 Geometry

The geometry of the model was accomplished through the use of two procedures. Firstly, it was assumed that the shape of the residual limb with the socket in place follows the shape of the socket. This assumption could be justified by the use of a total contact suction socket, which requires the residual limb soft tissue to be in constant contact with the socket to provide adequate suspension. Therefore, instead of acquiring the residual limb shape, the test sockets' shapes were defined using a 3-D mechanical digitiser. The digitiser, designed by Rassoulian (1989) in the Bioengineering Unit, was an inexpensive system used with an existing computer numerically controlled (CNC) milling machine. It consisted of a long pointed probe hinged to a main body (Fig. 7.2.1.1). At the hinged joint, a goniometer (Fig.

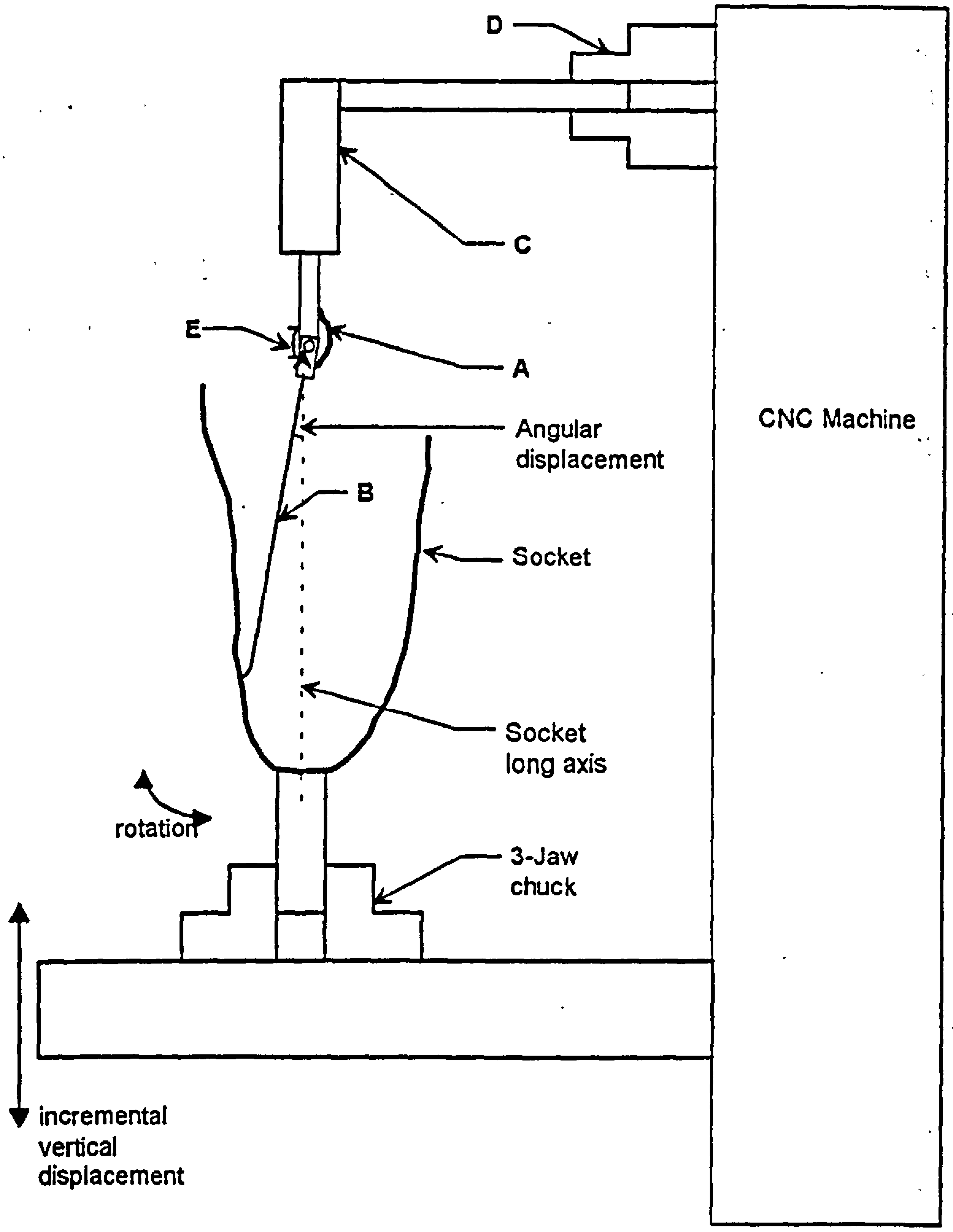

Fig. 7.2.1.1 Socket digitizer.

A - Goniometer
B - Probe
C - Body
D - Tool holder (CNC Machine)
E - Elastic band

7.2.1.1-A) tracked the angle of deflection between the probe (Fig. 7.2.1.1-B) and the main body (Fig. 7.2.1.1-C), while the main body itself was fixed on to the tool holder (Fig. 7.2.1.1-D) of the CNC machine. The socket to be measured was secured on the CNC machine table by a 3-jaw chuck. The digitiser probe was placed inside the socket with its axis aligned with the long axis of the socket. The long axis of the socket was obtained using the socket axis locater known as the SAL. The procedures in locating the socket's long axis was exactly the same as that described in section 4.5.1. for setting up the pressure measurement sites. Measurement began with the probe touching the inner surface of the socket at its most distal end. Tension was maintained at the hinged joint using an elastic band (Fig. 7.2.1.1-E), which ensured that the probe was in constant contact and followed the contours of the socket wall. The CNC machine table was lowered at an incremental vertical displacement of 5 mm for 46 times, while the goniometer tracked the angular displacement of the probe at each of these intervals. Upon completing the first column of measurements, the socket was rotated about its axis by an angle of 9 degrees and the probe was returned to its distal starting position, measurements corresponding to the second column are then taken. The completed measurements consisted of 40 columns and 46 rows making up 1840 points (Fig. 7.2.1.2).

The second procedure involved introducing a 3-D image of a femur to the digitised socket shape. Its geometry was obtained using magnetic resonance imaging (MRI) techniques performed by Torres-Moreno (1991). Torres-Moreno imaged a trans-femoral amputee lying in a supine position wearing a plaster cast over the residual limb to prevent tissue distortion. A total of 34 transverse images with a gap interval of 10 mm was acquired of the residual limb. These images were displayed on computer screen and digitised "on screen" using a "mouse" defining the contour of the skin and the severed femoral bone. In this part of the study, only the digitised contour of the bone (Fig. 7.2.1.3) was used. It must be noted that the bone in this case will be different to the bone of the three test subjects (U, M and H) in terms of geometry, though the body weight and build of these subjects and the length of their residual limbs do not differ greatly from the amputee on whom the MRI scan was performed. Incorporating the bone in this manner was considered to be a cheap and fairly

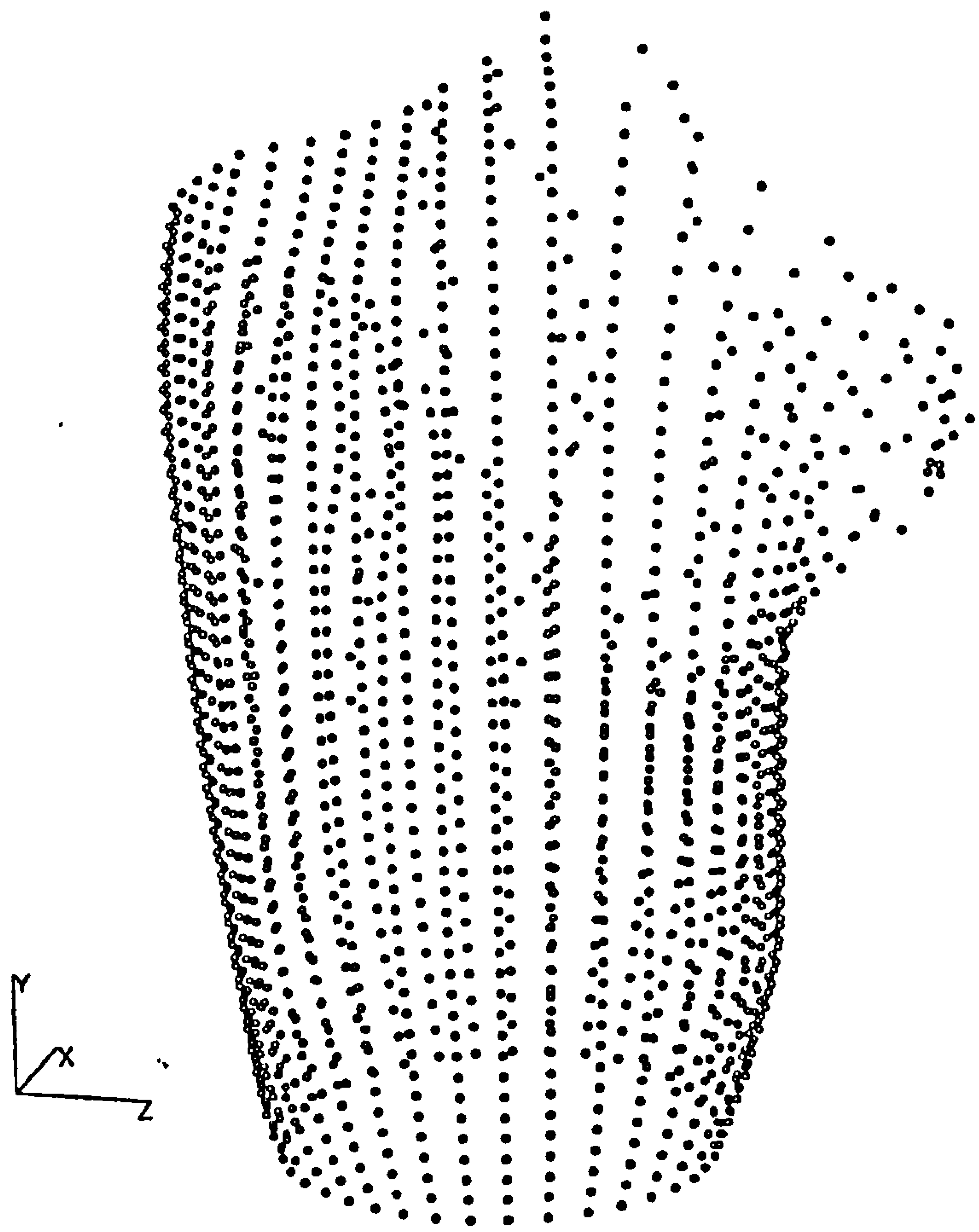

Fig. 7.2.1.2 Digitised points representing the geometry of the socket.

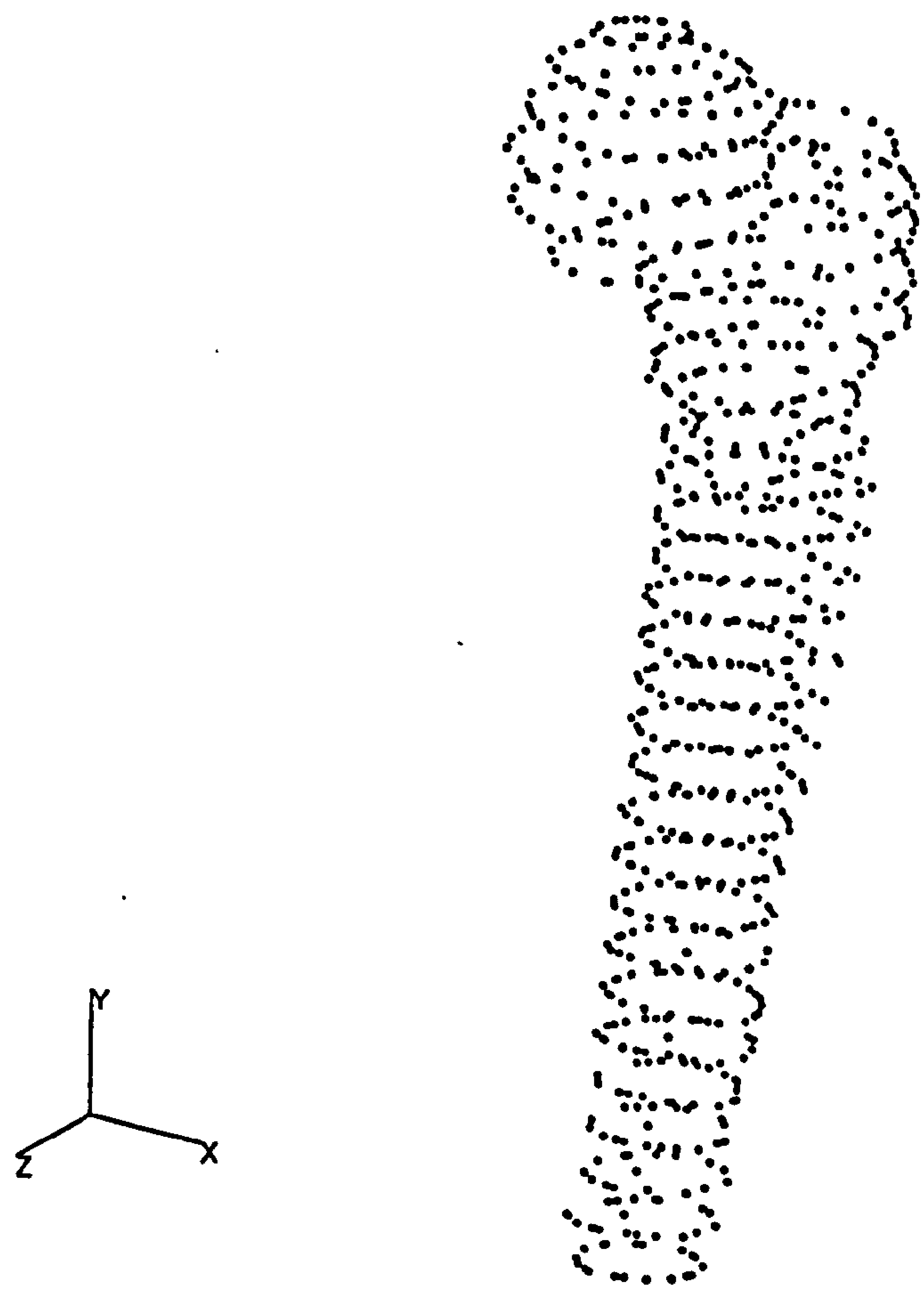

Fig. 7.2.1.3 Digitised points representing the femoral bone.

representative process where only slight modifications to the length of the femur was necessary. Part of the reason for adopting this procedure was, using anthropometric scaling, it was possible for the digitised femoral bone to be scaled to the different respective subjects based on their external anatomical landmarks. Thus by combining the image of the socket from probe digitisation with a scaled femoral bone from the MRI scans, a reasonably geometrically accurate FE model of the residual limb could be created avoiding the need for an individual MRI scan. However, this technique was not used in this part of the study because the method still needs to be thoroughly investigated, which is the subject of the next chapter.

7.2.2 Loading conditions

Inter segmental load actions at the residual limb hip were introduced to the FE model. The data were collected using a Vicon motion analysis system with six video cameras and three force platforms as described in chapter five of the thesis. Also shown in chapter five is the inter segmental load actions at the hip consisting of three forces Fx, Fy and Fz and three moments Mx, My and Mz (section 5.5). These were obtained by calculations and transformations of the ground reaction forces to the principal frame of reference of the thigh using directional cosine methods. The inter segmental load actions were calculated for standing and throughout the complete gait cycle. However, in terms of computational feasibility in the FE models only four loading conditions were input, these being the forces and moments during standing, 10% of gait cycle (early stance), 25% of gait cycle (mid stance) and 40% of gait cycle (late stance). The inter segmental load actions applied to the FE models for the three subjects can be found in Chapter five, Table. 5.5.4.1

7.2.3 Boundary conditions

The movements at the interface between the skin surface of the residual limb and the socket were assumed to be minimum since this was a suction socket, and large slippage at this interface would not allow socket suction to be maintained. In the FE model, fixed boundary conditions in the x, y and z direction were imposed on all the surface nodes of the model which described the interface between socket and residual limb. No restriction was placed at all the internal nodes of the elements that represented the tissues and bone. Similarly, the proximal surface nodes were also not restricted in the model. These nodes were therefore allowed to move freely in any direction.

7.2.4 Material properties

Constant elastic properties were assumed for the femoral bone (E = 15.5 MPa, $\nu = 0.33$) and 14 elastic moduli obtained by mechanical indentation on the soft tissues in the residual limb. The soft tissue was assumed to be incompressible having a Poisson's ratio of 0.4999. A full description of the process of obtaining material properties for the three subjects has already been discussed in chapter six.

7.3 FINITE ELEMENT SOFTWARE AND HARDWARE

Commercial FE analysis software packages were utilised ; these were PATRAN release 2.5-1 and ABAQUS version 4.9.1. Later versions of ABAQUS were also used, where the latest update was version 5.3. These program were marketed by different companies, the former by PDA Engineering, USA and the latter by Hibbitt, Karlsson & Sorensen, Inc. USA. Compatibility was maintained between the two software packages via software known as ABAPAT i.e ABAQUS to PATRAN and PATABA i.e. PATRAN to ABAQUS, provided by the companies.

Pre and post processing were performed using PATRAN release 2.5-1. Post processing was also possible using ABAQUS/POST especially when later versions of ABAQUS were used. This was due to certain areas of incompatibility arising between PATRAN 2.5-1 and ABAQUS version 5 and above. The only solver used during the analysis was ABAQUS / STANDARD.

The analysis was performed using the SUN Sparc workstation which was connected to the University network and maintained by the computer centre. The analyses were later transferred to a Silicon Graphics Indigo2 standalone workstation housed in the Bioengineering Unit. This system was powered by a RISC 4400 CPU at 133 MHz with 64 MBtyes RAM.

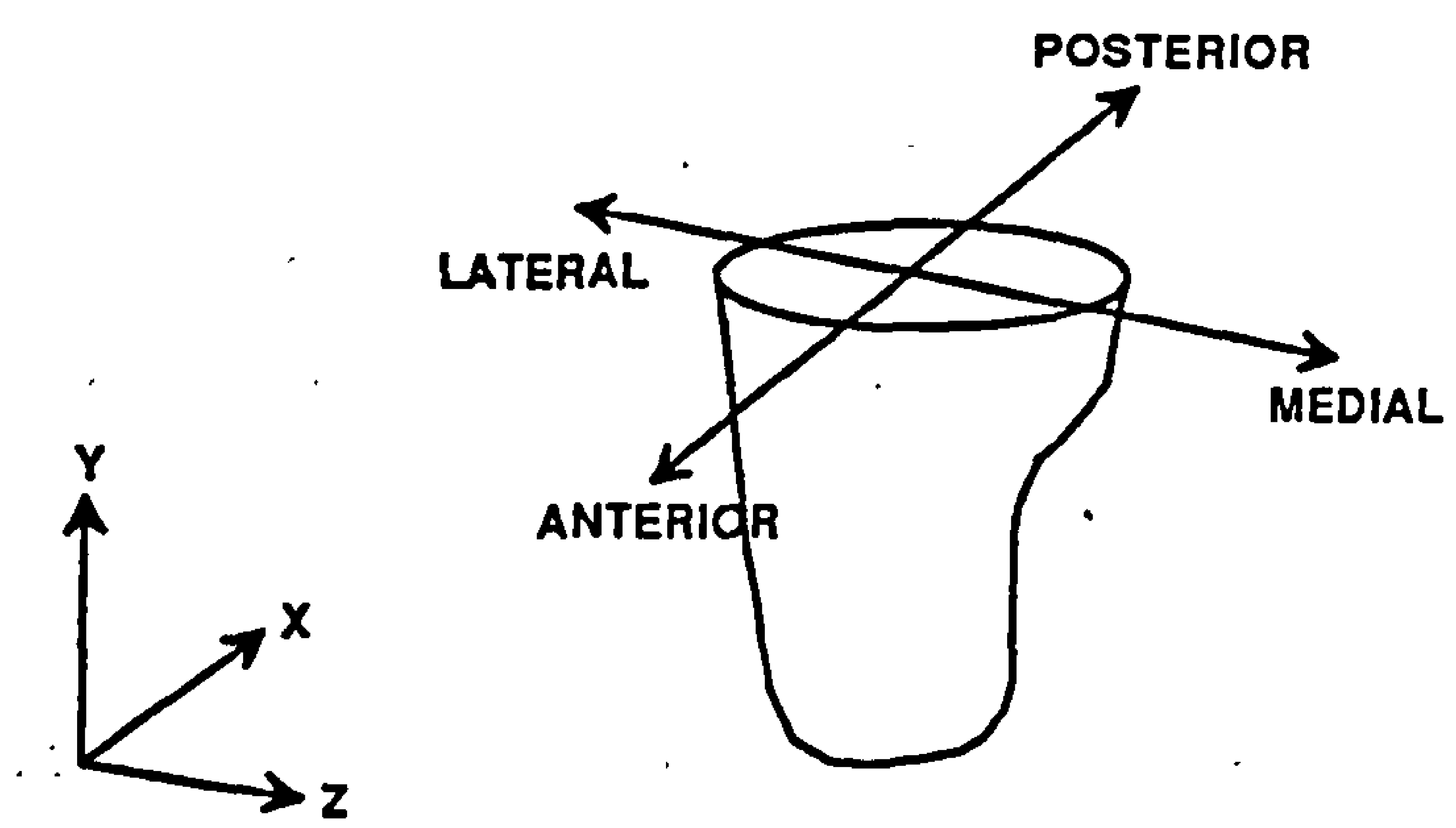

Co -ordinate system for right amputee

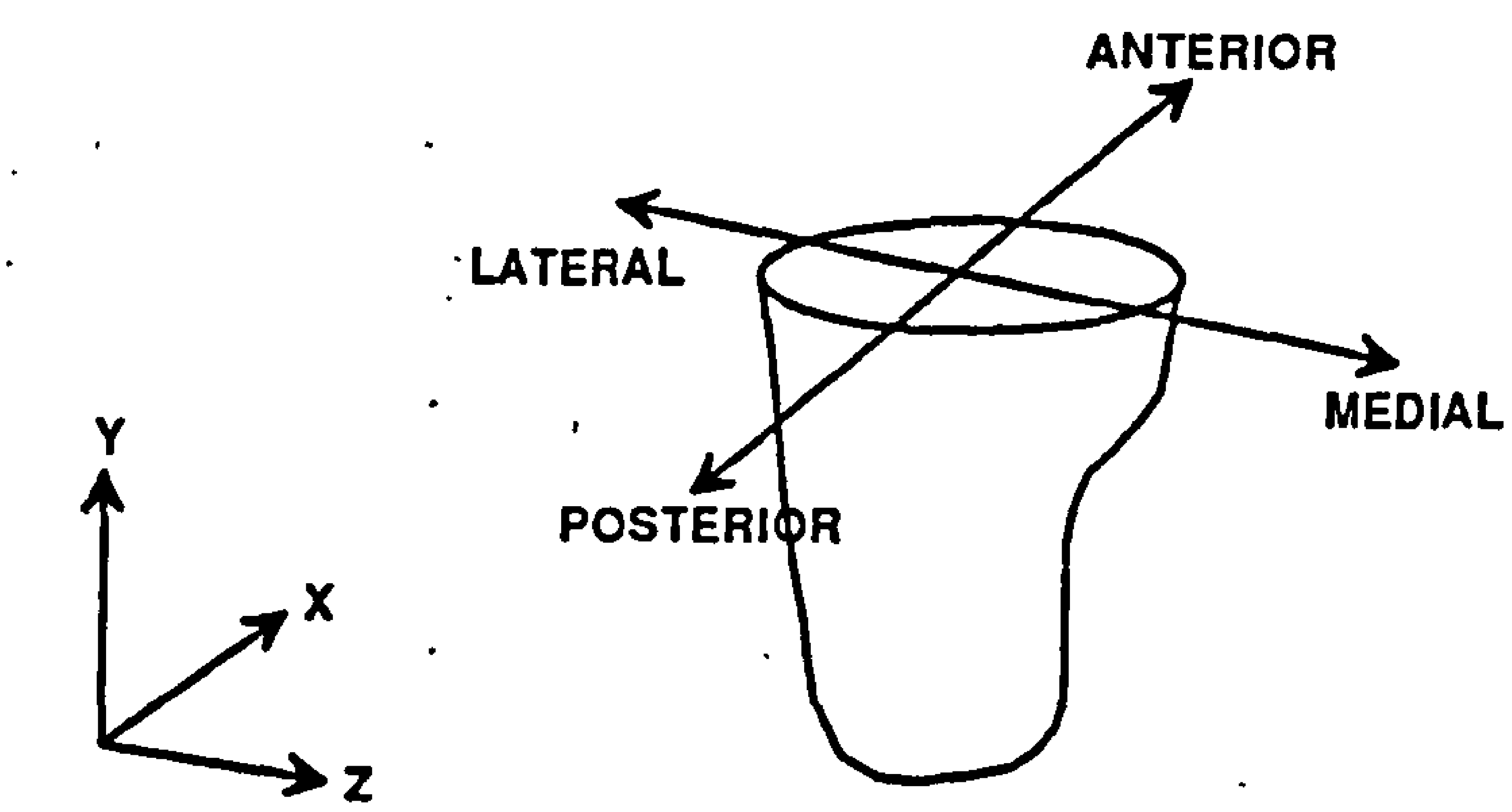

Co - ordinate system for left amputee

Fig. 7.4.2.1 Cartesian co-ordinate used in the FE models.

7.4 MODELLING TECHNIQUES

This section describes the pre processing stage in modelling the residual limb.

7.4.1 Three dimensional modelling

Two dimensional modelling is only suitable for planar structures (plane stress), structures with uniform cross-section (plane strain) or axisymmetrical conditions. It was considered insufficient to model the residual limb in two dimensions since there is neither a constant cross-section nor an axis of symmetry. Though assumptions could be made to reduce the modelling effort to two dimensions, as discussed in a later part of the thesis, this would made the task of validating the model at this stage difficult and inaccurate.

7.4.2 Co-ordinate system

The models were constructed under the Cartesian co-ordinate system similar to the co-ordinate system used in the gait laboratory (section 5.3.1). However, the two right amputee (M and H) sockets had to be oriented differently for reason of convenience during the modelling, where the direction of forward progression was in the opposite x-axis direction (Fig. 7.4.2.1). The axis system for the left amputee (U) remained consistent with that during gait analysis.

7.4.3 Element types

The ABAQUS 3-D solid (continuum) element types selected for the analysis were C3D8R and C3D6 (Fig. 7.4.3.1). The former was a reduced integration 8-noded linear brick element. The latter was a 6-noded linear triangular prism. The brick element was the main element used in the analysis. Only 16 triangular elements were used in order to close the end of the residual limb which will be described in section 7.4.7.

7.4.4 Number of elements

Increasing the number of elements generally leads to an increase in accuracy. However, this is only true when the model reaches the optimal number of elements.

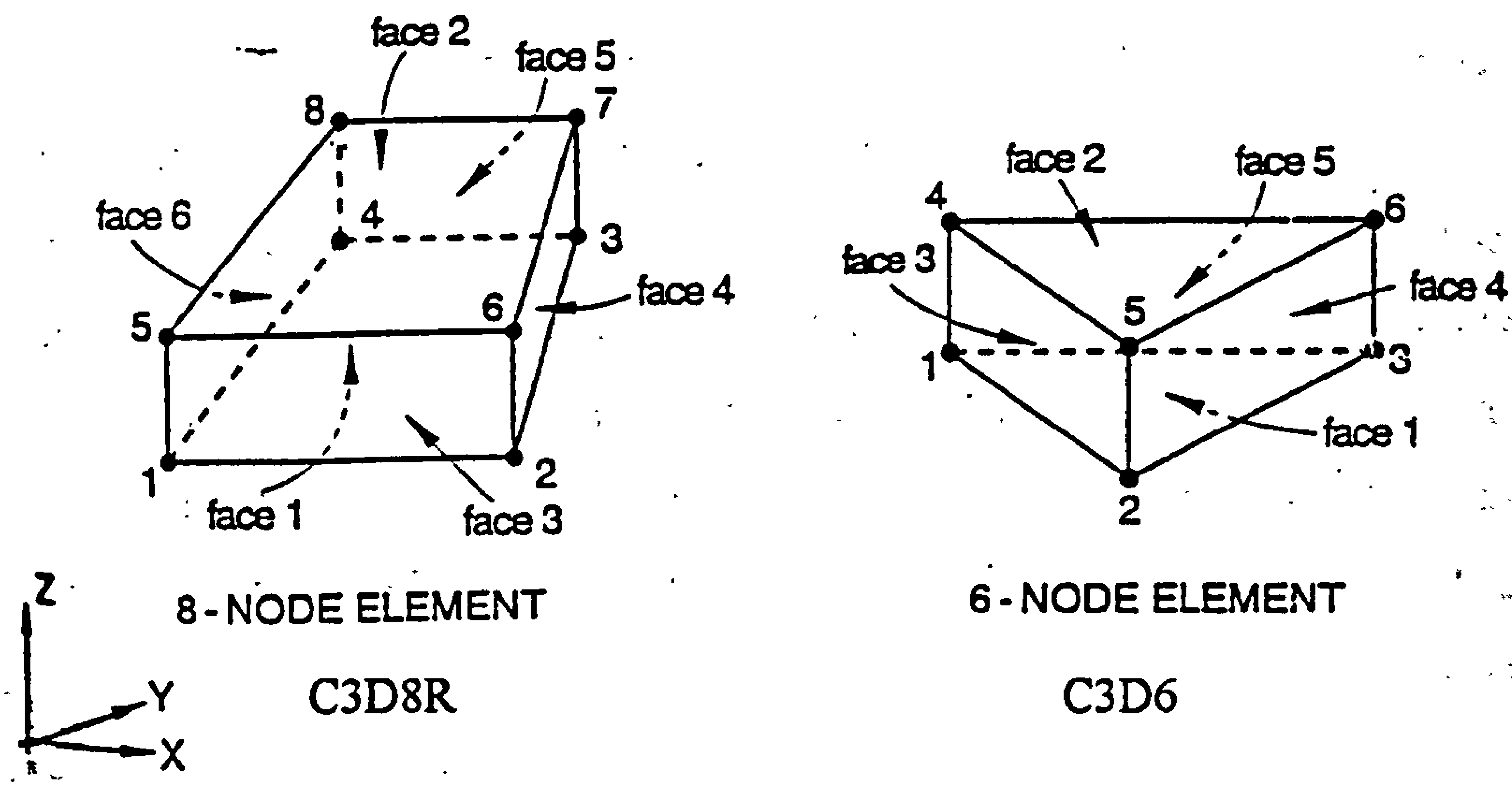

Fig. 7.4.3.1 Selected elements used in the modelling of the residual limb.

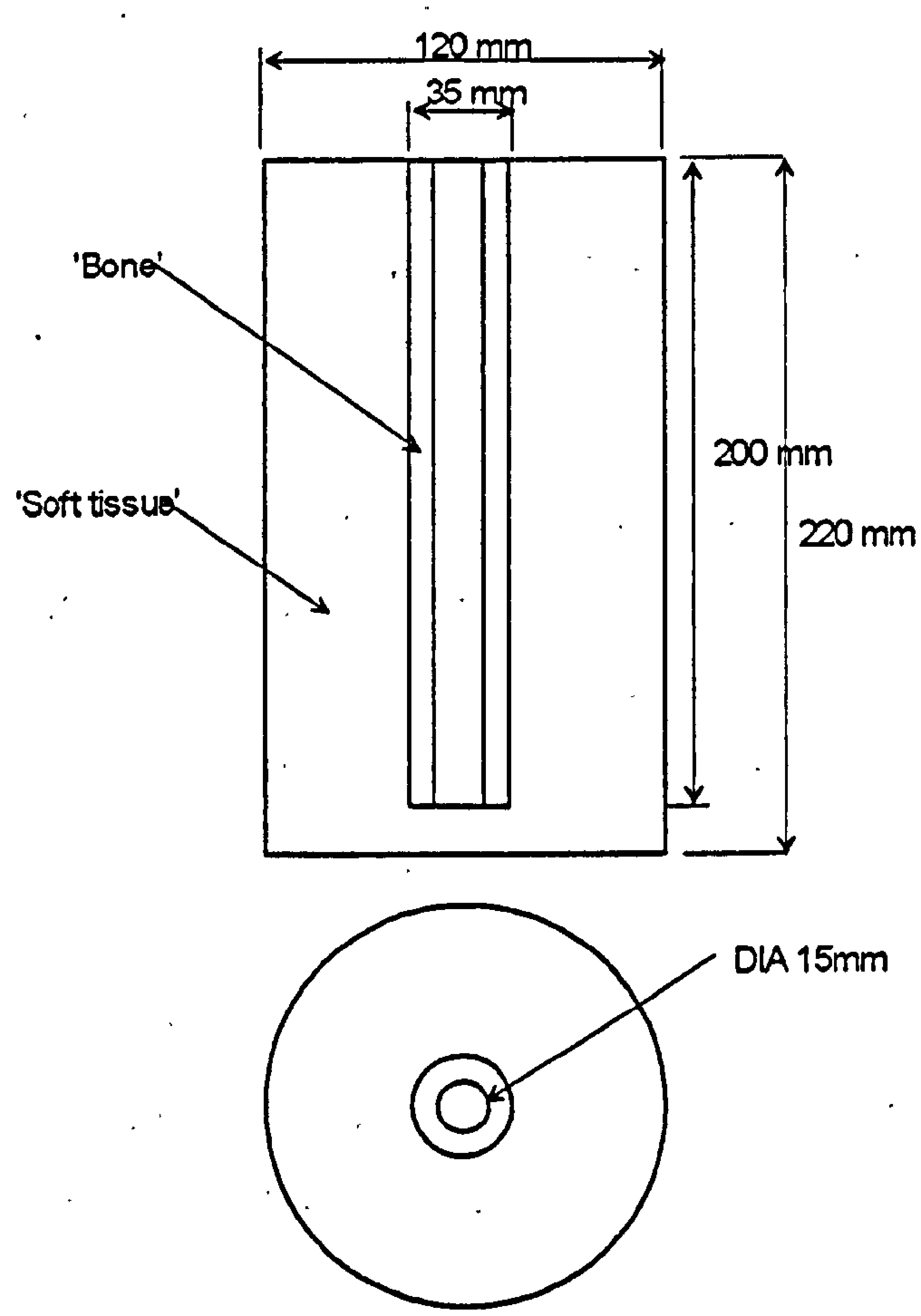

Fig. 7.4.4.1 Convergence test model.

Above this optimal value, there will be little or no increase in the accuracy of the prediction. The optimal number of elements in the model of the residual limb was determined from a convergence study on a cylindrical FE model of approximately the same size (Fig. 7.4.4.1) as the residual limb. This model was made up of two concentric cylinders, with the inner core representing the femoral bone and the outer core the soft tissue. Material properties for the former and latter were E = 15500 kPa, $\nu = 0.33$ and E = 100 kPa, $\nu = 0.49$ respectively. At the top surface of the "bone", a force of -200 N acted in the forward direction of the x-axis and a positive moment of 20000 Nmm about the x-axis. The loads were not distributed over the surface but act on a single node at the centre of the model. This node was however linked by rigid elements to neighbouring nodes that defined the internal circumference of the "bone". This procedure was similar to the loading introduced in the residual limb model and will be explained in more detail in section 7.4.8.

The aim of the FE experiment was to find a suitable number of elements to provide accurate results without excessive computational effort. Three sets of mesh densities were formed with C3D8R brick elements. These meshes were identified as rough, medium and fine (Fig. 7.4.4.2). The analysis assumed a large displacement analysis taking non-linear geometry into account. Fig. 7.4.4.3 plots the predicted displacements of the "bone", not to scale, for the three different mesh densities. The displacements in the x,y and z directions at a node situated at the centre of the top surface of the "bone" where the load had been applied are tabulated in Table. 7.4.4.1. The vector displacement at this particular node was 7.66 mm, 7.36 mm and 6.15 mm for the fine, medium and rough models repectively. The difference in the vector displacement between the rough and the medium model was 1.21 mm. This difference was observed by increasing the number of elements of the rough model by 2.7 times generating the medium model. In order to produce the fine model, the number of elements in the medium model was subsequently increased 4 times, which pushed the vector displacement up from 7.36 mm to 7.66 mm, an increase of 0.3 mm. This showed that the model gave a better accuracy with a finer mesh density, however, the increase in accuracy fell significantly as the number of elements approached an optimal level.

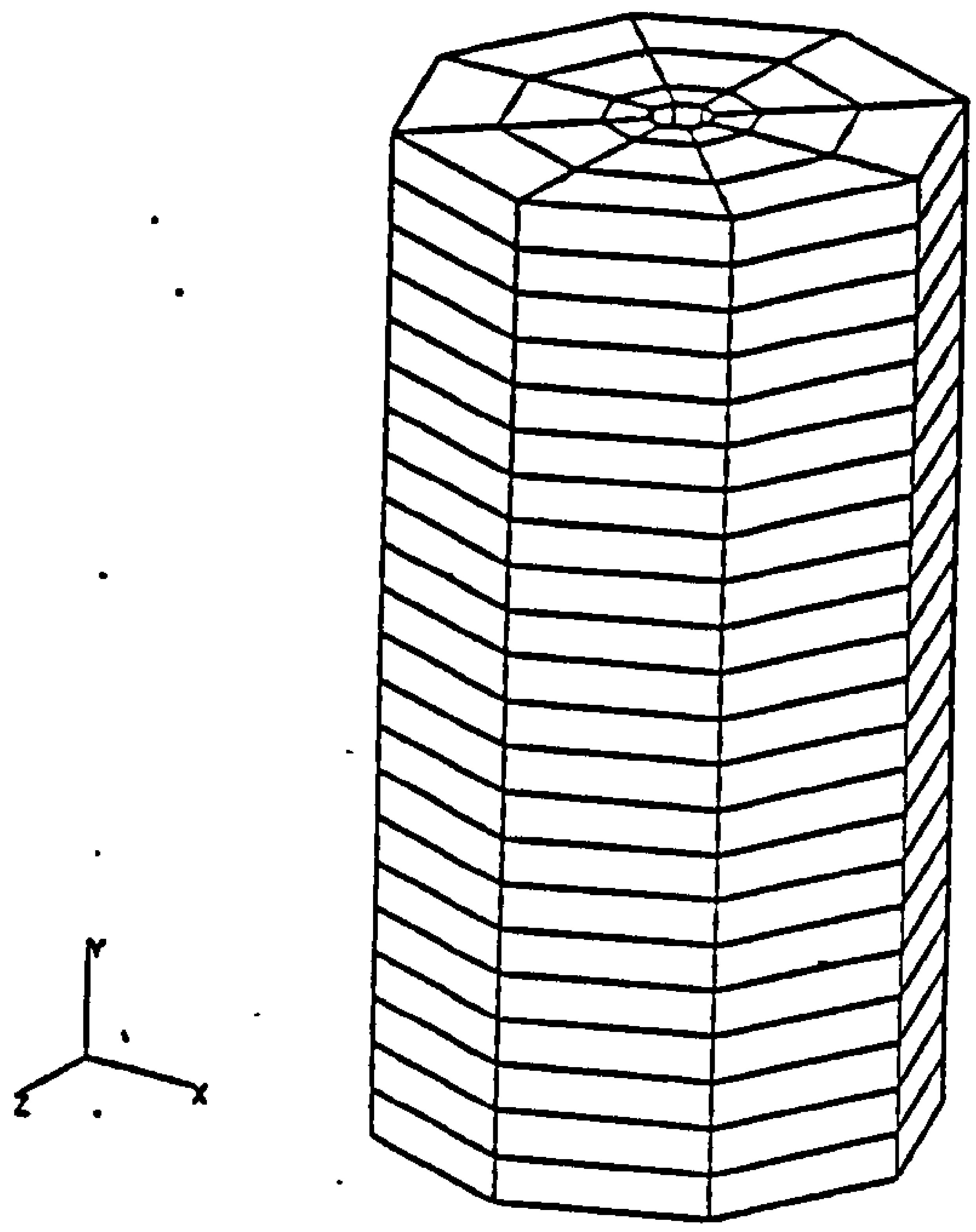

Rough
Nodes = 737
Elements = 530

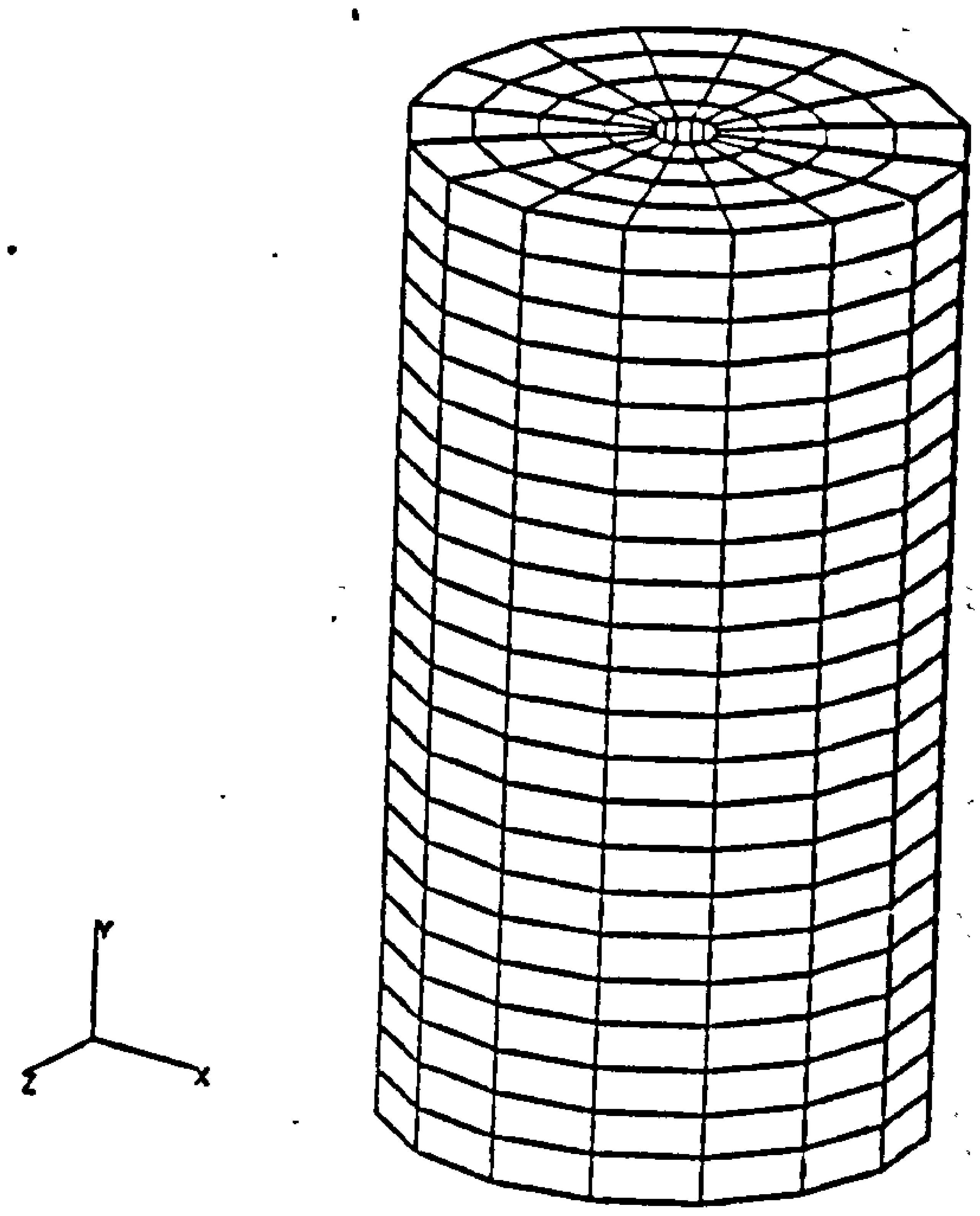

Medium
Nodes = 1841
Elements = 1410

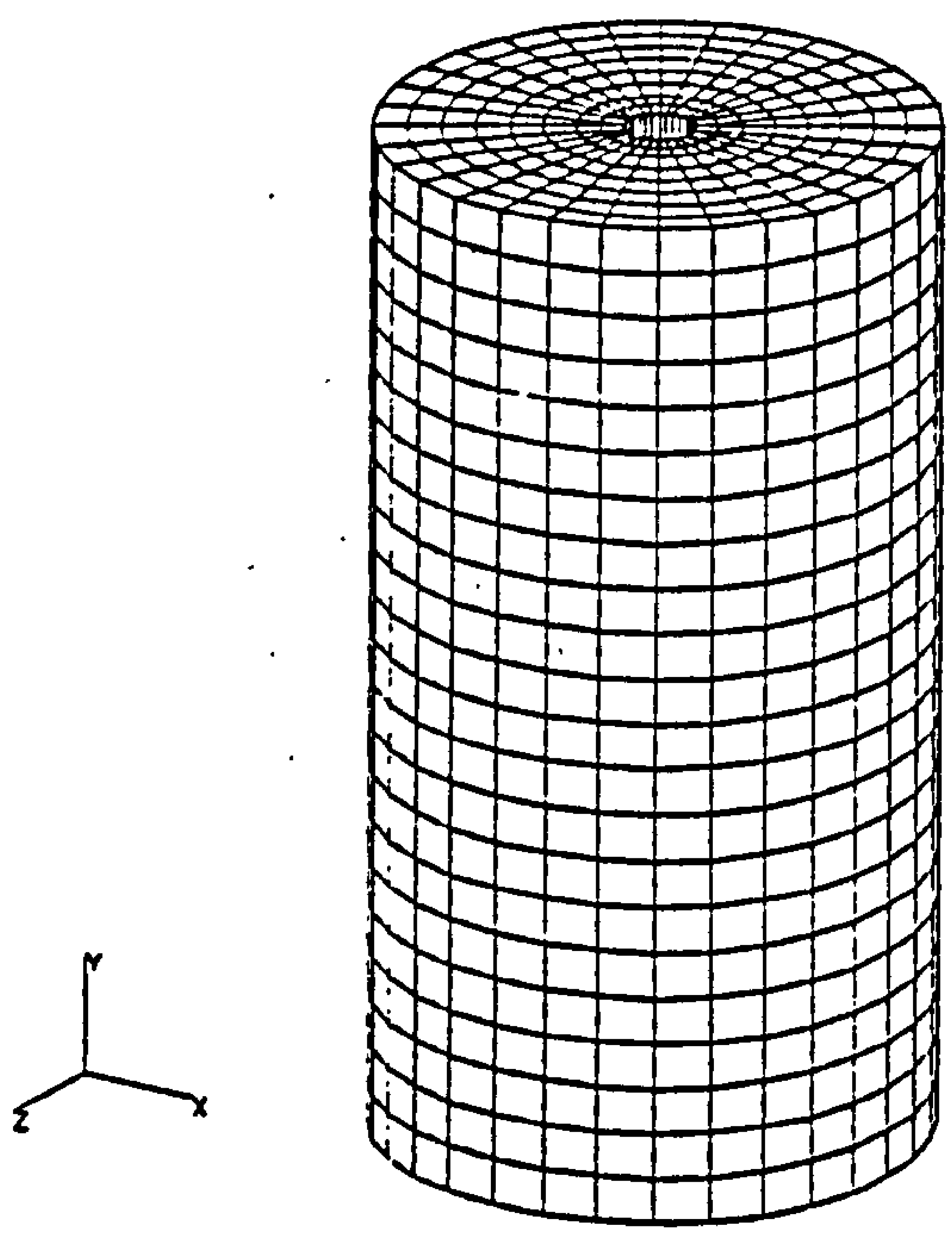

Fine
Nodes = 6625
Elements = 5634

Fig. 7.4.4.2 Three different mesh densities used in the convergence test.

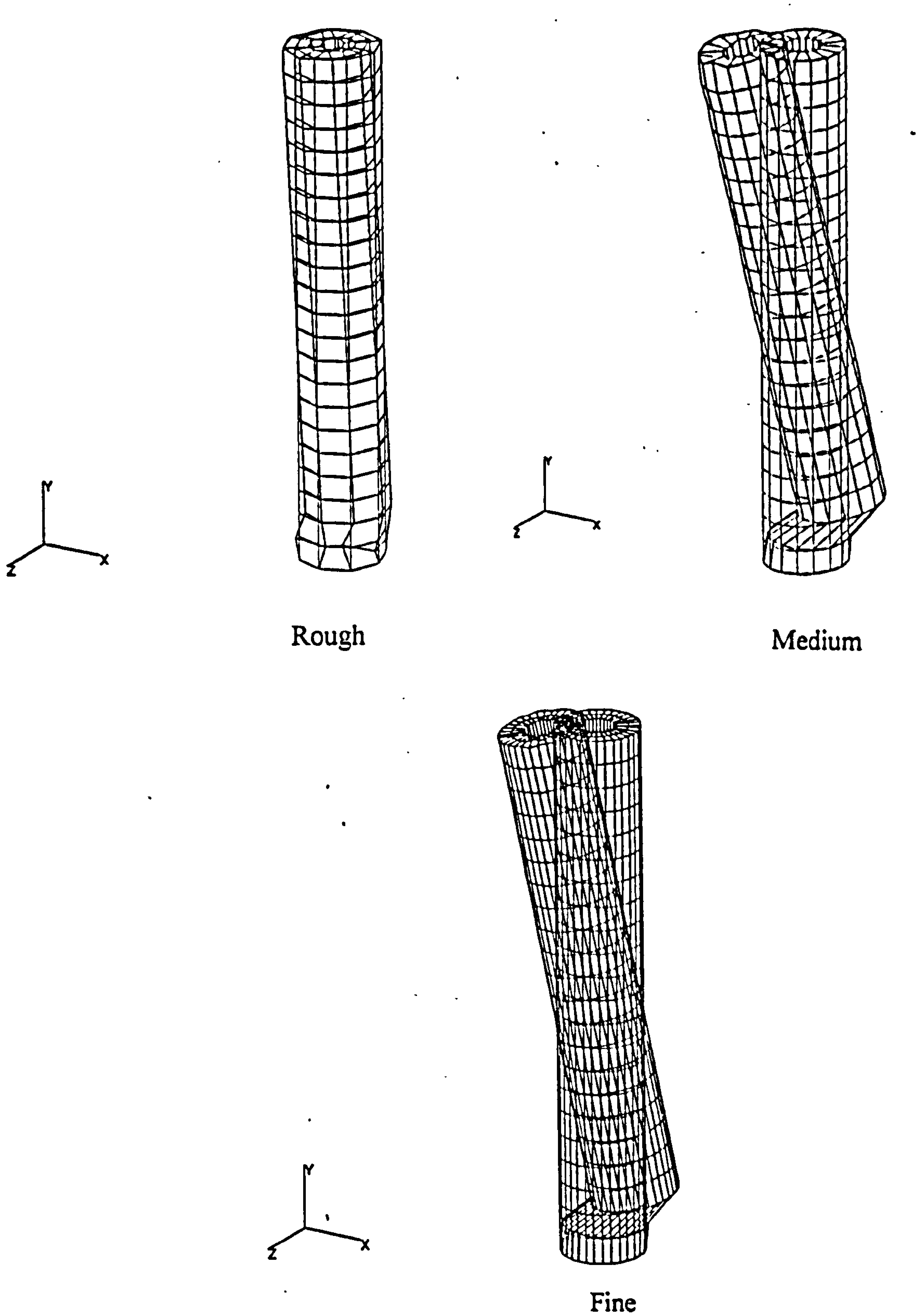

Fig. 7.4.4.3 Predicted displacements on the "bone" for the three different mesh densities.

FE model mesh	Displacement in mm		
	X	Y	Z
Fine	-6.2140	-0.1808	4.5060
Medium	-5.9270	-0.1687	4.3760
Rough	-5.6390	-0.4099	3.0910

Table 7.4.4.1 Predicted displacement at the centre of the top surface of the "bone".

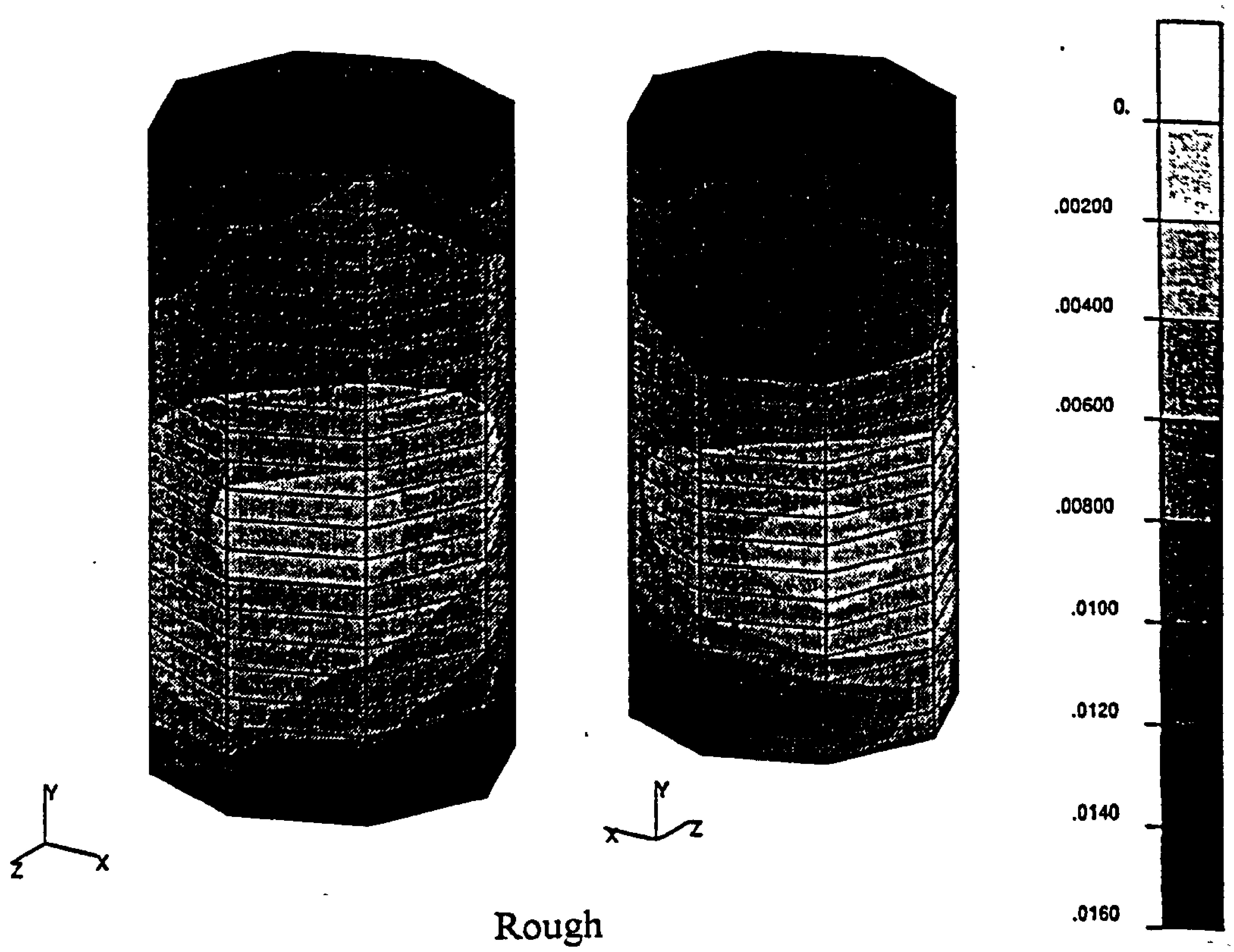

Rough

Fig. 7.4.4.4 Predicted surface stress distribution for the three different mesh densities.

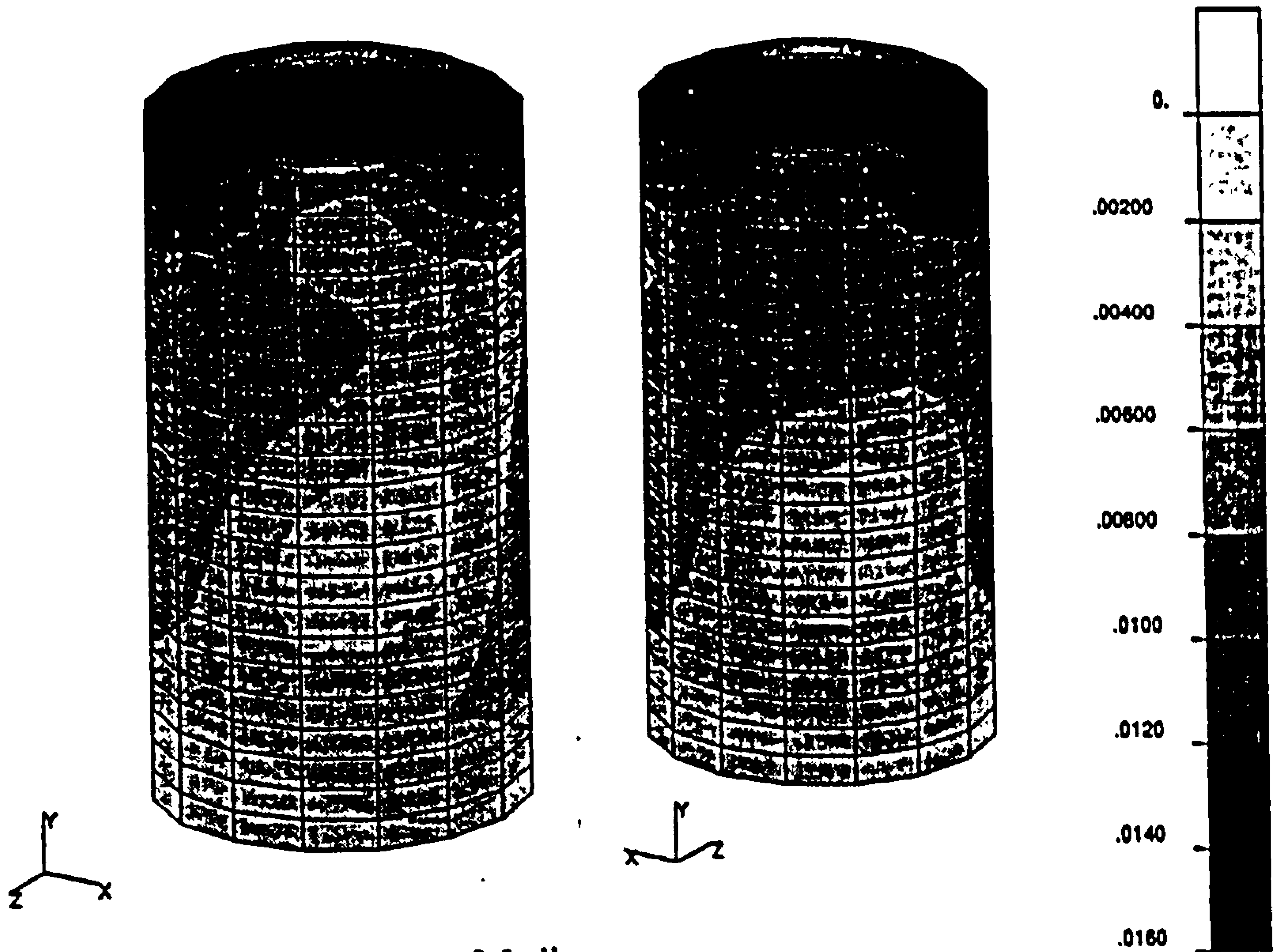

Medium

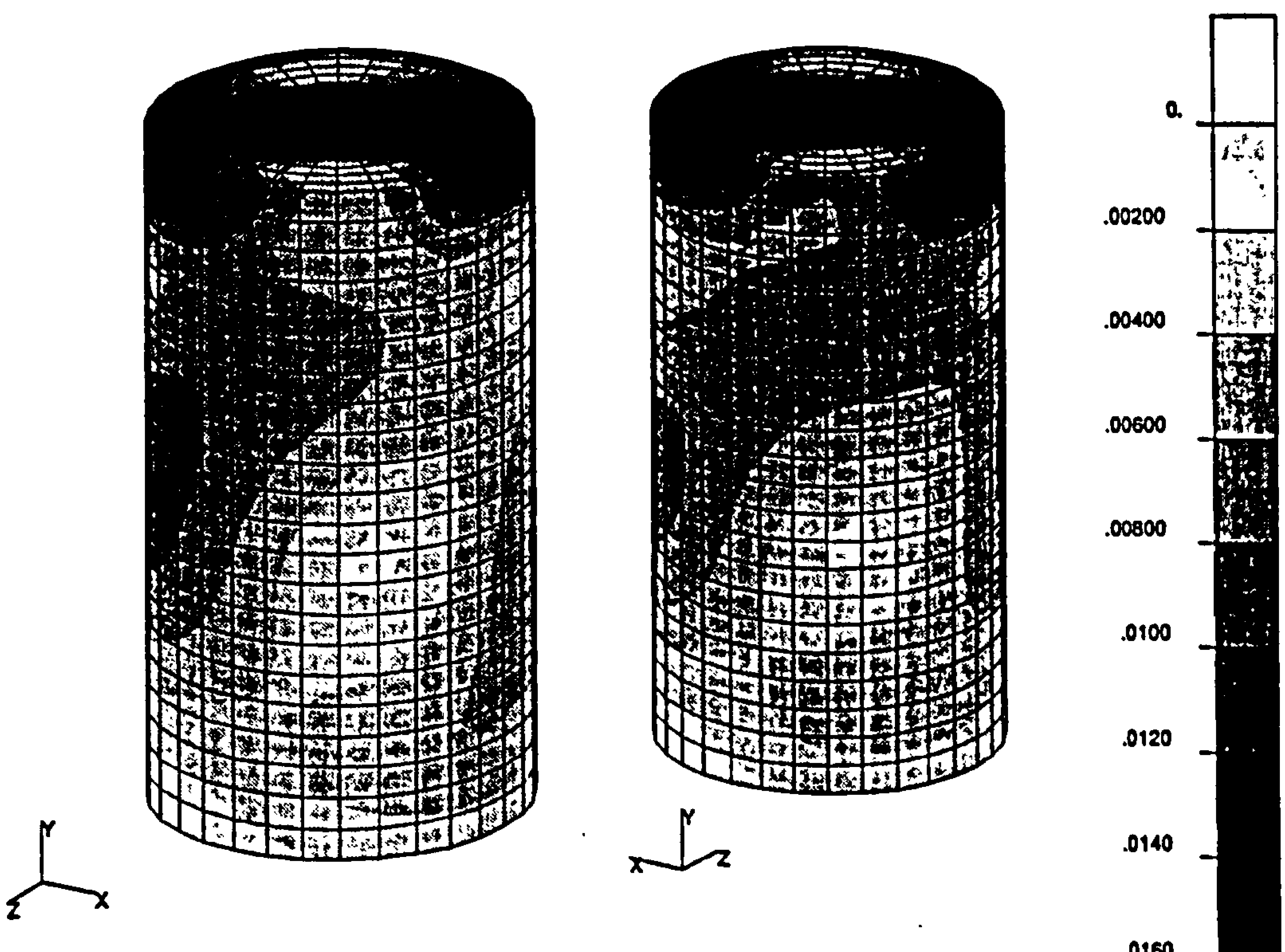

Fine

Fig. 7.4.4.4 Predicted surface stress distribution for the three different mesh densities.

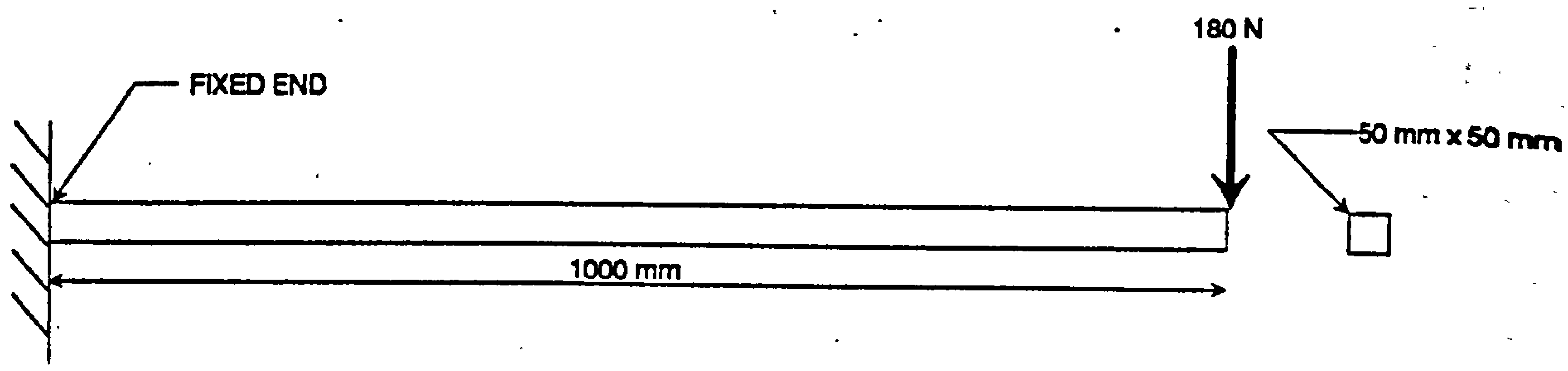

Fig. 7.4.5.1 Simple cantilever beam.

Comparing the predicted von Mises stress at the surface of the "tissue" (Fig. 7.4.4.4), the medium mesh model gave almost identical results with that of the fine mesh model in terms of magnitudes and distributions, even though the fine model did produce smoother stress contours. In the case of the rough mesh model, exceptionally high values were observed at the distal end of the cylinder which were not seen in the other two models. This was largely due to the limited deformation capabilities of the larger elements when subjected to large displacement.

The mesh density chosen for the residual limb model was approximately of the same order as that of the medium mesh. This decision was made based on a reasonable solution time with accurate results. The solution phase for the test models required 17 increments with an average of 2-4 iterations at each increment to obtain convergence. Using the Silicon Graphics workstation, the computation time for the fine, medium and rough model were 7 hrs, 30 min and 2 min respectively. With the Sun workstation, these computation times would be approximately three times greater. This made the fine model almost unreasonable. Furthermore, the residual limb models would be validated experimentally based on surface stresses, and the stresses predicted from the medium mesh cylinder model were very similar to that of the fine model and thus proved to be highly acceptable and accurate.

7.4.5 Element distortion

Several areas of the residual limb geometry especially that of the femoral bone were highly distorted with extreme curvatures. In order to conform to the residual limb geometry, the brick elements used would be subjected to distortion which could reduce the overall accuracy of the model. To understand the effect of element distortion, another FE experiment was performed. The experiment described below evaluates the performance of the brick elements used in this study (C3D8R) under several bending modes in highly distorted shapes.

A simple cantilever beam of uniform cross section (Fig. 7.4.5.1), fixed at one end and vertically loaded at the other end was modelled. From the given dimensions and loading, the maximum displacement at the loaded end is given by,

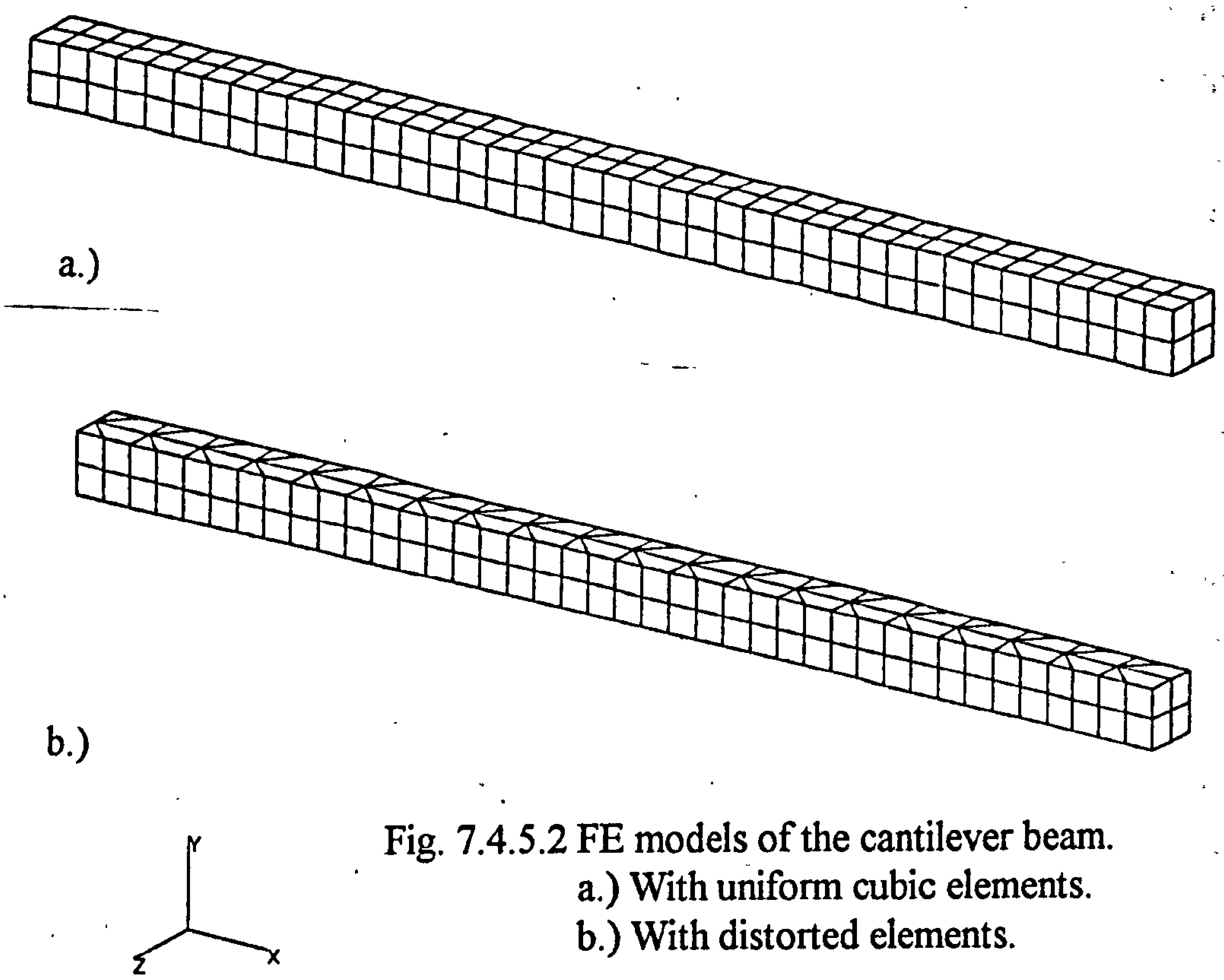

Fig. 7.4.5.2 FE models of the cantilever beam.
a.) With uniform cubic elements.
b.) With distorted elements.

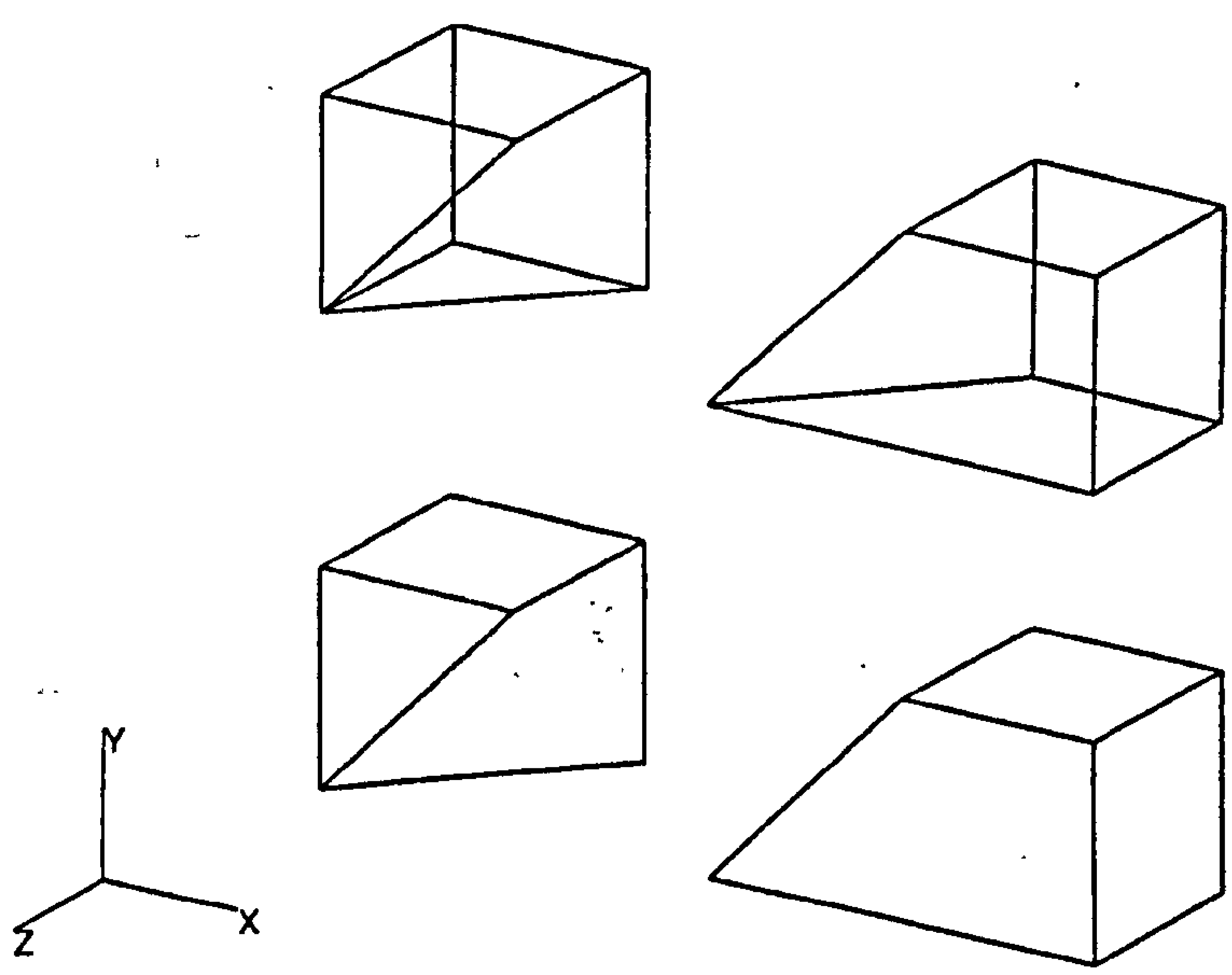

Fig. 7.4.5.3 Distorted elements used in the cantilever beam model.

$$d_{\max} = \frac{PL^3}{3EI} \qquad (7.4.5a)$$

where P is the applied force, L the length of the beam, E the Young's modulus and I the 2nd moment of inertia. Using the FE method assuming large displacement analysis, the beam was modelled using 40 8-noded brick elements of the most ideal shape, i.e. cube shape. The same beam was further modelled with similar type elements, but nodes at the top and bottom face of the elements had been moved to create internal angles of 45°/135°. Fig. 7.4.5.2 shows the two FE models of the cantilever beam and Fig. 7.4.5.3 shows the distorted elements in more detail.

A comparison was made with the $d_{\max}$ calculated using equation 7.4.5a with the approximation given by the two FE analyses based on cubic and distorted elements. The maximum displacement was 7.432 mm calulated from equation 7.4.5a, and 7.300 mm and 6.652 mm respectively from the cubic and distorted elements FE analyses. Fig. 7.4.5.4 shows that both analyses predicted similar deformed shapes, though deviations from the exact solution were 1.7% and 10.4% for cubic and distorted elements respectively. Fig. 7.4.5.5 plots the stress distribution of the models, and it could be noted that the maximum stress differed only by 0.04 N/mm^2 and the stress patterns were identical.

The experiment showed that errors could arise from distorted elements. However, the error would be confidently kept below the 10% level in the residual limb models, since the experiment with the beam was performed under the extreme condition of having all the elements in the model suffering from distortion. In the case of the residual limb models, the FE program detects an average of 85 out of 1600 elements to be highly distorted.

7.4.6 Meshing the bone

The 3-D co-ordinates of the bone from MRI scans were represented as grid points in PATRAN. Prior to meshing, standard steps were adopted to create suitable volumes from the grid points. Firstly, lines had to be formed by connecting the grids in the transverse plane, creating lines defining the outline of the bone in three dimensions. The lines in each transverse plane appeared circular where a centre point

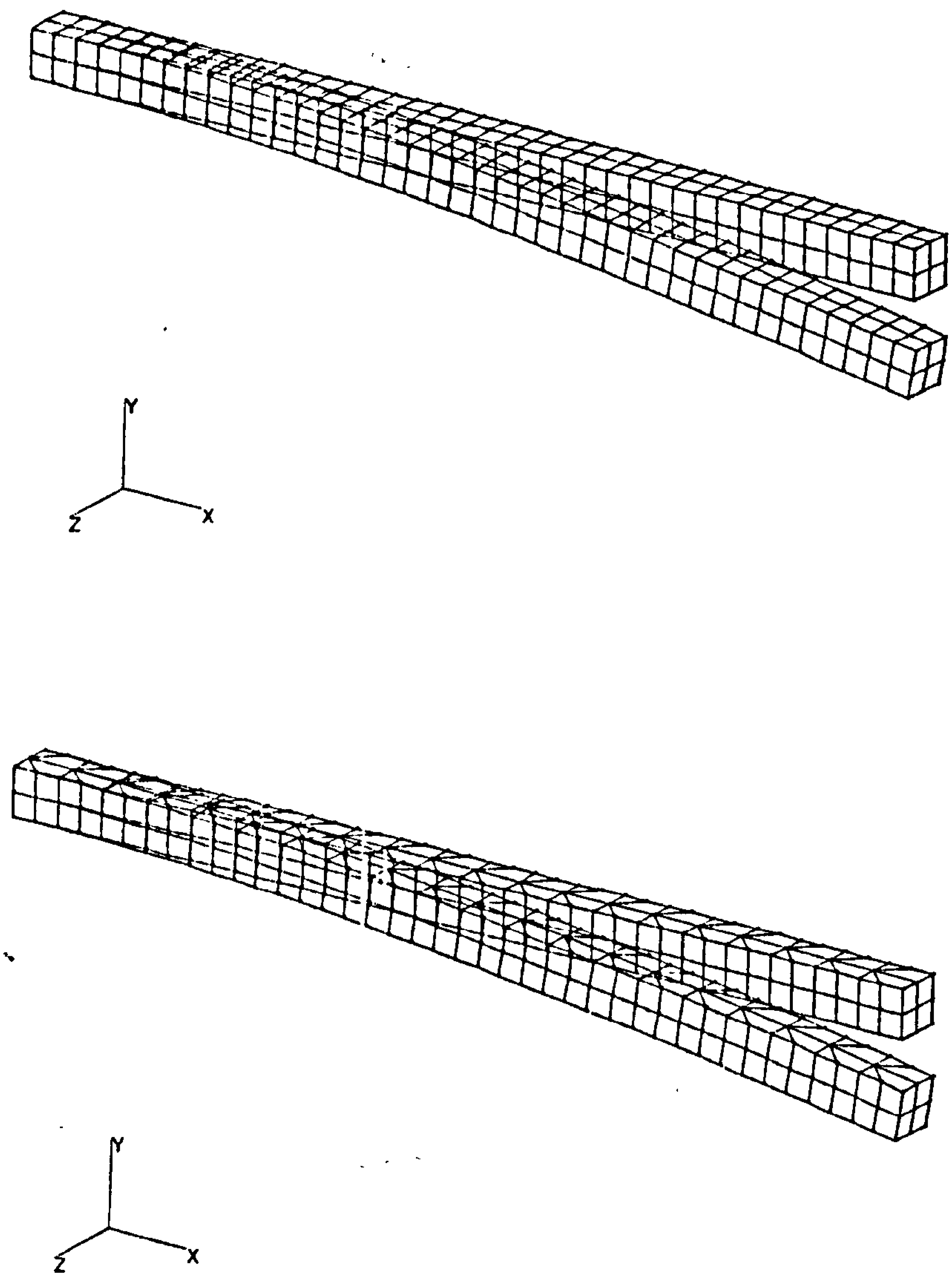

Fig. 7.4.5.4 Predicted deformation in the cantilever beam.

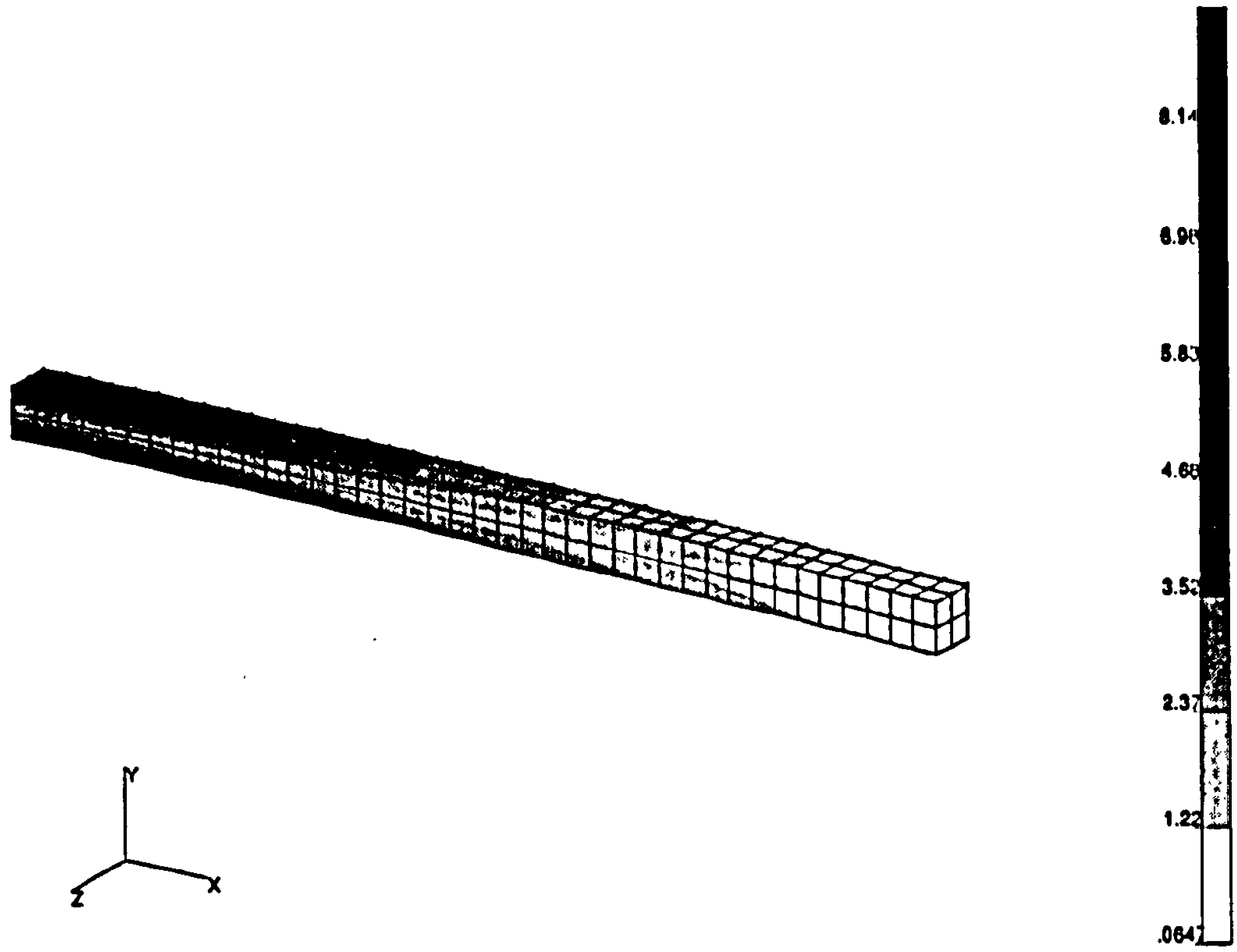

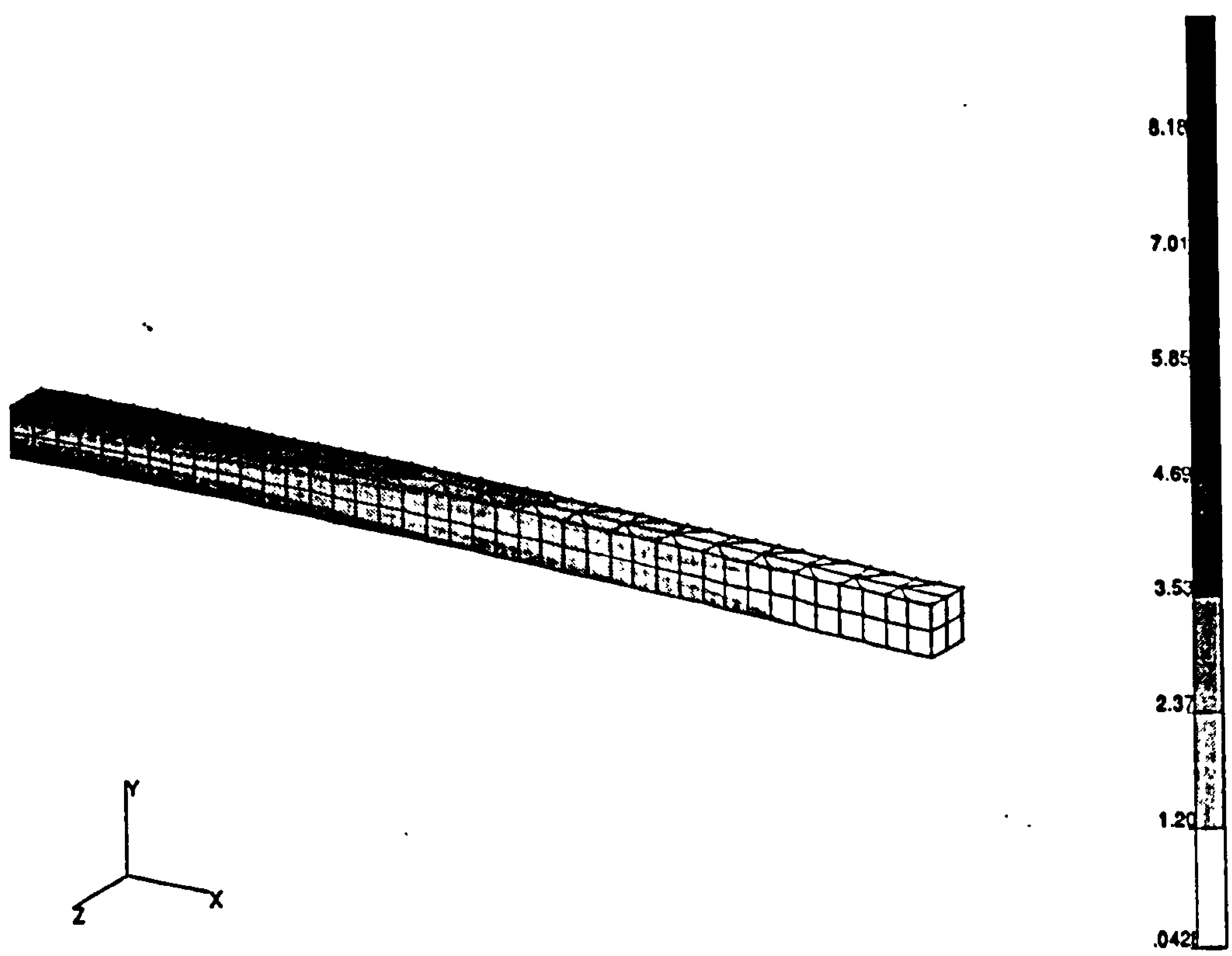

Fig. 7.4.5.5 Predicted stress distributions in the cantilever beam.

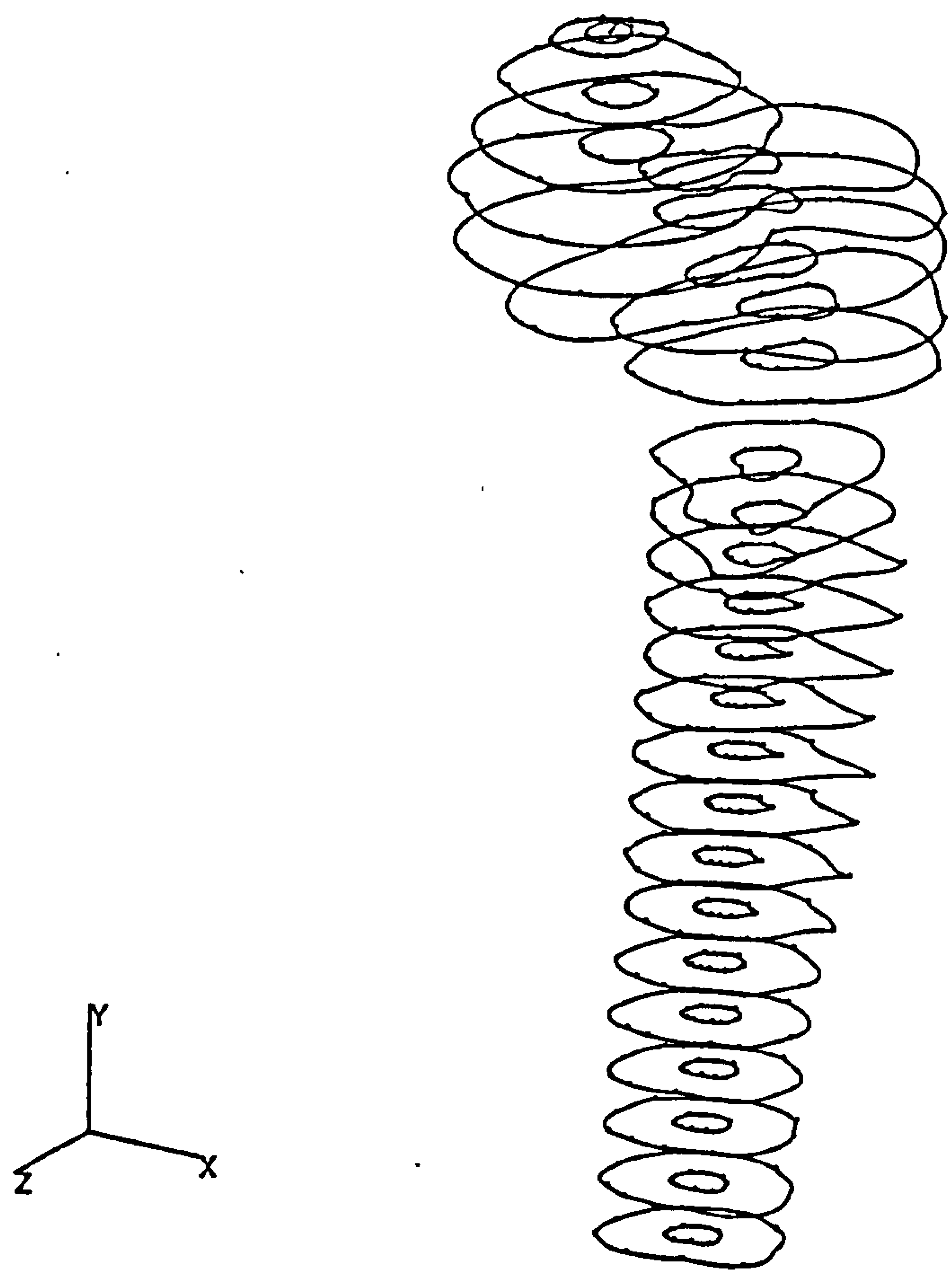

Fig. 7.4.6.1 Joining the grids to define lines of the bone.

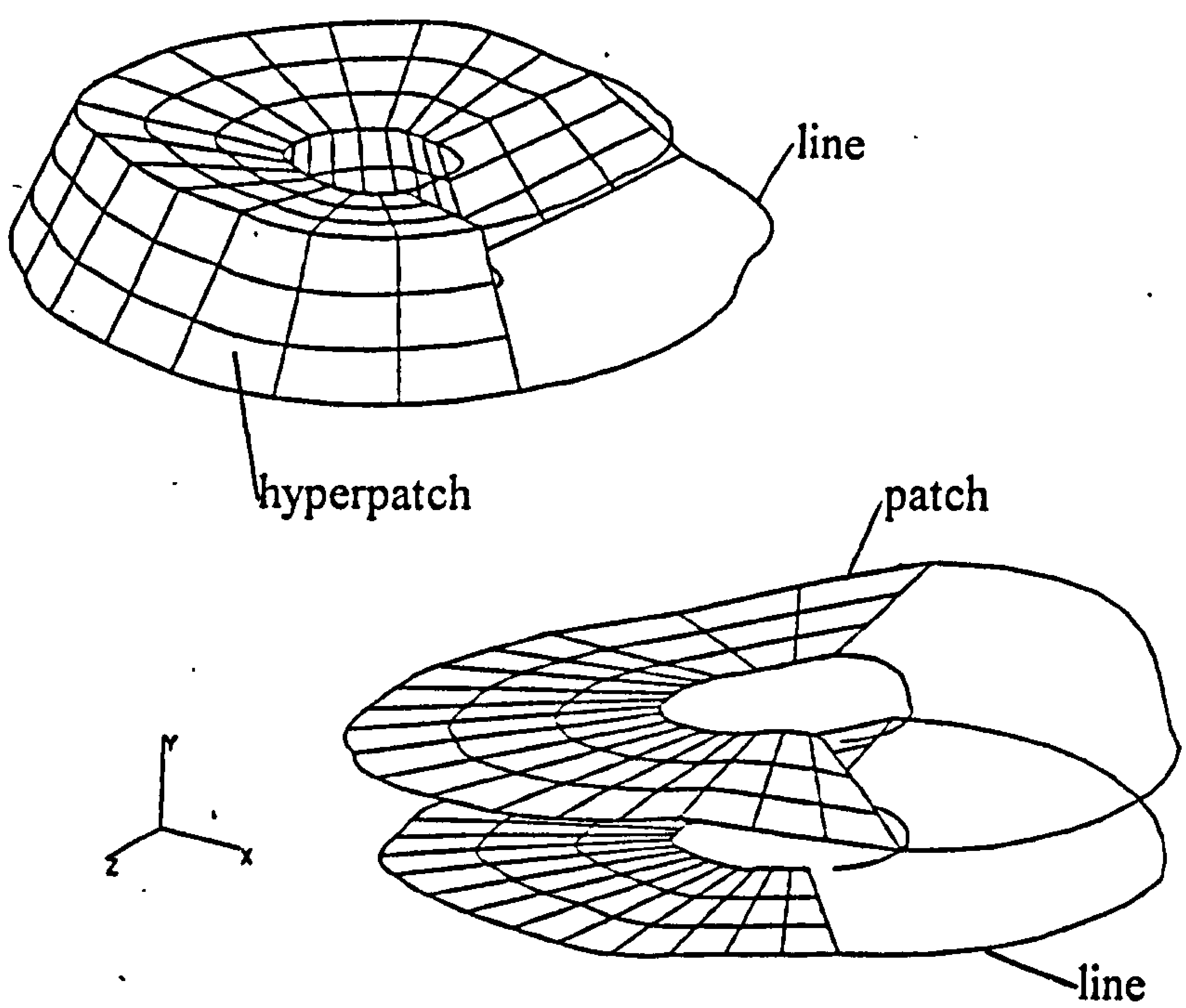

Fig. 7.4.6.2 Patches and hyperpatches of the bone.

could be approximated. Another set of lines was created by shrinking the first set of lines towards this centre point at each transverse plane (Fig. 7.4.6.1). With the second set of lines, appropriate areas (patches) were formed and finally volumes (hyperpatches) were formed with the adjacent transverse slices (Fig. 7.4.6.2). At each transverse section, eight volumes had been defined. Meshing was controlled by placing two elements in each volume (Fig. 7.4.6.3). The number of elements through the bone thickness was kept only to one since the material stiffness of the bone was 10^5 times that of the tissue, behaving almost like a rigid surface, a fine mesh would have little improvement to the overall model's accuracy. The complete bone mesh is as shown in Fig. 7.4.6.4. The total number of elements used was 448 and the number of nodes was 882.

7.4.7 Meshing the soft tissue

The process of meshing the soft tissue was exactly the same as that of the bone. The digitised socket shape was transferred to PATRAN and was represented by grid points as shown previously in section 7.2.1. The grid points were then joined to form lines that defined the external surface of the residual limb model (Fig. 7.4.7.1). Subsequent areas were formed by matching these lines with lines that outlined the bone geometry. Finally, volumes were formed and meshing commenced (Fig. 7.4.7.2). Each volume was meshed with six elements and each transverse soft tissue slice consisted of eight volumes (Fig. 7.4.7.3).

Meshing at the distal end of the residual limb was slightly different from that of the bone since the residual limb extends beyond the bone. Efforts were needed to close up the distal end by using 16 prism shape elements as shown in Fig. 7.4.7.4. Fig. 7.4.7.5 shows a plot of the completed FE mesh for subjects U, M and H. Subject's U model required 1618 elements and 2115 nodes. Subject's M model had a total of 1686 elements and 2163 nodes and finally subject's H model had 1650 elements and 2153 nodes.

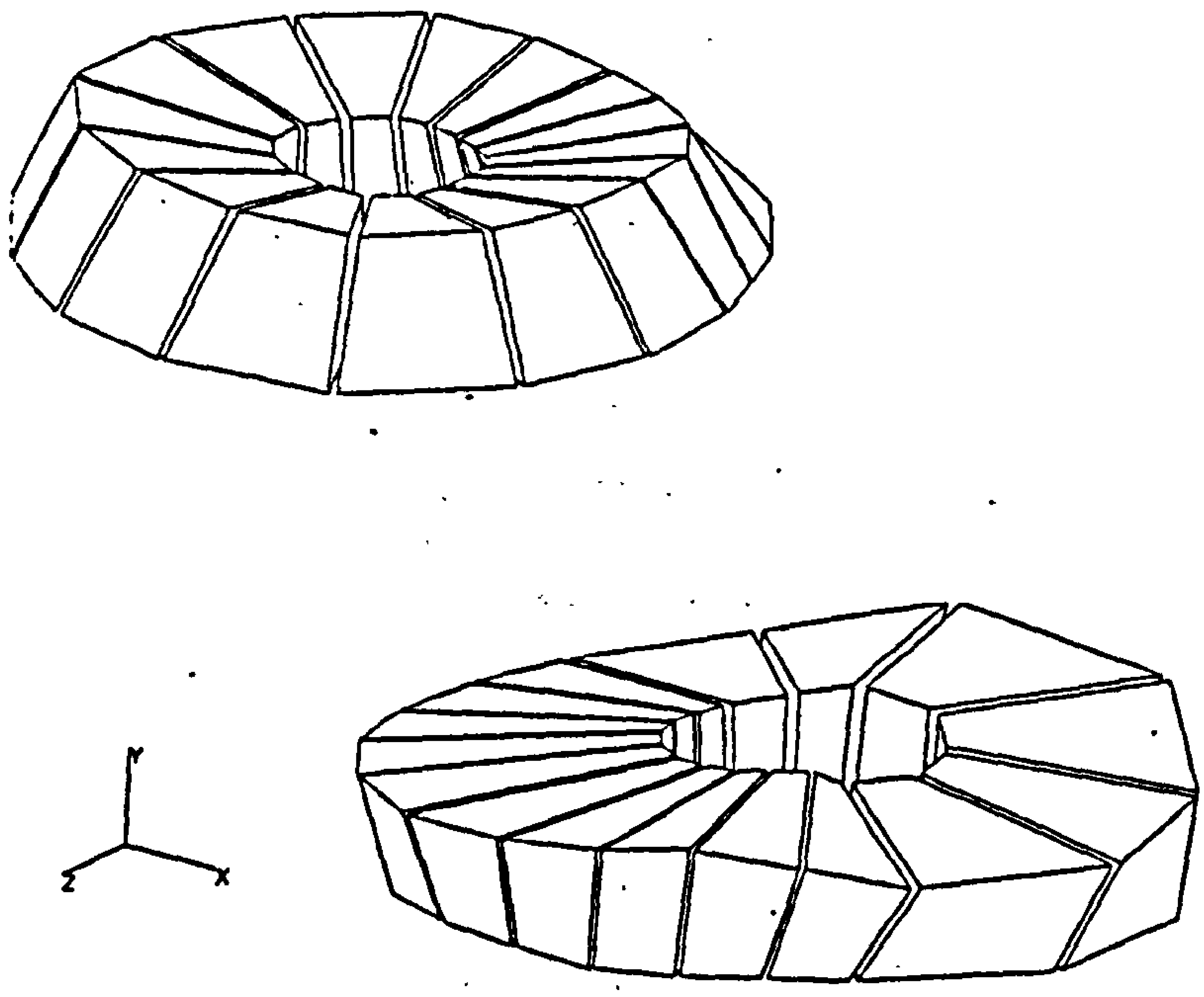

Fig. 7.4.6.3 Two elements placed in each hyperpatch.

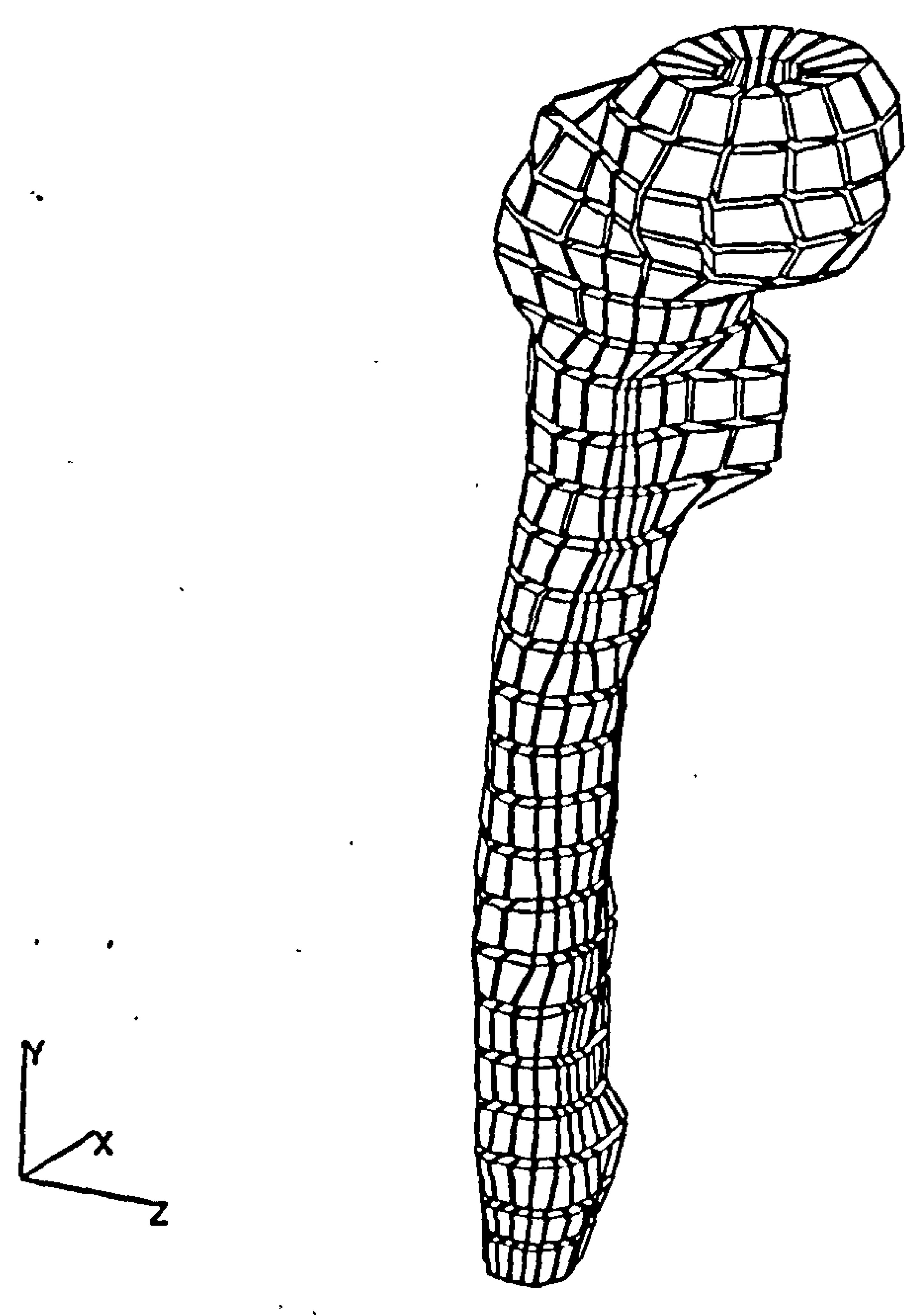

Fig. 7.4.6.4 Completed mesh of the bone.
(Note : Elements are shrunk by 20% in the plot for clarity.) .ty.)

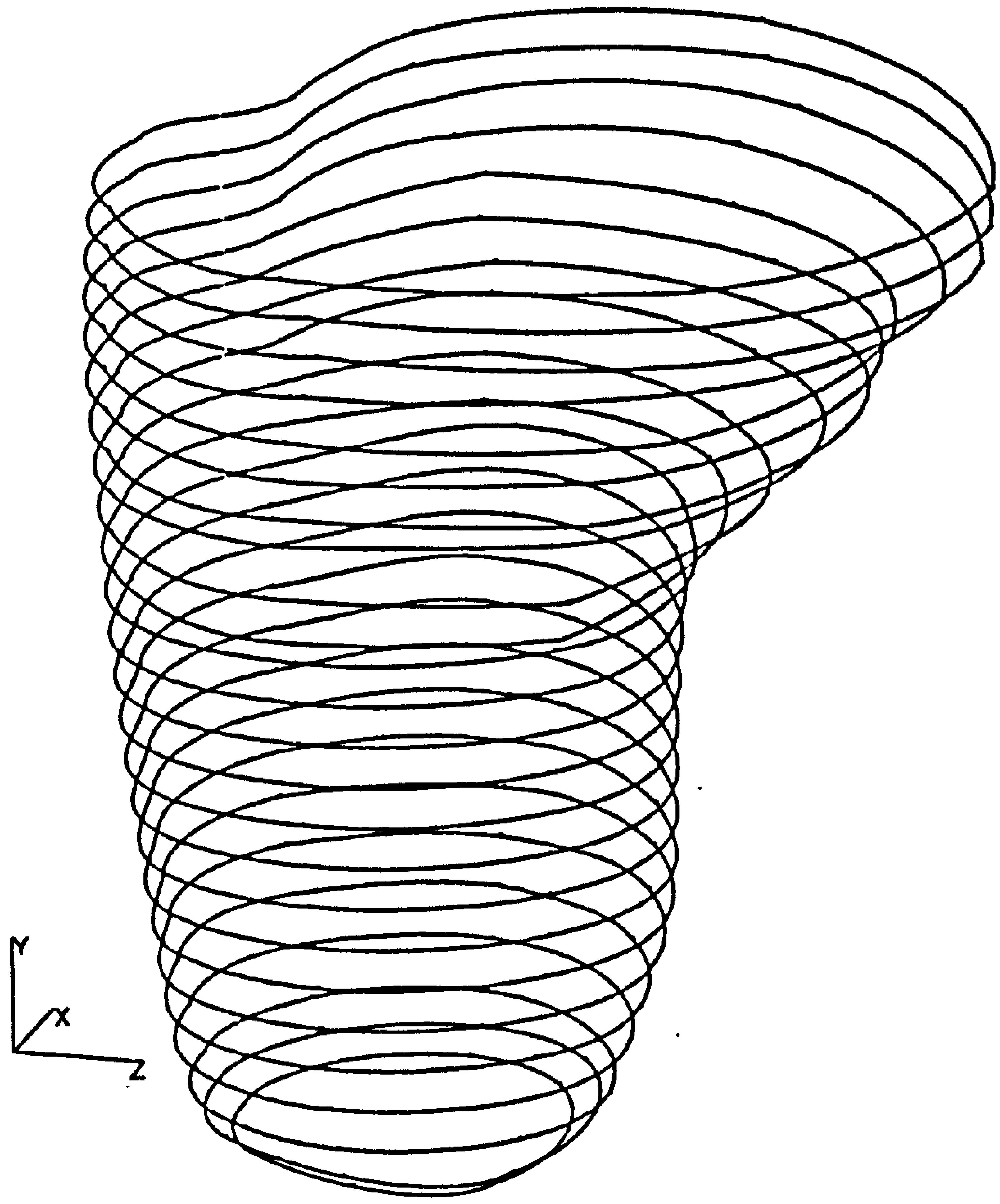

Fig. 7.4.7.1 Lines defining the external surface of the residual limb.

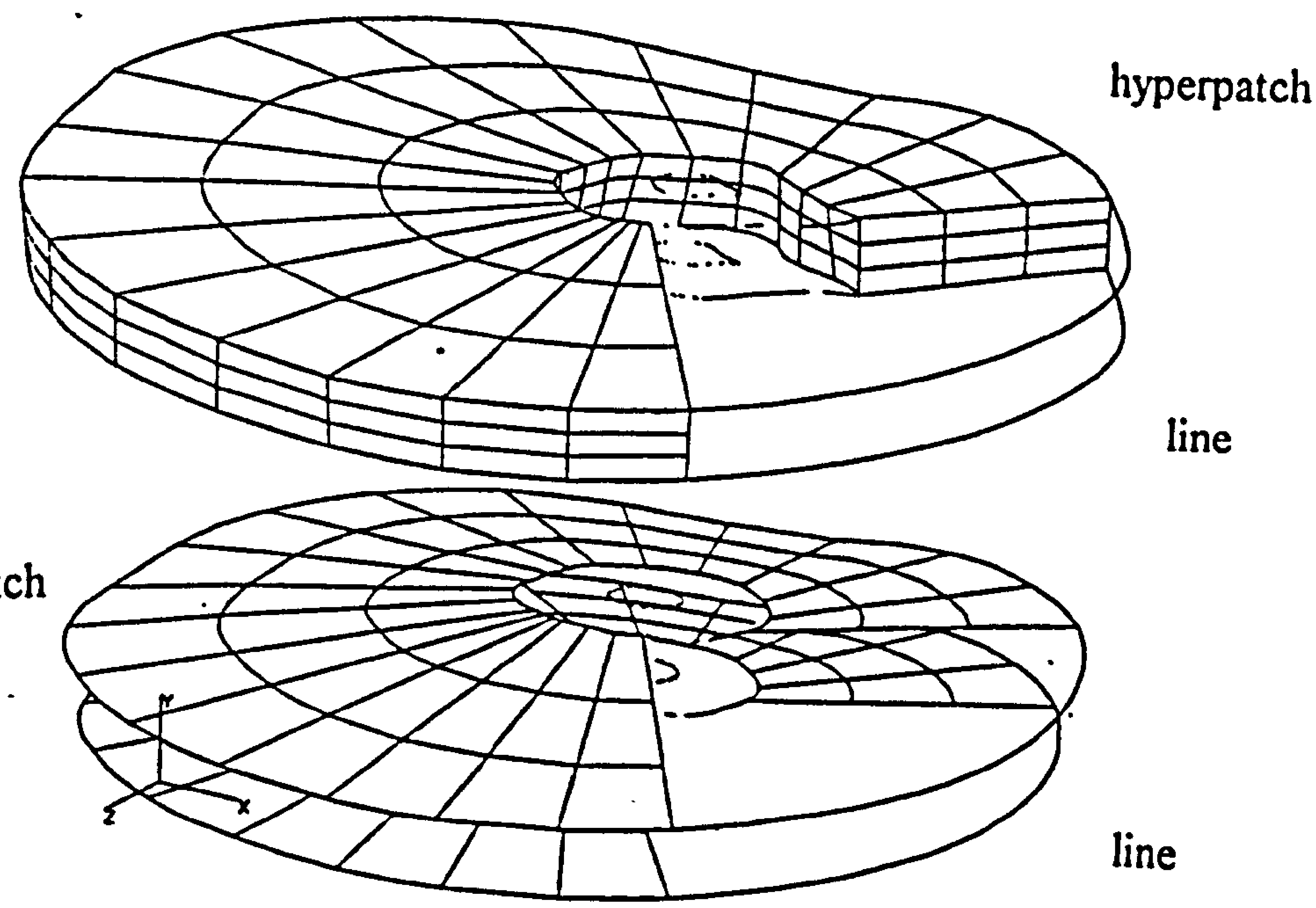

Fig. 7.4.7.2 Patches and hyperpatches of the soft tissue.

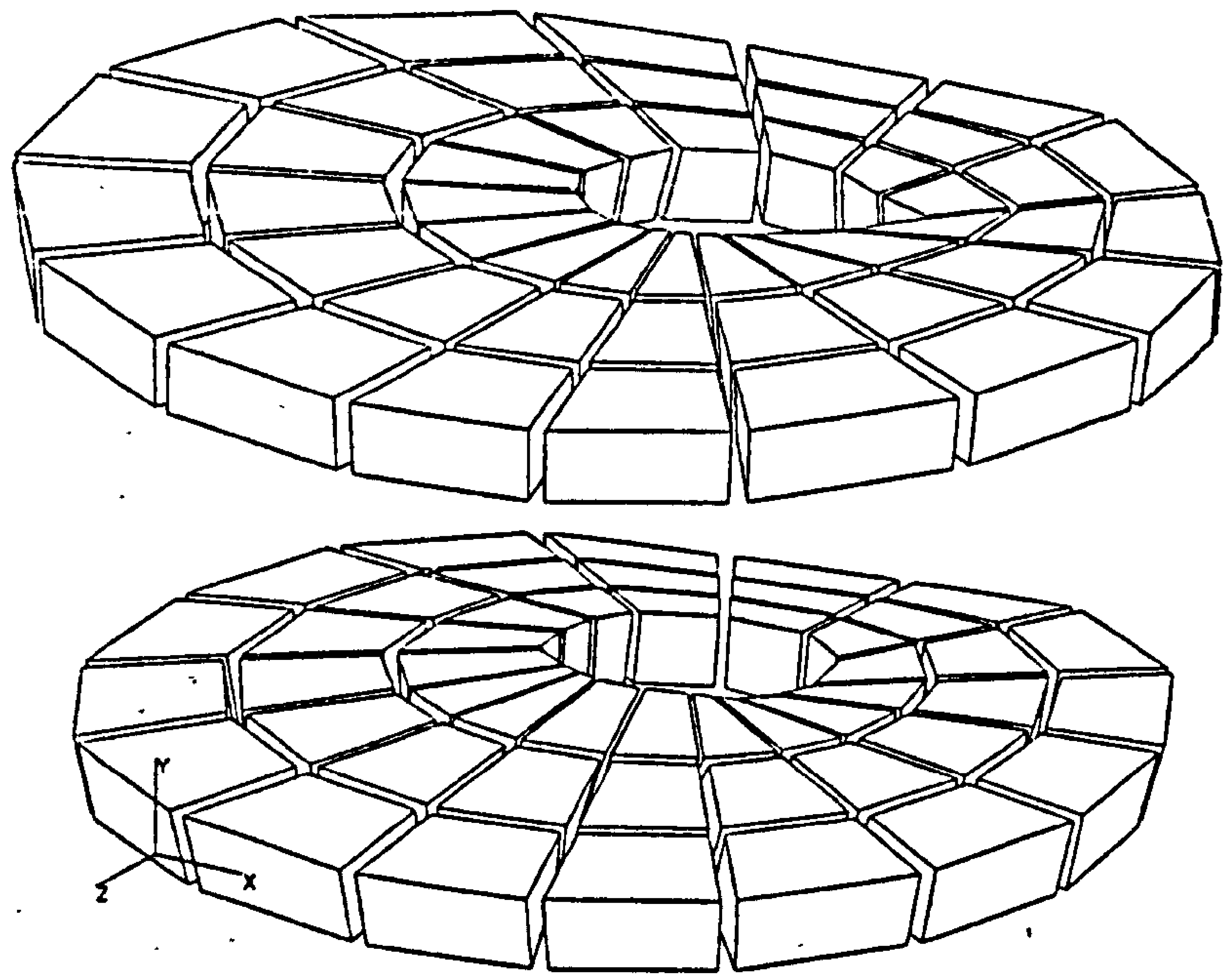

Fig. 7.4.7.3 Soft tissue meshed with 48 elements at each transverse slice.

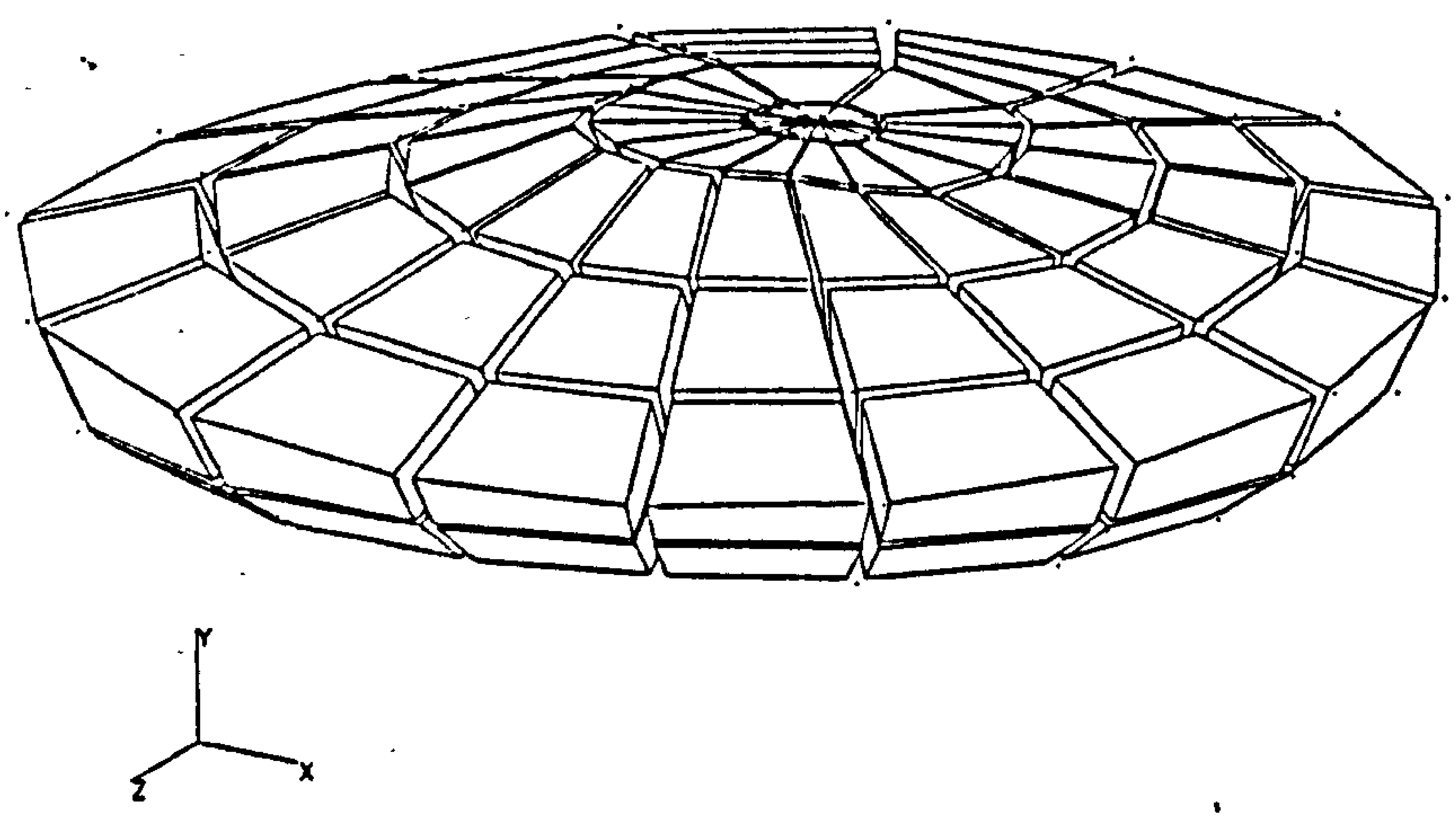

Fig. 7.4.7.4 Distal end meshed included prism shape elements.

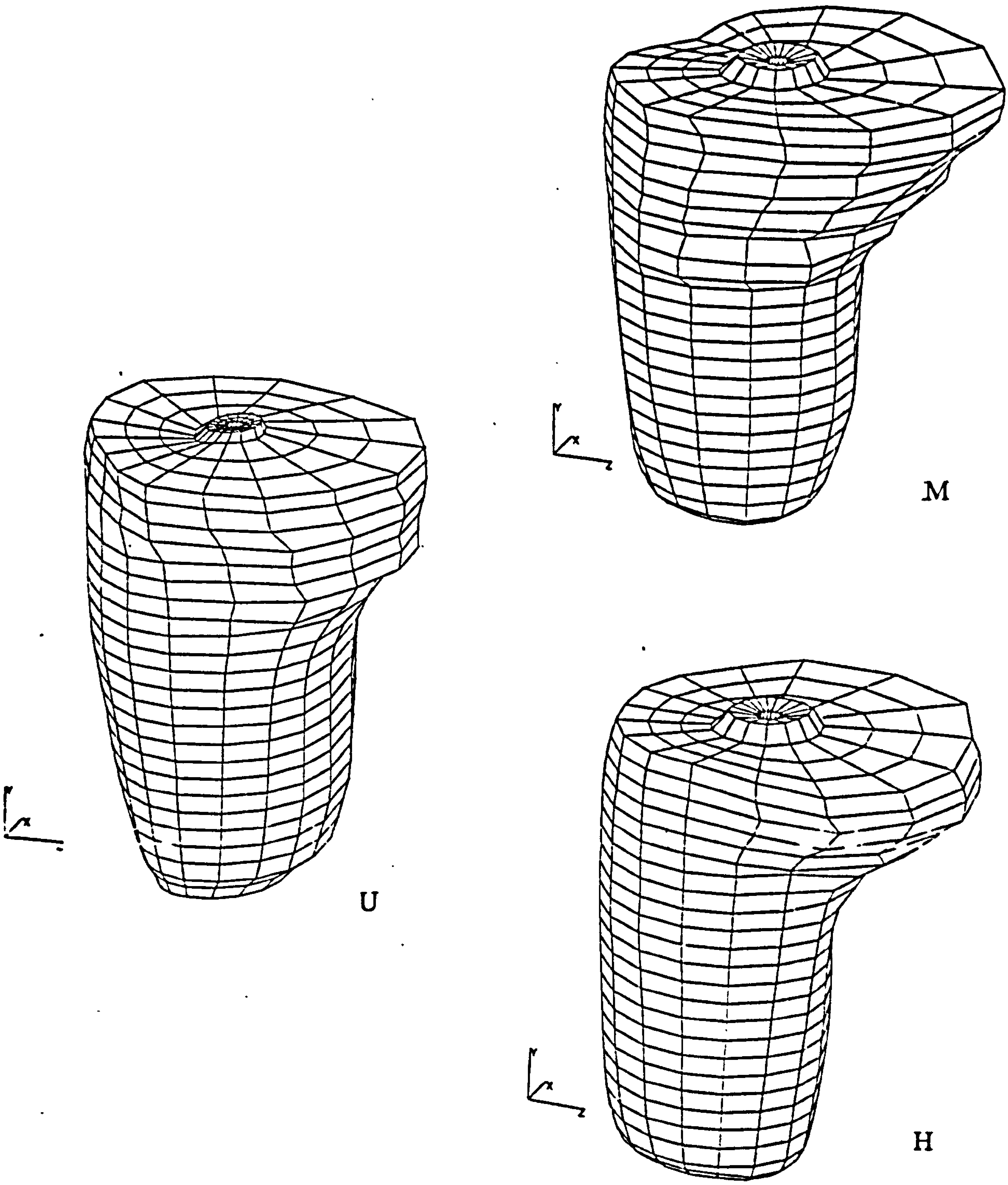

Fig. 7.4.7.5 Complete FE mesh of the residual limb for three subjects.

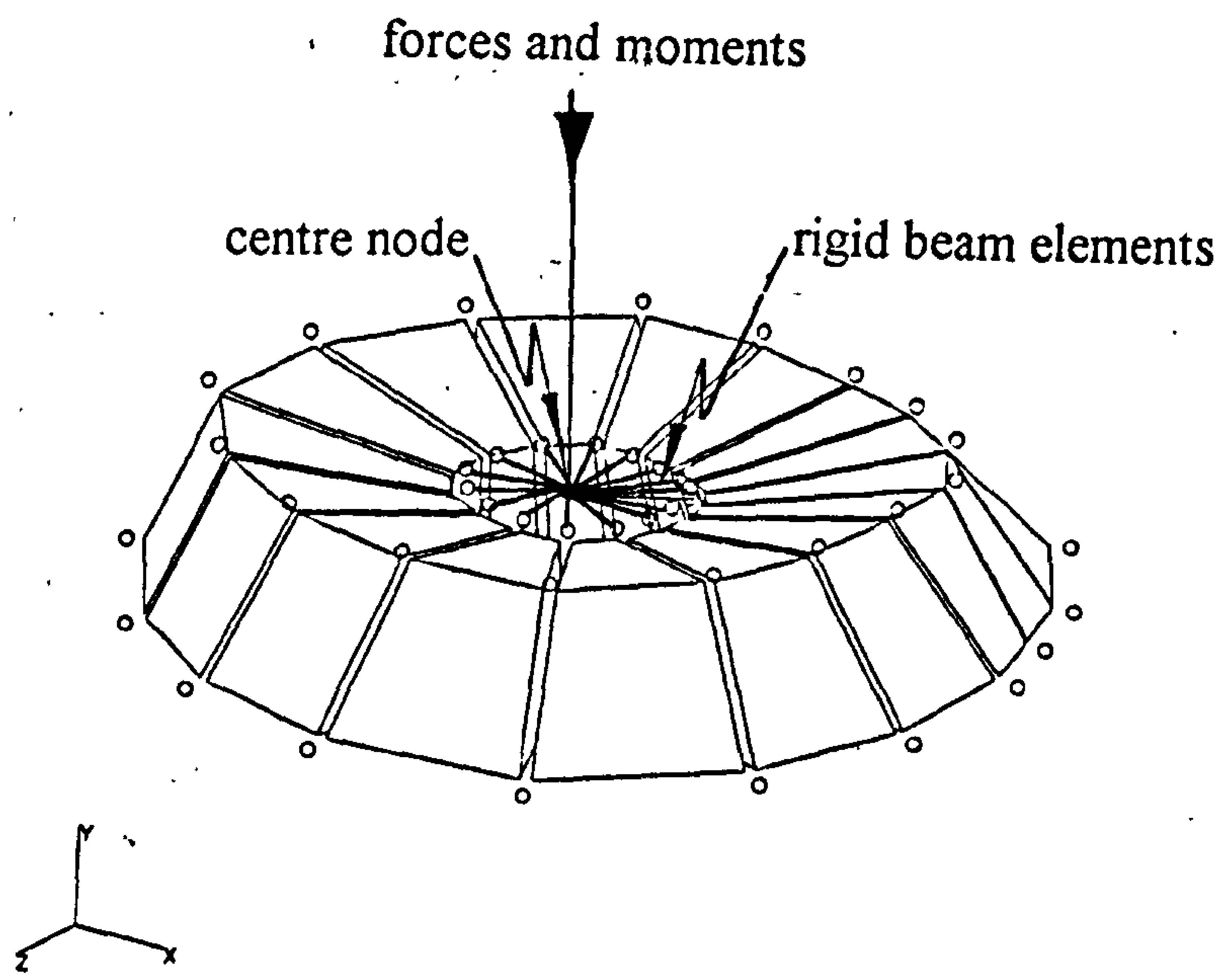

Fig. 7.4.8.1 A centre node linked by rigid elements to the surrounding nodes transferring load actions to the femur.

7.4.8 Loading on the bone

The inter segmental loads at the hip during standing and walking were input at a node placed at the centre of the head of the femur. This node was linked by rigid elements to the immediate nodes that surrounded the centre node (Fig. 7.4.8.1). Appropriate forces and moments applied at the centre node would be transferred to the bone through the rigid elements, causing it to behave as it would during standing and walking.

Several assumptions were made in loading the bone in this manner. Referring to chapter two (Table 2.3.1.1 and Fig. 2.3.2.1), a number of muscles are responsible for the movement of the thigh. The position, insertion and origin of the muscle determine its function. The author of this thesis reckons that loading the bone at the femoral head could only approximate certain muscle functions. Flexion of the thigh is provided by the psoas, iliacus, pectineus which originate at the pelvis and inserts at the lesser trochanter of the femur. The muscles' force are directed towards the proximal section of the femur which might be approximated by loading at the femoral head. However, flexion of the thigh is also provided by the adductor magnus which inserts along the linea aspera to the adductor tubercle of the femur. The model will not be able to simulate such loading due to lack of geometrical detail. Extension of the thigh also poses similar problem, since one of the main extensor is the adductor magnus. Nevertheless, another main extensor which is the gluteus maximus inserts at proximal section of the femur at the gluteal tuberosity.

Most muscles responsible for abduction of the thigh insert at the greater trochanter and therefore can be reasonably approximated by loading applied to the femoral head in the model. The abductors muscles are basically the gluteus medius, minimus, piriformis, obturator internus, superior and inferior gemellus. However, the main adductors, the adductor brevis, longus and magnus inserts at the linea aspera of the femur causing difficulties in specifying a suitable loading condition in the model.

7.4.9 Analysis type

The analysis type adopted was static and geometrically non-linear. The significantly large differences between the stiffness of the bone and soft tissues resulted in large movement of the femur in the residual limb during gait, which necessitated the use of a geometrically non-linear analysis. In ABAQUS, the analysis included large displacement effects, where large strains were no longer infinitesimal and shape changes were accounted for. The elements selected, C3D8R and C3D6 used a fully non-linear formulation, hence compatibility was maintained. In the analysis, a final solution was obtained by firstly breaking the load into a series of load increments and solving it. At the completion of each incremental solution, ABAQUS adjusted the stiffness matrix to reflect the non-linear changes in the structural stiffness before proceeding to the next increment. At each increment, the Newton Raphson equilibrium iterations were used to achieve equilibrium convergence. Therefore, a solution was obtained as a series of increments with iterations within each increment. In the residual limb model, the initial increment was kept small at 0.01% of the load, after which the ABAQUS automatic incrementation scheme was used. A direct user control incremental size was not used because it was difficult to predict the behaviour of the model before hand, therefore adopting too large an increment will result in more iterations or even an increment size which falls outside the Newton's radius of convergence preventing a solution. Automatic incrementation was considered a more economical approach. The residual limb models required about 23 increments and 4 iterations at each increment. The computation time with a Silicon Graphics Indigo II takes about an hour.

Material non-linearity was not considered in the models, as discussed earlier in chapter six, this effect was difficult to achieve at this level.

7.5 RESULTS AND VALIDATION OF FE MODELS

In the FE models considered in this thesis, the von Mises criterion was selected to interpret the stresses on the surface of the residual limb as interface pressures. The von Mises stress criterion is given by,

$$\sigma = \sqrt{\tfrac{1}{2}(\sigma_1 - \sigma_2)^2 + \tfrac{1}{2}(\sigma_2 - \sigma_3)^2 + \tfrac{1}{2}(\sigma_3 - \sigma_1)^2} \qquad (7.5a)$$

where $\sigma_1, \sigma_2, \sigma_3$ are the principal stresses in a three dimensional stress state. At the residual limb socket interface, the state of stress consists of components of normal and shear stresses which could be converted to the principal stresses. In the case of a trans-femoral amputee, shear stresses measured at the residual limb socket interface are much lower than normal stresses (Appoldt et al 1970). Therefore normal stresses would remain as the main stress component at the residual limb / socket interface. In addition to normal and shear stresses, hydrostatic stresses has been speculated to be present at the residual limb / socket interface (Readhead, 1979). However, hydrostatic stresses would have caused the least tissue damage. Instead, the main cause of soft tissue breakdown is the application of normal stress. Investigations in the development of pressure sores have shown that a normal pressure of 6.7 kPa could induce pathological changes in soft tissues (Husain 1953).

In a three dimensional stress state, the stresses in three directions are non zero and the overall stress state can be represented by the distortion energy or the von Mises criterion. The von Mises stress is the overall stress less the hydrostatic stress and has been used as a reliable prediction for failure in some engineering materials. It has also satisfied investigators as a source to predict tissue damage (Chow and Odell 1978). In this section, interface pressures and von Mises stresses will be used indiscriminately.

7.5.1 Comparison between FE predicted and experimental measured pressures

Comparison was made between predicted and measured pressures at the sites detailed in chapter four section 4.8, for sockets used in part one of the pressure measurement studies. The FE models were able to predict pressures at the entire residual limb, both on the surface and on the inside, including the bone. However, validation was only possible based on the interface pressure measured at the 14 locations. Though in the pressure measurement test and gait analysis, data were captured throughout the gait cycle, the FE models were only generated and validated on conditions during standing, and at 10%, 25% and 40% of the gait cycle from heel strike. It was considered extremely time consuming, costly and unnecessary to generate a model at every percentage of the gait cycle.

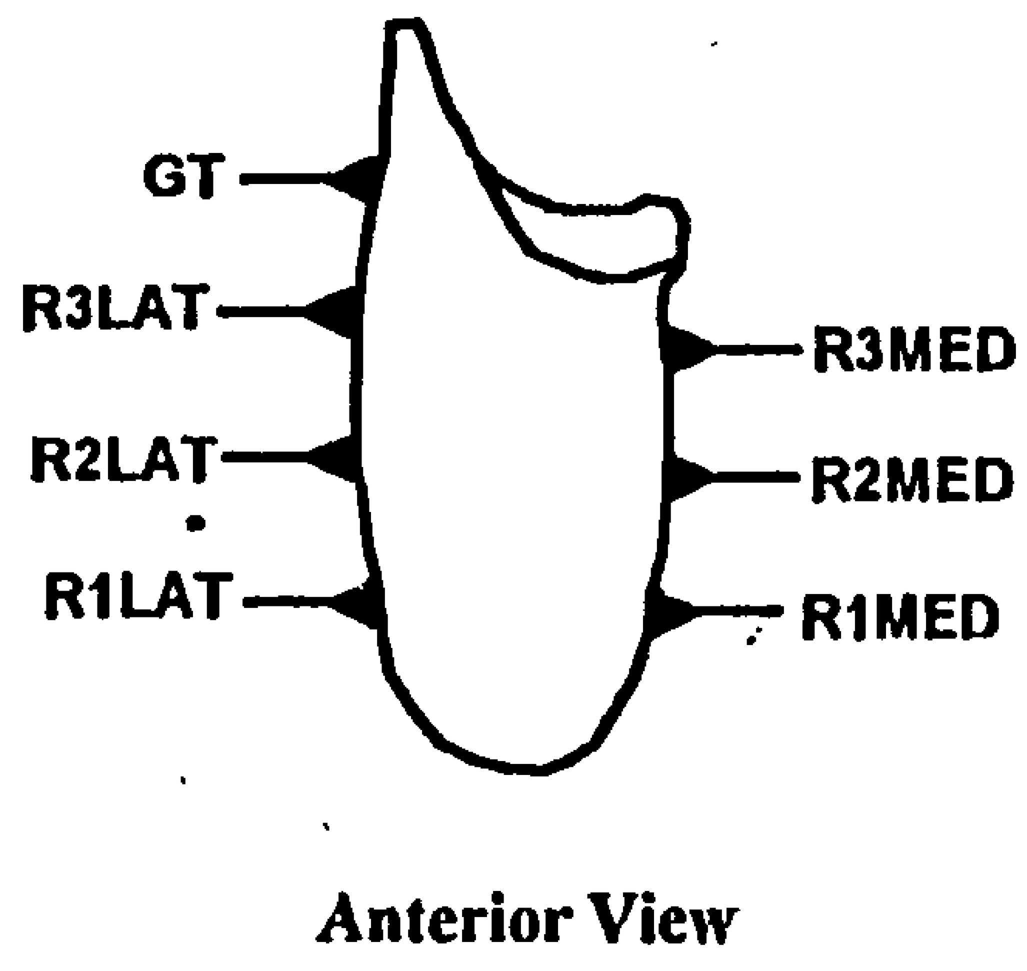

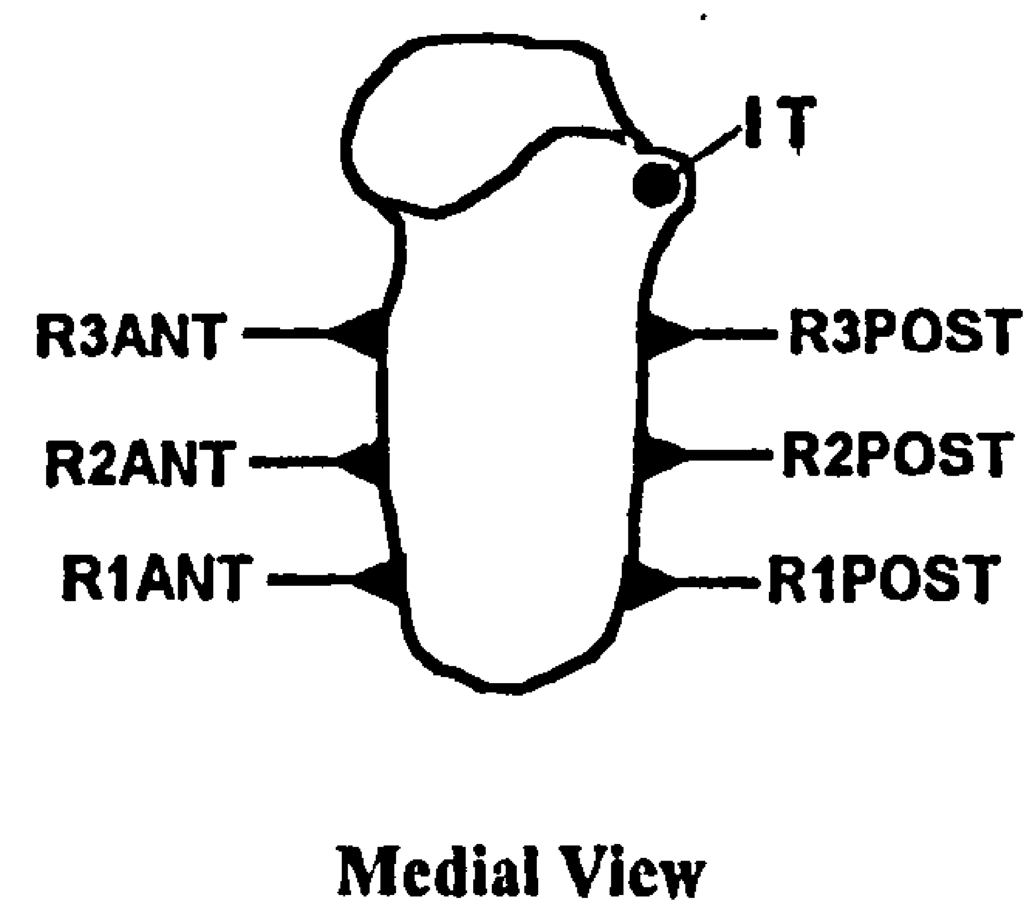

SUBJECT : H
All units in kPa.

	R1LAT	R2LAT	R3LAT	R1MED	R2MED	R3MED	R1ANT	R2ANT	R3ANT	R1POS	R2POS	R3POS	GT	I T
stand (Exp)	12.46	24.89	18.46	27.74	20.39	14.77	16.65	15.67	14.21	13.9	16.29	13.73	2.28	22.23
stand (FE)	3.3	2.75	2.2	3.3	3.3	6.05	3.85	2.2	1.65	3.85	3.3	4.95	2.2	4.95
10% (Exp)	23.09	76.27	44.89	56.92	56.25	34.08	46.46	43.37	38.12	52.13	64.71	45.19	-1.39	44.49
10% (FE)	40	32	36	28	20	12	36	20	16	20	8	24	44	16
25% (Exp)	19.88	73.06	45.16	53.9	51.54	33.65	47.12	42.31	38.36	48.02	56.35	42.86	-0.81	48.48
25% (FE)	27.5	22.5	25	12.5	12.5	7.5	17.5	10	7.5	12.5	5	15	27.5	10
40 % (Exp)	20.85	65.46	38.89	48.6	43.54	31.44	43.54	37.21	35.67	40.42	43.93	36.39	0.09	39.97
40 % (FE)	35	28	31.5	14	17.5	7	21	14	7	10.5	14	24.5	35	14

Table 7.5.1.1 Comparison between measured and predicted pressures in subject H obtained by experiment (Exp) and by finite element analysis (FE).

Interface pressures predicted by the model for subjects H, U and M ranged from 1-48 kPa, 2.5-66 kPa and 1-54 kPa, whereas the measured pressures ranged from 19-77 kPa, 11-48 kPa and 12-60 kPa respectively. Table 7.5.1.1, 7.5.1.2 and 7.5.1.3 tabulate the detailed pressures measured at the socket's sites with the corresponding FE predicted pressures. The difference in values of pressure were expressed as percentages of over (+) or under (-) estimation by the FE models as shown in table 7.5.1.4. The majority of the values were underestimated by the models. Higher correlation existed at sites towards the distal end of the residual limb. The percentage errors in subjects H and M were within the range of -91% to +101%, except at site GT where large errors prevailed. In subject U, large errors were seen in both R1LAT and the GT sites. The rest of the errors were distributed between -76% to +121%, except for site R1ANT (+183%) at 10% of gait.

7.5.2 FE model's results, subject H

During standing, the predicted interface pressures by FE analysis ranged from 0.5 kPa to 6.6 kPa (Fig. 7.5.2.1). A high pressure band (5 - 6.6 kPa) could be seen stretching from the anterior proximal surface to about two third proximally at the medial side. The high pressure band continued right up to the posterior side, just below the anatomical ischium's position. The model was sensitive enough to predict higher pressures at the medial and posterior regions due the loading at the femur. High pressures were evident at the anterior and posterior distal ends. This was largely caused by the vertical force component transferred through the femur. The low pressure areas (0.1 - 0.27 kPa) in the model were mainly situated at the mid anterior side of the residual limb. These low pressure regions spread out to an almost vertical band on the lateral side.

The interface pressure patterns predicted by FE analysis during the three percentages of gait were quite similar to each other, but different to that during standing (Fig. 7.5.2.2, Fig. 7.5.2.3, Fig. 7.5.2.4). All three stages of gait recorded high pressures at the greater trochanter, lateral and anterior distal ends. The pressure at these sites at 10% of gait were 44 kPa, 44 kPa and 48 kPa respectively. At 25% of gait the pressures reduced to 27.5 kPa, 30 kPa and 27.5 kPa respectively. At 40% of

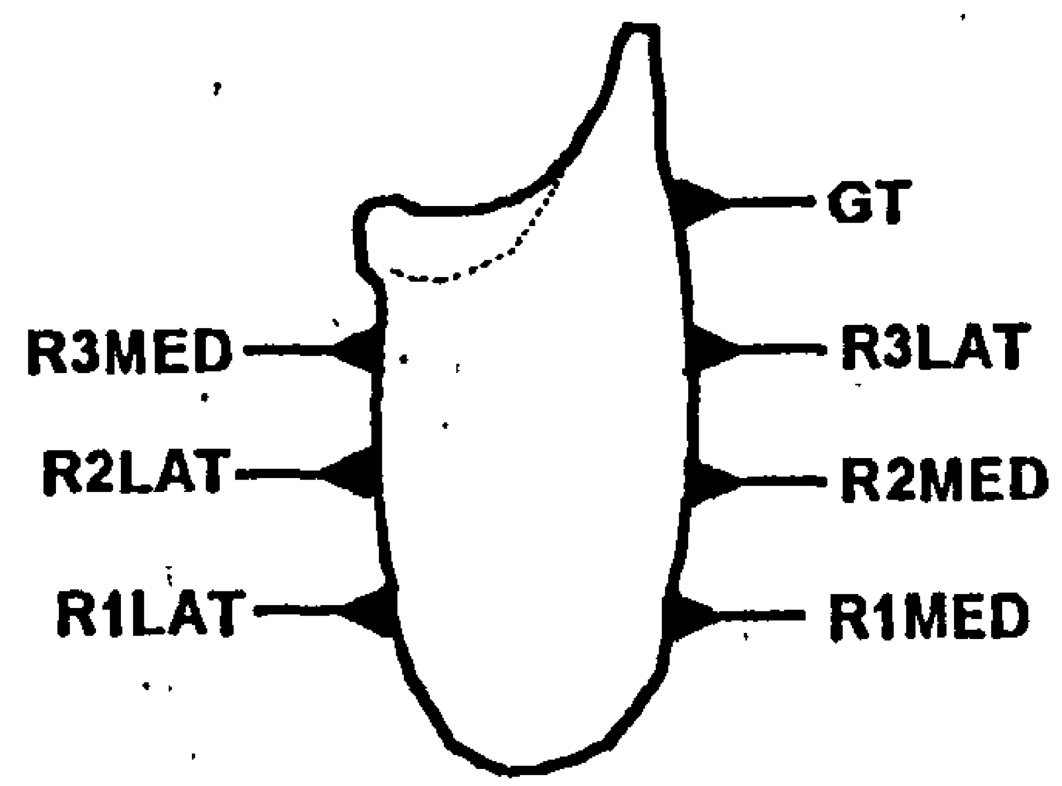

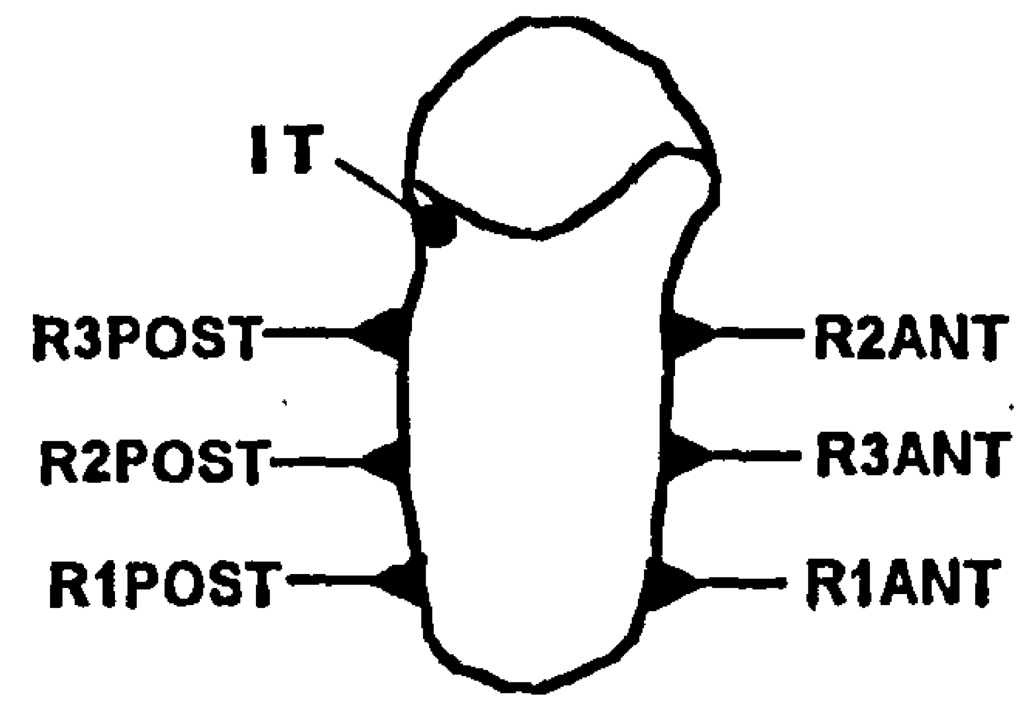

SUBJECT : U
All units in kPa.

	R1LAT	R2LAT	R3LAT	R1MED	R2MED	R3MED	R1ANT	R2ANT	R3ANT	R1POS	R2POS	R3POS	GT	I T
stand (Exp)	7.15	14.31	14.72	18.02	7.65	2.33	9.02	9.81	7.39	8.54	15.67	11.45	-0.18	15.04
stand (FE)	9	7.5	9	4.5	3	4.5	12	6	4.5	4.5	4.5	4.5	9	4.5
10% (Exp)	11.14	32.09	34.85	40.01	17.02	7.45	23.24	23.41	16.22	7.45	41.01	33.46	-0.41	24.22
10% (FE)	66	44	49.5	16.5	16.5	11	27.5	16.5	11	16.5	11	11	55	11
25% (Exp)	16.5	41.53	47.38	41.13	20.23	11.05	24.2	22.85	18.34	11.05	33.21	31.29	-0.07	30.28
25% (FE)	44	32	36	12	12	8	12	8	8	8	4	12	40	12
40 % (Exp)	16.08	39.57	43.89	40.07	21.36	11.02	26.19	25.08	21.52	11.02	32.24	31.3	1.59	38.84
40 % (FE)	40	40	45	15	15	10	15	10	5	10	15	20	55	15

Table 7.5.1.2 Comparison between measured and predicted pressures in subject U obtained by experiment (Exp) and by finite element analysis (FE).

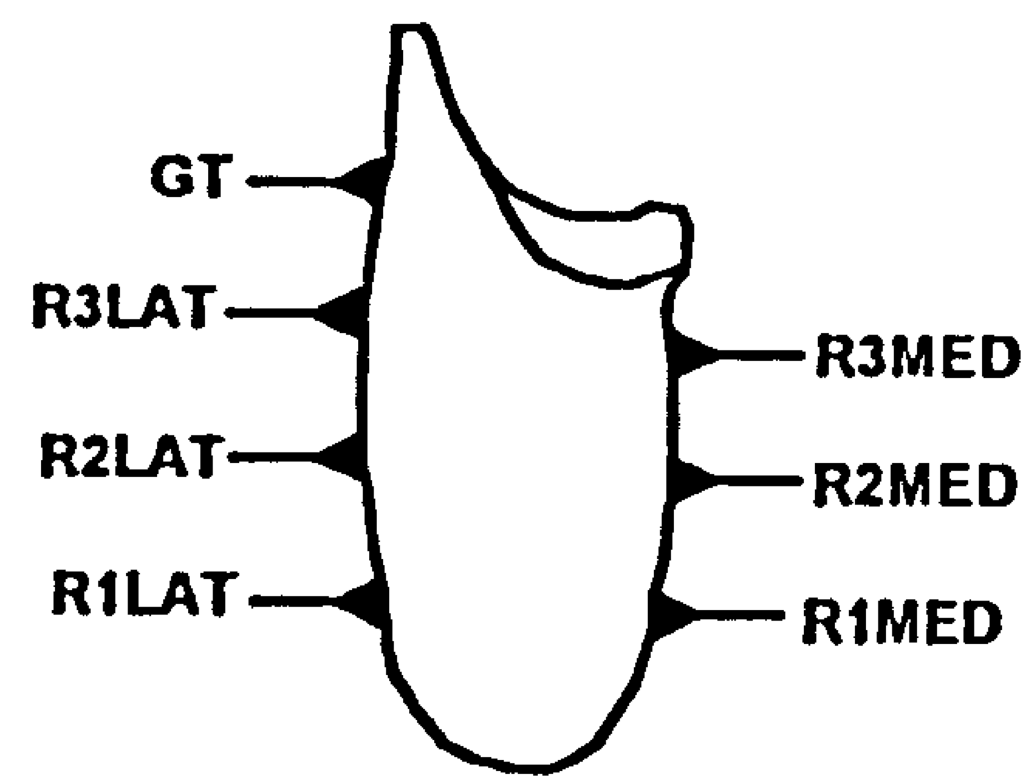

Anterior View

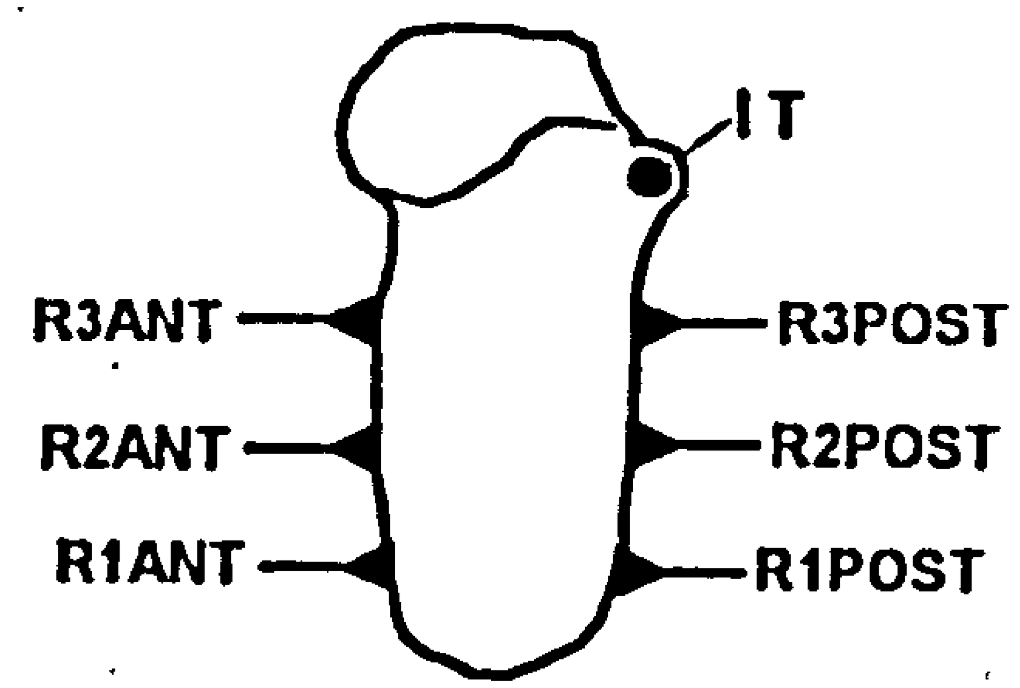

Medial View

SUBJECT : M
All units in kPa.

	R1LAT	R2LAT	R3LAT	R1MED	R2MED	R3MED	R1ANT	R2ANT	R3ANT	R1POS	R2POS	R3POS	GT	I T
stand (Exp)	11.64	13.06	10.38	10.68	9.22	8.72	13.49	12.43	11.63	12.02	10.77	10.65	9.34	29.91
stand (FE)	7	6	4	2	1	2	6	3	2	5	2	3	4	2
10% (Exp)	46.38	52.48	21.18	34.74	20.48	17.37	33.21	21.21	18.63	35.91	34.7	17.01	11.37	59.37
10% (FE)	40.5	31.5	36	22.5	9	9	31.5	13.5	9	22.5	18	18	45	9
25% (Exp)	26.53	36.92	16.87	24.44	15.75	13.28	22.34	14.81	12.69	22.58	18.58	12.61	15.49	52.42
25% (FE)	30	21	24	9	6	6	12	6	6	12	9	9	30	6
40 % (Exp)	25.64	25.51	19.89	27.92	19.02	16.54	28.39	19.14	18.88	25.67	21.04	19.87	22.52	46.08
40 % (FE)	36	32	40	12	12	8	24	12	12	20	16	20	48	12

Table 7.5.1.3 Comparison between measured and predicted pressures in subject M obtained by experiment (Exp) and by finite element analysis (FE).

SUBJECT : H

	R1LAT	R2LAT	R3LAT	R1MED	R2MED	R3MED	R1ANT	R2ANT	R3ANT	R1POS	R2POS	R3POS	GT	I T
standing	-73.52	-88.95	-88.08	-88.1	-83.82	-59.04	-76.88	-85.96	-88.39	-72.3	-79.74	-63.95	-3.51	-77.73
10 %	73.24	-58.04	-19.8	-50.81	-64.44	-64.79	-22.51	-53.89	-58.03	-61.63	-87.64	-46.89	-3265	-64.04
25 %	38.33	-69.2	-44.64	-76.81	-75.75	-77.71	-62.86	-76.36	-80.45	-73.97	-91.13	-65	-3495	-79.37
30 %	67.87	-57.23	-19	-71.19	-59.81	-77.74	-51.77	-62.38	-80.38	-74.02	-68.13	-32.67	38788	-64.97

SUBJECT : U

	R1LAT	R2LAT	R3LAT	R1MED	R2MED	R3MED	R1ANT	R2ANT	R3ANT	R1POS	R2POS	R3POS	GT	I T
standing	25.87	-47.59	-38.86	-75.03	-60.78	93.13	33.04	-38.84	-39.11	-47.31	-71.28	-60.7	-5,100	-70.08
10 %	492.46	37.11	42.04	-58.76	-3.06	47.65	18.33	-29.52	-32.18	121.48	-73.18	-67.12	-13514	-54.58
25 %	166.67	-22.95	-24.02	-70.82	-40.68	-27.6	-50.41	-64.99	-56.38	-27.6	-87.96	-61.65	-57242	-60.37
30 %	148.76	1.09	2.53	-62.57	-29.78	-9.26	-42.73	-60.13	-76.77	-9.26	-53.47	-36.1	3359	-61.38

SUBJECT : M

	R1LAT	R2LAT	R3LAT	R1MED	R2MED	R3MED	R1ANT	R2ANT	R3ANT	R1POS	R2POS	R3POS	GT	I T
standing	-39.86	-54.06	-61.46	-81.27	-89.15	-77.06	-55.52	-75.86	-82.8	-58.4	-81.43	-71.83	-57.17	-93.31
10 %	-12.68	-39.98	69.97	-35.23	-56.05	-48.19	-5.15	-36.35	-51.69	-37.34	-48.13	5.82	295.78	-84.84
25 %	13.08	-43.12	42.26	-63.18	-61.9	-54.82	-46.28	-59.49	-52.72	-46.86	-51.56	-28.63	93.67	-88.55
30 %	40.41	25.44	101.11	-57.02	-36.91	-51.63	-15.46	-37.3	-36.44	-22.09	-23.95	0.65	113.14	-73.96

All units expressed as percentage. ($\% = \frac{FE-Exp}{Exp}$)

+ indicates FE predicted interface pressure over estimated

- indicates FE predicted interface pressure under estimated

Table 7.5.1.4 Percentage difference in pressure between FE model prediction and experimental during standing, and at 10%, 25% and 40% of the gait cycle at locations represented in the figure in table 7.5.1.3.

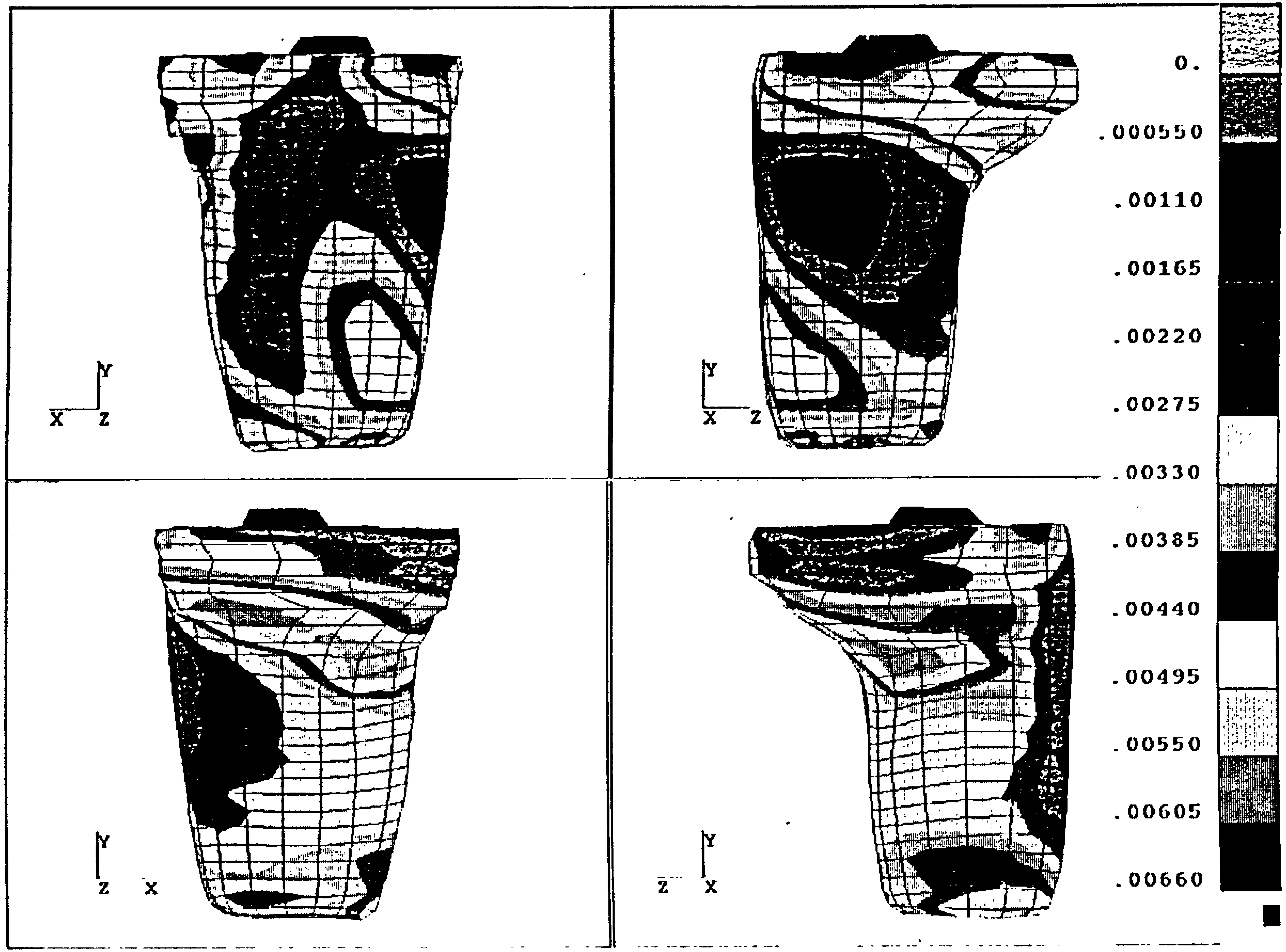

Fig. 7.5.2.1 Predicted interface pressures in N/mm^2 during standing for subject II.
From top left corner and clockwise : Lateral, anterior, posterior and medial view.

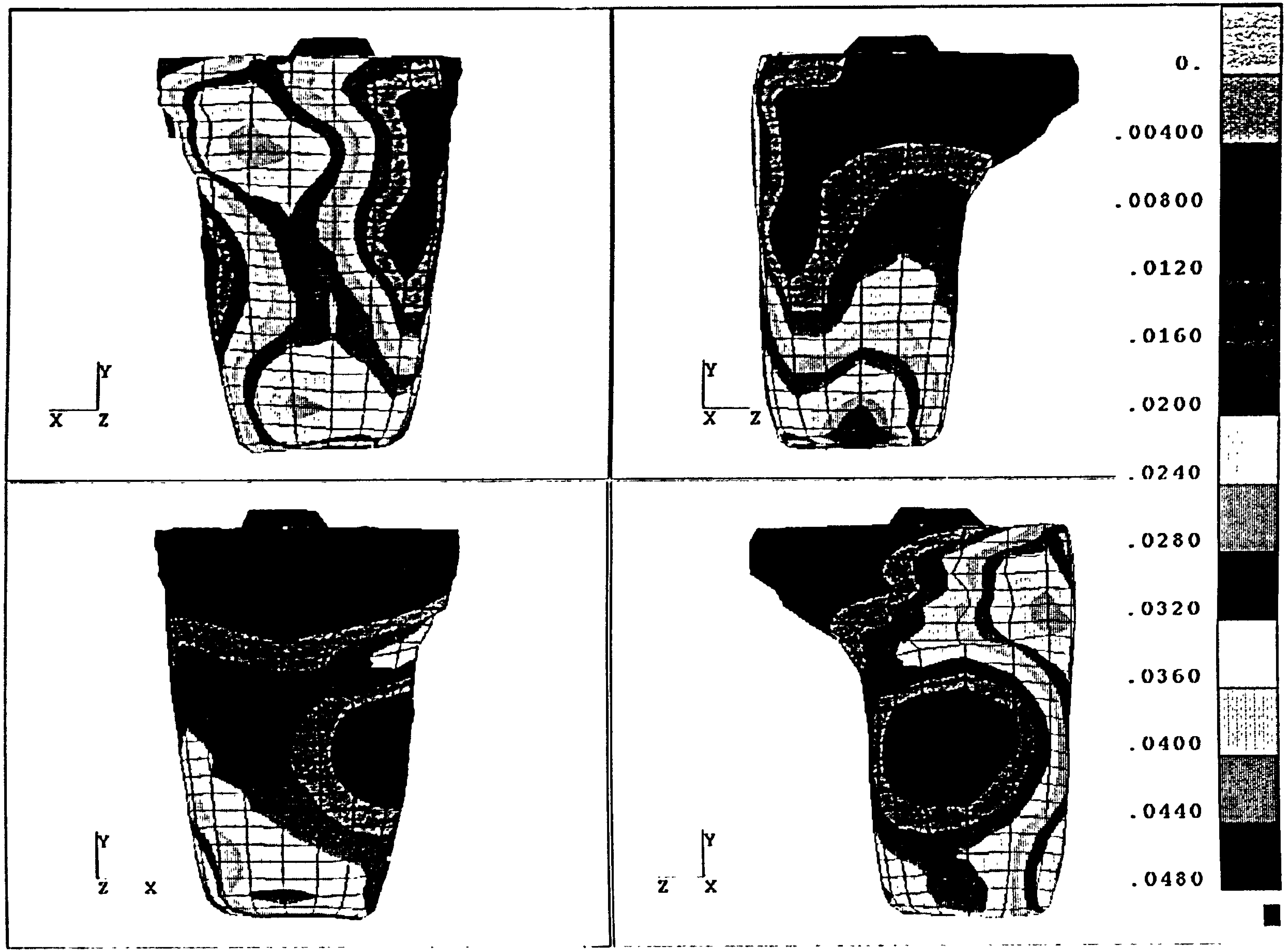

Fig. 7.5.2.2 Predicted interface pressures in N/mm^2 at 10% of gait cycle for subject II.
From top left corner and clockwise : Lateral, anterior, posterior and medial view.

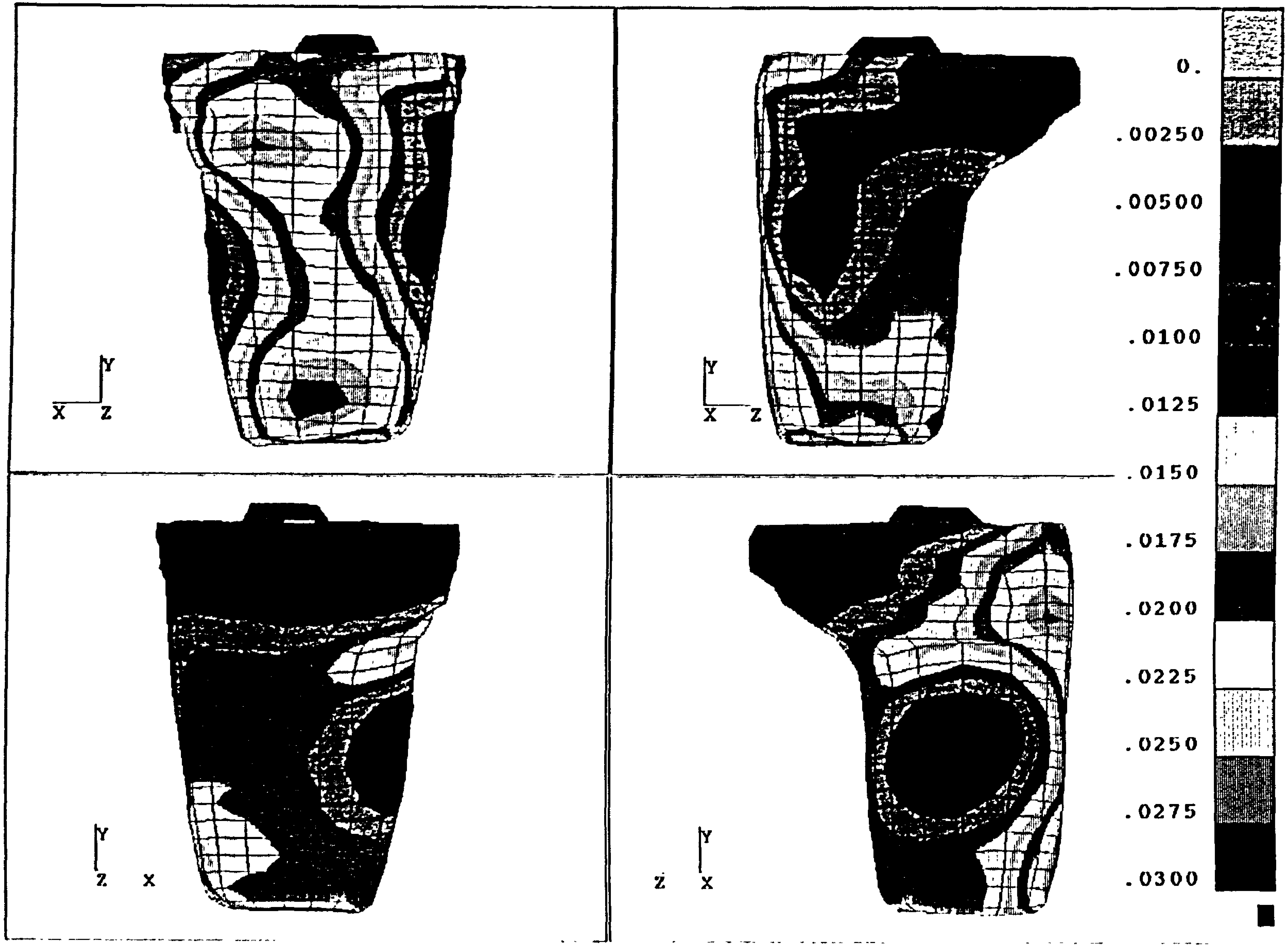

Fig. 7.5.2.3 Predicted interface pressures in N/mm^2 at 25% of gait cycle for subject II.
From top left corner and clockwise : Lateral, anterior, posterior and medial view.

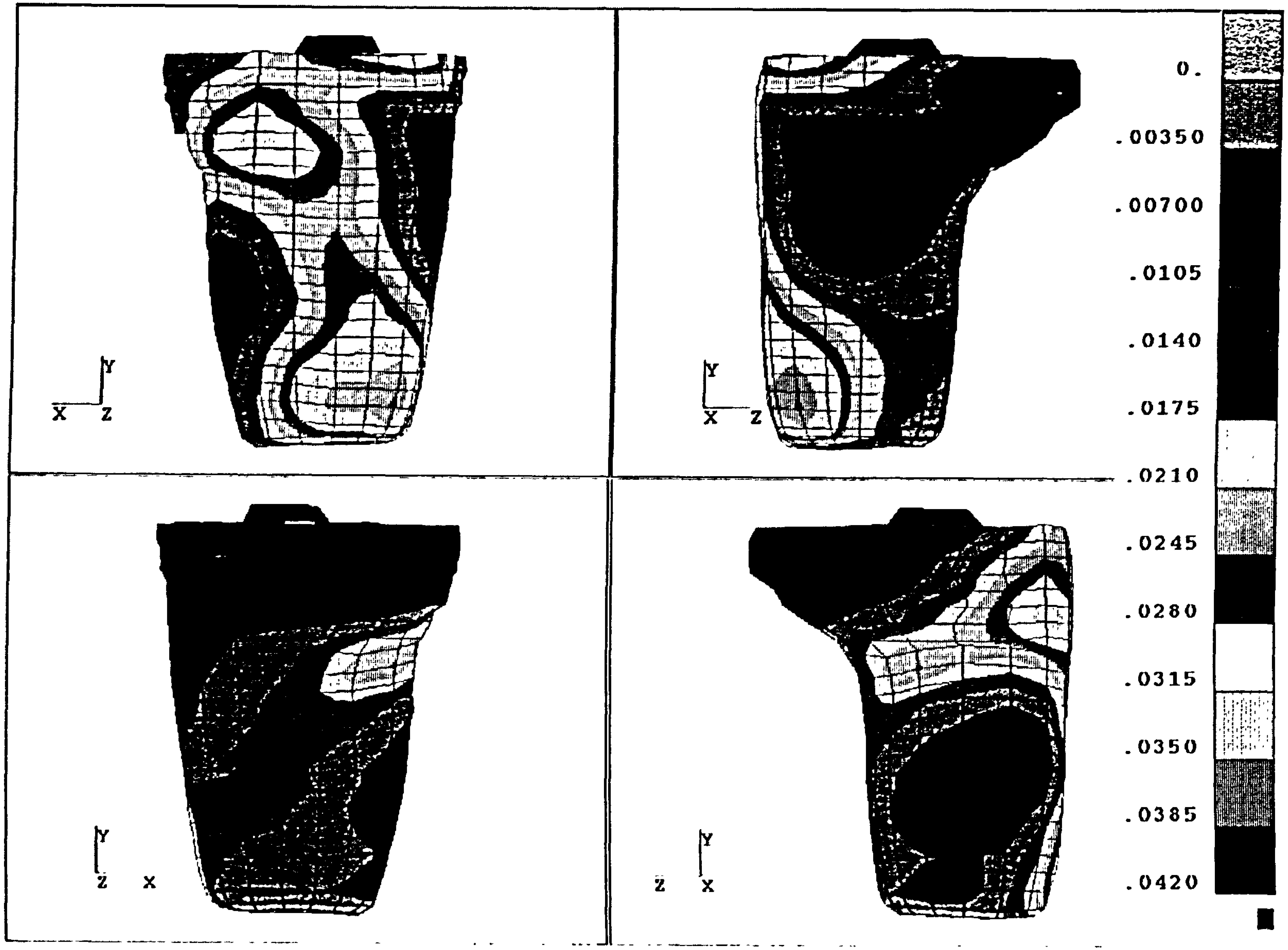

Fig. 7.5.2.4 Predicted interface pressures in N/mm^2 at 40% of gait cycle for subject II.
From top left corner and clockwise : Lateral, anterior, posterior and medial view.

gait cycle, the pressure at the lateral region increased again predicting pressure at the greater trochanter of 35 kPa and lateral distal end of 38.5 kPa. However, pressure at the anterior distal end remains much the same at 24.5 kPa. Fig. 7.5.2.5 shows the migration of high pressure contours at the lateral side throughout gait. At 10% of gait, the high pressure regions almost enclosed the whole of the lateral side of the residual limb. This region narrowed significantly at 25% of gait and magnitude at the greater trochanter and lateral distal end dropped by about 30%. At 40%, the magnitude increased but the pressure pattern remains largely unchanged from 25% of gait. Low pressures during gait were mainly predicted at the proximal anterior side, medial side and the mid region of the posterior side.

7.5.3 FE model's results, subject U

The high values of interface pressures (13-18 kPa) predicted in the FE analysis during standing (Fig. 7.5.3.1) were mostly situated in localised "spots". These "spots" existed at the lateral-posterior proximal area, lateral distal area and anterior distal area. Outwith these "spots", the pressure drops quickly to a range of 1- 7.5 kPa. The majority of the low pressures ranged only from 1-4.5 kPa and were found at the medial side and anterior proximal regions of the residual limb model. Unlike the pressure contour for subject H, no higher pressure areas near the ischium could be detected.

The predicted pressures at 10% of gait (Fig. 7.5.3.2) ranged from 5.5 - 66 kPa. Maximum pressures were located at the greater trochanter area and lateral distal end of the residual limb. The high pressure region was only concentrated around the lateral side; elsewhere, pressures were significantly lower especially at the medial side of the residual limb. At 25% of gait (Fig.7.5.3.3) the predicted pressures ranged from 4 - 48 kPa. There was little change in the pressure patterns from those of 10% of gait. At 40% of gait (Fig. 7.5.3.4), the high pressure region at the greater trochanter began to move posteriorly, while pressure at the lateral distal end moved anteriorly. The migration of pressure patterns indicated a movement of the femur in a similar direction. The pressures predicted at this phase of gait ranged from 5 - 60 kPa.

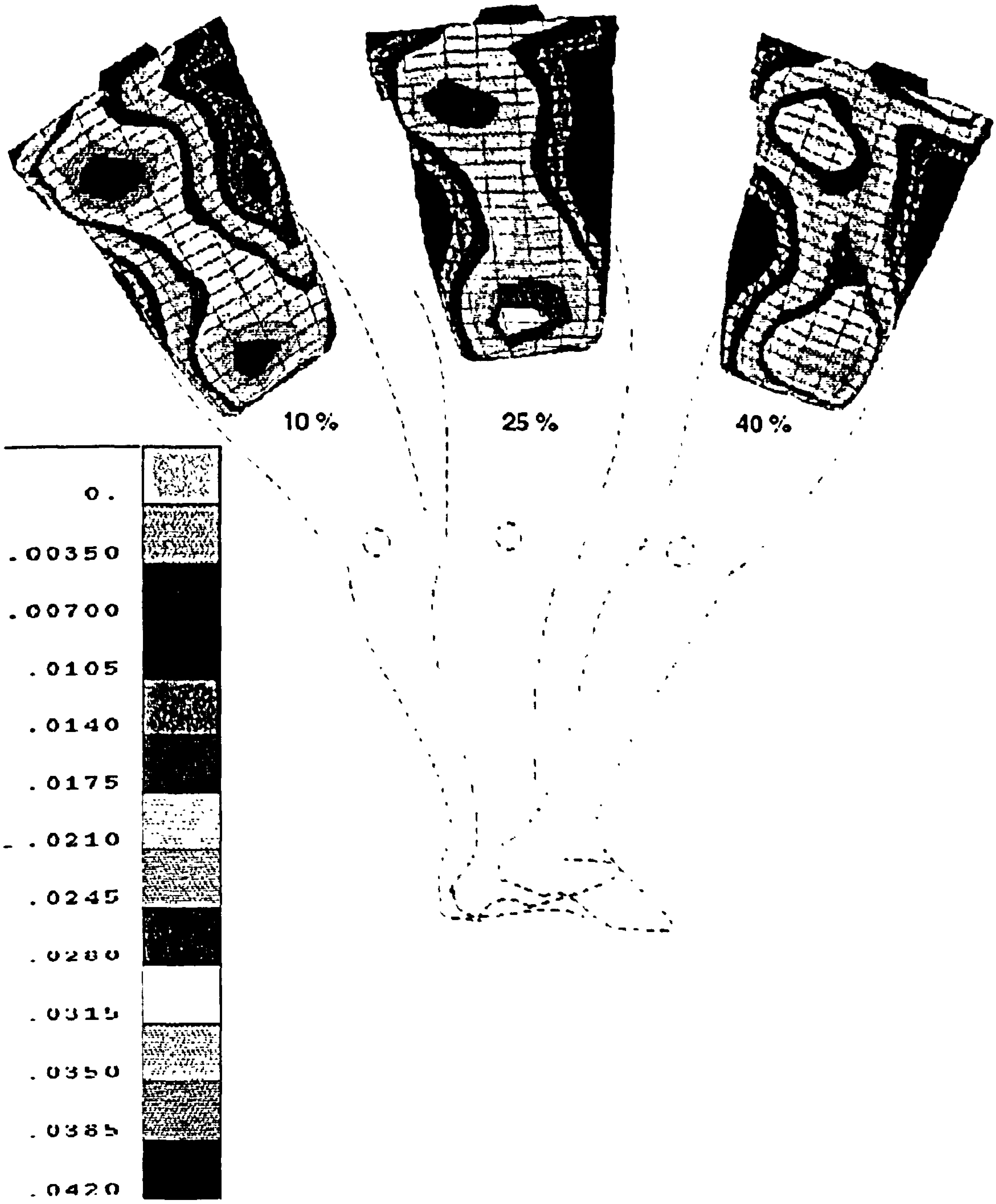

Fig. 7.5.2.5 Lateral pressures progressing from 10% - 25% - 40% of the gait cycle for subject H. (Units in N/mm²)

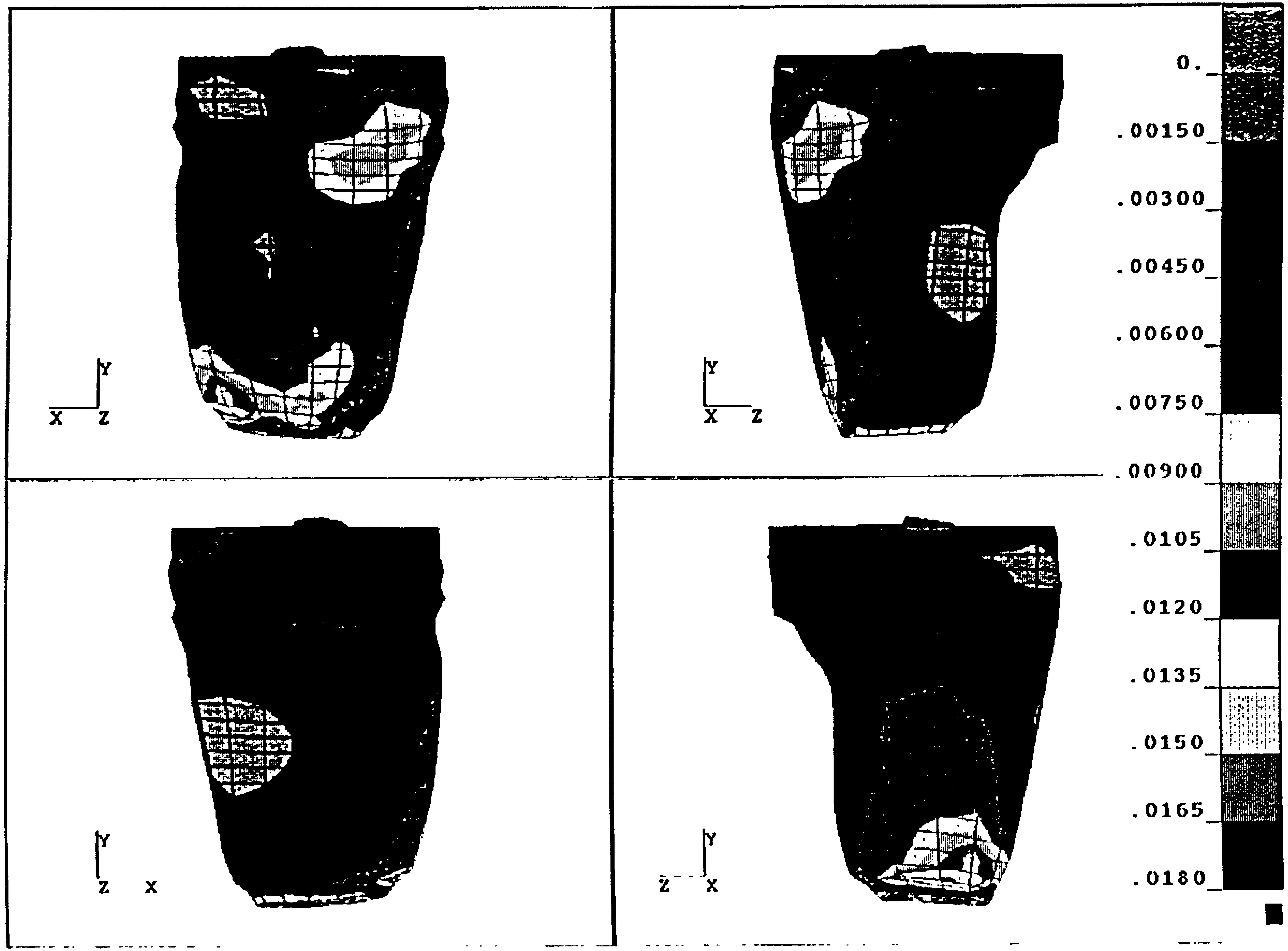

Fig. 7.5.3.1 Predicted interface pressures in N/mm^2 during standing for subject U.
From top left corner and clockwise : Lateral, posterior, anterior and medial view.

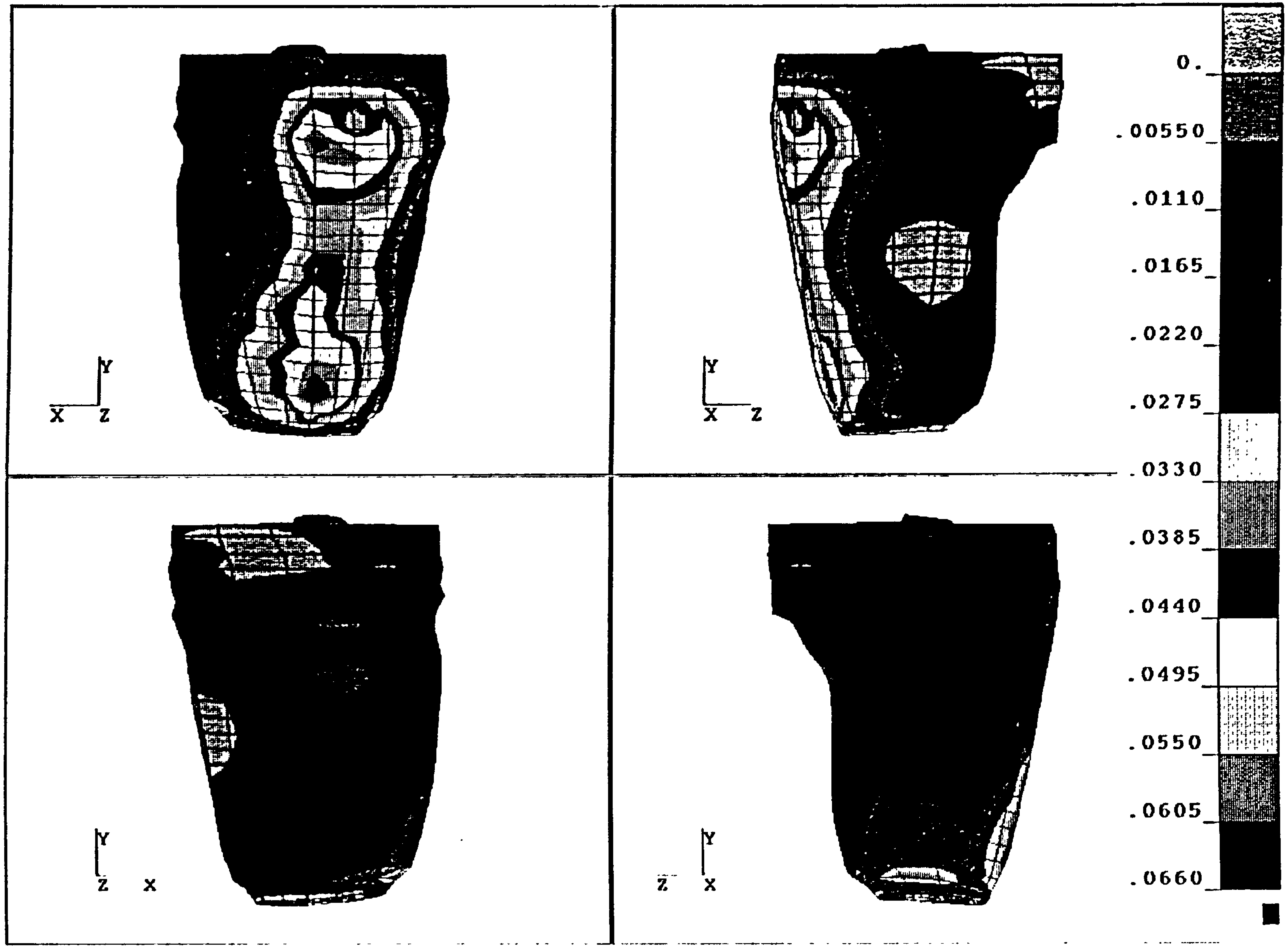

Fig. 7.5.3.2 Predicted interface pressures in N/mm^2 at 10% of gait cycle for subject U.
From top left corner and clockwise : Lateral, posterior, anterior and medial view.

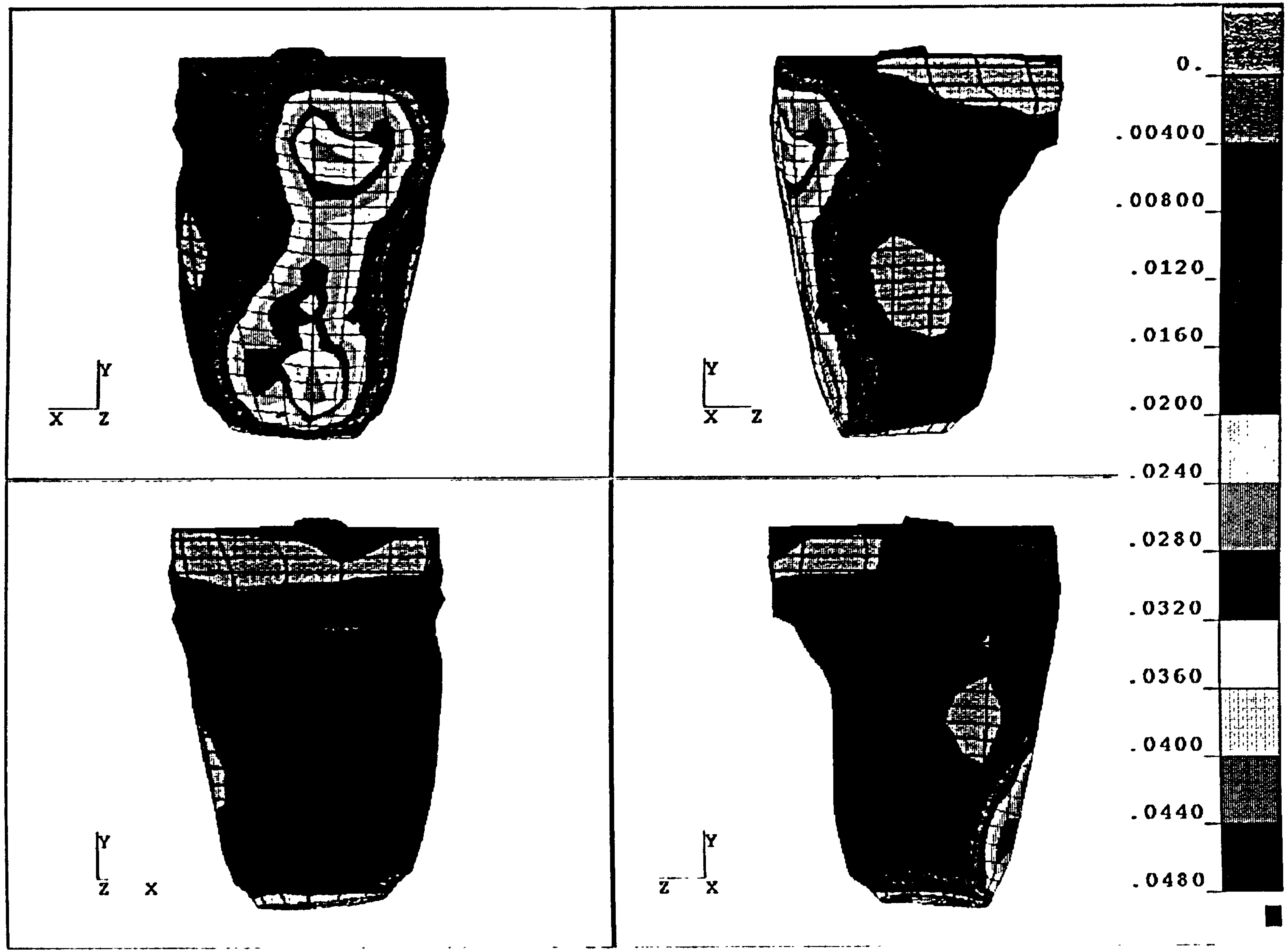

Fig. 7.5.3.3 Predicted interface pressures in N/mm² at 25% of gait cycle for subject U.
From top left corner and clockwise : Lateral, posterior, anterior and medial view.

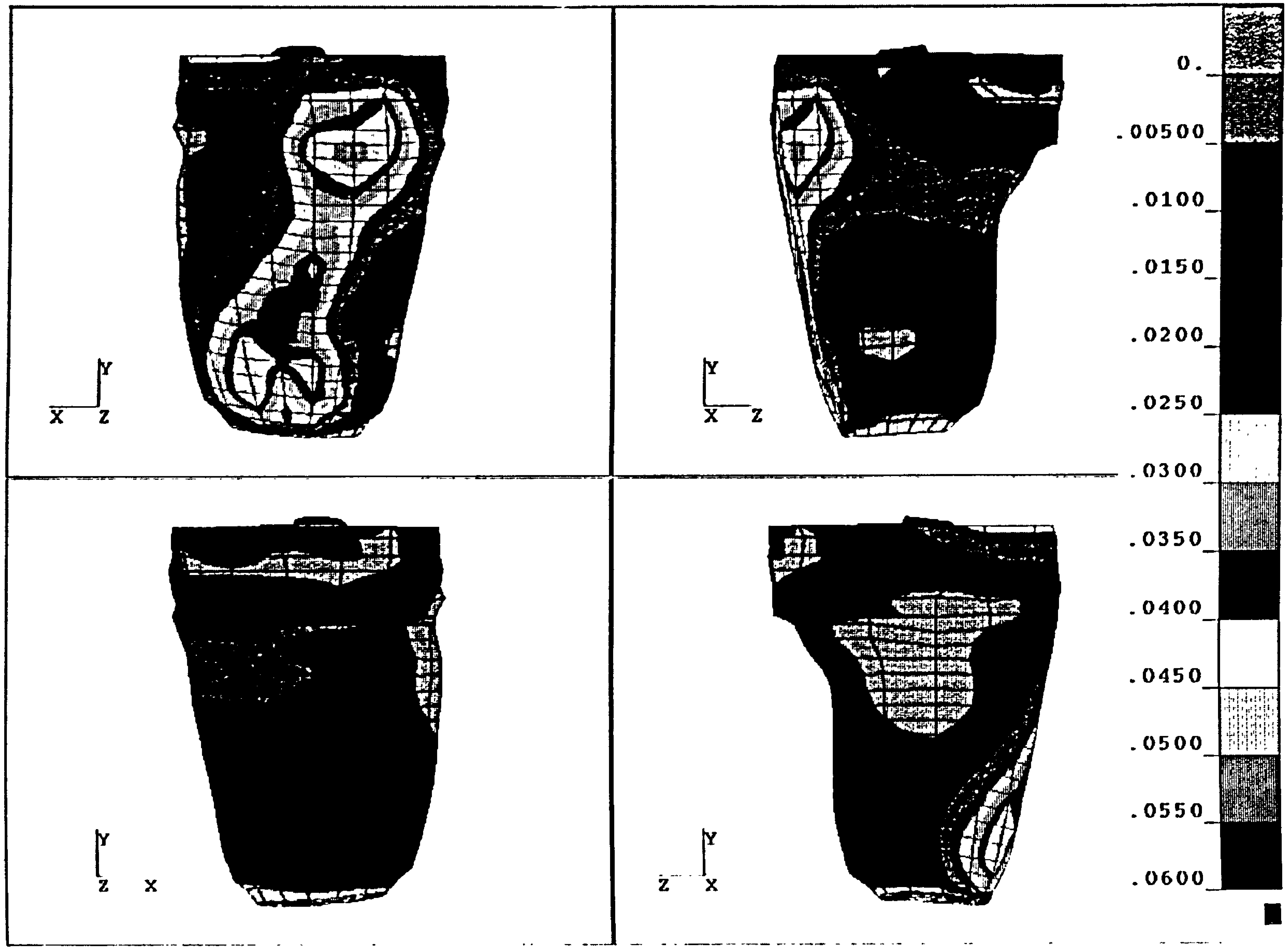

Fig. 7.5.3.4 Predicted interface pressures in N/mm^2 at 40% of gait cycle for subject U.
From top left corner and clockwise : Lateral, posterior, anterior and medial view.

7.5.4 FE model's results, subject M

The predicted standing pressure in subject M (Fig. 7.5.4.1) ranged mostly between 1 and 6 kPa. Higher pressures in the range of 6 - 12 kPa exist at the extreme proximal area on the lateral side of the model. High pressures (10 kPa) were also predicted at the distal regions of the lateral and posterior sides.

At 10% of the gait cycle (Fig. 7.5.4.2), high pressures (27 - 54 kPa) were predicted throughout the lateral side, peaking at two points, the greater trochanter area and distal end. The high pressure contours continued to the anterior distal end while the pressure at the proximal anterior region remained relatively low (4.5-18 kPa). Low pressures were also predicted at the medial side. At 25% of the gait cycle (Fig. 7.5.4.3), the pressure patterns remained unchanged. Pressure magnitudes ranged from 3-36 kPa indicating an approximate decrease of 33% from pressures predicted at 10% of the gait cycle. At 40% (Fig. 7.5.4.4), pressure patterns were again seen similar to the two previous gait cycles. The maximum pressure at the greater trochanter and lateral distal region increased slightly from the value at 25% of gait cycle to 48 kPa.

7.5.5 Femoral displacement predicted by the FE models

The predicted displacements of the femoral bone for the three subjects during standing, and gait were expressed as angles of flexion/extension, adduction/abduction and rotation of the femur as shown in Table 7.5.5.1. The angles were calculated using two axes, namely the vertical axis as defined by a plumbline and the axis of the bone, assigned as the line joining the hip joint centre to the distal end of the amputated femur (Fig. 7.5.5.1). These angles were therefore the difference between the angles which the axes of the deformed bone and the undeformed bone made with the vertical axis. Verification of the position of the femur through experimental means was not carried out. However, the femur adduction predicted was in agreement with current trans-femoral prosthetic practice.

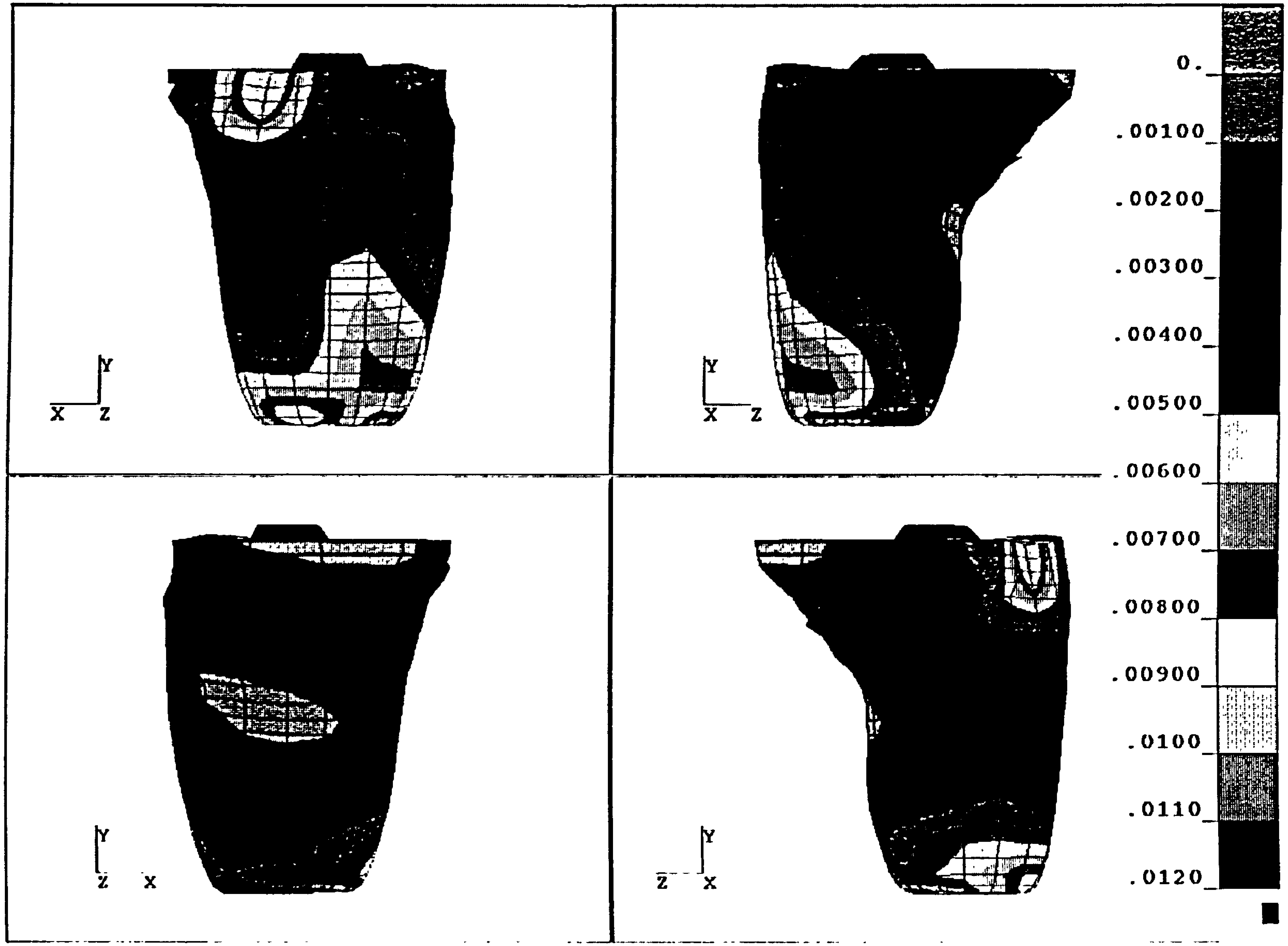

Fig. 7.5.4.1 Predicted interface pressures in N/mm^2 during standing for subject M.
From top left corner and clockwise : Lateral, anterior, posterior and medial view.

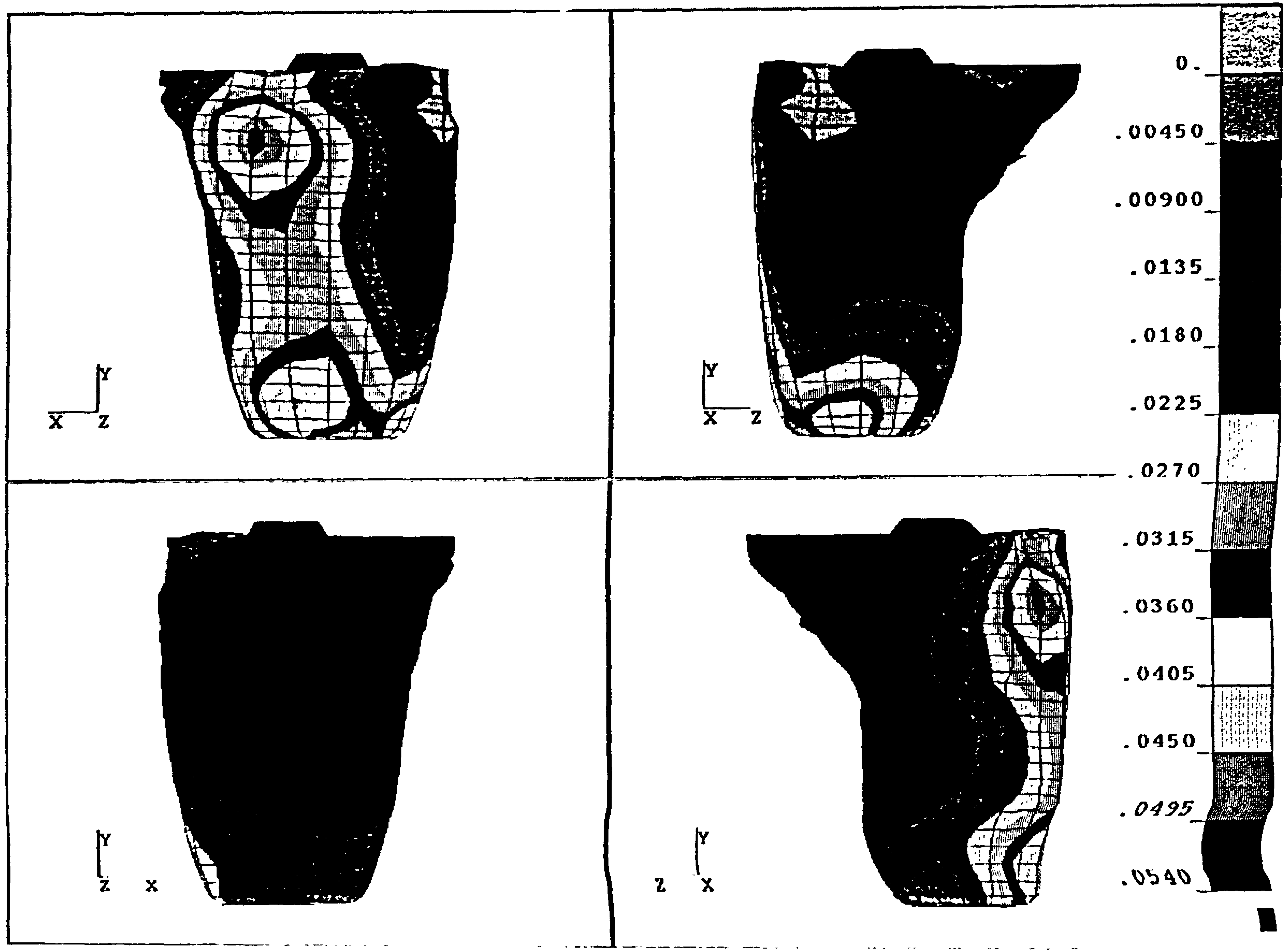

Fig. 7.5.4.2 Predicted interface pressures in N/mm^2 at 10% of gait cycle for subject M.
From top left corner and clockwise : Lateral, anterior, posterior and medial view.

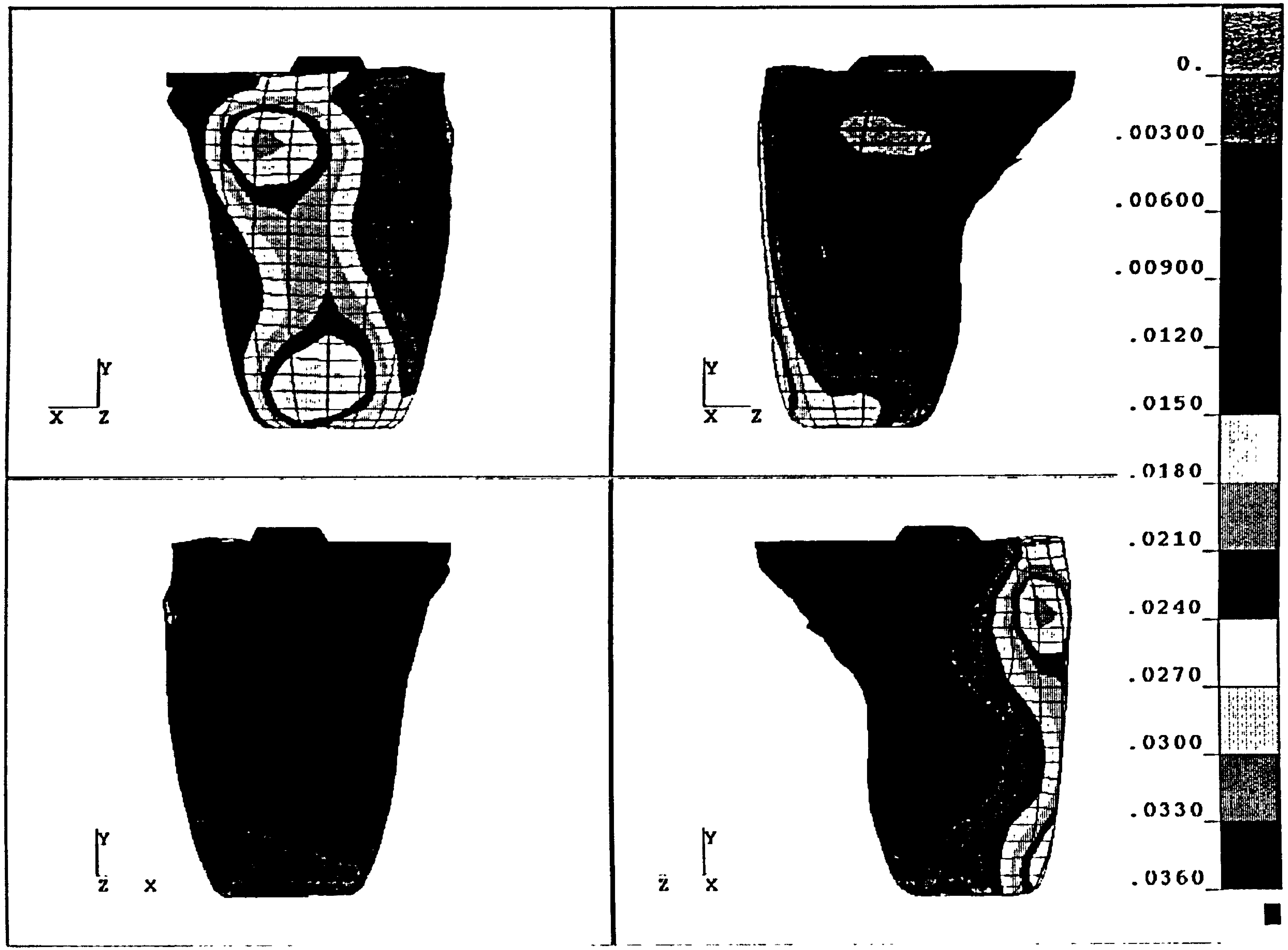

Fig. 7.5.4.3 Predicted interface pressures in N/mm^2 at 10% of gait cycle for subject M.
From top left corner and clockwise : Lateral, anterior, posterior and medial view.

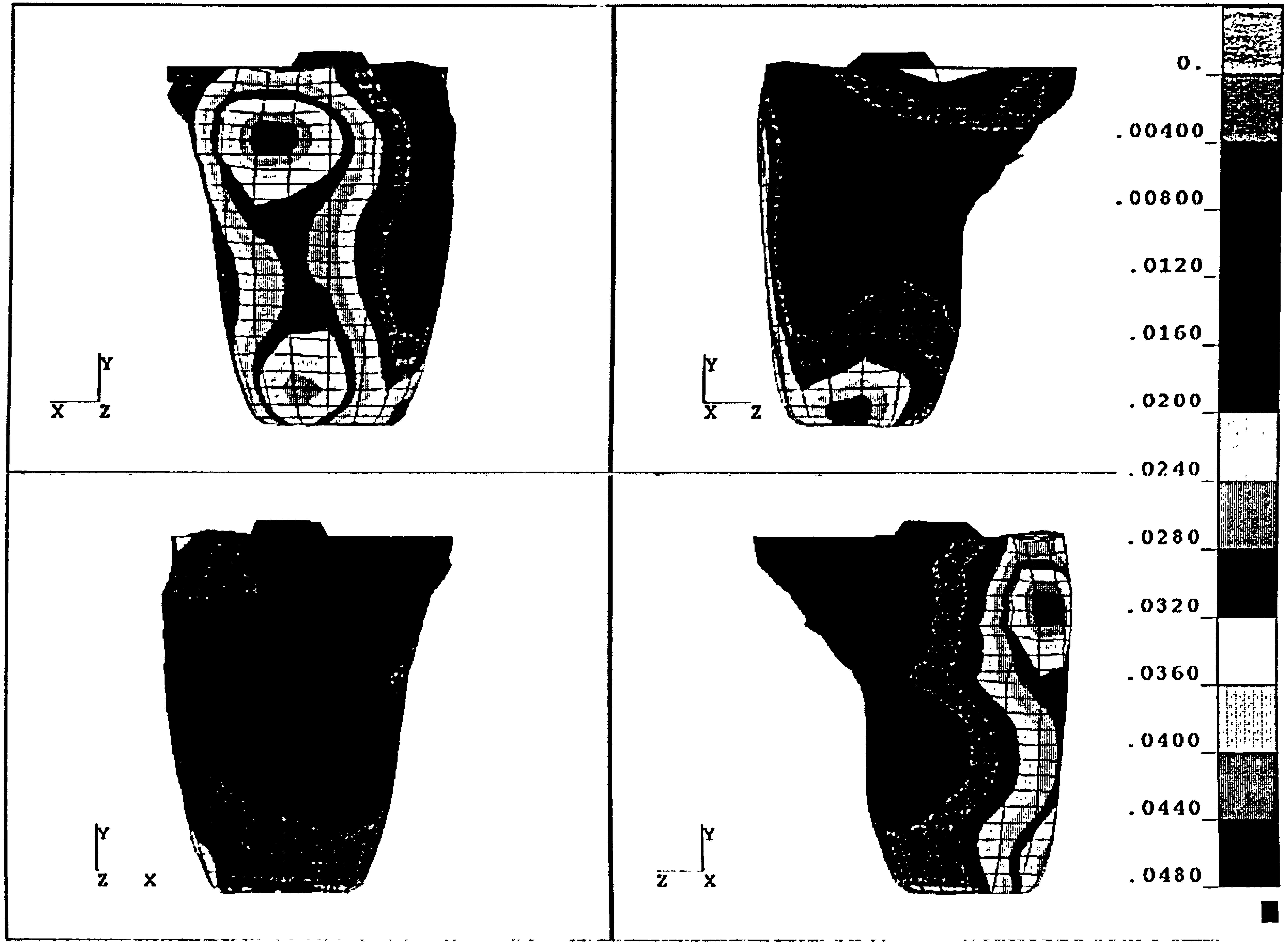

Fig. 7.5.4.4 Predicted interface pressures in N/mm^2 at 10% of gait cycle for subject M.
From top left corner and clockwise : Lateral, anterior, posterior and medial view.

SUBJECT : U

	Flexion	Extension	Adduction	Abduction	Internal Rot.	External Rot.
standing	2.09 deg	--	8.61 deg	--	21.05 deg	
10 %	5.53 deg	--	6.89 deg	--	47.96 deg	--
25 %	1.29 deg	--	5.22 deg	--	53.80 deg	--
40 %	--	2.77 deg	7.08 deg	--	--	10.69 deg

SUBJECT : M

	Flexion	Extension	Adduction	Abduction	Internal Rot.	External Rot.
standing	--	3.32 deg	0.14 deg	--	--	16.44 deg
10 %	4.42 deg	--	6.21 deg	--	41.42 deg	--
25 %	3.38 deg	--	6.62 deg	--	27.01 deg	--
40 %	5.67 deg	--	5.41 deg	--	42.03 deg	--

SUBJECT : H

	Flexion	Extension	Adduction	Abduction	Internal Rot.	External Rot.
standing	0.44 deg	--	2.31 deg	--	2.15 deg	--
10 %	4.51 deg	--	7.20 deg	--	50.36 deg	--
25 %	1.21 deg	--	5.32 deg	--	20.60 deg	--
40 %	--	2.45 deg	6.65 deg	--	--	13.69 deg

Table 7.5.5.1 Predicted difference in orientation between loaded and unloaded femur during standing and at 10%, 25% and 40% of the gait cycle.

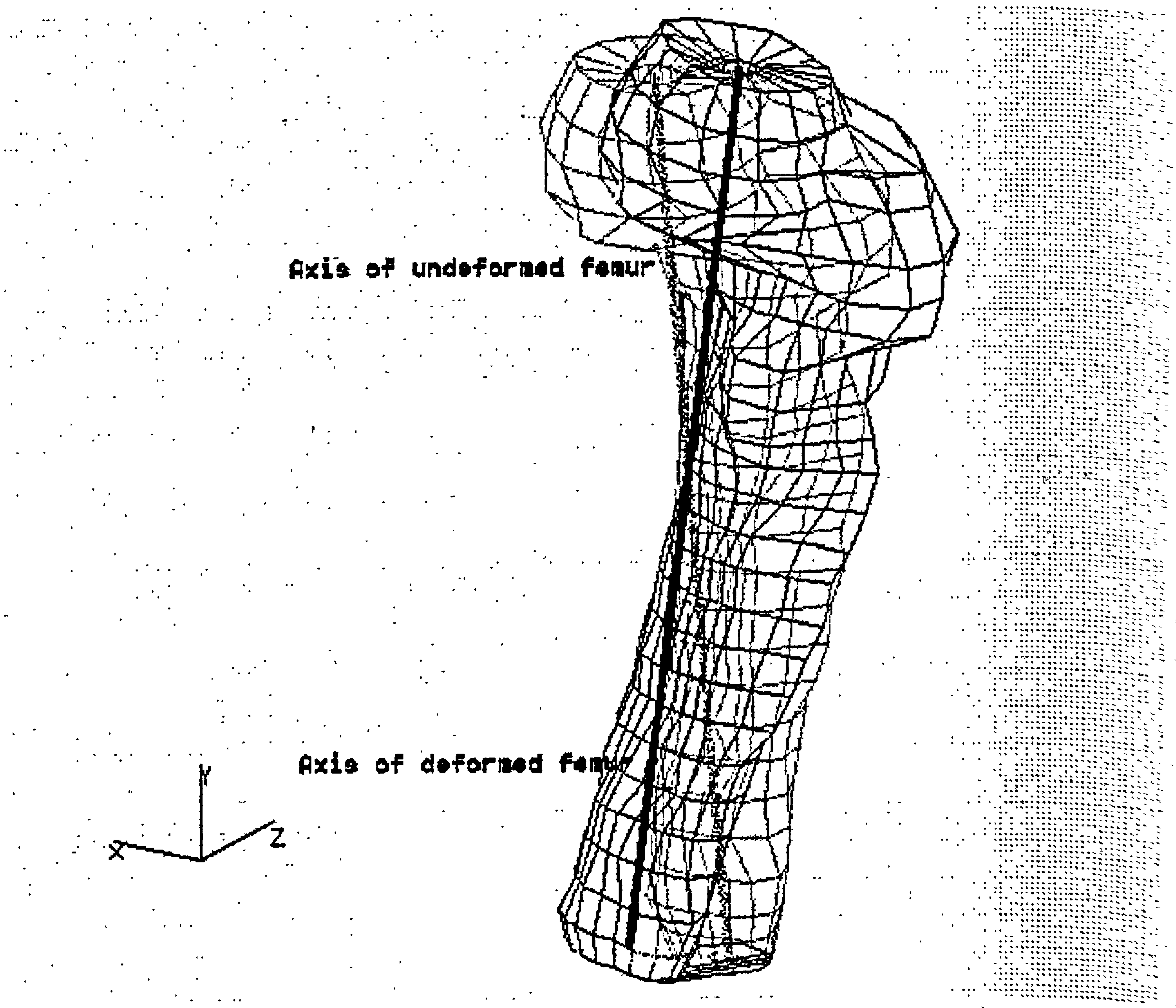

Fig. 7.5.5.1 Displacement plot of the femur with the two axes, i.e. the axis of the deformed and undeformed bone.

7.5.6 Internal stress distribution of the residual limb model

One of the main advantages of the residual limb model is the ability to calculate stresses within the limb. However, it is not possible to validate these stresses through experimental means. Thus, in an ideal situation, it could be assumed if the stresses at the surface were correctly validated, the stresses predicted within the limb should be relatively accurate. Fig. 7.5.6.1 shows the predicted von Mises stress plot of the model for subject M, at a transverse slice at the level of the greater trochanter. Loading conditions were those at 40% of the gait cycle. The maximum stress of 12000 kPa occurred at the bone. Immediately at the bone - soft tissue interface, a maximum stress of 8000 kPa was present at the medial side of the residual limb. However, the large tissue mass at this region did not allow the high stresses to be transferred to the surface. Instead stresses at the surface drop significantly to a level of only 10 kPa. The stresses at the greater trochanter reach 6000 kPa but, were again reduced to 45 kPa at the surface. The soft tissues at the immediate surroundings of the bone were subjected to an average pressure of 5000 kPa.

Fig. 7.5.6.2 plots the predicted stresses at the mid region of subject M residual limb. Loading was again taken at 40% of the gait cycle. The predicted stresses at the bone - soft tissue interface were in the range 3000 kPa - 6000 kPa. High stresses were concentrated at the latero-posterior and medio-anterior regions of the bone. Stresses on the surface were lower in magnitude compared to the proximal transverse slice mentioned above, mainly due to a small bone mass and a large soft tissue mass.

7.6 DISCUSSION

The FE models described in this study included many biomechanical assumptions. Errors encountered during pressure and kinetic measurement, together with the assumptions made in the FE models, contributed cumulatively to the overall difference between the measured and the predicted pressures' magnitudes. The departure from realism in the FE models can be discussed in three different areas, geometry, loading and boundary conditions, and material properties. Nevertheless, the models were promising in achieving good results even with the many assumptions

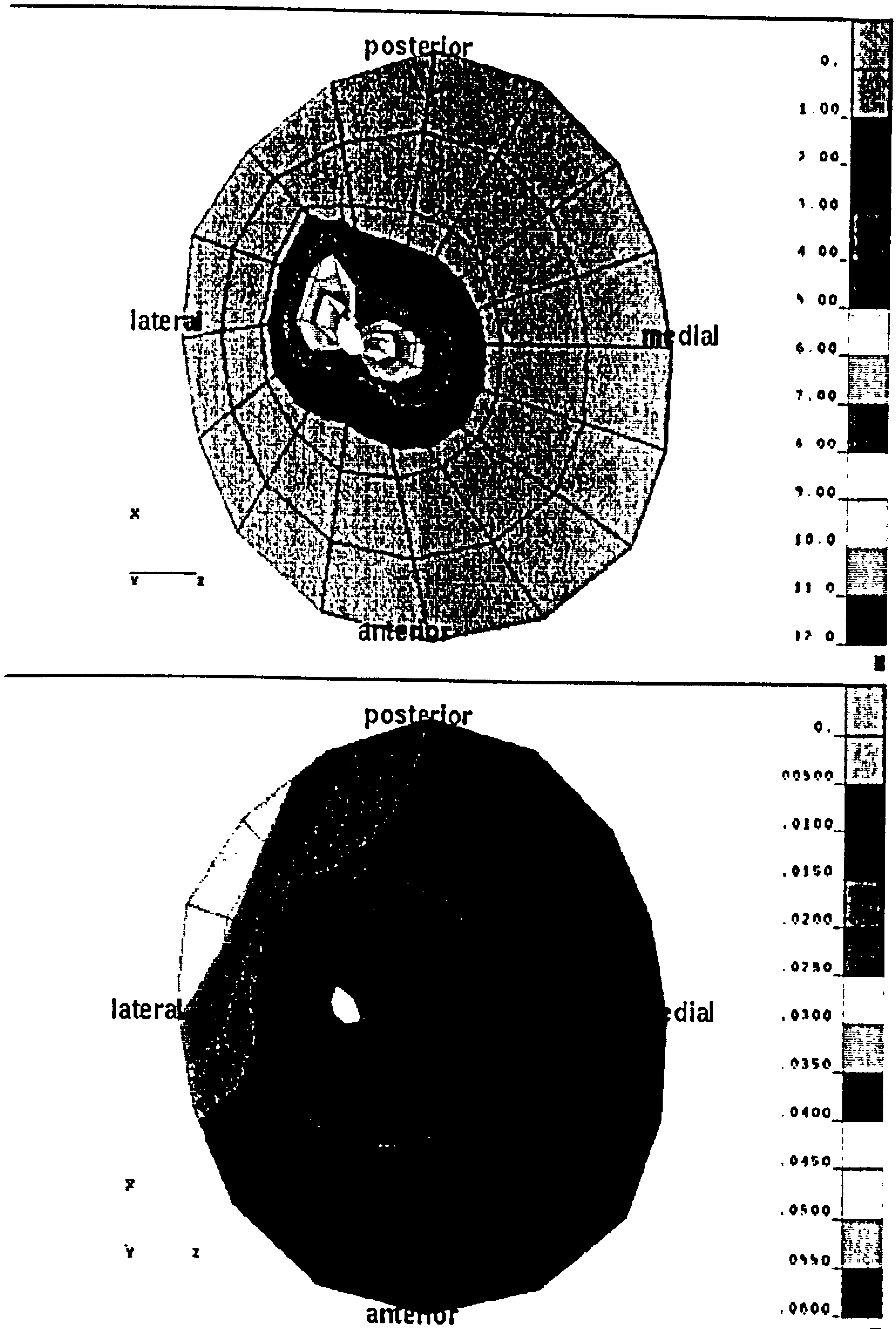

Fig. 7.5.6.1 Internal stress contours (von Mises stress) at the level of the greater trochanter of the residual limb. (Units in N/mm²)

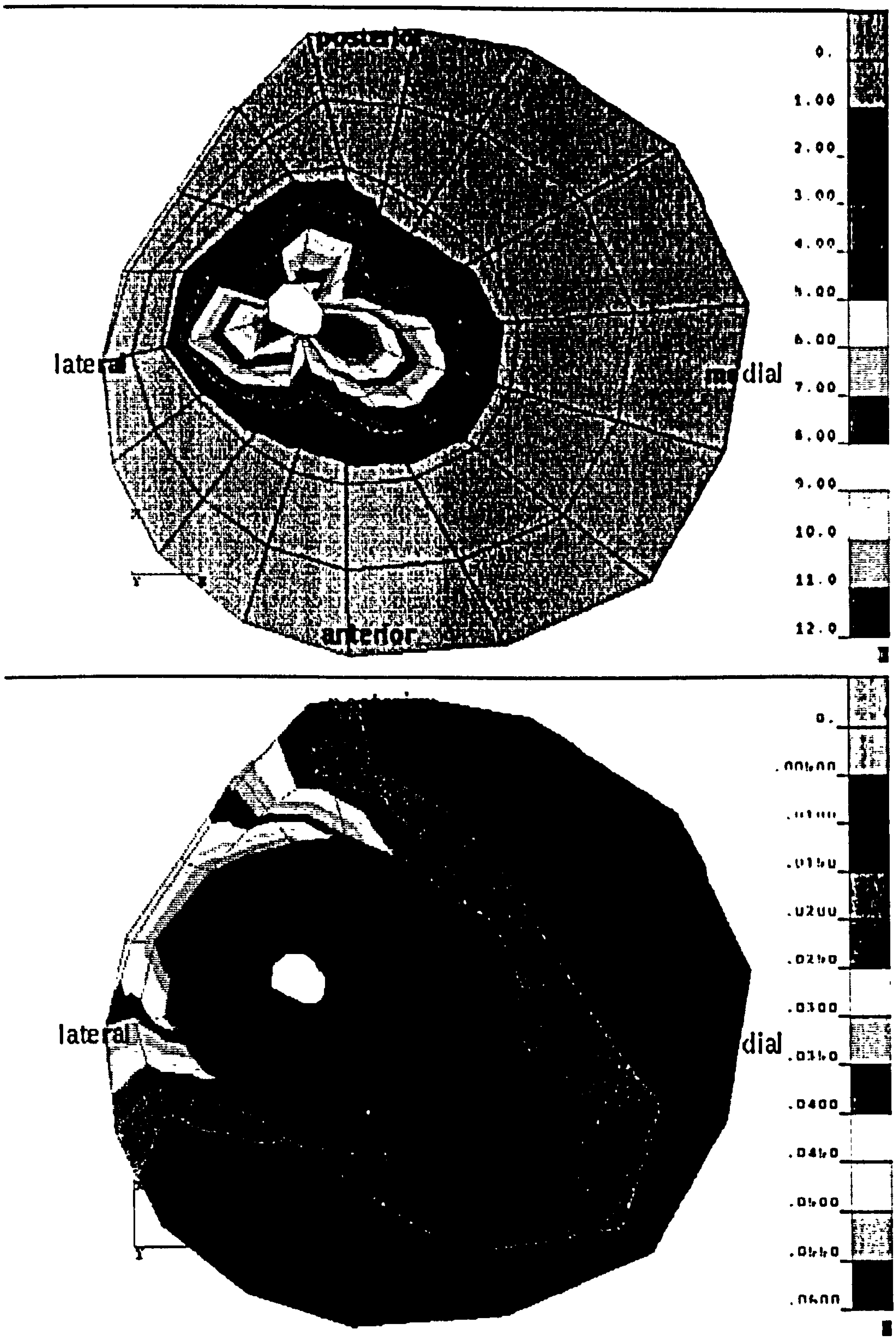

Fig. 7.5.6.2 Internal stress contours (von Mises stress) at the mid level of the residual limb. (Units in N/mm^2)

made. In the following section, the model can be seen to behave in a realistic manner in certain aspects.

7.6.1 FE models' prediction

In general, throughout gait, high pressures were predicted by the FE model at the lateral and the anterior sites, while pressures at the medial sites appeared low. Peak pressures were predicted at the greater trochanter, lateral and anterior distal ends of the residual limb. Low pressures were predicted at the medial side and anterior proximal area. According to the models, maximum pressure occurred at 10% of gait cycle, just after heel strike. The magnitude of pressure decreased at 25% of gait cycle by about 30%. At 40% of gait cycle, the pressure patterns remained similar to that at 10% of gait cycle, however, overall the pressure magnitude decreased by about 15%.

The pressure profiles predicted at most sites during gait generally follow a double peak curve, in phase with the vertical force component of the ground reaction force. A similar pattern was seen in the FE calculations when the predicted pressure at 10%, 25% and 40% of the gait cycle were plotted against the experimental pressure profile (Fig. 7.6.1.1).

In the comparison between predicted and measured pressure as presented in section 7.5.1, it was clear that a one to one match could not be achieved and predicted pressures were mostly lower than the measured values. However, when the predicted pressures along the entire length of the residual limb model were plotted with the measured pressures at corresponding sites as in Fig. 7.6.1.2, it could be seen that both predicted and measured values indicated decreasing pressures from the distal to the proximal end of the residual limb.

Most of the FE predictions erred within ± 70 % of the measured values. The deviation was mainly due to the limited available information to construct an accurate FE model. This will be addressed in more detail in the following sections.

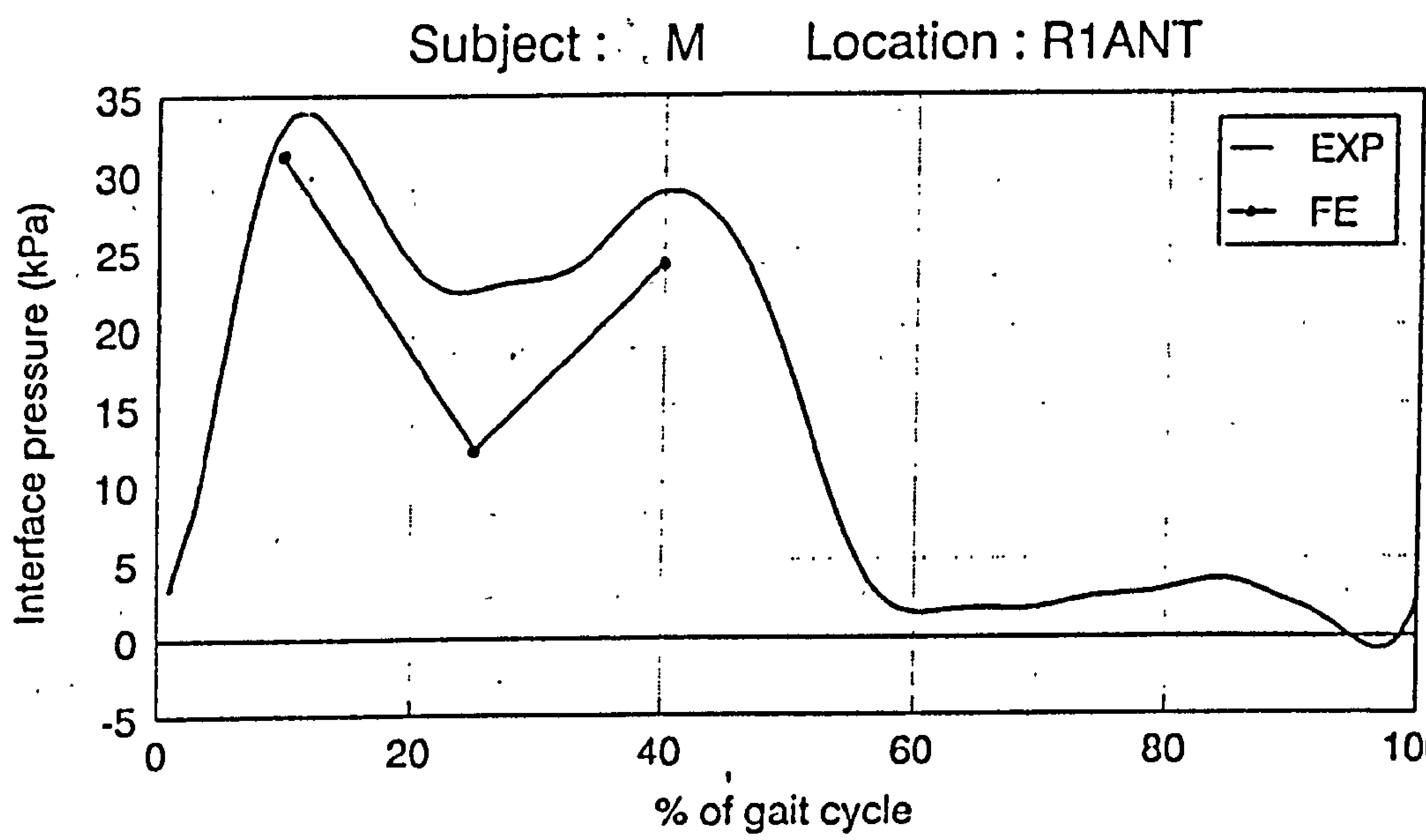

Fig. 7.6.1.1 The two peak pressure profile predicted at the R1ANT site follows the measured pressure profile. Subject M with IC socket.

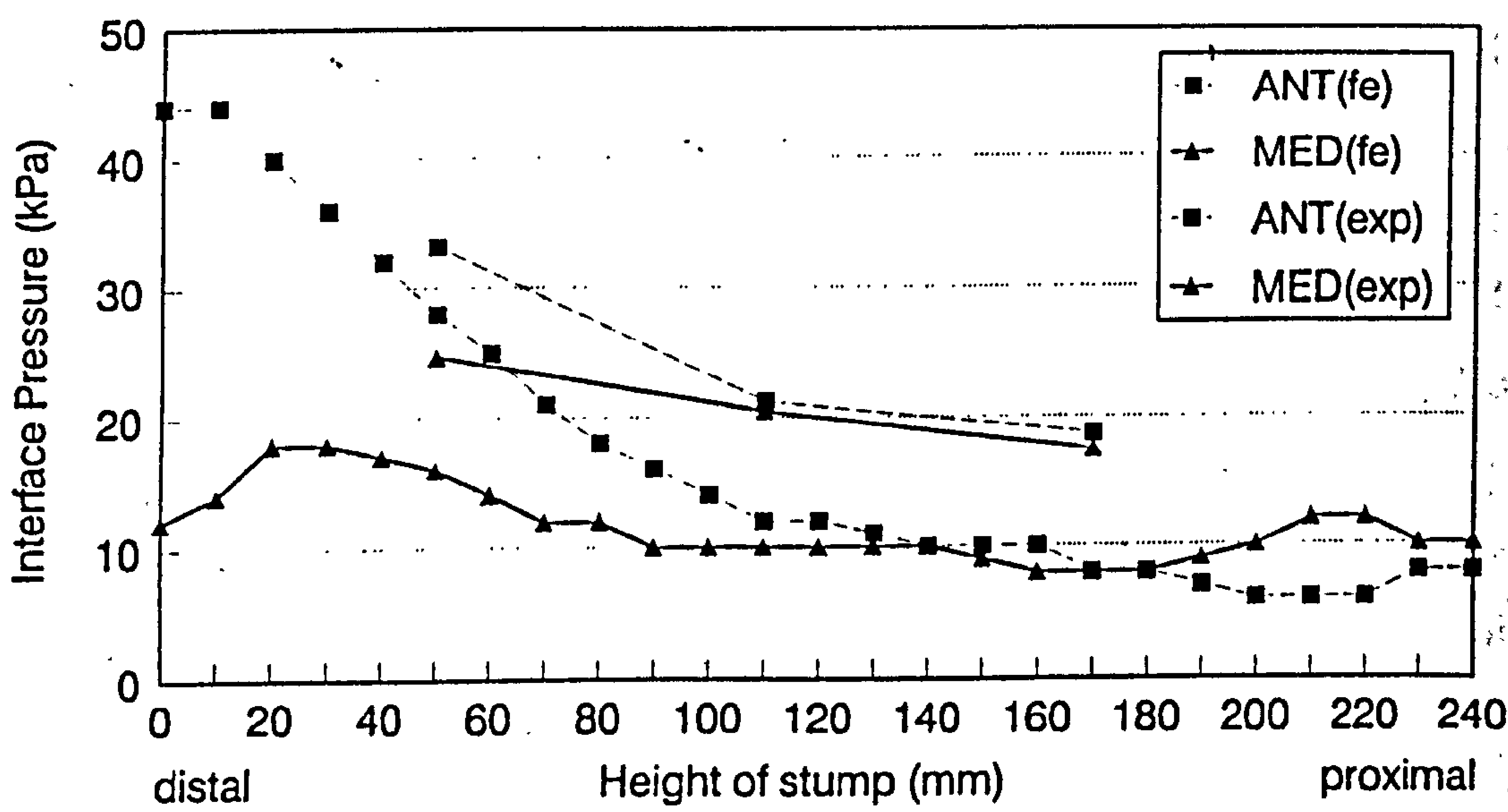

Fig. 7.6.1.2 The FE analysis predicted pressures follow an increasing trend towards the distal end of the residual limb, similar to experimentally measured pressures. Subject M at 10% of gait with IC socket.

7.6.2 Geometry

The geometry of the model was determined using two procedures as previously mentioned (section 7.2.1). The method did not allow an exact location of the femur within the socket to be determined. Thus, the position of the bone was only estimated through palpation of the amputee's residual limb on the distal end of the femur and the greater trochanter. The author of this thesis reckoned that the position of the bone was highly sensitive to the analysis, since all load actions were introduced to the bone in the model. Therefore a minor deviation from the exact position would affect the overall accuracy of the model.

The geometry of the pelvis was not defined in the model and all loading acted only on the hip joint. This was not true since the ischial tuberosity contained within the socket was load bearing. Pressures at the posterior proximal sites of the residual limb would therefore be underestimated.

The shape of the residual limb in the models was assumed to follow the shape of the sockets as in a total contact socket. This assumption, however, forced the FE analysis to begin at a zero stress state, though in reality the residual limb was in a pre-stress condition when the socket was in place. The pressures predicted were thus underestimated by at least an amount equivalent to the pre-load pressures. The pre-load pressures of the three subjects involved in this study had been measured by removing all the components of the artificial leg except the socket as described in chapter 4 section 4.6.3. The magnitudes were found to vary between -1 and 6 kPa for the 14 sites.

7.6.3 Loading and boundary conditions

As mentioned above, the boundary conditions did not consider the effect of pre stress introduced by the socket. There are basically two ways in which this effect could be assumed. Both procedures require the unloaded shape of the residual limb to be modelled. The first method assumes the entire surface of the residual limb is subjected to a set of displacements that will result in the model deforming to that of the socket shape, thus predicting a pre-stress condition. Upon achieving this, the loading on the femoral bone is then introduced. The second method is to mimic the effect of donning a socket by modelling a rigid surface or hard socket shell sliding onto the residual limb. Achieving this effect will allow the model to predict the pre-stress conditions, where further loading can then take place on the femur. In three dimensions, the latter procedure is highly complex as it involves dynamic modelling.

The above mentioned methods were not attempted in the FE models for the following reasons. From a preliminary model standpoint, the methods discussed above are highly complex in terms of boundary and loading conditions. This can lead to non-convergence in the FE solution and an increase in computational effort. The author of this thesis felt that the low pre-stress measured experimentally justified the cause of not attempting these complicated methods without firstly understanding the effect of a fixed boundary condition. In addition, the non-linear effect in the FE analysis at present were limited only to the geometry. If this effects is not significant, meaning the model behaves in a linear fashion, the overall pressure would mean adding up the predicted values with that of the measured pre-stress values. However, in this case adding the measured pre - stress values did not alter the predicted results significantly. This is expected as the inaccuracies in the models' predictions are contributing by other assumptions in geometry and material properties which could have a more significant effect on the predicted stresses. The two methods suggested were based on the logic that it approaches the real situation, but the methods are not impeccable. For example, introducing displacement to deform the surface of the model also introduced localised stresses which in reality do not exist. Modelling the donning of the socket requires specification of a suitable coefficient of friction and interface elements characteristics which are difficult to obtain experimentally and thus have to be assumed.

The fixed boundary conditions at the surface of the model assumed in this study concluded that a.) no movement existed between the surface of the residual limb and the socket and b.) that the socket rigidity exceeded that of the soft tissue by many times. In order to sustain suction, consistent contact at the interface between residual limb and the socket must be maintained, thus keeping movement to the minimum which satisfied condition (a). However, this assumption cannot be applied to the proximal brim area of the socket which was expected to lose contact with the residual limb on several occasions during gait in order to provide proper comfort to the amputee. The brim area thus posed extreme difficulty in defining a suitable boundary condition which varied throughout gait. The large percentage errors occurring at the GT site seen in this study was proof of such inconsistency. The GT site in prosthetic practice is defined as a 'pressure intolerant' area, with the greater trochanter acting as a bony prominence in contact with the prosthetic socket which becomes painful for the amputee. The prosthetist aims to direct pressure away by increasing the volume of the socket at the GT site, relieving pressures at the bony area. However, in the FE models, the surface nodes have been considered as fixed, i.e. analogous to direct contact with the socket, thus the pressure predicted at the GT area was expected to be much larger than the real socket which was provided with a relief at GT area. In the case of subject U, the measured pressures at the GT site during standing and gait were almost zero, compared to the FE predicted values, a huge percentage difference resulted. In subject H, the measured value at site GT during standing was 2.28 kPa and FE predicted 2.2 kPa. However during gait, surface contact was lost resulting in negative and zero pressure, and again the FE model assumed consistent contact throughout gait resulting in large errors. Subject M was the only one that maintained consistent contact at site GT throughout standing and gait, thus FE predictions were closer than in the other two subjects. This clearly indicates the difficulties in specifying a suitable boundary condition for all cases. Though all sockets were made by the same prosthetist, due to the unique characteristic (anatomical or physiological aspects) of the subjects' residual limb, consistency in boundary conditions was almost impossible to achieve by the prosthetist using artisan methods alone.

Lastly, the fixed boundary conditions proposed at the surface of the residual limb in essence defined a socket of infinite rigidity. The material of the socket used in the test was polypropylene, which though of relatively high stiffness still accounts for some flexibility.

7.6.4 Material properties

Characterising the mechanical properties of soft tissues was essential to allow any prediction of stresses and deformation on the residual limb imposed by external forces. Soft tissue in the residual limb could generally be grouped into skin, fascia and skeletal muscles. The FE models presented assumed the soft tissue in the residual limb as a single entity, homogenous, isotropic, nearly incompressible (ν = 0.4999) and linearly elastic, ignoring viscoelastic behaviour and assuming no hysteresis. This is not true in the case of soft tissue where the stress - strain behaviour is known to be highly non-linear. Also, the behaviour of live human tissue is expected to differ considerably from *in vitro* testing on animal and cadaver tissue where most mechanical testing has been performed and parameters derived. In this study, the mechanical properties of soft tissue were derived from *in vivo* indentation tests. However, the test limits the indentation force applied, therefore the mechanical behaviour is only applicable for lower load and characteristics at higher forces can only be obtained by extrapolation. From the indentation test, a suitable elastic constant was derived based on linear elastic theory with a flat cylindrical indentor indenting an infinite surface area.

The problem in choosing suitable material characteristics to represent soft tissue of the residual limb has already been highlighted in chapter six. FE experiments and mechanical tests of porcine tissue were conducted and several forms of modelling soft tissues, which include non-linear and hyperelastic material assumptions were attempted. One of the main reasons why a linear elastic material was chosen for the residual limb model was due to the lack of known parameters that could enable non-linear behaviour to be derived. A detailed explanation has been presented in chapter six and therefore will not be discussed further here.

7.7 CONCLUSION AND FURTHER WORK

The range of pressure predicted by the FE models compares well with measured values. However, an attempt to match pressure at individual measured sites with predicted values generated large percentage errors at several sites. Regardless, the study did show the possibility of using FE analysis to predict meaningful interface pressures at the residual limb.

Future efforts will be concentrated on refining the model in the area of geometry, boundary and loading conditions and material properties. In finite element modelling part two, chapter 10 of this thesis, a 2-D model with detail internal musculature of the residual limb will be attempted to study the effect of material non homogeneity, the biomechanical behaviour at the muscle / intermuscular tissue interface and the different types of loading and boundary conditions.

CHAPTER EIGHT
GENERIC GEOMETRICAL MODEL OF THE FEMUR

8.1 INTRODUCTION

Accurate location of the hip and knee joint centres, muscle's origins and insertions or obtaining the geometry of bones in a human subject without any imaging techniques can be difficult. Magnetic resonance imaging and computer aided tomography scans have been used successfully to obtain accurate geometry of bones, but these methods are not cost effective. This study is concerned with the use of homogeneous scaling as presented by Lew and Lewis (1977) to generate a generic model of the femur fit for finite element analysis. Homogeneous scaling can be visualised by the transformation of an initial object to that of a final object of the same shape but of different size.

The aim of the study is to transform a cadaveric femur to that of the human subject's femur based on the palpable anatomical landmarks of the human subject. In the case of a trans-femoral amputee subject, knowing the geometry of the femur allows a finite element model of the residual limb to be created by combining the scaled femur with a digitised shape of the prosthetic socket. Such a process would eradicate the need of either MRI or CT scans to define the amputee subject's femoral geometry.

In this investigation, homogenous scaling of the femur was thoroughly tested by scaling cadaveric femora with soft tissue still intact, and isolated by dissecting all soft tissue. Finally stress analysis was performed on the actual and scaled bones, to examine their mechanical behaviour due to geometrical changes contributed by the scaling technique.

The chapter begins with a review of several related investigations followed by detailed descriptions of the scaling method used in this study.

8.2 LITERATURE REVIEW

A three-dimensional description of the bony segments of the human body is often essential in several areas of biomechanics. Examples of these areas include the study of muscle, ligament or joint forces in the human body, design and evaluation of prosthetic devices and anthropometric analyses. As briefly discussed earlier, due to the high cost of imaging techniques, more economical methods have been developed

Femur No.	Condylar width	Condylar depth	Bone length
1	2.59	2.05	15.54
2	3.41	3.02	18.25

Table 8.2.1 Critical dimensions of femora. Note : the units are in inches.
(Lew and Lewis, 1977)

to obtain equivalent information. These latter methods are basically scaling techniques. Scaling is necessary because the size of an individual is different. However, the assumption that is often made in these techniques is that the shape of different individual remains largely the same.

Lew and Lewis (1977) performed an extensive study to evaluate the effectiveness of anthropometric scaling. Using adult cadaveric specimens, two femurs and three tibias which ranged considerably in sizes were selected. The scaling principles and experiments conducted by Lew and Lewis were similar for both femur and tibia, thus only the femur will be discussed in this review. Table 8.2.1 highlights the difference in dimensions of the femora. The anatomy of the femur was firstly studied in detail and six reference points were identified on the femur using a mechanical device which records 3-D global co-ordinates. These reference points were considered to be palpable anatomical landmarks on the human being. The points were ;

1.) tip of adductor tubercle,

2.) Lateral femoral epicondyle,

3.) greater trochanter,

4a.) medial ridge of the patellar surface,

4b.) medial femoral epicondyle and

4c.) joint space below adductor tubercle.

Using the 3-D co-ordinates of these points, transformation matrices were defined. However, only four of the six reference points were necessary for generating the transformation matrices. From the six reference points, Lew and Lewis tested four different combinations consisting of reference points 1 2 3 4a, 1 2 3 4b, 1 2 3 4c and 4a 2 3 1. In the four combinations, 4a, 4b, 4c and 1 were designated as the origin of the femur during the transformation. This will be made clearer in the next section which describes the theory involved with the scaling technique. The four combinations were tested to check which gave the most accurate transformation since the accuracy of the transformation was directly dependent on the location of the reference points and how they spanned the bone. The accuracy was also dependent on the exact location of the reference points, which would be highly dependent on the repeatability

Femoral Trial 1—Medial patella ridge as fourth reference points

Point	Absolute difference from measured position vector X1	X2	X3
1	0.09	0.12	0.34
2	0.28	0.07	0.07
3	0.12	0.17	0.00
4	0.19	0.04	0.27
5	0.11	0.00	0.24
6	0.13	0.00	0.17

Femorial Trial 2—Medial femoral epicondyle as fourth reference point

Point	Absolute difference from measured position vector X1	X2	X3
1	0.00	0.42	0.85
2	0.04	1.12	1.86
3	0.00	0.21	0.65
4	0.02	1.00	1.90
5	0.06	0.22	0.15
6	0.08	0.21	0.55

Femoral Trial 3—Joint space below adductor tubercle as fourth point

Point	Absolute difference from measured position vector X1	X2	X3
1	0.31	0.19	0.938
2	1.13	0.30	4.368
3	0.38	0.08	1.619
4	1.09	0.25	3.781
5	0.20	0.04	1.246
6	0.16	0.30	0.768

Femoral Trial 4—Reverse roles of adductor tubercle (origin) and medial patellar ridge

Point	Absolute difference from measured position vector X1	X2	X3
1	0.09	0.10	0.34
2	0.28	0.07	0.07
3	0.12	0.17	0.00
4	0.19	0.04	0.27
5	0.11	0.00	0.24
6	0.13	0.01	0.17

Table 8.2.2 The differences between the measured and the calculated positions vectors to the point of interest when scaling femur 1 to femur 2. Note: the units are in inches. (Lew and Lewis, 1977)

of palpating the reference points on the human subjects. In the test conducted by Lew and Lewis, the latter accuracy could not be evaluated since the study was conducted with isolated cadaveric femur. The influence of the soft tissue surrounding the femur was not considered.

Scaling was performed by transforming one bone to the another, femur 'one' was scaled to femur 'two'. To evaluate the accuracy of the scaling techniques, femur 'two' which was created by transforming femur 'one' was compared to the real femur 'two' bone. In the femoral scaling, six points of interest on the smaller bone were scaled to the larger bone i.e. femur one to femur two (table 8.2.1). These points were,

1. medial tip of lesser trochanter
2. lateral patellar ridge
3. middle of popliteal region
4. lower anterior third of shaft
5. centre of lateral articular groove
6. pit of popliteus tendon

Using the transformation matrices derived from the reference points, the six points of interest were transformed to their new co-ordinates which represent the scaled femur 'two'. In order to evaluate the errors between the scaled and the actual femur, the six points were compared to similar points measured on the actual femur two using the 3-D measurement device. Based on the four combinations of reference points, scaling was conducted and the absolute difference at the six points of interest was calculated (see table 8.2.2). The set of reference points in trial one, i.e. tip of adductor tubercle, lateral femoral epicondyle, greater trochanter and the medial ridge of the patellar surface as the origin gave the least difference between the scaled and the measured points. The other combinations had produced large errors. Lew and Lewis discussed three main sources of errors. The scaling technique being linear incorporated the assumption that the geometrical differences were accounted for by homogeneous deformation. However, this was only an approximation especially when large localised shape variation existed between specimens and subjects. Another source of errors was the repeatability of locating the reference points. In a human subject, this

Normative femur specimen landmark coordinates and standard deviations

Normative beagle left femur (dried)—dimensions in cm				
Landmark	$x \pm \sigma_x$ medial	$y \pm \sigma_y$ cranial	$z \pm \sigma_z$ proximal	σ_r
1. Dorsal extremity of greater trochanter	−1.002 ±0.125	−0.304 ±0.086	9.914 ±0.065	0.164
2. Cranial extremity of greater trochanter	−1.662 ±0.091	0.262 ±0.081	8.735 ±0.096	0.155
3. Tip of lesser trochanter	0.382 ±0.087	−0.359 ±0.104	7.359 ±0.122	0.183
4. Center of fovea	1.002 ±0.088	0.304 ±0.122	9.611 ±0.098	0.179
5. Center of trochanteric caudal cavity	−1.106 ±0.074	0.146 ±0.090	8.927 ±0.107	0.158
6. Nutrient foramen	−0.343 ±0.115	0.267 ±0.124	5.807 ±0.159	0.232
7. Center of extensor fossa	−0.515 ±0.048	0.769 ±0.084	−1.099 ±0.092	0.133
8. Center of popliteal fossa	−0.877 ±0.049	0.212 ±0.118	−1.063 ±0.131	0.183
9. Center of medial collateral ligament	1.102 ±0.054	0.085 ±0.077	−0.329 ±0.091	0.131
10. Center of lateral sesamoid of gastrocnemius	−0.916 ±0.054	0.000 ±0.093	−0.127 ±0.095	0.143
11. Center of medial sesamoid of gastrocnemius	0.916 ±0.093	0.000 ±0.040	0.000 ±0.095	0.136
7 Specimens	Overall σ = 0.166 cm			

Table 8.2.3 Errors (mm) in scaling canine femur.
(Sommers et al 1982)

Normative tibia specimen landmark coordinates and standard deviations

Normative beagle left tibia (dried)—dimensions in cm				
Landmark	$x \pm \sigma_x$ medial	$y \pm \sigma_y$ cranial	$z \pm \sigma_z$ proximal	σ_r
1. Center of popliteal notch	−0.139 ±0.032	−0.256 ±0.026	10.789 ±0.074	0.085
2. Tip of medial intercondylar eminence	0.225 ±0.060	−0.061 ±0.043	11.231 ±0.027	0.079
3. Tip of lateral intercondylar eminence	−0.225 ±0.044	0.061 ±0.068	11.240 ±0.050	0.096
4. Center of muscular groove	−0.447 ±0.043	0.892 ±0.050	11.044 ±0.045	0.080
5. Center of tibial tuberosity	0.608 ±0.075	1.755 ±0.029	10.699 ±0.067	0.105
6. Distal extent of tibial crest	0.829 ±0.049	1.477 ±0.043	8.571 ±0.086	0.108
7. Nutrient foramen	−0.109 ±0.061	0.420 ±0.054	7.421 ±0.312	0.323
8. Tip of medial malleolus	0.577 ±0.048	0.000 ±0.058	0.000 ±0.061	0.097
9. Tip of distal cranial lateral projection	−0.276 ±0.062	0.896 ±0.049	0.386 ±0.107	0.133
10. Tip of distal cranial intermediate projection	0.104 ±0.022	0.520 ±0.016	0.277 ±0.047	0.054
11. Tip of distal caudal medial projection	−0.104 ±0.048	−0.520 ±0.047	0.242 ±0.051	0.085
12. Proximal fibular articular facet	−0.961 ±0.038	0.732 ±0.071	10.810 ±0.103	0.131
13. Facet of medial collateral ligament	1.021 ±0.052	−0.469 ±0.039	10.855 ±0.056	0.085
8 Specimens	Overall σ = 0.129 cm			

Table 8.2.4 Errors (mm) in scaling canine tibia.
(Sommers et al 1982)

error would be much larger and could vary between 5 and 10 mm. Finally, the accuracy was limited by the co-ordinate measuring device.

Sommer et al (1982) extended the technique proposed by Lew and Lewis (1977) to include mirror kinematics and statistical calculation. The technique allowed for scaling mirror symmetrical (right versus left) specimens. In addition the authors claimed that the use of a direct least squares statistical method improved the overall scaling accuracy by reducing the effects of experimental and anatomical landmark errors, i.e., digitisation, palpation and morphological variation. Scaling was performed on three types of dried canine specimens, femur and tibia and humerus. Each specimen group consisted of 7-8 specimens. Several landmarks spanning across the bones were selected for evaluating the accuracy of the method. Table. 8.2.3, 8.2.4 and 8.2.5 display the co-ordinates of these selected landmarks and the errors (standard deviations) encountered in the scaling procedure. The overall standard deviation in the femur, tibia and the humerus were 16.6 mm, 12.9 mm and 19.3 mm respectively.

In order to overcome the limitations that exist in a linear homogeneous scaling, Lew and Lewis (1980) suggested a non homogeneous anthropometric scaling method based on finite element principles. As discussed earlier in a linear homogeneous scaling scheme, at least four bony references were needed in forming the scaling parameters. To achieve good accuracy, the four points were spanned over the bone essentially forming a tetrahedron. Thus a non-homogenous mapping could be achieved by using multiple tetrahedra, each with uniform but different scaling. In finite element analysis, the deformation of points within a single element can be formulated if the element's nodal displacement is known. This would enable the comparison of nodal positions of the equivalent element in the initial shape to its deformed shape, also enabling equivalent points in the initial shape to be located in the deformed shape (Fig. 8.2.1). In their study (Lew and Lewis 1980), a larger cadaveric femur was scaled to a smaller one. A total of 23 bony points on the femur were located in order to evaluate the scaling test (Fig. 8.2.2). Three scaling tests were performed. The first test applied a four noded tetrahedral element to represent the femur, requiring four of the 23 bony points measured on the femur (Fig. 8.2.3). The equivalent positions of the remaining 19 points were scaled from the larger bone to

. Normative humerus specimen landmark coordinates and standard deviations

Normative beagle left humerus (dried)—dimensions in cm

Landmark	$x \pm \sigma_x$ medial	$y \pm \sigma_y$ cranial	$z \pm \sigma_z$ proximal	σ_r
1. Cranial extremity of greater tubercle	−0.460 ±0.070	1.492 ±0.037	8.191 ±0.082	0.115
2. Caudal extremity of greater tubercle	−0.896 ±0.018	−0.239 ±0.044	8.706 ±0.107	0.117
3. Middle projection of greater tubercle	−1.116 ±0.040	0.470 ±0.035	8.523 ±0.067	0.086
4. Caudal proximal extremity of lesser tubercle	0.896 ±0.069	0.239 ±0.069	8.663 ±0.094	0.135
5. Center of bicipital groove	0.312 ±0.039	0.754 ±0.048	8.311 ±0.104	0.121
6. Distal extremity of deltoid tuberosity	−1.122 ±0.102	0.978 ±0.055	5.082 ±0.144	0.185
7. Nutrient foramen	−0.022 ±0.068	−0.016 ±0.070	3.851 ±0.485	0.495
8. Medial projection of medial epicondylar ridge	1.210 ±0.038	0.000 ±0.061	0.000 ±0.118	0.138
9. Caudal projection of medial epicondylar ridge	0.672 ±0.034	−0.987 ±0.049	−0.732 ±0.131	0.144
10. Center of proximal origin of extensors	−1.210 ±0.038	0.000 ±0.047	−0.318 ±0.090	0.109
11. Center of distal origin of extensors	−1.024 ±0.055	−0.183 ±0.050	−0.656 ±0.077	0.107
6 Specimens	Overall σ = 0.193			

Table 8.2.5 Errors (mm) in scaling canine humerus.
(Sommers et al 1982)

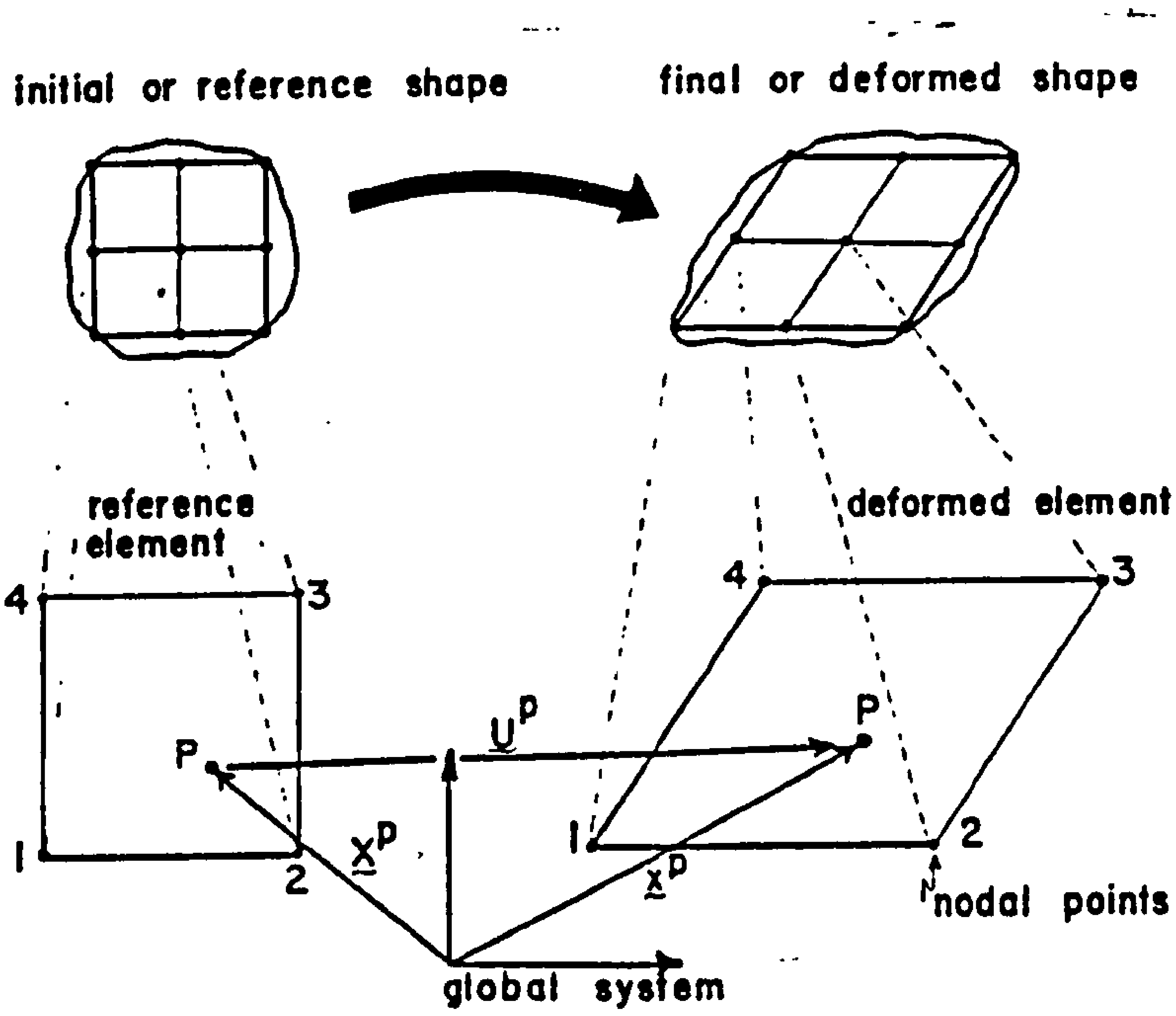

Fig. 8.2.1 A point p in a body may be located in the final or deformed shape by dividing the body into finite elements.
(Lew et al, 1980)

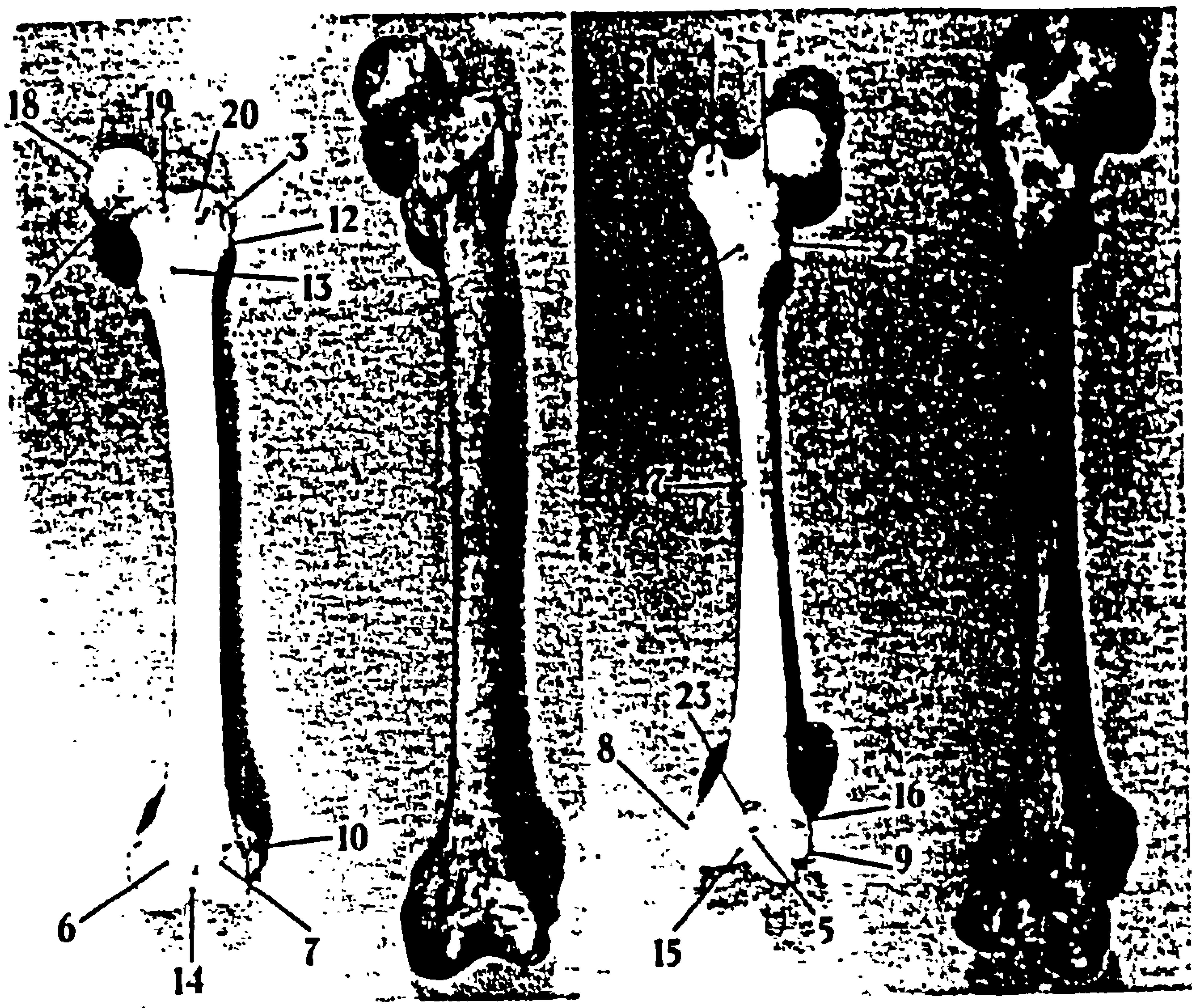

Fig. 8.2.2 Location of the 23 bony landmarks to be transformed.
(Lew et al, 1980)

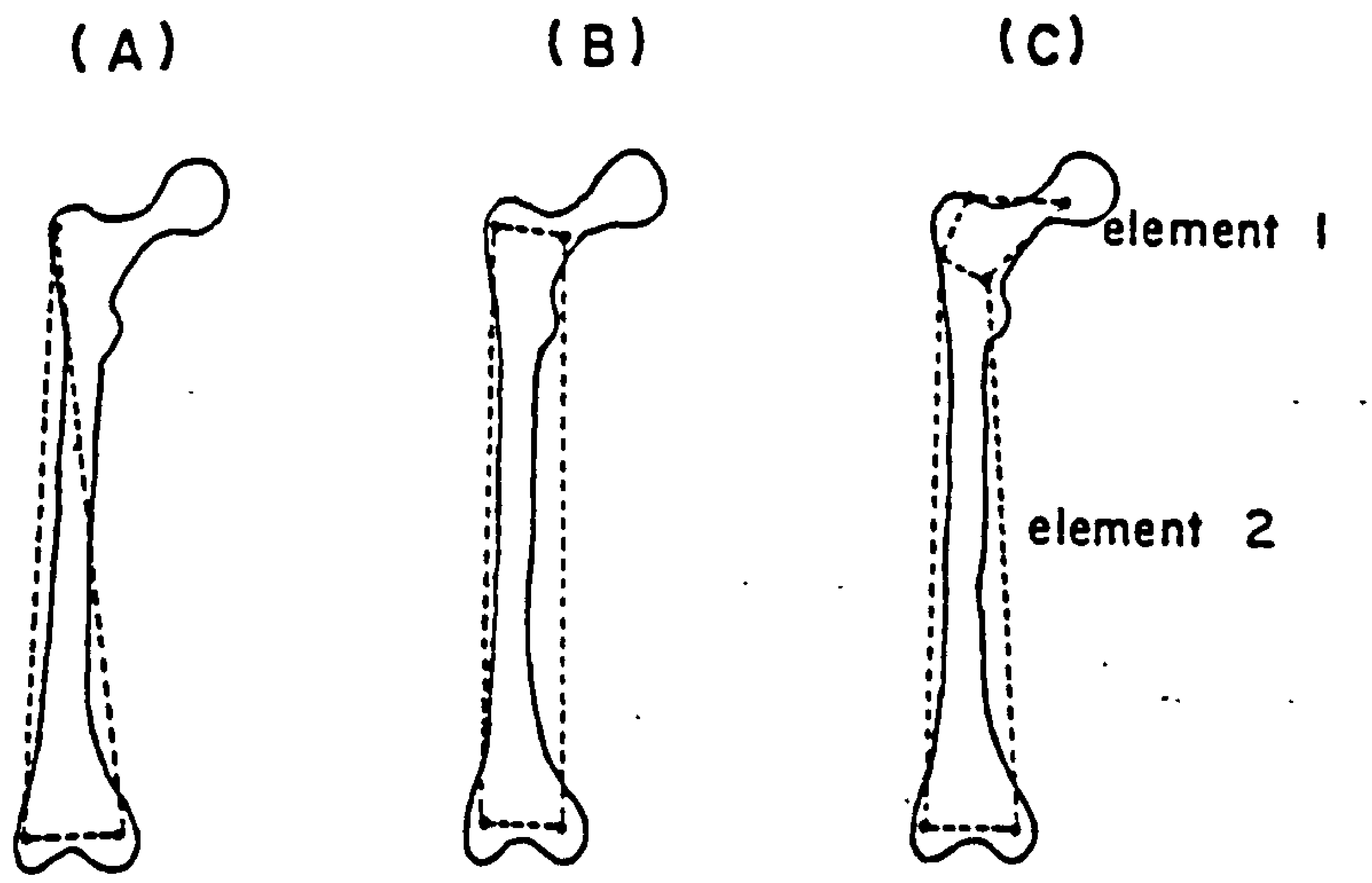

Fig. 8.2.3 The femur represented by
A.) a four noded tetrahedral element
B.) an eight noded element
C.) two eight noded elements. (Lew et al, 1980)

Bony point	Scaling by 4-noded element	Scaling by 8-noded element	Scaling by two 8-noded elements
1	9.76	*	4.06 (element 1)
2	12.86	*	*
3	9.45	*	6.59 (1)
4	9.24	*	*
5	9.40	*	*
6	14.43	*	*
7	*	*	*
8	8.01	*	*
9	7.48	7.65	6.70 (2)
10	*	5.43	5.42(2)
11	13.28	11.98	*
12	*	8.08	*
13	13.08	3.92	*
14	11.62	4.93	5.10 (2)
15	8.57	3.97	3.68 (2)
16	*	11.10	11.38 (2)
17	4.56	4.77	5.55 (2)
18	14.01	3.73	*
19	12.10	6.72	4.94 (1)
20	13.76	6.10	*
21	7.50	2.96	6.04 (1)
22	15.27	15.62	*
23	9.86	9.97	9.93 (2)
	mean for 19 points = 10.75	mean for 15 points = 7.13	mean for 11 points = 6.31

Table 8.2.6 Error (mm) vector between calculated and mesured values using the three different types elements for scaling. (Lew et al, 1980)

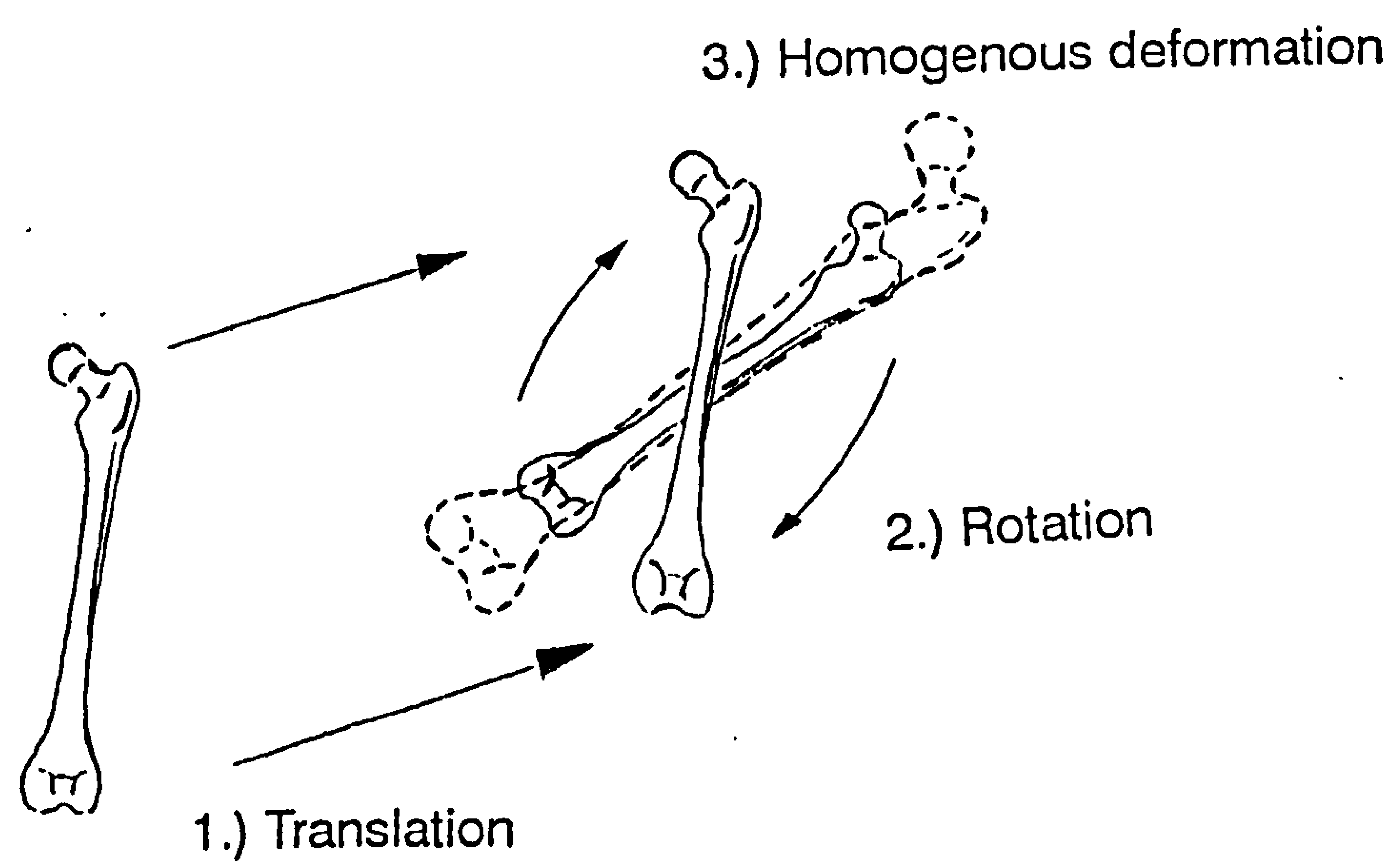

Fig. 8.3.1.1 The process of scaling the initial bone to the final bone.

the smaller one and their position compared. The second scaling test proposed an eight noded hexahedral element. Finally, moving on to non - homogeneous scaling, the femur was represented by two eight-noded element, separating the head-neck-trochanteric region from the shaft and the condyles. The magnitude of error vector between the calculated and those directly measured bony points were compared as tabulated in table 8.2.6.

Anthropometric scaling has been shown to be a viable method to locate positions that are inaccessible in the human subjects. Most studies conducted aimed at providing a means to locate several points of interest, for example muscles' insertions and origins at the femur for the purpose of force analysis. However, in order to produced a complete scaled femur, the method can be extended to include a multitude of points of interest which is sufficient to describe the 3-D geometry of the femur.

8.3 SCALING TECHNIQUE

8.3.1 Theory

The transformation of a body segment to be scaled is modelled by three successive motions ;

1.) a rigid body translation,

2.) a rigid body rotation and

c.) a homogeneous deformation of the initial body to the final body. Fig. 8.3.1.1 shows the three successive motions in the scaling of the initial bone to the final bone. The initial bone belongs to that of the cadaver, which is to be transformed to that of the human subject's bone (final bone). Representing the transformation in position vectors (Fig. 8.3.1.2), the position vector of a point in the initial bone is transformed to a new vector in the final bone by,

$$l_i = \underline{X}_I + \underline{V} + (\underline{U}\,\underline{T}(\underline{R}_{IL}))$$

where,

$\underline{l}_i$ is the position vector to the point of interest in the final bone (human subject)

$\underline{V}$ is the rigid body translation vector,

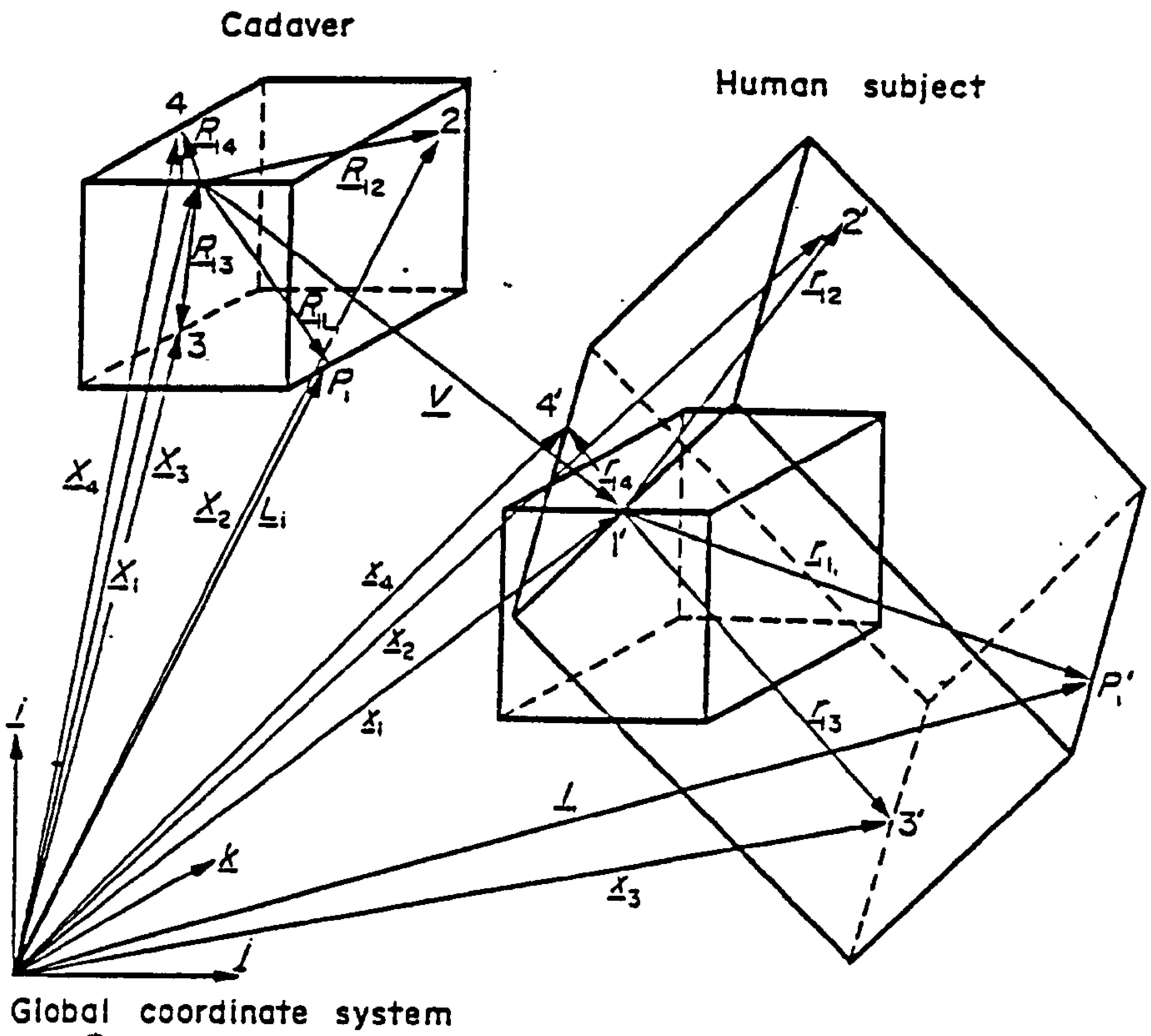

Fig. 8.3.1.2 Scaling transformation of a cadaver bone (initial) to a human bone (final). (Lew and Lewis, 1977)

$\underline{T}$ is the orthogonal matrix describing rigid body rotation

$\underline{U}$ is a 3 x 3 matrix describing homogeneous deformation of the initial bone to the final bone

$\underline{X}_I$ is the position vector of the origin of the initial bone

$\underline{R}_{IL}$ is the vector between the origin and the point of interest in the initial bone (cadaver)

The transformation required the knowledge of $\underline{V}$ and $\underline{U}\,\underline{T}$, which were derived from the four reference points selected on the initial and final bones. Thus, a point of interest in the initial bone $\underline{R}_{IL}$ can be transformed to a new point $\underline{l}_i$ in the final bone using $\underline{V}$ and $\underline{U}\,\underline{T}$

Referring to Fig. 8.3.1.2, reference point 1 i.e. $\underline{X}_I$ is selected as the origin of the initial bone, thus the vector between this origin and the three remaining reference points $\underline{R}_{pq}$ are given by ;

$$\underline{R}_{12} = \underline{X}_2 - \underline{X}_1$$
$$\underline{R}_{13} = \underline{X}_3 - \underline{X}_1$$
$$\underline{R}_{14} = \underline{X}_4 - \underline{X}_1$$

And the vector between the bone origin and any point of interest is,

$$\underline{R}_{ILi} = \underline{L}_i - \underline{X}_1$$

where $\underline{L}_i$ is the point of interest.

A set of local orthogonal co-ordinate axes $\underline{E}_1\ \underline{E}_2\ \underline{E}_3$ can defined at the origin of the initial bone using $\underline{R}_{12}$ and $\underline{R}_{13}$ and ,

$$E_{R12} = \frac{R_{12}}{|R_{12}|}$$

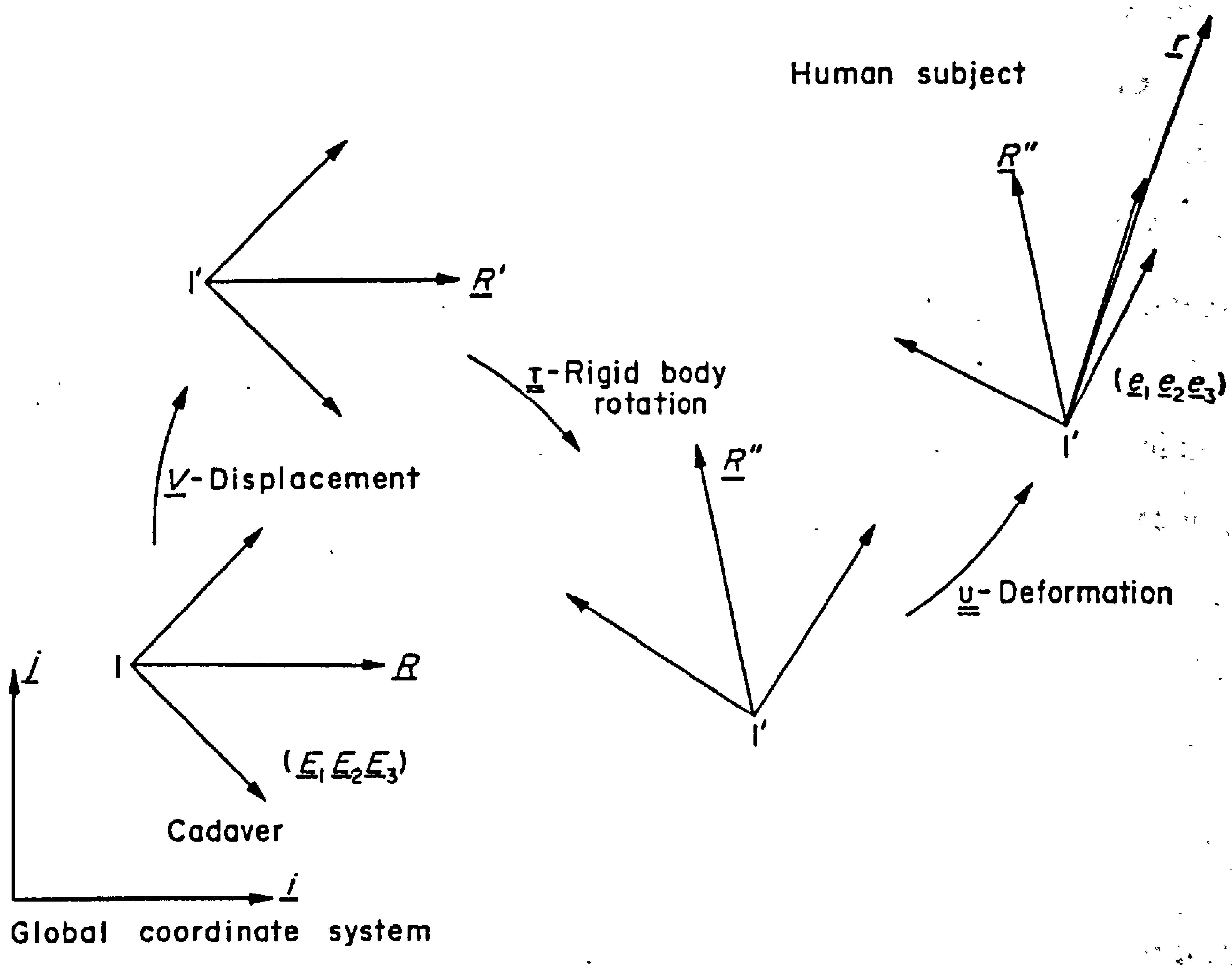

Fig. 8.3.1.3 Transformation of a line segment R to r.
(Lew and Lewis, 1977)

$$E_{R13} = \frac{R_{13}}{|R_{13}|}$$

thus,

$$E_1 = E_{R12}$$

$$E_3 = \frac{E_1 \times E_{R13}}{|E_1 \times E_{R13}|}$$

$$E_2 = \frac{E_3 \times E_1}{|E_3 \times E_1|}$$

The same also applied to the final bone where $\underline{x}_i$ are the reference points and $\underline{x}_1$ the origin. The vectors between the origin and the three reference points are therefore $\underline{r}_{pq}$ and the local orthogonal co-ordinate axes are $\underline{e}_1, \underline{e}_2, \underline{e}_3$.

Fig. 8.3.1.3 illustrates the transformation process, where $\underline{R}$ is firstly translated into $\underline{R}'$ by a displacement vector $\underline{V}$
which is defined by,

$$\underline{V} = \underline{x}_1 - \underline{X}_1$$

This is followed by a rigid body rotation about the final bone origin using matrix $\underline{\underline{T}}$ giving $\underline{R}''$. If the initial and final bone are of the same size, the transformation would only require $\underline{V}$ and $\underline{\underline{T}}$. In this case the deformation would be unity and,

$$\underline{\underline{T}}\,\underline{E}_i = \underline{e}_i$$

However, if the initial and final bone are of different sizes, a homogeneous deformation is required which is described with the matrix $\underline{\underline{U}}$ giving $\underline{R}'''$.

A FORTRAN program was written for the above computation. The input to the program are the four reference points on the initial and final bone. The program then reads a file containing all the points of interest on the initial bone and proceeds

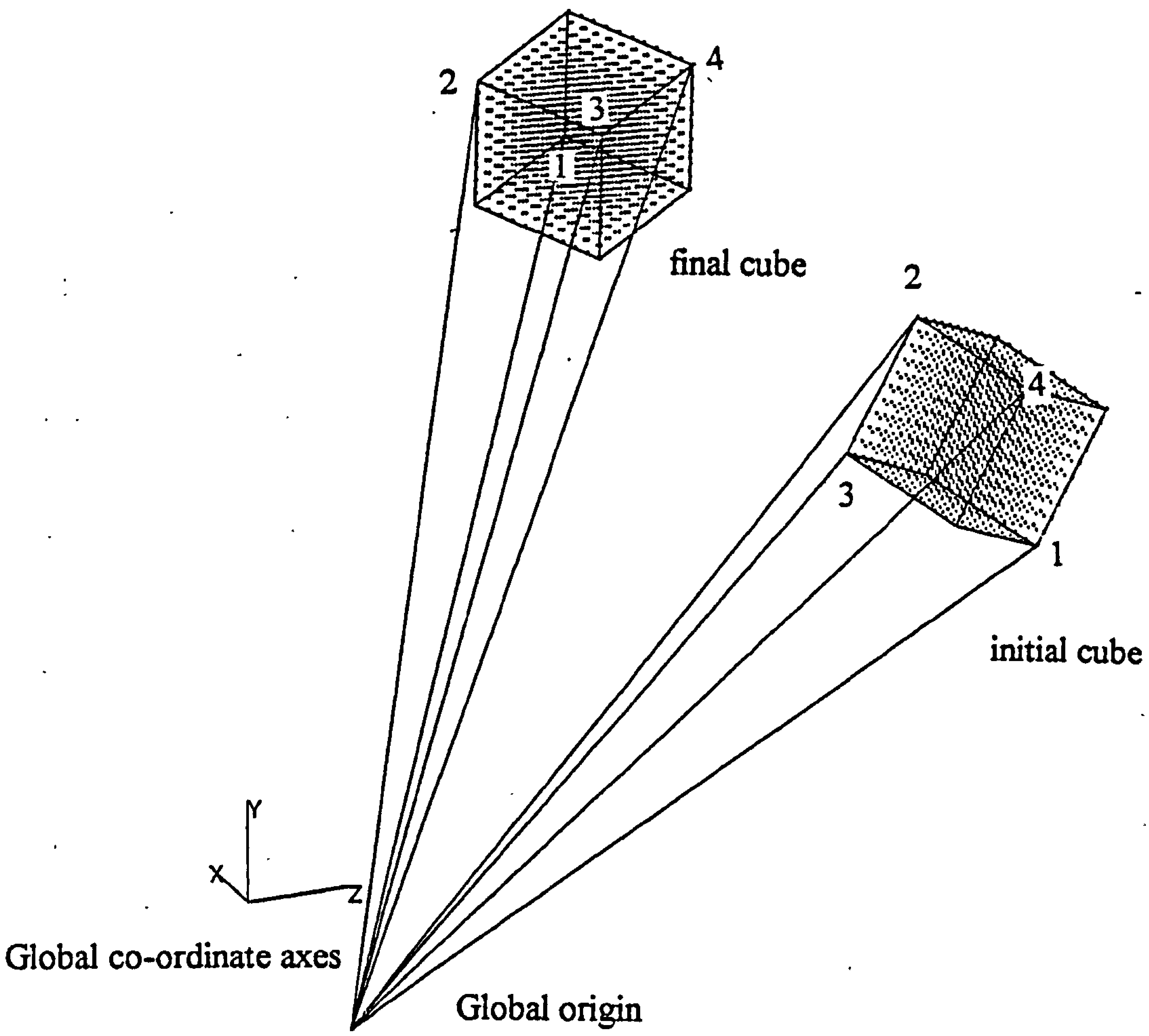

Fig. 8.3.2.1 Scaling of an initial cube to the final cube of the same size.
Point 1, 2, 3 and 4 define the reference points used in the scaling.
Point 1, the local origin also defines the location of the local orthogonal co-ordinates axes of the cube.

with the transformation of these points to that of the final bone.

8.3.2 Scaling of a cube

The FORTRAN program and the transformation method were tested by scaling a cube. Using the finite element modeller PATRAN (PDA Engineering), an initial cube of size 20 x 20 x 20 mm was constructed with 1331 equally spaced grid points. Another cube (final cube) of exactly the same size was also formed. However, the final cube was positioned and oriented differently from the initial cube in the global co-ordinate system (Fig. 8.3.2.1). The final cube also contained a total of 1331 grid points. Positioning and rotating the two cubes was possible using PATRAN commands and the exact position of the grid points was also known. The initial cube origin was positioned at 10, 50 and 100 mm according to the global x, y and z axes respectively. Two rotations were then introduced, a 60° clockwise rotation about the local x axis followed by a 30° anticlockwise rotation about the local z axis. The final cube was positioned in the global axis at 50, 100 and 50 mm in the x, y and z axes respectively. Again two rotations were introduced to the final cube, these were 30° anticlockwise rotation about the local x axis and a 50° clockwise rotation about the local z-axis. Having set the orientation of the two cubes, the scaling test was conducted by transforming the initial cube to the final cube. In this case, since both the cubes were of the same size, the transformation consisted of a rigid body translation and a rigid body rotation. To proceed with the scaling, four reference points were determined from the initial and the final cube. As discussed previously, the accuracy of the technique was dependent on the selection of these reference points. In a cube, one of the best possible combinations defining the overall span of the cube would be that shown in Fig. 8.3.2.1, which defined the corners of the cube. Once the reference points from the initial cube and the final were fed into the FORTRAN program, the transformation matrix representing the rigid body translation and rotation was calculated. The position vector of the point of interest in the initial cube was then transformed to a new position vector which should represent that of the final cube. To evaluate the scaling method, the absolute difference between the

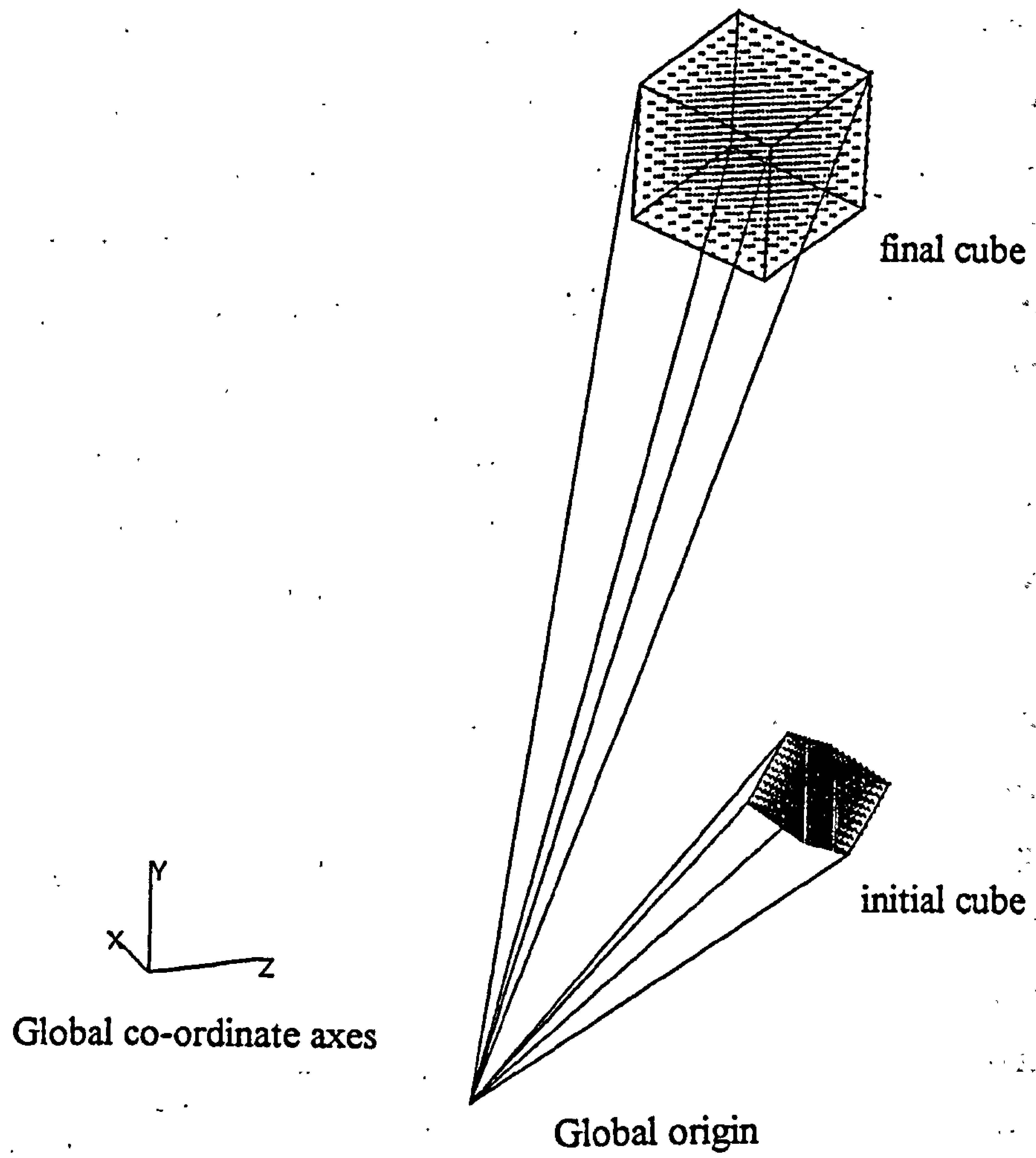

Fig. 8.3.2.2 Scaling of an initial cube to the final cube of different size.

new position vector was compared to that of the final cube. A total of 1327 (i.e. 1331 grid points minus the four selected reference points) points of interest in the initial cube were transformed to their new position vectors. Comparing the new position vectors with that of the final cube, the mean absolute difference of the 1327 points were 1.92 E -6, 2.06 E -6 and 2.52 E -6 mm in the x, y and z directions. The standard deviations were 4.03 E -6, 4.10 E-6 and 5.92 E -6 mm respectively. The values showed hardly any difference between the transformed cube and the final cube, indicating the FORTRAN program and the transformation method were working properly. The above results was achieved when the reference points were entered with accuracy of up to nine decimal places as represented in PATRAN. However, in the experiments described later, the reference points of the bones could only be measured up to one hundredth of a mm. Repeating the above test with the reference points entered with an accuracy of up to two decimal places, the mean absolute differences increased to 7.24 E -3, 4.76 E -3 and 2.05 E -3 mm and standard deviations 4.42 E -3, 2.15 E -3 and 2.69 E -3 mm in the x, y and z directions respectively.

Another scaling test which includes homogenous scaling was further conducted. For this test, the final cube from the previous test was enlarged to twice its size to a dimension of 40 x 40 x 40 mm using PATRAN commands (Fig. 8.3.2.2). The orientation of the final cube remained the same, however its origin was positioned at 100, 200 and 100 mm in the x, y and z axes of the global co-ordinate system. The initial cube being the same as the previous test was again scaled to the final cube, using similar reference points as that discussed in the first test. However, the transformation matrix generated in this test included a rigid body translation, rotation and a homogeneous deformation. The accuracy was again compared by taking the absolute difference between the new 1327 position vectors transformed from the initial cube to that of the final cube. Entering the reference points to an accuracy of a hundredth of a mm, the mean absolute difference in the x, y and z directions were 9.47 E -3, 4.53 E -3 and 8.93 E -4 mm, and standard deviations of 5.69 E -3, 2.27 E -3 and 2.87 E -3 mm respectively.

A different set of reference points was chosen to test its effect on the accuracy of the scaling method. Instead of a corner grid on the cube, a mid side grid was

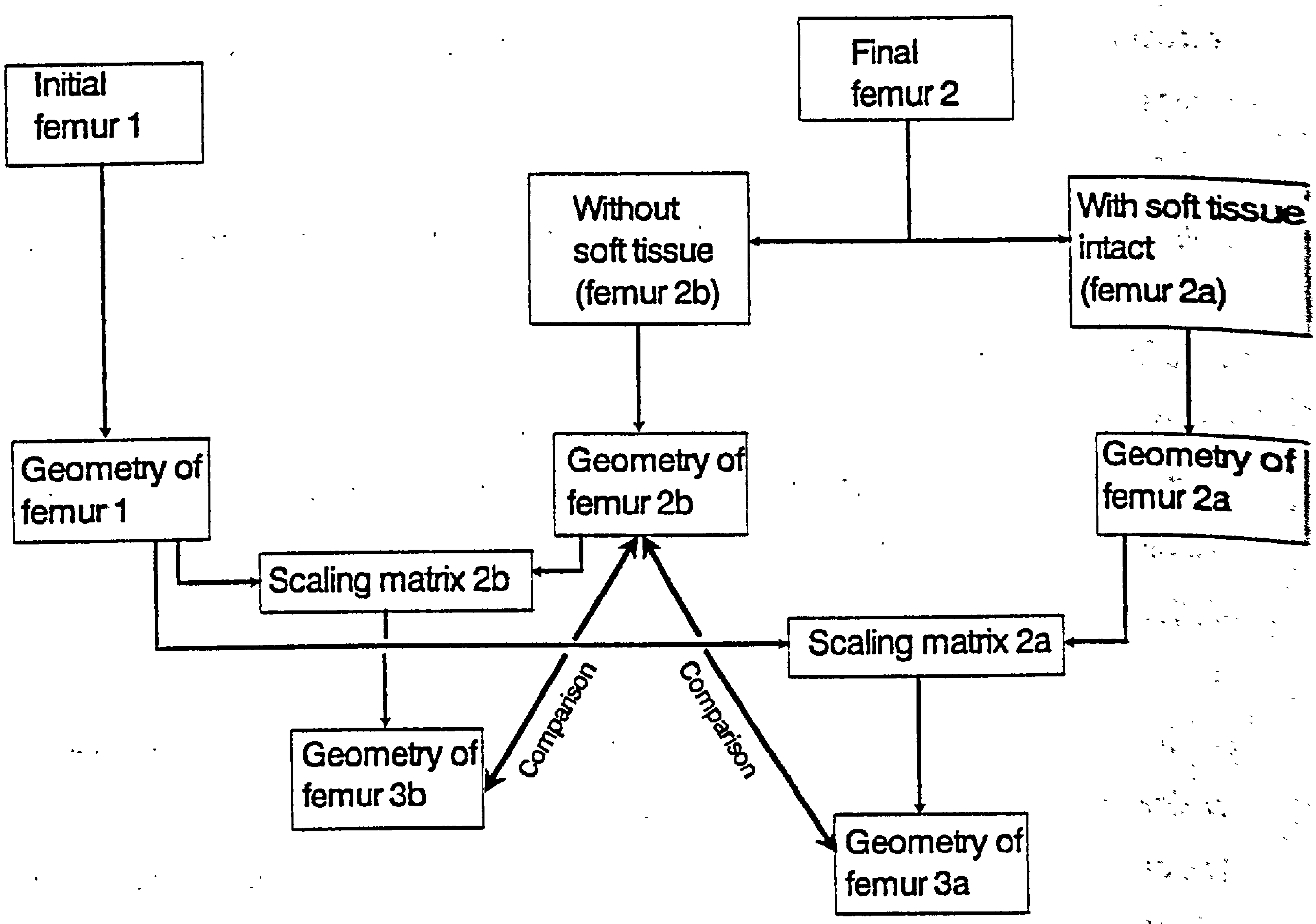

Fig. 8.4.1.1 Experimental procedures

selected as one of the four reference points. The test was similar to the previous one where the new position vectors of 1327 grids were compared to that of the final cube. The absolute errors generated were 9.46 E -3, 4.53 E -6 and 8.93 E -4 mm and standard deviation of 8.62 E -3, 5.68 E -3 and 2.67 E -3 mm in the x, y and z direction respectively. An approximately two fold increased in the standard deviation was observed in the x and y directions when compared to the previous test.

8.4 METHODOLOGY

This section outlined the steps taken to scale a femur using the above mentioned scaling techniques.

8.4.1 Experimental procedures

The ultimate aim of this study is to transform a cadaveric femur to that of the subject's femur. However, in order to evaluate the scaling technique, the femur has to be isolated for comparison. Therefore in this case, only cadavers were used in the study.

The experimental procedures is outlined in Fig. 8.4.1.1 At least two femora are required to test the scaling procedures. Firstly the initial femur 1 is to be scaled to the final femur, femur 2. In reality, the final femur 2 would be that of a living subject, while in this case it is cadaveric. Scaling proceeds under two conditions of femur 2, with soft tissue intact (femur 2a) and without soft tissue (femur 2b). Fig. 8.4.1.2 shows the scaling of femur 1 to femur 2a was performed by matching the bony landmarks (reference points) of femur 1 to similar palpable landmarks on the thigh based on the intact femur. After which the femur in the thigh is to be isolated by removing all the soft tissues of the cadaver's thigh which gives condition femur 2b. Fig. 8.4.1.3 shows the scaling of femur 1 to femur 2b.

In summary, femur 1 was transformed to the final femur 2 under two different conditions. The difference in the two conditions lies in the way the reference points in the final femur 2 were acquired. The first set of reference points on femur 2 was acquired by palpating the cadaver's thigh, and the second set was acquired by locating them directly on femur 2 that was isolated from the same cadaver's thigh. The two

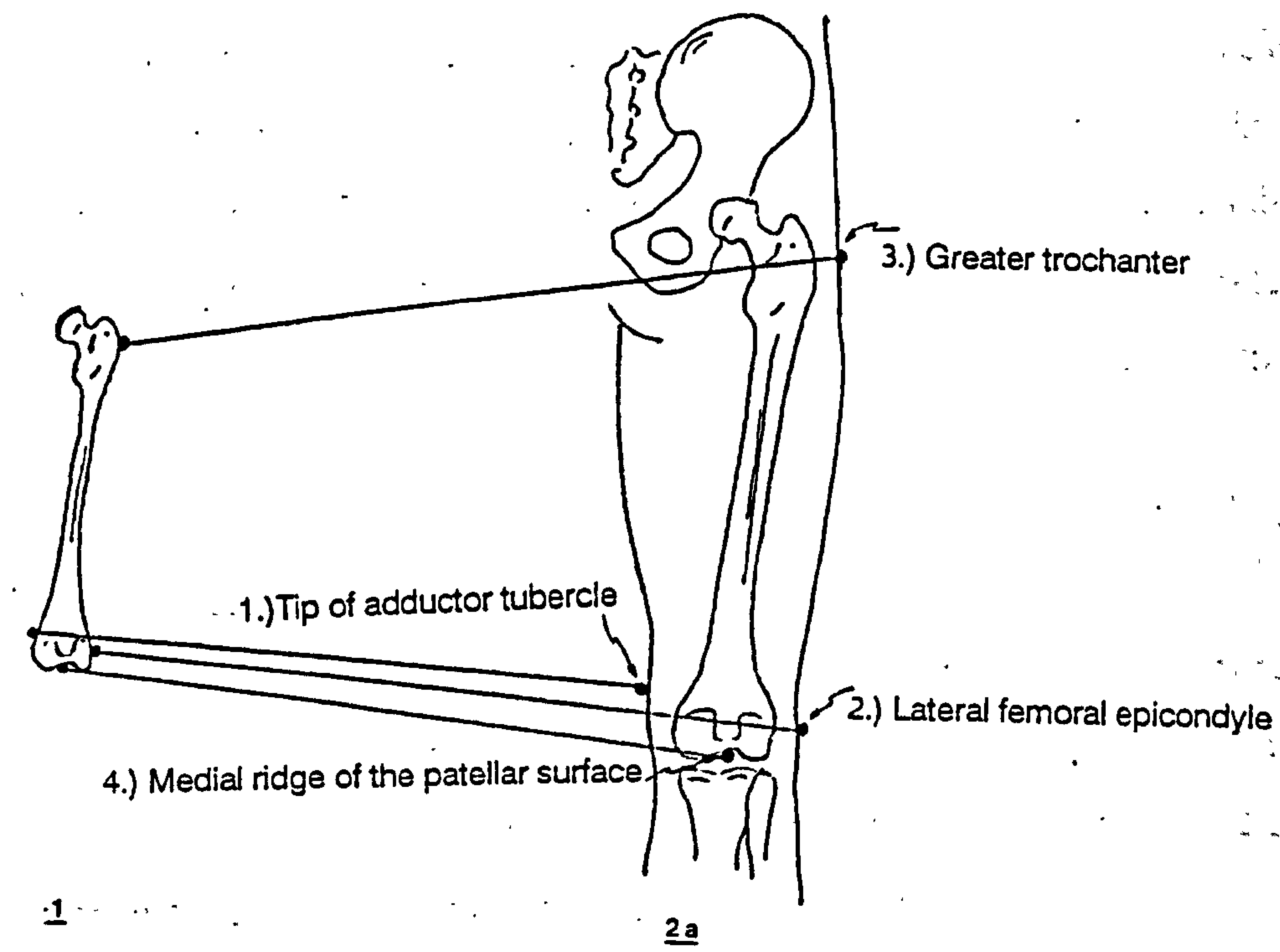

Fig. 8.4.1.2 Scaling of femur 1 to femur 2a with soft tissue intact.

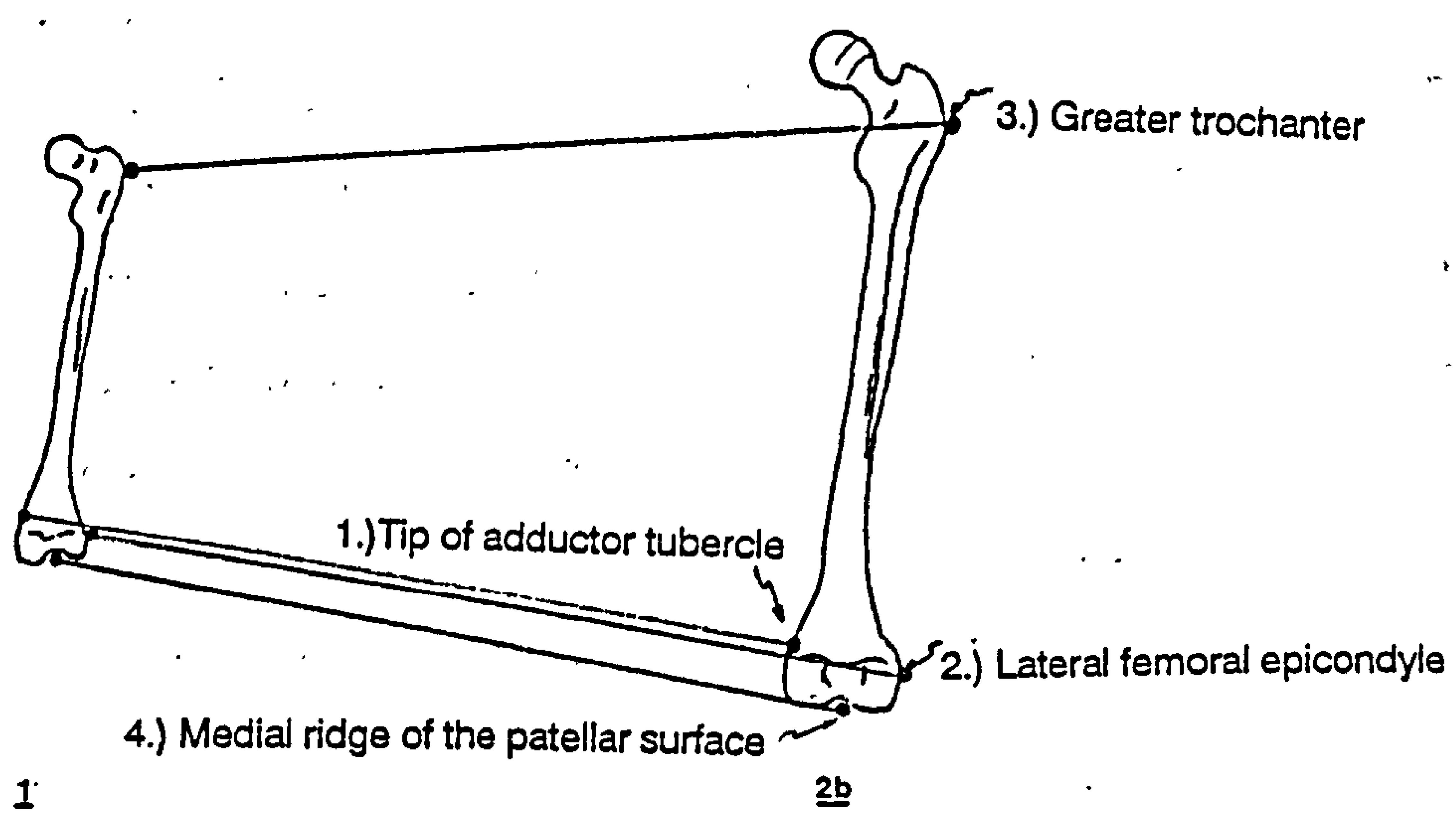

Fig. 8.4.1.3 Scaling of femur 1 to femur 2b without soft tissue.

different conditions could therefore give an indication of the error generated by palpating for reference points on the human subject thigh. In the study, two scaling matrix were therefore defined. One for scaling femur 1 to 2a giving femur 3a and the other for scaling femur 1 to 2b giving femur 3b. Finally, femur 3a and 3b which were generated by transforming the initial femur 1 were compared to the actual geometry of the final femur 2.

8.4.2 Cadaveric specimens

The study involved a total of four fixed cadavers with soft tissue still intact. The cadavers were two males and two females. Only one side of the lower limb was studied, and these were the right side for the male cadavers and the left side for the female cadavers. Since the scaling procedure required two femora, one was defined as the initial femur and the other the final femur in each sex group. Referring to table 8.4.2.1, the femur from the female cadaver 1-F-L was used as the initial femur and the femur from the female cadaver 2-F-L as the final femur. The same was adopted for the male cadavers. The measurements of the cadavers' lower limb are also presented in Table. 8.4.2.1.

As mentioned earlier, the cadaveric femora at some point need to be isolated by dissecting all soft tissues and dislocated from the joints. In order to make isolated femur transportable, they were chemically treated and dried. The process firstly required the main masses of soft tissue surrounding the bones to be removed, after which the femora were placed in a bath of 1 part antiformin, 6 part water. The solution with the bones was heated to just about boiling and maintained at this temperature. The bones were than examine from time to time to see how quickly they were being denuded. This takes between half to one hour. After removing from the bath, the bones were brushed clean to remove any remaining soft tissue and washed under running water and dried.

PARAMETERS	Cadavers' Code (1 - initial, 2 - final, F - Female, M - Male, L - Left and R - Right lower limb) 1-F-L (mm)	2-F-L (mm)	1-M-R (mm)	2-M-R (mm)
Height	1550	1560	1690	1720
Leg length	690	740	775	890
Inter ASIS distance	223	264	262	258
Distance between the ASIS and the patellar	440	435	420	500
Circumference of the pelvis at the ASIS	924	954	870	995
Circumference of the thigh at the ischium	496	463	457	509
Circumference of the thigh at the mid section	441	370	368	394
Circumference of the thigh at the condyles	399	351	360	376
Distance between the greater trochanter and the lateral condyle	340	335	345	420
Condylar width	114	101	106	110

Table 8.4.2.1 Two female and 2 male cadavers were selected for the experiment. Cadaver 1-F-L's femur was used as the initial femur, and cadaver 2-F-L's femur as the final femur in the scaling scheme. Similarly, the other set of femora selected for scaling were 1-M-R (initial) and 2-M-R (final). The table list the cadavers' height and lower limb measurements.

8.4.3 Reference points

The reference points or anatomical landmarks on the femur, used in this study for building up the scaling matrix are similar to that proposed by Lew and Lewis (1977). They are ;

a.) tip of the adductor tubercle

b.) lateral femoral epicondyle

c.) greater trochanter

d.) medial ridge of the patellar surface. (local origin)

As discussed in section 8.2, Lew and Lewis also tested two other anatomical position as reference points on the femur which were the medial femoral epicondyle and joint space below the adductor tubercle. However, lower accuracy had been obtained using these two points compared to the aforementioned combinations, which was tested and found to give the best accuracy. Therefore in this study, no effort was given in assessing the best combination of anatomical landmarks to obtain the best accuracy. The conclusion drawn from Lew and Lewis investigation regarding the best combination of reference points was accepted.

8.4.4 Locating the anatomical landmarks (reference points)

Locating the four anatomical landmarks of the femur (2a) with soft tissue still intact was performed on the skin of the cadavers limb using a 3-d co-ordinate marking table. The marking table was designed to measure prosthetic alignment for gait analysis, but after modification, was found suitable for this purpose. Fig. 8.4.4.1 shows the measurement set up. The table which was mounted on a heavy wooden base was made of hard perspex with the top surface marked with a grid of 1 cm squares. This allowed the co-ordinates of y and z to be measured to an accuracy of 0.3 mm (Marmar 1993). Distance in the x direction (height) was first recorded on a specially constructed marker. The marker has a long pointed arm which can be adjusted in two directions. The marker's long arm provided an added advantage when pin pointing awkward locations. The base of the marker is flat and slides on the perspex table. Once the height of the marker was set, it was then compared to a height gauge to obtain its numerical value. Using the method described, the x, y and z

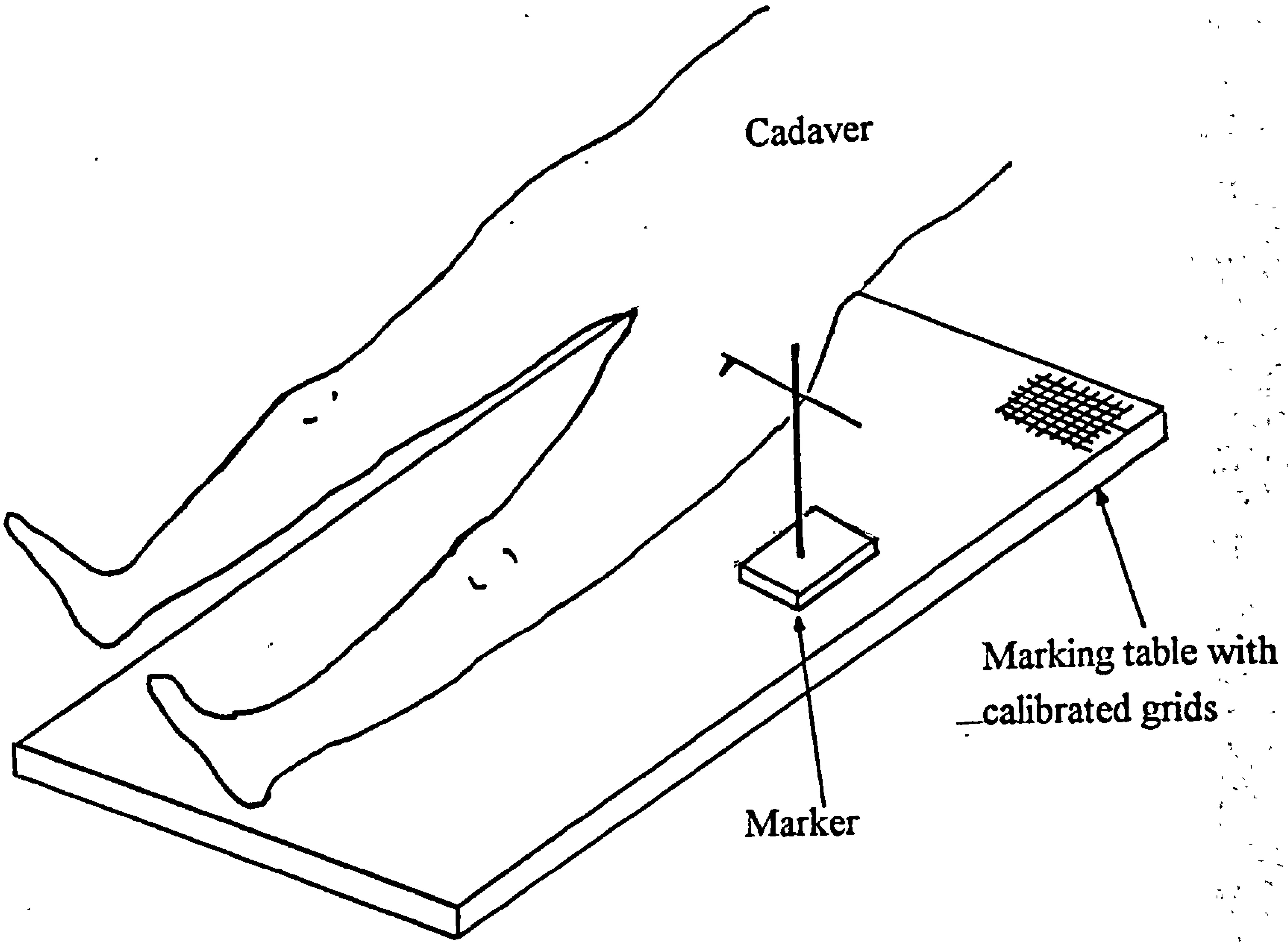

Fig. 8.4.4.1 Marking table measurement set up.

Cadaver 2-F-L

Locations	X (mm)	Y (mm)	Z (mm)
Tip of adductor tubercle	175.20	415.01	188.69
Lateral femoral epicondyle	120.84	387.12	136.99
Greater trochanter	113.72	773.59	125.98
Medial rigde of patellar surface	162.54	368.86	150.73

Cadaver 2-M-R

Locations	X (mm)	Y (mm)	Z (mm)
Tip of adductor tubercle	81.90	384.34	142.99
Lateral femoral epicondyle	85.17	377.25	61.42
Greater trochaniter	90.79	710.21	98.58
Medial rigde of patellar surface	53.40	350.11	95.91

Table 8.4.4.1 Location of the four reference points measured on cadavers 2-F-L and 2-M-R thighs using the marking table. In the scaling procedure, the reference points are designated for femur 2a.

co-ordinates of the four palpable anatomical landmarks of the femur were measured on cadavers 2-F-L and 2-M-R and tabulated in table 8.4.4.1.

The femora of cadavers 1-F-L and 1-M-R were used as the initial femur in the scaling process. Therefore there was no need for measurement to be taken with the cadaver's soft tissue still intact. The four anatomical landmarks of the initial femur were not obtained using the marking table, instead by another means as described in the next section.

8.4.5 Defining the geometry of the femur

A three dimensional geometry detail of the initial femur is required in order to produced a scaled femur of equal geometrical detail. Unlike studies conducted by previous investigators where a point of interest (eg. muscles insertion) in the initial femur is transformed to the final femur, the present study requires a multitude of points of interest which sufficiently define the 3-D shape of the initial femur to be transformed to the final femur.

The geometry of the four isolated femora were scanned using an optical laser scanner (Cyberware 4012). The cylindrical scanner produces 32 grid points on each transverse slice (representing the perimeter of the bone) at an interval of 3.175 mm. The scanner is well suited for objects of the cylindrical form but causes problems when scanning odd geometrical form like that of the femur. Thus in order to capture as much geometrical detail as possible, the femur was cut into three sections, the femoral head sectioned at just above the lesser trochanter, the shaft and finally the condyles sectioned approximately 2-3cm above the adductor tubercle. Each section was attached to a pin along its long axis which was secured onto a fixture attached to the scanner as shown in Fig. 8.4.5.1. On the average, approximately 6000-8000 grid points were required to completely described the geometry of the femur. Neutral files were generated containing the geometrical details of the femora and imported to the FE modelling software PATRAN (PDA Engineering, USA) which enabled the three separated sections of the femur to be joined graphically. Each femur represented in PATRAN provides information of the 3-D co-ordinates of individual grid points and the exact location of any anatomical feature of the bone. Therefore the four

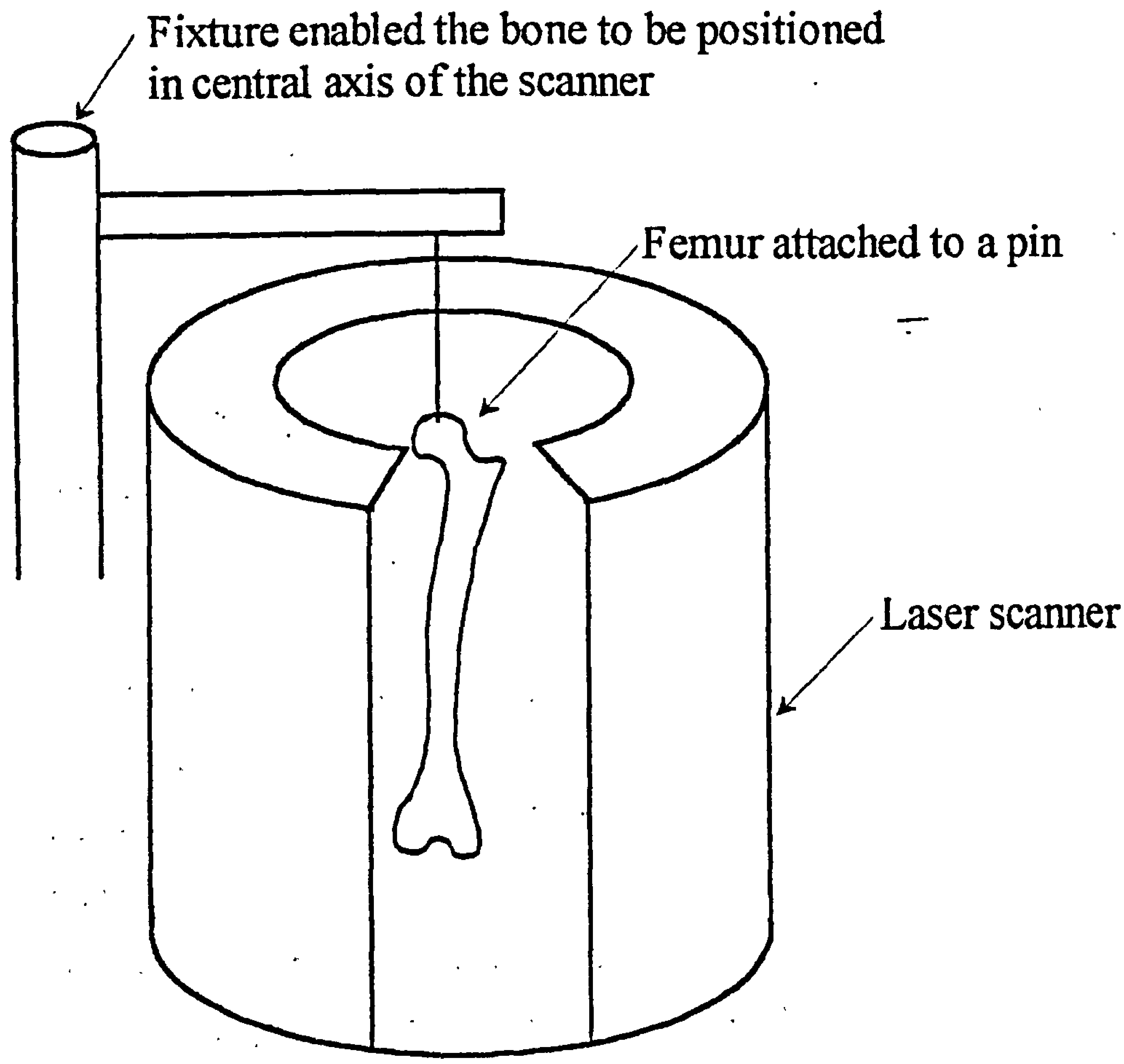

Fig. 8.4.5.1 Digitisation of the femoral bone using Cyberware laser scanner.

anatomical landmarks on the isolated initial femur 1 (cadavers 1-F-L and 2-M-R) could be identified from the grid points displayed in PATRAN instead of using a marking table for determining similar landmarks on the cadaver's thigh (Table 8.4.5.1). Similarly the geometry of the final femur (cadavers 2-F-L and 2-M-R) after isolating from the cadavers thigh were obtained using the laser scanner. Thus, the reference points on femur 2b (refer to fig. 8.4.1.3) , for the scaling of femur 1 to femur 2b could be determined. (Table 8.4.5.2)

Fig. 8.4.5.2 to Fig. 8.4.5.5 show the digitised femora as represented by PATRAN for 1-F-L (initial), 2-F-L (final), 1-M-R (initial) and 2-M-R (final) respectively.

8.5 RESULTS OF THE EXPERIMENT

This section presents a comparison between the shape of the transformed femora and that of the original femur. As described earlier, the scaling procedure was performed by scaling an initial femur 1 to femur 2 under two different conditions of obtaining the reference points, based on femur 2a with soft tissue intact and femur 2b without soft tissue. The transformed femora generated were therefore femur 3a and 3b respectively. Hence, in an ideal situation when the transformation are most accurate, the dimensions of femur 2, femur 3a and femur 3b would be the same.

In order to assess the accuracy of the scaling procedure, 18 locations were selected on the original femur 2 which were compared to the transformed femur 3a and 3b (see Fig. 8.5.1). The absolute differences between the x, y and z co-ordinates of these locations were calculated for femur 2 and femur 3a, and for femur 2 and femur 3b. Table 8.5.1 and 8.5.2 list these absolute differences as a result of scaling cadaver 1-F-L to 2-F-L and cadaver 1-M-R to 2-M-R respectively. Generally, a higher accuracy i.e. lower absolute differences, was obtained in the transformed femur 3b than in 3a. This was expected since the reference points in the transformation of femur 3b were measured directly on the bone, whereas in 3b the reference points were located on the cadavers' thigh by palpation. However, the average absolute differences in the 18 locations for both femur 3a and 3b were not significantly different.

Cadaver 1-F-L

Locations	X (mm)	Y (mm)	Z (mm)
Tip of adductor tubercle	-174.87	-135.1	-28.61
Lateral femoral epicondyle	-168.34	-137.48	40.09
Greater trochanter	-191.84	229.23	11.11
Medial rigde of patellar surface	-192.06	-159.77	11.19

Cadaver 1-M-R

Locations	X (mm)	Y (mm)	Z (mm)
Tip of adductor tubercle	112.57	-233.64	42.14
Lateral femoral epicondyle	123.13	-247.68	-58.91
Greater trochanter	106.01	148.24	-28.68
Medial rigde of patellar surface	86.16	-260.85	5.75

Table 8.4.5.1 Location of the four reference points measured on cadavers 1-F-L and 1-M-R femur using PATRAN. In the scaling procedure, the reference points are designated for femur 1.

Cadaver 2-F-L

Locations	X (mm)	Y (mm)	Z (mm)
Tip of adductor tubercle	25.15	-207.51	-44.66
Lateral femoral epicondyle	29.15	-217.99	25.82
Greater trochanter	15.61	163.70	2.09
Medial rigde of patellar surface	11.94	-235.92	3.77

Cadaver 2-M-R

Locations	X (mm)	Y (mm)	Z (mm)
Tip of adductor tubercle	33.42	-20.85	51.72
Lateral femoral epicondyle	41.10	-35.15	-12.38
Greater trochaniter	5.23	299.26	-25.41
Medial rigde of patellar surface	-6.73	-48.53	23.68

Table 8.4.5.2 Location of the four reference points measured on cadavers 2-F-L and 2-M-R femur using PATRAN. In the scaling procedure, the reference points are designated for femur 2b.

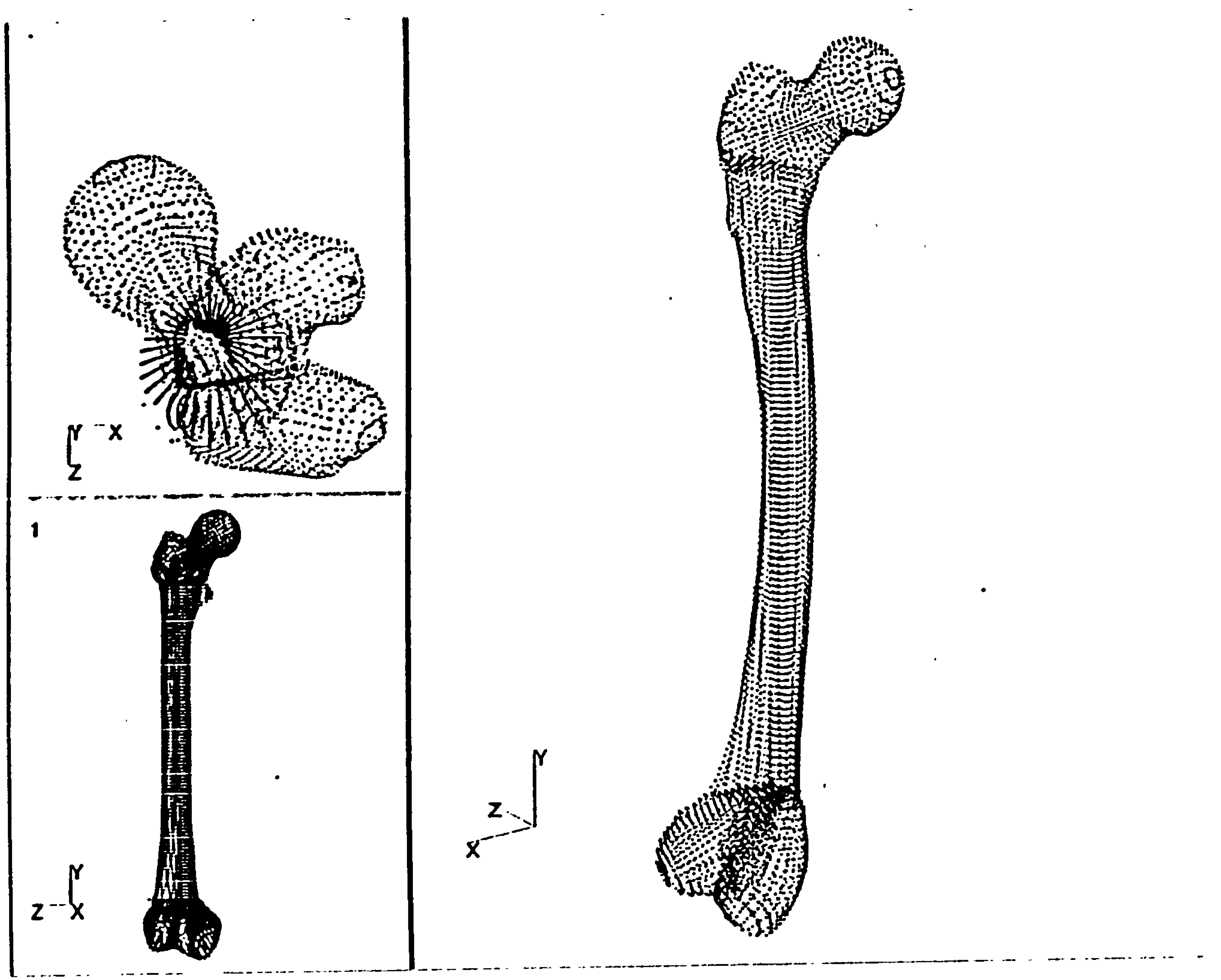

Fig. 8.4.5.2 Geometry of femur of cadaver 1-F-L represented in grid points using PATRAN.

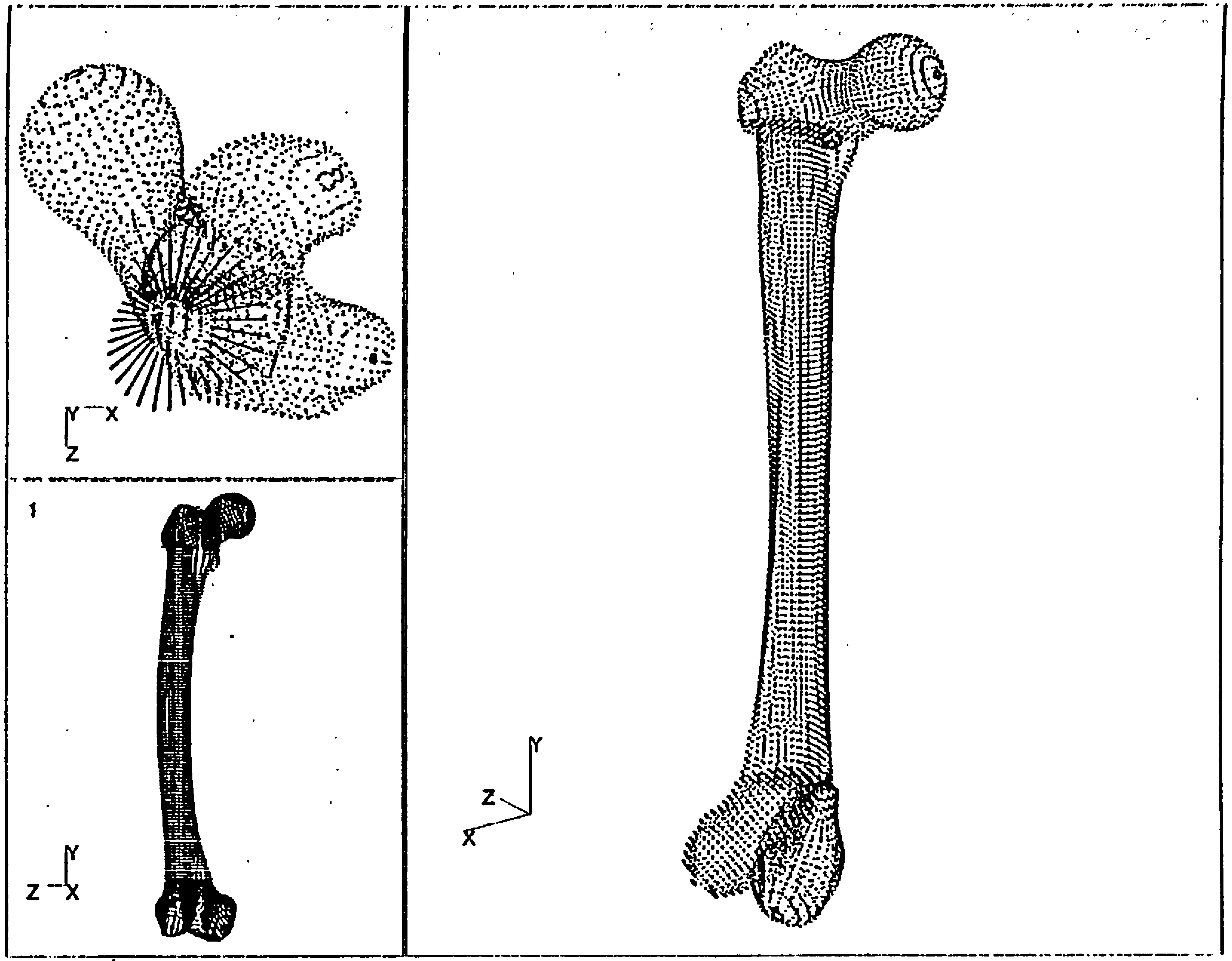

Fig. 8.4.5.3 Geometry of femur of cadaver 2-F-L represented in grid points using PATRAN.

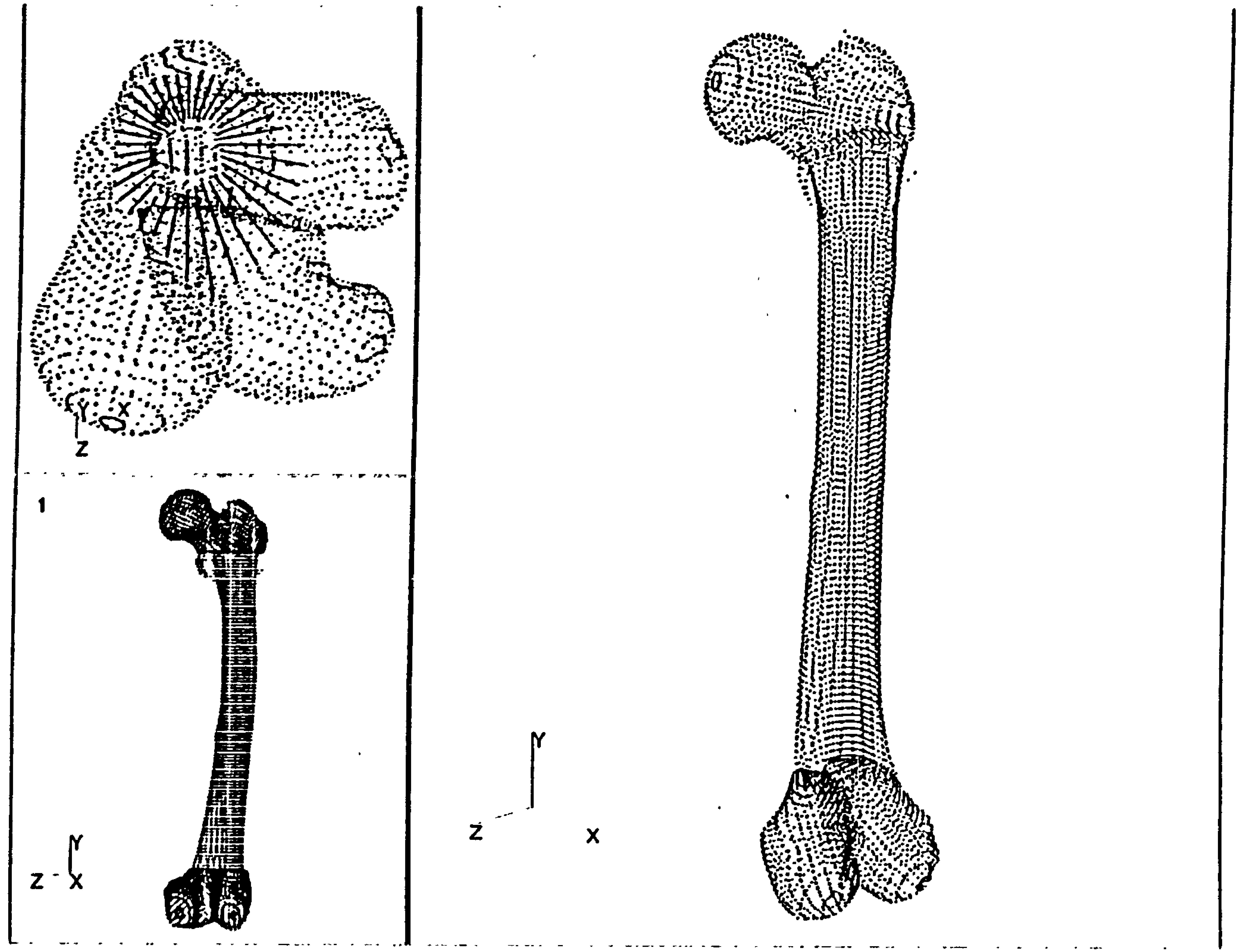

Fig. 8.4.5.4 Geometry of femur of cadaver 1-M-R represented in grid points using PATRAN.

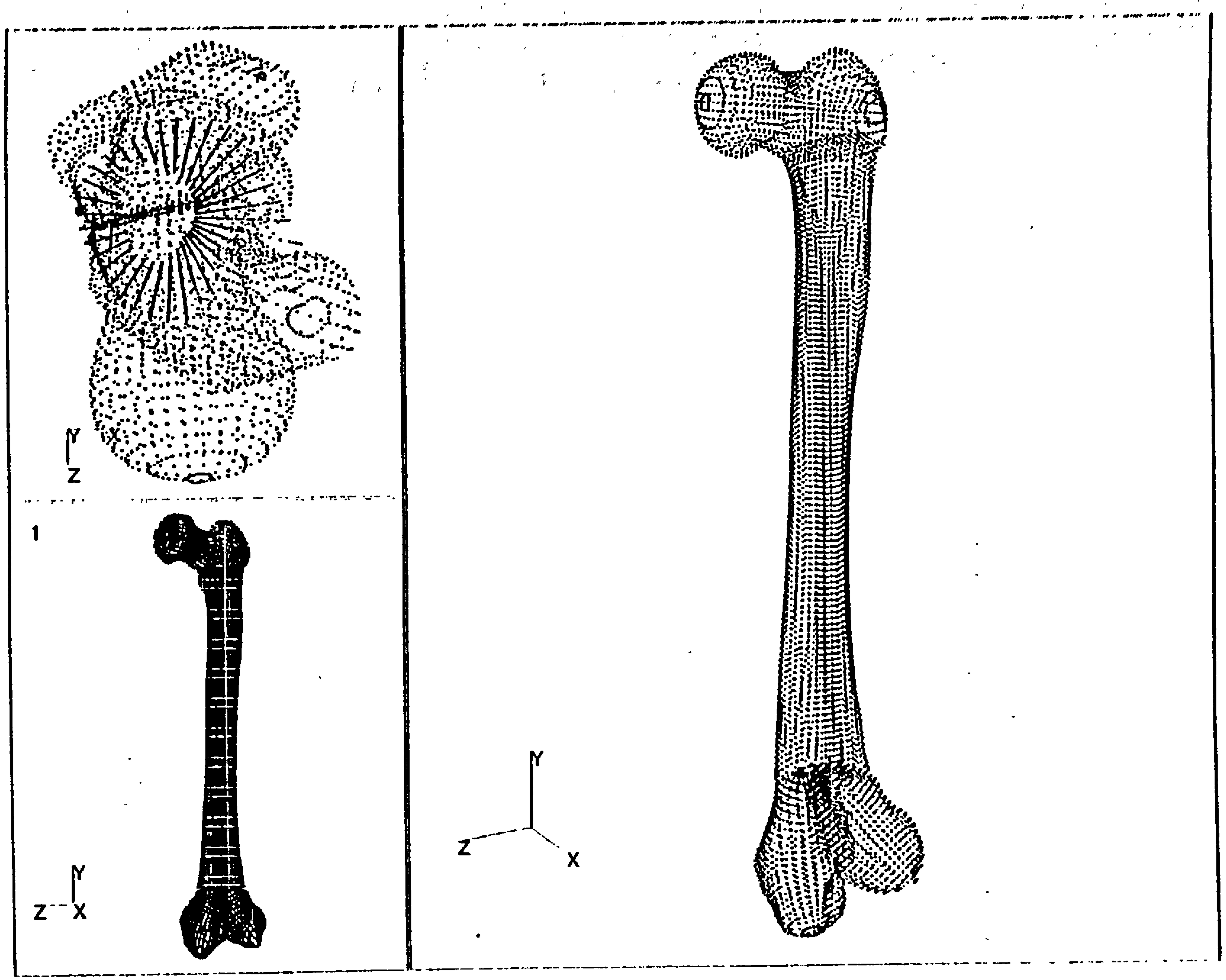

Fig. 8.4.5.5 Geometry of femur of cadaver 2-M-R represented in grid points using PATRAN.

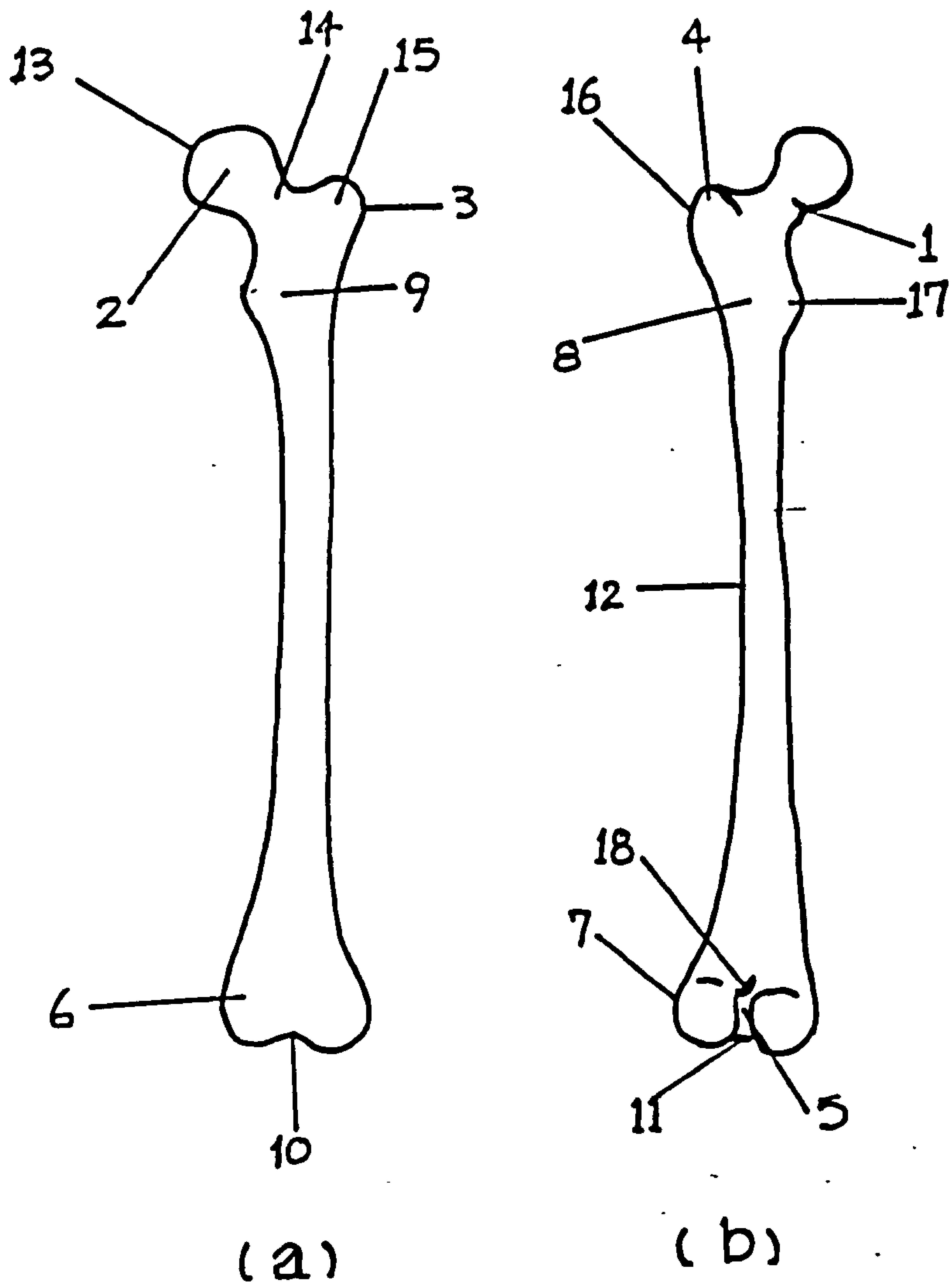

Fig. 8.5.1 Location of the 18 points selected on the femur for assessment of the accuracy achieved in the scaling procedure.
a.) Anterior view and b.) posterior view.

	Absolute difference comparing femur 2 and femur 3a.			Absolute difference comparing femur 2 and femur 3b.		
Locations	X (mm)	Y (mm)	Z (mm)	X (mm)	Y (mm)	Z (mm)
1	0.95	3.44	3.5	5.33	11.08	4.86
2	13.88	8.39	5.44	19.89	16.35	5.67
3	5.36	10.79	8.15	1.22	9.17	3.83
4	1.75	3.85	2.34	1.18	9.3	0.69
5	10.27	10.26	6.8	5.49	0.55	5.87
6	1.3	0.27	4.99	2.7	1.74	4.58
7	8.65	6.06	7.74	12.65	2.77	1.66
8	6.09	4.58	0.23	4.77	6.8	1.36
9	10.31	1.12	5.85	12.71	3.12	0.86
10	4.83	6.87	5.5	0.79	0.24	0.3
11	7.4	3.6	3.79	4.4	0.56	0.85
12	1.53	3.75	16.22	5.77	6.29	13.89
13	10.37	9.57	3.83	1.51	16.8	5.82
14	9.62	8.8	1.05	11.53	8.08	7.4
15	15.03	0.4	5.71	13.3	0.69	3.54
16	0.75	3.32	1.49	3.4	6.29	3.52
17	12.47	0.53	2.88	2.68	0.09	2.19
18	6.62	11.63	5.96	2.5	1.1	5.63
Average	7.06	5.4	5.08	6.21	5.61	4.03

Table 8.5.1 The absolute difference between the original femur of cadaver 2-F-L and the transformed femur 3a and 3b.

	Absolute difference comparing femur 2 and femur 3a.			Absolute difference comparing femur 2 and femur 3b.		
Locations	X (mm)	Y (mm)	Z (mm)	X (mm)	Y (mm)	Z (mm)
1	6.76	5.61	0.92	0.66	4.04	2.61
2	17.64	3.47	4.16	8.33	6.05	8.74
3	7.14	3.3	1.94	0.57	2.57	2.58
4	12.52	0.26	3.68	0.18	4.95	5.92
5	4.66	14.36	6.11	1.28	3.35	3.83
6	5.73	10.98	8.72	10.2	5.94	14.93
7	5.83	6.1	1.76	8.87	7.22	3.33
8	4.42	14.3	0.58	5.37	1.72	5.18
9	1.51	13.4	0.52	3.49	0.77	0.88
10	2.58	9.28	2.94	2.14	6.54	4.45
11	1.04	8.62	6.45	5.87	0.27	2.69
12	10.38	7.32	8.6	7.93	5.93	0.03
13	23.17	5.73	5.09	18.77	5.25	14.38
14	12.82	2.22	2.15	11.68	1.47	6.99
15	4.64	0.87	1.11	6.55	7.09	5.13
16	6.58	3.3	1.94	5.98	0.39	1.91
17	5.56	7.38	4.94	2.54	5.19	4.41
18	1.69	15.75	9.11	0.72	3.84	3.12
Average	7.48	7.34	3.93	5.61	4.03	5.06

Table 8.5.2 The absolute difference between the original femur 2 of cadaver 2-M-R and the transformed femur 3a and 3b.

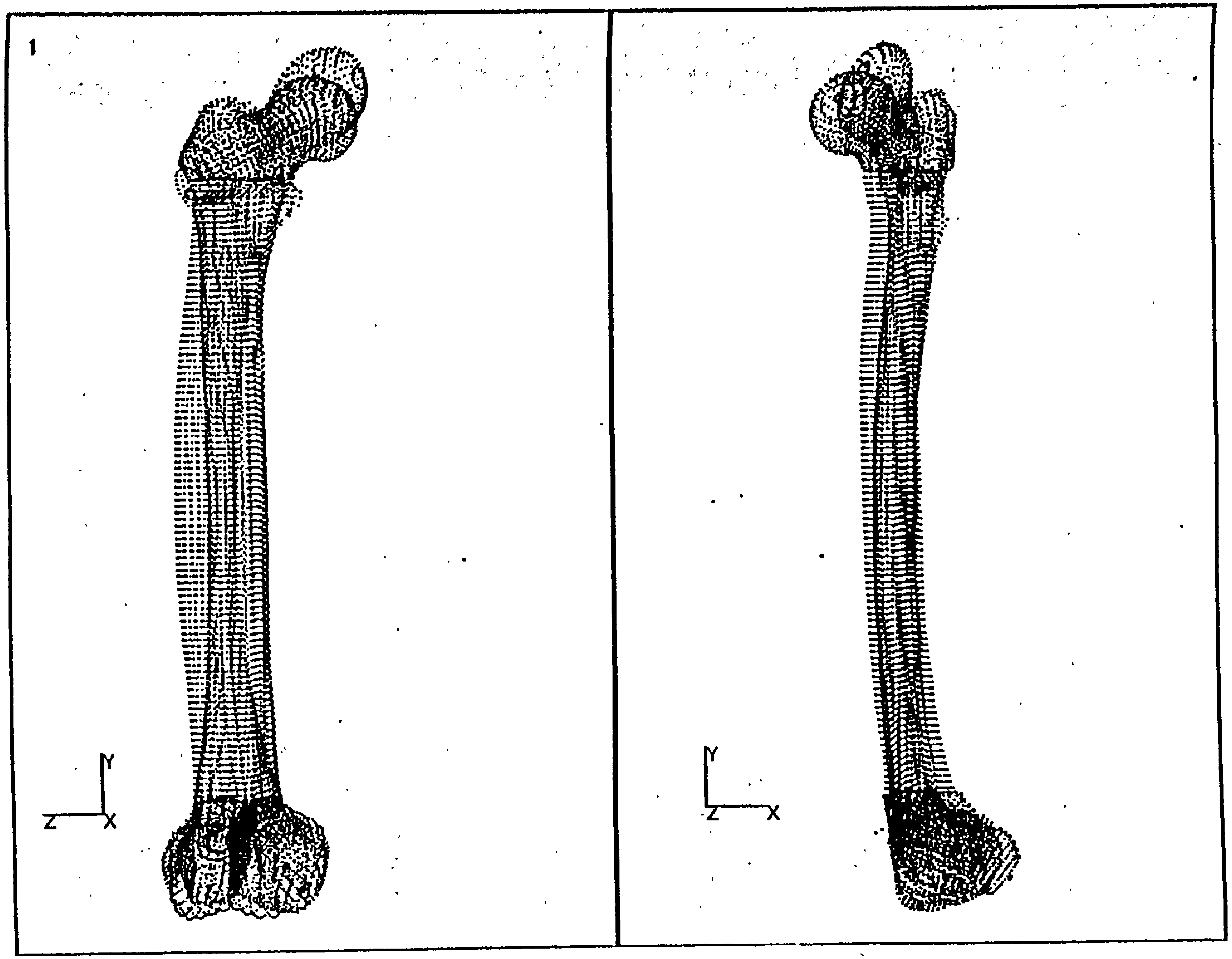

Fig. 8.5.2 Geometry of the transformed femur 3a superimposed on to the original femur 2 of cadaver 2-F-L.

Fig. 8.5.2 and Fig. 8.5.3 plot the transformed femur 3a and 3b superimposed over the original femur 2 for cadaver 2-F-L respectively. The transformed femur 3a and 3b for cadaver 2-F-L are also plotted in different views in Fig. 8.5.4 and Fig. 8.5.5 respectively. The transformed femora (3a and 3b) were geometrically distorted in several aspects. Comparing the two transformed femora to that of the original femur 2 of cadaver 2-F-L, as plotted earlier in Fig. 8.4.5.3, it can be seen that the transformation was not able to detect the curvature of the original femoral shaft in the coronal plane. In this plane, the transformed femora shaft appeared straight. Referring to table 8.5.1, point number 12 located on the femoral shaft recorded an absolute difference in the z-direction of 16.2 mm and 13.89 mm for femur 3a and 3b respectively. The overall cross section of the transformed femora shafts were also smaller than that in the original femur, which was probably due to the increased in the height of the transformed femur. The increase in height also caused the femoral head to be distorted in shape. The femoral head was elongated in the y-direction forming an elliptical ball shape. The transformed femoral condyles were able to maintain a shape very similar to that of the original femur, except for a reduction in the thickness of the condyles in the saggital plane i.e. dimension in the x-axis.

The plots of the transformed femora 3a and 3b superimposed on the original femur from cadaver 2-M-L are as shown in Fig. 8.5.6 and Fig. 8.5.7 respectively. Different views for femur 3a and femur 3b which can be compared to Fig. 8.4.5.5 (original femur 2 of cadaver 2-M-L) are plotted in Fig. 8.5.8 and Fig. 8.5.9. Generally throughout the whole femur, an increase in dimension was observed in the x-axis of the transformed femora. However at the coronal plane, the transformed femora showed a decrease in dimension in the z-axis. The difference in the y-axis between the transformed femora and the original femur were minimal. However, the minimal height change and the increased dimension in the x-axis of the transformed femora gave rise to a distorted femur. It subsequently caused the femoral head to appear flattened forming an elliptical ball with the long axis along the x-axis. However, in the case of femur 3a, the transformation has also caused the femur to be skewed approximately 45° in the saggital plane. The long axis of the elliptical femoral head of femur 3a thus lies at this angle. The condyles of the transformed femora also suffered

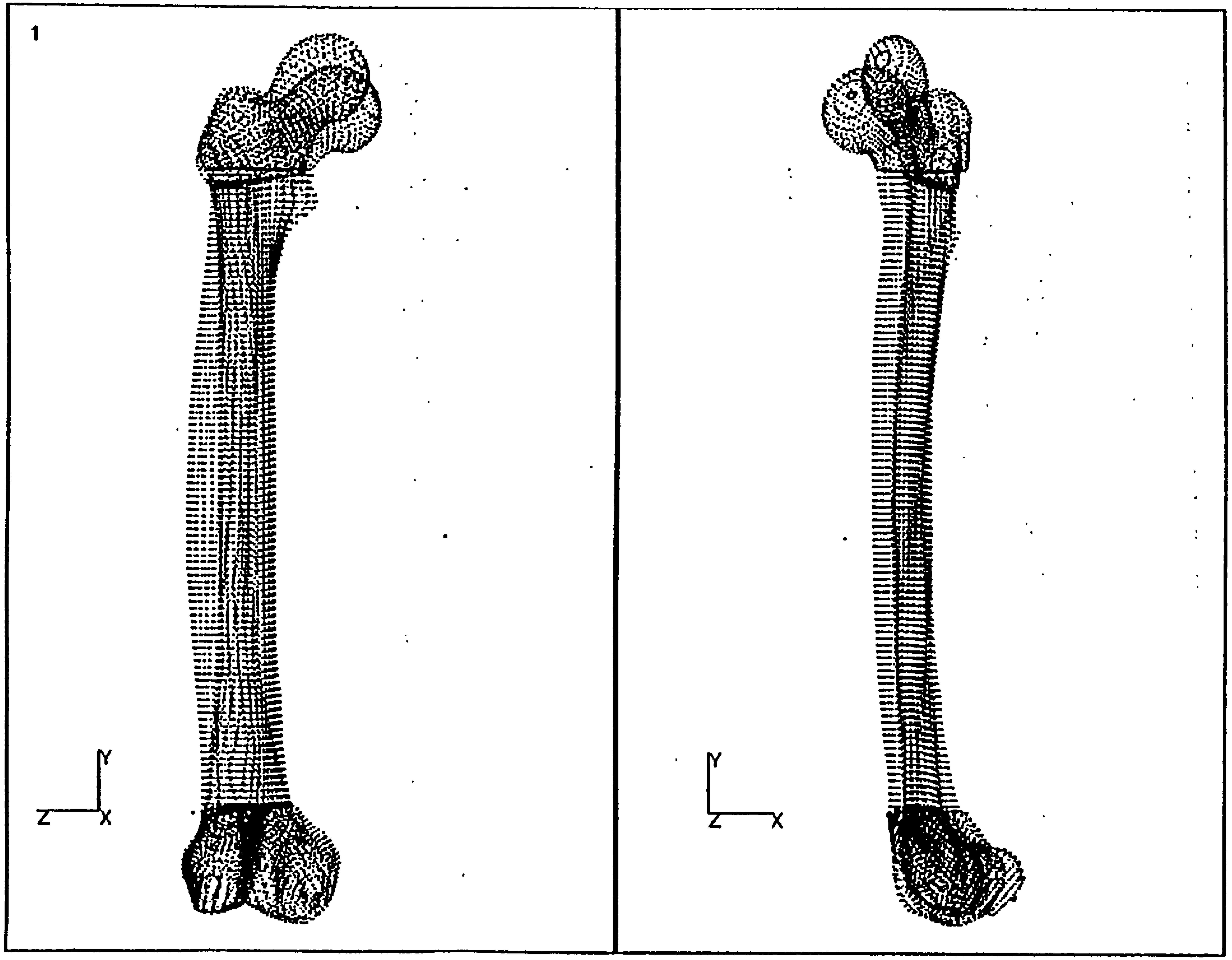

Fig. 8.5.3 Geometry of the transformed femur 3b superimposed on to the original femur 2 of cadaver 2-F-L.

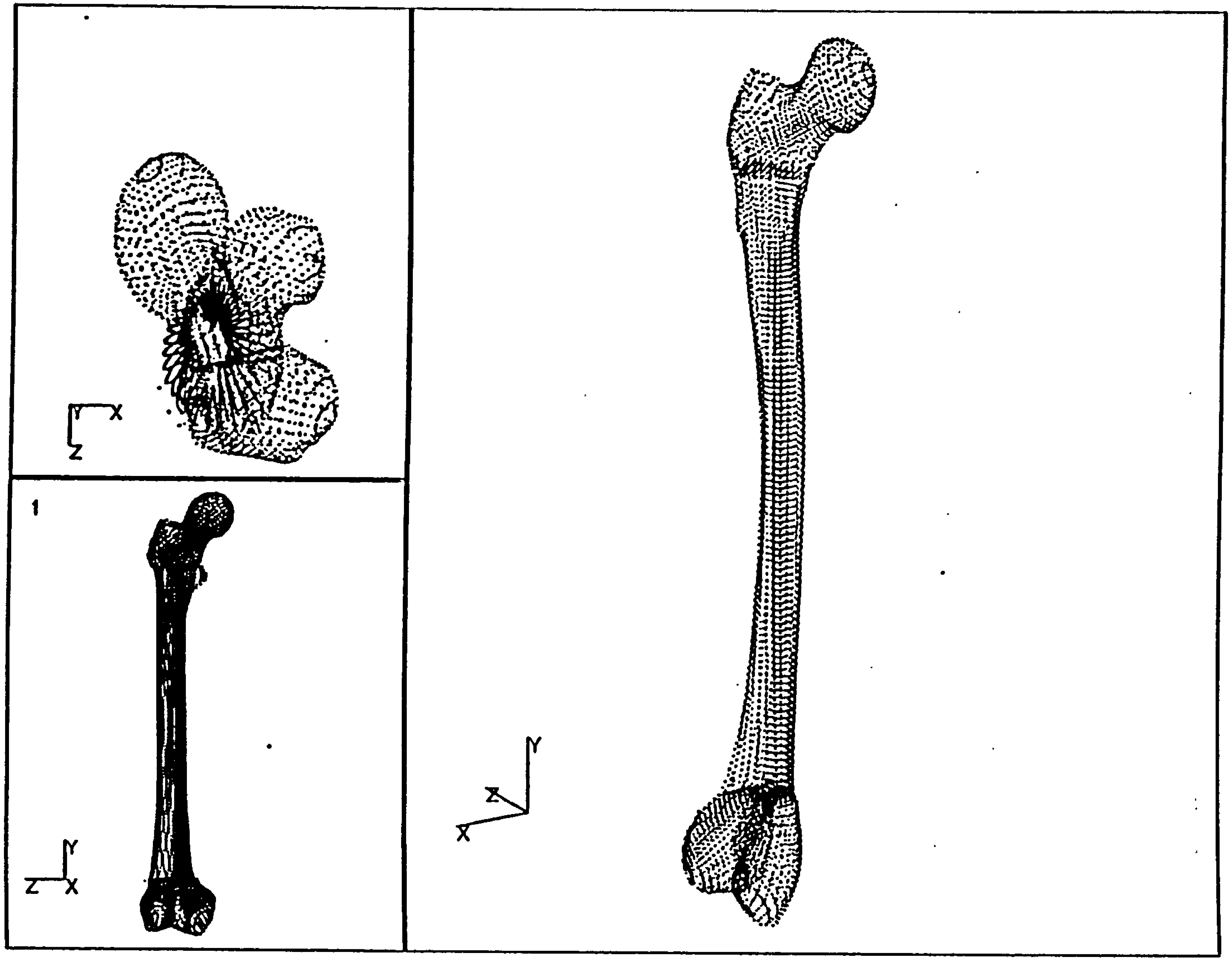

Fig. 8.5.4 Geometry of transformed femur 3a for cadaver 2-F-L.

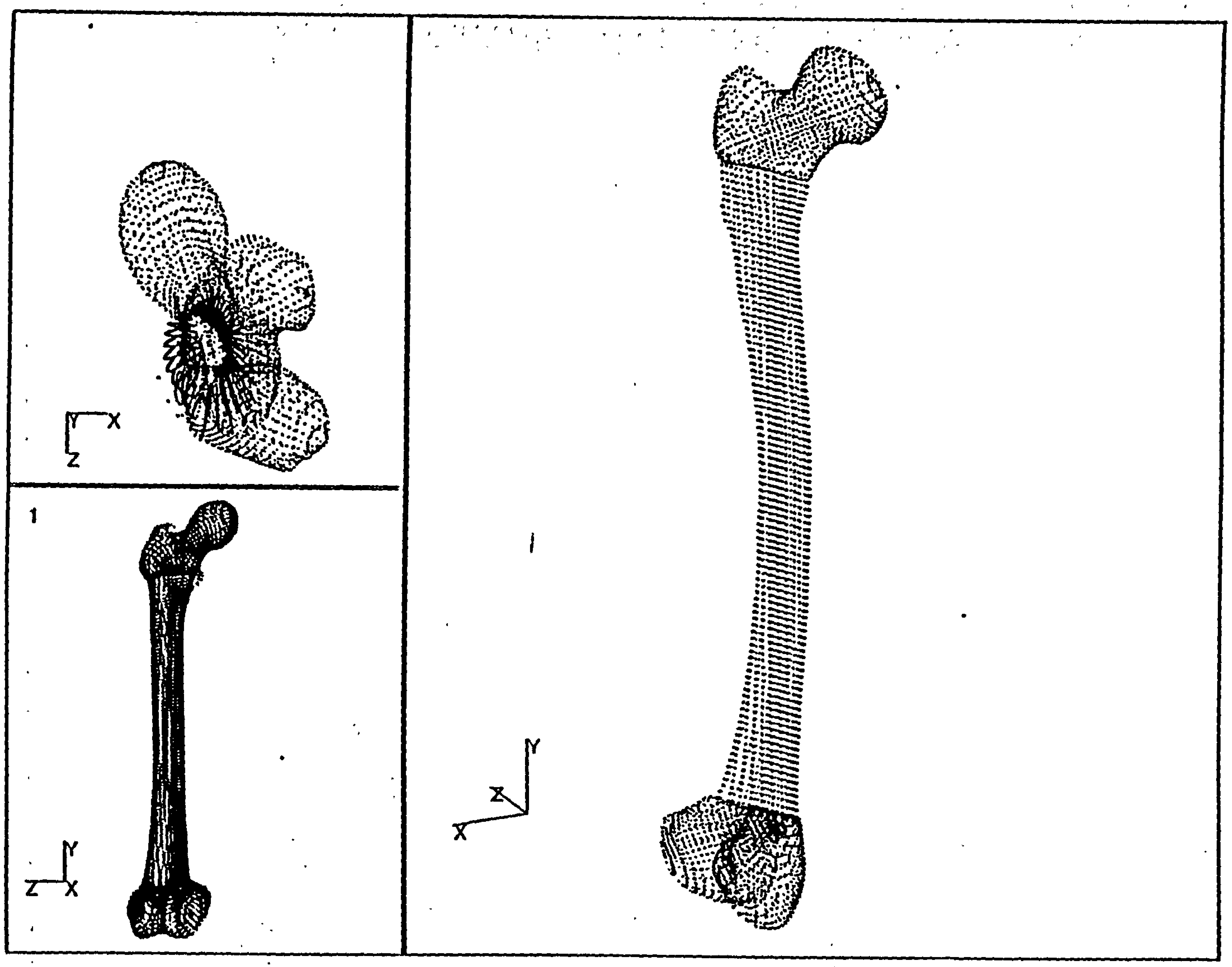

Fig. 8.5.5 Geometry of transformed femur 3b for cadaver 2-F-L.

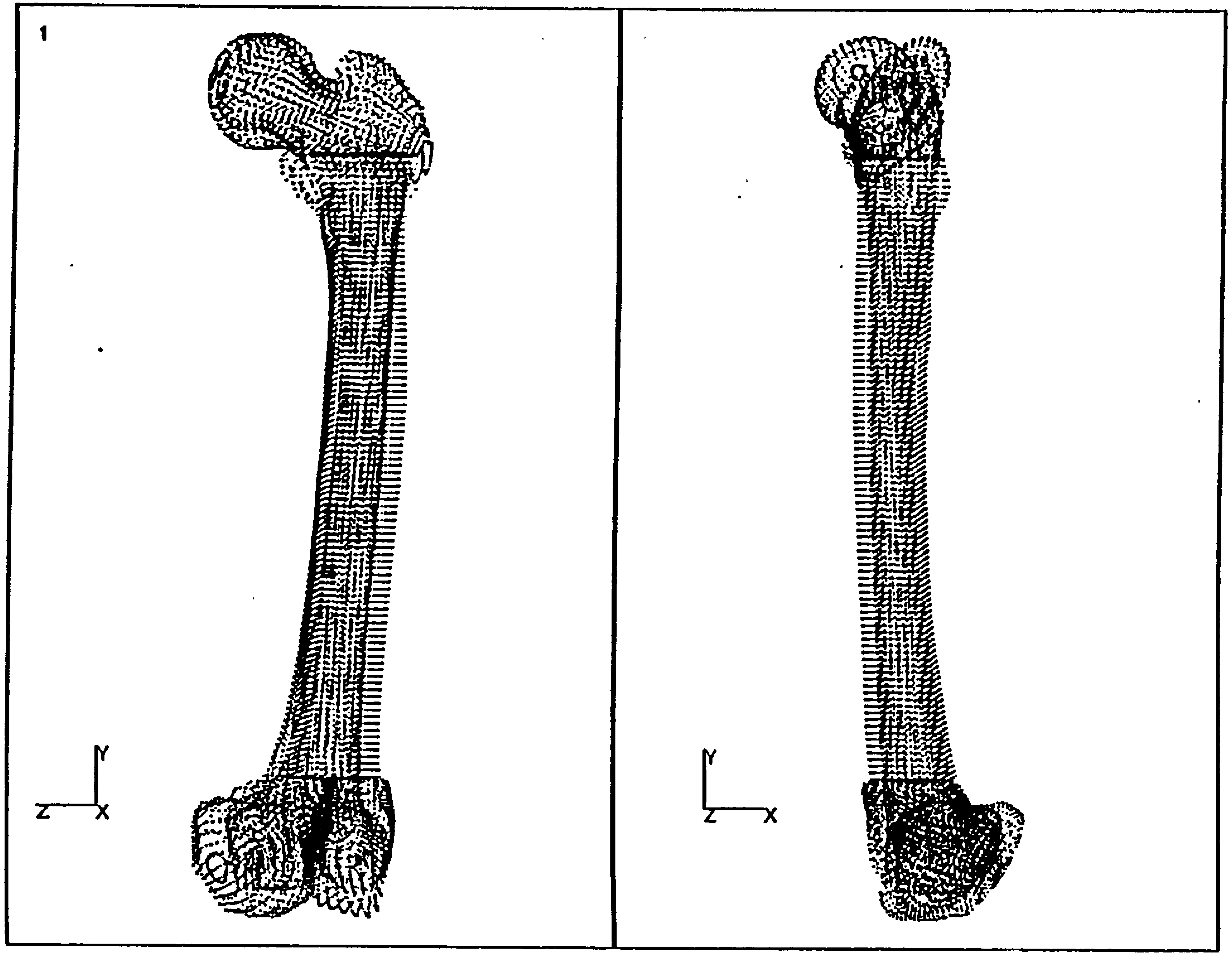

Fig. 8.5.6 Geometry of the transformed femur 3a superimposed on to the original femur 2 of cadaver 2-M-R.

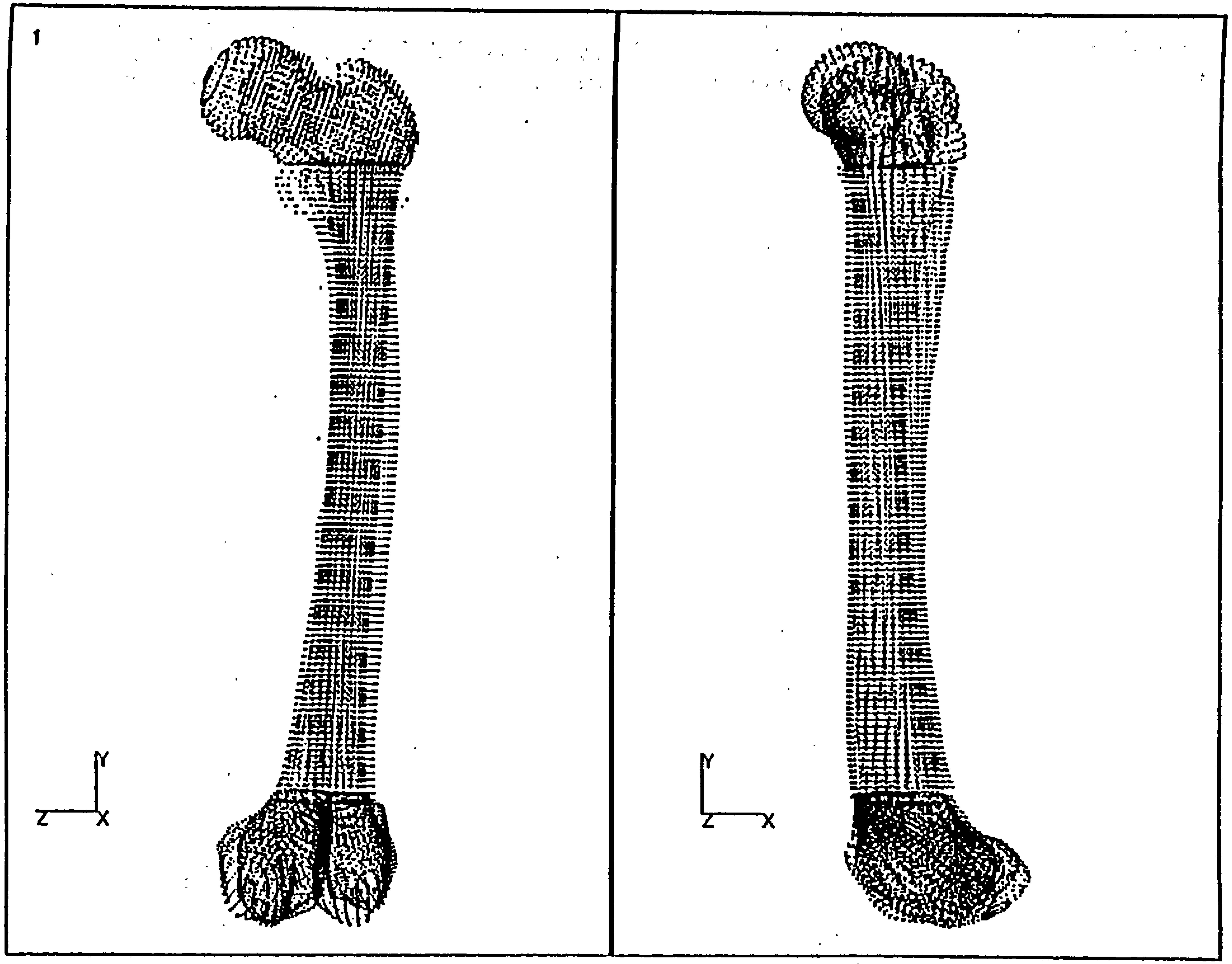

Fig. 8.5.7 Geometry of the transformed femur 3b superimposed on to the original femur 2 of cadaver 2-M-R.

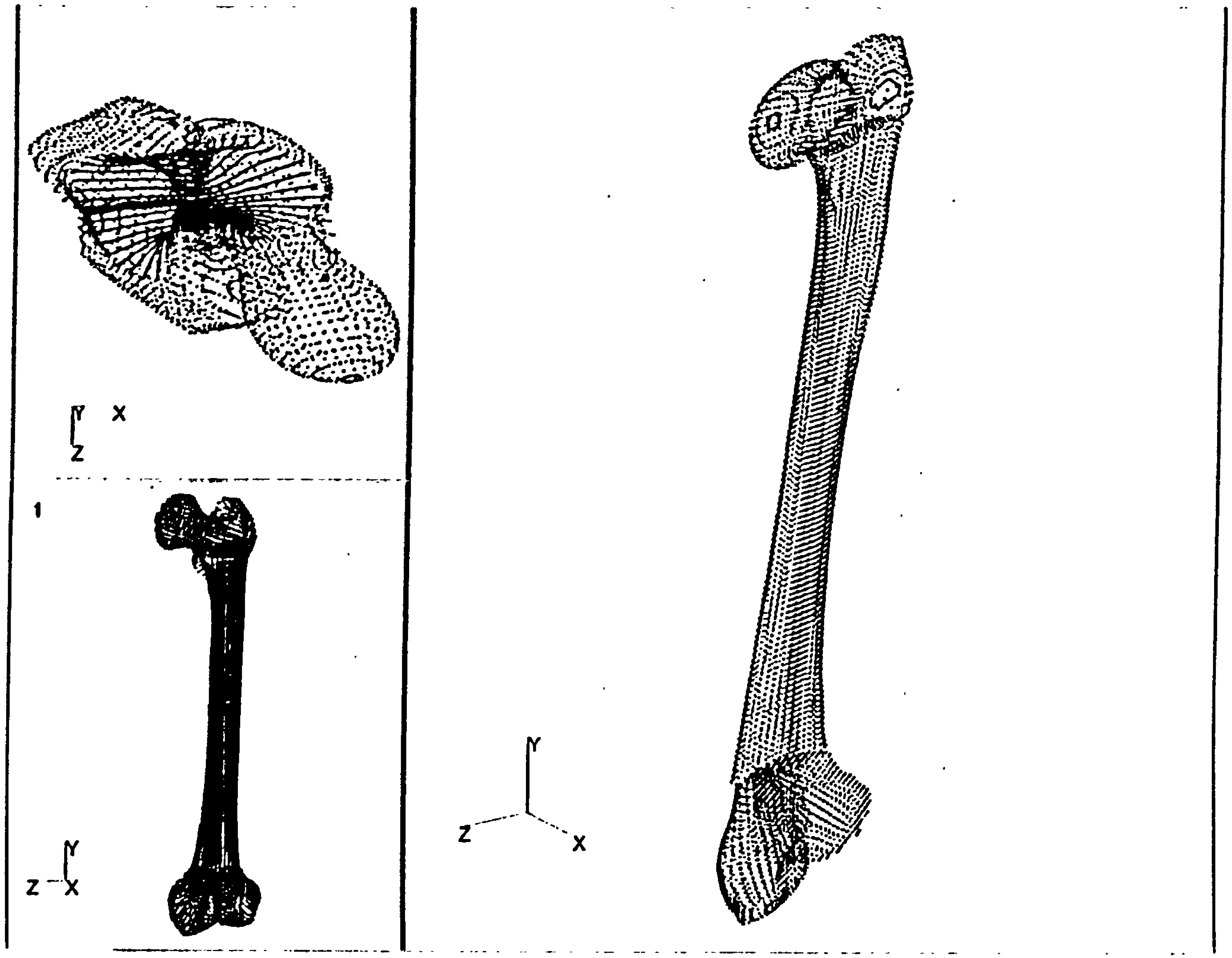

Fig. 8.5.8 Geometry of transformed femur 3a for cadaver 2-M-R.

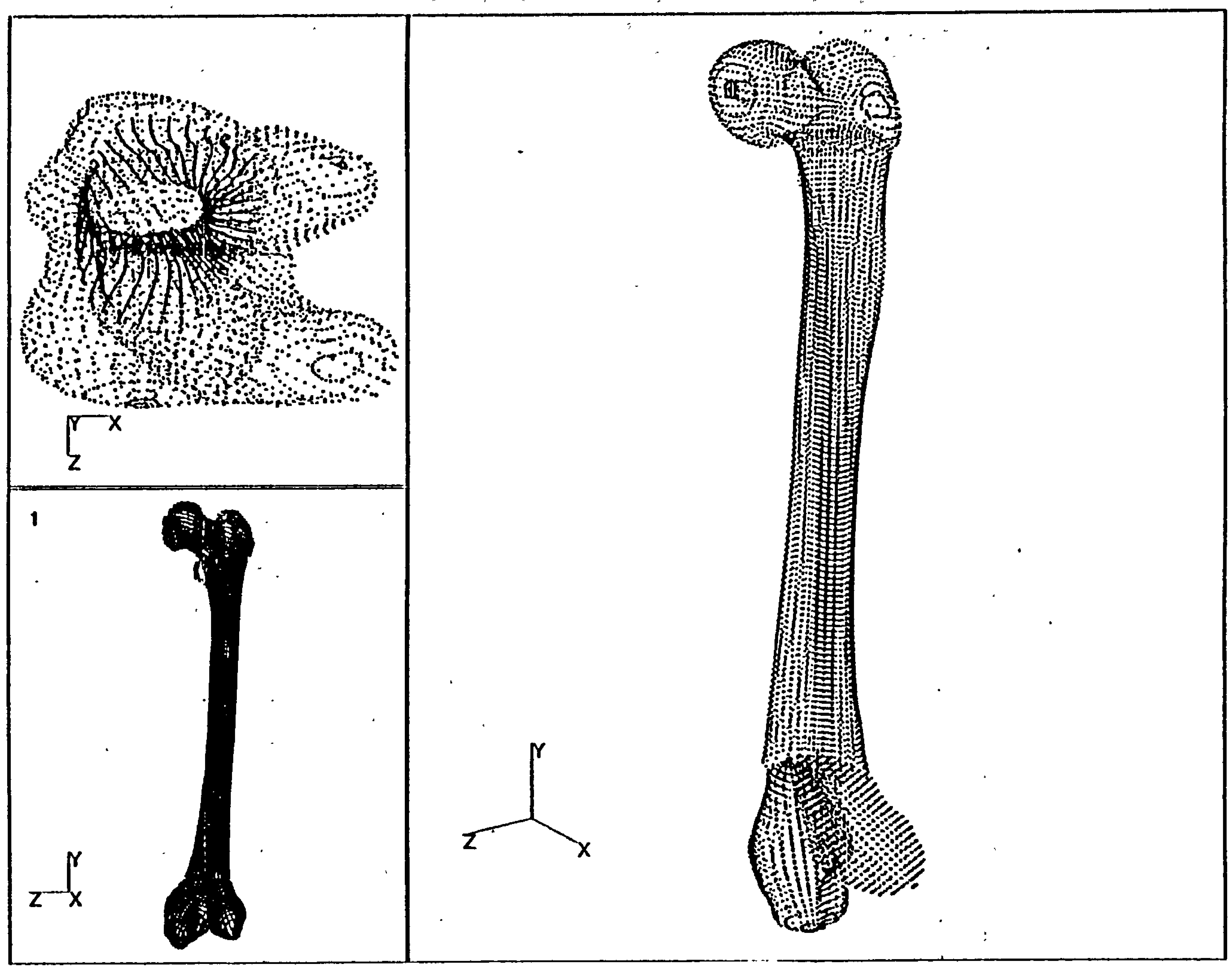

Fig. 8.5.9 Geometry of transformed femur 3b for cadaver 2-M-R.

similar distortion as that of the femoral head. The dimension in the x-axis has increased while the dimension in the z-axis was reduced slightly. The condyles were thus elongated along the x-direction. In the case of femur 3a, the elongation was maximum at an angle approximately 45° at the saggital plane.

8.6 FINITE ELEMENT MODEL OF THE FEMUR

The main purpose and potential of the transformed femur is its use in the creation of a FE model of a trans-femoral residual limb. However, as discussed in the previous section, the geometry of the transformed femur has deviated from the original femur in several aspects. Therefore proceeding with the creation of a FE model of the residual limb using the transformed femur is questionable and may require more work.

This section described further evaluation of the transformed femur using FE method. Three FE models of the femur were created based on geometry obtained previously using the scaling techniques. The femora modelled were (referring to Fig. 8.4.1.1),

a.) femur 2 (original femur)

b.) femur 3a (transformed femur)

c.) femur 3b (transformed femur)

The scaling test scaled femur 1 to femur 2 where the reference points in femur 2 were obtained with soft tissue intact (2a) and without soft tissue intact (2b). The procedures generated femur 3a and 3b respectively. In an ideal transformation femur 2, femur 3a and femur 3b would be the same, thus by comparing the stress patterns on the three supposed similar femora would lead to an understanding of the effectiveness and accuracy of the scaling technique for use in FE modelling.

8.6.1 Geometry

The geometry of the FE models created were based on the scaling of femur 1 (cadaver 1-M-R) to femur 2 (cadaver 2-M-R). In this evaluation, the scaling of the female cadavers (1-F-L and 2-F-L) were left out. Therefore, the FE model of femur 2 of cadaver 2-M-R being the original femur was compared to femur 3a and 3b

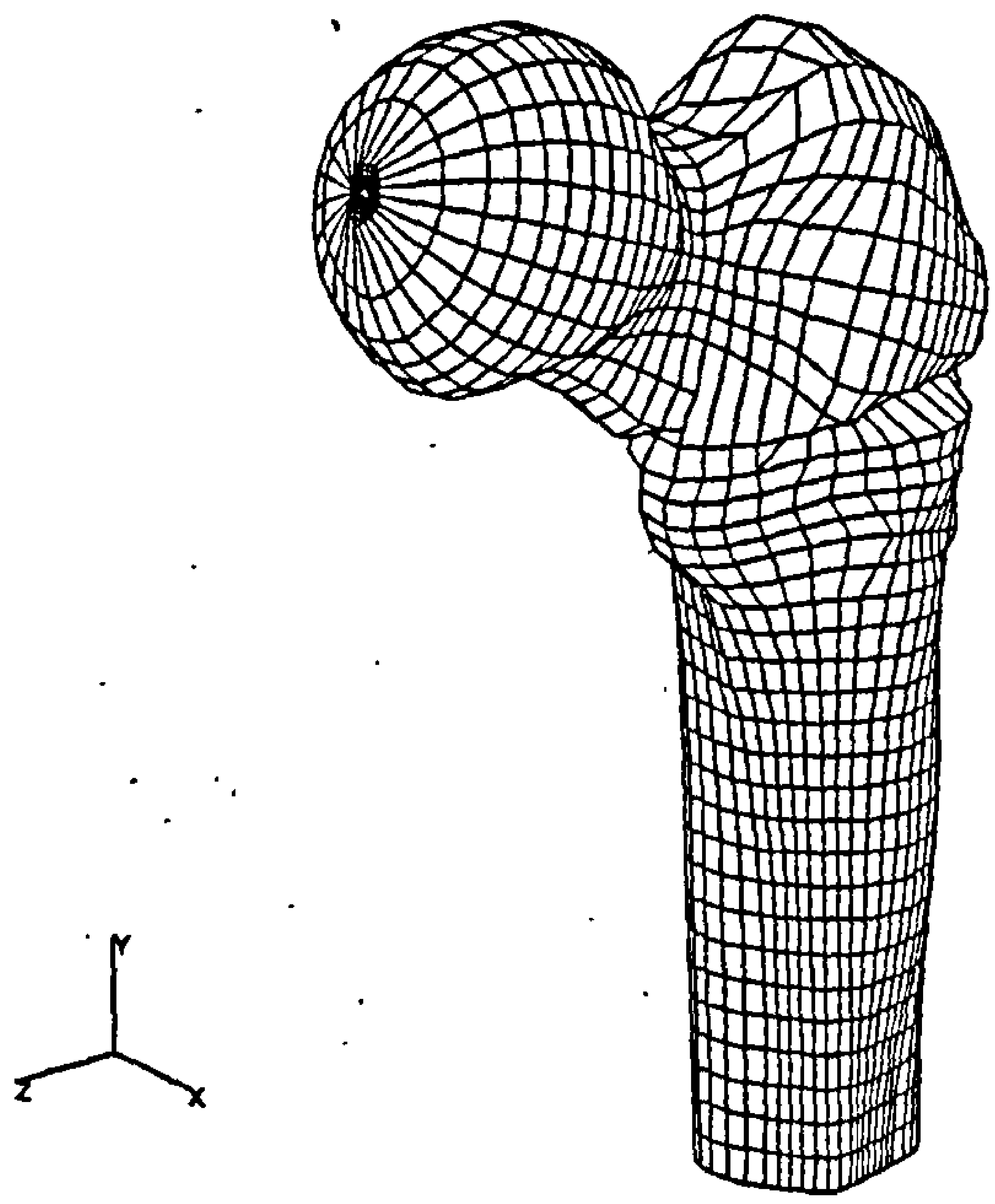

Femur 2

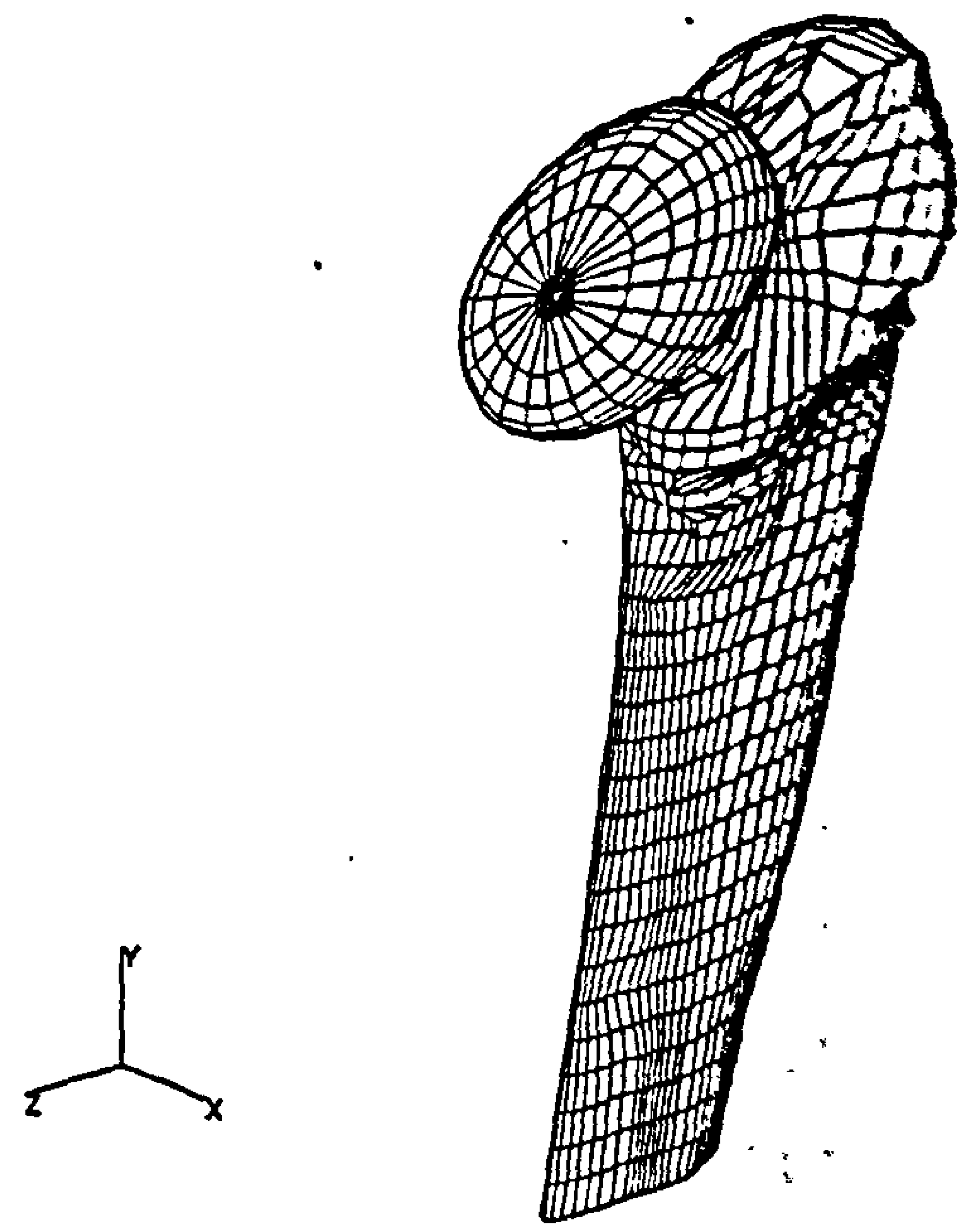

Femur 3a

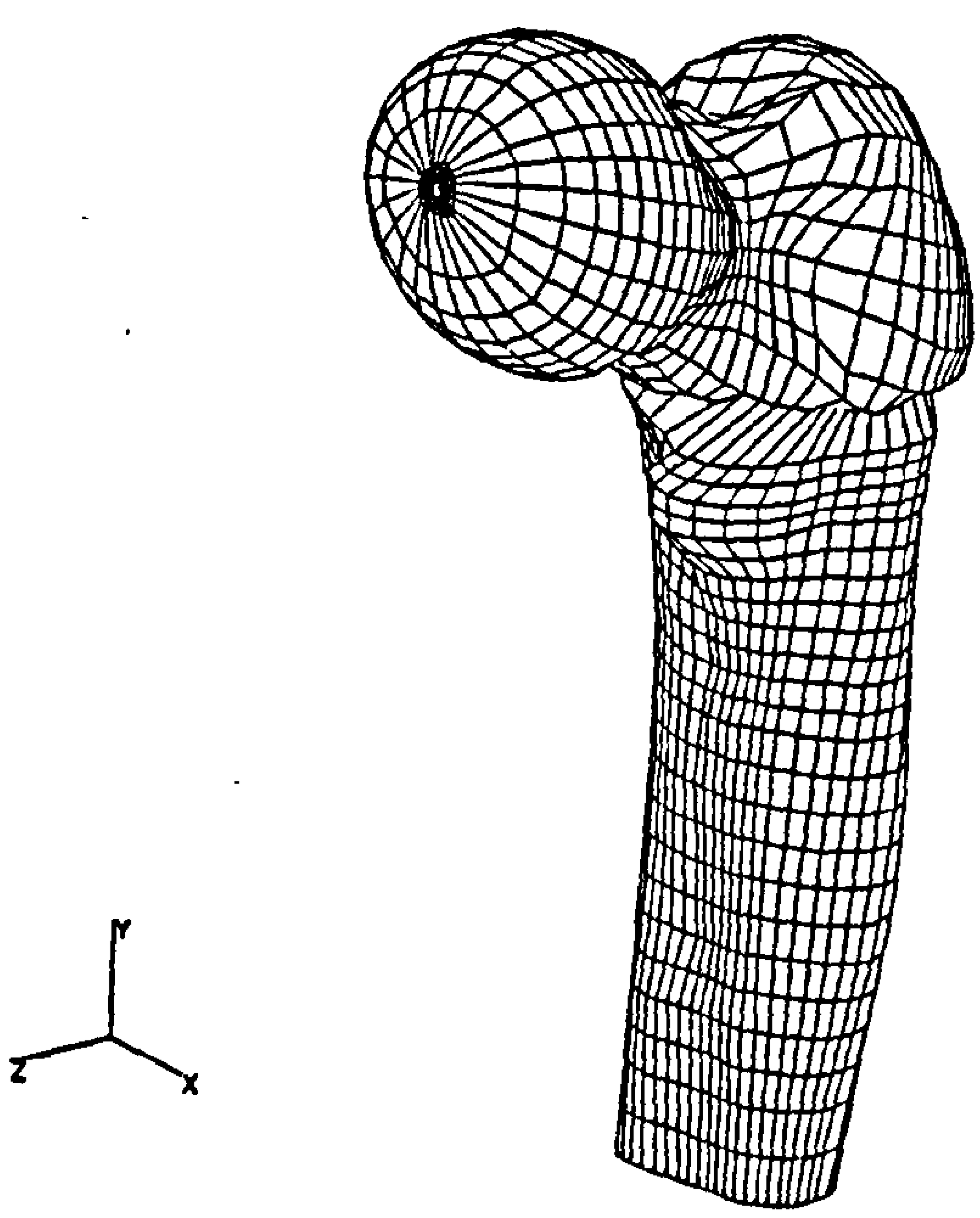

Femur 3b

Fig. 8.6.1.1 Finite element models of femur 2, 3a and 3b.

transformed from femur 1 of cadaver 1-M-R. From this point in the thesis, the three models will be identified as femur 2, 3a and 3b respectively. The FE models created consisted of the head-neck-trochanteric region and the proximal third of the shaft of the femur. The remaining shaft of the femur and the condyles were left out. The femur was assumed to be solid throughout its structure and no distinction was made between cortical and trabecular bone. Commercial Finite element codes were utilised, these were PATRAN as the pre and post processor and ABAQUS (Hibbitt, Karsson and Sorensen, Inc. USA) as the solver. The grid points as denoted in PATRAN in the scaling test, were used in creating the lines, areas and subsequently volumes for meshing with the finite elements. Three dimensional eight noded hexahedron elements (ABAQUS C3D8) were used.

The FE models of femur 2, 3a and 3b are as shown in Fig. 8.6.1.1. The anterior, posterior, medial and lateral view of the femoral model are also plotted in more detail in Fig. 8.6.1.2 and 8.6.1.3 and Fig. 8.6.1.4 respectively. The number of elements needed to construct femur 2, 3a and 3b were 5170, 5831 and 5260 and the corresponding number of nodes were 6601, 7201 and 6706 respectively.

8.6.2 Loading, boundary conditions and material properties

Load actions were applied to the greater trochanter and the head of the femur. The magnitude and direction of loads were based on experimentally measured loads at the hip joint taken from Rydell (1966). These loads are expressed schematically in Fig. 8.6.2.1. The proximal femoral model was assumed to be fixed at its cut distal end, i.e. potted. Hence, all the nodes at the distal end surface were fixed in the x, y and z directions. The material properties of the femur were assumed to be isotropic, linear elastic and homogeneous. The Young's modulus was 15.5 MPa and the Poisson's ratio 0.33.

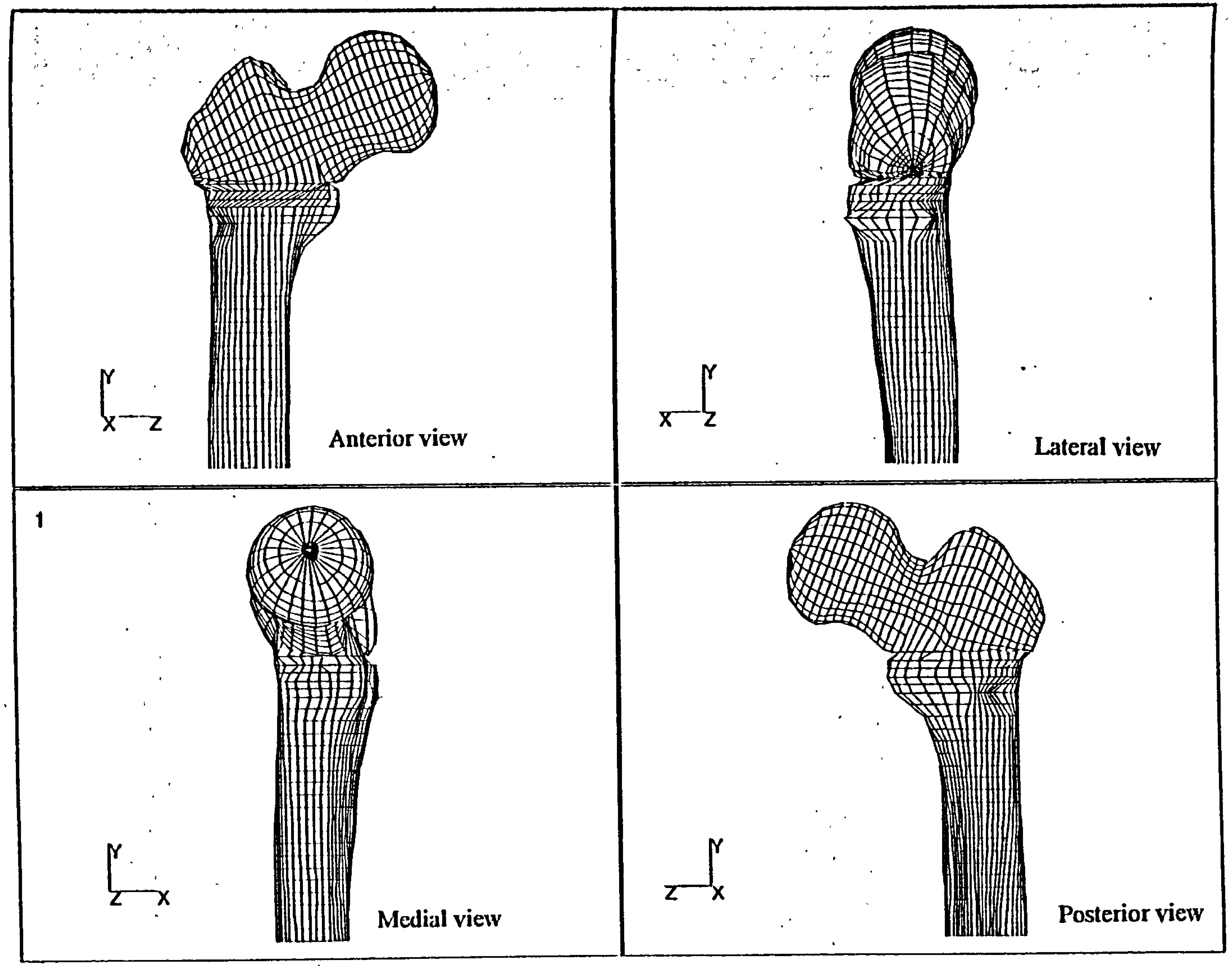

Fig. 8.6.1.2 Finite element model of femur 2.

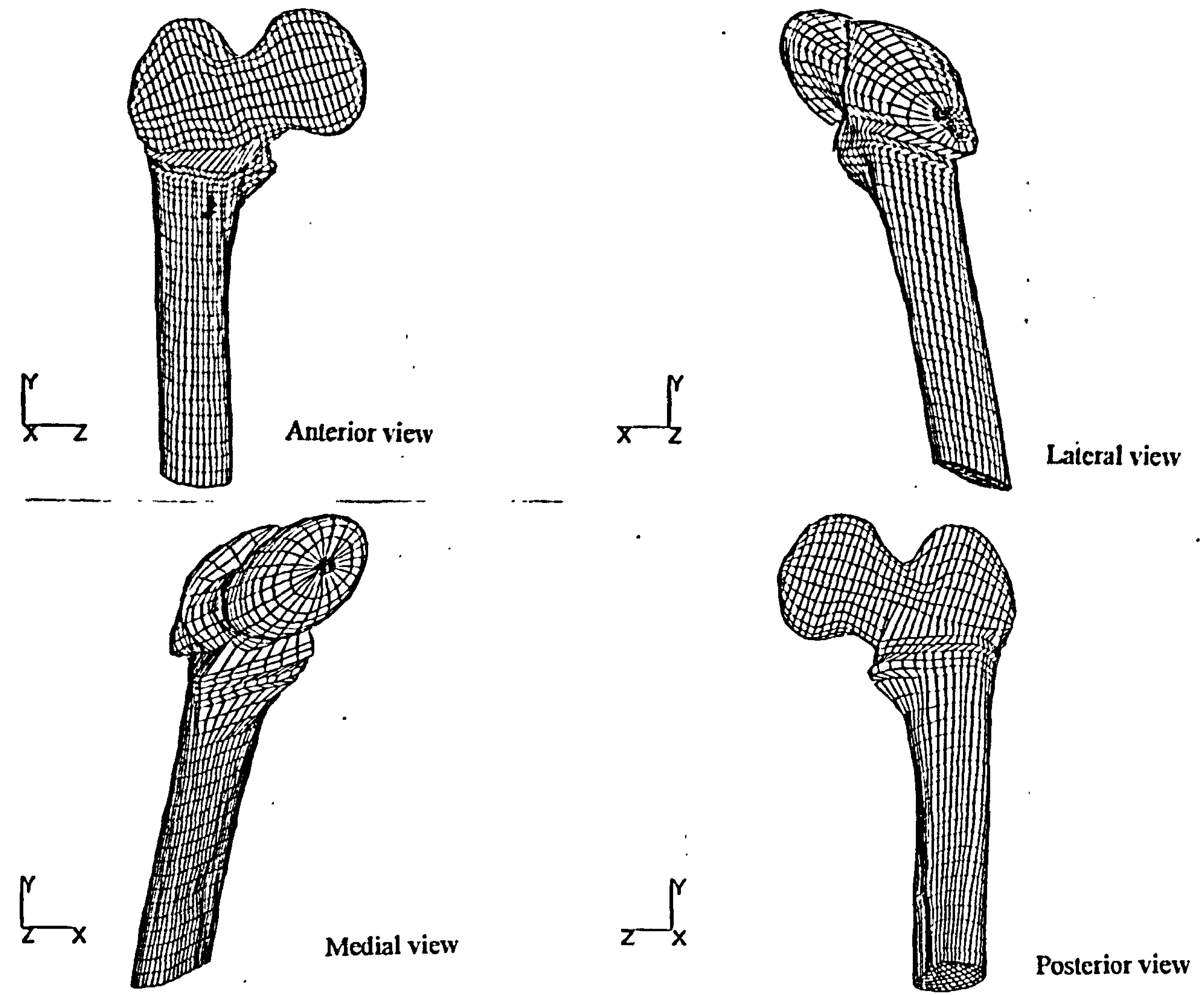

Fig. 8.6.1.3 Finite element model of femur 3a

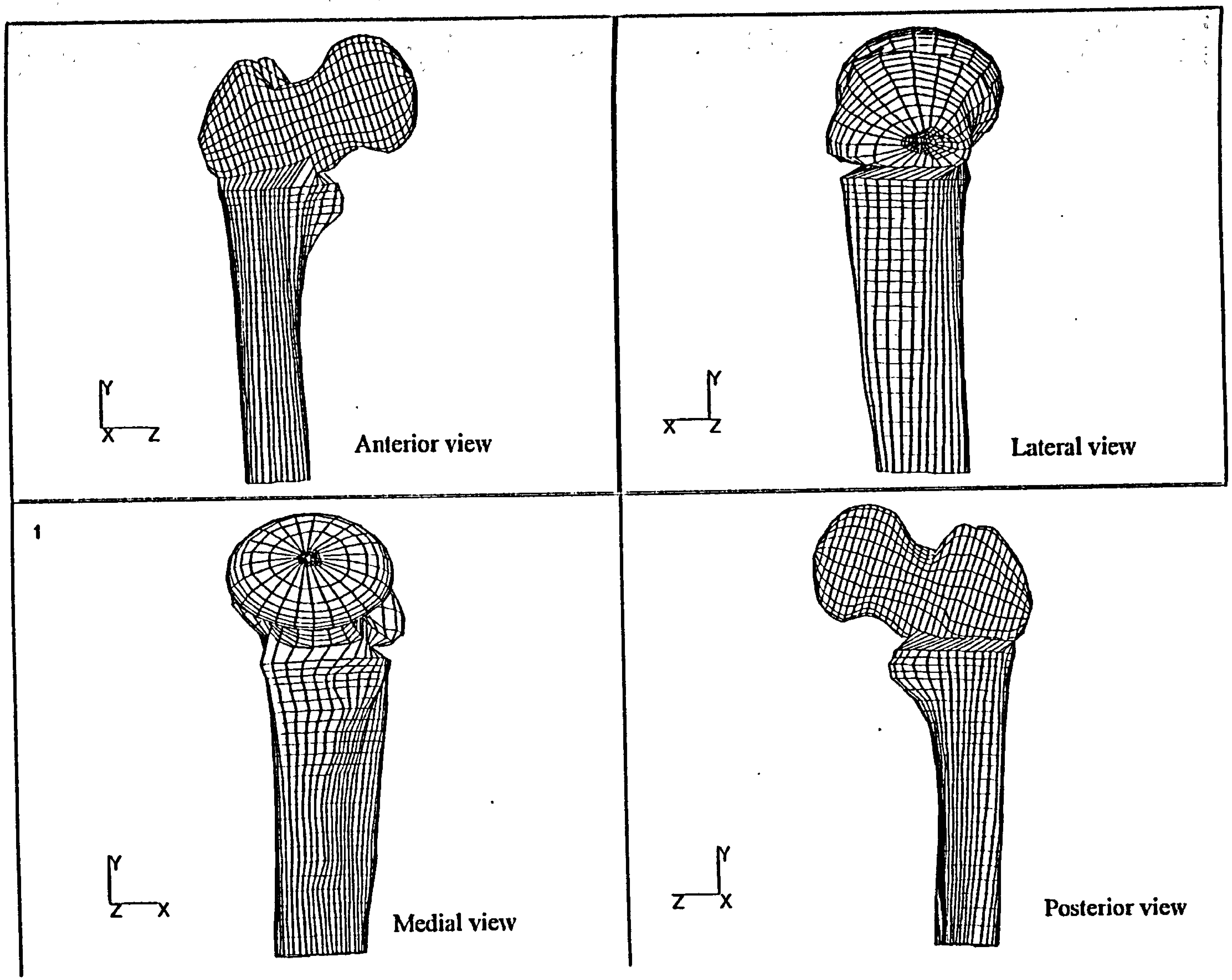

Fig. 8.6.1.4 Finite element model of femur 2.

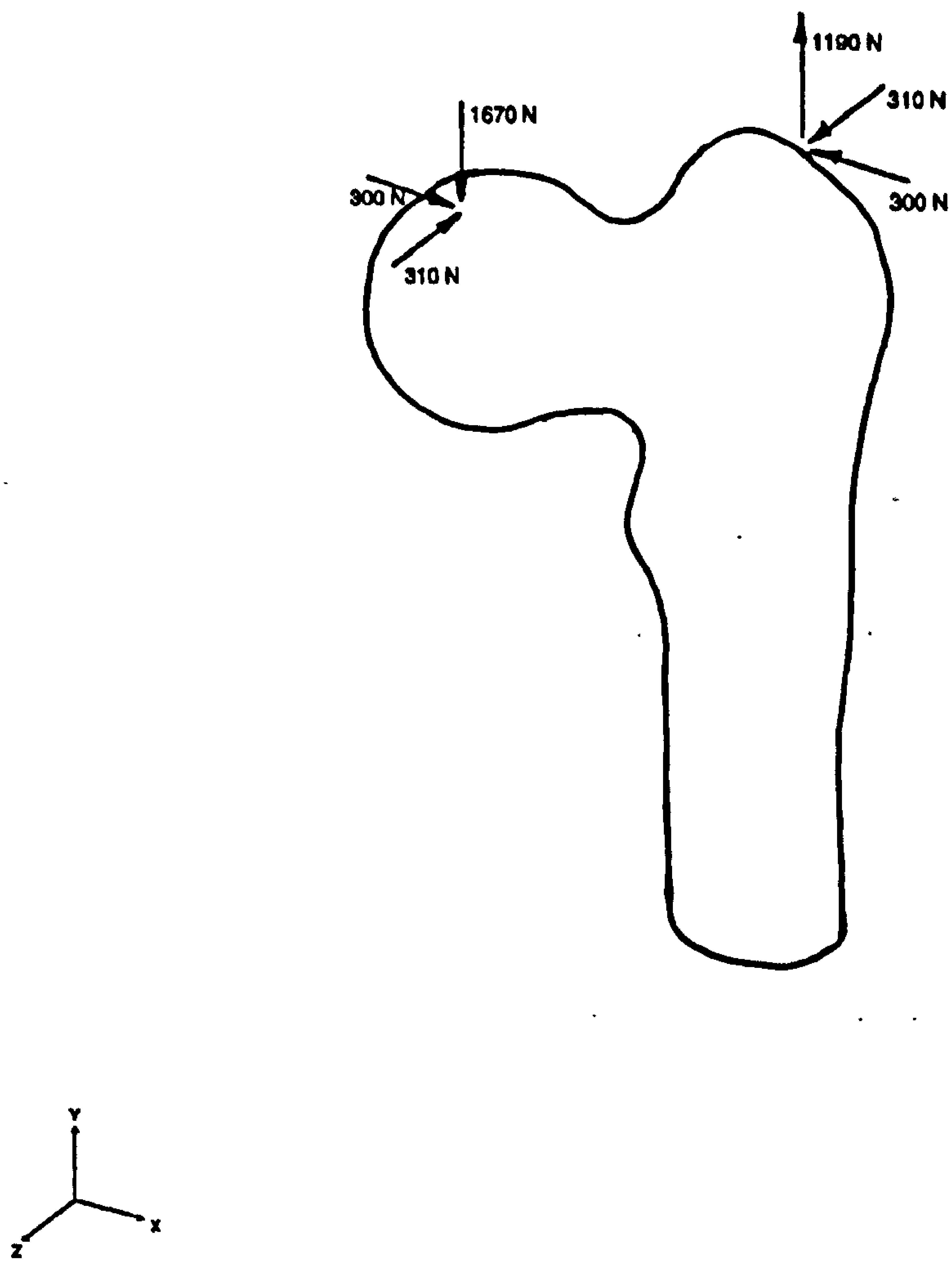

Fig. 8.6.2.1 Loading and boundary conditions introduced to the femoral FE model.

8.7 RESULTS OF THE FINITE ELEMENT MODEL

8.7.1 Displacements

The load actions introduced caused the femur to bend in the z-y plane or the coronal plane. Maximum displacement was thus recorded in the z - direction at femoral head. Fig. 8.7.1.1, 8.7.1.2 and 8.7.1.3 show the undeformed and deformed femur 2, 3a and 3b in two planes. The nodal displacements in the plots are amplified 20 times.The maximum displacment recorded in the z direction at the femoral head of femur 2, 3a and 3b were 1.51 mm, 2.07 mm and 1.96 mm respectively. The bending in the coronal plane has the effect of lowering the femoral head, which caused a displacement in the negative y-direction. The predicted values for the three femur in the y-direction were -0.62 mm, -1.61 mm and -0.63 mm respectively. In the x-direction, a negative displacement was predicted for femur 2 while femur 3a and 3b recorded positive displacements. However, the magnitude of displacements were minimal for femur 2 and 3b at -0.164 mm and 0.003 mm respectively. In femur 3a, the predicted displacement was 0.85 mm.

8.7.2 Stresses

The load actions introduced at the head and at the greater trochanter of the femoral bone produced maximum bending stress at the shaft. The maximum compressive stress was predicted at the medial side and tensile stress at the lateral side of the bone. The stress distribution is somewhat similar to that of loading a cantilever beam causing bending, with one end fixed and the other end loaded. The bending stress or stress in the y- direction of femur 2, femur 3a and femur 3b are plotted in Fig. 8.7.2.1, 8.7.2.2 and Fig. 8.7.2.3 respectively. All the three contour plots are displayed using the same stress contour level to enable comparison between one another. In the original femur 2, the maximum compressive and tenslie stresses were found at the fixed distal end of the femur to be -35.4 N/mm^2 and 34.2 N/mm^2 respectively. The stresses at the femoral shaft were almost symmetrical in pattern and magnitude. The head and the neck of the femur were mostly under low compressive stresses. Compressive stresses began to increase in magnitude at the neck just above the lesser trochanter and continued to spread in increasing magnitude to the fixed end

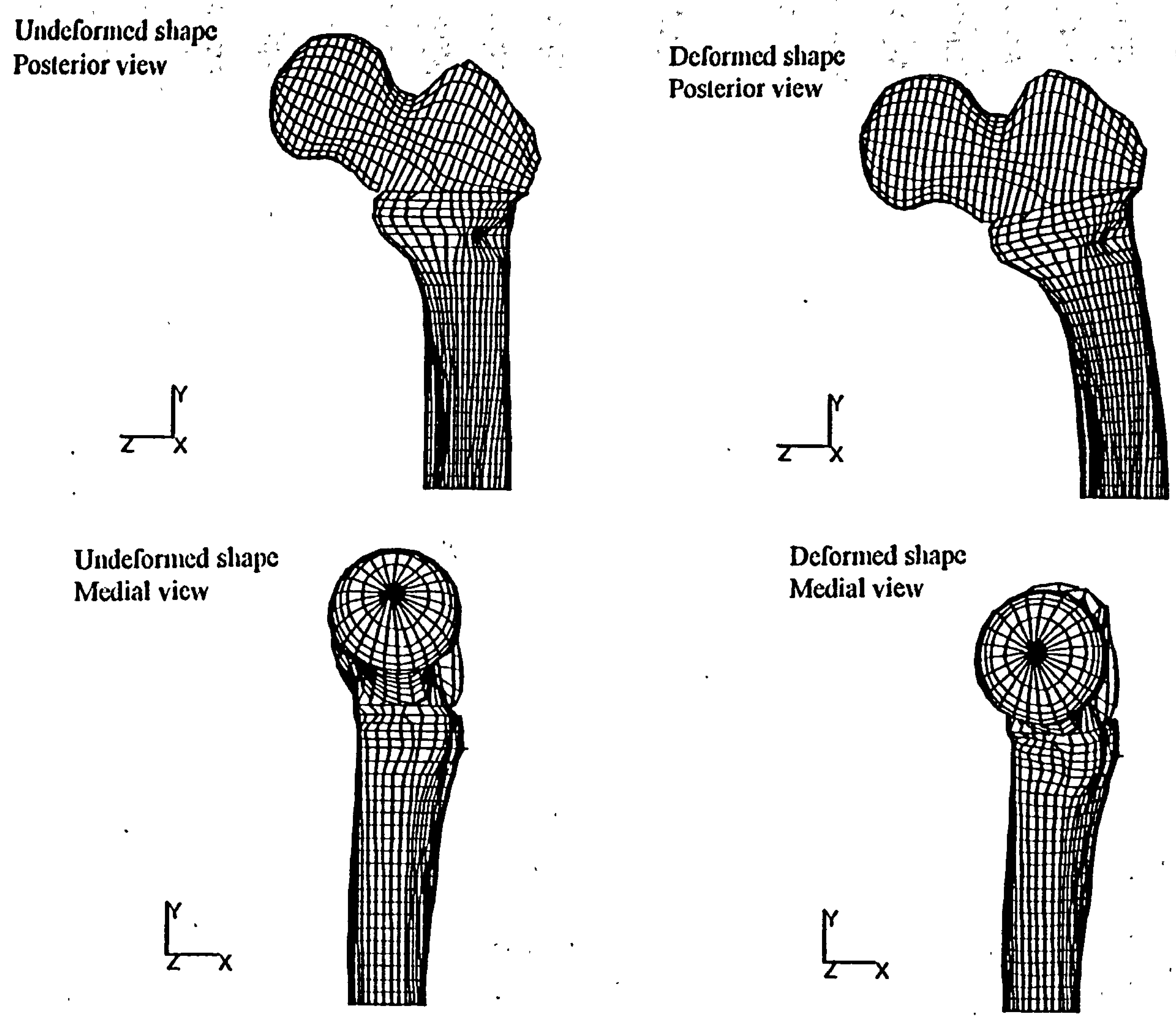

Fig. 8.7.1.1 Predicted deformation of model femur 2.

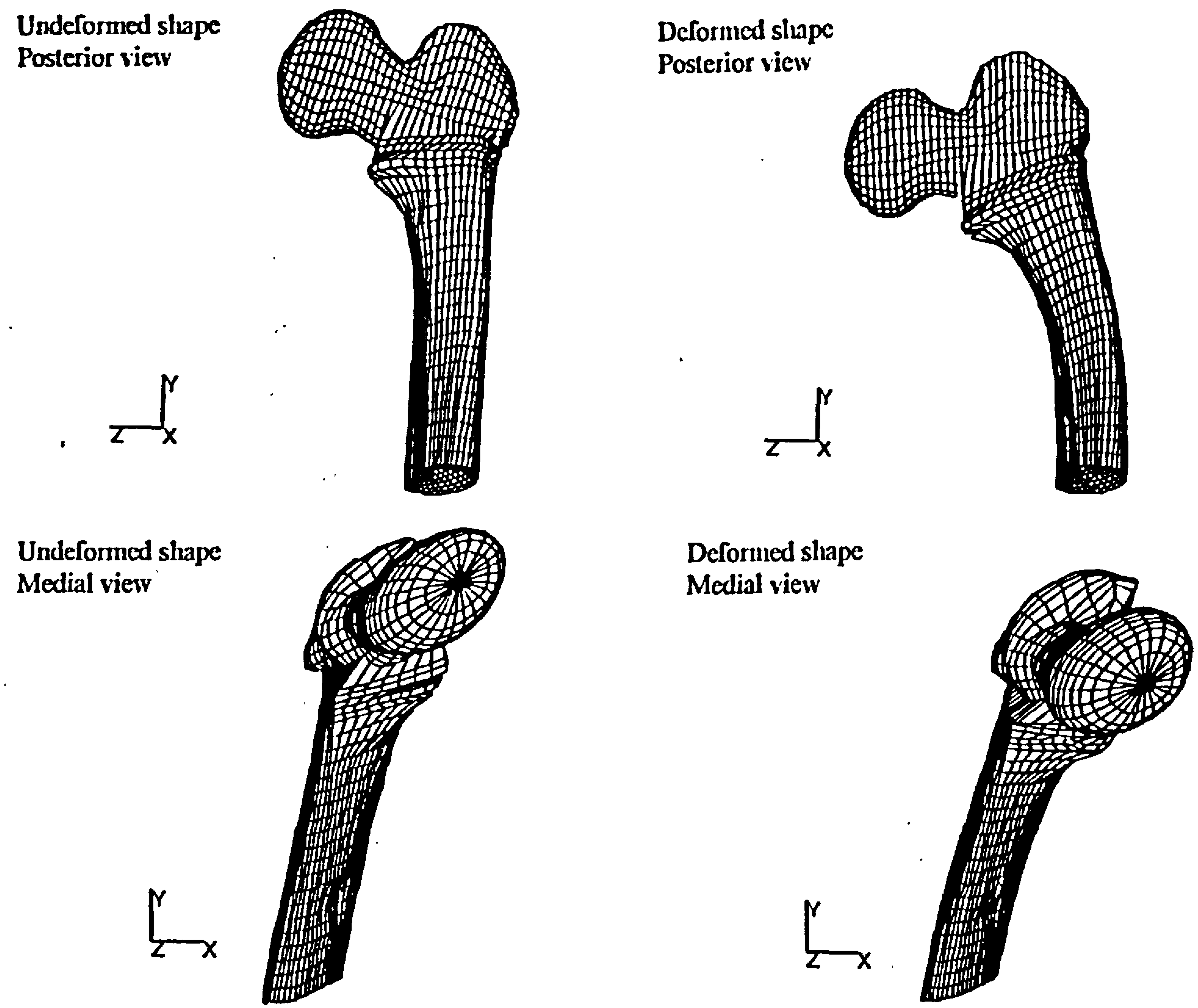

Fig. 8.7.1.2 Predicted deformation of model femur 3a.

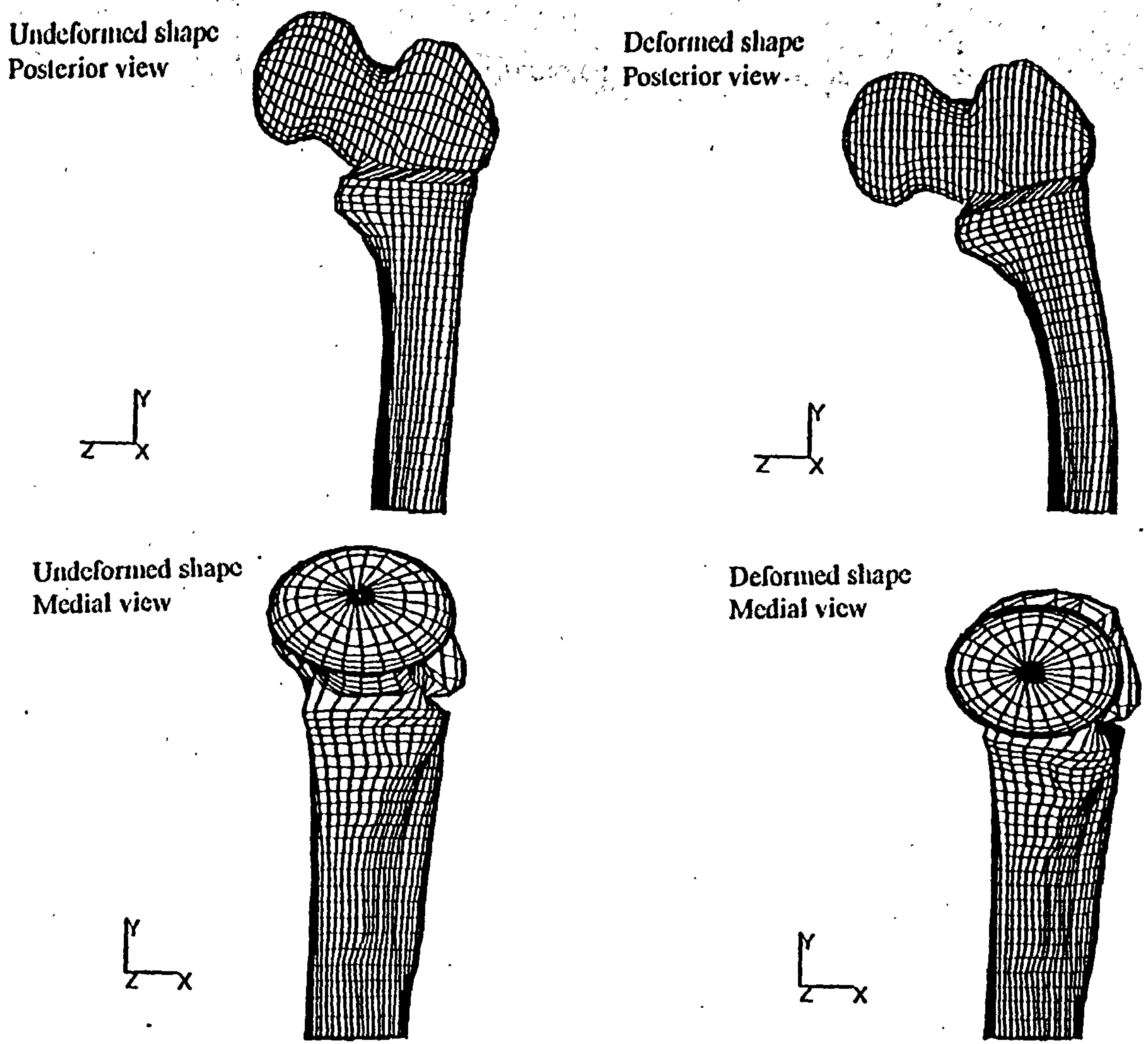

Fig. 8.7.1.3 Predicted deformation of model femur 3b.

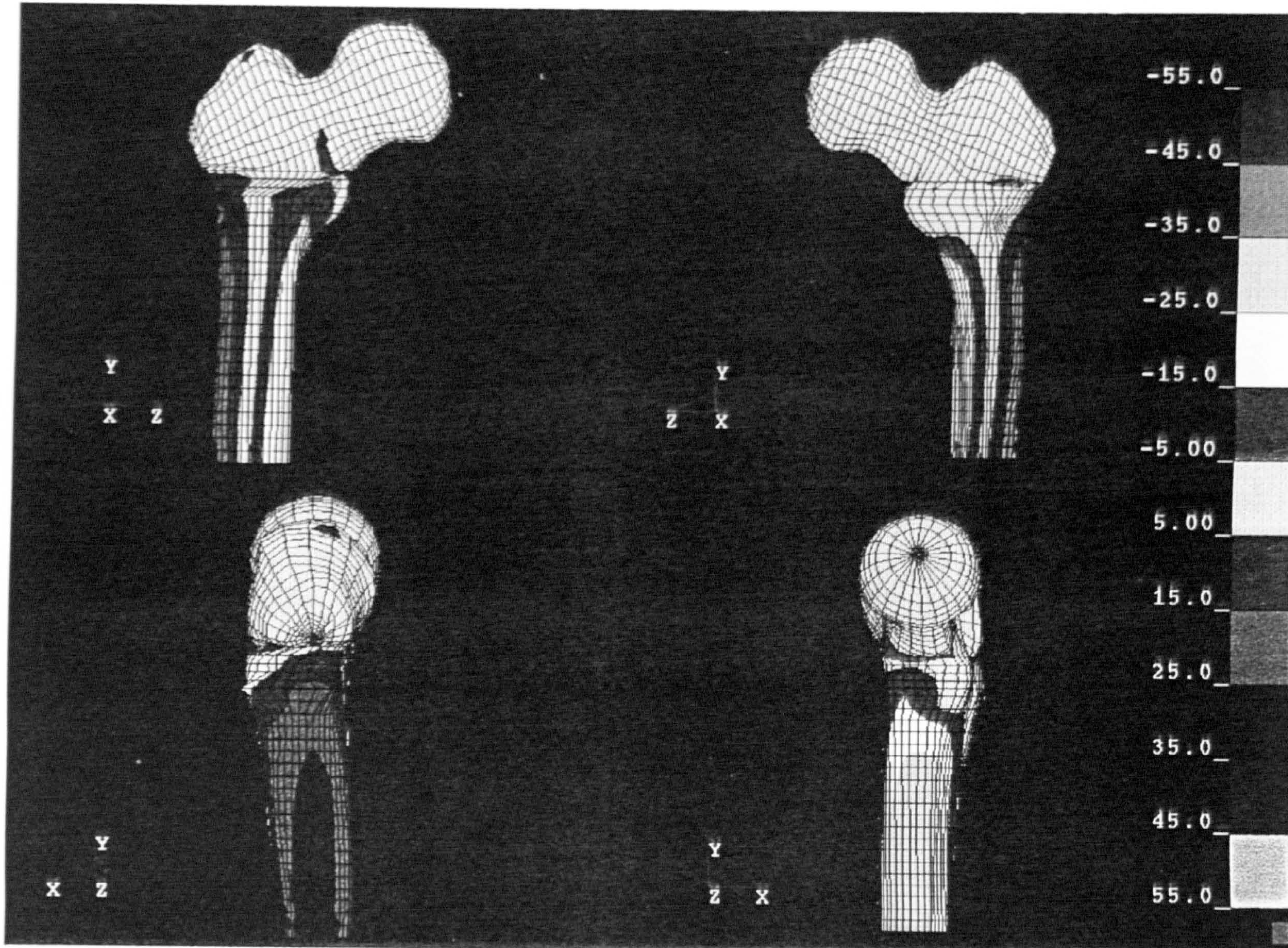

Fig. 8.7.2.1 Stress distribution in the y-direction for femur 2 in N/mm^2.

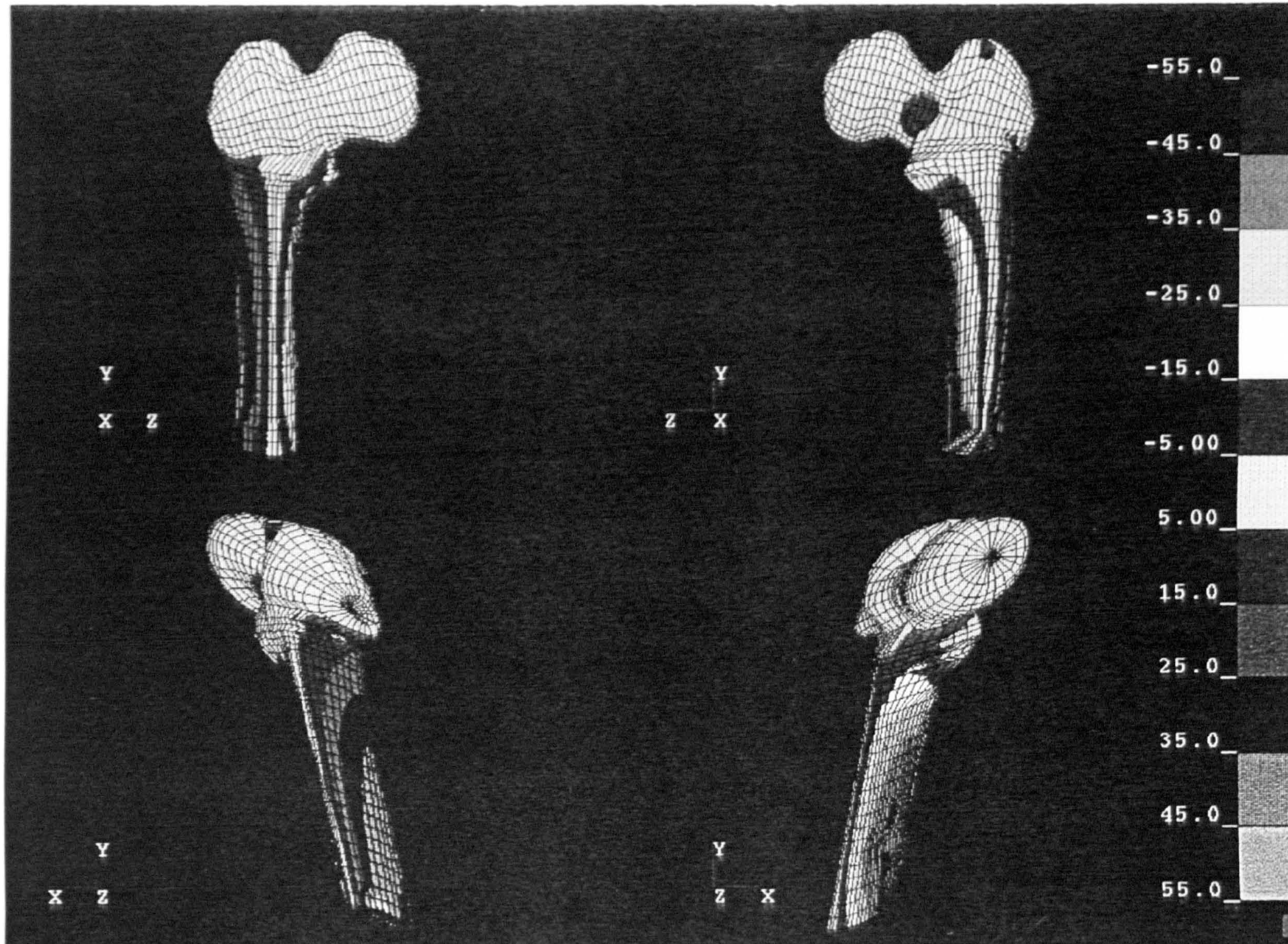

Fig. 8.7.2.2 Stress distribution in the y-direction for femur 3a in N/mm^2.

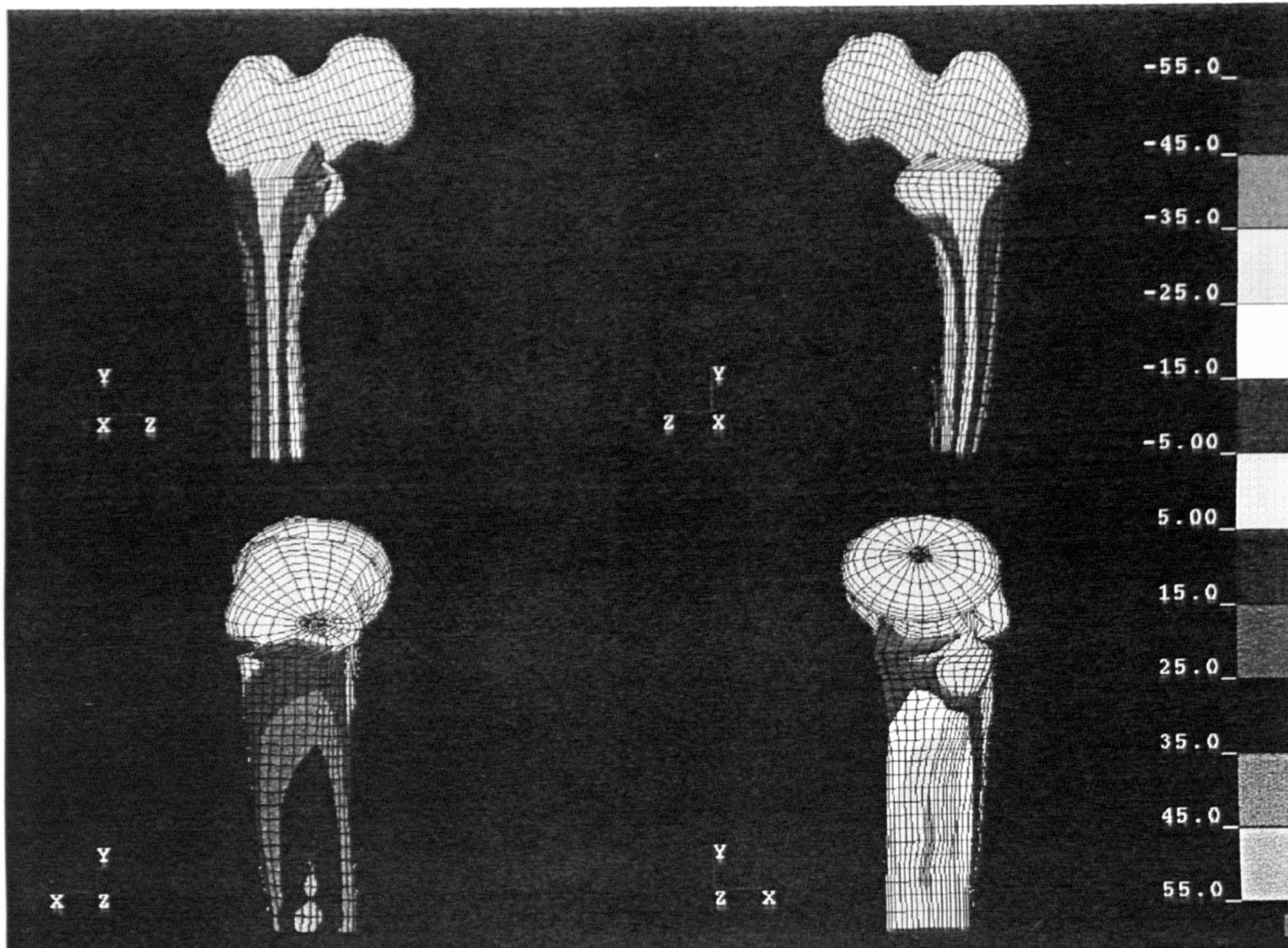

Fig. 8.7.2.3 Stress distribution in the y-direction for femur 3b in N/mm^2.

of the femur. Tensile stresses began to surface below the greater trochanter and spreading evenly in increasing magnitude until the maximum stress was reached at the fixed end of the femur. In the posterior view of the femoral shaft, the stresses in the y-direction reduced towards the centre and reached a minimum along the linear aspera of the femur. This pattern was repeated at the anterior view. Again comparing the femur to that of a cantilever beam, the neutral axis due to bending would be found at this region of low bending stresses.

Referring to Fig. 8.7.2.2, the stress pattern in femur 3a was almost identical to that of the original femur 2. However, difference in the stress magnitude was observed, where the predicted maximum compressive and tensile stresses were -56.6 N/mm^2 and 48.6 N/mm^2 respectively. The increased in stresses was due to the scaling process which caused the dimensions of the femoral shaft in the coronal plane to decrease reducing its capability to resist bending. Nevertheless, the symmetrical stress pattern about the saggital plane was still maintained.

Fig. 8.7.2.3 plots the stress distribution of femur 3b in the y-direction. Similar to femur 3a, due to the effect of scaling, the femoral shaft became thinner compared to the original femur in the coronal plane. Thus, an increased in the bending stresses could be observed when comparing it to femur 2. The maximum compressive and tensile stresses recorded were -43.4 N/mm^2 and 39 N/mm^2 respectively. The stress pattern in femur 2 was quite similar to femur 2 except the region where maximum compressive stress existed which was approximately 30 mm proximal to the distal end at the medial side in femur 3b instead of the fixed distal end in femur 2. However, the maximum tensile stress was similarly recorded at the distal end of the femoral shaft. Thus, the stress distribution was not equally distributed i.e. symmetrical as in femur 2.

The stresses in the x direction for femur 2, femur 3a and 3b were relatively low. The plots presented in Fig. 8.7.2.4, 8.7.2.5 and 8.7.2.6 show the stress patterns and magnitudes in the x-direction. The three plots were made using different stress contour levels with suitable range of values. The stress values were relatively low, thus defining a suitable stress range in the individual contour plots would enable the stress pattern to be highlighted clearer. In femur 2, the maximum and minimum stresses recorded in the x direction are 8.38 N/mm^2 and -8.14 N/mm^2 respectively.

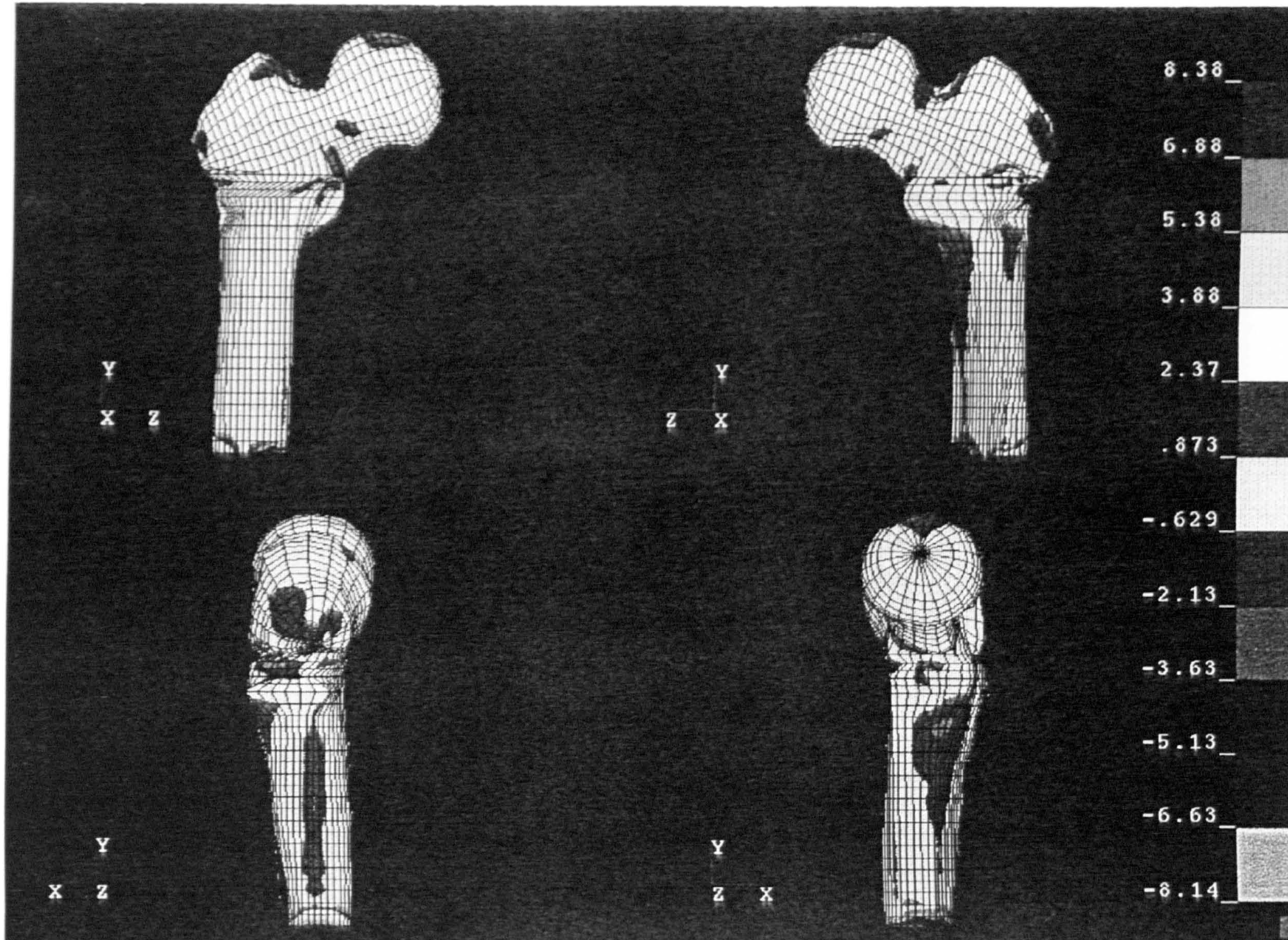

Fig. 8.7.2.4 Stress distribution in the x-direction for femur 2 in N/mm^2.

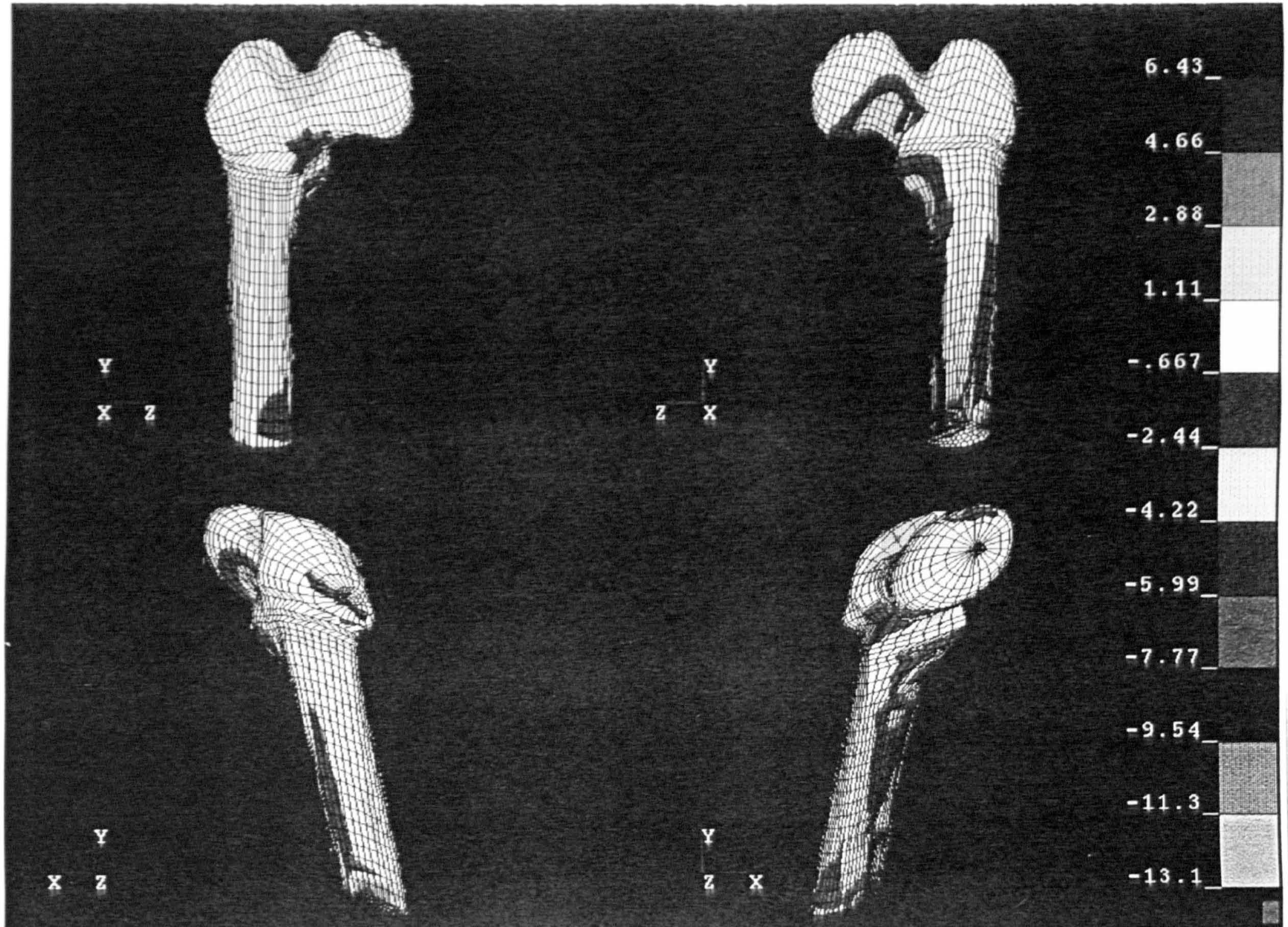

Fig. 8.7.2.5 Stress distribution in the x-direction for femur 3a in N/mm^2.

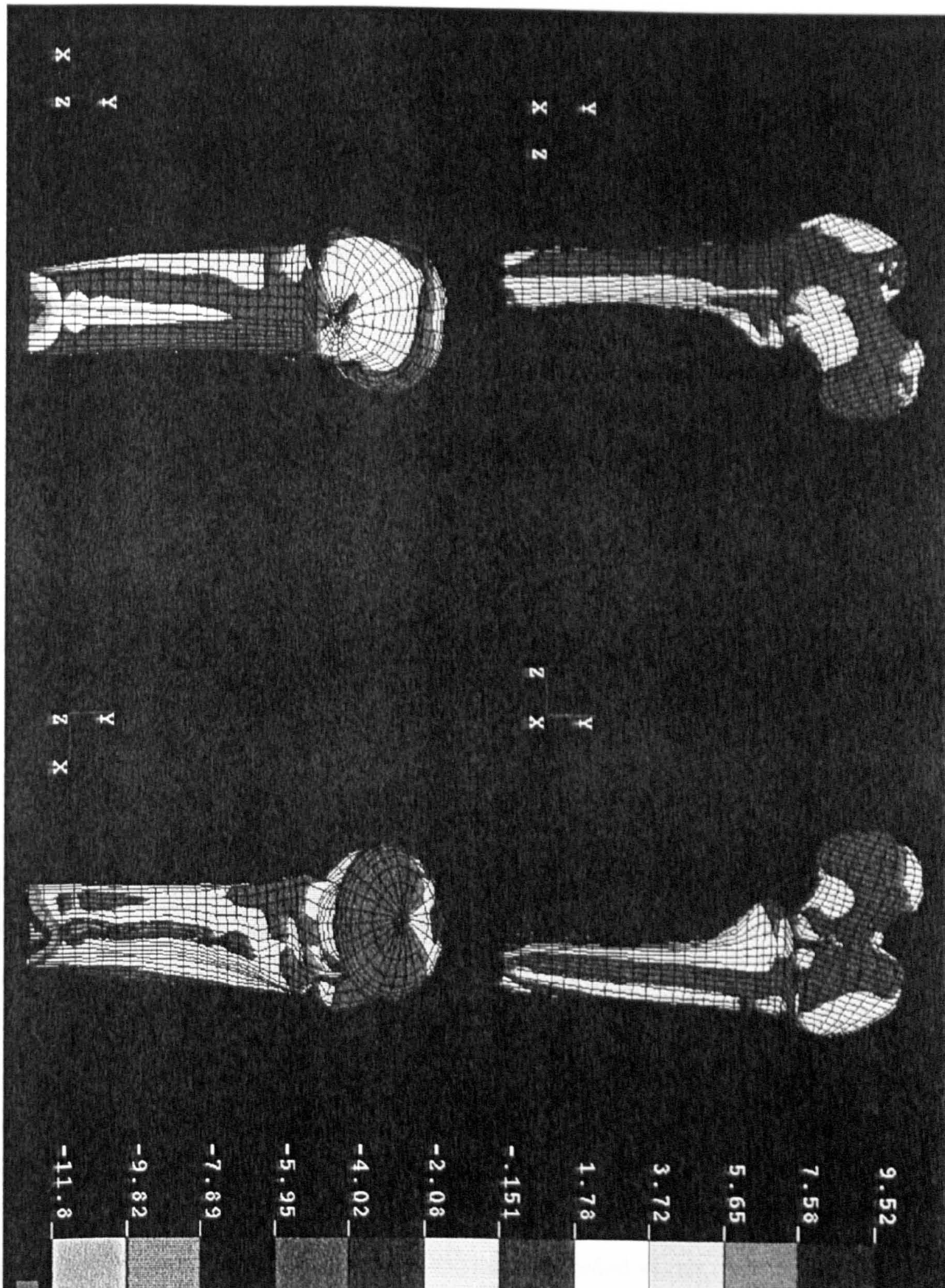

Fig. 8.7.2.6 Stress distribution in the x-direction for femur 3b in N/mm^2.

These were located at the fixed distal end at the lateral and medial sides respectively. This was expected since the the overall load actions introduced to the femur was causing bending in the x-y plane. An area of high stress magnitudes were also recorded at the proximal femoral neck region (3.88 N/mm^2) and the area just below the lesser trochanter (-3.63 N/mm^2). Other areas of the femur were in low stress, ranging from -0.6 N/mm^2 to 0.9 N/mm^2.

As shown in Fig. 8.7.2.5, the maximum (6.43 N/mm^2) and minimum (-13.1 N/mm^2) stresses were also located at the fixed distal end of femur 3a. However, due to the 'skewed' geometry of femur 3a, the location of the maximum and minimum stresses have migrated posteriorly instead of locating at the medial and lateral sides as in femur 2. Compared with femur 2, the maximum stress have decreased while the minimum stress (i.e. the stress in the negative x- direction) has increased in magnitude. The overall stress pattern was about the same as that of femur 2 with stress concentration appearing as positive at the proximal neck region (1.11 N/mm^2) and negative at the area below the lesser trochanter (-5.99 N/mm^2). A negative stress (-4.22 N/mm^2) area was also found at the neck region above the lesser trochanter. This area in particular was not obvious in the original femur 2.

Fig. 8.7.2.6 displays the stresses in the x-direction for femur 3b. Maximum and minimum stresses recorded were 9.52 N/mm^2 and -11.8 N/mm^2 respectively. The stresses are distributed in almost the same manner as that of femur 2. The magnitude of stresses displayed are also relatively close to that of femur 2. However, an exception was seen at the shaft of the femur. There was a proximal spread of high stresses, decreasing in magnitude from the distal end of the femur in the medial and lateral sides.

Fig. 8.7.2.7, 8.7.2.8 and 8.7.2.9 display the stresses of femur 2, 3a and 3b in the z-direction respectively. The stress distributions for the three bone were almost identical. Maximum stress concentration exist at the proximal neck of the femur and lateral distal end. Minimum stress was predicted at the neck of the femur just above the lesser trocahnter and medial distal end. The former recorded values of 13.9 N/mm^2, 14.5 N/mm^2 and 16.6 N/mm^2 while the latter recorded values of -8.44 N/mm^2, -8.91 N/mm^2 and -9.73 N/mm^2 respectively for femur 2, 3a and 3b.

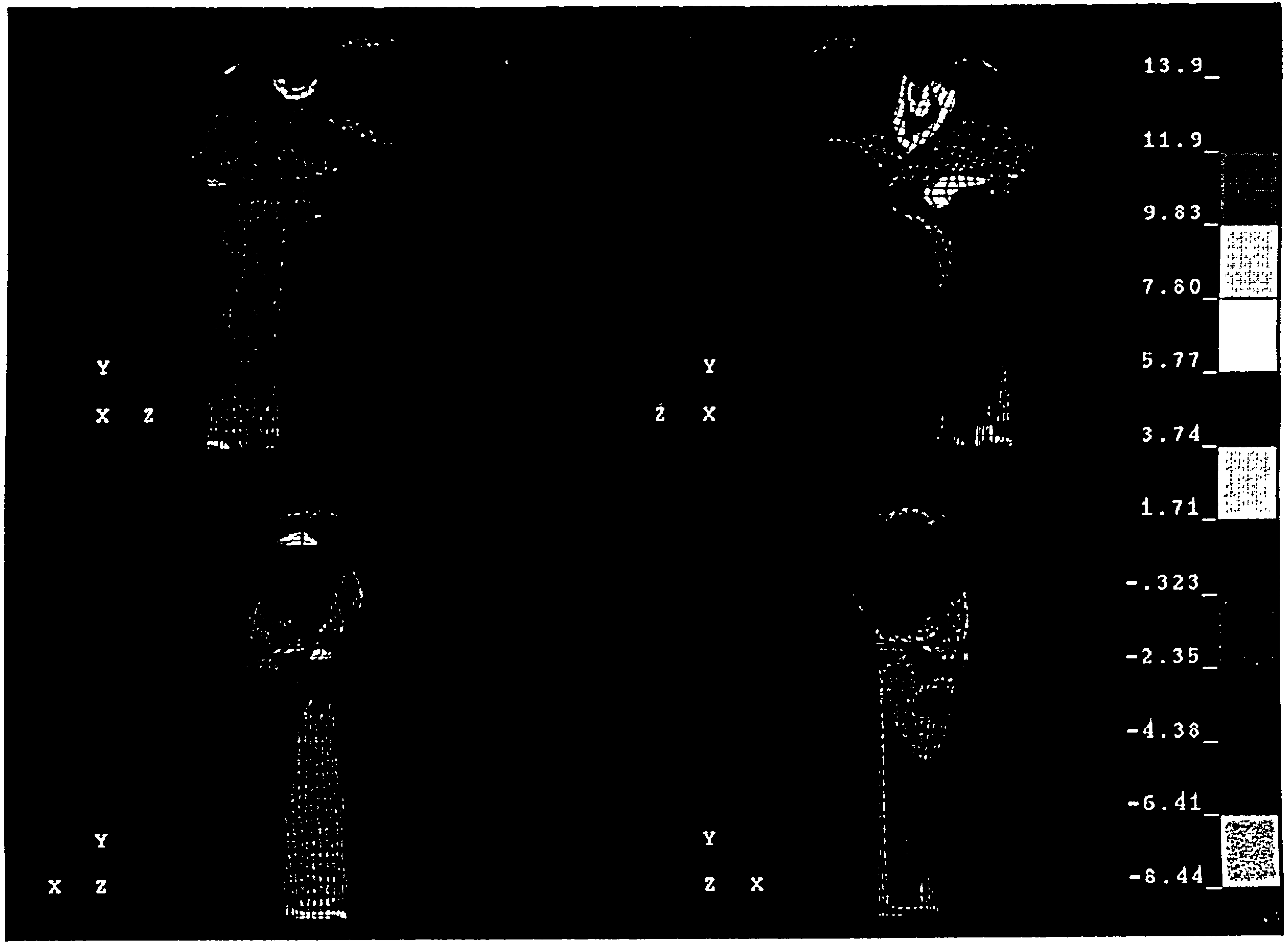

Fig. 8.7.2.7 Stress distribution in the z - direction for femur 2 in N/mm^2.

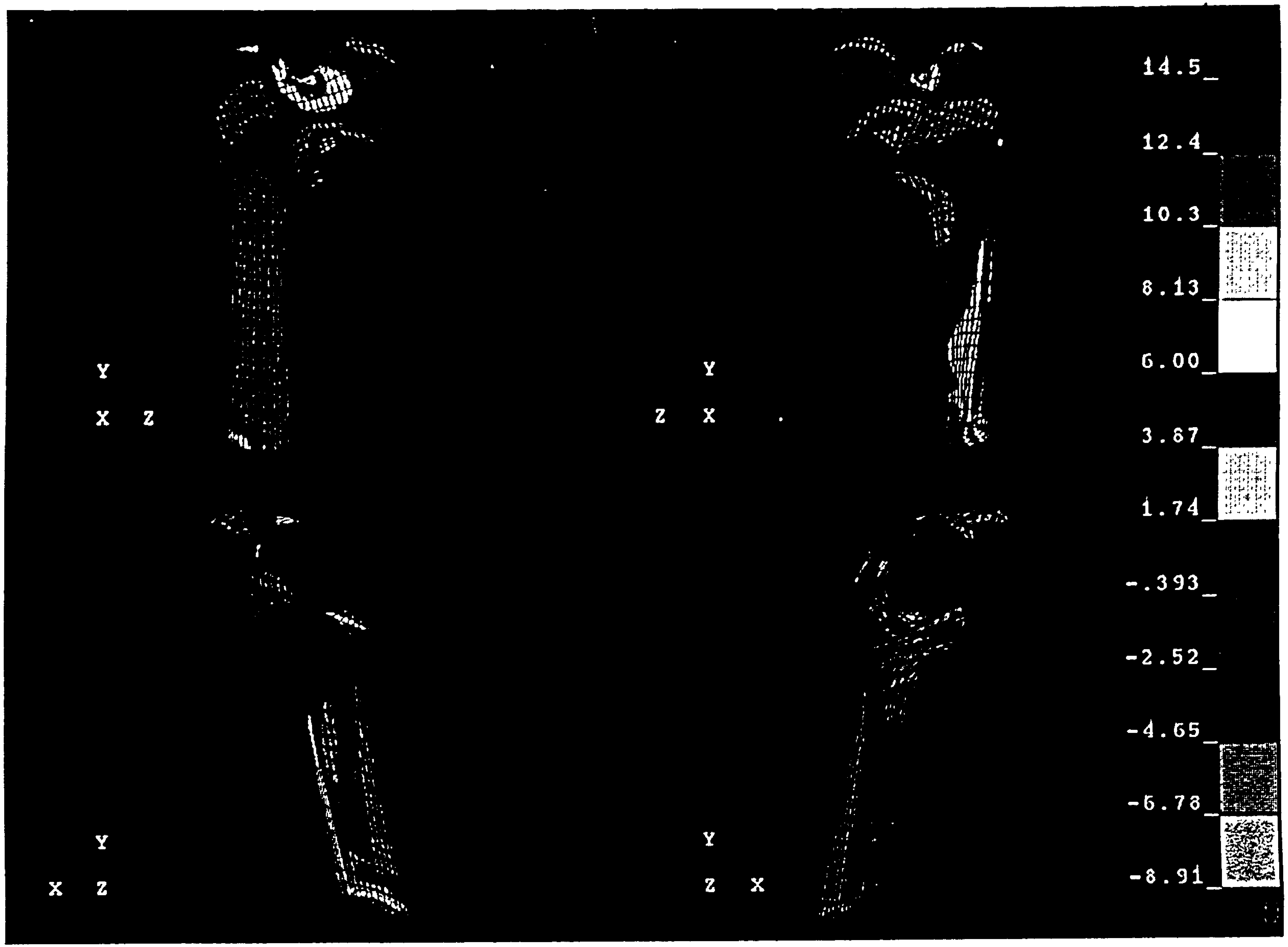

Fig. 8.7.2.8 Stress distribution in the z - direction for femur 3a in N/mm^2.

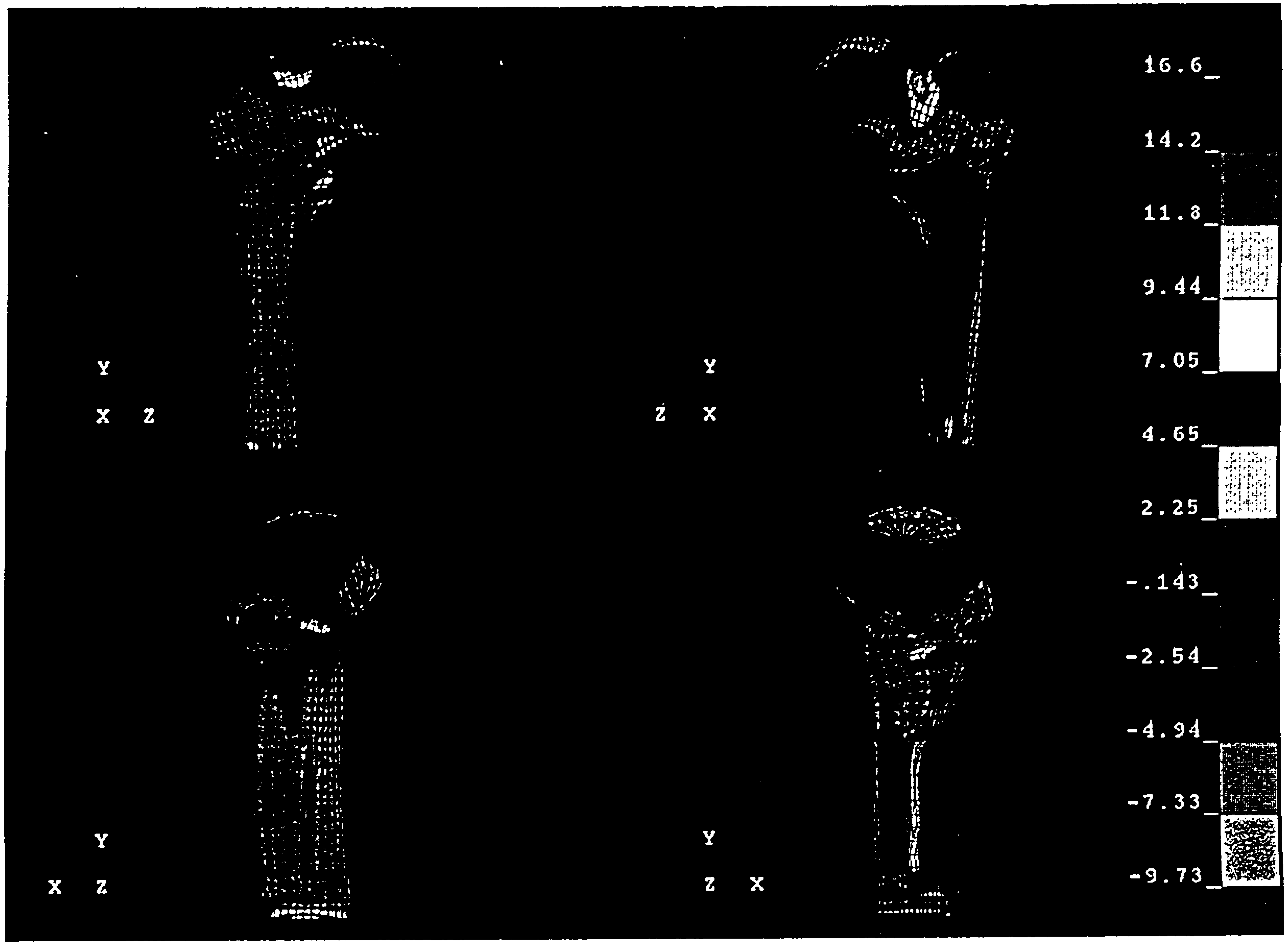

Fig. 8.7.2.9 Stress distribution in the z - direction for femur 3b in N/mm^2.

8.8 DISCUSSION

The preliminary test on the three dimensional cubes showed that the absolute differences in the x, y and z locations between the original and the scaled cube were less than 0.01 mm. It indicates than the methodology adopted and the FORTRAN program was correct.

The result obtained in the present study was comparable to previous attempts of scaling cadavers and animal bones by Lew and Lewis (1977) and Sommers et al (1982) (Previous study : Table 8.2.2 to 8.2.5 and present study : Table 8.5.1 to 8.5.2). In previous attempts, the reference points used in the scaling procedure were located directly on the bone. However, for the scaling procedure to be useful, the reference points on the femur would have to be located on the human subject's thigh. This condition was simulated in the present study by locating the reference points on the cadaver's thigh by palpating the bony landmarks of the femur. The scaling procedure based on the reference points obtained directly from bone was found to be more accurate, i.e. small differences between the original and transformed bone, than that obtained from the cadaver's thigh. This was expected since the fixed cadaver's tissue were relatively hard which made palpating for bony landmarks difficult.

Unlike previous studies where the investigators were only interested in scaling several point of interest i.e. muscles insertions and origins, the complete geometry of the transformed femur needed to be defined for generating FE models. This was accomplished with the aid of a laser scanner which produced an average of 6000-8000 grid points representing the geometry of the femur. However, due to the limitation of the scanner which was ideally designed to capture object of cylindrical form, several geometrical details were lost when scanning the femur. Particularly the neck of the femur and the intercondylar fossa, since the laser was blocked by the more prominent geometrical feature of the greater trochanter and the condyles respectively.

Errors in the scaling process can also be accounted by the assumption that the shape of the femur were similar regardless of the different human subjects. This is the basic assumption in a homogeneous deformation where high accuracy can be attained by scaling two objects of similar shape but of different size as seen in the preliminary test attempted on cubes. However it was clear from visual inspection that variation in shapes existed in the four cadaveric femur used in the present study. This was highlighted in the scaling performed on the female cadavers, i.e. scaling of femur in cadaver 1-F-L to that of 2-F-L. In the initial femur of cadaver 1-F-L, the femoral shaft was relatively straight compared to the final femur (2-F-L) where a distinct curvature in the coronal plane was observed. In the scaling of the initial femur to that of the final femur, the transformed femur did not produce the curvature in the final femur. This was because the transformed femur assumed that the final femur shape was similar to that of the initial femur, possessing a straight shaft.

The FE models created based on geometry obtained by the scaling process were able to replicate the stress distribution pattern of the original femur satisfactory. However, the stress magnitude differed from that of the original femur. The medial lateral dimensions of the transformed femur was reduced which made it less susceptible to bending loads in the medio-lateral plane. Thus, higher bending stresses were recorded at the fixed end of the transformed femur when compared to the original femur, which meant that the transformed femur would indicate mechanical failure first before the original femur. Nevertheless, the loading and boundary conditions introduced in this study would be considered excessive when compared to that of a trans-femoral amputee. In a trans-femoral amputee, the distal end of the severed femur is not fixed rigidly. Its resistance to bending loads is only offered by the surrounding soft tissues confined by the prosthetic socket, thus the bending stress experienced at the distal femur would be much lower.

Another area of high stress concentration as predicted in the FE models was the neck of the femur. The forces introduced in the FE models tend to bend and shear the femoral neck. Again, the loads introduced in the FE models are expected to be higher than that experienced in the trans-femoral amputee wearing a prosthetic socket. The load acting on the femoral head in the trans-femoral amputee would be shared by the pelvis and the ischial tuberosity supported by the socket. Furthermore, due to the severed muscles and the loss of limb, the muscles are usually weak reducing the loadings at the hip joint.

Presently, the need for an exact geometry of the femur in the modelling of the trans-femoral residual limb is yet to be clearly understood. The rigid nature of the bone had prompted some investigators to assume the bone to be of infinite stiffness compared to the surrounding soft tissue (Krouskop et al, 1989 and Todd and Thacker, 1994). The high stiffness of the bone compared to the soft tissue also encouraged these researchers to assume the geometry of the bone to be uniform, similar to that of a cylindrical bar. However, the author of this thesis firmly believes that the true geometry of the bone can significantly affect stresses both inside the residual limb and at the residual limb / socket interface. The simple fact that pressure sores usually appeared at bony prominence indicates the importance of a correct geometry of the bone in any analysis. For example, in the FE models presented in chapter 7, assuming the bone to be cylindrical in shape would have reduced the residual limb / socket interface at the greater trochanter significantly.

The aim of this investigation was to produced a transformed femur which represent the amputee subject femur geometrically. The transformed femur could then be used in the generation of a FE model of the residual limb. Several practical limitations would be encountered in such an attempt. Firstly, three of the four reference points used in the scaling procedure were located at the condyles. In a trans-femoral amputee the distal end of the femur would be amputated, thus the only possible way in locating the three reference points would be from the good limb. This led to the assumption that the femur is symmetrical in the sound and amputated side. The procedure would also assume that the shape and size of the bone does not change after amputation. The latter assumption is viable as seen in the MRI scans in chapter nine. The bone after amputation retained a similar size and shape except for the amount of cortical bone which was reduced, increasing the size of the marrow cavity.

The FE models of the transformed femora indicated that the stress pattern was similar to that of the original femur in several aspects. High bending stresses located at the femoral neck and the distal femoral shaft of the transformed femora were detected. Low stresses were also found at the posterior (linea aspera) and anterior side of the femoral shaft similar to that of the original femur. These results were obtained under a more severe loading condition than that of a residual limb when donning a prosthetic socket. Therefore the present FE model of the transformed femur could possibly be incorporated to a residual limb model resulting in an accurate representation of the femur. However, the author of the thesis recognised that more work may need to be done to improve the geometry of the transformed femur if more complex muscles loadings are considered.

Lastly, the accuracy of the scaling procedure is highly dependent on the equipment and methods used in locating the reference points. The marking table was able to provide sufficient accuracy in this study, however, locating the exact position of the reference points each time on a human subject was more difficult. Especially in the case with the intact femur. Lew and Lewis (1977) estimated such errors could ranged from 1.6 to 9.5 mm.

8.9 CONCLUSION

Antropomentric homogeneous scaling offer a cost effective method of acquiring the geometry of the femur which is fit for finite element modelling. In modelling the trans-femoral residual limb, this would mean eradicating the need for MRI or CT scans.

The feasibility of transforming a cadaveric femur to that of the human subject's femur based on palpable anatomical landmarks of the human subject was investigated. The transformed femur was able to reproduce the major geometrical aspects of the femur but also experienced distortion in shape in several regions. The finite element models of the transformed femur showed an increased in stress and deformation compared to the original femur.

The study indicated that anthropometric scaling is promising in predicting the shape of the femur in intact body. The FE models constructed evaluated the possible limitations and errors involved in using the transformed femur in a finite element model of the residual limb.

CHAPTER NINE
MRI OF TRANS-FEMORAL RESIDUAL LIMB

9.1 INTRODUCTION

The finite element model for three patients presented in chapter seven and the anthropometric scaling technique discussed in chapter eight highlighted the geometrical limitation in the creation of an accurate model of the residual limb. Using magnetic resonance imaging (MRI) technique, the following two aims can be achieved ;

a.) The morphology of the muscles in the amputee's lower limbs can be studied.

b.) The geometry of the femur, pelvis and the surrounding musculature in the residual limb can be acquired accurately.

This chapter begins with an introduction to MRI technology, describing its basic principle and its application as a clinical and research diagnostic tool. This is followed by three other sections, the first describing MR imaging on two trans-femoral amputees. The second and third sections discuss the morphology of the lower limb muscles and the geometry acquired for FE modelling respectively.

9.2 MAGNETIC RESONANCE IMAGING

The two groups who first discovered nuclear magnetic resonance* (NMR) were Bloch, Hansen and Packard (Bloch et al 1946) from Standford and the other Purcell, Torrey and Pound (Purcell et al 1946) from MIT. Both Bloch and Purcell were awarded the Nobel prize for physics for their achievements in 1952. The main discovery that led NMR to its application in analytical spectroscopy was that nuclei in chemically distinct sites resonate at slightly different frequencies. Further investigations in measuring the total intensity of the nuclear resonance as a function of position and finally, the application of a magnetic field enabling spatial information to be obtained, led to the first NMR image being published in 1973 (Lauterbur 1973). Following this achievement, anatomical cross-sectional details of human fingers and limbs have been produced using small laboratory systems. The goal to develop a whole body imager was accomplished by Damadian, Goldsmith and Minkoff in 1977 (Damadian et al 1977). Since then, commercial interest in NMR as an imaging tool has been developed. Industries began to get involved and together with the

*The terms Nuclear magnetic resonance (NMR) and magnetic resonance (MR) are used indiscriminately. Generally however, the latter has been preferred since the word nuclear could cause concern in the public.

advancements in computers, clinical trials with a prototype instrument was possible in the USA in 1983 (Morris, 1986).

9.2.1 Basic working principles

The display in MRI images appears as different levels of brightness usually in the form of 256 x 256 or 512 x 512 tiny squares. Each square is represented in numerical form in the computer. They are called pixels if the image was obtained as a single slice, or voxels if the image represents an entire volume. The value of the pixel or voxel reflects the strength of the radio frequency (RF) signal received during MRI. During imaging the patient lies in a magnetic field and is subjected to brief bursts of RF energy. In response to this stimulation, the mobile hydrogen nuclei in the patient's body act like miniature radio transmitters. Therefore, by systematically varying the strength of the magnetic field, the signals transmitted from the nuclei are recorded, and the computer can determine the signal attributable to their location in the patient's body. In simple terms, MRI subjects a sample (body) in a magnetic field to RF energy, so that spatial information of that sample can be obtained.

9.2.2 Magnetic field and magnets

The frequency at which a hydrogen nucleus resonates depends on the strength of the magnetic field. In order to know not just the number of nuclei but also the distribution, a magnetic field with varying strength is used. Most current techniques employ a linear gradient, dividing the magnet, hence the imaging volume according to the magnetic field strength. Nuclei in a stronger field will thus resonate at a higher frequency than nuclei in a weaker field. The signal from the transmitted nuclei is received as a function of time and subsequently reconstructed as an image through a process of Fourier transformation, converting the time domain signal into a frequency domain signal, which contains information about signal strength as a function of position. Present MRI systems have a magnetic field ranging from one kilo gauss (1 kG) or 0.1 Tesla (T) to 20 kG or 2T. For the purpose of comparison, the earth's magnetic field is about 0.5 G and the strength of a bar magnet is around 250 G. The determination of the optimal field strength for whole body imaging is highly complex, surrounded by a multitude of parameters. A few of the considerations are signal, noise, interpreter perception, chemical shift, pathological changes, imaging time, operational characteristics and energy dissipation. Weissman (1987) stated that in his clinical experience with different MRI systems operating at 0.15, 0.3, 0.6 and 1.5 T, images of the head seemed to be better with higher field strength systems, however there was no apparent effect on the detection of lesions.

There are mainly three types of magnets currently being used in MRI systems, permanent, resistive and superconducting types. Permanent magnets are limited in their field strength, but require very low maintenance cost with no need for electricity and cryogens. The main disadvantage is the size of the magnetic material, in a whole body imager this can go up to 100 tons. Having a permanent magnet also means that it is impossible to shut off the magnetic field, which can be a safety hazard. Resistive magnets have a maximum field strength ranging from 0.15 T to 0.25 T for a whole body imager. It is one of the currently most cost effective systems, where its main cost comes from the cooling system required to dissipate heat generated from the magnet coils. Superconducting magnets have the advantage of producing the highest magnetic field (above 2.0 T). The magnets are air core solenoids wound with fine superconducting wires which are capable of producing a more stable and uniform magnetic field than the other two types of magnet. There is no need for a larger power supply since it relies on the cryogens to maintain superconductivity. These systems are more expensive and the maintenance cost is high, requiring the replenishment of cryogens.

9.2.3 Radio frequency (RF) pulses

In MRI, a quick burst of RF pulsed from a rf transmitter is applied to the patient's body and the response is received by a RF receiver. The RF pulse is of the order of kilowatts and duration of tens or hundreds of microseconds. For a nucleus to produce a signal in a magnetic field, the RF pulse applied must be at the right frequency, duration and amplitude. The amplitude of the input signal must be many orders of magnitude higher than the amplitude of the signal with which the nuclei respond. Thus, one must turn off the RF transmitter in order to avoid drowning out

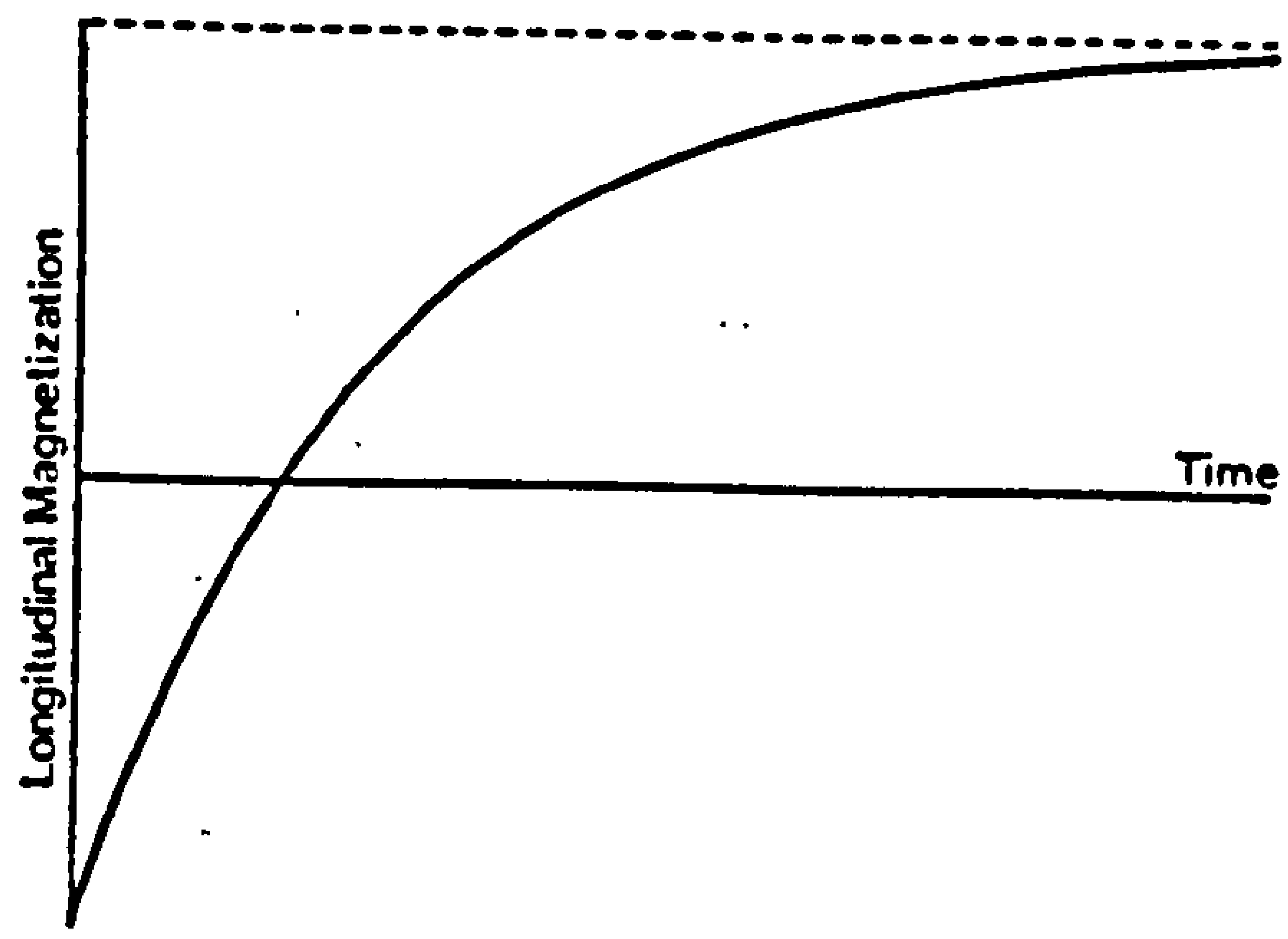

Fig. 9.2.4.1 T1 curve. Any RF pulse will set the longitudinal magnetisation of the sample to some point on this curve, from which the sample will regain its potential to produce a signal with time. (Hill and Waldo, 1985)

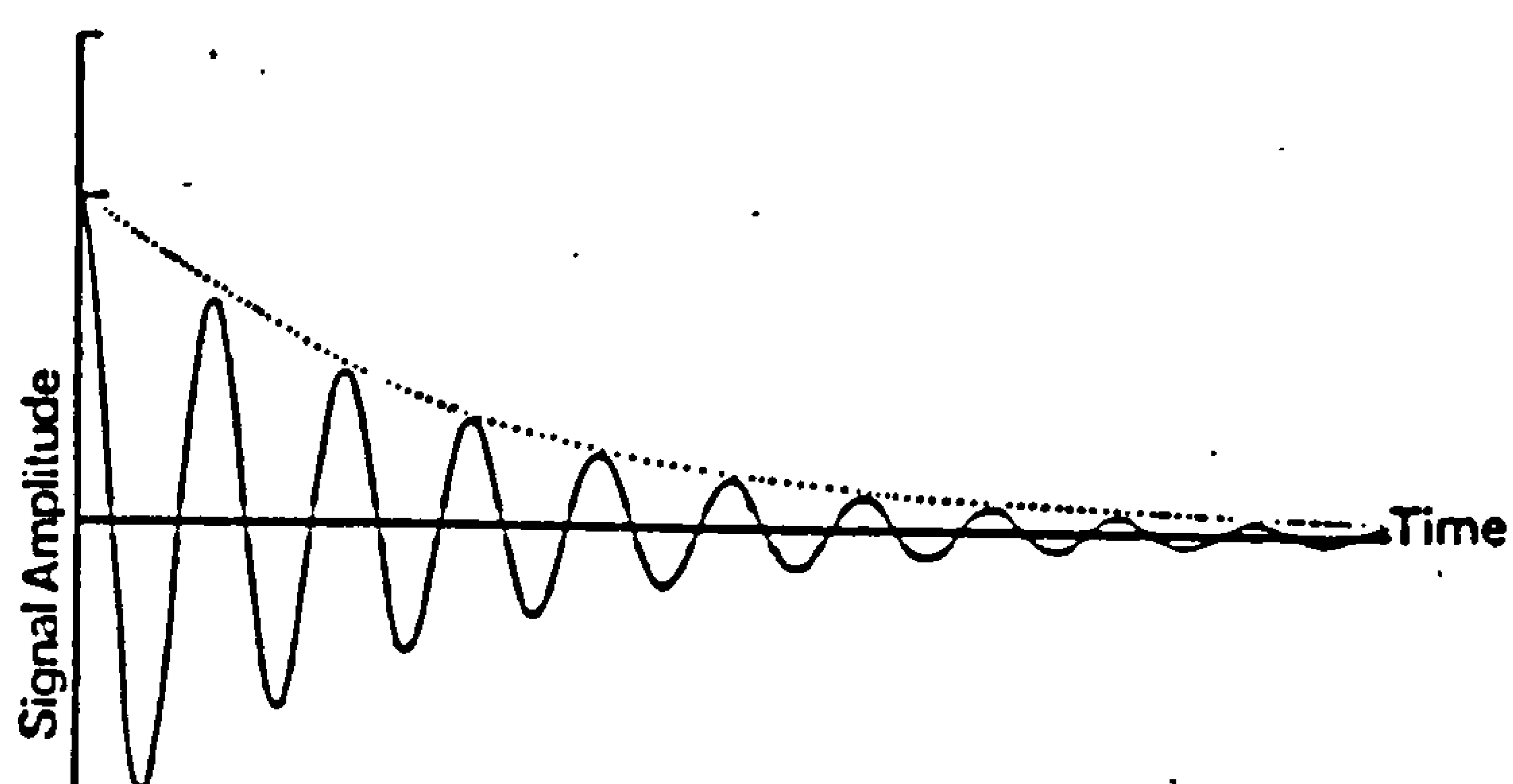

Fig. 9.2.4.2 Disappearance of the signal observed under perfect measuring conditions. The dashed line connecting successive peaks is the T2 curve of the substance. (Hill and Waldo, 1985)

the response entirely. Once the input RF field is turned off, the response signal becomes detectable. The response signal also begins to fade away immediately.

9.2.4 Relaxation processes

The fading of the MRI signal can be explained by two processes, T1 and T2 relaxation. Fig. 9.2.4.1 shows a T1 curve. It indicates how long a substance takes to regain its potential to produce an MRI signal after the nuclei have been disturbed from their preferred orientation in a magnetic field. T1 relaxation is therefore defined as the process of returning towards the equilibrium magnetisation. T1 has two implications for MR imaging. Firstly, the T1 of a substance limits how quickly the RF pulse can be repeated and still a measurable signal be achieved. Since if a sample is subjected to a continuous burst of RF pulse and does not allow enough time for the potential to grow between pulses, the potential signal never has a chance to develop. Secondly, the RF pulses can be patterned in ways that make image contrast heavily dependent on differences in T1. The process of losing the detectable signal is called T2 relaxation. Fig. 9.2.4.2 shows the T2 curve which is formed by connecting the diminishing peaks in a signal.

In summary, T1 can be considered as the time it takes the nuclei to regain their ability to produce a signal and T2 describes the time it takes a signal to disappear. The relaxation time constant is dependent on several variables like chemical and physical state of the substance, the strength of magnetic field, temperature, *in vivo* or *in vitro* observation, and in the last case contributing factors are how long the tissue has been excised and how was the tissue fixed. There have been many attempts to find suitable T1 and T2 for various tissues as shown in Fig. 9.2.4.3.

Often quoted parameters in MR images are the magnetic field of the MRI system in Tesla (T), the repetition time in ms (TR) and the echo time in ms (TE), slice thickness, and interslice thickness or slice gap. Repetition time indicates the time between successive RF pulses and the echo time is the time between the RF pulse and the echo peaks.

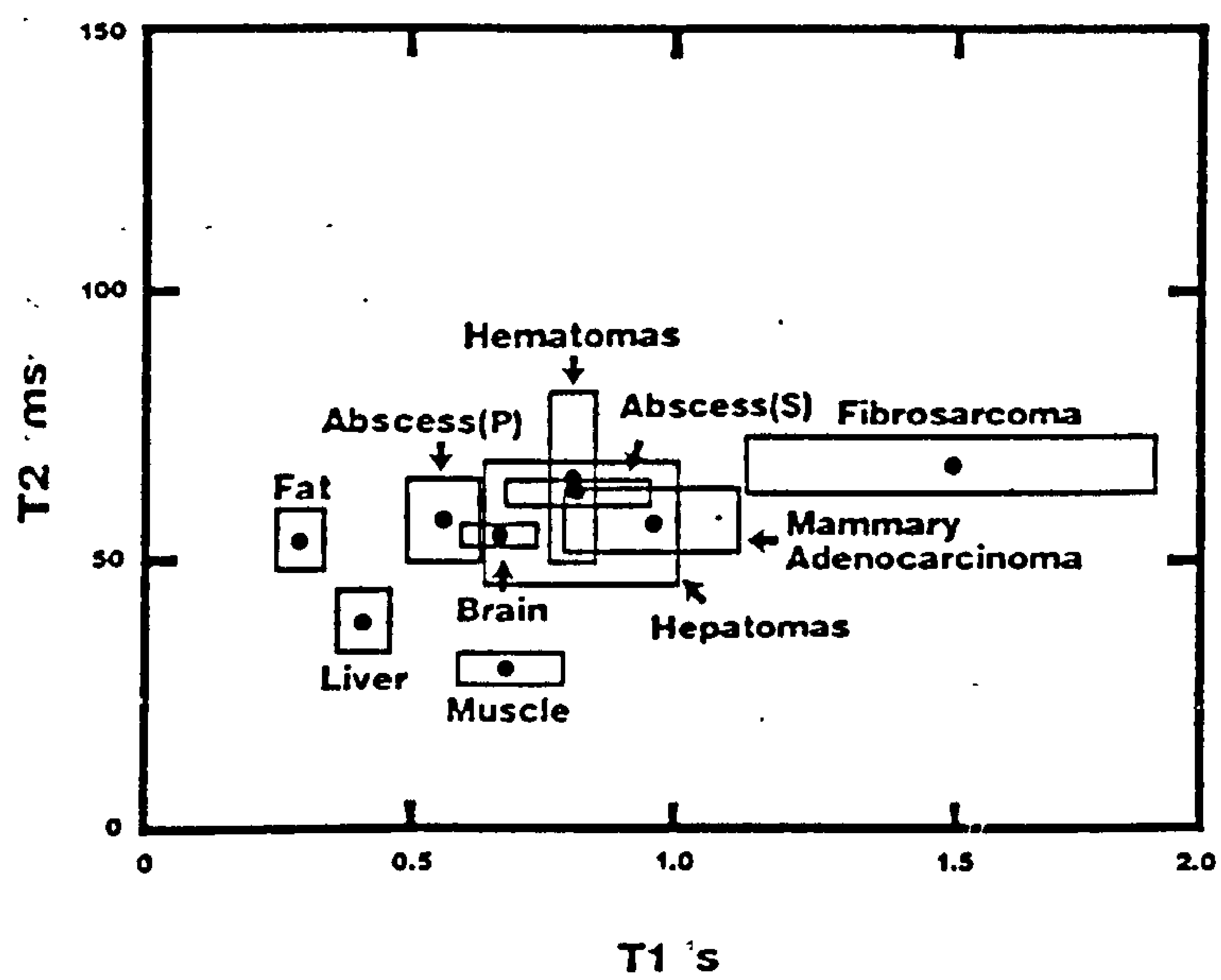

Fig. 9.2.4.3 Relaxation time constants T1 and T2 for various healthy and diseased tissues from a sample of 30 rats. The circle indicates mean values, while the rectangle plus or minus one standard deviation on either axis. (Crooks, 1985)

9.2.5 Safety aspects

MR imaging is not expected to be hazardous to the patient, although there is the presence of strong magnetic fields and radio frequency energy.

It has been reported that there is a possibility of reducing the nerve conduction velocity and affecting membrane permeability and chemical kinetics due to a steady magnetic field (Beischer and Knepton, 1964). Movement of the patient in the magnetic field will generate small voltages within the body tissue which are superimposed upon the natural biopotentials, however, these effects are not harmful. A changing magnetic field can induce a voltage producing currents in the body which could stimulate excitable tissue. Polson et al (1982) reported that the peripheral nerves of the limb can be stimulated by changing magnetic fields that are equivalent to those in present MR imagers. Lastly, radio frequency energy can produce heating in the patient. Mackay (1984) suggested that an absorbed power of 4 watts per kilogram of body weight may be harmful if applied for an extremely long period.

Generally, patients with cardiac pacemakers, large metallic implants and aneurysm clips are usually avoided. Failure or heating could take place with these devices.

9.3 A REVIEW OF THE APPLICATIONS OF MRI

The clinical and research applications of MRI are very diversified. One of its main clinical uses is the examination of injuries, especially in the area of head and spinal cord. Excellent contrast, absence of bone artifacts and high resolution images can be obtained. Furthermore, there is the advantage of multiplanar imaging without changing the patient's position. Perovitch et al (1992) discussed a typical study of examining 87 patients who had sustained spinal cord injuries using MRI. The paper also included a review of the recent advances in MRI as a diagnostic tool in this area, which encompassed image enhancement, fat tissue signal suppression, 3-D imaging and magnetic resonance angiography.

In the field of biomechanics, MRI has proved to be an effective research tool. Internal tissue movements and physiological behaviour can be visualised yielding useful information. Spoor and Van Leeuwen (1992) described a study using MR images to collect geometric data for moment arm estimates at the knee. A knee specimen was scanned in five successive flexion postures while the tendon positions of the loaded muscles were measured.

The ability to look inside the human body non invasively is the main aim in all imaging techniques like x-rays, computer tomography and MRI. Unlike the previous two techniques, MRI does not involves any radiation. Since its clinical implementation it has encouraged a vast amount of imaging not only on patients but also healthy subjects. The following look into some of the *in vivo* studies of the lower limb using MRI techniques. Ferkel et al (1991) described imaging of the foot and ankle. The aim of the study was to determine the MRI anatomy of normal subjects, and using this information correlate normal with pathological conditions. A total of 110 normal feet and ankles were scanned. A further 150 scans were performed to diagnose and characterise various abnormal conditions. Among the 150 scans, 42 had surgical confirmation of their disease process which allowed a direct correlation to the preoperative MRI scans. Imaging was performed on a 1.5 T General Electric system, with a slice thickness of 3 mm and 1 mm interslice gap. The authors considered the 1 mm gap was clinically acceptable but cautioned that scanning without gap may be necessary when looking for small structures such as neuromas. Coronal and axial images were acquired with a repetition time (TR) of 2000 ms and echo delay times (TE) of 40 and 80 ms respectively, whereas for saggital images the repetition time was 500 ms and echo delays of 20 ms. The investigation concluded that the soft tissue details in MR images could assist in early detection of tendon ruptures. Liagamentous injuries of the foot and ankle could also be diagnosed with greater accuracy.

Fukunaga et al (1992) presented a study of the human leg muscles using MRI. Twelve healthy subjects (11 male, 1 female) participated in the test where images were produced of the leg, from the knee to the ankle joint. MRI was performed using a 1.5 T scanner from General Electric Medical System, parameters were T1 weighted, TR was 600 ms and TE was 20 ms. A total of 41 images was acquired for the leg with slice thickness of 10 mm and interslice gap of 0 mm. The study was able to obtain geometrical information on the muscles in the leg. These included cross-sectional area, volume and length. The authors stated that though most of these parameters have been previously determined from cadaver studies; the samples were usually of older individuals with unknown health histories.

The morphology and function of muscles in the unilateral trans-femoral amputee has been studied by Jaegers (1993). Twelve amputees participated in the study. The MR system used was a Philips Gyroscan and the parameters were as follows, repetition time 1050ms, field of view 450 x 1.0 cm, 256 x 256 matrix, slice interval of 5.0 mm and slice thickness of 0.5 mm. The transverse MR images were digitised and individual muscles were identified in order to reconstruct the lower limb in 3-dimensions. The study looked at the muscles' volume changes after trans-femoral amputation. The muscles had atrophied by different amounts, from 4% to 50%. Muscles that were severed in amputation sustained higher atrophy while intact muscles showed minimal atrpohy. It was also found that muscles that were not fixed during surgery were retracted. Seven of the amputees' iliotibial tract was not fixed which resulted in the retraction of the tensor fascia lata and gluteus maximus and a higher percentage of muscle atrophy.

9.4 PROCEDURE ADOPTED FOR THE MRI IMAGING OF TRANS-FEMORAL AMPUTEES IN THIS PROJECT.

In this project two volunteer trans-femoral amputees participated in the test. Prior to the test, the subjects were thoroughly screened by a prosthetist, a medical physicist and a radiologist in order to satisfy all the safety aspects involved in MRI. A checklist and questionnaire were provided in conjunction with the fore mentioned task. A basic rule that was adopted in this study was to exclude subjects that had any metallic implants, which includes cardiac pacemakers, prostheses and aneurysm clips. The study was carried out at the Institute of Neurological Sciences, Southern General Hospital in Glasgow. The imager used was a Picker Vista resistive system with a field strength of 0.15 T. Imaging was performed with the subject in a supine position in the whole body imager. Three sets of scans of the pelvis and the residual limb were taken for the following conditions : a) wearing a plaster b.) wearing a quadrilateral (quad) socket and c.) wearing an ischial containment (IC) type socket. In the first condition, the plaster cast was applied to the residual limb and pelvis whilst the patient was in a relaxed standing position, in order to maintain the residual limb in its natural shape.

9.4.1 Volunteer subjects

The volunteer subjects for the MRI investigation were the same subjects who participated in the pressure measurement test (part two). These were therefore subjects U and M, information pertaining to the subjects remained similar as already highlighted in detail 4.3.2.

9.4.2 Preparation of plaster cast and prosthetic sockets

During imaging, the subject has to lie horizontally in the imager, which causes the residual limb to be distorted from its natural shape. The natural shape in this case could only be achieved with the amputee standing on the good leg and the residual limb without the prosthesis. To solve this problem, a plaster wrap cast was applied to the subject's residual limb while he was standing on the good leg. Care was taken not to apply any undue force during casting which might have distorted the residual limb. The plaster cast extended from the distal end of the residual limb right up to the anterior superior iliac spine (ASIS), covering also the buttock. This process was performed just before imaging commenced; thus once the wrap cast hardened the residual limb was prevented from any distortion when the amputee adopted a supine position in the imager. After imaging, the cast was removed immediately.

Imaging was also carried out with the amputees wearing the quad and IC sockets. The sockets were similar to sockets used in part two of the pressure measurement test except that they were made with clear plastic polypropylene and the sockets' valves had to be modified by replacing one of the metallic component with plastic. The transparent sockets enabled the prosthetist to check if donning was successful and total contact achieved. Donning of the socket was cumbersome since this had to be done without the rest of the distal artificial limb components, (knee, shank and foot) which consisted of metallic parts. Instead, a chair of suitable height was used so that the amputee could transmit his weight onto the socket during donning.

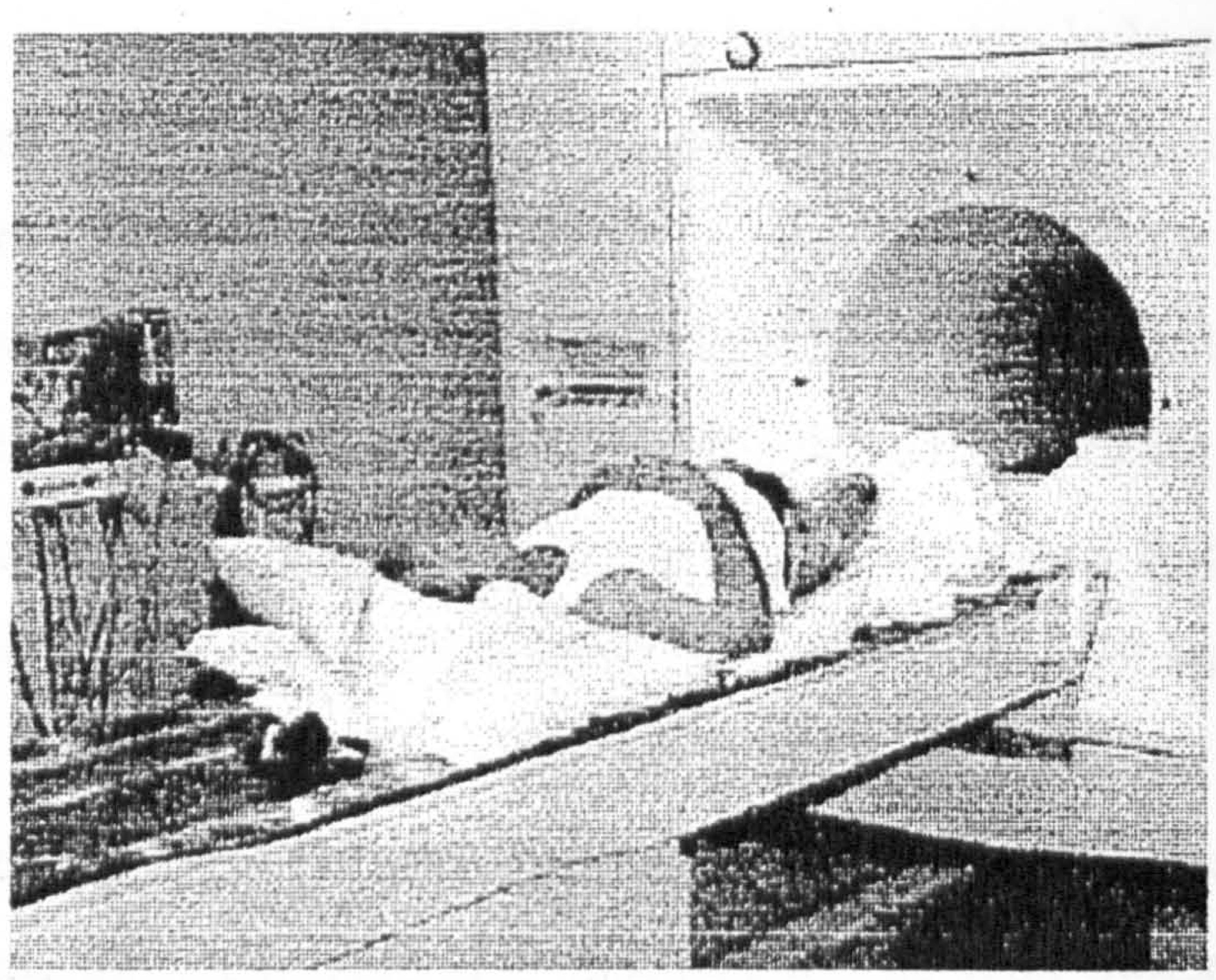

Fig. 9.4.3.1 Magnetic resonance imaging of trans-femoral amputee.

9.4.3 Imaging procedure

Once the subject's residual limb was plastered or fitted with either of the sockets, the subject adopted a supine position on the imager bed and padding was placed around the lower limbs to ensure that their position was within the field of view of the imager. The padding also ensured that the lower limbs were scanned in approximately the same position for the three different configurations. Imaging takes about 20 minutes for each configuration of the residual limb. The subjects were not sedated but requested to remain as still as possible throughout the procedure (Fig. 9.4.3.1).

Several coronal views of the residual limb were initially scanned. From these images, the length of the residual limb to be scanned transversely could be determined (Fig. 9.4.3.2). The imager was then set to acquire transverse images from the pelvis to the distal end of the residual limb. Due to the length of the residual limb and the limited field of view of the imager, imaging had to be split into two parts. The first covering a section from the ASIS to the middle of the amputated femur and the second starting near the ischium to the distal end of the residual limb. This meant that there was an overlap of images from the ischium to the middle of the amputated femur. The total number of transverse images captured for each of the two part was 29. Depending on the scanning configurations (plaster cast, quad and IC) and the subjects' residual limbs length, the number of overlapped images was approximately 16, thus about 42 transverse images were sufficient to describe the complete residual limb.

The transverse images were acquired with a slice thickness of 10 mm, interslice thickness of 0, repetition time (TR) of 1600 ms and echo time (TE) of 60 ms. The images were displayed as 512 by 512 pixel matrix, 256 grey levels and a pixel size of 1 mm.

Fig. 9.4.2.1 Coronal view showing that the images were acquired from the pelvis to the distal end of the residual limb.

9.5 THE MORPHOLOGY OF THE MUSCLES IN THE TRANS-FEMORAL RESIDUAL LIMB

In this part of the study, an attempt was made to provide geometrical information of the internal structures of the residual limb after trans-femoral amputation. Geometrical changes in the internal structures were also investigated when the residual limb donned the quadrilateral and the ischial containment type sockets. Information like soft tissue deformation and musculature position are useful in understanding the biomechanical principles applied to prosthetic sockets.

9.5.1 Interpretation of images

Generally, tissues with high water density such as fat, muscles, marrow and vessels appear clearer while bone emerges fainter in MR images. The darker grey colour in MR images could be associated with muscular tissues, while bone marrow emerges almost black. In contrast, the skin and the underlying fat and the cortical bone were almost white in colour. The images allowed the different muscle groups and bone to be identified fairly accurately. However, difficulty arises in differentiating muscles where the fascia surrounding the muscles could not be seen. The fascia normally act as an outline to the muscles since it would be appear in a lighter colour than the muscles in the images. Identifying the muscles was performed with the help of a cross-sectional anatomy text book by Eycleshymer and Schoemaker (1975) and also cadaveric specimens provided by the University of Glasgow Anatomy Department.

Fig. 9.5.1.1 and Fig. 9.5.1.2 show the transverse slice of the lower limb passing through the upper portion of the ischial tuberosity and the lower portion of the greater trochanter. The majority of the muscle groups can be identified clearly as seen in the figure, except for the adductor longus and brevis where a clear separation cannot be seen in the MR image. Muscles in the sound limb were clearly visible in the MR image. At the amputated side, minimal muscular atrophy had occurred and most muscles can still be clearly identified in the MR image.

Fig. 9.5.1.3 and Fig. 9.5.1.4 display the cross section at the ischial tuberosity level with the different muscles labelled accordingly. The muscles at this level were

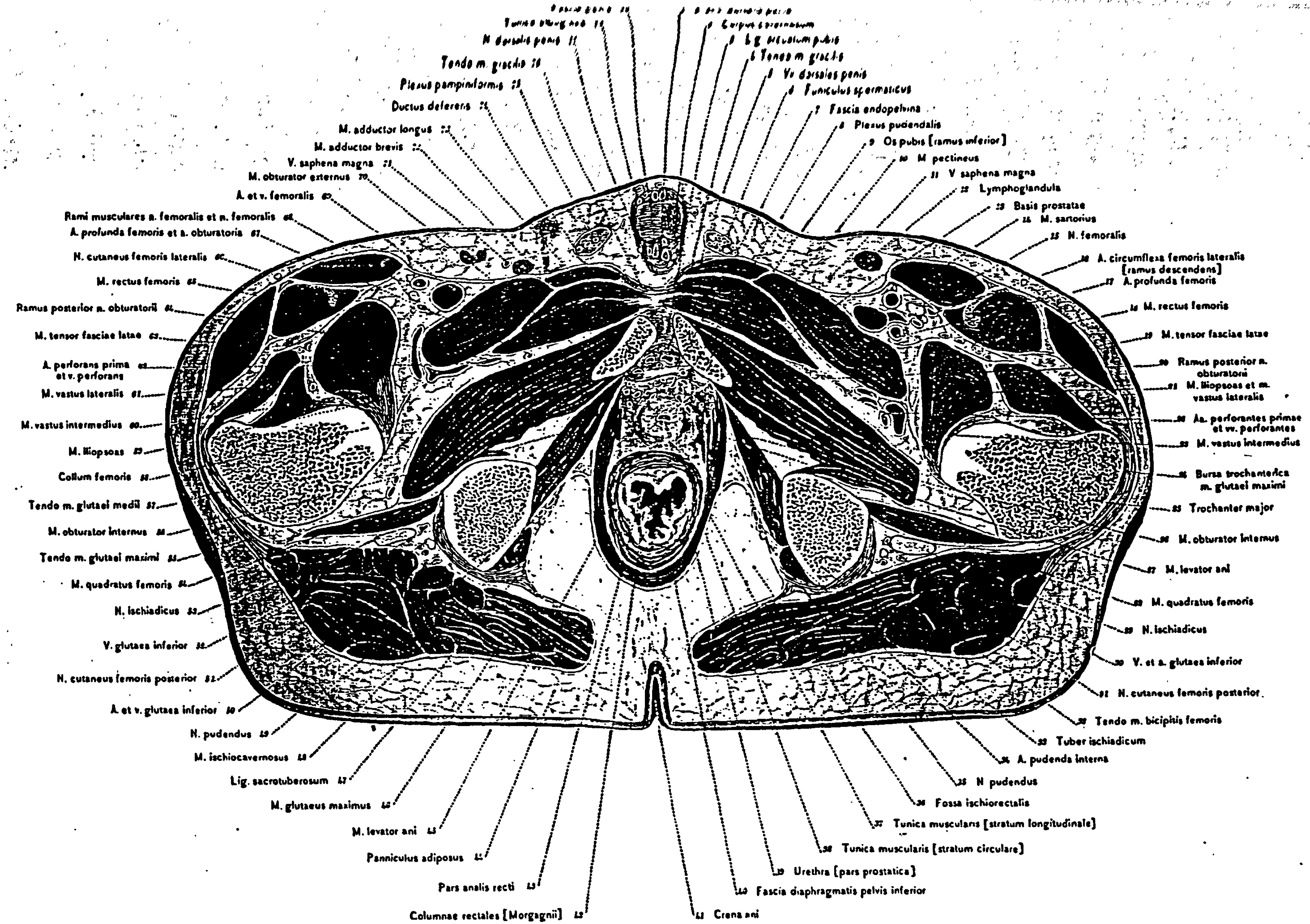

Fig. 9.5.1.1 Cross section through the upper portion of the ischial tuberosity. (Eycleshymer and Schoemaker, 1911)

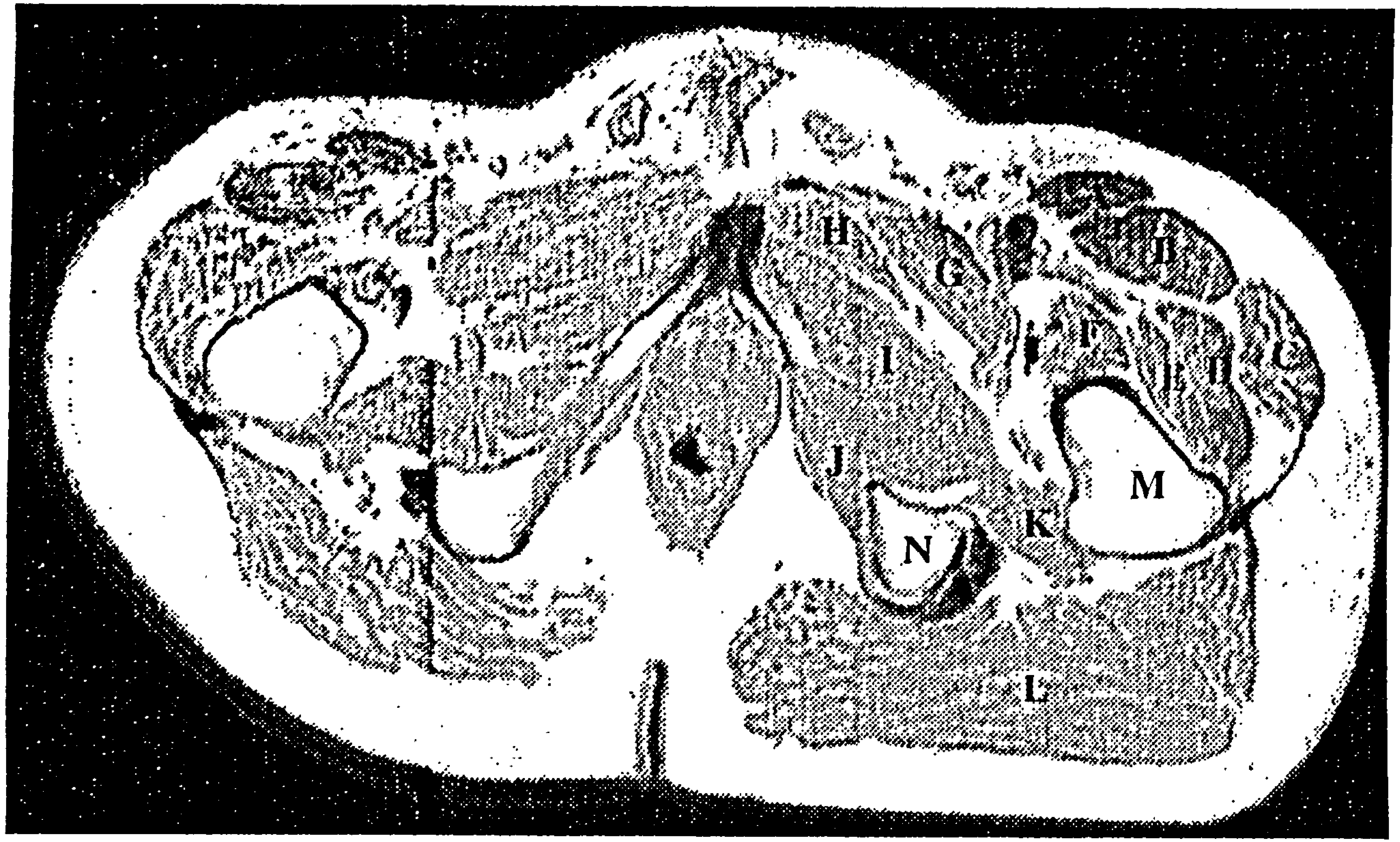

Fig. 9.5.1.2 Transverse section through the upper portion of the ischial tuberosity of subject M.

A – Sartorius

B – Rectus femoris

C – Tensor faciae latae

D – Vastus lateralis

E – Vastus intermedius

F – Iliopsoas

G – Pectineus

H – Adductor longus / brevis

I – Obturator externus

J – Obutrator internus

K – Quadratus femoris

L – Gluteus maximus

M – Femur

N – Ischial tuberosity

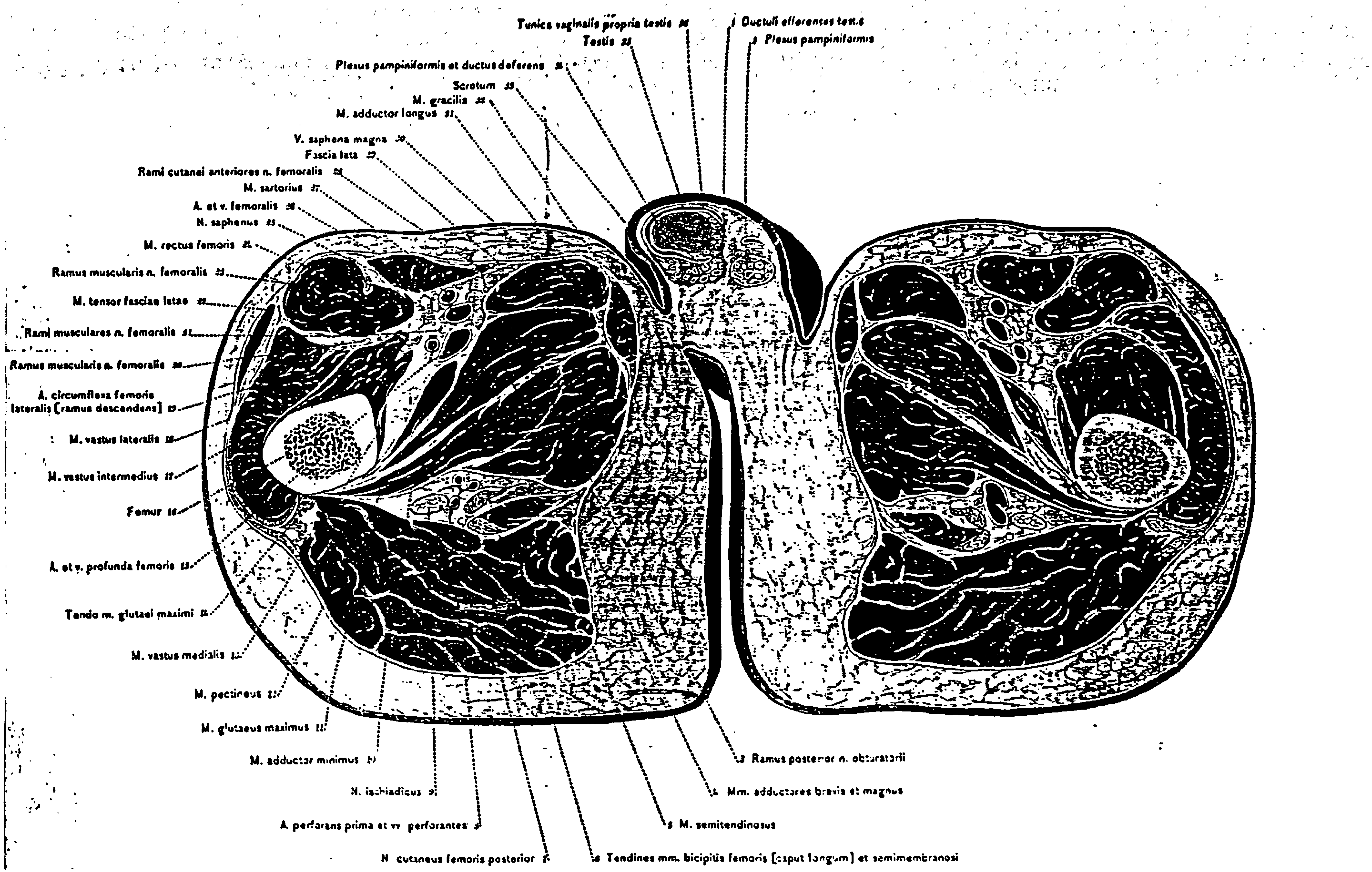

Fig. 9.5.1.3 Cross section through the ischial tuberosity. (Eycleshymer and Schoemaker, 1911)

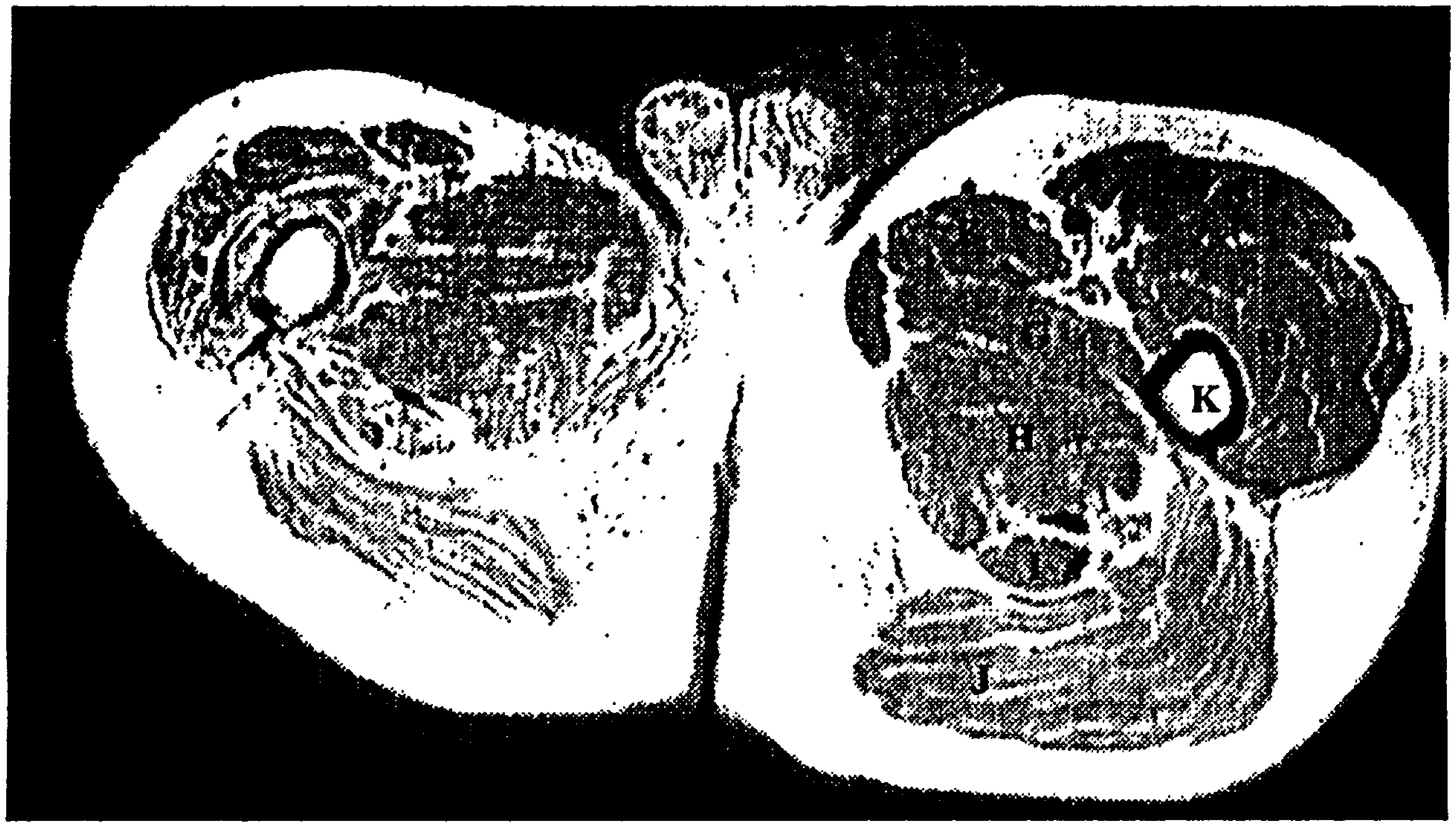

A – Sartorius

B – Rectus femoris

C – Tensor fascia latae

D – Vastus lateralis / intermedius / medialis

E – Adductor longus

F – Gracilis

G – Adductor brevis

H – Adductor magnus / minimus

I – Semitendinosus

J – Gluteus maximus

K – Femur

Fig. 9.5.1.4 Transverse section at the level of the ischial tuberosity of subject M.

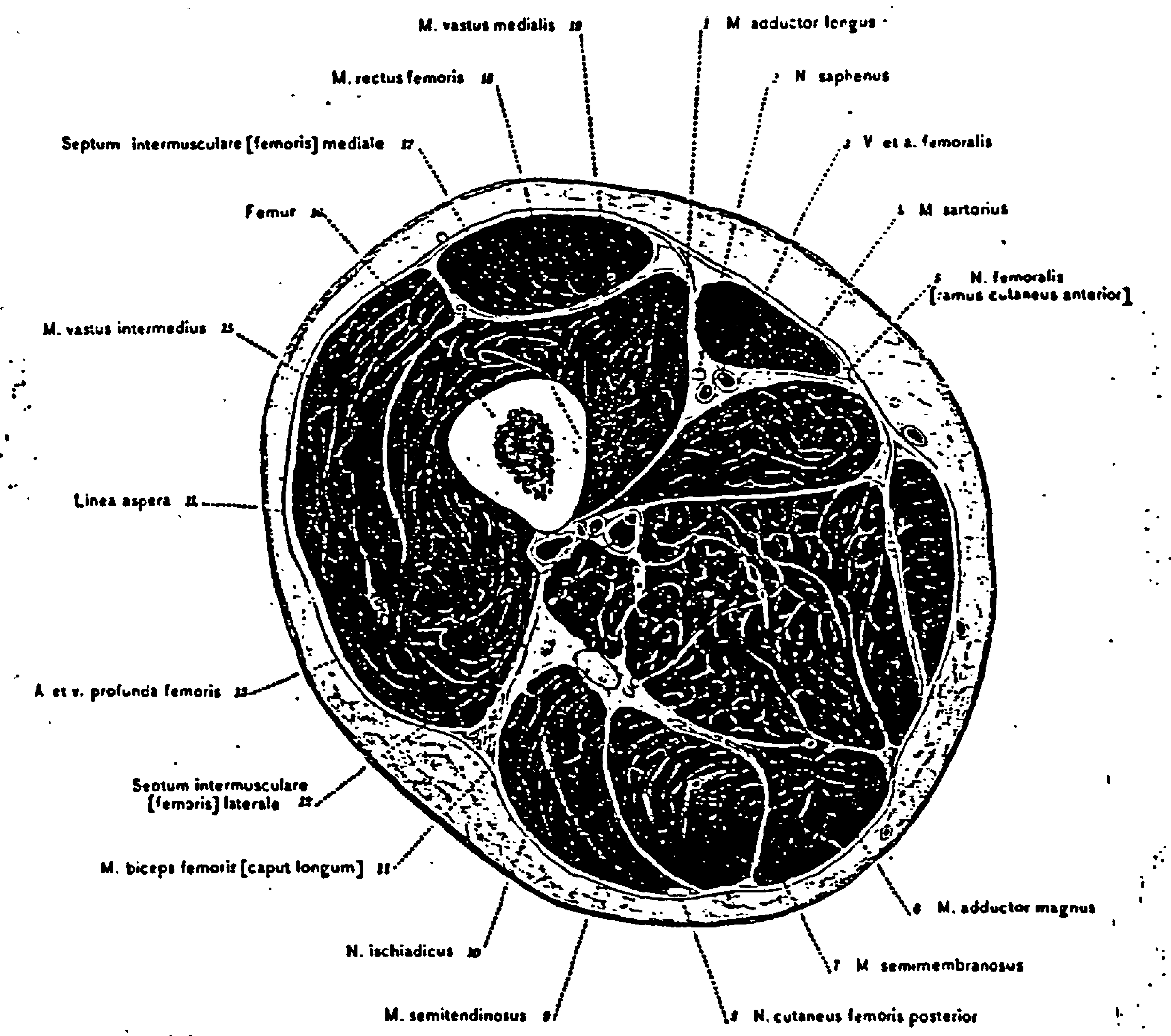

Fig. 9.5.1.5 Cross section through the upper third of the femur. (Eycleshymer and Schoemaker, 1911)

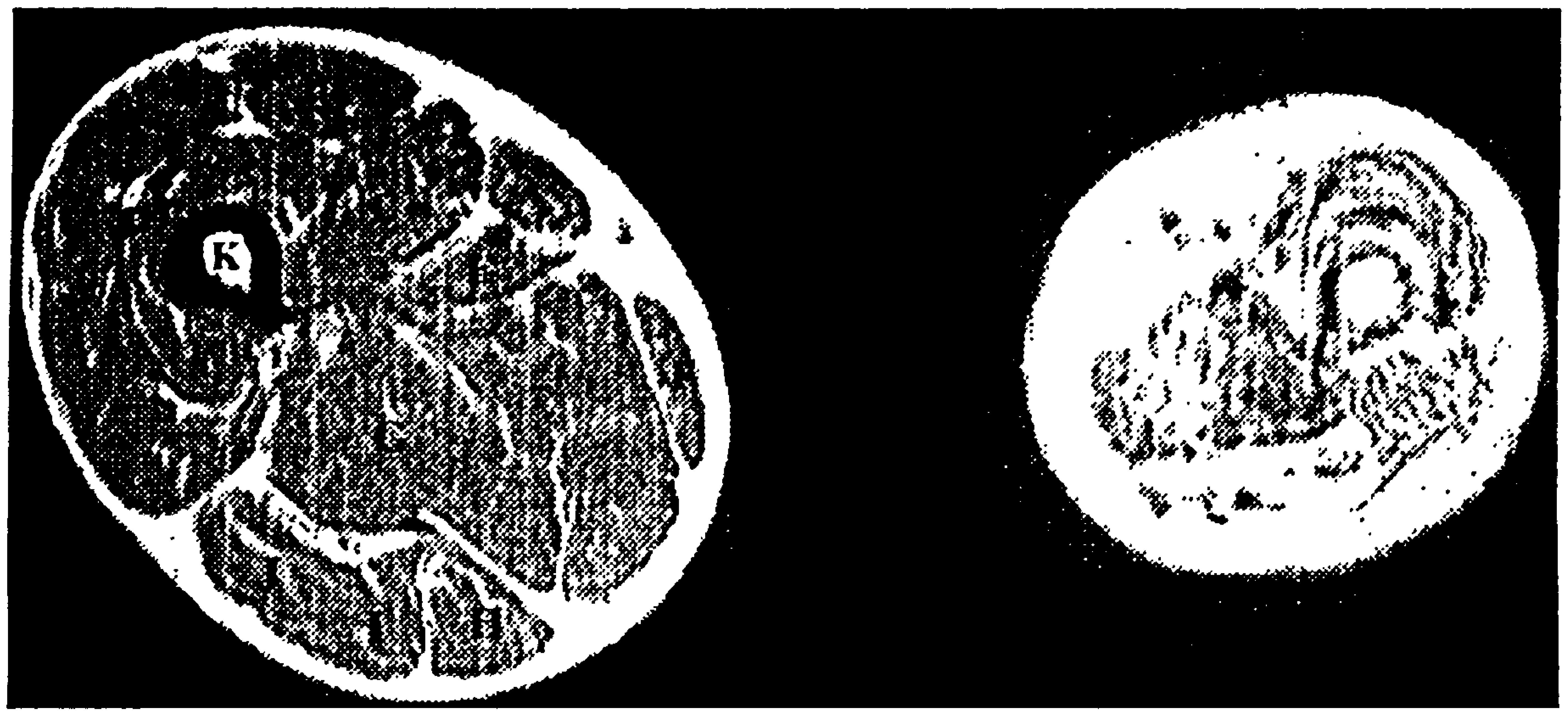

Fig. 9.5.1.6 Transverse section at the mid level of the residual limb of subject U.

A – Sartorius
B – Rectus femoris
C– Vastus medialis
D – Vastus intermedius
E – Adductor longus
F – Gracilis
G – Adductor brevis
H – Semimembranosus
I – Semitendinosus
J – Biceps femoris
K – Femur

tightly packed and separated by thin fascia. The vasti muscles were difficult to distinguish from each other and so was the adductor magnus and minimus in the MR image. The pectineus has reduced significantly in size at this level and could not be differentiated from the adductor brevis. Muscles atrophy in the amputated limb at this level was more severed than the previously described level, causing difficulties in identifying the following muscles in the MR image. Tensor fascia latae could not be differentiated from the vasti muscles. Furthermore, the pectineus and the semitendinosus were not clear.

Fig. 9.5.1.5 and Fig. 9.5.1.6 show the cross section at approximately the mid region of the residual limb. The adductor brevis and gluteus maximus do not extend into this region. In the sound side, the muscles were well defined and tightly packed. Nevertheless, the intermuscular fascia could be seen separating the different muscle groups. However, most muscles in the amputated limb had degenerated into fat, making it almost impossible to identify them.

9.5.2 Selection and processing of images

Two transverse images were selected from each of the imaging configurations (plaster cast, quad and IC). The first image described the cross-section at the ischial level, which in this case was the level immediately distal to the ischial tuberosity, or similarly the ischial seat level in the quadrilateral socket. This level was chosen due to the significance in weight bearing of trans-femoral prosthetic sockets. The second transverse image selected described the cross-section at the mid level of the residual limb. This level was examined because it would represent the overall condition of the residual limb outside the socket's proximal brim region.

The transverse images at the ischial level were identified based on the image obtained for the residual limb wearing the quad socket. The ischial level in the quad could be identified clearly from the ischial seat appearing as a dark shade at the posterior side of the residual limb in the MR image. The ischial level for the other two scanned configuration (plaster cast and IC socket) have to be of the same level as that obtained from the quadrilateral socket, in order to make comparison meaningful.

This was ensured by using the cross section of the femur as a reference since the femur was free from distortion.

The mid level of the residual limb was chosen by selecting a level 70 mm distal to the previously selected ischial level. This level was also the 7th transverse image distal to the ischial level, since the MR image was acquired at 10 mm slices. The images selected for both subjects are displayed in Fig. 9.5.2.1 to Fig. 9.5.2.6.

The MR images were examined using software provided by the University of Pennsylvania called 3dviewnix, installed in a SunSparc workstation. The software displayed the scanned images digitally and tissue structures of interest were digitised using the workstation's mouse. The different muscle groups were firstly identified and digitised around their circumference. Once the digitisation was completed, the software calculated the cross-sectional area based on the pixel information.

9.5.3 Tissue changes after trans-femoral amputation

Fig. 9.5.2.1a and Fig. 9.5.2.4a show the transverse sections of the good limb and the residual limb at the ischial level for subjects U and M respectively. These images were those captured with the subjects' residual limbs in plaster wrap cast simulating the natural state. To study the tissue changes after trans-femoral amputation, the cross sectional area of the muscles in the sound and the residual limb were measured and compared. Comparison were only performed for muscles which could be clearly identified in both the good limb and the residual limb in the MR images, and these were grouped into the following ;

a.) Vastus medialis, intermedius, lateralis and tensor fasciae latae,

b.) Rectus femoris,

c.) Sartorius,

d.) Adductor longus,

e.) Adductor brevis,

f.) Adductor magnus,

g.) Gracilis and

h.) Gluteus maximus.

a.)

b.)

c.)

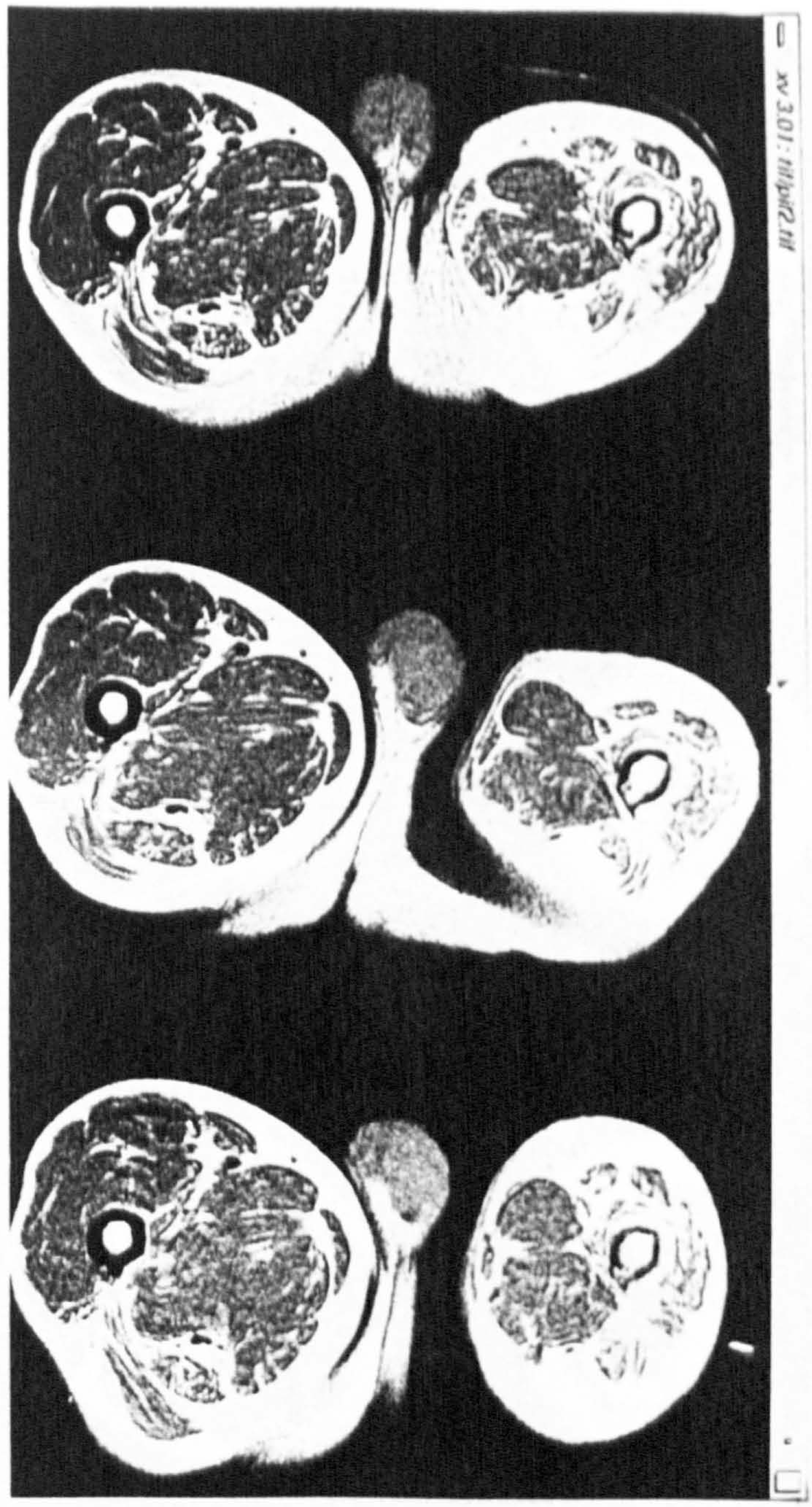

Fig. 9.5.2.1 Transverse sections immediately distal to the ischial tuberosity.
(Subject U)
a.) Residual limb in plaster cast (Natural shape).
b.) Residual limb after donning the quadrilateral socket.
c.) Residual limb after donning the ischial containment socket.

a.)

b.)

c.)

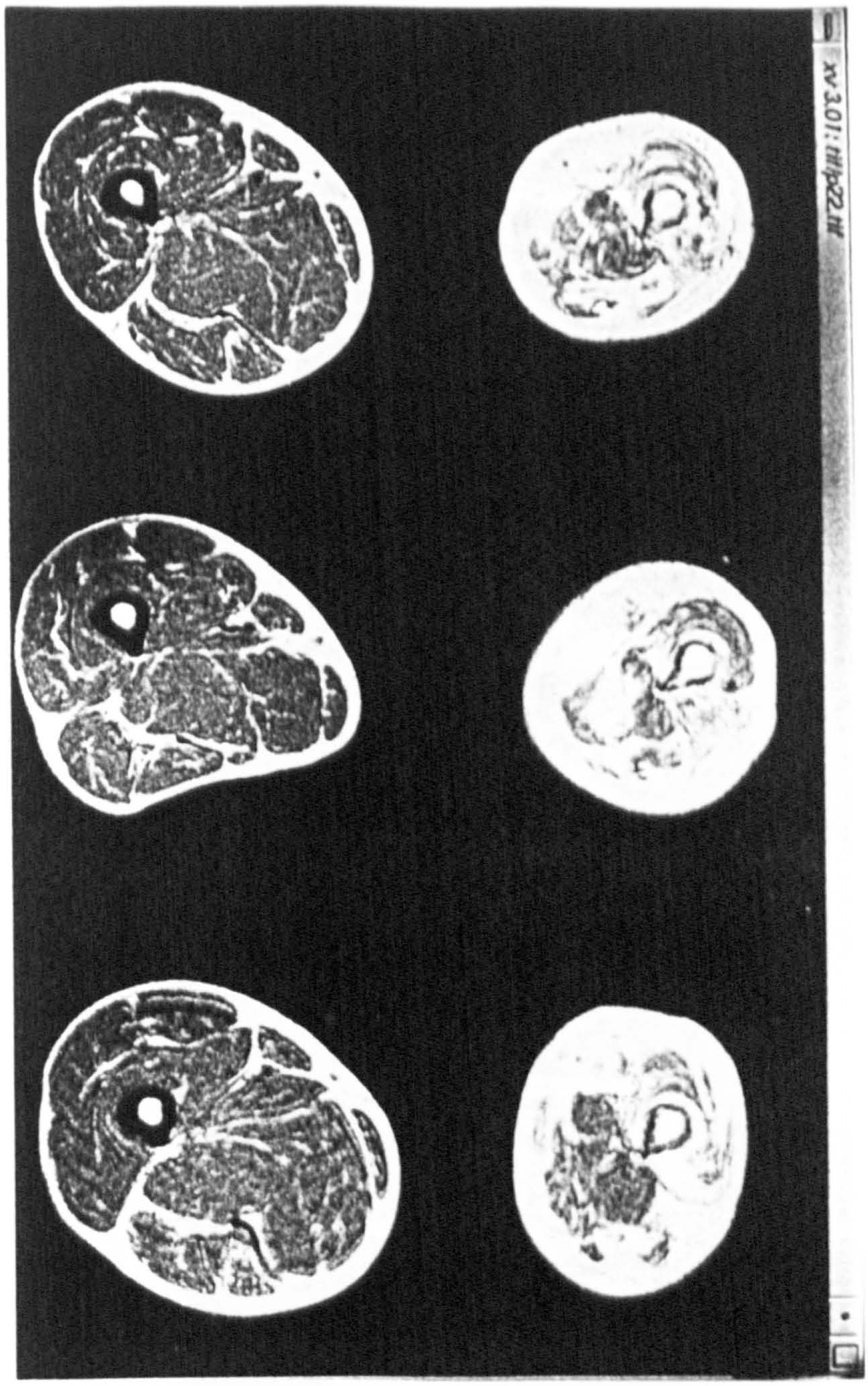

Fig. 9.5.2.2 Transverse sections at approximately 70 mm distal to the ischial tuberosity. (Subject U)

a.) Residual limb in plaster cast (Natural shape).

b.) Residual limb after donning the quadrilateral socket.

c.) Residual limb after donning the ischial containment socket.

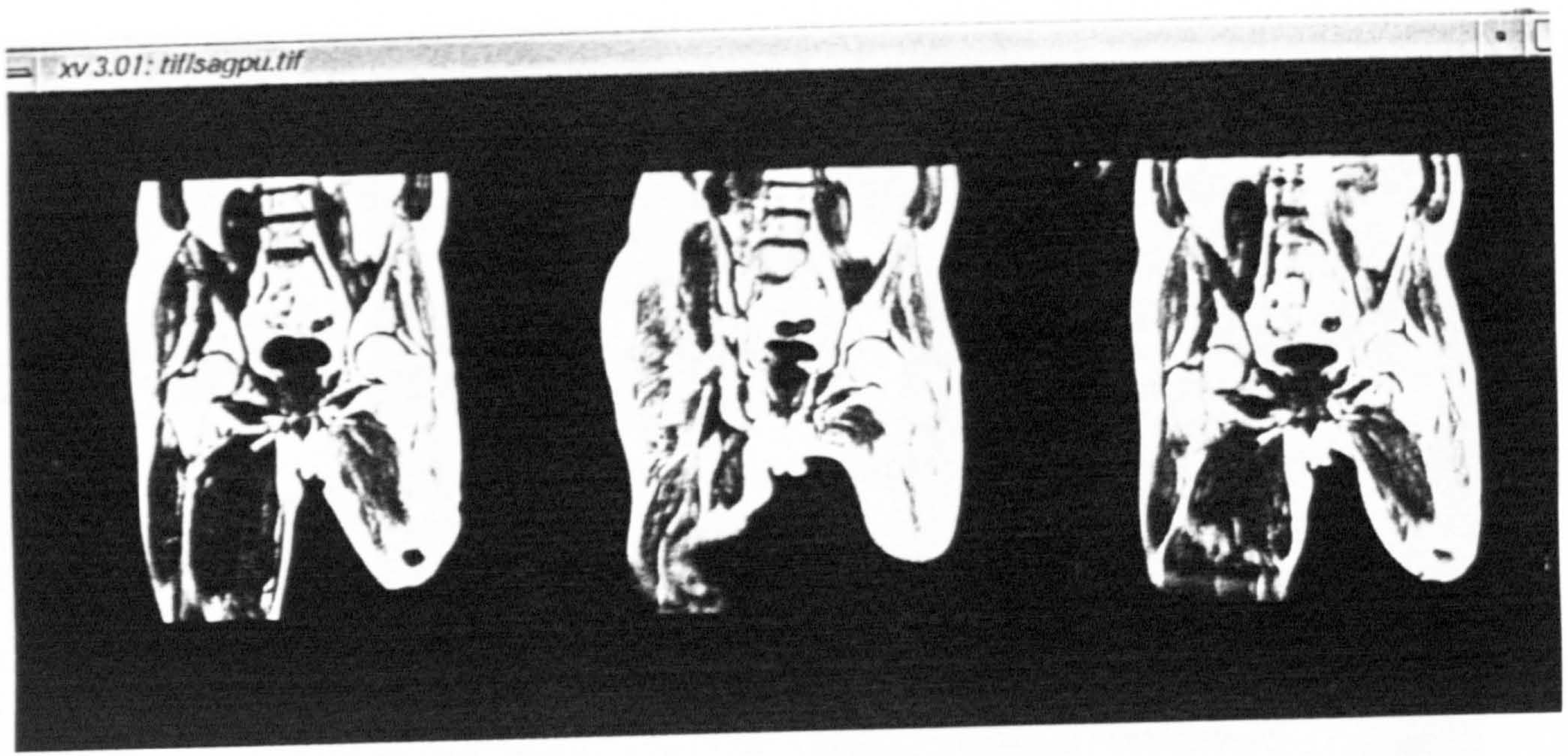

a.) b.) c.)

Fig. 9.5.2.3 Coronal view of subject U.
a.) Residual limb in plaster cast (Natural shape).
b.) Residual limb after donning the quadrilateral socket.
c.) Residual limb after donning the ischial containment socket.

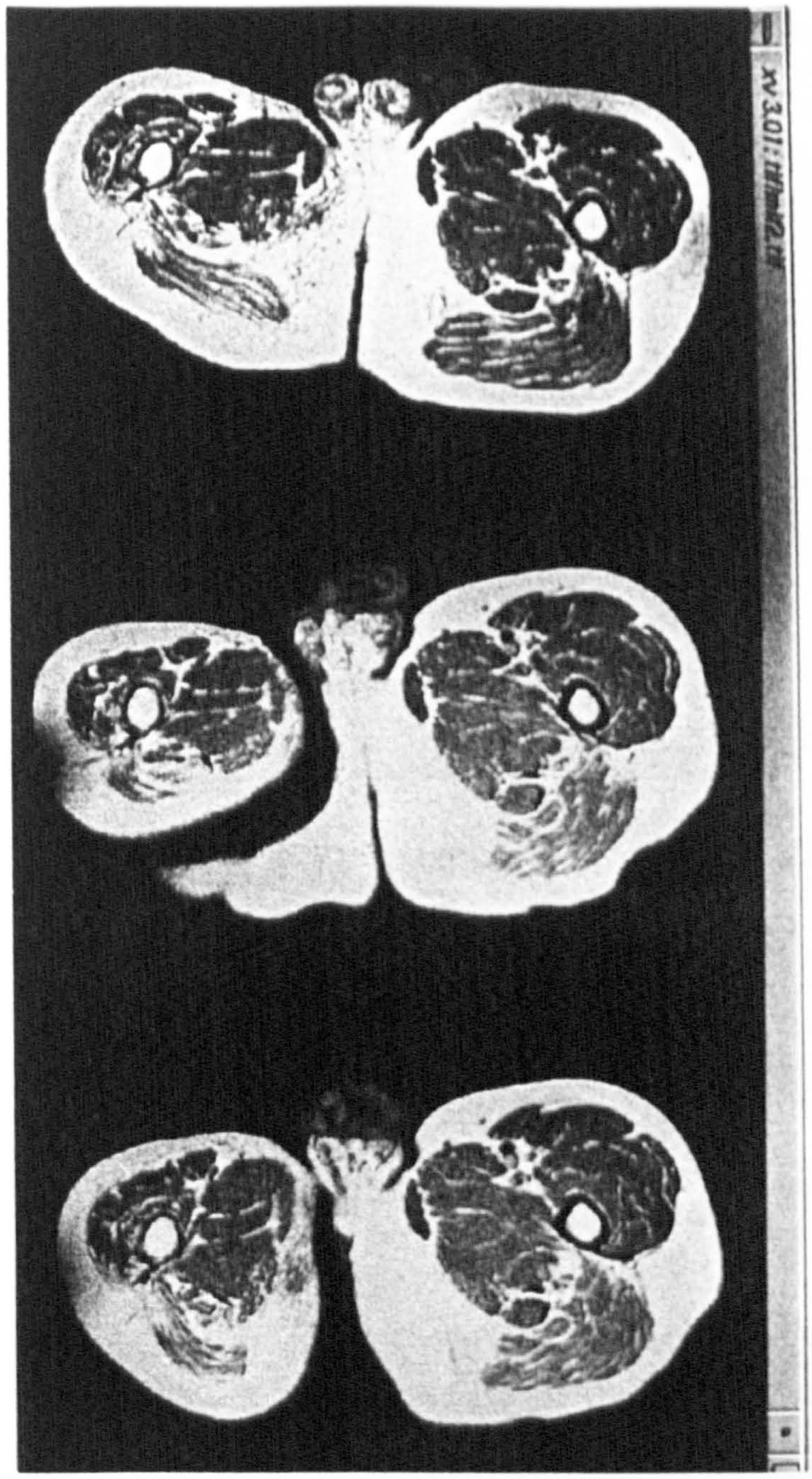

a.)

b.)

c.)

Fig. 9.5.2.4 Transverse sections immediately distal to the ischial tuberosity.
(Subject M)
a.) Residual limb in plaster cast (Natural shape).
b.) Residual limb after donning the quadrilateral socket.
c.) Residual limb after donning the ischial containment socket.

a.)

b.)

c.)

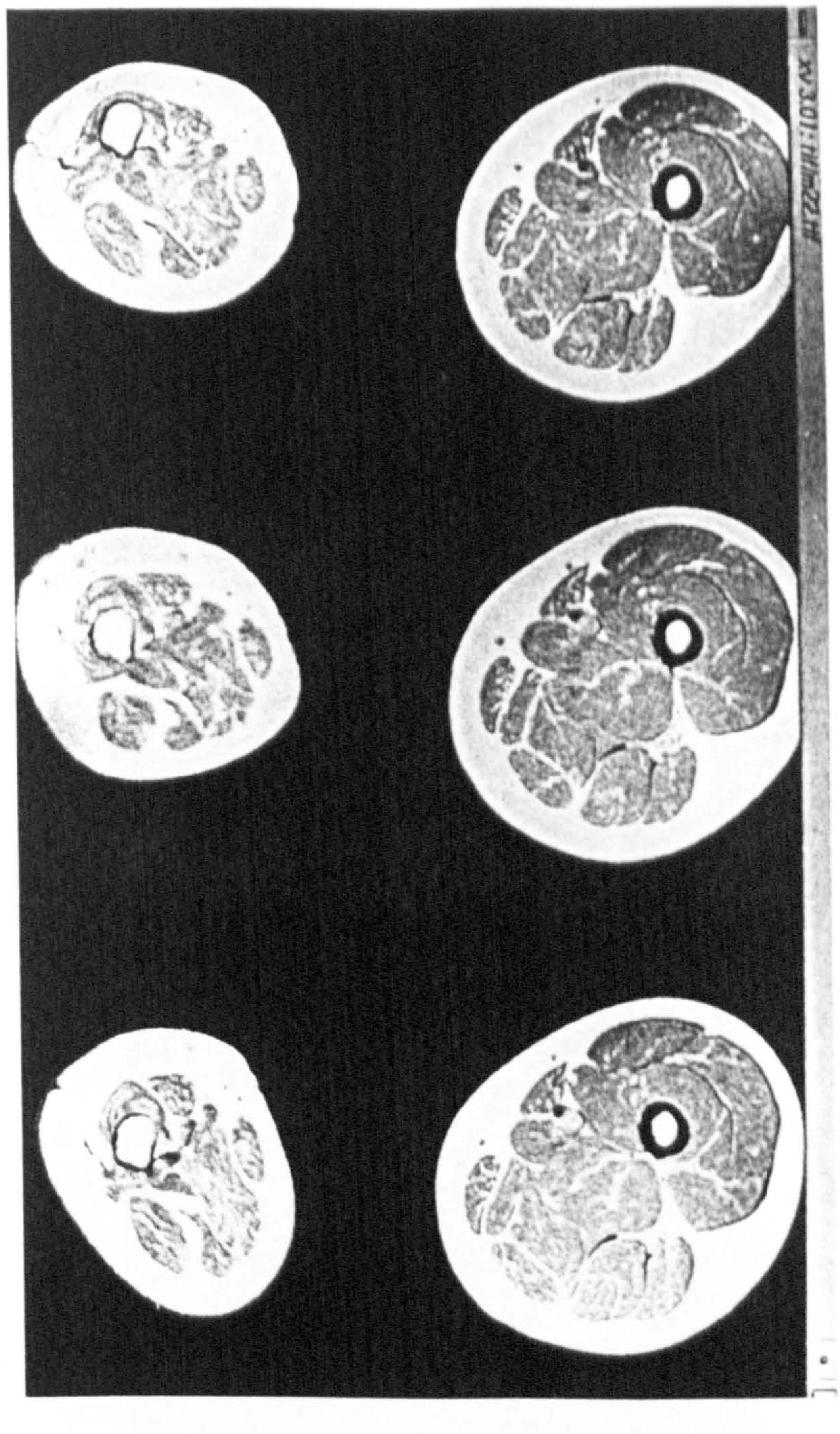

Fig. 9.5.2.5 Transverse sections at approximately 70 mm distal to the ischial tuberosity. (Subject M)
a.) Residual limb in plaster cast (Natural shape).
b.) Residual limb after donning the quadrilateral socket.
c.) Residual limb after donning the ischial containment socket.

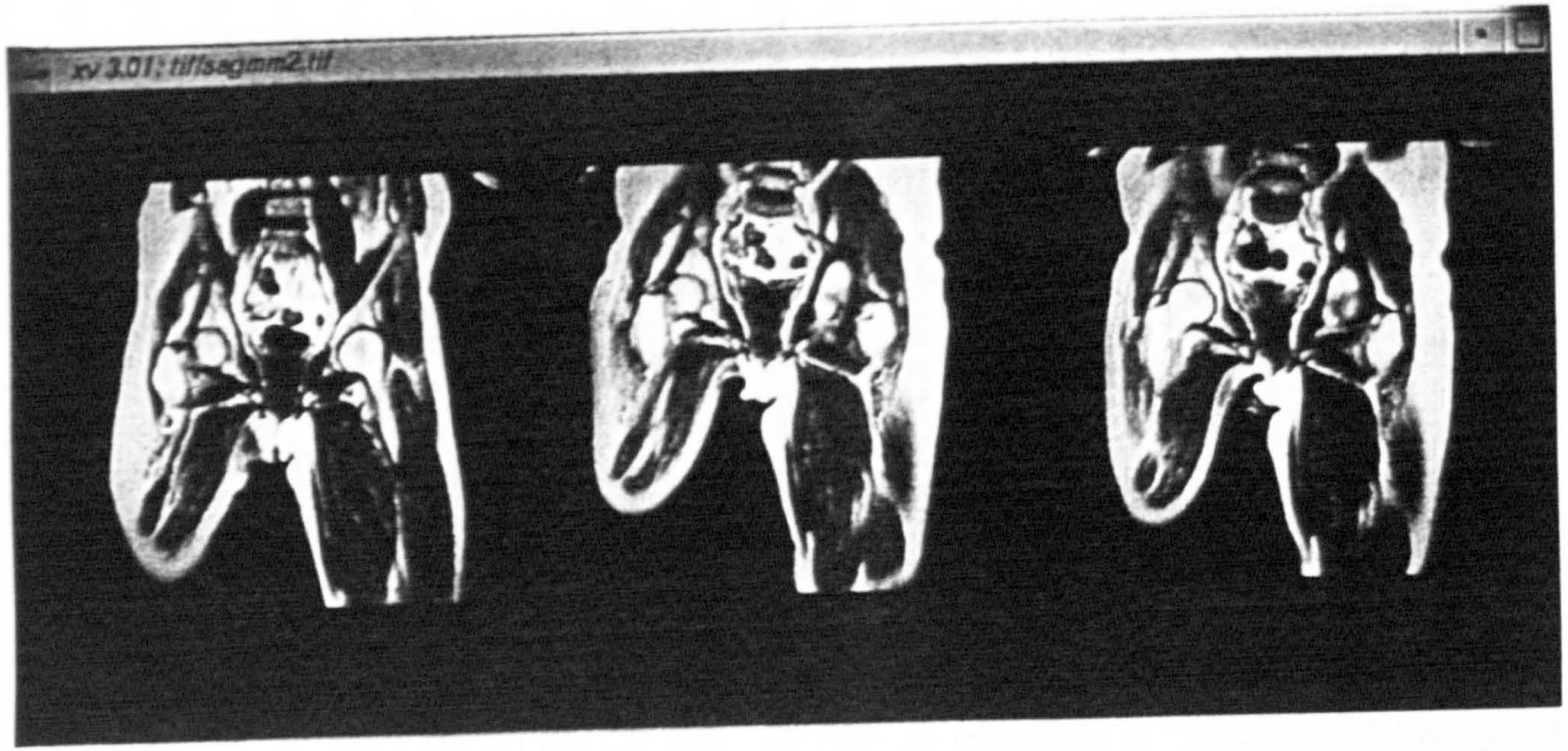

a.) b.) c.)

Fig. 9.5.2.6 Coronal view of subject M.
a.) Residual limb in plaster cast (Natural shape).
b.) Residual limb after donning the quadrilateral socket.
c.) Residual limb after donning the ischial containment socket.

Muscles	Sound limb (mm^2)	Residual limb (mm^2)	% difference
Vastus medialis / intermedius / lateralis. Tensor fascia latae	6275	3204	48.9
Rectus femoris	1903	732	61.5
Sartorius	516	383	25.8
Adductor longus	1748	1524	12.8
Adductor brevis	1094	638	41.7
Adductor magnus	4784	3705	22.6
Gracilis	562	262	53.4
Gluteus maximus	5658	2940	48.0

Table 9.5.3.1 Cross sectional area of the muscles at the ischial level (Subject U)

Muscles	Sound limb (mm^2)	Residual limb (mm^2)	% difference
Vastus medialis / intermedius / lateralis. Tensor fascia latae	5695	3290	42.2
Rectus femoris	1808	767	57.6
Sartorius	638	414	35.1
Adductor longus	1754	1556	11.3
Adductor brevis	1577	881	44.1
Adductor magnus	5719	3935	31.2
Gracilis	495	410	17.2
Gluteus maximus	8873	5055	43.0

Table 9.5.3.2 Cross sectional area of the muscles at the ischial level (Subject M)

Comparison was only performed for muscles at the ischial level, since muscles at the mid level of the residual limb were not discernible in the MR images.

The residual limb was significantly smaller in size compared to the good limb. Muscle atrophy occurred mainly at the gluteus maximus and the vastus muscles of the residual limb. These muscles appeared in the MR images as grey patches clouded with white spots, indicating muscles' degeneration to fat. The gracilis, sartorius, adductor longus, brevis and magnus though atrophied, experienced minimal fatty degeneration. There was almost no change in the size of the femur between the residual limb and the good limb, however, the marrow cavity in the residual limb was enlarged significantly reducing the thickness of the compact bone.

Table 9.5.3.1 and Table 9.5.3.2 tabulate the differences in the muscles cross-sectional area between the good limb and the residual limb at the ischial level for subjects U and M respectively. The difference in the size of the muscles can be attributed to muscle atrophy in the residual limb, or an increase in the muscle bulk in the good limb in order to compensate the limited functions of the residual limb. However, the author of this thesis reckons that muscle atrophy has indeed occurred as seen in the MR images which shows sign of muscle degeneration into fats. However, it is not clear how much of the difference in muscles size is due to the two above mentioned factors. Maximum difference was observed for both subject at the rectus femoris, 61% for subject U and 58% for subject M. The function of the rectus femoris was to extend the leg and flex the thigh, thus with the leg missing at the residual limb, the muscle was expected to degenerate. Most of the muscles controlling leg movement suffered similarly, the vasti muscles providing extension to the leg, the sartorius providing flexion to the leg. Among the adductor muscles, adductor brevis suffered the highest atrophy, this was followed by the adductor magnus and then the adductor longus. The main hip extensor, the gluteus maximus has atrophied above 40% in both amputees.

Besides the lack of muscular activities, the amount of muscle atrophy is also dependent on the level of amputation sites. Muscles which insert fully or partly on the shaft of the femur (adductor longus and magnus) will be least affected if the residual limb was kept long during amputation, retaining their functions. Another factor

Muscles	Natural (mm^2)	Quad (mm^2)	% difference
Vastus medialis / intermedius / lateralis. Tensor fascia latae	3204	2773	13.4
Rectus femoris	732	236	67.8
Sartorius	383	232	39.4
Adductor longus	1524	1505	1.2
Adductor brevis	638	459	28.1
Adductor magnus	3705	2580	42.4
Gracilis	262	202	22.9
Gluteus maximus	2940	1623	44.8

Table 9.5.4.1 Cross sectional area of the muscles at the ischial level (Subject U).
Natural - residual limb wearing plaster cast.
Quad - residual limb wearing quadrilateral socket

Muscles	Natural (mm^2)	Quad (mm^2)	% difference
Vastus medialis / intermedius / lateralis. Tensor fascia latae	3290	2620	20.4
Rectus femoris	767	660	14.0
Sartorius	414	361	12.8
Adductor longus	1556	1475	5.2
Adductor brevis	881	582	33.9
Adductor magnus	3935	2308	41.3
Gracilis	410	335	18.3
Gluteus maximus	5055	2585	48.9

Table 9.5.4.2 Cross sectional area of the muscles at the ischial level (Subject M).
Natural - residual limb wearing plaster cast.
Quad - residual limb wearing quadrilateral socket

affecting muscle atrophy is muscle attachment. Atrophy is likely to be more serious in muscles that are not attached during amputation. However, in this study the lack of surgical information on the subjects could not confirm this. The attachment techniques, myodesis or myoplasty may also have a bearing on muscle atrophy, again this could not be confirmed due to the lack of surgical information.

The difference in muscles size between the good limb and residual limb were quite similar for both subjects and could possibly be due to the long term used of the quad socket. Both subjects in the past have used the quad socket and recently been converted to the IC type of socket. It would be interesting to evaluate the same subjects again after several years to see any muscular changes had occurred with the use of the IC socket.

9.5.4 Residual limb changes after donning the quadrilateral socket

Fig. 9.5.2.1b and Fig. 9.5.2.4b display the transverse MR images with the subjects wearing the quad sockets at the ischial level. The gluteal musculature suffered high distortion due to the narrow anterio-posterior (A-P) dimension of the quad socket. All the muscles in general also experienced a slight lateral rotation and a reduction in cross sectional area. Table 9.5.4.1 and table 9.5.4.2 tabulates the residual limb muscles' cross sectional area in the natural state and after donning the quad socket at the ischial level. In both subjects, the cross sectional area of the gluteus maximus inside the socket was reduced by almost 50%. The quad compressed the residual limb in the A-P plane which forced the gluteus maximus to move proximally out of the socket onto the ischial seat. The rectus femoris and sartorius in subject U were also compressed considerably, 68% and 40% respectively, but in subject M these values were much lower, 15% and 14% respectively. The amount of fatty tissue that was observed in subject U was less than in subject M, which might explain why in the latter subject, the majority of the compression in the anterior posterior plane was taken up by the softer fat tissue leaving the deeper muscles less distorted.

Muscles	Natural (mm^2)	IC (mm^2)	% difference
Vastus medialis / intermedius / lateralis. Tensor fascia latae	3204	2396	25.2
Rectus femoris	732	407	44.3
Sartorius	383	290	24.2
Adductor longus	1524	1520	0.3
Adductor brevis	638	630	1.3
Adductor magnus	3705	2651	28.4
Gracilis	262	161	38.5
Gluteus maximus	2940	2014	31.5

Table 9.5.5.1 Cross sectional area of the muscles at the ischial level (Subject `U).
Natural - residual limb wearing plaster cast.
IC - residual limb wearing ischial containment socket.

Muscles	Natural (mm^2)	IC (mm^2)	% difference
Vastus medialis / intermedius / lateralis. Tensor fascia latae	3290	2744	16.6
Rectus femoris	767	760	0.9
Sartorius	414	377	8.9
Adductor longus	1556	1552	0.3
Adductor brevis	881	592	32.8
Adductor magnus	3935	3140	20.2
Gracilis	410	408	0.5
Gluteus maximus	5055	3104	38.6

Table 9.5.5.2 Cross sectional area of the muscles at the ischial level (Subject M).
Natural - residual limb wearing plaster cast.
IC - residual limb wearing ischial containment socket.

The muscles in the medial side were compressed considerably. The socket's medial brim progressed proximally until it was restricted by the adductor longus tendon, compressing the gracilis and the adductors muscles. However, the deeper adductor longus recorded almost no change in cross sectional area in both subjects. On the lateral side, the vastus muscles recorded a reduction of cross sectional area of 12% and 20% in subjects U and M respectively but the muscles did not show substantial alteration in their shape compared to those in the natural state.

At the mid level of the residual limb, Fig. 9.5.2.2b and Fig. 9.5.2.5b, it was observed that the muscle size in the quad socket was almost similar to those in their natural state. However, the muscles for both subjects were generally forced to rotate laterally, which causes some posterior muscles (biceps femoris, semitendinosus and semimembranosus) to alter their shape.

9.5.5 Residual limb changes after donning the ischial containment socket

Unlike the quadrilateral socket, the IC socket provides a posterior compartment to contain the gluteus maximus at the ischial level (Fig. 9.5.2.1c and Fig. 9.5.2.4c). Nevertheless, a substantial amount of soft tissue compression still took place at this region, reducing the cross sectional area of the gluteus maximus from its natural state by about 30% and 40% for subjects U and M respectively. Table 9.5.5.1 and table 9.5.5.2 show the changes in the cross sectional area due to the donning of the IC socket. The muscles at the anterior socket wall, the rectus femoris and the sartorius were reduced by 44% and 24% respectively for subject U. However in subject M, the cross-sectional area of these muscles only decreased by 1% and 8% respectively. This again could be reasoned by the larger amount of fat tissue present in subject M residual limb. In the medio-lateral plane, the adductor magnus and the gracilis at the medial wall and the vastus muscles at the lateral wall were reduced considerably for subject U. In subject M, the gracilis hardly showed any changes. Compression in the medial wall was mostly taken up by the adductor brevis and magnus. In both subjects, the adductor longus were left undistorted.

Moving down to the mid level (Fig. 9.5.2.2c and Fig. 9.5.2.5c), the residual limb in the IC socket was elliptical in shape. The muscles experienced a medial

Subject	Sound limb	Plaster cast (Natural)	Quad socket	IC socket
U (Ischial level)	45061	36506	28854	29720
U (Mid level)	35491	24335	23883	22842
M (Ischial level)	37980	23561	22106	21809
M (Mid level)	54124	42356	26785	33281

Table 9.5.6.1 Cross sectional area of the sound limb and the residual limb wearing the plaster cast, quadrilateral and ischial containment socket.
(All values in mm^2)

Subject	A	B	C
U (Ischial level)	19.0%	20.9%	18.5%
U (Mid level)	31.4%	1.9%	6.1%
M (Ischial level)	21.7%	36.8%	21.4%
M (Mid level)	38.0%	6.2%	7.4%

Table 9.5.6.2 Percentage difference in residual limb cross section area.
A - % difference between the sound limb and the residual limb.
B - % difference between the residual limb in plaster and residual limb in quad socket.
C - % difference between the residual limb in plaster and residual limb in IC socket.

rotation, where the vastus muscles were forced towards the anterior socket wall and the adductor muscles towards the posterior wall.

9.5.6 Discussion

Muscles atrophy

A varying degree of muscular atrophy was observed in the residual limb after trans-femoral amputation. Highest atrophy was observed at the rectus femoris in both subject. From the MR images, the gluteus maximus in both subjects were significantly degenerated into fat. The difference in the gluteus maximus cross sectional area between the good leg and the residual limb were greater than 40% for both subjects. At the ischial level of subject U, the overall cross sectional area on the good side was 45061 mm^2 and the amputated side was 36506 mm^2, a total difference of 19%. In subject M, this value was 21.7%. At mid level the difference between the good and the residual limb was greater, 31.4% and 38% were observed for subjects U and M respectively (see Table 9.5.6.1 and table 9.5.6.2).

Donning the prosthetic socket

The donning of the prosthetic socket caused the residual limb to be reduced in volume. This could be confirmed by the reduction in cross sectional area at the ischial and mid level of the residual limb as shown in table 9.5.6.1 and 9.5.6.2. The reduced volume was necessary for the residual limb to be in total contact with the socket inner surface, maintaining socket suspension. The prosthetist shapes the socket accordingly to obtain socket / residual limb stabilisation and comfort. Regions where the residual limb is sensitive to load are relieved by an increase in the socket volume while in regions where load can be tolerated, the volume is decreased.

Considering soft tissue to be incompressible, the decrease in volume leads to the conclusion that there was a redistribution of the residual limb soft tissues. The main bulk of the soft tissue was likely to be directed proximally out of the socket since the socket enclosed the distal end of the residual limb. However, it was difficult to track the exact behaviour of this effect from the MR scans.

Quad and the IC sockets

In general, the quad socket could be assumed to be smaller in volume compared to the IC socket. As shown in table 9.5.6.2, the residual limb cross sectional area was reduced by 20.9% in the quad and 18.5% in the IC for subject U at the ischial level, and for subject M these figures are 36.8% and 21.4%. The difference in the cross sectional area could be explained by the way the two types of sockets were designed to transmit load. As already elaborated in other parts of this thesis, the quad provides a flat seat and the IC a sloping seat for the ischial tuberosity. Therefore the quad's posterior wall ends just distal to the ischial tuberosity forming the ischial seat while the IC socket posterior wall extends above the ischial tuberosity enclosing it. For the ischial tuberosity to be positioned on the ischial seat, the anterior and posterior walls of the quad socket had to compress the residual limb tissue considerably at the region immediately distal to the ischial tuberosity, forcing the ischial tuberosity onto the seat. The posterior wall is therefore made flat. In contrast, the IC socket's posterior wall had to enclose the ischial tuberosity thus requiring more space which was provided by a curved posterior wall.

The difference in the cross sectional area between the quadrilateral and the IC socket was not as large as that at the ischial level. Subject U 's quadrilateral was in fact larger than the IC by 4.2% while subject M's quadrilateral was only smaller than the IC by 1.2%.

Antero-posterior dimension

It has been remarked that the larger AP dimension and the more anatomically shaped anterior and posterior walls of the IC socket allowed the residual limb flexors and extensors to expand naturally (Sabolich 1985). In several studies, it was also noted that by allowing the muscles to function naturally in the IC socket, hypertrophy of the AP muscles occurred, unlike the quad socket where muscles were squeezed, losing their effectiveness which leads to muscles atrophy (Flandry et al 1989, Sabolich 1985). From this study, it could be confirmed that the anterior muscles (rectus femoris and sartorius) and the posterior muscles (gluteus maximus) at the ischial level were in a state of higher compression in the quad than in the IC socket for both subjects. As

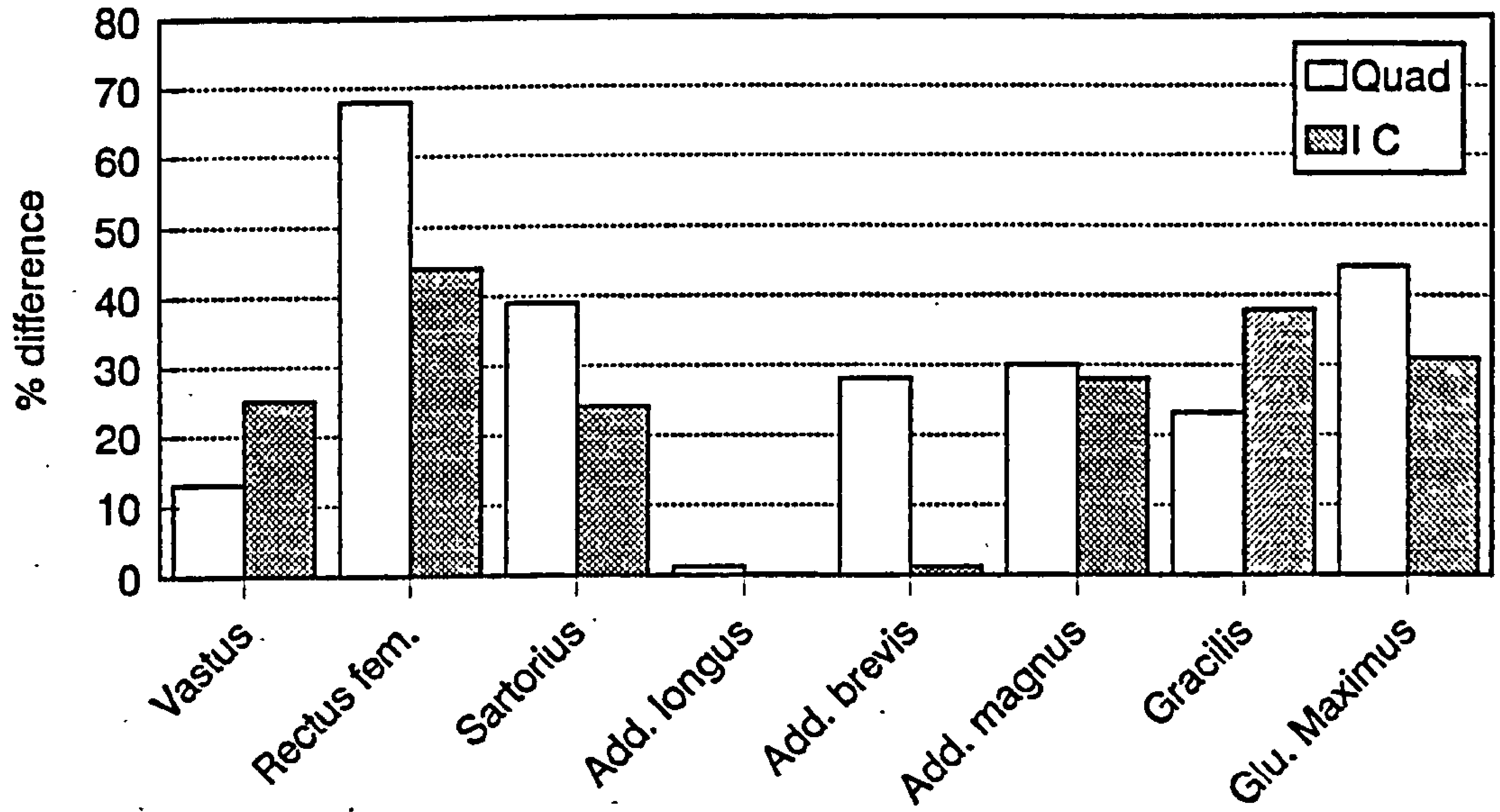

Fig. 9.5.6.1 Percentage difference in the muscles' cross sectional area between the residual limb wearing plaster cast and the two types of sockets. (Subject U)

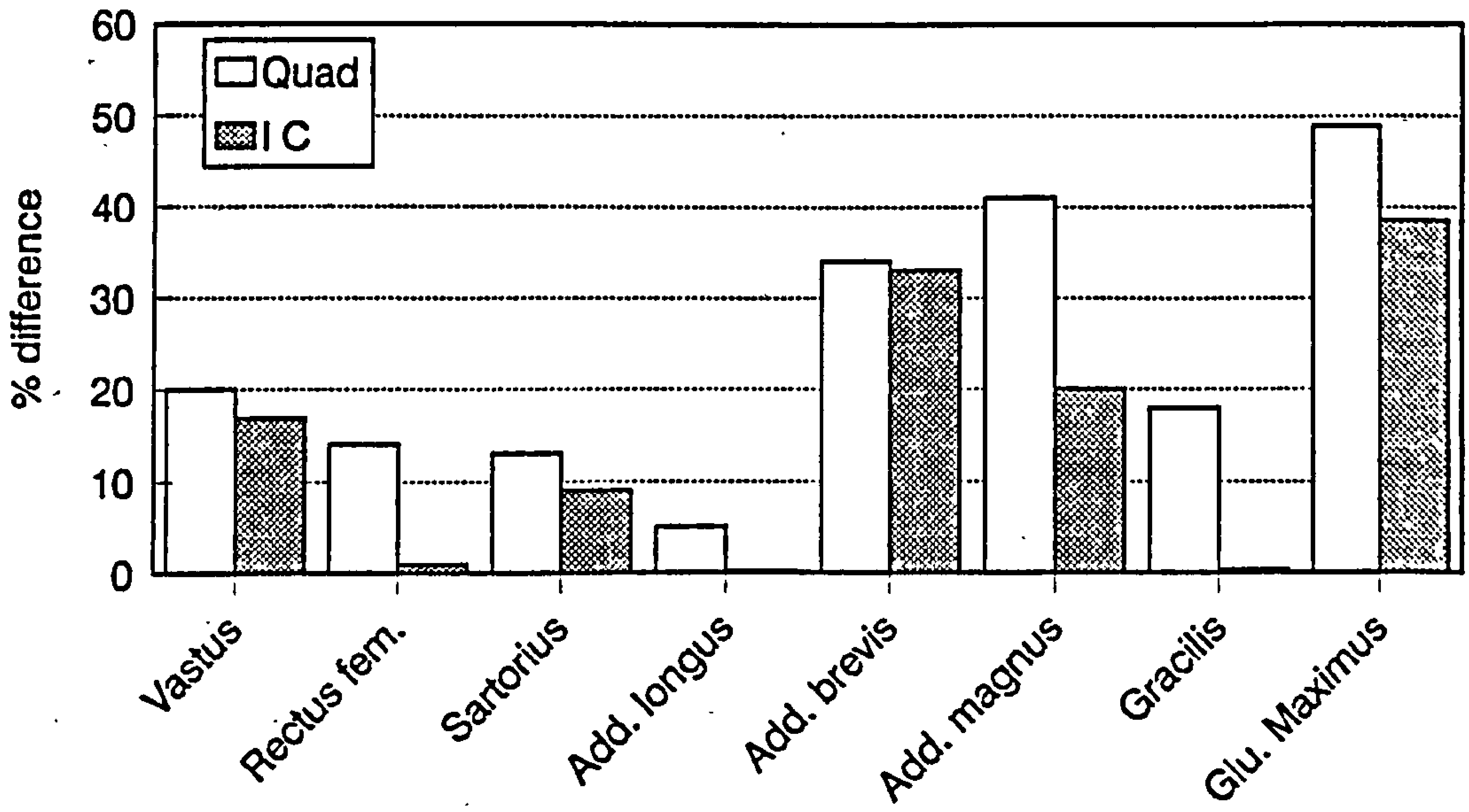

Fig. 9.5.6.2 Percentage difference in the muscles' cross sectional area between the residual limb wearing plaster cast and the two types of sockets.(Subject M)

shown in Fig. 9.5.6.1 and Fig. 9.5.6.2, subject U's rectus femoris, sartorius and gluteus maximus were 24%, 15.2% and 13.3% respectively smaller in the quad than in the IC, and in subject M, these figures were 13.1%, 3.8% and 10.3% respectively.

Medio-lateral dimension

Another criticism that the quad socket sustained from the advocates of the IC socket concerned the medial and lateral socket walls. Both Long (1985) and Sabolich (1985) described how the abduction of the femur in the quad socket was caused by its larger medio-lateral (M-L) dimension. The wider M-L dimension also allowed the ischial tuberosity to shift about on the ischial seat causing problems with stability in the M-L plane. It was claimed that the IC socket solved the problem by two means, a narrow medio-lateral socket dimension and a posteromedial wall that enclosed the ischial tuberosity and part of the inferior ramus of the ischium providing a bony lock that prevented the ischial tuberosity from shifting. With regards to the narrow ML dimension of the socket, Sabolich (1985) presented a schematic representation of the IC compared to the quad shown in Fig. 9.5.6.3. The diagram representing a plan view of both sockets at the level of the ischial tuberosity was different from than obtained from the MR images in this study. Fig. 9.5.6.4 shows a plan view traced from the MRI scans for subject M for the two sockets at a level immediately distal to the ischial tuberosity. The author of this thesis considers that two anatomical points, the position of the femur and the adductor longus tendon limit the medio-lateral dimension regardless of socket types. In Fig. 9.5.6.4 the lateral and anterior walls of the quad and the IC was almost identical. The medio lateral dimension of the IC begins to decrease with respect to the quad only when it was away from the adductor longus tendon. It was misrepresented in Sabolich's diagram that the adductor longus tendon could be shifted, and the difference in the ML dimension between the two sockets was overestimated. The narrow M-L dimension in the IC only becomes obvious towards the mid length of the sockets as shown in Fig. 9.5.6.5. Nevertheless, the curvature of the anterior and lateral wall of the IC at this level was still the same as that in the quad, but the IC socket's medial wall is displaced to form the narrower ML dimension.

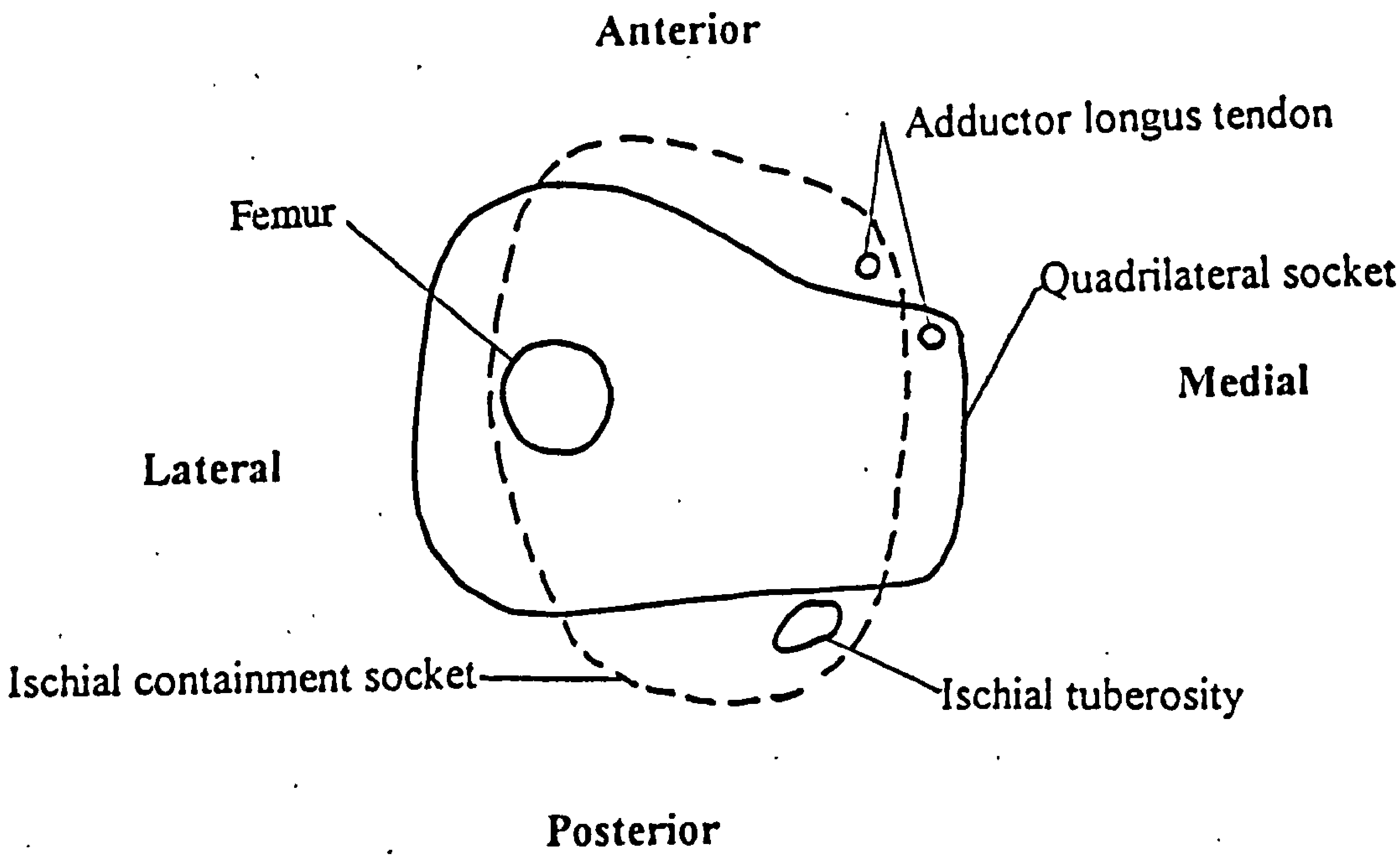

Fig. 9.5.6.3 Comparison of the quad and IC sockets as described by Sabolich, 1985.

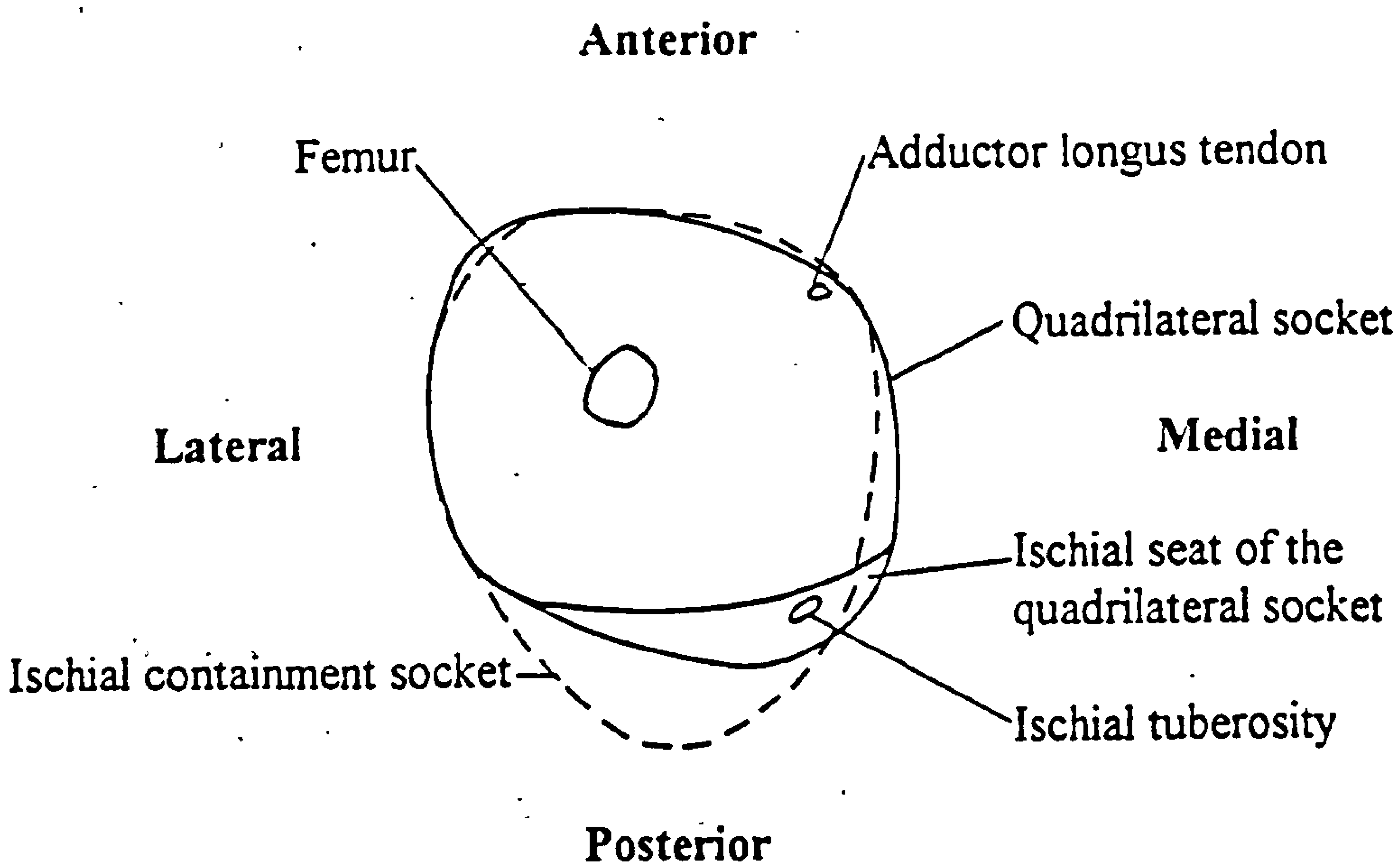

Fig. 9.5.6.4 Plan view immediately distal to the ischial tuberosity of the two types of sockets obtained from MRI scans..

In subject U (Fig. 9.5.6.1), based on the cross sectional area at the ischial level, the vastus and the gracilis were 16% and 12% smaller in the IC than in the quad socket. However, the adductors longus, brevis and magnus in the IC socket were larger than the corresponding muscles in the quad by 0.9%, 26.1% and 14% respectively. In subject M (Fig. 9.5.6.2), all the muscles in the IC at the ischial level were not squeezed as much as that in the quad as tabulated in table. 9.5.6.2.

Muscles shape

The author of this thesis understands that the 'more anatomical shape' as suggested by the advocates of the IC socket would mean that the residual limb muscles' shape in the socket should depart minimally from their natural unloaded state. Changes in the shape of individual muscles when the residual limb donned the two types of sockets could be observed from the MRI scans. Referring back to Fig. 9.5.2.1 to Fig. 9.5.2.6, the muscles' shape could be discussed by comparing the residual limb with and without the socket on. Upon donning the sockets, the residual limb medio-lateral dimension becomes smaller than its natural state which causes the adductor muscles to be circular in shape. However, due to the tight A-P dimension in the quad, the muscles were also flattened along the A-P plane causing the muscles to revert back to a shape quite similar to the natural condition. In the IC socket, the larger A-P dimension allowed the adductors to be maintained in their circular shape. The sartorius and rectus femoris in the quad were rectangular in shape while in the IC these muscles were again circular in shape, however, in the natural state these muscles are elliptical in shape. The vastus muscles remained largely unchanged in their shape for both sockets when compared to the natural state of the residual limb.

In the mid level of the residual limb, the narrow ML dimension of the IC caused the gracilis, adductors muscles and biceps femoris to be flattened along the medio-lateral plane. On the other hand, the quad at this level was able to maintain the muscles' shape similar to the residual limb in the natural condition.

It appears that to criticise that the quad is not anatomical in shape may be misleading. Besides the highly distorted gluteus musculature near the ischial

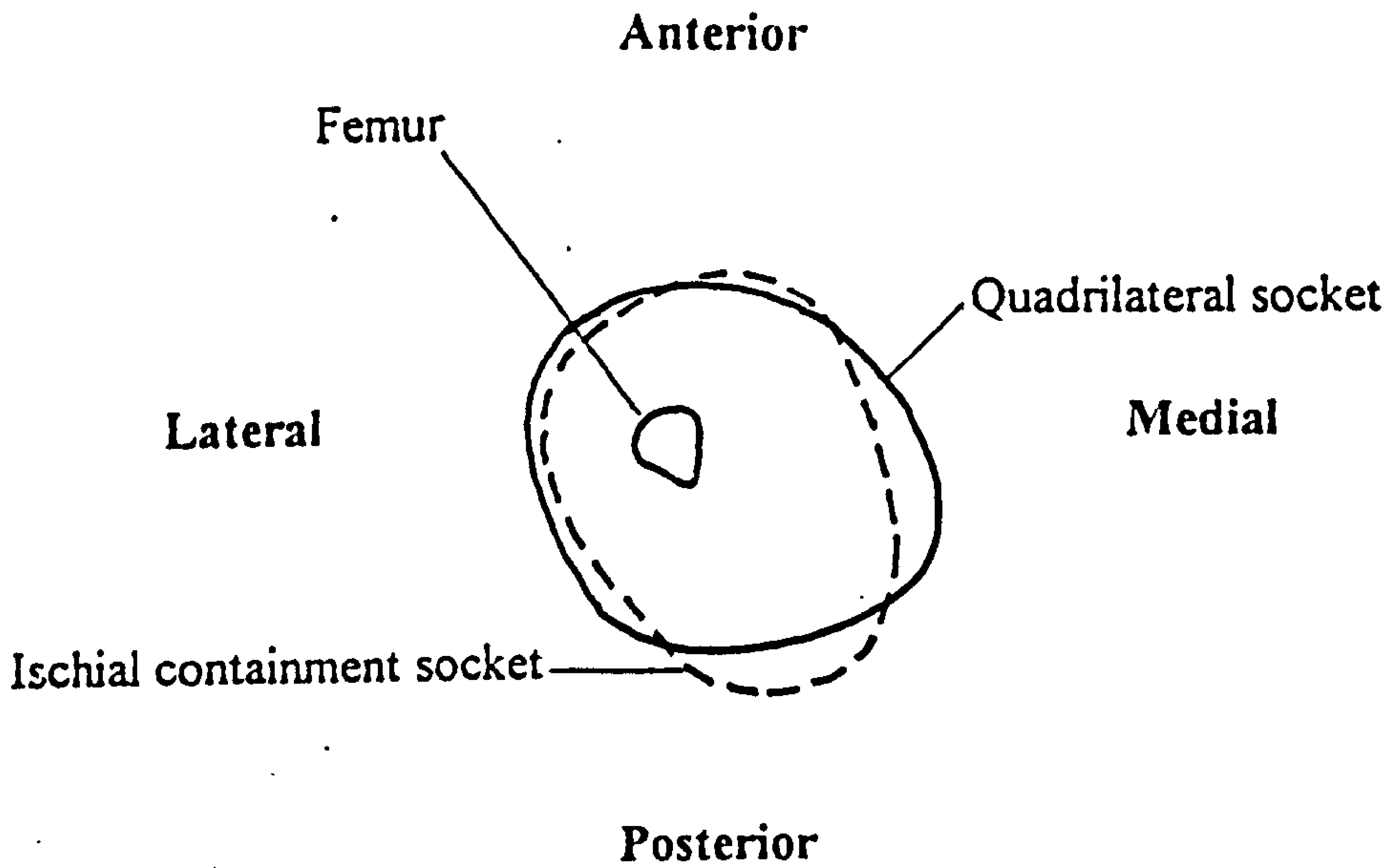

Fig. 9.5.6.5 Plan view of the quad and IC sockets at a level approximately mid length of the residual limb.

tuberosity, the muscles in the quad are shaped more like the natural state than in the IC.

9.5.7 Summary

Several claims for the IC socket should be reconsidered.

a.) The narrower ML dimension of the IC socket should apply mainly at the level below the ischuim.

b.) The claims that the IC socket is more anatomical in shape than the quad leading to better proprioception and muscles function is not clear.

From the result of this study, the IC socket does indeed allow more space for the muscles to expand at the ischial level, but at the mid level of the residual limb there is little difference between the two sockets. The author of this thesis believes that besides allowing space, the shape of the muscles would also have an effect of how well the muscles function. Though it is not clear at this point by distorting the shape of the muscles, what are the effects.

One main limitation in this study was that the imaging was performed under a non load bearing condition. The muscle size and shape relates only to the relaxed state. Nevertheless, all comparisons between the muscles' size and shape were carried out under the same condition. However, significant changes like femoral bone position, muscles' movement, shape and size should be expected under the load bearing condition.

9.6 GEOMETRICAL RECONSTRUCTION FOR FE MODELLING

In order to create 2-D or 3-D FE models based on the MR images, the transverse image data were reconstructed in a single slice or a series of slices respectively by digitisation. The data acquired with the Picker Vista imager were transferred into a SunSparc workstation in the University of Strathclyde. The data were in 8-bit integer form and each transverse image was contained in a single file. About 42 transverse slices were required for each scanned configuration, thus a similar number of files had to processed and digitised to obtain a 3-D image of the residual limb. A customised program was written in C programming language under

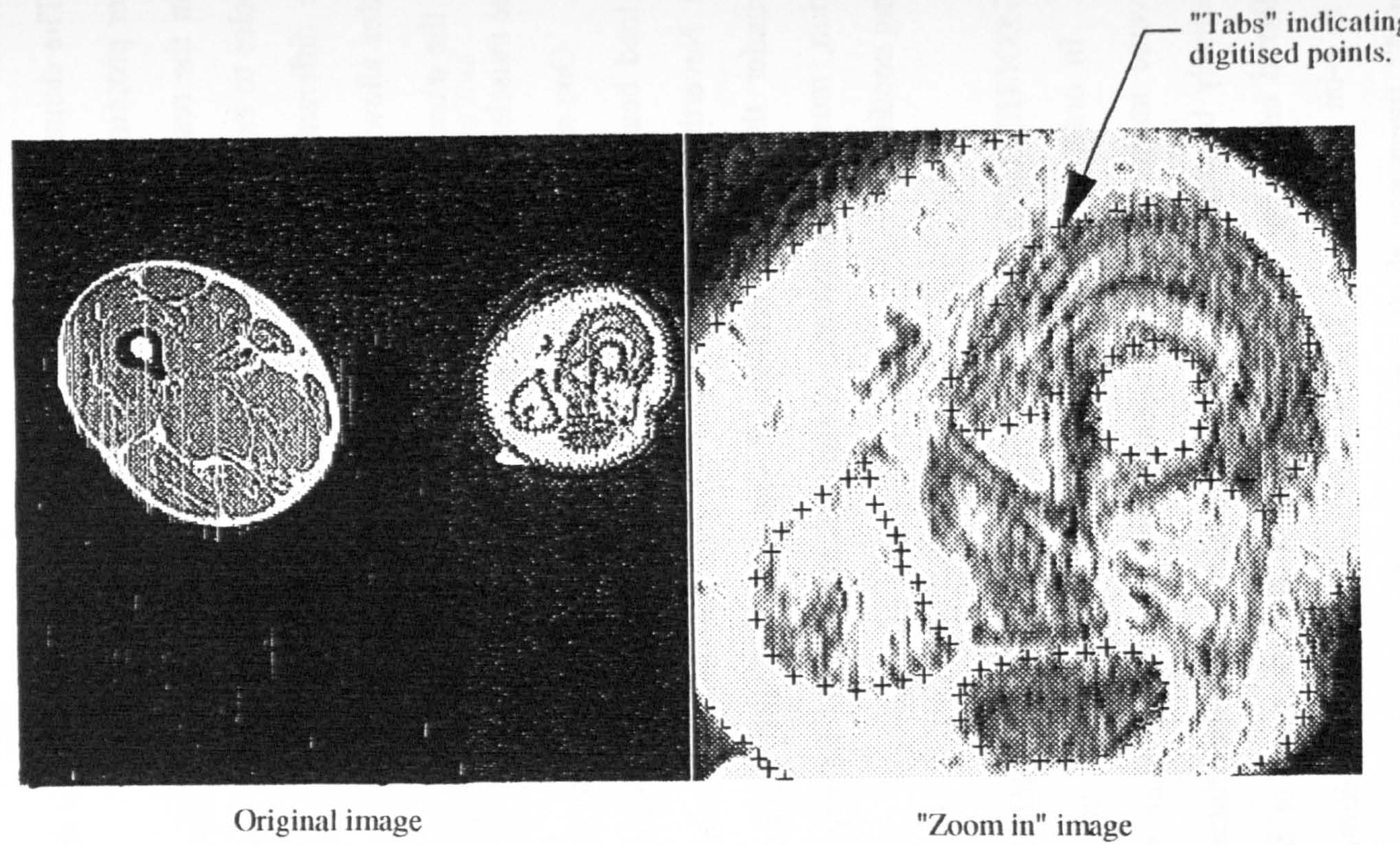

Fig. 9.6.1.1 Display of the digitisation software

the SunView environment for digitising the image. The program was designed to handle the different type of file format, view and digitised images using the workstation's keyboard and mouse.

9.6.1 Digitisation

The customised software written to process the image data have the following criteria ;

a.) read image data,

b.) create a window and display image,

c.) create another window to 'zoom in' image,

d.) vary grey level of image,

e.) digitise image and

f.) output digitised data in FE software package format.

In reading the image data, the program was designed to skip the header of each file and proceed straight into the pixel information. The header consisted of personal information on the subject which could jeopardise the anonymity of the subject. The data read were displayed as a 16 grey level image, 512 by 512 pixel (Fig. 9.6.1.1). The left window in Fig. 9.6.1.1 displayed the entire image of the transverse slice while the window on the right displayed an enlarged view of the left image. The latter image could be viewed in its entirety by shifting its view from left to right or up and down using the assigned arrow keys (←, →, ↑, ↓) on the workstation keyboard. The grey levels assigned to each pixel could be varied using the 'a' and 'z' keys. This helped in identifying different anatomical features, for example, by increasing the grey level of the bone, the bone appears in high contrast to the surrounding tissues.

The procedure of digitising was made easier by several features besides those already mentioned. The workstation mouse was the main 'pointer' during digitising. By moving the mouse hence moving a pointer on the right window ('zoom in' image) to the desired point, a tab which appeared as a '+' could be marked on the image by clicking the mouse. The tab also appeared in the left window showing the overall location of the digitised point. Any interesting feature of the image, for example, the outline of the residual limb could therefore be marked by continuously clicking the

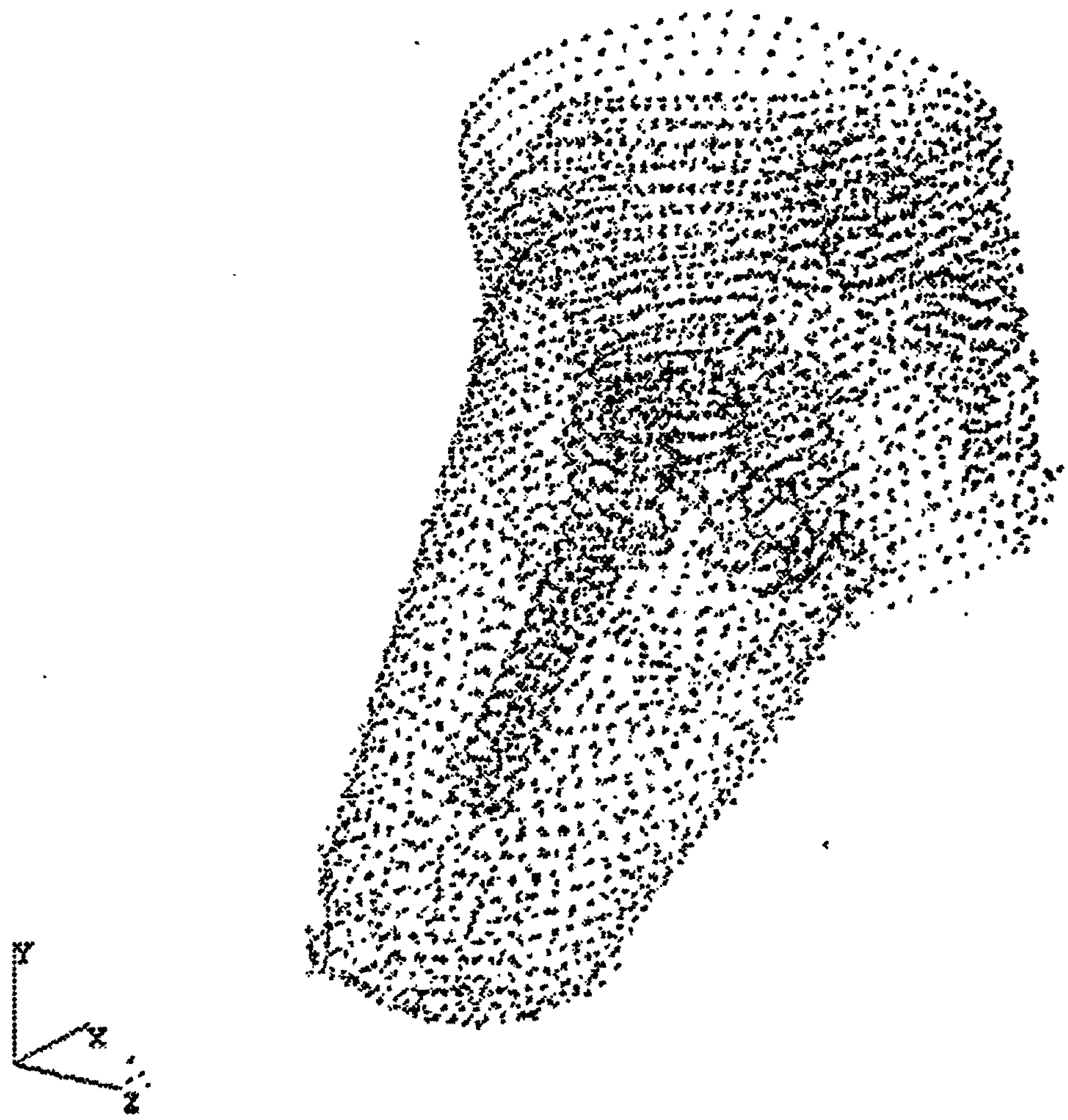

Fig. 9.6.2.1 Digitised points of the residual limb.

mouse, placing tabs on the skin surface of the transverse image. In the event of making a mistake, the 'x' key could be activated to erase the last digitised point and the 'r' key could be activated to re-display the image on the left window with the correct digitised points. Once the digitised points are confirmed to be correct, the pixel data are output to an ASCII file format comprehensible by the finite element packages used i.e. PATRAN and ANSYS.

9.6.2 Reconstruction

The ASCII file output from the digitisation program consisted of co-ordinates of the digitised points for each transverse MR image in a Cartesian co-ordinate system. Thus knowing the vertical distance between the images (10 mm), the digitised points could be built into a three dimensional model by 'stacking one ASCII file on top of the other' giving it depth. Fig. 9.6.2.1 shows the digitised points consisting of the femur, pelvis and the skin surface of the residual limb. Using these points, the geometry of the FE model can be determined, which will be discussed in more detail in the next chapter.

10.1 INTRODUCTION

In this final part of the thesis, the biomechanical behaviour of the trans-femoral residual limb was investigated in more detail using the finite element method. In chapter seven of this thesis, the residual limb models of three trans-femoral amputees demonstrated the ability to predict the interface pressures at the patient / prosthesis interface to a specific degree of accuracy. These previous models were attempted with limited geometrical, material, loading and boundary considerations. In terms of geometry, the model consisted of a bone surrounded by soft tissues. However, the soft tissues of the previous models were constructed without any differentiation into muscles, fascia and skin. Such simplifications were necessary in order to build a feasible 3-D model allowing the prediction of interface pressures which could be verified by pressure measurement techniques described in chapter four of the thesis. However, due to the simplifications, it becomes impossible to explore the response of the internal soft tissues to mechanical loading.

The imaging of the trans-femoral amputee's residual limb using MRI techniques, described in chapter nine of this thesis, enabled further modelling to include soft tissue geometrical details. This opened up a new avenue to look into the mechanical behaviour of the different soft tissues in the residual limb when subjected to loading introduced by the prosthetic socket. It is expected that material non-homogeneity and muscles' slippage have a significant effect on the stresses on the internal tissues structure. If this is the case, the previous 3-D model assuming a uniform bulk soft tissue would be insufficient in predicting the internal stress distribution, and may explain the discrepancy when comparing the predicted and measured pressure at the prosthesis / socket interface. However, to attempt a 3-D model which includes details of soft tissue geometry, the effect of muscle slippage and non - homogeneous material properties would be extremely difficult. Such a model can only be fulfilled with many assumptions leading to difficulties in evaluating its accuracy.

In this study, it is envisaged that the future aim is to create a 3-D model of the residual limb with sufficient detail to predict its mechanical responses accurately. The approach is to model a transverse section of the residual limb with accurate geometrical data obtained from MRI techniques in two dimensions. The 2-D model will concentrate on studying the three major aspects that affect stress distribution in the residual limb, material non - homogeneity, muscle slippage and changes in loading and boundary conditions. The versatility of the 2-D model allows parametric studies to be conducted leading to a better understanding of the biomechanical behaviour of the trans-femoral residual limb. In addition, the 2-D model also provides useful experience in understanding the capability and limitation in using the FE method for possible future 3-D model with similar amount of anatomical details.

10.2 OBJECTIVE

The objective of this part of the study is thus as follows ;

a.) To develop a two dimensional FE model of a transverse section of the residual limb with soft tissue geometrical detail.

b.) To study the biomechanical behaviour of the residual limb due to material non - homogeneity.

c.) To study the biomechanical behaviour of the residual limb due to muscle slippage.

d.) To study the biomechanical behaviour of the residual limb due to changes in the loading and boundary conditions.

d.) To investigate the feasibility of performing a 3-D model which includes more anatomical details.

10.3 TWO DIMENSIONAL MODEL OF A TRANSVERSE SECTION OF THE RESIDUAL LIMB

A transverse section of the residual limb was selected for modelling in 2-D. The transverse slice selected described the residual limb of subject M located at 30 mm distal to the ischial tuberosity. The study was split into three main sections, investigating material non - homogeneity, muscle slippage and changes in loading and boundary conditions. Under the three sections, several models investigating different parameters were attempted. In the model studying the material non - homogeneity of

a.)

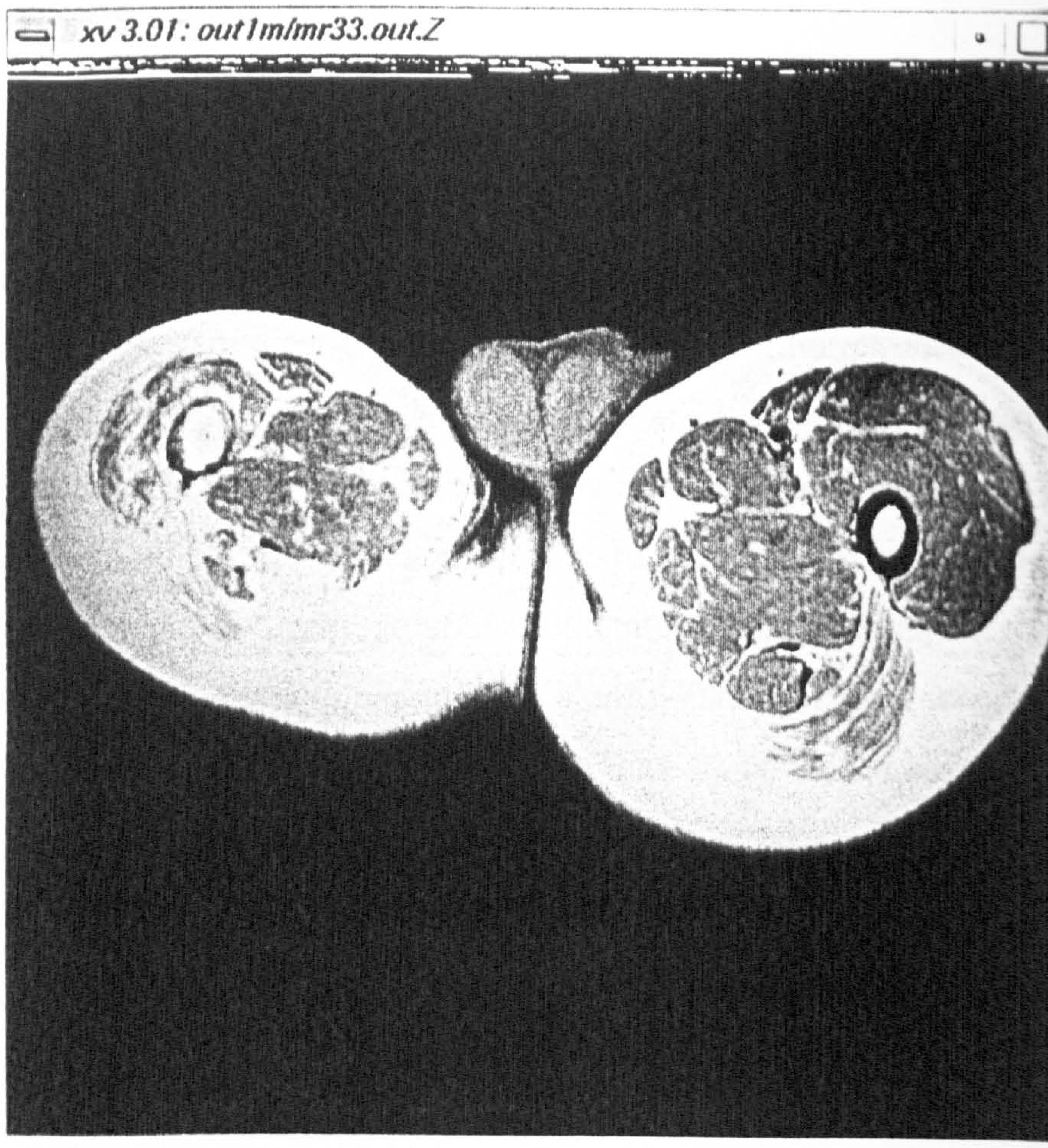

b.)

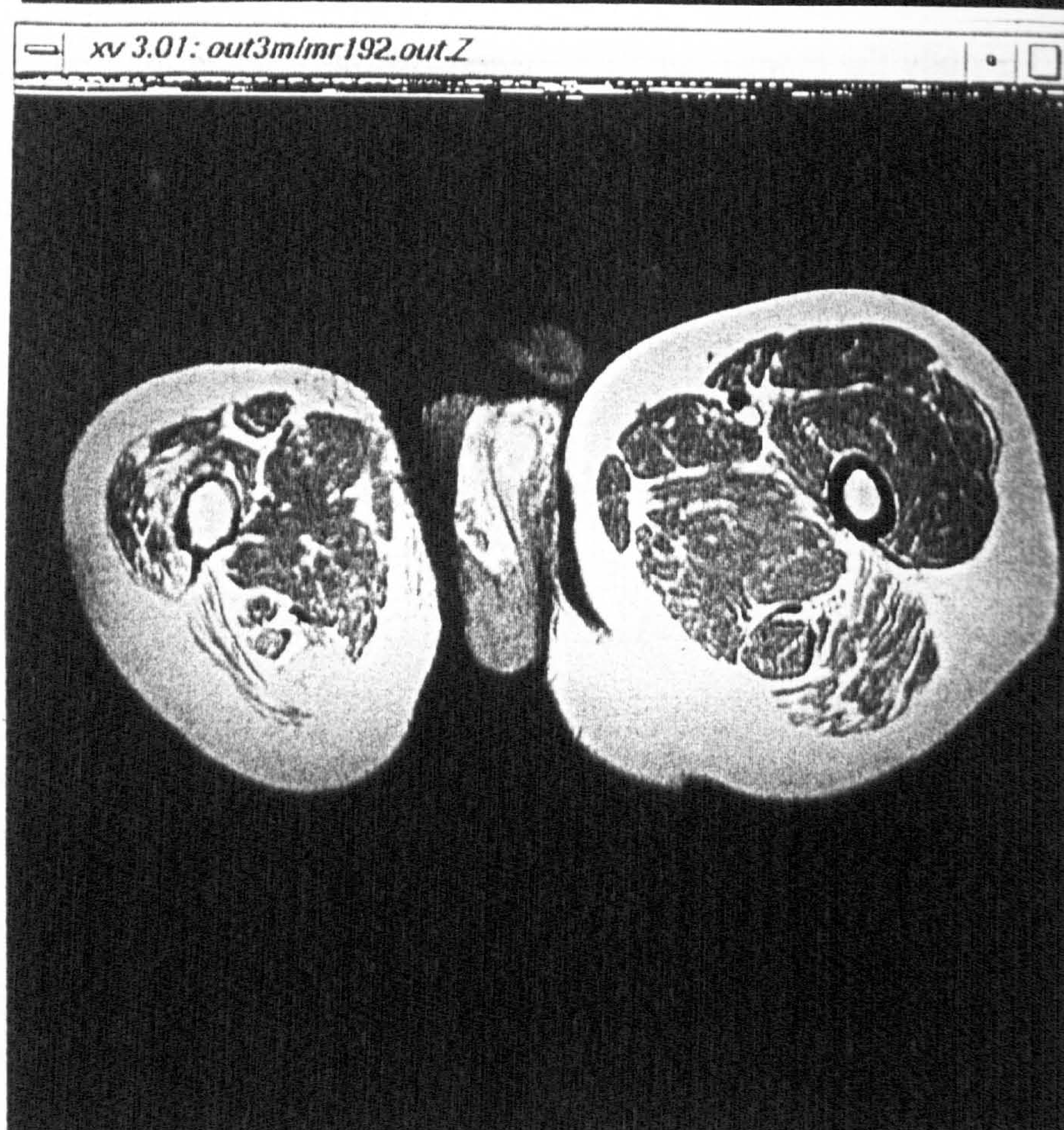

Fig. 10.3.1.1 Transverse section of a right trans-femoral amputee at a level 3 cm distal to the ischial tuberosity.
a.) The MRI image shows the natural unloaded state of the residual limb.
b.) The MRI image shows the state of the residual limb after donning an IC socket.

the residual limb, different elastic properties were assigned to fascia, intermuscular tissues and muscles. The muscle slippage models' main concerns were the behaviour at the interface between muscles and fascia, and muscles and muscles. Finally, different loading and boundary conditions at the residual limb / socket interfaces were also attempted.

10.3.1 Geometry

The geometry of the transverse section of the residual limb was digitised from MRI scans. The procedure has been described in full detail in chapter nine of the thesis. The level selected was 30 mm distal to the ischial tuberosity of the residual limb. Initially it was decided to study the level at the ischial tuberosity, due to its importance in prosthetic socket loading. However, at this level, muscles originate and insert at the tuberosity and pubis. In terms of geometry, this section was unique and its cross section differs considerably from the rest of the residual limb. This would mean that the section was less suitable to model in two dimensions, since a two dimensional model would assumes a uniform cross - sectional geometry in the out of plane dimension. In terms of material properties, the muscles at the origins and insertions would be significantly stiffer than muscles at other regions, thus the stress distribution at this particular level of the residual limb is dependent on the muscles' attachment. Considering the above mentioned variability, selecting a level 30 mm distal to the ischial tuberosity was considered most suitable. The level is proximally located where the residual limb tissue is subjected to large deformation caused by the socket brim, thus modelling is attempted at a severe loading situation. The muscles at this level are still actively used by the amputee and geometrically well defined.

The soft tissues in the model are generally divided into three main types, fascia, intermuscular tissues and muscles. In the MRI images, fascia, muscles and bone could be clearly distinguished, however it was impossible to define the epidermal layers. It was therefore considered suitable to model the geometry of the 2-D model by merging the epidermal layer with that of the hypodermis or the superficial fascia. This step was also taken to obtain a more uniform finite element mesh, since the

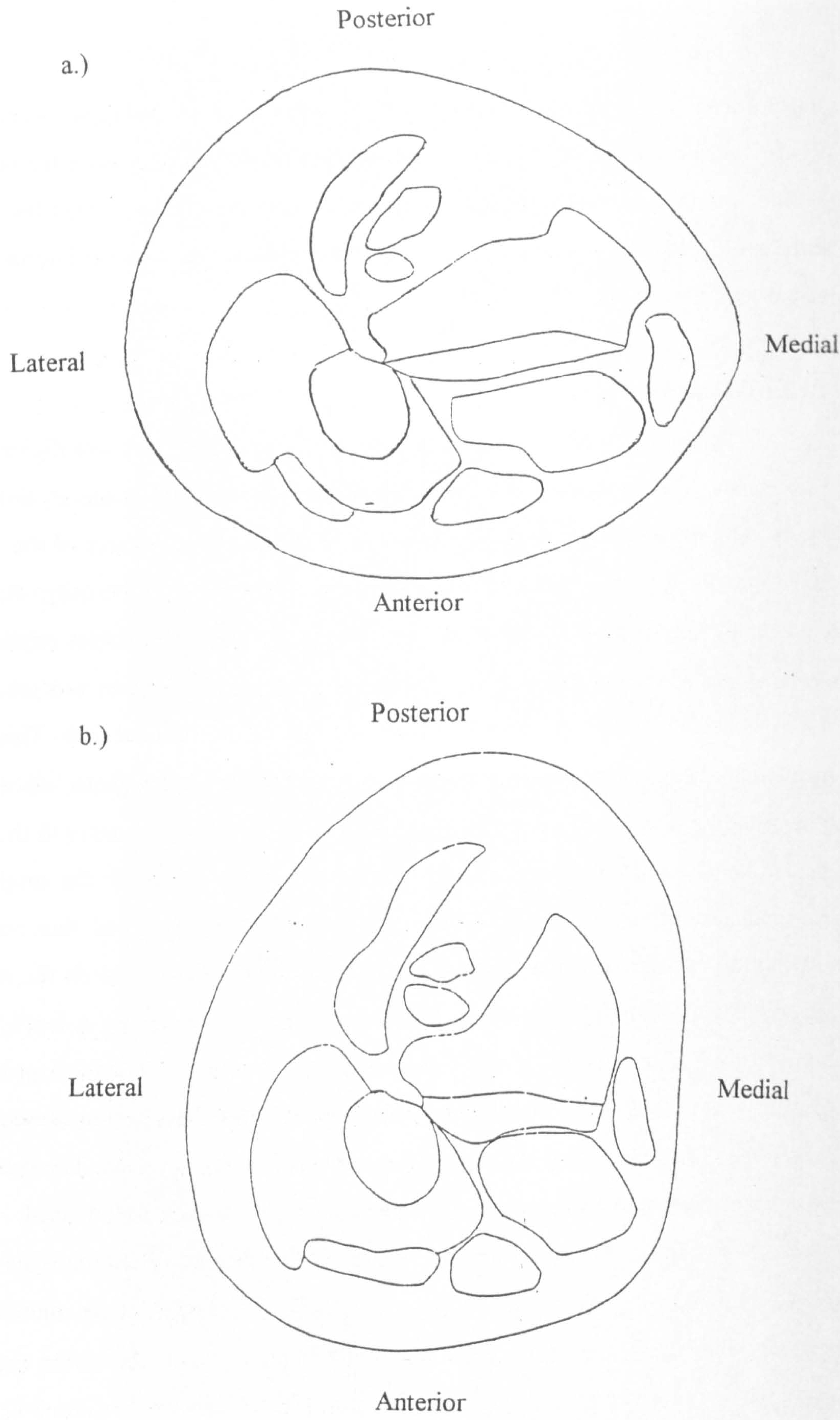

Fig. 10.3.1.2 The digitised points from the MRI images were connected by lines using ANSYS.
a.) The natural shape of the residual limb.
b.) The shape when wearing the IC socket.

inclusion of a thin epidermal layer could cause problems with meshing (elements' aspect ratio). The intermuscular tissue in the 2-D model are basically the deep fascia separating the different muscles group.

Another set of geometry was obtained for the purpose of specifying the loading and boundary constraints. It was based on the MRI image of the residual limb after donning the IC socket (Fig.10.3.1.1b). The image was of the same level and therefore could be compared directly to the natural unloaded shape of the residual limb.

The MRI scans were digitised as described previously in chapter nine. The digitised points were represented in x, y co-ordinates and were entered as keypoints into the FE software ANSYS 5.0 (Swanson Analysis Inc., USA). Fig. 10.3.1.2 shows the digitised points represented as lines in ANSYS. It also shows the location of the muscles of the residual limb in its natural unloaded shape and in the IC socket.

In the 2-D analysis, ANSYS was used throughout in pre-processing, solving and post processing. The hardware supporting ANSYS was a Silicon Graphics Indigo 2 workstation.

10.3.2 Meshing

The general element used was quadrilateral 4-noded elements (ANSYS PLANE42) (Fig. 10.3.2.1). In the model studying muscles' slippage, special elements were also included to describe the mechanics at the interface. These elements will be dealt with in more detail later. The most economical way to generate the elements was to use the procedure known as automatic mesh generation. This requires the specification of an ideal element size (4 mm face length) which ANSYS will attempt to maintain. Also in an attempt to control the distribution of elements, the lines representing the residual limb is firstly partition into suitable areas, ideally in rectangular form where quadrilateral elements could be fitted. In areas possessing large or small included angles, automatic meshing will invoke triangular elements (collapsed quadrilateral element) instead. Fig. 10.3.2.2 shows the final mesh of the

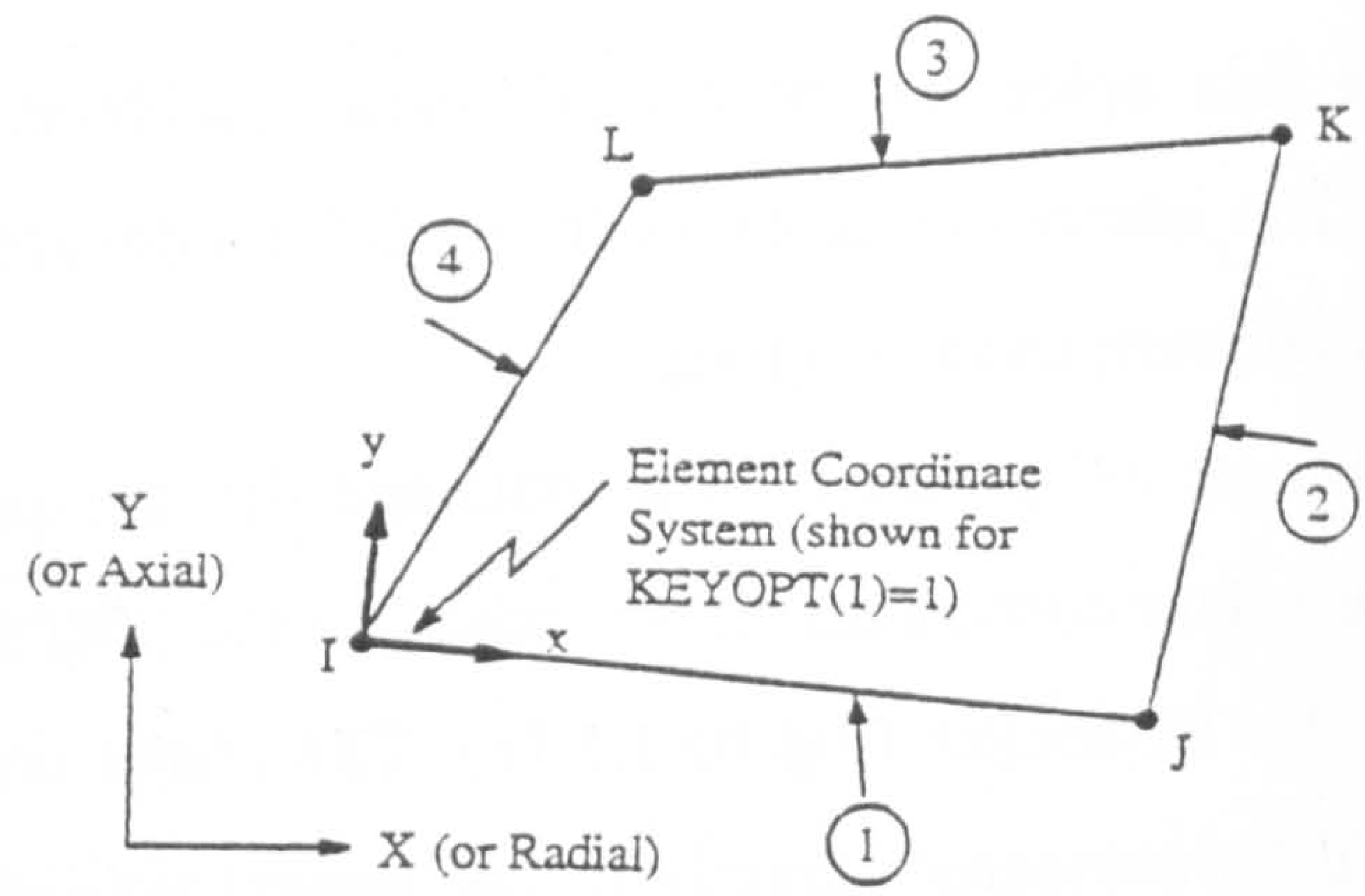

Fig. 10.3.2.1 ANSYS PLANE42, 2-D four noded quadrilateral element.
(Swanson Analysis System Inc, 1994)

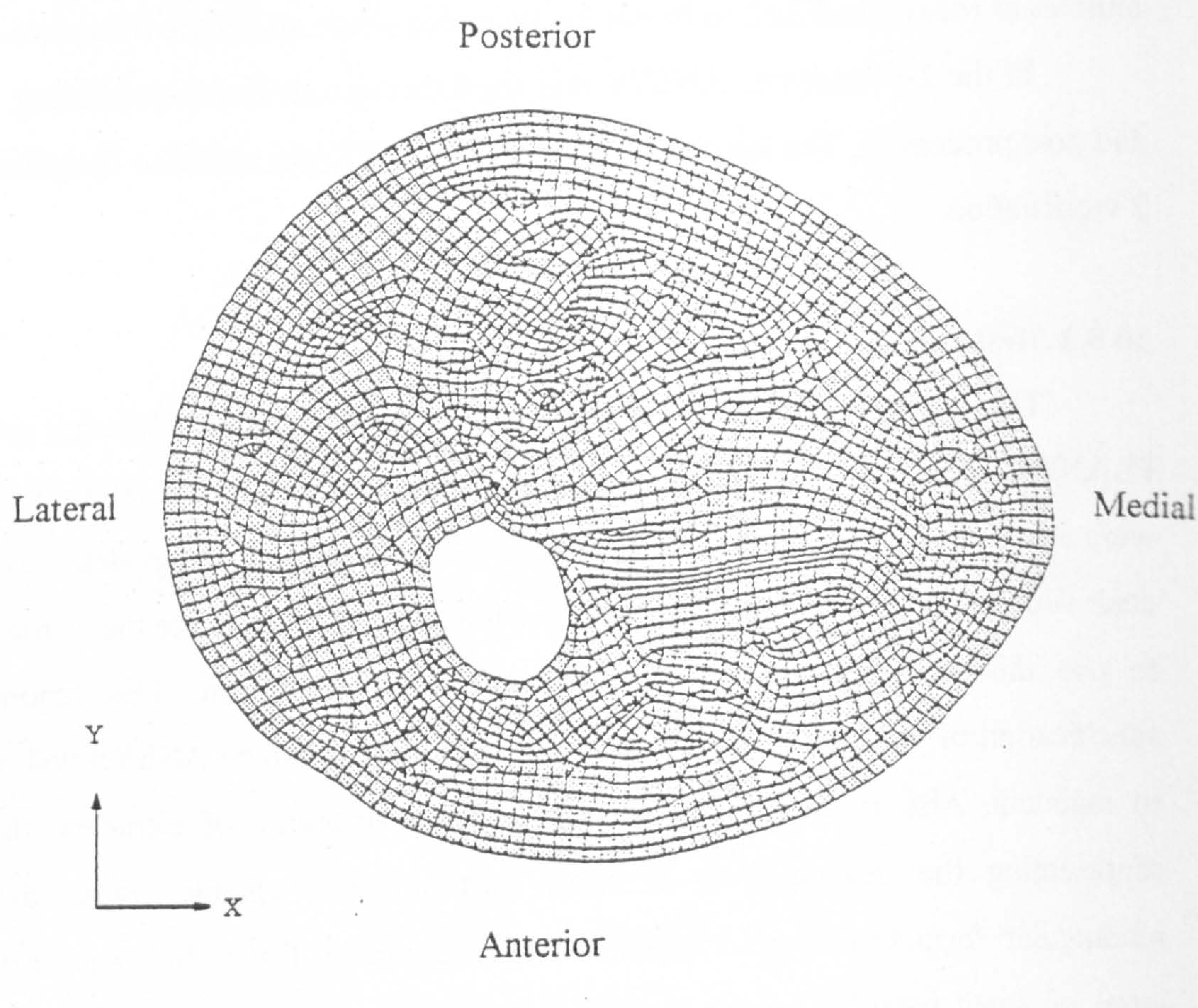

Fig. 10.3.2.2 Finite element mesh of the transverse section of the residual limb.

transverse slice in of the residual limb in its natural unloaded shape. The basic mesh consisted of 2826 elements and 8441 nodes.

10.3.3 Loading and boundary conditions

The 2-D model of the residual limb was loaded by displacing its external contour to the shape of the donned socket. This would enable the model to predict the soft tissue stress distribution and displacement caused by donning of the prosthetic socket. Based on the MRI scans, the digitised external contour of the residual limb in its natural unloaded state was superimposed onto the shape of the residual limb wearing the IC socket. The difference between the two shapes could therefore be calculated as x and y displacements and applied to the FE model. However, prior to calculating the displacements, the residual limb has to be brought to the same orientation. This was because the orientation of the residual limb when undergoing MRI was not the same due to physical constraints. The image obtained for the natural shape residual limb was slightly rotated and translated from the residual limb donning the IC socket. In order to transform them to similar orientation, a minimum of two landmarks were required. The two landmarks selected were found on the bone. They were the point where the adductor longus inserts and the linear aspera of the femur, where the adductor brevis inserts. The bone was logically chosen as a suitable landmark because it was the least affected by changes due to donning of the prosthetic socket. Using the global co-ordinates of the two landmarks, the transverse section of the residual limb wearing the IC socket was transformed to the same orientation as that of the residual limb in the natural state.

After the transformation, the displacements required to deform the residual limb to the shape of the IC socket were calculated. This was accomplished by identifying an arbitrary centre, where a multitudes of straight lines could be constructed by joining it to the nodal points at the external contour of the FE model (Fig. 10.3.3.1). The straight lines were further extended out so that they meet the contour of the socket forming a second intersection point. The difference between the

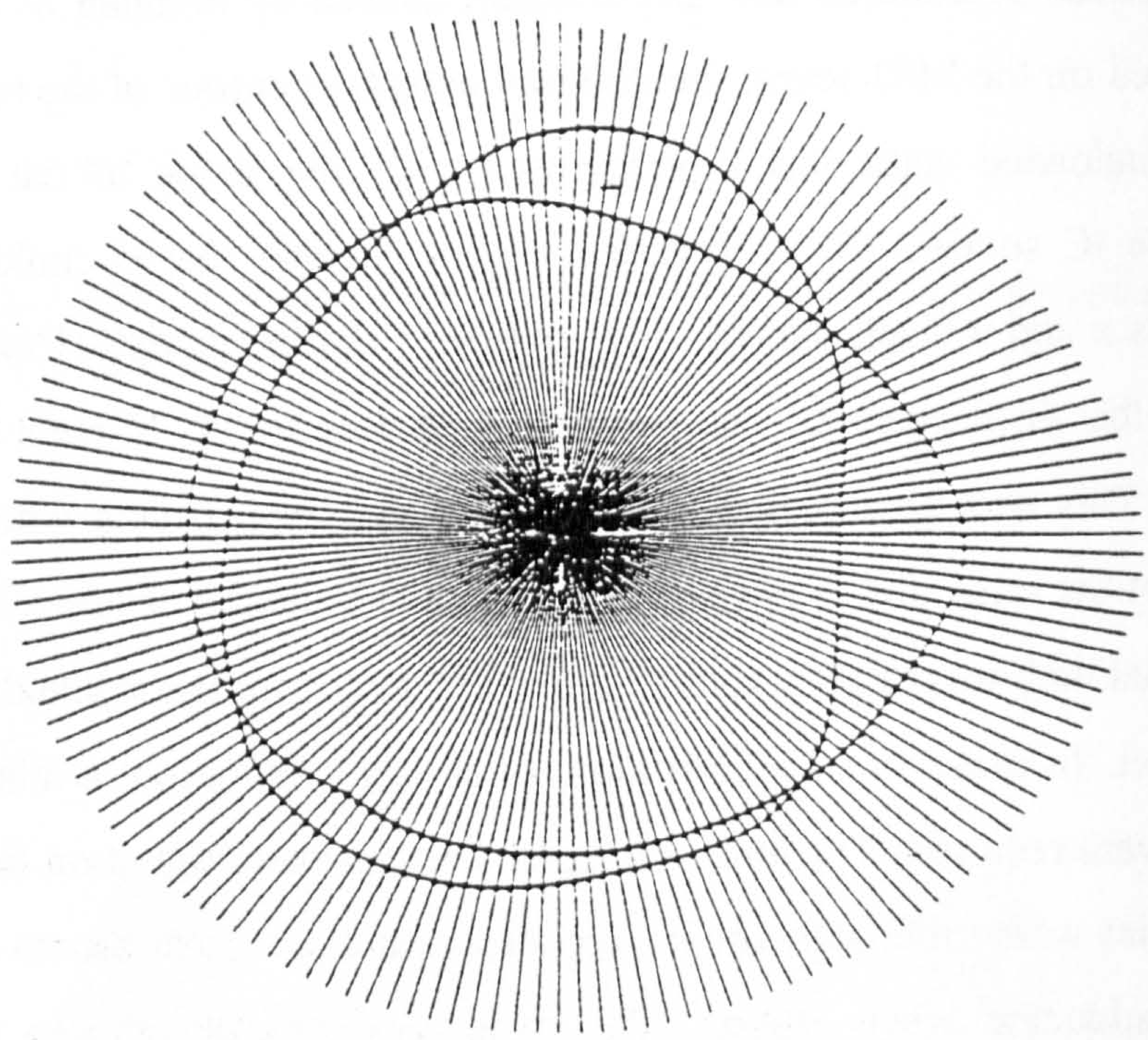

Fig. 10.3.3.1 The straight lines constructed intersect at two points which enabled the difference in the two shapes to be described in the x and y global co-ordinates.

two intersection points in the global co-ordinates would be the amount of displacement applied to the FE model.

The bone in the model was assumed to be infinitely rigid compared to the soft tissues. The nodes describing the contour of the bone were fixed in the x and y directions.

10.3.4 Additional loading and boundary conditions

As part of the study was to look further into the loading and boundary conditions due to donning of the prosthetic socket, three different sets of boundary conditions were investigated. The first set of boundary conditions was already mentioned in the previous section. The second set was similar to the first set except the bone was not fixed in position but allowed to move among the soft tissue. The bone was not modelled as a rigid surface but assigned a Young's modulus of 15.8 GPa and a Poisson's ratio of 0.3.

The third set of boundary conditions adopted a fixed rigid bone but allowed the external contour of the residual limb to slide within a specified boundary, which was equivalent to the shape of the IC socket. The nodes at the residual limb / socket interface could move in any directions in the 2-D plane except outside the boundary of the socket. To model this boundary effect in ANSYS, the nodes defining the external contours of the residual limb were firstly duplicated. Interface elements were set up between the original nodes and the new replica set of nodes. Finally, to bring the model to the shape of the socket i.e. to load the model, displacements were only introduced to the new duplicated set of nodes. The interface elements let the residual limb slide along the new duplicated set of nodes.

10.3.5 Assumptions in loading and boundary conditions

A two dimensional model assumes that the section to be analysed has a uniform cross-section hence uniform constraints in the third dimension. The loading and boundary constraints in a residual limb are clearly three dimensional. In the real situation, the residual limb exhibits both non-uniform geometry and constraints in the out of plane third dimension. Anatomical joint loading or loading transmitted due to ground reaction forces cannot be modelled. The only reasonable realism the 2-D model can achieve is to model the loading caused by donning of the prosthetic socket i.e. the stress and deformation generated on the residual limb when deforming to the shape of the socket. Nevertheless, the 2-D model offers a significant step in understanding the biomechanical behaviour of the internal residual limb tissue structure due to prosthetic socket loading.

The first set of boundary conditions explained in section 10.3.3 assumes that the bone is fixed in place and the external surface of the residual limb follows the shape of the socket. The assumption is viable considering that the bone does not move a lot relative to the soft tissues when the loading applied to the residual limb in the present FE model comes only from donning the socket. The next assumption is that the shape of the residual limb follows the shape of the socket. In the FE model, this would mean displacing all the surface nodes of the residual limb into positions that define the socket shape. This is again appropriate in the case of a suction socket, which is the type of socket used in the present study. In order to maintain suction, minimum slip is expected at the residual limb / socket interface. The residual limb should be in contact with the socket wall at all times.

The second set of boundary conditions which allows the bone to move was implemented to further understand muscle slippage. By not restricting the bone, the soft tissue movement is expected to increase thus decreasing shear stresses. In the actual case, the femur is not in a fully fixed position. It is restricted at one end at the hip joint while the distal cut end moves among the soft tissues which are restricted by the socket.

The third set of boundary conditions allows the skin surface of the residual limb to slip inside the socket. In the actual situation some slip may be present even though the socket is held onto the residual limb by suction. However, the interface elements were used in the model so that only compression forces could be applied at the residual limb / socket interface. In the first set of boundary conditions where nodal displacements were applied, in order to displace the residual limb to the shape of the

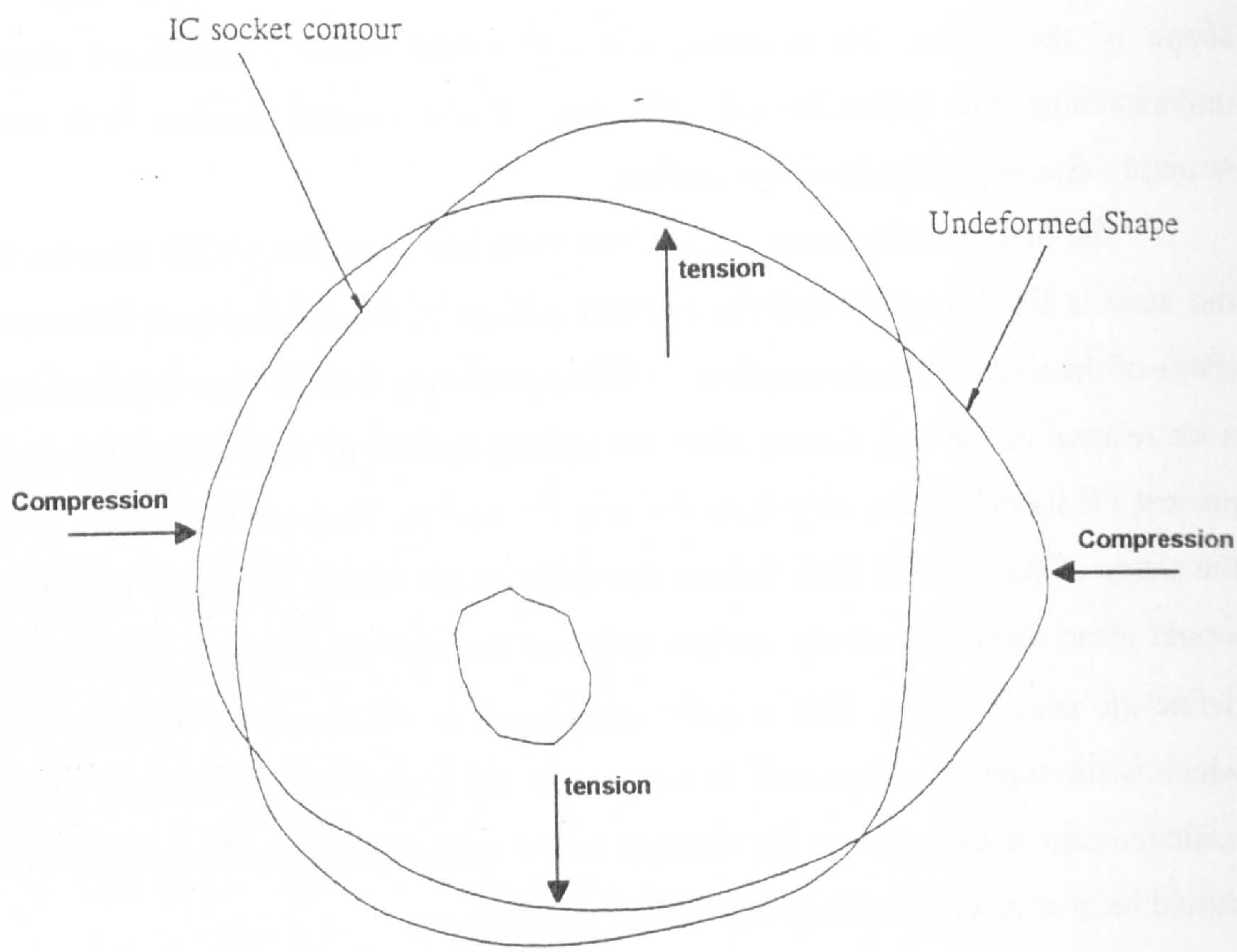

Fig. 10.3.5.1 Tension and compression forces were created by deforming the residual limb to the shape of the socket.

IC socket tension forces had to be introduced at the anterior and posterior regions (Fig. 10.3.5.1). This is necessary in order to guide the tissue to the exact geometry of the IC socket. In the real situation, the socket compresses the medial and lateral tissues and causes the anterior and posterior tissues to expand filling up the socket. It is not clear if the actions at the anterior and posterior tissues can be modelled by tension forces instead. Allowing the residual limb to slip inside the socket may give a more realistic stress pattern by eradicating any application of tension forces.

10.4 FE ANALYSIS STUDYING TISSUE NON - HOMOGENEITY

This section described the various material properties assigned to the model.

10.4.1 Model 1 (Uniform material properties)

The first model assumed all soft tissue to be of uniform material properties. This was considered a suitable first step to understand the effect of the applied loading and boundary conditions and the behaviour of the model. The soft tissue in the model was assumed to be linear elastic, isotropic and homogeneous. The Young's modulus selected was 36.6 kPa and Poisson's ratio of 0.49, assuming the tissues to be nearly incompressible. The boundary conditions in this model were set 'one', where the bone was fixed in place and the external contours of the residual limb were displaced to the shape of the socket by means of nodal displacements. The analysis was fulfilled under plane stress conditions assuming unit thickness. Large deflection analysis, i.e. geometrical non - linearity was also assumed.

10.4.2 Model 2 (Non uniform material properties)

It was hoped that varying the material properties of different soft tissues could give an indication of muscles contraction and slippage. This model bears a similarity to the Huang and Mak (1993) model of a transverse slice of the trans-tibial residual limb, where muscle contraction and slippage was studied by varying the material properties assigned to skin, fat and muscles. However, as discussed later, the characteristic at the interface is not effectively described using variation in material

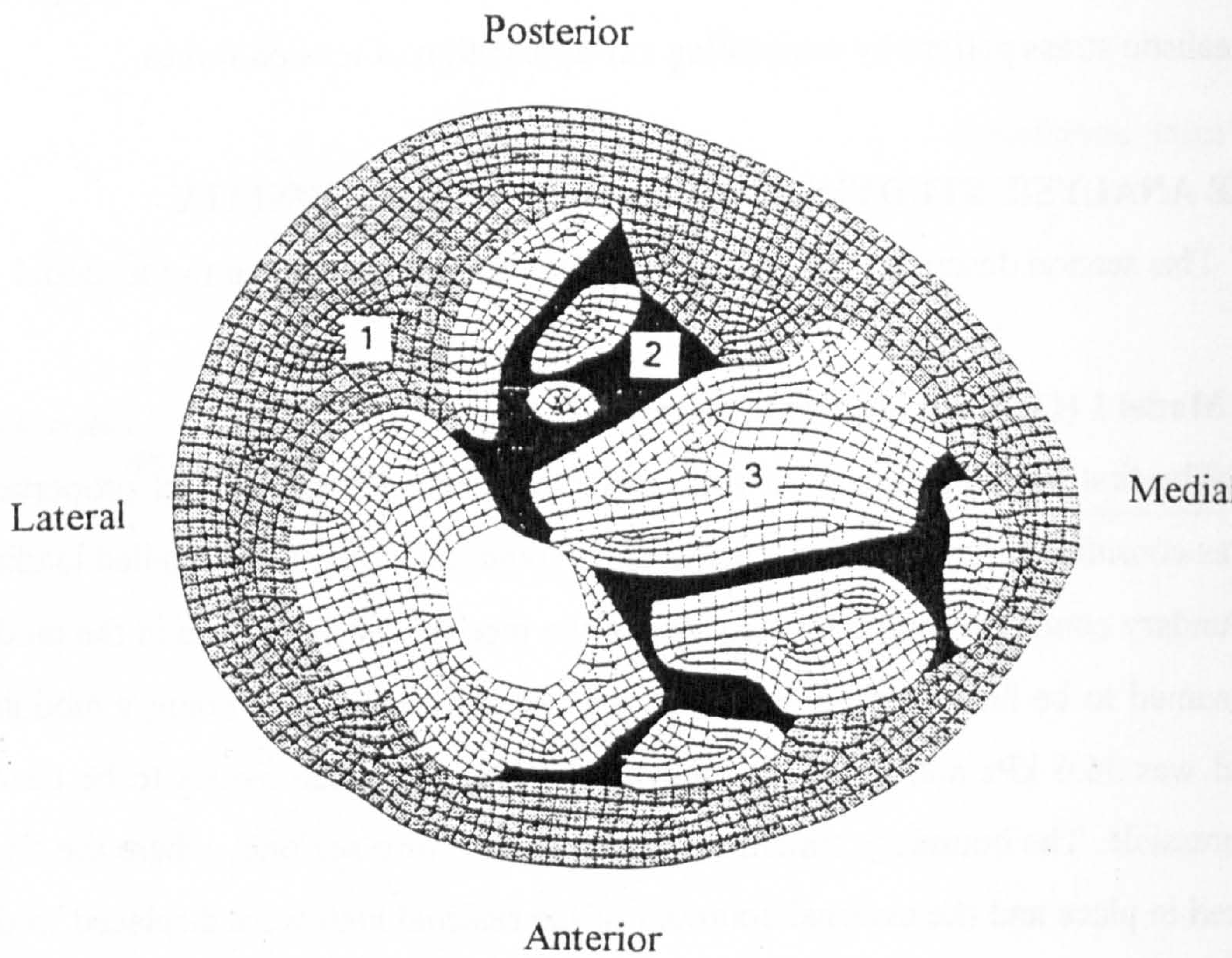

Fig. 10.4.2.1 The residual limb model is differentiated into three main tissue types.
1 - Fascia
2 - Intermuscular tissues
3 - Muscles

Anterior

Lateral

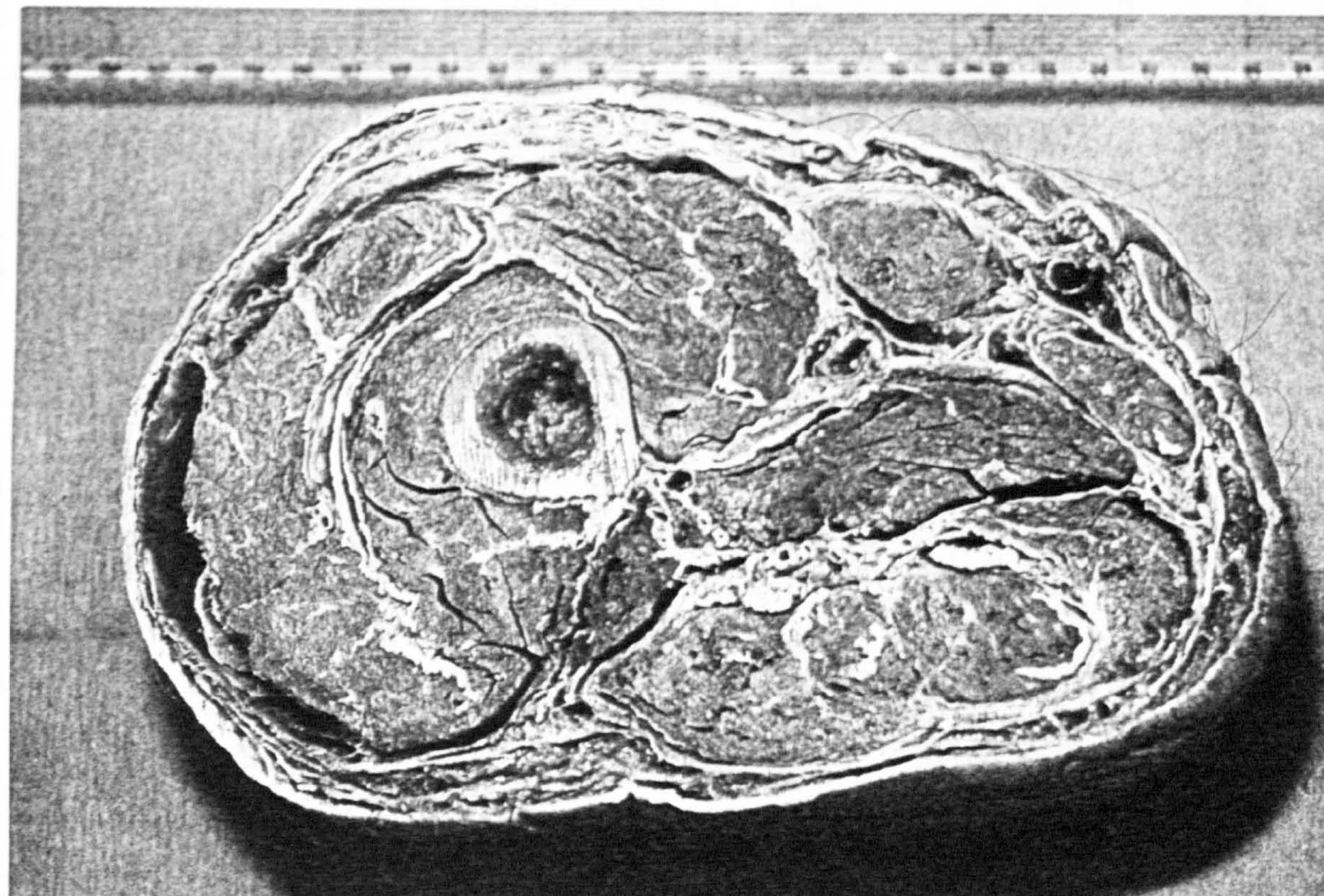

Medial

Posterior

Fig. 10.4.2.2 Cadaveric specimen of a transverse section of the thigh at a level approximately similar to the FE model.

	Elastic modulus (kPa) and Poisson's ratio				
Model no.	Fascia	Inter-muscular tissues	Muscles	Femoral bone	Loading and boundary conditions
1	36.6 / 0.49	36.6 / 0.49	36.6 / 0.49	Rigid	Nodal displacements at residual limb surface and fixed femoral bone.
2a	36.6 / 0.49	36.6 / 0.49	95.6 / 0.49	Rigid	Nodal displacements at residual limb surface and fixed femoral bone.
2b	36.6 / 0.49	12.2 / 0.49	95.6 / 0.49	Rigid	Nodal displacements at residual limb surface and fixed femoral bone.
2c	36.6 / 0.49	24.4 / 0.49	95.6 / 0.49	Rigid	Nodal displacements at residual limb surface and fixed femoral bone.
2d	36.6 / 0.49	36.6 / 0.49	see table 10.4.2.2	Rigid	Nodal displacements at residual limb surface and fixed femoral bone.
2e	36.6 / 0.1	36.6 / 0.1	see table 10.4.2.2	Rigid	Nodal displacements at residual limb surface and fixed femoral bone.
3	36.6 / 0.49	36.6 / 0.49	95.6 / 0.49	Rigid	Nodal displacements at residual limb surface and fixed femoral bone. Link elements were used to model the intermuscular septum.
4	36.6 / 0.49	36.6 / 0.49	95.6 / 0.49	Rigid	Nodal displacements at residual limb surface and fixed femoral bone. Interface elements were used to model muscle slippage.
5	36.6 / 0.49	36.6 / 0.49	95.6 / 0.49	15.8GPa / 0.3	Nodal displacements at residual limb surface and femoral bone was not fixed.
6	36.6 / 0.49	36.6 / 0.49	95.6 / 0.49	Rigid	Sliding allowed at residual limb surface and fixed femoral bone.

Table 10.4.2.1 Material properties, loading and boundary conditions applied to the 2-D model of the residual limb.

properties. This is because interface characteristics cannot be described fully by material properties alone. Nevertheless, the present model (model 2) provided a good background for more complicated models which incorporate interface characteristics. The analysis was carried out assuming plane stress conditions with unit thickness undergoing large deflection. The boundary conditions were those of model one (fixed bone and nodal displacement at the surface). The full nodal displacements were applied in 10 incremental load steps and the convergence tolerance residual was set to 1% of the applied load. The soft tissues were divided into three types, fascia, intermuscular tissues and muscles. The skin was not modelled in the present model and was assumed to be of similar properties to the fascia surrounding the muscles as shown in Fig. 10.4.2.1 in the region marked 1. The region marked 2 was termed the intermuscular tissues where it was made up of mainly of loose areolar tissue. The muscles were marked as region 3 in Fig. 10.4.2.1.

In model 2a, the tissues were assumed to be linear elastic, isotropic and nearly incompressible (v=0.49). The fats were assigned a Young's modulus of 36.6 kPa and the muscles, about 3 times higher (E=95.6 kPa). These values were taken from Huang and Mak (1993). As for the intermuscular tissues, there is no literature indicating a suitable value of Young's modulus. As a first approximation the intermuscular tissue in model 2a was assigned similar properties to the fascia. However, based on a cadaveric specimen at approximately the same level as the residual limb model (Fig. 10.4.2.2), the intermuscular tissue is made up of large fluid filled cells in a matrix less dense than that of fascia. It can be accurately described as softer than fats. Assuming the value of intermuscular tissue to be 3 times lesser than fascia (E= 12.2 kPa), model 2b was attempted. However, due to the low value of E introduced, problems with numerical convergence were encountered. Model 2b was only solved to 80% of the applied load. By trial and error, numerical convergence of 100% of the applied load was only possible when E for the intermuscular tissue was increased to 24.4 kPa, which was applied in model 2c (See table. 10.4.2.1).

The material properties of the residual limb tissues were further varied to study muscle contraction i.e. increasing the modulus of elasticity of the muscles, in

	Elastic modulus (kPa) and Poisson's ratio		
Model no.	-Vastus muscles -Rectus femoris	-Sartorius -Adductor longus -Gracilis -Adductor magnus	-Gluteus maximus -Semimembrinosus -Semitendinosus and long head of biceps femoris
2d	143.4 / 0.49	95.6 / 0.49	191.2 / 0.49
2e	143.4 / 0.3	95.6 / 0.3	191.2 / 0.3

Table. 10.4.2.2 Material properties assigned to the different muscles in model 2d and 2e.

model 2d. Due to muscle contraction, the geometry of the muscles are also expected to change. However there is no useful data available that allow the present analysis to include these geometrical changes. Muscle contraction was simulated by stiffening the muscles at the posterior and lateral regions of the residual limb without any geometrical changes. Stiffening the muscles at the posterior and lateral regions simulates an amputee in the standing position, where the hip extensors and the abductors are likely to be contracted. The E value selected for the posterior and lateral tissue were 2 times and 1.5 times the muscles in the anterior and medial side respectively. Table 10.4.2.2 shows the E values assigned to the different muscle groups in the residual limb model.

The final model in this section, model 2e has similar E values as model 2d but different Poisson's ratio. Instead of assuming the tissues to be nearly incompressible, the fascia and intermuscular tissues were assigned with a Poisson's ratio value $\nu = 0.1$ and the muscles $\nu = 0.3$.

10.5 FE ANALYSIS STUDYING MUSCLE SLIPPAGE

The muscle slippage in the trans-tibial residual limb has been studied by Huang and Mak (1993) by introducing very soft material (E = 0.956 kPa) in the intermuscular region. It was found in the present study that using a low value of E for the intermuscular tissues had produced severe numerical problems due to excessively distorted elements. The loading applied as displacements at the residual limb / socket interface in the present model were much larger than the trans-tibial model attempted by Huang and Mak (1993). The maximum displacement was six times more (32 mm compared to 5 mm) which explained the numerical problems encountered with the low Young's modulus value. Furthermore, the large tissue mass in the trans-femoral limb also gave rise to an unstable model caused by large tissue deformation and movement. The author of this thesis considered a more comprehensive approach is necessary in specifying the interface characteristics which is explained below.

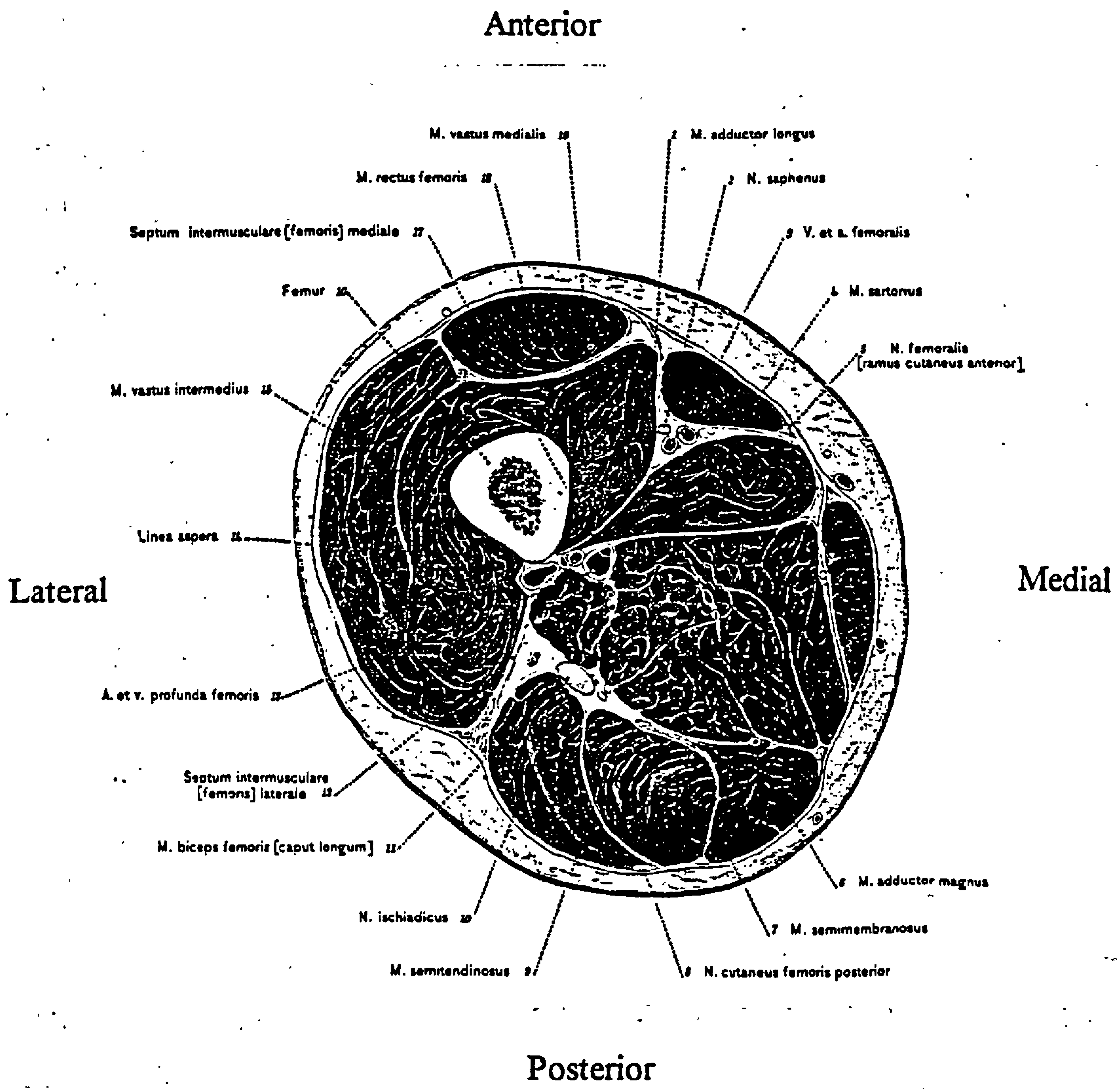

Fig. 10.5.1.1 Cross section of the thigh showing the intermuscular septa. (Eycleshymer and Schoemaker, 1911)

10.5.1 Model 3 (Incorporating intermuscular septa)

The aim of model three was to incorporate the intermuscular septum which surrounds the muscles. The septum is a tough connective tissue which binds muscle or muscle groups together. It can also be seen in Fig. 10.4.2.2 and Fig. 10.5.1.1 that the septa provides the means for the muscles to slide over each other. The thickness of septum was measured by Hinton et al (1992) to vary from 0.4 to 0.6 mm. To incorporate the septum in the transverse model of the residual limb using 2-D quad or triangular elements proved to be difficult due to its thinness. Unless a large number of elements was used, the aspect ratio of the elements making up the septum would be unacceptable. The alternative approach was to model the septum using link elements ANSYS LINK10 (Fig. 10.5.1.2). LINK10 is a 2-noded spar element having the unique feature of a bilinear stiffness matrix resulting in a uniaxial tension only element. Thus the stiffness is removed if the element goes into compression, very much like that of a slack cable. This assumption seems feasible since anatomically the septum only resists tension forces. The rest of the model was modelled using PLANE42 quadrilateral elements. The loading and boundary condition set 'one' was used. The Young's modulus assigned to the muscles and fascia were 95.5 kPa and 36.6 kPa respectively. The intermuscular tissues were also given a value of 36.6 kPa, as lower values were likely to give rise to convergence problems. Based on an experiment conducted by Hinton et al (1992), the estimated Young's modulus of the fascia lata was 400 kPa and Poisson's ratio of 0.4. The locations of the link elements are highlighted in Fig. 10.5.1.3. It was difficult to locate the septa from the MRI images, thus the locations of the septa surrounding the muscles and the points where it inserts the bone was based on the cadaveric specimen shown in Fig. 10.4.2.2.

10.5.2 Model 4 (Incorporating sliding between musculature)

The fourth model introduced interface elements between the muscles in order to allow muscle sliding to take place. Referring to Fig. 10.4.2.2, in some areas around the muscle tissues, a clear separation from the intermuscular tissues could be observed. Introducing interface elements in the model was thought to be most suitable

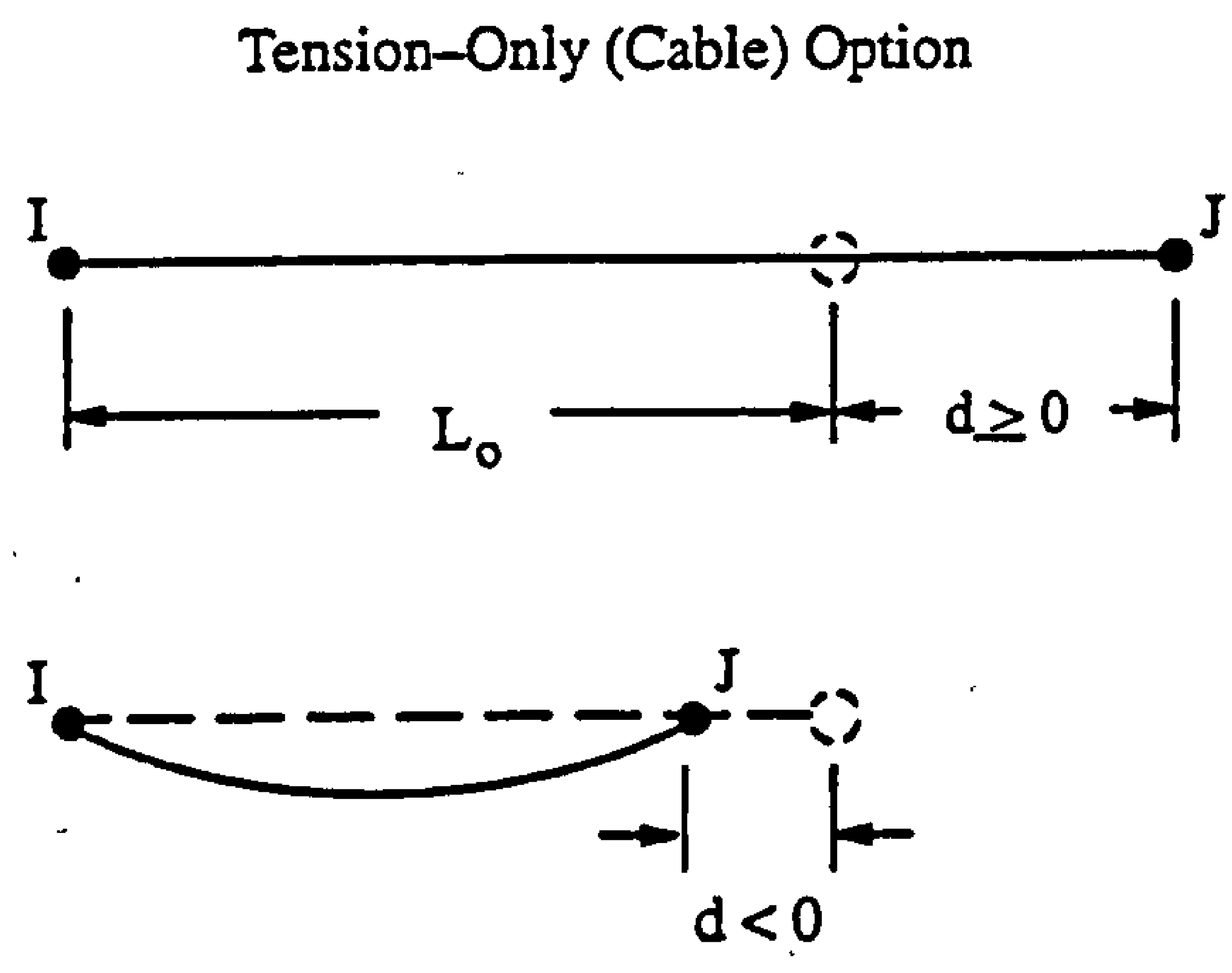

Fig. 10.5.1.2 ANSYS LINK10, 2-D two noded spar element.

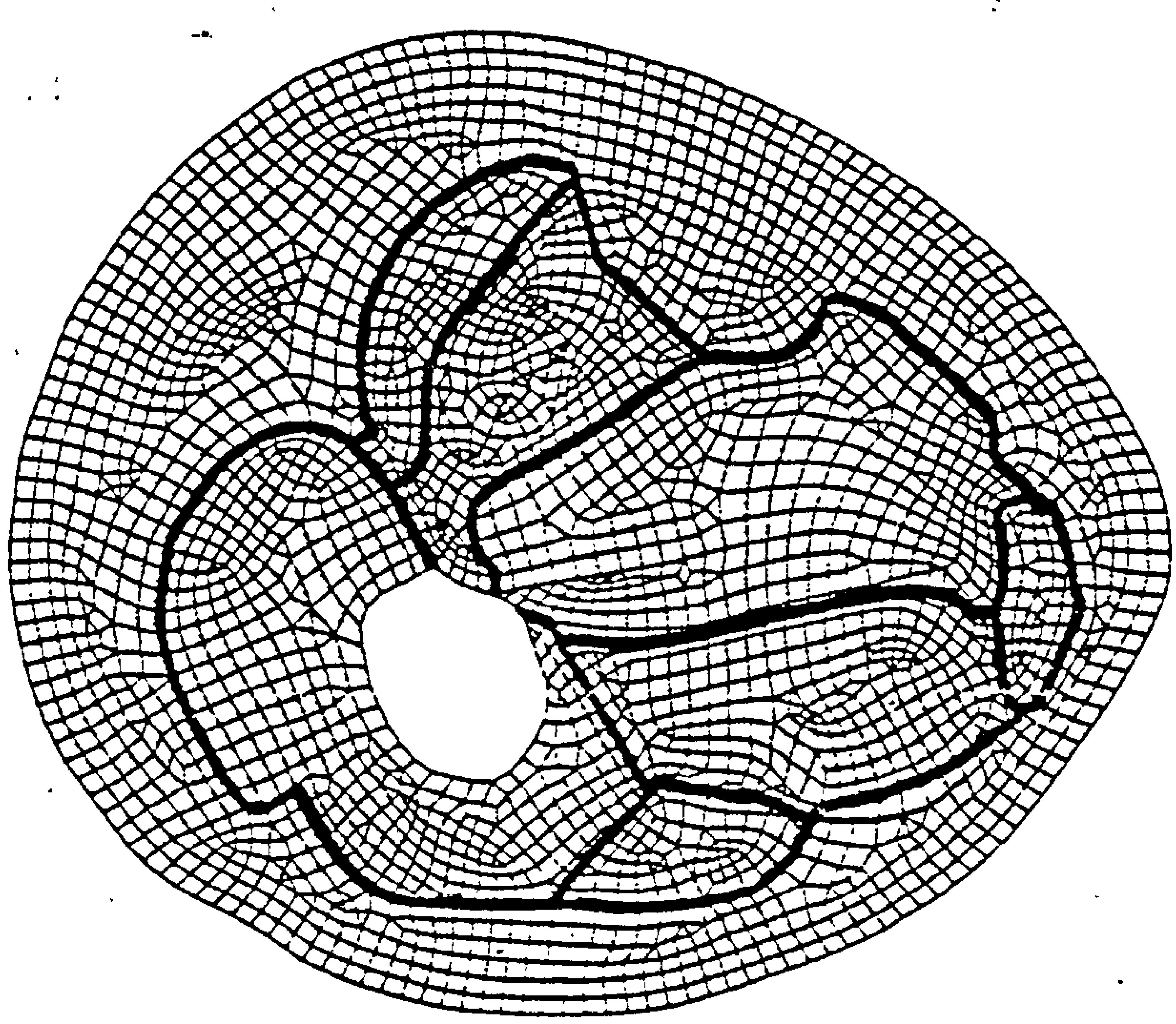

Fig. 10.5.1.3 The residual limb model showing the intermuscular septum modelled using link elements.

since it allows the muscles sliding and separation to take place. However, in other regions, the intermuscular tissues is connected to the muscles by very loose fibrous connective tissue. The loose fibrous tissues have very low stiffness which allow muscles to contract and slide. It was considered unsuitable to model these loose fibrous tissue by assuming a very low Young's modulus as this would cause excessive element distortion due to the much higher modulus of the muscles. To overcome this, interface elements were introduced in the regions surrounding the muscles regardless of whether they were connected by loose fibrous tissue or separated.

The type of interface element used is ANSYS CONTACT48 Fig. 10.5.2.1. It is a general purpose 2-D element with translation in the x and y directions. Contact occurs when the contact nodes penetrates the target line. Upon contact, the contact surface will slide along the target line and the amount of sliding is dependent on the coefficient of friction at the interface. Usually the contact nodes belong to the softer material which slides on the stiffer target material. However, sliding is also dependent on the geometry, boundary and loading conditions of the model. Therefore in the residual limb model, a fully symmetrical contact condition was assumed in which interface elements were specified on both the intermuscular tissues and the muscles, allowing them to act as either contact or target surfaces.

The applied boundary conditions were those of set 'one' where the bone was fixed and nodal displacements introduced at the surface of the residual limb. Referring to Fig. 10.4.2.2, it can be seen that the vastus muscles are secured to the bone. The adductor brevis and magnus are also connected to the linear aspera of the bone. These muscles were modelled using fixed boundary conditions at the surfaces where they contact the bone. Generally interface elements were situated at the boundary of individual muscles defined earlier (Fig. 10.5.2.2). However, sliding motion between the vastus muscles and the rector femoris was impossible at the aponeurotic connection at the lateral side. Another aponeurotic site exists posteriorly where the vastus muscles merge into the posterior intermuscular septum and connect to the linea aspera. Interface elements were therefore not assigned to both of these regions.

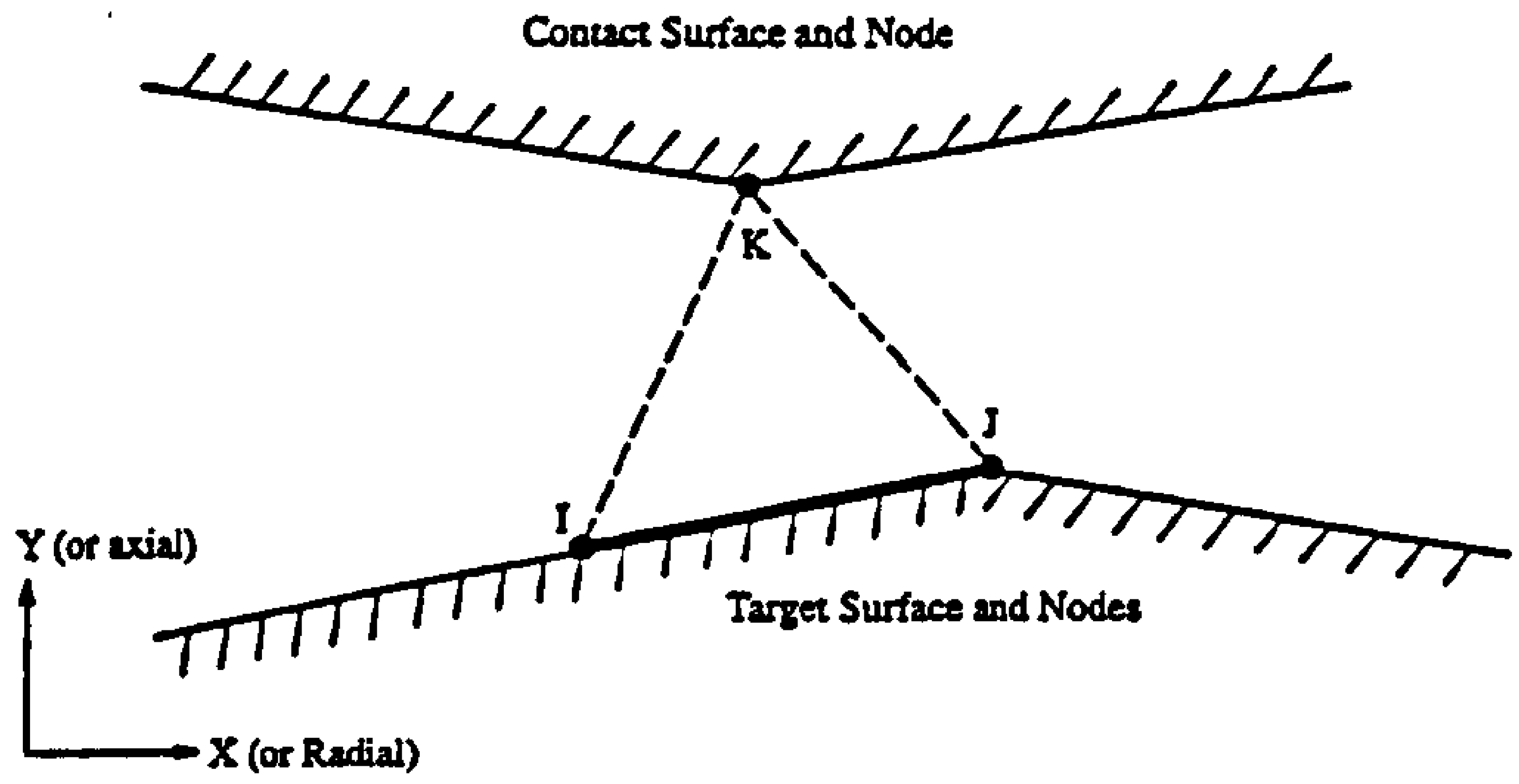

Fig. 10.5.2.1 ANSYS CONTACT48, 2-D point to surface contact element.

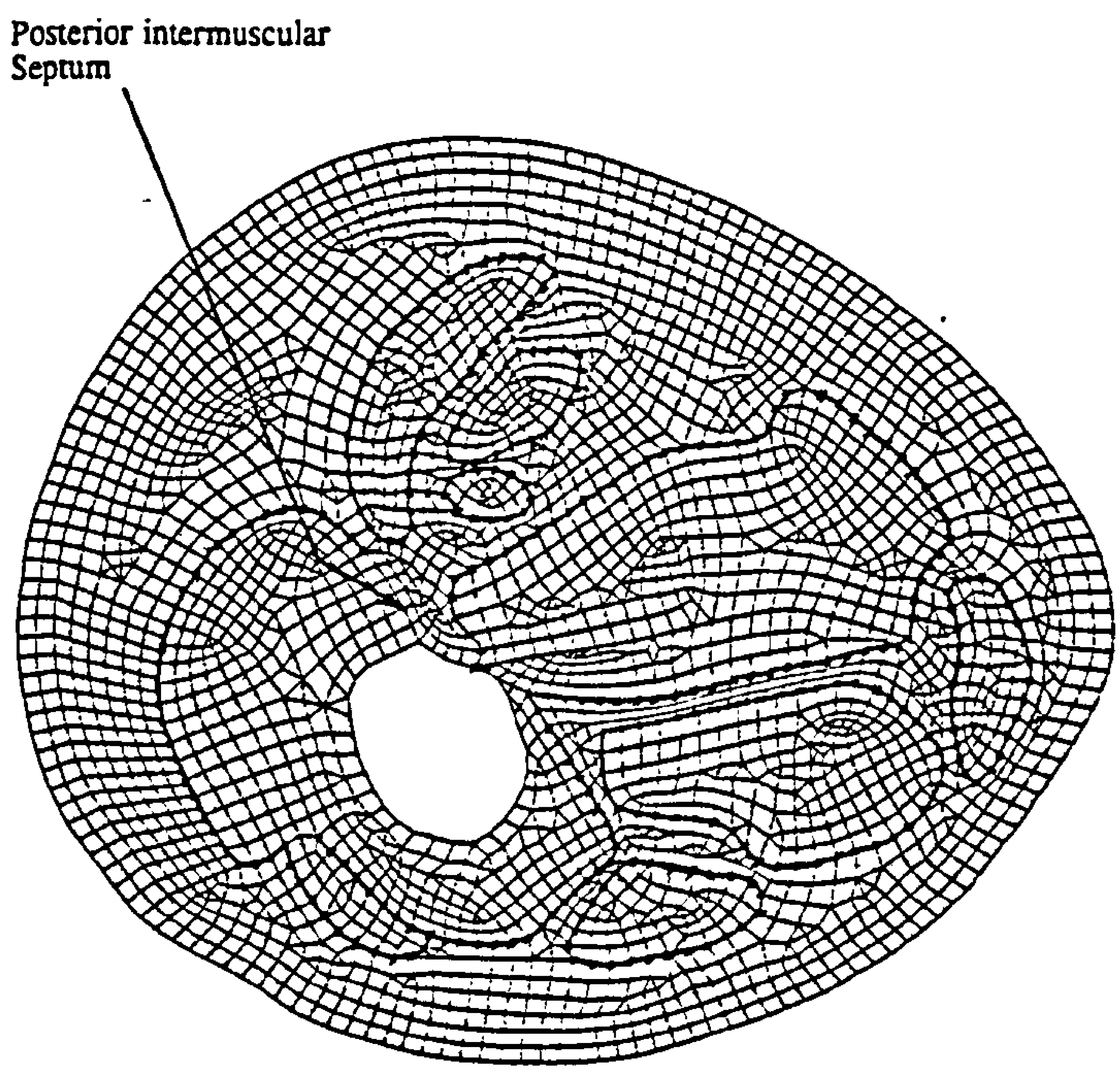

Fig. 10.5.2.2 Residual limb model incorporating interface elements.

The material properties used in model 3 were adopted. The Young's modulus of the muscles was 95.6 kPa. The moduli for both fascia and the intermuscular tissues were 36.6 kPa. The soft tissues were considered as nearly incompressible with ν=0.49. The contact parameters required in the model were contact stiffness and coefficient of friction. Contact stiffness (kN/m) determines the amount of penetration the contact node made on the target node. A high contact stiffness will satisfy compatibility (less penetration) between two materials i.e. muscles and intermuscular tissues, however numerical convergence difficulties can arise due to ill conditioning of the global stiffness. Using a low stiffness may solve numerical convergence problems but can give rise to too much material penetration. The selected contact stiffness was 50 kN/m which was estimated based on the stiffness of the muscles and intermuscular tissues using the recommended formulation in ANSYS where contact stiffness (KN) is given by,

$$KN = c\frac{AE}{h}$$

A = Typical contact area of an individual contact element
h = Typical contact length
E = Modulus of elasticity of solid bodies in contact
c = A factor typically varies from 1/100 to 100
The above formulation provides a relatively large range of contact stiffness. Thus, the estimated contact stiffness of 50 kN/m was also selected based on a compromise between compatibility and numerical convergence.

The coefficient of friction (μ) at the interface between the muscles and the intermuscular tissues could generally be regarded as low based on observations made in cadaveric specimens. To the author's knowledge, there are no known data describing this value. In the present study, a range of values from μ = 0 to 0.7 was tested.

10.6 FE ANALYSIS STUDYING DIFFERENT LOADING AND BOUNDARY CONDITIONS

10.6.1 Models 5 and 6 (Changes in loading and boundary conditions)

Model 5 and 6 were assigned with the second and third sets of loading and boundary conditions respectively as described in section 10.3.4. Model 5's femoral bone was allowed to move within the soft tissue mass and nodal displacements were applied to the surface of the residual limb. In model 6, interface elements were applied at the residual limb / socket interface which enabled the soft tissues to slide inside a boundary shaped according to the socket. The femoral bone was modelled as fixed in position. ANSYS PLANE42 2-D quadrilateral elements were used for both models and in addition, ANSYS CONTACT48 2-D interface elements were used in model 6. The Young's modulus assigned to the muscles, fascia and intermuscular tissues were 95.6 kPa, 36.6 kPa and 36.6 kPa respectively and Poisson's ratio was 0.49 for all three types of tissues. The assigned material properties allowed a direct comparison with model 2a in order to evaluate the stress distribution due to changes in boundary conditions.

10.7 RESULTS

The results will be presented according to the model number in ascending order. The different models will be compared with each other in order to study the effect due to material changes, muscle slippage and different loading and boundary conditions. The model will be analysed using von Mises yield criteria, a stress invariant considering the three principal stresses. The overall stress state, regions of maximum and minimum stress in the residual limb can be identified clearly using the von Mises criteria. In addition to von Mises stresses, stresses in the x and y directions i.e. medio-lateral and anterio-posterior planes respectively and the principal stresses were discussed.

Accompanied with the discussion on the results are plots of the model's predictions. The plots are presented in similar orientation as in Fig. 10.3.2.2 and the

ANSYS 5.0 A	Program version.
MAR 12 1996	Date of analysis.
18 : 36 : 29	Time of analysis.
NODAL SOLUTION	Solution based on nodal calculations.
STEP = 1	Number of load step. A load step is a discrete point on the load history curve.
SUB = 10	Number of substep which is an intermediate load level within a load step.
TIME = 1	Time is a history tracking parameter consisting of a monotonically increasing set of numbers that represent the precedence of the loading. Time = 1 indicates 100% of the applied load.
SEQV (AVG)	Equivalent or von Mises stress plots.
DMX = 0.035324	Maximum displacement in the model (m).
SMN = 1059	Minimum von Mises stress in the model (N/m^2).
SMX = 21923	Maximum von Mises stress in the model (N/m^2).

Table 10.7.1 Legends indicated in the stress plots in the results section.

legend accompany the stress plots are tabulated in table 10.7.1. All stress values in the plots are in units of N/m^2.

10.7.1 Model 1 (Uniform material properties)

Fig. 10.7.1.1 shows the von Mises stress distribution on the deformed residual limb. The elastic modulus applied to the soft tissue of the model was kept constant at 36.6 kPa. High stress was found at the medial side where large nodal displacements were imposed (maximum displacement of 32 mm in the negative x - direction). The maximum stress (21.9 kPa) was located at the surface of the residual limb at the medial side. In the anterior region of the residual limb, high stresses (17 kPa) were noticed at the bone / tissue interface. The increase in stresses in this region was largely due to the low thickness of the tissue between the bone and the socket. The majority of the residual limb experienced low stresses below 8 kPa. The lowest stress (1 kPa) was found at the lateral region of the residual limb.

In this model, there was no distinction between the different types of soft tissues in the residual limb.

10.7.2 Model 2 (Material non - homogeneity)

Model 2a

Fig. 10.7.2.1 displays the von Mises stress distribution of model 2a. Model 2a was kept similar to model 1 except that the muscles of the residual limb were assigned a modulus of 96.6 kPa. The fascia and intermuscular tissues remained as 36.6 kPa.

Due to the increased stiffness of the muscles, the maximum stress (35.3 kPa) in model 2a was 40% more than that in model 1. However, unlike model 1, the maximum stress in model 2a was located inside the residual limb, not at the residual limb / socket interface. The highest stress was found near the interface of the adductor magnus and the intermuscular tissues separating the adductor magnus/brevis and adductor longus. Another region of localised high stress (31.4 kPa) was found at the posterior bone / tissue interface, just medial to the linear aspera where the adductor

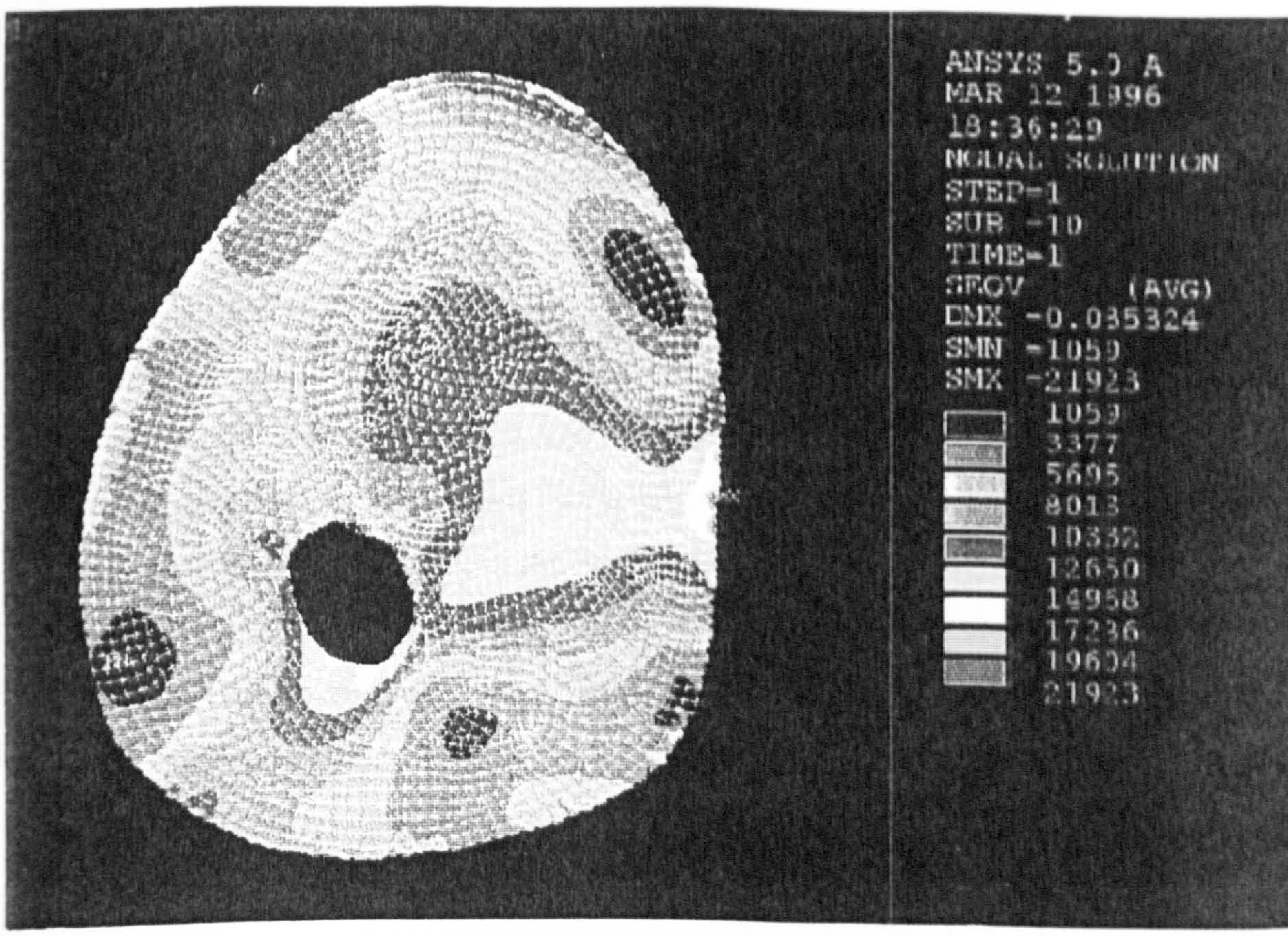

Fig. 10.7.1.1 Von Mises stress distribution of model 1 (Uniform material properties).

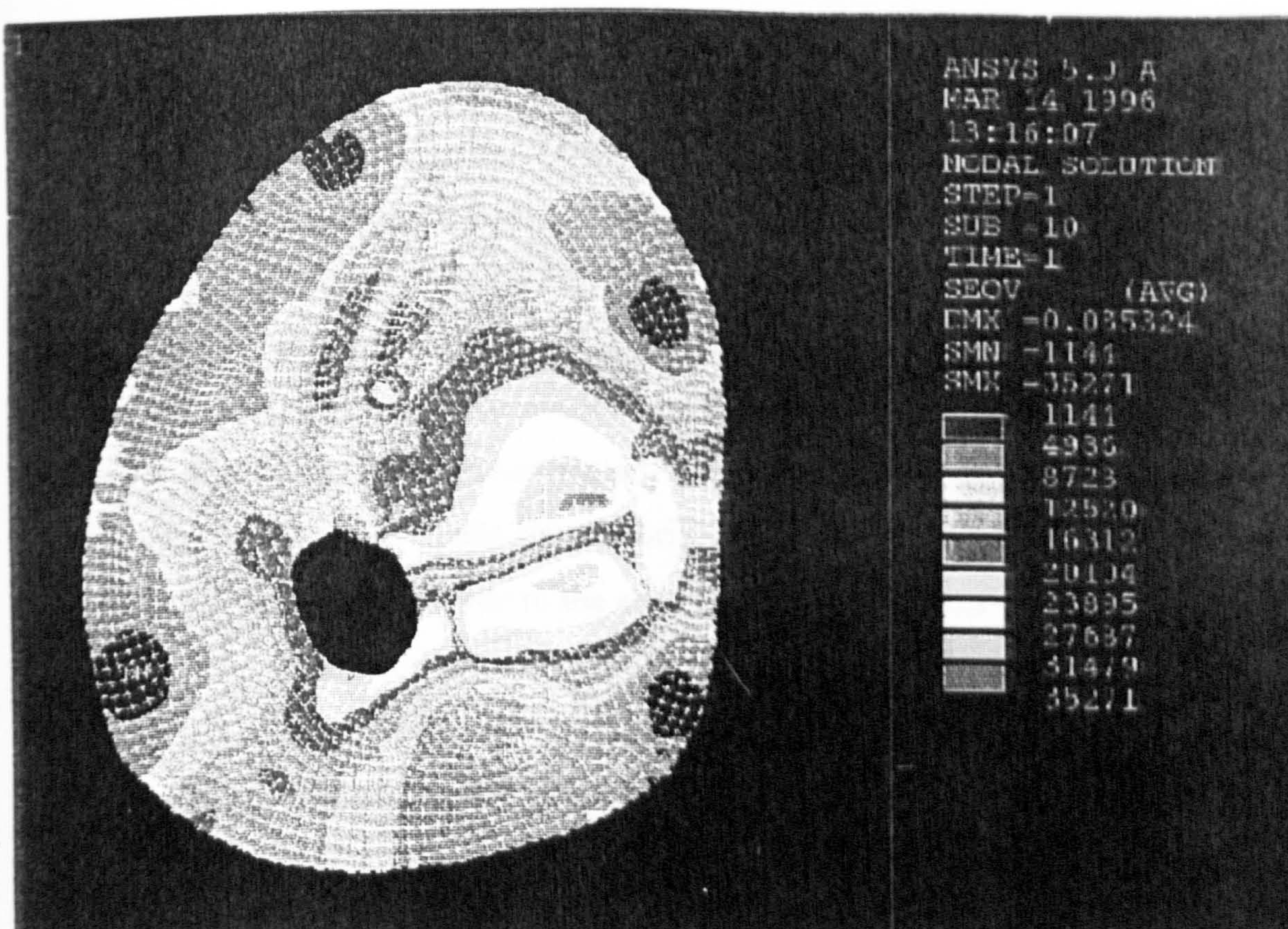

Fig. 10.7.2.1 Von Mises stress distribution of model 2a (non-uniform material properties).

magnus inserts into the femur. These regions of maximum stress could be explained by the displacements of the muscular tissue as shown in Fig. 10.7.2.2. The medial side of the residual limb was highly compressed which caused the gracilis, adductor magnus/brevis and longus to move laterally among the surrounding intermuscular tissue. The region of maximum stress recorded at the adductor magnus was caused by the gracilis moving into contact with the adductor muscles. The gracilis lies in a perpendicular fashion with respect to the adductor magnus and longus when viewed in the transverse plane. Thus when the gracilis was forced to move laterally, it began to push the adductor magnus upwards and longus downwards. As shown in Fig. 10.7.2.3 which plots the stresses in the x - direction with the surface and bone nodal reaction forces, high compressive stresses (up to -34 kPa) were seen at the region where the three muscles meet. The compressive stresses continued to exist along the adductors muscles right up to the bone. This was caused by the lateral posterior movement of the adductor magnus/brevis, increasing the compressive stress at the point where it attached the femur. Whereas the lateral anterior movement of the adductor longus collided with the vastus muscles at the anterior region which was attached to the bone, thus an increased in compressive stress was also seen.

Referring back to the Fig. 10.7.2.1, a region of high von Mises stresses was predicted just anterior to the femur. A plot of the stresses in the y direction showed the maximum tensile stress (25.5 kPa) was located at the same region (Fig. 10.7.2.4). In the same plot, the reaction forces indicated that the anterior tissues were undergoing tension. As the bone was fixed in position, the stiff vastus muscles (which were attached to the bone), when forced to move anteriorly lead to an increase in tensile stresses. The high tensile stresses originate at the vastus / femur interface and spread out in a triangular manner to the surface of the residual limb.

At the posterior region of the residual limb, the presence of the muscles (gluteus maximus, semimembrinosus, semitendinosus and long head of the biceps femoris) did not change the stress pattern significantly (comparing model 1 and model 2a). The tissue at this region was undergoing tension due to nodal displacement applied at the surface of the residual limb (Fig. 10.7.2.4). However, the muscles at the

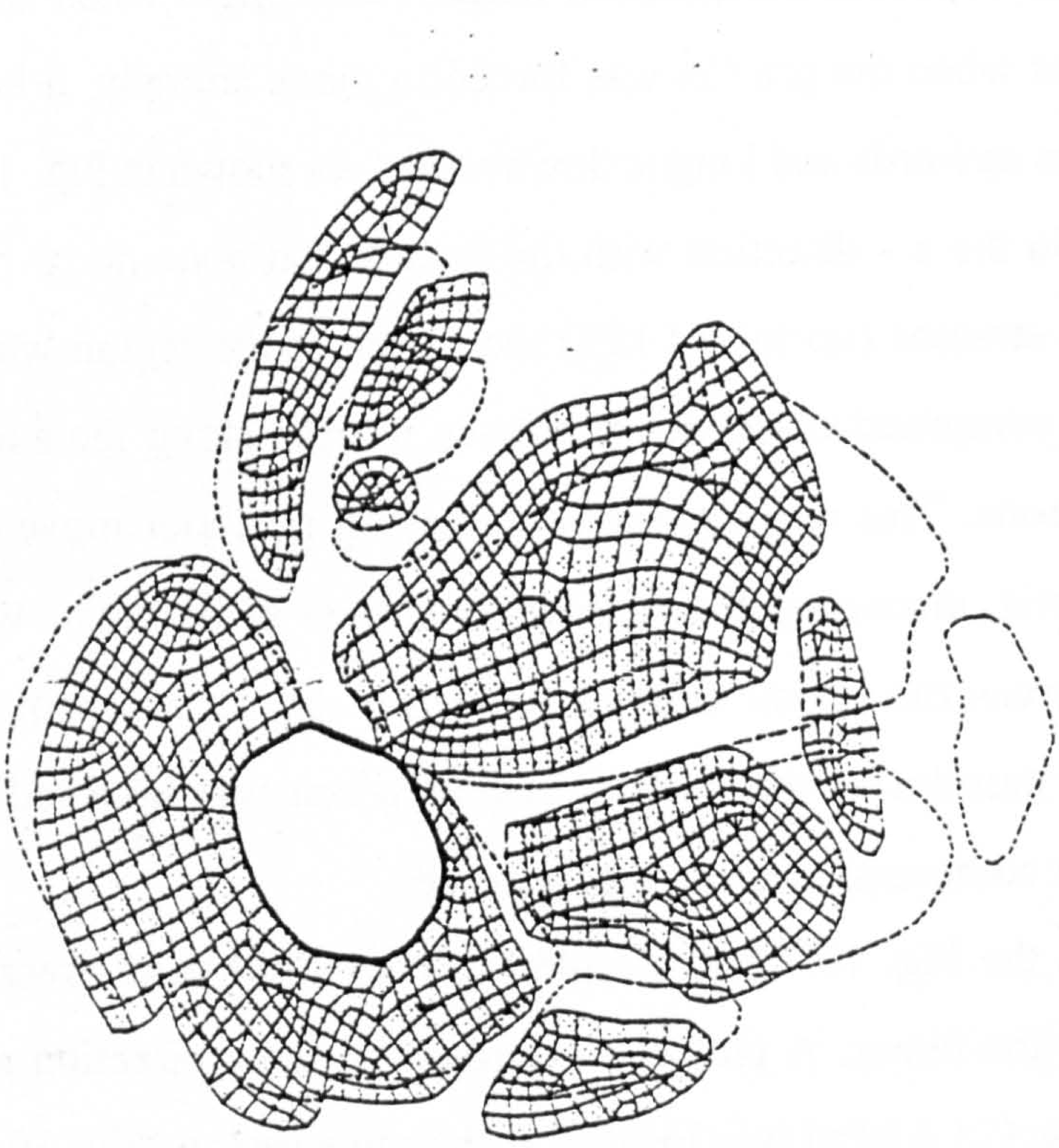

Fig. 10.7.2.2 Displacement of the different muscles in the model.
Dotted lines denote the original shape.

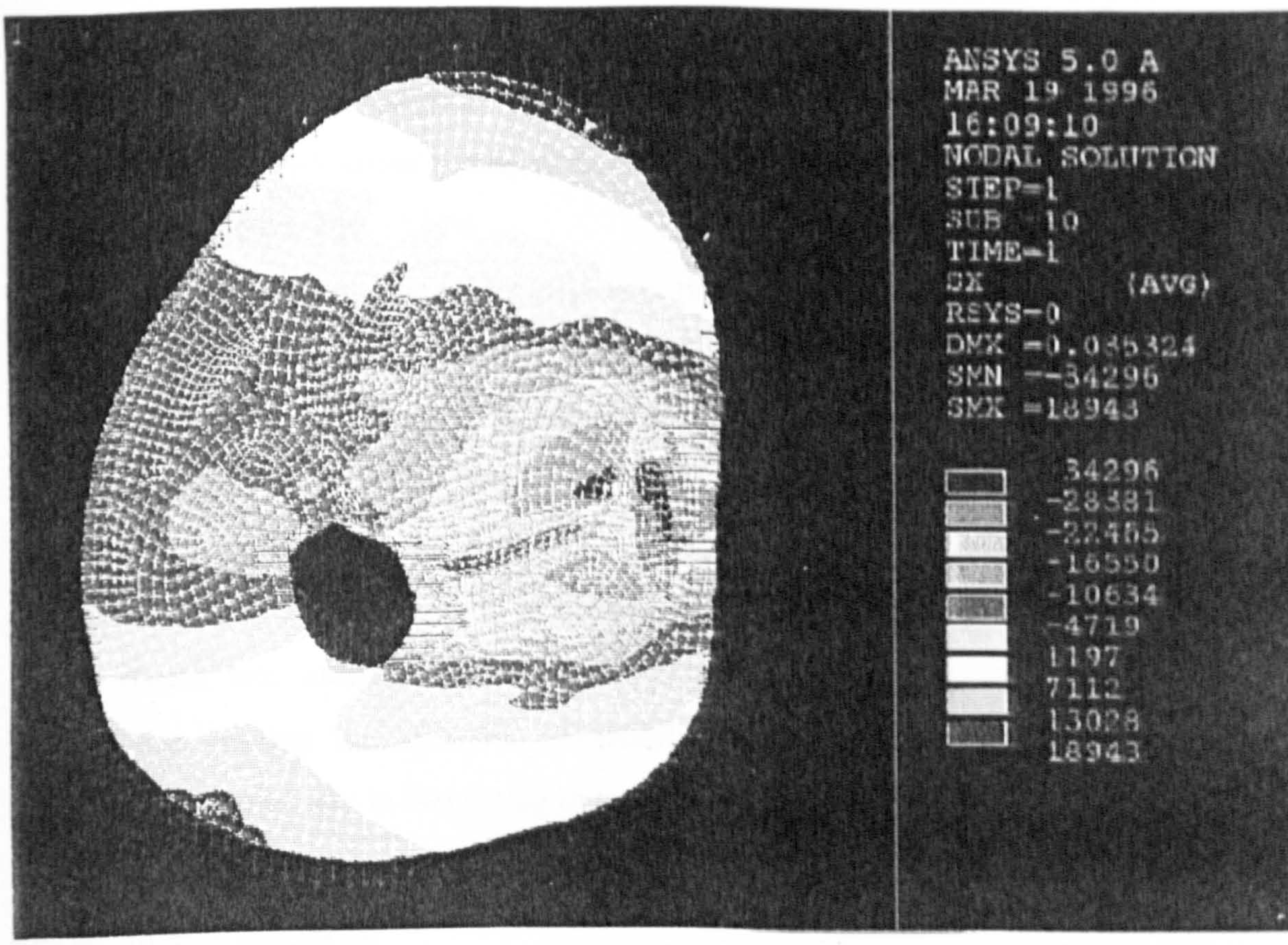

Fig. 10.7.2.3 Stress distribution in the x-direction of model 2a with nodal reaction forces. Forward x-direction is from the lateral to the medial side of the residual limb.

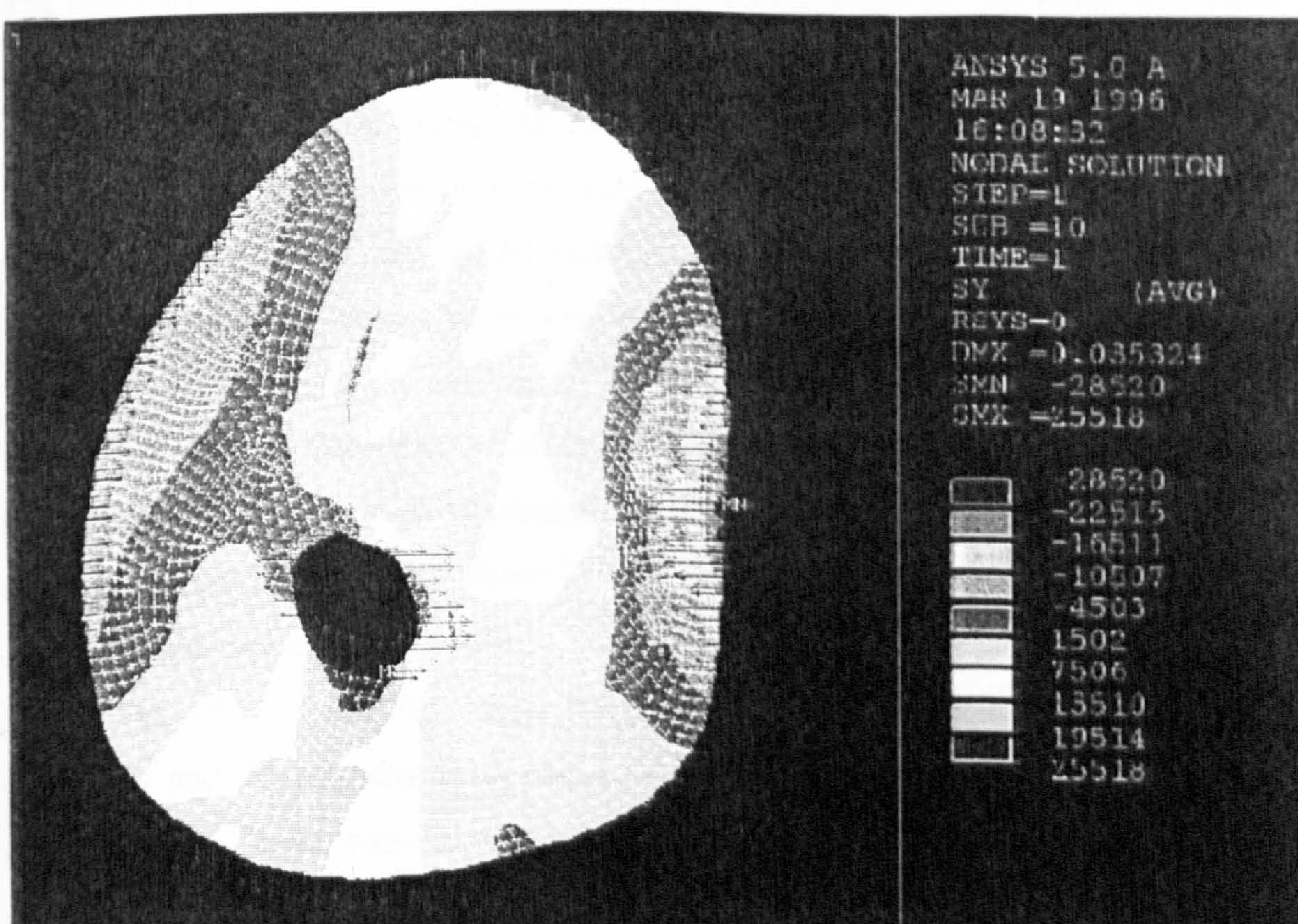

Fig. 10.7.2.4 Stress distribution in the y-direction of model 2a with nodal reaction forces. Forward y-direction is from the anterior to the posterior side of the residual limb.

posterior region were surrounded by a large amount fat which acted as a 'cushion'. Thus no area of high stress concentration was observed. At this region the tensile stresses ranged from 7 to 13 kPa.

One particular region of interest was the intermuscular tissue separating the adductor magnus/brevis and longus. The soft intermuscular tissue was sandwich between the stiffer muscles. Upon compressing the medial tissue, low compressive stress (-4.7 kPa) in the x - direction was predicted at the intermuscular tissue (Fig. 10.7.2.3). Instead as shown in Fig. 10.7.2.4, the intermuscular tissue predicted high positive stress (13.5 kPa) in the y - direction which indicated the intermuscular tissue at this region was under tension. As mentioned previously, the laterally displaced gracilis was forcing the adductor magnus/brevis and the longus apart, and the intermuscular tissue was in fact trying to resist this motion.

Model 2b and Model 2c

Model 2b and 2c investigates the effects of varying the intermuscular tissues. The intermuscular tissues was assigned a Young's modulus of 12.2 kPa and 24.4 kPa in model 2b and 2c respectively while the fascia and muscles were kept at 36.6 kPa and 95.6 kPa respectively. Numerical convergence problems were encountered with model 2b due to extreme element distortion experienced with the soft intermuscular tissue. The solution was only able to converge up to 80% of the applied displacements with the convergence criteria set at a residual of 0.1% of the applied displacements. However, by increasing the stiffness of the intermuscular tissue hence reducing the amount of element distortion, a solution which converges at 100% of the applied displacement was possible. It was found by trial and error that the minimum modulus assigned to the intermuscular tissue for the solution to converge at 100% of the applied displacement was 24.4 kPa.

Fig. 10.7.2.5 and Fig. 10.7.2.6 display the von Mises stress distribution of model 2b and 2c respectively in the same contour scale at 80% of the applied displacements. There was no significant different in the way the stresses were distributed. The maximum stress in model 2b was 29.7 kPa, which was located at the

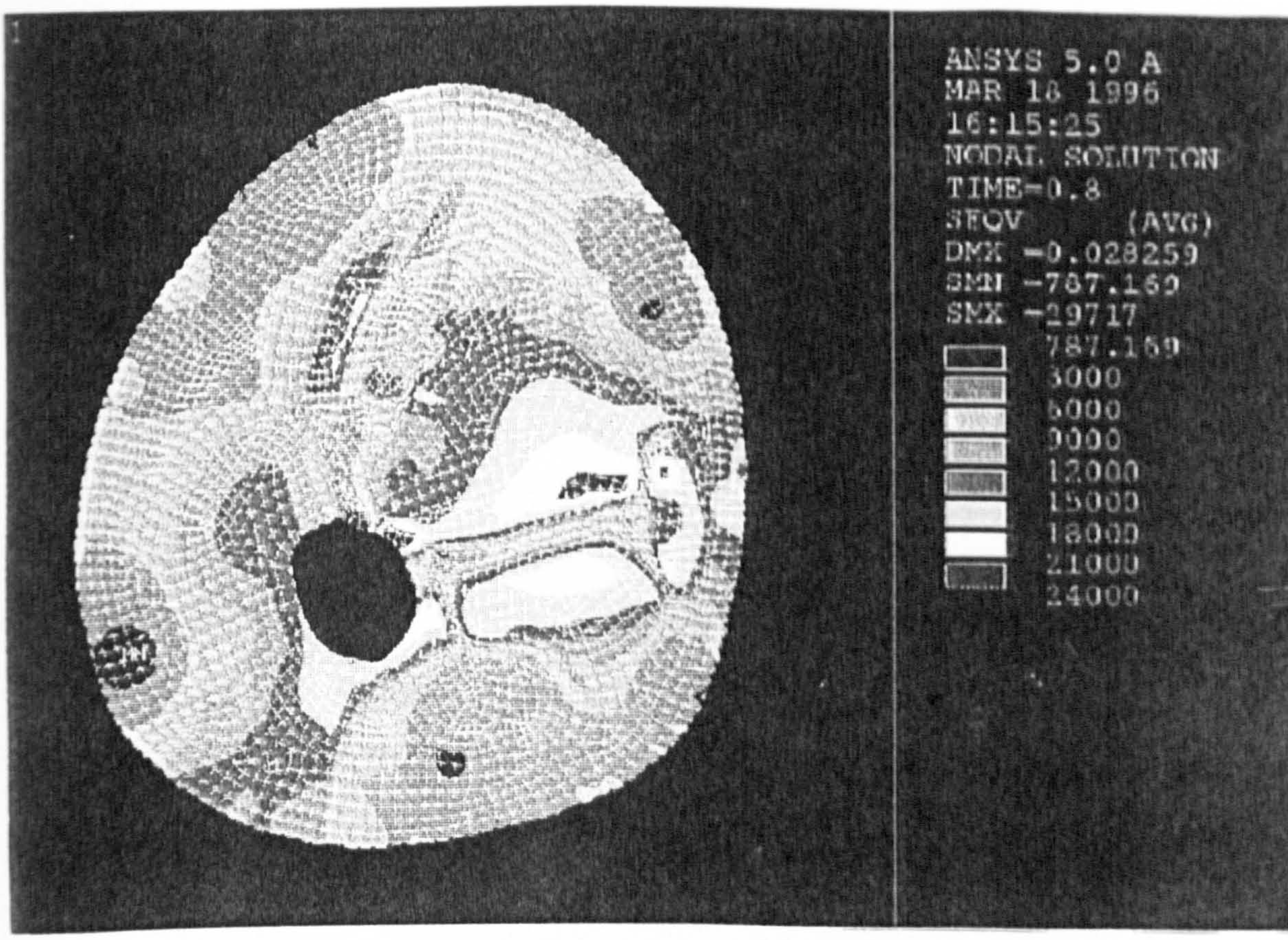

Fig. 10.7.2.5 Von Mises stress distribution of model 2b at 80% of the applied displacement. The intermuscular tissue elastic modulus was 12.2 kPa.

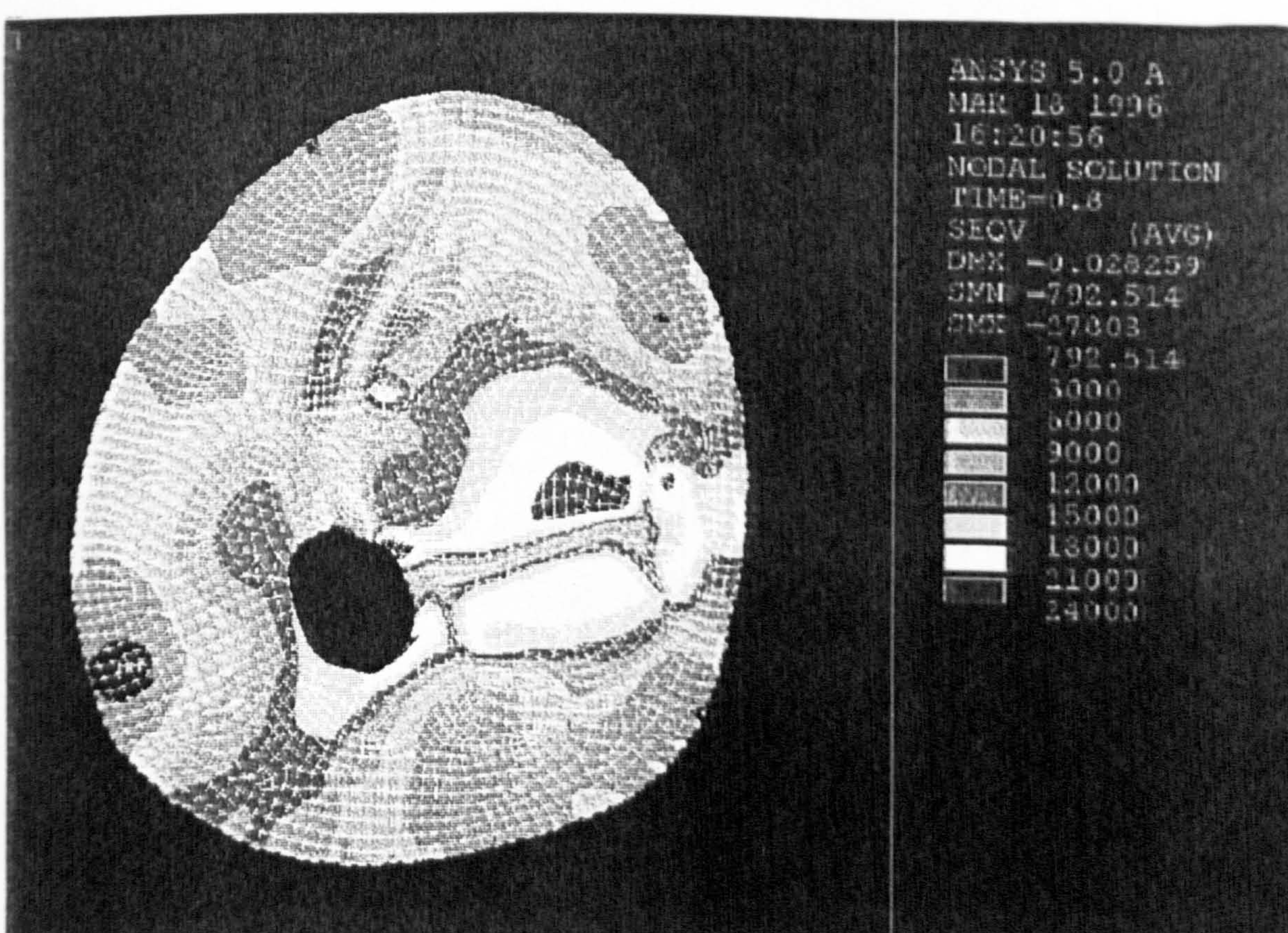

Fig. 10.7.2.6 Von Mises stress distribution of model 2c at 80% of the applied displacement. The intermuscular tissue elastic modulus was 24.4 kPa.

medial side of the adductor magnus/brevis muscle. Maximum stress was also found near the linear aspera where the adductor magnus/brevis muscle was attached to the bone. Increasing the stiffness of the intermuscular tissue has caused an overall increase in the stresses in the gracilis, the adductor magnus/brevis and the adductor longus. As seen in the figures, the area of high stress contours in these muscles were larger in model 2c than in 2b.

At 100 % of the applied displacements, model 2c predicted a maximum stress of 35.7 kPa. Comparing this with model 2a where the intermuscular tissue was assigned a modulus of 36.6 kPa, the maximum stress predicted was almost unchanged at 35.2 kPa. Increasing the modulus of the intermuscular tissue has the effect of reducing peak stress, though this reduction was minimal.

Model 2d and 2e

The stiffnesses of the different muscles were increased to simulate the residual limb in the state of muscle contraction. In model 2d, the posterior (gluteus maximus, semimembrinosus, semitendinosus and long head of biceps femoris) and the lateral (vastus muscles and rectus femoris) muscles were given elastic moduli of 191.2 kPa and 143.4 kPa respectively. The muscles at the anterior and medial regions (sartorius, adductor longus, gracilis and adductor magnus/brevis) of the residual limb were assigned with a modulus of 95.6 kPa.

All the models discussed so far have assumed the soft tissue to be nearly incompressible with a Poisson's ratio of 0.49. In model 2e, the elastic moduli were maintained as that of model 2d but a Poisson's ratio of 0.1 was assigned to the fascia and intermuscular tissue and 0.3 to the muscles.

Model 2d was discussed by comparing the von Mises stress plot (Fig. 10.7.2.7) to that of Model 2a (Fig. 10.7.2.1) where the elastic modulus of all the muscles was maintained uniform at 95.6 kPa. On the whole, stresses were increased in model 2d due to the effect of increasing the stiffness of the muscles. However, the effect was localised i.e. increased in stresses were only observed at the particular muscles assigned with a higher modulus. As seen in the figures, the stress distribution

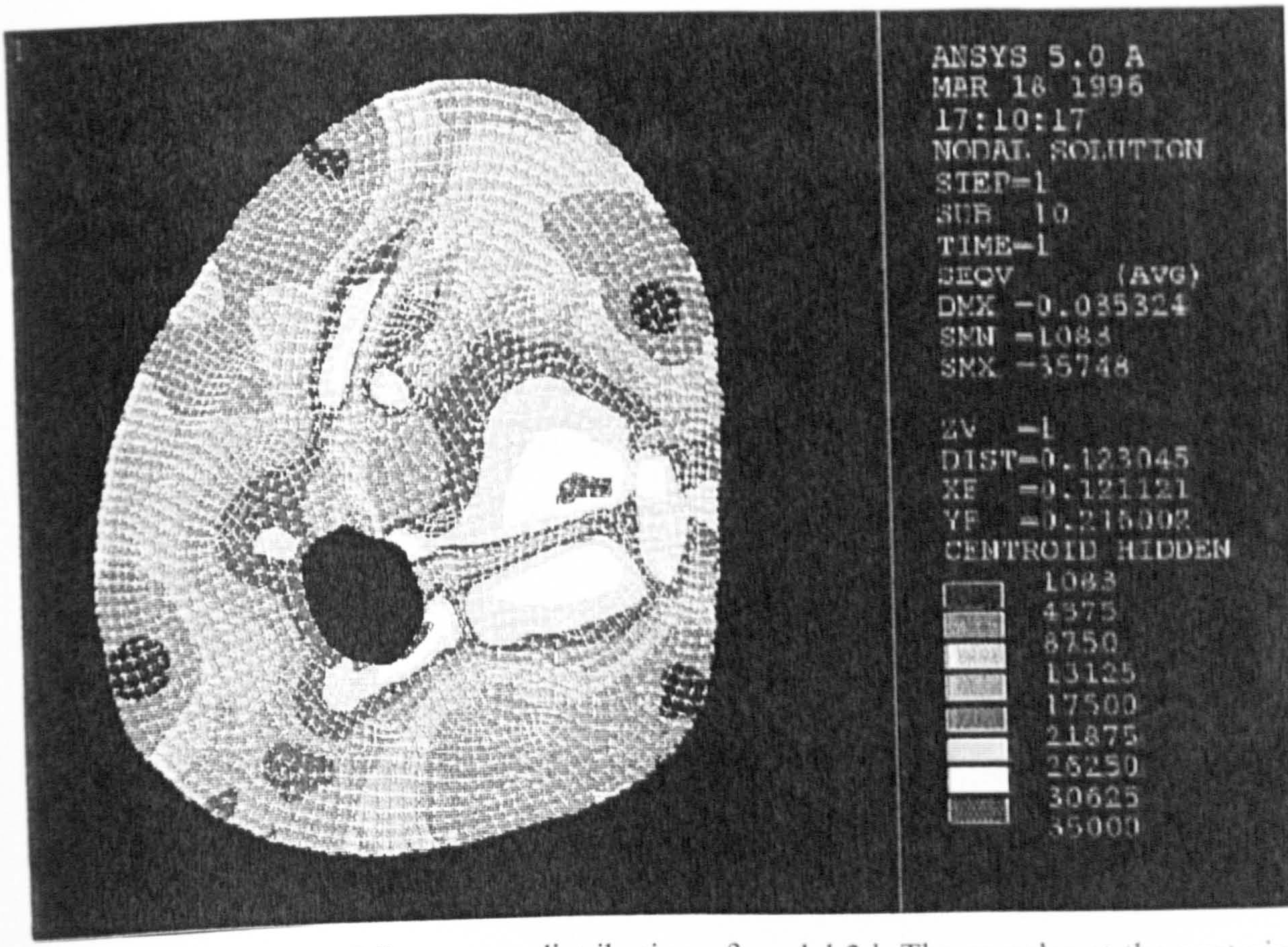

Fig. 10.7.2.7 Von Mises stress distribution of model 2d. The muscles at the posterior and lateral regions were assigned elastic moduli of 191.2 kPa and 143.4 kPa respectively.

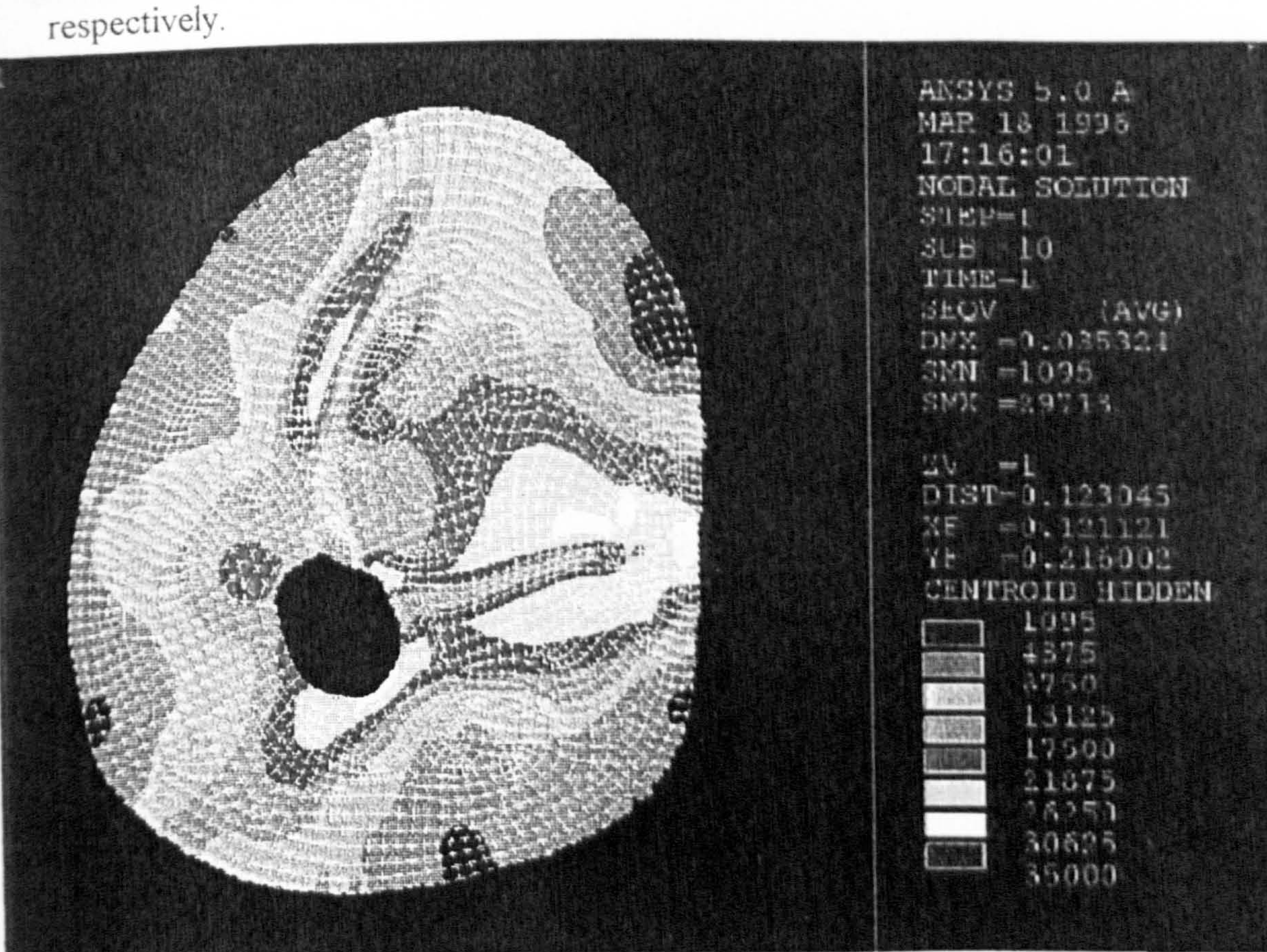

Fig. 10.7.2.8 Von Mises stress distribution of model 2e. The soft tissues were assumed to be compressible. The Poisson's ratio for fascia and intermuscular tissues was 0.1 and for muscles was 0.3.

at the medial region was almost unchanged, since the muscles at this region were of similar stiffness in model 2d and 2a. However, due to the increase in stiffness at the posterior region in model 2d, the gluteus maximus predicted higher stress at 30.6 kPa in model 2d compared with 20.1 kPa in model 2a. The effect was the same with the vastus muscles where the stress has increased 30% due to an increase in stiffness. There was no difference in the peak stress (35 kPa) recorded in both models, since the peak stress was located at the adductor magnus/brevis where the stiffness was the same in both models.

Significant changes in the von Mises stress distribution was realised when the tissues were assumed to be compressible instead of incompressible. Reducing the Poisson's i.e. assuming compressibility, has the effect of reducing the overall stresses. Comparing model 2d and 2e in Fig. 10.7.2.7 and Fig. 10.7.2.8 respectively, the maximum von Mises stress was reduced by 20% in the compressible model 2e.

10.7.3 Model 3 (Incorporating intermuscular septa)

The septa surrounding the muscles were modelled using link elements. The link elements were able to resist tension but upon compression, the elements became slack and did not transfer any load. The elastic modulus assigned to the tissues remained the same as that of model 2a, while the link elements were assigned a modulus of 400 MPa.

Model 3 suffered numerical problems at 95% of the applied displacements. This was due to the stiffening effect of the link elements, restricting movements in the quadrilateral elements. Fig. 10.7.3.1 plots the von Mises stress distribution at 80 % of the applied displacements. The maximum stress recorded was 27.4 kPa at the medial side of the adductor magnus/brevis. The location of maximum stress was exactly the same as that of model 2a which did not have any link elements. This was because the link elements were not effective at the medial side of the residual limb which was under compression. The addition of the link elements has the effect of reinforcing the residual limb structure, very much like that of steel beams in reinforced concrete. Though unlike the steel beams, the link elements used to model the intermuscular

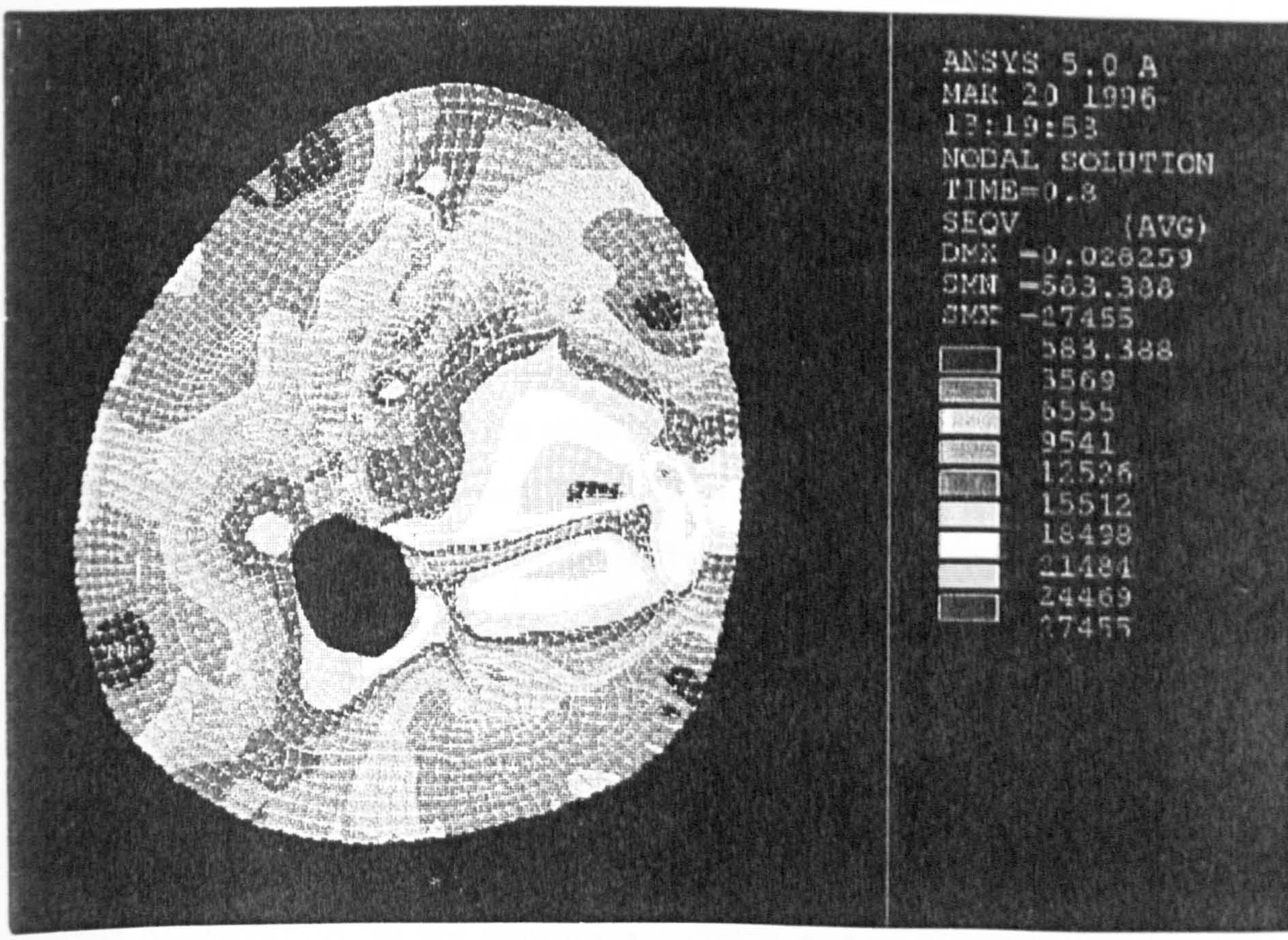

Fig. 10.7.3.1 Von Mises stress distribution of model 3 at 80% of the applied displacement. The intermuscular septa were modelled using link elements.

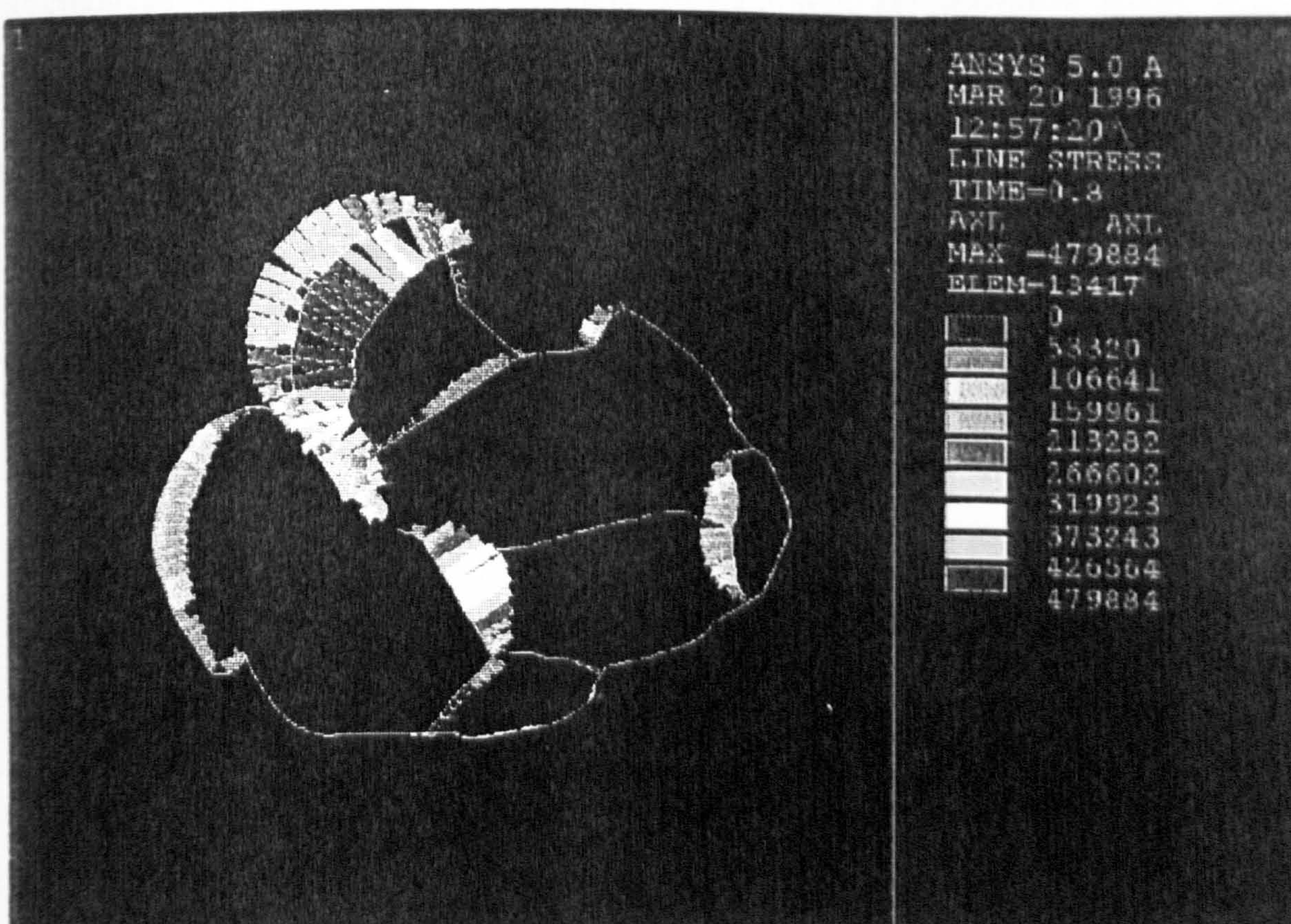

Fig. 10.7.3.2 Axial stresses at the link elements of model 3 at 80% of the applied displacement.

septa were only expected to resist tension. In the residual limb model, the nodal displacements introduced compression forces in the medio-lateral plane and tension forces in the anterio-posterior plane. Therefore the link elements resisted the tension in the anterio-posterior plane but appeared as slack cables at the medio-lateral plane. Fig. 10.7.3.2 plots the stress perpendicular to the link elements (axial stress). At the medial region, low axial stresses were predicted at the link elements. However, the link elements at the posterior region surrounding the gluteus maximus were particularly effective in restraining the applied tension forces. This lead to an overall decrease in the von Mises stresses in the posterior region where the gluteus maximus was located. Similarly, in the anterior region, the link elements which were connected to the femur were under high axial stresses.

The displacement plot of the link elements in Fig. 10.7.3.3 shows the large deformation at the medial side was not restricted in any way by the link elements. The effect of introducing the link elements was clearly seen by comparing the maximum tensile stress (principal stress) of model 3 with that of model 2a where no link elements was used. Fig. 10.7.3.4 and 10.7.3.5 plot the maximum tensile stress distribution of model 3 and 2a respectively. At the posterior region, the link elements surrounding the gluteus maximus were effective in resisting the applied tension forces, thus protecting the gluteus maximus from being stressed. This was confirmed by the tensile stress plots in model 3 where a much lower stress (2.3 kPa) was found in the gluteus maximus compared to model 2a (9.2 kPa). However, at the region just above the gluteus maximus where no link element was present, higher stress was predicted in model 3 (20.8 kPa) compared to model 2a (11.5 kPa). This was due to the tensile forces acting on a smaller area increasing stresses.

10.7.4 Model 4 (Incorporating sliding between muscles)

Interface elements enabled the muscles to slide or separate i.e. loose contact with the surrounding intermuscular tissues. This is a realistic assumption since some muscles are separated or loosely connected by fibrous tissue to the intermuscular tissue allowing very large movements to take place. Model 4 was attempted using

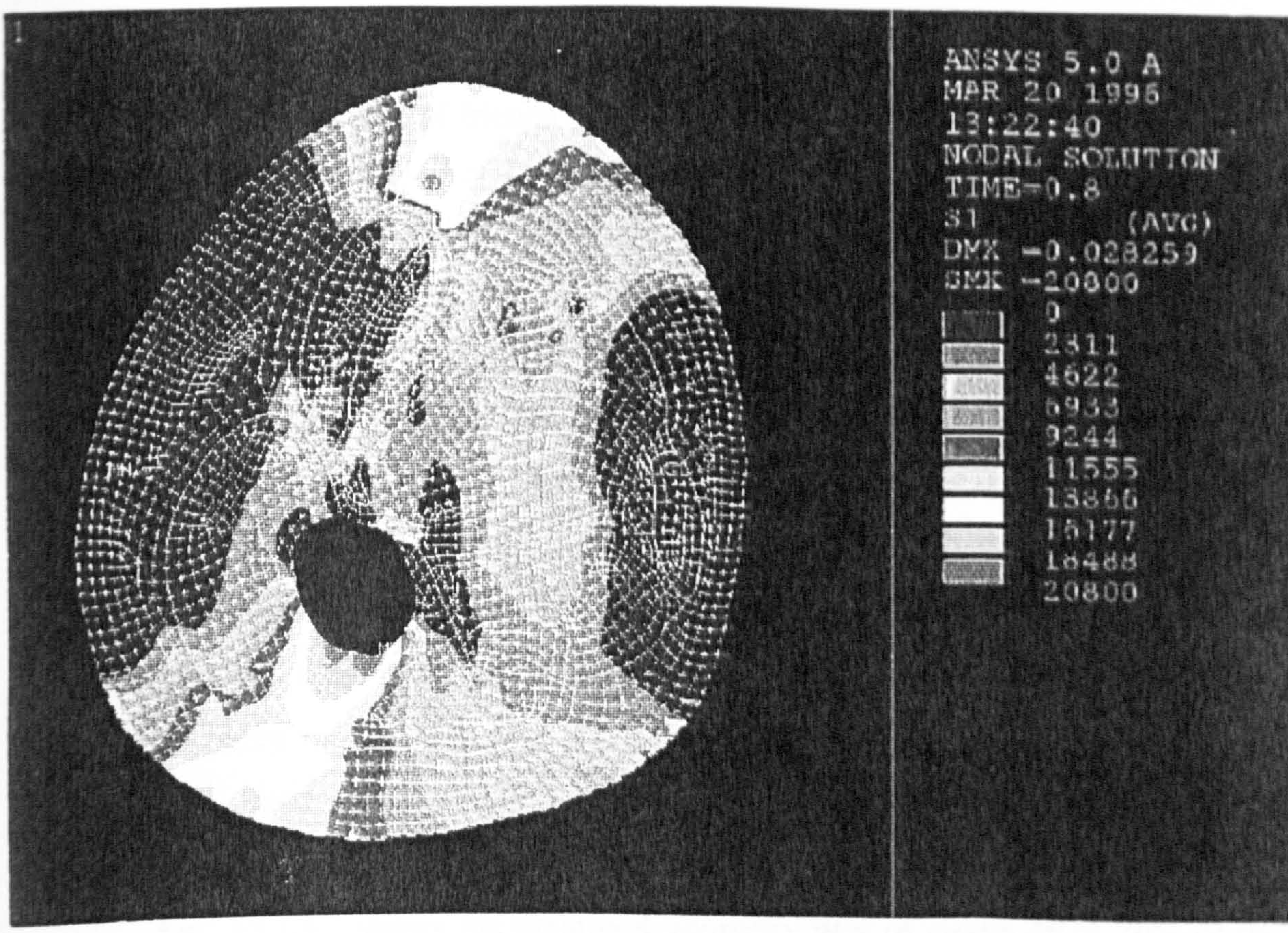

Fig. 10.7.3.4 Maximum tensile stress distribution of model 3 at 80% of the applied displacement.

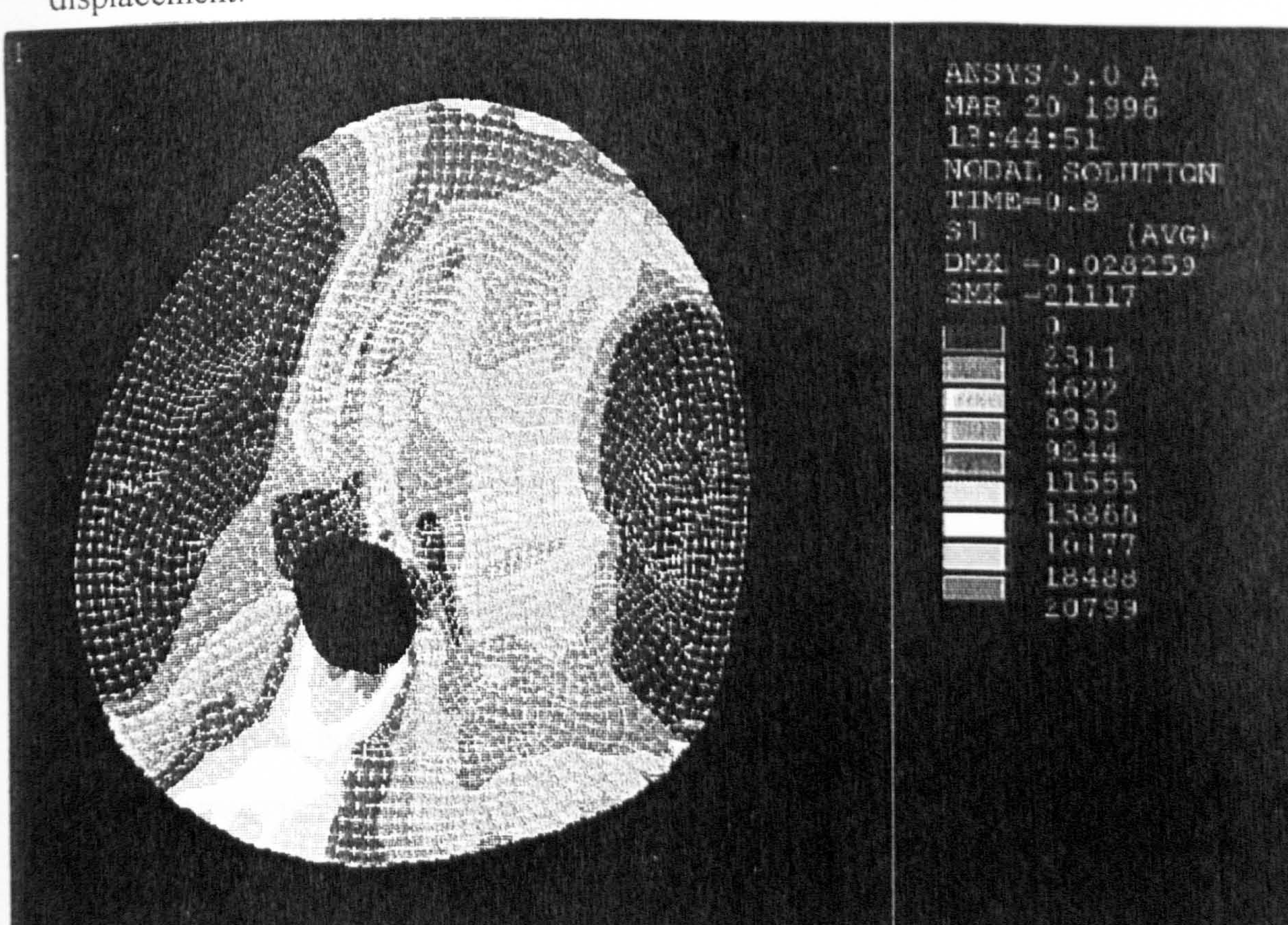

Fig. 10.7.3.5 Maximum tensile stress distribution of model 2a at 80% of the applied displacement. Model 2a was similar to model 3 except no link element was used.

three different coefficients of friction (μ) assigned to the interface elements. Model 4a , 4b and 4c were assigned μ of 0 (frictionless), 0.1 and 0.3 respectively.

Numerical convergence problems were encountered in all three models. Increasing the coefficient of friction also increased the computation time and risk of convergence difficulties. The model incorporated a total of 3279 interface elements and 2922 2-D solid elements. The maximum and minimum incremental load steps were set to 10% and 0.01% of the applied displacements. In order to achieve the optimal balance between computation time and solution, ANSYS automatic load stepping algorithm was utilised i.e. the load steps were increased or decreased automatically to achieve numerical convergence. Despite such caution, convergence difficulties were experienced with model 4a at 47% of the applied displacement. Computation time was also excessive, more than 30 hours with a standalone Silicon Graphics Indigo 2 workstation.

Fig. 10.7.4.1 shows the deformed geometry plot of model 4a at 20% of the applied displacements. Several muscles were separated from the intermuscular tissue. The largest separation was observed at the anterior region of the residual limb between the intermuscular tissue and the rector femoris and vastus muscles. The rectus femoris and the vastus muscles were practically rigid compared to the intermuscular tissue, since they were connected firmly to the bone. The tension forces applied were thus taken up by the anterior intermuscular tissue leaving the muscles unstressed. In the medial side, anterior and posterior regions of the adductor longus also experienced separation with the intermuscular tissue. Due to the compression at the medial side of the residual limb, the softer intermuscular tissue surrounding the adductor longus was forced to buckle, leaving a gap. At the posterior side of the residual limb, separation was encountered at the posterior of the gluteus maximus and the adductor magnus/ brevis with the intermuscular tissues. The tension forces applied at the posterior surface of the residual limb displaced the softer intermuscular tissue posteriorly causing the separation.

Due to numerical non-convergence in the subsequent models 4b and 4c and the large computation effort, the analyses were attempted using 10% of the applied displacement. To enable meaningful comparison, the following results were presented

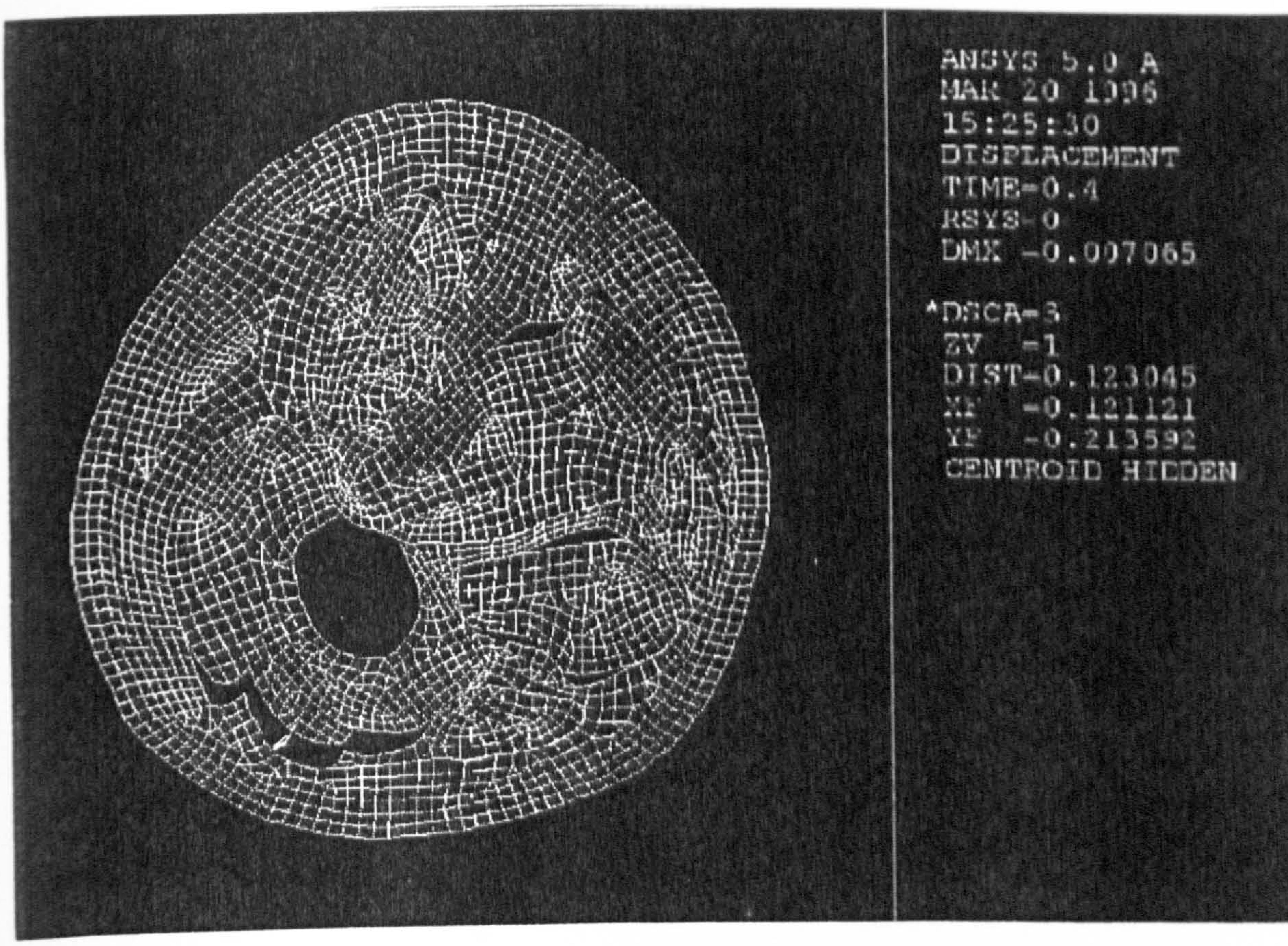

Fig. 10.7.4.1 Deform geometry of model 4a at 20% of the applied displacement. Model 4a consisted of frictionless interface elements which surrounded the muscles allowing sliding to take place. The displacements were enlarged three times in this plot for clarity.

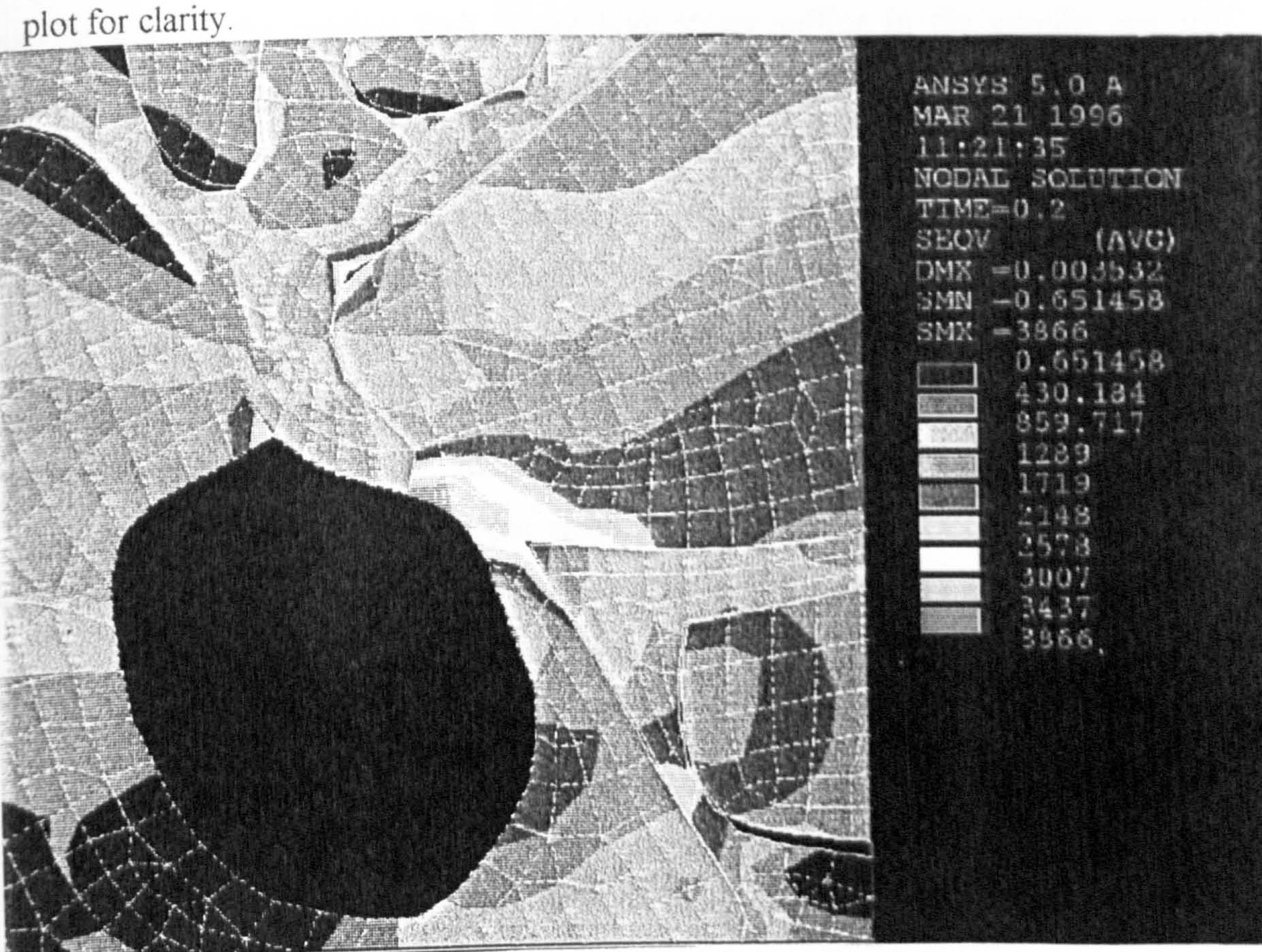

Fig. 10.7.4.2 Von Mises stress distribution at the bone / muscle interface in model 4a at 10% of the applied displacement.

based on 10% of the applied displacements. Fig. 10.7.4.2 shows the von Mises stress distribution at the adductor magnus/brevis insertion to the femur where maximum stress was observed for model 4a. The high stress was caused by the intermuscular tissue being forced into a corner penetrating the adductor magnus/brevis near the insertion to the bone. It was reckoned that numerical convergence could be improved by a finer mesh at this region. This was attempted but did not lead to any improvement.

The effect of allowing muscles to slip was evaluated by comparing model 4a with model 2a. Fig. 10.7.4.3 shows the maximum tensile stress in model 4a. By allowing the muscles to slip, the overall tensile stress was reduced as in model 4a, especially at the anterio-posterior plane. Near zero tensile stresses were predicted at the regions where the muscles were allowed to slip i.e. regions with interface elements. Fig. 10.7.4.4 and Fig. 10.7.4.5 show the von Mises stress plots for model 4a and 2a respectively at 10% of the applied displacement. There was a clear indication that a lower stress state was maintained when the muscles were allowed to slip. At the medial side of the residual limb where high stress suffice in the gracilis and the adductors, the stresses were 20% lower in model 4c than in model 2a. The stresses at the region where the vastus muscles attached the bone and the anterior side of the residual limb was reduced to a minimal of 0.4 kPa in model 4a. Similarly at the posterior side, the stresses at the gluteus maximus were within the region of 0.4 to 0.8 kPa. However, the peak stress recorded at the insertion of the adductor magnus/brevis was higher in model 4a than in model 2a. The localised stressed was caused by the ability of the adductor magnus/brevis to slip and generate larger displacements, putting stress on the small area at the muscle insertion point. Also discussed earlier, the intermuscular tissues at the medial side of the femur was pushed against the muscles' attachment causing an increase in stresses.

Fig. 10.7.4.6 and Fig. 10.7.4.7 display the von Mises stress distribution of model 4b and 4c at 10% of the applied displacement. Coefficient of friction of 0.1 and 0.3 were respectively allocated to the two models at the interface elements. An increase in maximum stress was observed when the coefficient of friction was

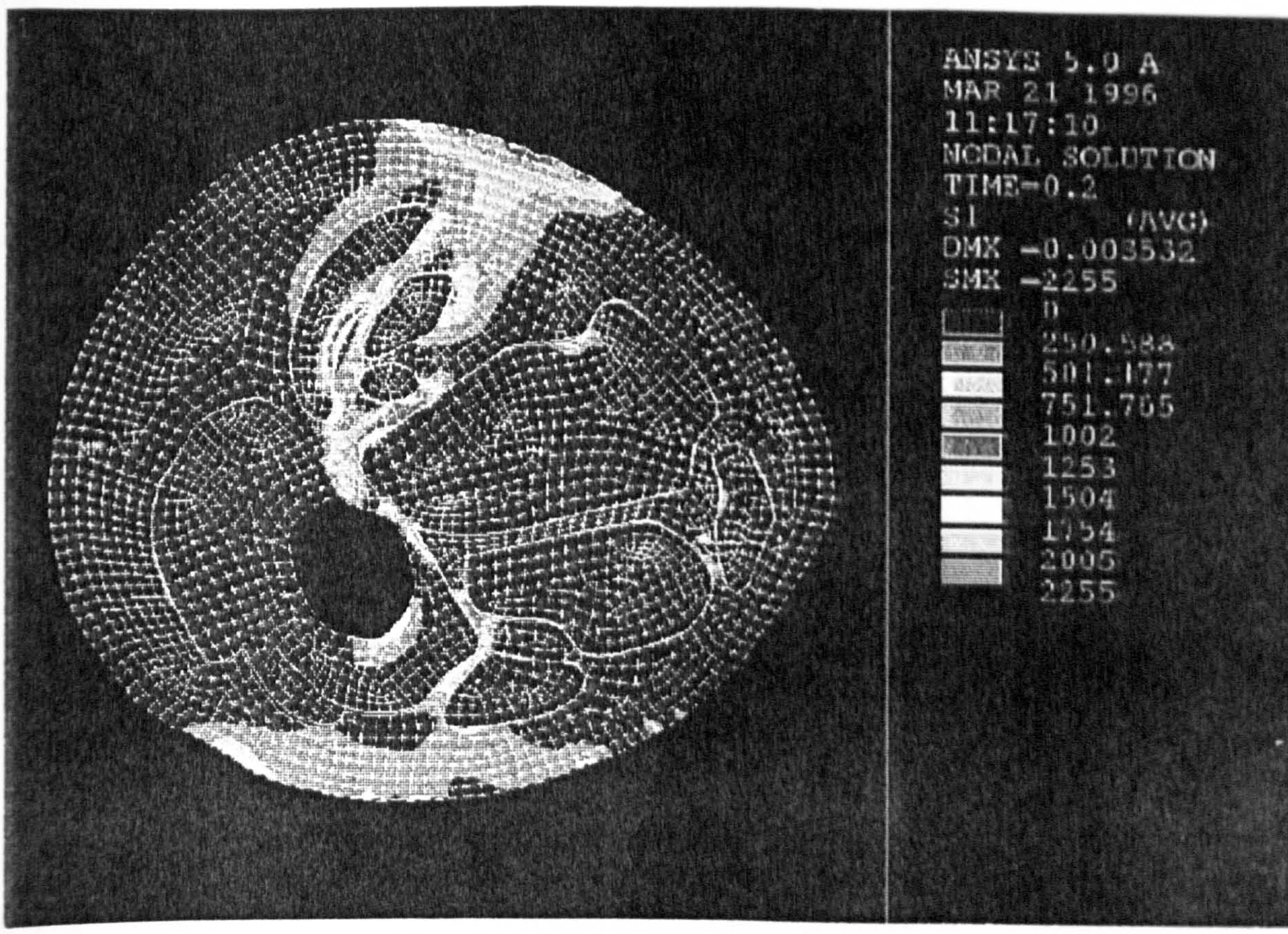

Fig. 10.7.4.3 Maximum tensile stress distribution of model 4a at 10% of the applied displacement.

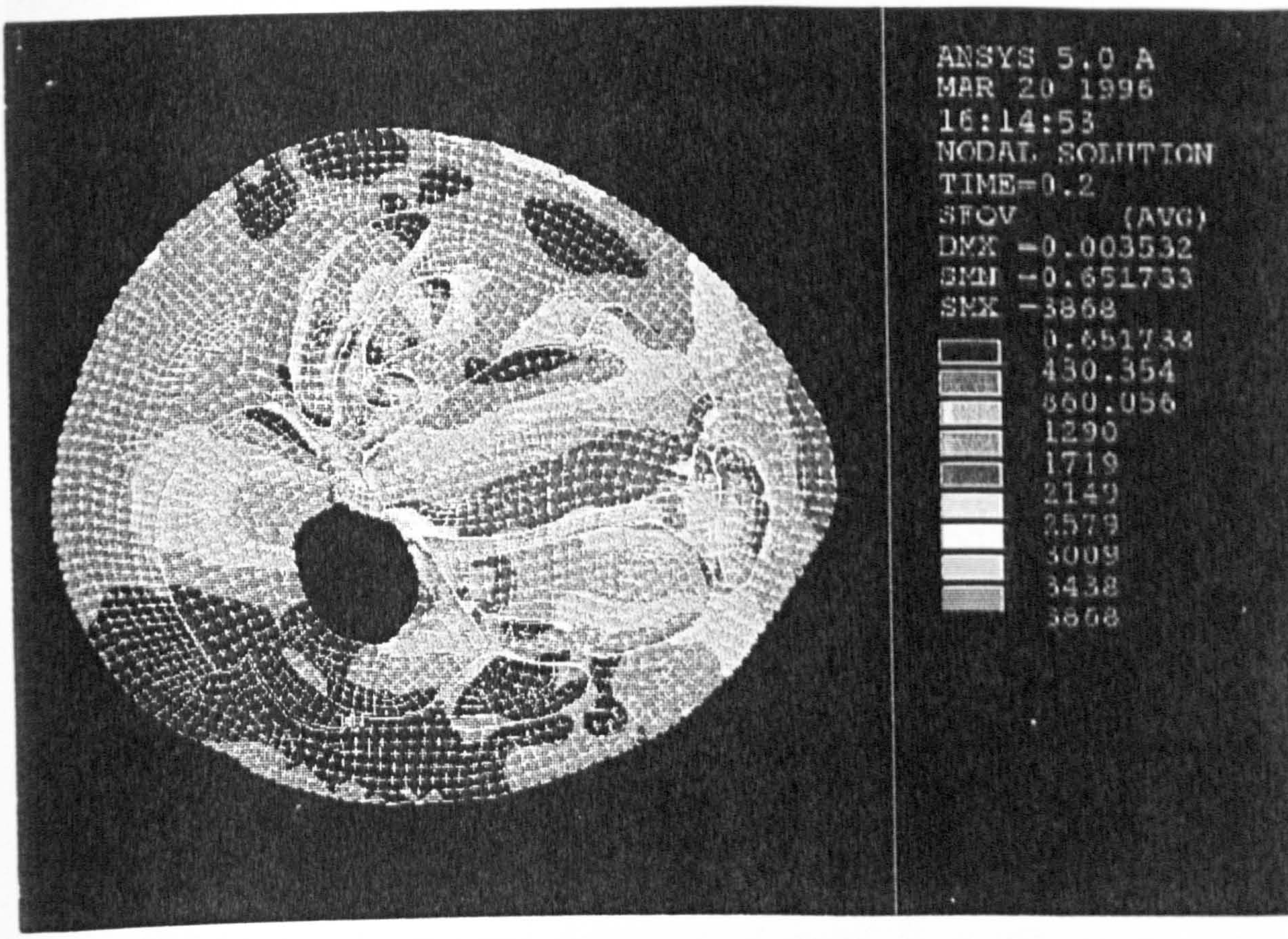

Fig. 10.7.4.4 Von Mises stress distribution of model 4a with frictionless interface elements at 10% of the applied displacement.

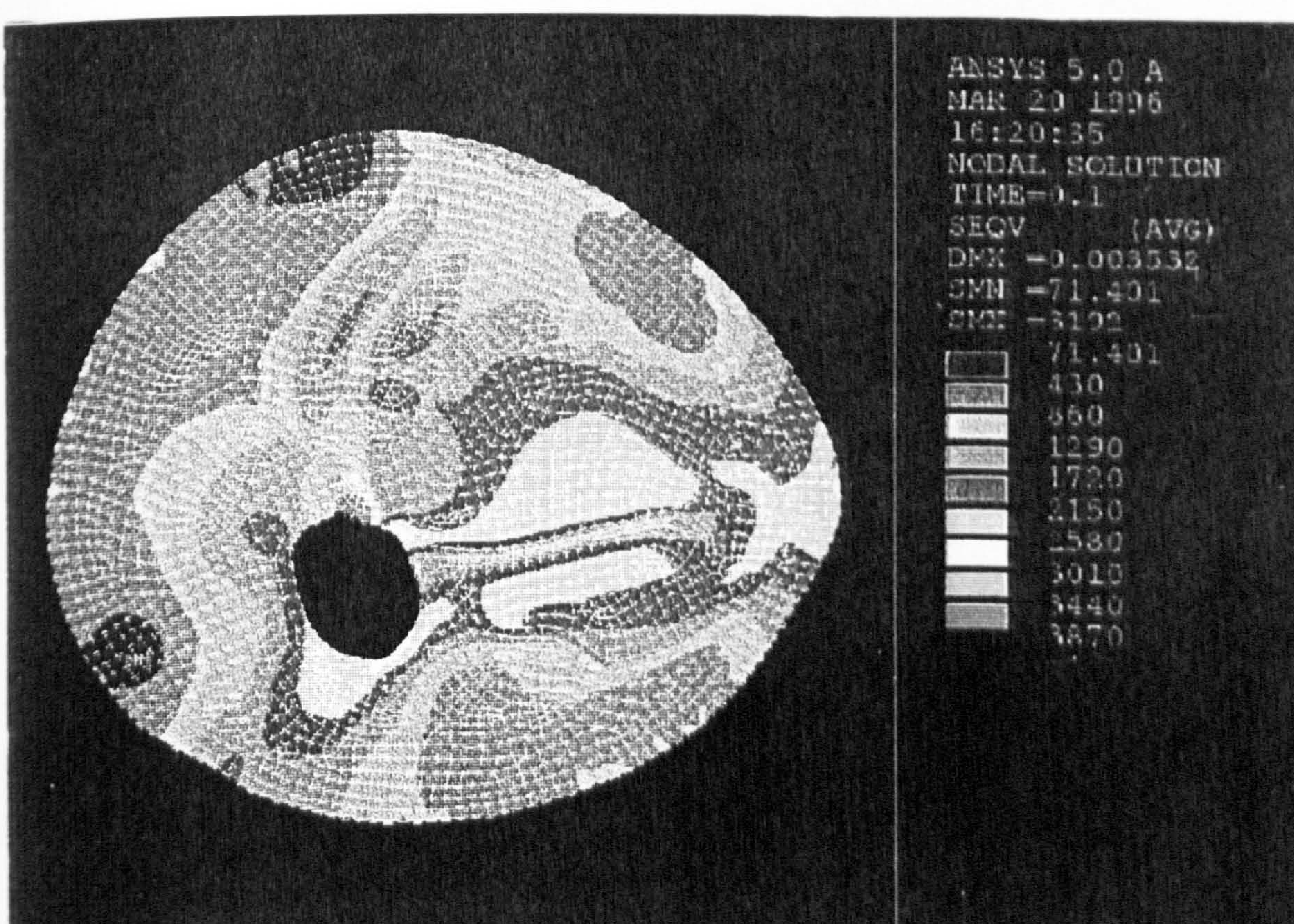

Fig. 10.7.4.5 Von Mises stress distribution of model 2a without any interface element.

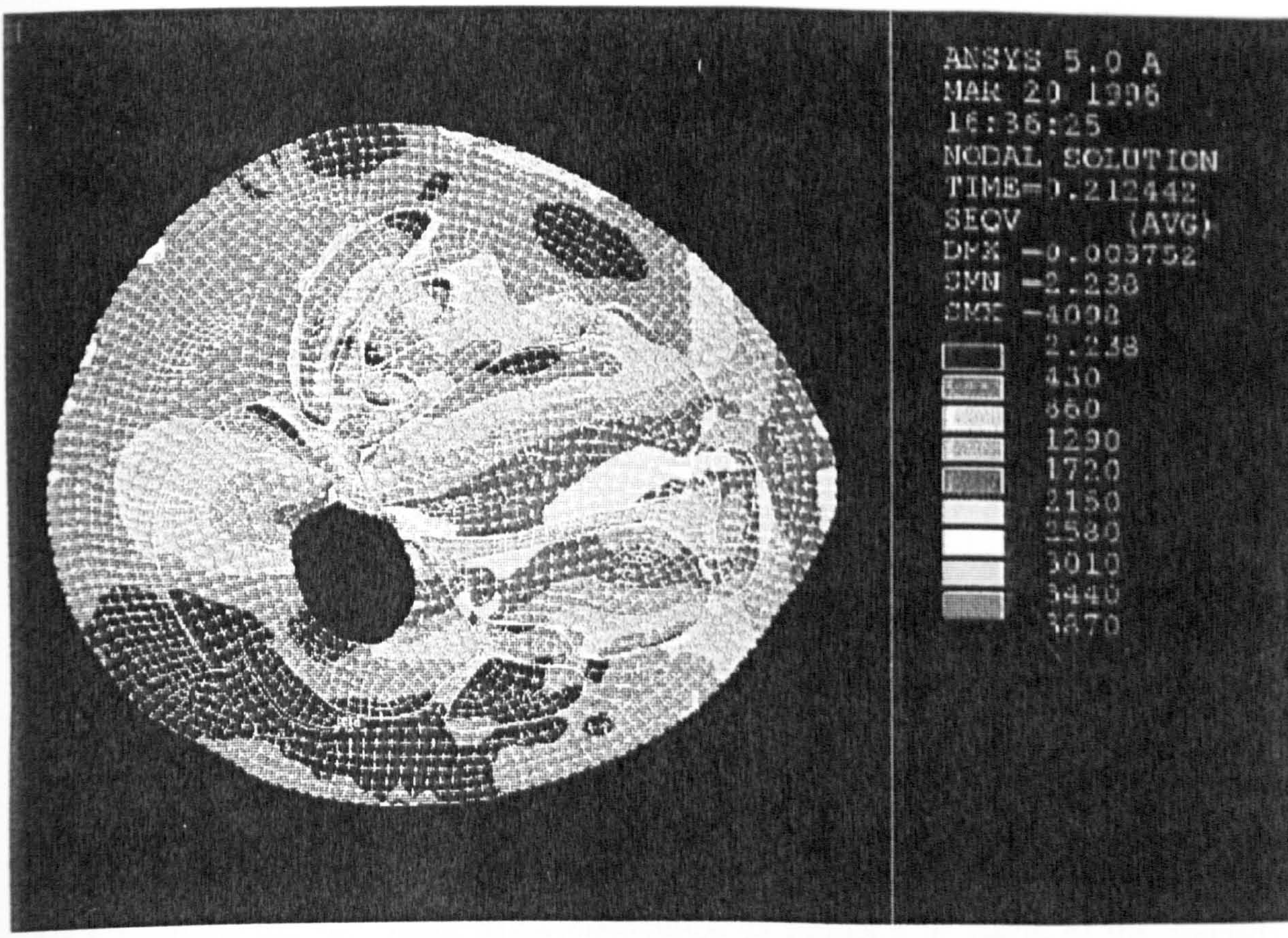

Fig. 10.7.4.6 Von Mises stress distribution of model 4b at 10% of the applied displacement. Coefficient of friction of 0.1 was introduced to the interface elements surrounding the muscles.

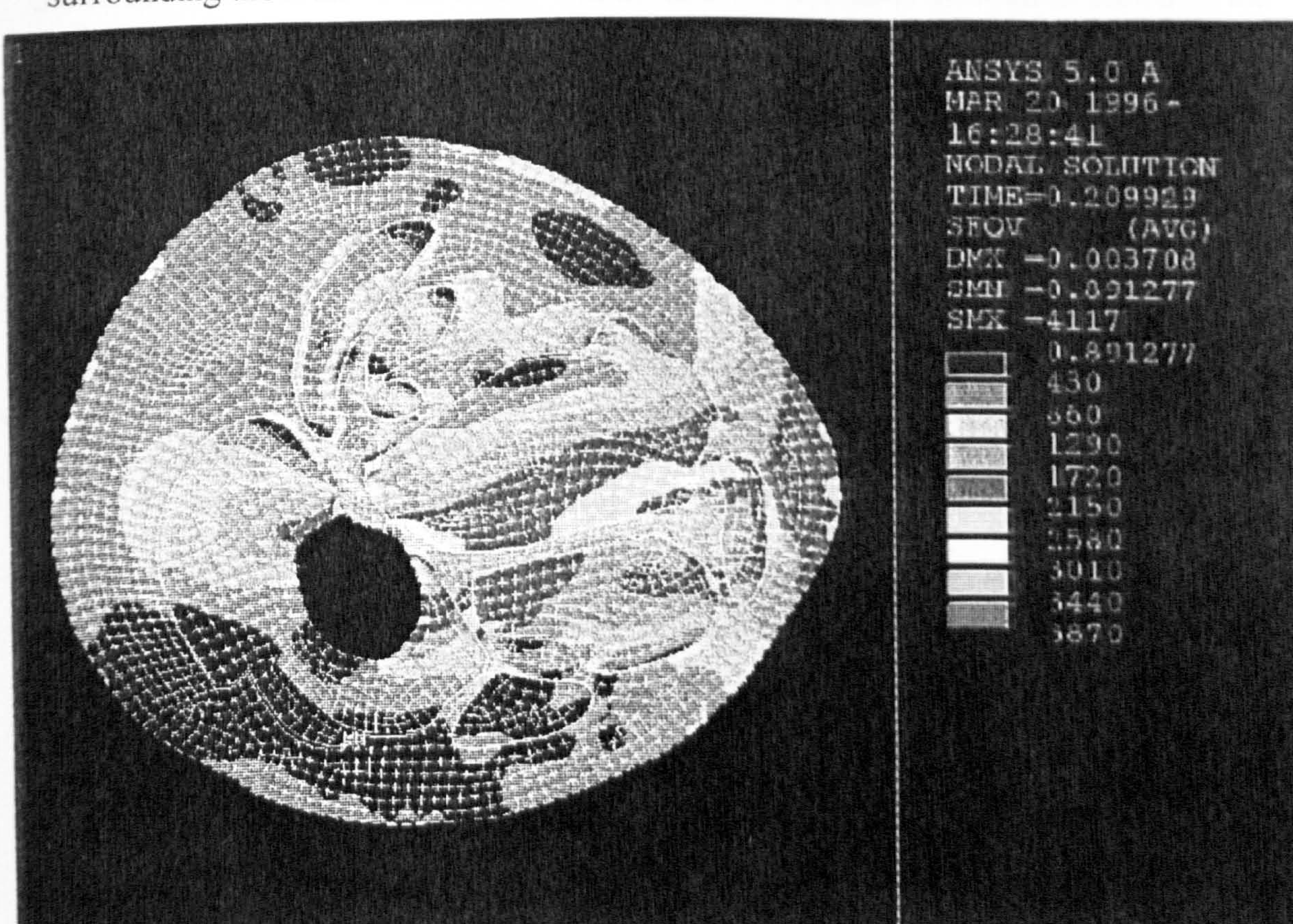

Fig. 10.7.4.7 Von Mises stress distribution of model 4c at 10% of the applied displacement. Coefficient of friction of 0.3 was introduced to the interface elements surrounding the muscles.

increased. Maximum von Mises stress at 10% of the applied displacement for frictionless, μ=0.1 and μ=0.3 models were 3.8 kPa, 4.0 kPa and 4.1 kPa respectively. As friction at the interface between muscles and intermuscular tissue was increased, localised stresses began to surface along the interface. However, the general stress pattern of model 4b and 4c were more or less indifferent when compared to the frictionless model 4a.

10.7.5 Model 5 (Allowing femur to move)

The femur was permitted to move among the soft tissue in model 5 by not restraining its boundary in the x and y directions. It was not modelled as a rigid boundary but given a high elastic modulus of 15.8 GPa and Poisson's ratio of 0.3. As expected, such a modification reduced the stress around the bone. At 100% of the applied load, the bone was found to move laterally 2.9 mm and anteriorly 8 mm. Fig. 10.7.5.1 plots the von Mises stress distribution of model 5 at 100% of the applied displacements. Comparing it to model 2a (Fig. 10.7.2.1) where the bone was fixed, the stress just anterior to the femur was 23 kPa. At the same location in model 5, the stress was 12 kPa. A discontinuous instead of a gradual change in the stress pattern was also observed at the adductor magnus/brevis muscle near the medial posterior region of the femur in model 5. The stresses at the medial region of the residual limb were lower in model 5 than in 2a since the bone had moved laterally provided stress relieve.

Fig. 10.7.5.2 plots the stress in the y- direction of model 5 which showed that the stress in the anterior posterior plane was relatively low between 11 kPa to 17 kPa. However, an exception existed at the point where the adductor magnus/brevis inserted the bone. A maximum stress of 31 kPa was predicted at this location. In the case where the bone was fixed in position (model 2a, Fig. 10.7.2.3), the stresses in the y - direction ranged from 7 to 25 kPa at the anterior posterior plane.

10.7.6 Model 6 (Sliding at the residual / socket interface)

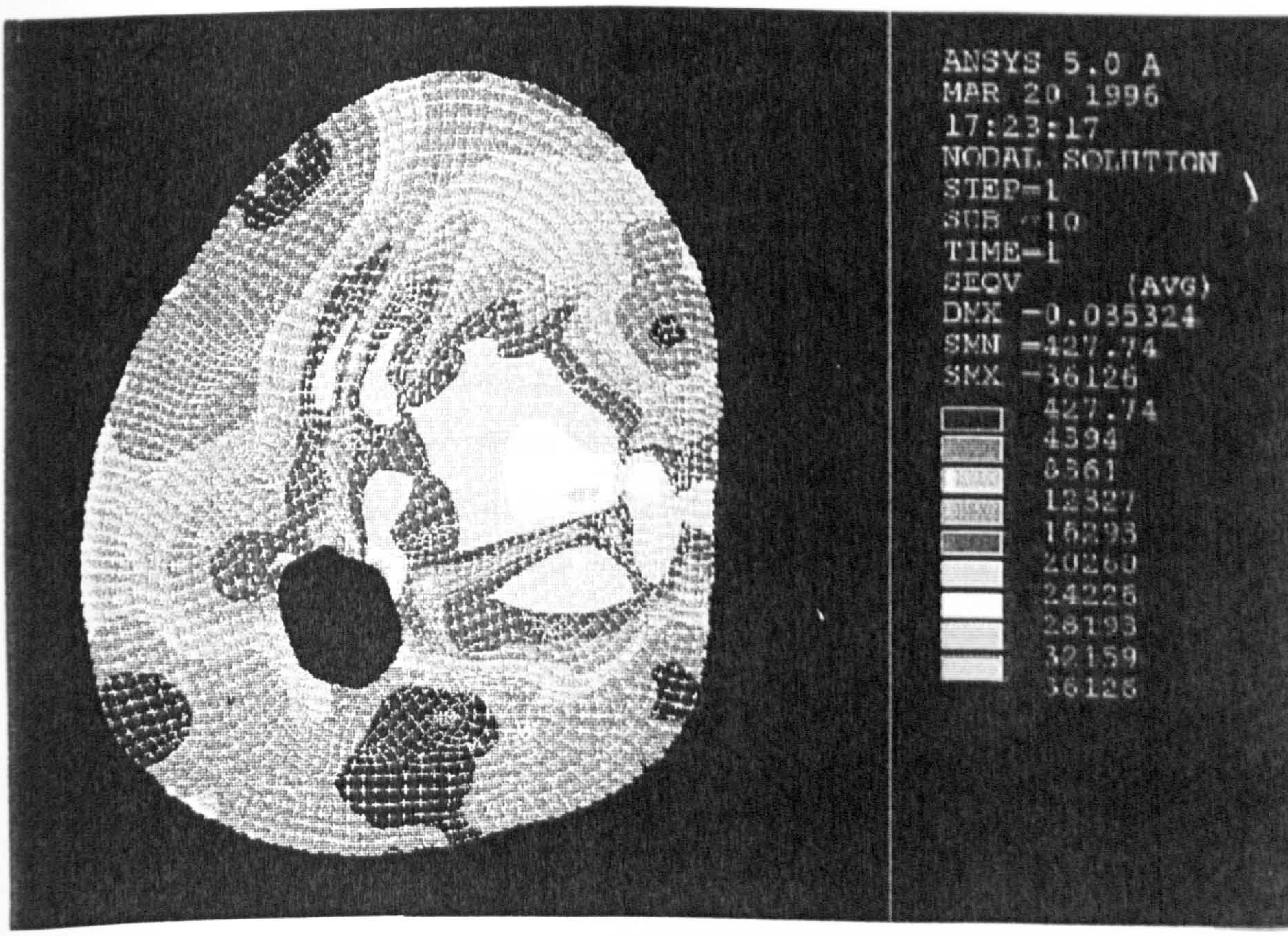

Fig. 10.7.5.1 Von Mises stress distribution of model 5 where the femur was not restrained in the x and y directions.

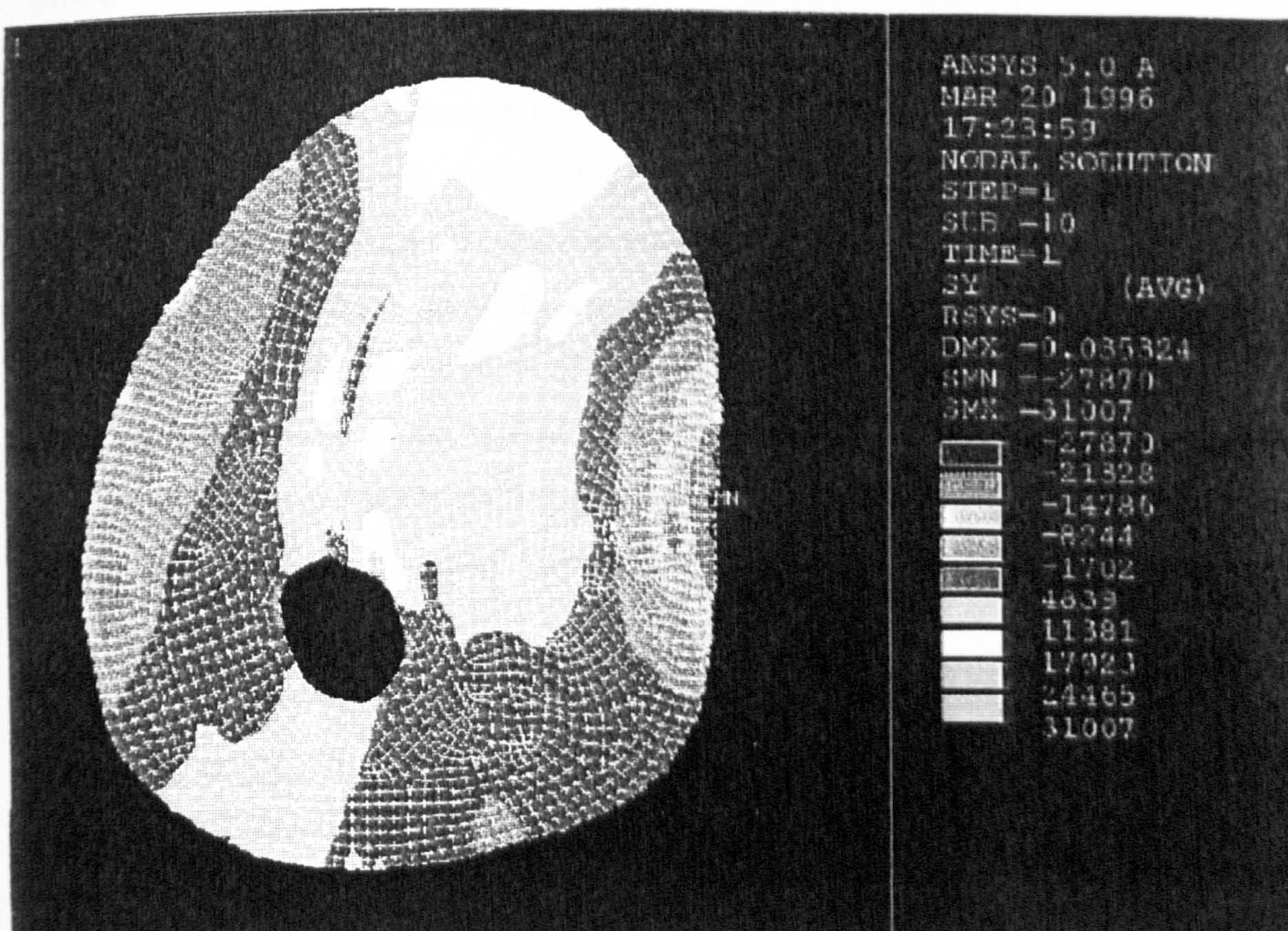

Fig. 10.7.5.2 Stress distribution in the y direction of model 5.

It is thought that a more realistic loading and boundary condition can be achieved by introducing only compressive forces at the residual limb / socket interface. The residual limb model was loaded by deforming the residual limb shape to the shape of the IC socket. In all the previous models attempted, the deformation was achieved by displacing the nodes at the residual limb surface i.e. the residual limb / socket interface. Therefore surface nodes that were displaced towards the femur would generate compressive forces while nodes that were displaced away from the femur would generate tension forces. The residual limb in the IC socket was compressed at the medio-lateral plane. However at the anterio-posterior plane, in order to fill the larger dimension of the socket, tension forces were applied at the residual limb surface.

The aim of model 6 was to eradicate the tension at the anterio-posterior plane. The approach was to allow the residual limb to slip at the interface restricted by a boundary equivalent to the shape of the IC socket. Numerical convergence in model 6 was achieved up to 56% of the applied displacements. Fig. 10.7.6.1 and Fig. 10.7.6.2 plot the maximum compressive stress at 40 % of the applied displacements of model 6 and model 2a (fixed nodal displacements at residual limb surface) respectively. Higher stresses were predicted with model 2a (maximum of 11.79 kPa) compared to model 6 (10.642 kPa). The overall stress pattern remained unchanged at the medio-lateral plane. However at the anterio-posterior plane, compressive stresses began to emerge with model 6, whereas in model 2a stresses at this region were mainly tensile. It can be further highlighted in the plots of Fig. 10.7.6.3 and Fig. 10.7.6.4, the maximum tensile stress at 40% of the applied displacements of model 6 and 2a respectively. Effectively no tensile stress existed at the anterio-posterior plane of model 6 but in model 2a, a maximum value of 10.6 kPa was present at the anterior region of the residual limb.

The boundary conditions applied in model 6 have successfully reduced the tensile stress at the anterio-posterior plane and maintained the loading at the medio-lateral plane similar to the previous models. However, the model was not able to preserve the shape of the IC socket in the predicted solution. This was evident in

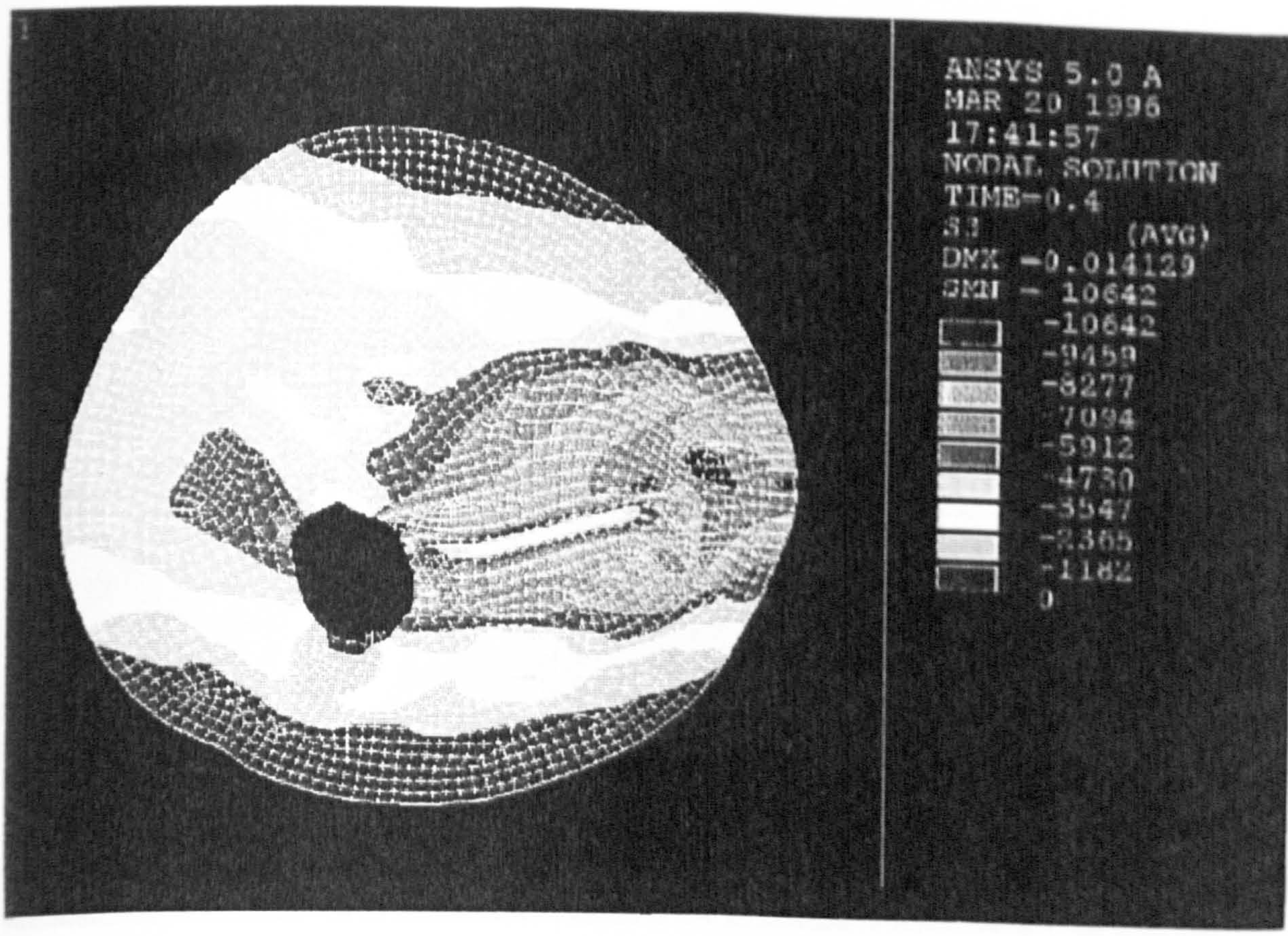

Fig. 10.7.6.1 Maximum compressive stress distribution at 40% of the applied displacement in model 6. Model 6 was allowed to slide within a boundary defined by the shape of the IC socket.

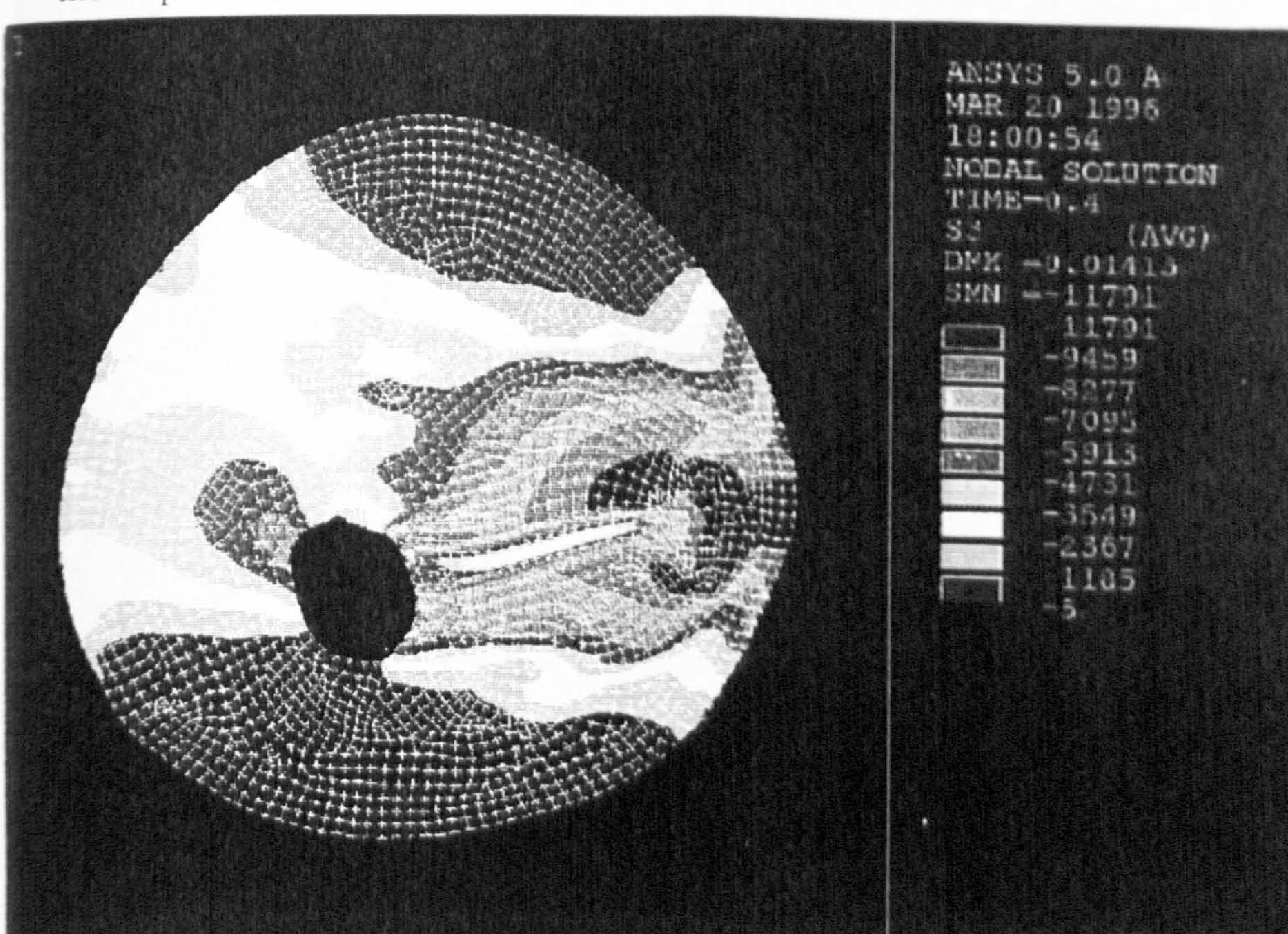

Fig. 10.7.6.2 Maximum compressive stress distribution at 40% of the applied displacement in model 2a. Model 2a possessed fixed nodal displacements defined by shape of the IC socket.

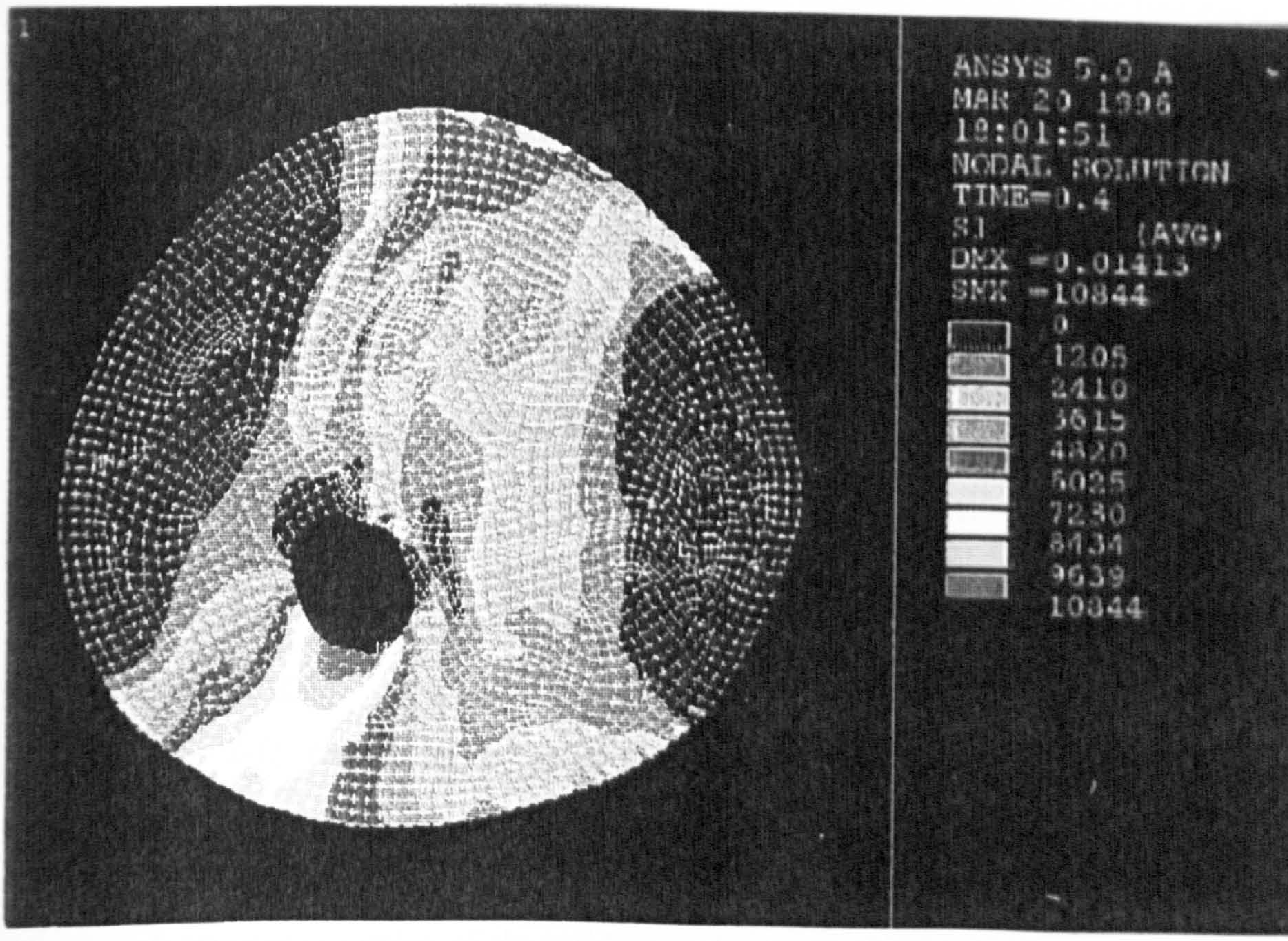

Fig. 10.7.6.3 Maximum tensile stress distribution in model 6 at 40% of the applied displacement.

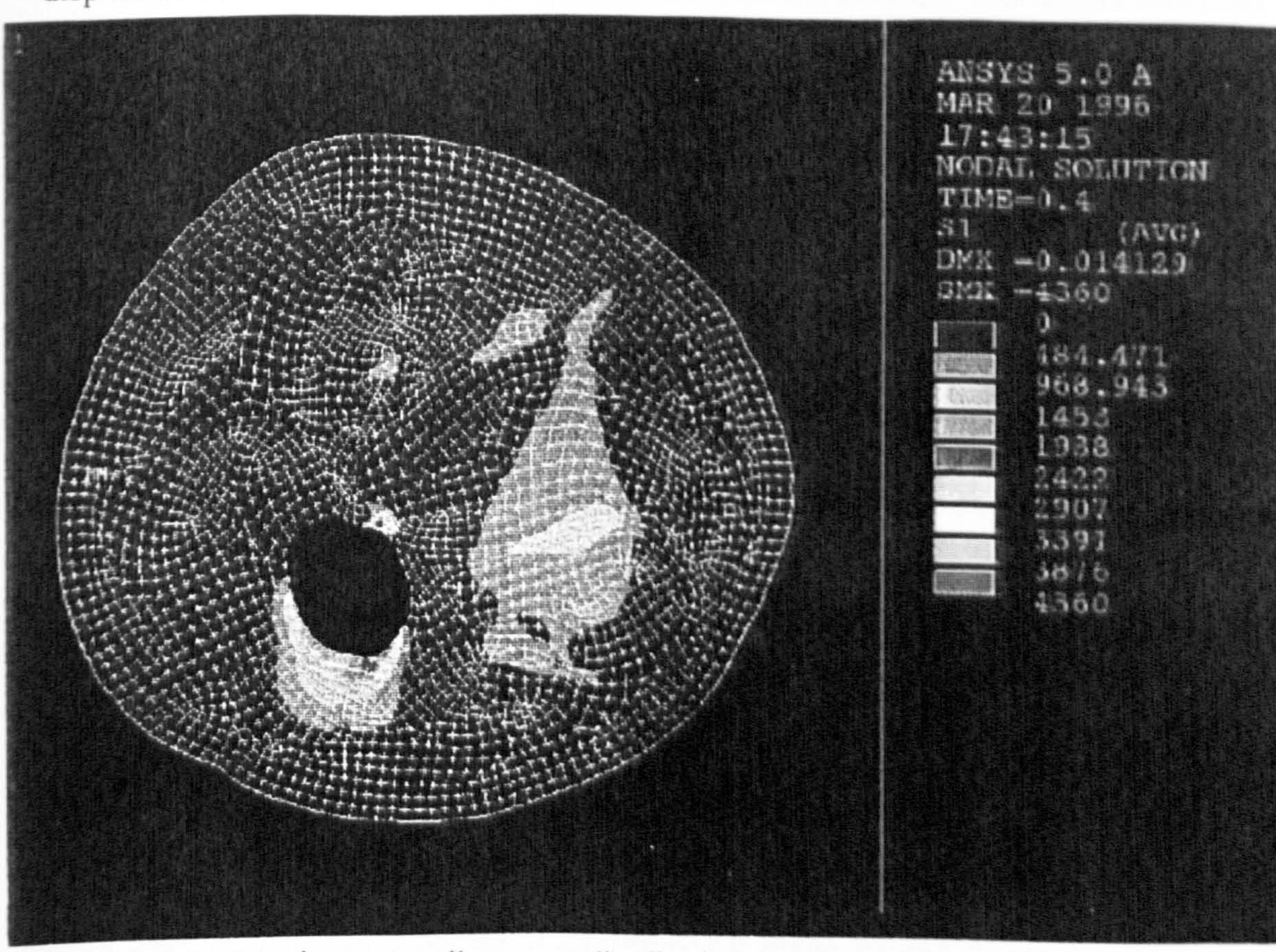

Fig. 10.7.6.4 Maximum tensile stress distribution in model 2a at 40% of the applied displacement.

Fig. 10.7.6.5, which shows the deformed geometry of the residual limb with respect to the shape of the IC socket at 50% of the applied displacements. The residual limb was in contact at the medial and lateral walls of the socket. However, at the anterior and posterior walls, the residual limb tissue was not in contact with the socket. The compression at the medial and lateral wall was not able to deform the residual limb so that it filled the anterior and posterior space of the socket. The deformation was therefore unrealistic, as confirmed by the MRI scan; the residual limb was in total contact with the socket.

10.8 DISCUSSION

The 2-D model of the residual limb will be discuss according to the assumptions employed. In addition, the possibility of a 3-D model with detailed geometry is discussed.

A transverse section of the residual limb at a level 30 mm distal to the ischial tuberosity was modelled in 2-D using the finite element method. The model was used to study the internal stress distribution of the residual limb when deformed to the shape of the IC socket. The geometry of the model was defined accurately with the aid of MRI images. The loading applied as displacements to the model was also based on accurate geometrical differences (MRI images) between the residual limb wearing an IC socket and not wearing any socket. The material properties assumed in the model were linear elastic and isotropic. The model assumed a geometrical non-linear analysis i.e. large displacement analysis.

The tissue components in the model were grouped into four types, fat, intermuscular tissue, muscles and bone. Skin was omitted because it was impossible to geometrically define it in the MRI scans. Furthermore, the mechanical response of skin was predominantly to resist tension, while in this case loading in the residual limb was mainly compressive. It was therefore assumed that the omission of the skin in the model would not affect the internal stress distribution of the residual limb severely. The model did not include any of the major vessels and nerves. These types of soft tissues were modelled as either fat or intermuscular tissue instead. Some muscles were

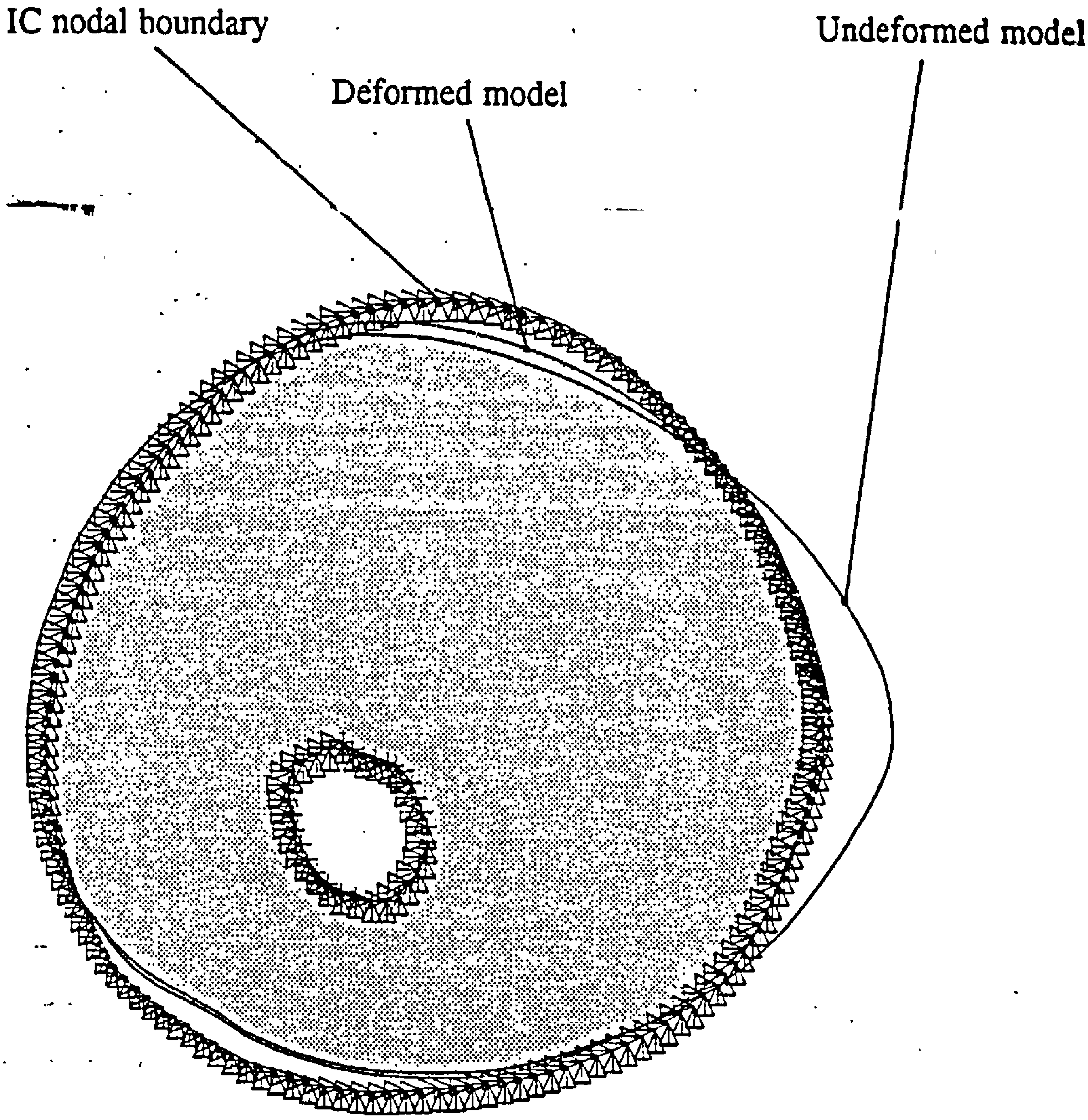

Fig. 10.7.6.5 Deform geometry of model 6 with respect to the shape of the IC socket.

difficult to define clearly based on the MRI images. These were the vastus intermedius, lateralis and medialis, and the adductor magnus, brevis and lateralis. In the model, these muscles were grouped together forming the vastus muscle and the adductor magnus/brevis muscle respectively.

As discussed previously in chapter six, modelling the soft tissue components as linear elastic material and isotropic was possibly the most feasible approach. Furthermore, restricting the model to only linear elastic material enabled an accurate evaluation of other forms of non linearity which arises due to geometry and interface characteristics of the soft tissues.

Several model configurations encountered numerical convergence problems. The main reason was attributed to the large displacements introduced at the surface nodes of the residual limb model in order for it to deform to the shape of the IC socket. The large displacements gave rise to extremely distorted elements causing numerical convergence problems. Another area which caused numerical divergence was the introduction of interface elements which allowed large movements at the muscles / intermuscular tissue interface.

The 2-D approach in modelling the transverse section of the residual limb could only provide limited information. As previously mentioned, anatomical joint loading or loading transmitted due to ground reaction forces cannot be modelled. The 2-D model was only feasible in predicting the stress and deformation generated on the residual limb when deforming to the shape of the socket. The 2-D analysis also assumed that the geometry of the residual limb was uniform along its length which was not realistic. Therefore the results of the analysis were only applicable to the modelled transverse slice.

In the model, plane stress elements were used. Unlike plane strain elements, out-of-plane movement was considered in plane stress elements. A more realistic model was thus achieved using plane stress elements since the soft tissue could move proximally or distally along the length of the residual limb when deformed by the prosthetic socket. In the case of using plane strain elements, the additional out-of-plane constraint would lead to unrealistic high stresses.

As seen in the complexity of the 2-D model and the non convergence solution in some models, the author of this thesis has proved that the best possible initial approach to study the internal stress distribution of the residual limb is a two, instead of a three dimensional model. The 2-D model was able to incorporate geometrical musculature details, material non - homogeneity, soft tissue interface characteristics and complex loading and boundary conditions. It would be an impossible task to incorporate similar specifications in a 3-D model with the present state of the art. Though limited, useful information was provided by the 2-D model in further understanding the biomechanical behaviour at the internal structure of the residual limb

The model was able to show the effect of non uniform material properties in the residual limb. The geometries of the muscles, fascia and intermuscular tissue also influence the stress distribution inside the residual limb. The model assuming uniform material properties and uniform geometry was unable to detect regions of maximum stress, which usually occurred near the muscle/intermuscular tissue interface. The 2-D model also showed that when assuming uniform material properties, the maximum von Mises stress was located at the residual limb / socket interface at the medial side. However, in a model with fascia, intermuscular tissues and muscles, each with different material properties, the maximum stress was located inside the residual limb at the adductor magnus/brevis and its point of attachment to the femur. The author of this thesis reckons that the internal stress distribution might be a more important factor in deciding socket fit than residual limb/ socket interface stresses. This is because the former stresses are of higher magnitude which can give rise to tissue breakdown. This hypothesis is also supported by pressure sores investigators whom predicted that pressure sores are initially generated from the inside near bony prominences and extend outward to the skin surface in a pyramidal fashion.

The interface characteristics between the muscles and the intermuscular tissues were realistically modelled using interface elements. The muscles were allowed to separate and slip from the intermuscular tissue, generating realisticlly large displacements inside the residual limb. However, slow numerical convergence thus excessive long computation time prevented the model from being analysed under the full loading conditions. Selecting a suitable coefficient of friction was also a problem as there was no suitable value available from literature. An experiment design to obtain the coefficient of friction *in vivo* would be impossible, and an *in vitro* test would be laborious and difficult to control. Nevertheless, at 10 % of the full loading, the three coefficient of friction tested in the model, μ=0, 0.1 and 0.3 did not affect the stress distribution inside the residual limb in a marjor way. However, it must be noted that the models were compared at only 10% of the full load due to numerical convergence difficulties. At full load, the difference might be more marked since the normal forces acting on the interface elements would be increased.

In the present study, muscle sliding was only investigated in the transverse plane. Furthermore, muscle contraction was simulated in the model by an increase in the elastic modulus of the muscles concerned. However, in the actual case, muscle contraction not only increases the stiffness of the muscles but also changes their geometries subsequently causing muscle slippage. The MRI imaging set up was not able to accommodate the amputee in a weight bearing situation. Hence, the geometry of the model using the MRI images was only representative of the muscles in the relaxed state. Muscle slippage was also expected to be more severe in the out-of-plane dimension than in the transverse plane, due to the shortening of the muscle fibres. However, this could not be modelled in two dimensions.

Loading and boundary conditions on the residual limb in the actual case is basically three dimensional and asymmetrical. This poses a problem if an attempt is made to reasonably represent the loading and boundary conditions in two dimensions. The loading in the 2-D model was introduced as displacements that caused the natural shape of the residual limb to deform into the shape of the IC socket. All other loadings have to be ignored. The only data available for specifying the loading and boundary definitions in the 2-D model was that obtained from 2-D MRI images. In this study, the three boundary conditions attempted shown significant changes in the way the internal stresses were distributed. The first set of loading and boundary conditions attempted applied nodal displacements at the residual limb / socket interface. The consequence of applying nodal displacements was to cause the anterior and posterior side of the residual limb to be in tension. As explained earlier, this might not be representative of the real situation where apparently the socket only compresses the residual limb's soft tissue. Another set of loading and boundary conditions was then introduced where interface elements were placed at the residual limb / socket interface. This allowed only compressive load to be transmitted. However as seen in the results, the residual limb was not able to deform to the shape of the IC socket, which again was not realistic. In summary, the first set of conditions was able to maintain the true surface deformation of the residual limb, but the state of stress may not be realistic due to the presence of tension forces. The latter condition was able to maintain only compression forces at the surface of the residual limb, but the resulting final deformation was not the shape of the IC socket. It must be noted that the failure of the latter condition could be due to other assumptions adopted for material properties, geometry and interface characteristics. In other words, the latter condition might actually be the correct loading and boundary condition for the model.

The other area of concern regarding boundary specification was that of the femoral bone. The bone was assumed to be fixed in most of the analysis attempted. However, in another analysis where the bone was allowed to move, the internal stresses in some regions were reduced by almost 50%. The bone had to be fixed because a reference was necessary in defining the geometrical difference between the residual limb with and without the IC socket on. As discussed earlier in section 10.3.5, fixing the bone was a realistic assumption. In addition, it enabled the model to be validated by comparing its internal musculature geometry using the bone as a reference landmark. As shown in Fig. 10.8.1, the predicted muscle displacements in model 1 were compared to the actual displacements obtained from the MRI image. In general, the model predicted the final position of the muscles to be slightly posterior to that of the MRI scan.

At present, the possibility of a three dimensional model with detailed musculature is highly doubtful. A model of this scale would have many assumptions leading to questionable results and numerical problems. Finite element mesh generation is laborious and difficult in the creation of a 3-D model. The problem could

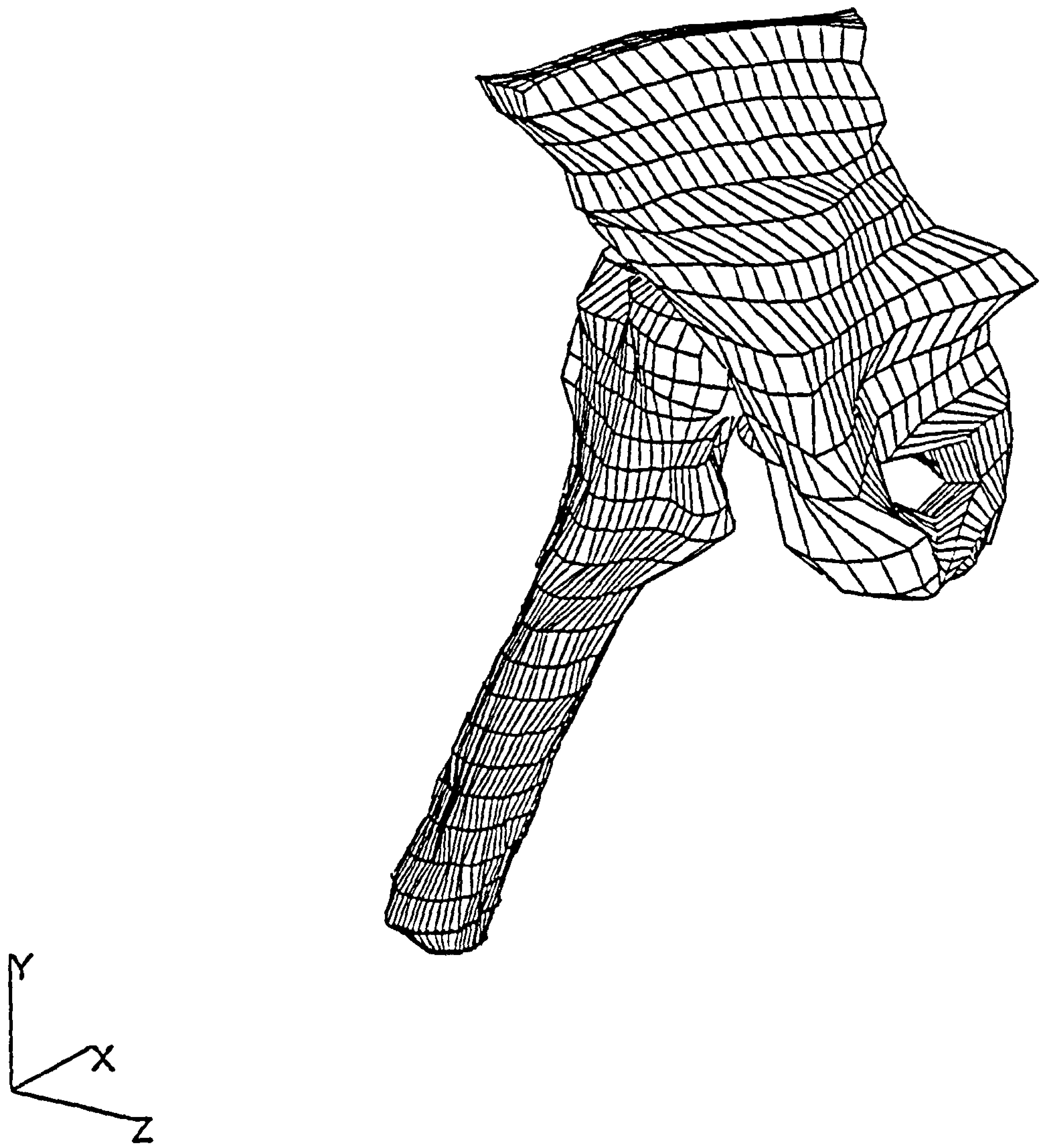

Fig. 10.8.2 Three dimensional mesh of pelvic bone and femur of subject M based on transverse MRI images.

be highlighted by an attempted mesh of the pelvic bone of the residual limb of subject M based on the MRI images. As shown in Fig. 10.8.2, the structure's geometry is very complicated. The geometrical resolution of the bone was decreased considerably due to the rough finite element mesh. In order to maintain a reasonable shape, a sizeable amount of elements need to be specified. There was also difficulties in managing the shape of the elements. Most elements suffered high distortion from a cube shape, which led to inaccurate prediction. The plot in Fig. 10.8.2 only highlighted some of the problems involving geometry. To complete the model, the geometry of individual muscle, its material properties, loading and boundary definitions need to be considered. The amount of information required becomes excessive. At this point, the author of this thesis would like to suggest that the creation of a useful model may not lie in the amount of detail the model possesses. This might contradict the norm. However, considering the amount of uncertainty in the loading and boundary conditions at the residual limb / socket interface, the highly non linear behaviour of the soft tissue and the complex biomechanical characteristic at the muscles / intermuscular interface, a model incorporating all these assumptions will be difficult to control and may not be a good model after all. The simpler 3-D models shown in chapter seven were able to predict interface pressures to a certain level of accuracy. Understanding their capabilities and limitations, the models might prove useful especially with the present CASD/CAM technology. The author of this thesis would also like to emphasize that a 3-dimensional model is still a basic requirement for use in conjunction with a CASD/CAM system. However, the future of residual limb modelling would likely to incorporate simpler and scaleable generic geometrical detail. This will be discussed further in the final chapter.

10.9 CONCLUSION

The 2-D model was able to predict stresses and deformations inside the residual limb. The predicted von Mises stresses at a transverse section 30 mm distal to the ischial tuberosity ranged from 0 kPa to 36 kPa. Assigning different material properties for fascia, intermuscular tissue and muscles was necessary for accurate prediction. Numerical convergence problems were encountered when the elastic modulus fell below 24.4 kPa for the soft intermuscular tissue. It was inaccurate to model muscle sliding by the use of very soft intermuscular tissue. Instead muscle sliding was modelled by incorporating interface elements at the muscle / intermuscular tissue interface. However, numerical convergence problems were encountered at 47% of the applied displacements with excessive computational time (> 30 h). The loading and boundary definitions at the residual limb / socket interface require more work. By allowing the femur to move within the residual limb soft tissue, the maximum von Mises stress was reduced by almost 50%.

CHAPTER ELEVEN
SUMMARY AND FINAL CONCLUSION

11.1 SUMMARY

11.2 FINAL CONCLUSION

11.1 SUMMARY

The residual limb / socket interface pressure was measured for three trans-femoral amputees. The pressure profile indicated a high proximal medial wall pressure and a high distal lateral wall pressure due to the abductor muscles contraction. The pressure profile in the anterio-posterior plane was more complex. A high proximal anterior and high distal posterior pressure profile was recorded at early stance due to the hip extensors being active. However, the measured pressure did not show the expected reversal of the pattern from early stance during late stance. The measured pressure at late stance remained the same as that of early stance but with the magnitude decreased. In the evaluation of the two types of socket, the quad was found to provide proximal support where pressure at the brim was considerably higher than at the distal end. In the IC socket, a more evenly distributed pressure profile was observed throughout the socket.

An *in vitro* study was conducted where a series of compression and indentation tests using the Instron machine were carried out on PVC rubber and porcine tissue. Finite element models based on the compression and indentation tests were subsequently constructed and validated by the experimental results. Three different material properties assumptions were investigated. These were linear elastic, non-linear elastic and hyperelastic (Mooney-Rivlin material) materials. The use of non-linear elastic material properties predicted the best results when comparing load - displacement plots obtained from experiments. The study also found that a suitable elastic modulus derived from the maximum stress or strain experienced by the specimen, can be used for predicting the final stress or strain state in a linear elastic analysis. The use of hyperelastic material in the modelling of bulk soft tissue under compression was found to be unsuitable.

Three 3-D FE models of the residual limbs were created which corresponded to the three amputee subjects who participated in the study, using data obtained from kinetics and kinematics studies. The model parameters were based on a mechanical digitizer and magnetic resonance imaging (MRI) scans. The model was used to predict residual limb / socket interface pressure during standing and at 10%, 25% and

40% of the gait cycle, and predicted pressure values were underestimated. Higher correlation was observed at sites towards the distal end of the residual limb. The percentage errors were within the range of -76% to +121%. At several sites the error were less than 5%. However, large error were seen at the greater trochanter and proximal lateral sites.

The study investigated the feasibility of transforming a cadaveric femur to that of the human subject's femur based on palpable anatomical landmarks of the human subject, assuming that the shape of the different individual subject's femur is the same. It was found in this study based on four cadaveric specimens, the variability in the curvature of the femoral shaft generated errors between the transformed femur and the original femur. The study indicated that anthropometric scaling is promising in predicting the shape of the femur in intact body.

Magnetic resonance imaging the residual limb of two trans-femoral amputees was accomplished, with the subject in a supine position to provide essential information for the creation of a FE model of the residual limb with internal musculature details. Muscle atrophy at the residual limb was found mainly at the gluteus maximum and vastus muscles. The investigation has raised several doubts regarding the IC socket which claims that it is more anatomical in shape than the quad, leading to better proprioception and muscle function. It was observed in the present study that the individual muscle shape in the IC socket was distorted from the natural shape due to its narrow medio-lateral dimension.

A two dimensional FE model of a transverse section 30 mm below the ischium was developed, using geometrical detailed from MRI images of the internal musculature. The loading in the model was based on deformations introduced by the IC socket shape. The maximum stress was recorded inside the residual limb near muscles / intermuscular tissue interface and at muscles / bone interface. It was observed that by allowing the femur to move within the residual limb in the model, the internal stresses in some regions were reduced by almost 50%.

11.2 FINAL CONCLUSION

The study has explored different areas related to the biomechanics of residual limb / socket interface. The models created have shown the potential of using the finite element method to predict stresses and deformation at the residual limb / socket interface and at the internal structure of the residual limb.

Several assumptions and simplifications have been investigated and adopted for the generation of the models. These were necessary steps in an attempt to further understand the complex behaviour of living tissues.

The findings presented in this investigation should stimulate further research in the area of prosthetic socket design. This includes understanding the biomechanics principles in trans-femoral prosthetic sockets, the possibility of new socket shapes and the manufacture of sockets based on quantitative analysis.

The future residual limb model is likely to incorporate simple and scaleable generic geometrical detail which can be incorporated to existing computer aided socket design and manufacturing system. The study has also provided the necessary background for a future program which aims at incorporating FE modelling techniques to the process of computer aided socket design and manufacturing.

APPENDIX A

KNEE DISARTICULATION AND TRANSFEMORAL AMPUTEE

Name

Date of examination .... Examiner ....

Over all situation

Described side — Right 1, Left 2
Bilateral amputees: Use two forms

ACTIVITY LEVEL: Average for age 1; Exceptionally active 2; Exceptionally low activity 3

SHAPE .... Cylindrical 1; Conical 2; Bulbous 3
Comments ....

SKIN SITUATION IN GENERAL — Normal 1; Sores 2
INCISION — Ok 1; Not healed 2; Fold or adh. 3
OTHER SKIN CONDITIONS — None 1; Descr. below 2
SENSIBILITY — Normal 1; Impaired 2

....

STATE OF TISSUE — AMOUNT: Ordinary 1; Scarce 2; Excessive 3
Prominent femur — Yes 1; No 2
FIRMNESS — Ordinary 1; Indurated 2; Flabby 3
OTHER CONDITIONS — None 1; Descr. below 2

....

CIRCULATION at rest — OEDEMA: None or minimal 1; Excessive 2
COLOUR OF SKIN — Normal 1; Cyanotic 2
TEMPERATURE OF SKIN — Normal 1; Cold 2
OTHERS CONDIT. — None 1; Descr. below 2

PAIN. Spontaneous pain at rest — Yes 1; No 2
Pain after exercise — Yes 1; No 2
Local stump pain — Yes 1; No 2
Palpable neuroma — Yes 1; No 2
Pain in hip joint — Yes 1; No 2
Other conditions — None 1; Descr. below 2

....

AMPUTATION DIAGNOSIS — Diabetes 1; Other vascular disease 2; Trauma 3; Tumor 4; Other 5

Not fitted before 1; Renewal 2
Date of previous renewal ....
Reason for present consultation ....

JOINT FUNCTION IN HIP — Normal 1; Not normal 2
Limited range of movement. Record deficit only — Degrees: Flexion; Extension; Abduction; Adduction
Other conditions — None 1; Descr. below 2

MUSCLE POWER — No or light reduction 1; Significant reduction 2
Specify: ....

OTHER LEG — Normal 1; Not normal 2. Specify: ....

OTHER FUNCTION REDUCING FACTORS — None 1; Descr. below 2

BODY BUILD — Average 1; Light 2; Heavy 3
Height
Kg

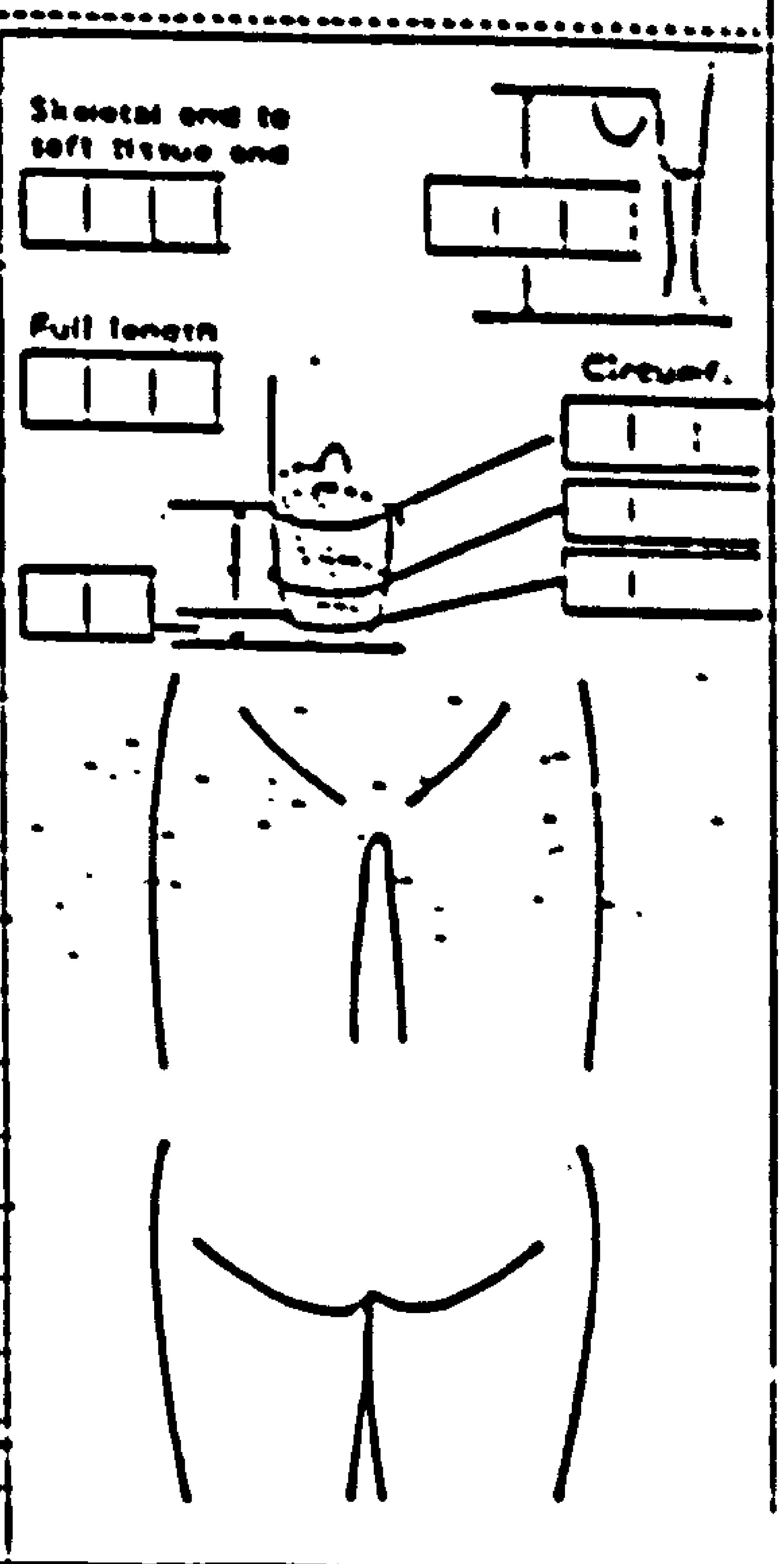

COMMENTS

[illegible]

UPPSALA UNIVERSITY WALKING SCHOOL
EEN & HOLMGRENS ORTOPEDISKA AB
INTERN. STANDARDS ORGAN. ISO

AMPUTEE ACTIVITY.

M F | M S W | AGE- ...... LEVEL- ....

CAUSE ....

DATE OF AMPUTATION

DATE OF ASSESSMENT

SCORE

CAN YOU-

Yes No PUT LEG ON?

Yes No TAKE LEG OFF?

LEG WORN DAYS per WEEK

LIVES- ALONE

WITH SPOUSE

WITH RELATIVE/FRIEND of SAME GEN.

WITH RELATIVE/FRIEND of YOUNGER GEN.

IN- HOUSE

BUNGALOW

FLAT LIFT

INSTITUTION

UPSTAIRS-

CAN YOU GO? Yes No

DO YOU GO? Yes No

FLIGHTS/DAY

LIMB WORN

hours/day

14+

11-14

6-10

3-6

<3

EMPLOYMENT.-Hours/Week

HOW MUCH

0 ¼ ½ ¾

SITTING

STANDING

WALKING

LOAD CARRYING

JOURNEYS-

WALKING DISTANCE

CYCLE

CAR

PUBLIC TRANSPORT

DO YOU USE STAIRS AT WORK?

No

Some

A lot

AIDS USED

FRAME

T/PODS CRUTCHES

STICKS-

INDOORS

2 STICKS

1 STICK

NONE

OUTDOORS

2 STICKS

1 STICK

NONE

WHAT DO YOU DO WITH YOUR (SPARE) TIME?-

HOURS PER [illegible]

TOTAL SCORE-

DO YOU DO YOUR OWN - ALL SOME NONE

SHOPPING

COOKING

CLEANING

CLOTHES WASHING

HAVE YOU HELP IN THE HOUSE?

WHEELCHAIR-

NEVER

SOMETIMES

OFTEN

ALWAYS

NEVER SOMETIMES OFTEN ALWAYS

REGULAR WALKING -

INDOOR

>75% 50-75% 25-50% 10-25% HARDLY ANY

OUTDOOR

>3 miles 1-3 miles ½-1 mile ¼-½ mile 50 yds-¼ HARDLY ANY

REFERENCES

REFERENCES

1 Aleshinsky SY and Zatsiorsky VM (1978), Human locomotion in space analysed biomechanically through a multi-link chain model. J. Biomech. 11, 101-108.

Amar J (1916), Trottoir dynamographique. Comptes Rendus de l'Academie de Sciences. 163, 130-132.

Andriacchi T. P., Galante J. O., Belytschko T. B. and Hampton S. (1976) A stress analysis of the femoral stem in total hip prostheses. J. Bone Jt Surg. 58A, 616-624

Appoldt FA, Bennett L, Contini R (1970), Tangential pressure measurements in above-knee suction
2 sockets. Bull. Prosthet. Res., 10(13), 70-86.

Appoldt FA, Bennett L, R Contini (1969), Socket pressure as a function of pressure transducer
3 protrusion. Bull. Prosthet. Res., 10(11), 236-249.

Appoldt F A and Bennett L (1967), Preliminary report on dynamic socket pressure. Bull. Prosthet. Res.,
4 10(8), 20-55.

Appoldt FA, Bennett L, Contini R (1968), Stump-socket pressure in lower-extremity prostheses. J.
5 Biomech. 1(4), 247-257.

Areblad M, Nigg BM, Ekstrand J, Olsson KO and Ekstrom H (1990), Three dimensional measurement of rearfoot motion during running. J. Biomech. 23, 933-940.

Bader D L and Hawken M B (1986), Pressure distribution under the ischium of normal subjects. J. Biomed. Eng., 8, 353-357.

Banerjee SN (1982), Limb amputation - incidence, cause and prevention, in Rehabilitation management
6 of amputees. Ed. SN Banerjee, 1-10. Rehabilation Medicine Library, Baltimore.

Barbenel JC (1979), Time dependent mechanical properties of skin. PhD thesis, University of Strathclyde, Glasgow, Scotland, UK.

Barbenel JC, Evans JH and Jordan MM (1978), Tissue mechanics, Engng. in Med., 7, 5-9.

Barbenel JC, Lee VSP (1994), Deformation and stress analysis of supported buttock contact. Proc Inst. Mech. Engrs., Part H, 208(H4), 263-266.

Barbenel J C and Sockalingham S (1990), Device for measuring soft tissue interface pressure. J. Biomed. Eng., 12, 519-522.

Bargar WL (1989), Shape the implant to the patient. A rationale for the use of custom fit cementless total hip implants. Clin. Orthop. Rel. Res., 249, 73-70.

Barnes RW, Shanik GD and Ehrenhaft JL (1976), An index of healing in below-knee amputation : leg blood pressure by Doppler ultrasound. J. Cardiovasc. Surg., 17, 100-102.

Bartel D. L. and Usloy G. A. (1975) The effect of stem length and stem material on stresses in bone-prosthesis systems. Proceedings 21st Annual Meeting Orthopaedic Research Society.

Bartel D. L. (1977) The calculation of stresses in bone prosthesis structures. Human Joints and their Artficial Replacement edited by Walker P. S., 440-448. Charles C. Thomas, Sprindfield IL.

7 Baumgartner RF (1988), Aetiology, priciples, operative techniques. In Amputation surgery and lower limb amputation. Ed. G Murdoch. Blackwell Scientific, Oxford, 97-104.

Beischer D and Knepton J (1964), Influence of strong magnetic fields on the ECG of squirrel monkeys. Aerosp. Med., 35, 939-944.

Berme N, Lawes P, Solomonidis SE and Paul JP (1976), A shorter pylon transducer for measurement of prosthetic forces and moments during amputee gait. Eng. Med., 4(4), 6-8.

BioSculptor (1994), Manufacturers catalogue. Finnieston Group. Coral Gables, USA.

Bloch F, Hansen WW and Packard ME (1946), The nuclear induction experiment. Physical Review. 70, 474-485.

8 Boenick U and Hasenpusch M (1992), The Berlin computerized system for socket design. Proceedings 7th world congress of ISPO. June 28-July 3. Chicago, Illinois, USA. 20.

Boone DA, Harlan JS, Burgess EM, (1994), Automated fabrication of mobility aids : review of the AFMA process and VA/Seattle Shape Maker software design. J. Rehabil. Res. Dev. 31(1), 42-49.

Boone DA and Harlan J (1992), Considerations for computer interface design for prosthetics and
9 orthotics : A user's perspective. Proceedings 7th world congress of ISPO. June 28-July 3. Chicago,
Illinois, USA. 157.

Borelli GA (1680), De motu animalium. Io: ALPHONSO BORELLI (1908-1679) : Opus posthumum. Ex typographica. Angeli Berbnabo, Rome. As reproduced on microcards, landmarks of science series. Readex microprint. New York, 1967.

Boudewijn JD, Rauwerda JA, Van Der Brock TAA, Hollander WD, Heidendal GAK and Van Rij GI
10 (1989), A modified scintigrafic technique for amputaion level selection in diabetics. Eur. J. Nucl. Med.,
15, 38-41.

Boyd HB (1947), Anatomic disaticulation of the hip. Surg. Gynecol. Obstet., 84, 346-349.

11 Braune W and Fischer O (1895), The Human Gait. English translation by Maquet P and Furlong R, 1987. Springer-Verlag, Belin Heideelberg, New York, London, Paris, Tokyo.

Brekelmans W. A. M., Poort H. W. and Slooff T. J. (1972) A new method to analyse the mechanical behaviour of skeletal parts. Acta Orthop. Scand. 43, 301-317.

Brennan JM and Childress DS, (1991), Finite element and experimental investigation of above-knee amputee limb/prosthesis systems : a comparative study. ASME Advances in Bioengineering, 20, 547-550.

Brunski J. B., Roth V., Reddy N. and Cochran G. V. B. (1980) Finite element sress analysis of a contact problem pertaining to the formation of pressure sores, in Advances in Bioengineering, ASME editied by Mow V. C. New York. 53-56

Burgess EM and Alexander AG (1973) The expanding role of the physical therapist on the amputee rehabilitation team. Phys. Ther., 53, 141-143

12 Burgess EM (1969), The below-knee amputation. ICIB, 8(4), 1-22.

13 Burgess E M and Moore A J (1977), A study of interface pressures in below-knee prosthesis (physiological suspension : an interim report). Bull. Prosthet. Res., 10(28), 58-70.

Burgess EM, Romano RL and Zettl JH (1969), Amputation management utilizing immediate postsurgical fitting. Prosthet. Int., 3(8), 28-37.

Burgess EM (1977), Disaticulation of the knee. Arch. Surg., 112, 1250-1255.

Campbell's Operative Orthopaedics (1971). Fifth Edition. Ed. Crenshaw AH. The CV Mosby Co.

CANFIT (1994), Manufacturers catalogue. Vorum Research Corporation. Vancouver, Bristish Columbia, Canada.

CAPOD (1994), Manufacturers catalogue. CAPOD SYSTEMS AB. Sweden.

14 Castronuovo JJ (1980), Below knee amputation : is the effort to preserve the knee joint justified ? Arch. Surg., 115, 1184-1187.

Chan RB, Childress DS, Brncick MD, Edwards M, Uellendahl E (1992), Clinical experience with CAD/CAM below knee socket fittings. Proceedings 7th world congress of ISPO. June 28-July 3. Chicago, Illinois, USA. 18.

Cheal E. J., Spector M. and Hayes W. C. (1992) Role of loads and prosthesis material properties on the mechanics of the proximal femur after total hip arthroplasty. J. Orthop. Res. 10(3). 405-22

Chow WW and Odell EI (1978), Deformations and stresses in soft body tissues of a sitting person. J. Biomech. Eng., 100, 79-86.

Chow W. W. and Odell E. I. (1978) Deformation and streese in soft body tissue of a sitting person. J Biomech. Eng. 100, 79-

Coombs AGA, Lawerence RB, Davies RM (1985), Rotational moulding in the production of prostheses. Prosthet. Ortot. Int., 9, 31-37.

Cowin S. C. and Hegedus D. H. (1976) Bone remodelling I : A theory of Adaptive Elasticity. J Elasticity. 6, . 313-326.

Crawford HV, Gellett P, Cousins S (1985), A low cost computer controlled machine. In : University College London Bioengineering Centre report. Roehampton. University College London. 43-44.

Crawford HV and Gellett P (1986), A low cost computer controlled machine. In : University College London Bioengineering Centre report. Roehampton. University College London. 19-20.

Crawford HV (1985), Computer aided socket design (CASD) : Medical Engineering Resource Unit (MERU) system based on reference socket. In : University College London Bioengineering Centre report. Roehampton. University College London. 39-42.

Crawford HV and Lord M (1985), Silhouette of below knee stumps. In : University College London
15 Bioengineering Centre report. Roehampton. University College London. 33-30.

16 Creaney MG, Chattopadhaya DK, Ward AS and Morris-Jones W (1981), Doppler ultrasound in the assessment of amputation level. J. Roy. Coll. Surg. Edin., 26, 278-281.

Crenshaw R P, Vistnes L M (1989), A decade of pressure sore research : 1977-1987. J. Rehabil. Res. Dev., 26(1), 63-74.

Crooks LE (1985), An introduction to magnetic resonance imaging. IEEE, Eng. Med. Bio., 4(3), 8-15.

Crowninshield RD, Brand RA and Johnston RC (1978), The effects of walking velocity and age on hip kinematics and kinetics. Clin. Orthop. and Relat. Res. 132, 140-144.

CRPD Committee on Prosthetic Research and Development (1976), Draft proposal for : Standardization
17 of Gait Analysis Parameters and Data Reduction Techniques - A Task Force Report.

Cummings JGR, Jain AS, Walker WF, Spence VA and Stewart C (1987), Fate of the vascular patient after lower limb amputation. Lancet, 613-615.

Cunningham DM and Brown GW (1952), Two devices for measuring the forces on the human body during walking. Proc. Soc. Exp. Stress Analysis 9, 2, 75-90.

Dabnichki PA, Crocombe AD and Hughes SC (1994), Deformation and stress analysis of supported buttock contact. Proc Instn. Mech. Engrs., Part H, 208(H1), 9-17.

Dai-L., Cheng-P., Zhang W., Xu Y. and Tu K. (1992) Stress distribution and bone density in the lumbar spine. Chin. Med. Sci. J. 7(2). 105-7.

Daly CH (1969), The role of elastin in the mechanical behaviour of human skin, PhD thesis, University of Strathclyde.

Damadian R, Minkoff L, Goldsmith M, Stanford M, Kontcher J (1976), Tumor imaging in a live animal by field focusing NMR. Physiol. Chem. Phys., 8, 61-65.

Daniel R K (1985) Pressure sores and paraplegia : An experimental model. Ann. Plast. Surg., 15(1), 41-9.

Davies RM, Lawrence RB, Routledge PE (1985), The Rapidform prcoess for automated themoplatic socket production. Prosthet. Orthot. Int., 9, 27-30.

١٨ Davis R B (1986), The measurement of prosthetic limb socket pressure. IEEE 8th Ann. Conf. Eng. Med. Biol. Soc., 1846-1849.

Dawson J. M. and Bartel D. L. (1992) Consequences of an interference fit on the fixation of porous-coated tibial components in total knee replacement. J. Bone Joint Surg. A. 74(2). 233-8.

Day, H. J. B. The assessment and description of amputee activity. Prosthet. Orthot. Int., 1981, 5, 23-28.

Dederich R (1985), Technik der amputation der unteren gliedmaBen (techniques for the amputation of the lower extremities). Unfallchirurgy, 88, 390-405.

Dederich (1963), Plastic treatment of the muscles and bone in amputation surgery: a method designed to produce physiological conditions in the stump. J. Bone Joint Surg., 1963, 45B, 60-66.

١٩ Department of Health and Social Security (DHSS) Amputation Statistics(1971-1989).

Dewar ME and Redhead RG (1992), A clinical trial of a prosthetic CADCAM system. Proceedings 7th world congress of ISPO. June 28-July 3. Chicago, Illinois, USA. 17.

Dewar M (1985), Computer aided socket design (CASD) : UCL system based on full shape sensing. In : University College London Bioengineering Centre report. Roehampton. University College London. 19-30.

Dewar M and Reynolds D (1986), Implementation of the UCL computer aided socket design system : In : University College London Bioengineering Centre report. Roehampton. University College London. 17-18.

Dietrich M., Kedzior K. and Zagrajek T. (1992) A biomechanical model of the human spinal system. Proc. Inst. Mech. Eng. H. 205(1). 19-26.

Dinsdale S M (1974), Decubitus ulcers; role of pressure and friction in causation. Arch. Phys. Med. Rehab., 55, 147-152.

Dormandy JA and Thomas PRS (1988), What is the nature of a critically ischaemic patient with and without a leg ? In Limb salvage and amputation for vascular disease. Ed. RM Greenhalgh, CW Jamieson and AN Nicolaides, Saunders, London, 58-60.

Eberhart HD and Inman VT (1947), Fundamental studies of human locomotion and other information relating to design of artificial limbs. University of California, Berkeley, report to National Research Council, committee on Artificial Limbs.

Eberhart HD, Inman VT and Bresler B (1954), The pricipal elements in human locomotion. In : Human limbs and their Subsitutes, Ed. Klopsteg PE and Wilson PD, Hafner Publishing Company, New York, London, 437-471.

Ebskov B (1988), Trends in lower extremity amputation (Denmark 1978-1983), In Amputation surgery and lower limb amputation. Ed. G Murdoch. Blackwell Scientific, Oxford, 3-8.

Engsberg JR, Springer MJN, Harder JA (1992), Quantifying interface pressures in below-knee-amputee
20 sockets. J. Assoc. Child. Prosthet. Orthot. Clin. 27(3), 81-88.

Engsberg JR, Clynch GS, Lee AG (1992), A CAD/CAM method for custom below-knee sockets. Prosthet. Orthot. Int., 16, 183-188.

Esquenazi A, Leonard JA, Meier RH, Hicks JE, Fisher SV and Nelson VS (1989), Prothetics, orthotics and assistive devices : 3. Prosthetics. Arch. Phys. Med. Rehabil., 70, S206-S209.

Eycleshymer AC and Schoemaker DM (1911), A cross section anatomy. Appleton - Century - Crofts. Education Division Meredith Corporation, New York.

Faulkner VW and Walsh NE (1990), Computer designed prosthetic socket from analysis of computed tomography data. J. Prosthet. Orthot., 1, 154-164.

Faulkner VW, Walsh NE, Gall NG (1988), A computerized ultrasound shape sensing mechanism. Orthot. Prosthet., 41(4), 57-65.

Feldkamp L., Goldstein S. A., Parfitt A. M., Jesion G. and Kleerekoper M., (1989) The direct examination of three dimensional bone architecture in vitro by computer tomography. J Bone Min. Res. 4, 3-11.

21 Ferguson-Pell MW (1980), Design criteria for the measurement of pressure at body support interfaces. Eng. Med., 9(4), 209-214.

Ferkel RD, Flannigan BD and Elkins BS (1991), Magnetic resonance imaging of the foot and ankle : correlation of normal anatomy with pathological conditions. Foot Ankle, 11, 289-305.

Fernie GR, Grigg S, Barlett S (1985), Shape sensing for computer aided below knee prosthetic socket design. Prosthet. Orthot Int., 9, 12-16.

Flandry F, Beskin J, Chambers RB, Perry J, Waters RL and Charez RC (1989), The effect of the CAT-CAM above knee prosthesis on functional rehabilitation. Clin. Orthop. Res., 239, 249-262.

Flandry F, Beskin J, Chambers RB, Perry J, Waters RL and Charez RC (1989), The effect of the CAT-CAM above knee prosthesis on functional rehabilitation. Clin. Orthop. Res., 239, 249-262.

22 Fleming HE (1992), Force plate, Subgoal A1, Internal Report, CAMARC II. Bioengineering Unit University of Strathclyde, Glasgow, Scotland, UK.

Foort J (1986), The Knud Jansen Lecture : Innovation in prosthetics and orthotics. Prosthet. Orthot. Int., 10, 61-71.

Foort J (1963), Adjustable brim fitting of the total contact above knee socket. San Francisco, Berkeley, University of California, Biomechanics Laboratory. 1-22.

Foort J (1965), Similarities of thigh stumps related to socket design, Manitoba Rehabilitation Hospital, Winnipeg, Report 5, March.

Foort J (1979), Socket design for the above-knee amputee. Prosthet. Orthot. Int., 3, 73-81.

Foort J, Lawerence RB, Davies RM (1984), Construction methods and materials for external prostheses : Present and future. Int. Rehabil. Med., 6, 72-78.

Friedmann LW (1972), Amputations and prostheses in primitive cultures. Bull Prosthet. Res. 10(17), 105-138.

Fukunaga T, Roy RR, Shellock FG, Hodgson JA, Day MK, Lee PL, Kwong-Fu H and Edgerton VR (1992), Physiological cross-sectional area of human leg muscles based on magnetic resonance imaging. J Orthop. Res., 10, 926-934.

Fung YC (1967), Elasticity of soft tissues in simple elongation. Am. J. Physiol., 213, 1532-1554.

Fung YC (1993), Biomechanics : Mechanical properties of living tissue. 2nd Edition. Springer-Velag. New York.

Furnee EH (1967), Hybrid instrumentation in prosthetic research. Proc. 7th. Int. Conf. on Med. Biol. Eng. Stockholm.

Furnee EH (1988), Advances in TV-based motion anlysis systems, in Progress in bioengineering , Ed Paul JP, Barbenel JC, Courtney JM and Kenedi RM, Adam Hilger, Bristol, 140-145.

Gage JR and Hicks R (1985), Gait analysis in prosthetics. Clin. Prosthet. Orthot. 9, 3, 17-23.

Gailey RS, Lawrence D, Burdi HC, Spyropoulos P, Newell C and Nash MS (1993), The CAT-CAM socket and quadrilateral socket : A comparison of energy cost during ambulation. Prosthet. Orthot. Int., 17, 95-100.

Gerhardt JJ, King PS and Zettl JH (1982), Amputations - immediate and early prosthetic management, Hans Huber Publishers, Berne Stuttgart.

Glattly HW (1963), A preliminary report on the amputee census. Artificial Limbs, 7(1), 5-10.

Glattly (1964) A statistical study of 12000 new amputees. South. Med. J. 57, 1373-1378.

Godfrey CM, Jousse AT, Brett R and Butler JF (1975). A comparison of some gait characteristics with six knee joints. Orthot. Prosthet. 29, 3, 33-38.

Goel VK, Nye TA, Clark CR, Nichitama K and Weinstein JN (1987), A technique to evaluate an internal spinal device by use of SELSPOT system - An application to the Luque closed loop. Spine, 12, 150-159.

Goel V K., Kong W., Han J. S., Weinstein J. N. and Gilbertson L. G. (1993) A combined finite element and optimization investigation of lumbar spine mechanics with and without muscles. Spine. 18(11). 1531-41.

23 Goh JCH (1982), Biomechanical evaluation of prosthetic feet, PhD thesis, Bioengineering Unit, University of Strathclyde, Glasgow, Scotland, UK.

Gottschalk F (1992), Transfemoral amputation. In Atlas of limb prothetics, American Academy of Orthopaedic Surgeons. Ed JH Bowkers and JN Micheal, London. 501-507.

Granholm JW, Roberston DD, Walker PS, Nelson PC (1987), Computer design of custom femoral stem prostheses. IEEE Computer Graphics and Applications., Feb. 26-35.

Green AE and Akins JE (1960), Large elastic deformations and nonlinear continuum mechanics. Oxford Univ. Press., London.

Haj F (1970), Disability in Antiquity. Philosophical Library, New York.

Ham RO, Luff R and Roberts VC (1989), A five year review of referrals for prosthetic treatment in England, Wales and Northern Ireland 1981-1985. Health Trends, 21, 25-30.

Ham R and Cotton L (1991), Limb Amputation : From aetiology to rehabilitation. Chapman and Hall, UK.

Ham R, Regan JM and Roberts VC (1987), Evaluation of introducing the team approach to the care of the amputee : the Dulwich study. Prosthet. Orthot. Int., 25-30.

Harrigan T. P., Kareh J, A., O'Connor D. O., Burke D. W. and Harris W. H. (1992) A finite element study of the initiation of failure of fixation in cemented femoral total hip components. J. Orthop. Res. 10(1). 134-44.

Harris RI (1961), The history and development of Syme's amputation. Artificial limbs. 6(1), 4-43.

Harris L. J., Chao R., Bloch R. and Weingarten V. (1978) A three dimensional finite element analysis of the proximal third of the femur. Proceedings of 24th Annaul Meeting of Orthopedic Research Society. 16. Chicago.

Hawkes B (1992), The CAD/CAM process. Pitman. London.

Hayes WC, Keer LM, Herman G, Mockros LF (1972), A mathematical analysis for indentation tests of articular cartilage. J. Biomech., 5(5), 541-551.

Hildebrandt J. Fukaya H, Martin CJ (1969), Completing the length tension curve of tissue. J. Biomech., 2, 463-467.

Hill BC and Waldo SH (1985), Fundamentals of NMR Imaging. In : Three dimensional biomedical imaging Volume 1. Ed. RA Robb. CRC Press, Inc. Boca Raton, Florida. 79-124.

Hinton R (1992), A biomechanical analysis of solvent dehydrated and freeze dried human fascia lata allografts - A preliminary report. Am. J. Sport. Med., 20(5), 607-611.

Hollister SJ and Kikuchi N (1993), Comparison of trabecular tissue strains computed by homogenization theory to direct finite element caluculations. ASME/AIChE/ASCE Summer bioengineering conference, Breckenbridge. June 25-29, 24, 258-261.

Hollister SJ and Goldstein SA (1993), Trabecular tissue strain estimates for bone adapted to controlled implant loads. ASME/AIChE/ASCE Summer bioengineering conference, Breckenbridge. June 25-29, 24, 254-257.

Holstein P (1982), Level selection in leg amputation for arterial occlusive disease : a comparison of clinical evaluation and skin perfusion pressure. Acta. Orthop. Scand., 53, 821-831.

Holstein D, Sager P, Lassen NA (1979), Wound healing in below-knee amputations in relation to skin perfusion pressure. Acta. Orthop. Scand., 50, 49-58.

Houle RJ (1969), Evaluation of seat devices designed to prevent ischaemic ulcers in parapelgic patients. Arch. Phys. med. and Rehab., 587-594.

Houston VL, Mason CP, LaBlanc KP, Beattie AC, Garbarini MA, Lorenze EJ (1994), Preliminary results with DVA Tekscan BK prosthetics socket/residual limb stress measurement system . Proceedings 20th Ann. Meet. Scientific Symposium. March 23-26. Nashville. USA.

Houston VL, Burgess EM, Childress DS (1992), Automated fabrication of mobility aids (AFMA) : below knee CASD/CAM testing and evaluation program results. J. Rehabil. Res. Dev., 29(4), 78-124.

Hoyt C (1987), The UCLA CAT-CAM above knee prosthesis. 3rd edition. Los Angeles CA. Prosthetics education and research program.

Huang D and Mak AFT (1993), The effects of sliding between muscle groups on the stress distribution within below-knee stumps. 8th Int. Conf. Biomed. Eng., Singapore, 348-350.

Huiskes R, Weinans H and van Rietbergen B. (1992) The relationship between stress shielding and bone resorption around total hip stems and the effects of flexible materials. Clin-Orthop. 274. 124-34.

Huiskes R. (1993) Stress shielding and bone resorption in THA: clinical versus computer-simulation studies. Acta. Orthop. Belg. 59 Suppl 1. 118-29.

Hulshof R (1995), Personal Communication. National Centre for Training and Education for Prosthetics and Orthotics. University of Strathclyde Glasgow. Scotland.

Husain T (1953), An experiment study of some pressure effects on tissue with reference to bed-sore problems. J. Path. Bact., 66, 347-358.

Husain T (1953), An experimental study of some pressure effects on tissues with reference to the bed sore problem. J. Pathol. Bact., 66, 347-358.

Huiskes R and Chao E (1983), A survey of finite element analysis in orthopaedic biomechanics : the first decade. J. Biomechanics. 16, 385-409

Huiskes R and Hollister SJ (1993) From structure to process, from organ to cell : Recent developmentsof FE analysis in orthopaedic biomechanics. J Biomech. Eng. 115. 520-527

Huiskes R, Janssen JD and Slooff TJ (1981), A detailed comparison of experimental and theoretical stress analyses of a human femur. Mechanical properties of bone edited by Cowin. S 211-234. American Society of Mechanical Engineers, New York.

Huiskes R., Elangovan P. T., Banens J. P. A. and Slooff T.J. (1978) Finite element computer methods for design and fixation problems of orthopaedic implants. Biomechanics VI-B edited by Asmussen E. and Jorgensen K. 229-238. University Park Press. Baltimore.

IPOS (1994), Manufacturers catalogue. IPOS GmbH & Co. KG. Luneburg, Germany.

ISPO (1975), Needs in prosthetics and orthotics world wide : Report of a workshop held at Les Diablerets. Switzerland. October, 1974.

Jaegers SM (1993), The morphology and functions of the muscles around the hip joint after a unilateral trans-femoral amputation. PhD thesis. Rijksuniversiteit Groningen.

Jamison CE, Marangoni RD, Glaser AA (1968), Viscoelastic properties of soft tissue by discrete model characterization. J. Biomech., 1, 33-46.

Jansson V. and Refior H. J. (1993) Mechanical failure of the femoral component in cemented total hip replacement--a finite element evaluation. Arch. Orthop. Trauma. Surg. 113(1). 23-7.

Jarrett MO (1976), A televison/computer system for human locomotion analysis. PhD thesis, University of Strathclyde, Glasgow, Scotland, UK.

Jones D, Mackie H and Taylor J (1992), Strathclyde experience of CAD/CAM in prosthetics. Proceedings 7th world congress of ISPO. June 28-July 3. Chicago, Illinois, USA. 19.

Kasra M, Shirazi-Adl A and Drouin G (1992), Dynamics of human lumbar intervertebral joints. Experimental and finite-element investigations. Spine. 17(1). 93-102.

Katz K, Susak Z, Seliktar R and Najenson T (1979), End-bearing characteristics of patellar-tendon-bearing prostheses - A preliminary report. Bull. Prosthet. Res., 10(32), 55-68.

Kay HW and Newman JD (1974), Amputee survey 1973-74 : Preliminary findings and comparisons. Orthot. Prosthet., 28(2), 27-32.

Kay HW and Newman JD (1975), Relative incidences of new amputations : statistical comparisons of 6000 new amputees. Orthot. Prosthet. 29(2), 3-16.

Keavenly D. L. and Bartel D. L. (1993) Effects of porous coating, with and without collar support, on early relative motion for a cementless hip prosthesis. J Biomechanics. 26(12). 1355-68

Kenedi R M, Gibson T and Daly C H (1965), Bio-engineering studies of the human skin II. In : Biomechanics and Related Bio-engineering Topics. Edited by Kenedi RM. Oxford, Pegamon, 147-158.

Keyak J. H. Fourkas M. G., Meagher J. M. and Skinner H. B. (1993) Validation of an automated method of three-dimensional finite element modelling of bone. J.Biomed.Eng. 15(6). 505-9.

Keyak JH, Meagher JM, Skinner HB, Mote CD Jr. (1990), Automated three-dimensional finite element modelling of bone : a new method. J Biomed. Eng., 1990, 12, 389-397.

Keyak J. H. and Skinner H. B. (1992) Three-dimensional finite element modelling of bone: effects of element size. J-Biomed-Eng. 14(6). 483-9.

King D and Steelquist J (1943), Transiliac amputation. J Bone Joint Surg., 25(A), 351-367.

Kistler Instrument (1975), Operating instructions (unpublished report), Kistler Instrument AG, CH-8408 Winterthur/Schweiz.

Klasson B (1985), Computer aided design, computer aided manufacture and other computer aids in prosthetics and orthotics. Prosthet. Orthot. Int., 9(1), 3-11.

Klein HM, Schneider W, Alzen G, Voy ED, Gunther RN (1992), Pediatric craniofacial surgery : Comparison of milling and stereolithography for 3D models manufacturing. Pediatric Radiology. 22(6), 458-460.

Koch J. C. (1917) The laws of bone architecture. Am. J. Anat. 21, 177-289

Kosiak M, Kubicek WG, Olson M, Danz JN, Kottke FJ (1958), Evaluation of pressure as a factor in the production of ischial ulcers. Arch. Phys. Med. Rehab., 623-629.

Kosiak M (1961), Etiology of decubitus ulcers. Arch. Phys. Med. Rehab., 42, 19-29.

Krebs DE and Tashman S (1985), Kinematic and kinetic comparison of the conventional and ISNY above-knee socket. Clin. Prosthet. Orthot. 9, 3, 28-36.

Krouskop TA, Muilenburg DL, Dougherty DR and Winningham DJ (1987), Computer-aided design of a prosthetic socket for above-knee amputee. J. Rehab. Res. Dev., 24(2), 31-38.

Krouskop TA, Malinauskas M, Williams J, Barry PD, Muilenburg DL and Winningham DJ (1989), A computer method for design of above-knee prosthetic sockets. J. Prosthet. Orthot. 1(3), April, 131-138.

Krouskop TA, Malinauskas M, Williams J (1989), A computerized method for design of above knee prosthetic sockets. J. Prosthet. Orthot., 1, 131-138.

Krouskop TA, Dougherty D, Yalcinkaya MI (1988), Measuring the shape and volume of an above-knee stump. Prosthet. Orthot. Int., 12, 136-142.

Lang Y (1988), The influence of limb alignment on the gait of above knee amputees. PhD thesis, University of Strathclyde, Glasgow, Scotland, UK.

Lauterbur PC (1973), Image formation by induced local interactions : Examples employing nuclear magnetic resonance. Nature. 242, 190-191.

Lavaste F, Skalli W, Robin S, Roy-Camille R and Mazel C (1992), Three-dimensional geometrical and mechanical modelling of the lumbar spine. J Biomech. 25(10). 1153-64.

Lawrence RB, Knox W, Mack A Crawford HV, Saunders C (1984), A computer controlled carving machine. In : University College London Bioengineering Centre report. Rochampton. University College London. 17-22.

Leavitt LA, Peterson CR, Canzoneri J, Paz R, Muilenburg AL, Rhyne VT (1970), Quantitative method to measure the relationship between prosthetic gait and the forces produced at the stump-socket interface. Am. J. Phys. Med., 49(3), 192-203.

Leavitt LA, Zuniga EN, Calvert JC, Canzoneri J, Peterson CR (1972), Gait analysis and tissue-socket interface pressure in above-knee amputees. Southern Med. J., 65(10), 1197-1207.

Lee EH, Goh JCH, Bose K (1992), Value of gait analysis in the assessment of surgery in cerebral palsy. Arch. Phys. Med. Rehab. 73, 2. 642-646.

Lee VSP, Solomonidis SE and Spence WD (1994), Biomechanical modelling of the interface between the residual limb and prosthesis for trans-femoral amputees using finite element analysis. Proc. 8th Int. Conf. on Biomed. Eng., Singapore, 333-335.

Lehneis HR (1985), Beyond the quadrilateral. Clin. Prosthet. Orthot., 9(4), 6-8.

Levenston ME, Beaupre GS, Schurman DJ and Carter DR (1993), Computer simulations of stress-related bone remodeling around noncemented acetabular components. J. Arthroplasty. 8(6). 595-605.

Lew WD and Lewis JL (1977), An anthropometric scaling method with application to the knee joint. J. Biomech., 10, 171-181.

Lew WD and Lewis JL (1980), A nonhomogeneous anthropometric scaling method based on finite element principles. J. Biomech., 13, 815-824.

Li QH (1993), Biomechanical analysis of aided gait in total hip replacement of total knee replacement patients. PhD thesis, University of Strathclyde, Glasgow, Scotland, UK.

Lilja M, Oberg T, Johansson T, Karsznia T (1992), Clinical evaluation of CAD/CAM made prosthetic sockets. Proceedings 7th World Congress of ISPO. June 28-July 3. Chicago, Illinois, USA. 16.

Lindan O (1961), Etiology of decubitus ulcers: An experimental study. Arch. Phys. Med. and Rehab., 42, 747-783

Lindholm LE (1974), An optoelectronic instrument for remote on line movement monitoring. In : Biomechanics IV. Ed. Nelson RC and Morehouse CA, University Park Press. Baltimore, 510-512.

Long IA (1985), Normal Shape-Normal Alignment (NSNA) above-knee prosthesis, Clin. Prosthet. Orthot., 9(4), 9-14.

Long IA (1975), Allowing normal adduction of femur in above-knee amputations, J. Orthot Prosthet., 8(1), 6-8.

Lyquist E (1970), The above knee prosthesis. In : Prosthetic and Orthotic Practice. Ed. Murdoch G., 199-211.

Maalej N, Zhu H, Webster J G, Tompkins W J, Wertsch J J and Bach-y-Rita P (1987), Pressure monitoring under insensate feet. In : Proc. Ann. Conf. IEEE Eng. Med. Biol. Soc., 1823-1824.

Mackay RS (1984), Medical images and displays (comparisons of nuclear magnetic resonance, ultrasound, x-rays and other modalities), John Wiley and Sons, New York.

Mak AFT, Liu GHW, Lee SY (1994), Biomechanical assessment of below knee residual limb tissue. J. Rehabil. Res. Dev., 31, 188-198

Mak AFT, Yu YM, Hong ML and Chan C (1992), Finite element models for analyses of stresses within above-knee stumps. Proceedings 7th World Congress of ISPO. June 28-July 3. Chicago, Illinois, USA. 147..

Malinauskas M, Krouskop TA, Barry PA (1989), Noninvasive measurement of the stiffness of tissue in the above-knee amputation limb. J. Rehabil. Res. Dev., 26(3), 45-52.

Malone JM, Leal JM, Moore WS, Henry RE, Daly MJ, Patton DD and Childers SJ (1981), The 'Gold Standard' for amputation level selection : Xenon - 133 clearance. J. Surg. Res., 30, 449-455.

Marey (1882), Analyse du mecanisme de la locomotion au moyen d' une serie d'images photographiques recueillies sur une meme plaque et representant les phases successives du mouvement. Comptes rendus 95, Naples, P14. (as quoted by Braune and Fischer 1895)

Marmar Z (1993), The effects of prosthetic alignment on the stability of the knee in above knee amputees. PhD thesis, University of Strathclyde, Glasgow, Scotland, UK.

Marsh JL, Vannier MW, Stevens WG (1985), Computerized imaging for soft tissue and osseous reconstruction in the head and neck. Plas. Surg. Clin. North Am., 12, 279-291.

McCollum PT, Spence VA and Walker WF (1984), Assessment of tissue viability in relation to the selection of amputation level. Prosthet. Orthot. Int., 8, 67-75.

McCollum PT, Spence VA and Walker WF (1988), Amputation for peripheral vascular disease : the case for level selection. Br. J. Surg., 75, 1193-1195.

McFarland DC and Lawrence PF (1982), Skin fluorescence, a method to predict amputation site healing. J. Surg. Res., 32, 410-415.

Mihalkow. M. Beaudoin A. J., Cardea J. A. and Krause W. R. (1992) Finite-element modelling of femoral shaft fracture fixation techniques post total hip arthroplasty. J Biomech. 25(5). 469-76

MIND (1994), Manufacturers catalogue. MIND Corporation. Seattle, USA

Mitchell CA, Versluis TL (1990), Management of an above-knee amputee with complex medical problems using the CAT-CAM prosthesis. Phys. Ther., 70, 389-393.

Mitchelson DL (1988), Automated three dimensional movement analysis using the CODA-3-system. Biomedizinische Technik, Band 33, Heft 7-8, 179-182.

Mizrahi J, Susak Z, Seliktar R Najenson T (1986), Alignment procedure for the optimal fitting of lower limb prostheses. J. Biomed. Eng., 8, 229-234.

Mizrahi J., Silva M. J. and Hayes W. C. (1992) Finite element stress analysis of simulated metastatic lesions in the lumbar vertebral body. J. Biomed. Eng. 14(6). 467-75.

Mizrahi J., Silva M. J., Keaveny T. M., Edwards W. T. and Hayes W. C. (1993) Finite-element stress analysis of the normal and osteoporotic lumbar vertebral body. Spine. 18(14). 2088-96.

Morris JRW (1991), An investigation of the sources and characteristics of noise in a video-based kinematic measurement system (unpublished report). Oxford Metrics Ltd. Unit 8, 7 West way, Botley, Oxford OX2 OJB, England, UK.

Morris PG (1986), Nuclear magnetic resonance imaging in medicine and biology, Oxford University Press, New York.

Motion Analysis System (1990), System Specifications, (unpublished report), Motion Analysis Corp. 3650 North Laughlin Road, Santa Rosa, CA 95403.

Murdoch G (1977), Amputation sugery in the lower extremity. Prosthet. Orthot. Int. 1, 72-83.

Murdoch G (1975), Below-knee amputation and its use in vascular disease and the elderly. Immediate prosthetic fitting and early walking. In Recent Advances in Orthopaedics, 21. Ed. B McKibbon. Edinburgh. Churchill. Livingston.

Murdoch G (1968), Myoplastic techniques. Bull. Prosthet Res., 10(9), 4-13.

Murdoch G, Condie DW, Gardiner D, Ramsay E, Smith A, Stewart CPU, Swanson AJG and Troup IM (1988), The Dundee experience. In Amputation Surgery and Lower Limb Prosthetics, Ed. G. Murdoch, Blackwell Scientific, Oxford, 450-457.

Murray MP, Sepic SB, Gardner GM and Mollinger LA (1980), Gait patterns of above-knee amputees using Constant-Friction knee components. Bull. Prosthet. Res., 10-34, 17, 2, 35-45.

Muybridge E (1887), Animal locomotion, an electro-photographic investigation of consecutive phases of animal movements (11 Vol.). Philadelphia, PA : J.B Lippincott. The human Figure in motion. New Edition 1955. Dover Publication, New York.

Naeff M and Van Pijkeren T (1980), Dynamic pressure measurements at the interface between residual limb and socket : The relationship between pressure distribution, comfort and brim shape, Bull. Prosthet. Res., 17(1), 35-50.

Narang IC and Jape VC (1982), Retrospective study of 14400 civilian disabled (new) treated over 25 years at an Artificial Limb centre. Prosthet. Orthot. Int., 6, 10-16

Natarajan-R. N., Ke J. H. and Andersson G. B. (1994) A model to study the disc degeneration process. Spine. 19(3). 259-65.

NCTEPO (1991), Above knee prosthetics. National Centre for Training and Education for Prosthetics and Orthotics. University of Strathclyde Glasgow. Scotland.

Neff G (1988), Surgery. In Amputation surgery and lower limb amputation. Ed. G Murdoch. Blackwell Scientific, Oxford, 117-129.

Nola GT, Vistnes LM (1980), Differential response of skin and muscle in the experimental production of pressure sores. Plast. Reconstr. Res., 10(33), 5-8.

Northern Digital Inc. (1983), Manufacturer of "WATSMART", 403 Albert Street, Waterloo, Canada, N2L 3V2.

Oberg K, Korman J, Karlsson A (1988), The CAPOD system, a Scandinavian CAD/CAM system for prosthetic sockets. J. Prosthet. Orthot., 1, 139-148.

Olofsson H. (1976) Three dimensional FEM calculation of elastic stress field in human femur. PhD Dissertation. Institute of Technology. University of Uppsala. Sweden.

Olson J (1991), Conventional pressure sensors. In : Prevention of Pressure Sores edited by Webster J G. IOP Publishing Ltd. Adam Hilger. Bristol, Philadelphia and New York.

Paul JP and Nicol AC (1981) , Usability of the SELSPOT system for biomechanical data acquisition. Report to the Scottish Home and Health Department (unpublished).

Pe H (1988), A 15 year survey of Burmese amputees. Prosthet. Orthot. Int., 2, 65-72.

Pearson J R, Holmgren G March L and Oberg K (1973), Pressure in critical regions of the below-knee patellar-tendon-bearing prosthesis. Bull. Prosthet. Res., 10(19), 52-76.

Perovitch M, Perl S, Wang H (1992), Current advances in magnetic resonance imaging (MRI) in spinal cord trauma : review article. Paraplegia, 30, 305-316.

Pollock SB and Ernst CB (1980), Use of Doppler pressure measurements in predicting success in amputation of the leg. Am. J. Surg., 139, 303-306.

Polson M, Barker A and Freeston I (1982), Stimulation of nerve trunks with time-varying magnetic fields. Med. Biol. Eng. Comput., 20, 243-244.

Porter D and Roberts VC (1989b), A review of gait assessment in the lower limb amputee. Part 1 : Kinetic and metabolic analysis. Clin. Rehab. 3, 157-168.

Porter D and Roberts VC (1989a), A review of gait assessment in the lower limb amputee. Part 1 : Temporal and kinematic analysis. Clin. Rehab. 3, 65-74.

Pritham CH (1988), The application of advanced technology to the production of positive models : A sceptics point of view. Report. ISPO workshop on CAD CAM in prosthetics and orthotics, USA, 8-12th June.

Pritham CH (1990), Biomechanics and shape of the above-knee socket considered in light of the ischial containment concept. Prosthet. Orthot. Int., 1990, 14, 9-21.

Purcell EM, Torrey HC and Pound RV (1946), Resonance absorption by nuclear magnetic moments in a solid. Physical Review. 69, 37-38.

Quesada P. and Skinner H. B. (1991) Analysis of a below-knee patellar-tendon bearing prosthesis : A finite element study. J. Rehab. Res. Dev. 28(3). 1-12.

Radcliffe CW (1977), The Knud Jansen Lecture : Above knee prosthetics. Prosthet. Orthot. Int., 1, 146-160.

Radcliffe CW (1955), Functional considerations in the fitting of above knee prostheses. Artificial limbs, 2(1), 35-60.

Radcliffe CW (1989), A short history of the quadrilateral above-knee socket. In Report of ISPO workshops. Ed. R Donovan, C Pritham and AB Wilson Jr. Copenhagen. ISPO, 4-12.

Rae J W and Cockrell J L (1971), Interface pressure and stress distribution in prosthetic fitting. Bull. Prosthet. Res., 10(16), 64-111.

Rakotomanana R. L., Leyvraz P. F., Curnier A., Heegaard J. H. and Rubin P. J. (1992) A finite element model for evaluation of tibial prosthesis-bone interface in total knee replacement. J Biomechanics. 25(12). 1413-24.

Rang M and Thomson GH (1981), History of amputation and prostheses, in Amputation Surgery and Rehabilitation - the Toronto Experience. Ed. JP Kostuik, Churchill Livingstone, New York, 1-12.

Rao SR, Clayton RM, Driessen KM, Torburn L, Winstein CJ and Perry J (1992), Vicon measurement error and reliability of joint kinematics in free and fast walking. Phys. Therapy. 72, 6 (Suppl)/June. S66.

Raschke SU and Saunders CG (1992), Custom design of spinal orthoses : The CANFIT-PLUS (tm) CAD/CAM software. Proceedings 7th world congress of ISPO. June 28-July 3. Chicago, Illinois, USA. 25.

Rassoulian SHR (1989), Design of a system for measurement of deformation due to shrinkage in themoplastic prosthetic sockets. MSc. thesis, University of Strathclyde, Glasgow, Scotland, UK.

Redhead RG (1979), Total surface bearing self suspending above knee sockets. Prosthet. Orthot. Int. 3, 126-136.

Rekow ED, Erdman AG, Riley DR, Klamecki B (1991), CAD/CAM for dental restorations - some of the curious challenges. IEEE Trans. Biomed. Eng., 38(4), 314-318.

Renstrom P (1981), A follow up study of 200 below knee amputees amputated between 1973-1977. In The below knee amputee, 7-25. MD Thesis. Gothenburg, Sweden.

Reswick JB, Lindan O, Lippay A (1964), A device to measure pressure distribution between the human body and various supporting surfaces. Report No. EDC 4-6407. Medical Engineering Group. Case Institute of Technology and Highland View Hospital. Cleveland. Ohio.

Reynolds DR (1988), Shape design and interface load analysis for below knee prosthetic sockets, PhD thesis, University of London, London, UK.

Rhodes ML, Kuo YM, Rothman SLG (1987), An applicaion of computer graphics and networks to anatomic model and prosthesis manufacturing. IEEE Computer Graphic and Applications., Feb. 12-24.

Ridge MD and Wright V (1966), Directional effects of skin. J. Invest. Derm., 46, 341-346.

Rogers WE, Crawford RH, Faulkner VF and Beaman JJ (1992), Fabrication of an integrated prosthetic socket using solid freeform fabrication. Proceedings 7th World Congress of ISPO. June 28-July 3. Chicago, Illinois, USA. 23.

Rohlman A., Bergmann G. and Koelbel R. (1982) The relevance of stress computation in the femur with and without endoprostheses in Finite Elements in Biomechanis. Edited by Gallagher R. H., Simon B. R., Johnson P. C. and Gross J. F. 361-377. John Wiley. New York.

Rovick JS (1992), An additive fabrication technique for computer aided manufacturing of sockets. Proceedings 7th World Congress of ISPO. June 28-July 3. Chicago, Illinois, USA. 24.

Rovick JS, Chan RB, Van Vorhis RL, Childress DS (1992), Computer aided manufacturing in prosthetics : various possibilities using industrial equipment. Proceedings 7th World Congress of ISPO. June 28-July 3. Chicago, Illinois, USA. 22.

Rubin P. J., Rakotomanana R. L., Leyvraz P. F., Zysset P. K., Curnier A. and Heegaard J. H. (1993) Frictional interface micromotions and anisotropic stress distribution in a femoral total hip component. J Biomecanics. 26(6). 725-39.

Rybicki E. F., Simonen F. A. and Weis E. B. (1972) On the mathematical analysis of stress in the human femur. J. Biomech. 5, 203-215

Rydell N (1966) Forces acting on the femoral head prosthesis. Acta. Orthop. Scand. Suppl. 88.

Sabolich J (1985), Contoured Adducted Trochanteric - Controlled Alignment Method (CAT-CAM) : Introduction and basic principles. Clin. Prosthet. Orthot., 9(4), 15-26.

25 Sanders J E, Daly C H and Burgess E M (1992), Interface shear stresses during ambulation with a below-knee prosthetic limb. J. Rehabil. Res. Dev., 29(4), 1-8.

Sanders J E, Daly C H and Burgess E M (1993), Clinical measurement of normal and shear stresses on a
26 trans-tibial stump: characteristics of wave-form shapes during walking. Prosthet. Orthot. Int., 17, 38-48.

Sanders JE and Daly CH (1993), Normal and shear stresses on a residual limb in a prosthetic socket during ambulation : Comparison of finite element results with experimental measurements. J. Rehab. Res. Dev., 30(2), 191-204.

Sanders GT (1986), Lower Limb Amputations: a guide to rehabilitation. FA Davis Co. Philadelphia.

Saunders CG and Vickers GW (1983), A generalized approach to the replication of cylindrical bodies with compound curvature. J. Mech. Transm-T ASME. 70-76.

Saunders CG, Bannon M, Sabiston RM, Panych L, Jenks SL, Wood IR, Raschke S (1989), The CANFIT system : Shape management technology for prosthetic and orthotic applications. J. Prosthet. Orthot., 1, 122-130.

Saunders CG (1983), Sculpting of 3-D free form objects using computer graphics techniques. A report. Medical Engineering Resource Unit. University of Bristish Columbia.

Saunders CG, Foort J, Bannon M (1985), Computer aided design of prosthetic sockets for below knee amputees. Prosthet. Orthot. Int., 9, 17-22.

Sawamura S (1988), A review and a modified surgical-prosthetic approach. In Amputation surgery and lower limb amputation. Ed. G Murdoch. Blackwell Scientific, Oxford, 81-86.

Schock RB (1981), A problem related to the biomechanics of pressure sores : Stress and strain analyses of soft tissue indentations. PhD thesis. Rensselaer Polytechnic Institute, USA.

Scholten R (1975), Ueber die Berechnung der mechanischen Beanspruchung in Knochenstrukturen mittels fuer den Flugzeugbau entwickelter Rechenverfahren. Med. Orthop. Technik 6, 130-138

Scholten PJM and Veldhuizen AG (1992), Computer aided spinal analysis. Proceedings 7th World Congress of ISPO. June 28-July 3. Chicago, Illinois, USA. 79.

Schuch CM (1988), Report from : International workshop on above-knee fitting and alignment techniques. Clin Prosthet. Orthot.,12(2), 81-98.

Seguchi Y, Tanaka M, Akazawa Y, Nakagawa A and Kitayama I (1988), Finite element analysis and load identification of above-knee prosthesis socket, at 4th Int. ANSYS Conf. Exhib., Proceedings, Abstract, Pittsburgh, USA, May,12.31 - 12.44.

Shirazi-Adl A. (1993) Finite-element simulation of changes in the fluid content of human lumbar discs. Mechanical and clinical implications. Spine. 17(2). 206-12.

Silver-Thorn MB and Childress DS (1992) Use of a generic, geometric finite element model of the below-knee residual limb and prostheic socket to predict interface pressures. Proceedings 7th World Congress of ISPO. June 28-July 3. Chicago, Illinois, USA. 272.

Skinner H. B., Cook S. D., Weinstein A. M. and Haddad R. J. (1982) Stress changes in bone secondary to the use of a canal plug with cemented hip replacement. Clin. Orthop. Rel. Res. 166, 277-283.

Skinner HB and Effeney DJ (1985), Gait analysis in amputees. Amer. J. Phys. Med. 64, 2 82-89.

Smith DM, Crew A, Hankin A (1986), Silhoutte shape sensor. In : University College London Bioengineering Centre report. Roehampton. University College London. 41-42.

Smolinski P. and Rubash H.E. (1992) Bone remodeling around total hip implants. Crit. Rev. Biomed. Eng. 20(5-6). 461-83

Soh AK, Soh CK and Law WS (1990), Method for the design and analysis of a non-linear anisotropic lower limb prosthetic socket. J. Biomed. Eng., 12(6), Nov., 470-476.

Sommer HJ, Miller NR, Pijanowski GJ (1982), Three-dimensional osteometric scaling and normative modelling of skeletal segments. J. Biomech., 15(3), 171-180.

Sonck W A, Cockrell J L, Koepke G H (1970), Effect of liner materials and interface pressure in
27 below-knee prostheses. Arch. Phys. Med. Rehab., 51, 666-669.

Spence VA, McCollum PT, Walker WF, Troup IM and Murdoch G (1981), Amputation of the ischaemic limb : selection of the optimum site by thermography. Angiology, 32, 155-169.

Spence WD (1992), Clinical and biomechanical evaluation of the ischial containment type socket for above-knee amputees- a pilot study. Proceedings of 7th World Congress of ISPO. June 29-July 3. Chicago Ilinois.

Spence WD (1994), Personal communication. University of Strathclyde. Bioengineering Unit. Glasgow. UK.

Spoor CW and Van Leeuwen JL (1992), Knee muscle moment arms from MRI and from tendon travel. J. Biomech., 25, 201-206.

Steege J W, Schnur D S and Childress D S (1987), Prediction of pressure at the below-knee socket interface by finite element analysis. ASME Symposium on the Biomechanics of Normal and Pathological gait, Boston, BED Vol. 4, DSC Vol. 6, 39-43.

Steege J. W. and Childress D. S. (1988) Finite element modelling of the below-knee socket and limb : Phase II, in Modelling and control, Issues in Biomechanical Systems. ASME, Chicago, 121-129

Steege J. W. Silver-Thorn M. B. and Childress D. S. (1992) Design of prosthetic sockets using finite element analysis. Proceedings 7th World Congress of ISPO. June 28-July 3. Chicago, Illinois, USA. 273.

Stokes VP, Andersson C and Forssberg H (1989), Rotational and translational movement features of the pelvis and thorax during adult human locomotion. J. Biomech. 22, 43-50.

Stokes VP (1984), A method for obtaining the 3-D kinematics of the pelvis and thorax during locomotion. Human Movement Sci. 3, 77-94.

Sugarbaker ED and Ackerman LV (1945), Disarticulation of the innominate bone for malignant tumors of the pelvic parietes and upper thigh. Surg. Gynecol. Obstet., 86, 36-52.

Suwito-W., Keller T. S., Basu P. K., Weisberger A. M., Strauss A. M. and Spengler D. M. (1992) Geometric and material property study of the human lumbar spine using the finite element method. J-Spinal-Disord. 5(1). 50-9.

Szulc JA (1983), development of the above knee telescopic limb prosthesis. PhD thesis, University of Strathclyde, Glasgow, Scotland, UK.

Taylor GW and Rodgers JR (1953), Hindquarter amputation: experience with eighteen cases. New. Engl. J. Med., 249, 963

Thomas SS, Sarwark JF, Porcelli R and Robinson C (1992) Preliminary report on the effect of gait analysis on the clinical decison making process for children with cerebral palsy. Orthop. Trans. 16.

Timoshenko S and Goodier JN (1970), Axially symmetrical stress distribution in a solid of revolution. In : Theory of Elasticity. Ed. S Timosheko and JN Goodier, McGraw-Hill, New-York, 3rd edition. 343-398.

Todd B. A. and Thacker J. G. (1994) Three dimensional computer model of the human buttocks, in vivo. J Rehab Res Dev. 31(2), 111-119.

Topper AK and Fernie GR (1990), An evaluation of computer aided design of below knee prosthetic sockets. Prosthet. Orthot. Int., 14, 136-142.

Torres-Moreno R, Morrison JB, Cooper D (1992), A computer aided socket design procedure for above knee prostheses. J. Rehabil. Res. Dev., 29(3), 33-44.

Torres-Moreno R (1991), Biomechanical analysis of the interaction between the above-knee residual limb and the prosthetic socket.PhD thesis, University of Strathclyde, Glasgow, Scotland, UK.

Torres-Moreno R, Foort J, Morrison JB (1989), A reference shape library for computer aided socket design in above-knee prostheses. Prosthet. Orthot. Int., 13, 130-139.

Tortora GJ (1989). Principles of human anatomy. Fifth Edition. Harper Collins Publishers. New York.

Totty WG, Vannier MW (1984). Analysis of complex musculoskeletal anatomy using three-dimensional surface reconstruction from CT scans. Electromedica, 53, 122-131.

Troung XT (1974), Viscoelastic wave propagation and rheologic properties of skeletal muscle. Am. J. Physiol., 226(2),256-264.

Troung XT, Jarrett SR, Nguyen MC (1978), A method for deriving viscoelatic modulus for skeletal muscle from transient pulse propagation. IEEE Trans. Biomed. Eng., 4, 382-384.

UCLA (1981), Prosthetic - orthotic education program : Total contact socket for the above knee amputation. 6th edition. Los Angeles. CA.

Houston VL, Manson CP, LaBlanc KP, Garbarini MA, Lorenze EJ (1992), Results of DVA RR&DS UCL-BC BK CASD/CAM system testing and evaluation program. Proceedings 7th World Congress of ISPO. June 28-July 3. Chicago, Illinois, USA. 15.

Valliappan S., Svensson N. L.and Wood R. D. (1977) Three dimensional stress analysis of the human femur. Comput. Biol. Med. 7, 253-264

Van Pijkeren T, Naeff M, Kwee H H (1980), A new method for the measurement of normal pressure
28 between amputation residual limb and socket. Bull. Prosthet. Res., 10(33), 31-34.

Van Rietbergen B., Weinans H., Huiskes R. and Odgaard A. (1993) Three dimensional analysis of a realistic trabecular bone structure, using large scale FE model. ASME/AIChE/ASCE Summer Bioengineering Conference, Breckenbridge. June 25-29, 24, 250-253.

Vannah WM and Childress DS (1993), Modelling the mechanics of narrowly contained soft tissues : The effects of specification of Poisson's ratio. J. Rehabil. Res. Dev., 30(2), 205-210.

Vannier MW, Totty WG, Stevens WG (1985), Musculoskeletal applications of three dimensional surface reconstructions. Orthop. Clin. North Am., 16, 537-549.

Veronda DR and Westmann RA (1970), Mechanical characterisation of skin finite deformations. J. Biomech., 3, 111-124.

Visser-Meily JMA, Cluitmans JJM, Deckers JHM and Ring S (1992), Experiences of above-knee amputees with an NML-Socket in comparison with a quadrilateral socket. J. Rehabil. Sci., 5(1), 22-25.

Vitali M (1987), Robinson KP, Andrews BG, Harris EE and Redhead RG (1986). A brief historical survey, in Amputations and Prostheses, Bailliere Tindall, London, 1-10.

Wall, M (1990), Stump descriptors. Report of ISPO Consensus Conference on amputation surgery, edited by G Murdoch, NA Jacobs, AB Wilson Jr, University of Strathclyde, Scotland, 1-5 October.

Walsh NE, Lancaster JL, Faulkner VW (1990), A computerized system to manufacture prostheses for amputees in developing countries. J. Prosthet. Orthot., 1, 165-181.

Weeks PM, Vannier MW, Stevens WG (1985), Three-dimensional imaging of the wrist. J. Hand Surg., 10A, 32-39.

Weinans H., Huiskes R. and Grootenboer H.J. (1992) Effects of material properties of femoral hip components on bone remodeling. J. Orthop. Res. 10(6). 845-53

Weinans H., Huiskes R., van Rietbergen B., Sumner D. R., Turner T. M. and Galante J. O. (1993a) Adaptive bone remodeling around bonded noncemented total hip arthroplasty: a comparison between animal experiments and computer simulation. J. Orthop. Res. 11(4). 500-13.

Weinans H., Huiskes R. and Grootenboer H. J. (1993b) Quantitative analysis of bone reactions to relative motions at implant-bone interfaces. J. Biomech. 26(11). 1271-81.

Weiss M (1966), The prosthesis on the operating table from the nerophysiological point of view. report of the Workshop Panel in Lower Extremity Prosthetics Fitting. Committee on Prosthetic Research and Development, National Academy of Science meeting, USA, 6-9 February 1966.

Weissman JD (1987), State of the art magnetic resonance imaging. In : Physics and Engineering of Medical Imaging. Edited by R. Guzzardi. NATO ASI Series. Martinus Nijhoff Publishers. Italy. 551-560.

Wells C (1964), Bones, Bodies and Disease, In Ancient peoples and places. Frederic Praeger.

Westbery G (1967), Hindquarter and Hip Amputation. Ann. R. Coll. Surg. Eng., 40, 226.

Whittle MW (1982), Calibration and performance of a 3-Dimensional televison system for kinematic analysis. J Biomech. 15, 3, 185-196.

Wilkinson J and Crawford H (1986), Ripple liners. In : University College London Bioengineering Centre report. Roehampton. University College London. 27-29.

Williams R B, Porter D and Roberts V C (1992), Triaxial force transducer for investigating stresses at the stump/socket interface. Med. Biol. Eng. Comput., 30, 89-96.

Wilson AB (1970), Limb prosthetics - 1970. Artificial limbs, 14(1), 1-52.

Wolff J. (1870) Ueber die innere Architekteur der Knochen und ihre Bedeutung fuer die Frage vom Knochenwachstum. Virchows Arch. Path. Anat. Physiol. 50, 389

Wood IR, Morrison JB, Saunders CG (1992), Computer aided design and alignment of limb shapes for below knee prostheses. Proceedings 7th world congress of ISPO. June 28-July 3. Chicago, Illinois, USA. 156.

Wood R. D., Valliappan S. and Svensson N. L. (1973) Stress analysis of the human femur in Theory and Practice in FEM Structural Analysis, Tokyo Seminar edited by Yamada Y. and Gallagher R. H. 461-478. University of Tokyo Press, Tokyo.

Yang L (1988), The influence of limb alignment on the gait of above-knee amputee. PhD thesis, University of Strathclyde, Glasgow, Scotland, UK.

Zahedi MS, Spence WD, Solomonidis SE and Paul JP (1988), The influence of alignment on prosthetic gait. In : Amputation sugery and lower limb prosthetics, Ed Murdoch G and Donovan RG, Blackwall Scientific Publications, Oxford, London, Edinburgh.

Zhang M. and Roberts C. (1993) Development of a nonlinear finite element model for analysis of stress distribution at stump/socket interface. in Computation Biomechanics, edited by Held K. D., Brebbia C. A., Ciskowski R. D. and Power H. Southamton. Computational Mechanics Publications. 209-214.

Zhang M, Lord M, Turner-Smith AR, Roberts VC (1995), Development of a non-linear finite element modelling of the below-knee prosthetic socket interface. Med. Eng. Phys. 17(8), 559-556.

Zhu H, Maalej N, Webster JG, Tompkins WJ, Bach-y-Rita P and Wertsch JJ (1990) An umbilical data-acquisition system for measuring pressure between the foot and shoe. IEEE Trans. Biomed. Eng., 37, 908-911.

Zuniga EN, Leavitt LA, Calvert JC, Canzorneri J and Peterson CR (1972), Gait patterns in above-knee amputees. Arch, Phys. Med. Rehab. 53, 373-382.